Sukumar Mishra
Yog Raj Sood
Anuradha Tomar   *Editors*

Applications of Computing, Automation and Wireless Systems in Electrical Engineering

Proceedings of MARC 2018

Volume 2

Springer

Lecture Notes in Electrical Engineering

Volume 553

The book series *Lecture Notes in Electrical Engineering* (LNEE) publishes the latest developments in Electrical Engineering - quickly, informally and in high quality. While original research reported in proceedings and monographs has traditionally formed the core of LNEE, we also encourage authors to submit books devoted to supporting student education and professional training in the various fields and applications areas of electrical engineering. The series cover classical and emerging topics concerning:

- Communication Engineering, Information Theory and Networks
- Electronics Engineering and Microelectronics
- Signal, Image and Speech Processing
- Wireless and Mobile Communication
- Circuits and Systems
- Energy Systems, Power Electronics and Electrical Machines
- Electro-optical Engineering
- Instrumentation Engineering
- Avionics Engineering
- Control Systems
- Internet-of-Things and Cybersecurity
- Biomedical Devices, MEMS and NEMS

For general information about this book series, comments or suggestions, please contact leontina.dicecco@springer.com.

To submit a proposal or request further information, please contact the Publishing Editor in your country:

China

Jasmine Dou, Associate Editor (jasmine.dou@springer.com)

India

Swati Meherishi, Executive Editor (swati.meherishi@springer.com)
Aninda Bose, Senior Editor (aninda.bose@springer.com)

Japan

Takeyuki Yonezawa, Editorial Director (takeyuki.yonezawa@springer.com)

South Korea

Smith (Ahram) Chae, Editor (smith.chae@springer.com)

Southeast Asia

Ramesh Nath Premnath, Editor (ramesh.premnath@springer.com)

USA, Canada:

Michael Luby, Senior Editor (michael.luby@springer.com)

All other Countries:

Leontina Di Cecco, Senior Editor (leontina.dicecco@springer.com)
Christoph Baumann, Executive Editor (christoph.baumann@springer.com)

** Indexing: The books of this series are submitted to ISI Proceedings, EI-Compendex, SCOPUS, MetaPress, Web of Science and Springerlink **

More information about this series at http://www.springer.com/series/7818

Sukumar Mishra · Yog Raj Sood ·
Anuradha Tomar
Editors

Applications of Computing, Automation and Wireless Systems in Electrical Engineering

Proceedings of MARC 2018

∞ Springer

Editors
Sukumar Mishra
Department of Electrical Engineering
Indian Institute of Technology Delhi
New Delhi, Delhi, India

Yog Raj Sood
Department of Electrical Engineering
National Institute of Technology
Hamirpur, Himachal Pradesh, India

Anuradha Tomar
JSS Academy of Technical Education
Noida, Uttar Pradesh, India

Preface

The papers presented at the International Conference on Manufacturing, Advanced Computing, Renewable Energy and Communication (MARC 2018) held at HMR Institute of Technology and Management in New Delhi, India, on July 19 and 20, 2018, are compiled in this volume. The International Conference on Manufacturing, Advance Computing, Renewable Energy and Communication focuses on advanced research in the area of electrical engineering and will provide a forum for sharing insights, experiences and interaction on various facts of evolving technologies and patterns related to these areas. The objective of MARC 2018 is to provide a platform for leading academic scientists, researchers, scholars and students to get together to share their results and compare notes on their research discovery in the development of electrical engineering and automation.

Numerous participants attended the conference, made technical presentations and indulged in various technical discussions. The number of paper published in this volume and the number of unpublished presentations at the conference indicate the evidence of growing interest among students, researchers and teachers in manufacturing and advanced computing. More than 500 research papers were submitted, out of which 113 were accepted and presented.

I would like to extend my sincere gratitude to Springer Nature for giving HMR Institute of Technology and Management the opportunity and the platform to organize this conference which helped in reaching out to the eminent scholars and the fellow researchers in the field of electrical engineering and helping them in widening the areas of the subject.

I express my sincere gratitude to our Program Chair Dr. Yog Raj Sood, NIT Hamirpur, for his motivation and support in hosting MARC 2018. I express my sincere gratitude to the management of HMR Institute of Technology and Management for their kind support and motivation.

New Delhi, India

Prof. (Dr). Sukumar Mishra
sukumar@ee.iitd.ac.in

Contents

Contents ix

About the Editors

Sukumar Mishra is a Professor at the Department of Electrical Engineering, Indian Institute of Technology, Delhi. He is a recipient of the INSA medal for young scientists, the INAE Young Engineer Award, and the INAE Silver Jubilee Young Engineer Award. In 2009, at the age of 38 he became the youngest fellow in the Electrical Engineering section of the INAE. He is also a fellow of the IET UK, IETE India and IE India. He is currently the NTPC Chair Professor as well as the Vice Chair of the Intelligent System Subcommittee of the IEEE Power and Energy Society. He is actively involved in academic and industrial research and development collaborations, and has been involved in numerous research projects and industrial consultancies. He has 25 years' professional experience and is currently serving as an Editor for the IEEE Transactions on Smart Grid and an Associate Editor for the journal IET Generation, Transmission & Distribution.

Yog Raj Sood is affiliated with the Department of Electrical Engineering, National Institute of Technology, Hamirpur, where he is currently working as a Professor. He has authored or co-authored several national and international publications and also acted as a reviewer for respected professional journals. He is actively associated with various societies and academies around the world, and has received several awards for his contributions to the scientific community. His major research interests are in the deregulated power sector and congestion management.

Anuradha Tomar is an Associate Professor at the Electrical Engineering Department, JSS Academy of Technical Education, Noida, India. She has authored or co-authored 68 research/review papers in various conference proceedings, national and international journals. Her research interests include photovoltaic systems, microgrids, energy conservation, and automation. In addition to having filed seven Indian patents, she is a member of the ISTE, IETE, IEI and IAENG.

Fault Detection in AC Transmission System Using Multiple Signal Classification Technique

Isarar Ahamad, Mohammed Asim, Archana Verma
and Mohammed Huzaifa

Abstract This paper presents the classification between permanent fault and transient fault by using multiple signal classification (MUSIC) technique for AC transmission systems. The time–frequency domain has often been exploited to analyze the signals with fast-changing spectral contents in MUSIC technique. By this, we classify the number of peaks from the spectral. If number of peak is one in the detection range, then this is the case of permanent fault and if more than one, then this is the case of transient fault. One of the most important methods that guarantee the safety and stability of power system is auto-reclosure. The signal which we mainly use is music signal. MATLAB/SIMULINK platform is used to calculate the power spectrums.

Keywords MUSIC technique · Concept of auto-reclosure · Spectral lines

1 Introduction

For the generation of goods and services, a large amount of energy is needed for the creation of modern ideal society and for providing services to ordinary man. All industrial plants need sufficient energy to fulfill the basic necessities of the society. The main motto of power system is to provide secure and reliable economic facilities to human being. Electrical energy is generated, transmitted and distributed by the various equipment of power system.

I. Ahamad · M. Asim (✉) · A. Verma · M. Huzaifa
Department of Electrical Engineering, Integral University, Lucknow, India
e-mail: asimamu@gmail.com

I. Ahamad
e-mail: isarar.iul@gmail.com

A. Verma
e-mail: vermaarchana201@gmail.com

M. Huzaifa
e-mail: huzaifa9807@gmail.com

Electric power system is a system which is very large and complex, and a large amount of investment is used for equipments and various facilities of power system. In the power system, various fault and failure take place. If the faults which occur in system are not promptly corrected, then this fault turns into a threat in the operation of system. An auxiliary system is needed for the corrective action when fault takes place in the system [1]. This type of auxiliary system is known as protection system. This protection system is the set of equipments and various types of policies which are used for the fault detection in the power system. They disconnect the faulty part of the system and continue the service. There are different types of operating state in which power system works, so the system provides different protective schemes for different types of operating states.

1.1 Protective Relay

Nowadays protection system has become very vast and complex system. Various types of changes take place in power system. Though it is a complex system, the relay provides protection to the power system from beginning of the electric industry. Earlier relays were made using solenoids and electromagnetic actuators. Those relays were very heavy and needed a lot of space to be mounted. Now electromechanical relay has become a standard device in power system protection. Modern relay is also working on the principle of electromagnetic relays, now solid-state relay uses electronic element in place of electromechanical actuators [2, 3]. Solid-state relay were proved very reliable for the power system and won the confidence of protection engineers due to their cost-effective operations, they also had various advantages over others.

The technology has changed tremendously in the recent past; we are using microprocessor in construction of relays. These types of relay are called digital relay and numerical relay. These are the multipurpose relays and also have the facility to record the fault and monitor them. For processing digital signal, numerical relay employs microprocessor which makes this very fast and powerful.

1.2 Numerical Relay

A numerical relay has following subsystem:

- Power supply
- Microprocessor
- Analog input system
- Digital output system
- Power supply

In numerical relay, some digital computations are performed. It works on the sampling of the signals. In sampling process, analog signal converts into digital signal, such as voltage and current. In electromechanical and static relay, these analog input signals are directly fed into electromagnetic winding or electronic circuit. For the protection of relay from large transient of input signal, we use surge filter. For the reconstruction of input signals that come from A/D sample/Hold section, an antialiasing filter is used to avoid errors. Harmonic components of order $N \pm 1, 2N \pm 1,\ldots, xN \pm 1$ (where N is no. of sample per cycle) in any signal can exhibit aliasing. Ideally, an antialiasing filter cut off all signal component above the Nyquist rate of $N/2$, but practically this is not possible with this filter. This filter cannot cut off all band frequencies because of this cut off frequency of antialiasing filter is set of $N/3$.

The sample value that represents the analog input signals gets converted into digital input signals by A/D. Since the conversion is not instantaneous, hence A/D system includes a sample and hold circuit. This sample and hold circuit confer ideal sampling holds the sample values for quantization by A/D converter [4, 5].

The relay algorithm stored in a microprocessor acts as the controller of the numerical relay. The microprocessor provides all control, computation, self-test and communication functions as a digital filter, the algorithm functions to extract the fundamental component of the input signal which is based on carrying of relay operation. The relay operation is based on the comparison of the signal of digital filter with pre-set threshold in the digital output system.

2 Permanent and Transient Fault

The fault in which insulation is damaged permanently is known as transient fault. The circuit regains its healthy state after a very short interval of time. Typical transient faults are insulation flashover on striking of lighting. These faults generally occur where the main insulating medium is air. Hence, they generally harm outdoor equipment.

On the other hand, permanent fault as the name suggests permanently damages the insulator. The equipment has to be repaired in case of permanent faults.

3 Adaptive Protection Scheme

The operating time of time delay over current relay is adapted to fault current magnitude. The direction relay set them to the direction of fault current. The harmonic restraint relay adapted to the difference between fault within a transformer and energizing a transformer [6, 7]. The scheme is part of the original system design. Adaptive technique is a protective scheme which seeks adjustment to different protective functions, in order to make them attained to different power system

conditions. This scheme protects buses, transformers, transmission line, etc. It also control and monitor substation [8, 9]. This paper discusses both the protection and control method of this adaptive protective scheme.

4 Methodology Used

We have studied about various signals processing techniques use in protection of power system. We will use the music technique for understanding about fault types and the nature of fault.

4.1 Multiple Signal Classification Technique

This method which is called the music method estimated the frequencies and the power of the harmonic signal employing a harmonic model. Basically, this method is a noise subspace-based method. When a data sequence has length $(L = M + N - 1)$, then its autocorrelation matrix R_v has size $M \times M$ (where M is the dimension of space spanned by $V(n)$ and K is the dimension of signal subspace $M > K$) and it can be estimated by $R_v = \frac{1}{N} V^H \cdot V$

where the size of V is $N \times M$ and is given by

$$V = \begin{bmatrix} V^T(0) \\ V^T(1) \\ \vdots \\ V^T(N-1) \end{bmatrix}^T = \begin{bmatrix} v(0) & v(1) & \cdots & v(M-1) \\ v(1) & v(2) & \cdots & v(M) \\ \vdots & \vdots & \ddots & \vdots \\ v(N-1) & v(N) & \cdots & v(N+M-2) \end{bmatrix}$$

where M = time window length of data vector and superscript $(\cdot)^H$ is the Hermitian operator.

$$\hat{R}_v = R_S + R_W = EPE^H + \sigma_W^2 I$$

where the matrix E and P are defined as:

$$E = \begin{bmatrix} e_1 & e_2 & \cdots & e_K \end{bmatrix}$$

$$P = \text{diag}\left\{ |\underline{A}1|^2 \quad |\underline{A}2|^2 \quad \cdots \quad |\underline{A}k|^2 \right\}$$

$$e^l = \begin{bmatrix} 1 & e^{jwl} & e^{j2wl} & \cdots & e^{j(M-1)wl} \end{bmatrix}^T \quad l = 1, 2, \ldots, K$$

are the eigenvectors of R_s.

4.2 Signal and Noise Subspace

Eigenvalue of R_v are arranged in decreasing order where rank of R_v is M (ie., $\lambda_1 > \lambda_2 > \cdots \lambda_m$) and the corresponding eigenvector is S_1, S_2, …, S_m, and it follows that:

$$\hat{R}_v S_i = \lambda_i S_i \quad \text{where } i = 1, 2, \ldots, M$$

K eigenvector which corresponds to the K largest eigenvalues belongs to the signal subspace and MK Eigen vector belongs to the noise subspace, are the two groups of eigenvectors. For estimating unknown harmonic frequencies, ω_k noise subspace is used in this music method.

Firstly we computed pseudo spectrum, $P_{\text{music}}(e^{j\omega}) = \frac{1}{\sum_{i=K+1}^{M} |e^H S_i|^2}$

Here, S_i ($i = K + 1$,…, M) is the eigenvector associated with the noise subspace which are orthogonal to the signal eigenvector $e = \begin{bmatrix} 1 & e^{j\omega} & e^{j2\omega} & \cdots & e^{j(M-1)\omega} \end{bmatrix}^T$, and e^H represents the complex conjugate transpose. The frequency related to the signal eigenvector has zero value at the denominator. The only objective of this pseudo spectrum is to generate the peaks frequencies corresponding to those of the dominant frequency component where the value of P_{music} component does not relate to any real power spectrum.

4.3 Case Studies

In this we, will study the response of the various faults on AC power system and H.V.D.C. power system with the help of music signal.

4.3.1 AC Power System

The simulation system as shown in Fig. 1 consists of 500 kV, 3000 MVA, EHV power transmission system, whose transmission line is 600 km in length (Table 1).

4.3.2 Analysis on Simulation Results

In order to observe the difference of power spectrum of different fault phase voltage, we take the fault occurring, both sides of the bus, away from the bus B_1, near the bus B_1 of line as example. When transient fault or permanent fault occurs, after the breakers tripping off, the wave of incoming voltage and its spectrum are shown in the figure below. When permanent fault occurs, there is one spectral line in the detection range.
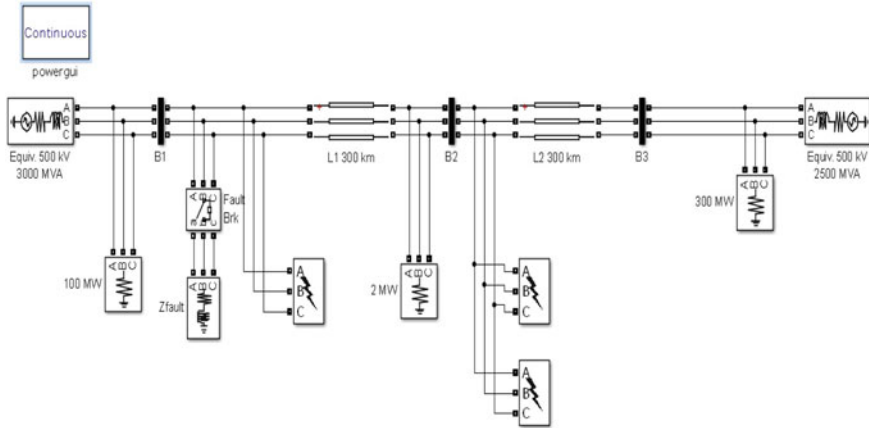
Fig. 1 Three-phase AC transmission system

Table 1 Three-phase source in series with RL branch

Phase-to-phase rms voltage	500 e^3 × 1.078 V
Phase angle	0°
Frequency	60 Hz
3-phase short-circuits level at base voltage	3000 MVA
3-phase circuit breaker transition time(s)	[0.2 0.4]

(1) When transient fault occurs, there are more than one spectral lines in the detection range.

Case 1 Three Phase-to-Ground Fault

(a) Fault occur on both sides of the buses

It is clearly visible from Figs. 2 and 3 of fault phase voltage and fault phase current that whenever any sort of fault occurs in the system, the system voltage may decay or rise for a moment and after the fault is cleared, it again regains new stable voltage level. Similarly for a current during fault, it may increase or decrease but when fault is cleared, it comes back to a new stable current level.

Also the different power spectrums as shown in Fig. 4 depict that when transient fault occurs, there are more than one spectral lines in the detection range: one reflects the frequency of free content, the other reflects power frequency. When permanent fault occurs, there is only one spectral line which reflects power frequency in the detection range, and the grounding resistance has no effect to it. As a
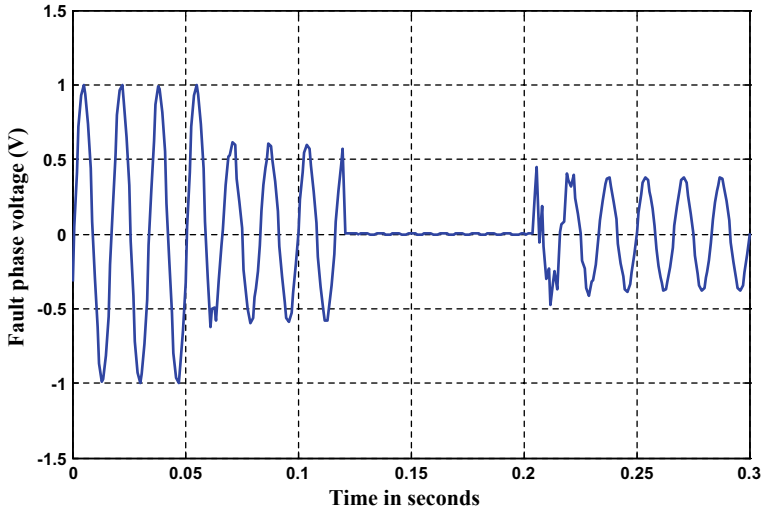
Fig. 2 Fault phase voltage
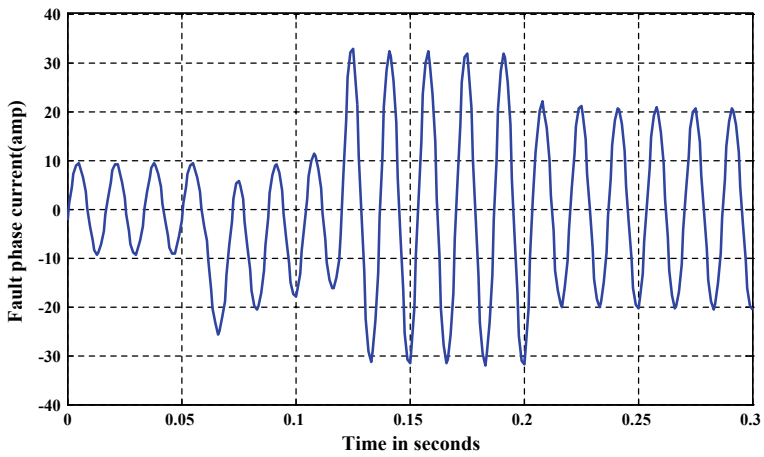
Fig. 3 Fault phase current

result, the fault type is easy to judge by the number of spectral lines. To validate the validity of criterion, we have done simulations of the system above in different operation modes and different compensation degrees (Table 2).
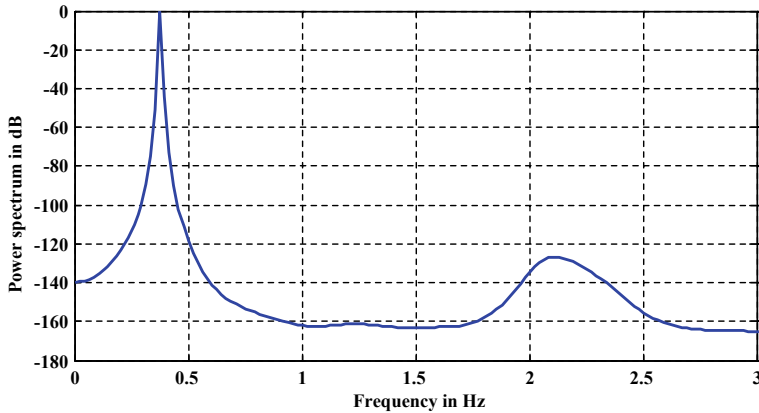
Fig. 4 Power spectrum

Table 2 Testing result

S. No.	Types of fault	No. of peaks	Music power (W)
1	*Three phase-to-ground fault*		
	(1) When fault occur both sides of the buses	2	2.2081×10^4
	(2) When fault occur away from the bus B_1	3	2.4963×10^4
	(3) When fault occur near the bus B_1	1	2.4887×10^4
2	*Single phase-to-ground fault*		
	(1) When fault occur both sides of the buses	1	2.2808×10^4
	(2) When fault occur away from the bus B_1	2	3.1373×10^4
	(3) When fault occur near the bus B_1	1	3.2263×10^4

5   Conclusions

This paper presents various simulation results in different fault conditions, by using the music signal in auto-reclosure method. By using this method, the nature of fault that is permanent or transient can be easily classified. When permanent fault occurs, there is one spectral line in the detection range. When transient fault occurs, there is more than one spectral line in the detection range.

References

1. Jongepier AG, Vander Sluis L (1994) Adaptive distance protection of a double-circuit line. IEEE Trans Power Deliv 9:1289–1297
2. Chen W, Malik OP, Yin X, Chen D, Zhang Z (2003) Study wavelet-based ultra high speed directional transmission line protection. IEEE Trans Power Deliv 18(4):1134–1139

3. Pathirana V, McLaren PG (2005) A hybrid algorithm for high speed transmission line protection. IEEE Trans Power Deliv 20(4):2422–2428
4. Darwish HA, Taalab AMI, Ahmed ES (2005) Investigation of power differential concept for line protection. IEEE Trans Power Deliv 20(2):617–624
5. Yusuff AA, Fei C, Jimo AA, Munda JL (2011) Fault location in a series compensated transmission line based on wavelet packet decomposition and support vector regression. Elsevier J Power Syst Res 81:1258–1265
6. Asim M, Tariq M, Mallick MA, Ashraf I (2016) An improved constant voltage based MPPT technique for PMDC motor. Int J Power Electron Drive Syst 7(4)
7. Hu Y, Novosel D, Saha MM, Leitloff V (2002) An adaptive scheme for parallel-line distance protection. IEEE Trans Power Deliv 17(1):105–110
8. Ahamad I, Asim M, Sarkar PR, Khan FA (2016) Comparison of conventional PFC boost converter and bridgeless PFC boost converter. Int J Innovative Res Electr Electron Instrum Control Engineering 4(5)
9. Conde A, Vazquez E (2010) Application of a proposed over current relay in radial distribution networks. Elsevier J Power Syst Res 81:570–579

Steady-State Performance of DFIG with Stability Assessment in Wind System

Sandeep Gupta and Indubhushan Kumar

Abstract In past few years, it has been realized that the wind power, as a source of renewable energy, has proved to be one of the most reliable and developing energy sources. The share of wind energy has been a significant contribution in the total installed power capacity worldwide. In the present study, the system under consideration is a variable speed wind generation system, which is a doubly fed induction generator (DFIG). Therefore, in this paper, steady-state performance and stability assessment of DFIG is analyzed with 4 bus system. On applying the converged power flow solution, the steady-state performance has been also calculated using *PQ* Bus Model-based method. The method presented in this paper does not deploy the use of d–q reference frame. Here, steady-state performance of the DFIG is analyzed under different leading and lagging conditions with the help of MATLAB programming. In this paper, stability assessment results of the test system are also included with the different loading condition.

Keywords *PQ* bus model · DFIG · Wind power ·
Stability and steady-state analysis

1 Introduction

The energy crisis as well as the associated environmental problems is the major cause of concern throughout the world nowadays. However, due to limitations of conventional resources in terms of their availability and sustainable utilization, attention and interest is being paid for the efficient and sustainable exploitation of renewable energy sources such as wind, fuel cell and photovoltaic, hydro, biomass,

S. Gupta (✉)
JECRC University, Jaipur 303905, Rajasthan, India
e-mail: jecsandeep@gmail.com

I. Kumar
JECRC University, Jaipur, Rajasthan, India
e-mail: indubhushan.kumar@gmail.com

etc. [1]. Out of all the renewable energy sources present condition, the share of wind power in the total installed power capacity is very vast area in the worldwide.

In early nineteenth century, largest share of wind installation was concentrated in European and American country. But after 2010, capacity addition of wind power was much more prominent due to advancement in technologies in rest of the world. In the global scenario, it is observed that there is 43.44% increment in installed capacity between years 2009 and 2012. China is giant contributor in the world with 26.75% along with India 6.52%, ranking 5th in world in total installed capacity [2].

Torkaman et al. [3] discussed reactive power loading ability of DFIG under steady-state condition. They concluded that magnetic flux saturation, converter voltage and output current, nonlinear relation between junction temperature, and rotor current restricted the loading capability of reactive power for a given active power. Banakar et al. [4] have revealed the fact that DFIG operating under decoupled control of P–Q has an extensive stable operating region. Vargas et al. [5] have simulated and verify the behaviors of DFIG wind turbine system during grid disturbances. This analysis also measures impacts on power quality by the DFIG integration. Developed model [6] is based on the vectorized dynamic approach and can be usable to every kind. El Moursi et al. [7] have investigated reactive power management and secondary voltage control scheme to analyze stability of DFIG. It has concluded that communication delays efficiently worsen the performance of system during transient conditions. Babypriya et al. [8] have presented system performance by taking d–q reference frame for voltage orientation using MATLAB. It has concluded that under a subsynchronous condition generator will behave as capacitive and otherwise inductive.

With growing penetration of wind power in interconnected power systems, it is necessary to find generator which has variable speed constant frequency features. DFIG is the most favorable choice under such condition. Therefore, steady-state analysis of DFIG is explained with problem formulation in Sect. 2. PQ bus model-based methodology is also discussed in this section. The analysis is carried out on a 4-bus system with simulation software in Sect. 3. Outcomes of the test system with different cases (such as lagging or leading power factors) are shown in this section. Stability assessment results are also shown in this section. Finally, Sect. 4 concludes this paper.

2   Steady-State Analysis of DFIG

Analysis of steady-state simulation is essential to recognize the behavior of DFIG such that it can operate a maximum power producing point for a given wind speed and for good dynamic modeling of these machines. Performance evolution and conversion efficiency of generator is largely depends on steady state.

2.1 Problem Formulation

The objective of the steady-state simulation is to find steady-state operating point under various conditions. These variables can be obtained after joint solution of nonlinear differential equation describing the stator and rotor dynamics.

From equivalent circuit shown in Fig. 1, we have following equations:

$$V_s \angle \varphi_s = -(R_s + j(X_s + X_m))I_s \angle \varnothing_s + jX_m I_r \angle \varnothing_r \tag{1}$$

$$V_r \angle \varphi_r = (R_r + js(X_r + X_m))I_r \angle \varnothing_r - jsX_m I_s \angle \varnothing_s \tag{2}$$

Separating real and imaginary parts of Eqs. (1) and (2).

$$f_1 = V_s \cos \varphi_s + R_s I_s \cos \varnothing_s - (X_s + X_m)I_s \sin \varnothing_s + X_m I_r \sin \varnothing_r \tag{3}$$

$$f_2 = V_s \sin \varphi_s + R_s I_s \sin \varnothing_s - (X_s + X_m)I_s \sin \varnothing_s - X_m I_r \cos \varnothing_r \tag{4}$$

$$f_3 = V_r \cos \varphi_r - R_r I_r \cos \varnothing_s + s(X_s + X_m)I_r \sin \varnothing_r - sX_m I_s \sin \varnothing_s \tag{5}$$

$$f_4 = V_r \sin \varphi_r - R_r I_r \sin \varnothing_r - s(X_r + X_m)I_r \sin \varnothing_r + sX_m I_s \cos \varnothing_s \tag{6}$$

$$f_5 = P - V_s I_s \cos(\varphi_s - \varnothing_s) + V_r I_r \cos(\varphi_r - \varnothing_r) \tag{7}$$

$$f_6 = Q - V_s I_s \sin(\varphi_s - \varnothing_s) \tag{8}$$

$$f_7 = P - k_o * (1 - s)^3 + I_s^2 R_s + I_r^2 R_r \tag{9}$$

Thus, a set of seven nonlinear equations has seven possible unidentified values, depending on the method used for simulating the bus, and has explored for to find steady-state parameter. In NR method, increments can calculate as follows:

$$X^{n+1} = X^n - J^{-1}\Delta f \tag{10}$$

$$\Delta x = X^{n+1} - X^n = -J^{-1}\Delta f \tag{11}$$
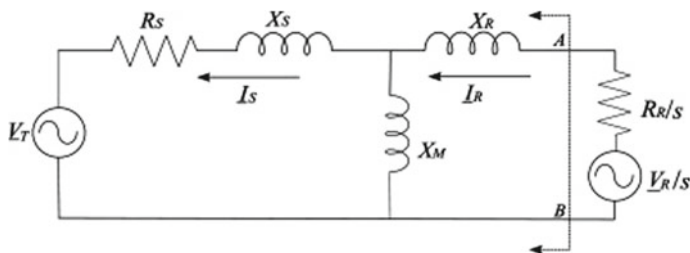
Fig. 1 Equivalent circuit of doubly fed induction generator [9, 10]

where variable

$$\Delta f = (f_1, f_2, f_3, f_4, f_5, f_6, f_7)^{\mathrm{T}} \tag{12}$$

$$\text{Jacobian matrix, } J = \begin{pmatrix} \dfrac{\partial f_1}{\partial V_r} & \dfrac{\partial f_1}{\partial_r} & \dfrac{\partial f_1}{\partial I_r} & \dfrac{\partial f_1}{\partial \theta_r} & \dfrac{\partial f_1}{\partial I_s} & \dfrac{\partial f_1}{\partial \theta_s} & \dfrac{\partial f_1}{\partial S} \\[2mm] \dfrac{\partial f_2}{\partial V_r} & \dfrac{\partial f_2}{\partial_r} & \dfrac{\partial f_2}{\partial I_r} & \dfrac{\partial f_2}{\partial \theta_r} & \dfrac{\partial f_2}{\partial I_s} & \dfrac{\partial f_2}{\partial \theta_s} & \dfrac{\partial f_2}{\partial S} \\[2mm] \dfrac{\partial f_3}{\partial V_r} & \dfrac{\partial f_3}{\partial_r} & \dfrac{\partial f_3}{\partial I_r} & \dfrac{\partial f_3}{\partial \theta_r} & \dfrac{\partial f_3}{\partial I_s} & \dfrac{\partial f_3}{\partial \theta_s} & \dfrac{\partial f_3}{\partial S} \\[2mm] \dfrac{\partial f_4}{\partial V_r} & \dfrac{\partial f_4}{\partial_r} & \dfrac{\partial f_4}{\partial I_r} & \dfrac{\partial f_4}{\partial \theta_r} & \dfrac{\partial f_4}{\partial I_s} & \dfrac{\partial f_4}{\partial \theta_s} & \dfrac{\partial f_4}{\partial S} \\[2mm] \dfrac{\partial f_5}{\partial V_r} & \dfrac{\partial f_5}{\partial_r} & \dfrac{\partial f_5}{\partial I_r} & \dfrac{\partial f_5}{\partial \theta_r} & \dfrac{\partial f_5}{\partial I_s} & \dfrac{\partial f_5}{\partial \theta_s} & \dfrac{\partial f_5}{\partial S} \\[2mm] \dfrac{\partial f_6}{\partial V_r} & \dfrac{\partial f_6}{\partial_r} & \dfrac{\partial f_6}{\partial I_r} & \dfrac{\partial f_6}{\partial \theta_r} & \dfrac{\partial f_6}{\partial I_s} & \dfrac{\partial f_6}{\partial \theta_s} & \dfrac{\partial f_6}{\partial S} \\[2mm] \dfrac{\partial f_7}{\partial V_r} & \dfrac{\partial f_7}{\partial_r} & \dfrac{\partial f_7}{\partial I_r} & \dfrac{\partial f_7}{\partial \theta_r} & \dfrac{\partial f_7}{\partial I_s} & \dfrac{\partial f_7}{\partial \theta_s} & \dfrac{\partial f_7}{\partial S} \end{pmatrix} \tag{13}$$

Unknown variables

$$\Delta x = \begin{pmatrix} V_r & \phi_r & I_r & \theta_r & I_s & \theta_s & S \end{pmatrix} \tag{14}$$

These unknown variables are nothing but the steady-state operating variables which we need to calculate, i.e., stator current and its angle, rotor voltage and its angle, rotor current and its angle, slip. Initials values considered for desired accuracy and fast convergence of systems of nonlinear equations are 0.1, 0.1, 1.0, 0.1, 1.0, 0.1, and 0, respectively, with angle in radian and others are in per unit (pu). This process will iterative till the above-mentioned equation converges to zero. From these variables, we can easily find steady-state parameters using following method.

2.2 PQ Bus Model-Based Methodology

Considered system bus is modeled as a method can be described using given flowchart (Fig. 2):

The solution of Eqs. (3)–(9) can be obtained by means of an iterative process, NR method. The final consequence will be steady-state operating parameters of proposed system. By taking P and Q as input data, and stator and rotor currents and rotor voltage are obtained, along with the value of slip. Finally, value of the variable called mechanical power can be obtained with the help of flowchart. Using the

Fig. 2 Steady-state calculations using *PQ* bus model
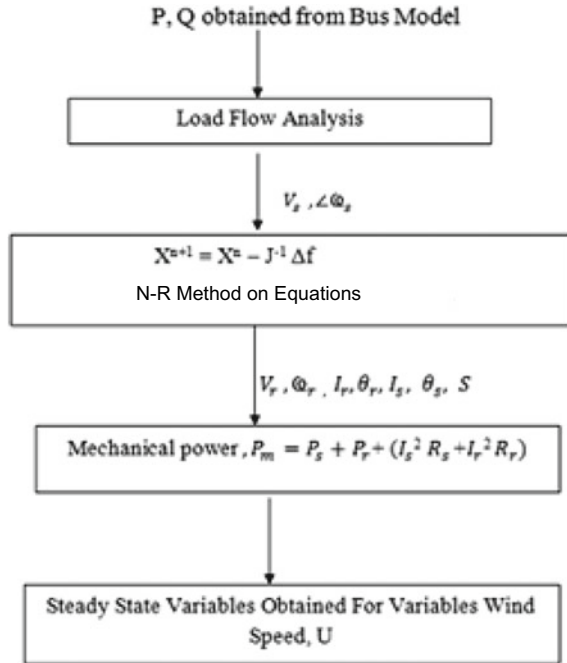
above used dynamic equations, we can easily describe validity of stationary operation values, i.e., steady-state values with dynamic model.

Conditions for validation of steady-state parameter for dynamic model are as follows:

$$\frac{\mathrm{d}E'}{\mathrm{d}t} = \Delta E' = 0 \tag{15}$$

$$\frac{\mathrm{d}s}{\mathrm{d}t} = \Delta s = 0 \tag{16}$$

The results obtained are directly used as initial values in the third-order dynamic model of doubly fed induction generator if above proposed condition fulfilled. Stability assessment of considered system depends on the suitability of obtained steady-state parameters in the dynamic model. The performance of this generator also depends on field orientations or vector control applied to it, but in proposed system, this condition is not considered.

3   Result Analysis and Discussion

The investigation of steady-state execution of DFIG, as mentioned in the algorithm, has been done in two steps. Firstly DFIG is coupled with test system as *PQ* bus, and the production point of DFIG is supposed to be fixed. After that, load flow calculations are obtained. Stator voltage V_s and stator voltage angle are bus voltage and bus voltage angle of the bus to which DFIG is connected. The analysis is carried out on a 4-bus system. The bus data and line data for this 4-bus system are given in Tables 1 and 2. In this system, generator parameters such as stator impedance, rotor impedance, and mutual reactance are $0.01 + j0.04$, $0.01 + j0.05$, and 2.9 pu, respectively.

3.1   Case Studies

Given analysis is carried out on 4-bus system with integration of DFIG. The performance of this generator is carried out for leading power factor, lagging power factor, and unity power factor condition. In considered system, generated power *P* is varying from 0.1 to 1.2 pu with the step of 0.1 pu. These steady-state parameters are obtained by using *PQ* bus method described in previous section, and this has completed with the help of developed MATLAB program. These results are summarized in Tables 3 and 4, respectively, for 0.95 (lagging and leading) power factors.

3.1.1   System Operating at 0.95 Leading Power Factor (pf = 0.95 Lead)

It is observed from given Table 3 that stator voltage increases for the leading power factor operation of DFIG. For leading power factor operation, the slip decreases for initial values of *P* and after attaining a minimum positive value at 0.9 pu value of *P* the slip start attaining higher negative value. The stator and rotor current has the

Table 1 Bus data for 4-bus system

Bus No.	Bus type	Specified voltage (pu)	Load	
			Active power (MW)	Reactive power (MVAR)
1	Swing bus	1.05	0	0
2	*P–Q* bus	1	45	15
3	*P–Q* bus	1	51	25
4	*P–Q* bus	1	60	30

Table 2 4-bus line data

Opening bus	Closing bus	Impedance (pu)
1	2	0.08 + j0.2
1	4	0.05 + j0.1
2	3	0.04 + j0.12
3	4	0.04 + j0.15

Table 3 Steady-state parameters at 0.95 leading pf

P (pu)	Q (pu)	S (pu)	V_s (pu)	I_s (pu)	V_r (pu)	I_r (pu)	P_s (pu)	P_r (pu)
0.1	0.033	0.531	0.957	−0.098	0.681	0.376	−0.094	0.176
0.2	0.066	0.412	0.965	0.072	−0.612	0.402	0.069	0.105
0.3	0.099	0.326	0.972	0.116	−0.562	0.442	0.113	1.035
0.4	0.131	0.258	0.981	0.201	−0.513	0.497	0.197	−0.031
0.5	0.164	0.201	0.987	0.304	0.461	0.571	0.300	−0.086
0.6	0.197	0.151	0.994	0.423	−0.396	0.663	0.420	−0.130
0.7	0.231	0.105	1.001	0.559	0.315	0.776	0.560	−0.153
0.8	0.263	0.063	1.008	0.708	0.215	0.906	0.714	−0.140
0.9	0.296	0.024	1.015	0.871	−0.096	1.054	0.884	−0.077
1	0.329	−0.012	1.021	1.047	−0.047	1.217	1.069	0.055
1.1	0.362	−0.046	1.028	1.229	−0.211	1.391	1.263	0.272
1.2	0.394	−0.079	1.034	1.418	−0.396	1.573	1.466	0.586

Table 4 Steady-state parameters at pf = 0.95 lag

P (pu)	Q (pu)	S (pu)	V_s (pu)	I_s (pu)	V_r (pu)	I_r (pu)	P_s (pu)	P_r (pu)
0.1	−0.033	0.531	0.951	−0.052	−0.621	0.295	−0.049	0.122
0.2	−0.066	0.412	0.952	0.101	0.501	0.268	0.096	0.032
0.3	−0.099	0.327	0.954	0.214	0.418	0.294	0.204	0.026
0.4	−0.131	0.258	0.956	0.244	0.395	0.281	0.233	−0.030
0.5	−0.164	0.201	0.957	0.461	−0.287	0.462	0.441	−0.097
0.6	−0.197	0.151	0.961	0.587	−0.227	0.572	0.564	−0.108
0.7	−0.231	0.104	0.962	0.715	0.168	0.691	0.688	−0.103
0.8	−0.263	0.063	0.963	0.708	0.107	0.811	0.810	−0.080
0.9	−0.296	0.025	0.964	0.841	0.046	0.929	0.930	−0.039
1	−0.329	−0.011	0.965	0.965	0.021	1.045	1.047	0.021
1.1	−0.362	−0.044	0.966	1.085	−0.082	1.158	1.160	0.095
1.2	−0.394	−0.075	0.967	1.131	0.146	1.265	1.094	0.185
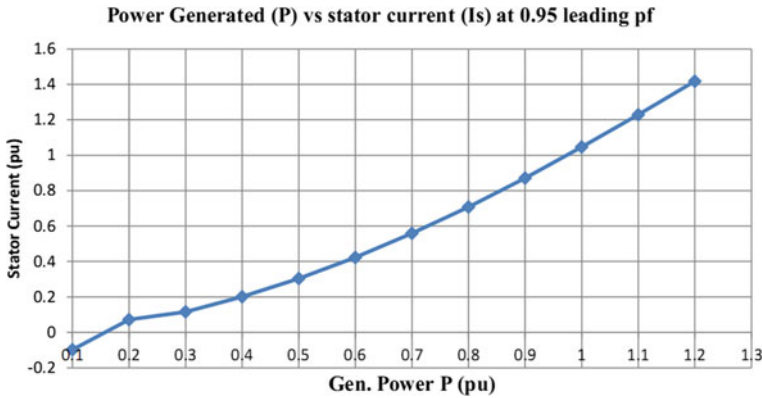
Fig. 3 Stator current versus generated power curve

same trend as obtained for unity power factor operation as shown in Fig. 3. With increase in P, the P_s increases and so the magnitude of rotor current also increase with increase in P. The rotor voltage magnitude decreases when P increases. After attaining the minimum value about rated 1.0 of P, the rotor voltage starts increasing. Using P_s and P_r value, rotor voltage angle and rotor current angle, stator current angle can easily be calculated.

3.1.2 System Operating at 0.95 Lag Power Factor

It is observed from Fig. 4 that stator voltage decreases comparatively for lagging power factor operation of DFIG with respect to leading and unity stator voltage. For lagging power factor, however, the stator current value increases significantly in comparison with respective value at leading power factor operation which restrict its operation in lagging mode. It is also observed that the value of slip continuously decreases up to 0.9 pu, than −ve. It means under −ve slip operation, power is delivered through both start and rotor which can be observed from Table 4. Rotor current and stator current increases as slip varies from 0.531 to −0.394 pu.

3.2 Stability Assessment-Based Results

Steady-state values obtained under above-mentioned conditions are directly used as initial values in the third-order dynamic model of doubly fed induction generator Eqs. (15) and (16) are satisfied. Stability assessment of considered system depends on the suitability of obtained steady-state parameters in the dynamic model. Initials values for proposed dynamic model and their relative error for unity pf, 0.95 leading can be described using form Tables 5 and 6.
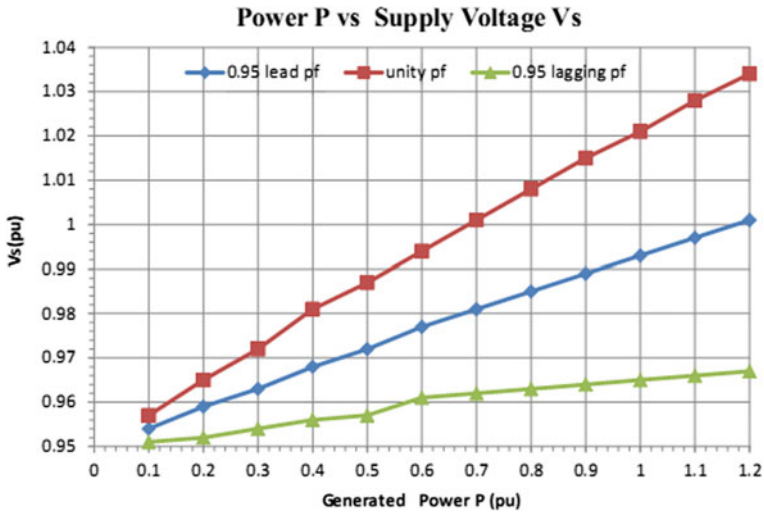
Fig. 4 Supply voltage versus power generated

Table 5 Initial values for dynamic model at unity pf and error obtained

U (m/s)	E' (pu)	S (pu)	$\Delta E'$	ΔS
5	0.6194	0.531	10^{-5}	10^{-7}
8	0.8236	0.411	10^{-8}	10^{-9}
10	1.0233	0.326	10^{-8}	10^{-12}
12	1.0445	0.261	10^{-8}	10^{-12}
14	1.0739	0.202	10^{-8}	10^{-12}

Table 6 Initial values for dynamic model at 0.95 leading pf and error obtained

U (m/s)	E' (pu)	S (pu)	$\Delta E'$	ΔS
5	1.0032	0.531	10^{-8}	10^{-12}
8	1.0489	0.412	10^{-8}	10^{-12}
10	1.0733	0.327	10^{-8}	10^{-12}
12	1.0956	0.258	10^{-8}	10^{-12}
14	1.1623	0.201	10^{-8}	10^{-12}

Since required conditions in Eqs. (15) and (16) are approaches to zero. It means that obtained steady-state variables can be used as initial values for the dynamically proposed system model as stable under varied wind conditions.

4 Conclusion

In this paper, the steady-state operation of DFIG connected to power system and its stability has been analyzed. This analysis carried out the integration of considered generator on 4-bus system. The operation in leading power factor, lagging power factor, and unity power factor made has been investigated along with its stability. From the simulation results, we can say that stator current is more for lagging load with respect to leading. Higher stator current at lagging load restricts its operation for higher power outputs. Slip may be positive and negative for lower and higher power generation, respectively. From data analysis of outputs, system stability highly depends on slip characteristics. Therefore slip value must be range for its stable operation. The stator voltage is decided by the power system, i.e., for leading power factor operation; voltage is more, whereas for lagging power factor operation, the stator voltage is less.

References

1. Khan BH (2006) Non-conventional energy resources. Tata McGraw-Hill Education
2. Gupta S, Sharma A (2018) Global scenario of solar photovoltaic (SPV) materials. In: Advanced computational and communication paradigms. Springer, Singapore, pp 126–133
3. Torkaman H, Keyhani A (2018) A review of design consideration for doubly fed induction generator based wind energy system. Electr Power Syst Res 160:128–141
4. Banakar H, Luo C, Ooi BT (2006) Steady-state stability analysis of doubly-fed induction generators under decoupled P-Q control. IEE Electr Power Appl 153(2):300–306
5. Vargas U, Ramirez A, Lazaroiu GC (2018) PSCAD simulation and experimental validation of a synchronous generator-based wind turbine generator. In: 18th IEEE international conference on harmonics and quality of power (ICHQP)
6. Karakasis NE, Mademlis CA (2018) High efficiency control strategy in a wind energy conversion system with doubly fed induction generator. Renew Energy 125:974–984
7. El Moursi M, Joos G, Abbey C (2008) A secondary voltage control strategy for transmission level interconnection of wind generation. IEEE Trans Power Electron 23(3):1178–1189
8. Babypriya B, Anita R (2009) Modelling, simulation and analysis of doubly fed induction generator for wind turbines. J Electr Eng 60(2):79–85
9. Shukla RD, Tripathi RK, Gupta S (2010) Power electronics applications in wind energy conversion system: a review. In: IEEE international conference on power, control and embedded systems (ICPCES), Nov 2010, pp 1–6
10. Debouza M et al (2018) Direct power control for grid-connected doubly fed induction generator using disturbance observer based control. Renew Energy 125:365–372

Comparison of Two Design Methods of Triboelectric Nanogenerator for Building Efficient Energy Harvesting and Storage

Khushboo and Puneet Azad

Abstract Triboelectric nanogenerators are used to convert all kinds of mechanical vibrations such as human motions, vibrations from industrial machinery, automobiles, etc. into useful electrical energy. In this paper, we compared two design methods of efficient energy harvesting systems in vertical contact-separation and lateral-sliding mode with respect to their implementation and experimental results. We have demonstrated the charging behavior of two modes of TENG using polytetrafluoroethylene (PTFE), aluminium, and copper used as triboelectric materials. We have observed a maximum open circuit voltage of 4.9 V across 4.7 µF capacitor, maximum energy of 270 µJ/cm^{-3} across 100 µF capacitor, and maximum output power of 0.9 µW across 4.7 µF load capacitor with 7.8 MΩ load resistor in vertical contact-separation mode.

Keywords Vertical contact-separation mode · Lateral sliding mode · Triboelectric materials · Energy harvesting

1 Introduction

In recent years, there has been growing interest in the triboelectric nanogenerator, another optimistic approach of mechanical/vibration energy harvesting. The original idea of triboelectric nanogenerator was proposed in 2012 by Z. L. Wang's group. The working principle of triboelectric nanogenerator is depending upon triboelectric effect, a prominent category of contact electrification. According to triboelectric effect, two non-identical materials are brought into contact with each

Khushboo (✉)
USICT, Guru Gobind Singh Indraprastha University, Delhi, India
e-mail: kkhushboo_2008@yahoo.com

P. Azad
Department of Electronics and Communication Engineering, Maharaja Surajmal
Institute of Technology, Delhi, India
e-mail: puneet.azad@msit.in

other after applying an external force and the materials are electrically charged [1]. Electrical charge transfer then takes place at the contact area. This is also known as "static electricity." The charges of the materials are in different polarity. There is a huge list of TENG materials; the selection of the materials depends on its polarity of gaining/losing electron. Materials normally are less conductive or insulator so that they can store transferred charges and preserve them for a long interval of time. TENG has so many numerous advantages; it is low in density, light in mass, low in cost, ideal at low frequency (<5–10 Hz), and can be manufactured easily [2, 3]. Examples of applications include for energy harvesting from human body motion, elbow motion, walking, rotating tire, vibration or mechanical motion, and wind energy, etc. for applications in transportable/wearable devices, sensor networks, bioelectronics, Internet of things (IoT), infrastructure monitoring, smart electronic devices, etc. Several other energy harvesting sources are available in our living environment, such as solar energy, pyroelectricity [4, 5], mechanical vibration, biomechanical energy, and bio fuels. To differentiate from others, TENG is the one that is available almost everywhere. The fundamental modes of operation of TENG are divided into four groups:

(a) Vertical contact-separation mode (V-TENG): This method has two working state: the first one is pressed mode, and the second one is released mode. During pressed mode, two non-identical materials are brought into contact with each other through an external force; hence, the materials get electrically charged, and due to the triboelectric effect, this charge then deposits at the contact area. In released mode, the two opposite materials are separated and an electric potential is created between the electrodes. This mode can be practically achieved by vibration and shock events, by finger/palm tapping, human walking motion, and motor vibration, etc.

(b) Lateral sliding mode (LS-TENG): This mode uses horizontal motion. It has two states of operation, sliding inward and sliding outward. When an external force is applied, these materials are sliding inwards and outwards. Due to this motion, there is an electric potential created across the electrodes. It can be achieved by rotation of a wheel and useful for harvesting planar or rotational mechanical energy.

(c) Single-electrode mode (SE-TENG): The working mechanism of this mode is familiar with vertical contact-separation mode, except that it has only one primary electrode and ground as the second electrode which is used to capture the induced electrical charge. In this mode, triboelectric material allowed to move more freely. Due to this freedom of movement, this mode can be applicable to harvest mechanical energy from the flow of water and wind [6].

(d) Freestanding triboelectric mode (F-TENG): In this mode, electrodes are kept at fixed position, whereas the triboelectric material keeps moving to and fro between the electrodes. Hence, a potential drop starts passing through the load.

In this paper, we present two modes of TENG: vertical contact-separation and lateral sliding mode implementing using three triboelectric materials: polytetrafluoroethylene (PTFE), aluminium (Al), and copper (Cu), and the thickness of

each is 50 µm. We choose these materials on the basis of their ability of a material for gaining/losing electron depends on its polarity. As per this polarity, PTFE is the most negative charged material, and Cu is less negative than PTFE and Al having positive charge. Furthermore, aluminium (Al) and copper (Cu) are used as positive and negative charged electrodes to capture and transfer the electric charge through the load resistor. PTFE has the tendency to retain the charge for a longer period of time and converted it into electricity. Both modes are using the same type of materials; the only difference between these two modes is their design approach.

2   Modeling of a Proposed Techniques and Materials

The primary working operation of the two modes of TENGs is shown in Fig. 1, which utilizes the coupling of contact electrification and electrostatic induction. As shown in Fig. 1b, the right side of the schematic diagram is often regarded as lateral sliding mode and left side Fig. 1a is often called as vertical contact-separation mode [7, 8]. In both modes, we have same top and bottom electrode as Al and Cu. The only difference is in the selection of triboelectric materials. In such a way, maximum number of charge gets transferred and collected by the triboelectric materials. Figure 1c demonstrates a practical application of triboelectric nanogenerator based on human walking.
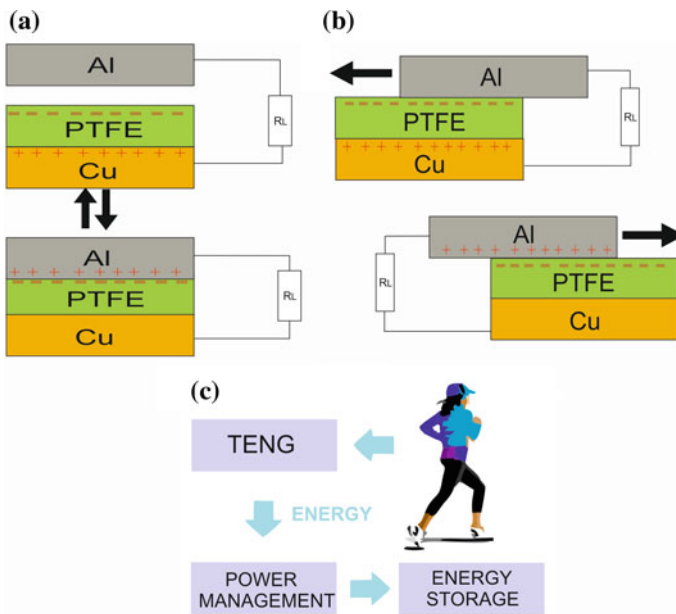
Fig. 1 Block diagram of **a** V-TENG, **b** LS-TENG, and **c** practical application

3   V-TENG and LS-TENG Schematic Design

We demonstrate a practical model of the above said two mechanisms as shown in Fig. 2. The first V-TENG mode is the simplest design of TENG. In this mode, two plates coated with two distinct triboelectric materials are placed opposite to each other such as case (a) vertical contact-separation mode using the combination of Al + PTFE + CU and case (b) lateral sliding-contact mode using the combination of Al + PTFE + CU.

An external force is applied through a DC motor, doing so these plates come in physical contact (pressed mode) and charge gets transferred. In contrast to release mode, a voltage drop is created. Here the two electrodes are directly coupled with a load resistor so that free electrons can easily move from one electrode to other to establish an opposite charge in order to balance the electrostatic field. Once the gap is closed, the triboelectric charge created potential disappears, and the electrons flow back [9–11]. The structure of second contact-sliding mode is same as that for the vertical contact-separation mode. The only difference is in the position of the two plates. These plates are arranged in sliding direction by repetitive back and forth motion through an external force generates an AC output. Both modes can operate simultaneously without the need of two external forces. Two separate full wave bridge rectifier circuit, a capacitor and a load is connected with both the mechanism to get DC output voltage.

The DC output voltage across capacitor load C_L is given as:

$$C\frac{\mathrm{d}v}{\mathrm{d}t} + \frac{V_{\text{out}}}{R_L} = I \tag{1}$$

In this paper, resistors were used to calculate the electric output power on the external load. The power output (P_{out}) across resistor load R_L is found as:

$$P_{\text{out}} = \frac{V_{\text{out}}^2}{R_L} \tag{2}$$
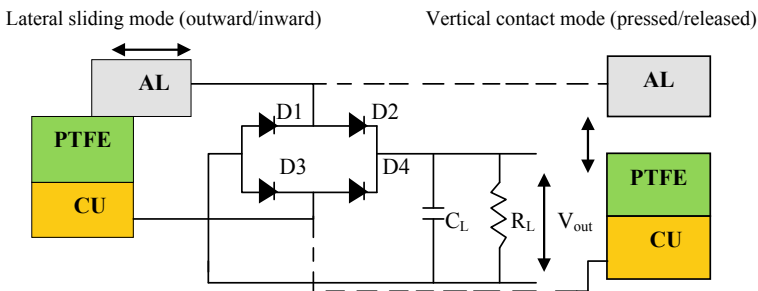
Fig. 2 Schematic view of V-TENG and LS-TENG

The stored energy is determined using the equation:

$$E = \frac{1}{2} C_L V_{out}^2 \tag{3}$$

4 Simulated Results of V-TENG and LS-TENG

To store the generated DC voltage, various load capacitor (C_L) is parallel connected together with the FWR and measured voltages are recorded on Fluke 287 an electronic logging multimeter. The experimental results shown in Fig. 3 represent charging voltage across different capacitors using V-TENG mode and LS-TENG mode both are designed using three different triboelectric materials (AL + PTFE + Cu). The graph shows the correlation between V_{out} (V) versus time (s) across the different value of capacitor load C_L (4.7, 33, 47, and 100 µF) without any resistor load R_L in Fig. 3a, b. It illustrates an output voltage variation across different C_L in respect of time. We have observed that the DC output voltage across low value capacitors like 4.7 µF in this paper increase quickly and reached
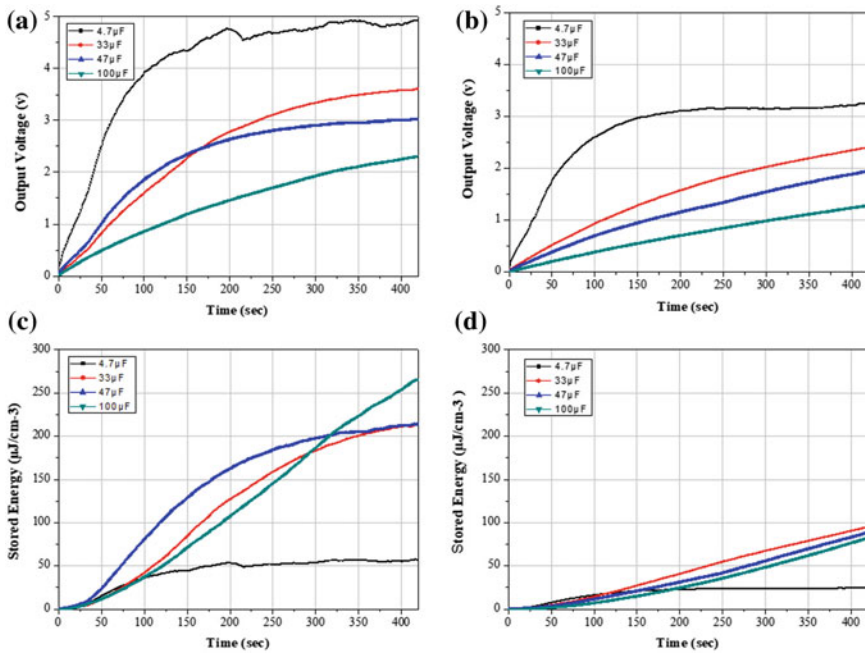
Fig. 3 Capacitor charging voltage and energy with two modes of TENG **a** vertical mode output voltage, **b** vertical mode stored energy, **c** sliding mode output voltage, and **d** sliding mode stored energy across various load capacitors (4.7, 33, 47, and 100 µF)

saturation owing to smaller time constant in contrast to high value capacitors like 47–100 μF [12–15]. This will result in fast charging and discharging of small value capacitor. Large value capacitors like 100 μF charges gradually but preserve charge for longer duration than small value capacitors and resulting in delayed in saturation. Figure 3c, d shows the stored energy in different capacitors in respect to time as evaluated using Eq. (3). We have found that 270 μJ/cm^{-3} across 100 μF capacitor is the maximum stored energy density observed in case (a) as compared to
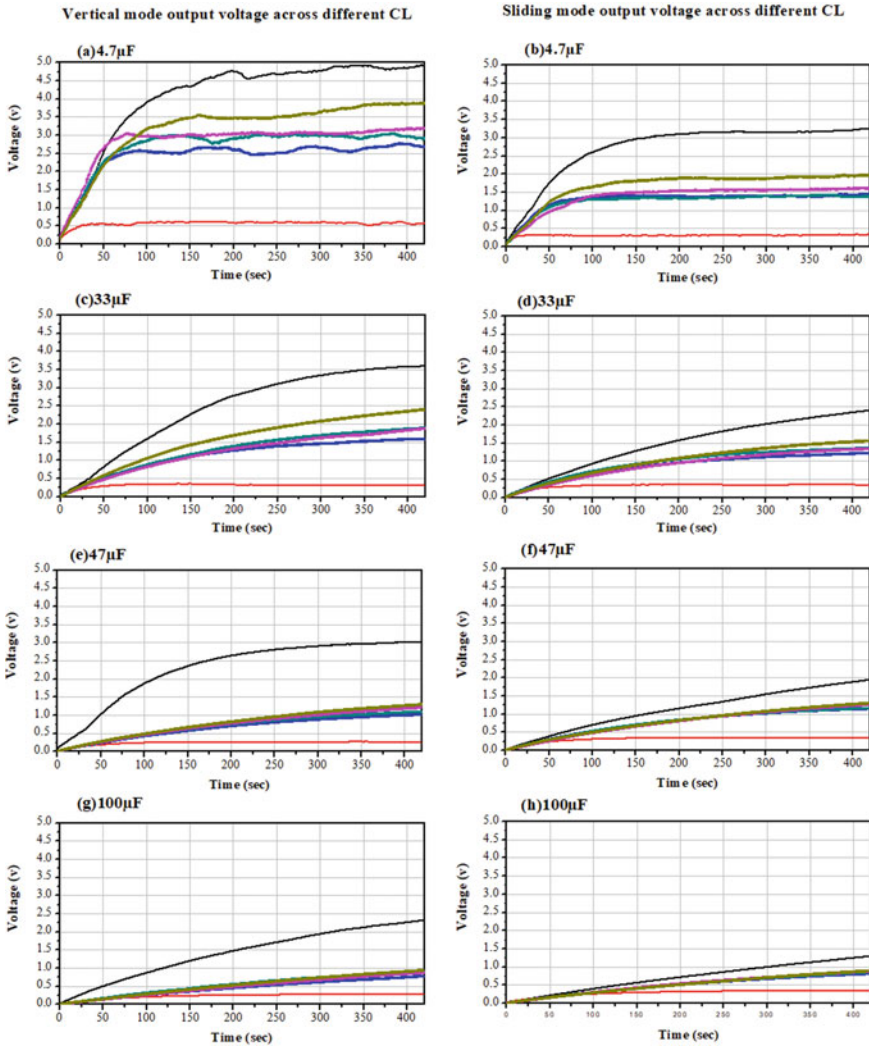
Fig. 4 Output voltage versus time at no load and with load condition across different load capacitor C_L (4.7, 33, 47, and 100 μF)

Table 1 Comparative analysis of maximum power output across different capacitors

Capacitance (µF)	Maximum power output (µW)									
	V-TENG					LS-TENG				
	1 M Ω	7.8 M Ω	10.4 M Ω	13 M Ω	20.80 M Ω	1 M Ω	7.8 M Ω	10.4 M Ω	13 M Ω	20.80 M Ω
4.7	0.57	0.90	0.84	0.78	0.71	0.10	0.25	0.18	0.20	0.18
33	0.29	0.32	0.36	0.27	0.27	0.11	0.19	0.18	0.13	0.11
47	0.25	0.16	0.13	0.12	0.89	0.11	0.13	0.12	0.11	0.82
100	0.27	0.83	0.81	0.60	0.42	0.11	0.76	0.71	0.59	0.38

case (b) energy of 98 µJ/cm^{-3} both are across 33 µF capacitor [16–18]. The reason is that V-TENG is able to transfer and store more electric charge as compared to LS-TENG. It is noticed that energy of small value capacitor is less than large value capacitor as small amount of charge is stored by small value capacitor.

Furthermore, different resistor load R_L (1, 7.8, 10.4, 13, and 20.8 MΩ) are connected in parallel with capacitor load (C_L) to calculate electric output power at the load. Further, the output voltage versus time at no load and with load resistor is plotted to monitor the effect of load resistance and capacitance as shown in Fig. 4. We found that maximum output power measured with 7.8 MΩ across 4.7 µF load capacitor in case (a) vertical contact-separation mode using Al + PTFE + Cu (0.90 µW) and in case (b) lateral sliding mode using Al + PTFE + Cu (0.25 µW) with same load resistor 7.8 MΩ and 4.7 µF load capacitor was observed [19–21]. Measured result shows that both modes are using the same type of material but vertical contact-separation mode has the simplest design approach and provides maximum dc output voltage and energy and power as compared to lateral sliding mode. These results also represent the future prospective of triboelectric nanogenerators in the future applications, so that we will obtain the large amount of voltage, power, and energy with the hybridization of both modes together (Table 1).

5 Conclusion

In this paper, an energy harvesting system is demonstrated that is based on the working principle of triboelectric nanogenerator (TENG). This newly designed approach successfully converted the mechanical energy from human motion powered into electricity with a maximum output power up to 0.90 µW across 4.7 µF load capacitor and 7.8 MΩ load resistor in V-TENG mode and second LS-TENG mode provides maximum power of 0.25 µW across same load resistor and load capacitor using Al + PTFE + Cu combination within 450 s. Moreover, we have successfully compared the results of two modes of TENG and finally realized the significant of one mode over the other. We have used combination of three triboelectric materials for this purpose such as PTFE, aluminium, and copper. It is

observed that a maximum of 4.9 V DC voltage is obtained across 4.7 µF capacitor and maximum energy of 270 µJ/cm^{-3} across 100 µF capacitor in V-TENG mode, whereas LS-TENG mode gives the maximum of 3.2 V DC voltage across 4.7 µF and energy of 98 µJ/cm^{-3} across 33 µF load capacitor within 450 s. A subsequent work could be designing in hardware with the hybridization of above two modes and analyzed the performance of the circuit.

References

1. Wang ZL, Lin L, Chen J, Niu S, Zi Y (2016) Triboelectric nanogenerators. Springer International Publishing, Switzerland
2. Wang ZL, Chen J, Lin L (2015) Progress in triboelectric nanogenerators as a new energy technology and self-powered sensors. Energy Environ Sci 8:2250–2282
3. Lee JH, Kim J, Kim TY, Hossain MSA, Kim SW, Kim JH (2016) All-in-one energy harvesting and storage devices. J Mater Chem A 4:7983–7999
4. Azad P, Singh VP, Vaish R (2018) Candle soot-driven performance enhancement in pyroelectric energy conversion. J Electron Mater. 47(8):4721–4730. ISSN 0361-5235. https://doi.org/10.1007/s11664-018-6357-8
5. Sharma M, Singh VP, Singh S, Azad P, Ilahi B, Madhar NA (2018) Porous $Ba_{0.85}Ca_{0.15}Zr_{0.1}Ti_{0.9}O_3$ ceramics for pyroelectric applications. J Electron Mater. 47(8):4882–4891. ISSN 0361-5235. https://doi.org/10.1007/s11664-018-6375-6
6. Azad P, Vaish R (2017) Portable triboelectric based wind energy harvester for low power applications. Eur Phys J Plus 132:253
7. Khushboo, Azad P (2016) Triboelectric nanogenerator based on vertical contact separation mode for energy harvesting. In: IEEE, ICCCA 2017. IEEE, India, pp 1499–1502
8. Khushboo, Azad P Design and implementation of conductor to dielectric lateral sliding TENG mode for low power electronic. In: Springer, accepted in signals, machines and automation (SIGMA 2018). Applications of Artificial Intelligence Techniques in Engineering. Advances in Intelligent Systems and Computing, vol 698. Springer, Singapore, pp 167–174. https://doi.org/10.1007/978-981-13-1819-1_17
9. Mao Y, Genga D, Liang E, Wang X (2015) Single-electrode triboelectric nanogenerator for scavenging friction energy from rolling tires. Nano Energy 15:227–234
10. Vaish M, Sharma M, Vaish R, Chauhan V (2015) Electrical energy generation from hot/cold air using pyroelectric ceramics. Integr Ferroelectr J Integr Ferroelectr 167(1):90–97 (Taylor & Francis)
11. Wang ZL (2014) Triboelectric nanogenerators as new energy technology and self-powered sensors—principles, problems and perspectives. Energy Environ Sci Faraday Discuss 176:447–458
12. Zhu G, Chen J, Liu Y, Bai P, Zhou YS, Jing Q, Pan C, Wang ZL (2013) Linear-grating triboelectric generator based on sliding electrification. ACS Publ Nano Lett 13:2282–2289
13. Zil Y, Wang J, Wang S, Li S, Wen Z, Guo H, Wang ZL (2016) Effective energy storage from a triboelectric nanogenerator. Nat Commun 7
14. Fan FR, Tian ZQ, Wang ZL (2012) Flexible triboelectric generator. Nano Energy 1:328–334 (Elsevier Ltd.)
15. Niu S, Liu Y, Zhou YS, Wang S, Lin L, Wang ZL (2015) Optimization of triboelectric nanogenerator charging systems for efficient energy harvesting and storage. IEEE Trans Electron Dev 62(2):641–647
16. Proto A, Penhaker M, Conforto S, Schmid M (2017) Review nanogenerators for human body energy harvesting. Trends Biotechnol 35(7):610–624 (Elsevier Ltd.)

17. Shaikh FK, Zeadally S (2016) Energy harvesting in wireless sensor networks: a comprehensive review. Renew Sustain Energy Rev 55:1041–1054 (Elsevier Ltd.)
18. Yang W, Chen J, Zhu G, Yang J, Bai P, Su YJ, Jing QS, Wang ZL (2013) Harvesting energy from natural vibration of a human walking. ACS Nano 7(12):11317–11324. https://doi.org/10.1021/nn405175z
19. Vaish M, Sharma M, Vaish R, Chauhan VS (2015) Experimental study on waste heat energy harvesting using lead zirconate titanate (PZT-5H) pyroelectric ceramics. Wiley Energy Technol 3:768–773
20. Zhong J, Zhong Q, Fan F, Zhang Y, Wang S, Hu B, Wang ZL, Zhou J (2013) Finger typing driven triboelectric nanogenerators and its use for instantaneously lighting up LEDS. Nano Energy. 2(4):491–497. https://doi.org/10.1016/j.nanoen.2012.11.015
21. Xia X, Lie G, Chen L, Li W, Xi Y, Shi J, Hu C (2015) Foldable and portable triboelectric-electromagnetic generator for scavenging motion energy and as a sensitive gas flow sensor for detecting breath personality. Nanotechnology 26. https://doi.org/10.1088/0957-4484/26/47/475402

Maximization of Plug-In Electric Vehicle's Exploitation for Load Flattening with Consideration of Customer Satisfaction

K. Ramakrishna Reddy and S. Meikandasivam

Abstract Vehicle-to-grid (V2G) feature in electric vehicles enables ancillary support to the grid due to its bidirectional power capability. This work mainly focuses on effective utilization of PEV's storage capacity to suppress solar PV and load power fluctuations using PEV's storage capacity. A win-win strategy between customer and utility is proposed by maximizing revenue for customer and to minimize demand fluctuations. Water Filling Energy Dispatch Algorithm (WFEDA) is used to optimally schedule PEV's available energy. Adaptive neuro-fuzzy inference system (ANFIS) is designed and implemented to prioritize PEVs with revenue maximization and load flattening as the key objectives.

1 Introduction

Recent developments in the battery technology of electric vehicles have shown remarkable positive signs toward cost reduction and range improvement of plug-in electric vehicle (PEV) batteries [1]. Integration of PEVs into the grid imposes complexities if their daily plug-in timings coincide with massive number of PEVs. The effect on load profile as a result of uncertainty in electric vehicles charging is studied in [2]. On the other hand, PEV's storage capacity can be exploited for the grid ancillary services such as load flattening, frequency regulation, and voltage regulation. V2G power flow brings advantages along challenges with bidirectional power flow feature that increases network complexity [3].

K. Ramakrishna Reddy (✉) · S. Meikandasivam
Vellore Institute of Technology, Vellore, Tamil Nadu, India
e-mail: ramu.svce@gmail.com

S. Meikandasivam
e-mail: meikandasivam@gmail.com

Uncontrolled or unscheduled PEV charging will create a lot of disturbances to the utility operator in terms of frequency and voltage deviations. Solar PV which delivers maximum amount of power during midday time is another big concern to deal with in distribution networks. Thanks to ICT which has created new opportunities to transform adverse effect of PEVs integration into an advantage. PEV proliferation can facilitate grid ancillary services such as load flattening [4], reducing cost of charging electric vehicles, and improving revenue by assisting grid support [5] and more importantly to reduce spinning reserves [6] from utility prospective.

PEV stochastic load modeling is presented [7]. In [8], dynamic programming method is used for frequency regulation using PEVs in which final state of charge (SoC) set point and customer revenue are the main considerations. Customer revenue is the key factor that encourages PEV's owners to participate in grid support. It is utility's prime responsibility toward customers to maximize their revenue in order to make them feel comfortable to cope with scheduled charging/discharging times. However, primary purpose of the electric vehicle is traveling, and hence, it has to be given highest priority while scheduling. Authors in [9] have prioritized PEVs based on electricity price, capacity, and power rate, and in [10], electricity price and charging requirements are used for prioritization. SoC is taken as key variable to assign priority in [11]. Most of the works have been done with the priority based on time left for the vehicle, SoC, and electricity price in order to minimize cost of charging [8, 12, 13]. In this work, a new strategy has been developed based on five parameters (SoC, laxity, capacity, electricity price, and customer revenue). A win-win situation is analyzed between customers and utility while prioritizing. ANFIS is trained with random input variables to assign rank for each PEV during each interval of time (Sect. 5).

The novel contribution of this work includes the following aspects:

1. Day-ahead power demand estimations are used to schedule PEVs for grid support by identifying zones of charging and discharging requirements.
2. WFA is used to optimally distribute available energy from PEVs among the intervals in each zone.
3. To improve the customer satisfaction without compromising utility need, a prioritization procedure is implemented using ANFIS.

2 Estimation of Power Fluctuations

Solar PV power generation which depends on irradiation will be maximum during midday in which residential loading will be very less. In order to deal with this situation, it needs storage units installed in coordination with solar PV. On the other side, PEV loading (charging or G2V) creates extra burden on transformers if more

number of PEVs are plugged in for charging simultaneously. Here $P_{\text{spec}}^{\text{grid}}$ is taken as reference for flattening of load curve. Estimation of PEV availability and their capacities for the following day and hour is the key factor that determines level of exploitation of PEV storage space. Each hour divided into four equal intervals denoted by 't' (each of 15 min). Equation (1) gives net power need from grid which is the average aggregated sum of solar PV and load demand along with PEVs charging during tth interval. Energy need $\left(E_{\text{need}}^{t,\text{pev}}\right)$ from PEVs during tth interval of time is given in Eq. (3), where total need of energy from grid $\left(E_{\text{need}}^{t,\text{grid}}\right)$ for tth interval is given by Eq. (2). Here P_{solar}^{t}, P_{load}^{t}, $P_{\text{pev}}^{t,\text{ch}}$, and $E_{\text{spec}}^{\text{grid}}$ are total solar PV power, aggregate load demand, PEV charging load, and specified energy from grid. Here, the actual data is used to represent day-ahead forecast data by adding an error of $\pm 10\%$ deviation.

Let, $x + y + z = N$
where N = Total number of PEVs.

x = Number of PEVs getting charge for trip purpose.
y = Number of PEVs participating grid support.
z = Number of PEVs away from home.

$$p_{\text{need}}^{t,\text{grid}} = P_{\text{solar}}^{t} - P_{\text{load}}^{t} - P_{\text{pev}}^{t,\text{ch}} \tag{1}$$

$$E_{\text{need}}^{t,\text{grid}} = \sum_{i=t}^{t+15} P_{\text{need}}^{i} * \mathrm{d}i \tag{2}$$

$$E_{\text{need}}^{t,\text{pev}} = E_{\text{need}}^{t} - E_{\text{spec}}^{\text{grid}} \tag{3}$$

where $E_{\text{spec}}^{\text{grid}} = \sum\limits_{i=t}^{t+15} P_{\text{spec}}^{\text{grid}} * \mathrm{d}i$

Here $\mathrm{d}i$ is the time difference between two consecutive samples.

Figure 1a shows the forecasted power demand from grid and energy demand during each interval of time is shown in Fig. 1b. Based on power demand shown in Fig. 1c, charging and discharging zones are identified as +ve or −ve depending on whether power demand is greater or less than the specified grid power. Expected aggregated power available from all available PEVs is shown in Fig. 1d. PEV availability and mobility are discussed in Sect. 3. Constraints on PEV battery usage are given by Eqs. (4)–(6). Here $P_{\text{rate}}^{i,\text{min}}$, $P_{\text{rate}}^{i,\text{max}}$, and $P_{\text{rate}}^{i,t}$ are minimum, maximum power rates, and power rate of ith PEV during tth interval, respectively. Here $\text{SoC}_{\text{min}}^{i}$, $\text{SoC}_{\text{max}}^{i}$, and SoC_{t}^{i} are ith PEV's minimum, maximum SoC limits, and SoC during tth interval, respectively. $P_{\text{rate}}^{i,\text{dif}}$ is allowable change in PEV power rate in each step.
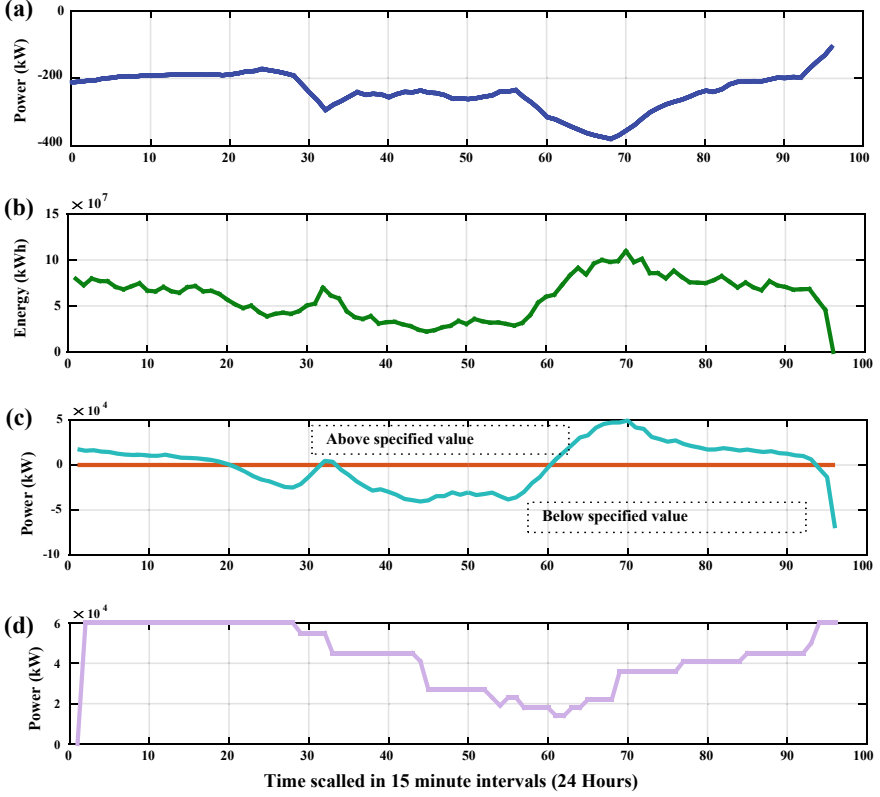
Fig. 1 Estimation for the following day in terms of power and energy demand: **a** load demand, **b** energy demand, **c** deviation in power from specified value, and **d** expected available power from PEVs

$$SoC^i_{\min} \le SoC^i_t \le SoC^i_{\max} \tag{4}$$

$$P^{i,\min}_{\text{rate}} \le P^{i,t}_{\text{rate}} \le P^{i,\max}_{\text{rate}} \tag{5}$$

$$P^{i,t}_{\text{rate}} - P^{i,t-1}_{\text{rate}} \le P^{i,\text{dif}}_{\text{rate}} \tag{6}$$

When it comes to utility, the objective is to minimize the deviations in power drawn from grid (Eq. 7) and the second objective is to minimize the cost of charging (Eq. 8). Customer benefit due to grid support is the key factor that drives coordination of PEVs with power fluctuations. Hence, the whole objective is to maximize utilization of available PEV capacity while maximizing revenue for the customer without disturbing trip schedules. The constraints are substantiated in Eqs. (4)–(6), (14), and (17).
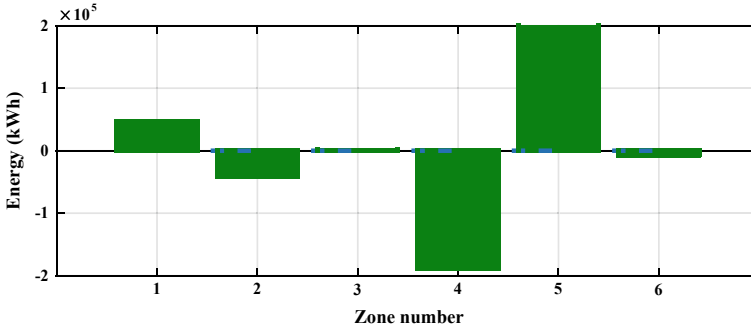
Fig. 2 Energy demand during each zone ('−' charging and '+' discharging)

Energy demand $\left(E_{\text{need}}^{z,\text{grid}}\right)$ for each zone 'z' is given in (11), and energy need in all the zones is shown in Fig. 2.

$$\min, \Delta P$$
$$= \min, \left| \sum P_{\text{solar}}^t - \sum P_{\text{load}}^t - \sum_{i=1}^{x} P_{\text{pev,trip}}^{t,\text{ch}} + \sum_{i=1}^{y} P_{\text{pev,trip}}^{t,\text{dc}} - \sum_{i=1}^{y} P_{\text{pev}}^{t,\text{ch}} - P_{\text{spec}}^{\text{grid}} \right| \tag{7}$$

$$\min, C_{\text{pev}}^i = \min, \sum_{t=1}^{96} \left(C_{i,\text{ch}}^{e,t} + C_i^{t,\text{bd}} - C_t^{\text{reg}} + C_{i,\text{dc}}^{e,t} \right) * E_{\text{pev}}^{t,i} \tag{8}$$

$$C_{\text{pev}}^{i,t,\text{bd}} = \frac{C_{b,i}E_{b,i} + C_{L,i}}{L_{c,i}E_{b,i}\text{DoD}_i^t} E_{\text{ch/dc}}^{t,i} \tag{9}$$

$$C_{i,\text{ch}}^{e,t} = a_1 + a_2 \alpha^{\left(P_t^{\text{grid}} - P_{\text{spec}}^{\text{grid}}\right)/P_{\text{spec}}^{\text{grid}}} \tag{10}$$

Here ΔP is deviation in grid power from specified value, and the terms 3, 4, and 5 in Eq. (7) pertains to PEVs' charging load, discharging contribution for grid support, and charging contribution for grid support, respectively. In Eq. (8), C_{pev}^i is the cumulative sum of cost paid by PEV for charging over 96 intervals, $C_{i,\text{ch}}^{e,t}$ is cost of electricity during tth interval, $C_{i,\text{dc}}^{e,t}$ is cost paid to PEV owner for discharging which is taken as same as $C_{i,\text{ch}}^{e,t}$, and C_t^{reg} is amount paid to owner due to participation in regulation. Equation (9) represents battery degradation cost $\left(C_{\text{pev}}^{i,\text{bd}}\right)$ of ith PEV which depends on its battery initial cost $(C_{b,i})$, battery capacity $(E_{b,i})$, life

cycle of battery $\left(C_{\mathrm{L},i}\right)$, depth-of-discharge $\left(\mathrm{DoD}_i^t\right)$, and energy charged/discharged $\left(E_{\mathrm{ch/dc}}^{t,i}\right)$ during interval 't'. Smart pricing which is shown in Eq. (10). The values of a_1, a_2, and α are pricing constants and are taken as 0.1, 0.2, and 10, respectively.

$$E_{\mathrm{need}}^{z,\mathrm{grid}} = \sum_{t=1}^{M} E_{\mathrm{need}}^{t,\mathrm{grid}} \tag{11}$$

3   Modeling of PEV and Estimation of Energy Availability

Data from National Travel Survey (NTS) [14] (NTS0503-trip purpose, NTS0405-average trip length, and NTS0409-average number of trips) is referred to in the work in order to estimate the probability of PEV availability at plug point, trip return time, and energy discharged during travel [15]. After arrival from trip, the energy level of the PEV is calculated using total trip length l (km) and mileage γ (kWh/km) using (13) where $\mathrm{SoC}_{\mathrm{arraiv}}^{i,t=t_a}$ and $\mathrm{SoC}_{\mathrm{depart}}^{i,t=t_d}$ are SoC levels at arrival and departure times of ith PEV.

$$P_{\mathrm{rate}}^{i,t,\mathrm{pev}} = \begin{cases} P_{\mathrm{rate}}^{i,t}; & \text{if } \mathrm{PEV}_{\mathrm{avail}}^{i,t} = 1 \\ 0; & \text{if } \mathrm{PEV}_{\mathrm{avail}}^{i,t} = 0 \end{cases} \tag{12}$$

$$\mathrm{SoC}_{\mathrm{arraiv}}^{i,t=t_a} = \begin{cases} \mathrm{SoC}_{\mathrm{depart}}^{i,t=t_d} - \gamma * l; & \text{if } \mathrm{PEV}_{\mathrm{avail}}^{i,t} = 1 \ \& \ \mathrm{PEV}_{\mathrm{avail}}^{i,t-1} = 0 \\ 0; & \text{if } \mathrm{PEV}_{\mathrm{avail}}^{i,t} = 0 \end{cases} \tag{13}$$

Depending on trip purpose (commute, education, shopping, business, etc.), trip starting probability and cumulative distribution function (CDF) are used to find the availability of vehicle [16]. Laxity of each vehicle is calculated using on (14) taken from [17] which is the indication of vehicle flexibility and availability for grid support. Higher the laxity of a given PEV more will be the flexibility of scheduling it and vice versa. Laxity of ith PEV at tth interval $\left(L_{\mathrm{pev}}^{i,t}\right)$ also depends on SoC, capacity, and power rate. It is ensured that the vehicle is ready with maximum SoC before it leaves for trip. Here t_d^i and t_a^i are departure and arrival timings of ith PEV, and t_{ch}^i is the tame taken to get charge up to 0.8 SoC.

$$L_{\mathrm{pev}}^{i,t} = \frac{\left(\mathrm{SoC}_{\mathrm{pev}}^{i,t=t_d} - \mathrm{SoC}_{\mathrm{pev}}^{i,t}\right)E_{\mathrm{cap}}^{i,\mathrm{pev}}}{\eta P_{\mathrm{rate}}^{i,\mathrm{pev}} \Delta t} = \begin{cases} t_d^i - t; & \text{if '} - \text{ve' zone} \\ t_d^i - t - t_{\mathrm{ch}}^i; & \text{if '} + \text{ve' zone} \end{cases} \tag{14}$$

$$E_{\text{avail},t=1}^{z,\text{pev,ch}} = \sum_{i=1}^{x+y} \left(0.8 * E_{\text{cap}}^{i,\text{pev}} - E_{\text{level}}^{i,t,\text{pev}} \right) \text{PEV}_{\text{avail}}^{t,i} \tag{15}$$

$$E_{\text{avail},t=1}^{z,\text{pev,dc}} = \sum_{i=1}^{x+y} \left(E_{\text{level}}^{i,t,\text{pev}} - 0.2 * E_{\text{cap}}^{i,\text{pev}} \right) \text{PEV}_{\text{avail}}^{t,i} - \sum_{i=1}^{x} \left(E_{\text{cap}}^{i,\text{pev}} - E_{\text{level}}^{i,t,\text{pev}} \right) \tag{16}$$

Here $E_{\text{avail},t=1}^{z,\text{pev,ch}}$ and $E_{\text{avail},t=1}^{z,\text{pev,dc}}$ are available storage capacity from PEVs at starting interval of zone z. $E_{\text{cap}}^{i,\text{pev}}$ is capacity of ith PEV, and $E_{\text{level}}^{i,t,\text{pev}}$ is energy level at tth interval. Energy storage capacity available from PEVs for charging and discharging can be estimated using (15) and (16).

4 Proposed Control Strategy for PEV Scheduling

In the study, a new smart energy management strategy is proposed for scheduling PEVs charging and discharging. Based on day-ahead forecast power demand and solar PV power generation, charging (−ve) and discharging (+ve) zones are identified (Fig. 2). From PEV availability model, available power, power requirement for charging the vehicle, and laxity are estimated. Each zone is considered individually for optimum power dispatch among the time intervals included in that zone. Let N be the number of zone and M be the number of time intervals in each zone on a given day.

Energy distribution among intervals in each zone is carried out using WFA, and prioritization of PEVs is done by using ANFIS; this process is discussed later in this section. The flowchart shown in Fig. 3 shows the proposed PEV control strategy which. Based on energy availability, WFA will optimally distribute the PEVs' energy among all time intervals in each zone. WFA is dedicated to do favor to utility, whereas ANFIS is designed with PEV's owner prospective in order to increase revenue without compromising grid support.

5 Energy Distribution and Prioritization

WFEDA is used in allocation of available storage capacity in each zone, and ANFIS is trained to prioritize PEVs. Water Filling Algorithm is generally used in maximizing communication channel capacity based on noise levels and constraints on power [18]. In [19], authors have used WFA to achieve flat load profile using electric vehicles storage capacity while fulfilling energy need for trip requirements. In this work, WFA is used to dispatch available energy among intervals involved in each zone. Here the objective is to reduce power deviation during each zone which
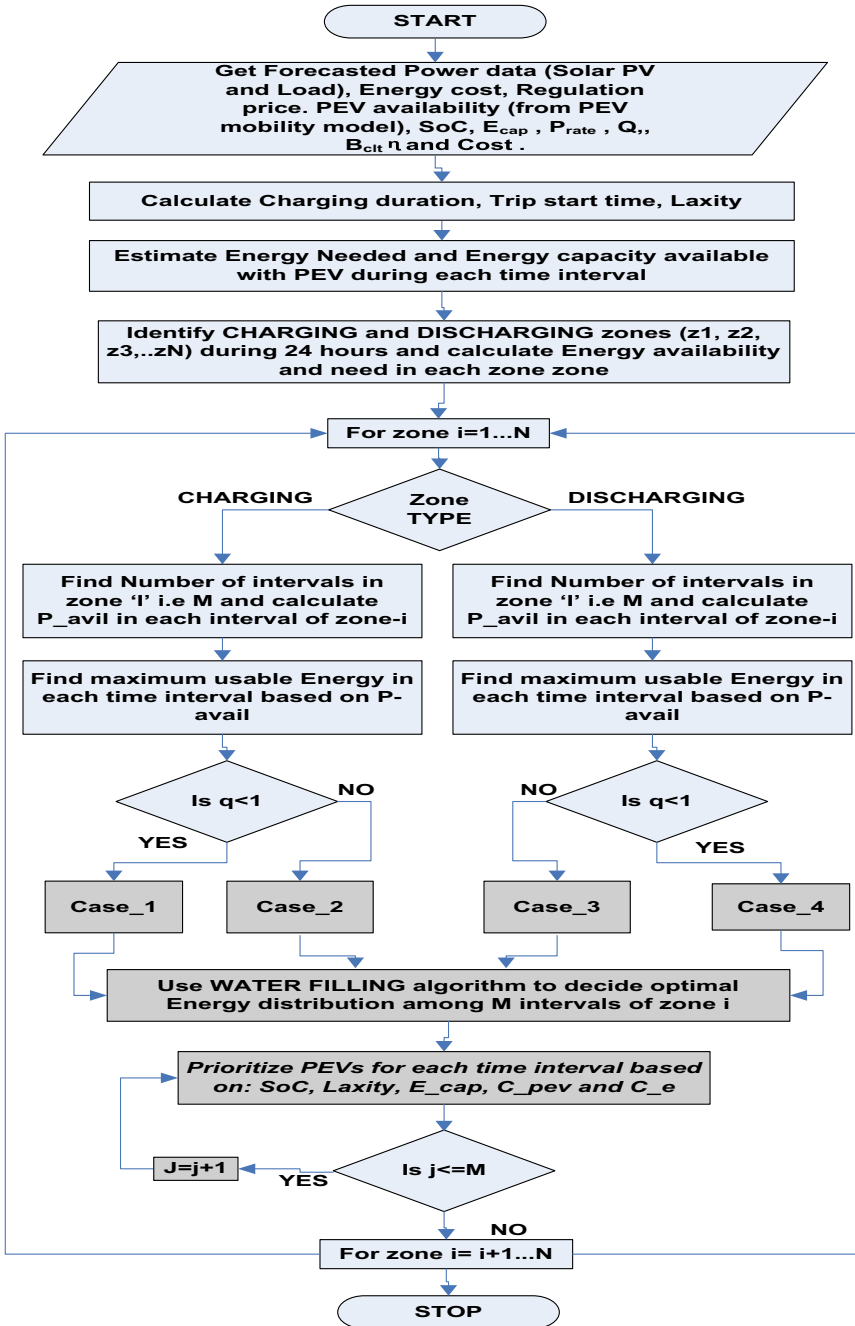
Fig. 3 Storage unit prioritization and estimation of usable energy for grid support during interval '*t*'

is taken as variance (Eq. 17). The constraints are given in Eqs. (19) and (20). The useable energy limit in each zone is restricted to not to exceed while dispatching. Aggregated power from available PEVs at a give time interval is another main constraint.

$$\sum_{t=1}^{M} \left(P_{\text{need}}^{t,\text{grid}} + \sum_{i=1}^{x} P_{\text{rate}}^{i,t,\text{pev}} + \sum_{i=1}^{y} P_{\text{rate}}^{t,i,\text{pev}} - P_{\text{spec}}^{\text{grid}} \right)^2 \tag{17}$$

In terms of energy, the above equation can be rewritten as follows:

$$\sum_{t=1}^{M} \left(E_{\text{need}}^{i,t,\text{grid}} + \sum_{i=1}^{x} \left(E_{\text{cap}}^{i,\text{pev}} - E_{\text{level}}^{i,t,\text{pev}} \right) \pm \sum_{i=1}^{y} E_{\text{pev}}^{\text{reg},t,i} - E_{\text{spec}}^{\text{grid}} \right)^2 \tag{18}$$

Under the following constraints: The constraint on maximum usable energy during zone 'z' ensures not to exceed available aggregated energy from PEVs.

$$\text{In charging zone} \quad \sum_{t=1}^{M} \sum_{i=1}^{y} E_{\text{pev}}^{\text{reg},t,i} \le E_{\text{avail},t=1}^{z,\text{pev,ch}} \tag{19}$$

$$\text{In discharging zone} \quad \sum_{t=1}^{M} \sum_{i=1}^{y} E_{\text{pev}}^{\text{reg},t,i} \le E_{\text{avail},t=1}^{z,\text{pev,dc}} \tag{20}$$

Here $E_{\text{pev}}^{\text{reg},t,i}$ is energy contribution to regulation from ith PEV at tth interval. Another constraint on usable aggregated power in each interval of zone 'z' ensures not to exceed maximum available power from aggregated sum.

$$-\sum_{i=1}^{y} P_{\text{rate}}^{i,\text{pev}} * (0.25) \le \sum_{i=1}^{y} E_{\text{pev}}^{\text{reg},t,i} \le \sum_{i=1}^{y} P_{\text{rate}}^{i,\text{pev}} * (0.25) \tag{21}$$

The value 0.25 in (21) is to convert interval into an hour so that all the terms are in kWh. While evaluating available storage from PEVs, SoC and power limits are taken into consideration based on Eqs. (4)–(6) and (12). Using Lagrange multiplier method, Eq. (18) can be deduced by adding constraint that gives Eq. (22).

$$\Gamma\left(E_{\text{opt}}^{t}, \lambda\right) = \left(E_{\text{need}}^{i,t,\text{grid}} + \sum_{i=1}^{x} \left(E_{\text{cap}}^{i,\text{pev}} - E_{\text{level}}^{i,t,\text{pev}} \right) \pm \sum_{i=1}^{y} E_{\text{pev}}^{\text{reg},t,i} - E_{\text{spec}}^{\text{grid}} \right)^2$$
$$- 2\lambda \left(\sum_{t=1}^{M} \sum_{i=1}^{y} E_{\text{pev}}^{\text{reg},t,i} - E_{\text{avail},t=1}^{z,\text{pev,ch}} \right) \tag{22}$$

By differentiating Eq. (21) with respective decision variable and equating it to zero, we get the following condition (Eq. 23) which is simplified in Eq. (24). In Eq. (24), the '+' and '−' are to indicate charging and discharging zones, respectively.

$$E_{\text{need}}^{i,t,\text{grid}} + \sum_{i=1}^{x} \left(E_{\text{cap}}^{i,\text{pev}} - E_{\text{level}}^{i,t,\text{pev}} \right) \pm \sum_{i=1}^{y} E_{\text{pev}}^{\text{reg},t,i} - E_{\text{spec}}^{\text{grid}} - \lambda = 0 \qquad (23)$$

$$\pm \sum_{i=1}^{y} E_{\text{pev}}^{\text{reg},t,i} - \lambda + \delta = 0 \qquad (24)$$

where $\delta = E_{\text{need}}^{i,t,\text{grid}} + \sum_{i=1}^{x} \left(E_{\text{cap}}^{i,\text{pev}} - E_{\text{level}}^{i,t,\text{pev}} \right) - E_{\text{spec}}^{\text{grid}}$

The symbol λ is Lagrange multiplier. The optimal energy dispatch task can be accomplished by finding height of filling (the value of 'α'), and it can be obtained using simple line search method.

PEV's owner cost minimization or maximization of revenue attracts the customer to actively participate in grid ancillary services like load flattening, voltage, and frequency regulation. But vehicle prioritization is an important issue so as to ensure equal profit (per kWh of capacity) to all customers based on their energy capacity and also laxity. ANFIS is trained with random training data obtained by manually mapping all the five inputs $\left(E_{\text{pev}}^{\text{cap}}, \_\text{SoC}, \_L_i^t, C_i^t \text{ and } C_{\text{pev}}^t \right)$ to output (priority/rank). Training data is prepared with five input variables, and a few samples of random mapping used in training data are shown in Table 1.

Table 1 Sample mapping of input variables to output (rank)—for charging case

S. No.	$E_{\text{pev}}^{\text{cap}}$	SoC	L_x^t	C_i^t	Revenue	Rank
1	0.1	0.1	0.1	0.1	0.1	0.1
2	0.3	0.3	0.3	0.1	0.3	0.3
3	0.5	0.5	0.5	0.1	0.5	0.5
4	0.7	0.7	0.7	0.1	0.7	0.7
5	0.9	0.9	0.9	0.1	0.9	0.9
6	1.0	1.0	1.0	0.1	1.0	1
7	0.9	0.9	0.9	1.0	0.9	0.9
8	0.7	0.7	0.7	1.0	0.7	0.7
9	0.5	0.5	0.5	1.0	0.5	0.5
10	0.3	0.3	0.3	1.0	0.3	0.3

The input variables are converted into per unit quantities so as to make mapping easer while preparing training data. Output (rank) is taken in between 0 and 1. Lower the rank, higher the priority given for PEV to participate in grid support and vice versa. Revenue is accounted as inverse of cost of charging ($/kWh-capacity) and cumulative sum is taken as input at each t. For a given time interval, if revenue of ith PEV is highest and if cost of electricity is very less, then that PEV is given less rank. But if SoC and capacity of ith PEV are at highest levels, then the rank is increased based on relative difference. In Table 1, few samples of training data are shown that gives the idea of inputs to output mapping is carried out. Suppose, in charging case for a particular PEV, if SoC is low, then rank should be high and vice versa. Prioritization is done with consideration of five input variables in which SoC, laxity, and capacity are pertaining to utility perspective, whereas electricity price and coast paid by PEV are considered in customer perspective.

6 Results and Discussions

An active residential distribution network with four small-scale solar PVs, residential loads, and 13 PEVs at residential plug points is considered to implement proposed methodology. Data available with DiSC (MATLAB-based distribution network simulation platform with heterogeneous entities) simulation framework is used for simulation purpose [14]. Figure 4 shows the layout of distribution network which is adopted to implement proposed methodology.
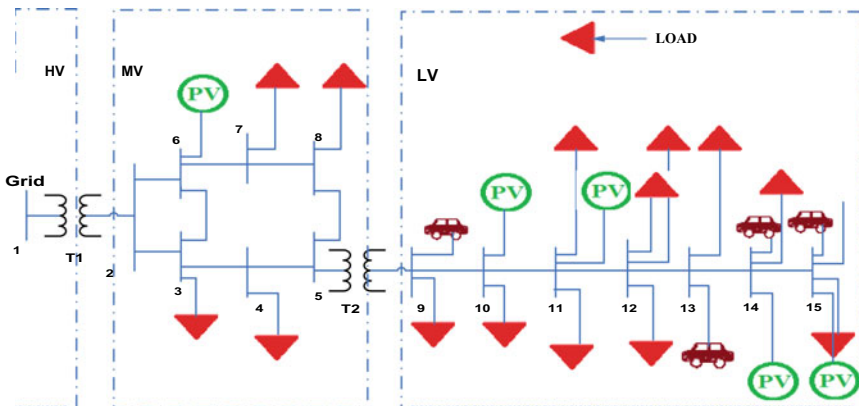
Fig. 4 Active distribution network with solar PVs and PEVs
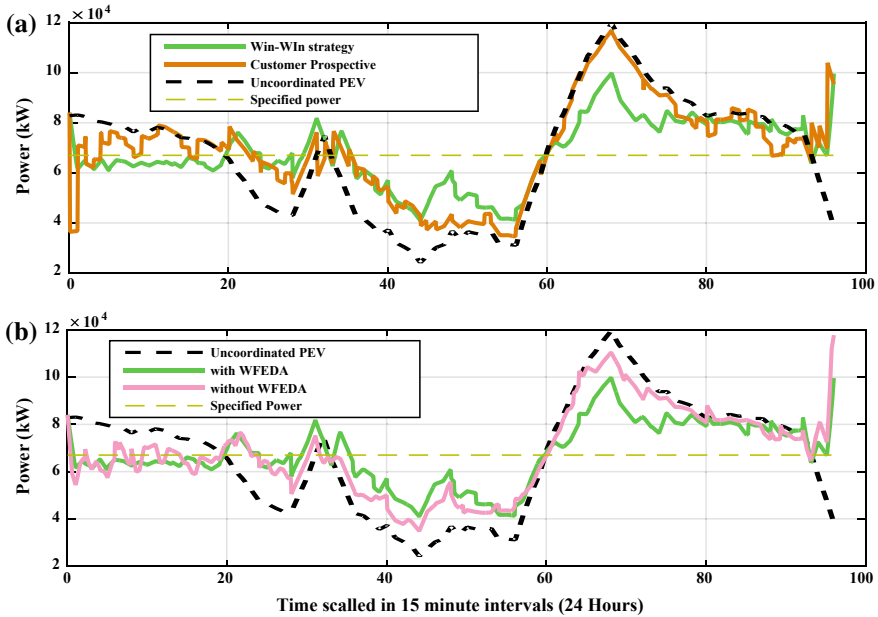
Fig. 5 Comparison of power drawn from grid: **a** from customer and utility prospective and **b** with and without WFEDA

All the four solar PVs are of same capacity (with maximum power of 10 kW). Each bus from 9 to 15 is connected with 20 houses. Buses 9, 13, 14, and 15 are connected with 1, 3, 4, and 5 number of PEVs. Fixed charging/discharging rates are considered for PEVs. And it is assumed that authenticated PEV consumers are always flexible enough to synchronize with utility operator decisions. Different cases are compared with proposed one in Fig. 5a, and the results are compared between the cases with and without WFEDA in Fig. 5b from which it can be observed that energy deficiency is present without WFEDA.

Grid power and power available from all PEVs are compared with and without prioritization (using ANFIS) based on SoC and laxity in Fig. 6a, b. Cost paid for PEV charging with and without consideration of electricity price and revenue is presented in Fig. 6c. Here the negative value of cost paid for charging indicates that owner has gained profit due to participation in grid regulation. The vehicles 12 and 13 are not gained any profit rather they paid for charging unlike others. The reason is that they are not present at plug point during low electricity price in charging case or during peak price in discharging case.
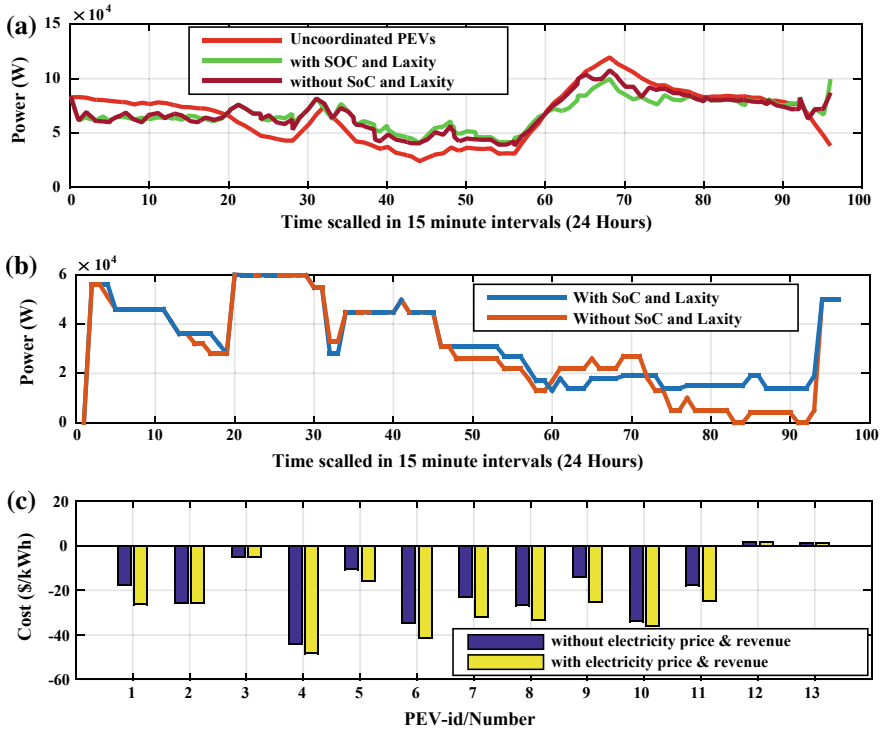
Fig. 6 Comparison of power and cost with and without SoC and laxity consideration in prioritization: **a** power drawn from grid, **b** aggregated power available with PEVs, and **c** cost paid by PEV owner with and without consideration of electricity price and revenue

7 Conclusion

WFEDA is used for this task in order to distribute energy among all time intervals in each zone based on constraints. Available storage capacity is estimated based on NTS data, and trip requirements are ensured with vehicle laxity and SoC. ANFIS is trained to prioritize PEVs based on all the variables that affect both utility and customer benefits. Hence, both utility and customer benefits are given equal importance to encourage PEV owners toward grid ancillary services. Load flattening is archived with maximum utilization of PEVs and without disturbing trip schedule.

References

1. Conti J et al (2016) International energy outlook 2016 with projections to 2040. No. DOE/EIA-0484 (2016). USDOE Energy Information Administration (EIA), Washington, DC (United States). Office of Energy Analysis
2. Shahidinejad S, Filizadeh S, Bibeau E (2012) Profile of charging load on the grid due to plug-in vehicles. IEEE Trans Smart Grid 3(1):135–141
3. Sovacool BK, Hirsh RF (2009) Beyond batteries: an examination of the benefits and barriers to plug-in hybrid electric vehicles (PHEVs) and a vehicle-to-grid (v2g) transition. Energy Policy 37(3):1095–1103
4. Rotering N, Ilic M (2011) Optimal charge control of plug-in hybrid electric vehicles in deregulated electricity markets. IEEE Trans Power Syst 26(3):1021–1029
5. Guo F, Inoa E, Choi W, Wang J (2012) Study on global optimization and control strategy development for a PHEV charging facility. IEEE Trans Veh Technol 61(6):2431–2441
6. Viswanathan VV, Kintner-Meyer M (2011) Second use of transportation batteries: maximizing the value of batteries for transportation and grid servieces. IEEE Trans Veh Technol 60(7):2963–2970
7. Tan J, Wang L (2014) Integration of plug-in hybrid electric vehicles into residential distribution grid based on two-layer intelligent optimization. IEEE Trans Smart Grid 5 (4):1774–1784
8. Han S, Han S, Sezaki K (2010) Development of an optimal vehicle-to-grid aggregator for frequency regulation. IEEE Trans Smart Grid 1(1):65–72
9. Wencong S, Mo-Yuen C (2012) Performance evaluation of an EDA-based large-scale plug-in hybrid electric vehicle charging algorithm. IEEE Trans Smart Grid 3(1):308–315
10. Gan L, Topcu U, Low S (2013) Optimal decentralized protocol for electric vehicle charging. IEEE Trans Power Syst 28(2):940–951
11. Escudero-Garzas JJ, Garcia-Armada A, Seco-Granados G (2012) Fair design of plug-in electric vehicles aggregator for V2G regulation. IEEE Trans Veh Technol 61(8):3406–3419
12. Shiyao C, Lang T, Ting H (2011) Optimal deadline scheduling with commitment. In: Proceedings of 49th annual Allerton conference communication control computing, pp 111–118
13. Clement-Nyns K, Haesen E, Driesen J (2010) The impact of charging plug-in hybrid electric vehicles on a residential distribution grid. IEEE Trans Power Syst 25(1):371–380
14. Pedersen R, Sloth C, Andersen GB, Wisniewski R (2015) DiSC: a simulation framework for distribution system voltage control. In: European control conference, Linz, Austria, July 2015
15. National Travel Survey (2012) Department of Transport, Tech. Rep., 2014 (Online). Available: https://www.gov.uk/government/publications/national-travel-survey-2014
16. Wu Q, Nielsen AH, Ostergaard J, Cha ST, Marra F, Chen Y, Traeholt C (2014) Driving pattern analysis for electric vehicle (EV) grid integration study. In: Proceedings of the IEEE PES innovative smart grid technology conference Europe (ISGT Europe), pp 1–6
17. Zhang H, Hu Z, Xu Z, Song Y (2017) Evaluation of achievable vehicle-to-grid capacity using aggregate PEV model. IEEE Transactions on Power Systems, 32(1), pp 784–794
18. Zhou XS, Rui Y, Huang TS (1999) Water-filling: a novel way for image structural feature extraction. In: Proceedings of IEEE international conference on image processing (ICIP), Kobe, Japan, pp 570–574
19. Mou Y, Xing H, Student Member, IEEE, Lin Z, Senior Member, IEEE, and Fu M, Fellow, IEEE (2014) Decentralized optimal demand-side management for PHEV charging in a smart grid

A Novel Strategic Scheduling of Plug-in-Electric Vehicles to Reduce Power Fluctuations in an Active Distribution Network

K. Ramakrishna Reddy and S. Meikandasivam

Abstract The penetration of plug-in-electric vehicles (PEVs) on the grid causes additional problems if they are not strategically scheduled for charging. Storage capacity of available PEVs can be utilized for grid ancillary support such as load flattening, voltage regulation and frequency regulation. In this work, an intelligent control strategy is developed for PEVs in order to mitigate power fluctuations caused by load demand and solar power together. The effect of PEV scheduling in coordination with energy storage units (ESU) is also analysed. An effort is made to reduce slack bus power deviations from specified value with maximum utilization of available PEV storage capacity. Day-ahead power demand and solar power generation during upcoming hours are considered while scheduling storage units (ESU and PEV). Fuzzy logic controller is implemented to decide power rate of storage units for optimal usage of PEV's storage capacity.

1 Introduction

Uncontrolled or unscheduled PEV charging will create a lot of disturbances to the utility operator in terms of frequency and voltage deviations. Solar PV which delivers maximum amount of power during mid-day time is another big concern to deal with distribution networks. Thanks to ICT which has created new opportunities to transform adverse effect of PEVs integration into an advantage. PEV proliferation can facilitate grid ancillary services such as load flattening [1], reducing cost of charging electric vehicles and improving revenue by assisting grid support [2] and more importantly to reduce spinning reserves [3] from utility prospective.

K. Ramakrishna Reddy (✉) · S. Meikandasivam
Vellore Institute of Technology, Vellore, Tamil Nadu, India
e-mail: ramu.svce@gmail.com

S. Meikandasivam
e-mail: meikandasivam@gmail.com

The transformation of legacy electric grid with integration of heterogeneous power sources like solar photovoltaic (solar PV), wind, biomass and other RES along with plug-in-electric vehicles (PEV) and energy storage units (ESU) brought so many advantages and challenges too. Solar and wind are purely dependent on weather conditions and hence power generation is naturally uncertain. Also, PEV's plugging timings are unpredictable. So, the penetration of these variants into the existing grid makes it more complex and causes degradation in the performance of power system [4]. In this scenario, if there is no real-time control and monitoring of power system all the time, it leads to poor power quality and system instability. The introduction of smart grid technologies brought unlimited possibilities in effective monitoring and control over power system. The distribution system operator (DSO) can make utilize of sophisticated technologies available in this smart grid era in order to make the grid more reliable and economical.

PEV is an important asset of the smart grid as it can be used for either to supply power to the grid (V2G) or to consume power from grid (G2V) on a schedule basis. The electric vehicle market has been dramatically increasing globally and huge change in market can be seen from 2014 to 2016 during which the market was doubled [5]. PEV integration at higher level of penetration causes voltage instability, frequency fluctuation power losses [6]. It is mainly because of increase in energy density and reduction of cost of PEV. In near future, more number of PEVs are expected to be connected to distribution grid. Uncoordinated PEVs causes problems with its uncertainties in daily charging patterns [7, 8]. On the other hand, PEV can be considered as a flexible load/source through which active and reactive power fluctuations can be suppressed. PEV is one of the best assets for demand-side management in peak load shaving and voltage regulation. Many researchers have come up with different ways of utilizing PEVs for demand-side management [9, 10]. Coordination among all the PEVs and ESUs is an important concern that determines the level of feasibility and participation in power quality improvisation.

Many authors have proposed different methodologies to exploit the available PEV storage space (G2V) and stored energy (V2G) in PEVs in order to support stochastic RES such as solar PV and wind. Authors in [11] have proposed an approach to utilize PEV aggregator to compensate fluctuations in the wind power plant. Mitigation of the collective impact of solar PV and PEV was discussed by Aguero et al. [12] and Marra et al. [13]. PEV capacity was utilized to support solar PV fluctuations instead of using separate storage [14]. Alam et al. [15] have developed a control strategy for peak load support at evening times and to reduce solar PV impact using battery storage (without PEV) integrated to solar PV.

In this work, unit commitment of storage units (ESU and PEV) and scheduling are accomplished with consideration of feature demand variation (during hour ahead). This work mainly focuses on the following factors in the proposed control strategy for scheduling of storage units:

1. Reduction of deviations in slack bus power (*P*-slack) drawn by distribution network, thereby reducing spinning reserve capacity requirement by effectively utilizing the ESU and PEV in coordination.

2. Storage units charging and discharging rates are decided based on forecasted load demand and solar PV power.
3. PEV's trip requirements are given highest priority while accounting them for grid support activity.
4. Storage unit prioritization is carried out by considering all the battery parameters that affects performance and lifetime of the battery.
5. Novel intelligent control strategy using fuzzy controller is designed to schedule both ESU and PEV strategically.

The rest of this paper is organized as follows: Sect. 2 deals with fluctuations in energy requirements; Sect. 3 is dedicated for estimation of available storage capacity. Mobility model of PEV is discussed in Sect. 4. A new control strategy for storage units scheduling was presented in Sect. 5; finally, the impacts of proposed control scheme are discussed with the help of simulation results in Sect. 6.

List of Variables and Symbols

t	Time interval (=15 min)
α	Drain rate of the battery unit
η	Battery efficiency
p	Ratio that decides charging/discharging
q	Ratio that decides excess/deficit storage
SoC	State of charge
DoD	Depth of discharge
P_{rate}^{t}	Rate of charge/discharge
$P_{\text{rate}}^{\min}$	Minimum power rating of a storage unit
$P_{\text{rate}}^{\max}$	Maximum power rating of a storage unit
$P_{\text{rate}}^{\text{dif}}$	Maximum allowable rate of change in P_{rate}^{t}
$P_{\text{rate}}^{\text{ref},t}$	Reference power rate during interval 't'
P_{load}^{t}	Aggregated average load demand during interval 't'
$P_{\text{es}}^{t,c}, P_{\text{ev}}^{t,c}$	Aggregated charging power of ESUs and PEVs during interval 't'
$P_{\text{es}}^{t,c}, P_{\text{ev}}^{t,c}$	Aggregated charging power of ESUs and PEVs during interval 't'
$\boldsymbol{ES^{in}}, \boldsymbol{EV^{in}}$	Vectors to represent ESU and PEV that are in grid support during 't'
$\boldsymbol{SoC^{ES}}, \boldsymbol{SoC^{EV}}$	Vectors of energy levels of ESU and PEV during interval 't'
ES^{N}, EV^{M}	Vectors to represent storage units that are in grid support
E_{bal}^{t}	Energy required during time interval 't'
$E_{\text{es}}^{\text{cap},i}$	Energy capacity of ith ESU
$E_{\text{ev}}^{\text{cap},i}$	Energy capacity of ith PEV
$E_{\text{es}}^{i,t}$	Energy level of ith ESU during interval 't'
$E_{\text{ev}}^{i,t}$	Energy level of ith PEV during interval 't'
$E_{\text{es}(t)}^{\text{4dish}}$	ESU energy available for discharge in tth interval
$E_{\text{es}(t)}^{\text{4chrg}}$	ESU energy available for charge in tth interval

(continued)

(continued)

$E_{ev(t)}^{4dish}$	PEV energy available for discharge in tth interval
$E_{ev(t)}^{4chrg}$	PEV energy available for charge in tth interval
$E_{avail(t)}^{4disch}$	Total available stored energy for discharge operation
$E_{avail(t)}^{4charg}$	Total available storage space for charging operation
E_{need}^{t}	Storage capacity needed during time interval 't'
E_{avail}^{t}	Storage capacity available during time interval 't'
$E_{need}^{(t+2:t+4)}$	Forecasted energy need during $(t+2)$ to $(t+4)$ intervals
E_{spec}^{slack}	Specified power drawing from grid

2 Estimation of Load and Solar PV Fluctuations

Generally, PEVs will be plugged into get charge during evening times (as soon as vehicle reaches home). Hence, inclusion PEV charging in load demand curve causes worst situation with rapid power fluctuations and voltage deviations. However, these adverse effects caused by PEVs and others can be converted into advantage with proper planning of PEV plugging (V2G and G2V). This can be achieved by strategically committing or choosing right storage unit at right time and by scheduling their charging/discharging rates. Both ESU and PEV are considered to support the grid or in other words to mitigate the impact of RES and demand fluctuations. Danish active distribution network with medium voltage level of 20 kV and low voltage level of 400 V is considered with four different types of loads, five solar PV, 13 PEVs, three ESUs and other entities [16]. All the PEVs are connected to residential side (low voltage).

In this work, a complete day is considered and each hour is sliced into four equal intervals (each is of 15 min duration). From Eq. (1) in which each term represents an aggregated power of respective load and source. The terms in right-hand side of Eq. (1) represents Solar PV power, load power, ESS charging power, PEV charging power, ESS discharging power and PEV discharging power, respectively. Power balance P_{bal}^{t} is calculated (from Eq. 1) and thereby energy balance is calculated at the end of each 15th min using Eq. (2). E_{bal}^{t} is the estimated energy that the grid has to supply during time interval $(t+1)$. The $E_{bal}^{t+2:t+4}$ is the energy requirement during $(t+2)$ to $(t+4)$ which is taken from historical data of the same day of previous week.

$$P_{bal}^{t} = P_{res}^{t} - P_{load}^{t} - P_{es}^{t,c} - P_{pev}^{t,c} + P_{es}^{t,dc} + P_{pev}^{t,dc} \tag{1}$$

$$E_{\text{bal}}^t = \int_{t=1}^{t+15} P_{\text{bal}}^t(t) * \mathrm{d}t \qquad (2)$$

$$E_{\text{sneed}}^t = E_{\text{bal}}^{t+1} - E_{\text{spec}}^{\text{slack}}$$

Charging and discharging modes of operations for storage are decided based on E_{bal}^{t+1} and $E_{\text{spec}}^{\text{slack}}$. The ratio of E_{bal}^{t+1} and $E_{\text{spec}}^{\text{slack}}$ is taken as p. If $p < 1$, it implies that the energy required from grid to distribution network is lesser than the specified value (storage units are kept in charging mode). If $p > 1$, it implies that the energy required from grid to distribution network is greater than the specified value (storage units are kept in discharging mode)

$$p = E_{\text{bal}}^{t+1} / E_{\text{spec}}^{\text{slack}}$$

3 Available Storage Capacity Estimation

3.1 ESU and PEV Penetration

Continuous monitoring of energy levels of storage units (both ESU and PEV) is required to schedule the charging and discharging operations. It has been assumed that DSO has enabled with sophisticated communication and information technologies. It is also assumed that the owner of PEV has got an agreement to participate in grid support activities (ancillary services like voltage and frequency regulation and demand-side management). The revenue to the PEV's owners during grid support will be decided by utility and the cost analysis regarding this is not studied in this work.

$\boldsymbol{SoC^{ES}} = \begin{bmatrix} \text{SoC}_1^{\text{ES}} & \text{SoC}_2^{\text{ES}} & \cdots & \text{SoC}_N^{\text{ES}} \end{bmatrix}$ is the vector representation of state of charge (SoC) of 'N' number of ESUs and $\boldsymbol{SoC^{EV}} = \begin{bmatrix} \text{SoC}_1^{\text{EV}} & \text{SoC}_2^{\text{EV}} \cdots \text{SoC}_N^{\text{EV}} \end{bmatrix}$ represents SoC of 'M' number of PEVs. Calculating SoC and finding its viability for grid support is an easy job in case of static storage units (ESU). On the other hand, it is very difficult task in the case of PEV. Probability model of vehicle availability for grid support has been estimated with the help of data availed from National Travel Survey (NTS), Great Britain [16]. The further discussions about PEV mobility model discussed in Sect. 4.

3.2 Available Capacity in ESU and PEV

Net available storage space (for charging) and stored energy (for discharging) are considered under battery constraints that affects the lifetime and performance.

Battery lifetime depends on so many factors, and it is a complicated issue to analyse for a particular application with consideration of all the parameters [15]. One of the main objectives of this work is to determine P_{rate}^t by ensuring the energy fluctuations in the hours ahead, available storage capacity, energy needed during present time interval and trip requirements.

Energy level (SoC), change in P_{rate} and rate of change in P_{rate} are controlled under the constrains shown in Eq. (3). It is preferable to maintain SoC in between 20 and 80% of its full capacity. However, aging of battery still reduces these boundaries.

$$\text{Battery constraints}: \quad \text{SoC}_{min} \leq \text{SoC}(t) \leq \text{SoC}_{max}$$
$$P_{rate}^{min} \leq P(t) \leq P_{rate}^{max}$$
$$P_{rate}^t \leq \left| P_{rate}^{t-1} - P_{rate}^{ref} \right| \tag{3}$$

Storage Unit Commitment Based on Constraints and PEVs Availability Depending on the availability of PEV storage space, availability for grid support and other factors that affects the battery lifetime are considered in prioritizing storage units for grid support. The prioritization process is accomplished as shown in the following steps.

(1) Identifying the storage units (ESU and PEV) to participate in grid support (only available PEVs are considered from mobility model discussed in Sect. 4).
(2) ESUs that are within SoC limits are taken into consideration.
(3) PEVs that are about to leave immediately are preferred for charging mode and those are about to stay long at plug point are chosen to operate discharge mode.
(4) Charging rate of PEV which about to leave for a trip is decided individually based on SoC level, maximum power rate and time left.
(5) The storage units that are outside the SoC limits are eliminated.
(6) In case of excess storage capacity, the storage units eliminated based on SoC levels and DoD is reduced for those that are participating.
(7) If the required storage capacity is lesser than the available capacity (charging/discharging), then next level of filtering will be initiated through step-2.

Total available capacity for discharging is taken as the sum of all storage units energy levels after filtering process. Equations (4) and (5) give storage capacity available during time interval 't'. As already mentioned, 24 h are sliced into 96 intervals each spans for 15 min duration. Vectors $\boldsymbol{ES^{in}} = [0\,1\,1\,1\,0\,0\ldots0]$ and $\boldsymbol{EV^{in}} = [0\,1\,1\,1\,0\,0\ldots0]$ give information about PEVs and ESUs' participation in grid support. Here '0' represents that the particular storage unit is not participating during grid support and '1' represents the vehicle availability.

$$E_{es(t)}^{4dish} = \sum_{i=1}^{N} \left\{ \left[E_{es}^{i,t} \right] - \left[0.2 * E_{es}^{cap,i} \right] \right\}$$

$$E_{ev(t)}^{4dish} = \sum_{i}^{M} \left\{ \left[E_{es}^{i,t} \right] - \left[0.2 * E_{es}^{cap,i} \right] \right\}$$

$$E_{es(t)}^{4chrg} = \sum_{i=1}^{N} \left\{ \left[0.8 * E_{es}^{cap,i} \right] - \left[E_{es}^{i,t} \right] \right\}$$

$$E_{ev(t)}^{4chrg} = \sum_{i=1}^{M} \left\{ \left[0.8 * E_{ev}^{cap,i} \right] - \left[E_{ev}^{i,t} \right] \right\}$$

$$E_{avail(t)}^{4disch} = E_{es}^{4dish}(t) + E_{ev}^{4dish}(t) \tag{4}$$

$$E_{avail(t)}^{4charg} = E_{es}^{4charg}(t) + E_{ev}^{4charg}(t) \tag{5}$$

$$E_{savail}^{t} = \begin{cases} E_{avail(t)}^{4disch} & \text{for discharing} \\ E_{avail(t)}^{4charg} & \text{for charing} \end{cases}$$

$$E_{sneed}^{t} = \begin{cases} \text{For Discharing;} & \text{if } p > 1 \\ \text{For Charing;} & \text{if } p < 1 \end{cases}$$

The ratio of E_{savail}^{t} and E_{sneed}^{t} is represented by 'q'. $q < 1$ indicates deficit in available storage capacity and $q > 1$ indicates that excess in available storage capacity.

$$q = E_{savail}^{t} / E_{sneed}^{t}$$

Next levels of eliminating the storage unit depend on the value of q (as mentioned above in step 5). So, charging and discharging mode will be decided by the value of p.

4 PEV Mobility Model

To find the PEV arrival time, departure time and SoC after arrival the Eq. (6) has been used. NTS data [NTS0503 (trip purpose), NTS0405 (average trip length) and NTS0409 (average number of trips)] have been considered in this work to estimate probability of vehicle availability at charging point and energy spent during trip [16]. During vehicle unavailability, the P_{rate}^{t} and E are taken as zero. After the

completion of trip, the SoC level of PEV is calculated by using total trip length
L (km) and mileage Υ (kWh/km) as shown in Eq. (6).

$$P_{\text{rate}}(\boldsymbol{t}) = \begin{cases} P_{\text{rate}}^{\text{ref}}(t) & \text{if } \text{avail}(t) = 1 \\ 0 & \text{if } \text{avail}(t) = 0 \end{cases}$$

$$\text{SoC}_{\text{new}}^{\text{ev}} = \begin{cases} \text{SoC}_{\text{old}}^{\text{ev}} - \Upsilon L; & \text{if } \text{avail}(t) = 1 \text{ and } \text{avail}(t-1) = 0 \\ 0; & \text{if } \text{avail}(t) = 0 \end{cases} \tag{6}$$

Here, $\text{SoC}_{\text{new}}^{\text{ev}}$ is SoC pf PEV after finishing the trip, $\text{SoC}_{\text{old}}^{\text{ev}}$ is SoC level of PEV
before starting the trip, $\text{avail}(t)$ indicates availability of PEV during time interval
't', Υ is the mileage of PEV, L is length travelled.

5 Novel-coordinated Control Strategy for ESU and PEV

5.1 Mode of Storage Unit and Constraints Applied

Charging Mode If the ratio 'p' is greater than 1, then it indicates charging mode of
operation. If the ratio 'q' is greater than 1, then it indicates that the storage space
available for charging is more than what is required and q less than 1 reflects the
opposite case.

Discharging Mode If the ratio p is less than 1, then it indicates discharging mode of
operation and the ratio q decides excess or deficit in stored energy for discharging.
If q is greater than 1, then it indicates available stored energy for discharging is
more than what is required and if q is less than 1 reflects opposite case.
The power rate of charging or discharging $\left(P_{\text{rate}}^{t}\right)$ is bounded by the limits $P_{\text{rate}}^{\text{min}}$,
$P_{\text{rate}}^{\text{max}}$ and $P_{\text{rate}}^{\text{dif}}$(rate of change in power rate). Charging mode is considered as
consumption ($-$ve), and discharging mode is considered as generation ($+$ve). The
P_{rate}^{t} constraints are also bounded by SoC limitations. Rate of change in P_{rate}^{t} which
is indicated as $P_{\text{rate}}^{\text{dif}}$ is another constraint applied to limit abrupt change in P_{rate}^{t}, and
it is shown in Eq. (9). SOC at the end of $(t + 1)$th interval starting time is calculated
using Eq. (9); here, α is drain rate (here taken as 1), and η represents efficiency of
the battery (considered same for both charging and discharging).

$$P_{\text{rate}}^{t} = \begin{cases} P_{\text{rate}}^{\text{min}}; & \text{if } 0 < \text{SoC} < \text{SoC}_{\text{max}} \text{ and } P_{\text{rate}}^{\text{ref},t} < P_{\text{rate}}^{\text{min}} \\ P_{\text{rate}}^{\text{max}}; & \text{if } 0 < \text{SoC} < \text{SoC}_{\text{max}} \text{ and } P_{\text{rate}}^{\text{ref},t} < P_{\text{rate}}^{\text{max}} \\ P_{\text{rate}}^{\text{ref}}; & \text{if } 0 < \text{SoC} < \text{SoC}_{\text{max}} \text{ and } P_{\text{rate}}^{\text{min}} < P_{\text{rate}}^{\text{ref},t} < P_{\text{rate}}^{\text{max}} \end{cases} \tag{7}$$

$$P_{\text{rate}}^{t} = \begin{cases} P_{\text{rate}}^{(t-1)} - P_{\text{rate}}^{\text{dif}} & \text{if } \left| P_{\text{rate}}^{\text{ref},t} - P_{\text{rate}}^{(t-1)} \right| > P_{\text{rate}}^{\text{dif}} \\ P_{\text{rate}}^{(t-1)} + P_{\text{rate}}^{\text{dif}} & \text{if } \left| P_{\text{rate}}^{\text{ref},t} - P_{\text{rate}}^{(t-1)} \right| < P_{\text{rate}}^{\text{dif}} \end{cases} \tag{8}$$

$$\mathrm{SoC}(t+1) = \alpha\,\mathrm{SoC}(t) \pm t\eta P_{\mathrm{rate}}(t) \tag{9}$$

5.2 Proposed Control Strategy for ESU and PEV

In this paper, the main contribution reflects in consideration of energy fluctuations during the hours ahead, slicing each hour into four uniform intervals and consideration of the factors that affects battery performance degradation. From Fig. 1, it can be seen that there is power requirement from the grid all the time (i.e., local generation is always lesser than the minimum demand). But, due to the stochastic nature of load and solar power, power drawing from the main grid (slack bus power) is fluctuation around a specified value.

Energy demand from the grid for the upcoming time interval $(t+1)$ is calculated using the average power consumption at the end of previous interval of time (t). From the historical data, the energy demand need from the grid is calculated for next three consecutive time intervals. It is done by taking average of energy demands during $(t+2)$th, $(t+3)$th and $(t+4)$th time intervals. So, one complete hour has been considered to account the demand fluctuations that are expected to arise.

After applying the battery constraints, available storage capacity is calculated and compared with energy needed. The value of 'p', which is the ratio of energy demand $\left(E_{\mathrm{dmnd}}^{t}\right)$ to expected grid energy $\left(E_{\mathrm{spe}}^{t}\right)$ during interval 't' decides whether
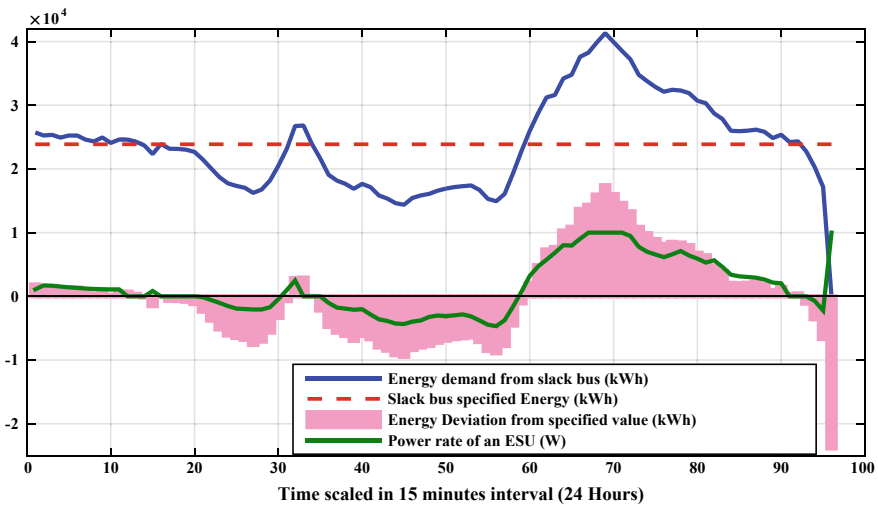
Fig. 1 Aggregated power fluctuations (around specified/average load) in power drawing from slack bus and respective P_{rate}^{t}

charging operation ($p < 1$) or discharging operation ($p > 1$). Here, supporting grid implies reduction of energy demand fluctuations on grid. The value of 'q', which is the ratio of storage availability $\left(E_{savail}^{t}\right)$ to storage capacity needed $\left(E_{sneed}^{t}\right)$ decides whether excess ($q > 1$) or deficit ($q < 1$) storage capacity during time interval.

The vectors ES^{in} and EV^{in} represents the storage unit's participation in grid support. In these vectors, '1' indicates storage unit participation and '0' indicates no-participation in grid support. In case of deficit storage capacity, maximum utilization of storage is preferred for both charging and discharging operations. On the other hand, the excess capacity available gives choice to schedule the storage units depending on utility requirements. In this case, as a first step, the storage units which are suitable to participate (within constraints) are selected.

5.3 Design of Fuzzy Controller to Set P_{rate}^{t}

Fuzzy controller is used to take decision on P_{rate}^{t}. As mentioned in the previous section, 15 min duration is considered as the time interval during which P_{rate}^{t} is maintained constant. As we go on reducing the time span of interval and altering control mechanism, performance of the proposed control scheme can be improved. But more frequent changing of P_{rate}^{t} is not preferable as it affects the battery lifetime and performance. At the same time, high power rates are not preferable and hence an optimal power rate based on all the constraints need to be chosen. Input variables (decision variables) for the fuzzy controller are taken as: energy need E_{need}^{t}, energy available E_{avail}^{t} and forecasted energy average demand in the next three consecutive time intervals $E_{need}^{(t+2:t+4)}$ (next three consecutive time intervals). Output is taken as the power rate reference $\left(P_{rate}^{ref}\right)$ at which charge or discharge should be done, so that there would not be much deviation (P-slack) in the next time intervals also.

P_{rate}^{t} for each storage unit (ESU or PEV) depends on its rated value of the particular storage unit and percentage set by the fuzzy controller output. Mandani-type fuzzy inference system and triangular membership functions are used for both input and output variables. Inputs and output variables are classified into five membership functions (LOW MEDIUM_LOW MEDIUM MEDIUM_HIGH HIGH). Output of fuzzy controller lies from 0 to 100 which indicates percentage of maximum power rate. This output is taken as reference power rate $P_{rate}^{ref,t}$ and new power rate will be set for each storage unit based on Eq. (8). Rules are framed in such a way that the P_{rate} value is chosen to satisfy all the three inputs. As an example, if E_{need}^{t} is in L while E_{avail}^{t} and $E_{need}^{(t+1:t+4)}$ are in H then P_{rate}^{t} is L. If E_{need}^{t} is in H while E_{avail}^{t} and $E_{need}^{(t+1:t+4)}$ are in H and L, respectively, then P_{rate}^{t} is H.

6   Results and Discussion

The proposed control strategy is implemented in a 20 kV medium voltage
(MV) distribution network with 400 V low voltage (LV) feeders. The 60 kV bus is
considered as slack bus. Different loads (house, commercial, industrial and agri-
culture) are connected in both MV and LV feeders. Danish electric grid real-time
data (DiSC—a MATLAB-based simulation plot form for smart grid simulation with
heterogeneous entities [17]) is used to investigate the proposed control strategy.
Five solar PV units are connected—one at MV level and four at LV level.
Four ESU units and 13 residential PEVs are connected in the LV network.

A clear comparison in between the cases with and without PEV support is shown
in Fig. 2a, and respective deviations of P-slack are represented with the help of
histogram in Fig. 2b, c. The specified value of power from slack bus is taken as
65 kW with 10% deviation in this case (between 60 and 70 kW). It can be seen
from Fig. 2b that P-slack deviations are violated the limits (without PEV support).
In Fig. 2c, deviation is limited in the boundaries (between 60 and 70 kW) for
maximum duration.
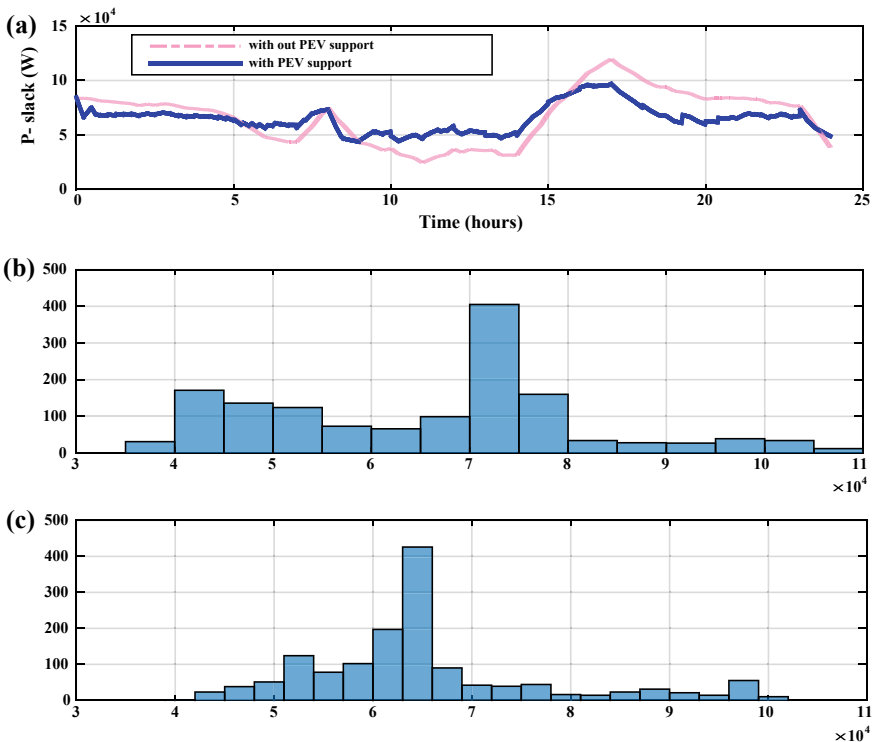
Fig. 2   **a** P-slack comparison with and without PEV support. **b** P-slack deviation from specified
value without PEV support. **c** P-slack deviation from specified value with PEV support

Another comparison is made with different power rate settings (power rates around the optimal power rate decided by the fuzzy controller) for storage units in Fig. 3a. Also, the standard deviation values are compared with uncoordinated PEV case (Fig. 3a). It can be seen that the uncoordinated case of PEV is showing around 40 kW deviation at maximum, whereas the best case with the proposed strategy is
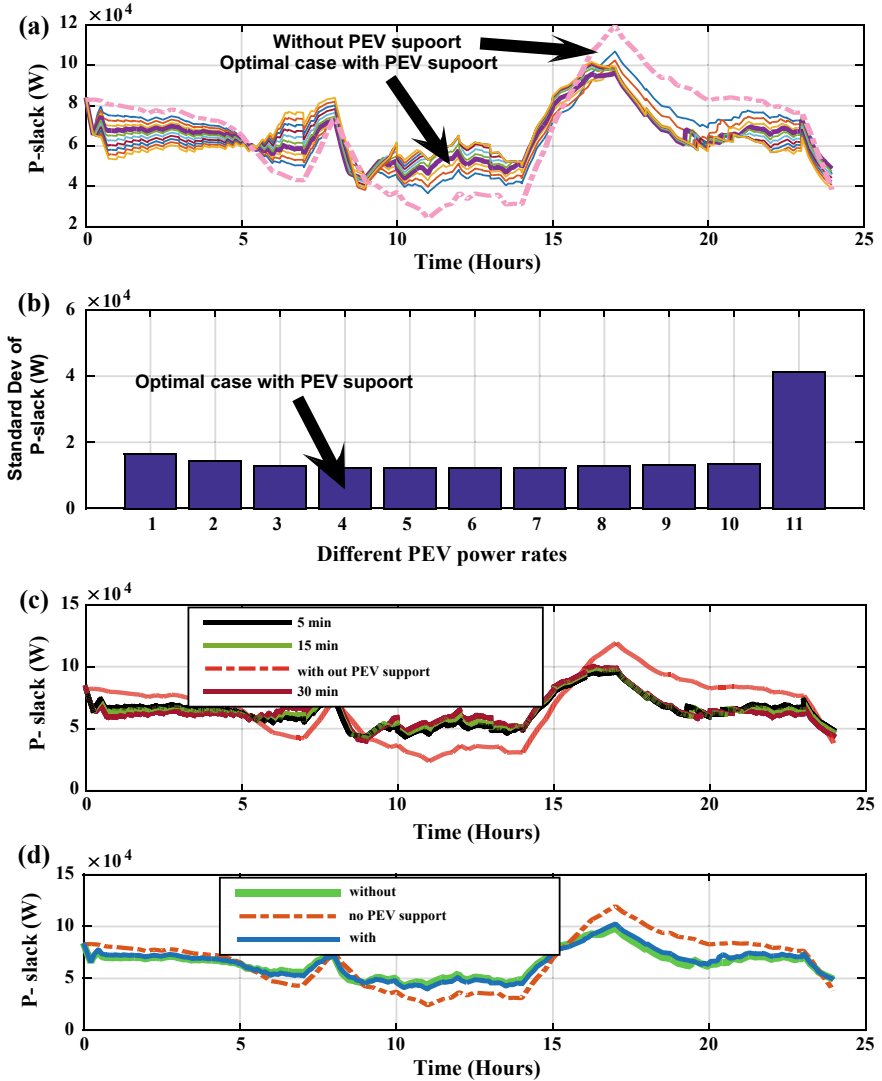
Fig. 3 **a** Comparison of P-slack in different charging/discharging rates. **b** Comparison of standard deviation in P-slack for (**a**). **c** Time interval slicing effect on P-slack. **d** With and without consideration of energy fluctuations during upcoming hour $\left(E_{\text{need}}^{(t+1:t+4)}\right)$

showing just in and around 10 kW deviation (in Fig. 3b, fourth bar indicates the best case, whereas eleventh bar indicates uncoordinated PEV case).

Duration of time interval slicing effect on P-slack deviation is shown in Fig. 3c with three different time intervals (5, 15 and 30 min). Lesser the time interval span, lesser will be the deviation of P-slack as the control action can be well coordinated with current power fluctuations. However, frequency of altering and setting power rates for storage units affects battery lifetime. Hence, a suitable time interval has to be chosen for better battery lifetime. In this work, 15-min duration is considered in a randomly manner and the study is not focused on optimal duration of time interval. However, it mainly depends on data available.

The case with consideration of power fluctuation during hours ahead is compared with the case without consideration (shown in Fig. 3d). If future energy requirement is not taken into account, optimal usage of storage can be achieved as it effects energy availability for next time interval. This work can be extended by including other parameters which influences PEV's owners' profit and economy analysis while utilizing for grid support.

7 Conclusion

In this work, an attempt is made to maximize the utilization of available PEV's storages in coordination with ESU. Mitigating the impact of solar and wind along with demand fluctuations at distribution level effectively reduces the spinning reserve capacity. This will be more prominent if all the individual distribution networks connected to main grid can precisely handle the scheduling process of ESU and PEV units. This paper mainly focuses on effective utilization of both ESU and PEV storage capacities in coordination.

References

1. Rotering N, Ilic M (2011) Optimal charge control of plug-in hybrid electric vehicles in deregulated electricity markets. IEEE Trans Power Syst 26(3):1021–1029
2. Guo F, Inoa E, Choi W, Wang J (2012) Study on global optimization and control strategy development for a PHEV charging facility. IEEE Trans Veh Technol 61(6):2431–2441
3. Viswanathan VV, Kintner-Meyer M (2011) Second use of transportation batteries: maximizing the value of batteries for transportation and grid servieces. IEEE Trans Veh Technol 60(7):2963–2970
4. Kushalini S, Solanki JM, Schulz NN (2007) Development of 3-phase unbalanced power flow using PV and PQ models for DG and study of impact of DG models. IEEE Trans Power Syst 22(3):1019–1025
5. Global EV (2016) Outlook 2016, beyond one million electric cars. France, International Energy Agency

6. Deilami S, Masoum AS, Moses PS, Masoum MAS (2011) Real-time coordination of plug-in electric vehicle charging in smart grids to minimize power losses and improve voltage profile. IEEE Trans Smart Grid 2(3):456–467
7. Clement-Nyns K, Heasen E, Driesen J (2010) The impact of charging hybrid plug-in electric vehicles on a residential distribution grid. IEEE Trans Power Syst 25(1):371–380
8. Sikai H, Infield D (2010) The impact of domestic plug-in hybrid electric vehicles on power distribution system loads. In: Proceedings of international conference power system technology (POWERCON), Hangzhou, China, pp 1–7
9. Padiha-Feltrin A, Rodezno DAQ, Mantovani RA (2015) Volt-VAR multi objective optimization to peak-load relief and energy efficiency in distribution networks. IEEE Trans Power Deliv 30(2):618–626
10. Hu W et al (2013) Optimal operation of plug-in electric vehicles in power systems with high wind power penetration. In: IEEE Trans Sustain Energy 4(3):577–585
11. Vaya MG, Anderson G (2016) Shelf scheduling of plug-in electric vehicle aggregator to provide balancing services for wind power. IEEE Trans Sustain Energy 7(2):886–899
12. Aguero JR et al (2012) Integration of plug-in electric vehicles and distributed energy resources on power distribution systems. In: Proceedings of IEEE international electric vehicle conference (IEVC), Greenville, SC, USA, pp 1–7
13. Marra F et al (2013) EV charging facilities and their application in LV feeders with photovoltaics. IEEE Trans Smart Grid 4(4):1533–1540
14. Marra F et al (2013) Improvement of local voltage in feeders with photovoltaic using electric vehicles. IEEE Trans Power Syst 28(3):3515–3516
15. Alam MJE, Muttaqi KM, Sutanto D (2013) Mitiogation of rooftop solar PV impacts and evening peak support by managing available capacity of distributed energy storage systems. IEEE Trans Power Syst 28(4):3874–3884
16. Pedersen R, Sloth C, Andersen GB, Wisniewski R (2015) DiSC: a simulation framework for distribution system voltage control. In: European control conference, Linz, Austria, July 2015
17. National Travel Survey (2012) Department of Transport, Tech. Rep., 2014 (Online). Available: https://www.gov.uk/government/publications/national-travel-survey-2014

Design of an Effective Control Structure to Grid-Interfaced Solar Inverter with Fault Stability Performance

Krishna Chaitanya Marri, Sambasivarao Gudapati, Amarendra Matsa and M. A. Chaudhari

Abstract Grid-interfaced solar power generation is intensifying its importance day to day due to the less cost and performance led to installation of MW solar power plants. With the increased system network, reliability and stability are most considerable factors. Under abnormal and faulted conditions, system has to connect to utility to improve stability of the system by supporting reactive power according to grid standards. In this research work, an advanced algorithm with efficient control structure has developed under different fault conditions (LLLG and LG faults). The research conclusions presented in this work will be helpful for the next-level smart grid control actions.

Keywords Power electronics · Solar power and reactive power control

1 Introduction

Solar energy generation capacity is continuously increasing rapidly last ten years due to the reduction of PV panels cost and social awareness improvement. But, as the MW of solar power is emerging to grid, the system has to face certain challenges like majorly stability and power quality [1]. More number of research

K. C. Marri
Acharya Nagarjuna University, Guntur 522510, India
e-mail: mleela.venkata@gmail.com

S. Gudapati
R.V.R. & J.C. College of Engineering, Guntur 522019, India
e-mail: sambasiva.gudapati@gmail.com

A. Matsa (✉)
KITS, Guntur 522017, India
e-mail: amarmeetsyou@gmail.com

M. A. Chaudhari
VNIT, Nagpur 440010, India
e-mail: macavc@yahoo.com

attempts are done to simulate and investigate the grid-interfaced system stability [2–5]. The solar power penetration will be helpful to increase the system stability and also increase reactive power support to system [6–8]. This paper presented the objective of solar power grid-integrated control system with preforming fault stability tolerance.

2 Grid-Interfaced Solar Inverter Under Fault Conditions

Figure 1 shows a simplified diagram of a solar energy system connected to the grid network. The system is connected with the solar power source, controlled grid-interfaced inverter and the utility grid.

2.1 Reference Reactive Current Calculation During Voltage Disturbances

Reactive current injection during fault and recovery is required to minimize the voltage drop in the grid and to ensure a fast voltage recovery after the failure. Depending on the voltage at the PCC, the grid-interfaced inverter has to feed in a certain reactive current as shown in Fig. 2. This support improves the stability of the power system and increases the quality and reliability of the network. The parameters of the reactive standard curve [9] vary depending on the regulations of each country; however, efforts are being made to unify the criteria of this requirement.

2.2 Proposed Control Scheme

Figure 3 shows the flowchart of the control algorithm of grid-interfaced solar system under fault conditions. If RMS value of PCC is within the range of 0.9–1.1 pu, the system is operating under steady-state condition. At normal steady-state condition, the active and reactive power at PCC is calculated, and these values are

Fig. 1 Grid-connected solar inverter
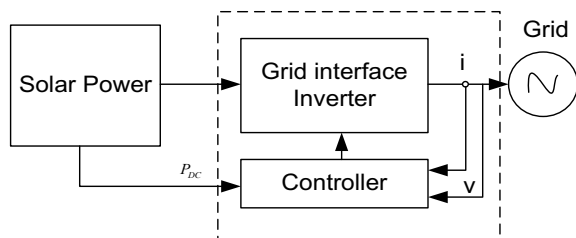
Fig. 2 Reactive current requirement adopted from Spanish GC
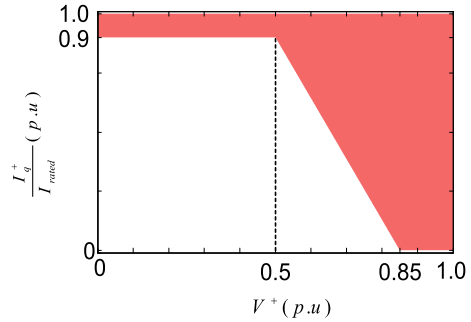
used to find maximum value to injected reactive power. However, if voltage is not in the prescribed range, then the system is under abnormal faulted conditions.

In the fault conditions, system must be connected and support more demanded reactive power to the grid to improvise the stability of the system. The reactive power demand supplied is based on the fault condition and the voltage drop of a PCC shown in Fig. 2. The reference q-component of current is determined based on voltage drop; this will influence the reactive power injection to the grid. Finally, controlled current signals are given to the modulation method of the gird inverter, which generates controlled pulses to the inverter switches.

3   Results and Analysis

A three-phase ground (symmetrical LLLG) fault is initiated at the utility at $t = 0.05$ s and recovered at $t = 0.2$ s shown in Fig. 4. There is a small transient increase in PCC current from steady-state condition due to the parasitic capacitance. The PCC current is observed as balanced at the faulted duration, because the system is balanced under LLLG fault condition. At $t = 0.2$ s (fault recovery condition), again the transient nature in the PCC current is emerged.

During the fault, RMS voltage at PCC is dropped to zero per unit from normal condition; this will cause reduction of I_{dref} to zero shown in Fig. 5.

The reduced capacity of reference current is allocated to I_{qref} to compensate reactive power demand during fault. After the fault cleared, the d-axis currents reach normal condition and q-axis currents will be zero per unit. The active and reactive powers at PCC during the fault (shown in Fig. 6) collapse to zero due to the zero PCC voltage.

From Fig. 7 solar PV voltage, MPP voltage and PV current are observed. At $t = 0.05$ s, the PV voltage is increased to supply reactive currents and PV current is reduced to zero. At fault recovery condition, PV voltage reduced and current increased to normal conditions.
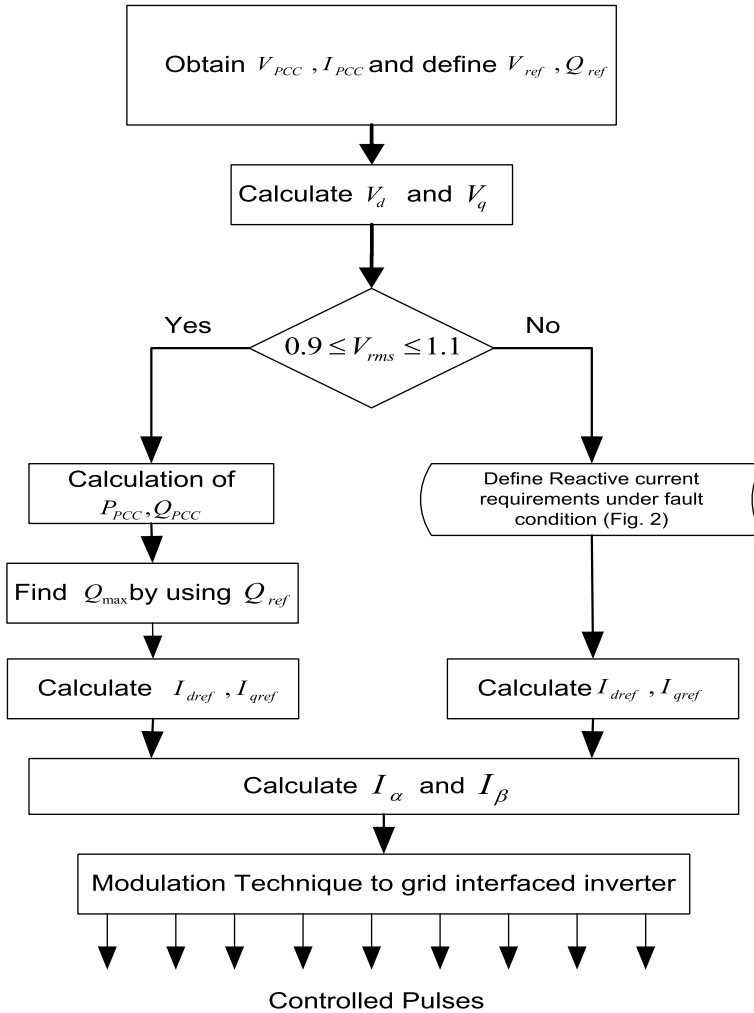
Fig. 3 Flowchart of proposed control algorithm

In Fig. 8 a LG fault is observed at AC host system at $t = 0.05$ s. It is observed that the utility system behaves unbalanced at fault duration and current at PCC will also be observed unbalanced.
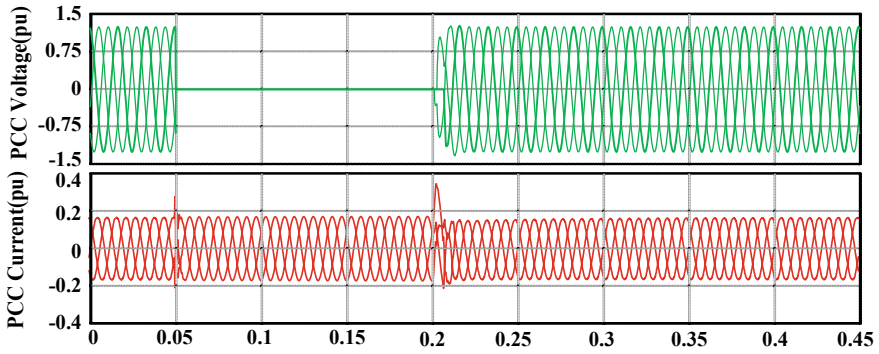
Fig. 4 Voltage and current at PCC during a three-phase ground fault (LLLG fault)
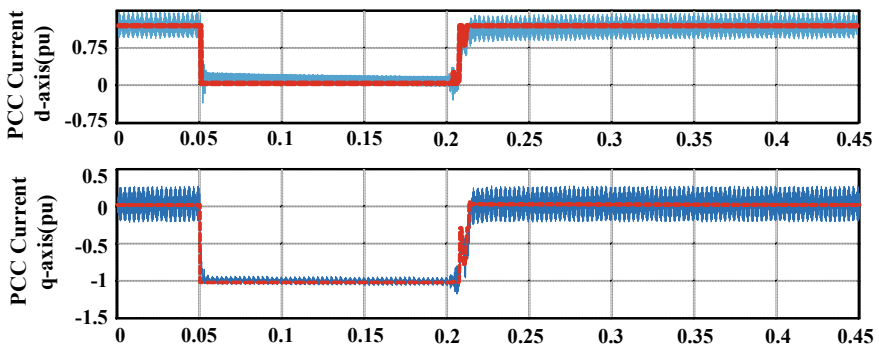
Fig. 5 PCC *d*-axis and *q*-axis currents merged with reference (redline) *d*-axis and *q*-axis currents with LLLG fault
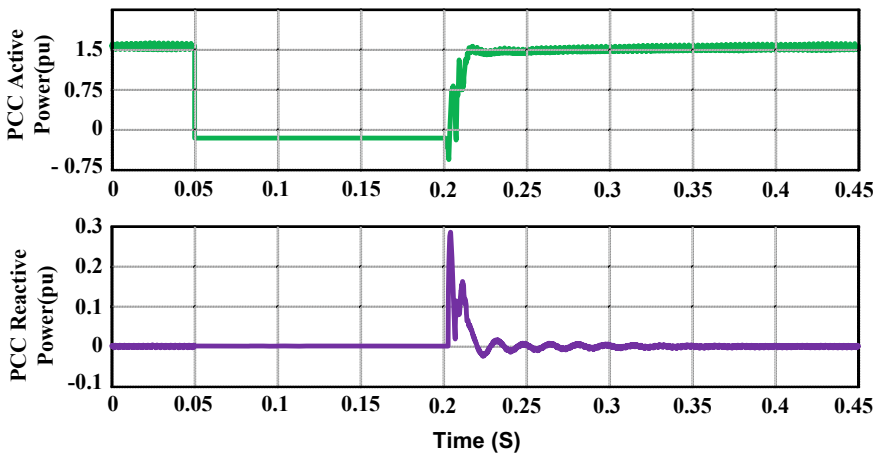
Fig. 6 Active and reactive power at PCC with LLLG fault
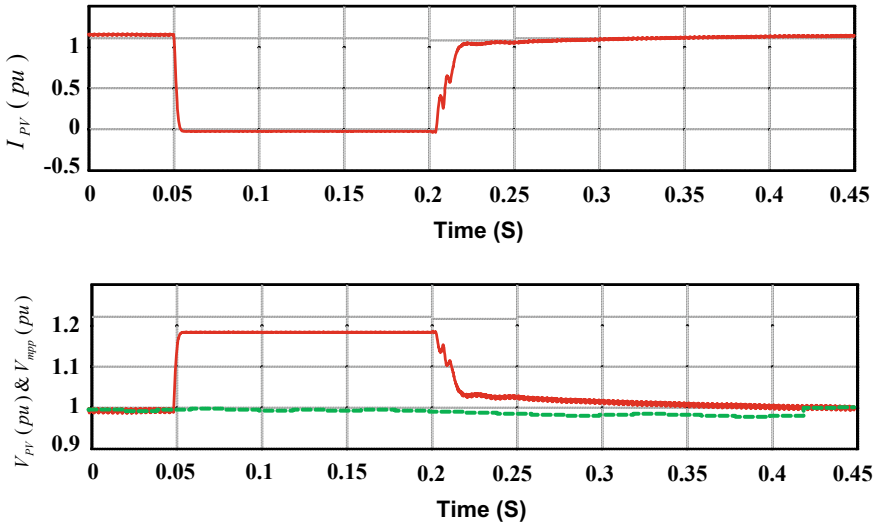
Fig. 7 V_{pv}, V_{Mpp} and I_{pv} with LLLG fault
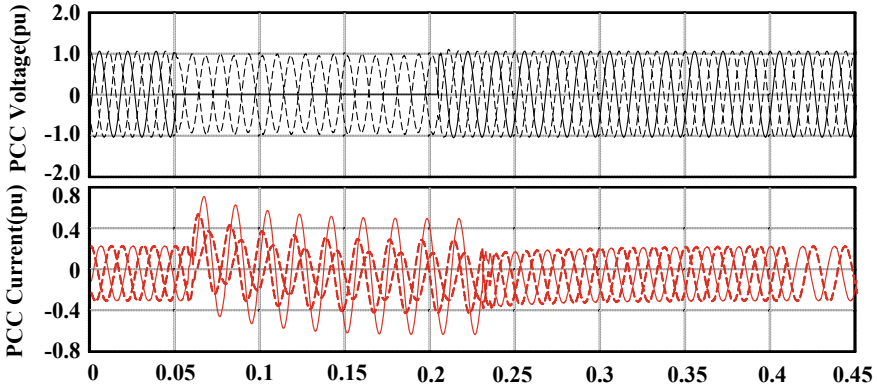
Fig. 8 Voltage and current at PCC during a three-phase ground fault (LG fault)

Due to the existence of negative sequence components during the fault, the active and reactive power at PCC consists in oscillations because the power exchange takes place between solar system and unbalanced AC system as shown in Fig. 9.

These oscillations are also present in solar system voltage and currents as shown in Fig. 10.
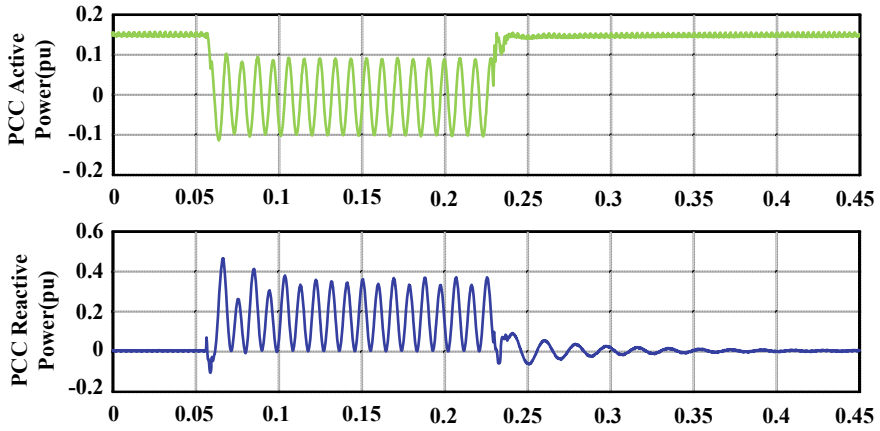
Fig. 9 Active and reactive power at PCC with LG fault
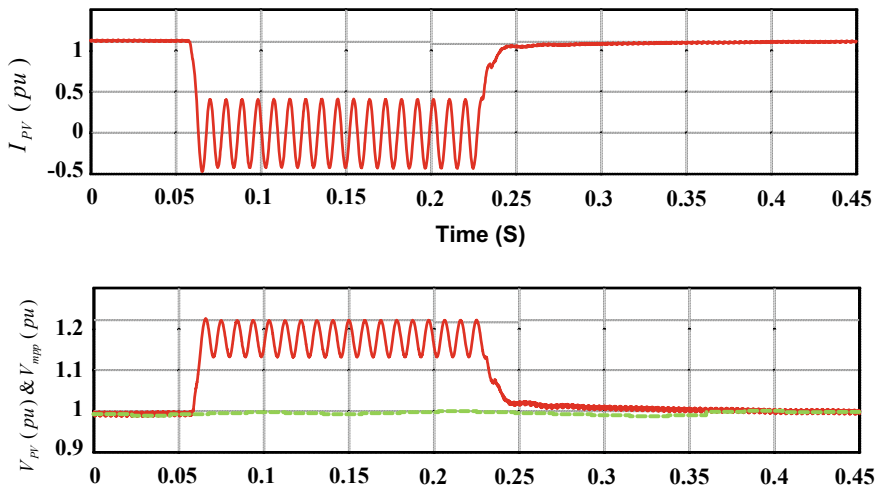
Fig. 10 V_{pv}, V_{Mpp} and I_{pv} with LG fault

4 Conclusions

This research work presents the results of three phases to ground (LLLG) and single phase to ground fault (LG) results. The fault in the grid-interfaced system has the very high effect of solar system due to the physical vicinity. It is observed from the both fault results that there is a high transient current in the LLLG fault, whereas negative sequence components will affect the system in case of LG fault.

References

1. Enslin JHR (2010) Network impacts of high penetration of photovoltaic solar power systems. IEEE PES General Meeting, Minneapolis, MN, pp 1–5
2. Lin Y et al (2016) Integrating high-penetration renewable energy into power system—a case study. In: China international conference on electricity distribution, Xi'an
3. Matsa A, Chaudhari MA, Suryawanshi HM (2017) Modified synchronous vector control design of multilevel inverters for AC grid applications. Electr Power Compon Syst 45:881–893
4. Matsa A, Chaudhari MA (2015) Synchronous vector control design of multilevel inverters for AC grid applications. TENCON 2015—2015 IEEE Region 10 Conference, Macao, pp 1–6
5. Hossain MJ, Saha TK, Mithulananthan N, Pota HR (2012) Robust control strategy for PV system integration in distribution systems. Appl Energy 99:355–362
6. Azmi SA, Adam GP, Ahmed KH, Finney SJ, Williams BW (2014) Grid interfacing of multimegawatt photovoltaic inverters. IEEE Trans Power Electron 8:2770–2784
7. Mahalakshmi D, Archana VS, Komathi J (2016) Reactive power control in microgrid by using photovoltaic generators. In: International conference on computation of power, energy information and communication (ICCPEIC), pp 762–767
8. Sourkounis C, Tourou P (2013) Grid code requirements for wind power integration in Europe. Conf Pap Energy 2013:1–9
9. P.O. 12.3. (2006) Requisitos de respuesta frente a huecos de tensión de las instalaciones eólica. Red Eléctrica de España (REE)

Whale Optimization Algorithm Tuned Fuzzy Integrated PI Controller for LFC Problem in Thermal-hydro-wind Interconnected System

Nimai Charan Patel and Manoj Kumar Debnath

Abstract The research work employed a modern optimization method recognized as whale optimization algorithm (WOA) to tune the gain factors of fuzzy integrated PI (FIPI) controller in an interconnected system consisting of two areas. Area 1 in the scrutinized system consists of thermal and hydro generating units, whereas area 2 comprises thermal and wind generating units. To investigate the behavior of the system, an abrupt disturbance of 1.5% is employed to area 1, and the controller constraints are tuned with the help of WOA considering proper objective function (ITAE). To confirm the robustness of the suggested controller, the load disturbance is applied in both the areas as an extension of case studies. Throughout the analysis, the dominance nature of FIPI controller is proved over conventional controllers like PID controller.

Keywords Whale optimization algorithm · Fuzzy integrated controller · PID controller · Load frequency control · Renewable sources

1 Introduction

The foremost challenges in a unified power system are to supply secured and reliable energy to the consumers maintaining the prescribed power quality. The voltage and frequency profile is a measure of the power quality of a unified power system. Hence, it is always desirable to uphold the voltage and frequency of such system within the acceptable tolerance limits. The main objective of the AGC is to retain the system frequency at a nominal value while the main objective of AVR is

N. C. Patel (✉)
Government College of Engineering, Keonjhar 758002, Odisha, India
e-mail: ncpatel.iter@gmail.com

M. K. Debnath
Siksha 'O' Anusandhan Deemed to Be University,
Bhubaneswar 751030, Odisha, India
e-mail: mkd.odisha@gmail.com

to maintain the voltage profile. Whenever there is any disturbance or sudden change of active power demand, the system frequency differs from its nominal value due to mismatch between the generation and demand [1, 2]. AGC works on the principle of retaining the balance within power generation and load demand which facilitates to reduce the frequency oscillation during transient state and to keep the system frequency constant at a nominal value after the transient is over.

Since the inception of AGC, many researchers have contributed their work in this field. Cohn is the first one to start the research on AGC in the year 1956 [3]. In 1970, Elgerd and Fosha introduced the concept of optimal control strategy for AGC and proposed a proportional controller with different feedback schemes [4]. An adaptive controller for AGC was proposed by Pan and Liaw [5]. In 1991 for the very first time, Lee et al. illustrated a technique named as the gain scheduling-based fuzzy control for the LFC problem of a unified system [6]. Thereafter, Talaq and Al-Basri added a fuzzy-based adaptive technique along with gain scheduling process for PI type traditional controller in 1999 [7]. For AGC of interconnected power systems, many classical controllers such as proportional integral (PI), proportional integral derivative (PID), and integral double derivative (IDD) controllers and their enactment comparison have been reported in the literature [8, 9]. Apart from these classical controllers, several other controllers for AGC of unified systems have also been described in many literatures. In recent years, many optimization algorithms have been developed and implemented successfully for tuning the constraints of the controller parameters to obtain improved dynamic performance of AGC system. Sahu et al. have implemented a fuzzy PID controller tuned by TLBO algorithm for AGC of two-area power system, and its performance was found to be superior to Lozi map along with genetic algorithm, chaotic optimization algorithm and simulated algorithm optimized PID controller [10]. Mohanty et al. has demonstrated the performance superiority of a derivative filter along with fuzzy PID controller over PID/PIDF/fuzzy PID controllers, and also it was shown that the performance of PIDF controller is better than the simple PID controller for AGC of multi-area interconnected power system [11]. Hybrid local unimodal sampling–teaching learning-based optimization (LUS-TLBO) algorithm was employed to tune the implemented controller constraints in the above work. Kennedy and Eberhart developed the particle swarm optimization method in 1995 for solving optimization problems [12]. PSO was introduced to optimize the gains of employed PID controller in fuzzy-based AGC of multi-thermal units [13]. Later on, many optimization algorithms were developed and implemented for AGC. A hybridization of differential evolution particle swarm optimization (DEPSO) technique was used for AGC to optimize the constraints of fuzzy PID controller, and it was shown that it gives superior performance than differential evolution/PSO tuned fuzzy PID controller [14]. Nanda et al. are the first to introduce bacteria foraging (BFO) algorithm for optimization of the various parameters of AGC system which has faster convergence than GA [15]. It was shown that cascaded PI and PID controllers tuned by artificial bee colony (ABC) algorithm for AGC of unified reheat-based thermal power system has superior tuning performance than PSO [16]. Sharma et al. implemented a new optimization technique called as Grey Wolf Optimizer

(GWO) algorithm to optimize the constraints of classical controllers for AGC of multi-unit interconnected power system having solar thermal power plant (STTP) in one area [17]. The performance superiority of hybrid algorithm optimized fuzzy-based PID controller was verified by Singh et al. [18].

This paper basically focuses on the tuning of PID and fuzzy integrated PI controller using whale optimization algorithm for load frequency control in an interconnected system which consists of conventional thermal and hydro generating units as well as renewable generating unit like wind generating system.

2   Scrutinized System

Generally, a wide-ranging power system includes many interconnected areas that are connected through the tie-line. However, here the investigation takes account of a two-area interconnected system which includes thermal as well as hydro unit in area 1 and thermal along with wind unit in area 2. Initially, the investigations take place over the proposed power system which consists of FIPI controller that is optimally tuned by a novel optimization process known as whale optimization algorithm (WOA) while giving a load disturbance of 1.5% to area 1. The detailed modeling about the proposed fuzzy PI controller used over two-area interconnected system is presented in Fig. 1. The operation and evaluation of the responses were conducted in the MATLAB version 7.10.0.499 (R2010a). The nominal parameters used in this work have been taken from the reference paper [18]. Then, the extended investigations include load disturbance of 1.5% in both the areas. The performance results of the proposed FIPI controller tuned WOA optimization technique are compared with the results of a PID controller.

3   Controller Configuration

The integral action in the PI controller tends to result large oscillations along with excessive overshoots, and hence, to overcome this problem, fuzzy integrated PI (FIPI) controllers are used. The proposed controllers are designed in such a manner to eliminate the unwanted overshoots as well as the oscillations caused by the integral action. The transient response of the second-order systems with integrating element is improved after the usage of these controllers. The outline of the mentioned FIPI controller is shown in Fig. 2. Every area in the system is implemented with a FIPI controller.

Error along with the derivative of the error is utilized as the input signals for the fuzzy controller. u_1 and u_2 are the outputs of the fuzzy controller but are the inputs to the power system which are termed also as the reference power settings (ΔP_{ref1} and ΔP_{ref2}). C_1 and C_2 are two input scaling factors in the controller as well as C_3 and C_4 are proportional and integral gains of the fuzzy controller correspondingly.
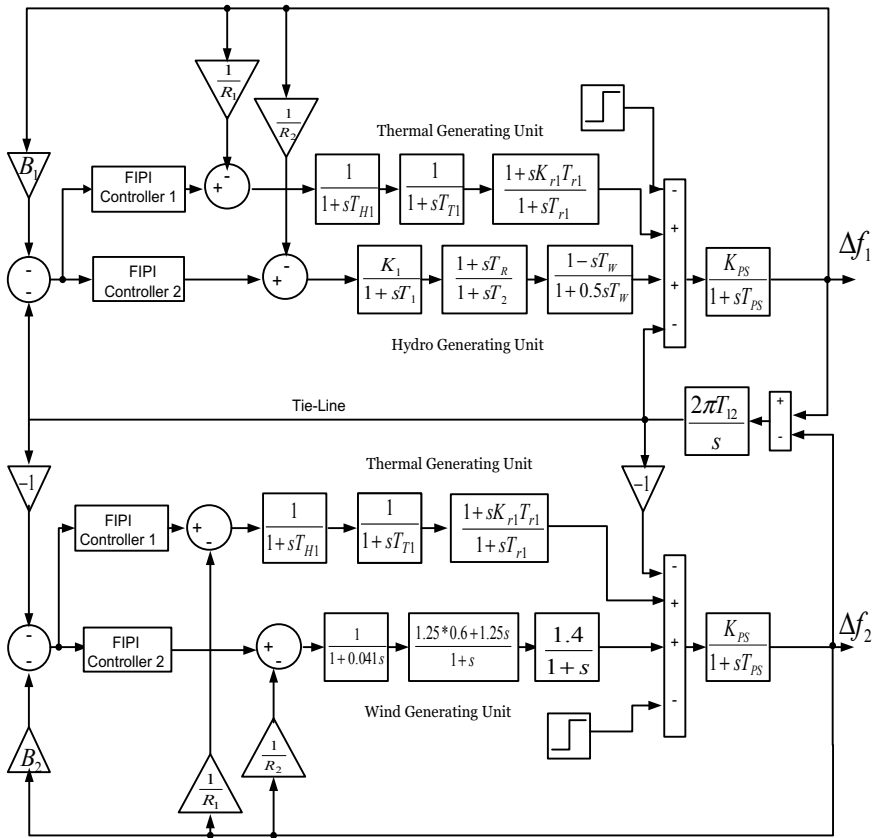
Fig. 1 Interconnected power system with thermal-hydro and thermal-wind generating units
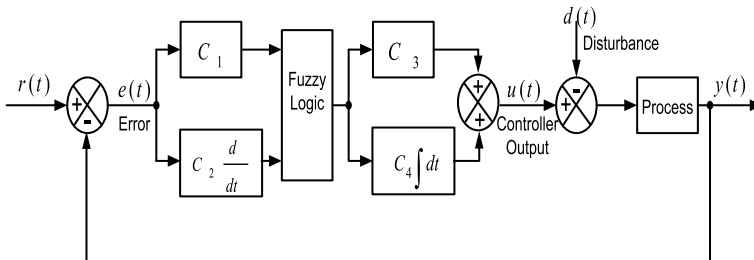
Fig. 2 Internal diagram of fuzzy integrated PI controller
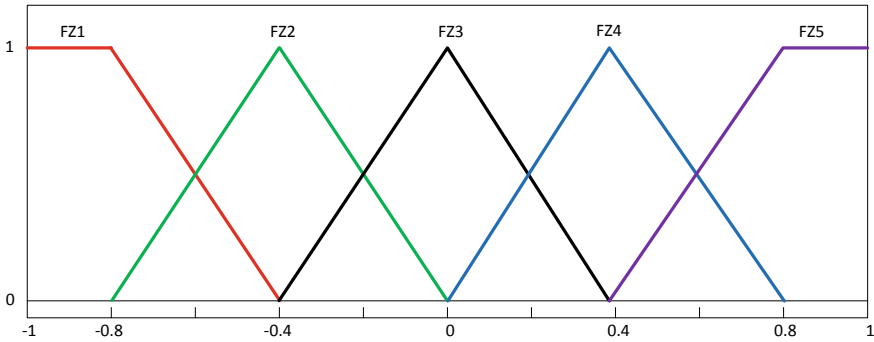
Fig. 3 Triangular-shaped membership functions of FIPI controller

Table 1 Fuzzy IF-THEN rules of FIPI controller

Error	Error Derivative				
	FZ1	FZ2	FZ3	FZ4	FZ5
FZ1	FZ1	FZ1	FZ2	FZ2	FZ3
FZ2	FZ1	FZ2	FZ2	FZ3	FZ4
FZ3	FZ2	FZ2	FZ3	FZ4	FZ4
FZ4	FZ2	FZ3	FZ4	FZ4	FZ5
FZ5	FZ3	FZ4	FZ4	FZ5	FZ5

Figure 3 illustrates the membership functions of fuzzy logic controller (FLC) output, error along with error derivative values. Five fuzzy linguistic variables such as FZ1, FZ2, FZ3, FZ4 and FZ5 in the form of triangular membership functions are utilized mutually for the inputs as well as output. By the usage of center of gravity method, the fuzzy logic controller output is firmed. Table 1 represents the fuzzy rules for the FIPI controller output, error along with error derivative values.

4   Whale Optimization Algorithm (WOA)

Meta-heuristic optimization algorithms gain the attention due to its easy implementation nature, no need for gradient information and lastly it can be applied widely for several disciplines. New whale optimization meta-heuristic optimization process belongs to the performance of humpback whales. Exploration and exploitation are two phases of search process. Maintaining proper balance is a very difficult task between these two search processes during the development of any meta-heuristic algorithm. Generally, whales are the biggest mammals and one of the fancy creatures in the world. Researchers also revealed that there are some

cells inside the brain of whales which is similar to the spindle cell of human being. Due to these facts, whales are known as the smartest animal with emotions. Humpback whales are one of the biggest whales, and their exceptional hunting method made them unique among all other whales. Searching is achieved by forming individual bubbles along a '9'-shaped path called bubble-net feeding method. In this technique, firstly whales dive 12 m down and start to create bubble in a spiral shape around the prey and again swim up toward the surface. To execute WOA optimization technique, it should have an idea about encircling prey, spiral bubble-net feeding maneuver and search of prey which is described in the below section.

Encircling prey:

Humpback whales start their hunting by encircling the location of prey. The target solution which is nearer to the optimal value is considered as the best candidate solution. The other search agents update their locations by moving onward to the best-fitted agent which is followed by the below equation

$$\vec{D} = |\vec{C} \cdot \vec{X}^*(t) - \vec{X}(t)|$$
$$\vec{X}(t+1) = \vec{X}^*(t) - \vec{A} \cdot \vec{D}$$

Here X^*, $\vec{X}$, and t are known as location vector of finest solution, position vector, and the current iteration, respectively.

The vectors $\vec{A}$ and $\vec{C}$ are known as coefficient vectors and calculated by using the below equation

$$\vec{A} = 2\vec{a} \cdot \vec{r} - \vec{a}$$
$$\vec{C} = 2 \cdot \vec{r}$$

Here, $\vec{r}$ is the random vector in [0, 1], and the value of $\vec{a}$ is linearly decreased from 2 to 0 at every iteration.

Bubble-net-attacking method (exploitation phase):

Two methodologies are applied for mathematical modeling of the bubble-net-attacking hunting method of humpback whales.

(1) Shrinking encircling mechanism
(2) Spiral updating position

(1) *Shrinking encircling mechanism*: In this approach, the value of $\vec{a}$ is decreased which in turn affects the variation range of $\vec{A}$. Earlier, the fluctuation of $\vec{A}$ is set in the interval of $[-a, a]$. In order to get the new location of search agent, the random values of $\vec{A}$ are set in $\lceil -1, 1 \rceil$.

(2) *Spiral updating position*: In this method, we have to calculate the space within the whale location (X, Y) and the prey location (X^*, Y^*). To represent the helix-shaped movement of humpback whales, a spiral equation is made between the location of whale and prey as follows

$$\vec{X}(t+1) = \vec{D}' \cdot e^{bl} \cdot \cos(2\Pi l) + \vec{X}^*(t)$$

In this equation, the logarithmic spiral nature is defined by constant 'b' and 'l' is an arbitrary number in the range $[-1, 1]$. During hunting process, humpback whales move around with a spiral-shaped path along with shrinking circle simultaneously. During optimization, there is a chance of 50% whether the whales do the shrinking encircling or the spiral model to update their positions. To solve these problems mathematical model is as follows

$$\vec{X}^*(t) - \vec{A}.\vec{D} \quad \text{if} \quad p < 0.5$$
$$\vec{D}' \cdot e^{bl} \cdot \cos(2\Pi l) + \vec{X}^*(t) \quad \text{if} \quad p \geq 0.5$$

In the above equation, p specifies an arbitrary value in the limit $[0, 1]$.

Hunt for prey:

During exploration for prey method, the variation of $\vec{A}$ has been taken either bigger than 1 or lower than -1. Now, update the location of a search agent in the exploitation phase. The below mathematical model is used to perform global search for $|\vec{A}| > 1$.

$$\vec{D} = |\vec{C} \cdot \vec{X}_{\text{rand}} - \vec{X}$$
$$\vec{X}(t+1) = \vec{X}_{\text{rand}} - \vec{A} \cdot \vec{D}$$

Here $\vec{X}_{\text{rand}}$ is a random location vector which is chosen from existing population.

5   Simulation and Result

At first, the two-area unified system with multi-source units is examined while comparing the performance results of the proposed FIPI tuned by WOA technique to PID controller allowing the load disturbance of 1.5% to area 1. All the examinations were carried out under the surroundings of MATLAB/SIMULINK software. The objective function of this paper included integral time absolute error (ITAE) (Eq. 1). The performance comparison between the parametric gain constraints after optimizing via WOA of the FIPI with PID controller is recorded and shown in Table 2. The variations of frequencies are denoted as Δf_i, and the oscillations due to interline power are denoted as ΔP_{tie}. The deviations Δf_1, Δf_2, and ΔP_{tie12} are shown in Figs. 4, 5, and 6, respectively. Table 3 represents the response

Table 2 Tuned values of gain parameters obtained by WOA

Controllers		Thermal	Hydro	Thermal	Wind
FIPI	C1	2.1345	2.1345	1.1987	2.1345
	C2	1.0123	1.0123	1.8854	1.0123
	C3	2.1142	2.1142	1.2342	2.1142
	C4	1.9977	1.9977	1.4321	1.9977
PID	Cp	2.1121	2.1121	0.7100	0.7100
	Ci	3.4865	3.4865	0.5984	0.5984
	Cd	3.8550	3.8550	0.6548	0.6548

Fig. 4 Frequency swinging in area 1
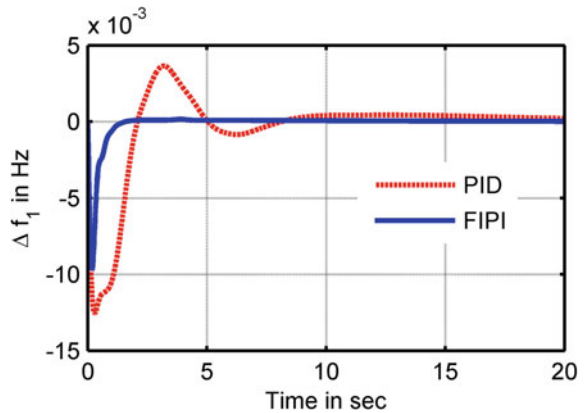
Fig. 5 Frequency swinging in area 2
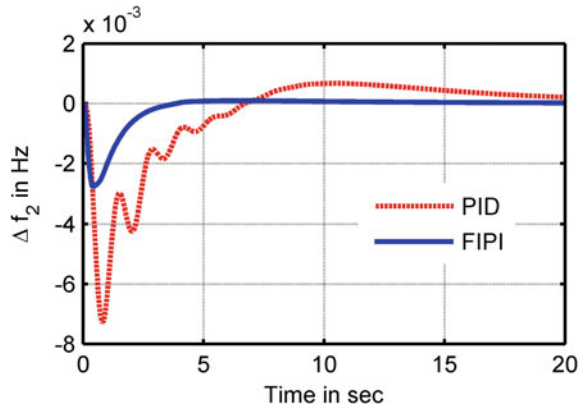
indices such as peak overshoot, minimum undershoot as well as settling time. The result of the performance regarding the second case as taking 1.5% of load disturbance to both the areas is displayed in Figs. 7, 8, and 9, respectively. Table 3 along with Figs. 4, 5, 6, 7, 8, and 9 proves the dominance of FIPI controller over PID type conventional controller.
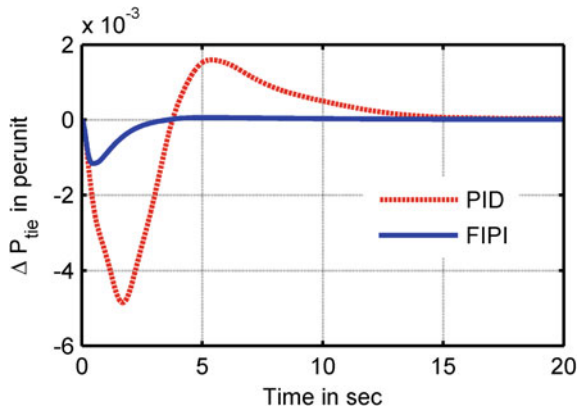
Fig. 6 Tie-line power swinging

Table 3 Different performance specifications achieved with various methods

Deviations	Performance specifications	PID	FIPI
Δf_1	Overshoots	0.0037	0.0001665
	Undershoots	−0.0125	−0.0097
	T_s in seconds	7.1400	1.0600
Δf_2	Overshoots	0.0007	0.0000959
	Undershoots	−0.0073	−0.0028
	T_s in seconds	13.9800	2.2100
ΔP_{tie}	Overshoots	0.0016	0.0000572
	Undershoots	−0.0049	−0.0012
	T_s in seconds	9.9800	1.6100
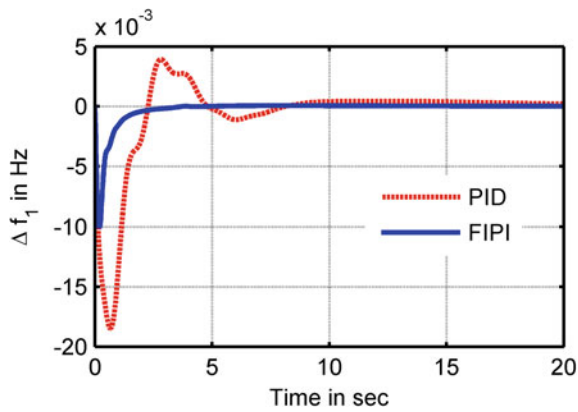
Fig. 7 Frequency swinging in area 1 with SLP in both areas

Fig. 8 Frequency swinging in area 2 with SLP in both areas
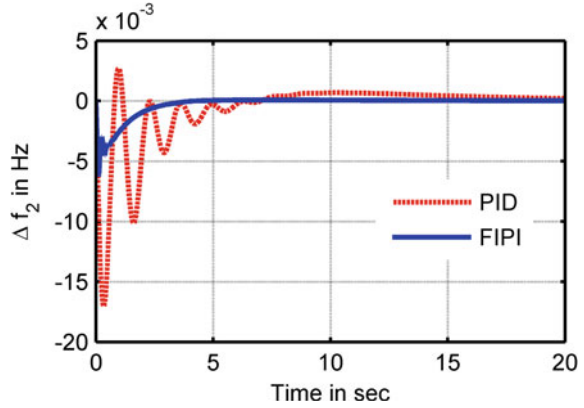
Fig. 9 Tie-line power swinging with SLP in both areas
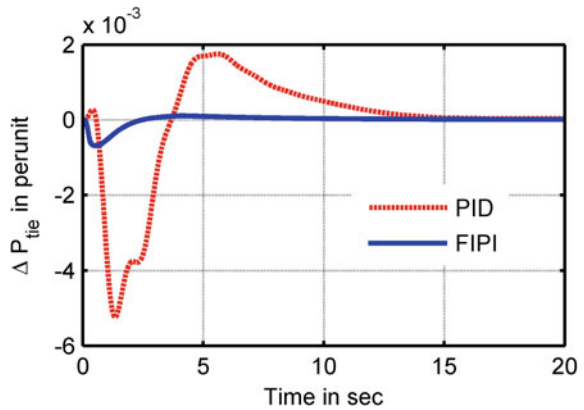
$$\text{ITAE} = \int \left(|\Delta f_1| + |\Delta f_2| + |\Delta f_3| \right) \cdot t \cdot \mathrm{d}t \qquad (1)$$

6 Conclusion

The WOA technique is successfully applied in this research work to tune the gains of FIPI controller implemented in the two-area thermal-hydro-thermal-wind unified system. The system behavior was analyzed in two conditions, i.e., disturbance in one area and disturbances in both the area. For both the cases, the dominating nature of fuzzy integrated PI controller is shown over PID type conventional controller in consideration of response indices like peak overshoots, minimum undershoots, and the response settling time. Here, we confined the analysis in a

two-area system which can also be extended to multi-area system with many generating units.

References

1. Kundur P, Balu NJ, Lauby MG (1994) Power system stability and control, vol 7. McGraw-hill, New York
2. Elgard OI (1982) Electric energy systems theory. McGraw-Hill, New York, pp 299–362
3. Cohn N (1956) Some aspects of tie-line bias control on interconnected power systems. Trans Am Inst Electr Eng Part III Power Appar Syst 75(3):1415–1436
4. Elgerd OI, Fosha CE (1970) Optimum megawatt-frequency control of multi area electric energy systems. IEEE Trans Power Appar Syst 4:556–563
5. Pan CT, Liaw CM (1989) An adaptive controller for power system load-frequency control. IEEE Trans Power Syst 4(1):122–128
6. Lee KA, Yee H, Teo CY (1991) Self-tuning algorithm for automatic generation control in an interconnected power system. Elect Power Syst Res 20(2):157–165
7. Talaq J, Al-Basri F (1999) Adaptive fuzzy gain scheduling for load frequency control. IEEE Trans Power Syst 14(1):145–150
8. Nanda J, Mangla A, Suri S (2006) Some new findings on automatic generation control of an interconnected hydrothermal system with conventional controllers. IEEE Trans Energy Convers 21(1):187–194
9. Saikia LC, Nanda J, Mishra S (2011) Performance comparison of several classical controllers in AGC for multi-area interconnected thermal system. Int J Electr Power Energy Syst 33 (3):394–401
10. Sahu BK et al (2015) Teaching–learning based optimization algorithm based fuzzy-PID controller for automatic generation control of multi-area power system. Appl Soft Comput 27:240–249
11. Mohanty PK et al (2016) Design and analysis of fuzzy PID controller with derivative filter for AGC in multi-area interconnected power system. IET Gener Transm Distrib 10(15):3764–3776
12. Kennedy J, Eberhart R (1995) Particle swarm optimization. In: Proceedings of IEEE International Conference on Neural Networks, Perth, Australia, vol 4, pp 1942–1948
13. Ghoshal SP (2004) Optimizations of PID gains by particle swarm optimizations in fuzzy based automatic generation control. Electr Power Syst Res 72(3):203–212
14. Sahu BK, Pati S, Panda S (2014) Hybrid differential evolution particle swarm optimisation optimised fuzzy proportional–integral derivative controller for automatic generation control of interconnected power system. IET Gener Transm Distrib 8(11):1789–1800
15. Nanda J, Mishra S, Saikia LC (2009) Maiden application of bacterial foraging-based optimization technique in multiarea automatic generation control. IEEE Trans Power Syst 24 (2):602–609
16. Gozde H, Taplamacioglu MC, Kocaarslan I (2014) Comparative performance analysis of Artificial Bee Colony algorithm in automatic generation control for interconnected reheat thermal power system. Int J Electr Power Energy Syst 42(1):167–178
17. Sharma Y, Saikia LC (2015) Automatic generation control of a multi-area ST–thermal power system using Grey Wolf Optimizer algorithm based classical controllers. Int J Electr Power Energy Syst 73:853–862
18. Rajesh KS, Dash SS, Rajagopal R (2018) Hybrid improved firefly-pattern search optimized fuzzy aided PID controller for automatic generation control of power systems with multi-type generations. Swarm Evolut Comput

Mamdani-Based Fuzzy PI Controller Tuned by Binary GWO Technique for LFC Problem in Solar-Thermal Interconnected System

Manoj Kumar Debnath and Priyambada Satapathy

Abstract Here an advanced Mamdani-based fuzzy proportional–integral (MFPI) controller is employed over a two-area solar-thermal interconnected system for LFC. The tuning of constraints of the recommended MFPI controller is accomplished by binary grey wolf optimization (BGWO) technique. The application of an abrupt disruption of 1% load is taken in control area 1, and for tuning process ITAE is being considered as the objective function. The offered work reflects two dissimilar sources of generating system, namely, a solar and a reheat thermal unit. The toughness of the planned controller is further placed to investigate by introducing a time delay. Investigations of the dynamic features of the arrangement are accomplished in view of various dynamics response indices, i.e. peak overshoot, settling time and least undershoot. Throughout the investigation, the attained finest values are compared with conventional PID method so as to demonstrate the ascendancy of this presented controller.

1 Introduction

At the present rapidly growing power demand scenario, it is definitely a challenge to all electric utilities to afford secure and consistent power within a sound quality to the consumer. Swapping of power among lots of generating stations in the enormous power system has done through tie lines in the bulk power system. Sustaining stability in the entire power system zone is a very tough job by balancing overall produced power and power demand simultaneously [1]. Active power and

M. K. Debnath (✉) · P. Satapathy
Siksha 'O'Anusandhan Deemed to Be University, Bhubaneswar 751030, Odisha, India
e-mail: mkd.odisha@gmail.com

P. Satapathy
e-mail: lirasatapathy@gmail.com

reactive power stability mechanism has been followed to balance the total power of the system. Automatic generation control (AGC) is accountable for upholding the system frequency within accepted targeted range by taking care of the active power. In order to bring the area control error (ACE) to zero, AGC changes the set position of the generators by estimating the net change in the required generation due to the significant level of uncertainties and nonlinearities of real industrial system [2].

AGC gains the attention of many researchers relating to its demand to regulate the instabilities in the system constraints during uncertainties and nonlinearities operation of the interlocked power system. The closed-loop control programs of AGC assign automatically the generations to meet the predefined frequency and tie line interchange schedule by keeping both economic and regulation restrictions and protect the system from governor wind up. Basically appropriate design of AGC system is preferred to accomplish the challenging tasks regarding stochastically variations in the power demands, faults during system modelling, etc. [3–6]. In recent times, many relevant researches have been developed which are discussed in the next section. Dated back, nonreheat thermal-type turbines are mostly considered to keep an eye on AGC problems, but presently combination of multi-source generators like thermal with reheat turbine, hydro and gas sources is more fruitful to observe the load frequency control (LFC) [7]. Increasing complexity in power generation and declining conventional energy sources lead to the integration of renewable energy sources (RESs). Recent survey reveals that the scope of solar energy and wind energy becomes the most alternative generating sources with large potential. To mature renewable sources in 2015, researchers introduced solar-type thermal generating system as well as wind turbine-based generating system for surplus generation of power in a hybrid two-area system [8]. The inadequacy of fossil fuels will adversely have a great impact to contribute wind energy resources to reduce the conventional generation in most of the parts of the world. A modern approach of variable speed wind turbines along with integrated control mechanism is implemented to control over active and reactive power [9]. In [10], to mitigate the problem of automatic load shedding and regulation of frequency the wind and solar plants are used as a backup of conventional generation assets. Two-area hybrid thermal system has considered with biogeography-based optimization (BBO)-tuned integral (I), proportional–integral (PI) and proportional–integral–derivative (PID) as secondary controller along with solar- and wind-type generating system [11]. An innovative idea of hybrid combination of wind turbine, solar thermal, solar photovoltaic, diesel engine generator, fuel cell and battery energy storage system is injected to an autonomous hybrid generation system [12]. It is very dangerous to make change in the control mechanism of generator, so that flatness-based control structure is investigated with high penetration of wind energy [13]. The main job of a controller is to get a suitable set of instructions that can help the system to easily reach the required state with minimal deviations. A new robust imperialist competitive algorithm optimized PID controller in Ref. [14] to bring the system from instability. Fuzzy logic deals with approximate rather than fixed and exact having binary sets have two-valued logic; true or false. Many researchers implemented and experimented robust fuzzy logic-based PID controller which is self-tuned and tuned

by particle swarm optimization and hybrid PSO–PS for the regulation of frequency in multi-area power system [14–20]. Fuzzy proportional–integral (PI) and PID controllers are tested on two-area and multi-area network to challenge the problems during instability [20, 21].

2 Scrutinized System

A solar-thermal-based power system of 2000 MW in each area is considered in this proposed research work. The transfer function model of this simulated model is shown in Fig. 1. Governor, turbine and reheat system and a solar module are mentioned in the model of solar-thermal-based power system.

Here T_g, T_t, K_r, T_r, K_p, T_p, K_{SO} and T_{SO} are the gains of time constant of governor, time constant of turbine, gain and time constant of reheat system, gains of generator, time constant of power system and lastly gains and time constant of solar
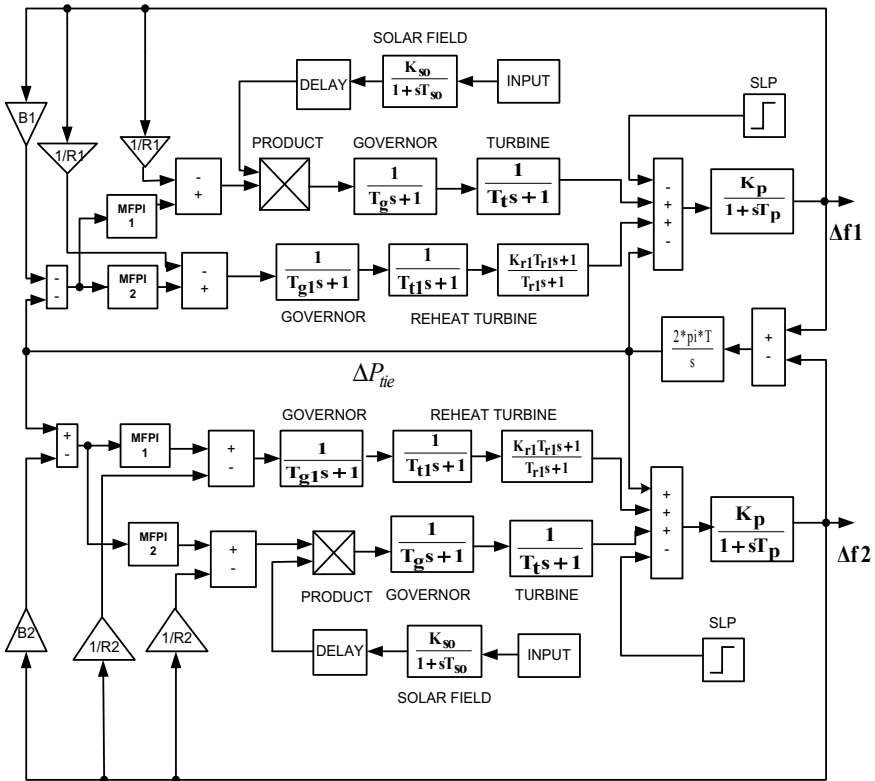
Fig. 1 Two-area solar-thermal multi-unit power system

unit, respectively. Mamdani-based fuzzy PI controller tuned by binary GWO algorithm has been introduced here along with integral time absolute error as objective function.

Solar system:

Photovoltaic cells (PV) play a vital role for generating power from solar system. The main role of collectors is that they absorb the solar rays to the pipe in a heat exchanger. The mathematical modelling of solar power system has described below.

$$\frac{dT_0(t)}{dt} = \frac{A\eta_0}{C} I(t) - \frac{U_L A}{C}[T_\alpha(t) - T_e(t)] + \frac{v(t)}{V}[T_0(t) - T_e(t)]$$

where $T_\alpha(t) = \frac{T_i(t) + T_0(t)}{2}$.

The above expression denotes the alternation of output results. The above equation can be modified by keeping the temperature unchanged.

$$\frac{dT_0(t)}{dt} + \left[\frac{U_L A}{2C} + \frac{v}{V}\right] T_0(t) = \frac{A\eta_0}{C} I(t) + \left[\frac{v}{V} - \frac{U_L A}{2C}\right] T_i(t) + \frac{U_L A}{2C} T_e(t)$$

The Laplace transform of the above equation is

$$T_0(s) = \frac{T_{SO}}{T_{SO} + 1} \frac{A\eta_0}{C} I(s) + \frac{T_{SO}}{T_{SO} + 1} \left[\frac{v}{v} - \frac{U_L A}{2C}\right] T_i(s) + \frac{T_{SO}}{T_{SO} + 1} \times \frac{U_L A}{2C} T_e(s)$$

Here the time constant of solar field is

$$T_{SO} = 1 / \frac{U_L A}{2C} + \frac{v}{V}$$

The mathematical expression of solar radiance in terms of Laplace operator is

$$G(s) = \frac{K_{SO}}{1 + T_{SO} S}$$

Here K_{SO} is known as the gain of solar field.

3 Mamdani-Based Fuzzy PI (MFPI) Controller Outline

Mamdani fuzzy and Takagi–Sugeno (T–S) are two fuzzy rule-based inference systems. Spontaneous and widespread reliability is the most advantages of Mamdani fuzzy rule base, and along with that it is suitable for human perception. In this research work to update the gain parameters with the surroundings, a human

Table 1 Fuzzy IF–THEN rules of MFPI controller

Error	Error derivative				
	Func1	Func2	Func3	Func4	Func5
Func1	Func1	Func1	Func2	Func2	Func3
Func2	Func1	Func2	Func2	Func3	Func4
Func3	Func2	Func2	Func3	Func4	Func4
Func4	Func2	Func3	Func4	Func4	Func5
Func5	Func3	Func4	Func4	Func5	Func5
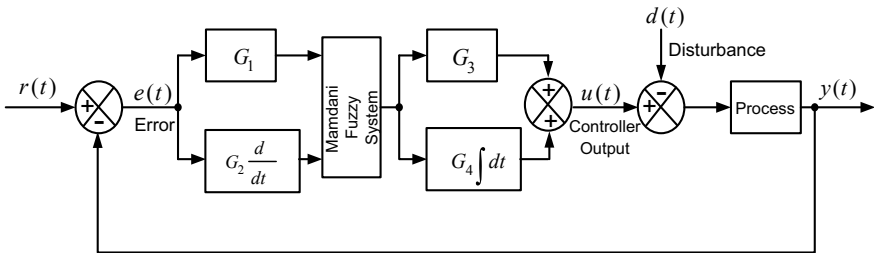
Fig. 2 Internal diagram of Mamdani-based Fuzzy PI controller
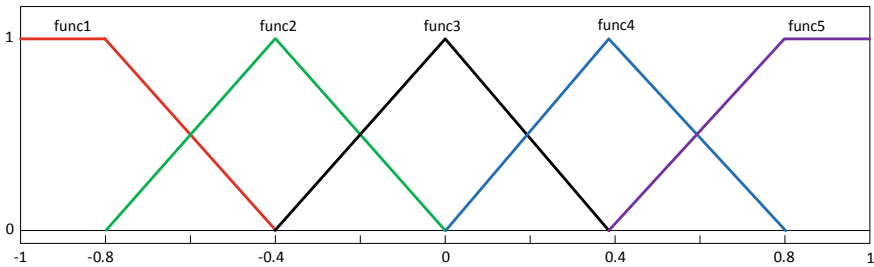
Fig. 3 Triangular-shaped membership functions of FIPI controller

logic-based fuzzy logic controller is employed over described system. The rule base and the fuzzy membership function are shown in Table 1 and Fig. 3, respectively. Figure 2 demonstrates the model structure of MFPI controller. Proportional–integral controller has the advantages to overcome the problems during offsets which are a major disadvantage of only proportional controller.

4 Grey Wolf Optimization

The grey wolf generally survives and attacks in a pack and obeys certain pecking order. The topmost order of the pyramid is obtained by alpha wolf which is knowledgeably considered as the toughest of the group. The rest of the wolves except alpha wolf show their respect towards the decisions made by alpha wolf during the completion of task. The beta wolf is considered as the second topmost order of the pack which communicates between alpha wolf and remaining wolves of the group. Beta wolf suggests alpha wolf on making decisions and is also considered the best following candidate in case the alpha wolf is dead. In this pecking order, omega wolves occupied the last order of the pyramid and they are permitted to have their food lastly in a group. Wolves in the pack that does not belong to any group are considered as deltas. The location of wolf is updated by calculating the space from the updated location of prey as per the three best solutions $(\alpha, \beta \text{ and } \delta)$ which are as follows

$$\vec{D} = \left| \vec{C} X_p(t) - \vec{X} \right|$$
$$\vec{X}(t+1) = \vec{X}_P(t) - \vec{A} \cdot \vec{D}$$
$$\vec{A} = 2\vec{a}\vec{r}_1 - \vec{a}$$
$$\vec{C} = 2\vec{r}_2$$
$$r_1, r_2 \in [0, 1]$$

t, A and C, X_P and X are the iteration number, coefficient, vector of prey position and vector of grey wolf position, respectively.

Binary grey wolf optimizer (BGWO):

The two methodologies like binarization model 1 (BGWO1) and binarization model 2 (BGWO2) are employed in this research process.

A. *Binarization model 1 (BGWO1)*

Crossover strategy is implemented in this described model, and the following equation is followed to update the position of wolf.

$$\varkappa_i^{k+1} = Crossover \quad (\gamma_1, \gamma_2, \gamma_3),$$

The above equation is used to complete the crossover method which affects the finest three wolves' locations like alpha, beta and delta. $\gamma_1, \gamma_2, \gamma_3$ are the binary vectors updated with the help of below transformation

$$\gamma_1^D = \begin{cases} 1 & \text{if } (\gamma_\alpha^D + q_\alpha^D) \geq 1 \\ 0 & \text{Else} \end{cases}$$

Here γ_α^D shows the location of alpha wolf with respect to dimension 'D' and the binary step q_α^D is expressed by

$$q_\alpha^D = \begin{cases} 1 & \text{if} \quad p_\alpha^D \geq r \\ 0 & \text{Else} \end{cases}$$

Here r is an arbitrary value that has considered within [0, 1] and p_α^D is updated using sigmoid transformation

$$p_\alpha^D = \frac{1}{1 + \exp(-10 * (A_1^D D_\alpha^D - 0.5)}$$

The updating of beta and gamma wolves of grey wolf optimizer has been done in the similar updating way of alpha wolf.

The wolf position of $\gamma_1^D, \gamma_2^D, \gamma_3^D$ is updated by crossover operation

$$\gamma^D = \begin{cases} \gamma_1^D & \text{if} \quad r < \frac{1}{3} \\ \gamma_2^D & \text{if} \quad \frac{1}{3} \leq r \leq \frac{2}{3} \\ \gamma_3^D & \text{Else} \end{cases}$$

B. *Binarization model 2 (BGWO2)*

In the second model, the direct sigmoid transformation has been implemented to obtain binary values which is specified as

$$\gamma_D^{k+1} = \begin{cases} 1 & \text{if} \quad S\{X(k+1)\} > r \\ 0 & \text{Else} \end{cases}$$

where r is random number considered between [0, 1] and the expression for sigmoid transformation is given by

$$S\{X(k+1)\} = \text{sigmoid}(\gamma(k+1) = \frac{1}{1 + e^{-10\{(\frac{X_1 + X_2 + X_3}{3}) - 0.5\}}}$$

Here X_1, X_2, X_3 are the real valued position of three best wolves of (α, β, δ) in a group.

5   Simulation and Result

At first, the two-area interconnected power system with solar-thermal source units in each area is examined while comparing the performance results of the proposed Mamdani-based fuzzy PI controller (MFPI) tuned by binary grey wolf optimization (BGWO) technique to PID controller based on the same optimization technique allowing the load disturbance of 1% to area I. All the examinations were carried out with the help of MATLAB/SIMULINK software. The objective function of this

paper included integral time absolute error (ITAE) (Eq. 1). The performance comparison between parametric gain constraints after optimizing via BGWO of the MFPI with PID controller is recorded and shown in Table 2. The variations in frequencies are denoted as Δfi, and the oscillations due to interline power are denoted as ΔP_{tie}. The deviations Δf_1, Δf_2 and ΔP_{tie12} are shown in Figs. 4, 5 and 6, respectively. Table 3 represents the response indices such as peak overshoot, minimum undershoot as well as settling time with and without time delay. The result of the performance regarding the second case as taking the time delay of 0.1 s is displayed in Figs. 7, 8 and 9, respectively.

Table 2 Tuned gain parameters obtained by BGWO

MFPI controller							
Controller 1				Controller 2			
G1	G2	G3	G4	G1	G2	G3	G4
2.1346	1.2116	1.8854	2.2465	1.2534	1.7895	1.3246	1.4526
PID controller							
Gp	Gi	Gd	Gp	Gi	Gd		
2.2214	3.9875	1.9857	2.1435	0.01124	0.3428		

Fig. 4 Swinging of frequency in area 1
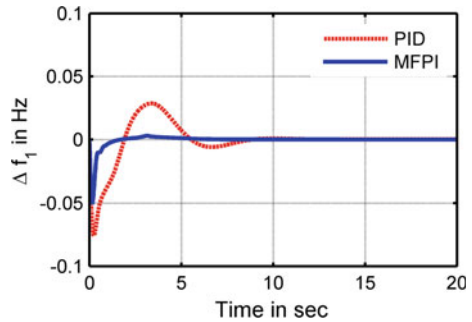
Fig. 5 Swinging of frequency in area 2
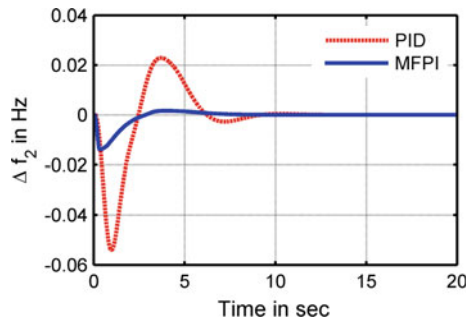
Fig. 6 Swinging of tie line
power
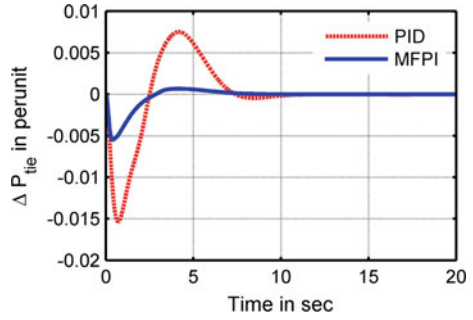
Table 3 Different performance specifications achieved with various methods

Deviations	Performance specifications	Without delay		With delay	
		PID	MFPI	PID	MFPI
Δf_1	Overshoots	0.0286	0.0030	0.0321	0.0027
	Undershoots	−0.0757	−0.0504	−0.1197	−0.0550
	T_s in seconds	12.4600	7.4800	12.2900	7.3200
Δf_2	Overshoots	0.0229	0.0017	0.0247	0.0016
	Undershoots	−0.0541	−0.0141	−0.0648	−0.0166
	T_s in seconds	12.4700	9.2300	12.4400	9.1500
ΔP_{tie}	Overshoots	0.0075	0.0007	0.0081	0.0007
	Undershoots	−0.0154	−0.0055	−0.0191	−0.0057
	T_s in seconds	10.9700	8.4100	10.7300	8.4600

Fig. 7 Swinging of
frequency in area 1 with delay
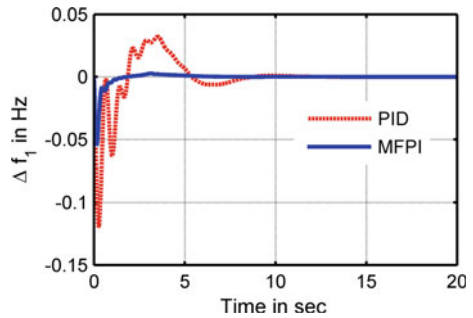
Fig. 8 Swinging of
frequency in area 2 with delay
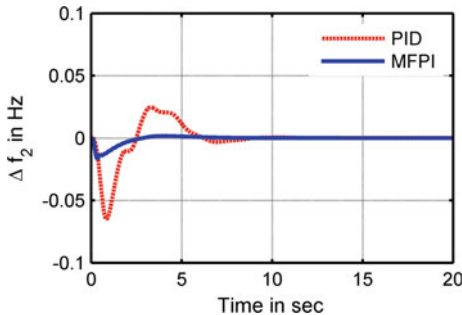
Fig. 9 Swinging of tie line
power with delay
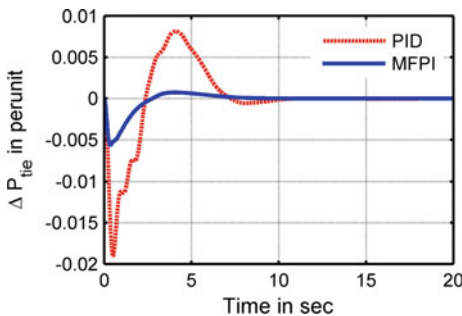
$$\text{ITAE} = \int \left(|\Delta f_1| + |\Delta f_2| + |\Delta f_3| \right) \cdot t \cdot \mathrm{d}t \tag{1}$$

6   Conclusion

This article presented a two-area interconnected power system utilizing a MFPI controller which is being tuned by a novel algorithm, i.e. binary grey wolf optimization algorithm. The proposed methodology was implemented considering solar units as well as thermal units in both the areas, and a load disturbance of 0.1 per unit in area I is applied. The operation and evaluation of the responses were carried out in the MATLAB version 7.10.0.499 (R2010a). The results from the simulation of the MFPI controller are compared with the PID controller, and the output result established the supremacy of the proposed controller. The extended study included a time delay of 0.1 s, and the performance result was also supreme as compared the BGWO-MFPI to BGWO-PID controller. Hence, it indicated that the proposed controller can guarantee the stability for the overall system for large parametric uncertainties. The performance of the MFPI controller is also far superior regarding

the maximum overshoot along with minimum undershoots and settling time. The simulation results showed that the proposed controller guarantees the robust stability as well as robust performance.

References

1. Kundur P (1994) Power system stability and control. McGraw-Hill, New York
2. Wood AJ, Wollenberg BF (2012) Power generation, operation, and control. Wiley, New York
3. Patel MR (2005) Wind and solar power systems: design, analysis, and operation. CRC Press, Boca Raton
4. Jaleeli N et al (1992) Understanding automatic generation control. IEEE Trans Power Syst 7 (3):1106–1122
5. Kumar P, Kothari DP (2005) Recent philosophies of automatic generation control strategies in power systems. IEEE Trans Power Syst 20(1):346–357
6. Nanda J, Kaul BL (1978) Automatic generation control of an interconnected power system. In: Proceedings of the Institution of Electrical Engineers, vol 125.5 IET Digital Library
7. Parmar KPS, Majhi S, Kothari DP (2012) Load frequency control of a realistic power system with multi-source power generation. Int J Electr Power Energy Syst 42(1):426–433
8. Sharma Y, Saikia LC (2015) Automatic generation control of a multi-area ST–thermal power system using Grey Wolf Optimizer algorithm based classical controllers. Int J Electr Power Energy Syst 73:853–862
9. Amenedo R, Luis J, Arnalte S, Burgos JC (2002) Automatic generation control of a wind farm with variable speed wind turbines. IEEE Trans Energy Convers 17(2):279–284
10. Delille G, Francois B, Malarange G (2012) Dynamic frequency control support by energy storage to reduce the impact of wind and solar generation on isolated power system's inertia. IEEE Trans Sustain Energy 3(4):931–939
11. Rahman A, Saikia LC, Sinha N (2017) Automatic generation control of an interconnected two-area hybrid thermal system considering dish-stirling solar thermal and wind turbine system. Renew Energy 105:41–54
12. Das DC, Roy AK, Sinha N (2012) GA based frequency controller for solar thermal–diesel–wind hybrid energy generation/energy storage system. Int J Electr Power Energy Syst 43 (1):262–279
13. Variani MH, Tomsovic K (2013) Distributed automatic generation control using flatness-based approach for high penetration of wind generation. IEEE Trans Power Syst 28(3):3002–3009
14. Shabani H, Vahidi B, Ebrahimpour M (2013) A robust PID controller based on imperialist competitive algorithm for load-frequency control of power systems. ISA Trans 52(1):88–95
15. Ghosal SP (2004) Optimization of PID gains by particle swarm optimization in fuzzy based automatic generation control. Electr Power Syst Res 72(3):203–212
16. Cam E, Kocaarslan I (2005) Load frequency control in two area power systems using fuzzy logic controller. Energy Convers Manag 46(2):233–243
17. Visioli A (2001) Tuning of PID controllers with fuzzy logic. IEE Proc Control Theory Appl 148(1):1–8
18. Güzelkaya M, Eksin I, Yeşil E (2003) Self-tuning of PID-type fuzzy logic controller coefficients via relative rate observer. Eng Appl Artif Intell 16(3):227–236
19. Sahu BK, Pati S, Panda S (2014) Hybrid differential evolution particle swarm optimisation optimised fuzzy proportional–integral derivative controller for automatic generation control of interconnected power system. IET Gener Transm Distrib 8(11):1789–1800

20. Sahu RK, Panda S, Sekhar GTC (2015) A novel hybrid PSO-PS optimized fuzzy PI controller for AGC in multi area interconnected power systems. Int J Electr Power Energy Syst 64:880–893

21. Yogendra A, Narendra (2017) Design and analysis of BFOA-optimized fuzzy PI/PID controller for AGC of multi-area traditional/restructured electrical power systems. Soft Comput 21(21):6435–6452

Emerging Green Energy Potential: An Indian Perspective

Jasmine Kaur, Yog Raj Sood and Rajnish Shrivastava

Abstract One of the major challenges faced by developing nations nowadays is the growing gap between energy demand and supply. Also, the quick depletion of fossil fuels is adding fuel to this burning issue. Nations like India, which is fortunately bestowed with ample renewable energy, are able to see a silver lining in this scenario. The concept of microgrids in such nations would prove to be a boon, as far as reducing the main grid burden is concerned. This work reviews the electricity market evolution in India and the transition of the Indian power scenario from conventional to renewable sources of generation. A detailed analysis of the state-wise solar and wind potential in India is aptly described in this paper.

Keywords Deregulation · Electricity market · Microgrids · Renewable energy

1 Introduction

The outreach of power to distant rural areas would serve as a major poverty alleviation tool for the generations to come. With the ever-increasing gap in energy demand and supply along with the alarming depletion of fossil fuels, it seems quintessential for an alternate source of energy to not only substitute but completely replace the conventional sources of energy. In this scenario, microgrids seem the most appropriate technology option. Microgrids can be sized in order to meet with the local demand and can be powered by renewable energy sources available locally [1]. Thus, microgrids are a promising solution to meet the global energy demand

J. Kaur (✉) · Y. R. Sood
Department of Electrical Engineering, NIT Hamirpur, Hamirpur, H.P, India
e-mail: jasminekaur.nith@gmail.com

Y. R. Sood
e-mail: yrsood.nith@gmail.com

R. Shrivastava
Mahindra Ecole Centrale College of Engineering, Hyderabad, Telangana, India
e-mail: rajnishshri@gmail.com

owing to their non-polluting nature [2]. Microgrids may be powered using microgeneration sources such as wind turbines, small hydro and solar photovoltaics, owing to their contribution in significantly reducing CO_2 emissions and improving energy efficiency [3].

2 Electricity Market Evolution

The concept of a centralized electrical system, i.e. vertical integrated regulated monopoly, is being followed in both developed and developing nations since time immemorial. The performance of this system is seen to be poor in developing nations owing to the weak financial capacity for infrastructure development. The introduction of the competitive electricity market, firstly, in developed countries, ended the primacy of this system, which then spread across the world from 1980s onwards [4]. This reform has helped in attracting foreign capital and has contributed effectively to improving the efficiency of the existing power system [5]. Countries around the globe are shifting to restructuring, thus allowing wholesale suppliers of electricity to compete in providing energy and other reliability services. The upcoming research in this area introduces microgrids in a deregulated market scenario. The system operator of the main grid, i.e. Independent System Operator (ISO), typically operates various markets that include energy and several types of ancillary services [6]. Electricity market design has evolved phenomenally owing to the availability of abundant variable energy sources.

The Federal Energy Regulation Commission (FERC) has listed various principles in its recent price initiative [7]:

(i)   Maximizing market surplus for both suppliers and consumers
(ii) Providing incentives for market participants and ensure that they follow dispatch instructions and maintain reliability
(iii) Providing transparency in order to ensure that the market participants understand how prices affect the actual marginal cost of the load being served
(iv) The suppliers must have the opportunity to recover their invested costs

In a nutshell, any new design must hold the capacity to improve at least one of these: economic efficiency, reliability and incentive compatibility. In the power market of a developing country like India, Indian Energy Exchange (IEX) serves as a premier power trading platform. Catering to more than 5800 registered participants located across 29 states and 5 union territories, IEX serves as an automated platform for the delivery of electricity, physically. Apart from the participants who traded electricity contracts, participants also registered trade Renewable Energy Certificates which include about 1,000 renewable energy generators and approximately 2,900 industry customers, as of March 2017 [8].

3 Transition from Conventional to Renewables

The Indian power scenario has shown a leap of growth since last decade. During the last 5 years, the installed capacity has increased at a compound annual growth rate (CAGR) of 10%. Figure 1 illustrates the growth of installed generation capacity, clearly bifurcating the share of different generating sources available, i.e. gas and diesel, coal, hydro, nuclear and renewable energy sources (RES). It is seen that the share of RES and hydro shows a gradual rise every year, thus subtly setting hope that it may replace the conventional fuels of generation in the near future [10]. Thus, RES hold the potential to replace conventional sources completely, in a few years from now.

3.1 Solar Energy in India: A Vast Potential

Indian subcontinent is blessed with a vast solar energy potential waiting to be tapped. It witnesses about 300 sunny days, i.e. considering most parts of the country, the average solar radiation incident lies between 4 and 7 kWh per day. The direct conversion of sunlight into energy is possible by utilizing solar photovoltaic technology. Last few decades saw the advent of several solar energy-based systems which were deployed in different parts of India, providing energy solutions for varied purposes such as cooking, water heating, lighting and most importantly electricity generation. The National Solar Mission (NSM) was launched by the Government of India on 11 January 2010 with a target to include [9]:
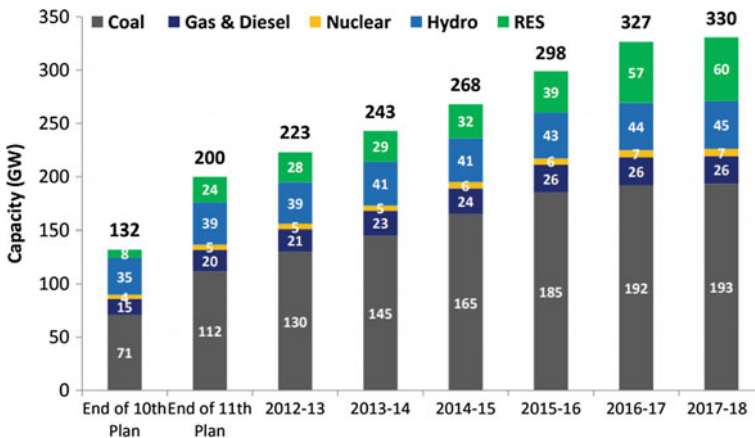
Fig. 1 Installed generation capacity of India. *Source* CEA, GOI, As on 31 December 2017

Table 1 State-wise grid-connected solar projects commissioned under the RPSSGP scheme [9]

State	No. of projects	Capacity (MW)
Andhra Pradesh	10	9.75
Chhattisgarh	2	4
Haryana	8	7.8
Jharkhand	8	16
Madhya Pradesh	3	5.25
Maharashtra	3	5
Odisha	7	7
Punjab	5	6
Rajasthan	12	12
Tamil Nadu	6	6
Uttarakhand	3	5
Uttar Pradesh	4	7
Total	71	90.8

  (i)   20,000 MW of grid-connected solar power deployment by the year 2022.

 (ii) Off-grid solar applications of 2000 MW which includes about 20 million solar lights by the year 2022.

(iii) Solar thermal collector area of about 20 million m^2.

(iv) Conditions favourable for development of solar manufacturing in the country.

 (v) Capacity building activities and support research and development in order to achieve grid parity by the year 2022.

Ministry of New and Renewable Energy (MNRE) announced guidelines, for power plants powered by solar energy below 33 kV, connected to the distribution network. They were named Rooftop PV and Small Solar Power Generation Programme (RPSSGP). This scheme was aimed at setting up small grid-connected solar projects in various states of India. Seventy-eight projects were chosen to be set up with a capacity of 98 MW from 12 States. Also, 71 projects with a total capacity of 90.80 MW are grid-connected. The state-wise data is given in Table 1.

The data given in Table 1 are the clear indication of the growing potential of grid-connected solar systems across the nation and the fact that they can be banked upon as the future substitute to the existing, pollution causing fuels.

3.2 Wind Energy: The Indian Scenario

Early 1990s saw wind power development peaking in the country. Wind power installed capacity presently in India is about 32.5 GW, i.e. approximately 55% of the power generation capacity with renewable installed. Wind energy contribution

Wind Potential at 100 metres (GW)
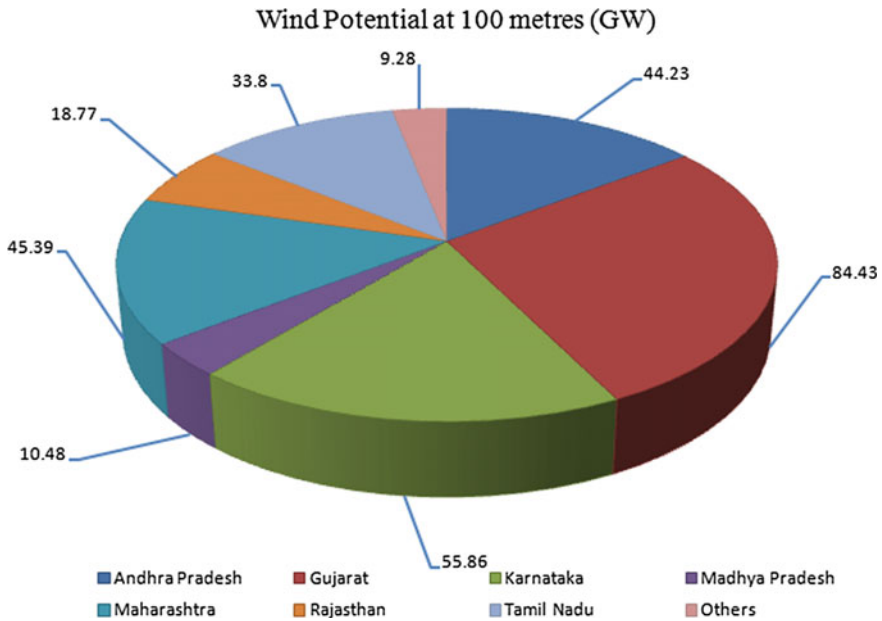
Fig. 2 Pie chart showing wind energy potential in different Indian states. As on 31 March 2017

in the total renewable generation was 55, 50 and 56% during the year 2014–15, 2015–16 and 2016–17, respectively.

Few Indian states (as shown in Fig. 2) show remarkable wind energy potential [10], which is being exploited well by the Indian Government, in order to sustainably manage the rising energy demand of the country.

The huge potential in various Indian states opens new avenues of opportunities waiting to be tapped to their maximum capacity. India has set a goal of powering 40% of its installed electric capacity by renewable or clean energy sources by 2030. This would help in drastically reducing the "emissions intensity". Wind energy, being clean and non-polluting, would play a significant role in achieving this goal.

4 Conclusion

The advent of microgrid technology will prove to be a boon for the remote areas where power transmission is both cumbersome and expensive. Power generation using green fuels would be a befitting solution for the pollution caused to the environment by fossil fuels. The huge potential in various Indian states, as reviewed in this work, opens wide avenues of possibilities for renewable generation to be tapped to its maximum capacity. It is thus realized that developing countries like India hold a bright potential in terms of ample renewable availability, thus making it

utmost suitable for microgrid installation. It thus can be foreseen that microgrids would be powering the future, especially in countries like India, where varied renewable sources are available in plenty. The Indian electricity market is ready to witness a transition to a completely deregulated market. Also, the abundant renewable sources, it is bestowed with, when used as generating fuels, would help reduce drastically the energy demand–supply gap that the country faces.

References

1. Mandelli S, Mereu R (2013) Distributed generation for access to electricity: "off-main-grid" systems from home-based to microgrid. In: Renewable energy for unleashing sustainable development. Springer International Publishing, pp 75–97
2. Kaur J, Sood YR, Shrivastava R (2017) A two-layer optimization approach for renewable energy management of green microgrid in deregulated power sector. J Renew Sustain Energy 9(6):065905
3. Infield D, Li F (2008) Integrating micro-generation into distribution systems—a review of recent research. In: IEEE PES General Meeting, pp 1–4
4. Varley C, Lammers G (1999) Electricity market reform: an IEA handbook. Organization for Economic
5. Mostert W (2008) Review of experiences with rural electrification agencies: lessons for Africa. European Union (EU) Energy Initiative Partnership Dialogue Facility, Eschborn
6. Banshwar A, Sharma NK, Sood YR, Shrivastava R (2017) Market based procurement of energy and ancillary services from renewable energy sources in deregulated environment. Renew Energy 101:1390–1400
7. Ela E, Wang C, Moorty S, Ragsdale K, O'Sullivan J, Rothleder M, Hobbs B (2017) Electricity markets and renewables: a survey of potential design changes and their consequences. Power Energy Mag 15(6):70–82
8. Indian Energy Exchange Jan. 2018 https://www.iexindia.com/Uploads/Presentation/IEX_DAM_TAM_WEB_2017.pdf
9. National Solar Mission Annual Report (2016–2017) https://mnre.gov.in/annual-report
10. Ministry of New and Renewable Energy. Wind Energy Programme https://mnre.gov.in/wind

Performance Analysis of Interactive Thermal Process Using Various MRAC Techniques

Shubham Kulthe, Chandra Shekher Purohit, Saibal Manna, R. Sudha, B. Jaganatha Pandian and Anis Kazi

Abstract The recent day's chemical processes are widely used in industrial applications. These chemical processes are nonlinear in nature. This nonlinearity can cause instability in process. In this paper, different types of control techniques are studied for control of CSTR with external heat exchanger. Control of this type of CSTR is tedious and arduous because of varying system dynamics and handling of chemical process. This paper presents performance evaluation on the comparison of different adaptive control scheme. MRAC scheme is used as adaptive technique. MRAC with Lyapunov, MRAC with MIT rule, and MRAC with a modification in MIT rule are used for developing adaptive law. MATLAB–Simulink^{TM} is used for simulating all the aforementioned control techniques, and results have been analyzed. Results indicate that MRAC with modified MIT gives better performance compared to other techniques. To quantitatively analyze and compare the performance of all techniques performance, measure such as mean square error (MSE), integral absolute error (IAE), integral time absolute error (ITAE) is applied, and result is compared for the same.

Keywords Continuous stirred tank reactor · Model reference adaptive control · MIT rule · Lyapunov stability method · MRAC-PD

S. Kulthe · C. S. Purohit · S. Manna · R. Sudha · B. J. Pandian · A. Kazi (✉)
School of Electrical Engineering, VIT University, Vellore, Tamil Nadu, India
e-mail: aniskazi17.ak@gmail.com

S. Kulthe
e-mail: Shubhamkulthe584@gmail.com

C. S. Purohit
e-mail: purohit37@hotmail.com

S. Manna
e-mail: mannasaibal1994@gmail.com

R. Sudha
e-mail: sudha.r@vit.ac.in

B. J. Pandian
e-mail: jaganathapandian@vit.ac.in

1   Introduction

In the field of control system, it is often required to handle system which varies their characteristics with time and subjected to occurrence of frequent perturbation, externally as well as internally. Such dynamic and time-varying predicaments of control system are arduous to handle. For aforementioned situation, classical control technique performs poorly as they are unable to handle dynamic system as the matter of fact is classical techniques used for control application are generally designed to handle the process with static or specified tendency [1]. Analysis of various available control techniques to handle system with time-varying and nonlinear dynamics is area of interest. In chemical and crude oil distillation plant, CSTR, which is indeed a tank reactor system, is widely utilized. Control of this dynamic and nonlinear control system is an arduous control problem. Various control techniques have been used for controlling of this nonlinear system, but finding best suitable technique is matter of interest specifically for CSTR with external heat exchanger. Any real-time system can be considered as adaptive system if it is able to maintain the required performance even if large perturbations are present [2]. For such nonlinear system, adaptive controller can provide ameliorated steady-state as well as superior set-point tracking [3]. In real time, it is found that chemical processes are too complex to handle, but adaptive controller can provide better result. These adaptive control techniques were first exploited in 1950 for autopilot mechanism [4]. As an adaptive controller has to adapt according to situation or changing environment, two techniques can be utilized. First one is based on performance, and second one is based on parameter. Gain scheduling is widely accepted adaptive technique, and it is based on adaption of performance. Here, output of the system itself is exploited as a variable for scheduling [5]. Implementation of fuzzy logic with gain scheduling for nonlinear system is discussed [6]. Application of MRAC on CSTR shows fine-tuned and expedites following response with diminished overshoot [7]. Effectiveness of MRAC can be enhanced using fuzzy logic for transient condition [8]. Selection of adaption gain can affect the efficacy of performance of MRAC [9]. The implicate information for application of Lyapunov approach and MIT approach is discussed [10]. In this reported work for a typical CSTR system which is considered to be an arduous control, problem is controlled using various different techniques. Application and performance analysis have been done for Lyapunov approach, MIT rule, and one modified technique named as MRAC-PD which is in turn modification of MIT rule. Finally to quantitatively analyze and compare the performance of all techniques performance, measure such as mean square error (MSE), integral absolute error (IAE), integral time absolute error (ITAE) is applied, and result is compared for the same.

1.1 Model Reference Adaptive Control

The model reference adaptive control (MRAC) is a major controller where desired performance is given as reference model. It termed as an adaptive servo mechanism. It consists of two feedback loops, first one is of process and controller, and second is feedback loop that can change the parameters of controller. Error is generated from taking the difference of system output and reference model output. This error is used to change the controller parameter. There are couples of methods to derive the tools for regulating the constraints in a model. One is gradient method or by applying stability theory. Error among model and process output along with input signal and process output is used to formulate adaption law. Variation of parameters is amid to reduce the error (Fig. 1).

1.2 MRAC MIT Algorithm

The adaptation law challenges to discover a set of constraints that reduce the error among the plant and the model outputs. To achieve it, constraints of the controller are changed till error has condensed to zero. Many adaptation laws have been derived. The two important are the gradient and the Lyapunov approach. In this system reference model, adjustment mechanisms with controller are the main parts. Reference model gives desired state of input and output. Control signal (U) is driven by controller to maintain the closed loop characteristics of plant, i.e., command signal (U_c) to the plant output (Y) is same as dynamics of reference model.

The modeling error e is given by Eq. (1):

$$e = Y - Ym \tag{1}$$

The controller parameters are adjusted with the loss function $J(\theta)$:

$$J(\theta) = e^2/2 \tag{2}$$

Fig. 1 General block diagram of model reference adaptive control
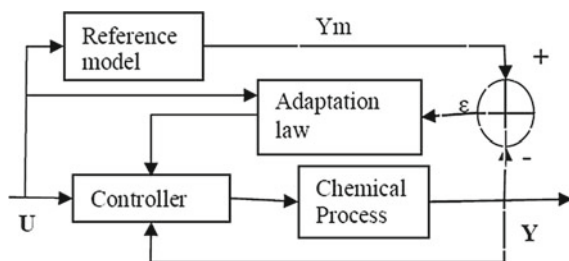
To minimize J, the parameters can be changed in the direction of negative gradient of J. The following parameter adjustment mechanism, called MIT algorithm and represented as in Eq. (3), is used to control the interactive thermal system:

$$\frac{\mathrm{d}\theta}{\mathrm{d}t} = -\gamma e \frac{\partial e}{\partial t} \tag{3}$$

Adaptive control technique can be applied for gray, black, and white—box problems. But it is more appropriate for gray box problems because when process is clear applying 'no model' control method is of no use. Also, dealing with black box problem without studying the actual process is a bad idea. Using prior knowledge here, the process is modeled as second order.

1.3   MRAC with Lyapunov Stability Method

In adaptive control, MIT rule could result in unstable system. Hence, it is always better to use Lyapunov stability method along with MRAC which guarantees systems stability in closed loop.

Consider a time-varying nonlinear system as

$$\dot{x} = f(x, t). \tag{4}$$

$$\text{If } t = t_0 \|x(0)\| = \delta. \tag{5}$$

i.e., the initial state is not the equilibrium state $x^* = 0$ then, the system will be stable if δ is sufficiently small and x stays within ε and x^*. The δ can be selected independently of $t0$, and hence, system is said to be uniformly stable. The system will be unstable if it is possible to find ε which does not allow any δ value. It is said to be asymptotically stable for $\delta < R$ and an arbitrary ε. If this asymptotical stability is guaranteed for any δ, then it is said to be globally asymptotically stable.

1.4   MRAC with PD Feedback

In this paper, a novel technique utilized for improving performance of model reference adaptive control has been studied. In this, an additional PD block has been used with MRAC to improve its performance, and it is termed as MRAC-PD. In control system, proportional derivative is used to handle sudden changes, and same property of PD is utilized in this special type of MRAC so that it gains the capability to handle frequent change in load during transient as well as during steady-state condition. Figure 2 depicts block diagram of MRAC-PD technique.

Fig. 2 Interactive thermal process
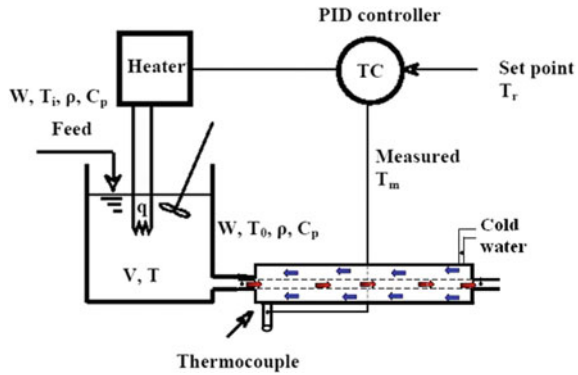
It shows that PD block is connected in feedback to improve the performance of the system. Sole purpose of this technique is to remove oscillation from response of system and make it smooth as much as possible. Here, the value of gain of PD controller is taken as $K_p = 1.2$ and $K_d = 0.05$. Control law for modified MRAC techniques is given by efficacy of this modified technique which is analyzed for a second-order underdamped system. Performance measures such as ISE and IATE are also done to explore and show enhance capabilities of MRAC, to handle large change in load.

2 Process Description and Modeling

A CSTR with a non-isothermal reaction is considered. External heating coil is used to heat the liquid with heat input Q (Kj/min). For controlling temperature in tank closed loop, feedback circuit is used. Output of tank is used as input of heat exchanger. In this process, counter-current tubular heat exchanger is used. The reactor hot fluid crosses the circular duct and cold fluid, i.e., water circulate in annular duct. The thermocouple probes are placed at outlet of cold fluid of tubular heat exchanger. Flow rates of fluid are constant. Reactor parameters are as follows. Continuous stirrer thermal process is classical problem. The interactive thermal process is shown (Fig. 2) along overall material balance.

The CSTR system is modeled using basic accounting and energy conservation principles.

Rate of material accumulation = rate of material in − rate of material out.

$$\frac{dV\rho}{dt} = F_{in}\rho - F_{out}\rho \tag{6}$$

$$A\frac{dh}{dt} = F_i - F_o \tag{7}$$

Energy balance equation is given by,

$$V\rho Cp\frac{dT}{dt} = F\rho Cp(T_i - T) + UA(Q - T) \tag{9}$$

Similarly, heat balance equation for heat exchanger can be derived as (Tables 1 and 2)

$$\rho_w \text{Vol}_w C_{pw}\frac{\partial Tw}{\partial t} = h_h A_h(T_h - T_w) + h_c A_c(T_c - T_w) \tag{10}$$

System transfer function is given by

$$G_p(S) = \frac{0.13S + 4.79}{S^2 + 8.38s + 13.4} \tag{11}$$

Model transfer function is given by

$$G_m(S) = \frac{3.56}{S^2 + 2.67S + 3.56} \tag{12}$$

Table 1 Process parameters for interactive thermal process

Reactor parameters	Value
F/V, hr-l	4
K_o, hr-l	15e12
$(-\Delta H)$, BTU/lbmol	40,000
ρCp, BTU/ft^3	54.65
T_f, c	70
Caf, lbmol/ft^3	0.132
UA/V	122.1
E, BTU/lbmol	33,500

Table 2 Dimensions of external heat exchanger

	L (m)	D (m)	a (m)	P (Kg/m^3)	Cp (J/KgK)
Inner	4.5	0.02	0.001	8900	394
Outer	4.5	0.04	0.003	7850	490

3 Results

Different types of model reference adaptive control techniques had been applied to the interactive thermal process explained before. Using different MRAC techniques, different results have been obtained. Comparing the control action, theta and other parameters of all three MRAC techniques give the brief idea about with adaptation technique is best suited for the problem statement considered here. The simulation results for MRAC MIT rule, MRAC with Lyapunov stability method, and MRAC with PD feedback are compared using various performance measures to know which MRAC technique is more precise. The Simulink models and various results obtained are as follows

3.1 MRAC MIT Rule

(Figure 3) shows simulation of MRAC MIT method, (Fig. 4) shows response for system and (Fig. 5) shows adaption parameter.

3.2 MRAC with Lyapunov Stability Method

(Figure 6) shows simulation for Lyapunov method, (Fig. 7) shows response for the same and (Fig. 8) shows adaption paramter.
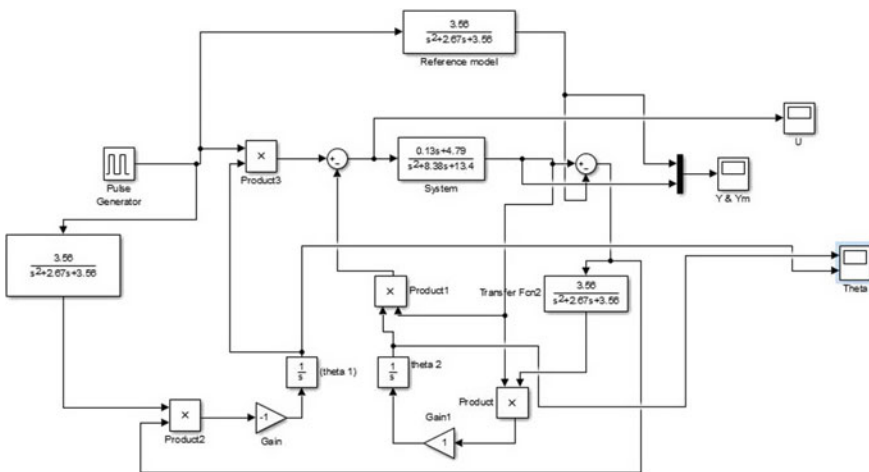
Fig. 3 Simulink model of MRAC MIT rule
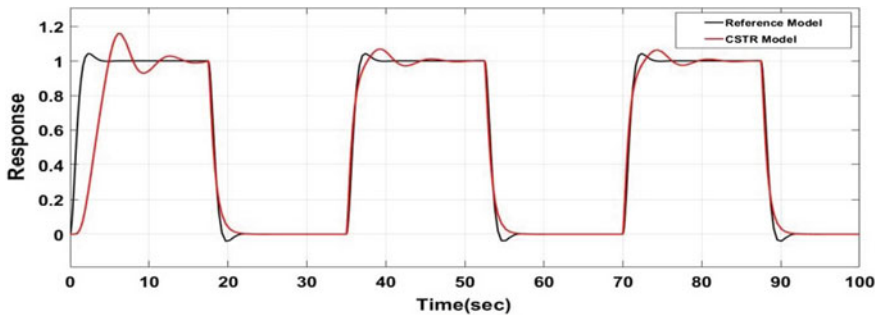
Fig. 4 Response of the system with MRAC MIT model
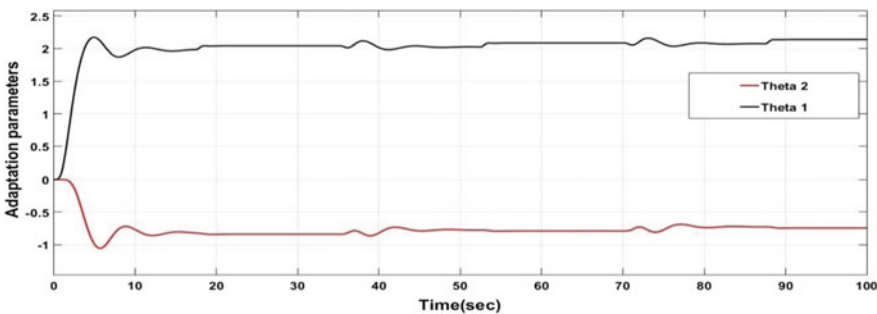
Fig. 5 Theta for MRAC MIT model
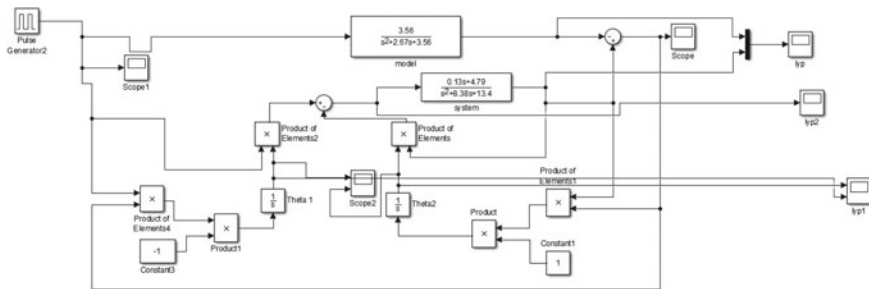
Fig. 6 Simulink model for MRAC with Lyapunov stability method
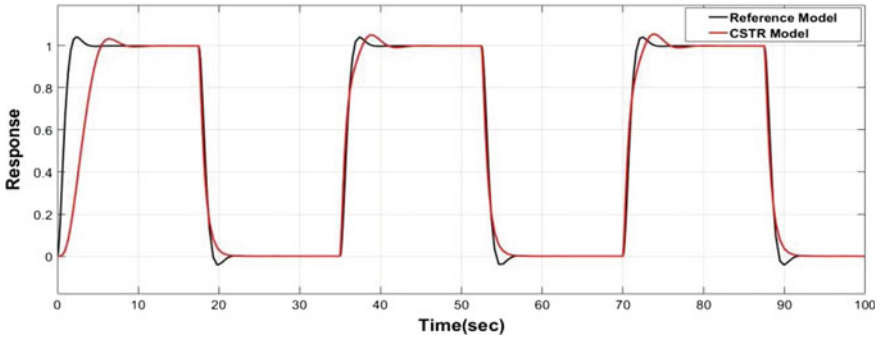
Fig. 7 Response of the system with MRAC with Lyapunov stability method
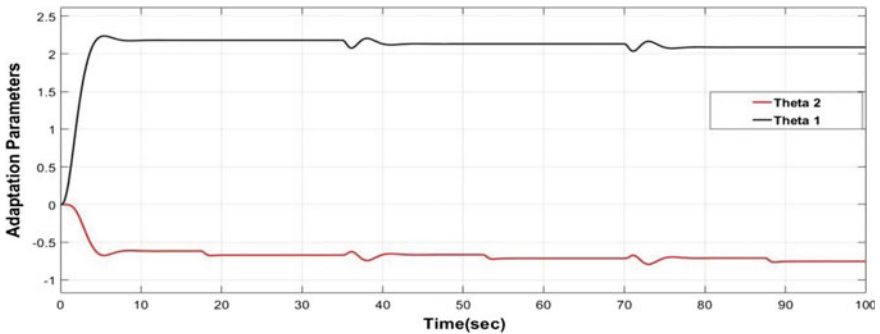
Fig. 8 Theta for MRAC Lyapunov model

3.3   MRAC with PD Feedback

(Figure 9) shows simulation for MRAC-PD method, (Fig. 10) shows response for the same and (Fig. 11) shows adaption parameter. Control action for all three method is shown(Fig. 12). Response comparistion for all three method is shown (Fig. 13), quantitative analysis is presented in Table 3.
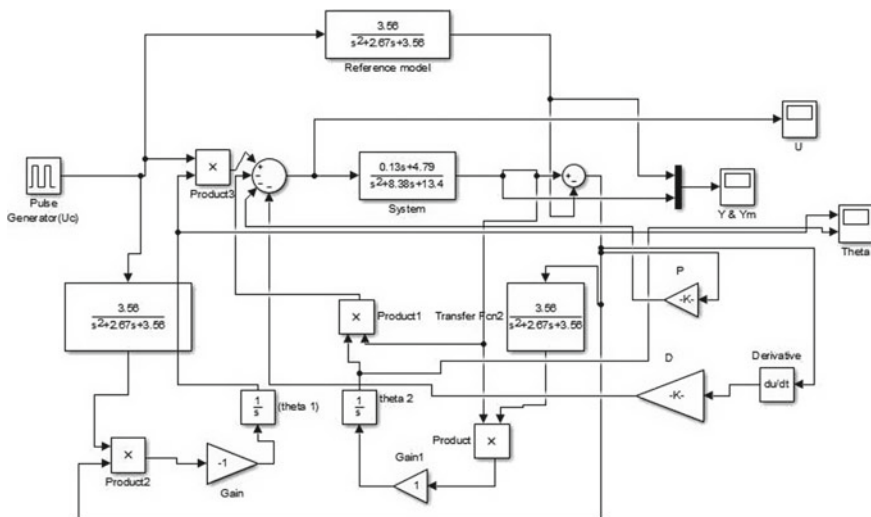
Fig. 9 Simulink model of MRAC with PD feedback
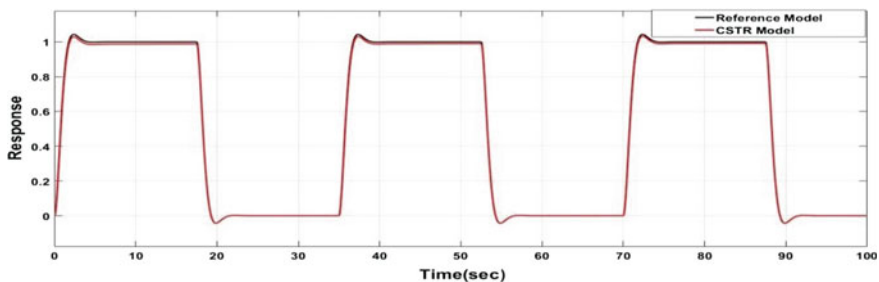
Fig. 10 Response of the system with MRAC-PD
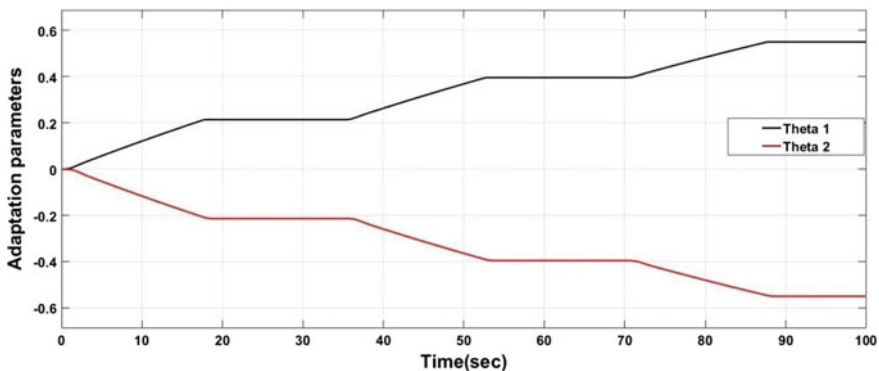
Fig. 11 Theta for MRAC-PD model
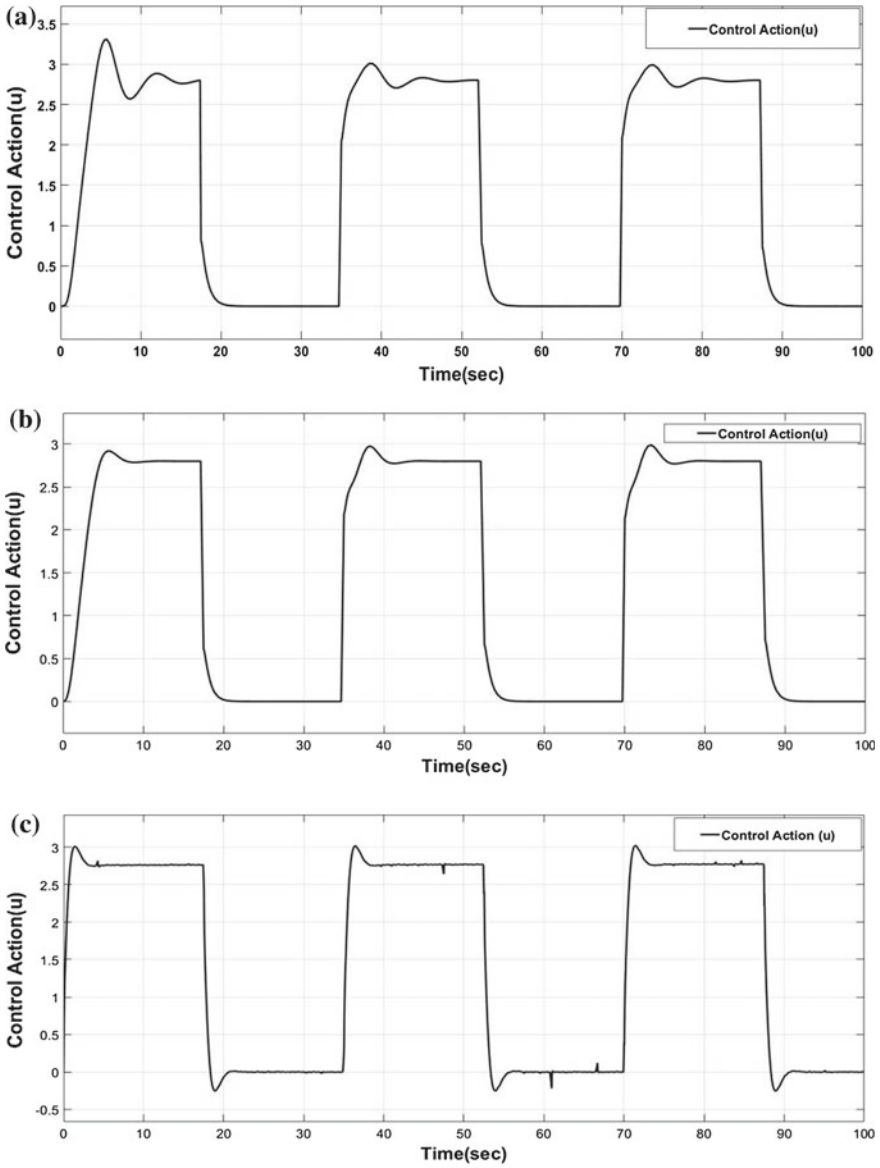
Fig. 12 Control action for **a** MRAC MIT, **b** MRAC Lyapunov, and **c** MRAC-PD
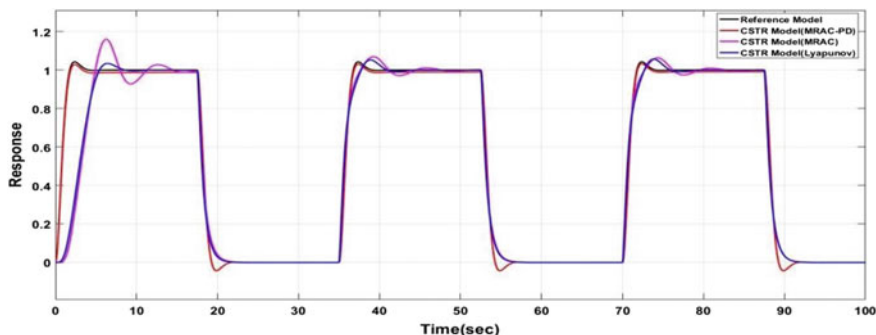
Fig. 13 Response of the system with all the MRAC models

Table 3 Performance analysis of different MRAC techniques for interactive thermal process

Controller mode	Error	ISE	IAE	ITAE
MRAC MIT	4.54×10^{-06}	2.061×10^{-11}	4.54×10^{-06}	0.000454
MRAC Lyapunov	4.573×10^{-05}	2.091×10^{-9}	4.573×10^{-05}	0.004573
MRAC-PD	4.126×10^{-08}	1.702×10^{-15}	4.126×10^{-08}	4.126×10^{-06}

4 Conclusion

In this paper, we reviewed different control strategies for MRAC that is Lyapunov, MIT, and modified MIT (MIT-PD) for temperature control of CSTR with external heat exchanger. After simulating all three control strategies, we can conclude that Lyapunov adaption rule for MRAC shows lesser overshoot as compared to MRAC with pure MIT, but it takes more time to adapt. Whereas we can say that modified MIT rule that is addition of proportional derivative controller in MIT rule for adaption law shows better response, ameliorated error handling fast adaption, and lesser error value as compared to both MRAC with MIT and Lyapunov both. This paper presents performance analysis for underdamped and second-order system only so application of these techniques for higher-order system could be considered for the future work.

References

1. Seborg DE, Edgar TF, Mellichamp DA (2004) Process dynamic and control, 2nd edn. Wiley, New York
2. Black WS, Haghi P, Ariyur KB (2014) Adaptive systems: history, techniques, problems, and perspectives. Systems 2:606–660. https://doi.org/10.3390/systems2040606
3. Astrom KJ, Wittenmark B (2009) Adaptive control, 2nd edn. Dover Publications

4. Whitaker H, Yamron J, Kezer A (1958) Design of model reference adaptive control systems for aircraft (Report R-164);: Cambridge. MIT Press Instrumentation Laboratory, Cambridge, MA, USA

5. Yuan C, Liu Y, Wu F, Duan C (2016) Hybrid switched gain- scheduling control for missile autopilot design. J Guid Control Dyn 39(10):2352–2363

6. AbuNasr MS, Elaydi HA (2017) Fuzzy gain scheduling control for a special case of 2nd order non-linear systems. In: 2017 international conference on promising electronic technologies (ICPET), Deir El-Balah, pp 20–25. https://doi.org/10.1109/icpet.2017.10

7. Ratnakumari UV, Triven MB (2016) Implementation of adaptive model predictive controller and model predictive control for temperature regulation and concentration tracking of CSTR. In: 2016 international conference on communication and electronics systems (ICCES), Coimbatore, pp 1–6. https://doi.org/10.1109/cesys.2016.7889843

8. Bojan-Dragos CA, Precup RE, Hergane S, Teban TA, Petriu EM (2017) Fuzzy logic-based adaptive control scheme for magnetic levitation systems. In: 2017 IEEE international symposium on robotics and intelligent sensors (IRIS), Ottawa, ON, pp 160–165. https://doi.org/10.1109/iris.2017.8250115

9. Swarnkar P, Jain S, Nema RK (2011) Effect of adaptation gain in model reference adaptive controlled second order system. Eng Technol Appl Sci Res 1(_o.3):70–75

10. Chen Y-R, Wu J, Cheung NC (2004) Lyapunov's stability theory-based model reference adaptive control for permanent magnet linear motor drives. In: 1st IEEE international conference on power electronics system and applications, Hong Kong, China, pp 260–266

Wind Speed and Power Forecast for Very Short Time Duration Using Neural Network Approach—A Case Study

M. B. Hemanth Kumar and B. Saravanan

Abstract The effective operation of the wind farm is decided by the accuracy of forecasted wind speed and the wind power generated. In this paper, an improved neural network based on radial basis function is implemented for very short-term duration forecasting. For training, the neural network Gaussian function is included in the hidden layer to find the initial values which are key parameters for training the neural network. A case study is carried out for the wind farm located at Seshachalam hills near Tirupati as the target location. Test data are considered for different months of 2017 for training and compared with other artificial neural network methods. The accuracy of all the methods has been studied and presented, showing that the proposed model is having less forecast error.

Keywords Wind forecast · Wind power · Radial basis function · Neural network

1 Introduction

With depleting fossil fuels, there is an increased focus on wind power generation and various aspects associated with it. It is also an alternative to the conventional energy source and the future energy for the world that need to be focused [1, 18]. Even though there are many benefits of integrating wind energy into the electricity network, few limitations are stressed in operation and planning. These problems are mainly caused due to intermittency and uncertainty in its availability in nature.

In power system planning and scheduling of generators, it is better to have a forecast from 1 to 72 h. This is also beneficial for the electricity trading between two regions. Once the forecast has been done accurately, we can have a better trade

M. B. Hemanth Kumar (✉) · B. Saravanan
VIT, Vellore, Tamil Nadu, India
e-mail: hemanthkumar.b@vit.ac.in

B. Saravanan
e-mail: bsaravanan@vit.ac.in

in terms of energy storage and wind power. This short-term forecasting also benefits the wind farm for improving the efficiency and decreasing the overloading on the power plants [2, 19]. By this, the reserve capacity can be reduced ultimately, thereby decreasing the cost of installing power plants.

Machine learning (ML) [3] is an interesting area that can be applied to many areas of optimization problems and most preferably probabilistic nature. Artificial intelligence [4] and machine learning are nearly same, but machine learning can learn by experience based on historical events. While artificial intelligence needs well training and cannot identify new environment easily. There are few techniques which include recurrent neural networks [5], support vector machine [6], and multilayer perception [7]. When an ML is introduced for any problem, it can solve nonlinear problems like forecasting.

Nowadays, a lot of work is being done in the area of wind and power forecasting. From the literature, it is well known that numerical weather prediction (NWP) gives better accuracy compared to other methods. The only disadvantage in using NWP is that it requires more data information and it is better suited for longtime predictions. In [8], NWP combined with Kalman filter was used to improve the accuracy of forecasting, and in [9] a performance comparison is made among autoregressive moving average (ARIMA), artificial neural network (ANN) and support vector machine (SVM) for short-period prediction applications.

The hybrid models, i.e., ARIMA-SVM and other such models, gave better performance in terms of forecast error compared to individual models. In [10], backpropagation NN, radial basis function neural network (RBFNN), and artificial neural network fuzzy inference system (ANFIS) were used for wind forecasting. The studies showed that the hybrid models are performing better compared to individual models for wind forecasting applications. Among all the above models, RBFNN is having greater flexibility in time series analysis and predictions. It has the capability to manage higher-order nonlinear functions and the usage of approximations [11, 12].

While implementing the RBFNN, it finds difficult for tracing the parameters and standard deviation for the Gaussian basis function. Irrespective of the approach being supervised or unsupervised, the parameters play an important role in estimating the forecasting error. The RBFNN methods are often affecting the time of convergence and accuracy due to parameter settings.

For improving the forecasting accuracy and to overcome the drawbacks in the literature, the error feedback in a neural network is included. By this, the convergence and the accuracy of the model improve in terms of wind speed and power forecasting.

2 Wind Speed and Power Forecasting

The need to perform the wind forecasting is to provide the energy competitors and marketing personals to estimate the amount of energy that will be available in future time intervals. The forecasting can be classified into four types based on the time intervals: long, medium, short, and very short time intervals. Among these, very short time forecasting is used to perform the energy trading and regulations [13].

This forecasting can also be used for economic dispatch; long terms are used for scheduling the machines. For forecasting the wind speed, some of the tools use the terrain data at which the wind turbines are located as one of the inputs. The forecasting uses physical and statistical methodologies, and further, some may use a combination of both to form a hybrid approach. This hybrid model includes the advantages of both individual models.

The physical model for forecasting uses the physical properties of the site [14] taken under study. The wind farm physical description includes the farm layout, terrain information, and power curve. The statistical modeling requires past data for forecasting [15]. Commonly used forecasting models use the time series for forecasting the data. The forecasting has majorly four steps that include identifying the model, estimating the inputs, checking, and at last forecasting. Some of the time series models are autoregressive (AR), autoregressive moving average (ARMA), and moving average (MA). By using ANN, the input datasets are given as training input for obtaining the future outputs. We can also obtain a hybrid model by merging two models having different advantages to improve the accuracy [16, 17].

3 Proposed Forecasting Model

An improved RBFN with an error feedback is introduced for estimating minimum error which is shown in Fig. 1. For increasing the searching range, a Gaussian basis function, i.e., a shape parameter, is included. This will estimate the initial value of standard deviation and center values. The forecasting model is performed by taking 150 min of wind speed as input and used for forecasting 210 min of wind speed. The procedure is explained below.

The RBFNN consists of a three-layer network, and each input represents a multi-dimensional vector. A single hidden layer has M neurons known as RBF units and is connected to the output layer.

The Gaussian function for an RBFNN is given by

$$\varphi_j(x) = \exp\left(-\frac{S_j^2(x-c_j)^2}{\sigma_j^2}\right), \ j = 1, 2, 3, \ldots, M+N \tag{1}$$
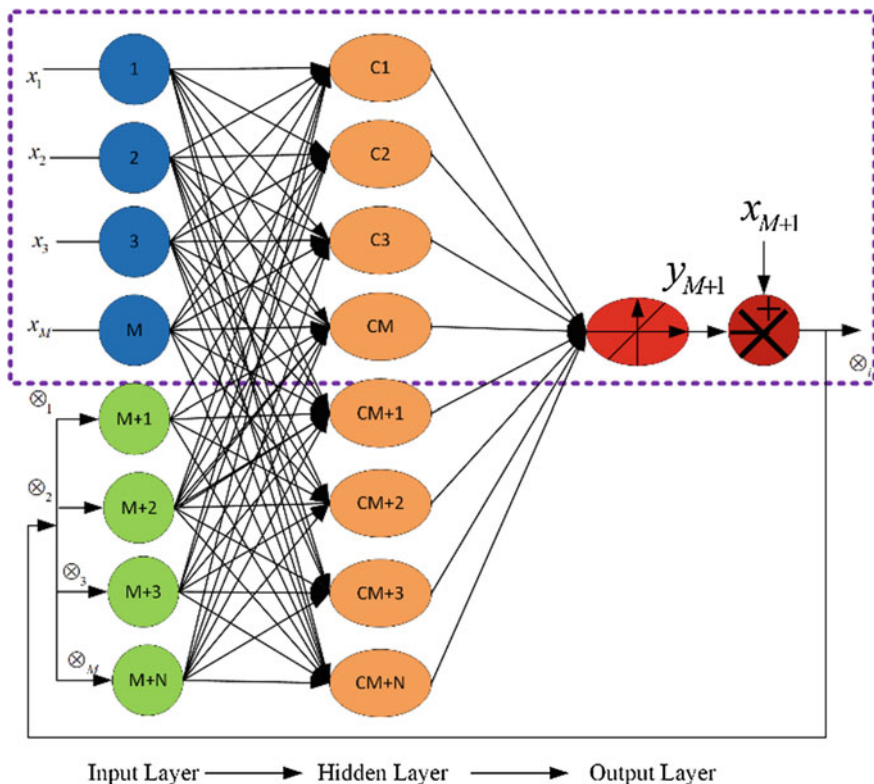
Fig. 1 Neural network training process

$$y_{M+i} = \sum_{j=1}^{J} w_j \varphi_j(x), \quad i = 1, 2, 3, \ldots, N_I \tag{2}$$

$$\xi(n) = \frac{1}{2}(x_{M+i} - y_{M+i})^2 = \frac{1}{2}\varepsilon_i^2(n) \tag{3}$$

$$\mu^* = \left(\sum_{j=1}^{J} x_j\right)/(M+N) \tag{4}$$

$$\sigma^* = \sqrt{\sum_{j=1}^{J}(x_j - \mu^*)^2/(M+N)} \tag{5}$$

$$w_j(n+1) = w_j(n) - \eta_1 \frac{\partial \xi(n)}{\partial w_j(n)} = w_j(n) - \eta_1 \frac{\partial \xi(n)}{\partial y_{M+i}(n)} \frac{\partial y_{M+i}(n)}{\partial w_j(n)} \tag{6}$$

$$c_j(n+1) = c_j(n) - \eta_2 \frac{\partial \xi(n)}{\partial c_j(n)} = c_j(n) - \eta_2 \frac{\partial \xi(n)}{\partial \varphi_j(n)} \frac{\partial \varphi_j(n)}{\partial c_j(n)} \tag{7}$$

$$\sigma_j(n+1) = \sigma_j(n) - \eta_3 \frac{\partial \xi(n)}{\partial \sigma_j(n)} = \sigma_j(n) - \eta_3 \frac{\partial \xi(n)}{\partial \varphi_j(n)} \frac{\partial \varphi_j(n)}{\partial \sigma_j(n)} \tag{8}$$

$$s_j(n+1) = s_j(n) + \eta_4 \frac{\partial \xi(n)}{\partial s_j(n)} = s_j(n) + \eta_4 \frac{\partial \xi(n)}{\partial \varphi_j(n)} \frac{\partial \varphi_j(n)}{\partial s_j(n)} \tag{9}$$

$$w_j(n+1) = w_j(n) + \eta_1 \xi(n) \varphi_j(x(n)) \tag{10}$$

$$c_j(n+1) = c_j(n) + 2\eta_2 \frac{s_j^2(n)w_j(n)\xi(n)}{\sigma_j^2(n)} \varphi_j(x(n))(x(n) - c_j(n)) \tag{11}$$

$$\sigma_j(n+1) = \sigma_j(n) + 2\eta_3 \frac{s_j^2(n)w_j(n)\xi(n)}{\sigma_j^3(n)} \varphi_j(x(n))||(x(n) - c_j(n)||^2 \tag{12}$$

$$s_j(n+1) = s_j(n) - 2\eta_4 \frac{s_j(n)w_j(n)\xi(n)}{\sigma_j^2(n)} \varphi_j(x(n))||(x(n) - c_j(n)||^2. \tag{13}$$

In the modified RBFNN with feedback, the additional N error terms are feedback to N additional neurons in the input layer.

On considering shape parameter S_j in the hidden neurons, the function can be written as (1), where x is the input with N number of data from the feedback. σ_j represents the standard deviation. The output layer with the weighted matrix is given by (2), where N_I is the total input in order to train and w_j gives the weight in between the hidden and output neurons.

The neural networks can be subjected to error feedback in order to forecast the data precisely. At a point, the present value is considered as the error from the network. When the learning is progressing, the model will reach the approximate value.

4 Forecasting Procedure

The first phase is to train the input from M datasets consisting of 150*M with M data for each hour of measured wind velocity. While training the output, error is fed back to the input for N points to improve the accuracy during the training process.

When the training process is completed, we get weight, shape parameter, and standard deviation for individual hidden neurons. These values are placed in a lookup table for calling these values for forecasting wind speed and power values.

From (1) and (2), estimate the target output with the trained datasets. Now, we repeat the process from (10) to (13) from steepest descent method and we update these values with the previously stored values in the lookup table.

Now calculate the error for N number of input neurons and verify if the parameters are meeting the threshold value once the condition is satisfied to update the values.

Once the training process is completed, the lookup table values are used to forecast the wind speed and power by implementing a new wind data as input. The forecasted wind speed and power are calculated from (2). After the process has been completed, check whether the number of output data to be forecasted has reached, else increase the data at the input and use forecasted values as the final input and repeat the process.

5 Results

The wind data are collected from National atmospheric research laboratory located near Tirupati. The average wind speed is about 3 m/s at that location for the year and also in the surrounding areas.

Here, we have considered wind data for different months for and ahead time of 210 min with a 10 min of resolution. In this study, 150-min data are taken as training with 10 min of resolution.

The learning rate is fixed at 0.05 for effective forecasting accuracy of wind speed and power. The proposed model is compared with conventional forecasting models ANFIS, RBFNN, and BPNN. The threshold values for each parameter are maintained at 10^{-6}. Figure 2 shows the input wind speed taken for training the forecast model.
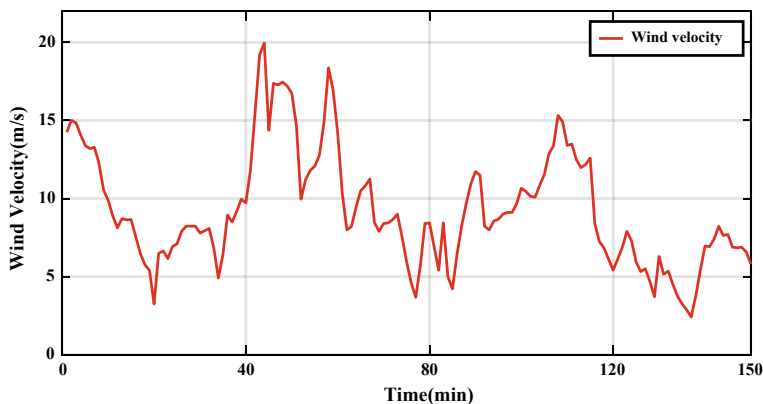
Fig. 2 Wind speed taken at the target location for training the neural network
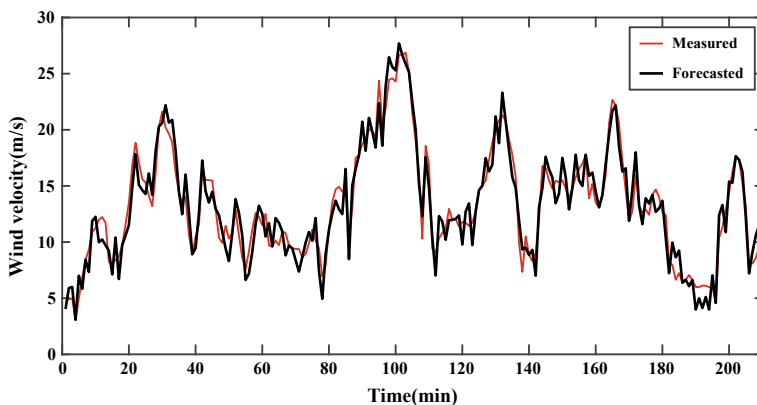
Fig. 3 Forecasted wind speed for the proposed model with measured wind speed

Figure 3 shows the forecasted wind speed for the next day with the actual measured wind speed. The table shows the error for the forecasted wind speed with the parameters of mean absolute percentage error (MAPE) and root-mean-squared percentage error (RMSPE).

$$\text{MAPE} = \frac{\sum_{q=1}^{Q_T} \frac{|x_{q,\text{measured}} - x_{q,\text{forecast}}|}{x_{q,\text{measured}}}}{Q_T} \times 100\% \tag{14}$$

$$\text{RMSPE} = \frac{\sqrt{\sum_{q=1}^{Q_T} \left(\frac{|x_{q,\text{measured}} - x_{q,\text{forecast}}|}{x_{q,\text{measured}}}\right)^2}}{Q_T} \times 100\%. \tag{15}$$

The wind power forecast is also performed by measuring the power output for 24 h with 10-min resolution. For forecasting, the next three days' wind power is taken for validating the forecasted values.

Figure 4 shows the training wind power data, and Fig. 5 shows the forecasted power with the measured power. Tables 1 and 2 give the error for wind power forecast.
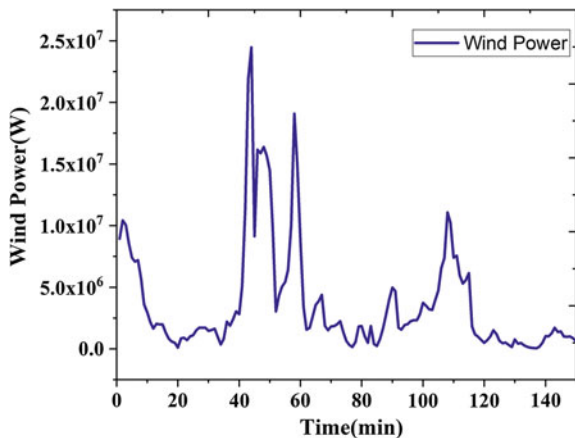
Fig. 4 Wind power for a time scale of 150 min for training the network
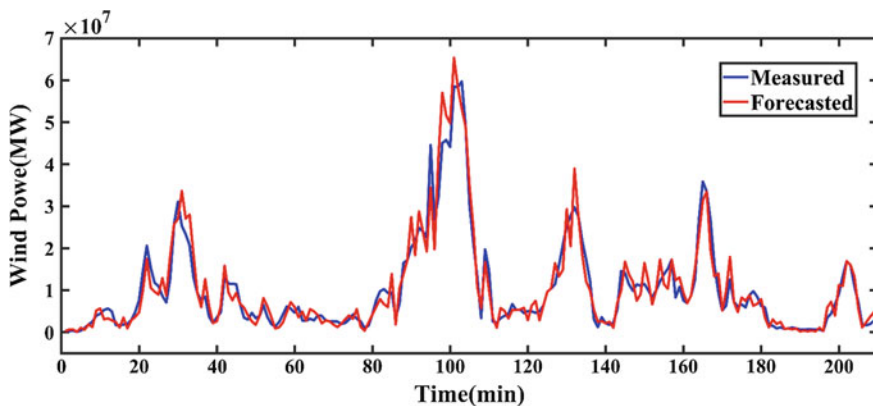
Fig. 5 Forecasted wind power and measured power for 210 min

Table 1 Forecast error for the wind speed with conventional methods

	MAPE%	RMSPE%	No. of iterations
RBFNN	23.645	27.392	650
RBFNN-EF	3.642	4.253	532
BPNN	28.743	27.432	942
ANFIS	2.345	4.281	915
Proposed	2.015	4.103	465

Table 2 Forecast error for the wind power with conventional methods

	MAPE%	RMSPE%	No. of iterations
RBFNN	23.375	23.401	675
RBFNN-EF	3.925	4.682	524
BPNN	26.691	28.026	916
ANFIS	2.024	4.936	928
Proposed	2.011	4.472	436

6 Conclusion

Wind forecasting is very important to predict the energy section in terms of trading, managing resources, transporting, and making profits. With the advancement of technology and globalization, there is a need for huge amount of power for the future and we must be in a situation to forecast the energy available. It may be a day ahead or week ahead or month ahead. Everything has its own merits and applications. Here, the proposed model is compared with conventional forecasting models to estimate the effectiveness. It is clear from the results that the modified RBFNN, ANFIS, and RBFNN are more accurate in forecasting wind speed and power. The ANN is more complex in modeling nonlinear relationship and extracting the relationship between input and output data by learning and training, while the hybrid approach performs better than individual models. With the addition of parameter in the Gaussian function between input and output layer, it provides highly accurate forecasting than conventional models. From the table, it is clear that the proposed model has an error of 2.015% for wind speed and about 4.472% for wind power.

References

1. Monteiro C, Bessa R, Miranda V, Botterud A, Wang J, Conzelmann G (2009) Wind power forecasting: state-of-the-art 2009, Report ANL/DIS-10e1, Argonne Natl. Lab.
2. Riahy G, Abedi M (2008) Short term wind speed forecasting for wind turbine applications using linear prediction method. Renew Energy 3:35e41
3. Rani MS (2017) Analysis on various machine learning based approaches with a perspective on the performance 1–7
4. Lei M, Shiyan L, Chuanwen J, Hongling L, Yan Z (2009) A review on the forecasting of wind speed and generated power. Renew Sustain Energy Rev 13(4):915–920
5. Chow TW, Li SD, Fang Y (2000) A real-time learning control approach for nonlinear continuous-time system using recurrent neural networks. IEEE Trans Ind Electr 47:478e486
6. Santamaría-Bonfil G, Reyes-Ballesteros A, Gershenson C (2016) Wind speed forecasting for wind farms: a method based on support vector regression. Renew Energy 56:790e806

 7. Gnana Sheela K, Deepa SN (2013) Neural network based hybrid computing model for wind speed prediction. *Neurocomputing* 122:425–429
 8. Cassola F, Burland M (2012) Wind speed and wind energy forecast through Kalman filtering of numerical weather prediction model. Appl Energy 99:154–166
 9. Shi J, Guo JM, Zheng SY (2012) Evaluation of hybrid forecasting approaches for wind speed and power generation time series. Renew Sustain Energy Rev 16:3471–3480
10. Haque AU, Mandal P, Kaye ME, Meng J, Chang L, Senjyu T (2012) A new strategy for predicting short-term wind speed using soft computing models. Renew Sustain Energy Rev 16:4563–4573
11. Haykin SS (1999) Neural networks: a comprehensive foundation. Prentice Hall
12. Kasabov NK (1996) Foundations of neural networks, fuzzy systems, and knowledge engineering. MIT Press
13. Elattar EE (2013) Day-ahead price forecasting of electricity markets based on local informative vector machine. IET Gen Trans Dist 7:1063–1071
14. Hemanth Kumar MB, Saravanan B (2017) Impact of global warming and other climatic condition for generation of wind energy and assessing the wind potential for future trends (2018) 2017 Innovations in Power and Advanced Computing Technologies, i-PACT 2017, 2017-Jan 1–5
15. Lange M, Focken U (2006) Physical approach to short-term wind power prediction. Springer
16. Hibon M, Evgeniou T (2005) To combine or not to combine: selecting among forecasts and their combinations. Int J Forecast 21:15–24
17. Sanchez I (2006) Short-term prediction of wind energy production. Int J Forecast 22:43–56
18. Mekalathur HKB (2017) An improved resonant fault current limiter for distribution system under transient conditions. Int J Renew Energy Res (IJRER) 7(2):547–555
19. Ganesh C, Anupama S, Kumar MH (2016) Control of wind energy conversion system and power quality improvement in the sub rated region using extremum seeking. Indonesian J Electr Eng Inf (IJEEI) 4(1):14–23

Photovoltaic Module Designing with Comparison of Different MPPT Techniques

Sandeep Gupta, Navdeep Singh and Shashi Bhushan Singh

Abstract Energy production from solar panels is one of the fastest growing ways of receiving environmental-friendly power. Energy saving is the biggest issue in these days. Therefore, this paper presents a comparison of three different solar panels made by companies from India, Canada and Poland to bring the power of the sun to people in the most efficient and cost-effective way. For this comparison, the number of cells and datasheets are given by the manufacturer. This paper presents PV-cell-based circuit model equations, which define the model for estimating the PV characteristic curves of photovoltaic panel with respect to changes on climate parameters such as irradiance and temperature. In this paper, the MPPT (maximum power point tracking) with DC–DC buck/boost converter is used to obtain time-dependent graphs with the help of MATLAB simulation. The incremental conductance (INC) and perturb and observe (P & O) methods are used to obtaining the maximum efficiency of MPPT. The comparison results of these both methods are also given in this paper.

Keywords MPPT · Photovoltaic · Perturb and observe · Incremental conductance and solar energy

S. Gupta (✉)
JECRC University, Jaipur 303905, Rajasthan, India
e-mail: jecsandeep@gmail.com

N. Singh
MMMUT, Gorakhpur, India
e-mail: navdeepsingh26nov@gmail.com

S. B. Singh
National Institute of Technology, Kurukshetra, India
e-mail: sbsingh@nitkkr.ac.in

1   Introduction

Solar energy in its direct form is used to produce electricity by photovoltaic energy and for the production of heat. Silicon-based semiconductor photoelectric cells are characterized by high reliability and long service life [1]. Photovoltaic (PV) systems directly change the energy of sunrays into electrical energy [2]. The photovoltaic efficacy was discovered in 1954 [1]. After a long time, with many researches today, solar cells are used to power calculators, watches and space satellites, etc. Solar panel has a lot of advantages. From solar panel, electricity is produced directly without any additional conversion, i.e., less loss [3]. There is energy efficiency in the same regardless of the scale of production. Power is generated even during cloudy weather with diffused light [4]. No harmful gases are produced during electricity generation [5]. Solar panel required minimal effort for operation and maintenance.

The disadvantage of photovoltaic cells is their cost and very low efficiency. Solar energy is not 100% reliable. The easiest way to explain it is sun movement, i.e., when the sun is not lucent or cloudy time, energy generation is zero through PV cells. Therefore, power production is generally influenced at the hours of darkness and during wintry weather. This problem is short out with the help of battery backup system, which accumulates the power to be used when the sun is going down and not shining.

For the first time, the photovoltaic effect has been examined by A. C. Becquerel in 1839. W. Adams and R. Day, 37 years later, observed this phenomenon at the boundary of two solid bodies [6]. This crystal which releases paper was taken the center of attention on the photovoltaic modules modeling with composition of different cells. The MPPT charge controller ensures that the loads receive maximum current to be used [7]. The maximum power point is obtained when the solar panel operates, characteristic of a solar panel curvature is knee formed and the position at which the maximum power is obtained, i.e., at MPP, the current and voltage values are given own best output values [8]. The main paper objective is to compare the solar systems of the different manufacturer panels with the help of MPPT algorithms which are based on two different methods such as incremental conductance (INC) and perturb and observe (P & O).

2   Ideal PV Cell Model

A photovoltaic cell is a semiconductor-based appliance that transforms sunlight and reflections of illumination precisely into electricity by the photovoltaic effect. The material from which most of the panels are made is silicon electrons [1]. In the ideal photovoltaic cell, it is assumed that $R_{sh} = R_s = 0$ where R_s is the series resistance which affects more accurate shape between open circuit voltage and MPP—maximum power point. R_{sh} is shunt resistance; this one corresponds to leakage current

Fig. 1 The circuit of platonic photovoltaic cell using a single diode
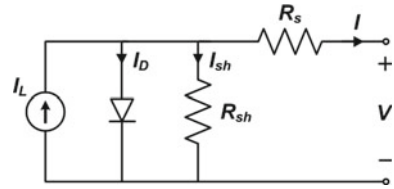
to the ground. Figure 1 shows the circuit diagram of PV cell. Appropriate equations to describe and define the model of PV cell are presented below:

$$V_{\text{oc}} = V_t \ln\left(\frac{I_{\text{ph}}}{I_{\text{s}}}\right) \tag{1}$$

$$I_{\text{d}} = \left[e^{\frac{(V + IR_s)}{(nV_t CN_s)}} - 1\right] I_s N_p \tag{2}$$

$$I_{\text{s}} = I_{\text{rs}}\left(\frac{T_{\text{op}}}{T_{\text{ref}}}\right)^3 e^{\left[\frac{qE_g}{nk}\left(\frac{1}{T_{\text{op}}} - \frac{1}{T_{\text{ref}}}\right)\right]} \tag{3}$$

$$I_{\text{rs}} = \frac{I_{\text{sc}}}{\left[e^{\left(\frac{V_{\text{oc}} q}{kCT_{\text{op}} n}\right)} - 1\right]} \tag{4}$$

$$I_{\text{sh}} = \frac{V + IR_{\text{s}}}{R_{\text{p}}} \tag{5}$$

$$I_{\text{ph}} = G_{\text{k}}\left[I_{\text{sc}} + k\left(T_{\text{op}} - T_{\text{ref}}\right)\right] \tag{6}$$

$$I = I_{\text{ph}} N_{\text{p}} - I_{\text{d}} - I_{\text{sh}} \tag{7}$$

$$V_t = \frac{kT_{\text{op}}}{q} \tag{8}$$

where the series resistance is represented by R_{s}, the photo-current value is denoted by I_{ph}, the reverse saturation current of diode is represented by I_{s}, the output voltage is denoted by V_{oc}, the parallel resistance is denoted by R_{p} symbol, k is Boltzmann's constant (=1.38064852 × 10–23 J/K) and the charges on electron is symbolized by q. Using Eqs. (1)–(8), the solar panel module is formed. Figure 2 shows the basic I–V characteristic of the photovoltaic solar cell. In this figure, the total current (I) in the cell is the combination of the generated current (I_{pv}) by light and the current (I_{d}) in the diode.

The atmospheric conditions are very important for the operation of photovoltaic cells, which determine the changes in sunlight and the working temperature of the
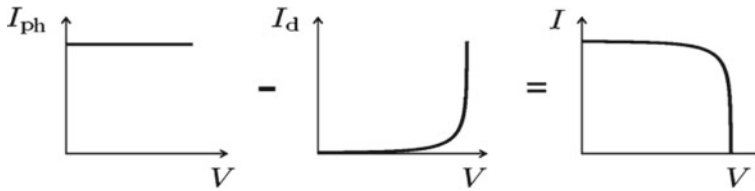
Fig. 2 I–V characteristic curve of the photovoltaic cell
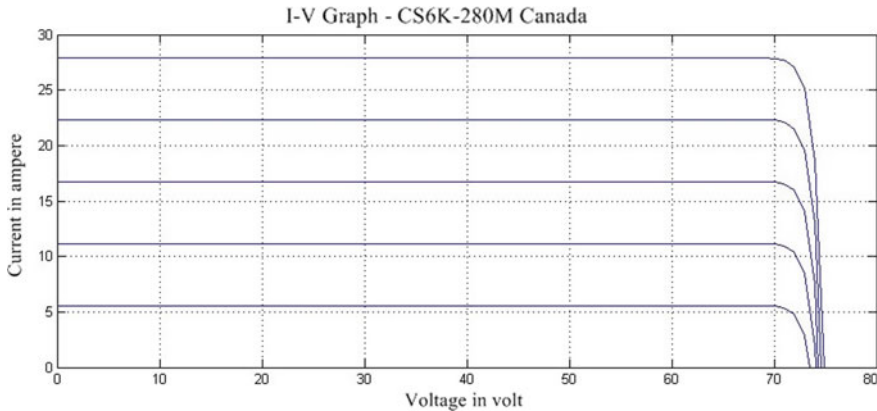
Fig. 3 Characteristic I–V curve of the CS6K-280M PV cell

cell. Thus, they influence the shape of the current–voltage curve. Key influences on the work of photovoltaic cells are atmospheric changing, which determine sunshine changes and temperature of work.

Figure 3 shows the I–V characteristics based on Canadian 72 cells solar panel datasheet CS6K-280M. This figure also shows the MPPT location. In the first graph (in Fig. 3), maximum power point should be at the point where the graph falls, i.e., the voltage is around 75 V, and current is 27.5 A at maximum power point. Therefore, from Fig. 4, two more remarkable points are observed: short circuit (0 V, 27.5 A) and open circuit (75 V, 0 A).

3   Maximum Power Point Tracking

MPPT is an higher power point tracking system, which one can increase the amount of energy obtained by up to 20% (in relation to the inverter without MPPT) [9]. This point changes primarily in shading of modules. All modern inverters have at least one arrangement like that. Photovoltaic modules do not have a single

maximum power point (MPP). It changes according to the intensity of radiation and temperature, because the shape of the power characteristic changes as the function of voltage changes. The purpose of the MPPT is to "track" this point and to adapt as fast as possible to the new value. In fact, the efficiency and speed of the MPPT system guarantee the highest values of processed energy of solar panel.

3.1 Efficient MPPT Commands Algorithms

There are three basic and most used types of maximum power point tracking: hill climbing, perturb and observe and incremental conductance. The problem of local maximum comes in the hill-climbing method [9, 10]. Therefore, in this paper, perturb and observe and incremental conductance methods are used for comparison.

3.2 Perturb and Observe Command Principle

One of the most frequently used algorithms for finding the maximum working point (MPP) is used to find the optional voltage: the perturb and observe (PO) algorithm. This method is nowadays widely used because of its ease of implementation. This algorithm consists in small periodic increases or decreases in voltage and then compares the power delivered at a given moment and the power delivered before the voltage change. On the basis of the power comparison, another value of the voltage increases and its sign is determined. The process of perturb and observe algorithm is explained clearly in Fig. 4.

3.3 Incremental Conductance

This method is based on the principle of impedance matching. Here, power controlling is used to match the internal resistance of the PV module to the input resistance of the converter. The incremental conductance method utilizes the two sensors for the current and voltage measurement to impression the voltage and current outcomes of the photovoltaic array.

From Fig. 5, we can say that incremental conductance method gives greater accuracy than the P & O method under very drastically changing conditions and provides a local maximum MPP. But the weakness of this technique is the greater number of calculations compared to the P & O method. Figure 6 presents a flowchart of incremental conductance algorithm method for solar panel model tracking MPP.
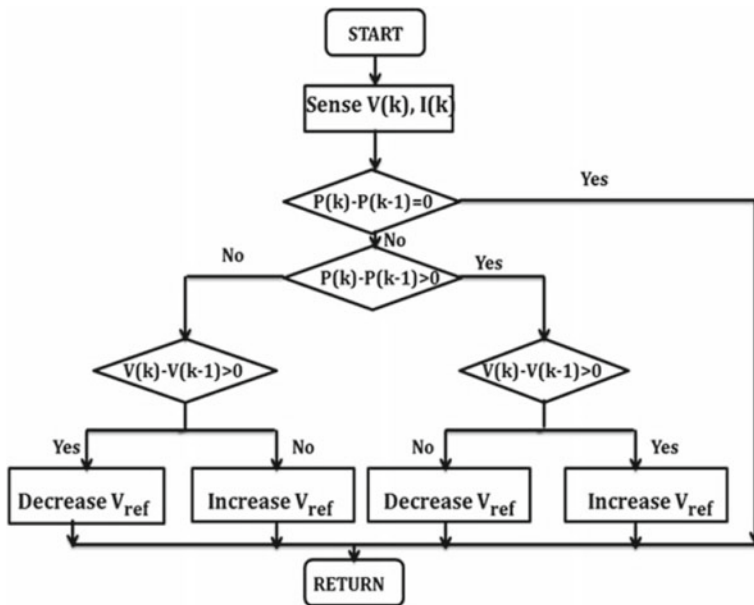
Fig. 4 Flowchart for perturb and observe algorithm
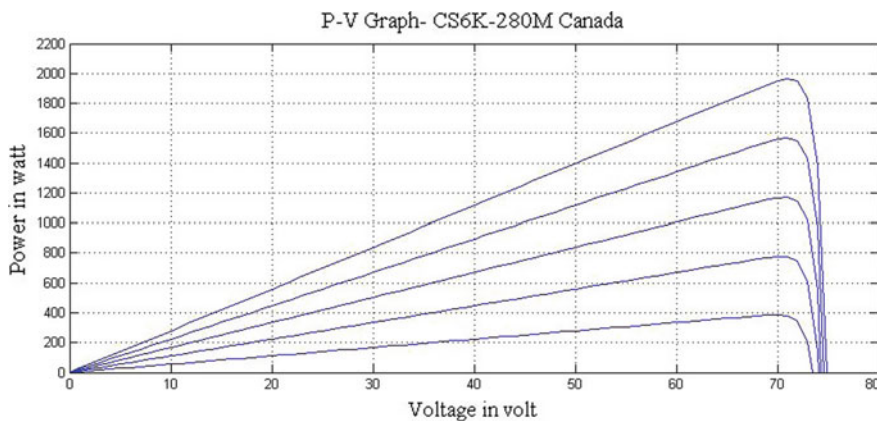
Fig. 5 Characteristic P–V curve of the CS6K-280M PV cell CANADA

4 Simulation Results of Solar System

The model that is devoted to this paper is the design of solar panels enriched with the maximum power point tracking system and DC-to-DC-type converter, which is also called Buck–Boost. This solar system has three components: active switch,
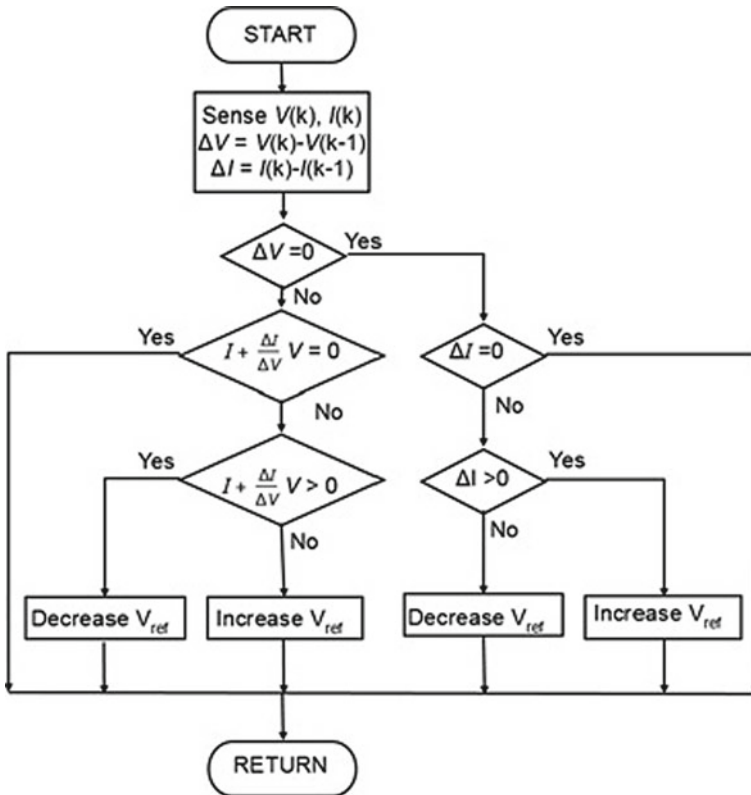
Fig. 6 Flowchart for incremental conductance algorithm

passive switch and inductor. The main task of the converter is buck—means decrease the voltage, and boost—means increase the voltage, relative to the input voltage. In Fig. 7, based on PV system, two different methods (perturb and observe and incremental conductance) are used for making the maximum power point tracking (MPPT) block.

For simulation results, two types of solar panel (CS6K-280M & PVMU60-210) are used in the PV system model. Figure 8 shows the voltage, power and current graphs with solar panel CS6K-280M model. Figure 9 shows the voltage, power and current graphs with solar panel PVMU60-210 model. Results of Figs. 8 and 9 are obtained with the help of incremental conductance topology. Figures 10 and 11 are obtained with the help of perturb and observe method with solar panel models CS6K-280M & PVMU60-210, respectively. These results are given in Tables 1 and 2.
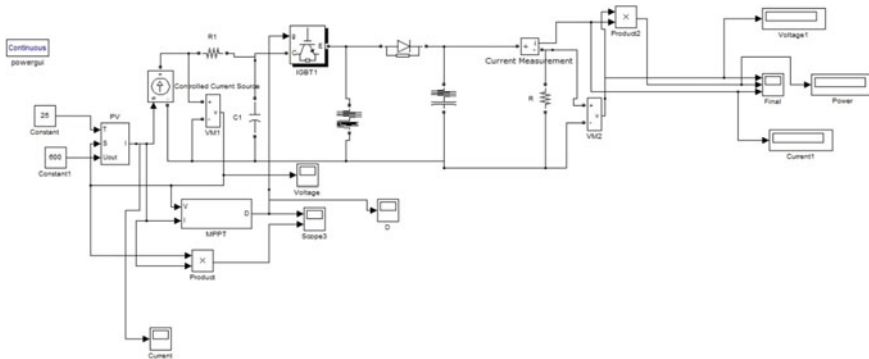
Fig. 7 Simulink model of PV system with MPPT
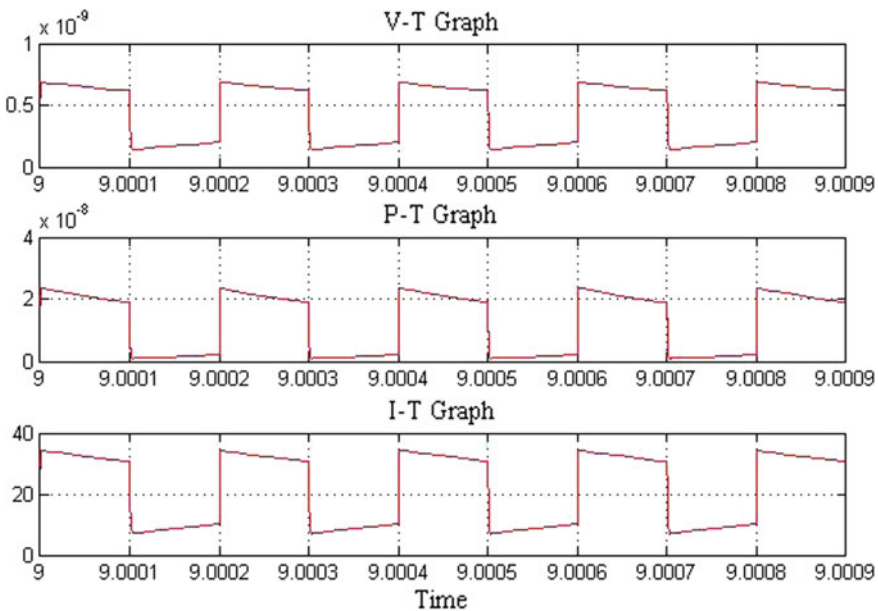
Fig. 8 Voltage, power and current versus time graphs with solar panel CS6K-280M model using incremental conductance method

5 Conclusion

This paper covered the incremental conductance and perturb & observe-based MPPT algorithms. The modeling and simulations of these methods have been introduced and done in MATLAB/Simulink. From the simulation results, we can state that the tracking speed of INC method is faster compared to P & O method.
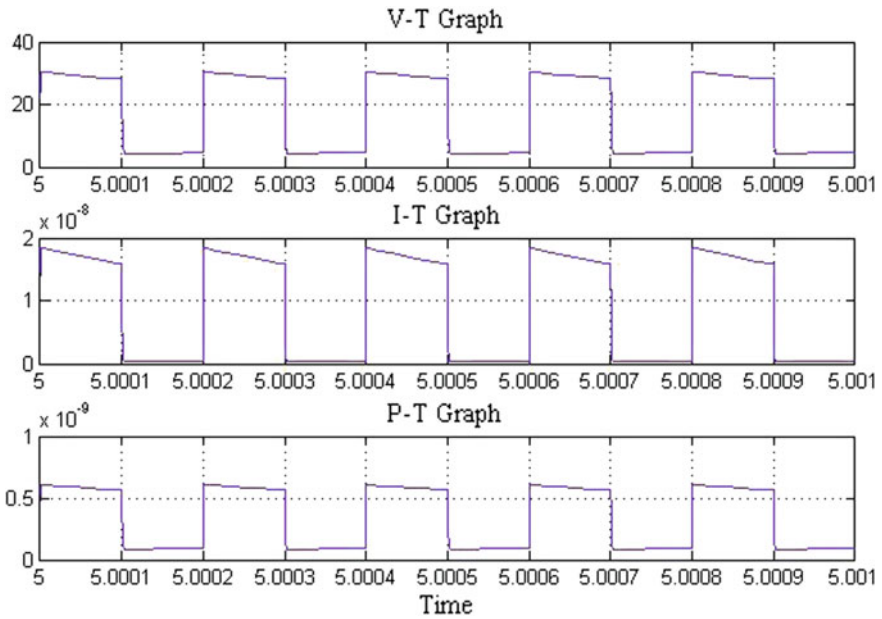
Fig. 9 Voltage, power and current versus time graphs with solar panel PVMU60-210 model using incremental conductance method
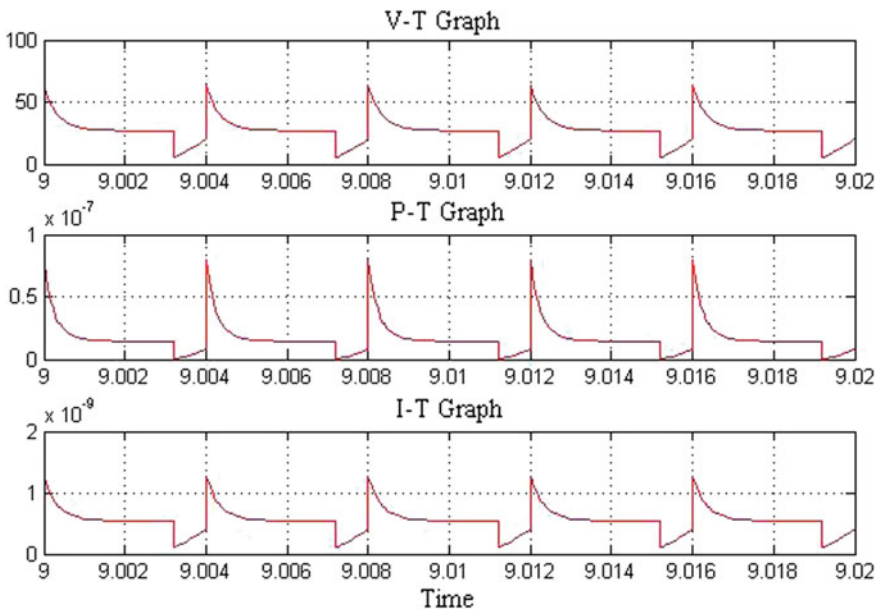
Fig. 10 Voltage, power and current versus time graphs with solar panel CS6K-280M model using perturb and observe method
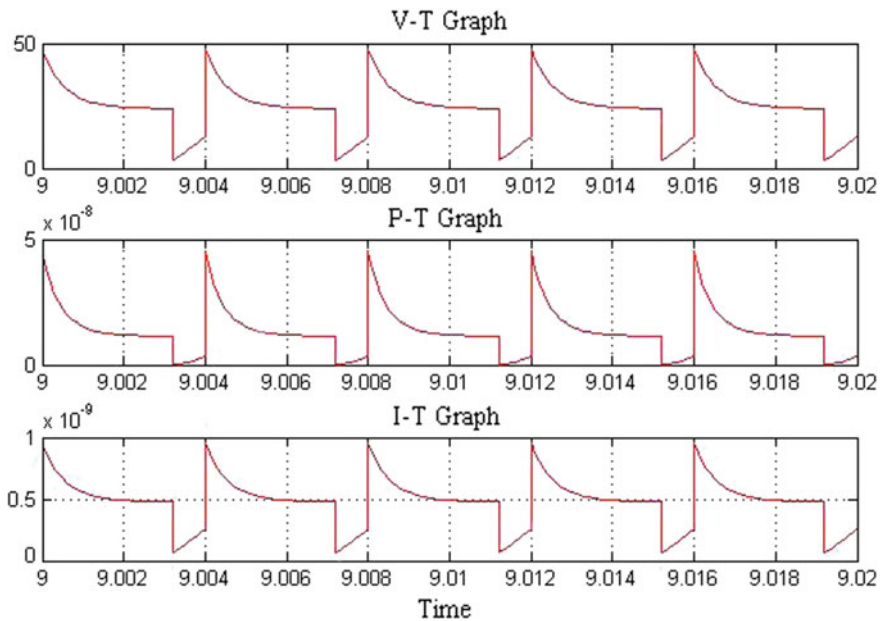
Fig. 11 Voltage, power and current versus time graphs with solar panel PVMU60-210 model using perturb and observe method

Table 1 Outcomes of solar panel using incremental conductance tracking method

Country	Canada	Canada	Canada
Constant	1000	800	600
Current (nA)	20.11	21.68	23.12
Voltage (V)	10.08	10.87	11.6
Power (nW)	2.027	2.357	2.682
Country	Poland	Poland	Poland
Constant	1000	800	600
Current (nA)	971.3	10.64	11.56
Voltage (V)	4.843	5.306	5.765
Power (nW)	47.04	56.46	66.64

It is also found that in perturb and observe algorithm, the number of component used is less as compared to INC algorithm. In this paper, MPPT technique is used to achieve high efficiency. Complexity of P & O method implementation is low. The INC method is more complex. Therefore, the major disadvantage of the INC method is a long calculation time because of much more complicated structure. From simulation outcomes, another important aspect is the power achieved by the P

Table 2 Outcomes of solar panel using perturb and observe tracking method

Country	Canada	Canada	Canada
Constant	1000	800	600
Current (nA)	39.85	42.86	45.62
Voltage (V)	19.95	21.45	22.83
Power (nW)	7.951	9.196	0.1042
Country	Poland	Poland	Poland
Constant	1000	800	600
Current (nA)	25.88	28.18	30.37
Voltage (V)	12.93	14.08	15.17
Power (nW)	3.345	3.966	4.608

& O method which is much larger than that obtained with INC method. Finally, by comparing both methods, we can say that the perturb and observe method-based MPPT tracking is definitely better.

References

1. Gupta S, Sharma A (2018) Global scenario of solar photovoltaic (SPV) materials. In: Advanced computational and communication paradigms. Springer, Singapore, pp 126–133
2. Villalva MG, Gazoli JR, Ruppert Filho E (2009) Comprehensive approach to modeling and simulation of photovoltaic arrays. IEEE Trans Power Electron 24(5):1198–1208
3. Saini P, Patil DV, Powar S (2018) Review on integration of solar air heaters with thermal energy storage. In: Applications of Solar Energy. Springer, Singapore, pp 163–186
4. Jacobs WA, Hertz AD, Tam MK (2018) Solar energy collecting apparatus and method. U.S. Patent No. 9,865,760. 9 Jan
5. Kabir E et al (2018) Solar energy: potential and future prospects. Renew Sustain Energy Rev 82:894–900
6. Johansson TB, Burnham L (1993) Renewable energy: sources for fuels and electricity. Island press
7. Tian H, Boschloo G, Hagfeldt A (2018) Molecular devices for solar energy conversion and storage. Springer, Singapore
8. Shahid H et al (2018) Implementation of the novel temperature controller and incremental conductance MPPT algorithm for indoor photovoltaic system. Solar Energy 163:235–242
9. Hohm DP, Ropp ME (2000) Comparative study of maximum power point tracking algorithms using an experimental, programmable, maximum power point tracking test bed. In: Photovoltaic specialists conference, conference record of the twenty-eighth IEEE
10. Hua C-C, Fang Y-H, Wong C-J (2018) Improved solar system with maximum power point tracking. IET Renew Power Gener 12(7):806–814

Performance Optimization of a Grid-Connected PV/Biomass-Based Hybrid Energy System Using BBO Algorithm

Anurag Chauhan, Mohd Tauseef Khan, Ashish Srivastava and R. P. Saini

Abstract The concerns of depletion of the fossil fuel reserves and climate change have encouraged the utilization of renewable energy resources to fulfill the ever-growing demand. Renewable resources are sustainable and environment friendly. This paper is focused on design and performance optimization of a grid-connected hybrid energy system for an un-electrified village of Indian state of Uttar Pradesh. Three different combinations of renewable sources in grid environment are considered and investigated for achieving the required power reliability at user end. The total cost (TC) of each combination has been optimized under technical, social and environmental constraints using biogeography-based optimization (BBO) algorithm. Finally, a suitable combination is recommended for the selected site which offers the minimum cost for the design of the hybrid system. A sensitivity analysis has also been conducted to evaluate the most sensitive parameter of the system.

Keywords Solar · Wind · Hybrid · Renewable energy · Demand

A. Chauhan (✉) · M. T. Khan · A. Srivastava
Rajkiya Engineering College, Banda 210201, Uttar Pradesh, India
e-mail: anurag.chauhan36@gmail.com

M. T. Khan
e-mail: tauseefkhan_alig@yahoo.co.in

A. Srivastava
e-mail: iitrashish220@gmail.com

R. P. Saini
Alternate Hydro Energy Centre, Indian Institute of Technology Roorkee,
Roorkee 247667, Uttarakhand, India
e-mail: saini.rajeshwer@gmail.com

1 Introduction

In order to meet out the ever-increasing global energy demand and the concern of the global rise in temperature, it is now widely acknowledged that renewable energy sources are the best option in place of the conventional energy sources (coal, oil, gas, etc.). The government of many countries has implemented the policy for power utilities to increase the share of renewable energy sources as part of their energy portfolio. Utilization of renewable resources offers minimal environment impact compared to coal-, hydro- and gas-based power plants [1–8].

Ahadi et al. [9] optimized the annual capital cost of a system consisting of wind and PV array resources. They minimized the system cost under the operating constraints of reserve of 50% of wind turbine output, 10% of the load and 25% of PV output. Maleki et al. [10] carried out the optimal sizing of various combinations of renewable energy sources such as photovoltaic/fuel cell systems, hybrid photovoltaic/wind turbine/fuel cell and wind turbine/fuel cell. They minimized the life cycle cost by fulfilling the maximum allowable loss of power supply probability. Maleki et al. [11] included the uncertainties of resources and load during the cost optimization of grid-isolated hybrid system.

Nadjemi et al. [12] proposed a novel cuckoo search (CS) algorithm for grid-connected hybrid PV/wind energy system. They minimized the total cost under different economic, technical and environmental constraints. Rahman et al. [13] investigated various scenarios of hybrid system for a remote society of Canada. They also conducted sensitivity analyses to evaluate the impact of different parameters on system's design. Sanajaoba et al. [14] performed the optimal sizing of three schemes of hybrid system. They optimized the total cost of hybrid system with the consideration of outage rate and the seasonal variation of load. Yang et al. [15] developed a power management system for household PV–battery hybrid system.

Based on the available literature, it has been found that most of the researchers do not perform the studies related to the grid-connected hybrid system with consideration of carbon emission, land use, seasonal variation of renewable sources and demand [16–23]. The present paper is focused on performance optimization of grid-connected hybrid energy system for rural area. The total system cost of hybrid system has been optimized to find the optimum size of system components.

2 Modeling of Hybrid Energy System

A grid-connected PV-biomass-based hybrid system has been considered for a small village located in Bijnour district of Uttar Pradesh state of India as shown in Fig. 1.
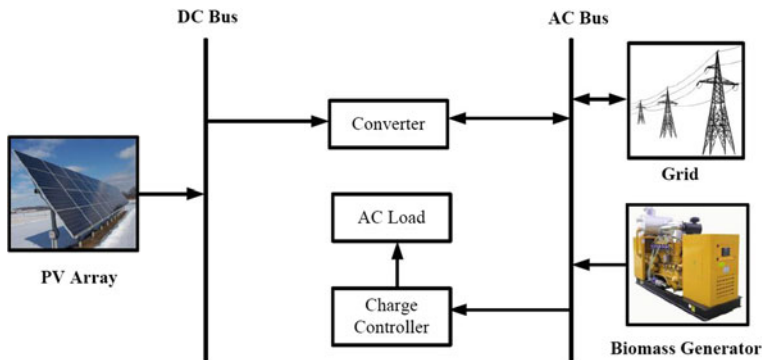
Fig. 1 Configuration of grid-connected PV–biomass-based hybrid system

2.1 PV Array

Mathematical model of PV array is described in Eqs. (1–3) as:

$$P_{PV}(k) = [N_{PV} \times V_{OC}(k) \times I_{SC}(k) \times FF]/1000 \qquad (1)$$

$$I_{SC}(k) = \left[I_{SC,STC} + K_I \{ T_C(k) - 25 \} \right] \frac{\beta(k)}{1000} \qquad (2)$$

$$V_{OC}(k) = V_{OC,STC} - K_V T_C(k) \qquad (3)$$

where $P_{PV}(k)$ is power output of PV array at kth hour, I_{SC} is short-circuit current, N_{PV} is number of PV modules, V_{OC} is open-circuit voltage and FF is fill factor, $I_{SC,STC}$ is short-circuit current under STC, T_C is cell temperature, K_I is short-circuit current temperature coefficient, $V_{OC,STC}$ is open-circuit voltage under STC and K_V is open-circuit voltage temperature coefficient and β is hourly average solar radiation (W/m^2).

2.2 Biomass Operated Generator

Hourly power output of biomass generator can be modeled by Eq. (4) as:

$$P_B = \frac{Q_B \times CV_B \times \eta_B \times 1000}{365 \times 860 \times H} \qquad (4)$$

where Q_B is availability of forest foliage (ton/year), η_B is conversion efficiency (20%), CV_B is calorific value of biomass and H is daily operating hours.

2.3 Utility Grid

The surplus amount of electricity sold to grid and grid purchase is estimated as:

$$E_{GS}(k) = E_{EE}(k) = [(E_{PV}(k) \times \eta_I) + E_{BM}(k) - E_{Load}(k)] \qquad (5)$$

$$E_{GP}(k) = E_{DE}(k) = E_{Load}(k) - [(E_{PV}(k) \times \eta_I) + E_{BM}(k)] \qquad (6)$$

where E_{GS} is amount of electricity sold to grid, E_{EE} is excess electricity, η_I is inverter efficiency, E_{PV}, E_{BM}, E_{Load}, respectively, represent hourly PV array generation, biomass gasifier generation and load demand, E_{DE} is hourly deficit electricity and E_{GP} is grid purchase electricity.

3 Problem Framework

The total cost (TC) of grid-connected hybrid system is considered as the objective function. The total cost has been optimized under the several operating constraints.

3.1 Objective Function

The total cost of hybrid system is the sum of costs of individual system components during the lifetime of the project, and it can be calculated as:

$$TC = C_{PV} + C_{BM} + C_{Conv} + C_{grid,sale} - C_{grid,pur} \qquad (7)$$

where C_{PV}, C_{BM}, C_{Conv}, respectively, represent the total cost of PV array system, biomass gasifier system and converter, $C_{grid,sale}$ is total revenue from grid sale and $C_{grid,pur}$ is total cost of grid purchase.

The total cost of individual system components can be estimated as:

$$C_{PV} = \sum_{i=1}^{N_{PV}} (A_i P_i \times CRF) + OM(P_i) + REP(P_i) \qquad (8)$$

$$C_{BM} = \sum_{j=1}^{N_{BG}} (A_j P_j \times CRF) + OM(P_j) + REP(P_j) \qquad (9)$$

$$C_{Conv} = \sum_{k=1}^{N_{Conv}} (A_k P_k \times CRF) + OM(P_k) + REP(P_k) \qquad (10)$$

where CRF is capital recovery factor, N_{PV}, N_{BG} and N_{Conv}, respectively, are the numbers PV panels, biogas generators and converter; A_i, A_j, A_k are the unit cost (INR/kW); P_i, P_j, P_k are the required power capacity (kW); $OM(P_i)$, $OM(P_j)$, $OM(P_k)$ are the operation and maintenance cost; $REP(P_i)$, $REP(P_j)$, $REP(P_k)$ are the replacement cost.

The cost of energy generation (COEG) for the considered system depends upon annual demand (E_D) and annual electricity sold to grid (E_{GS}) and can be estimated as:

$$COEG = \frac{TC}{E_D + E_{GS}} \tag{11}$$

3.2 Operating Constraints

3.2.1 Upper and Lower Limit of Power Output

The power output of PV array, biomass generator and converter is limited as:

$$0 \leq N_{PV} \leq N_{PV,max} \tag{12}$$

$$0 \leq N_{BG} \leq N_{BG,max} \tag{13}$$

$$0 \leq N_{Conv} \leq N_{Conv,max} \tag{14}$$

3.2.2 Grid Sale and Grid Purchase Constraint

Grid sale and grid purchase of electricity are subjected to the condition of upper limit as:

$$E_{gs}(t) \leq E_{gs,max} \tag{15}$$

$$E_{gp}(t) \leq E_{gp,max} \tag{16}$$

3.2.3 Loss of Load Expected

The loss of load expected (LOLE) is defined as the total number of annual hours for which the load is likely to more than the generation, and it can be calculated as [13]:

$$LOLE = \sum_{d=1}^{365} \sum_{t=1}^{24} h_{outage}(d,t)$$

where d is day of the year, t is hour of the day and h_{outage} is equal to 1 under the condition when load is greater than the generation and 0 otherwise.

3.2.4   Carbon Emission and Land Requirement

The CO_2 emission generated by hybrid energy system in grid environment has been incorporated as environmental constraint. In the present study, emission from the utilization of solar photovoltaic, biomass gasifier and grid electricity is considered. Also, land requirement for the development of hybrid system is considered as social constraint that depends upon the component's size and land used for 1 kW of system component.

4   BBO Algorithm

In the paper, biogeography-based optimization (BBO) algorithm has been used to optimize the total system cost. BBO algorithm is inspired from the migration strategy of animals or other species. Like other meta-heuristic algorithms, BBO is also a population-based algorithm in which global optimum solution depends upon the population of candidate solutions. In BBO, each habitat with its habitat suitability index (HSI) is considered individually. Low HSI signifies a poor solution, whereas high HSI represents good solution. The major steps of the algorithm are given as follows:

  step 1: Initialize the population, upper bound, lower bound, mutation rate
  step 2: Objective function values for are each habitat are calculated
  step 3: Check the stopping criteria
  step 4: Best habitat are stored in an array
  step 5: Habitat suitability index is mapped with the number of species for each habitat
  step 6: Select the immigration island using the probabilistic approach
  step 7: Based on the island selected, suitability index variables are migrated randomly
  step 8: Mutate the population randomly and evaluate the objective function values.
  step 9: Select the best value of objective function

5 Database

5.1 Solar Potential

In the present paper, three seasons of four months each are considered. Hourly solar radiation availability in the study area for different seasons is depicted in Fig. 2. It has been observed that the highest radiation of 800, 700 and 600 W/m^2 is recorded during season 1 (March–June), season 2 (July–October) and season 3 (November–February), respectively. Hourly average temperature for the area is shown in Fig. 3 [24].
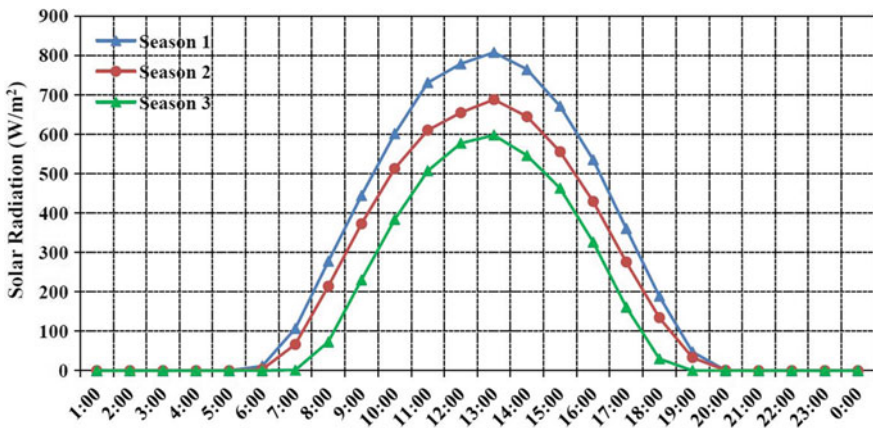
Fig. 2 Hourly average solar radiation availability in the study area [24]
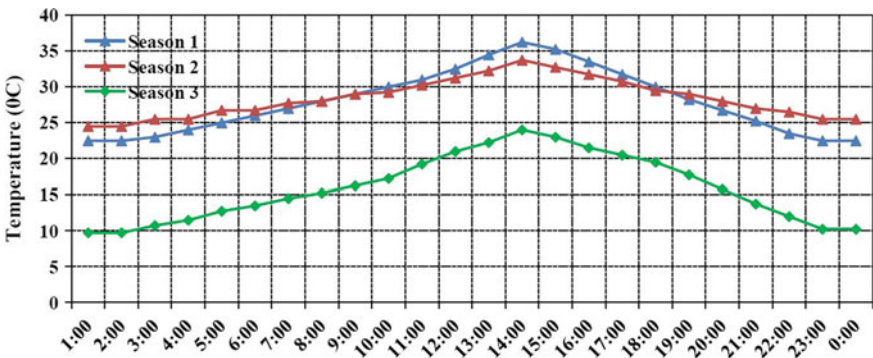
Fig. 3 Hourly average temperature of the study area [24]
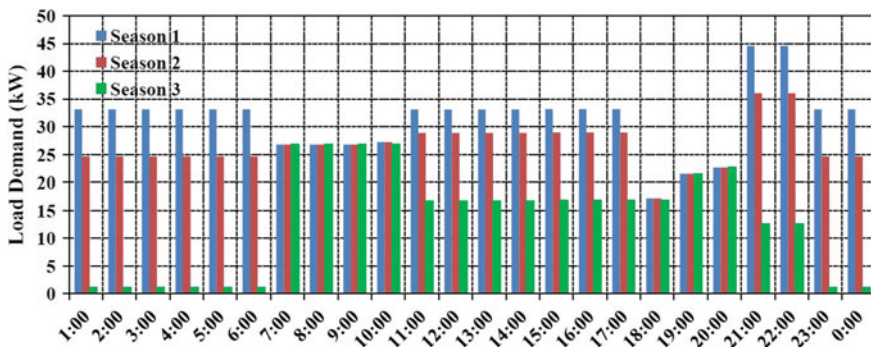
Fig. 4 Seasonally varying load demand of the study area

5.2 Load Profile

Hourly load profile of the study area is depicted in Fig. 4. Peak demand is estimated as 44.57, 36.07 and 22.63 kW for season 1, season 2 and season 3, respectively.

5.3 Techno-Economical Data of System Components

Technical and economical data of different system components are given in Table 1. During simulation, 1 kW_p PV module, 1 kW size of biomass gasifier system and 1 kW converter have been considered. Annual real interest rate of 6% and project lifetime of 25 years have been considered under the present study. Price of grid sale and grid purchase is INR 6.50/kWh and INR 3.25/kWh which are considered.

Table 1 Techno-economical data

Indicators	Unit	PV array	Biomass gasifier system	Converter
Capital cost	INR	80,000	45,000	3000
O & M cost	INR	1600	2250	0
Replacement cost	INR	80,000	45,000	3000
Lifetime	Year	25	5	10

Table 2 CO_2 emission rate and land needed for different technologies

Energy technologies	CO_2 Emission (g/kWh)	Land needed (m^2/kW)
PV array system	130	30
Biomass gasifier system	20	90
Grid electricity	955	–

5.4 CO₂ Emission Rate and Land Requirement

Emission from the utilization of solar photovoltaic, biomass gasifier and grid purchase (coal based) for electricity generation is considered, and its rate is given in Table 2. Requirement of land for the implementation of 1 kW of system components is given in Table 2.

6 Results and Discussions

Three different combinations of renewable sources are considered during size optimization of grid-connected hybrid system as:

Combination 1: Grid-connected PV-based system
Combination 2: Grid-connected biomass-based system
Combination 3: Grid-connected PV/biomass-based system.

6.1 Optimum Size of System Components

The considered combinations are optimized for the power reliability value of zero LOLE using BBO algorithm. Codes are developed in MATLAB environment to obtain the optimum size of system components. Based on hourly simulation, the optimum sizes for different combinations are reported in Table 3. For combination 1, the optimum size for this combination is comprised of 50.40 kW$_p$ PV array system and 41 kW converter. The total cost of this configuration has been estimated as INR 1.2484 million at the COEG of INR 5.79 per kWh. For combination 2, the

Table 3 Optimum size of system components

Combination	PPV (kW$_p$)	PBMG (kW)	P_{Conv} (kW)	TC (in million INR)	COEG (INR/ kWh)
1	50.40	0	41	1.2484	5.79
2	0	25	0	1.2832	5.96
3	48.90	24	40	1.1933	5.28

optimum configuration consists of 25 kW biomass gasifier system. The total cost and cost of energy generation of this configuration are calculated as INR 1.2832 million and INR 5.96 per kWh, respectively. Among all the combinations, combination 3 offers minimum total cost of INR 1.1933 million at the COEG of INR 5.28 per kWh. The optimum size of system components is obtained as: 48.90 kW$_p$ PV array, 24 kW biomass gasifier system and 40 kW converter.

6.2 Carbon Emission and Land Requirement

Carbon emission and land requirement for each combination are given in Table 4. Based on the grid electricity purchase, carbon emission of 66.50 ton/year has been found minimum for combination 3. The total land requirement for the development of optimum configuration of combination 1, combination 2 and combination 3 is found to be as 1512, 2250 and 3627 m^2, respectively.

6.3 Sensitivity Analysis

Finally, a sensitivity analysis for the optimum configuration of combination 3 has been performed as shown in Fig. 5. The price of PV array, biomass gasifier system, grid sale and grid purchase is varied by ±20% of the base cost. Accordingly, the total system cost has been calculated. It has been observed that the total system cost is more sensitive to PV array price, biomass gasifier price and grid purchase price. The total cost is deviated from INR 1.088 million to INR 1.261 million for grid purchase price varying from INR 5.20/kWh to INR 7.80/kWh. Further, it has been found that for the variation of PV array price from INR 64,000/kW to INR 96000/kW, the total cost is changed from INR 1.1091 million to INR 1.2664 million.

Table 4 CO_2 emission and land requirement for each combination

Combination	CO_2 emission (ton/year)	Land requirement (m^2)
Combination 1	136.34	1512
Combination 2	120.32	2250
Combination 3	66.50	3627
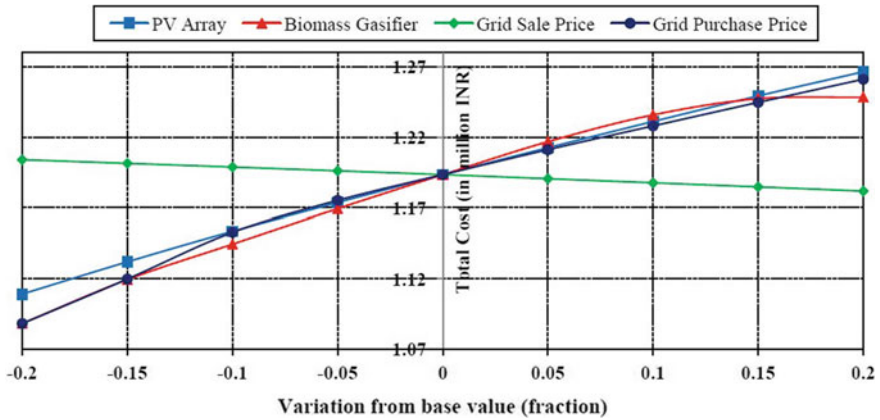
Fig. 5 Effect of various different parameters on total system cost

7   Conclusions

In the present paper, a grid-connected PV–biomass-based hybrid energy system has been designed for a small village located in India. Performance optimization of the developed model has been carried out by using BBO algorithm. Three different combinations of renewable sources have been considered and compared based on the total system cost. Based on hourly analysis, it has been found that the combination consisting of PV array and biomass gasifier in grid-connected mode offers minimum cost and CO_2 emission.

The optimal model consists of 48.90 kW_p PV array system, 24 kW biomass generator and 40 kW converter. The total cost of this combination has been calculated as INR 1.1933 million at the COEG of INR 5.28/kWh. The results obtained under the present study may be helpful for the design and development of hybrid system for other similar un-electrified rural households.

References

1. Bossink BAG (2017) Demonstrating sustainable energy: a review based model of sustainable energy projects. Renew Sustain Energy Rev 1349–1362
2. Vidal-Amaro JJ, Østergaard PA, Sheinbaum-Pardo C (2015) Optimal energy mix for transitioning from fossil fuels to renewable energy sources—the case of the Mexican electricity system. Appl Energy 150:80–96
3. Chauhan A, Saini RP (2016) Techno-economic optimization based approach for energy management of a stand-alone integrated renewable energy system for remote areas of India. Energy 138–156
4. Kaldellis JK (2010) Optimum hybrid photovoltaic—based solution for remote telecommunication stations. Renew Energy 2307–2315

5. Chauhan A, Saini RP (2015) Renewable energy based off-grid rural electrification in Uttarakhand state of India: technology options, modelling method, barriers and recommendations. Renew Sustain Energy Rev 662–681

6. Chauhan A, Saini RP (2014) A review on integrated renewable energy system based power generation for stand-alone applications: configurations, storage options, sizing methodologies and control. Renew Sustain Energy Rev 99–120

7. Sims REH, Rogner H, Ken Gregory K (2003) Carbon emission and mitigation cost comparisons between fossil fuel, nuclear and renewable energy resources for electricity generation. Energy Policy 1315–1326

8. Chauhan A, Saini RP (2013) Renewable energy based power generation for stand-alone applications: a review. In: Proceedings of the international conference on energy efficient technologies for sustainability (ICEETS) 424–428

9. Amir A, Sang-Kyun K, Jang-Ho L (2016) A novel approach for optimal combinations of wind, PV, and energy storage system in diesel-free isolated communities. Appl Energy 101–115

10. Maleki A, Pourfayaz F, Rosen MA (2016) A novel framework for optimal design of hybrid renewable energy based autonomous energy systems: a case study for Namin, Iran. Energy 168–180

11. Maleki A, Morteza Khajeh MG, Ameri M (2016) Optimal sizing of a grid independent hybrid renewable energy system incorporating resource uncertainty, and load uncertainty. Electr Power Energy Syst 514–524

12. Nadjemi O, Nacer T, Hamidat Salhi AH (2017) Optimal hybrid PV/wind energy system sizing: application of cuckoo search algorithm for Algerian dairy farms. Renew Sustain Energy Rev 1352–1365

13. Rahman MM, Khan MMUH, Ullah MA, Zhang X, Kumar A (2016) A hybrid renewable energy system for a North American off-grid community. Energy 151–160

14. Sanajaoba S, Fernandez E (2016) Maiden application of Cuckoo search algorithm for optimal sizing of a remote hybrid renewable energy System. Renew Energy 96:1–10

15. Yang F, Xia X (2017) Techno-economic and environmental optimization of a household photovoltaic-battery hybrid power system within demand side management. Renew Energy 132–143

16. Chen J, Garcia HE (2016) Economic optimization of operations for hybrid energy systems under variable markets. Appl Energy 177:11–24

17. Kaldellis JK, Zafirakis D (2017) Optimum energy storage techniques for the improvement of renewable energy sources-based electricity generation economic efficiency. Energy 2295–2305

18. Kenfack J, Neirac FP, Tatietse TT, Mayer D, Fogue M, Lejeune A (2009) Micro hydro-PV-hybrid system: sizing a small hydro-PV-hybrid system for rural electrification in developing countries. Renew Energy 2259–2263

19. Ogunjuyigbe ASO, Ayodele TR, Akinola OA (2016) Optimal allocation and sizing of PV/Wind/Split-diesel/Battery hybrid energy system for minimizing life cycle cost, carbon emission and dump energy of remote residential building. Appl Energy 153–171

20. Rahman MM, Khan MM, Ullah MA, Zhang X, Amit A (2016) A hybrid renewable energy system for a North American off-grid community. Energy 151–160

21. Chauhan A, Saini RP (2017) Size optimization and demand response of a standalone integrated renewable energy system. Energy 59–73

22. Chauhan A, Saini RP (2016) Techno-economic feasibility study on integrated renewable energy system for an isolated community of India. Renew Sustain Energy Rev 388–405

23. Chauhan A, Saini RP (2016) Discrete harmony search based size optimization of integrated renewable energy system for remote rural areas of Uttarakhand state in India. Renew Energy 587–604

24. NASA (2017) Surface meteorology and solar energy: a renewable energy resource website. Available from: https://eosweb.larc.nasa.gov/sse/. Accessed 5.07.17

Wide Area Control of Power System Using FACTS Device

Mohd Tauseef Khan, Anurag Chauhan and Anwar Shahzad Siddiqui

Abstract Advent of phasor measurement unit (PMU) technology has resulted in efficient wide area monitoring of power system which was previously done through state estimators at relatively slow rate. As status of power system changes dynamically, PMU devices provide reliable data synchronized with time. FACTS devices along with PMUs and phasor data concentrator (PDC) can be an efficient tool for real-time monitoring and control of power system. This paper provides a technique to study the localized control and wide area control of power system through a FACTS device. IEEE-14 bus system has been considered for analysis of the control process. First, optimal location and number of PMU is determined through network topology features analysis, and then, localized control and wide area control are simulated in MATLAB software.

Keywords Wide area control · PMU · FACTS device

1 Introduction

Deregulation of power system has resulted in decentralized control of power system, where different market participants work and strive for their own profits thereby neglecting system security. So, the main responsibility of network security lies on the shoulders of transmission grid operator who not only manages the power transactions, but also prepares for contingencies and ancillary service requirements

M. T. Khan (✉) · A. Chauhan
Rajkiya Engineering College, Banda, Uttar Pradesh, India
e-mail: tauseefkhan_alig@yahoo.co.in

A. Chauhan
e-mail: anurag.chauhan36@gmail.com

A. S. Siddiqui
Jamia Millia Islamia, New Delhi, India
e-mail: anshsi@yahoo.co.in

[1]. With advancement of technology, synchronized phasor measurements are becoming popular for advanced power system monitoring and control. Phasor measurement unit (PMU), used for synchronized measurements, provides real-time voltages and currents phasors synchronized through timing signals obtained from global positioning system (GPS) [2].

Large numbers of PMUs are being installed around the globe by utility companies to synchronize the measurement at geographically dispersed areas for post-mortem analysis, adaptive system protection and state estimation applications [3]. Taking economic consideration, PMUs should be installed at optimal location. Three techniques present in the literature are compared in [4] for determining optimal placement of PMUs based on maximum observability information. Authors in [5] presented a model for placement of contingency constrained PMUs in electricity network. State estimators are used conventionally to enhance the power system security by estimating the voltages, currents, active and reactive power at different buses [6]. Optimal placement of PMU enhances the state estimation by taking a real-time snapshot of power system. Authors in [7] developed a strategic PMU placement algorithm for improving bad data processing capability of state estimation, while in [8], phasor measurements are included along with conventional measurements in state estimator. Unified approach is proposed in [9] for state estimation and determination of optimal locations and number of PMUs to make system observable.

A number of PMU making a wide area monitoring system (WAMS) are also prevalent for analysis of major blackouts [10] and specially designed control actions [11]. Using suitable standards and protocols in a wide area network (WAN) communication, synchrophasors acquired from PMU is transferred to phasor data concentrator (PDC) [12].

FACTS devices are usually placed at specific locations for providing appropriate control to network abnormalities. The control of FACTS devices basically depends on the requirements of the bus on which it is connected or in the line where it is placed [13]. The primary controller of FACTS devices takes control action according to local requirements. However, fulfilling the local requirements may sometimes result in system wide abnormality. So, a secondary controller for FACTS devices is needed which works according to wide area needs of the network [14].

In this paper, wide area control of power system using FACTS device is discussed. The settings of the secondary control are decided based on real-time data coming from PDC. For real-time operation, triggering signal is fed to FACTS controller based on these settings. A case study of IEEE-14 bus having a TCSC and wide area monitoring through PMUs is studied in this paper. This paper consists of six sections. Section 2 discusses the basics fundamentals of PMU, while Sect. 3 discusses the technique used for determining the optimal location of PMU in this paper. Section 4 presents the wide area control scheme with the use of FACTS devices. Section 5 gives the major results obtained and discusses its implications. Section 6 concludes the results obtained in this paper.

2 Phasor Measurement Unit (PMU)

Phasor measurement unit (PMU) is a device which provides synchronized measurements of real-time voltages and currents phasors (both magnitude and phase angle). Timing signals from global positioning system (GPS) is used for same-time sampling of voltages and currents in order to achieve the synchronization [15]. Referring the phase angle of PMUs to a global reference time makes possible to capture the wide area snapshot of power system. PMU is helpful in monitoring the status and real-time behaviour along with the recording of sequence of event in case of blackouts or major faults in power system [16].

A GPS receiver is installed in the substation or may be built in PMU for providing the synchronization pulse to PMU. For providing the synchronization, GPS receiver provides one-pulse-per-second signal phase-locked to a sampling clock. The time tags for PMU are in multiples of the nominal frequency period. On the output of PMU, positive sequence current and voltage phasors are normally received. However, phasors of individual phase currents and voltages can also be provided by PMU [17].

3 Optimal Location of PMU

Optimal locations for PMUs should be found in order to attain complete observability of the entire network along with economic considerations. A number of researchers have studied the concept of observability and classified it into two approaches [18]. These approaches are based on numerical observability and topological observability. Numerical observability method utilizes the Jacobian matrix along with the measurement set, whereas the topological observability requires analysis based on network topology.

In this paper, optimal location of PMU is found using network topology features. Network topology features arise from structure or geometry of the network that depends solely on the interconnection of the network. Further analysis needs to be carried out only after the introduction of certain mathematical parameters related to network topology.

3.1 Network Topology Features

The symbols used in the following context have following meanings:

i = node in the graph
n = no of nodes
b = no of branches
N = no of nodes in the network

(a) **Incidence Matrix**

It is a matrix (denoted as A) of order $(n \times b)$ with following conventions. Any element in the incidence matrix is described as:

$$a_{pq} = \begin{cases} 1, & \text{branch} q \text{ incident at node } q \text{ oriented away from node } p \\ -1, & \text{branch } q \text{ incident at node } q \text{ oriented towards node } p \\ 0, & \text{branch } q \text{ not incident at node } q \end{cases} \quad (1)$$

(b) **Laplacian Matrix**

It determines whether the network is well connected and how fast it shared the information across the network (denoted as L).

$$L = A \times A^{\mathrm{T}} \quad (2)$$

(c) **Adjacency Matrix (M)**

It represents which vertices (or nodes) of the graph are adjoining to which other vertices. It is given as:

$$M = (-L) + \mathrm{diag}(L) \quad (3)$$

(d) **Number of Links (m)**

A link is a connection between two nodes. It is given as:

$$m = \frac{1}{2} \sum_i L(i, i) \quad (4)$$

where $\sum_i L(i, i)$ is the summation of all diagonal values of Laplacian matrix.

(e) **Average Nodal Degree (k)**

The degree of the vertex of the graph is the number of edges incident to the vertex. It is given as:

$$k = \frac{1}{N} \sum_i L(i, i) \quad (5)$$

(f) **Ratio Parameter (R)**

It defines the maximum node degree of the nodes of network graph. It is given as:

$$R = \frac{\max(k_i)}{N} \quad (6)$$

(g) **Clustering Coefficient (C_i)**

It is a measure of degree to which nodes in a graph tend to cluster together. It is given as:

$$C_i = e_{jk}/k_i \times (k_i - 1)/2 \tag{7}$$

where $e_{jk} = 1$ if there exists a branch in a closed triplet otherwise it is zero. The rules for PMU placement on a node is that the nodes in the cluster having a nodal degree value around the value of ratio parameter are positively biased for the PMU location.

4   Wide Area Control Scheme Using FACTS Devices

The P- or PI-type controllers are typically embedded in FACTS devices along with special supplementary controllers like damping controllers [19]. The set-points of FACTS devices are normally kept constant or manually changed according to optimal power flow calculations or market activities. Basically, the controllers of FACTS devices operate with the objective of serving the local criterion such as voltage or power flow rather than the effect of FACTS devices on whole power system. For its optimal utilization, a secondary control loop is required which generates the set-points to the FACTS controllers. This secondary control loop analyses the effects of FACTS device operation in a specified region on the whole power system. The set-points of secondary controllers are pre-calculated using the optimization algorithm for various contingencies. This approach results in avoiding any conflict of secondary control with objectives undertaken by local primary controller.

If a power flow control device is used for reduction of power flow in a load centre, it can jeopardise stability of system as it would introduce additional reactance thereby contributing in the voltage instability. So, it is beneficial to relax objectives of primary control whenever system operates close to or beyond stability limits. Secondary controllers should be able to detect the conditions when stability margins are small in order to correct the set-points appropriately for improving the stability margins [20].

For demonstrating the benefits of wide area FACTS control, three conditions are taken here, viz. without FACTS device, FACTS device with traditional local controller, FACTS device with optimal set-points (set-points corrections are made by secondary controller) for maximizing transmission capability to load region.

Figure 1 represents the flow chart of wide area control scheme using FACTS devices utilizing the WAMS available through PMUs. The figure also shows the direction of synchrophasors and commands. The rate of data sent by PMU to PDC through communication link for IEEE C37.118-based PMU is 30–60 samples per second. For IEC-61850-90-5-based PMU, the rate of data sent by PMU to PDC is 4000 samples/s [21].
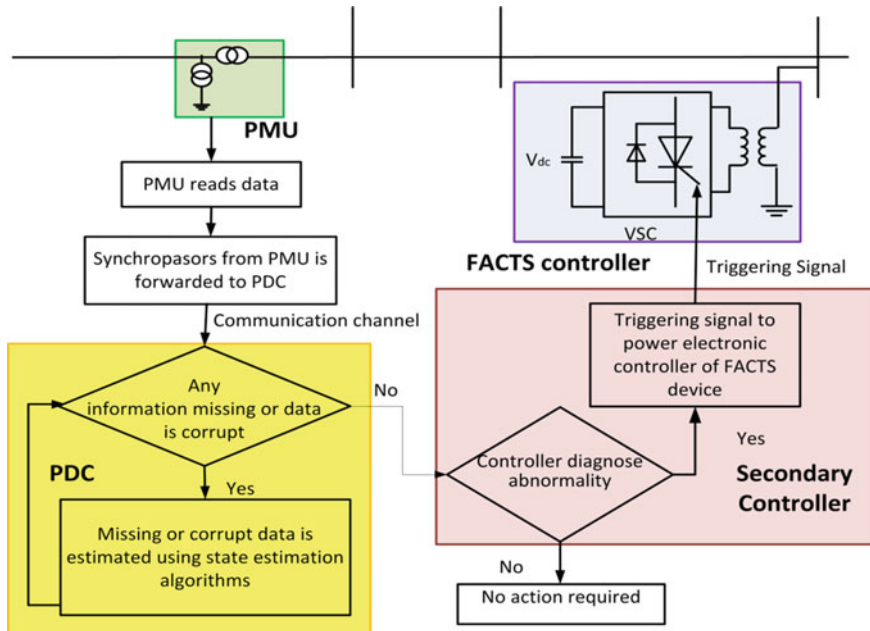
Fig. 1 Flow chart of wide area control scheme

PMU units uninterruptedly forward synchrophasors to PDC which is coupled to the secondary controller via communication channel. The secondary control settings are provided to primary controllers of FACTS devices based on requirements of whole system.

5 Simulation Result and Discussion

The wide area control scheme for optimal control of power system using the FACTS devices is tested on IEEE-14 bus network. Before control of power system, monitoring is required. So, wide area monitoring of power system is carried out through optimal PMU placement on this network.

For the IEEE-14 bus network, directed graph is made as shown in Fig. 2 which consists of 14 buses and 20 interconnected lines. The bus bars are replaced by nodes, and load flows are carried out to find the direction of current flow for drawing a directed graph of the single line diagram.

For the network topology analysis of IEEE-14 bus network, model parameters like incidence matrix (A), Laplacian matrix (L) and adjacency matrix (M) are obtained through the linear graph. Incidence matrix gives the information about incidence of branches (i.e. lines) on nodes (i.e. buses) along with direction and is

Fig. 2 Linear graph for
IEEE-14 bus network
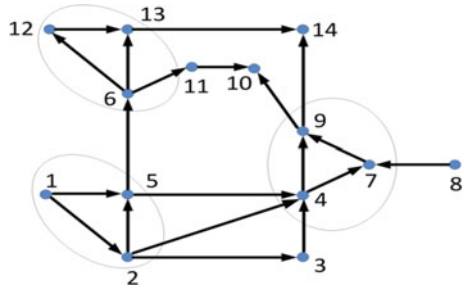
obtained through Eq. (1). The whole network can be represented by a matrix of
order ($n \times b$) and is crucial for network topology analysis. Incidence matrix (A) for
IEEE-14 bus network is represented as:

$$
A = \begin{bmatrix}
0 & 1 & 0 & 0 & 1 & 0 & 0 & 0 & 0 & 0 & 0 & 0 & 0 & 0 \\
-1 & 0 & 1 & 1 & 1 & 0 & 0 & 0 & 0 & 0 & 0 & 0 & 0 & 0 \\
0 & -1 & 0 & 1 & 0 & 0 & 0 & 0 & 0 & 0 & 0 & 0 & 0 & 0 \\
0 & -1 & -1 & 0 & -1 & 0 & 1 & 0 & 1 & 0 & 0 & 0 & 0 & 0 \\
-1 & -1 & 0 & 1 & 0 & 1 & 0 & 0 & 0 & 0 & 0 & 0 & 0 & 0 \\
0 & 0 & 0 & 0 & -1 & 0 & 0 & 0 & 0 & 0 & 1 & 1 & 1 & 0 \\
0 & 0 & 0 & -1 & 0 & 0 & 0 & -1 & 1 & 0 & 0 & 0 & 0 & 0 \\
0 & 0 & 0 & 0 & 0 & 0 & 1 & 0 & 0 & 0 & 0 & 0 & 0 & 0 \\
0 & 0 & 0 & -1 & 0 & 0 & -1 & 0 & 0 & 1 & 0 & 0 & 0 & 1 \\
0 & 0 & 0 & 0 & 0 & 0 & 0 & 0 & -1 & 0 & -1 & 0 & 0 & 0 \\
0 & 0 & 0 & 0 & 0 & -1 & 0 & 0 & 0 & 1 & 0 & 0 & 0 & 0 \\
0 & 0 & 0 & 0 & 0 & -1 & 0 & 0 & 0 & 0 & 0 & 0 & 1 & 0 \\
0 & 0 & 0 & 0 & 0 & -1 & 0 & 0 & 0 & 0 & 0 & -1 & 0 & 1 \\
0 & 0 & 0 & 0 & 0 & 0 & 0 & 0 & -1 & 0 & 0 & 0 & -1 & 0 \\
\end{bmatrix}
$$

Laplacian matrix (L) found through Eq. (2) provides the communication feasi-
bility and network connectivity.

$$L = \begin{bmatrix}
2 & 1 & -1 & -2 & -1 & -1 & 0 & 0 & 0 & 0 & 0 & 0 & 0 & 0 \\
1 & 4 & 1 & -2 & 2 & -1 & -1 & 0 & -1 & 0 & 0 & 0 & 0 & 0 \\
-1 & 1 & 2 & 1 & 2 & 0 & -1 & 0 & -1 & 0 & 0 & 0 & 0 & 0 \\
-2 & -2 & 1 & 5 & 1 & 1 & 1 & 1 & -1 & -1 & 0 & 0 & 0 & -1 \\
-1 & 2 & 2 & 1 & 4 & 0 & -1 & 0 & -1 & 0 & -1 & -1 & -1 & 0 \\
-1 & -1 & 0 & 1 & 0 & 4 & 0 & 0 & 0 & -1 & 0 & 1 & -1 & -1 \\
0 & -1 & -1 & 1 & -1 & 0 & 3 & 0 & 1 & -1 & 0 & 0 & 0 & -1 \\
0 & 0 & 0 & 1 & 0 & 0 & 0 & 1 & -1 & 0 & 0 & 0 & 0 & 0 \\
0 & -1 & -1 & -1 & -1 & 0 & 1 & -1 & 4 & 0 & 1 & 0 & 1 & 0 \\
0 & 0 & 0 & -1 & 0 & -1 & -1 & 0 & 0 & 2 & 0 & 0 & 0 & 1 \\
0 & 0 & 0 & 0 & -1 & 0 & 0 & 0 & 1 & 0 & 2 & 1 & 1 & 0 \\
0 & 0 & 0 & 0 & -1 & 1 & 0 & 0 & 0 & 0 & 1 & 2 & 1 & -1 \\
0 & 0 & 0 & 0 & -1 & -1 & 0 & 0 & 1 & 0 & 1 & 1 & 3 & 0 \\
0 & 0 & 0 & -1 & 0 & -1 & -1 & 0 & 0 & 1 & 0 & -1 & 0 & 2
\end{bmatrix}$$

Matrix M indicates the adjacency matrix. The network's average nodal degree value $k = 2.8571$ is obtained using Eq. (5). As this value of k is above 2.8, it indicates that the IEEE-14 bus system is a well-clustered network. The value of ratio parameter is found to be 0.1429 and is calculated using Eq. (6). Node clustering coefficient limits the locations of PMU within clusters and obtained through this parameter. It assesses the degree to which nodes are clustered with each other.

$$M = \begin{bmatrix}
0 & -1 & 1 & 2 & 1 & 1 & 0 & 0 & 0 & 0 & 0 & 0 & 0 & 0 \\
-1 & 0 & -1 & 2 & -2 & 1 & 1 & 0 & 1 & 0 & 0 & 0 & 0 & 0 \\
1 & -1 & 0 & -1 & -2 & 0 & 1 & 0 & 1 & 0 & 0 & 0 & 0 & 0 \\
2 & 2 & -1 & 0 & -1 & -1 & -1 & -1 & 1 & 1 & 0 & 0 & 0 & 1 \\
1 & -2 & -2 & -1 & 0 & 0 & 1 & 0 & 1 & 0 & 1 & 1 & 1 & 0 \\
1 & 1 & 0 & -1 & 0 & 0 & 0 & 0 & 0 & 1 & 0 & -1 & 1 & 1 \\
0 & 1 & 1 & -1 & 1 & 0 & 0 & 0 & -1 & 1 & 0 & 0 & 0 & 1 \\
0 & 0 & 0 & -1 & 0 & 0 & 0 & 0 & 1 & 0 & 0 & 0 & 0 & 0 \\
0 & 1 & 1 & 1 & 1 & 0 & -1 & 1 & 0 & 0 & -1 & 0 & -1 & 0 \\
0 & 0 & 0 & 1 & 0 & 1 & 1 & 0 & 0 & 0 & 0 & 0 & 0 & -1 \\
0 & 0 & 0 & 0 & 1 & 0 & 0 & 0 & -1 & 0 & 0 & -1 & -1 & 0 \\
0 & 0 & 0 & 0 & 1 & -1 & 0 & 0 & 0 & 0 & -1 & 0 & -1 & 1 \\
0 & 0 & 0 & 0 & 1 & 1 & 0 & 0 & -1 & 0 & -1 & -1 & 0 & 0 \\
0 & 0 & 0 & 1 & 0 & 1 & 1 & 0 & 0 & -1 & 0 & 1 & 0 & 0
\end{bmatrix}$$

The value for node clustering coefficient C_i is found as

$$C_i = [1, 0.1667, 0, 0.1, 0.1667, 0.1667, 0.3333, 0, 0.1667, 0, 0, 1, 0.3333, 0]$$

According to above methodology, the nodes on which clustering coefficient is near about value to that of ratio parameter are positively biased for PMU placement. Thus, PMU can be placed on node 2, 5, 6 and 9. However, bus 5 can be observable from PMU at bus 6 and bus 2. So, according to optimal observability with

minimum PMU criterion, PMU placement on bus 5 can be minimized. Thus, optimal location for PMU placement is 2, 6 and 9. The results obtained for optimal PMU location verify the results reported in [22].

Figure 3 shows the IEEE-14 bus system which is divided into three areas, where Area 1 is exporting region, Area 2 is export–import region, while Area 3 is only importing region. Three PMUs are placed in the network at bus 2, 6 and 9 while a TCSC, one of the FACTS devices, is placed in line 4–5. A secondary controller is provided for wide area control of the TCSC.

In this paper, three cases are considered:

(a) Without TCSC in the network
(b) TCSC with local control
(c) TCSC with secondary control

The percentage loading for the base case having no abnormalities is shown in Fig. 4. It is visible in the figure that percentage loading at each bus is below 100% or 1 pu.
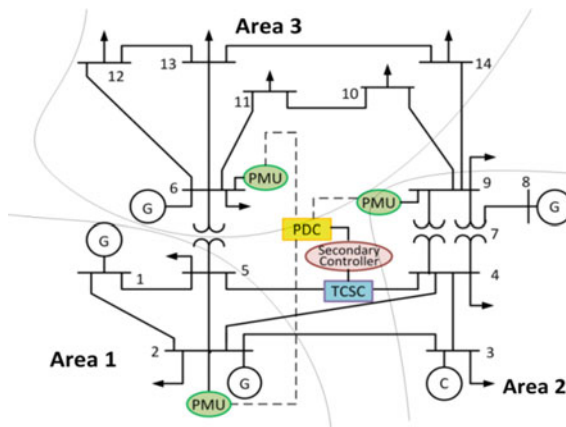
Fig. 3 IEEE-14 bus system divided into three areas with optimal PMU placement and secondary control for TCSC
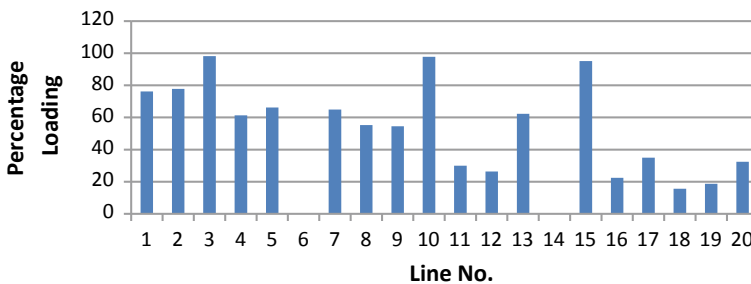
Fig. 4 Percentage loading in each line of IEEE-14 bus network without having any abnormality
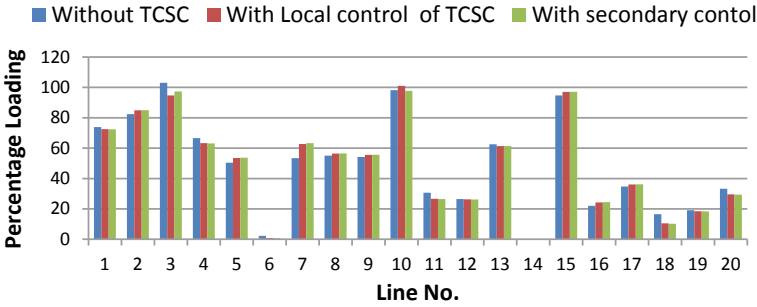
Fig. 5 Percentage loading in each line of IEEE-14 bus network with reduction in maximum capacity of line 5 (between bus 2 and 5), with local control and with secondary control of TCSC

Due to contingency or tripping of few lines, maximum capacity of line 5 (between bus 2 and bus 5) is reduced by 25%. This reduction in capacity results in increment of power flows in few lines, an overload or congestion in line 3 (between bus 2 and bus 3) as shown in Fig. 5 represented as without TCSC case.

This congestion in line 3 can be mitigated through the change in power flows using TCSC placed in line 7 (between bus 4 and bus 5). The local control of TCSC results in congestion mitigation in line 3, but introduction of congestion in line 10 (between bus 5 and bus 6) as also indicated in Fig. 5. It is also visible in Fig. 5 that with the wide area control or through the secondary controller not only congestion in line 3 is mitigated but also there is no occurrence of congestion in line 10. This is due to the reason that input through wide area control takes care of the whole network.

6 Conclusions

With the improvements in monitoring infrastructure of the transmission networks like the PMUs, PDCs, etc., whole power system can be mapped on a single time stamp. This has resulted in the improvement of overall visibility of the system at every instant. As electrical network is very vast, there should be certain phenomenon through which optimal locations of multiple PMUs can be found. Certain techniques are already being used in this field, but there is a need for better techniques. So, research is being carried out across the globe for determination of optimal location of PMUs. The control actions should be adopted in such a way so as to fulfil maximum needs of the network. So, use of FACTS devices was proposed by researchers and being implemented in developed countries as these devices are costly. Developing countries have also started procuring and installing it in their networks for advance control of power system. FACTS devices provide stability improvement, reactive power compensation, voltage stability improvement, voltage profile improvement, etc., to modern power system. The control

settings of FACTS devices should adapt according to requirements of whole network. Use of a secondary control, based on wide area measurements and control, is investigated in this paper and tested on IEEE-14 bus network. A simple case study demonstrates that if FACTS device is controlled by its local controller, it works to fulfil the local commitments and requirements. With local control, the control actions resulted in mitigation of congestion in targeted line, but may result in congestion on some other line of the network. If wide area monitoring is not available, then it will be a major problem. On the contrary, wide area control of FACTS device resulted in mitigation of congestion in targeted line, but not at the expense of other lines in the network.

References

1. Khan MT, Siddiqui AS (2017) Congestion management in deregulated power system using FACTS device. Int J Syst Assur Eng Manag 8:1–7
2. Phadke AG, Thorp JS (2008) Synchronized phasor measurements and their applications. Springer, New York
3. Mohammadi MB, Hooshmand RA, Fesharaki FH (2016) A new approach for optimal placement of PMUs and their required communication infrastructure in order to minimize the cost of the WAMS. IEEE Trans Smart Grid 7:84–93
4. Almutairi AM, Milanovi JV (2009) Comparison of different methods for optimal placement of PMUs. In: 2009 IEEE Bucharest PowerTech conference, June 28th–July 2nd, Bucharest, Romania
5. Aminifar F, Lucas C, Khodaei A, Fotuhi-Firuzabad M (2009) Optimal placement of phasor measurement units using immunity genetic algorithm. IEEE Trans Power Deliv 24:1014–1020
6. Momoh JA, Xia Y, Boswell G (2008) Voltage stability enhancement using phasor measurement unit (PMU) technology. In: 2008 40th North American power symposium, Calgary, AB, pp 1–6
7. Chen J, Abur A (2006) Placement of PMUs to enable bad data detection in state estimation. IEEE Trans Power Syst 21:1608–1615
8. Chakrabarti S, Kyriakides E, Gustavo V, Terzija V (2009) State estimation including synchronized measurements. In: 2009 IEEE Bucharest Power Tech conference, June 28th–July 2nd, Bucharest, Romania (2009)
9. Nabil HA, Hanafy MI (2009) A unified approach for the optimal PMU location for power system state estimation. IEEE Trans Power Syst 24:806–813
10. Kosterev DN, Taylor CW, Mittelstadt WA (1999) Model validation for the August 10, 1996 WSCC system outage. IEEE Trans Power Syst 14:967–979
11. Kosterev DN, Estergalyos J, Stigers CA (1998) Feasibility study of using synchronized phasor measurements for generator dropping controls in the colstrip system. IEEE Trans Power Syst 13:755–762
12. Petrone G, Spagnuolo G, Teodorescu R, Veerachary M, Vitelli M (2008) Reliability issues in photovoltaic power processing systems. IEEE Trans Ind Electron 55:2569–2580
13. Siddiqui AS, Khan MT, Iqbal F (2017) Determination of optimal location of TCSC and STATCOM for congestion management in deregulated power system. Int J Syst Assur Eng Manag 8:110–117
14. Nguyen MY, Yoon YT (2014) A comparison of microgrid topologies considering both market operations and reliability. Electr Power Compon Syst 42:585–594

15. Murthy C, Mishra A, Ghosh D, Roy DS, Mohanta DK (2014) Reliability analysis of phasor measurement unit using hidden Markov model. IEEE Syst J 8:1293–1301
16. Gong Y, Schulz N, Guzmán A, Laboratories SE (2006) Synchrophasor-based real-time voltage stability index. In: 2006 IEEE PES power systems conference and exposition, Atlanta, pp 1–8
17. Wang Y, Li W, Lu J (2009) Reliability analysis of phasor measurement unit using hierarchical Markov modeling. Electr Power Compon Syst 37:517–532
18. Exposito AG, Abur A (1998) Generalized observability analysis and measurement classification. IEEE Trans Power Syst 13:1090–1095
19. Zhang X-P, Rehtanz C, Pal B (2012) Flexible AC transmission systems: modelling and control. Springer, Heidelberg
20. Drouineau M, Maïzi N, Mazauric V (2014) Impacts of intermittent sources on the quality of power supply: the key role of reliability indicators. Appl Energy 116:333–343
21. Khan MT, Siddiqui AS (2016) FACTS device control strategy using PMU. Perspect Sci 8:730–732
22. Singh SP, Singh SP (2014) Optimal PMU placement in power system considering the measurement redundancy. Adv Electron Electr Eng 4:593–598

Battery Energy Storage System for Solar PV and Wind Power Smoothing Considering Economic Aspects

Chinmay Kumar Nayak and Manas Ranjan Nayak

Abstract This paper introduces an avant-garde method to minimize the uncertainty in power output of a hybrid PV and wind plant (HPW) with the help of BESS which stores excess power generated and supplies the load when the renewable power generated is insufficient. Hence, BESS, in a way, smoothes the HPW power output. Here, the simulation was carried out for an IEEE-RBTS basic system to optimize the size of the solar PV arrays, wind turbine and BESS so that obtained annual cost benefit would be maximized. For cost benefit analysis of the system, economic loss as a result of electricity outage and BESS costs were taken into account.

Keywords Solar photovoltaic · Wind energy · Battery energy storage system · Power system reliability · Techno-economic analysis

1 Introduction

Harnessing renewable energy like solar and wind energy and utilizing it to meet global electricity demands is challenging as these sources are uncertain and unpredictable. Integrating them to a conventional thermal powered distribution system poses a great deal of problems to the control and scheduling. In case of renewable power generation more than that is required for the load, the system has to divert the power flow elsewhere to maintain the power system stability. High rush of power from PV and wind units accompanied with drastic fluctuations in

C. K. Nayak (✉)
Department of Electrical Engineering, Indira Gandhi Institute
of Technology, Sarang, Dhenkanal 759146, Odisha, India
e-mail: chinmaynayak009@gmail.com

M. R. Nayak
Department of Electrical Engineering, Biju Patnaik University
of Technology, Rourkela 769015, Odisha, India
e-mail: manasnk72@gmail.com

load demand put up many severe power quality issues like voltage surge, huge line losses and detrimental voltage stability [1]. These problems can be addressed by using BESS in order to smooth the power output of the renewable sources which eventually leads to better power system reliability.

Various factors inducing intermittency in wind power generation were summarized, and mitigating solutions to these problems were reviewed from different aspects such as wind farms alterations, load demand management and use of different energy storage systems [2]. A novel wind farm modelling was proposed, and the system reliability was investigated considering the universal generating functions utilizing z-transform and composition operators, taking factors influencing the wind power generation into account [3]. A control strategy has been proposed for optimal use of BESS in a large wind farm for the purpose of making the wind farm more dispatchable [4]. Facilitating penetration of very huge amount of renewable power with the integration of BESS in a small isolated system was investigated [5]. The reliability of a power system fed by wind generator was investigated. The reliability improvement achieved by using energy storage system along with the wind generator has been addressed [6]. A hybrid solar-wind model integrated with a battery bank was proposed to optimize the sizes of different system components considering loss of power supply probability (LPSP) subjected to system reliability requirements [7].

Here, the BESS is used primarily to reduce the difference between the actual and the expected renewable power generation in order to supply the load reliably. The capacity of the BESS and hybrid PV and wind plant was optimized for an IEEE-RBTS basic system [8] in order to retain maximum reliability benefit considering costs associated with BESS and electricity outage.

In Sect. 2, the system schematic is described. Sections 3 and 4 present the strategy to level generated PV/wind power and the problem formulation, respectively. Section 5 discusses the simulation results, and Sect. 6 lists the conclusions drawn from the results.

2 System Modelling

The detail system schematic is illustrated with the direction of power flow in Fig. 1.

The PV panel along with the wind turbine supply power to the load through an AC bus. In case of power surplus, the controller converts ac power into dc and charges the BESS. In case of power deficit, it converts the discharged dc power output of the BESS into ac and supplies the load.

Fig. 1 System model
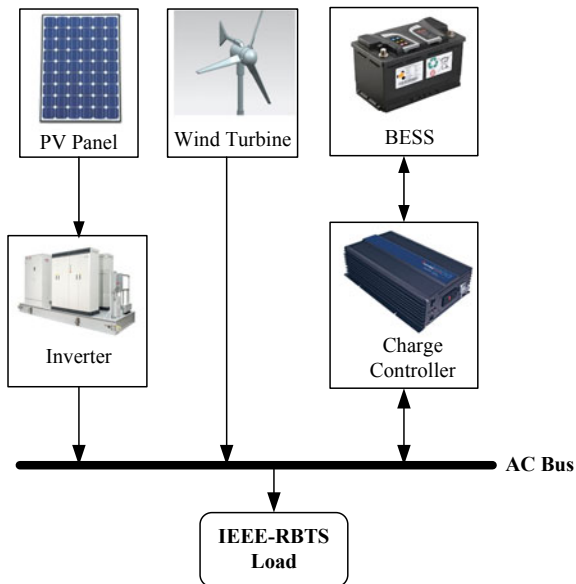
2.1 PV Modelling

The power contribution of PV array (in kW) to the AC bus bar is evaluated as [9]:

$$P_{pv}(t) = G(t) \times \eta_{pv} \times \eta_{mppt} \times a_{pv} \times \eta_{inv} \times \eta_{cable} \times N_{pv} \times d_{man} \times d_{dirt} \times d_T \times 10^{-3}$$

$$(1)$$

where η_{pv} is the efficiency of the PV cell (= 20%), a_{pv} is the area of the array (= 1.67 m^2 for rated power of 250 Wp), η_{mppt} is the efficiency of the maximum power point tracker (= 93%), η_{inv} is the inverter efficiency, η_{cable} is the factor by which the output is affected by cable losses, $G(t)$ is the hourly global horizontal irradiance (GHI) in W/m^2, N_{pv} is the number of PV arrays, d_{man} is the tolerance specified by the manufacturer, d_T is the efficiency of the panel resulting from derating due to the effect of temperature, and d_{dirt} is the factor by which the output power is derated because of accumulation of dirt over the panels. Annual hourly GHI data are considered for Bhubaneswar, India [10]. The GHI data are presented in Fig. 2.
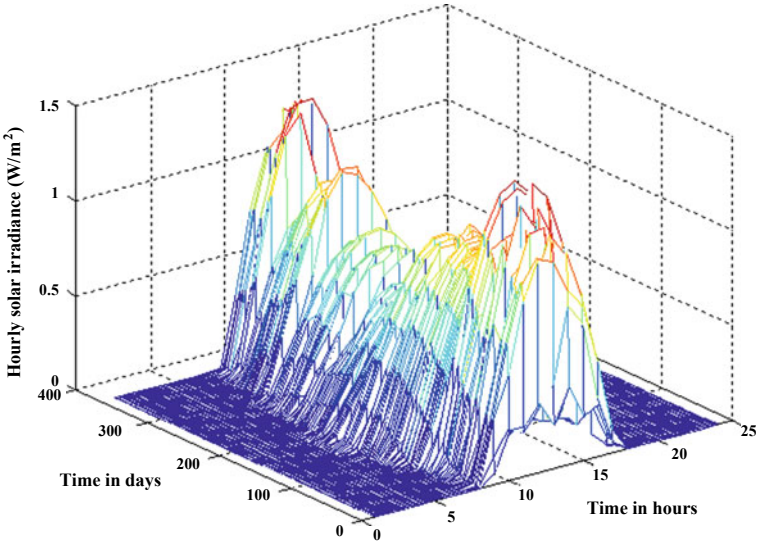
Fig. 2 Hourly variations of solar irradiance in a year

2.2 Wind Turbine Modelling

The output power of the wind generator is calculated as follows [11]:

$$
P_{WT}(t) = \begin{cases}
0, & v(t) < v_c \\
(A + B.v(t) + C.(v(t))^2) \times P_{rated}, & v_c \leq v(t) \leq v_r \\
P_{rated}, & v_r \leq v(t) \leq v_f \\
0, & v(t) > v_f
\end{cases} \tag{2}
$$

where $v(t)$ is the hourly wind velocity, v_c is the cut-in speed (= 3 m/s), v_r is the rated speed (= 11 m/s), v_f is the furling speed (= 25 m/s), and P_{rated} is the rated power output of the wind turbine. The constants A, B and C are derived from v_c, v_r and v_f. The wind speed data over the year 2015 are given in Fig. 3.

The total renewable power generated is calculated as follows:

$$
P_t(t) = P_{pv}(t) + P_{WT}(t) \tag{3}
$$

2.3 Load Modelling

A predictive load demand model is prepared considering IEEE-RBTS platform with peak and average demand of 185 and 160 MW, respectively. The hourly load factor of all 8760 h of a year is calculated by
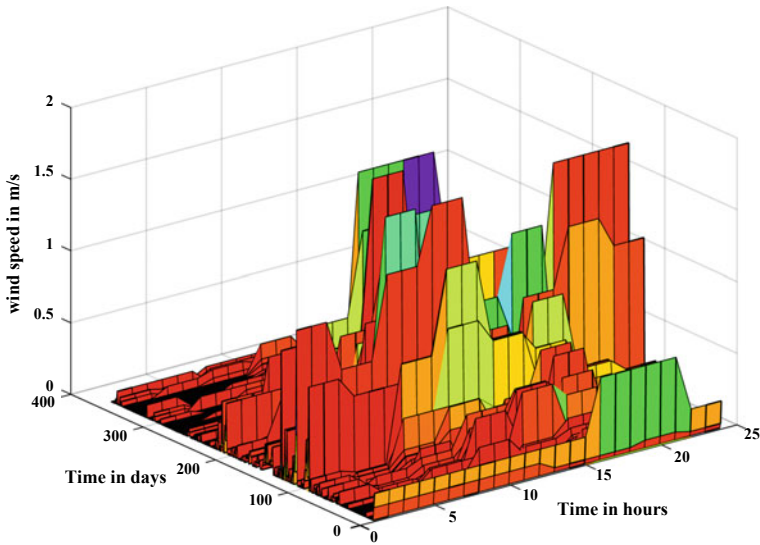
Fig. 3 Hourly variations of wind speed in a year

$$w = w_{\mathrm{w}} \times w_{\mathrm{d}} \times w_{\mathrm{h}} \tag{4}$$

where $w_{\mathrm{w}}, w_{\mathrm{d}}$ and w_{h} are the weekly, daily and hourly load factors, respectively [12]. The hourly load can be calculated as

$$P_{\mathrm{L}}(t) = w(t) \times P_{\mathrm{P}} \tag{5}$$

where P_{P} is the peak load. The load factors over one year are presented in Fig. 4.

3 Power Smoothing Strategy

To ensure power supply without any outage, BESS can be utilized. They are able to smooth the power output of the HPW by storing the excess power generated and releasing it during energy deficit. A new coming of age strategy is devised to smooth the power output of the HPW plant. An optimal size of the BESS is found out as larger size leads to higher initial cost whereas smaller size of BESS is only able to smooth a little part of the output power profile.

The average of the actual power output during a particular interval of length 'T' hours is calculated as:
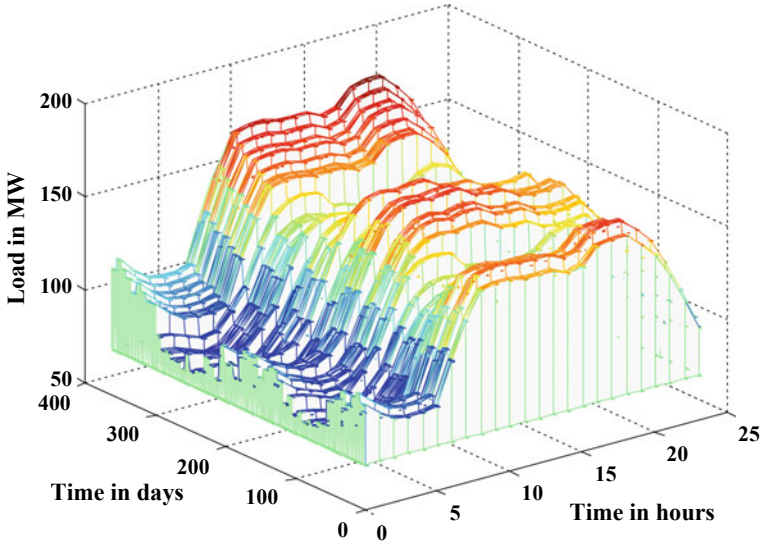
Fig. 4 Hourly load profile in a year

$$P_s = \frac{1}{T} \int\limits_{(i-1)T}^{iT} P_t \, dt \quad (i = 1, 2, 3 \ldots N) \tag{6}$$

where P_s is the desired power and N is the total no. of hours. The mean value is compared with the hourly actual output to determine the required size of the BESS. If the desired output is higher than the actual value, the BESS is allowed to discharge to compensate the difference. Otherwise, it charges to consume the extra power generated. The size of the BESS can be calculated as:

$$E_t = \sum_{i=1}^{m} \int\limits_{(i-1)T}^{iT} (P_t - P_s).\eta.dt + \int\limits_{mT}^{t} (P_t - P_{k+1}).\eta.dt + E_0 \tag{7}$$

where E_0 is the energy stored in the BESS initially and m is an integer. η can be expressed as:

$$\eta = \begin{cases} \eta_c, & P_t - P_i \geq 0 \\ \frac{1}{\eta_d}, & P_t - P_i < 0 \end{cases} \tag{8}$$

where η_c and η_d are the charging and discharging efficiencies, respectively.

4 Problem Formulation

The main objective of this paper is to determine the most favourable size of the PV panel, wind turbine and the BESS to obtain maximum cost benefit. The objective function is defined as follows:

$$f_{\text{obj}} = \max(B) \tag{9}$$

where B is the cost benefit obtained due to smoothing of generated power using BESS. It is calculated as follows:

$$B = B_{\text{R}} - C \tag{10}$$

where B_{R} is the reliability benefit which is the benefit obtained due to improvement in reliability of the system and C is the annual operating cost of the BESS.

4.1 Reliability Benefit

The reliability benefit is calculated as follows:

$$B_{\text{R}} = \left(E_a^{\text{NS}} - E_a^{\text{NS}}\right) \times c \tag{11}$$

where E_a^{NS} and E_b^{NS} are the energy not available following the integration of BESS and prior to it, respectively, and c is the loss due to black-outs expressed in financial terms (400 INR/kWh). Different factors that amount to economic loss as a result of power outage include food replacement due to loss of refrigeration, alternative light and heat source, backup diesel and other generators, reduction in no. of working hours and property damage [13].

The energy shortage E_{NS} can be determined as:

$$E_{\text{NS}} = \sum_{l=0}^{k} p_n \int_{t=0}^{8760} \Delta P_n(t)\mathrm{d}t \tag{12}$$

where k is the states of operation of the pre-existing generators, p_n is the probability of the generator to remain in kth state, and $\Delta P_n(t)$ is the power deficit while the generator is in nth state which is determined as:

$$\Delta P_n(t) = \begin{cases} P_L(t) - P_{c,n}(t) - P_t(t), & P_L(t) > \left(P_{c,n}(t) + P_t(t)\right) \\ 0, & P_L(t) \leq \left(P_{c,n}(t) + P_t(t)\right) \end{cases} \tag{13}$$

where $P_{c,l}(t)$ is the generator power output.

4.2 BESS Cost

The cost associated with the BESS due to its replacement after its life span is calculated as:

$$C = (1 + \alpha) \times c_b \times E_b \times \text{CRF}_b \tag{14}$$

where α is a cost coefficient and can be determined as:

$$\alpha = \frac{\text{BESS maintenance cost}}{\text{BESS investment cost}} \tag{15}$$

c_b is the initial BESS cost in INR/kWh, E_b is the energy storage capacity in MWh, and CRF_b is the capital recovery factor [14]. The details of the BESS considered are given in Table 1.

5 Simulation Result and Analysis

The simulation is carried out using Matlab (release 2016a, 9.0.0). The sizes of the solar PV array and wind farm are varied between 5 to 100 MW. Table 2 lists the result obtained from the optimization.

The results show that the retained profit is maximized when the HPW plant capacity is 75 MW with PV plant and wind farm contributing 37.5 MW each along with BESS capacity of 270.06 MW. The optimal smoothing time T is determined to be 6 h. The maximum annual profit retained is Rs. 143,219,950.90.

The output power smoothened by the BESS is shown and collated with the actual power output of the HPW plant in Fig. 5. The BESS stores energy in power surplus scenario and releases it to serve the load if the load becomes greater than the generated power. Thus, it reduces the ripples in power generation profile, ultimately compensating for the uncertain nature of PV and wind energy sources and improving system reliability.

Figure 6 shows the variation of the profit obtained by the 75 MW HPW plant when smoothened by the BESS for different smoothing time. It is observed that the annual profit increases initially with the increase in smoothing hours. But after a certain point (in this case $T = 6$), an increase in smoothing hour brings down the smoothened power output. Hence, the difference between actual power output (P_t)

Table 1 BESS parameters [15]

Parameters	Value	Parameters	Value
η_c	98%	c_b	4000 INR/kWh
η_d	95%	α	2%

Table 2 Optimization results

Wind farm size (MW)	Solar PV plant size (MW)	BESS capacity (MWh)	Smoothing time (h)	Retained annual profit (Rs.)
2.5	2.5	18	3	−3,375,757.45
5	5	36	3	−8,672,776.43
7.5	7.5	54.01	2	−5,666,074.20
10	10	72.02	3	1,813,708.66
12.5	12.5	90.02	6	13,504,811.62
15	15	108.02	6	45,554,696.69
17.5	17.5	126.03	6	71,291,923.11
20	20	144.03	6	93,722,740.06
22.5	22.5	162.04	6	109,572,758.60
25	25	180.04	6	121,374,648.10
27.5	27.5	198.04	6	129,918,621.80
30	30	216.05	6	136,245,483.30
32.5	32.5	234.05	6	139,444,840.20
35	35	252.06	6	142,228,984.30
37.5	**37.5**	**270.06**	**6**	**143,219,950.90**
40	40	288.06	6	142,735,254.20
42.5	42.5	306.07	6	140,888,559.10
45	45	324.07	6	138,776,835.90
47.5	47.5	342.08	6	137,019,723.30
50	50	360.08	6	134,414,294.00

and the smoothened power output (P_s) increases which increases the size of the BESS. Larger size of BESS leads to higher cost which eventually decreases the profit.

Figure 7 illustrates the variation of state of charge (SOC), an indicator of the mode of operation of the BESS for a day along with the variations in actual and desired power output. It is evident that the BESS discharges during the starting hours of the day as the actual generation lags the expected generation, decreasing the SOC. After 7 a.m., the real power becomes more than the desired smoothened power. So, the BESS charges with the excess energy. Hence, SOC starts increasing. Depending on whether the real power output is more or less in comparison with the expected smooth power output, the BESS charges or discharges. Figure 5 also ensures the health of the BESS, as the SOC, under no circumstances, goes beyond its prescribed limits of minimum of 30% to a maximum of 90%.
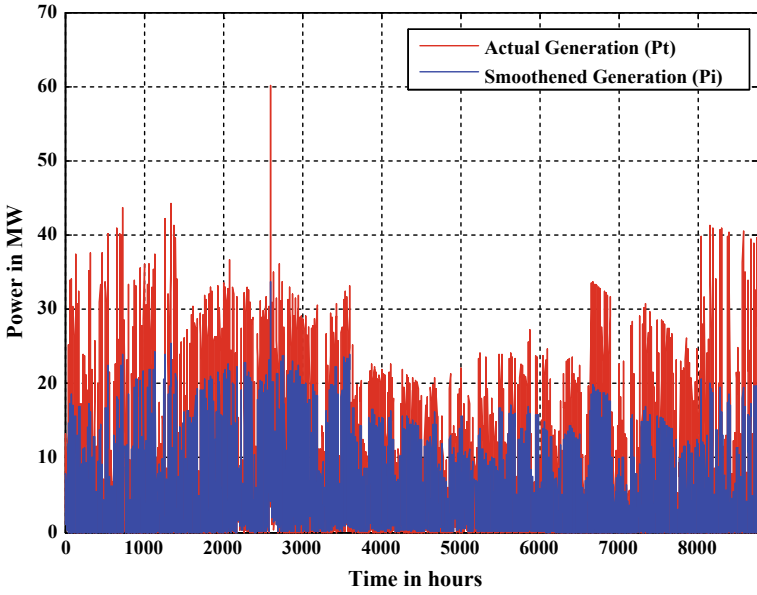
Fig. 5 Power output before and after smoothening with a smoothing period of 6 h
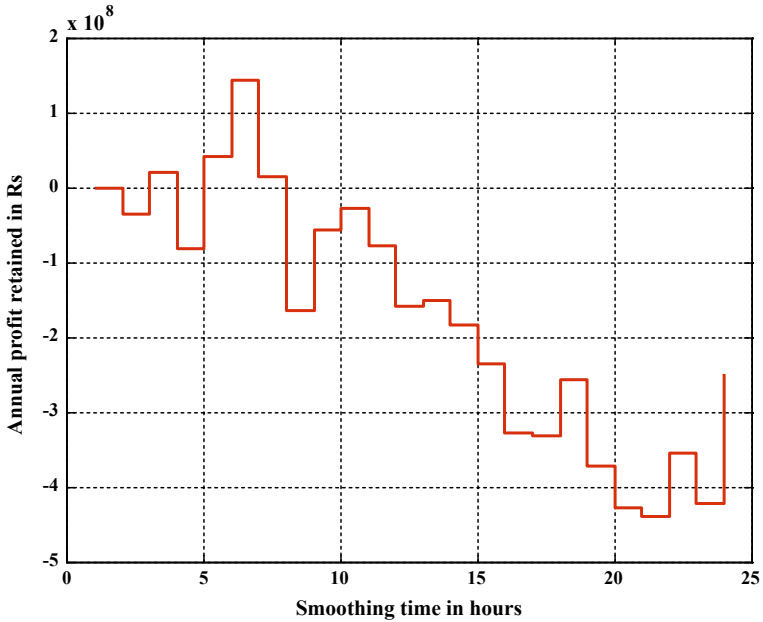
Fig. 6 Annual profit for 75 MW HPW plant for different smoothing time
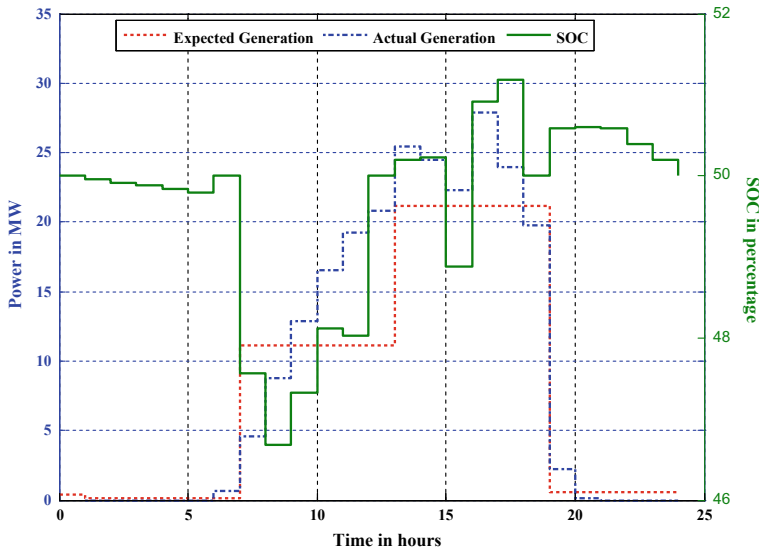
Fig. 7 Expected generation, actual generation and SOC in a day

6   Conclusions

This paper proposes a novel strategy to smooth quite uncertain and unpredictable PV/wind hybrid energy system using BESS. Analytical method is utilized here to evaluate the optimal size of the PV and wind farms as well as the BESS capacity in order to maximize the annual profit. It considers the expenses regarding wear and tear of the BESS as well as the benefits that would be acquired by improving the system reliability in supplying the load. Hence, the results promise practical viability from both technical and economical points of view. Consideration of different vital factors affecting the power output of renewable energy systems with real time hourly data for a year enhances its proximity to implications in real-world applications.

References

1. Sugihara H, Yokohoma K, Saeki O, Tsuji K, Funaki T (2013) Economic and efficient voltage management using customer-owned energy storage systems in a distribution network with high penetration of photovoltaic systems. IEEE Trans Power Syst 28(1):102–111
2. Ren G, Liu J, Wan J, Guo Y, Yu D (2017) Overview of wind power intermittency: Impacts, measurements, and mitigation solutions. Appl Energy 204:47–65
3. Di Fazio AR, Russo M (2008) Wind farm modelling for reliability assessment. IET Renew Power Gener 2(4):239–248

4. Teleke S, Baran ME, Bhattacharya S, Huang AQ (2010) Optimal control of battery energy storage for wind farm dispatching. IEEE Trans Energy Convers 25(3):787–794
5. Vrettos EI, Papathanassiou SA (2011) Operating policy and optimal sizing of a high penetration RES-BESS system for small isolated grids. IEEE Trans Energy Convers 26 (3):744–756
6. Shahooei Z, Fotuhi-Firuzabad M, Abbaspour A (2015) Reliability improvement of power system utilizing BESS with wind farm. In: Environment and electrical engineering (EEEIC), 2015 IEEE 15th international conference; 10 June 2015. IEEE, New York, pp 1120–1125
7. Yang H, Lu L, Zhou W (2007) A novel optimization sizing model for hybrid solar-wind power generation system. Sol Energy 81(1):76–84
8. Billinton R, Kumar S, Chowdhury N, Chu K, Debnath K, Goel L, Khan E, Kos P, Nourbakhsh G, Oteng-Adjei J (1989) A reliability test system for educational purposes-basic data. IEEE Trans Power Syst 4(3):1238–1244
9. Kusakana K (2015) Optimal scheduled power flow for distributed photovoltaic/wind/diesel generators with battery storage system. IET Renew Power Gener 9(8):916–924
10. Indian Meteorological Department, Bhubaneswar, 2015. http://www.imd.com/ (accessed 30 Aug 2016)
11. Giorsetto P, Utsurogi KF (1983) Development of a new procedure for reliability modelling of wind turbine generators. IEEE Trans Power Appar Syst 1:134–143
12. Allan RN, Billinton R, Sjarief I, Goel L, So KS (1991) A reliability test system for educational purposes-basic distribution system data and results. IEEE Trans Power Syst 6 (2):813–820
13. Su CL, Teng JH (2007) Outage costs quantification for benefit–cost analysis of distribution automation systems. Int J Electr Power 29(10):767–774
14. Nayak CK, Nayak MR (2018) Technoeconomic analysis of a grid-connected PV and battery energy storage system considering time of use pricing. Turk J Electr Eng Comput 26(1): 318–329
15. Ton D, Peek GH, Hanley C (2008) Solar energy grid integration systems–energy storage (SEGIS-GS). EERE Publication and Product Library, Washington, DC, United States

Economic and Technical Analysis of the Power System with Electric Vehicles Enabling G2V and V2G

Kumari Kasturi, Chinmay Kumar Nayak and Manas Ranjan Nayak

Abstract Adoption of electric vehicles (EVs) is globally accepted as an alternative option in transportation sector due to energy crisis and environmental issues. EVs' role in the form of vehicle to grid discharging is an advanced concept in evolution of smart grid in power system. A practical driving pattern is chosen for EVs. Salp Swarm Algorithm (SSA) optimization technique is used to obtain the optimal number of EVs and location of electric vehicle charging station (EVCS) in distribution network in order to minimize feeder power loss cost, cost of power drawn from the main grid and EV owner power purchase cost. It is verified that the algorithm does not only provide the social optimality—minimizing the impact of EV charging/discharging on the grid and utility's operating cost—but also satisfies EV owners' charging preferences.

Keywords Electric vehicle · Distribution system · Salp Swarm Algorithm · Vehicle to grid charging

K. Kasturi
Department of Electrical Engineering, Institute of Technical Education
and Research, Siksha 'O' Anusandhan University, Khandagiri Square,
Bhubaneswar 751030, Odisha, India
e-mail: kumari.kasturi1986@gmail.com

C. K. Nayak (✉)
Department of Electrical Engineering, Indira Gandhi Institute of Technology,
Sarang, Dhenkanal 759146, Odisha, India
e-mail: chinmaynayak009@gmail.com

M. R. Nayak
Department of Electrical Engineering, Biju Patnaik University of Technology,
Rourkela 769015, India
e-mail: manasnk72@gmail.com

1   Introduction

Transportation sector consumes major share of world's total energy consumption, as economy and population grow all around the globe [1], for each incremental demand of energy will have negative impact on environment and may lead to energy crisis [2]. Electric vehicle (EV) is a clean and green alternative option in transportation sector. Integration of EVs in radial distribution system (RDS) gives some new technical and economic challenges. Charging of EVs limits the capacity supply, exposing power system to acute security risk. EVs can give benefits due to a useful concept of vehicle to grid (V2G) charging [3]. V2G charging means EV has an option to sell the stored electrical energy to distribution company (DC) during peak periods and so reliability of the grid is increased. Several methods have been proposed for finding appropriate EV charging/discharging schedules.

A new demand response model has been proposed in [4] by which EV owners can change their trip plan to offer energy reduction. The paper introduced an energy scheduling for smart grid considering large number of EVs. In [5], for charging of plug-in electric vehicles (PEVs) in distribution system, a load management method has been suggested. A control technique was used for minimizing cost of power loss and generated energy. In [6], a multi-objective method was used to minimize total operation cost of distribution system and emission cost of DGs to get optimal charging/discharging schedule of EVs. In [7], the effects of EVs in grid balancing and demand side management have been discussed. V2G participation of EVs were shown to have benefited the EV owners.

An optimal location and number of EVs of each electric vehicle charging station (EVCS) are the problem variables for techno-economic aspects of DC and EV owners'. Salp Swarm Algorithm (SSA) optimization technique is used to solve single objective function. The suggested method provides EV charging/discharging schedule that can reduce the impact of EV integration in RDS without upgrading the power equipment.

In Sect. 2, the distribution system model is illustrated. Section 3 presents the electric vehicle model. In Sect. 4, the problem formulation is discussed and SSA is described in Sect. 5. In Sect. 6, simulation and result analysis are presented. Conclusions are detailed in Sect. 7.

2   Distribution System Model

The propose method is tested on the 33-bus radial distribution system (RDS) [8]. The total load on this system is 3715 kW. The backward and forward sweep-based algorithm is used for power flow calculation of RDS [9]. Hourly weight factors are used to model the 33-bus load demand of RDS. The hourly weight factor and electricity price for a day are shown in Fig. 1.
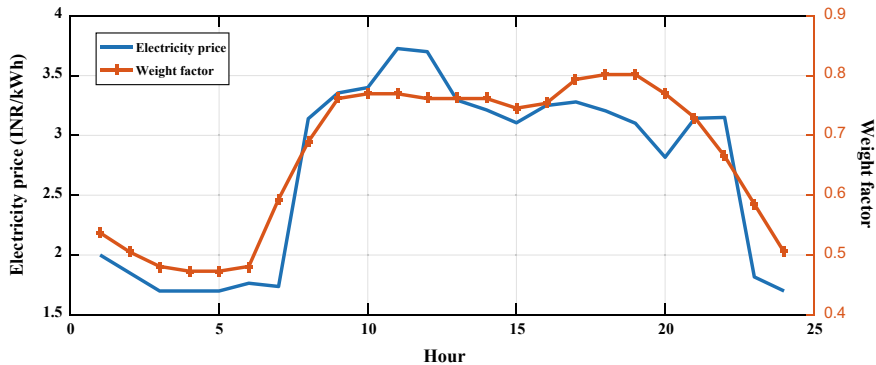
Fig. 1 Hourly weight factor and electricity price in a day

Power loss for RDS can be expressed as:

$$\sum_{t=1}^{n_t} P\text{Loss}, ij(t) \tag{1}$$

$$P_{\text{Loss},ij}(t) = R_{ij}I_{ij}^2(t) \tag{2}$$

where ijth is the branch number, R_{ij} is the resistance of ijth branch, $I_{ij}(t)$ is the current at ijth branch at time t and $P_{\text{Loss},ij}(t)$ is the active power loss of ijth branch at time t, n_t is the time slot (24 h for one day).

Power drawn from main grid can be expressed as:

$$\sum_{t=1}^{n_t} P_g(t) \tag{3}$$

$$P_g(t) = \text{real}\big(V_{\text{sub}}(t) \times I_{\text{sub}}^*(t)\big) \tag{4}$$

where $P_g(t)$ is the power drawn from main grid, $V_{\text{sub}}(t)$ is the voltage at substation at time t, $I_{\text{sub}}(t)$ current at the substation flowing into the RDS.

3 Electric Vehicle Model

3.1 Electric Vehicle User Behaviour

Two EVCSs are present in 33-bus RDS, and maximum 80 EVs can connect to each of EVCS. In this paper, the charging hours are the hours during which EVs are

parked at home or at workplace. EVs are parked at home during the hours 01:00–06:00 and 17:00–24:00 and parked at workplace during the hours 08:00–15:00. The EVs are charged/discharged during these parking hours by connecting to the RDS. It is assumed that EVs are running with constant speed. The average speed of the EV is 3 kWh/h. It should be ensured that EVs should have sufficient stored energy for next hour to travel the required distance.

3.2 EV Charging/Discharging Model

In this paper, two modes for charging of EVs are addressed. When EVs receive energy from the grid, it is stated as grid to vehicle (G2V) or EV charging and when EVs inject energy to the grid it is stated as vehicle to grid (V2G) or EV discharging [10]. Both types of charging are carried out during parking hours of EVs. Total available charging hours include both peak and off-peak hours as per the electricity price. From the total parking hours, hours having lower electricity price are chosen for G2V charging, whereas hours having higher electricity price are chosen for V2G discharging.

The power output of ith EVCS is

$$P_{\text{EVCS},i}(t) = \begin{cases} 0 & \text{when no EV is connected} \\ \alpha_i(t)P_{\max} & \text{else} \end{cases} \tag{5}$$

where $P_{\max}$ is the maximum charging/discharging rate of EV, and $\alpha_i(t)$ is time function of charge/discharge status which is the ratio of actual to maximum charging/discharging rate, i.e. $\alpha_i(t) \in [-1, 1]$.

$$\begin{cases} -1 \leq \alpha_i(t) < 0 & \text{G2V} \\ \alpha_i(t) = 0 & \text{idle} \\ 0 < \alpha_i(t) \leq 1 & \text{V2G} \end{cases} \tag{6}$$

The total power of EV for all EVCS can be calculated as

$$P_{\text{V2G/G2V}}(t) = \sum_{i=1}^{N_{\text{EVCS}}} P_{\text{EVCS},i}(t) \tag{7}$$

where N_{EVCS} is the number of EVCS connected to RDS. The EV charging/discharging rate of kth EV connected to ith EVCS at time t is

$$P_{\text{EV},i,k}(t) = \begin{cases} P_{\text{EVCS},i}(t) & t_{s,i,k} \leq t \leq t_{e,i,k} \\ 0 & \text{else} \end{cases} \tag{8}$$

where $t_{s,i,k}$ and $t_{e,i,k}$ are the start and end time of kth EV connected to ith EVCS. The state of charge (SOC) of EV battery is updated as

$$SOC(t+1) = SOC_{initial} + \sum_{t=1}^{T} SOC(t) \tag{9}$$

where SOC (t) is the state of charge at time t.

4 Problem Formulation

The primary objective of optimal placement of EVCS and number of EVs charging/ discharging in RDS is to minimize feeder power loss cost, power drawn cost from main grid and EV owner power purchase cost within the limitation of system operational constraints.

4.1 Objective Function

$$\text{Minimize} \left(F = f_{obj}^1 + f_{obj}^2 + f_{obj}^3 \right) \tag{10}$$

- Minimization of feeder power loss cost: This objective represents operating objective of DC which is given as:

$$f_{obj}^1 = \sum_{i=1}^{n} \left[\left(P_{Loss,EV}(t) - P_{Loss,Base}(t) \right) \times price(t) \right] \tag{11}$$

where $P_{Loss,EV}(t)$ is the active power loss at time t with EVCS, $P_{Loss,Base}(t)$ is the active power loss at time t without EVCS (Base case) and $price(t)$ is the electricity price.

- Minimization of power drawn cost from main grid: This objective also represents operating objective of DC which is given as:

$$f_{obj}^2 = \sum_{k=1}^{n_n} \left[\left(P_{g,EV}(t) - P_{g,Base}(t) \right) \times price(t) \right] \tag{12}$$

where $P_{g,EV}(t)$ is the power drawn from main grid at time t with EVCS and $P_{g,Base}(t)$ is the power drawn from main grid at time t without EVCS.

- Minimization of EV owner's power purchase cost: This objective represents operating objective of EV owners which is given as:

$$f_{\text{obj}}^3 = \sum_{t=1}^{n_t} [(\text{charge}(t) - \text{discharge } e(t)) \times \text{price}(t)] \tag{13}$$

where charge(t) is the power receive from grid during G2V charging at time t and discharge(t) is the power inject to the grid during V2G discharging at time t.

4.2 Constraints

The system operates within the framework of some equality and inequality constraints which are given below.

$$\text{EV}_{\text{ch/disch}} \leq \text{EV}_{\text{available\_parkinging\_hour}} \tag{14}$$

$$\text{EV}_{\text{demand}} = \sum_{n=1}^{N_{\text{EV}}} (\text{SOC}_{\text{max}} - \text{SOC}_{\text{initial}}) \tag{15}$$

$$\text{SOC}^{\text{min}} \leq \text{SOC}(t) \leq \text{SOC}^{\text{max}} \tag{16}$$

$$P_{\text{sub}}(t) = P_{\text{Load}}(t) + P_{\text{Loss}}(t) + P_{\text{EV}}(t) \tag{17}$$

$$Q_{\text{sub}}(t) = Q_{\text{Load}}(t) + Q_{\text{Loss}}(t) + Q_{\text{EV}}(t) \tag{18}$$

$$V_i^{\text{min}} \leq V_i(t) \leq V_i^{\text{max}} \tag{19}$$

$$I_{ij}(t) \leq I_{ij}^{\text{max}} \tag{20}$$

where $\text{EV}_{\text{ch/disch}}$ is the EV charging demand, $EV_{\text{available\_parkinging\_hour}}$ is the available parking hours, N_{EV} is the number of EVs, $P_{\text{sub}}(t)$ and $Q_{\text{sub}}(t)$ are the active and reactive power injection of substation at time t, respectively, $P_{\text{Loss}}(t)$ and $Q_{\text{Loss}}(t)$ are the active and reactive power losses of branch at time t, $P_{\text{Load}}(t)$ and $Q_{\text{Load}}(t)$ are the active and reactive loads of bus at time t, $P_{\text{EV}}(t)$ and $Q_{\text{EV}}(t)$ are the active and reactive charging/discharging capacity of EV, V_i^{min} and V_i^{max} are the lower and upper limit of voltage at bus i, I_{ij}^{max} is the maximum current at ijth branch and $I_{ij}(t)$ is the current at ijth branch at time t.

5 Salp Swarm Algorithm (SSA)

Salps are oceanic creatures from Salpidae family having transparent barrel-shaped body. Salps tissues are very similar to jelly fish. They move their body by pumping water through their body, propelling them. [11]. Sometimes Salps form Salp chain to get the better locomotion using rapid coordinated changes and foraging.

This swarming behaviour of Salps can be mathematically modelled. The Salps chain can be broadly divided in two groups, i.e. leader and followers. The Salp at the front of the chain is the leader and others are followers. As the name suggests, the leader guides the swarms and the others follow each other, in a way following the leader directly or indirectly.

In this optimization technique, n-dimensional search space is created where the number of variables of the problem is n. A two-dimensional matrix is created where all the position of Salps are stored. Swarm's target is assigned as a food source f.

The position of the leader Salp is updated as follows:

$$x_{j,1} = \begin{cases} f_i + c_1\big((vb_j - mb_j)c_2 + mb_j\big) & c_3 \geq 0 \\ f_j + c_1\big((vb_j - mb_j)c_2 + mb_j\big) & c_3 < 0 \end{cases} \tag{21}$$

where j is the dimension, $x_{j,1}$ is the first Salp position, f_j is the food source position, vb_j and mb_j are the upper and lower bounds, respectively. c_1, c_2 and c_3 are the random numbers. c_2 and c_3 are uniformly generated in [0, 1].

c_1 can be derived as follows:

$$c_1 = 2e^{-\left(\frac{4i}{I}\right)^2} \tag{22}$$

where i and I are the current and maximum iteration, respectively.

The position of follower is updated using the 2nd law of kinematics which can be modelled mathematically as follows:

$$x_i^k = \frac{1}{2}at^2 + u_0 t \tag{23}$$

$$a = \frac{u_{\text{final}}}{u_0} \tag{24}$$

$$u = \frac{x - x_0}{t} \tag{25}$$

where x_j^k is the position of the kth follower Salp in jth dimension with $k \geq 2$, u_0 is the initial speed, t is the time period which is equivalent to difference between consecutive iterations, i.e. 1 in case of optimization.

If $u_0 = 0$, then Eq. (23) can be rewritten as

$$x_j^k = \frac{1}{2}\left(x_j^k + x_j^{k-1}\right) \tag{26}$$

After first iteration, a swarm is created and it moves effectively using the above suggested model. Over the upcoming iterations, the superior Salp updates its position around the pray and other Salps try to chase it slowly. During optimization, food source is updated to find the space for the Salp chain model. Also Salp chain has the ability to chase a moving prey. Hence, the Salp chain has the capability to find the global optimum that change over iterations. The determination process and the procedure of SSA are discussed as follows:

Step 1. Quality of Salps (swarm size = 50) and the maximum iterations (iteration = 100) are specified for the problem. Assign the minimum and maximum values for variables
$x_j = [L_{\text{EVCS}}, N_{\text{EV}}]$.
where, L_{EVCS} is the location of the EVCS.
Step 2. Calculate the fitness of each Salp.
Step 3. Determine the Salp with best fitness value and assign it to f as the target for the Salps.
Step 4. Update c_1 by using Eq. (22).

6 Simulation and Result Analysis

The proposed technique is tested in 33-bus RDS. Maximum iteration number and number of search agents of 100 and 50, respectively, are chosen as the parameters for SSA. For power flow calculation, the base values are set to 100 MVA and 12.66 kV. The load bus is considered as the location for EVCS. The bus voltage variation is restricted to $\pm10\%$. EV batteries have the charging and discharging capacities of 40 kW each with a battery inverter efficiency of 94%. The maximum charging/discharging time of EV battery is 8 h. $\text{SOC}_{\text{inital}}, \text{SOC}^{\max}$ and $\text{SOC}^{\min}$ of EV batteries are considered as 50, 100 and 10%, respectively. The objective function value with EVCS locations are illustrated in Table 1.

Table 1 Optimization results

Parameters	Value
Location	32, 16
Number of EVs in EVCS	8, 10
f_{obj}^1 (INR)	32.2100 (Benefit)
f_{obj}^2 (INR)	10.8902 (Benefit)
f_{obj}^3 (INR)	22.6876
Power loss (kW)	2206.9
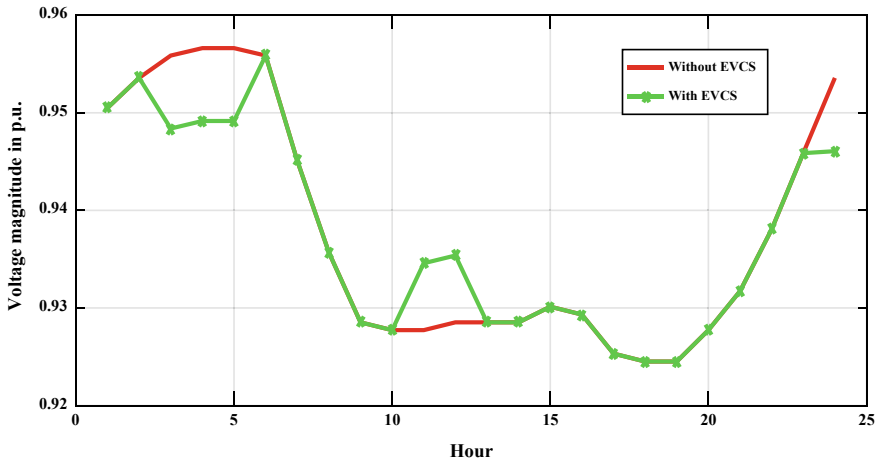
Fig. 2 Voltage profile of bus 18
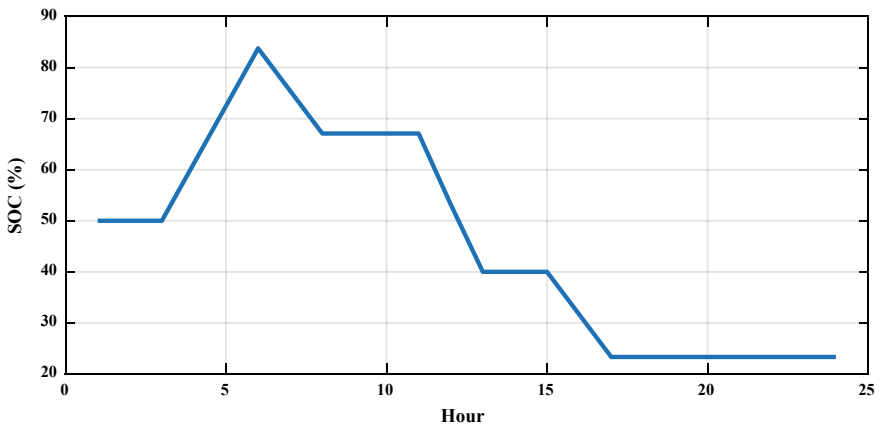
Fig. 3 SOC for optimal EVs

Voltage profile of bus 18 is shown in Fig. 2 as the voltage profile of this bus is low as compared to other buses in 33-bus RDS. It can be observed that during off-peak hours, from 03:00 to 05:00, when the electricity price is less, EVs are operated as G2V charging. So the voltage profile is more affected. During peak hours 11:00 and 12:00 when price is higher, EVs are operated as V2G charging the voltage profile is significantly improved. Due to V2G charging, the minimum voltage is improved from 0.9277 p.u. to 0.9346 p.u.

SOC curves for all EVs are same, because same types of batteries are used in all the EVs. Figure 3 depicts the SOC of EV battery. The EV battery remains idle until 03:00 h, and then, it charges till 06:00 h as electricity price is less in those hours. It
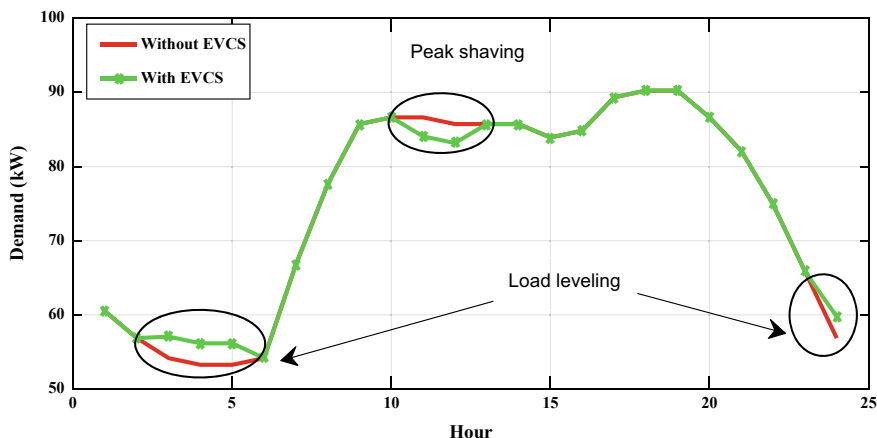
Fig. 4 Grid load demand in one day

starts discharging from 06:00 h to 08:00 h in order to arrive at the workplace. Then it remains idle until 11:00 h even if it has sufficient power to discharge, because lower electricity price during those hours does not benefit the EV owner. Then it starts discharging up to 13:00 during higher electricity price periods. Then it remains idle up to 15:00 in order to store sufficient energy for returning home. It starts discharging until 17:00 h to reach at home. Then it remains idle as the SOC reaches at 23.34%. Then for next day sufficient charging hours are available to charge the EV battery.

Excessive EVs energy can support the power grid as V2G charging. The grid load profile is flatten due to use of V2G charging by load levelling and peak load shaving. Figure 4 describes the comparison of grid load after and before implementation of load levelling and peak load shaving. At 11:00–12:00 h, the load as well as electricity price is high, so to shave off the peak load EVs can be used to supply energy which is economically viable. The stress on components of RDS can be reduced by this method during peak hours, and it is also benefited to EV owners. EVs can be operated as G2V charging during off-peak hours with lower electricity price.

The total active power loss is increased from 2206.9 to 2220.9 kW after installation of EVCS in RDS. But it is reduced in peak hours due to V2G discharging as shown in Fig. 5. V2G discharging during peak hours can provide more benefit as compared to off-peak hour discharging. Before using the V2G discharging, the power equipment is less utilized during off-peak hours as it is meant to handle peak loads. So V2G charging can enhance the power equipment capacity which reduces the upgrade cost of those equipment. So the proposed method can maximize the benefits of EV owners and DC.
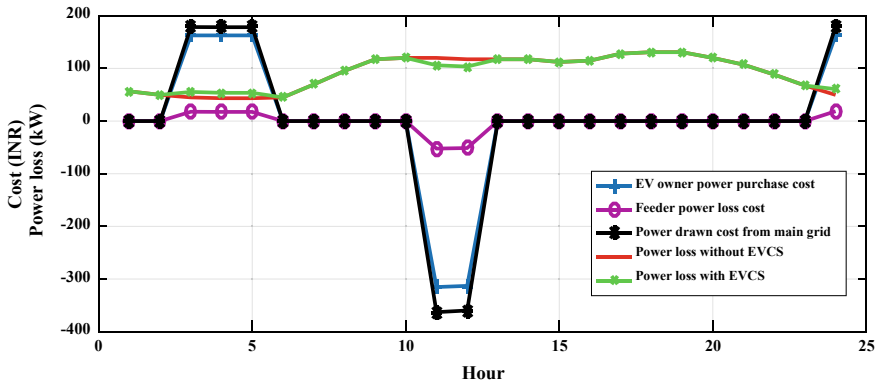
Fig. 5 Different objective function values and power loss in one day

7   Conclusion

Results of this proposed technique make it clear that use of EV as G2V and V2G charging is beneficial for both DC and EV owners. The proposed optimization technique minimizes feeder power loss cost, power drawn cost from main grid and EV owner power purchase cost to get optimal placement of EVCS and number of EVs charging/discharging in RDS. SSA is adopted as optimization tool. G2V and V2G charging of EVs are able to support power grid, such as load levelling, peak load shaving and ancillary services.

References

1. Tan KM, Ramachandaramurthy VK, Yong JY (2016) Integration of electric vehicles in smart grid: a review on vehicle to grid technologies and optimization techniques. Renew Sustain Energy Rev 53:720–732
2. Organization of the petroleum exporting countries OPEC (2013) World oil outlook. ISBN 978-3-9502722-6-0
3. Kempton W, Tomić J (2005) Vehicle-to-grid power fundamentals: calculating capacity and net revenue. J Power Sour 144(1):268–279
4. Soares J, Morais H, Sousa T, Vale Z, Faria P (2013) Day-ahead resource scheduling including demand response for electric vehicles. IEEE Trans Smart Grid 4(1):596–605
5. Deilami S, Masoum AS, Moses PS, Masoum MA (2011) Real-time coordination of plug-in electric vehicle charging in smart grids to minimize power losses and improve voltage profile. IEEE Trans Smart Grid 2(3):456–467
6. Zakariazadeh A, Jadid S, Siano P (2014) Multi-objective scheduling of electric vehicles in smart distribution system. Energy Convers Manag 79:43–53
7. Druitt J, Früh WG (2012) Simulation of demand management and grid balancing with electric vehicles. J Power Sour 216:104–116

8. Nayak MR, Kasturi K, Rout PK (2013) optimal placement and sizing of multiple capacitors in radial distribution systems using modified TLBO algorithm. Int Rev Autom Control 6 (6):701–713
9. Nayak MR, Nayak CK (2013) Distributed generation optimal placement and sizing to enhance power distribution network performance using MTLBO. Int Rev Electr Eng-I 8 (6):1857–1869
10. Alipour M, Mohammadi-Ivatloo B, Moradi-Dalvand M, Zare K (2017) Stochastic scheduling of aggregators of plug-in electric vehicles for participation in energy and ancillary service markets. Energy 118:1168–1179
11. Mirjalili S, Gandomi AH, Mirjalili SZ, Saremi S, Faris H, Mirjalili SM (2017) Salp swarm algorithm: a bio-inspired optimizer for engineering design problems. Adv Eng Softw 114:163–191

Simscape Modelling and Analysis of Photovoltaic Modules with Boost Converter for Solar Electric Vehicles

Mohammad Waseem, A. F. Sherwani and Mohd Suhaib

Abstract Solar/battery electric vehicles are the future vehicles in place of the conventional engine vehicles to meet the sustainable development goal. Solar electric vehicles have several advantages over conventional vehicles such as eco-friendly, fewer emissions at the tail point and improved transmission efficiency. Photovoltaic (PV) panels can mount on the roof or suitable available area on a vehicle that converts solar irradiation into useful electric energy. Generally, the output power of PV module is low or insufficient to charge the batteries of electric vehicles due to variation in solar irradiation. Hence, there is need to boost up the output power/voltage of PV panel. In this paper, modelling and analysis of DC-boost converter for a solar electric vehicle are presented. The physical model of DC-boost converter is designed and developed in Simscape environment of MATLAB tool. Simulations of DC-boost converter model are carried out at irradiation values of 1000, 800, 600, 400 W/m^2 for 200 ms that uses 75 and 80% duty cycle of pulse width modulation (PWM). Finally, simulation results are analysed at irradiation values of 1000, 800, 600, 400 W/m^2 for 75 and 80% duty cycle.

M. Waseem (✉) · A. F. Sherwani · M. Suhaib
Department of Mechanical Engineering, Faculty of Engineering & Technology,
Jamia Millia Islamia (A Central University), New Delhi 110025, India
e-mail: waseem159088@st.jmi.ac.in

A. F. Sherwani
e-mail: asherwani@jmi.ac.in

M. Suhaib
e-mail: msuhaib@jmi.ac.in

1 Introduction

Solar energy is considered as one of alternate sustainable resource to meet the future energy demand. Due to limited energy resources of conventional fuel and pollution issues, conversion of solar energy into electric power is a promising solution to make eco-friendly environment [1]. Literature suggests that conventional resources of fuel are diminishing. Fossil fuel and uranium are the only available conventional energy resources. Uranium is mostly used for nuclear power production, and it required careful attention to operating [2]. Hence, the main sources of energy are fossil fuels like petroleum, coal, and natural gas. Harmful gasses such as carbon dioxide (CO_2) and nitrogen oxide (NO_x) are produced in the environment by the combustion of fossil fuels [3].

In the current era, research towards photovoltaic (PV) technology is expanding significantly. PV technology has positive environmental impacts to control global warming and pollution issues [4]. Due to numerous eco-friendly characteristics, PV technology is considered as one of the important sources for future energy [5]. In the existing automobile transportation system, internal combustion engines (ICEs) technology is used most widely. Vehicles using ICEs technology have several negative environmental issues such as air, land and water pollution [6]. Electric vehicle technology has a positive environmental effect and zero emissions at the tail point. The automobile industries introduce electrical and hybrid vehicle technology to reduce fossils fuel consumption [7]. Solar/battery electric vehicles are introduced for further advancement of technology which utilizes sustainable solar energy. Electric propulsion systems are employed in solar/battery electric vehicles to impart necessary power [8].

Approximately 21 V is produced by PV module consisting 36 cells in series only for few hours during maximum sunlight condition [9]. Hence, the output voltage from PV module is not sufficient to charge 12–48 V batteries. Therefore, boost-up device can fulfil this need to charge the 12 V batteries regularly. This technique can also be applied to boost up PV output voltage during low incoming solar irradiation.

2 Methodology

Power electronic devices are the integrated part of the renewable energy system. The Literature discussed above suggests that some boost-up device is needed to ensure the desired output of PV module. Firstly, selection of appropriate PV module is conducted. Next, the physical model of selected PV module is designed and simulated in Simscape environment of MATLAB. Thereafter, the physical model of DC-boost converter is developed in Simscape library tool to boost up the output voltage and current of PV module. Appropriate designing values of inductor and capacitor are estimated for the physical model of the boost converter.

Now, simulations are carried out at irradiation values of 1000, 800, 600, 400 W/m^2 for 200 ms using 75 and 80% duty cycle of pulse width modulation (PWM). In the next section, selection of PV module for the solar electric vehicle is discussed.

3   PV Module for Solar Electric Vehicles

The scope of solar energy in India is excellent due to its geographical characteristics. Being a tropical country, India received 3×10^3 h sunshine of solar radiation throughout the year. Almost 4–7 kWh per square metre, solar radiation is being received by all parts of India [10]. PV technology is an innovative technique to coverts solar energy into electricity. Various operating characteristics/parameters of PV module such as efficiency, dimensions, weight, maximum nominal output power, operating cost are responsible to select appropriate module. PV modules of five manufacturing companies are considered to analyse various parameters as shown in Table 1. From the analysis, it is found that X21-345 series module of Sunpower company has the highest rank out of five modules. Therefore, X21-345 series module is considered for the present work.

3.1   Simscape Physical Modelling of PV Module

Several solar cells in series and parallel combinations are arranged to construct PV module. The equivalent electrical circuit network of a solar cell is shown in Fig. 1. The output current of the solar cell is governed by Eq. (1).

$$I = I_p - I_d \left(\exp\left[\frac{V + IR_s}{NV_T}\right] - 1 \right) - \left[\frac{V + IR_s}{R_{sh}}\right] \tag{1}$$

where I = cell output current (A), I_p= light (photon) produced current, I_d is reverse saturation currents for diode, V = cell output voltage, R_s= series resistance, R_{sh} = shunt resistance, N is quality factor for diode and V_T = thermal voltage of cell.

Simscape library is a powerful tool of MATLAB for modelling a complex engineering system. Therefore, physical model of X21-345 module is designed and developed in Simscape MATLAB environment library tool. The developed physical model of PV array in Simscape MATLAB is shown in Fig. 2. It consists of physical blocks such as PV subsystem, current sensor, voltage sensor, scopes, PS constant, Simulink-PS converter and ramp. PS constant block is used to specify the intensity of solar irradiation. The output physical signal of voltage and current is measured with the help of voltage and current sensor blocks. Now, these physical signals are converted into Simulink signals by PS-Simulink converter block. Finally, Simulink signals are sent to scope blocks for analysing. PV subsystem is

Table 1 Operating characteristics of PV modules

Characteristics of PV panel modules at standard test condition (25 °C)

Company/Brand	Waaree [11]	Sunsolar [12]	Sunpower [13]	Tatapower solar [14]	Alpex [15]
Panel series	WSMP-350	SS MONO 265	X21-345-COM	TP 300	X-FACTOR
Maximum power (W)	350	265	345	310	330
Module efficiency (%)	18.07	15.90	21.5	15.63	17.28
Panel weight (kg)	22.50	19.00	18.60	24.00	22.50
Panel dimensions ($l \times b \times h$) mm	1960 × 990 × 40	1663 × 997 × 35 mm	1556 × 1046 × 46	1984 × 1000 × 40	1966 × 40 × 982
Number of cells per module	72	72	96	72	72

Fig. 1 Equivalent solar cell diagram with a single diode
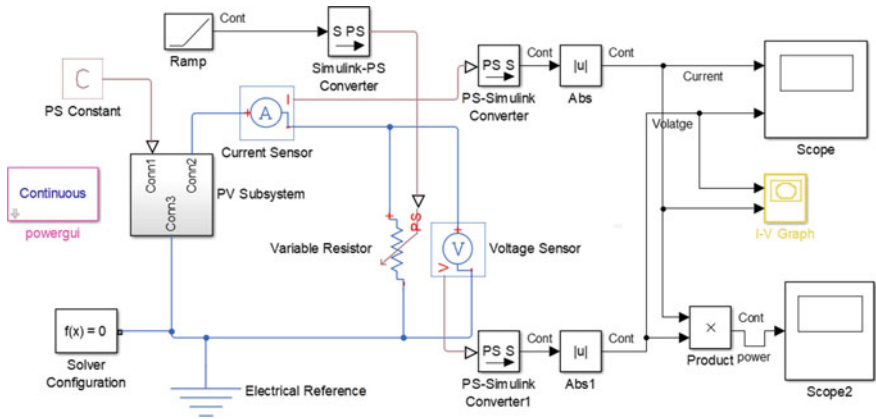
Fig. 2 Simscape physical model of X21-345 PV module

PV module that consists of 96 solar cells. A total of 96 monocrystalline Maxeon Gen III cells are connecting in series-wise to construct one PV module.

The developed physical model of PV module is compiled in Simscape environment. Thereafter, output current and voltage of physical model of X21-345 are analysed through simulations. The simulations have been carried out for 250 s at irradiation values of 1000, 800, 600, 400, and 200 W/m^2, respectively. The output current of PV module at irradiation values of 1000, 800, 600, 400, and 200 W/m^2 is plotted as shown in Fig. 3. The output results signify that there is a significant downfall in output current and power magnitude at irradiation 200 W/m^2. Hence, it is important to boost up the output voltage for maintaining desired output level. Therefore, Simscape modelling of DC-boost converter is presented in the next section to maintain the desired output level.
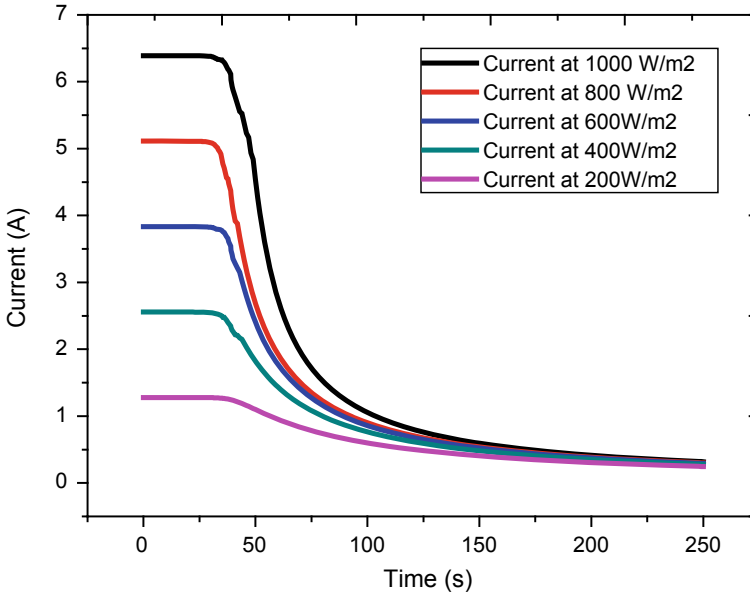
Fig. 3 Simscape physical model of X21-345 PV module

3.2 Simscape Modelling of Boost Converter for Solar Electric Vehicle

To boost up the output voltage and power of PV module, physical model of the DC-DC-boost converter is developed in Simscape environment of MATLAB tool. The block diagram of Simscape physical model of the DC-DC-boost converter is shown in Fig. 4. The model of boost converter consists of various physical blocks such as PV subsystem, inductor, controlled PWM voltage, diode, N-Channel MOSFET, capacitor, resistor, a current sensor, a voltage sensor, PS-Simulink converter, and scope. Switching operation time of MOSFET is controlled by the PWM pulses with defined duty cycle. Finally, physical signal of current and voltage is converted into Simulink signal. Inductor and capacitor are the important components of the boost converter. Minimum designed values of inductance and capacitance are calculated from Eqs. (2) and (3), respectively.

$$L_{min} = \frac{V_{in} \times D}{f_{pwm} \times \Delta I_L} \qquad (2)$$

$$C_{min} = \frac{D}{f_{pwm} \times V_r \times R} \qquad (3)$$
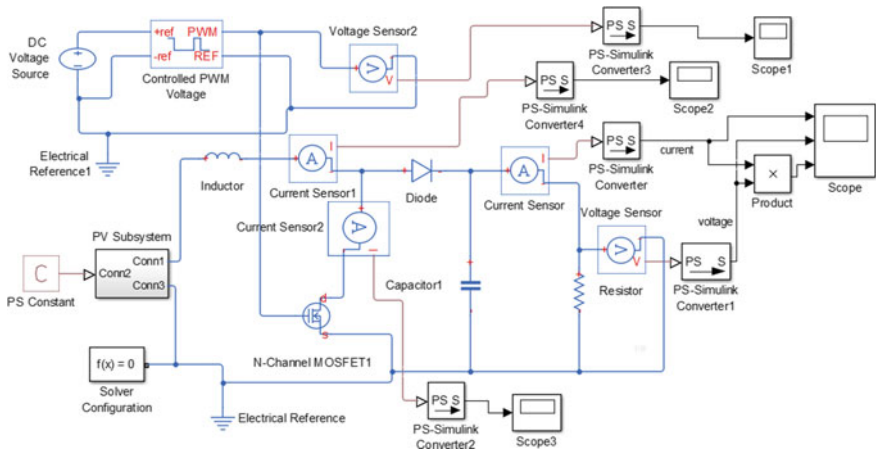
Fig. 4 Simscape physical model of DC-boost converter

Table 2 Parameters of DC-boost converter at 1000 W/m² irradiation

S. No.	Parameters	Numerical value	Unit
1	Input voltage to boost converter	68	V
2	Output voltage from boost converter	282	V
3	Frequency of PWM	10	kHz
4	Duty cycle	80	%
5	Inductance of inductor	2800	μH
6	Capacitance of capacitor	12.8	μF
7	Load resistance	250	Ω
8	Voltage ripple factor	0.0125	

where V_{in} is input voltage of boost converter, D is the duty cycle, and f_{pwm} is the frequency of pulse with modulation (Hz); ΔI_L is desired ripple current, V_r is the desired output voltage ripple, and R is the load resistance (Ω).

Designing parameters for DC-DC-boost converter and the solar cell are given in Tables 2 and 3, respectively.

Table 3 Specifications of the solar cell at 1000 W/m^2 irradiation

S. No.	Parameters	Numerical value	Unit
1	Open circuit voltage (V_o)	0.7083	V
2	Short circuit current (I_{sc})	6.39	A
3	Irradiance (I_{rr})	1000	W/m^2
4	Number of cells in PV module (n)	96	
5	Quality factor of diode (N_q)	1.5	
6	Series resistance (R_s)	0.0	Ω
7	Energy gap (E_g)	1.11	eV
8	Operating temperature of cell	25	°C

4 Results and Discussions

Firstly, appropriate PV module is selected from the survey of variously available panels in the market. The physical model of selected PV module (Sunpower-345) is designed in Simscape environment of MATLAB tool. Next, the physical model of PV module is simulated for 250 s to find out the effects of solar irradiation on the output voltage and current. Thereafter, the physical model of DC-boost converter is designed and developed in Simscape library. Appropriate designing values of inductor and capacitor are estimated and assigned to the physical model of the boost converter. Now, simulations have been carried out at irradiation values of 1000, 800, 600, 400 W/m^2 for 200 ms using 75 and 80% duty cycle of PWM. Simulation response of output boosted voltage and current for 80% duty cycle are shown in Figs. 5 and 6, respectively. The output voltage has been boosted up from 68 to 282 volts using 80% duty cycle for 1000 irradiance.
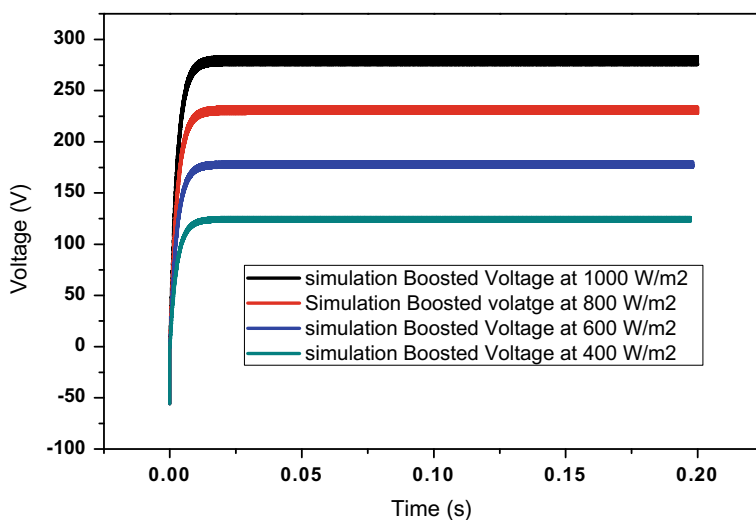
Fig. 5 Voltage response of DC-boost converter at 1000, 800, 600, and 400 W/m^2 irradiation
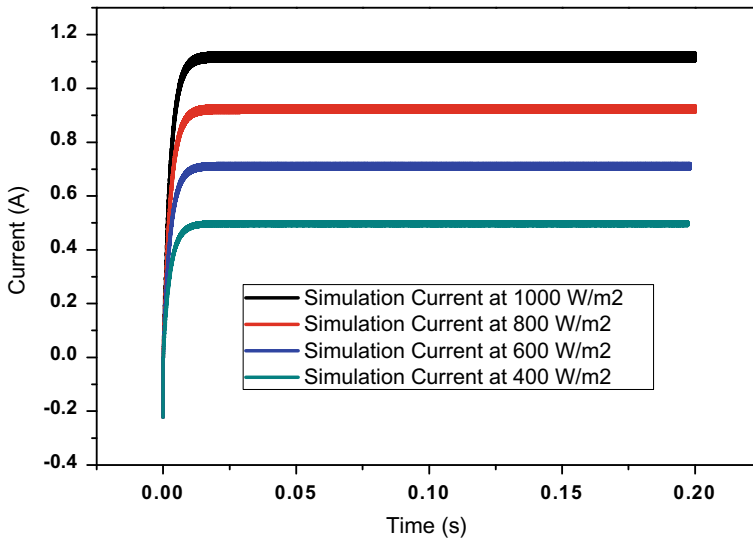
Fig. 6 Current response of DC-boost converter at 1000, 800, 600, and 400 W/m^2 irradiation

DC-boost converter's input and output parameters for 75% and 80% duty cycles of PWM are given in Tables 4 and 5, respectively.

Simulated results of DC-boost converter are analysed for 75 and 80% duty cycle. It is concluded from the results that maximum output power is obtained for 80% duty cycle at 1000 W/m^2 irradiation while minimum output power is also obtained for 80% duty cycle at 400 W/m^2 irradiations. So, results are further analysed by taken mean values of output power for 75 and 80% duty cycle, respectively. The mean values of output power from DC converter are 196.827 and 182.349 for duty cycle 75 and 80%, respectively. Hence, more average output power is obtained from the DC-boost converter that has 75% duty cycle of PWM.

Table 4 DC-boost converter data for 75% duty cycle

Boost parameters	Unit	Data 1	Data 2	Data 3	Data 4
Irradiation I_{rr}	W/m^2	1000	8000	600	400
Simulation time t	ms	200	200	200	200
Panel current I_{pv}	A	6.39	5.1	3.9	2.6
Inductance L_{min}	mH	2.7	3.3	4.4	6.5
Capacitance C_{min}	μF	12	12	12	12
Boosted voltage V_{boost}	V	258.72	248.214	214.115	149.772
Boosted current I_{boost}	A	1.0349	0.9929	0.8565	0.5991
Boosted power P_{boost}	W	267.76	246.44	183.38	89.727

Table 5 DC-boost converter data for 80% duty cycle

Boost parameters	Unit	Data 1	Data 2	Data 3	Data 4
Irradiation I_{rr}	W/m^2	1000	8000	600	400
Simulation time t	ms	200	200	200	200
Panel current I_{pv}	A	6.39	5.1	3.9	2.6
Inductance L_{min}	mH	2.8	3.6	4.6	7.0
Capacitance C_{min}	μF	12.8	12.8	12.8	12.8
Boosted voltage V_{boost}	V	282.81	233.83	180.146	123.892
Boosted current I_{boost}	A	1.1319	0.9347	0.7206	0.4956
Boosted power P_{boost}	W	319.93	218.43	129.64	61.397

5 Conclusions

Solar energy has excellent potential in India; implementation of sustainable solar energy with an electric vehicle is proposed in the presented work. Firstly, the physical model of Sunpower X21-345 module is developed in Simscape library of MATLAB tool. Next, output voltage and current from panel are simulated for 250 s from this physical model. Thereafter, Simscape physical model of DC-boost converter is designed and modelled to boost up the panel output voltage. Now, simulations of Simscape DC-boost converter model are carried out at irradiation values of 1000, 800, 600, 400 W/m^2 for 200 ms that uses 75% and 80% duty cycle of PWM. Results show that maximum output power is obtained from the proposed DC-boost converter that uses 80% duty cycle of PWM at 1000 W/m^2 irradiation. While in terms of overall average output power for irradiation values of 1000, 800, 600, and 400 W/m^2, the DC-boost converter that uses 75% duty cycle of PWM is more efficient. In future, the DC-boost converter will be implemented with solar/battery electric vehicle to reduce the pollutions issues.

References

1. Glaser PE (1977) The potential of satellite solar power. Proc IEEE 65:1162–1176
2. Masood B, Naqvi RAH, Asif RM (2015) Designing of a control scheme for the solar rickshaw in comparative study with conventional auto rickshaw. In: 2014 4th international conference on engineering technology and technopreneuship, ICE2T 2014, pp 324–329
3. Sarkar T, Sharma M, Gawre SK (2014) A generalized approach to design the electrical power system of a solar electric vehicle. In: 2014 IEEE students' conference on electrical, electronics and computer science. IEEE, New York, pp 1–6
4. Elmenshawy M, Elmenshawy M, Massoud A, Gastli A (2016) Solar car efficient power converters' design. ISCAIE 2016—2018 IEEE symposium on computer applications & industrial electronics, pp 177–182
5. Gitano-Briggs H (2010) Small wind turbine power controllers. In: Wind power, pp 165–188. InTech

6. Simaes MG, Franceschetti NN, Adamowski JC (1998) A solar powered electric vehicle. Appl Power Electron Conf Expo 1:49–55
7. Hannan MA, Azidin FA, Mohamed A (2014) Hybrid electric vehicles and their challenges: a review. Renew Sustain Energy Rev 29:135–150
8. Vas JV, Venugopal S, Nair VG (2008) Control scheme for electrical drive of solar powered vehicles. In: Proceedings of the INDICON 2008 IEEE conference and exhibition on control, communications and automation, pp 75–80
9. Matsuo H, Hayashi H, Kurokawa F, Koga T (1991) A general analysis of the zero-voltage switched quasi-resonant buck-boost type DC-DC converter in the continuous and discontinuous modes of the reactor current. In: [Proceedings] Thirteenth international telecommunications energy conference—INTELEC 91, pp 472–479
10. Genta G (2012) Introduction to the mechanics of space robots. Springer, Netherlands
11. documents_WSMP-350_4BB_40mm_datasheet. http://www.waaree.com/download-center. Accessed 09 Mar 2018
12. SunSolar-Datasheet_Silver-Sterling-SS-265-1. http://www.sunsolarenergy.co.uk/downloads/. Accessed 10 Mar 2018
13. https://us.sunpower.com/sites/sunpower/files/media-library/data-sheets/ds-x21-series-335-345-residential-solar-panels.pdf. Accessed 10 Apr 2018
14. http://www.tatapowersolar.com/images/module/downloads/Datasheet%20-%20TP300%20[June2015].pdf. Accessed 09 Mar 2018
15. http://www.alpexsolar.com/assets/diamond-xxx-pv-modules-final_315-330.pdf. Accessed 09 Apr 2018

Comparison of Heuristic Approach in Renewable Power Optimization and Environmental Analyses

Trina Som and Vishal Rajak

Abstract Optimal power generation (OPG) through reliable and clean technologies is nowadays of high concern. Meta-heuristic algorithms are attractive for robust and adaptable solutions to OPG problems. However, no algorithm can result in the most desirable solution to OPG problems. In the present work, two novel methods, namely improved colliding body optimization and tuned genetic algorithm have been proposed for electric power production through combination of renewable and non-conventional energy resources. Solar photovoltaic module and biomass gasification systems have been used to deliver power reliably for a real-time load data in an Indian scenario, with battery used for energy storage. Two case studies have been conducted considering different loading scenarios. To quantify the environmental impact, carbon footprint and carbon tax have been computed for the defined case studies. ICBO has been found to provide more consistent result, in generating optimal renewable power as well as computing carbon tax.

Keywords Biomass · Solar · Carbon footprint · Heuristic · Optimization

1 Introduction

This ever-increasing demand for energy, continuous rise in fuel costs, diminution of conventional fuel reserves, and concern for environmental pollution have brought to prominence a wide array of power generation technologies. The new energy-producing systems, comprising of different forms of DERs are usually adept at protecting environment from pollution, and been studied by several researchers

T. Som (✉) · V. Rajak
Department of Electrical and Electronics, Delhi Technical Campus, 28/1,
Knowledge Park-III, Greater Noida 201306, Uttar Pradesh, India
e-mail: trinasom@gmail.com

V. Rajak
e-mail: vishalrajakvishal@gmail.com

[1, 2]. In reduction of environmental pollution by utilization of different non-conventional energy sources *viz.* wind power, fuel cells, solar power, and biomass units, DERs play a key task though share of various-sized markets. In regard to function and design of DERs, a number of works [3, 4] are available in the literature.

The difficulties faced by conventional power delivery system, in terms of distribution, control, and protection have been surmounted through the conception of microgrid as a new power delivery system [5]. Microgrid [6] is locally controlled energy system that uses different types of renewable energy resources (solar, wind, biomass, hydro, and ocean), energy generators (diesel, gasoline, biogas, and biodiesel), energy storage systems (batteries, flywheel, hydrogen, and thermal), loads (residential, commercial, and industrial), and control equipment (inverters and converters) integrated with loads. Development of potential microgrids including DERs has been mentioned in the literature [7]. Even though several researchers [8, 9] are dealing with the technical aspects of the microgrid, the newly built microgrids are still struggling in standardization through optimal power generation and flow pertaining to the reliability and economics.

Huang et al. [10] presented an improved direct search method of optimal power dispatch considering microgrid energy delivery system. Different aspects of micropower generating system which are accessible to deterministic solution techniques are dealt with in [11, 12]. Although an exact solution can be obtained from these methods, they fail to consider the aspects such as uncertainty, partial truth, imprecision, and approximation. Integration of these features should result in robust, tractable, easily implementable solution with low cost, a soft computing techniques, or heuristic methods that provide an useful and adaptive approach, wherein the above-mentioned features are integrated naturally [9], and could, therefore, be capable of providing a better solution.

Applications of different evolutionary methods on various aspects of microgrid are available in the literature. In order to size power equipment for an islanded microgrid operation, a comparison between a classical integer minimization problem (IMP) and evolutionary strategy (ES) method (a generic population-based optimization meta-heuristic algorithm) has been studied by Logenthiran et al. [13]. Erdinc and Uzunoglu [14] also highlighted a few techniques to solve for hybrid renewable energy systems sizing. These methods include GA, PSO, SA, Ant Colony, and AIS. In order to improve system efficiency of energy utilization and other constrains, a combined cooling and heating power model for a rural microgrid system has been built and optimized by using a MINLP optimization process with a BONMIN solver [15]. A probabilistic approach for economic/emission management of microgrids [16] has been performed, which is based on the MGSA to find pareto-optimal front of the operation management problem. Heuristic methods are designed to find a good solution among a large set of feasible solutions with less computational effort than optimization techniques. However, application of improved evolutionary approach in exploring the optimal power generation for a micropower system with different frameworks of renewable energy delivery resources, in an Indian scenario are rare in the literature.

At present, two methods, namely solar thermal and photovoltaic (PV) are in use for solar electricity generation. PV system which directly converts solar power in electricity with photoelectric effect is preferable for local small-scale power generating utilities [17]. Optimal operation non-conventional hybrid power generation including solar power has been studied by Som and Chakraborty [18]. In Indian context, Kumar et al. made an optimization study regarding the size and control strategies of solar PV with diesel generator (DG) for both grid-active microgrid and remote location [19]. Hybrid technology combination for electricity generation from a mix of renewable energy resources to satisfy the electrical needs in India was investigated by Sen and Bhattacharyya [20]. Further, optimization and comparison of results for various microgrid configurations have been carried out for remote village, in terms of reliable supply and reasonable cost [21]. Nevertheless, it can be concluded that, though optimization in meeting load demand has been studied by few authors in Indian scenario, but various improved methodology have hardly been explored and implemented toward a more specific solution.

No one algorithm can result in best solution to OPG problems; hence, there is always a requirement for a new algorithm. Over the last few decades, constant evolution in search of advanced computational techniques gave rise to the development of what is called meta-heuristics method. A meta-heuristic technique inspired by the process of natural selection have been modified and implemented in the current work.

The colliding bodies optimization (CBO) is a new nature-inspired meta-heuristic which is based on the law of collision between two bodies, and has been used in exploring better solutions under the consideration of different constraining factors. The other method used is TGA [18], which has also been developed for the present problem.

2 Problem Modeling

A study on optimal power generation through renewable energy resources has been performed. Optimal power generation has been computed for a real-time load scenario of a specific Indian location. In order to explore better reliability, effectiveness, and environment friendly alternative, the operation of current renewable-based power delivery system has been defined and formulated with the following key features.

- A combination of solar and biomass power generation have been explored
- Nature-inspired heuristic methods based on CBO and GA-based have been implemented as control method

- Modifications have been done to improve the optimized results in terms of parametric variation, which resulted as an improved colliding body optimization (ICBO) and tuned genetic algorithm (TGA)
- Carbon footprint and carbon tax have been computed for the defined case studies and comparative study have also been presented in this regard.

The objective function pertaining to optimal power generation depending on various side constraining factors is as follows;

A. Objective function

The power deviation in meeting the load demand by the power generated from different renewable energy sources, *viz.* solar photovoltaic, biomass gasifier unit, and a battery backup system has been defined as the main objective function, which has to be minimized for both summer and winter seasonal load as shown in Eq. (1)

$$\sum_{hr=1}^{24} P_d(\text{ss}, \text{hr}) = \sum_{hr=1}^{24} P_l(\text{ss}, \text{hr}) - [P_{SO}(\text{ss}, \text{hr}) + P_{BM}(\text{ss}, \text{hr}) \pm P_{bt}(\text{ss}, \text{hr})] \quad (1)$$

Here, P_d, P_l, are the power difference and load demand, respectively. P_{SO}, P_{BM}, and P_{bt} are the power generations from solar photovoltaic, biomass gasifier unit, and battery, respectively. The subscripts ss and hr denotes the seasonal and hourly variation of load and power generation.

The power generated from solar energy depends on certain geographical and environmental factors which are expressed [22] as shown below in Eq. (2)

$$P_{SO} = (Y_{PV})(f_{PV}) \frac{G_T}{G_{T,STC}} \left[1 + \alpha_P (T_C - T_{C,STC})\right] \quad (2)$$

Here, f_{PV} is the derating factor, Y_{PV} is the rated capacity for solar panel, and G_T is the global solar irradiation on the surface of solar panel, and $G_{T,STC}$ is the solar irradiation at standard test condition, *viz.* 25 °C. The parameter α_P is the temperature coefficient of power (%/°C) and T_C is the PV cell temperature at the current time step (°C), and $T_{C,STC}$ is the PV cell temperature under standard test conditions (25 °C). In addition, the PV cell temperature at current time step (°C) has been calculated, considering the real temperature over 8 h on daily basis corresponding to the load-specific locality. The governing equation is given below as

$$T_C = T_{air} + \frac{(\text{NOCT} - 20) \times S}{80} \quad (3)$$

where NOCT is nominal operating cell temperature, S is the isolation in MW/cm^2. T_{air} is the temperature of the air [23].

The biomass gasifier unit (BMGU), used in the present work [18] operates on the principle of biomass gasification, utilizing the wastes like wood wastes, bio-degradable materials, and agricultural crops. The transfer function is given by

$$P_{\mathrm{BM}} = \frac{M \times \eta_0 \times \mathrm{LHV_b}}{3600 \times \mathrm{hr}} \tag{4}$$

Here, M is the mass flow rate of biomass waste mixture, $\mathrm{LHV_b}$ is the low heating value of the mixture, η_0 is the overall efficiency of the biomass production unit, and hr is the operating hours.

In order to minimize the power deviations on hourly basis, the optimal power operation planning of DERs is performed considering the following constraining factors;

$$0 \leq P_{\mathrm{SO}}(\mathrm{ss}, \mathrm{hr}) \leq IC_{\mathrm{SO}} \tag{5}$$

$$0 \leq P_{\mathrm{BM}}(\mathrm{ss}, \mathrm{hr}) \leq IC_{\mathrm{BM}} \tag{6}$$

$$0 \leq P_{\mathrm{bt}}(\mathrm{ss}, \mathrm{hr}) \leq IC_{\mathrm{bt}} \tag{7}$$

$$0 \geq P_{\mathrm{SO}}, P_{\mathrm{BM}} P_{\mathrm{bt}}, IC_{\mathrm{SO}}, IC_{\mathrm{BM}} IC_{\mathrm{bt}} \tag{8}$$

The Eqs. (5)–(7) give us the upper and lower limits of power output from distributed generators such as solar photovoltaic system, biomass gasified unit, and battery backup system to meet the electric load, respectively, while Eq. (8) ensures that all of the variables as power generated and installed capacities are positive for solar PV system, BMGU, fuel cell, and the battery energy storage system (BESS), respectively.

3 Solution Technique

The optimized algorithms used for solving optimal power generation problem meeting various side constraints are based on natural selection and law of collision-inspired meta-heuristic techniques, i.e., genetic algorithm and colliding bodies optimization. Further, tuning and modifications have been made in order to achieve better results in the above-mentioned problem. These are explained in detail as below.

A. Tuned Genetic Algorithm (TGA)

Genetic algorithm is a nature-inspired technique, which is based on genetic reproduction theory. The GA operation generally follows the steps given below:

I. On the basis of constraining ranges, populace of solutions is generated randomly, which generally vary in terms of their fitness value, as shown in equation below

$$p = \frac{fi}{\sum_{i=1}^{Nv} fi} \tag{9}$$

II. A group of better solutions are probabilistically selected, depending on the fitness value of the objective function. This forms a mating pool consisting of new solutions.

III. Better children solutions are obtained through a probabilistic check and implementation of crossover operation [7].

$$C = 0.5(\text{Expt} + 1)sf^{\text{expt}} \tag{10}$$

$$E = 0.5(\text{Expt} + 1)/sf^{(\text{expt} + 2)} \tag{11}$$

IV. To bring a local change over the current solutions, iteration is performed over the better children solutions to produce mutated children solution, as given below

$$\text{Ch}_{\text{mutated}} = \text{Ch}_{\text{original}} + pf \times \Delta_{\text{max}} \tag{12}$$

A comparison between the fitness values between the best one and the better one among two consecutive iterations can be made, resulting in a modified method is named as tuned genetic algorithm [7]. This procedure, involving tuning in choosing better set of population, continues until the difference between the fittest values between every generation reaches within a predefined acceptable value. The above-mentioned technique has been developed in consideration of finding better optimized results for the present problem.

B. Colliding Bodies Optimization (CBO)

The colliding bodies optimization (CBO) is a novel meta-heuristic method, whose concept relates to nature-inspired law of collision between two bodies. The algorithm has been proposed by Kaveh and Mahdavi [24], where each CB has a varying mass and a velocity before and after every collision.

The operation of CBO follows the steps as given below

Step 1: At first, a population set is generated in the search space of colliding bodies.

Step 2: Secondly, mass of each CB is computed using the equation:

$$m_K = \frac{1/F(K)}{\sum_n^{i=1} \frac{1}{F_i}} \tag{13}$$

where F denotes the objective function for a population size of n.

Step 3: The population comprising the best value among all the masses are being selected and ranked as first. Thereafter, the pool of population is divided into two equal groups, depending on the best to worst values of CBs... The CBs of the first group (i.e., the best ones) are considered as stationary while, the CBs of the second group (the worst ones) move toward the first group.

The velocities of stationary CBs, before collision are given by:

$$v_i = 0, \quad i = 1 \ldots \frac{n}{2} \tag{14}$$

and for the moving group CBs, they are given by:

$$v_i = x_i - x_{i-n/2}, \quad i = \frac{n}{2+1} \ldots n \tag{15}$$

where v_i and x_i are the velocity and the position of the ith CB, respectively.

Step 4: Further, new velocities are computed, after the pairwise collision between the members of the first group and the ones of the second group. Thus, the velocities after collision for the first group are given by:

$$v_i' = \frac{\left(m_{i+\frac{n}{2}} + \varepsilon\left(m_{i+\frac{n}{2}}\right)\right) v_{i+\frac{n}{2}}}{m_i + m_{i+\frac{n}{2}}} \tag{16}$$

and for the second group are given by:

$$v_i' = \frac{\left(m_i - \varepsilon\left(m_{i-\frac{n}{2}}\right)\right) v_{i+\frac{n}{2}}}{m_i + m_{i-\frac{n}{2}}} \tag{17}$$

Here, v_i' is the velocity after collision and the coefficient of restitution (COR) is ε, in order to have a good balance between the exploitation and exploration between the phases of the CBO, the coefficient of restitution (COR) is defined as

$$\varepsilon = \frac{1 - \text{iter}}{\text{iter}_{\max}} \tag{18}$$

where iter is the present iteration and $\text{iter}_{\max}$ is the maximum number of iterations.

Step 5: New positions have been evaluated for every CBs after collision have been evaluated. The expression governing the position upgradation for moving CBs is:

$$x_i^{\text{new}} = x_{i-\frac{n}{2}+} \text{rand} \times v_i', \quad i = \frac{n}{2} + 1, \ldots, n \tag{19}$$

while the equation computing for position upgradation of stationary CBs are as follows:

$$x_i^{\text{new}} = x_i + \text{rand} \times v_i', \quad i = 1, \ldots \frac{n}{2} \tag{20}$$

where x_i^{new} is the new position of the ith CB after collision. The steps from 2 to 5 continue to repeat until a termination criterion has been satisfied.

4 Input Data

A typical load variation of a specific residential locality of India has been considered for the present study. The summer and winter solar irradiations over a day, for the given specific Indian locality have been considered [25] for the present case study. Descriptions for the distributed power generation system components are presented in Table 1.

Table 1 System components and its specifications

System components	Description
Solar photovoltaic	Solar photovoltaics capacity, Y_{PV} = 250 kW Efficiency, η = 14% Temperature effects on power, α_P = 0.5%/°C Derating factor f_{PV} = 80%, tracking system: dual axis tracking system; electrical bus DC, and life time = 25 years % solar radiation at standard test condition; $G_{T,\text{ STC}}$ = 1 kW/m; at 25 °C isolation; S = 80 MW/cm^2 Nominal operating cell temperature, NOCT = 48 °C PV cell temperature under standard test condition; $T_{C,\text{ STC}}$ = 25 °C
Biomass gasifier	Efficiency of biomass generator: N = 17 Biomass gasifier capacity: 200 kW Mass flow rate: M = 885 kg/h Low heating value of mixture: LHV = 152
Lithium-ion battery	Rated capacity of battery (Li-ion) energy storage system = 75 Ah Rated output voltage = up to 54 V (CC/CV) Nominal voltage = 48 V Current rating = 75 A/37.5 A Overall efficiency >97% charge/discharge cycle

5   Result

A comparative study has been performed with the purpose of generating power more optimally with respect to the load demand, by the application of two ICBO and TGA. The optimal power distribution for the given residential load during summer and winter demand condition is computed for 24 h in terms of power deviation.

The power deviations are calculated as positive where the demand is more than the generation, while they are negative when the generation is more than demand. The negative power differences obtained from the optimal operation are used to charge the battery energy storage system, while the positive power deviations are met by the battery through its electrical discharge. A typical result for optimal power generation during summer as evaluated by ICBO is shown in Fig. 1.

Similarly, Fig. 2 portrays the optimal power generations from the solar photovoltaic and biomass gasifier unit for summer load using TGA.

Fig. 1 Optimal power generation by ICBO for summer load
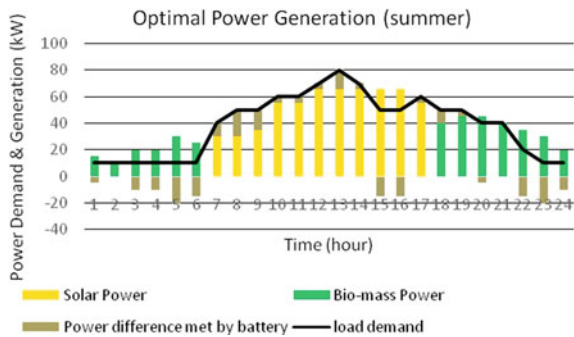
Fig. 2 Optimal power generation by TGA for summer load
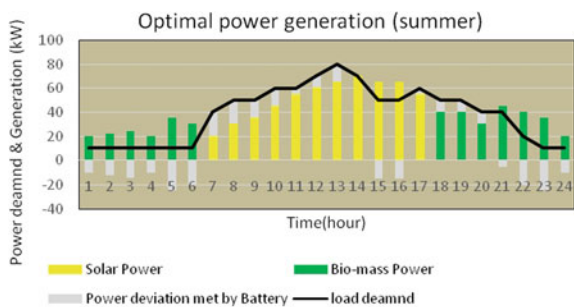
Fig. 3 Fitness function versus number of iterations using ICBO for winter
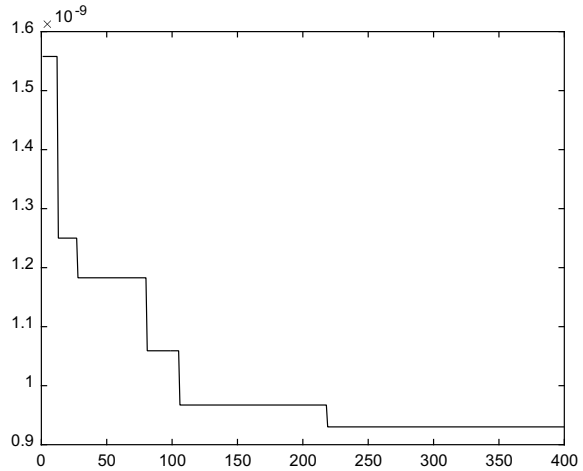
The optimal power generation values obtained by TGA have been found to be better in case of summer demand than that of winter. While, on the other hand, implementation of ICBO resulted in almost same pattern of optimal generation for both summer and winter loading. It can be interpreted in such a manner, that TGA works better, for a large dimension of problem; as for summer load, the hourly irradiation are two hours more than that of winter along with the load demands. It has also been noted that, though tuned genetic algorithm (TGA) reaches optima much early than improved colliding bodies optimization (ICBO), but the absolute minimum value obtained by TGA are many times more than that obtained by ICBO. The representation of convergence plot toward optimal results for ICBO during winter load has been presented in Fig. 3.

It has also been inferred from the results, that the ICBO has a better consistency in handling the variations in the number and range of the problem dimension.

The economic evaluation performed for two different sets of loading, catered by two different types of renewable energy resources, with the application of nature-inspired modified soft computing controlling techniques are shown below as follows;

A. CO_2 emission during optimal power generation for summer load demand as calculated by ICBO
B. CO_2 emission for generating optimal power to meet winter load demand as calculated by ICBO
C. CO_2 emission for generating optimal power to deliver summer load demand using TGA
D. CO_2 emission during optimal power generation for winter load demand as evaluated.

The estimated carbon tax computed for the above-calculated CO_2 has been presented in Table 2, and compared with the same (carbon tax) computed for conventional (coal) power generating system. The estimated cost for carbon

Table 2 Comparison of carbon footprint tax for conventional and non-conventional power generation system

	Carbon tax (non-conventional) (biomass integrated gasification combine cycle)				Carbon tax (conventional) (coal-based thermal power plant)			
	A	B	C	D	A	B	C	D
Total carbon emitted (g/kWh)	46	46	46	46	1022	1022	1022	1022
Total CO_2 emitted (ton)	0.226044	0.175260	0.240396	0.216660	5.022108	3.893820	5.340972	4.813620
Cost ($/ton)	85	85	85	85	85	85	85	85
Total carbon tax ($)	19.21374	14.8971	20.43366	18.4161	426.87918	330.9747	453.98262	409.1577

footprint as discussed in Nordhaus [26] has been considered for the calculation of carbon tax, in the present test cases.

The above-mentioned result in Table 2 predicted an estimated cost which a consumer has to pay as carbon tax, for consumption of power depending on the type of generation. It has further been observed that, the costs for winter load demand have been found to be lower than that for summer loading, for both techniques used for optimal power generated. Further, by the application of ICBO, more optimal power generation was achieved, as the costs for both summer and winter load were lower as compared to that obtained by the application of TGA. So, it can be inferred that economically, ICBO technique has been found to be a better numerical technique in evaluating, the present optimal generation problem. Further, an economic comparison, in terms of carbon tax have also been made, between biomass-based (integrated gasification combined cycle) and coal-based (thermal power plant) power generation. By the application of modified heuristic techniques, the cost incurred for conventional power system is much more than that obtained by non-conventional power system. The application of ICBO resulted in 95% carbon tax savings for summer load and 96% savings for winter load. TGA implemented results were 96% economical in terms of carbon tax for both summer and winter loading.

6   Conclusion

Improved forms of two nature-inspired meta-heuristic techniques have been implemented and developed for solving the optimal operation of non-conventional micropower generation units. For same loading scenario, a more optimized result has been obtained by the application of ICBO than TGA. Further, the role of algorithmic parameters has been studied in detail. In both the cases, though TGA delivered better results for large dimension problems ICBO resulted in good consistency. In terms of environmental impact, the application of ICBO and TGA resulted in 96 and 94% savings in terms of carbon tax, with respect to that calculated for conventional power delivery system.

References

1. Wang Q, Zhang C, Ding Y, Xydis G, Wang J (2015) Review of real-time electricity markets for integrating distributed energy resources and demand response. Appl Energy 138:695–706
2. Bruce, Justo JJ, Mwasilu F (2013) AC-microgrids versus DC-microgrids with distributed energy resources: a review. Renew Sustain Energy Rev 24:387–405
3. Chandel SS, Shrivastva R, Sharma V, Ramasamy P et al (2016) Overview of the initiatives in renewable energy sector under the national action plan on climate change in India. Renew Sustain Energy Rev 54:866–873
4. Chaouachi A et al (2013) Multiobjective intelligent energy management for a microgrid. IEEE Trans Ind Electron 60(4):1688–1699

5. Panora R (2014) Real-world performance of a CERTS microgrid in Manhattan. IEEE Trans Sustain Energy 5(4):1356–1360
6. Hatziargyriou N (ed) (2014) Microgrids: architectures and control. Wiley/IEEE Press
7. Som T, Chakraborty N (2014) Evaluation of different hybrid distributed generators in a microgrid—a metaheuristic approach. Distr Generat Altern Energy J 29(4):49–77
8. Memon AA, Kauhaniemi K (2015) A critical review of AC microgrid protection issues and available solutions. Electr Pow Syst Res 129:23–31
9. Buigues G, Dyśko A, Valverde V, Zamora I, Fernández E (2013) Microgrid protection: technical challenges and existing techniques. In: International conference on renewable energies and power quality (ICREPQ'13)
10. Huang WT, Yao KC, Wu CC, Chang YR, Lee YD, Ho YH (2016) A three-stage optimal approach for power system economic dispatch considering microgrids. Energies 9(11):976
11. Motevasel M, Seifi AR (2014) Expert energy management of a micro-grid considering wind energy uncertainty. Energy Convers Manag 83:58–72
12. Zoka Y, Sugimoto A, Yorino N, Kawahara K, Kubokawa J (2007) An economic evaluation for an autonomous independent network of distributed energy resources. Int J Elec Power Syst Res 77(7):831–838
13. Logenthiran T, Srinivasan D, Khambadkone AM, Sundar Raj T (2010) Optimal sizing of an islanded microgrid using evolutionary strategy. In: Proceedings of the 2010 IEEE 11th international conference on probabilistic methods applied to power systems, IEEE, p 12–7
14. Erdinc O, Uzunoglu M (2012) Optimum design of hybrid renewable energy systems: overview of different approaches. Renew Sustain Energy Rev 16:1412–1425
15. Zhang X, Sharma R (2012) Optimal energy management of a rural microgrid system using multi-objective optimization. In: 2012 IEEE PES innovative smart grid technologies, IEEE, p 1–8
16. Reddy YJ, Kumar YP, Kumar VS, Raju KP (2012) Distributed ANNs in a layered architecture for energy management and maintenance scheduling of renewable energy HPS microgrids. In: Proceedings of 2012 international conference on advances in power conversion and energy technologies, IEEE, p 1–6
17. Sharma V, Chandel SS (2013) Performance analysis of a 190 kWp grid interactive solar photovoltaic power plant in India. Energy 55:476–485
18. Som T, Chakraborty N (2014) Studies on economic feasibility of an autonomous power delivery system utilizing alternative hybrid distributed energy resources. IEEE Trans Power Syst 27(1):172–181
19. Kumar A, Verma A (2016) Optimization and implementation of hybrid energy sources in remote and grid active microgrids–a case study for Indian scenario. In: 2016 IEEE 7th power India international conference (PIICON), IEEE
20. Sen R, Bhattacharyya SC (2014) Off-grid electricity generation with renewable energy technologies in India: an application of HOMER. Renew Energy 62:388–398
21. Phurailatpam C, Rajpurohit BS, Wang L (2018) Planning and optimization of autonomous DC microgrids for rural and urban applications in India. Renew Sustain Energy Rev 82:194–204
22. Ghenai C, Janajreh I (2016) Design of solar-biomass hybrid microgrid system in Sharjah. Energy Procedia 103:357–362
23. Ross Jr RG, Smokler MI (1986) Flat-plate solar array project: final report: volume 6, engineering sciences and reliability. No. DOE/JPL-1012-125-Vol. 6. Jet Propulsion Lab., Pasadena, CA (USA)
24. Kaveh A, Mahdavi VR (2014) Colliding bodies optimization: a novel meta-heuristic method. Comput Struct 139:18–27
25. Som T, Pathak R (April 2015) Maximum solar power generation through optimization of tilt solar angles of solar panels by heuristic technique. Int J Innovative Res Electr Electron Instrum Control Eng 3(4)
26. Nordhaus W. Critical assumptions in the stern review on climate change. In: Science magazine's state of the planet 2008–2009

Reliability Evaluation of Power System Expansion Incorporating Wind Energy: A State-of-the-Art Review

Tulasi Ramakrishna Rao Ballireddy and Pawan Kumar Modi

Abstract With ever-increasing demand for electrical energy day by day, fast depletion in fossil fuels and concern for environment, it is the need of the hour to go for alternative means of generating electrical energy, i.e. renewable energy sources so as to bridge the gap between generation and demand and to reduce the impact of carbon emission by the conventional generation plants on the environment. Solar and wind are becoming a significant portion of renewable generation portfolios. Besides incorporating the non-conventional sources, its impact on the performance, stability and reliability are also the key aspects. This paper presents a state-of-the-art review pertaining to the reliability assessment incorporating wind power generation, modelling of wind generation firms, optimal sizing and location of wind firms. Energy storage system is included to smoothen the unpredictability and uncertain natures of wind generation.

1 Introduction

To deal with the deficit of electrical energy generation, incorporation of non-conventional energy sources has gained momentum in the recent past. This also counters the environmental issues, global warming and depletion of fossil fuels [1]. Generally, the renewable energy sources are small-scale generating units ranging from few KWs to 100 MWs: installed at the load centres to minimize the cost of

T. R. R. Ballireddy (✉) · P. K. Modi
Department of EE, VSSUT, Burla, Odisha, India
e-mail: btrkrao2002@gmail.com

P. K. Modi
e-mail: pkmodi_ee@vssut.ac.in

generation, carbon emission and burning up of fossil fuels, the intermittence, and uncertain nature [2–7]. Likewise, keeping up the efficiency and reliability of the grid, in presence of non-conventional energy sources has turned into a testing errand [5]. A few examinations have demonstrated that high penetration level of renewable energy sources could altogether influence power system quality and security because of its intermittency [6–10]. By considering renewable energy sources for integration process, wind power generation plays a major role [11, 12]. A wind farm involves a huge number of wind turbine generators (WTGs). The working qualities of wind turbines contrast from those of traditional power plants as far as their capability and dispatch ability [13]. Wind turbines on a similar farm create yield control that are identified with the occurrence wind speed and are corresponded between turbines [14]. Hence, forced outages such as unexpected turbine failure and relationship between the wind turbine power outputs are also to be considered besides the stochastic nature of wind speed in the planning phase [15–17].

2 Wind Farms Perspective

Study of Reliability assessment of power system including the wind farms is given a special focus in this section.

Zhang et al. [18] have discussed about the Bayesian attack graph models applicable to address the cyberattack scenarios on the wind farm SCADA/EMS system. The reliability for the above-mentioned case is evaluated based on the IEEE RTS79 system. Xiang et al. [19] have developed a holistic way of evaluating the reliability of the system so as to incorporate the proposed model that is based on Monte Carlo simulation. Adefarati and Bansal [20] have presented a complete reliability estimation of the distribution system which satisfies the end-user demand necessities through the incorporation of wind turbine generator (WTG), electric storage system (ESS) and photovoltaic (PV). Liniger et al. [21] have presented a qualitative design tool for evaluation of the risk for fluid power pitch systems. The design tool was developed with special attention to industry standard failure analysis methods and was aimed at the early phase of system design. The methodology was conducted solely on a circuit diagram and functional behaviour. The failure mode and effects criticality analysis were subsequently employed to determine the failure mode risk via the risk priority number. The failure mode and effect criticality analysis were based on past research concerning failure analysis of wind turbine drive trains. Rocha et al. [22] assessed the reliability considering the effects of deviation in voltage and frequency and consequences of failure of components. The model was proposed depending on the mix of probabilistic method of evaluating reliability with the dynamic simulation of the islanding process.

Nguyen et al. assessed the reliability of an integrated system considering the system security, and found to be decreased. Also presented how the reliability is influenced by the random and low-inertia characteristics of wind power and energy

storage [23]. Billinton and Chowdhury proposed possible WECS that can be included into the existing power system so as to meet the unexpected load demand or to act as backup and the corresponding reliability is evaluated [24]. Singh and Lago-Gonzalez presented a separate model each for conventional and renewable energy sources (hourly based) to determine loss of load and hourly capacity deficiency [25]. Considering the random nature of wind, Sayas and Allan [26] developed a probabilistic wind model for distribution system that can be incorporated with a single or multiple wind turbines for reliability evaluation. Leite et al. proposed a wind model based on the operating and failure states whose rates are represented by λ and μ, respectively [27]. Manco et al. proposed a model using Markovian approach to find the energy that can be produced and to know the availability of power from a wind turbine [28]. Sulaeman et al. developed a wind model considering wind variability, correlation between turbine outputs and forced outages of turbines using a recursive technique. The proposed analytical method is verified by applying it on IEEE RTS [29] consisting of 32 generating units with a capacity of 3405 MW in total and 2850 MW peak. Also the comparison of various reliability indices such as LOLP, EENS, expected demand not supplied (EDNS) and LOLF have been carried out with and without turbine-forced outages and the outcomes are validated by means of Monte Carlo simulation [30].

The power output of a wind turbine can be determined from Eq. (1) [31]

$$P = 1/2\, C_p \rho A v^3 \tag{1}$$

where,

P—Power output in watts; ρ—Air density in Kg/m^3; v—Wind speed in m/s
A—Area swept in m^2; C_p—Power coefficient.

The combination of power output curve and Eq. (1) can be expressed as

$$\left. \begin{array}{ll} P = 0, & \text{if } v < v_{\text{cut in}} \\ 1/2\, C_p \rho A v^3, & \text{if } v_{\text{cut in}} \leq v < v_{\text{r}} \\ P_{\text{r}}, & \text{if } v_{\text{r}} \leq v < v_{\text{cut out}} \\ 0, & \text{if } v_{\text{cut out}} \leq v \end{array} \right\} \tag{2}$$

Dobakhshari and Fotuhi-Firuzabad made use of frequency and duration method, an analytical technique to develop a wind generation farm as a conventional unit with derated output states. The reliability indices LOLE and LOLF are also evaluated [32]. Vallée et al. [33] proposed Monte Carlo simulation-based equivalent wind capacity calculations so that wind equivalent capacities can be determined from reliability perspective. Taking nine different aspects into considerations which influence offshore installation reliability, Negra et al. presented the calculation for wind farm reliability [34]. The inclusion of wake effect and its impact on the computation of reliability indices such as LOLE, EENS, load-carrying capacity benefit ratio (LCCBR), equivalent capacity rate (ECR) and wind generation

interrupted energy benefit (WGIEG) is studied by Kim et al. [35]. Billinton et al. computed reliability of the system including WECS using a sequential Monte Carlo sampling technique [36].

Wang and Billinton [37] evaluated the reliability of a distribution system including WTG using a time-sequential simulation technique. The advantages of including WTG in a distribution system by introducing the reliability indices the wind generation interrupted energy benefit (WGIEB), the wind generation interruption cost benefit (WGICB) and the equivalent number of conventional generators (ENCG). Reliability analysis of a large power system incorporating WECS is carried out by Wangdee and Billinton [38] and found that WECS location has impact on the reliability analysis. Maximum amount of wind power absorbed satisfying the system constraints is also investigated. Halamay et al. concluded that penetration of various non-conventional energy sources like wind, solar and wave into the existing power system yields significant impact rather than considering only a single renewable source [39]. Nguyen and Mitra studied the effect of wind power on load frequency control that provides a basis for estimating the penetration levels of wind-generated power depending on systems configuration, disturbance in maximum load and frequency limitations [40]. Hossain et al. presented how high levels of wind generation penetration and compensation have their affect on power system dynamic performance [41]. Vittal et al. proposed a method that is suitable for analysing a bulk power system in which the combination of power flow, economic dispatch, unit commitment and historical time-series data is made use of to know the wind variation. It also helps in estimating the voltage stability with high levels of wind penetration [42]. Billinton and Bai concluded that the conditions of the wind contribute mostly to the reliable operation of the generating system and the same is validated using a sequential Monte Carlo simulation technique on RBTS and IEEE-RTS [43]. For an independent electric power system network, the extent up to which the wind energy can be penetrated is estimated by integrated numerical algorithm proposed by Kaldellis et al. [44]. To account for the intermittent and the unpredictable nature of generating wind power, physical and economic constraints are included and a hybrid dynamic programming (HDP) technique was proposed by Chen to accomplish a compromise between system security and total production cost [45]. The reduction in system inertia and primary frequency responses because of high-level penetration of non-conventional energy sources is addressed by Ahmadi and Ghasemi using a security-constrained unit commitment (SCUC) satisfying frequency limits [46].

In order to reduce the impact of indecisive nature of wind power and to provide continuous supply, an energy storage is provided. In the process of developing energy storage, models in various feasible operating strategies are taken into account by Hu et al. [1]. The developed wind model including energy storage is shown in Fig. 1, where transmission line is used as a means to provide connection between the system and the wind farm.

Mitra et al. presented simulated annealing (SA) technique to optimally position the distributed generators (DG's) with feasible size in a microgrid, so that the set criterion of reliability is attained [47]. Sulaeman et al. [48] evaluated reliability
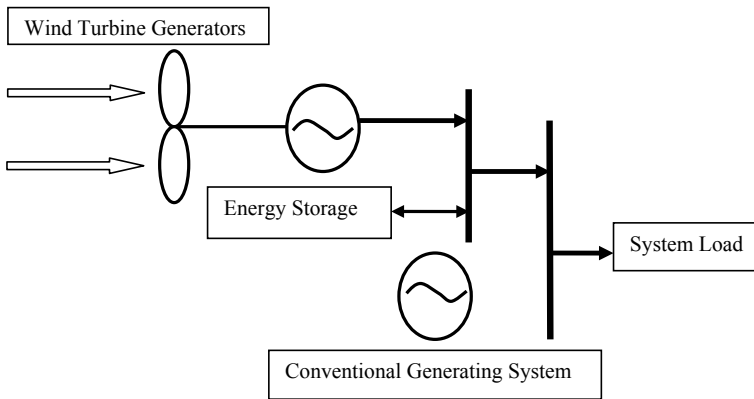
Fig. 1 Wind conventional generating system model with inclusion of energy storage

indices using sequential Monte Carlo simulation to determine size and location of energy storage system which are included with wind energy. Sulaeman et al. [15] assessed the reliability of the system by using an analytical method considering wind unpredictability, forced outages of turbines and also the correlation between turbine outputs. Nguyen and Mitra [49] evaluated the power system reliability by taking intermittent nature of wind in addition to its low-inertia characteristic into consideration. The evaluated indices are presented in Table 1

Base case: Modified IEEE-RTS system with 26 conventional generators and 43 identical wind farms. Each wind farm has 10 wind turbines, each with 8 MW rated power.

Scenario 1: Considering the effects of intermittence and low inertia of wind generation.

Scenario 2: The spinning reserve requirement is considered.

Scenario 3: Both the spinning reserve requirement and the limit of wind penetration due to frequency security are considered.

Scenario 4: Large-scale energy storage is considered.

Table 1 Evaluated reliability indices for different cases

Index	LOLE (h/year)	LOLF (f./year)	LOLP	EDNS (MW/year)	LOEE (MWh/year)
Base case	9.369	2.016	0.0012	0.1641	1433.75
Scenario 1	17.52	9.636	0.002	0.2190	1918.44
Scenario 2	48.18	26.28	0.0055	0.5840	5115.84
Scenario 3	73.584	37.668	0.0084	0.9125	7993.50
Scenario 4	64.531	34.660	0.0074	0.7956	6969.50

3   Power System Uncertainties and Reliability Assessment

See Figs. 2 and 3.

4   Conclusion

This paper presents a state-of-the-art review where one can get the information pertaining to the modelling of wind generation firms, optimal sizing and location of wind firms. To overcome the unpredictability and uncertain nature of wind energy, storage systems have been included that helps in improving the reliability of the system. The reliability assessment by evaluating the reliability indices such as LOLP, LOLE, LOLF and EDNS has been discussed. The impact of combining two or more renewable energy sources on the system performance to account for the
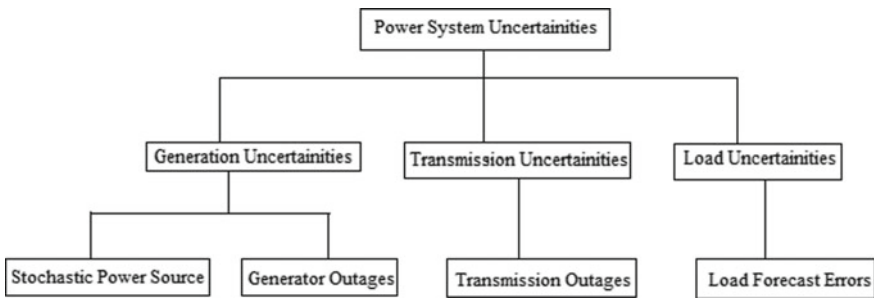
Fig. 2 Typical uncertainties in power system
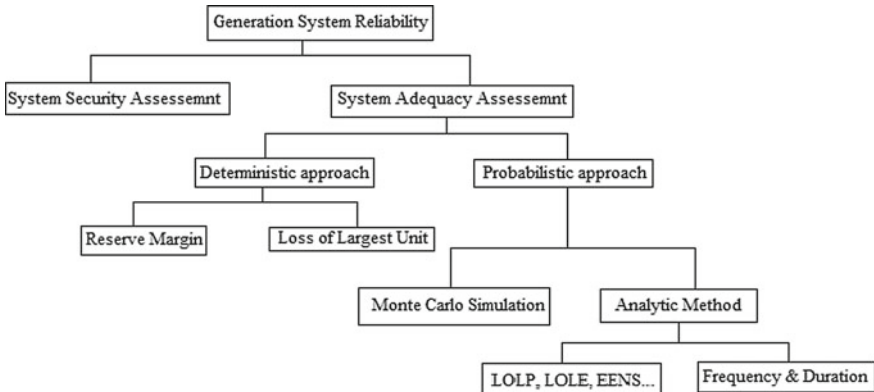
Fig. 3 Generation system reliability assessment indices

system security, stability, reliability and electric power quality may be carried out. The optimal sizing and placement of various non-conventional sources to further improve the reserve requirements can be studied. The reliability of possible combination can be assessed by evaluating the various reliability indices discussed in the literature and then the optimal location of the renewable energy sources can be found by using various optimization techniques. In addition, the systems' reliability can also be assessed including the transmission lines.

References

1. Hu P, Billinton R, Karki R (2009) Reliability evaluation of generating systems containing wind power and energy storage. IET Gener Transm Distrib 3(8):783–791
2. Karki R, Hu P, Billinton R (2006) A simplified wind power generation model for reliability evaluation. IEEE Trans Energy Conver 21(2):533–540
3. Billinton R, Wangdee W (2007) Reliability-based transmission reinforcement planning associated with large-scale wind farms. IEEE Trans Power Syst 22(1):34–41
4. Karki R, Hu P, Billinton R (2010) Reliability evaluation considering wind and hydro power coordination. IEEE Trans Power Syst 25(2):685–693
5. Qiu Y, Feng Y, Tavner P, Richardson P, Erdos G, Chen B (2011) Wind turbine SCADA alarm analysis for improving reliability. Wind Energy 15(8):951–966
6. Xie K, Billinton R (2009) Considering wind speed correlation of WECS in reliability evaluation using the time-shifting technique. Electr Pow Syst Res 79(4):687–693
7. Atwa Y, El-Saadany E (2009) Reliability evaluation for distribution system with renewable distributed generation during islanded mode of operation. IEEE Trans Power Syst 24(2):572–581
8. Bie Z, Zhang P, Li G, Hua B, Meehan M, Wang X (2012) Reliability evaluation of active distribution systems including microgrids. IEEE Trans Power Syst 27(4):2342–2350
9. Arabian-Hoseynabadi H, Oraee H, Tavner P (2010) Wind turbine productivity considering electrical subassembly reliability. Renew Energy 35(1):190–197
10. Arifujjaman M, Iqbal M, Quaicoe J (2009) Reliability analysis of grid connected small wind turbine power electronics. Appl Energy 86(9):1617–1623
11. Jiang W, Hu Z, Yan Z (2011) Reliability assessment of composite generation and transmission system with wind farms. Adv Mater Res 347–353:879–883
12. Zhang Y, Chowdhury A, Koval D (2011) Probabilistic wind energy modeling in electric generation system reliability assessment. IEEE Trans Ind Appl 47(3):1507–1514
13. Mehrtash A, Wang P, Goel L (2013) Reliability evaluation of restructured power systems using a novel optimal power-flow-based approach. IET Gener Transm Distrib 7(2):192–199
14. Choi J, Lim J, Lee K (2013) DSM considered probabilistic reliability evaluation and an information system for power systems including wind turbine generators. IEEE Trans Smart Grid 4(1):425–432
15. Sulaeman S, Benidris M, Mitra J, Singh C (2017) A wind farm reliability model considering both wind variability and turbine forced outages. IEEE Trans Sustain Energy 8(2):629–637
16. Sulaeman S, Tian Y, Benidris M, Mitra J (2017) Quantification of storage necessary to firm up wind generation. IEEE Trans Ind Appl 53(4):3228–3236
17. Nguyen N, Mitra J (2017) Reliability of power system with high wind penetration under frequency stability constraint. IEEE Trans Pow Syst, 1
18. Zhang Y, Xiang Y, Wang L (2017) Power system reliability assessment incorporating cyber attacks against wind farm energy management systems. IEEE Trans Smart Grid 8(5):2343–2357

19. Xiang Y, Ding Z, Zhang Y, Wang L (2016) Power system reliability evaluation considering load redistribution attacks. IEEE Trans Smart Grid, 1
20. Adefarati T, Bansal R (2017) Reliability assessment of distribution system with the integration of renewable distributed generation. Appl Energy 185:158–171
21. Liniger J, Soltani M, Pedersen H, Carroll J, Sepehri N (2017) Reliability based design of fluid power pitch systems for wind turbines. Wind Energy 20(6):1097–1110
22. Rocha L, Borges C, Taranto G (2016) Reliability evaluation of active distribution networks including islanding dynamics. IEEE Trans Pow Syst, 1
23. Nguyen N, Mitra J. Reliability of power system with high wind penetration under frequency stability constraint. IEEE Trans Pow Syst. https://doi.org/10.1109/tpwrs.2017.2707475
24. Billinton R, Chowdhury AA (January 1992) Incorporation of wind energy conversion systems in conventional generating capacity adequacy assessment. In: IEE Proceedings-C, vol 139, no I
25. Singh C, Lago-Gonzalez A (May 1985) Reliability modeling of generation systems including unconventional energy sources. IEEE Trans Pow App Syst PAS-104(5)
26. Sayas FC, Allan RN (September 1996) Generation availability assessment of wind farms. IEE Proc Gener Transm Distrib 143(5)
27. Leite AP, Borges CLT, Falcao DM (November 2006) Probabilistic wind farms generation model for reliability studies applied to Brazilian sites. IEEE Trans Pow Syst 21(4)
28. Manco, Member, Testa A (2007) A markovian approach to model power availability of a wind turbine. In: Power tech 2007
29. Reliability test system task force (1999) The IEEE reliability test system-1996. IEEE Trans Pow Syst 14(3):1010–1020
30. Sulaeman S, Benidris M, Mitra J, Singh C (2017) A wind farm reliability model considering both wind variability and turbine forced outages. IEEE Trans Sustain Energy. https://doi.org/10.1109/tste.2016.2614245
31. Manwell JF, McGowan JG, Rogers AL (2010) Wind energy explained: theory, design and application. Wiley, New Jersey
32. Dobakhshari AS, Fotuhi-Firuzabad M (September 2009) A reliability model of large wind farms for power system adequacy studies. IEEE Trans Energy Convers 24(3)
33. Vallee F, Lobry J, Deblecker O (August 2008) System reliability assessment method for wind power integration. IEEE Trans Pow Syst 23(3)
34. Negra NB, Holmstrom O, Bak-Jensen B, Sorensen P (March 2007) Aspects of relevance in offshore wind farm reliability assessment. IEEE Trans Energy Convers 22(1)
35. Kim H, Singh C, Sprintson A (April 2012) Simulation and estimation of reliability in a wind farm considering the wake effect. IEEE Trans Sustain Energy 3(2)
36. Billinton R, Chen H, Ghajar R (December 1996) A sequential simulation technique for adequacy evaluation of generating systems including wind energy. IEEE Trans Energy Convers 11(4)
37. Wang P, Billinton R (June 2001) Reliability benefit analysis of adding WTG to a distribution system. IEEE Trans Energy Convers 16(2)
38. Wangdee W, Billinton R (2007) Reliability assessment of bulk electric systems containing large wind farms. Electr Pow Energy Syst 29:759–766
39. Halamay DA, Brekken TKA, Simmons A, McArthur S (July 2011) Reserve requirement impacts of large-scale integration of wind, solar, and ocean wave power generation. IEEE Trans Sustain Energy 2(3):321
40. Nguyen N, Mitra J (January 2016) An analysis of the effects and dependency of wind power penetration on system frequency regulation. IEEE Trans Sustain Energy 7(1)
41. Hossain MJ, Pota HR, Mahmud MA, Ramos RA (March 2012) Investigation of the impacts of large-scale wind power penetration on the angle and voltage stability of power systems. IEEE Syst J 6(1)
42. Vittal E, O'Malley M, Keane A (February 2010) A steady-state voltage stability analysis of power systems with high penetrations of wind. IEEE Trans Pow Syst 25(1)

43. Billinton R, Bai G (September 2004) Generating capacity adequacy associated with wind energy. IEEE Trans Energy Convers 19(3)
44. Kaldellis JK, Kavadias KA, Filios AE (2009) A new computational algorithm for the calculation of maximum wind energy penetration in autonomous electrical generation systems. Appl Energy 86:1011–1023
45. Chen C-L (March 2008) Optimal wind–thermal generating unit commitment. IEEE Trans Energy Convers 23(1)
46. Ahmadi H, Ghasemi H (July 2014) Security-constrained unit commitment with linearized system frequency limit constraints. IEEE Trans Pow Syst 29(4)
47. Mitra J, Vallem MR, Singh C (2015) Optimal deployment of distributed generation using a reliability criterion. 978-1-4799-8374-0/15/$31.00 © IEEE
48. Sulaeman S, Tian Y, Benidris M, Mitra J (2017) Quantification of storage necessary to firm up wind generation. IEEE Trans Ind Appl. https://doi.org/10.1109/tia.2017.2685362
49. Nguyen N, Mitra J (2018) Reliability of power system with high wind penetration under frequency stability constraint. IEEE Trans Power Syst 33(1):985–994

A Comparative Analysis of Different Maximum Power Point Tracking Algorithms of Solar Photovoltaic System

Md. Sabir Hassan, Shafqat Nabi Mughal,
R. K. Jarial and Yog Raj Sood

Abstract The demand for power is increasing day by day, and working with fossil fuels is associated with global warming problem, so renewable resource is better option to fulfil ever-increasing power demand without affecting climate. Among renewable resources, solar energy is widely adopted due to its availability in abundance. The power output for a solar photovoltaic (SPV) cell depends on the operating temperature, solar irradiation and load impedance. So maximum power point of SPV is not constant and keeps on changing under different conditions. Therefore, maximum power point tracking is used to uphold the point to extract maximum power from PV system under different working conditions. In this paper, we have described many maximum power point tracking algorithms commonly used for extracting maximum power out of a solar panel. We have also done a comparative analysis among them for various parameters using a common Simulink model in MATLAB. It has been found that among different methods, artificial intelligence method is most efficient compared to all existing methods and perform well under different conditions of solar irradiations and temperatures.

Keywords SPV cell · MPPT · Open-circuit voltage · Short-circuit voltage · Perturb and observe · Hill climbing · Incremental conductance · Artificial intelligence · Fuzzy logic control · Neural network · Converter

Md. S. Hassan (✉) · R. K. Jarial · Y. R. Sood
Department of Electrical, National Institute of Technology Hamirpur,
Hamirpur, Himachal Pradesh, India
e-mail: mdsabirhassan@gmail.com

R. K. Jarial
e-mail: jarial0@gmail.com

Y. R. Sood
e-mail: yrsood.nith@gmail.com

S. N. Mughal
Department of Electrical and Renewable Energy Engineering,
Baba Ghulam Shah Badshah University, Rajouri, Jammu and Kashmir, India
e-mail: snmughal.bgsbu@gmail.com

1 Introduction

The earth natural resources are depleting day by day, to meet the ever-increasing power demand. Another major concern with working fossil fuels is the pollution associated with their combustion. The power sector is looking at alternate energy resources which can overcome problem of global warming condition. Out of various prevalent renewable energy sources SPV abundantly available robust, noiseless and reliable energy resource in which light energy directly converted into electricity by means of SPV module. SPV module has low efficiency approximately 15–30%, due to which, it is challenging for user as an alternative option [1]. The relation between output power and voltage of a SPV cell is a nonlinear curve [2]. From this nonlinear characteristic curve, it is to be noted that there is a unique point, under given irradiation and temperature, at which the SPV cell produces maximum power, and that point is called maximum power point (MPP). The output power of PV cell varies due to solar irradiation and operating temperature. The MPP of SPV array will change with external environment condition. Maximum power available in SPV array is very difficult to harness, so it is operated at its highest energy conversion output, due to which, the SPV module has to be operated at the maximum power output point. Since the MPP varies with irradiation show in Fig. 1 and temperature show in Fig. 2. Maximum power point tracking (MPPT) is the technique/algorithm that has been widely employed to extract possible maximum available power from the SPV systems under any working condition. Different types of algorithms have been proposed to realize MPP. These MPPT algorithms vary in complexity, steady-state error, oscillation, accuracy, convergence/tracking speed, cost, implementation complexity, dynamic response, popularity and other respects. Among different types of algorithm open-circuit voltage method, perturb and observe method, incremental conductance method, etc., are most commonly used.

Fig. 1 PV curve at different irradiation levels
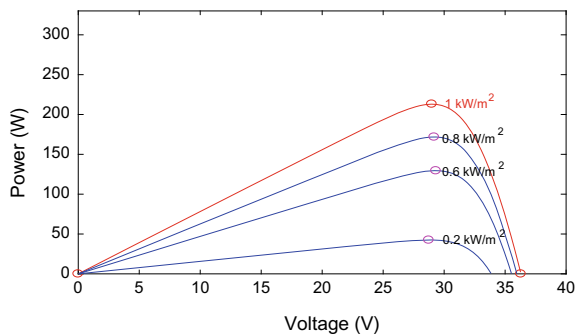
Fig. 2 PV curve at different temperature levels
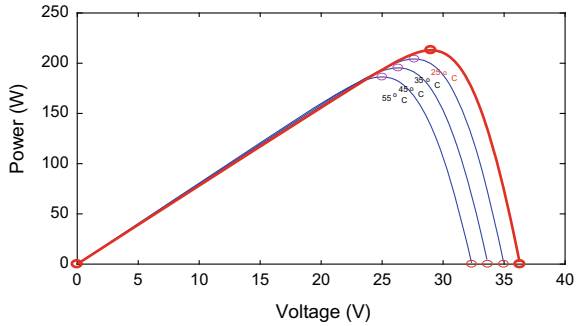
2 Ideal Model of PV Cell

The PV cell is a solid-state p-n semiconductor device in which light energy is converted directly into electricity on the principle of photo-effect. The equivalent circuit of a SPV cell can be represented by a current control source in which antiparallel with a loss diode and the non-ideal are represented by the insertion of the parallel resistance (R_p) and series resistance (R_s) is shown in Fig. 3.

The SPV module equation is based on the output current of one PV cell equivalent model, and its mathematical equation is represented by [3, 4]

$$I = I_{ph} - I_o \left(e^{\frac{q(V + R_s . I)}{A.K.T}} - 1 \right) - \frac{V + R_s . I}{R_p} \tag{1}$$

where

I_{ph}: light generated current (A);
I_o: dark saturation current;
R_s: series resistance (Ω);
R_p: shunt resistance (Ω);
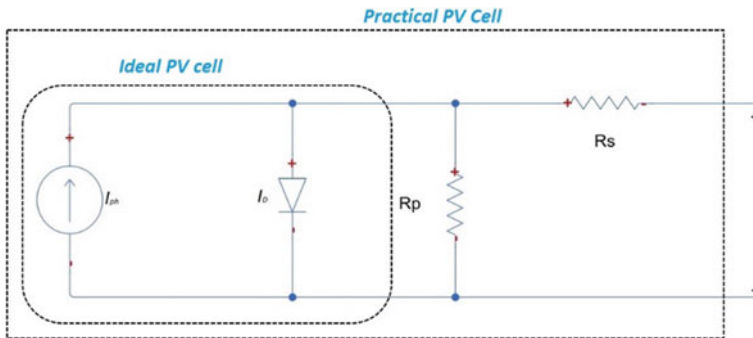
Fig. 3 One-diode model equivalent circuit of a SPV cell

A: diode ideality factor;
q: electron charge $(1.6 * 10^{-19}\,\text{C})$;
K: Boltzmann's constant $(1.38 * 10^{-23}\,\text{J/K})$;
T: ambient temperature, (K);
V: cell output voltage (v);
I: cell output current (A);

3 Maximum Power Point Tracking Method

An MPPT is the essential component of the SPV system to sustained point at which maximum power is producing. The proposed MPPT method can be divided into main two categories:

(1) Conventional methods and
(2) Artificial intelligence methods.

(1) Conventional Method

It is a traditional method widely adopted due to ease in hardware implementation and simple in use. It can be further divided as:

(a) Indirect methods,
(b) Direct methods.

(a) Indirect methods

Extraction of maximum power from SPV array in an indirect method is from its output characteristics. Short-circuit current (SCC) [5] and open-circuit voltage (OCV) [6] methods are a simple and efficient approach to achieve the MPP. The drawback of indirect method is that for every interval of time, it is isolated from the system which causes power losses, so it is used for low-power applications.

(b) Direct Methods

Direct methods are also called true searching methods, in which MPP is obtained by a regular change in the operating point of the SPV array. Hill climbing (HC) method is widely adopted in PV systems which is a direct method [7]. Perturb and observe (P&O) [8] and incremental conductance (INC) [9] methods are based on the "hill-climbing" principle. In P&O method, operation voltage of the PV array increases, decreases or remains constant which cause duty cycle perturbs with the help of the DC–DC interface converter to obtain the MPP. Alike the P&O method, INC method also perturbs the duty cycle of the DC–DC interface converter to obtain the MPP. These methods are simple and easily implemented; however, intrinsic steady-state oscillation occurs in P&O methods which causes low-power applications. This drawback can be overcome by the incremental conductance

method, which is based on the slope at MPP of power versus voltage curve which is zero.

(2) Artificial Intelligence Methods

For improvement in the dynamic response, eliminate the steady state oscillation, proper uphold of MPP tracking artificial intelligence method work in an efficient manner which provide a fast result without demanding any equation for the MPPT problem.

4 Characterization of MPPT Algorithms

(A) Open-Circuit Voltage

This is an observance method; in this, the ratio of maximum power voltage to its open-circuit voltage is approximately a constant value of a PV module, i.e.

$$\frac{V_{\mathrm{MPP}}}{V_{\mathrm{OC}}} < K_1 < 1 \tag{2}$$

This method is simple; however, it is difficult to select the appropriate value of the constant K_1. The value of K_1 ranging from 0.71 to 0.78 is obtained from literature reports.

The flowchart of OCV is shown in Fig. 4. For measurement of V_{OC} solar array temporary isolated from the MPPT. Next from pre-set value of K_1, and equation

Fig. 4 Flowchart for CV algorithm
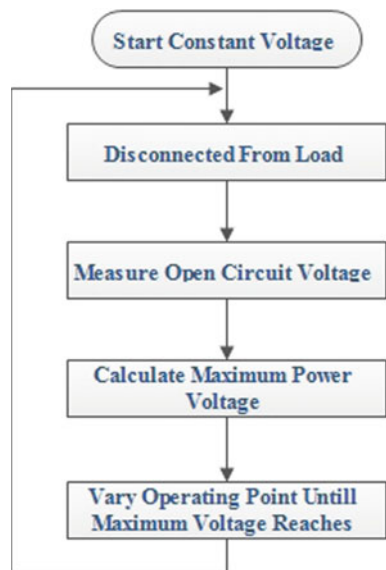
MPPT calculated and adjusts the array's voltage until the calculated V_{MPP} is reached. This operation is continuously repeated to track the position of the MPP [10].

In measurement V_{OC}, the MPPT has to be isolated temporary from PV array, so, in each measurement, a power loss occurs. Another problem associated with this is unable to track the MPP under different irradiations and temperatures. The MPP obtained in this method is fictitious, not real because the relationship is only an assumption.

(B) Short-Circuit Current Method

This method is also an observance method; in this, the ratio of current at maximum power point (I_{MPP}) to the short-circuit current (I_{SC}) is approximately a constant value of the PV array, i.e.

$$\frac{I_{MPP}}{I_{SC}} = K_2 < 1 \tag{3}$$

Like open-circuit voltage method, K_2 is not constant value. It is found that value of K_2 ranging from 0.78 and 0.92 is obtained from the literature report. The accuracy and tracking speed depend on the accuracy of K_2 and periodic measurement of I_{SC}. The problem associated with SCC method is same as OCV method, but OCV performance is better than SSC method.

(C) Hill-Climbing Method

Hill climbing (HC) method is widely adopted in PV systems which is direct method. Perturb and observe (P&O) and incremental conductance (INC) methods are based on the "hill-climbing" principle, in which operating point of the PV array is moving in the direction in which power increases. Hill-climbing methods are easy to implement and have good performance when solar irradiation is constant [11]. Problem associated with hill-climbing technique is steady-state oscillations around the MPP and MPP lost or move in the wrong direction during rapidly change solar irradiation and temperature.

(1) Perturb and Observe

The P&O method is more popular and widely adopted because of its simple feedback structure and optimum number of hardware parameters required [12, 13]. The operation of P&O is based on the perturbation of duty cycle of DC–DC interface converter in which PV array voltage increases or decreases according to PV array power output [14, 15]. If the power of PV array increases, then perturbation will continue in the same direction, otherwise in reversed direction. The flowchart of P&O is shown in Fig. 5 [16].

Fig. 5 Flowchart for P&O algorithm
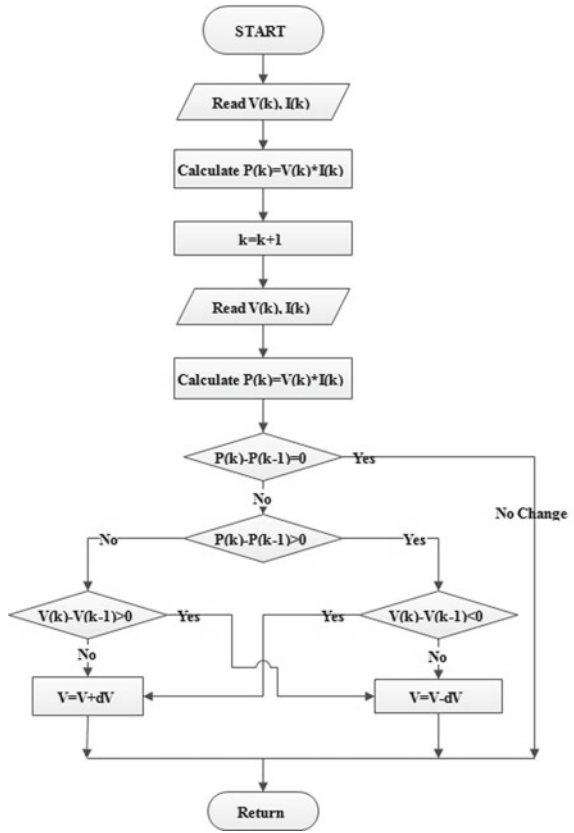
Fig. 6 Basic idea of INC method on an SPV curve
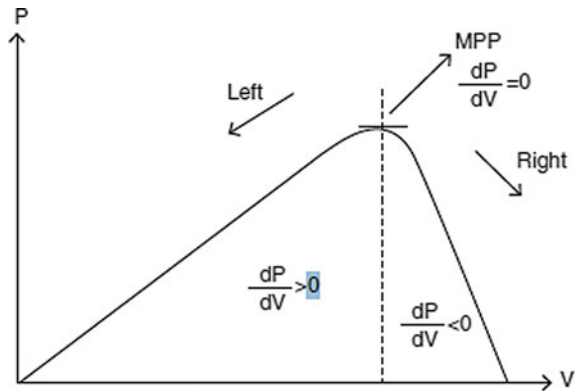
(2) Incremental Conductance Method

The operation of INC method is based on slope at the MPPT which is zero, left side positive, and right side negative on the MPP of power versus voltage curve. This statement is shown in Fig. 6, and the equation of INC method is as follow:

We know that

$$P = VI$$

Differentiating w.r.t V, we get

$$\frac{\mathrm{d}P}{\mathrm{d}V} = \frac{V\mathrm{d}I}{\mathrm{d}V} + I$$

at MPP

$$\frac{\mathrm{d}P}{\mathrm{d}V} = 0$$

which yield at MPP

$$\frac{\mathrm{d}I}{\mathrm{d}V} = -\frac{I}{V}$$

From the above-obtained equation, we conclude that change in instantaneous output conductance is equal to the negative output instantaneous conductance; then, array will operate at MPP [17]

$$\frac{\mathrm{d}I}{\mathrm{d}V} > -\frac{I}{V} \quad \text{at left side of MPP}$$
$$\frac{\mathrm{d}I}{\mathrm{d}V} = -\frac{I}{V} \quad \text{at MPP}$$
$$\frac{\mathrm{d}I}{\mathrm{d}V} < -\frac{I}{V} \quad \text{at right side of MPP}$$

where V and I are PV array output voltage and current, respectively. The left-hand side of equations represents instantaneous incremental conductance, and the right-hand side represents the instantaneous conductance of PV module [18]. The flowchart of the INC algorithm is depicted in Fig. 7

(D) Artificial Intelligence Method

1. Fuzzy Logic Control

Over a last decade MPPT made with the microcontroller by using FLC more popular due to advantages of working with guessed input, output, and not required an exact mathematical equation and handling nonlinearity very easily [19]. The FLC works exactly like adaptive P&O and adjusts the duty cycle according to the requirement. The FLC helps to reduce oscillation near MPP by decreasing the duty cycle step [20–22]. Algorithm flowchart of FLC MPPT is depicted in Fig. 8
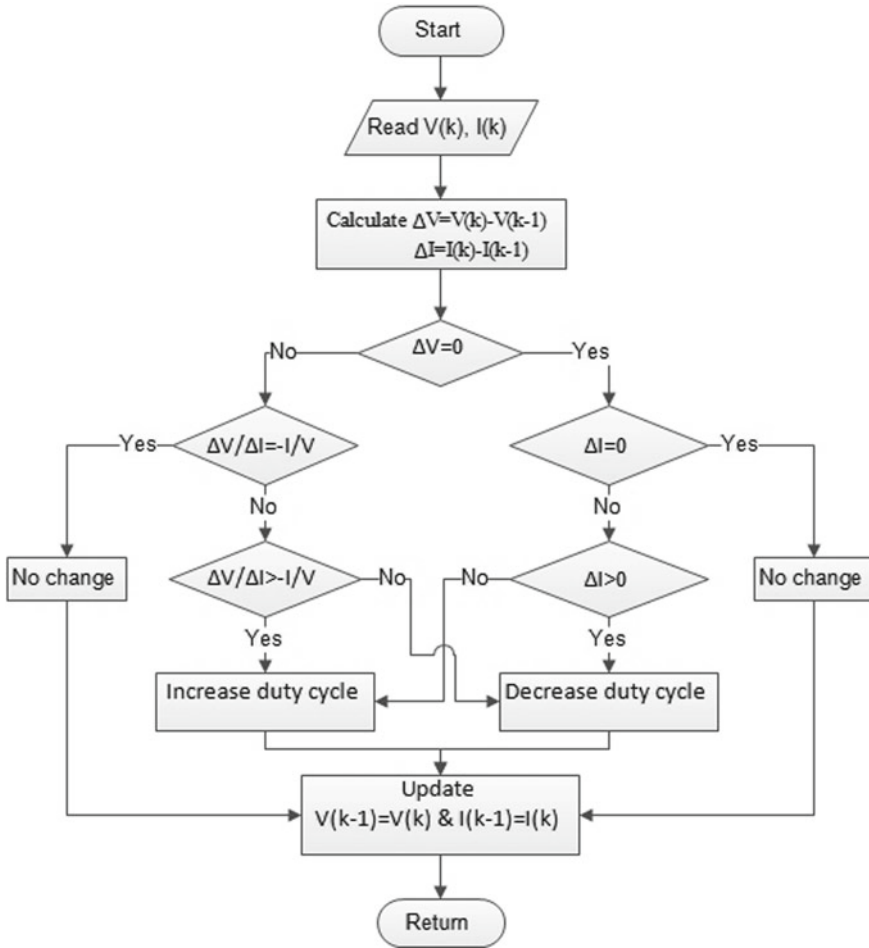
Fig. 7 Flowchart for INC algorithm

The fuzzification, fuzzy logic inference system and defuzzification are the three major stages of FLC. The fuzzification is the conversion of real data into fuzzy linguistic variable based on the membership function (MF). A defuzzification is the conversion of the output linguistic variable into a suitable control signal. The If-then relations between the input variable and the output signal are set in the fuzzy inference system block. The accuracy is achieved by resolution of the membership function and fuzzy levels.

2. Neural Network-Based MPPT

Neural networks are also well adapted in microcontrollers for MPPT for control an MPP. An NN generally has three layers: input, hidden and output layers which are
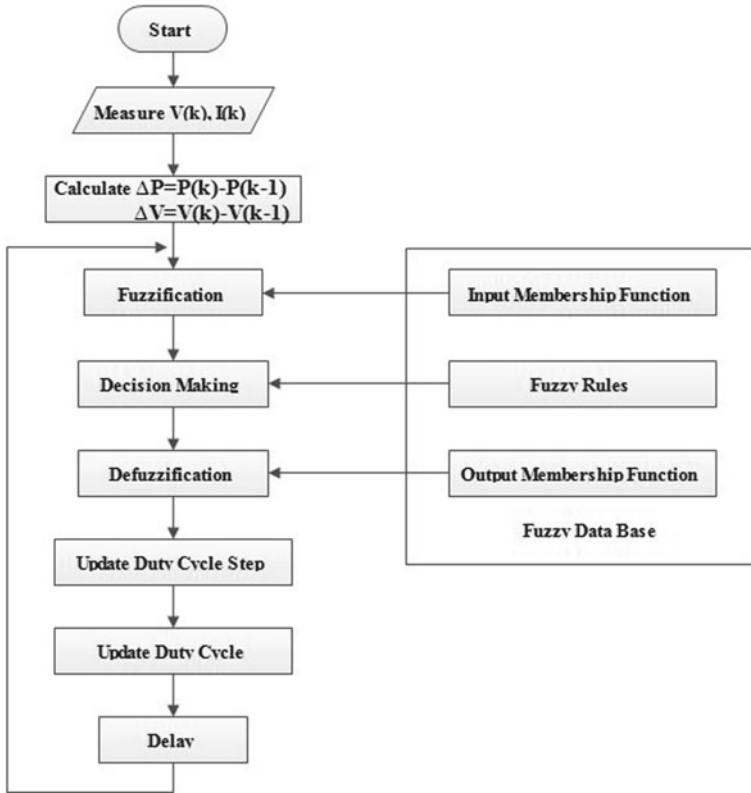
Fig. 8 Algorithm for FLC MPPT

shown in Fig. 9. The number of nodes in any layer variable and it is user dependent. In the input layer, input may be OCV, SSC, irradiation, temperature or any combination of these parameters [23, 24]. The output is generally one or more reference signal(s). In MPPT output is duty cycle to control DC-DC converter for PV array

Fig. 9 Example for neural network
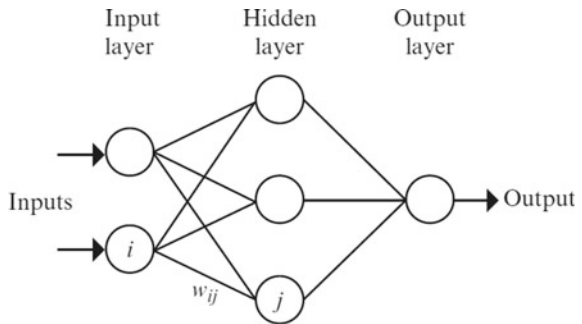
Table 1 Comparison Table

Type	Conventional methods	Artificial intelligent methods
Tracking speed	Slow	Fast
Tracking accuracy	Low	High
Implementation complexity	High	Low
Dynamic response	Oscillatory	Good
Steady-state oscillations	Yes (slow)	Very slow
Cost	Low	High

operate at MPP [25]. The performance of the NN depends on how well the neural network has been trained and hidden layer function is used. The connection between the nodes is weighted. In Fig. 9, the weight between the nodes i and j is represented by W_{ij}. The weights are adjusted in the training process. Over a long period of time, the input and output data of pattern are collected for training process of NN so that the MPP of PV array can be attained accurately [22].

5 Comparative Analysis

The performance of the conventional technique is compared with AI technique under varying insolation and temperature; we observe that in the case of cost factor, the conventional method is more economical than AI method. But in other parameters such as tracking speed, accuracy, implementation complexity, dynamic response and steady-state error, AI technique performs better than conventional technique. Some comparisons are listed in Table 1.

6 Conclusion

In this paper, various maximum power point tracking (MPPT) techniques for solar Photovoltaic have been discussed and a comparison among different parameters of interest has been made. Out of the comparison, we saw that artificial intelligent methods are very accurate and computationally less, while conventional method is easy to use, but accuracy is not well. It is interesting point that various MPPT techniques have a slight difference in all aspects. Nevertheless, among different types of MPPT algorithms, choosing the right algorithm depends on cost.

References

1. Yoshikawa K, Kawasaki H, Yoshida W (2017) Silicon heterojunction solar cell with interdigitated back contacts for a photo conversion efficiency over 26%. Nature energy
2. Salas V, Olias E, Barrado A, Lazaro A (2006) Review of the maximum power point tracking algorithms for stand-alone photovoltaic systems. Sol Energy Mater Sol Cells 90:1555–1578
3. Rauschenbach HS (1980) Solar cell array design handbook. Van Nostrand Reinhold, New York, NY, USA
4. Villalva MG, Gazoli JR, Filho ER (2009) Comprehensive approach to modelling and simulation of photovoltaic arrays. IEEE Trans Power Electr 24(5):1198–1208
5. Masoum MAS, Dehbonei H, Fuchs EF (2002) Theoretical and experimental analyses of photovoltaic systems with voltage- and current-based maximum powerpoint tracking. IEEE Trans Energy Convers 17(4):514–522
6. Schoeman JJ, Van Wyk JD (1982) A simplified maximal power controller for terrestrial photovoltaic panel arrays. In: Proceedings of the IEEE 13th annual power electronics specialists conference (PESC '82), pp 361–367
7. Koutroulis E, Kalaitzakis K, Voulgaris NC. Development of a microcontroller-based, photovoltaic maximum power point tracking control system. IEEE Trans on Power Electron
8. Wasynczuk O (1983) Dynamic behaviour of a class of photovoltaic power systems. IEEE Trans Power App Syst 102(9):3031–3037
9. Hussein KH, Muta I, Hoshino T, Osakada M (1995) Maximum photovoltaic power tracking: an algorithm for rapidly changing atmospheric conditions. IEE Proc Generat Transm Distrib 142(1):59–64
10. Hohm DP, Ropp ME. Comparative study of maximum power point tracking algorithms. Prog Photovoltaics Res Appl. Accessed on 22 Nov 2002
11. Lyden S, Haque ME, Mahmud MA (June 2016) Maximum power point tracking methods for PV systems. In: Advances in solar photovoltaic power plants, green energy and technology, pp 79–105
12. Femia N, Petrone G, Spagnolo G, Vitelli M. Optimizing duty-cycle perturbation of P&O MPPT technique. In: IEEE 35th annual power specialists conference, Aachen, Germany, 2004
13. Femia N, Petrone G, Spagnolo G, Vitelli M. Increasing the efficiency of P&O by converter dynamic matching. In: IEEE 35th annual power specialists conference, Aachen, Germany, 2004
14. Mughal S, Sharma N. Green energy resources/technologies scenario in India. In: Proceeding of national conference on emerging technologies in renewable energy and electrical engineering-2012 (EREEEE-2012), Sangam University Rajasthan, 25–26 Feb 2012
15. Hussein KH, Muta I, Hoshino T, Osakada M (1995) Maximum power point tracking: an algorithm for rapidly chancing atmospheric conditions. IEE Proc Generat Transm Distrib 142:59–64
16. Amrouche B, Belhamel M, Guessoum A (2007) Artificial intelligence based P&O MPPT method for photovoltaic systems. Revue des Energies Renouvelables ICRESD-07 Tlemcen, 11–16
17. Hussein KH, Muta I, Hoshino T, Osakada M (1995) IEE Proc Generat Transm Distrib 142:59–64
18. Esram T, Chapman PL (June 2007) Comparison of photovoltaic array maximum power point tracking techniques. IEEE Trans Energy Convers 22(2)
19. Li J, Wang H (1989) Maximum power point tracking of photovoltaic generation based on the fuzzy control method. In: Young M (ed) The technical writer's handbook. University Science, Mill Valley, CA
20. Al Nabulsi A, Dhaouadi R (August 2012) Efficiency optimization of a DSP-based standalone PV system using fuzzy logic and dual-MPPT control. IEEE Trans Ind Informat 8(3):573–584

21. Zainuri MAAM, Radzi MAM, Soh AC, Rahim NA (March 2014) Development of adaptive perturb and observe-fuzzy control maximum power point tracking for photovoltaic boost dc–dc converter. IET Renew Power Gener 8(2):183–194
22. El Khateb A, Rahim NA, Selvaraj J, Uddin MN (August 2014) Fuzzy-logic-controller-based SEPIC converter for maximum power point tracking. IEEE Trans Ind Appl 50(4):2349–2358
23. Mughal S, Sharma N. 3E's in exploring green word. In: National conference on technology advances in electrical and renewable energy engineering (EREECON-2013), Techno India NJR Institute of Technology Udaipur
24. Mughal S, Sood YR, Jarial RK. A review on solar photovoltaic technology and future trends. Int J Sci Res Comput Sci Eng Inform Technol (IJSRCSEIT-2018) 4(1)
25. Ramaprabha R, Gothandaraman V, Kanimozhi K, Divya R, Mathur BL (January 2011) Maximum power point tracking using GA optimized artificial neural network for solar PV system. In: 1st international conference on electrical energy systems (ICEES), pp 264–268
26. Sedaghati F, Nahavandi A, Badamchizadeh MA, Ghaemi S, Abedinpour Fallah M (2012) PV maximum power-point tracking by using artificial neural network. Math Probl Eng 2012

Design and Techno-Financial Analysis of Solar Photovoltaic Plant for School of Engineering and Technology at BGSB University, Rajouri (J&K)

Shafqat Nabi Mughal, Yog Raj Sood and R. K. Jarial

Abstract Solar power technology was present in India from a very long time, but due to its high purchase cost, only few were able to reap its benefits. It was very costly and less efficient during its early phase, but due to the increase in efficiency of solar modules and drop in the prices of solar PV along with various government schemes and policy implementations, solar PV technology has gained prime importance as a source of electricity. In this paper, we have carried out design, technical and financial analysis along with optimisation of solar PV plant for the School of Engineering and Technology, Baba Ghulam Shah Badshah University (BGSBU), Rajouri, Jammu and Kashmir, India. This paper uses two-way approaches for the design and analysis of feasibility of solar PV plant. We have not limited our design and analysis to the use of simulation software like PV GIS, etc., but also making use of the actual physical cost for the various items needed for building this plant prevailing these days in India. This has helped us to calculate the cost expenditures much closer to that would be spent in building this plant in the future. In this paper, we have estimated the energy demand of the School of Engineering and Technology, and based on the energy demand and location, we have proposed this solar PV system to solve much-awaited issue of power scarcity in such locations of educational and economic importance. This system will not only help the university to lower down the burden of money spent on the usage of electricity but will also help in reducing the quantity of carbon dioxide emission into the atmosphere.

S. N. Mughal (✉)
Department of Electrical and Renewable Energy Engineering,
Baba Ghulam Shah Badshah University, Rajouri, Jammu and Kashmir, India
e-mail: snmughal.bgsbu@gmail.com

Y. R. Sood · R. K. Jarial
Department of Electrical, National Institute of Technology Hamirpur,
Hamirpur, Himachal Pradesh, India
e-mail: yrsood.nith@gmail.com

R. K. Jarial
e-mail: jarial0@gmail.com

1 Introduction

A huge surge could be seen in the technology developments related to solar pho-
tovoltaics, resulting in more competition among the PV technology industries
causing heavy reduction in panel prices and other cost components of this tech-
nology. Solar photovoltaic technology is renewable, pollution-free and with
advancement taking place each day it is swiftly reaching grid parity [1]. It is a very
reliable source of free energy requiring no fuel to burn, hence preserving our natural
resources which are already being depleting at a very high rate. The PV technology
has reached to a state which ones was considered a very costly affair to a very
lucrative technology which could be used not only by utility service providers but
by anybody. It is very famous among public and can be easily seen in the rooftops
of residential and commercial users. With the advancement of PV technology,
rising prices of fossil fuels, new governmental incentives and schemes, the PV
set-up prices have fallen drastically, resulting in the huge market growth rate of this
technology. The top market leaders among them are China, Japan, Germany and the
USA [2]. Apart from them, a surge in PV market is also witnessed in India, UK and
the Middle East. The main constituent of PV system is PV module, and it indi-
vidually constitutes 50% of the total cost of PV system [3]. With the advancement
of new materials and techniques, new and improved panels with high efficiency and
low costs are being developed. This has resulted in improving the competitiveness
of solar photovoltaics than any other renewable energy technologies. There are
several types of PV technologies, but crystalline silicon photovoltaic (c-Si PV) has
highest market share so far, and however, with new innovations and research
developments, there is still a significant room for further decline in prices of solar
PV. According to one study [4], both low-cost and high-cost manufacturers of solar
PV will halve their production costs in the coming years. Apart from decline in
panel costs, decline in cost of balance of system (BOS), operation and maintenance
cost are other important drivers which need to be taken care of for reducing the
overall cost of PV system. At the present, the residential tariffs are increasing day
by day due to the increase in the fuel prices, and however, by adopting solar PV
system, one can reduce the tariffs to a large extent. Also, the present worldwide
installed PV capacity has reached more than 300 gigawatts (GW). There are several
agencies which have anticipated the falling prices of solar PV. According to
European Photovoltaic Industry Association (EPIA), the LCOE of PV would
reduce from $0.22/kWh (kilowatt hour) in 2010 to $0.06/kWh by 2020 [5], while
analysis of the US market projected that the LCOE of residential PV would reduce
from $0.10/kWh in 2015 to $0.07/kWh by 2020.

As far as India is concerned due to its climatology and new renewable energy
policies and schemes, it is becoming the favourite choice among the market leaders

for deploying renewable energy investments. A project is already being launched by the Government of India (GOI) known as Jawaharlal Nehru National Solar Mission (JNNSM) with a mission of deploying 100 GW solar PV by 2022. One of the prime objectives of JNNSM is to utilise the large area of rooftop for installation [6]. In addition to the initiates taken at national level, many Indian states are devising policies to fulfil their renewable power obligations (RPOs) through solar PV. The main course of action to achieve these RPOs targets involves better designing procedures, deep technical and financial analysis of solar PV technology. A number of studies have been carried out for designing solar photovoltaics. In one study, a framework was suggested to cater the energy demand of six top cities of India up to 2025 using solar PV [7]. Amal Marrekchi studied the ways to size the inverter and made a practical guide to connect to it to the grid [8]. In another study performance of a grid-connected solar PV set-up at Sivagangai district in Tamil Nadu (South India) was evaluated and validated by Sundaram and Babu [9]. Moreover, a techno-economic analysis of solar photovoltaic power plant was carried out to cater the energy demand of garment zone at Jaipur [10]. In another paper, optimal sizing of grid-connected photovoltaic energy system was studied [11]. Other studies [12, 13] also found that solar PV system is the most suitable replacement for powering the Indian process industries, particularly the garment industry.

2 Site Location

The Baba Ghulam Shah Badshah University is located on the terrains of Dhanidar mountains which is the peripheral part of the gigantic Pir Panjal mountain range in Rajouri (Jammu and Kashmir state). The University campus is located (latitude 33° 38′N. longitude 74°36′E.) at an altitude of 975 m above the mean sea level. The climate of the place varies from subtropical to temperate. Presently, the university is powered by Jammu and Kashmir Power Development Department (JKPDD); however, due to the remote location of the university, it often suffers frequent power cuts, which leads the university to switch to install diesel generator sets, resulting in additional power expenditure. The majority of the problem is faced by School of Engineering and Technology (SOET) which is one of the most important constituents of the varsity. SOET comprises of following blocks/departments.

   i. COET: College of Engineering and Technology (Main building).
  ii. ERE: Electrical and Renewable Energy Engineering Block.
 iii. R&D Wing: Research and Development Wing Building.
 iv. Workshop: Civil Workshop Building.

We are seeking the self-sustainable solution for the School of Engineering and Technology since it is the major constituent of the university. Figure 1 shows the satellite location of the School of Engineering and Technology as given by PV GIS simulation software.

Fig. 1 Satellite aerial view of location for installation of solar PV. *Source* Google maps/PV GIS simulation software

3 Energy Demand Calculation

Energy Demand assessment is done by finding out the number of equipments installed in the premises consuming power, calculating the number of kWh used by the equipments on daily, monthly or yearly basis. When properly executed, a load analysis can yield valuable insight into facility energy usage that can be used to save on energy costs, increase productivity and protect critical assets [14]. Table 1 shows the different equipments installed in the SOET premises along with their quantities and ratings.

The daily average load consumption is calculated based on the ratings and the approximate hours of usage given in Table 1. The approximate daily load utilisation is 396 kWh. Considering the futuristic increase in demand and seasonal variation of load, the daily load requirement is kept 400 kWh.

4 Designing Methodology for Solar PV

4.1 Feasibility of Solar Radiations

In this study, average solar radiations were estimated using PV GIS simulation software. Based on location coordinates, data can be accessed from the NASA website with meteorological data. The average solar radiation at the proposed site, i.e. SOET, BGSB University, was found around 5.61 kWh/m^2/day. Table 2 shows the solar radiation data for different months of the whole year at the proposed site

Table 1 Different equipments installed in the SOET premises along with their quantities and ratings

S. No.	Item/equipment	Quantity	Rating (in watts)	Approximate watt hours utilised
1	LEDs	500	15	500 × 15 × 8 = 60,000
2	Fans	150	50	150 × 50 × 8 = 45,000
3	Computers	100	300	100 × 300 × 8 = 150,000
4	Air conditioners (all weather AC)	10	1500	10 × 1500 × 6 = 75,000
5	Scanners	4	35	4 × 35 × 1 = 140
6	Printers	5	50	5 × 50 × 2 = 500
7	Xerox machines	5	1200	5 × 1200 × 2 = 12,000
8	Water coolers	3	90	3 × 90 × 8 = 2160
9	Geysers	2	2000	2 × 2000 × 5 = 20,000
10	Exhaust fans	5	25	5 × 25 × 5 = 625
11	Miscellaneous			30,000
Total watt hours				395,425 Wh

Table 2 Solar radiation data for different months of the whole year

Fixed system: inclination = 34°, orientation = 0°

Month	E_d	E_m	H_d	H_m
Jan	376	11,700	4.90	152
Feb	354	9920	4.68	131
Mar	444	13,800	6.07	188
Apr	433	13,000	6.03	181
May	454	14,100	6.50	201
Jun	400	12,000	5.76	173
Jul	368	11,400	5.21	161
Aug	363	11,200	5.09	158
Sep	422	12,700	5.92	178
Oct	472	14,600	6.51	202
Nov	424	12,700	5.71	171
Dec	376	11,600	4.94	153
Yearly average	408	12,400	5.61	171

which is used in the simulation. Also, Fig. 2 shows monthly energy output from fixed-angle PV system. Figure 3 shows the monthly in-plane irradiation for fixed angle, and Fig. 4 shows outline of horizon with the sun path for winter and summer solstice for the proposed site.

Where

E_d: Average daily electricity production from the given system (kWh),

E_m: Average monthly electricity production from the given system (kWh),

PV estimate: 33°23'42" North, 74°21'4" East

-Fixed system, incl.=   34°
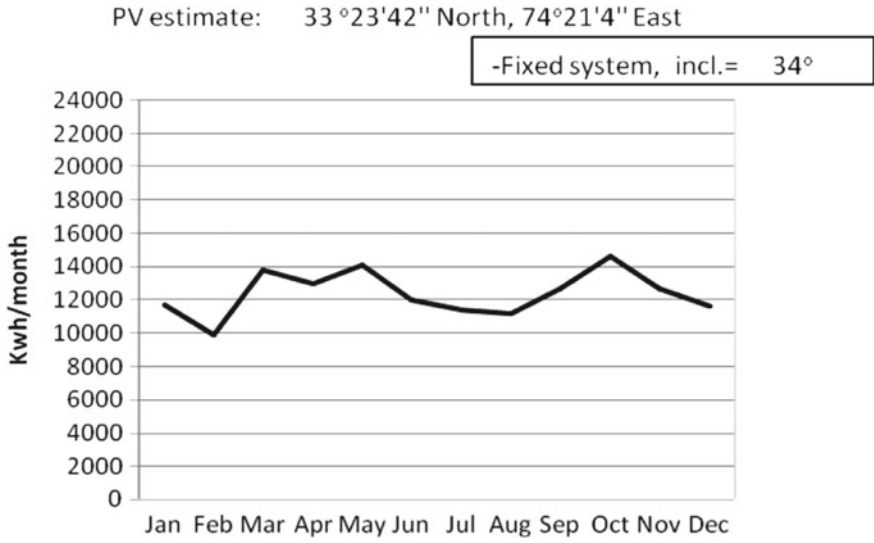
Fig. 2 Energy output (monthly) for fixed-angle PV system

Irradiation estimate: 33°23′42"North, 74°21′4"East

— Fixed system, incl.= 34
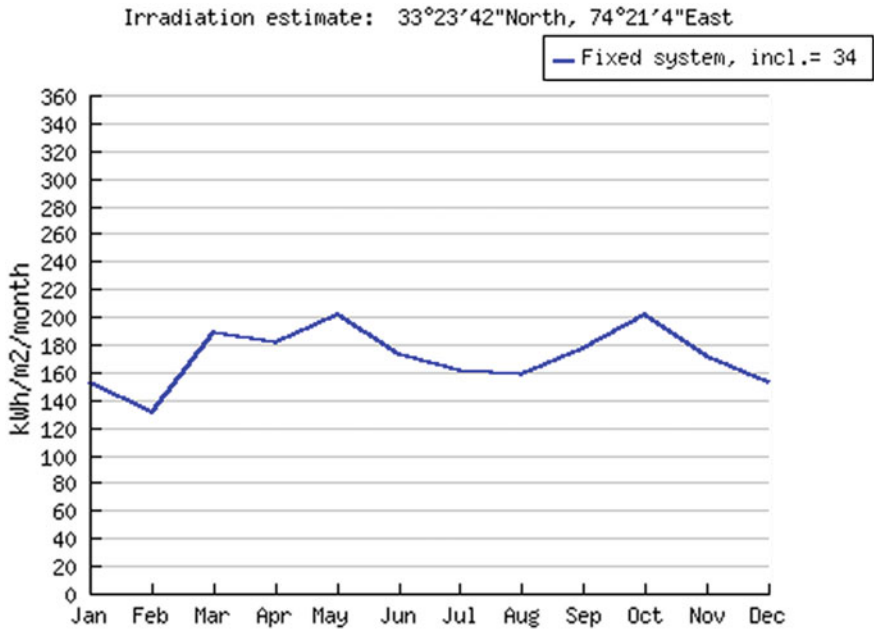
Fig. 3 In-plane irradiation (monthly) for fixed angle
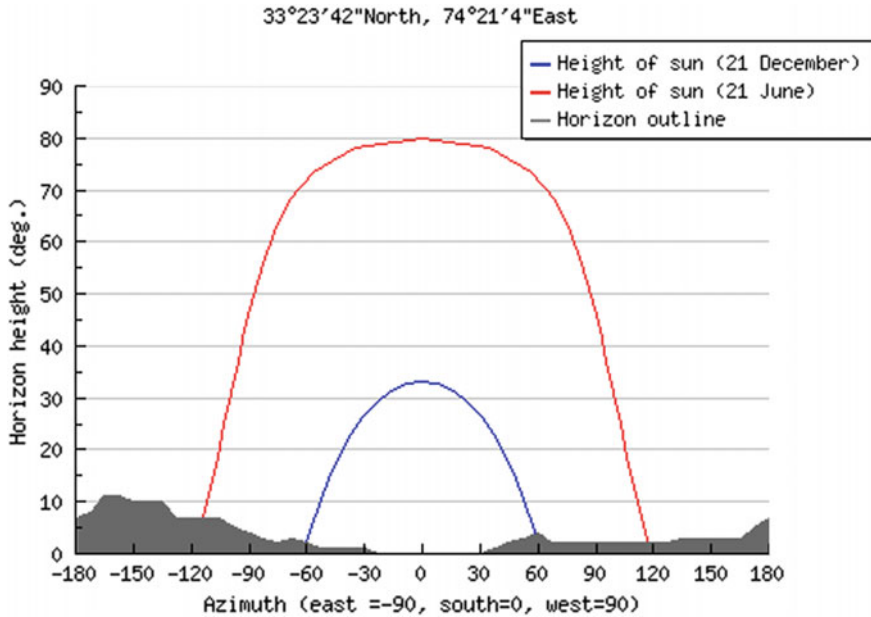
Fig. 4 Outline of horizon with the sun path for winter and summer solstice

H_d: Average daily sum of global irradiation per square metre received by the modules of the given system (kWh/m^2) and

H_m: Average sum of global irradiation per square metre received by the modules of the given system (kWh/m^2).

The average daily energy production from the plant is 408 kWh which is very similar to the desired demand requirement of 400 kWh.

4.2 Capacity of the Plant

The capacity of the plant is dependent upon many factors. To get the optimal design, various parameters should be taken into consideration. The design steps are divided into the following:

4.2.1 No. of Modules Required

The number of PV modules required to meet the daily energy demand can be calculated by two methods. In one method, numbers of modules are determined using the wattage of the module and the mean daily solar insolation in the region.

Table 3 Parameters and values

S. No.	Parameter	Value
1	Daily load	400 kWh
2	Insolation	5.61 kWh/m^2/day
3	Battery efficiency	90%
4	Charge controller efficiency (MPPT type)	95%
5	Mismatch factor	0.85%
6	Array load	467,836.26 W
7	Array size	98,109.73 Wp = 100 kWp
8	Number of modules required	400

In other method, numbers of modules are determined first by calculating array load and then the array size. The second method is used in our calculation. Assuming the battery efficiency of 90%, charge controller efficiency of 95% [15] and mismatch factor of 0.85%, the following calculations are made [16]

$$\text{Array load} = \frac{\text{Total daily load}}{\text{Battery efficiency} \times \text{charge controlle efficiency}}$$

$$\text{Array size} = \frac{\text{Array load}}{\text{Insolation} \times \text{mismatch factor}}$$

$$\text{Number of PV modules required} = \frac{\text{Array size}}{\text{PV module peak rated output}}$$

Using the above equations, the following parameters are obtained as shown in Table 3.

The size of the plant we are suggesting should be 100 kW because in the future, the demand would rise. Therefore, the array size would be 100 kWp. Hence, the number of modules taken is 400.

4.2.2 Inverter Sizing

Inverter sizing is very important as it converts DC current from panels to AC current required by majority of the appliances. It must ensure that PV modules should operate at their maximum power point tracking (MPPT). Hence, proper sizing of inverter is necessary for safety and higher efficiency of the system. The chosen inverter must be of that rating which could handle the total peak watt requirement of the site at any time. The inverter rating should be 20–25% bigger than the peak load of the system to handle futuristic increase in load. Since the peak demand for the given site is around 80 kW, hence, inverter size = 80 kW × 1.25 = 100 kW.

4.2.3 Battery Sizing

The fact that the proposed PV system is being used for powering engineering college which is very important as far as regular electricity is concerned since without electricity no practicals can be performed, so we are suggesting that the size of batteries should be such that we could get two days of power autonomy. Also, depth of discharge of battery being considered here is 25%.

Load requirement for day = 400 kWh

The suggested battery is 12 V/200 VA. Hence, the amount VA requirement is given by the expression as follows [16].

$$\text{VA of battery} = \frac{\text{Daily load} \times \text{depth of discharge} \times \text{days of autonomy}}{\text{Votage of the system}}$$
$$= \frac{400,000 \times 1.25 \times 2}{12}$$
$$= 83,333.34 \approx 84,000 \text{ Ah}$$

5 Project Cost

The project cost is evaluated by considering individual items cost as provided by various vendors and suggested by government agencies [17–19]. Two scenarios are considered, one with battery backup and the other without battery backup. Table 4 gives cost statistics with battery backup, and Table 5 gives cost statistics without battery backup.

The Jammu and Kashmir state is getting subsidy from MNRE up to 70% [20]. Based on this, the solar PV project cost statistics dropped considerably making solar PV plant more competitive. The new cost statistics are summarised as shown in Table 6.

6 Financial Analysis

Considering the annual yield per kWp of 1488 kWh with useful life of plant of 25 years and feed in Tariff of Rs. 5.005 (the commercial tariff charged per kWh presently in the campus) for 25 years, the various parameters are evaluated for both cases without and with subsidy as shown in Tables 7 and 8, respectively.

Table 4 Cost statistics with battery backup

Item/component	Quantity	Cost/unit	Total cost
Solar panels	400	Rs. 35/W	Rs. 3,500,000
Inverter	1 (100 kW)	Rs. 10/W	Rs. 1,000,000
Mounting structure	–	Rs. 3500/KW	Rs. 350,000
Cables	–	Rs. 2000/KW	Rs. 200,000
Battery, 12 V/200 Ah [MNRE]	420	Rs. 16 per Ah	Rs. 1,344,000
Combiner box	20	Rs. 6000	Rs. 120,000
Main junction box	10	Rs. 7500	Rs. 75,000
Fuses and disconnects	Set	Rs. 2500	Rs. 250,000
Protection switches	50	Rs. 500	Rs. 25,000
Energy monitoring metre	2	Rs. 4000	Rs. 4000
Total			Rs. 6,868,000
GST	5%		Rs. 343,400
Transport and installation	10%		Rs. 686,800
Project management, design and engineering	5%		Rs. 343,400
Miscellaneous	5%		Rs. 343,400
Total cost			Rs. 8,585,000
Total cost (considering 5% increase from expenditure being calculated)			Rs. 9,014,250
Total cost (considering 5% decrease from expenditure being calculated)			Rs. 8,155,750

Table 5 Cost statistics without battery backup

Item/component	Quantity	Cost/unit	Total cost
Solar panels	400	Rs. 35/W	Rs. 3,500,000
Inverter	1 (75 kW)	Rs. 10/W	Rs. 750,000
Mounting structure	–	Rs. 3500/kW	Rs. 350,000
Cables	–	Rs. 2000/kW	Rs. 200,000
Battery, 12 V/200 Ah [MNRE]	420	Rs. 16 per Ah	Rs. 1,344,000
Combiner box	20	Rs. 6000	Rs. 120,000
Main junction box	10	Rs. 7500	Rs. 75,000
Fuses and disconnects	Set	Rs. 2500	Rs. 2,50,000
Protection switches	50	Rs. 500	Rs. 25,000
Energy monitoring metre	2	Rs. 4000	Rs. 4000
Total			Rs. 5,524,000
GST	5%		Rs. 276,200
Transport and installation	10%		Rs. 552,400
Project management, design and engineering	5%		Rs. 276,200
Miscellaneous	5%		Rs. 276,200
Total cost			Rs. 6,905,000
Total cost (considering 5% increase from expenditure being calculated)			Rs. 7,250,250
Total cost (considering 5% decrease from expenditure being calculated)			Rs. 6,559,750

Table 6 PV project cost statistics

PV configuration	Cost
PV set-up with battery backup	Rs. 8,585,000
PV set-up without battery backup	Rs. 6,905,000
PV set-up with battery backup considering subsidy	Rs. 2,575,500
PV set-up without battery backup considering subsidy	Rs. 2,071,500

Table 7 PV set-up without subsidy

Parameter	PV set-up with battery backup	PV set-up without battery backup
Purchase value (in Rs.)	8,585,000	6,905,000
Own funds (in Rs.)	8,585,000	6,905,000
Present value of net income (in Rs.)	9,896,399	10,238,875
Levelised energy cost (Rs./kWh)	4.609	3.707
Amortisation Time (in years)	11.8	10
IRR before tax (%)	4.9	7.7

Table 8 PV set-up with subsidy

Parameter	PV set-up with battery backup	PV set-up without battery backup
Purchase value (in Rs.)	2,575,500	2,071,500
Own funds (in Rs.)	2,575,500	2,071,500
Present value of net income (in Rs.)	11,080,695	11,224,209
Levelised energy cost (Rs./kWh)	1.490	1.112
Amortisation time (in years)	3.2	2.2
IRR before tax (%)	25.1	34.3

7 Conclusion

The School of Engineering and Technology being the epitome of providing education in the far-flung area on the hills of Dhanidar mountain range consumes more or less 396 kWh monthly. The average solar radiation at the proposed site, i.e. SOET, BGSB University, was found around 5.61 kWh/m^2/day, which is having

average daily energy production of 408 kWh. The cost of the plant with battery backup was estimated around Rs. 8,585,000 and without battery backup, Rs. 6,905,000. Also considering the subsidy as provided by the Ministry of New and Renewable energy department, the cost of the PV set-up was found to slide down to Rs. 2,575,500 and Rs. 2,071,500 for PV set-up with and without battery backup, respectively. As far as financial analysis is considered, for PV set-up without subsidy the levelised energy cost was calculated at Rs. 4.609/kWh and Rs. 3.707/kWh with amortisation time of 11.8 and 10 years for PV set-up with battery backup and without battery backup, respectively. Also for PV set-up with subsidy, the levelised energy cost was calculated at Rs. 1.490/kWh and Rs. 1.112/kWh with amortisation time of 3.2 and 2.2 years for PV set-up with battery backup and without battery backup, respectively.

References

1. Goodrich A, James T, Woodhouse M (2012) Residential, commercial, and utility-scale photovoltaic (PV) system prices in the United States: current drivers and cost reduction opportunities. NREL, Golden, CO
2. Green MA (2009) The path to 25% silicon solar cell efficiency: history of silicon cell evolution. Prog Photovoltaics 17(3):183–189
3. http://www.eai.in/ref/ae/sol/rooftop/cost
4. Mehta S, Maycock P (2010) The PV supply chain: manufacturing, technologies, costs. Greentech Media Res PV Energy Syst
5. EPIA, Kearney AT (2011) Solar photovoltaics: competing in the energy sector. EPIA, Brussels
6. https://www.mnre.gov.in/solar-mission/jnnsm/introduction
7. Muneer T, Asif M, Munawwar S (2005) Sustainable production of solar electricity with particular reference to the Indian economy. Renew Sustain Energy Rev 9:444–473
8. Marrekchi A, Kammoun S, Sallem S, Kammoun MBA (2015) A practical technique for connecting PV generator to single-phase grid. Sol Energy 118
9. Sundaram S, Babu JSC (2015) Performance evaluation and validation of 5 MWp grid connected solar photovoltaic plant in South India. In: Energy conversion and management, Elsevier, pp 429–39
10. Chandel M, Agrawal GD, Mathur S, Mathur A (2014) Techno-economic analysis of solar photovoltaic power plant for garment zone of Jaipur city. In: Case studies in thermal engineering, Elsevier
11. Ramli MAM, Hiendro A, Sedraoui K, Twaha S (2015) Optimal sizing of grid-connected photovoltaic energy system in Saudi Arabia. Renew Energy 75:489–495
12. Mekhilef S, Saidur R, Safari A (2011) A review on solar energy use in industries. Renew Sustain Energy Rev 15:1777–1790
13. Gupta S (1989) Scope for solar energy utilization in the Indian textile industry. Sol Energy 42:311–318
14. https://www.poweringhealth.org
15. https://www.solar-electric.com/learning-center/batteries-and-charging/solar-charge-controller-basics.html
16. Deambi S (2015) From sunlight to electricity: a practical handbook on solar photovoltaic application. Teri press

17. https://www.business-standard.com/article/pti-stories/solar-pv-benchmark-capital-cost-down-by-75-lakh-mw-116042800807_1.html
18. https://mnre.gov.in/file-manager/UserFiles/ready_reconer_list_batteries.doc
19. https://dir.indiamart.com/impcat/solar-combiner-box.html
20. https://mnre.gov.in/file-manager/UserFiles/gcrt-cfa-notification-04-03-2016.pdf

Study on Placement of Sensors for Readings Accuracy Level Enhancement in Greenhouse

Yogesh Kumar Chauhan and Rajeev Ratan

Abstract The present study tells about the sensors topology followed in a greenhouse to enhance their accuracy. Sensors are deployed in the greenhouse agriculture to enhance their productivity and efficacy. Use of sensors and other actuators have resulted in better surveillance and improved yield for the greenhouse crop. Proper installation of these sensors, after analyzing the coverage region limitations of a sensor is suggested after completion of the present study. By means of this study, it is suggested that the whole crop region should be divided into cells, confirming homogeneity regardless of plant growth, nutrient deposition in the roots. These cells should be equipped with one sensor sending the reading for their region so that the need for unnecessarily increasing the number of sensors in a greenhouse is avoided. The factors which are taken into consideration, first one is ventilation did in a greenhouse that can alter the actual readings of a temp or relative humidity sensor, and second is sunlight on the sensors, it can add additional temperature on the meter.

Keywords Greenhouse · Humidity · Sensor · Temperature

1 Introduction

The world is almost on the brink of food scarcity. There are a lot of reasons culminating to this issue. Lesser availability of arable land due to rapid modernization, extreme weather conditions, diminishing water resources, and the high cost of energy are some of the major aspects, contributing to the problem. A greenhouse

Y. K. Chauhan (✉)
School of Engineering and Technology, MVN University, Haryana, India
e-mail: yogesh.chauhan9@gmail.com

R. Ratan
Department of Electronics and Communication Engineering, MVN University, 121105 Palwal, Haryana, India
e-mail: rajeev.arora@mvn.edu.in

is a remarkable asset to the agriculture worldwide by the modern technology. This technology has enabled us to grow crops almost everywhere and replenish our food resources. Greenhouses are a revolutionary technology in modern agriculture. It can surpass the challenges posted by irregularity in temperature, changing precipitation levels, and rising level of CO_2 in the environment. Greenhouses provide a breathable ambiance to the crop and let it flourish under the controlled conditions. A greenhouse is generally a prominent area, having proper control over the climatic conditions, giving a relief from outside disturbances. In a greenhouse (maybe an acre in size or so), it has been observed that it is not always a homogenous environment from one corner to another, while it is a heterogeneous portion having temperature differences of almost 3–4 °C between two sensors readings area, showing the highly heterogeneous nature of a greenhouse [1]. We can readily switch crop cycles, sowing seasons. The dependency over the basic necessities like irrigation waters and fertile lands has been reduced considerably. These green-houses are considered as one of the promising solutions to extreme climate whom every year destroy a huge yield, especially in countries like India and China. These nations are listed as the top three countries with the most arable land. Greenhouses provide a controlled environment and considerably reduce the impact of extreme conditions outside, thus enhancing the yields. Regardless of the demography, cli-mate control is a remarkable feature for all greenhouses. Ambient temperature, radiations by the sun, and relative humidity are the crucial factors which are expected to be controlled by these structures. These factors can adversely affect the crop yield, duration, and quality. A significant amount of total production cost is invested in controlling these factors [2, 3]. Earlier, it was considered that green-houses maintain a homogenous environment inside and provide the excellent environment for the crop. But with the infusion of sensors in greenhouses, it became evident that there are anomalies inside. Sensors are deployed to give temperature and relative humidity readings, and accordingly, suitable steps are taken to maintain the favorable environment homogenously.

The assumption of the homogenous environment inside a modern greenhouse is not possible. Various studies have indicated such heterogeneous environment. In a modern greenhouse, with all modern facilities, these disparities could be up to 5 °C in temperature. These variations can further be introduced by the ventilation sys-tems [4]. Solar radiations are avoided by using radiation shields in many structures, but practically, even after using these shields, the ambient temperature in a greenhouse is affected by the radiations [5]. There are certain issues which have to be tackled with sheer attention, about their accuracy and reliability. This is a result of spatial patchiness existing in a crop region and due to temporal variability in the disturbances occurring in a greenhouse. Similar results were accumulated from humidity sensors placed at multiple locations. Areas near to the ventilation ducts/ fans were considerably better, and remote locations were a bit uncomfortable. In a greenhouse field, the maximum ambient temperature should not surpass from 35 °C for long periods, and similarly, the relative humidity readings should not surpass from 95% to avoid large-scale damages to the crop [3]. Thus, it is a requisite to measure the ambient temperature and relative humidity precisely as they fluctuate

considerably inside the greenhouse field. These variations create non-uniformity along with that can lead to problems like pests and diseases inside. Not only this, the stated heterogeneity in the climate inside can increase energy, water, fertilizers, and pesticides consumption about 15%. With wireless technology, sensors are placed at random places inside a greenhouse and that is the problem [1]. To enhance crop yield and quality and reduce the chances of diseases, designing of a modern greenhouse should consider these anomaly patches. Sensors can be used in a much more efficient manner, by a smart field placement. The placement should consider the number of sensors placed as well as the accuracy.

2   Materials and Methods

2.1   Sensors and Other Devices

Temperature and relative humidity are considered as the main variants while ambient CO_2 concentrations and ambient luminous intensity are excluded from this study. IC LM35 as a temperature sensor and SY HS 220 as humidity sensor were used for the experiment. The LM35 temperature sensor has a range from −55 to 150 °C with 0.5 °C ensured accuracy at 25 °C. It provides a typical accuracy of ±3/4 °C over its full range from −55 to 150 °C. Relative humidity sensor SY HS 220 has a range from 30 to 90% RH with operating temperature range from 0 to 60 °C, with an accuracy of 5% RH (at 25 °C, 60% RH). These specifications and accuracy level make these sensors the best suitable for the proposed study.

2.2   Experimental Section

It has been revealed from various studies that sensors used in a greenhouse in similar conditions may give different results due to variations in different factors. Standard sensors also can vary in their output in the same environment. In order to stabilize their output, sensors are placed under stable conditions something like 25 °C for some time. After that, these sensors should be deployed for the actual measurements.

There could be two different topologies of the sensors in the field for this study. In the first case, the sensors can be placed randomly inside a greenhouse, placed at random distances and at random points. While in the other case, there can be a proper grid-like structure for placement of the sensors inside a greenhouse, to have uniformity in their position and the area covered by surveillance. Figure 1 shows sensors in a proper grid-style arrangement where all the sensors are placed at a proper distance of 3 m from each other. This topology makes uniformity in the design and covers almost the whole of the field for surveillance. Figure 2 shows the
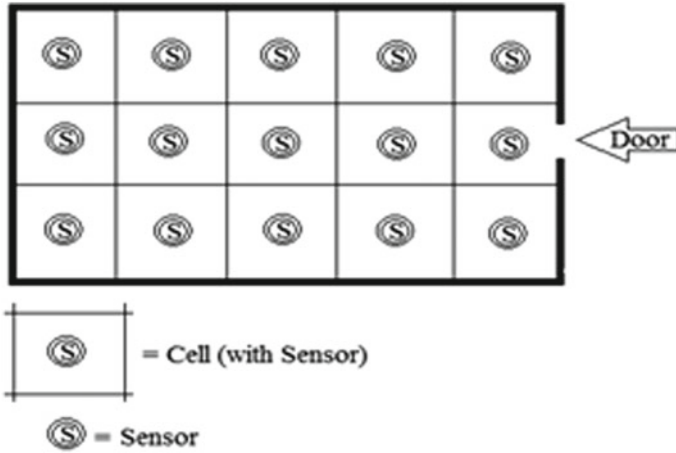
Fig. 1 Proper arrangement of sensors
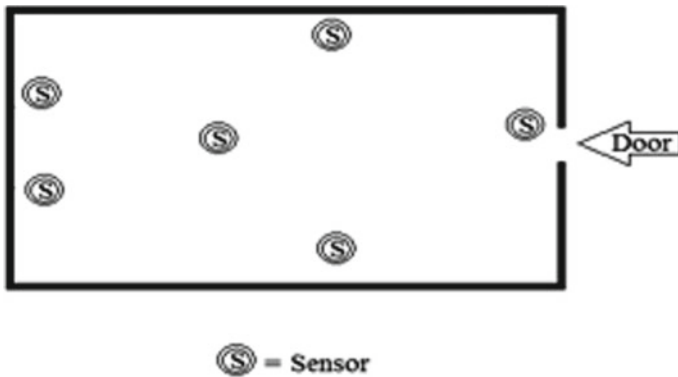
Fig. 2 Random arrangement of sensors

random placements of the sensors, and their position is random which may lead to improper coverage of the field. While placing too few sensors might lead to inaccuracy about the measurements in the field, adding too much of them can swell the cost of production. So we have to make a balance for both the scenarios. A closed greenhouse has larger vertical gradients of ambient temperature and humidity than a natural ventilated system. But for mechanical ventilated, the gradients are even higher [4]. Placing the sensors just near to the ventilation area or the wall facing, the sun could experience a spike as compared to other sensors.

For the present study, an experiment was done at 12 O' clock noon and at 1 p.m. to have an equal impact of luminous intensity and heat due to sunlight on all the sensors [6]. All the sensors placed were kept there for almost 1 min before the

actual reading taken from them. The place selected is a mechanically ventilated greenhouse in Gurgaon, Haryana. The readings were taken from each sensor after their stabilization in the current conditions, and their mean value is taken into consideration for the ventilation automation purpose. The mean values will illicit about the actual temperature levels inside a greenhouse, whereas the values noted in a single sensor can indicate the level of heterogeneity inside a greenhouse and can help in marking the heterogeneous patches. The similar activity was done for relative humidity-level measurements in the same greenhouse field structure.

3 Result and Discussion

Table 1 shows the results of temperature readings noted at two separate intervals for the random field placement, and Table 2 displays the same for a grid-style topology.

Temperature variations are experienced in the case of sensors placed near the mechanical ventilated system or door and those placed very near to the walls of a greenhouse [7]. The heterogeneous environment, created due to plant development cycle, soil characteristics, seed genetics, pests, or any other kind of infestation, can further add to the inaccuracy. Improper measurements can lead to failure of an automated greenhouse structure and can even damage a semi-automated structure whose dependency is somewhat lower on such sensors. While with a grid system, the scenario is somewhat improved, and proper placement helps to achieve a greater level of accuracy. The readings noted by the sensors in a grid-like structure are not varying much as compared to the readings taken during random placement. The random topology is having a variation of about 7 °C whereas the same variation has reduced up to 4 °C when placed in a proper grid. This grid is covering the whole region and preventing any false spike in the readings just by staying at the right place.

Random topology

	Maximum temperature (°C)	Minimum temperature (°C)	Range
12 noon	45.7	38.3	7.4
1 p.m.	47	39.7	7.3

Smart-grid topology

	Maximum temperature (°C)	Minimum temperature (°C)	Range
12 noon	44.5	41.0	3.5
1 p.m.	45.9	42.1	3.8

Tables 3 and 4 show the readings for the relative humidity at two separate intervals for random field placement and a grid topology.

Table 1 Temperature sensors placed randomly

Time	Temp. sensor 1	Temp. sensor 2	Temp. sensor 3	Temp. sensor 4	Temp. sensor 5	Temp. sensor 6	Temp. sensor 7	Temp. sensor 8	Temp. sensor 9
12 noon	41.2° C	45.7° C	38.3° C	43.4° C	42.1° C	41.9° C	40.4° C	43.1° C	41.8° C
1 p.m.	42.1° C	47° C	39.7° C	44.7° C	43.1° C	43.2° C	41.9° C	44.6° C	43.2° C

Table 2 Temperature sensors placed in grid pattern

Time	Temp. sensor 1	Temp. sensor 2	Temp. sensor 3	Temp. sensor 4	Temp. sensor 5	Temp. sensor 6	Temp. sensor 7	Temp. sensor 8	Temp. sensor 9
12 noon	41.5° C	43,4° C	41.0° C	44.5° C	43.2° C	42.6° C	41.5° C	44.2° C	42.7° C
1 p.m.	42.1° C	43,9° C	42.1° C	44.6° C	44.3° C	43.8° C	43° C	45.9° C	44.0° C

Table 3 Relative humidity at field for random placement

Sensor no.	RH 1	RH 2	RH 3	RH 4	RH 5	RH 6	RH 7	RH 8	RH 9
12 noon	65.32	69.82	61.43	65.67	63.79	64.30	66.21	64.80	65.10
1 p.m.	71.37	76.20	63.43	72.12	69.62	69.78	71.31	70.43	72.23

Note Here, RH is relative humidity

Table 4 Relative Humidity for a grid structure

Sensor no.	RH 1	RH 2	RH 3	RH 4	RH 5	RH 6	RH 7	RH 8	RH 9
12 noon	66.62	68.37	64.80	66.01	63.64	65.2	69.32	66.23	66.78
1 p.m.	72.12	74.89	71.56	72.90	69.34	72.23	76.45	73.21	74.58

Similar to temperature variations, even relative humidity has experienced the heterogeneous behavior much higher than actual. The sensors placed near to the ventilator or door have recorded differently. The variations of level in readings noted by sensors are greater in case of random arrangement, and it reduces when placed in a proper arrangement. It shows that the heterogeneous nature of a greenhouse can be more extreme if it is partially opened to the outer environment.

Random topology

	Max. (%)	Min. (%)	Range
12 noon	69.82	61.43	8.39
1 p.m.	76.20	63.43	12.77

Smart-grid topology

	Max. (%)	Min. (%)	Range
12 noon	69.32	63.64	5.68
1 p.m.	76.45	69.34	7.11

The values of relative humidity have reduced from 8.39 and 12.77 with random topology to 5.68 and 7.11 with grid-like structure, respectively. False spikes are reduced by proper sensor placement inside a heterogeneous greenhouse. Clearly, the variations generated other than by the plant development cycle can be minimized by proper arrangement of sensors and considering a proper grid can reduce the used sensor numbers while enhancing their precision.

4 Conclusion

It has been concluded from the study that increasing the number of sensors will enhance the accuracy of the system but it also proliferates the cost of production. While making a trade-off between the sensors numbers and accuracy, there should be the consideration about anomaly inside a greenhouse. These variations may arise due to variation in plant growth patterns, soil textures, seed genetics, varying seasons and crop cycle, ventilation mechanism, and its vicinity for other plants. Sensors should be placed near to the plants and should consider the incident sunlight along with the ventilators. Field placement should be similar to what is done in the cellular networks, while covering the maximum region, their placement should be done away from the walls of a greenhouse. The sensors placed randomly may get arbitrary measurements and can generate a false need of action. They can sometimes miss a crucial moment where the action was much needed, thus inviting damages to the yield. Avoiding improper sensor placement can reduce such conditions and help in determining the actual heterogeneity of the greenhouse system [8]. Temperature is one of the most crucial attributes in a greenhouse as the rates of many biological processes are affected considerably by it [9]. Thus, a special consideration has to be done for such disturbance in a greenhouse. A grid structure covers the maximum region, and sensors placed in close vicinity to each other can easily detect the distress patch. It even helps in avoiding the unknown duplicacy by sensors for measuring the same area. A well-connected grid can accumulate a much relevant data, and proper analysis can guide a farmer toward genuinely needed steps. Placing the sensors high in the greenhouse will mostly consider the ambient temperature, and this can neglect the actual temperature experienced by the plant. Placing them too close to plants is also not advised as due to transpiration relative humidity levels might shoot up and temperature levels will be reduced [2]. Plant-centric approach for automating a greenhouse can be a much reliable way for improving the crop yield and reducing the burden of other resources. Use of porous structures can improve the greenhouse interaction with outer environment, and they can exchange heat radiations and get a relief from the pests and infestation. Such interactions help a crop to improve its microclimate and reduce the need for water [9]. This can help in improving the damages done by the faulty sensor measurements.

Improved placement of sensors can help in detecting the heterogeneous patches, and actuating a suitable action can diminish the chances of pests and diseases in a greenhouse. A greenhouse could be a superb incubator for the pests or diseases occurred and can lead to large-scale damage to the crop. A proper systematic placement of the sensors can be an answer to such problems and enhance the efficiency of a greenhouse by considerably reducing the surveillance efforts of the farmers. This effective use of available sensors can reduce the cost of production and will lead to proper utilization of resources like energy, fertilizers and water, etc. It can considerably improve the utility of fully or semi-automatic greenhouses

which are otherwise less popular due to their large cost of input. A crop is affected by a lot of other factors like soil characteristics, seed genetics, pests, and variations in seasonal lengths, but at least a better prediction can help in reducing the damages [10].

References

1. Lamprinos I, Charalambides M, Chouchoulis M (2015) Greenhouse monitoring system based on a wireless sensor network. In: 2nd international electronic conference on sensors and applications
2. Bartzanas T, Kittas C (2007) Greenhouse microclimate and dehumidification effectiveness under different ventilators configuration. Build Environ 42(10):3774–3784
3. Kittas C, Katsoulas N, Bartzanas T, Bakker S (2013) Greenhouse climate control and energy use. In: Baudoin W, Castilla N, Qaryouti M (eds) Good agricultural practices (GAPs) principles for greenhouse vegetable production in the Mediterranean region, FAO publications, pp 63–96
4. Zorzeto TQ, Leal PAM, de Souza Coutinho V, de Arajo HF (2014) Gradients of temperature and relative humidity of air in greenhouse with wireless sensor network. In: 2nd international conference on agriculture and biotechnology, PCBEE, vol 79, IACSIT Press, Singapore
5. Balendonck J, van Os EA, van der Schoor R, van Tuijl BAJ, Keizer LCP (2010) Monitoring spatial and temporal distribution of temperature and relative humidity in greenhouses based on wireless sensor technology. In: International conference on agricultural engineering-AgEng, Cemagref, France, pp 443. ISBN: 978-2-85362-684-2
6. Runkle E (2011) Measuring greenhouse temperature. https://www.Gpnmag.com, retrieved from http://www.flor.hrt.msu.edu/assets/Uploads/Measuringtemperature.pdf, Mar 2011
7. Flores-Velazquez J, Montero JI, Baeza EJ, Lopez JC (2014) Mechanical and natural ventilation systems in a greenhouse designed using computational fluid dynamics. Int J Agric Biol Eng 7(1):1–16
8. Ryu M, Chung S, Kim K, Huh Y Determination of sensor locations for monitoring of greenhouse ambient environment, proceedings international society of precision agriculture
9. Tanny J (2013) Microclimate and evapotranspiration of crops covered by agricultural screens: a review. Biosys Eng 114(1):26–43
10. Khan SA, Kumar S, Hussain MZ, Kalra N (2009) Climate change, climate variability and indian agriculture: impacts vulnerability and adaptation strategies. In: Singh SN (ed), Climate change and crops, environmental science and engineering, Springer, Berlin, Heidelberg. https://doi.org/10.1007/978-3-540-88246-6_2

Load Comparison of Solar Plant Generation and Solar Hydrogen Energy System

Rashmi Jain, Rahul Sharma and Preeti Dahiya

Abstract This paper deals with the design, implementation, and operation of a solar hydrogen energy system. The hydrogen system consists of electrolyzer, pressurized gas storage, and compressor. The electrolyzer converts the electrical energy into chemical energy in the form of hydrogen during daytime which is stored for further usage. This stored hydrogen can be used to drive vehicles and in case of shortage of power supply, and it can be reconverted to electrical energy by reverse electrolysis that takes place in a fuel cell. This results in improved efficiency of renewable energy system by the use of hydrogen energy systems. This proposed work has the advantage of efficiency enhancement as well as reduces the environmental issues such as pollution. The different parameters such as number of photovoltaic (PV) modules, current drawn, power delivered, battery bank capacity, and hydrogen plant are studied, and the calculations for solar-integrated hydrogen module present at National Institute of Solar energy is presented in this chapter.

Keywords Electrolyzer · Compressor · Buffer tank · Distribution box · Solar modules · Battery banks · Energy calculation

R. Jain (✉) · R. Sharma
Department of Electrical Engineering, J.C. Bose University of Science & Technology, YMCA, Faridabad, Haryana, India
e-mail: rashmiagarwal404@gmail.com

R. Sharma
e-mail: rahulsharma41295@gmail.com

P. Dahiya
Department of Electrical and Electronics Engineering, ABES Engineering College, Ghaziabad, Uttar Pradesh, India
e-mail: preetieednith@gmail.com

1 Introduction

Nowadays, energy demand has been continuously increasing, and to attain the power balance between generation and load demand is a very tedious task for the electrical engineers. The 1973 energy crisis brought the world to the fact that sooner or later the fossil fuels will be depleted. In the present scenario, the power generation using conventional power sources posed the problems such as acid rain, global warming, ozone layer depletion, and oil spills [1]. This arise the need to use alternative sources of energy which reduces the environmental problems and helps in achieving the sustainable energy. Basically, there are two possible approaches to achieve sustainable energy production, namely Olle and radical approach. The efficiency of energy production is improved using Olle method. In this approach, the ratio between energy input and desired energy output is improved which in turn improves the system efficiency, whereas radical approach aims to find the alternative of the present sources of energy. Keeping the limitations posed by the fossil fuels, during recent times, renewable sources of energy, namely solar power, wind power, etc. are being used for electric power generation as they are environmental friendly and helps in achieving the sustainable energy.

The present paper has focused on solar energy because solar energy is available in plenty and is widespread everywhere on the earth. Due to improved technology and reduced costs, the photovoltaic cells have become a great area of research for engineers for generating electricity. The advancements in technology are likely to bring further significant cost reductions in the future. The low intensity and wide distribution of renewable sources favor decentralized power generation. Therefore, energy from renewable sources will often not require much further distribution since the resources are already distributed. The solar energy has a great variation on daily and seasonal basis which is the major concern for researchers for obtaining the constant power. This problem can be solved if there must be a relation between load and present energy availability. However, this is not possible on practical basis. The intermittent nature of renewable sources of energy arise the need of efficient storage, so that the alternative sources of power generation can be utilized to full extent. Contrary to its need and high efficiency, the battery energy storage is expensive.

This issue of storing the renewable energy got resolved with the introduction of hydrogen which can be effortlessly produced by the electrolysis process. Hydrogen can be produced at any location using local renewable energy sources and reconverted to electricity by using the fuel-cell power plants. The solar and wind energy can be easily stored by the hydrogen which can then be converted to electricity, and hence hydrogen forms a renewable storage carrier of electric power and gives reliable output. Compared to battery storage, hydrogen storage has improved storage density, economies of scale, temperature response characteristics, and lifetimes. Considering these advantages, hydrogen is considered to be the cheaper and compact storage source. Hydrogen (H) is the lightest and most abundant element in the universe. On a molar basis, 2/3 of the oceans is hydrogen. The advantages of hydrogen make it the ideal component of a renewable sustainable

energy system of the future. Hydrogen is a useful energy carrier for numerous reasons, namely easily producible, storable, environmental friendliness, etc. The problems that are faced during the development of the hydrogen production by solar thermal water splitting (HSTWS) process are [2]:

a. Using secondary concentration of solar energy to attain high temperatures in hydrogen reactors;
b. Manufacturing of materials for the solar reactor; and
c. Improvement in ceramic membranes for resisting the clogging.

Theoretical thermal efficiency of hydrogen production can be calculated by one-step water splitting utilizing solar heat at high temperatures where Carnot efficiency is assumed as effective work input, and the solar collection efficiency is assumed as the total energy input [3]. In 1977, Nakamura investigated the possibilities of producing hydrogen and oxygen from water utilizing solar heat at high temperatures. The thermodynamic requirements for the direct thermal decomposer are difficult to realize from the structural viewpoint and that existing separation methods are not applicable to attain sufficiently high thermal efficiencies [4, 5]. Fuel cells can use hydrogen as a fuel, offering the prospect of supplying the world with clean, sustainable electrical power [6, 7].

In the present paper, the load balancing of solar-powered hydrogen plant of National Institute of Solar Energy is studied. The different parameters, namely number of photovoltaic (PV) modules, current drawn, power delivered, battery bank capacity, hydrogen plant, etc. are studied, and the calculations are presented in Sects. 3 and 4.

2 System Modeling and PV Solar Specification

Hydrogen production facility at National Institute of Solar Energy (NISE) is installed in December 2013. This plant is India's second hydrogen production plant after Indian Oil Corporation Limited (IOCL) research at Faridabad. But, it is the first with integration with solar plant, i.e., purely renewable hydrogen production. The production facility consists of two plants which are:

a. Solar plant for electric energy generation.
b. Hydrogen plant for hydrogen production from electrolysis of water.

2.1 Modules Arrangements

Modules are arranged in a systematic manner, so that required level of voltage maintained for the proper functioning of inverter and energy requirement is fulfilled
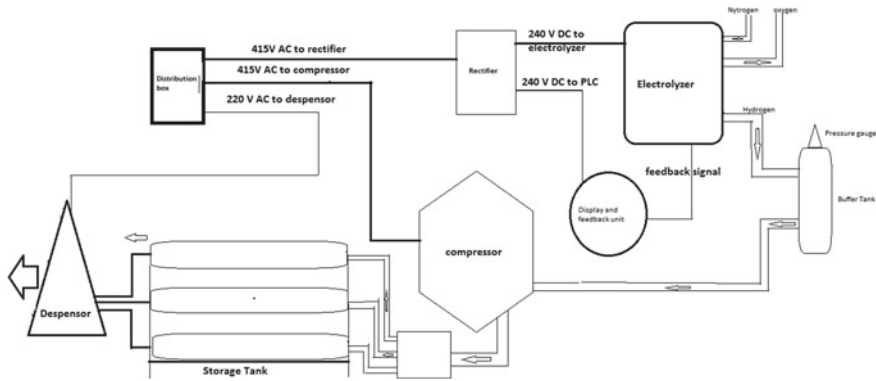
Fig. 1 Block diagram representation of solar-powered hydrogen generation and dispensing facility

for satisfactory operation of load (hydrogen plant). The arrangement of the modules according to inverter specification is shown in Fig. 1. The required value of voltage for operation of inverter is 440 V (DC). The maximum voltage generated by one photovoltaic (PV) module is 36.7 V (DC).

Number of modules in series to get required voltage is = 440/36.7 = 11.98 (say 12 modules).

Max current drawn from single module is 8.04 A.

Power from string of 12 modules in series is = 12 * 36.7 * 8.04 = 3.54 KW.

Power is delivered to the inverter through the junction boxes. The maximum capacity of single junction box is to transfer 25 KW power.

The number of string connected to single junction box is = 25/3.54 = 7.06 (7 strings as shown in Fig. 1).

The required capacity of the plant is 120 kW.

The power delivered by one junction box is = 7 * 3.54 = 24.78 kW.

The number of junction boxes required for 120 kW power delivery is = 120/24.78 = 4.843 (not possible).

The number of junction boxes chosen is 5 which are arranged as shown in Fig. 2.

The power generation capacity of plant is = 5 * 24.78 = 123.9 kW.

The power generated by single module is 295 W_P.

The arrangement of string and power division between hydrogen plant and grid is shown in Fig. 3. The number of PV modules required to generate this power is 408 which is mounted on the rooftop of the workshop of NISE whose arrangement layout is shown in Fig. 4. The generated power through this plant is supplied to the hydrogen plant and rest is fed to the grid. During foul and stormy weather, solar plant is not able to generate the required level of energy for the plant. A battery bank is installed in NISE premises that take care of these types of disturbances. The capacity of battery bank is discussed in the subsequent section.
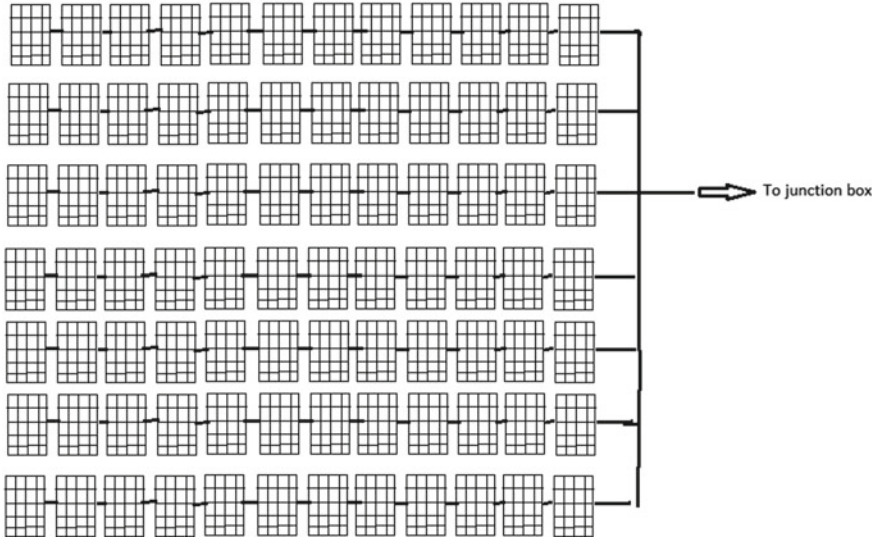
Fig. 2 Arrangement of solar panels at each junction box
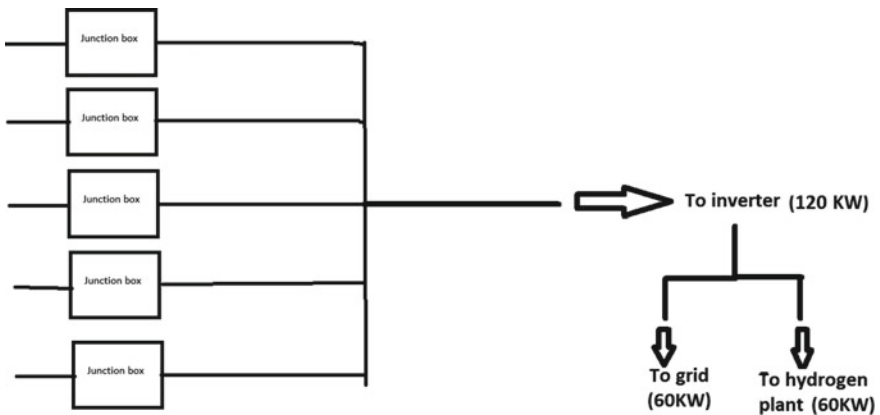
Fig. 3 Arrangement of string and power division between hydrogen plant and grid

2.2 Battery Bank Capacity

The battery bank for power backup is made up of 2 V, 850 Ah cells arranged in array (string) of 240 V (DC).

The number of cells in each string = 240/2 = 120
Total energy stored by each string = 240 * 850 = 204 kWh
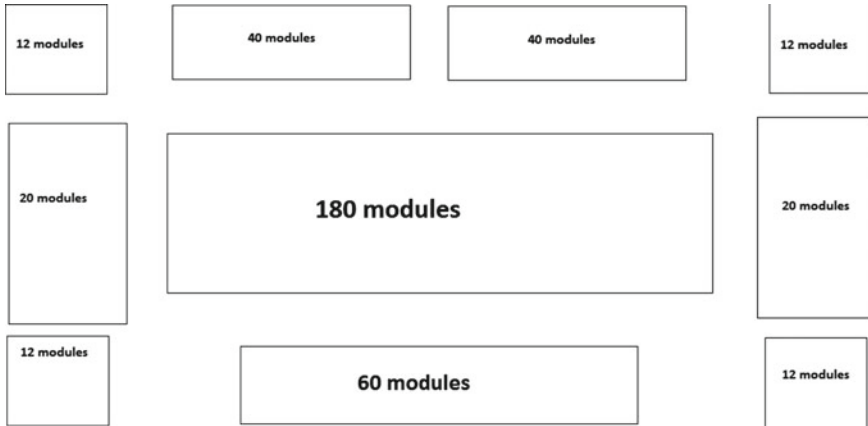
Fig. 4 Module structure arrangement at rooftop (top view)

Total number of battery string = 5
Therefore, total power stored by battery bank = 5 * 204 = 1020 kWh

So, a load of 102 kW can be drawn for duration of 10 h approximately.

2.3 Hydrogen Plant

The production of hydrogen takes place in the compartment by electrolysis of water by alkaline-based electrolyzer (KOH). The hydrogen produced so is stored in pressure by a two-step process, i.e., from electrolyzer to buffer tank at low pressure (9.5–10.5 bars) and from buffer to high pressure storage tank using compressor at high pressure (up to 350 bar). The impurity during the production process went out by using nitrogen and electrolyzer delivers hydrogen at the purity level of 99.999% to buffer tank. The flowchart of energy in electrical and chemical form is shown in Fig. 5.

3 Observations

See Table 1.
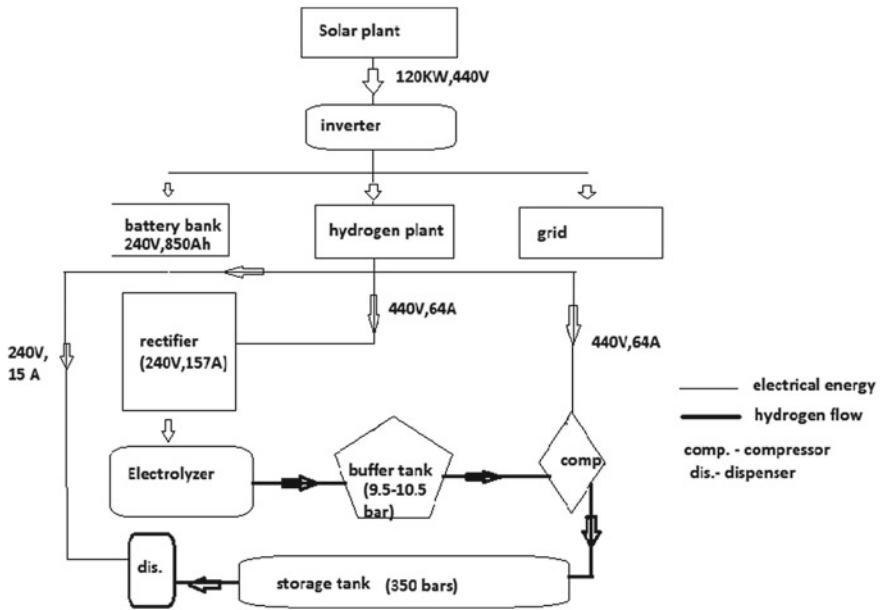
Fig. 5 Flowchart of energy in electrical and chemical form

4 Results

The energy calculation sheet on which different parameters are measured to analyze the performance of the plant is shown in Table 1. The hydrogen production by the plant with respect to electric energy consumed depicted in Fig. 6 and hydrogen delivered to buffer from the electrolyzer with respect to the electric energy consumed shown in Fig. 7 are plotted using the energy calculation sheet given in Table 1. It can be observed from Figs. 6 and 7 that the electric energy consumed shows sudden rise due to continuous energy consumption by the auxiliary components on 21 August, 2017 they consume energy in that interval of time, but the production of hydrogen is not there. Therefore, considers hydrogen production of one day and auxiliary consumption is of more than two days, i.e., after 18 August, 2017 16:45 to 21 August, 2017 up to 17:28 energy consumed is 470 kWh, but production is only 35.7 Nm^3 which is actually generated on 21 August, 2017 from 9:00 am only.

Table 1 Energy calculation sheet

Date	Time	Total running time	Electric energy consumed	H₂ produced	H₂ Delivered	Energy/H₂ produced	Duration (h)	H₂/day	Energy
11-08-17	16:35	542.56	48.29	2752.1	2262.7	17.3913	5.11	27.6	480
14-08-17	16:58	547.67	48.77	2779.7	2282.4	11.86944	6.23	33.7	400
16-08-17	17:45	553.9	49.17	2813.4	2305.9	8.648649	6.9	37	320
17-08-17	18:30	560.8	49.49	2850.4	2334.7	8.579088	7	37.3	320
18-08-17	16:45	567.8	49.81	2887.7	2364.3	13.16527	6.62	35.7	470
21-08-17	17:28	574.42	50.28	2923.4	2391.2	8.743169	6.85	36.6	320
22-08-17	17:31	581.27	50.6	2960	2420.1	9.142857	3.23	17.5	160
23-08-17	11:38	584.5	50.76	2977.5	2430.1	8.189655	8.75	46.4	380
24-08-17	17:39	593.25	51.14	3023.9	2467	9.230769	4.87	26	240
25-08-17	16:24	598.12	51.38	3049.9	2487.3	14.91935	4.6	24.8	370
28-08-17	17:40	602.72	51.75	3074.7	2499.4	8.12892	6.03	30.4	270
29-08-17	17:03	608.75	52.02	3105.1	2522.9	8.8816	5	28.7	250
30-08-17	17:21	613.75	52.27	3133.8	2544.3	8.71	5.53	29.4	260

Fig. 6 Hydrogen produced (Nm^3) with energy consumed (in MWh)
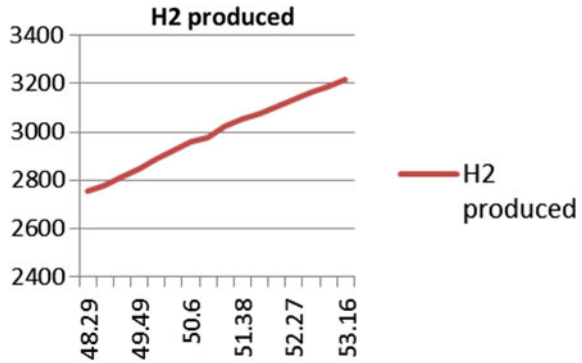
Fig. 7 Hydrogen delivered (in Nm^3) with respect to energy consumed (in MWh)
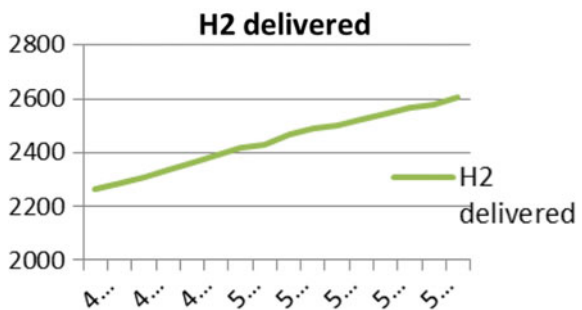
4.1 Energy Required by Hydrogen Plant

Energy required by plant for generating 35 Nm^3 of hydrogen with losses = 338.8847 kWh
Energy required by auxiliary devices = 80 kWh (16 h)
Energy required per day for generating without losses = 258.847 kWh
Energy required per annum = 338.847 * 365 = 123.679 MWh approx.

Energy generated by solar plant

Length of PV module = 203 cm
Breadth of PV module = 114 cm
Area of module = 23,142 cm^2
As total no of module in the plant are 408
So total area exposed to sun is = 9,441,936 cm^2 = 944.1936 m^2
And the efficiency of plant is approx. = 20%
Average annual radiation received on ground = 1,544,193 Wh/m^2

Temperature coefficient is taken as 0.45% per degree rise in temperature above STC.

Fig. 8 Hydrogen delivered
(in Nm^3) with respect to
energy consumed (in MWh)
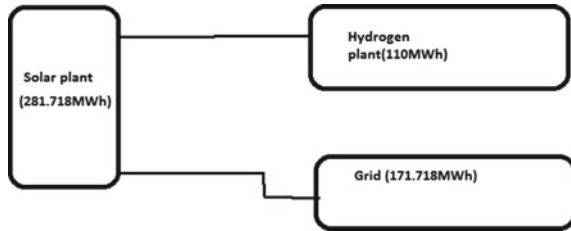
Therefore, Energy generated = GHI $[1 - 0.45/100(T - 25)]$ * Efficiency
Total energy generated annual per m^2 is = 298.369 kWh/m^2
Total energy generated by plant = 298.369 * 944.1936 = 281.718 mWh annually

Figure 8 shows the distribution of energy between hydrogen plant requirement
and excess energy to the grid of Haryana power utility. The generating ability of
solar plant is 281.718 MWh. Energy required by hydrogen pant is 110 MWh, and
energy supplied to grid is 171.718 MWh.

5   Conclusion

In the present paper, the load balancing of solar-powered hydrogen plant of
National Institute of Solar Energy is studied and it is concluded that the plant is
purely renewable and independent source of energy and do not require any energy
from grid.

The hydrogen produced is able to meet the load demand in addition to the solar
energy produced using the specified number of PV modules.

References

1. Ma J, Renewable energy system for house hold applications. Master of Science program in Environmental Science, Lund University
2. Kogan A (1998) Direct solar thermal splitting of water and on-site separation of the products-II experimental feasibility study. Int J Hydrog Energy 23:89–98
3. Ihara S (1980) On the study of hydrogen production from water using solar thermal energy. Int J Hydrog Energy 5:527–534
4. Nakamura T (1977) Hydrogen production from water utilizing solar heat at high temperature. Solar Energy 19:467–475
5. Cook B (2002) Introduction to fuel cell and hydrogen technology. Eng Sci Educ J, 11
6. Lina FS, Iqbal MT (2009) Remote control of power connected to grid in a small distributed generation system. Electr Comput Eng
7. Dawood N (2016) Review of different DC to DC converters based on renewable energy applications. IRJET 3:46–50

Techno-Economic Evaluation of AC and DC Microgrid Systems

Sandeep Dhundhara, Yajvender Pal Verma and Arthur Williams

Abstract The paper presents the comparative techno-economic analysis of AC and DC microgrid systems. Both microgrids consist of PV–wind renewable energy sources (RESs) based generating system, battery bank to store and supply the excess electricity and a diesel generator for reliable operation under the absence of intermittent generation. The performance of the two types of microgrids has been evaluated using real load profile, actual prices of components, and realistic wind and solar resources data. The load profile of the business organization (IT building) of the city Hyderabad in India has been considered. The results include the response of microgrid in the day of summer and winter, various generators electricity generation response, overall cost of AC–DC microgrid under the given scenarios, detail comparison between the various components cost and battery state of charge. It has been validated through simulations that DC microgrid system requires lesser converter unit as compared to AC microgrid system. Further analysis revealed that DC microgrids are economically more feasible as compared to AC microgrid and reduce the losses significantly which are associated with AC–DC conversion in several applications of electric power system.

Keywords AC–DC microgrid · Wind · Solar · HOMER

S. Dhundhara (✉) · Y. P. Verma
UIET, Panjab University, Chandigarh 160014, India
e-mail: sandeepdhundhara@gmail.com

Y. P. Verma
e-mail: yp_verma@pu.ac.in

A. Williams
University of Nottingham, Nottingham NG7 2RD, UK
e-mail: arthur.williams@nottingham.ac.uk

1   Introduction

A microgrid is a small-scale local power system that consists of distributed generators, converters, energy-storage units and loads, which can be operated independently or collaboratively with the main power grid. The major fraction of total power can be generated by renewable energy sources (RESs) based generators in the microgrids that contribute greener, reliable power with reduced losses and lesser network congestion as compared to conventional generation systems [1]. They are becoming a good medium for integrating RESs and also provide support to overcome the energy challenges and reliability problems of the power systems. The microgrid configuration can be AC, DC or hybrid [2].

The arrival of electronically based distributed generation has upheld attention on the DC paradigm for power distribution owing to drastic changes within the nature of loading. Also, the greater economies are possible when RESs such as photovoltaic (PV) and wind along with energy-storage systems (ESSs) are incorporated into DC instead of an AC system [3].

Various studies related to operational issues of several types of microgrids (AC, DC and hybrid AC/DC) are available in recently published literature [1–10]. The detailed review about the possible control strategies employed in an AC microgrid system is given in Ref. [2]. Li et al. proposed a droop-control-based technique to maintain the small-signal stability of islanded hybrid AC/DC microgrids. The time-/frequency-domain analyses have been performed to explore the small-signal enactment of hybrid DC/AC microgrids in this study [4]. An in-depth overview about the most recent advances in DC distribution systems has been discussed by Elsayed et al. [5]. The reviews on the different interconnection-based topologies of the AC/DC networks and the conventional electrical network have been deliberated by Unamuno et al. [6]. The substitute DG units' configurations in the low-voltage AC/DC distribution networks in the perspective of the existing and the forthcoming consumer equipment's in future electricity market have been discussed by Justo et al. [7]. The advantages and application of AC–DC and hybrid microgrids which includes grid architecture, operation control, energy management and protection strategy have been introduced and analysed by Zhu et al. [8]. Planning of AC/DC microgrids to reduce total planning cost, which comprises the cost of converters, DER's investment and operational, reliability and energy purchase from the grid has been done by Lotfi et al. [1, 9]. Fregosi et al. have evaluated the DC and AC microgrid systems for commercial buildings and explored that the generated PV energy utilization in Bosch DC microgrid is 6–8% more proficiently than conventional AC systems [10]. An in-depth study about the planning and optimization of the DC microgrid system for various load scenarios is presented in Ref. [11].

In literature, many authors have worked on the various issues of AC, DC and hybrid microgrid systems. However, the techno-economic assessment of AC and DC microgrid systems is not well studied in the literature. Therefore, an attempt has been made to execute the techno-economic investigation of AC–DC microgrid systems. The main contributions of this study are as follows:

- The isolated AC and DC microgrid systems consisting of diesel, PV and wind-resource-based generators with battery bank in an urban scenario has been designed.
- The real resources data with real-time load profile, and actual prices of components have been used to investigate the performance of proposed microgrids.
- The optimum size of the microgrid components on the basis of least cost of energy and minimum total net present cost (TNPC) has been attained.
- Finally, the techno-economic performances of the AC and DC microgrids have been investigated and compared.

The remaining paper is organized as follows: brief detail about microgrid components modelling and their economic parameters are presented in Sect. 2. The information about the load profile and the resources data of the selected locations are represented in Sect. 3. Sections 4 and 5 include the simulation results and conclusion, respectively.

2 Modelling and Economic Parameters of the Microgrid Components

Microgrid generally consists of different generating sources such as microturbine (MT), diesel–biodiesel/biogas generator, fuel cell, wind generator, PV system, centralized control system, loads and storage system which situated inside a clearly defined electrical boundary [12]. In this study, both AC and DC MGs consist of conventional (diesel) units, solar plant, wind plant, AC–DC converter and battery energy-storage system as depicted in Fig. 1.
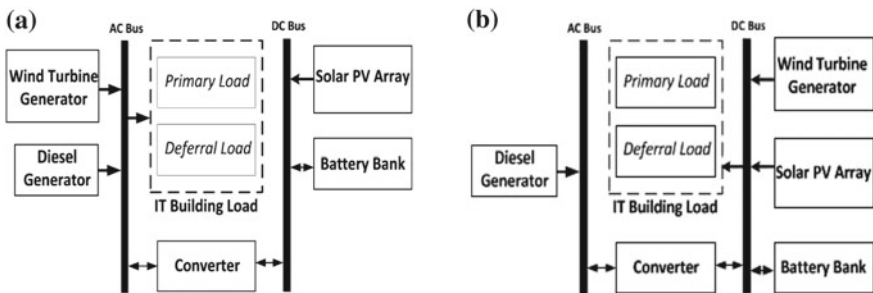
Fig. 1 Block diagram of microgrid system having PV/battery/wind/diesel hybrid system **a** AC microgrid, **b** DC microgrid

2.1 Solar Photovoltaic Generator

The solar energy available from the sun is converted into useful electrical energy with the help of solar PV generator. This photoelectric conversion mainly relies on the geographical locations and atmospheric conditions of the installed PV generators [13]. The electrical power output (P_{SPV}) of a solar PV generator can be expressed as follows:

$$P_{SPV} = G_{PV} f_{PV} \left(\frac{I_T}{I_{T,STC}}\right) \left[1 + \alpha_P \left(T_C - T_{C,STC}\right)\right] \tag{1}$$

where, I_T and $I_{T,STC}$ denote the radiation (kW/m^2) incident on the PV panels at any instant of time and at standard test conditions (STC) (1 kW/m^2), respectively. The rated capacity of the PV generator is denoted by G_{PV}. T_C and $T_{C,STC}$ denote the cell temperature (°C) of the PV panels at any instant of time and at STC (25 °C), respectively. f_{PV} represents the derating factor of the PV system, α_P is the temperature coefficient of power (%/°C) [11, 13–15].

Further, the velocity of wind and temperature around the cell of PV panels primarily impact the output power of the PV generator. The energy balance corresponding to PV system can be stated as given below:

$$(\tau\alpha)I_T = I_T\eta_{PV} + U_L(T_C - T_a) \tag{2}$$

where, $(\tau\alpha)$ represents the actual transmittance-absorptance of the PV panel, η_{PV} and U_L denote the efficiency and surroundings heat-transfer coefficient of the PV array, T_C and T_a designate the cell and ambient temperature of the PV module, respectively [14]. Equation (2) can be rewritten as shown below:

$$T_C = T_a + I_T \left(\frac{\tau\alpha}{U_L}\right)\left(1 - \frac{\eta_{PV}}{\tau\alpha}\right) \tag{3}$$

The value of η_{PV} considered as zero at no load conditions. Then, Eq. (3) can be expressed as follows:

$$\frac{\tau\alpha}{U_L} = \frac{T_C^{NOCT} - T_a^{NOCT}}{I_T^{NOCT}} \tag{4}$$

where, the solar irradiation at NOCT (0.8 kW/m^2) is denoted by I_T^{NOCT}, $T_{C,NOCT}$ denotes the nominal operating cell temperature (NOCT) and T_a^{NOCT} represents the atmospheric temperature at NOCT of the PV array. Hybrid Optimization Model for Multiple Energy Resources (HOMER) takes the value of $(\tau\alpha)$ as 0.9. By utilizing the value of $(\tau\alpha)$, the temperature at the cells of a PV panel can be stated as follows [14]:

$$T_C = T_a + I_T \left(\frac{T_{C,NOCT} - T_{a,NOCT}}{I_{T,NOCT}} \right) \left(1 - \frac{\eta_{PV}}{\tau\alpha} \right) \tag{5}$$

This study has been carried out on PV module of multi-crystalline structure and flat-plate type. The efficiency at STC (%) has been taken 14.5%, whereas lifetime and derating factor of the PV panels are 20 years and 80%, respectively [11]. The overall capital cost which comprises panels, installation, delivery, wiring and mounting hardware charges is 840 $/kW, whereas the replacement and operation and maintenance (O&M) costs are $800 per kW and 10 $/kW/year, correspondingly for the PV system [16].

2.2 Wind Generator

A wind turbine generator (WTG) produces electrical energy by using mechanical energy of the wind. The wind turbine generator's power output (P_{wt}) can be expressed as given below:

$$P_{wt}(v) = \begin{cases} \frac{P_r(V - V_{cin})}{V_{rat} - V_{cin}} & V_{cin} \leq V \leq V_{rat} \\ P_r & V_{rat} \leq V \leq V_{CO} \\ 0 & V \leq V_{cin} \text{ and } V \geq V_{CO} \end{cases} \tag{6}$$

where P_r denotes the rating of a WTG, V_{CO} and V_{cin} represent the cut-out and cut-in speed. V_{rat} and V denote the rated wind speed and wind velocity at chosen height, respectively [14]. Mainly, the wind speed depends on the geographic location and the particular hub height at which the WTG is installed.

Further, the velocity (V) of wind at a height of 'H' can be expressed as shown below:

$$V = V_{ref} \left(\frac{H}{H_{ref}} \right)^{\alpha} \tag{7}$$

where, V_{ref} describes the velocity of wind considered at the reference height (H_{ref}), α denotes the exponent that relies on season, speed of the wind, roughness of the surface, time of day and temperature. The exponent value at constant wind flow is 1/7 in this study [14]. The generated power of the WTG varies with change in wind speed or air density. To standardize the realistic conditions, the power value and air-density ratio which are prophesied by the power curve is utilized by the HOMER which can be expressed as follows:

$$P_{wt} = \left(\frac{\rho}{\rho_O} \right) P_{wt,(STP)} \tag{8}$$

where the power output of a WTG at standard temperature and pressure (STP) is denoted by $P_{wt,(STP)}$, ρ represents the actual density, and ρ_O denotes the density at STP (1.220 kg/m^3) of the air [14, 15].

A generic WTG of 10 kW rating capacity having capital and replacement cost of equal values amounting $11,539 and O&M cost of 230 $/year has been considered in the study. The lifetime of the WTG is 20 years, and it is operated at a hub height of 25 m. The rated speed of the WTG is 12 m/s, whereas the cut-out (V_{CO}), and cut-in (V_{cin}) speed are 24, 3 m/s, respectively [11].

2.3 Diesel Generator

The fuel-consumption rate to generate electricity by a diesel generator (DG) can be denoted as given below:

$$F = F_{0,DG}Y_{DG} + F_{1,DG}P_{DG} \tag{9}$$

where, F_1 and F_0 represent slope and intercept coefficient of the fuel curve, Y_{DG} and P_{DG} denote the rated capacity and maximum power generated by the DG [11, 14].

A generic DG set of rated capacity 1 kW having capital and replacement cost of 385 $/kW, each is considered for simulation. The lifetime of the genset is 15,000 h, whereas the cost of O&M of the genset unit per kW is 0.150 $/h. [11]. The price of the fuel (diesel) is considered as 1 $/l [11].

2.4 Power Converter

A power converter is used to synchronize the AC–DC bus and other components of the microgrid system for AC–DC conversion as presented in Fig. 1. The required capacity of the converter generally depends on peak load demand (P_L^{max}) [14]. The rating of the inverter (P_{inv}) can be represented as given below:

$$P_{inv} = P_L^{max}/\eta_{inv} \tag{10}$$

where η_{inv} designates the efficiency of the inverter [13, 15].

Here, the capital and replacement cost of the converter is taken as $127 per kW. While, the O&M cost of the converter is considered as 1 $/kW/year. The round-trip efficiency of 90% with lifetime of 15 years is considered for the converter unit in this study [13, 15].

2.5 Battery

The surplus energy from renewable generators is stored in the battery bank during low power demand. Then, the stored energy is utilized back into the microgrid during insufficient electricity generation from renewable generators as well as during peak or sudden load demand. The flooded lead-acid (LA) battery of 1 kWh (12 V, 83.4 Ah) has been used for simulation in this study. The battery has 40% of minimum SOC, 100% of initial SOC, with 80% round-trip efficiency. The cost of the battery is 124 $/kWh with same replacement cost. The floating life of the battery is 4 years with 800 cycle life at maximum depth of discharge (DOD) [11, 17, 18].

2.6 About Economic Parameters

The total net present cost (TNPC) and per-unit cost of energy (COE) are the main parameters to estimate the economic viability of any microgrid system.

2.6.1 Cost of Energy

The COE is the ratio of the annual cost of the components of the microgrid system with respect to energy generated/served by the different generators. The amount of actual demand served by the generated after excluding excess energy gives the energy generated/served. Mathematically, the COE can be expressed as follows:

$$\text{COE} = \frac{C_A}{E_S} \tag{11}$$

where 'E_S' is the energy served during the year and 'C_A' represents the overall yearly cost [14]. The overall annual cost includes C_{A_CC} (annual capital cost), $C_{A\_O\&M}$ (annual operation and maintenance cost), and C_{A_rep} (annual replacement cost) which can be calculated as follows:

$$C_A = C_{A\_CC} + C_{A\_rep} + C_{A\_O\&M} \tag{12}$$

2.6.2 Net Present Cost

The present value of all the costs (initial capital costs, O&M, replacement and fuel costs) of the microgrid system incurs over its lifespan, minus the current value of all the revenue it makes over its lifetime gives the total net present cost (TNPC) of the system. The revenues consist of salvage values of components of the whole system for the total lifetime of the project. The TNPC is stated as follows:

$$\text{TNPC} = \frac{C_A}{\text{CRF}(n,i)} \tag{13}$$

where the capital recovery factor can be symbolized by $\text{CRF}(n,i)$, n stands for total number of years and i represents the real yearly interest rate [14]. Moreover,

$$\text{CRF}(n,i) = \frac{i(i+1)^n}{(i+1)^n - 1} \tag{14}$$

where $i = \frac{-f + i_{\text{nom}}}{f+1}$.

where i_{nom} is the nominal rate of interest and f indicates yearly rate of inflation. The lifespan for the project is assumed 20 years with 2% yearly rate of inflation and a discount rate of 8% [15].

3   Introduction About Resources Data and Estimated Load Profile

The simulation study has been done for AC and DC microgrid systems by using the load data of an IT building of the city Hyderabad in India. The complete detail about the demanded load is given in Ref. [11]. The organization (IT building) considered for study incorporates a total area of 3.81 km^2. The electrical load of the building is distributed into deferrable and priority loads. Figure 2 shows the average daily load pattern of the priority load of the building. The building has an average daily demand of 2.8 MWh with a peak demand of 245 kW. The nature of load demand is AC for AC microgrid and DC for DC microgrid with the same rating. There is good obtainability of wind and solar resources all over the year at the selected location for microgrid study. The real data of wind and solar resources obtained from NASA(National Aeronautics and Space Administration) surface meteorology and solar energy database are considered for simulation in this study. Figure 3a and b shows the yearly average solar radiation having value of 5.24 kWh/m^2/day and yearly average wind speed having value of 5.45 m/s [11].
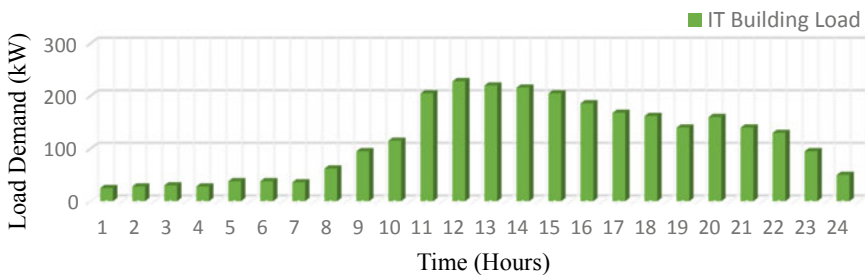
Fig. 2 Average load profile (24 h) of an IT building of city Hyderabad in India

(a)

(b)
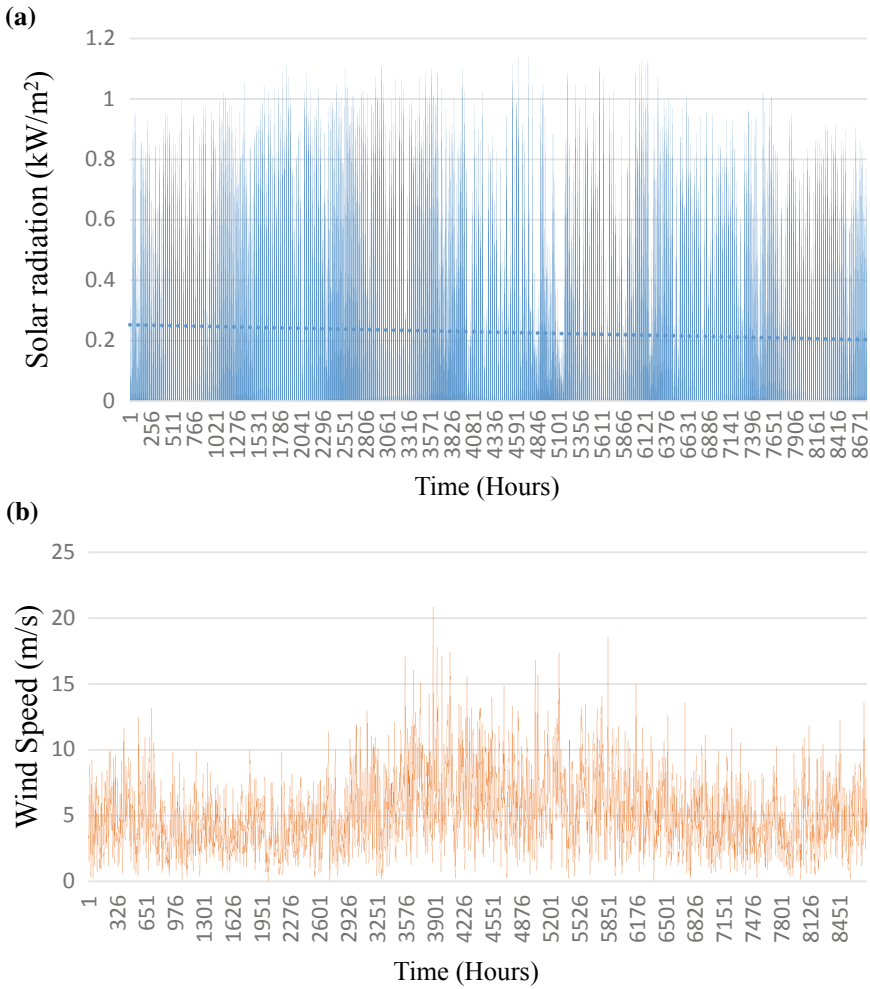
Fig. 3 Resource data of the selected location **a** solar Global Horizontal Irradiance (GHI) data, **b** average monthly wind speed data

4   Simulation Results and Discussion

The simulation results obtained demonstrate the performance of AC and DC microgrid systems. DC and AC microgrids having different sources of generation which include PV, DG, WTG and storage batteries, have been executed using HOMER-2018 (13.11.3) software. The realistic electricity load profile has been

used for carrying out the simulations and deriving analysis from them. One USD dollar has been assumed equivalent to ₹64 Indian rupees (INR) and USD dollar ($) is the currency used for the study. The following case studies have been performed to investigate the microgrid's response.

The simulation was performed and an optimal combination component for AC and DC microgrid systems was obtained. A 732-kW PV system, 120-kW WTG, 200-kW DG and 2000 units of 1 kWh each lead-acid (LA) batteries with combined dispatch (CD) dispatch strategy are needed to satisfy the load demand of IT building. The main difference between the AC and DC microgrid system components is the inverter rating. AC microgrid system requires a converter unit of 417 kW, but DC microgrid system requires a converter unit of 219 kW. A cost of approximately 0.205 $/kWh is required to have a continuous supply of power from the AC microgrid, whereas it is 0.198 $/kWh for the DC microgrid system. The simulation results of a DC microgrid system consisting of PV, wind and diesel generator have been shown in Figs. 4, 5 and 6.

Figure 4(a and b) shows the waveforms depicting the power generated by the various generators, SOC of battery and load power demand for the month of June (summers) and December (winters). Figure 4a depicts the total primary load and battery's SOC, and Fig. 4b shows the power generation response from PV, WT and diesel generator. It can be seen from the results that RESs not only meets the load demand but also keep the full charging state of the battery. When PV and wind generation is not available, diesel generator comes into play and balances the deficits. Thus, the microgrid system maintains reliable power supply besides meeting energy demand through PV, wind, batteries and diesel generator.

Annual power generation share of different generating sources of the microgrid is shown in Fig. 5. As the rating of PV is higher, the annual average production of power from the PV is higher than WTG. Availability of solar irradiances and wind speed at a particular location decide the power generated by PV and WTG, respectively. The power generation variability of PV and WTG is countered by the application of DG.

Figure 6 represents the average SOC of the lead-acid battery units for every month of the year. It can be analysed from the results that the SOC is retained well inside the stated limit of LA (40–100%) batteries. The obtained results in the figure also reveal that the consumption of power from the battery banks increases during summers as compared to winters. The batteries are utilized maximum during the cold-season months of January and hot-weather season spanning May to September.

The detailed investigation of the different components of AC and DC microgrid costs has been shown in Table 1. The net cost of AC microgrid is around $2,409,391.34 and for the DC microgrid, it is around $2,332,552.72. It is assumed that the lifespan of PV and WTG is equal to that of the project lifetime; hence, replacement cost of the two has not been taken. However, for diesel generator, the
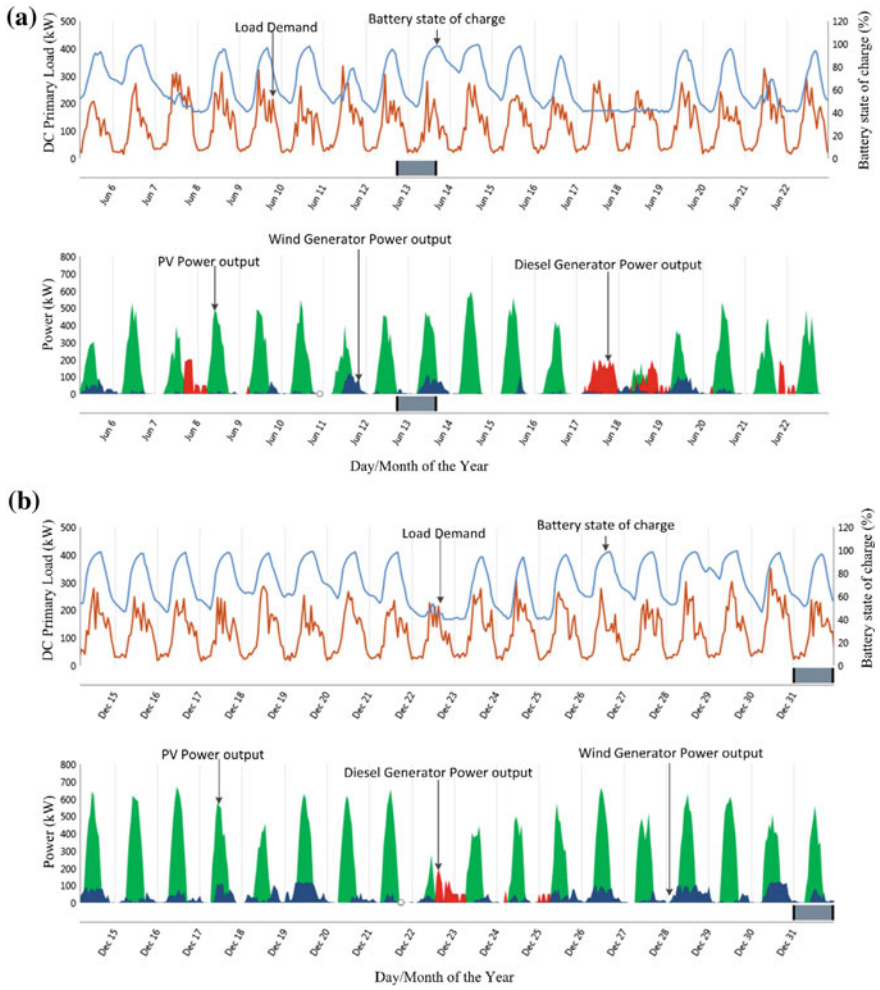
Fig. 4 Power generation by different sources and SOC of battery for a load of **a** second week of June, **b** third week of December
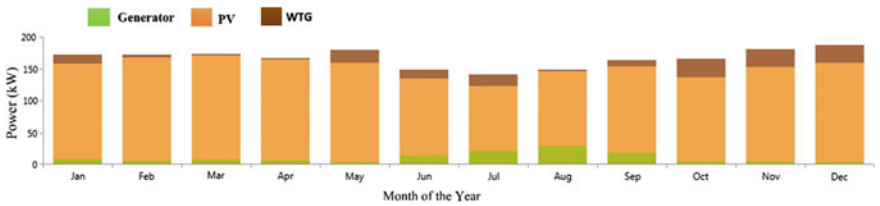
Fig. 5 Annual power generation share of different generating sources
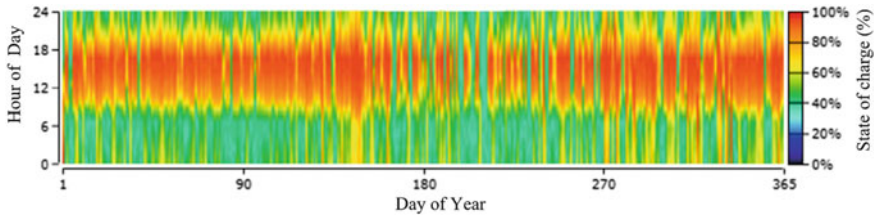
Fig. 6 Lead-acid battery SOC

lifespan is counted on the basis of hours for which it is operated instead of its life in years. The operating hours of diesel generator are less which gives longer life, hence no replacement is required. The negative values in the table show the salvage value. This is the value of the power system components that remains at the end of the project lifetime. The converter units and the battery banks are the parts of the microgrid that require replacement. The battery unit covers the replacement and maintenance cost of these components. Based on usage and lifetime of batteries, they need to be replaced. The lifetime of the converter is 15 year in this study. It can be perceived from the obtained results that the AC microgrid system requires higher rating of converter unit having cost of $77,753.03 whereas, DC microgrid system requires lower rating converter unit having cost of $40,820.34.

The detailed comparative analysis of the AC and DC microgrids in terms of components rating, battery units, generator operating hours, TNPC, per-unit COE, renewable fractions and dispatch strategy employed during simulation are displayed in Table 2. It can be noted that same number of battery units, equal rating of the generator (PV, WTG, DG), with similar cycle dispatch strategy are required in the designed AC and DC microgrids to fulfil the load demand. The number of generator operating hours is little bit higher in AC microgrid system as compared to DC microgrid system due to the difference in their renewable fraction. The major difference in both microgrid systems is in the utilization of converter units for AC–DC conversion. The converter units required in AC microgrid system (417 units) is approximately double as compared to DC microgrid system (219 units). Due to this, the per-unit cost on energy in DC microgrid system (0.198 $/kWh) is less than the AC microgrid system (0.205 $/kWh). Therefore, it can be determined through simulations that DC microgrid system requires less number of converter units that result lower AC–DC conversion losses and is economically more feasible than AC microgrid system.

Table 1 Cost summary of the different components utilized in microgrid system

Components	Microgrid types	Capital ($)	Replacement ($)	O&M ($)	Salvage ($)	Fuel ($)	Total ($)
PV	AC	614,880.00	0.00	84,767.61	0.00	0.00	699,647.61
	DC	614,880.00	0.00	84,767.61	0.00	0.00	699,647.61
Wind generator	AC	138,468.00	0.00	31,961.56	0.00	0.00	170,429.56
	DC	138,468.0	0.00	31,961.56	0.00	0.00	170,429.56
Battery	AC	248,000.00	559,912.89	231,605.50	0.00	0.00	1,039,518.39
	DC	248,000.00	559,912.89	231,605.50	0.00	0.00	1,039,518.39
Diesel generator	AC	77,000.00	0.00	2051.45	−14,884.37	357,875.6	**422,042.74**
	DC	77,000.00	0.00	1816.95	−15,989.04	319,308.9	**382,136.81**
Converter	AC	**64,166.67**	**27,224.24**	0.00	**−13,637.87**	0.00	**77,753.03**
	DC	**33,687.50**	**14,292.72**	0.00	**−7159.88**	0.00	**40,820.34**
Total system	AC	1,142,514.6	587,137.13	350,386.12	−28,522.24	357,875.6	2,409,391.34
	DC	1,112,035.5	574,205.62	350,151.62	−23,148.92	319,308.9	2,332,552.72

Table 2 AC–DC microgrid system comparative analysis

Microgrid types	PV (kW)	Wind turbine (kW)	Diesel generator (kW)	Gen. running (Hrs.)	Batteries (Units)	Inverter (Units)	Total NPC ($)	Operating cost ($)	COE ($/ kWh)	Renewable fraction (%)
AC	732	120	200	1120	2000	**417**	2,421,999	109,171	0.205	90.0
DC	732	120	200	1086	2000	**219**	2,345,026	105,156	0.198	90.9

5   Conclusion

In this paper, the optimal design and comparative analysis of the stand-alone AC and DC microgrid systems have been studied for an urban scenario consisting of wind–PV, battery bank and diesel generators. The techno-economic analysis of both the microgrids has been executed through simulations on real load data, actual resource data and prices of components at present. The analysis shows that both microgrids satisfy the load demand. However, the DC microgrid has the lower net present cost and the least cost of energy as compared to an AC microgrid system. It has also been validated through the simulation that DC microgrid system requires lesser converter units for AC–DC conversion as compared to AC microgrid. In addition, the comparative analysis shows that DC microgrids could be potentially more economically beneficial than AC microgrids, as they require less converter units, have simplified interfaces and have reduced losses associated with the AC–DC energy conversion.

References

1. Lotfi H, Khodaei A (2016) Hybrid AC/DC microgrid planning. Energy 118:1–5
2. Rajesh KS, Dash SS, Rajagopal R, Sridhar R (2017) A review on control of ac microgrid. Renew Sustain Energy Rev 71(January):814–819
3. Hamad AA, Nassar ME, El Saadany EF, Salama MMA (2018) Optimal configuration of isolated hybrid AC/DC microgrids. IEEE Trans Smart Grid 3053(no. c):1–10
4. Li Z, Shahidehpour M (2018) Small-signal modeling and stability analysis of hybrid AC/DC microgrids. IEEE Trans Smart Grid 10(2):2080–2095
5. Elsayed AT, Mohamed AA, Mohammed OA (2015) DC microgrids and distribution systems: An overview. Electr Power Syst Res 119:407–417
6. Unamuno E, Barrena JA (2015) Hybrid ac/dc microgrids—Part I: Review and classification of topologies. Renew Sustain Energy Rev 52:1251–1259
7. Justo JJ, Mwasilu F, Lee J, Jung JW (2013) AC-microgrids versus DC-microgrids with distributed energy resources: a review. Renew Sustain Energy Rev 24:387–405
8. Zhu JP, Zhou JP, Zhang H (2014) Research progress of AC, DC and their hybrid micro-grids. Conference proceedings—2014 international conference on system science and engineering, ICSSE 2014, pp 158–161
9. Lotfi H, Member S, Khodaei A, Member S (2017) AC versus DC microgrid planning. IEEE Trans Power Syst 8(1):296–304
10. Fregosi D et al (2015) A comparative study of DC and AC microgrids in commercial buildings across different climates and operating profiles. In: 2015 IEEE first international conference on DC microgrids, pp 159–164
11. Phurailatpam C, Rajpurohit BS, Wang L (2018) Planning and optimization of autonomous DC microgrids for rural and urban applications in India. Renew Sustain Energy Rev 82:194–204

12. Soshinskaya M, Crijns-Graus WHJ, Guerrero JM, Vasquez JC (2014) Microgrids: experiences, barriers and success factors. Renew Sustain Energy Rev 40:659–672
13. Singh S, Chandra Kaushik S (2016) Optimal sizing of grid integrated hybrid PV-biomass energy system using artificial bee colony algorithm. IET Renew Power Gener 10(5):642–650
14. Das BK, Hoque N, Mandal S, Pal TK, Raihan MA (2017) A techno-economic feasibility of a stand-alone hybrid power generation for remote area application in Bangladesh. Energy 134:775–788
15. Singh S, Singh M, Kaushik SC (2016) Feasibility study of an islanded microgrid in rural area consisting of PV, wind, biomass and battery energy storage system. Energy Convers Manag 128:178–190
16. "Solar Panels prices," [Online]. Available: http://www.solarenergypanels.in/solar-panels/75w-80w-100w-solar-panels
17. Podder S, Khan MZR (2016) Comparison of lead acid and Li-ion battery in solar home system of Bangladesh. In: 5th international conference on informatics, electronics, and vision, pp 434–438
18. "Battery Prices." [Online]. Available: http://www.powerwale.com/store/amaron-12v-100ah-cr1000h29r-inverter-ups-battery/77232

Adaptive Neuro-Fuzzy-PID and Fuzzy-PID-Based Controller Design for Helicopter System

Rupam Singh and Bharat Bhushan

Abstract The paper presents designing and control of two-degree-of-freedom helicopter system, with two degrees of freedom. The helicopter is a combination of rotor motors which helps to lift the body of system. This is a nonlinear and unstable system in nature. The control techniques focused are adaptive neuro-fuzzy inference-PID and fuzzy-PID. Helicopter system has been analysed using MATLAB software and analysed in terms of transient response, root-mean-square error, steady-state error and total harmonic distortion analysis for performance assessment. The controllers have been designed with and without integral action.

Keywords Helicopter system · Adaptive neuro-fuzzy inference system with PID · Fuzzy with PID control · PID

1 Introduction

Helicopters are one of the most navigable and adaptable platforms. The best part of helicopter is, it is easy to take-off and land without an airstrip and can float in a small area, due to which autonomation of miniature helicopters becomes possible. These capabilities enhance huge applications of helicopters in various zones in a wide manner such as military, civil for surveillance of traffic, rescue operations, search operations, charting of area, monitoring of air pollution, farming claims and building and bridge constructions inspection. For the safe execution of these various tasks, great handling and controllers' robustness in the presence of high turbulences are desirable. This has engendered substantial interest in the design of robust flight control.

R. Singh (✉) · B. Bhushan
Department of Electrical Engineering, Delhi Technological University,
Shahbad Daulatpur, Main Bawana Road, Delhi, India
e-mail: singhrupam99@gmail.com

B. Bhushan
e-mail: bharat@dce.ac.in

The twin-rotor multi-input multi-output (MIMO) system, i.e., (TRMS), is an aerodynamical system like a helicopter; it is a highly coupled nonlinear system. TRMS has been modelled by various methods such as physical–mathematical modelling [1], quasi-LPV modelling [2], Euler–Lagrange method [3] and chirp input-based modelling [4]. The main objective is to track a determined path rapidly by positioning its yaw and pitch angles in the presence of cross-couplings of TRMS. Many approaches have been made to control the system, and various methods have been established to solve the trajectory following problems. These methods are offered under plenty of names, such as classical, hybrid and intelligent controlling. PID has been tuned by various methods previously such as real-value-type genetic algorithm [5] and fractional-order reference model approximation [6]. On the other side, in intelligent controlling, yaw and pitch of helicopter are also controlled by fuzzy LQR [7], fuzzy sliding [8] and adaptive fuzzy [9] methods to achieve stabilized and disturbance less output. For adaptive fuzzy design, gradient descent method is used and stability is analysed by Lyapunov theory. One-degree-of-freedom helicopter model studied based on inversion modelling and controlled through artificial neural network [10] provides satisfactory control, while Chebyshev neural network [11] guarantees excellent stability. The other nonlinear control methods implemented on helicopter are stable model predictive control (MPC) [12] and MPC with states based on Kalman [13], adaptive sliding mode controller [14] and disturbance observer-based sliding control [15]. Further work in helicopter system is trajectory accurately tracked by shaping input using active disturbance rejection controller [16] and designing of backstepping controller for adding integral gain to stabilize pitch against gravitational force [17].

Helicopter is nonlinear, complicated, multi-input, multi-output control benchmark system. In this paper, a comparison has been made between three techniques. First one, conventional technique, PID, and rest two are hybrid techniques, fuzzy logic controller with PID (FPID) and adaptive neuro-fuzzy inference system with PID (ANFIS-PID) have been designed to control the yaw and pitch angles of helicopter system in two degrees of freedom. The rest of the paper is organized as follows. Helicopter system equation is represented in Sect. 2. Designing and implementation of controllers for system are presented in Sect. 3. Result analysis has been done in Sect. 4 based on time response analysis, root-mean-square error (RMSE) and total harmonic distortion (THD) values. The paper is concluded in Sect. 5 followed by references.

2 Helicopter System

Two-degree-of-freedom (2DOF) helicopter system comprises of two propellers and a fixed base. These propellers are basically rotors and operated by dc motors. The propeller placed on the front end is used for elevation control about its pitch, whereas the second propeller on the back-end controls yaw axis for side motion.

Two-degree-of-freedom helicopter model is illustrated in Fig. 1 by its free-body diagram. Z-axis represents yaw motion of the helicopter denoted by φ, and *Y*-axis displays pitch control denoted by α.

For the implementation of PID, FPID and ANFIS-PID control methods with state feed-forward controller, linear model system dynamics needed to be considered. The linearization of the nonlinear model of the system is taken place by substitution of following values of $\alpha = 0, \varphi = 0, \dot{\alpha} = 0, \dot{\varphi} = 0$. This results into

$$\ddot{\alpha} = \frac{k_{\text{ppi}}v_{\text{mpi}}}{J_{\text{eq}_{\text{pi}}} + m_{\text{heli}}l_{\text{CM}}^2} + \frac{k_{\text{pya}}v_{\text{mya}}}{J_{\text{eq}_{\text{pi}}} + m_{\text{heli}}l_{\text{CM}}^2} - \frac{B_{\text{p}}\dot{\alpha} + m_{\text{heli}}gl_{\text{CM}}}{J_{\text{eq}_{\text{pi}}} + m_{\text{heli}}l_{\text{CM}}^2} \tag{1}$$

$$\ddot{\varphi} = \frac{k_{\text{ypi}}v_{\text{mpi}}}{J_{\text{eq}_{\text{ya}}} + m_{\text{heli}}l_{\text{CM}}^2} + \frac{k_{\text{yya}}v_{\text{mya}}}{J_{\text{eq}_{\text{ya}}} + m_{\text{heli}}l_{\text{CM}}^2} - \frac{B_{\text{p}}\dot{\varphi}}{J_{\text{eq}_{\text{ya}}} + m_{\text{heli}}l_{\text{CM}}^2} \tag{2}$$

By using the input $u = \begin{bmatrix} V_{\text{mpi}}, V_{\text{mya}} \end{bmatrix}^{\text{T}}$ and states as $x = [\alpha, \varphi, \dot{\alpha}, \dot{\varphi}]^{\text{T}}$, the state space representation without integrator can be carried out as:

$$
\begin{bmatrix} \dot{\alpha} \\ \dot{\varphi} \\ \ddot{\alpha} \\ \ddot{\varphi} \end{bmatrix} =
\begin{bmatrix}
0 & 0 & 1 & 0 \\
0 & 0 & 0 & 1 \\
0 & 0 & \frac{-B_{\text{pi}}}{J_{\text{eq}_{\text{pi}}} + m_{\text{heli}}l_{\text{CM}}^2} & 0 \\
0 & 0 & 0 & \frac{-B_{ya}}{J_{\text{eq}_{\text{ya}}} + m_{\text{heli}}l_{\text{CM}}^2}
\end{bmatrix}
\begin{bmatrix} \alpha \\ \varphi \\ \dot{\alpha} \\ \dot{\varphi} \end{bmatrix}
$$
$$
+ \begin{bmatrix}
0 & 0 \\
0 & 0 \\
\frac{k_{ppi}}{J_{\text{eq}_{\text{pi}}} + m_{\text{heli}}l_{\text{CM}}^2} & \frac{k_{pya}}{J_{\text{eq}_{\text{pi}}} + m_{\text{heli}}l_{\text{CM}}^2} \\
\frac{k_{ypi}}{J_{\text{eq}_{\text{ya}}} + m_{\text{heli}}l_{\text{CM}}^2} & \frac{k_{yya}}{J_{\text{eq}_{\text{ya}}} + m_{\text{heli}}l_{\text{CM}}^2}
\end{bmatrix}
\begin{bmatrix} V_{\text{mpi}} \\ V_{\text{mya}} \end{bmatrix}
\tag{3}
$$
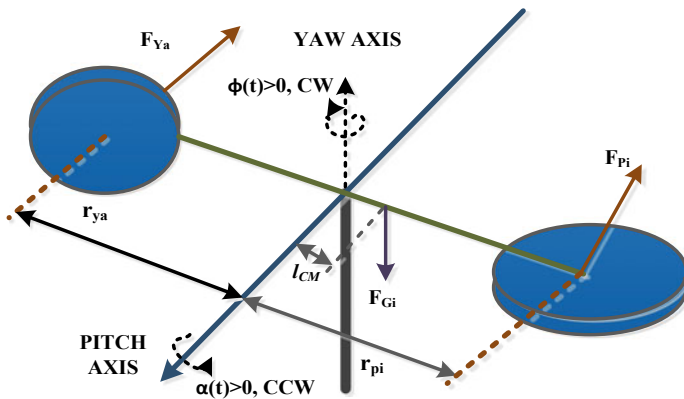
Fig. 1 Graphic representation of helicopter model

For reducing the pitch and yaws steady-state error due to gravitational disturbance, two integrals are taken into consideration. Two state variables are included with pitch and yaw for the above purpose. The values of α_d and φ_d depict the designed pitch and yaw set values. For 2DOF helicopter system, a new state vector is formulated by combining the state model with integrator, which is formulated as $x = \left[\alpha, \varphi, \dot{\alpha}, \dot{\varphi}, \dot{\lambda}, \dot{\beta}\right]$ and can be described as:

$$
\begin{bmatrix} \dot{\alpha} \\ \dot{\varphi} \\ \ddot{\alpha} \\ \ddot{\varphi} \\ \dot{\lambda} \\ \dot{\beta} \end{bmatrix} = \begin{bmatrix} 0 & 0 & 1 & 0 & 0 & 0 \\ 0 & 0 & 0 & 1 & 0 & 0 \\ 0 & 0 & \frac{-B_{pi}}{J_{eq_{pi}}+m_{heli}l^2_{CM}} & 0 & 0 & 0 \\ 0 & 0 & 0 & \frac{-B_{ya}}{J_{eq_{ya}}+m_{heli}l^2_{CM}} & 0 & 0 \\ 0 & 0 & 0 & 0 & 1 & 0 \\ 0 & 0 & 0 & 0 & 0 & 1 \end{bmatrix} \begin{bmatrix} \alpha \\ \varphi \\ \dot{\alpha} \\ \dot{\varphi} \\ \dot{\lambda} \\ \dot{\beta} \end{bmatrix}
$$

$$
+ \begin{bmatrix} 0 & 0 \\ 0 & 0 \\ \frac{k_{ppi}}{J_{eq_{pi}}+m_E l^2_{CM}} & \frac{k_{pya}}{J_{eq_{pi}}+m_{heli}l^2_{CM}} \\ \frac{k_{ypi}}{J_{eq_{ya}}+m_{heli}l^2_{CM}} & \frac{k_{yya}}{J_{eq_{ya}}+m_{heli}l^2_{CM}} \\ 0 & 0 \\ 0 & 0 \end{bmatrix} \begin{bmatrix} V_{mpi} \\ V_{mya} \end{bmatrix} \tag{4}
$$

3   Controller Design

PID, FPID and ANFIS-PID are designed separately for the control of pitch and yaw motion of helicopter system. Controllers are designed with and without integrator to check the performance of helicopter for different control strategies.

3.1   PID Controller

Feed-forward control is integrated with PID to provide necessary gain to the pitch. This control passes a dominant signal from a supply in its external loop and solely responds to gain based approach. Forward control responds to compensatory signal during a predefined method. Here, it compensates the gravitational forces which force pitch angle down. The response is controlled by defining the suitable value of proportional, derivative and integral constants.

In addition to PID, due to a huge change in set points values of pitch and yaw error, a large voltage is induced which can saturate the amplifier. This mechanism

Fig. 2 PID without integrator
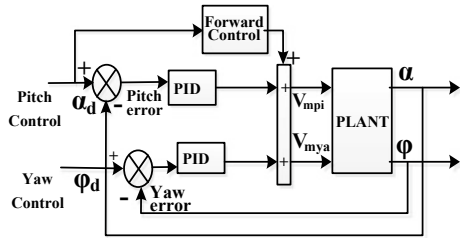
Fig. 3 PID with integrator
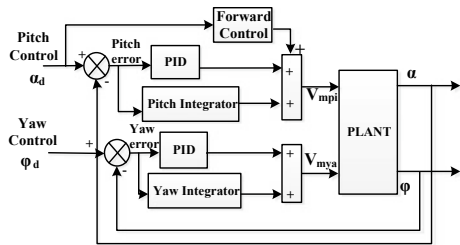
causes oscillations and disrupts the desired output. To avoid this situation, integral windup is used which makes the saturation error negative during large voltages. This error is later divided by reset time and added with the input of the integrator. The block diagram for PID with integral and without integral is shown in Figs. 2 and 3.

3.2 Fuzzy-PID Controller

The hybrid FPID controller is to be found within the control loop and used to calculate PID constants with fuzzy inference. For designing FPID controller, five standards and consistent gaussian membership functions are defined for error and three membership function for change in error input parameter, and fifteen rules have been set on the output to make complete fuzzy rule base. PID with integral and without integral is shown in Figs. 4 and 5.

3.3 Adaptive Neuro-Fuzzy Inference System-PID (ANFIS-PID)

The structure of neuro-fuzzy controller combines the advantages of both fuzzy and artificial neural networks. The fuzzy model generated after training the adaptive neural network optimization technique is called adaptive neuro-fuzzy inference system. ANFIS architecture is shown in Fig. 6. Neural nets adopt the environments
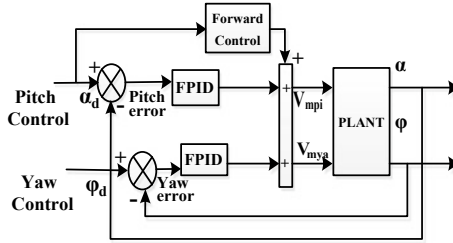
Fig. 4 FPID without integrator
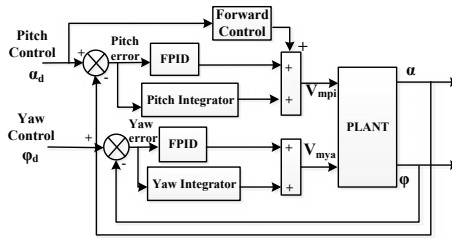
Fig. 5 FPID with integrator
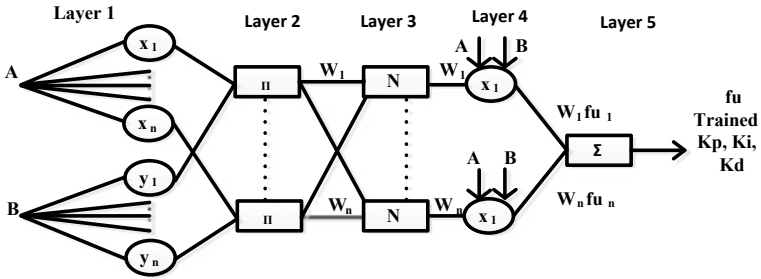
Fig. 6 Schematic diagram of neural network designed for ANFIS

and train data from previous standards, while fuzzy offers flexibility in framing system. The algorithm used is a combination of gradient descent and least square estimate methods. The block diagram for PID with integral and without integral is shown in Figs. 7 and 8.

Fig. 7 ANFIS-PID without integrator
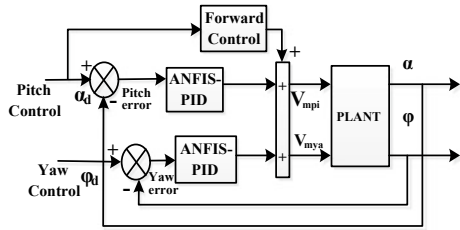
Fig. 8 ANFIS-PID with integrator
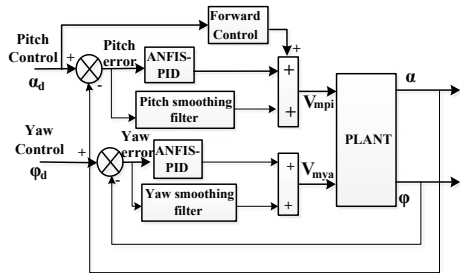
4 Results and Discussion

PID, FPID and ANFIS-PID have been designed for the study of helicopter system using Simulink using MATLAB. The square input signal is of 0.05 Hz with an amplitude of 5. Implementation of LQR, fuzzy-P and ANFIS-P controllers on helicopter system and their precise results are discussed below.

4.1 PID Outcomes

Proportional, derivative and integral gain values are shown in Table 1.

4.2 Fuzzy-PID Controller Outcomes

For the pitch and yaw angle control purpose, Takagi–Sugeno-type fuzzy inference system has been used. Designed fuzzy controller has pitch and yaw error and three

Table 1 PID gain values

Controller	Without integrator			With integrator		
	k_p	k_i	k_d	k_p	k_i	k_d
PID for pitch	1	0.04	0.25	1.05	0.1	0
PID for yaw	1.5	0.01	0.27	1.5	0.4	0
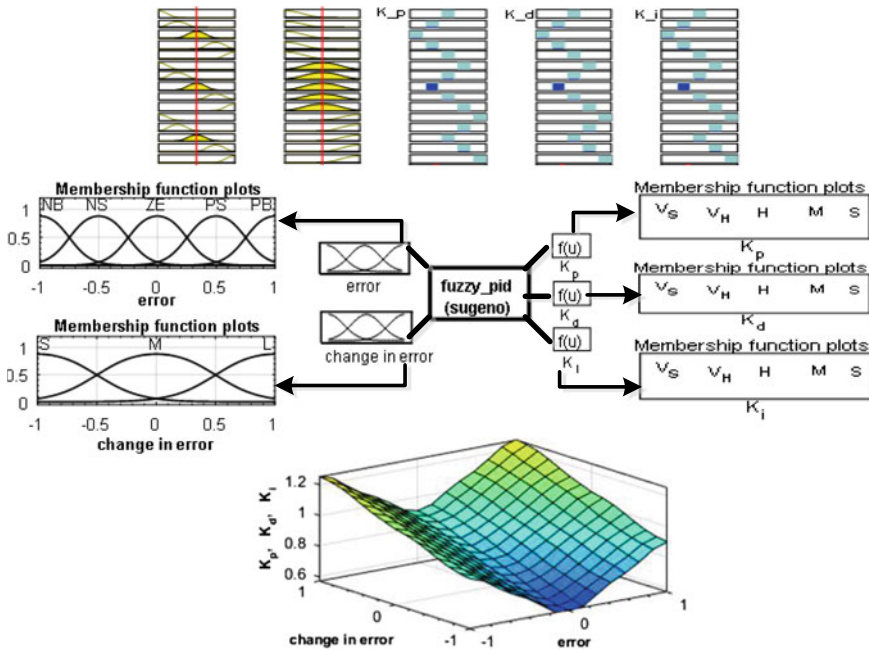
Fig. 9 Complete fuzzy model for yaw control of helicopter control

Controller	Without integrator			With integrator		
	k_p	k_i	k_d	k_p	k_i	k_d
Fuzzy-PID for pitch	3.2	1.1	0.1	1.5	0.2	0.01
Fuzzy-PID for yaw	5	0	0.3	3.5	0.01	0.89

Table 2 Gain values for FPID

constants outputs named as k_p, k_i and k_d. The membership function for inputs, output, fuzzy rules and surface viewer is shown in Fig. 9 for controlling of pitch and yaw. Gain values for FPID are shown in Table 2.

4.3 ANFIS-PID Controller Outcomes

Fuzzy control is fed as a target output to obtain control signal. The universe of discourse is chosen to be [−0.2, 0.2] for yaw error and yaw derivative, [−0.35, 0.35] for pitch error and [−1 1] for pitch derivative error as shown in Fig. 10.
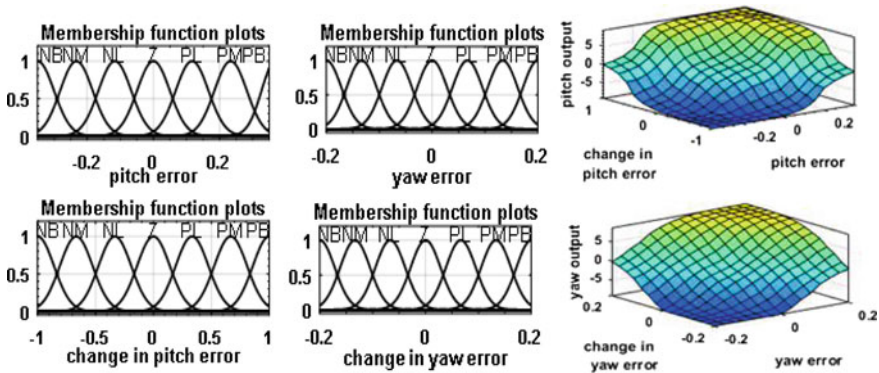
Fig. 10 Pitch and yaw membership function, surface viewer after training
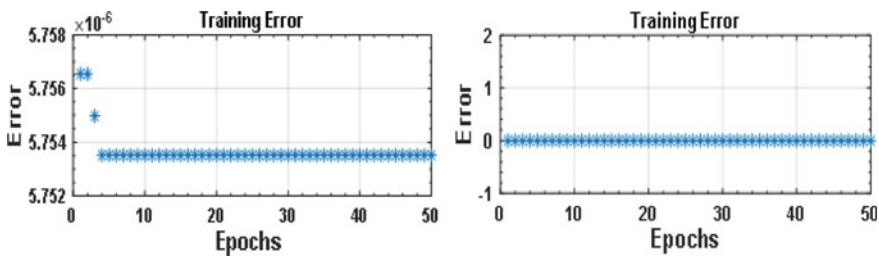
Fig. 11 Training error versus epochs for pitch and yaw ANFIS

A hybrid training algorithm is used for training of pitch and yaw data for 50 epochs as shown in Fig. 11. Consequently, membership function parameters of single-output, Sugeno-type fuzzy inference system are obtained. Seven linguistic variables (NB, NM, NL, Z, PL, PM and PB) are associated with each input, so the input space is partitioned into 49 fuzzy subspaces, each of which is governed by fuzzy if-then rules. The Scaling factor for pitch control is obtained as $M_{Pe(t)} = n/e$ (t) = 20; $N_{Pde(t)/dt} = n/\{de(t)/dt\} = 7$ for input and $O_{Pu(t)} = U/n = 0.7$ for output. For yaw control the input scaling factors are $M_{Ye(t)} = N_{Yde(t)/dt} = 35$, and output scaling factor is $O_{Yu(t)} = U/n = 0.7$. The learning coefficient for this system starts $\eta = 5.75352e^{-6}$ with minimal training RMSE = 0.000006 for pitch and $\eta = 6.95252e^{-6}$ with minimal training RMSE = 0.000006 for yaw. Gain values for ANFIS-PID are shown in Table 3.

Table 3 Gain values for ANFIS-PID

Controller	Without integrator			With integrator		
	k_p	k_i	k_d	k_p	k_i	k_d
ANFIS-PID for pitch	0.3	0.335	0	0.7	0.1	0
ANFIS-PID for yaw	1	0.1	0	0.4	0.01	0

4.4 Validation of Controllers

It was found that a simulation of the helicopter system responded very nicely to PID, FPID and ANFIS-PID controllers. For controller validation, root-mean-square error has been considered and shown in Table 4. From RMSE values, it is clear that observed pitch and yaw angle are close to reference angle for ANFIS-PID with minimum RMSE. A comparative assessment of controller's performance through time domain analysis is shown in Tables 5 and 6. Simulation output after implementation of PID, FPID and ANFIS-PID is shown in Figs. 12 and 13. Distortion in output waveform with respect to sine wave has been measured by calculating THD values in Table 7. Pitch and yaw velocities have been considered for the comparison of distortion in output waveforms of controllers.

Table 4 RMSE values

Controllers	Without integrator		With integrator	
	Pitch	Yaw	Pitch	Yaw
PID	3.6816	8.6938	3.0112	1.0253
FUZZY-PID	2.4160	0.2991	2.4404	0.1880
ANFIS-PID	2.1863	0.1148	2.0471	0.1758

Table 5 Comparative assessment of controllers on helicopter model without integrator

Controller	Pitch control response without integrator				Yaw control response without integrator			
	t_p	t_s	PO	Error	t_p	t_s	PO	Error
PID	45.6	4.72	1.92	0.99	5.42	5.42	0.284	9.82
FUZZY-PID	4.7	4.7	0.40	0.45	4.94	4.24	0.12	0.26
ANFIS-PID	4.12	4.12	0.10	0.18	4.74	4.07	0.01	0.11

Table 6 Comparative assessment of controllers on helicopter model with integrator

Controller	Pitch control response with integrator				Yaw control response with integrator			
	t_p	t_s	PO	Error	t_p	t_s	PO	Error
PID	2.35	4.89	6.70	1.32	1.24	4.49	75.4	0.62
FUZZY-PID	2.86	4.39	0.31	0.64	24.9	4.27	1.12	0.11
ANFIS-PID	3.98	3.98	0.12	0.55	4.73	4.09	0	0.04
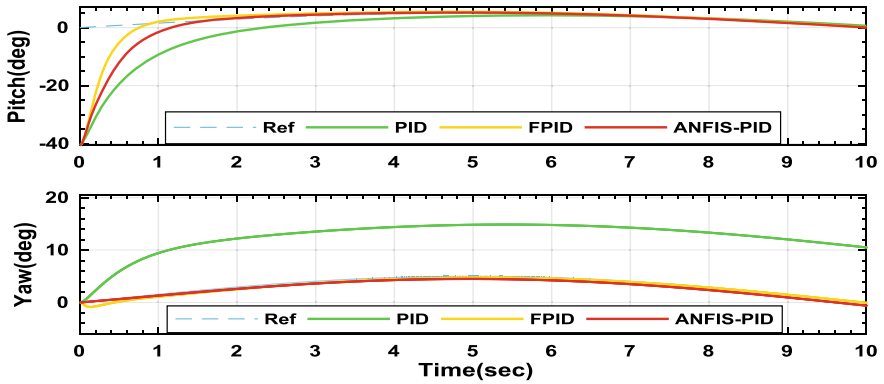
Fig. 12 Pitch and yaw angle control without integrator
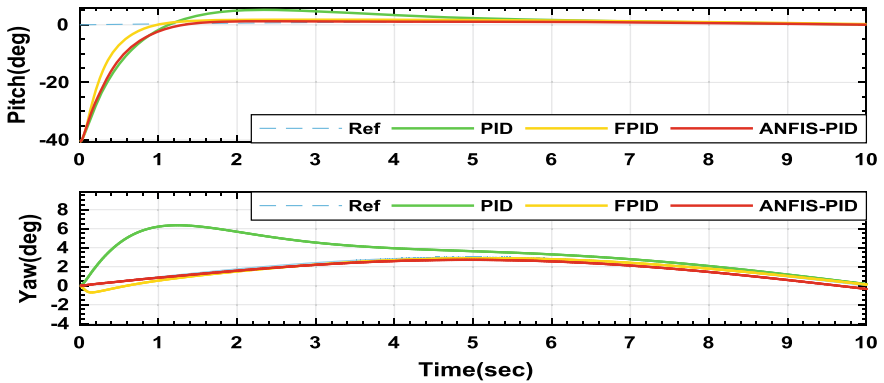
Fig. 13 Pitch and yaw angle control with integrator

Table 7 THD values

Total harmonic distortion (THD)				
Controller	Without integrator		With integrator	
	Pitch velocity (%)	Yaw velocity (%)	Pitch velocity (%)	Yaw velocity (%)
PID	78.30	78.27	77.68	77.80
FUZZY-PID	78.17	78.16	78.17	78.16
ANFIS-PID	77.86	50.14	77.72	54.38

5   Conclusion

This paper depicts design and implementation of conventional PID, hybrid FPID and ANFIS-PID controllers for helicopter pitch and yaw control. Fuzzy and ANFIS are employed with PID and accomplish constant gain that eliminates cross-coupling that occurs between the motor rotors. The performance of controllers is assessed based on various parameters such as THD, time response analysis and RMSE. For the comparison of the controller's results, time response analysis has been carried out. Pitch settling time and yaw settling time are 4.12 and 4.07 without integrator, whereas 3.98 and 4.09 with integrator which shows that helicopter will take less time to settle in case of ANFIS-PID. The results from simulation provide the values of steady-state error, peak time and settling time; RMSE and THD are minimum for ANFIS-PID as compare to FPID and PID. The ANFIS-PID controller has the adaptability, excellent control performances and strong robustness.

References

1. Chalupa P, Přikryl J, Novák J (2015) Modelling of twin rotor MIMO system. In: Proceedings 2015 20th international conference on process control. PC 2015, vol. 2015–July, pp. 314–319
2. Rotondo D, Nejjari F, Puig V (2013) Quasi-LPV modeling, identification and control of a twin rotor MIMO system. Control Eng Pract 21(6):829–846
3. Tastemirov A, Lecchini-Visintini A, Morales-Viviescas RM (2017) Complete dynamic model of the twin rotor MIMO system (TRMS) with experimental validation. Control Eng Pract 66 (July):89–98
4. Paul PK, Jacob J (2017) On the modeling of twin rotor MIMO system using chirp inputs as test signals. Asian J Control 19(5):1731–1740
5. Juang JG, Te Huang M, Liu WK (2008) PID control using presearched genetic algorithms for a MIMO system. IEEE Trans Syst Man Cybern Part C Appl Rev 38(5):716–727
6. Alagoz BB, Ates A, Yeroglu C (2013) Auto-tuning of PID controller according to fractional-order reference model approximation for DC rotor control. Mechatronics 23 (7):789–797
7. Tao CW, Taur JS, Chen YC (2010) Design of a parallel distributed fuzzy LQR controller for the twin rotor multi-input multi-output system. Fuzzy Sets Syst 161(15):2081–2103
8. Tao CW, Taur JS, Chang YH, Chang CW (2010) A novel fuzzy-sliding and fuzzy-integral-sliding controller for the twin-rotor multi-input multi-output system. IEEE Trans Fuzzy Syst 18(5):893–905
9. Jahed M, Farrokhi M (2013) Robust adaptive fuzzy control of twin rotor MIMO system. Soft Comput 17(10):1847–1860
10. Rahideh A, Bajodah AH, Shaheed MH (2012) Real time adaptive nonlinear model inversion control of a twin rotor MIMO system using neural networks. Eng Appl Artif Intell 25 (6):1289–1297
11. Shaik FA, Purwar S, Pratap B (2011) Real-time implementation of Chebyshev neural network observer for twin rotor control system. Expert Syst Appl 38(10):13043–13049
12. Rahideh A, Hasan Shaheed M (2011) Stable model predictive control for a nonlinear system. J Franklin Inst 348(8):1983–2004
13. Rahideh A, Shaheed MH (2012) Constrained output feedback model predictive control for nonlinear systems. Control Eng. Pract 20(4):431–443

14. Mondal S, Mahanta C (2012) Adaptive second-order sliding mode controller for a twin rotor multi-input–multi-output system. IET Control Theory Appl 6(14):2157–2167
15. Rashad R, El-Badawy A, Aboudonia A (2017) Sliding mode disturbance observer-based control of a twin rotor MIMO system. ISA Trans 69:166–174
16. Yang X, Cui J, Lao D, Li D, Chen J (2014) Input shaping enhanced active disturbance rejection control for a twin rotor multi-input multi-output system (TRMS). ISA Trans 62: 287–298
17. Haruna A, Mohamed Z, Efe M, Basri MAM (2017) Dual boundary conditional integral backstepping control of a twin rotor MIMO system. J Franklin Inst 354(15):6831–6854

Measurement and Controlling of pH and TDS in Automated Hydroponics System

Devvrat and Rajeev Ratan

Abstract Development, signifying a vital viewpoint in gross domestic product, has been influenced massively in the course of recent decades because of the utilization of chemicals. Due to quick urbanization and industrialization, arable land under development is diminishing hugely. Natural cultivating, being the need of great importance, is selected as one of the generally picked systems to conquer the predominant issue in development. Headways in farming have demonstrated to serve the cultivators in various ways. Development of yields is being done at home, which expends restricted measure of room and cost. To get another innovative progression by breaking all hindrances, for natural cultivating is where utilization of room also, water is much excessively negligible. Hydroponics is a strategy for developing plants simply utilizing water and supplements, without soil. The proposed hydroponic framework is based upon the ideas of the inserted framework. The framework encourages the development of numerous trims under a solitary controller. Vital supplements for the crops are given in light of the sources of info got from the pH sensor and the water level sensor utilized. The water and supplement supply to the diverse assortments of product is controlled and observed at customary time interims. A proficient calculation has been proposed for controlling every one of the functionalities. Robotization of the hydroponic framework enhances the proficiency and diminishes manual work.

Keywords Hydroponics · Fertilizers · Water flow · Controller · Crops · Nutrients

Devvrat (✉) · R. Ratan
Department of Electronics and Communication Engineering,
MVN University, Palwal 121105, India
e-mail: akheriya@yahoo.co.in

R. Ratan
e-mail: rajeev.arora@mvn.edu.in

1 Introduction

Sustenance being the essential prerequisite worldwide for driving a stimulated and solid life must be liberally created furthermore, made accessible. This creation is extended by the system called development. Agribusiness encourages in giving the most basic product required as a profession which is sustenance. Various vegetables, natural products, nuts, and flavors are on the whole continually being developed by different strategies. Each trim is developed in an alternate domain requiring a wide scope of fundamentals, contingent on the product's hereditary association. Compound composts which are thought to be risky for humanity are lavishly utilized as a part of the present-day cultivating. To conquer this, a domain inviting methodology has been embraced called the natural cultivating. To think upon with the viewpoint of considering human well-being as the at most vital factor, natural cultivating should be actualized everywhere throughout the world. New methods and an assortment of methodologies are required to be actualized keeping in mind the end goal to accomplish this natural method for development. One such conspicuously utilized natural cultivating system is the hydroponics. Hydroponics principally includes the development of harvests without the utilization of soil and synthetic composts, which unwinds the danger of bug assaults and other product maladies. The supplements required for the plant development are provided in the frame a supplement arrangement with a particular blend of required parts relying upon the plant's need. The framework is assembled in a shut situation as the yields developed in here have the potential to sustain without daylight. This thusly keeps the green growth development in the supplement arrangement which the yields are inclined to. The current hydroponic framework can be utilized to develop different harvests at the same time. Be that as it may, at that point it requires the use of all the important parts of development autonomously. Too these frameworks are made to take a shot at a simultaneous premise. Despite the fact that this enhances the execution, it needs trustworthiness. We have received a strategy to overcome these with sensible gathering of assets and organizing their requirements [1].

In this paper, existing works identified with hydroponics and Arduino writing computer programs are exhibited in segment II took after by a portrayal of the proposed framework modules in area III, additionally, a calculation formulated for keeping up the stream of control has been incorporated. Advance the framework's execution has been examined and contrasted and the current framework in segment IV [2].

1.1 Existing Work

The thought proposed by Saaid actualizes one of the hydroponic framework models which are deepwater culture. In this model, roots are submerged in supplement and

oxygen-rich water. pH sensors are being utilized to screen the supplement content in water. The framework proposed by Lenord presents a proficient framework controlling the hydroponic supplement arrangement by utilizing hereditary calculation and streamlining the framework parameters. To get to the nature of arrangement utilized, a Mamdani fluffy impedance framework utilizes an arrangement of parameters as it's wellness work. Light is thought to be the fundamental factor impacting plant development. The thought proposed by Rongsheng Chen talks about the development of lettuce and how light influences it in the hydroponic framework. Red light was utilized as an improving parameter to empower the development of shoot and root. What's more, it was recorded that the development expanded with a bring up in force of red light. The framework proposed by Saaid et al. depends on aquaponics which is only the joint effort of hydroponics and water culture. Arduino writing computer programs is utilized to acquire data from the sensors and process the important yield back. Specifically, the development of goldfish is examined. Notwithstanding these current takes a shot at hydroponics, few different takes a shot at the utilization of Arduino board and programming certain applications were alluded to L. Buechley et al. has proposed and detailed a toolbox for e-materials which is drifting in the previous couple of decades. It empowers the clients to outline their own particular one of a kind plan and construct their own particular e-materials. In the framework proposed by M. S. Perez et al. time synchronization is approved tentatively for genuine frameworks like Bluetooth correspondence channels. The framework is actualized in an Arduino-based system, for which acoustic occasions are thought to be of at general significance. The thought proposed by T. O. Loup et al. is to assemble a room-safe security framework with the assistance of installed framework. Here the temperature is considered and an edge esteem is set. Once the temperature surpasses security levels, a message is sent through Bluetooth for security reasons [3]. The thought proposed by A. A. Murthy et al. depicts the working of the electric guitar where in the bending impacts are essentially considered. Arduino UNO board is utilized for measuring and investigating this impact in guitars. This is one vital impact that is found in all the melodic instruments. Contrasted with all the current works in this space, our framework varies basically as it coordinates the natural setup for developing diverse assortments of products. A solitary controller empowered framework overseeing development of numerous of crops which if physically took care of will represent various challenges.

2 Proposed Work

2.1 Overview

The development condition contrasts for every single edit in light of the morphological and hereditary structure. The proposed work manages incorporating the

developing condition for singular products on to a solitary framework. This framework is composed and based upon for growing three distinct sorts of crops which can be additionally stretched out to numerous various crops. An efficient setup is worked for the smooth working of the framework. Fitting supplement arrangement is provided to the products, blending them with the required amount of water. Different sensors are utilized for observing the pH level of the supplement arrangement and the water level . The info got from these sensors will empower the controller to direct the water and supplement stream in redress extent. The controller is customized with an effective calculation which will efficiently manage the stream. The framework once assembled is tried upon for meeting an individual product's necessity and at that point which is all incorporated. This coordinated framework will extemporize the development of products quickly.

2.2 Architecture Diagram

The spirit of this framework is the controller which empowers the whole working. Arduino UNO processor plays out all the control activities fundamental for the framework. pH meter and water level sensors are utilized for aligning the proper estimations required for the plant development. All the water and supplement arrangement are put in a store from which they are sent to the products. The proposed hydroponic framework module is portrayed in Fig. 1.

The framework involves L293d engine driver which goes about as a valve for controlling the supplement and water supply, specified in Fig. 2. Furthermore, it has a blending tank to weaken the supplement arrangement with water and this arrangement is nourished to the yields. There are sensors being set in the blending tank to continually screen the qualities and encourage the outcomes to the controller. The controller works the engines in light of the pH estimations of the supplement arrangement and the level of the blend . This aids in the best possible working of the framework.

Fig. 1 Hydroponic system module
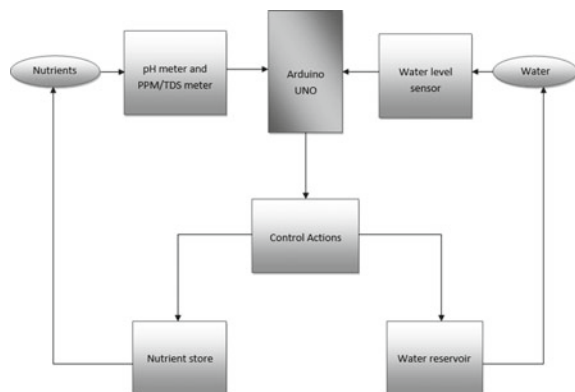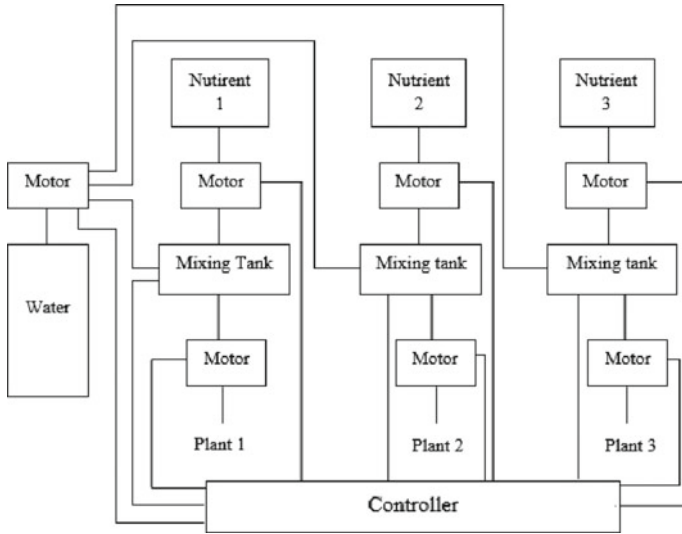
Fig. 2 Control-oriented architecture

2.3 Proposed Modules

The structure is figured by at first working up a setup for a productive stream and working. This is essential as there are different points of view that manage the advancement of plants (Fig. 3). Not only the saplings and supplements would take care of business the improvement; nevertheless, an overall constructed condition is fundamental. The setup as in Fig. 4 depends on by using PVC channels, which is required as a conveyor for stream of water through it. Inside this, net pots are set for holding the plants upright and empowering their improvement. These net pots contain mud balls that are porous and specific to invigorate and set the right condition for plants as showed up in Fig. 3. The minor pores engage holding of water by these balls.

Fig. 3 Plant saplings

Water and supplement supply required for the harvests are made open in a store. Motors for the control and course of water and supplement supply are settled in the setup. This setup enables a methodical working of the hydroponic system which is essential. The resulting stage is laid ahead with the control part as in Fig. 5. Arduino UNO processor is used for the general control of the system. Key writing computer programs is done and the processor is made to play out the required functionalities. It drives the motors and controls the water and supplement stream. Distinctive sections used are L293d motor driver, pH sensor, and water level identifying anodes. Besides, fundamental IC's are used for working the system. These sections are generally required for advancement of individual collects too anyway a setup being composed to consolidate diverse such yields is done.

Fig. 4 Initial setup

Fig. 5 Arduino controller
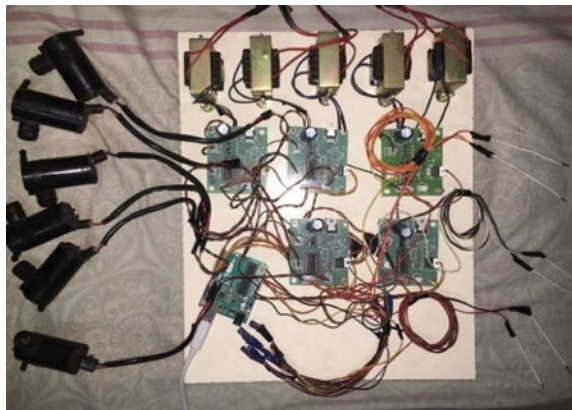
2.4   Alignment of Networks

A consistent watching and a watch out for the water level and the supplement course of action used for the item advancement should be done. Adjusting their estimations as required in perspective of the plant's need is essential. The pH estimation of the supplement game plan used for each yield is inspected under various conditions. This regard will be used as an edge for choosing the supplement course of action essential. The Arduino UNO processor is modified with these pH esteems and once the pH esteem changes from the required one, the processor will empower the engine driver. This will manage the supplement supply until the point that the coveted pH esteem is gotten. The water level detecting cathodes are utilized for adjusting the amount of water required for each harvest. Any errors in these qualities will be as a contribution to the processor, and it will either empower or impair the engines in like manner.

S. No.	Crops	pH value
1.	Mint	6–6.8
2.	Tulsi	6–7.5
3.	Diffenbachia	5–6

In view of the above, pH esteems and water levels crops are nourished with the fundamental supplements and water. For instance, the pH regard required for the Mint plant is around 6–6.8 and this regard is adjusted into the Arduino processor. The pH sensor consistently screens the pH of the supplement course of action gushing to the items and once the regard drops down the breaking point, the controller will get the data. Further, it enables the motor driver to supply the supplements from the supplement store for the harvests till it accomplishes the best possible pH regard. After the desired pH regard for this collect has been expert, the processor impedes the motor driver and stops the supplement supply. This technique goes over reliably till the yield is procured. The pH of a gather course of action may reduce on account of bounteous supply of water to it when the water level of the game plan diminishes as plants take in this response for improvement. As and when water is fed, the pH content varies in light of which pH is managed into it . The riches in the plants improvement is kept up by the precision in working of this system.

2.5   Programming

The working of the controller ought to be gainfully definite. For this, a practical count has been proposed for coding the Arduino UNO processor as shown up in Fig. 6. The computation is invented to such an extent that the entire hydroponic system works in a perfect world without any blemishes. Commitment to the count is

Fig. 6 Growth rate of crops
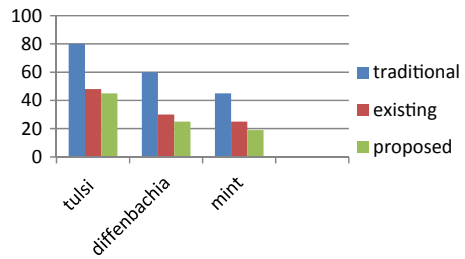
got from the characteristics gained from the pH sensor and the water level sensor. An edge has been set for these qualities in the estimation and if the condition is met appropriate limits are performed. The computation oversees reasonably and rapidly enabling the motor drivers once the characteristics procured from the sensors are sustained into the processor. Here the most basic viewpoint is enabling and crippling the motor drivers inside piece of seconds. The proposed count satisfies this condition and aides in dealing with the smooth working of the system.

3   Integration of Controller

The setup worked for making a development domain for the crops is incorporated with the controller which has been customized. The incorporation is exceptionally basic for a methodical stream of control to happen. The primary piece of this reconciliation is consolidating the development of different harvests under a solitary framework. It is basic for the yield of products to boost. Another favorable position of such incorporation is computerization of framework empowers decrease in manual workforce. Encouraging the successful incorporation of wide assortment of harvests lessens time utilization. It is exceptionally easy to deal with supplement adjust. Thus, a persistent checking of the supplement focus in the coursing water is done to keep up the level of natural substances that we supply.

4   Performance Analysis

The underneath diagram delineates on the time a harvest takes to be become under various ecological conditions. Customary technique takes after the traditional method for developing products utilizing soil. The current approach develops singular yields in hydroponic condition though the proposed work manages an incorporated hydroponic condition empowering development of numerous products.

The aftereffects of the diagram as in Fig. 7 give an unmistakable picture on which technique is invaluable and gives snappier yields. The proposed framework

Fig. 7 Initial setup cost
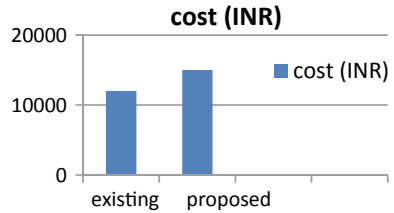
Fig. 8 Cost per crop
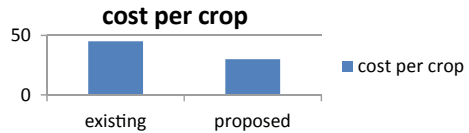
enables plants to be developed at a mightier pace and the yields are given at productive and reasonable costs. The following diagram in Fig. 8 clarifies about how fetched parameter influences the hydroponic framework. The cost of development of a current hydroponic framework for developing individual harvests independently is around Rs. 13,000 as cited in Fig. 6. The proposed framework because of its need to coordinate repays on cost factor charging Rs. 15,000. Despite the fact that the costs are more on beginning setup, it overcomes the use by diminishing expense per development of harvests.

Figure 8 outlines the cost for every harvest in existing and in addition the proposed framework. Since the current framework manages singular products, the cost is very high. Be that as it may, the proposed framework incorporates various harvests which impressively lessen the cost.

These measurable relationships between's the customary, existing and the proposed framework underscore that the proposed framework outnumbers the others . This examination made by utilizing the cost and development as elements makes it apparent.

5 Conclusion

The proposed hydroponic structure from this time forward completes the blend of different collections of harvests. The deficiencies of the present system like advancement of a singular kind of item in the entire structure have been survived. A methodological approach has been taken forward to coordinate the working of the structure. The plants created under this system is inspected with for the most part grown ones and has been found that these plants grow an extensive measure snappier with slightest need of supplements. They are much cleaner with slightest substance constituents spending simply required water, preventing loss of water. In like manner, the cost for trimming is apparent on thought of its positive conditions.

Accordingly, this model invigorates sharpening of a substitute approach toward developing that is eco-friendlier and capable on connection with expected frameworks.

References

1. Saaid MF, Sanuddin A, Ali M, Yasin MSAIM (2015) Automated pH controller system for hydroponic cultivation. In: 2015 IEEE international conference on system engineering and technology (ICSET)
2. Devvrat, Ratan R, (2017) Automated hydroponics system to deliver nutrients directly to the root of plants. In: IJERT, Special issue, pp 327–330. ISSN No: 2278-0181
3. Lenord Melvix JSM, Sridevi C (2014) Design of efficient hydroponic nutrient solution control system using soft computing based solution grading. In: 2014 international conference on computation of power, energy, information and communication (ICCPETC)

Identification of Industrial Nonlinear Loads Using S-Transform Aided Fuzzy Classifier

Pullabhatla Srikanth and C. Koley

Abstract This paper presents a system for identification and localization of type of load in an industrial power system. A simulated standard IEEE 5-bus industrial power system has been considered in the work, where the variations of the supply frequency harmonics remain within the limit as per IEC-61000 standard. The current waveforms recorded at the point of common coupling (PCC) are used for identification of the unknown nonlinear loads. Stockwell transform (ST) has been used to transform the recorded time domain signal into time–frequency domain. Further, ST is used to identify different non-stationary signatures present in the current waveforms of different power electronic drives. A comprehensive analysis has been performed to find suitable set of reduced number of features from the obtained ST coefficients, to make the system computationally light and to limit the response time to one-half of the fundamental supply frequency. The obtained optimum set of features then has been fed to fuzzy machine, for possible identification of type and location of load. Obtained results found to be robust enough to identify the nonlinear loads, even in poor quality of supply voltages.

Keywords Power quality · Nonlinear loads · Fuzzy logic · Signal processing · Harmonics

P. Srikanth (✉)
Defence Research and Development Organization (DRDO),
DRDO HQ, New Delhi 110011, Delhi, India
e-mail: srikanth.srikki@gmail.com

C. Koley
NIT Durgapur, Gandhi More, Durgapur 713209, India
e-mail: chiranjib_k@yahoo.com

1   Introduction

The presence of huge power electronic loads leads to increase in nonlinearity, thereby causing harmonics to inject into the healthy power system and exceeding the defined harmonic limits. As the power system is majorly interconnected, these harmonics superimpose with the cleaner waveforms and disturb the quality of power [1, 2]. The consequences of harmonic injection are amplification of harmonic levels due to series and parallel resonance, reduction in efficiency, ageing of insulation and system malfunctioning [3]. Due to increase in many power electronic-based industries and inclusion of power electronic equipment in large-scale residential areas, identification of type and location power electronic loads has become the prime interest to the present day power system engineers. Further, the identification and location of harmonic sources are heavily useful for utilities for harmonic assessment of the power system [4].

Vast research has been done in identification of harmonic loads in the power system. Among these, harmonic state estimation (HSE) is one of the methodologies reported in the literature [5–7]. HSE unlike the other identification techniques is only capable of estimating the net current inflow and outflow of a busbar. Generally, it may not give any information about the composition of the load. It requires the spectrogram of the nonlinear loads for running the load flow. Kalman filtering approach has also been implemented with HSE, and however, the query of identifying type of load remains unanswered [8, 9]. Similar to HSE, simultaneous measurements and constrained neural network-based identification follow the same path [10, 11]. Some advanced techniques like independent component analysis have also been reported in the literature [12]. However, the drawback is same as with HSE that the type of load is not predicted.

Few signal processing techniques like short-time Fourier transforms (STFT) and wavelet transform (WT) were testified for identification of nonlinear loads [13–16]. But the identification is purely based on visual signatures obtained from different waveforms. On the other hand, wavelet transform returns wavelet coefficients, which are basically correlation coefficients of the signal with the mother wavelet in time and scale plane, and therefore, it does not directly provide the information about the harmonic contents, i.e. magnitude at some particular frequency of interest. Though, application of STFT can directly provide the idea of harmonic contents, but it suffers from poor time and frequency resolution due to finite window length. Further, S-Transform derived from theory of wavelet transform, which is basically 'phase correction' of CWT and is obtained by multiplying the CWT with a phase factor. In the case of S-Transform, the scale factor is the inverse of the frequency. In this work, the properties of ST have been effectively applied for identification of various types of load as the time and frequency information is different for various types of loads. The present approach shall be able to automatically identify the type and location of nonlinear loads by using minimal number of extracted features from the S-Transform coefficients.

ST is an advanced and effective technique in comparison with STFT and WT [17–19]. Its unique and dynamic Gaussian window dilation with change in signal frequency provides a strong platform for time-frequency resolution (TFR). Unlike the previous TFR techniques, it overcomes the disadvantages of poor resolution of both time and frequency. In recent times, ST and inverse ST have been extensively used as a tool for analysis of power system signals [20–28]. The current waveforms of various loads at loading conditions and different locations of a five-bus power system are fed to the ST algorithm. The obtained TFR matrices are then processed through a search algorithm for extraction of minimal number of features through Mahalanobis distance approach [29, 30]. Further, the obtained features are fed to a fuzzy machine for identification of type and location of the nonlinear load [31–33]. The proposed methodology is advantageous in comparison with the techniques discussed earlier. However, the results have not been compared as the approach used here is unique and novel. The extracted features are from a TFR matrix where both time and frequency information is retained. Such information found to be effective in order to discriminate various nonlinear loads due to non-stationary nature of nonlinear load currents. A detailed explanation about the proposed methodology is provided in the following sections of this paper.

2 Simulation Model

Identification, analysis and study of nonlinear loads in a power system require accurate and practical data. However, due to the data privacy policies of utilities, it is difficult to obtain the recorded information. Though, individual nonlinear practical loads can be considered for analysis, but the effect of line impedances and source cannot be observed. Hence, a simulation of the equivalent circuits of the industrial loads has been adopted in the present work to get data of the current waveforms. Typical nonlinear loads, viz. AC regulator, cycloconverter, and DC traction, have been considered for identification. All the nonlinear loads have been rightly modelled to suit the power system considered in the work. A five-bus system has been considered for capturing the waveforms of various nonlinear loads at various locations and loadings. The single-line diagram (SLD) of IEEE standard five-bus system is shown in Fig. 1, where all the quantities are represented in per unit (PU). Complete data regarding the IEEE 5-bus system are provided in Tables 1 and 2.

The values of impedance, initial voltages have been scaled to the level of 6.6 kV with a base of 25 MVA. The positions of feed generators and consuming loads have been kept unaltered. The waveforms are recorded at the point of common coupling (PCC) which is formed at the generator bus, to make the proposed system more suitable, for practical applications.
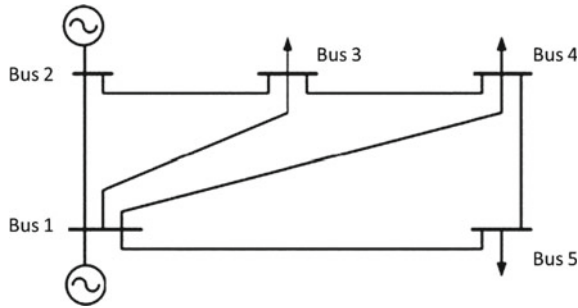
Fig. 1 Standard IEEE 5-bus system considered for simulation

Table 1 Line impedance data of IEEE 5-bus system

Source bus	End bus	R (p.u)	X (p.u)	Ys	Tap
1	2	0.02	0.06	0.03	1
1	3	0.08	0.24	0.025	1
2	3	0.06	0.18	0.02	1
2	4	0.06	0.18	0.02	1
2	5	0.04	0.12	0.015	1
3	4	0.01	0.03	0.01	1
4	5	0.08	0.24	0.025	1

Table 2 System operating parameters data

Bus no.	Generation		Load		Voltage	Q min.	Q max.	V min.	V max.
	Real	Reactive	Real	Reactive					
1	0	0	0	0	1.06	0	0	0.95	1.1
2	0.4	0.3	0.2	0.1	1	−0.4	0.5	0.95	1.1
3	0	0	0.45	0.15	1	−0.06	0.24	0.95	1.1
4	0	0	0.4	0.05	1	0	0.4	0.95	1.1
5	0	0	0.6	0.1	1	−0.06	0.24	0.95	1.1

Simulation of the shown SLD has been done using MATLAB®/SIMULINK 7.6 version [34]. However, the simulation model is not shown. Following assumptions have been considered, for simulating different practical situations that may be faced by the proposed system, when implemented:

1. Different types of nonlinear loads can be switched ON and OFF at any bus and at any instant of time. All the loads may be running at 25, 50, 75 and 100% loading condition when connected.

2. The generators are assumed to inject harmonics (under the limit of IEC-61000) and can have supply unbalances, frequency variations and transients under the limit. The harmonic injection ratios and unbalances were also varied time-to-time.
3. An allowable Gaussian noise has been added to the simulated data samples to emulate the effect of measurement error and to reach near practical situation.

These considerations are required to match the obtained data with actual behaviour. The sampling frequency was initially taken as 5 kHz, so that most of the harmonics can be considered. The recorded signals were scaled down to per unit values and stored in database experiment-wise for further analysis and identification. All the test signals are obtained using MATLAB®/SIMULINK 7.6 version.

The tests have been categorized into four types of loads as shown below:

1. Linear loads
2. AC Reg. loads
3. Cycloconverter loads and
4. Traction loads

As assumed all these loads may act in any of the three load buses with various loading values, i.e. 25, 50, 75 and 100%. As the objective is to find the type and location of the load (bus number) through classification technique, therefore each load type along with the location has been used to form as a class, and subsequently, various classes as formed are presented in Table 3. For each class, measurement has been taken from PCC with various conditions such as variation in load, supply harmonics and unbalance. At least nine set of tests have been performed for each of the class, accumulating total of 90 set of recordings. Among 90 recordings, 30 recordings (randomly chosen three recordings from each class) have been used for training, another set of 30 recordings have been used for validation and remaining 30 have been utilized for independent testing of the proposed system.

Table 3 Definition of types of classes

Class No.	Description	Variable name
1	AC regulator load at Bus-3	C1
2	AC regulator at Bus-4	C2
3	AC regulator at Bus-5	C3
4	Cycloconverter at Bus-3	C4
5	Cycloconverter at Bus-4	C5
6	Cycloconverter at Bus-5	C6
7	Traction load at Bus-3	C7
8	Traction load at Bus-4	C8
9	Traction load at Bus-5	C9
10	All linear loads	C10

3 Methodology

The present section discusses the methodology adopted for identification and localization of loads in the above-mentioned IEEE 5-bus power system. For easy understanding, a flow diagram is presented in Fig. 2. The description of each step in Fig. 2 is provided from the next subsection.

3.1 Signal Conditioning

In order to obtain the reference supply signal for detection of zero crossings, a suitable 50 Hz band-pass filter has been applied on the buffered signal, during simulation. Thereafter, a complete cycle of the actual supply current has been extracted for further processing, which acts as a reference supply signal. The amplitude and the frequency of the reference supply signal have been used for normalization of the buffered signal. It is assumed that the harmonic injection is same in both positive and negative cycles. It is also assumed that in any one half cycles, no significant information is present during the starting and ending of the half-cycle waveform. Therefore, the amplitude and phase normalized buffered signal of one half-cycle duration with phase variation from 43° to 153° is transformed to time–frequency domain using Stockwell transform (ST) [17–19]. The equation which generates the time–frequency matrix using ST is shown in Eq. (1).

$$S\left[kT, \frac{n}{NT}\right] = \sum_{k=0}^{N-1} H\left[\frac{m+n}{NT}\right].e^{\frac{-2\pi^2 m^2}{n^2}} e^{\frac{i2\pi mk}{N}} \text{ for } n \neq 0 \tag{1}$$

where k, n, $m = 0$, …, $N - 1$, T = Sampling time and N = Number of samples.

During phase normalization, the buffered signal was down-sampled to the value of the number of samples present in 51.5 Hz, i.e. $f_s/51.5$ where f_s is the sampling frequency.

3.2 Selection of Most Discriminatory Features

The ST matrix in Eq. (1) returns large number of ST coefficients in phase (normalized time domain) frequency plane, which depends on the initially chosen sampling frequency and the frequency resolution. Choosing high resolution in each of the cases results higher number of coefficients and produces huge computation burden. Since the proposed algorithm is aimed to identify the loads in real time, therefore it should be computationally less intensive in terms of required memory and number of mathematical operations. Therefore, the following steps have been adopted to obtain few set of features, which will be robust enough to discriminate different types of load irrespective of different situations.
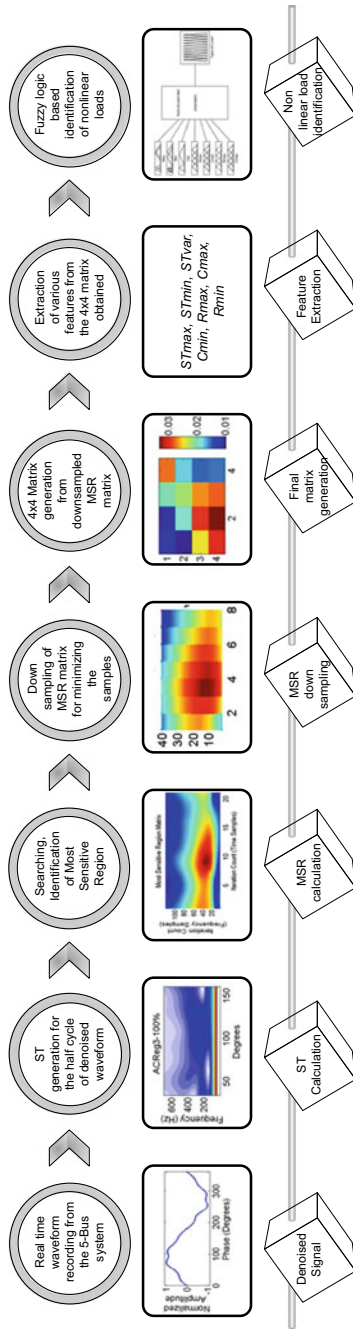
Fig. 2 Graphical representation of the overall process of nonlinear load identification

3.2.1 Searching Most Discriminatory Region

The ST coefficients matrix obtained from the normalized buffered signal contains a region which is helpful in discriminating the type nonlinear load. This region has to be identified and called as most sensitive smallest region (MSR). The MSR is a rectangular window in the ST plane, with some random initial coordinates (m, n) and having width w and breadth b, which has to be found using some search algorithms. Accordingly, an algorithm is designed which initially finds the difference between the interclass coefficients, i.e. the coefficients of classes $C_1, C_2, C_3 \ldots$ and so on. The number of coefficients to be considered depends on the window size of width w and breadth b.

When the median value of the differences (M_{avg}) between the interclass coefficients is maximum, the algorithm returns the dimensions of the MSR with coordinates. As higher median values indicate high discrimination, it is expected that better classification accuracy is achieved. However, it has been observed that this exercise generally returns larger area in the ST plane, thereby results in more number of coefficients to be computed. Therefore, in order reduce the number of coefficients, another objective, i.e. to have smallest area $A = w \times b$, has been added apart from the maximization of the mean differences. The dual objective function H is represented in Eq. (2), where maximization of M_{avg} has been converted to minimization problem. The function H leads to dual optimization problem, which has been solved through quadratic programming 'QP' optimization and using Lagrange multipliers.

$$H(m, n, w, b) = \alpha \times \frac{1}{M_{avg}} + \beta \times A \tag{2}$$

The α and β are the weights adjusted heuristically and m, n are the randomly chosen initial coordinates in H plane for the window. The optimization returns the MSR with starting coordinates of the window, i.e. m_o, n_o and the w_o and b_o. By such optimization, the MSR with minimum window width is found.

3.2.2 Reduction in Sampling Frequency and Number of Frequency Components

After selecting suitable MSR in the computed ST coefficients matrix, the sampling frequency and consequently the frequency resolution have been reduced. The reduction will make the system computationally light but may lead to loss of information which is significant for classification. In order to reduce the dimension of the MSR matrix, the sampling frequency (i.e. phase resolution) and frequency resolution have been decreased from the level of 5 kHz to 500 Hz and 1–50 Hz, respectively. While carrying out such exercise, the drop in the values of M_{avg} has been observed. Finally, by selecting a suitable M_{avg} value, the matrix size has been

reduced. However, it has been observed that the matrix can be further downscaled, by down-sampling and by averaging the values of the nearest neighbours of each element of the matrix. By doing so, very few features are fed to the fuzzy logic tool box which lessens the computation time further.

4 Feature Extraction

For classification using fuzzy logic, various features have been extracted from the down-sampled ST coefficients matrix. These are minimum and maximum values of the down-sampled matrix and their respective relative positions in the matrix-, row- and column-wise average values, variance and other statistical measures of the matrix elements. The generalization performance of a classifier depends primarily, on the selection of good features, i.e. features that represent maximal separation between the classes. Consequently, the efficacy of Mahalanobis distance is used to access discrimination ability of the reduced set ST coefficients. Here, higher distance indicates higher discrimination ability [29, 30]. Since this is a multiclass problem, therefore median value (M_d) of the Mahalanobis distances between the classes has been considered. Mahalanobis distance is defined by (3),

$$D_M(x) = \sqrt{(x - \mu)^T S^{-1}(x - \mu)} \tag{3}$$

where observation x is $(C_1, C_2)^T$ or $(C_2, C_3)^T$ or $\ldots (C_m, C_n)^T$.

Among various features, only those have been selected, which has reasonable higher Mahalanobis distance. Thereafter, the set of the selected features has been fed to fuzzy logic machine for identification of the type of nonlinear load. In most of the applications of fuzzy logic, a fuzzy logic solution is, in reality, a translation of a human solution into Fuzzy Dependency and Command Language (FDCL). Hence, the fuzzy logic technique is considered here for identification or classification of nonlinear loads based on the parameters extracted from the feature matrix obtained. A fuzzy decision box consisting of input and output membership functions with a rule base embedded inside has been always used as the tool for identification of power quality problems [31–33]. A similar system has been used here, and the detail about fuzzy system is provided in the next section.

5 Fuzzy Classification System

A fuzzy if-then logic has been used to identify the type of load. The rules have been defined based on the range of values obtained for every feature of each type of load. The overlap in the area of the membership functions has been chosen according to the range. The membership values have been assigned using intuition method.
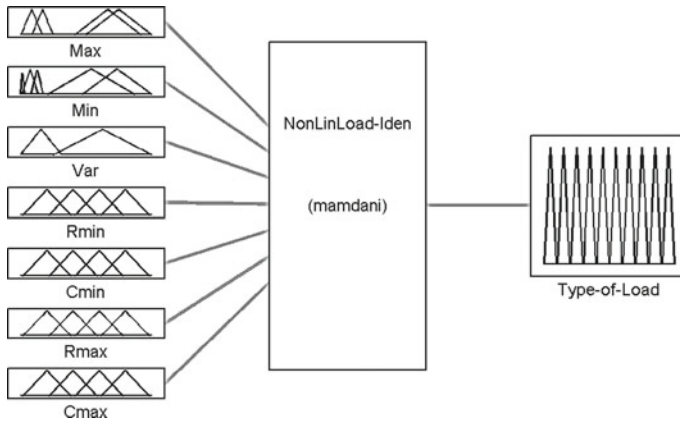
Fig. 3 Fuzzy system block diagram used for identification of nonlinear load

A triangular functioned fuzzifier has been used, and for defuzzification, centroid method has been adopted. The overall diagram of the fuzzy system has been graphically presented in Fig. 3. In order to test the robustness and accuracy of the designed fuzzy system, some random samples are fed. It is found that the system is able to identify the type of load, and hence, the same system has been considered for identification.

6 Results and Discussion

This section presents the obtained results, starting from signal conditioning section. Figure 4a shows the reference signal obtained through 50 Hz band-pass filter for an AC regulator type load placed at Bus-3, with 100% load level. The corresponding plot for normalized buffered signal in Fig. 4b. It can be seen that buffered signal is distorted as it contains other harmonics due to nonlinear load, and this indicates the need for filtering the signal to obtain the reference signal in order to find the zero crossings accurately. It also can be observed that the buffered signal mainly contains the fundamental frequency along with the other harmonics. In most of the cases, the buffered signal is almost symmetrical over the half-cycle. A surface plot of the ST coefficients for the same buffered signal is shown in Fig. 4c.

In the surface plot, the horizontal axis and vertical axis are the phase and frequency, respectively, and the magnitude of the ST coefficients is presented by colour, as presented in the colour bar. From the figure, it can be observed that, at frequency 50 Hz ST coefficients are having highest value over the entire cycle. The magnitudes decrease with the increase in the frequency, but the harmonic composition does not remain same for the time duration. It has been further observed that among the ST coefficients over the half cycle, i.e. from 0° to 180°, the

Fig. 4 Signal conditioning for current signal of AC regulator type load placed at Bus-3, with 100% load level, **a** reference signal obtained through 50 Hz band-pass filter, **b** corresponding normalized buffered signal and **c** surface plot of the ST coefficients for the same buffered
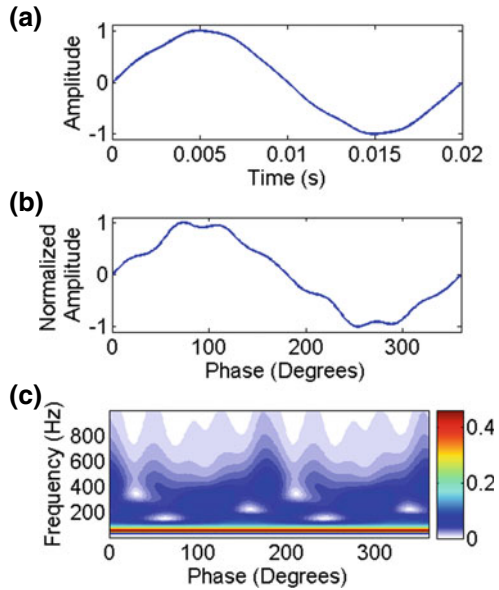
coefficients do not vary significantly with different loads, when the amplitude of the current is low. Therefore, the coefficients, i.e. from 0° to 43° and from 153° to 180°, have been eliminated for further processing, in order to reduce unnecessary computation. From the plot of different load current, it was also concluded that the ST coefficients of the fundamental and the higher-order harmonic, i.e. above 13th (650 Hz), are also not contributing significantly for classification of different load. The final ST matrix for the selected region of the load current is shown in Fig. 5.

As mentioned earlier, in order to further reduce the computation burden, the sampling frequency has been varied from 5 kHz to 500 Hz. This leads to variation in M_{avg} with respect to variation in sampling frequency, and the same has been shown in Fig. 6. It is clearly visible that reducing sampling frequency beyond 1500 Hz creates high loss in M_{avg}, thereby decreasing the discriminating ability.

The value of M_{avg} at 1500 Hz is found out to 3.455 and has dropped drastically to 3 when sampled at 1000 Hz. But sampling with 1 kHz will lead to information loss of few key harmonic components. Therefore, sampling frequency of 1.5 kHz was chosen, strategically. This leads to matrix size of [640 × 8] for the MSR. Similarly, the study on reducing frequency resolution to 50 Hz from the actual 1 Hz

Fig. 5 Surface plot of ST coefficients for MSR region 43° to 153°
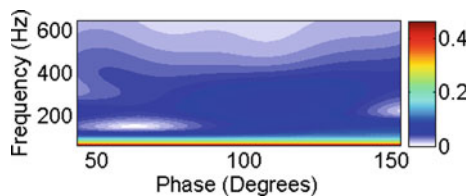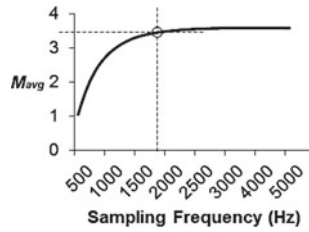
Fig. 6 Variation of average median values (M_{avg}) with sampling frequency (Hz)
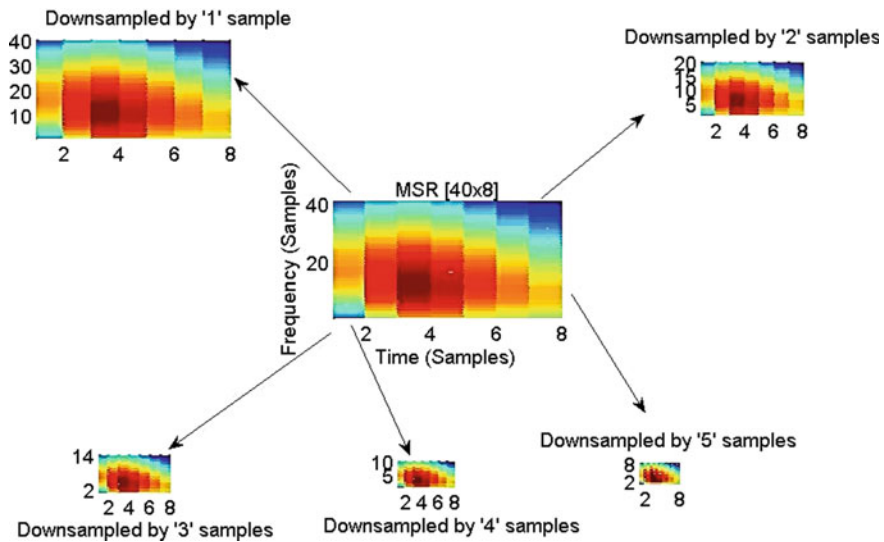
Fig. 7 Various plots of MSR after feature matrix compression. The compressed images with their respective down-sampling rate have been shown

within the MSR leads to 16 Hz as the reasonable choice, which provides 40 samples, along with the frequency axis. The final matrix of [40 × 8] size is shown in Fig. 7. This matrix size of [40 × 8] is now down-sampled to a matrix of size [8 × 8]. Further, it is reduced to the value of [4 × 4] matrix by using the average of its nearest neighbours. This makes the identification faster by reducing computation, as the size of the matrix is low. The obtained final 4 × 4 matrices for each load at each bus are shown in Fig. 8.

It is visually clear that the obtained [4 × 4] matrix is different for various loads considered at various locations (viz. Bus 3, 4 and 5). The range of values is represented in the colour bar. As automatic identification is envisaged in this work, there is a requirement of extracting the features from the matrices shown in Fig. 8. It is observed that there are numerous features available. For example, it can be observed that all the plotted 4 × 4 matrices are having different combinations of
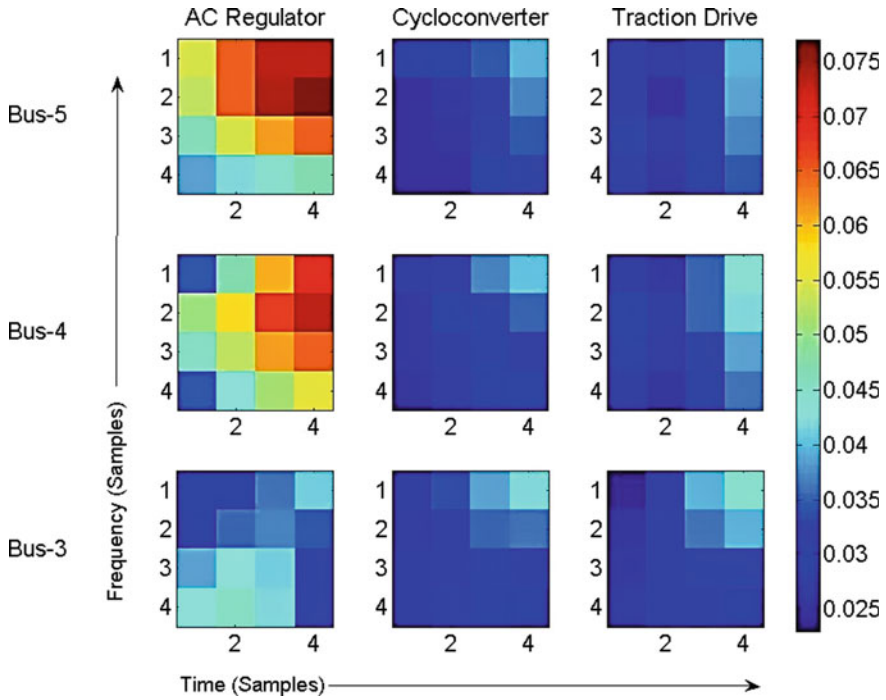
Fig. 8 Final 4 × 4 matrix (with normalized colour bar), dark brown cells indicate the highest value and dark blue cells indicate least value

colours, which represent that the values are different. Also, the maximum and minimum values obtained are positioned in various cell addresses. Hence, for extraction out of many important features available only the best suited are considered. In order to find out the best feature for feeding the fuzzy box, ranking procedure has been adopted. Such prioritized feature selection helps in accurate identification. The ranking has been done based on the Mahalanobis distance obtained, as explained in Sect. 4, for each type of feature as shown in Table 4. In total, seven types of features have been outlined and tabulated. The range of values

Table 4 Extracted features with respective rank and Mahalanobis Distance

No	Feature name	Rank	M_d
1	Maximum value of the reduced ST matrix (ST_{Max})	1	131.7
2	Minimum value of the reduced ST matrix (ST_{Min})	2	60.74
3	Variance of the reduced ST matrix (ST_{Var})	3	6.92
4	Row of Minimum values of reduced ST matrix R_{min}	4	0.98
5	Column of Maximum values of reduced ST matrix C_{max}	5	0.88
6	Column of Minimum values of reduced ST matrix C_{min}	6	0.55
7	Row of Maximum values of reduced ST matrix R_{max}	7	0.30

Table 5 Range of the extracted features nos. 1–3 defined in Table 2

Class No.	Range obtained with simulations at various loadings (25, 50, 75 and 100%)	Maximum value of the reduced ST matrix (ST_{Max})	Minimum value of the reduced ST matrix (ST_{Min})	Variance of the reduced ST matrix (ST_{Var})
1	Min	0.0533	0.0223	0.2612
	Max	0.0776	0.0399	0.8556
2	Min	0.0477	0.011	0.2668
	Max	0.0744	0.0325	0.6804
3	Min	0.0262	0.0052	0.256
	Max	0.0323	0.0081	0.4979
4	Min	0.0236	0.0023	0.1734
	Max	0.025	0.0029	0.2551
5	Min	0.0263	0.0047	0.2495
	Max	0.0269	0.0049	0.2609
6	Min	0.0285	0.0046	0.2302
	Max	0.0289	0.0052	0.2522
7	Min	0.0237	0.0028	0.031
	Max	0.0242	0.0066	0.2965
8	Min	0.0249	0.0029	0.0448
	Max	0.0299	0.0068	0.1947
9	Min	0.028	0.0038	0.1729
	Max	0.0327	0.0046	0.2457
10	Min	0.0264	0.0032	0.2997
	Max	0.0264	0.0032	0.2997

for different classes has been obtained after simulating and testing the data. The same is shown in Tables 5 and 6.

Table 5 consists of the range of values for the first three ranked features. The minimum and maximum values of the features for all the classes have been listed out in the table. It is clear that the magnitude and position of minimum and maximum value of the matrix are varying in Fig. 8. Hence, the cell addresses of the maximum and minimum value of the [4 × 4] matrix have been considered as one of the key features for identification. Table 6 consists of the details of the last four ranked features of Table 4.

Now the features with their respective ranges have been extracted, and the fuzzy rule base has been framed as shown in Table 7. It has already been explained that all the MFs of the fuzzy system are considered to be triangular as the variation in the range of values is linear. The output MFs are also considered as triangular in line with the input MFs. In the rule base, the names of various classes defined in Table 1 are used for identifying different types of loads and locations.

As mentioned earlier, one-third of the data set obtained has been used to train the proposed fuzzy system. The other one-third part has been used for validation, and

Table 6 Cell addresses of minimum (blue coloured) and maximum (brown coloured) values obtained from the 4 × 4 matrix shown in Fig. 8

Features→ Class↓	Row of minimum values of reduced ST matrix $[R_{\min}]$	Column of minimum values of reduced ST matrix $[C_{\min}]$	Row of maximum values of reduced ST matrix $[R_{\max}]$	Column of maximum values of reduced ST matrix $[C_{\max}]$
Class 1	2	4	2	1
Class 2	1	2	4	1
Class 3	4	2	4	1
Class 4	2	1	4	1
Class 5	3	1	4	1
Class 6	4	1	4	1
Class 7	1	1	4	1
Class 8	4	1	4	2
Class 9	2	1	4	2
Class 10	1	4	2	4

Table 7 Set of rules defined in the FIS rule base for identifying the type of load

S No	Feature Name
1	1. If (Max is mf4) and (Min is mf5) and (Var is mf2) and (Rmin is mf2) and (Cmin is mf4) and (Rmax is mf2) and (Cmax is mf1) then (Type-of-Load is Class1-Load) (1)
2	2. If (Max is mf3) and (Min is mf4) and (Var is mf2) and (Rmin is mf1) and (Cmin is mf2) and (Rmax is mf4) and (Cmax is mf1) then (Type-of-Load is Class2-Load) (1)
3	3. If (Max is mf2) and (Min is mf3) and (Var is mf2) and (Rmin is mf4) and (Cmin is mf2) and (Rmax is mf4) and (Cmax is mf1) then (Type-of-Load is Class3-Load) (1)
4	4. If (Max is mf1) and (Min is mf1) and (Var is mf1) and (Rmin is mf2) and (Cmin is mf1) and (Rmax is mf4) and (Cmax is mf1) then (Type-of-Load is Class4-Load) (1)
5	5. If (Max is mf1) and (Min is mf2) and (Var is mf1) and (Rmin is mf3) and (Cmin is mf1) and (Rmax is mf4) and (Cmax is mf1) then (Type-of-Load is Class5-Load) (1)
6	6. If (Max is mf1) and (Min is mf2) and (Var is mf1) and (Rmin is mf4) and (Cmin is mf1) and (Rmax is mf4) and (Cmax is mf1) then (Type-of-Load is Class6-Load) (1)
7	7. If (Max is mf1) and (Min is mf1) and (Var is mf1) and (Rmin is mf1) and (Cmin is mf1) and (Rmax is mf4) and (Cmax is mf1) then (Type-of-Load is Class7-Load) (1)
8	8. If (Max is mf1) and (Min is mf1) and (Var is mf1) and (Rmin is mf4) and (Cmin is mf1) and (Rmax is mf4) and (Cmax is mf2) then (Type-of-Load is Class8-Load) (1)
9	9. If (Max is mf2) and (Min is mf2) and (Var is mf1) and (Rmin is mf2) and (Cmin is mf1) and (Rmax is mf4) and (Cmax is mf2) then (Type-of-Load is Class9-Load) (1)
10	10. If (Max is mf1) and (Min is mf2) and (Var is mf1) and (Rmin is mf1) and (Cmin is mf4) and (Rmax is mf2) and (Cmax is mf4) then (Type-of-Load is Class10-Load) (1)

Table 8 Extracted parameters values obtained from simulations of various case studies

Load type and location	Count of correct identifications for 30 simulations	Accuracy (%)
AC regulator @ Bus-3	28	93.3
AC regulator @ Bus-4	29	96.7
AC regulator @ Bus-5	28	93.3
Cycloconverter @ Bus-3	29	96.7
Cycloconverter @ Bus-4	28	93.3
Cycloconverter @ Bus-5	28	93.3
Traction drive @ Bus-3	28	93.3
Traction drive @ Bus-4	29	96.7
Traction drive @ Bus-5	29	96.7
Linear load	28	93.3

the output obtained is as desired. The remaining one-third values have been used to obtain as given in Table 8. It is seen that the proposed ST methodology-based nonlinear identification in a 5-bus power system has produced exact and unique values for easy identification of different nonlinear loads. With the addition of the fuzzy decision box, the level of accuracy has been maintained at nearly 95%. Thus, the blend of ST and FL serves as a robust platform for identifying various types of nonlinear loads.

7 Conclusion

This paper presents a new methodology based on ST for identification of different types of nonlinear loads which exists in a power system. In total, ten combinations of nonlinear loads have been identified. The MSR technique used at pre-parameter extraction is effective with least number of calculations. Implementation of Mahalanobis distance approach is explored to find suitable set of features. The proposed concept can be scaled up to higher number of buses in power system. Further, in order to reduce the misinterpretation and increase the accuracy of the proposed technique, a fuzzy decision box is incorporated. The implementation provided reasonable good results for automatic identification of the nonlinear loads.

It is found that the fuzzy decisions are 95% accurate in identifying the unknown group of nonlinear loads. In the proposed method, an attempt has been made to reduce the computational burden, so that it can be realized into a real-time-low-cost system. It is envisaged that the exact identification of nonlinear loads shall facilitate in taking up proper remedial action for the harmonic mitigation and will prove to be an effective tool for nonlinear loads identification.

References

1. Dugan RC, Mcgranaghan MF, Santoso S, Beaty HW (2008) Electrical power systems quality, 2nd edn, chap 1. Mc.Graw Hill, USA
2. Duffy CK, Stratford RP (1989) Update of harmonic standard IEEE-519: IEEE recommended practices and requirements for harmonic control in electric power systems. IEEE Trans Ind Appl 25:1025–1034
3. Arrilaga J, Watson NR (2003) Power system harmonics, 2nd edn, chap 1. Wiley, England
4. Santoso S, Powers EJ, Grady WM, Hofmann P (1996) Power quality assessment via wavelet transform analysis. IEEE Trans Power Deliv 18:924–930
5. D'Antona G, Muscas C, Sulis S (2009) State estimation for the localization of harmonic sources in electric distribution systems. IEEE Trans Instrum Meas 58:1462–1470
6. De Arruda EF, Kagan N, Ribeiro PF (2010) Harmonic distortion state estimation using an evolutionary strategy. IEEE Trans Power Deliv 2:831–842
7. Gelagaev R, Vermeyen P, Driesen J (2008) State estimation in distribution grids. In: 13th international conference on harmonics and quality of power, 1–6
8. Yu KKC, Watson NR, Arrillaga J (2005) An adaptive Kalman filter for dynamic harmonic state estimation and harmonic injection tracking. IEEE Trans Power Delivery 20:1577–1584
9. Du ZP, Arrillaga J, Watson NR, Chen S (1999) Identification of harmonic sources of power systems using state estimation. In: IEEE proceedings-generation, transmission and distribution, vol 146, pp 7–12
10. Morimoto K, Konishi K, Miki T, Nagaoka N, Ametani A (2007) Harmonic source identification by simultaneous-multipoint harmonic measurements. In: 42nd international universities power engineering conference, 322–327
11. Hartana RK, Richards GG (1993) Constrained neural network-based identification of harmonic sources. IEEE Trans Ind Appl 29:202–208
12. Gursoy E, Niebur D (2009) Harmonic load identification using complex independent component analysis. IEEE Power Energy Soc Gen Meet 1:26–30
13. Rönnberg SK, Wahlberg M, Bollen MHJ, Lundmark CM (2008) Equipment currents in the frequency range 9–95 kHz, measured in a realistic environment. In: 13th international conference on harmonics and quality of power, ICHQP, 1–8, Sept. 28 2008–Oct. 1 2008
14. Larsson EOA, Lundmark CM, Bollen MHJ (2006) Measurement of current taken by fluorescent lights in the frequency range 2–150 kHz. In: IEEE power engineering society general meeting, 6
15. Yu XD, Wang K (2009) Digital system for detection and classification of power quality disturbance. In: Asia-Pacific Power and Energy Engineering Conference, vol 1, pp 27–31
16. Chan WL, So ATP, Lai LL (2000) Harmonics load signature recognition by wavelets transforms. In: International conference on electric utility deregulation and restructuring and power technologies, pp 666–671
17. Stockwell RG, Mansinha L, Lowe RP (1996) Localization of the complex spectrum: the S transform. IEEE Trans Signal Process 44:998–1001
18. Stockwell RG (1999) S-transform analysis of gravity wave activity from a small scale network. Ph.D. dissertation, Dept. of Physics, Western Ontario Univ., London, Ontario
19. Ventosa S, Simon C, Schimmel M, Dañobeitia JJ, Mànuel A (2008) The S-Transform from a wavelet point of view. IEEE Trans Signal Process 44:2771–2777
20. Dash PK, Panigrahi BK, Panda G (2003) Power quality analysis using S-transform. IEEE Trans Power Deliv 2:406–411
21. Lee IWC, Dash PK (2003) S-Transform-based intelligent system for classification of power quality disturbance signals. IEEE Trans Ind Electr 50:800–805
22. Zhao F, Yang R (2006) Power quality disturbance recognition using S-Transform. IEEE Conf 6:1–7

23. Zhang M, Li KC, Hu WB (2008) Automated classification of power quality disturbances using the S-Transform. In: Proceeding of the 2008 international conference on wavelet analysis and pattern recognition, vol 8, pp 321–26
24. Reddy MJB, Sagar K, Mohanta DK (2014) A multifunctional real time power quality monitoring system using Stockwell transform. IET Sci Measur Technol 8:155–169. ISSN: 17518822
25. Reddy MJB, Raghupathy RK, Venkatesh KP, Mohanta DK (2013) Power quality analysis using discrete orthogonal s-transform (DOST). Digit Signal Process 23:616–626
26. Reddy MJB., Mohanta DK, Karan BM (2004) Power system disturbance recognition using wavelet and stransform techniques. Int J Emerg Electr Power Syst 1:116
27. Srikanth P, Chandel AK, Naik KA (2011) Identification of power quality events using inverse properties of s transform. In: IEEE PES power system conference and exposition, pp 1–7
28. Srikanth P, Chandel AK, Naik KA (2011) Inverse S-Transform based decision tree for power system faults identification. Telkomnika J Electr Eng Indonesia 9:99–106
29. Jin X, Ma EWM, Cheng LL, Pecht M (2012) Health monitoring of cooling fans based on mahalanobis distance with mRMR feature selection. IEEE Transa Instrum Meas 61:2222–2229
30. Kumar S, Chow TWS, Pecht M (2010) Approach to Fault identification for electronic products using Mahalanobis distance. IEEE Trans Instrum Meas 59:2055–2064
31. Banshwar A, Chandel AK (2010) Identification of harmonic sources using fuzzy logic. In: IEEE PEDES, pp 1–6
32. Sivanandam SN, Sumathi S, Deepa SN (2007) Introduction to fuzzy logic using MATLAB. Springer, Berlin
33. Ibrahim WRA, Morcos MM (2000) Preliminary application of an adaptive fuzzy system for power quality diagnostics. Proc. IEEE Power Eng Rev 20:55–58
34. MATLAB/SIMULINK 7.6

Differential Positive Sequence Impedance-Based Transmission Line Protection Scheme

T. Manikanta Varma, Ch Durga Prasad and N. Srinivasu

Abstract In this paper, a new fault detection scheme based on a cumulative sum of differential positive sequence impedance component is presented for the application of relaying in the power system. The performance of the proposed method is tested for various fault conditions that usually occur in a power system by carrying simulations in MATLAB/Simulink. Along with faults at normal operating condition, several faults at extreme operating condition are also investigated to test the superiority of the method. From the simulation studies, it is observed that the proposed method produced acceptable performance in detecting all types of faults at different fault conditions.

Keywords Positive sequence impedance · Fault detection · Transmission line protection

1 Introduction

Transmission lines are crucial elements in the power system, as they are exposed to atmosphere over a hundred kilometers unlike other components; therefore, the chance for fault occurrence is more. Thus, they require fast and reliable protection schemes to maintain system stability and power transmission capability [1]. In transmission line protection, the tripping of relay is important as it shows a direct impact on the damage of components during fault and the relay's tripping directly depends on fault detection unit as it identifies the faulty situation. Thus, the important task in transmission line protection is the detection of a fault.

Conventionally, the protection of the transmission line is done by distance and overcurrent and differential relays. The performance of overcurrent relay is dependent on the impedance of source and fault type, which is an undesirable feature, and it is not applicable for network transmission line [2]. The drawbacks of

T. Manikanta Varma (✉) · C. Durga Prasad · N. Srinivasu
SRKR Engineering College, Bhimavaram, India
e-mail: varma251351@gmail.com

distance protection include its sensitivity for the effect of fault resistances, remote end faults, etc. The advancement of communication technologies has made pilot protection application practical. The most widely used pilot protection scheme is current differential protection. Its principle for fault detection is simple and straightforward. Its implicit selectivity, desirable sensitivity, and its fast tripping made this scheme suitable for the protection of short- and medium-transmission lines [3]. However, this scheme is affected by capacitive current due to distributed capacitance in long transmission lines [4]. Impedance-based pilot protection methods are proposed, and these methods provide some advantages [5, 6] to eliminate the effect of capacitive current when compared with current differential protection scheme.

As fault detection is a crucial task, the fault detection unit that identifies the fault in relay plays an important role in the protection of transmission line. Sample-to-sample and cycle-to-cycle comparison are the traditional methods for fault detection. These have limitations during frequency deviations from nominal value and during the presence of noise [2, 7]. A statistical approach method [8] and some complicated methods have been presented in the literature. These methods include complex calculations and are also prone to harmonics, deviations in frequency, etc. [10]. For fault detection, a moving sum approach has been implemented [9], and this method is not so effective during large frequency variations, as it requires an adaptive setting. Fault detection scheme based on cumulative sum is proposed [10], and it has problems in detecting high impedance faults.

In this paper, a new fault detection algorithm based on cumulative sum (CUSUM) of differential positive sequence impedance has been presented. The proposed algorithm has been studied under different conditions to show its effectiveness.

2 Proposed Method

Here, a method is presented to detect the faults in transmission line based on CUSUM of differential positive sequence impedance component measured at the line section to be protected.

2.1 Positive Sequence Network for Normal State

Initially, consider the positive sequence network of the power transmission system under no-fault condition as shown in Fig. 1.

E_R and E_S are positive sequence voltage sources of sending end and receiving end, respectively; Z_{SR1} and Z_{SS1} are the positive sequence source impedances; Z_{PQ1}
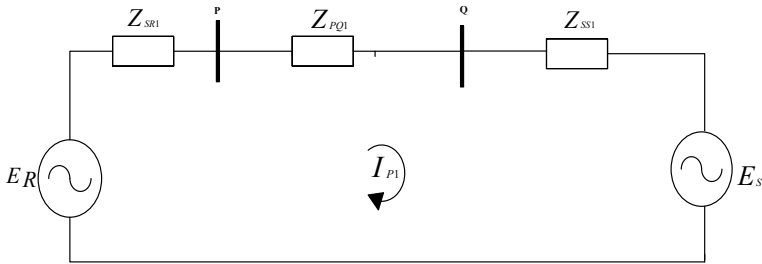
Fig. 1 Positive sequence network for no-fault condition

is the positive sequence impedance of the line section PQ. Let V_{P1}, I_{P1} and V_{Q1}, I_{Q1} be the positive sequence voltage and currents at the bus P and bus Q of the line section PQ, respectively. Let Z_{P1} and Z_{Q1} be the positive sequence impedances at the bus P and Q, respectively. Under no-fault condition,

$$\left| Z_{P1} - Z_{Q1} \right| = Z_{PQ1} \tag{1}$$

Equation (1) represents the differential positive sequence impedance of the line section PQ under no-fault condition.

2.2 Positive Sequence Network for an Internal Fault

Now, consider the positive sequence network of the power transmission system with fault initiated in between the line section PQ as shown in Fig. 2.

For fault at F_x, the positive sequence fault current through bus P and bus Q will be I_{PF1} and I_{FQ1}, respectively. Z_{PF1} and Z_{FQ1} are the equivalent positive sequence impedances of the line between bus P and F_x and between F_x and bus Q, respectively.
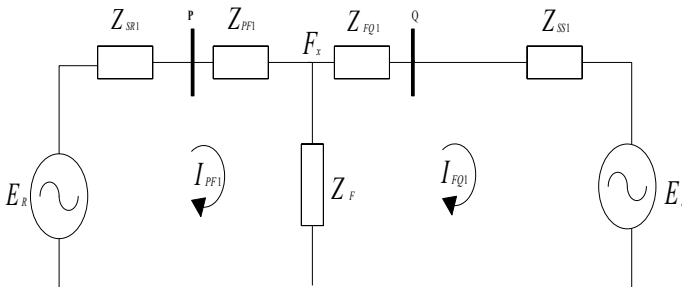
Fig. 2 Positive sequence network for fault at F_x

Applying KVL to the left loop of Fig. 2,

$$E_R - I_{PF1}(Z_{SR1} + Z_{PF1} + Z_F) + I_{FQ1}Z_F = 0 \tag{2}$$

Applying KVL to the right loop of Fig. 2,

$$-I_{FQ1}(Z_{SS1} + Z_{FQ1} + Z_F) - E_S + I_{PF1}Z_F = 0 \tag{3}$$

By solving (2) and (3), I_{PF1} and I_{FQ1} can be obtained

$$\left|Z_{P1} - Z_{Q1}\right| = \frac{E_R}{I_{PF1}} - \frac{E_S}{I_{FQ1}} - (Z_{SR1} + Z_{SS1}) \tag{4}$$

Equation (4) represents differential positive sequence impedance which is actuating signal, and to detect the fault, cumulative sum technique is applied to this signal.

Let $Z_{d1}(k)$ be the current sample of the actuating signal, and CUSUM applied actuating signal can be expressed as:

$$g(k) = g(k-1) + \max(abs((Z_{d1}(k) - Z_{d1}(k-1)) - v, 0))$$

where $g(k)$ indicates cumulative sum applied actuating signal and v is the peak value of the absolute difference between $Z_{d1}(k)$ and $Z_{d1}(k-1)$ under no-fault condition.

The fault is identified when the value of $g(k)$ exceeds the predefined setting value (threshold), i.e., $g(k) >$ threshold and

For no-fault case, $g(k) = 0$.

Hence, by this method, the faults can be detected that occur on the transmission line.

3 Algorithm Assessment

To evaluate the performance of the proposed method, a 230 kV, 50 Hz transmission system is chosen which is shown in Fig. 3 and the load angle difference of 10º is maintained between two areas.

Fig. 3 Test power system

P   Q

200km

230KV,50HZ   230KV,50HZ
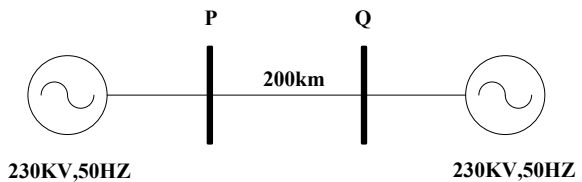
A. *Performance During unsymmetrical Faults:*

(1) L-G Fault: A fault type of B-G, at a distance of 100 km from end P with fault resistance 10 Ω, is initiated at 0.04 s. The differential positive sequence impedance signal dZpos is processed through the proposed method, and corresponding indices are plotted in Fig. 4. From Fig. 4, it is observed that the variations in positive sequence impedance (Zpos) signals of bus P and bus Q due to fault inception and CUSUM of dZpos (differential positive sequence impedance), i.e., $g(k)$, which is indicated as Index β in the plot start growing after the inception of fault and fault is identified when Index β crosses the threshold ε; here, ε is taken as 4 by doing various case studies, the corresponding trip decision is also shown in Fig. 4, and the corresponding fault detection time is 6 ms.

(2) LL Fault: A fault type of BC, at 80 km from end P having fault resistance 1 Ω, is initiated at 0.06 s, corresponding indices are plotted in Fig. 5, and the corresponding fault detection time is 5 ms.

(3) LL-G Fault: A fault type of BC-G, at 140 km from end P having fault resistance 10 Ω, is initiated at 0.03 s, corresponding indices are plotted in Fig. 6, and the corresponding fault detection time is 5 ms.
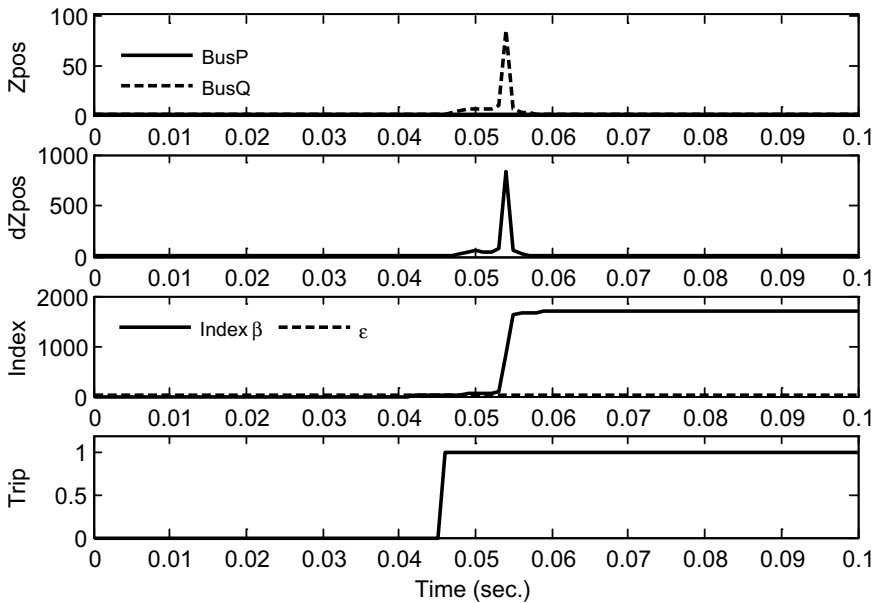
Fig. 4 **a** Positive sequence of impedance signals of buses P and Q (Zpos), **b** differential positive sequence impedance, **c** CUSUM of dZpos, **d** trip signal
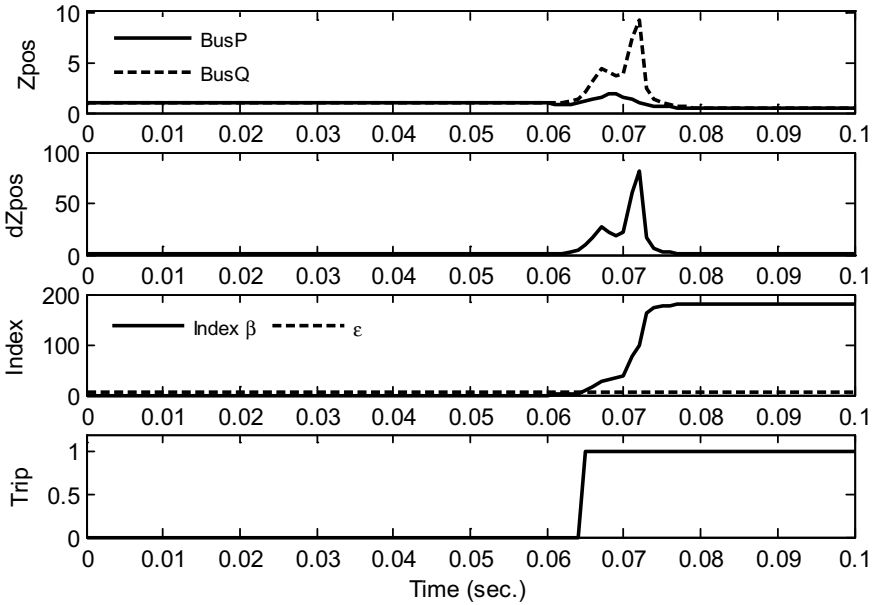
Fig. 5 **a** Positive sequence of impedance signals of buses *P* and *Q* (Zpos), **b** differential positive sequence impedance, **c** CUSUM of dZpos, **d** trip signal
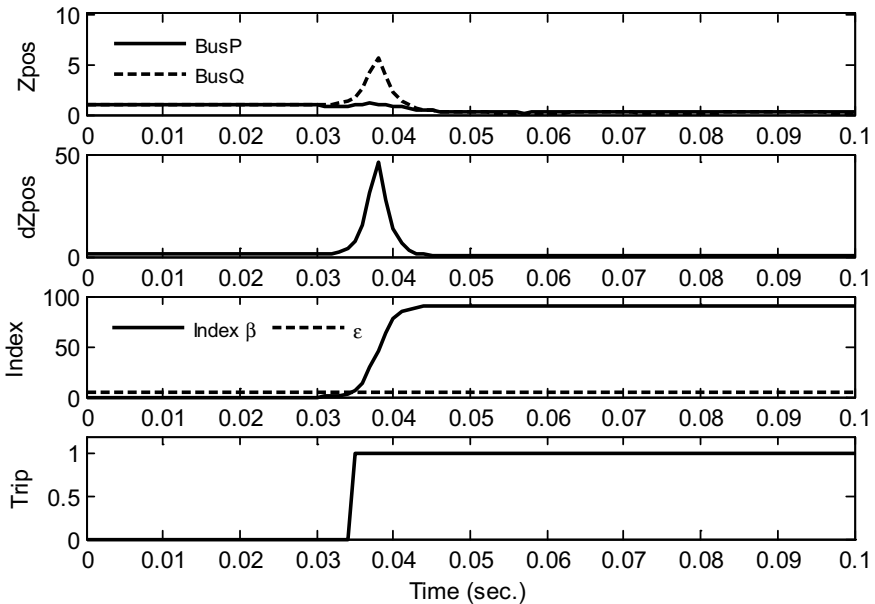
Fig. 6 **a** Positive sequence of impedance signals of buses *P* and *Q* (Zpos), **b** differential positive sequence impedance, **c** CUSUM of dZpos, **d** trip signal

B. *Performance During Symmetrical Faults:*

(1) LLL Fault: A fault type of ABC, at 180 km from end P having fault resistance 1 Ω, is initiated at 0.05 s, corresponding indices are plotted in Fig. 7, and the corresponding fault detection time is 7 ms.

(2) LLL-G Fault: A fault type of ABC-G, at 180 km from end *P* having fault resistance 10 Ω, is initiated at 0.05 s, corresponding indices are plotted in Fig. 8, and the corresponding Fault detection time is 7 ms.

C. *Effect of Fault Resistance:*

An AB-G fault is created at 50 km from end P, fault initiation is at 0.06 s and fault resistance is varying from 50 to 300 Ω. Similarly An A-G type fault at 120 km from end *P*, fault initiation is at 0.04 s and fault resistance is varied from 50 to 300 Ω. The corresponding indices for both these cases are plotted in Figs. 9 and 10, respectively. The corresponding fault detection times for both these cases are given in Tables 1 and 2, respectively.

D. *Performance During Remote End Faults:*

An A-G fault is created at 190 km from end P, fault initiation is at 0.04 s having fault resistance 10 Ω and a ABC-G type fault created at 190 km from end *P*, fault initiation is at 0.04 s having fault resistance 40 Ω. The performance of the proposed method for these faults is plotted in Fig. 11.
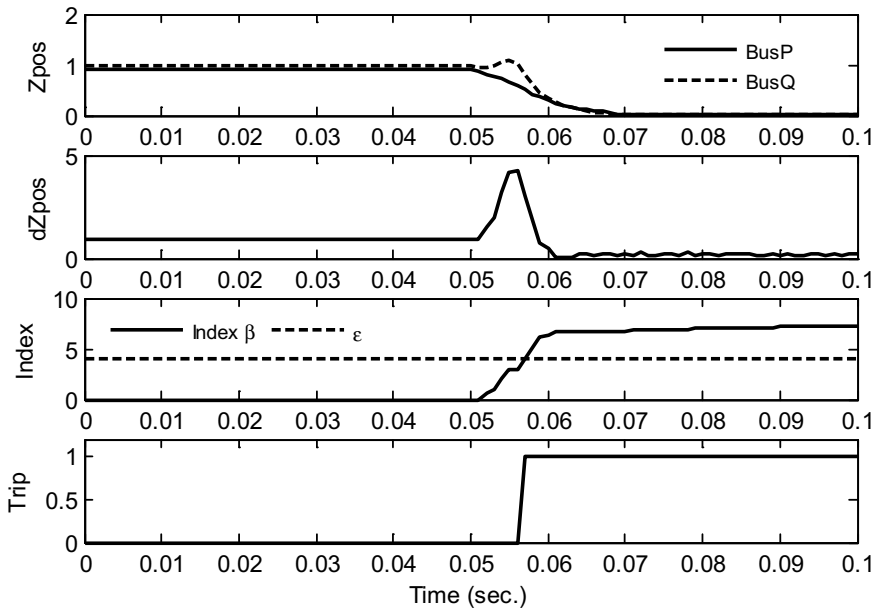
Fig. 7 **a** Positive sequence of impedance signals of buses *P* and *Q* (Zpos), **b** differential positive sequence impedance, **c** CUSUM of dZpos, **d** trip signal
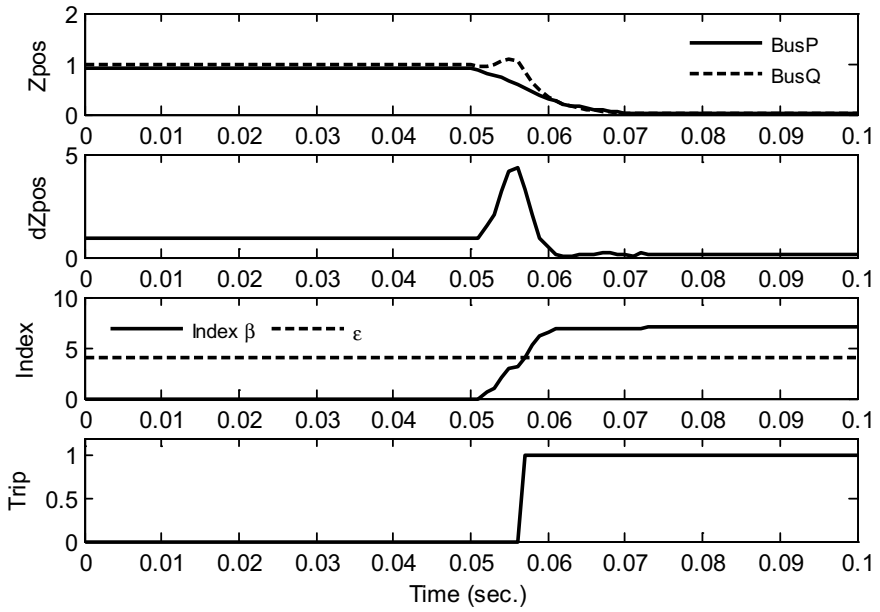
Fig. 8 **a** Positive sequence of impedance signals of buses *P* and *Q* (Zpos) **b**, differential positive sequence impedance, **c** CUSUM of dZpos, **d** trip signal

Fig. 9 Detection indices of AB-G-type fault for various fault resistances
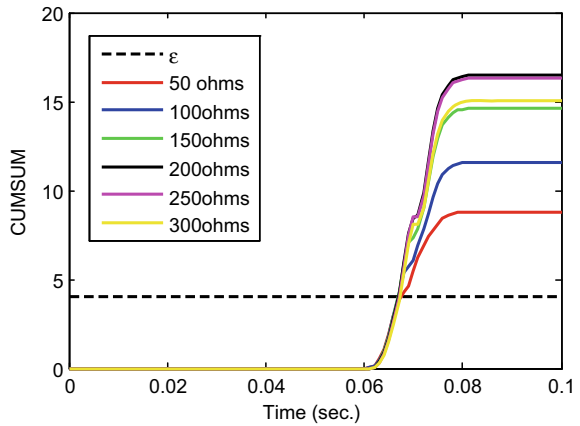
Fig. 10 Detection indices of A-G-type fault for various fault resistances
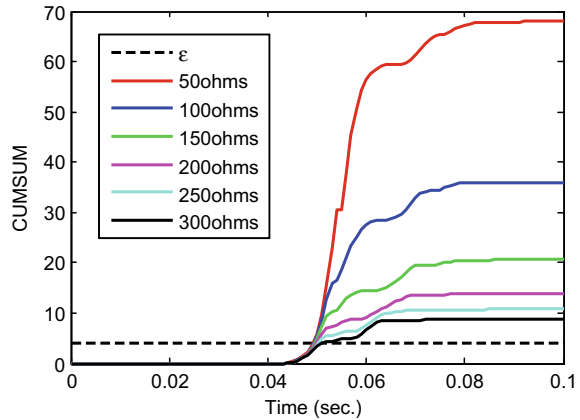
Table 1 Fault detection times for AB-G fault

Fault type	Fault inception time (s)	Fault resistance (Ω)	Fault detection time (ms)
AB-G	0.06	50	8
		100	7
		150	7
		200	7
		250	7
		300	8

Table 2 Fault detection times for A-G fault

Fault type	Fault inception time (s)	Fault resistance (Ω)	Fault detection time (ms)
A-G	0.04	50	10
		100	10
		150	10
		200	10
		250	11
		300	11

4 Conclusion

In this paper, a new fault detection scheme based on a cumulative sum of differential positive sequence impedance is presented. The performance of this method is analyzed during all fault types, high fault impedances, and remote end faults. Finally, it is observed that the proposed method is effective in detecting faults and also shows its effectiveness for remote end faults and for faults having high fault impedances.

Fig. 11 Detection indices of
A-G and ABC-G-type fault
for remote end faults
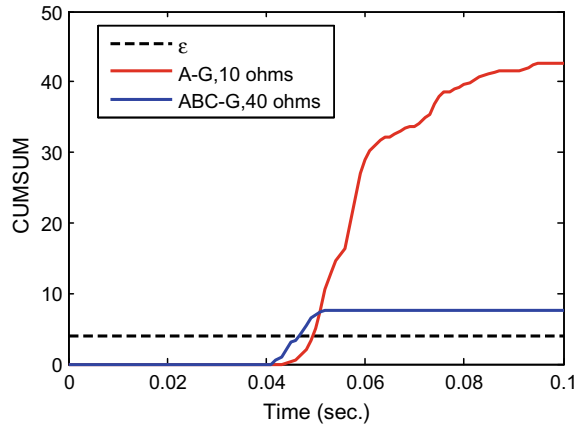
References

1. Oliveira ALP (2009) The use of real time digital simulation for performance analysis of distance protection and differential protection in short transmission lines. In: 20th international conference on electricity distribution, Prague, 8–11 June 2009
2. Phadke G, Thorp JS (2009) Computer relaying for power systems, 2nd edn. Wiley, Hoboken, NJ, USA
3. Xu ZY et al (2007) A current differential relay for a 1000 kV UHV transmission line. IEEE Trans Power Deliv 22(3):1392–1399
4. Bi TS, Yu YL, Huang SF, Yang QH (2005) An accurate compensation method of distributed capacitance current in differential protection of UHV transmission line,". In: Proceedings IEEE power engineering society of general meeting, vol 1–3, pp 770–774
5. Suonan JL, Li K, Song GB (2011) A novel UHV/EHV transmission line pilot protection based on fault component integrated impedance. IEEE Trans Power Deliv 26(1):127–134
6. Xia J, Jiale S, Deng X, Wang L, He S, Liu K (2011) Enhanced transmission line pilot impedance and pilot protection. IET Gen Trans Distrib 5(12):1240–1249
7. Gilcrest GB, Rockefeller GD, Udren EA (1972) High speed distance relaying using a digital. computer—Part I: system description. IEEE Trans Power App Syst 91(3):1235–1243
8. Gilbert BDM, Morrison IF (1997) A statistical method for the detection of power system faults. Elect Power Energy Syst 19:269–275
9. Pradhan AK, Routray A, Mohanty S (2006) A moving sum approach for fault detection of power systems. Elect Power Compon Syst 34:385–399
10. Mohanty SR, Pradhan AK, Routray A (2008) A cumulative sum based fault detector for power system relaying application. IEEE Trans Power Deliv 23(1):79–86

Optimal Planning Strategies of DG in Distribution Systems

Tarannum Bahar, Omveer Singh and Vinod Yadav

Abstract The allocation of distributed generation (DG) units has gained a lot of attraction in DNs in recent years because of their ability to reduce the burden on DN by minimizing system losses, improve the voltage profile, increase reliability and reduce overall cost of distribution system (DS). The major challenge in the installation of DG is to optimize the appropriate location and size of DG. A number of techniques are proposed by various writers in the literature that deals with the optimal DG allocation solution. This paper offers comprehensive review on dissimilar approaches of the DG placement and the numerous methods applied to planning of DG.

Keywords Distributed generation · Optimization techniques · DN · Optimal siting and sizing

1 Introduction

The traditional electrical energy systems are basically large centralized power plants [1–3]. These systems are using conventional resources of energy such as fossil fuels or the large hydro plants and nuclear plants which are more polluting and cause various environmental issues, and on the other hand, they require a long chain of transmission and DN (DN) which cause various energy loss issues. The most commonly used rules for loss reduction in DS are reconfiguration and capacitor allocation, but they are not much efficient. Among of various methods used to

T. Bahar (✉) · O. Singh
EED, SoE, GBU, G.B. Nagar, UP, India
e-mail: tannu007tannu@gmail.com

O. Singh
e-mail: omveer.singh@gbu.ac.in

V. Yadav
EED, DTU, New Delhi, India
e-mail: v3k5y7@gmail.com

reduce power loss, installation of DG is well-known method and is mostly used for its excellent results. During the last few years, the penetration of DG has got an excessive concern and can be elaborate, aspects like environmental, use of improved technologies for small generating units, power electronics devices and devices for energy-storing options for prompt backup into distribution system [4, 5]. DGs have some other technical and environmental benefits. The technical benefits include installation of DG units for power loss reduction, voltage profile improvement, enhancement of system reliability and stability, increase overall efficiency of the system, etc. [4–9].

2 Distributed Generation

Distribution generation (DG) include installation of generators which are scattered throughout power system to provide electrical power needs of consumers, in simply words they include small capacity generators which are connected near the load centres. According to CIGRE, DG as the power plant ranging from 100 MW to less than this, generally coupled with DNs and those neither centrally planned nor dispatched [8], an another organization EPRI defines, DG size ranges as from few kW up to 50 MW [9]. International Energy Agency (IEA) defines DG as generating plants that are serving customers on site connected to grid at distribution level voltage [10]. Considering the different definitions, it is evident that the meaning of DG is small-scale electricity generation. Installation of DGs using renewable energy resources is the centre of attraction by recent decades to reduce greenhouse emission such as wind, solar and biomass are often used. Other DGs options include micro- and gas turbines, diesel, internal combustion reciprocating and Stirling engines and fuel cells [11–13]. Based on generated power DGs can be grouped [7]: Type I: DG supplying of active power only (solar, fuel cells, etc.); Type II: DG supply only reactive power to enhance the voltage profile (kVAr enhancer, synchronous machine as compensator and capacitor); Type III: DGs that can supply real and reactive power both (synchronous compensators); and Type IV: DG supply active power but consume reactive power (induction generators).

2.1 Objective of DG Installation

There should be a single or multiple objectives behind optimal allocation of DG such as:

- Minimization of power losses of DN.
- Minimization of system average interruption duration index (SAIDI).
- Minimization of DG size without disturbing the constraints. Minimization of cost.

2.2 Constraints

The constraints which are majorly covering in optimal DG placement are:

- Power flow equality constraint.
- Maximum and minimum voltage limits constraint.
- Current limit constraint.
- Reliability constraints.
- Budget limit constraint.

3 Problem Statement

Installation of DG is a point of interest by recent decades, and extensive publications are available in this field, but the study shows that suitable optimal planning strategies have to be adopted before installation of DG. The main problem ensued during the installation is to determine appropriate location and size of DG. Installation of DG into existing network subjects to the various electrical constants and cost factors. For a given type of the DS, it is not logical to install the DG of any size in DN. The capacity of DG should in limit so that it does not increase line losses and also does not violate other required operating constraints [14–18].

4 Optimal Placement of DG Techniques—A Review

Area of optimal DGs placement is vast, and consequently, the available references are extensive. The aim of this work is to perform comprehensive study of the problems related to optimal allocation of DGs in DS to reduce the real power loss, improve the voltage profile and maximize the benefits. Existing literature on several aspects of optimum allocation of dissimilar kinds of DGs in DS has been grouped as follows.

4.1 Analytical Methods

Analytical methods have also been proposed in optimal placement and sizing of DG. In DN, a feeder supplying uniform distributed load for installation of DG is generally known as 'Golden Rule' or '2/3 Rule' was first introduced by Willies [14]. An analytical method has been proposed in [19], to calculate the optimum size and best location of DG in a primary DS, by reduction in real power losses. However, optimal placement of the DG violates the minimum typical service

voltage limit. An analytical expression has been proposed in [15] that determines the optimal location of DG in a radial network for minimizing loss with time-invariant and loads vary with time. Gozel et al. [20] also used the analytical approach to determine the optimal size and location considering loss sensitivity factor based on equivalent current injection method. Bhowmik et al. [21] developed a method to predict allowable DGs in a radial feeder in order to limit the voltage harmonics. Kashem et al. [22] presented an analytical approach to minimize power loss by optimizing the size, location and operating point of DGs. Tuba et al. [17] found the optimum location and capacity of DG in order to minimize network losses using an analytical strategy for uniform, centrally and increasing loads for single DG. Popovic et al. [23] developed an iterative method using loss and voltage sensitivity analysis to identify the best locations of DGs in DN. Hung et al. [24] determined the optimal size and location of different DGs types by analytical approach to minimize the losses and improve voltage profile. In [25], extended the above method to determine the optimal placement of multiple DGs by improved analytical (IA) method for same objective along with optimal pf. In [26, 27], presented a simulation study based on analytical formulation without formation of bus impedance matrix for optimum allocation of wind-based DG in a primary DS. Viral and Khatod [28] presented a fast and efficient analytical method for optimum allocation of single and multiple DG units in DN.

4.2 Classical Methods

Classical methods are those techniques in which mathematical problems are formulated and solved with the arithmetic operations. A Gradient search using second-order method to minimize power loss is proposed in [29, 30]. Authors in [31] presented a linear programming (LP) to solve optimal placement of DG for embedded DS and, in [32] with an objective to improve voltage stability, optimum allocations of DG using MINLP. Ant Lion optimization algorithm in siting & sizing of DGs in [33]. Similarly, a classical method using AIMMS and GAMS is proposed in [34].

4.3 Heuristic Methods

Heuristics approaches are based on clues, ideas or rules of thumb that are formed over insight, knowledge and decision. Some algorithms based on meta-heuristic process are as.

4.3.1 Genetic Algorithm (GA)

GA is the specific type of evolutionary algorithms which enthused by an evolutionary process for instance selection, crossover and mutations. GA with improved Hereford ranch algorithm is proposed [35] for the optimal sizing of DG. GA is used to optimize the lessening of active loss [36, 37]. Placement and bond pricing of DG to maximize owners profit is presented [38] with hybrid Immune-GA. In [39, 40], GA is used to minimize the operating cost considering the discrete size of DG. GA is integrated with the LP to minimize the power loss by increasing DG capacity in [41].

4.3.2 Tabu Search (TS)

The optimal DG placement problem is resolved by TS algorithm for equally distributed loads in [42, 43]. An incessant stochastic DG problem is resolved by hybrid GA and TS method [44]. Multiobjective TS algorithm is used to solve a dynamic DG placement problem in [45, 46].

4.3.3 Particle Swarm Optimization (PSO)

PSO is implemented to unravel an optimal DG placement in DS having varying loads and non-unity pf [47]. In [48], a PSO is to find the optimal solution of DGs allocation; the solution is compared with GA and ABC. In [48], a meta-heuristic approach is applied for DG allocation to minimize real and reactive power losses. PSO with probabilistic load flow and viability analysis is presented in [49]. A multiobjective PSO to optimize sizing and placement of DGs from DG owners has been proposed in [50]. A new multiobjective PSO (MOPSO) has been proposed considering load uncertainty in DS for allocation of DGs and shunt capacitor bank [51]. Further, a hybrid PSO with gravitational search to improve voltage profile improvement is presented in [52].

4.3.4 Ant Colony Optimization (ACO)

The author reconfigured the DN using ACO algorithm to minimize system loses [53]. Minimization of DG investment and total operating cost is solved by ACO [54]. An ACO algorithm is suggested for optimum location of DGs in [55].

4.3.5   Artificial Bee Colony (ABC)

An ABC method, with dual controlling constraints for optimal DG allocation, is proposed in [56]. ABC is used to compute the network reinforcements and commitment schedule for installed generating units is presented in [57].

4.3.6   Harmony Search (HS)

A loss sensitivity factor based scheme is used for optimal DG siting and solved by HS technique in [58]. An improved multiobjective HS to improve voltage profile is presented in [4].

4.3.7   Practical Heuristic Algorithm

An approach using heuristic value for optimum location of a single DG by minimizing system reliability cost is described in [59]. Heuristic optimal DG placement scheme depends on continuous power flow is offered in [60]. The DG placement is elucidated by using the constructive heuristic algorithm in [61, 62]. The heuristic iterative method using clustering and exhaustive search method to find optimal location of DG [63, 64]. A heuristic method based on uniform voltage distribution based constructive reconfiguration algorithm (UVDA) is proposed for DG siting and sizing in [65].

5   Evaluation of Optimal DG Allocation Methods

This section extends the evaluation methods used for DG placement.

5.1   Evaluation of Analytical Methods

Analytical methods are easily implemented and executed quickly, but obtained results are only indicative, due to dependency on simplified assumptions.

5.2   Evaluation of Numerical Methods

The optimal results can be obtained by numerical methods but usually inaccurate and time-consuming due to complex optimization model, hence difficult for large system.

5.3 Evaluation of Heuristic Methods

Heuristic techniques are having easy in use. Due to their robustness can give near-optimal solution for intricate and large size network.

6 Taxonomy and Input of Revised Work

Table 1 illustrates brief taxonomy and key contribution of reviewed work of DG planning techniques for power loss minimization. Summary of different objectives considered in past work is given in Table 2, whereas comparison of various technique reviewed above is presented in Table 3.

Table 1 Summary of techniques for DG planning considering power loss

Objective function	DG locations	DG modelling as real/reactive source	Techniques implemented	Contribution & inferences
Minimize line losses	Only single optimal location [15], single DG with uniform, central and increasing load [53, 59], only optimal locations [16, 55], single DG placement [4, 17–29], multiple DG [25–29, 45, 56, 57, 66], Type I, II & III DG at single location [25, 49]	Real power [15–19, 36–46], real and reactive [26–28, 46–49], real and reactive with unspecified pf [17], Type I and Type II [48], DG and capacitor option [67]	**Analytical**: Analytical approaches [15–28], Iterative technique [16, 17], Analytical techniques with and without considering P and QV buses [18, 27]. **Classical**: **Gradient** [29, 30], LP [31], MINLP [32], hybrid SQP and BAB [33]. **Heuristic**: GA [36–38, 40, 41], TS [43, 47], PSO [50, 52, 58], Ant colony [54–56], ABC [57, 58], HS [4, 59], practical heuristics [60–66]	(1) Optimal DG allocation problem by classical methods is not fully explored. Therefore, optimal planning by classical approach need to be extend further (2) DG is modelled as a real power source by most of the researches. Further research can be proceed by modelled DG as both real and reactive source (3) In the literature, DG is modelled at UPF or constant pf. But, DG modelling can be include by considering optimal DG pf too

Table 2 Summary of different objectives used in the literature

Objective function	Techniques used	Remarks
Min. of energy loss	Analytical approaches [15–27], classical approach using AIMMS [20], classical approach using GAMS [25], classical approach using LP [32], ACO [55, 56]	Actual wind generation case study considered in [24, 25]
Min. of power loss, voltage profile improvement, DG capacity maximization.	Hybrid PSO with gravitational search [67, 68], ABC [57, 58], constructive heuristic algorithm [62, 63]	Multiobjective optimization with weighted average
Multiobjective with weighted average for voltage profile improvement, line loss reduction, line loading and short circuit	GA and fuzzy set theory [69], PSO with different load models [48], MOPSO with uncertainty load [67]	$W = W1$ VPI $+ W2$ PLI $+ W3$ QLI $+ W4$ LLI $+ W5$ SCI, VPI—Voltage profile index, PLI, QLI—Active and reactive power loss, index LLI—Line loading index, SCI—Short-circuit current index, $W1$, $W2$, $W3$, $W4$, $W5$ weights of different index.
Reliability improvement	Analytical method for benefit and maximization with min. of cost for voltage profile and reliability improvement using GA technique [70, 71]	
Multiobjective for max. of DG owner profit and min. of DISCO cost	GA [71], Immune-GA [39], MOPSO [48]	Single objective [71], modelled as multiobjective [42, 48]
Min. power loss, voltage deviation and voltage stability improvement	MINLP [29], TS [42, 45, 46]	
Min. loss and voltage improvement	HS [4], IMOHS Multiobjective harmony search [59]	Min. power loss and voltage profile improvement with network reconfiguration and DG [4], multiobjective [59]

Table 3 Comparison of different optimization techniques

Objective function	Objectives considered	Technique implemented	Contribution & conclusion
Min. cost	Min. cost. discrete size of DG considered while environment criterion not considered [39]; min. investment and operational cost with DG modelled as per the capability curve, environment criterion not considered [46]; planning with renewable resources for emission reduction along with cost minimization [72]; Min. of cost integrated with technical and environment criterion [73]; min. energy and loss cost along with emission reduction [74]; min. generation cost and line loss cost without environment criterion [75]; min. generation, operational and network enforcement cost without environment criterion [76]; probabilistic approach for cost and emission reduction [77]; consideration of reactive power limit for min. of economic, emission and reliability cost with load and generation uncertainty [69]	MILP approach [46], MINLP approach [40], multiobjective with GA and NSGA [39, 59, 79], multiobjective optimization using NSGA and fuzzy set to handle uncertainty [67], PSO [48, 69], multiobjective using shuffled frog leap algorithm [74], ε-constraint method [42], back-propagation approach [65], UVDA [66]	(1) DG modelling without reactive power capability may lead to suboptimal location, thereby underutilization of DG power. Also, optimal DG size is also not same when modelled as real power source or real and reactive power source (2) DG planning at peak load may lead to overestimation of DG size. Therefore, DG planning at discrete load levels give more realistic DG location, size and time of installing new unit (3) The eco-environment criterion should be considered fully for sustainable development (4) Some RES cannot compete with conventional sources in its present form

7 Conclusion

This paper discussed overview of different methods used for the optimal allocation of DGs. The work illustrates that during optimal allocation of DG in DS, need proper concern of voltage profile, losses, load ability, reliability, etc. The important contribution of this study is to summarize those methods that minimize real and reactive loss and thus reduce installation cost of DG without violating the constraints. The methods used for the DG planning are categorized into three groups,

namely analytical, classical and heuristic approaches. The study concludes that the analytical methods are easy to implement, but they offer approximate results. The classical methods are suitable for small DN but become complex for large network. Moreover, heuristic techniques are popular as they are fast and modification can be done easily, such as GA and practical heuristic algorithms.

References

1. Federico J, Gonzalez V, Lyra C (2005) Learning classifiers shape reactive power to decrease losses in power distribution networks. In: Proceedings of IEEE power engineering society general meeting, vol 1, pp 557–562
2. Baran ME, Wu FF (1989) Network reconfiguration in distribution systems for loss reduction and load balancing. IEEE Trans Power Delivery 4(2):1401–1407
3. Haque MH (1996) Efficient load flow method for distribution systems with radial or mesh configuration. IEE Proc Gen Trans Distrib 143(l):33–38
4. Rao RS, Ravindra K, Satish K, Narasimham SVL (2013) Power loss minimization in distribution system using network reconfiguration in the presence of distributed generation. IEEE Trans Power Syst 28(1):317–325
5. Ackermann T, Andersson G, Soder L (2001) Distributed generation: a definition. Electr Power Syst Res 57(3):195–204
6. Viral R, Khatod DK (2012) Optimal planning of distributed generation systems in distribution system: a review. Renew Sustain Energy Rev 16(7):5146–5165
7. Hung DQ, Mithulananthan N (2011) Multiple distributed generator placement in primary distribution networks for loss reduction. IEEE Trans Ind Electron 60(4):1700–1708
8. CIGRE (1999) Impact of increasing contribution of dispersed generation on the power system. Working Group 37.23, p 44
9. Schmill JV (1965) Optimum size and location of shunt capacitors on distribution feeders. IEEE Trans Power App Syst 84(9):825–832
10. IEA (2018) Distributed generation in liberalised electricity markets. OECD Publishing, http://dx.doi.org/10.1787/9789264175976-en. Accessed on 2018
11. Martin G (2003) Renewable energy gets the green light in Chicago. IEEE Power Ener. Mag 99(6):34–39
12. Sonderegger RC, Henderson D, Bubb S, Steury J (2004) Distributed asset insight. IEEE Power Energy Mag 3(1):32–39
13. Rahman S (2003) Green power: what is it and where can we find it? IEEE Power Energy Mag 99(1):30–37
14. Willis HL (2000) Analytical methods and rules of thumb for modeling DG distribution interaction. In: Proceedings of IEEE Power Engineering Society. Summer Meeting (2000), pp 1643–1644
15. Wang C, Nehrir MH (2004) Analytical approaches for optimal placement of distributed generation sources in power systems. IEEE Trans Power Syst 19(4):2068–2076
16. Hedayati H, Nabaviniaki SA, Akbarimajd AA (2008) Method for placement of DG units in distribution networks. Power Deliv IEEE Trans 23:1620–1628
17. Tuba G, Hocaoglu MH, Eminoglu U, Balikci A (2005) Optimal placement and sizing of distributed generation on radial feeder with different static load models. In: IEEE international conference on future power system, Amsterdam, pp 2–6
18. Ghosh S, Ghoshal SP (2010) Optimal sizing and placement of distributed generation in a network system. Int J Elect Power Energy Syst 32(8):849–856
19. Acharya N, Mahat P, Mithulananthan N (2006) An analytical allocation in primary distribution network. Elect Power Energy Syst 28(10):669–678

20. Gozel T, Hocaoglu MH (2009) An analytical method for the sizing and siting of distributed generators in radial systems. Elect Power Syst Res 79(6):912–918
21. Bhowmik A, Maitra A, Halpin SM, Schatz JE (2003) Determination of allowable penetration levels of distributed generation resources based on harmonic limit considerations. IEEE Trans Power Delivery 18(2):619–624
22. Kashem MA, Le ADT, Negnevitsky M, Ledwich G (2006) Distributed generation for minimization of power losses in distribution systems. In: Proceedings of PES general meeting, Montreal, pp 1–6
23. Begovic DH, Pregelj A (2005) Placement of distributed generators and reclosers for distribution network security and reliability. Elect Power Energy Syst 27(5–6):398–408
24. Hung DQ, Mithulananthan N, Bansal RC (2010) Analytical expressions for DG allocation in primary distribution networks. IEEE Trans Energy Conf 25(3):814–820
25. Hung DQ, Mithulananthan N (2013) Multiple distributed generator placement in primary distribution networks for loss reduction. IEEE Trans Ind Electron 60:4
26. Mahat P, Ongsakul W, Mithulananthan N (2006) Optimal placement of wind turbine DG in primary distribution systems for real loss reduction. In: Proceedings of energy for sustainable development, Thailand, pp 1–6
27. Tha A, Das D (2016) Novel analytical method for the placement and sizing of distributed generation unit on distribution networks with and without considering P and PQV buses. Electr Power Energy Syst 78:401–413
28. Viral R, Khatod DK (2015) An analytical approach for sizing and siting of DGs in balanced radial distribution networks for loss minimization. Int J Electr Power Energy Syst 67:191–201
29. Rau NS, Wan YH (1994) Optimum location of resources in distributed planning. IEEE Trans Power Syst 9(4):2014–2020
30. Vovos PN, Bialek JW (2005) Direct incorporation of fault level constraints in optimal power flow as a tool for network capacity analysis. IEEE Trans Power Syst 20(4):2125–2134
31. Keane A, O'Malley M (2005) Optimal allocation of embedded generation on distribution networks. IEEE Trans Power Syst 20(3):1640–1646
32. Al Abri RS, El-Saadany EF, Atwa YM (2013) Optimal placement and sizing method to improve the voltage stability margin in a distribution system using distributed generation. IEEE Trans Power Syst 28(1):326–334
33. Ali ES, Abd Elazim SM, Abdelaziz AY (2017) Ant lion optimization algorithm for optimal location and sizing of renewable distributed generations. Renew Energy 101:1311–1324
34. Kaur S, Kumbhar G, Sharma J (2014) MINLP technique for optimal placement of multiple DG units in distribution systems. Int J Electr Power Energy Syst 63:609–617
35. Ochoa LF, Dent CJ, Harrison GP (2010) Network distributed generation capacity analysis using OPF with voltage step constraints. IEEE Trans Power Syst 25(1):296–304
36. Kim JO, Nam SW, Park SK, Singh C (1998) Dispersed generation planning using improved Hereford ranch algorithm. Electr Power Syst Res 47(1):47–55
37. Singh RK, Goswami SK (2009) Optimum siting and sizing of distributed generations in radial and networked system. Elect Power Comp Syst 37:127–145
38. Shukla TN, Singh SP, Srinivasarao V, Naik KB (2010) Optimal sizing of distributed generation placed on radial distribution systems. Elect Power Comp Syst 38:260–274
39. Soroudi A, Ehsan M, Caire R, Hadjsaid N (2011) Hybrid immune-genetic algorithm method for benefit maximisation of distribution network operators and distributed generation owners in a deregulated environment. IET Gen Trans Distr 5:961–972
40. Jalali M, Zare K (2004) A multi-stage MINLP-based model for sub-transmission system expansion planning considering the placement of DG units. Int J Electr Power Energy Syst 63:8–16
41. Liu K, Shen W, Liu Y (2014) Optimal allocation of distributed generation in distribution system considering time sequence data and low-carbon economy. In: PES General Meeting Conference & Exposition. National Harbor, MD, USA, pp 1–5
42. Soroudi A, Ehsan M (2010) A distribution network expansion planning model considering distributed generation options and techo-economical issues. Energy 35:3364–3374

43. Nara K, Hayashi Y, Ikeda K, Ashizawa T (2001) Allocation of Tabu search to optimal placement of distributed generators. In: IEEE power engineering society winter meeting, vol 2, pp 918–923
44. Golshan MEH, Arefifar SA (2007) Optimal allocation of distributed generation and reactive sources considering tap positions of voltage regulators as control variables. Eur Trans Electr Power 17(3):219–239
45. Novoa C, Jin T (2011) Reliability centered planning for distributed generation considering wind power volatility. Elect Power Syst Res 81(8):654–1661
46. Pereira Junior BR, Cossi AM, Contreras J, Mantovani RS (2014) Multiobjective multistage distribution system planning using Tabu search. IET Gen Trans Distr 8(1):35–45
47. Koutsoukis NC, Georgilakis PS, Hatziargyriou ND (2014) A Tabu search method for distribution network planning considering distributed generation and uncertainties. In: Proceedings of PMAPS, Dhuram, UK
48. Gomez GM, Lopez A, Jurado F (2012) Optimization of distributed generation systems using a new discrete PSO and OPF. Elect Power Syst Res 84(1):174–180
49. El-Zonkoly AM (2011) Optimal placement of multi-distributed generation units including different load models using particle swarm optimization. IET Gen Trans Distr 5(7):760–771
50. Jain N, Singh SN, Srivastava SC (2012) Meta-heuristic approach for distributed generation planning in electricity market paradigm. In: IEEE power energy society general meeting, CA, USA, pp 1–6
51. Jain N, Singh SN, Srivastava SC (2013) A generalized meta-heuristic approach for distributed generation planning in electricity market paradigm approach for DG planning and viability analysis under market scenario. IEEE Trans Ind Electr 60(11):5075–5085
52. Ameli A, Bahrami S, Khazaeli F, Haghifam MR (2014) A multiobjective particle swarm optimization for sizing and placement of DGs from DG owner's and distribution company's viewpoints. IEEE Trans Power Delivery 29(4):1831–1840
53. Wen Shan T, Hassan MY, Rahman HA, Abdullah MP, Hussin F (2013) Multi-distributed generation planning using hybrid particle swarm optimisation-gravitational search algorithm including voltage rise issue. IET Gen Trans Distrib 7(9):929–942
54. Su CT, Chang CF, Chiou JP (2005) Distribution network reconfiguration for loss reduction by ant colony search algorithm. Electr Power Syst Res 75(2–3):190–199
55. Falaghi H, Haghifam MR (2007) ACO based algorithm for distributed generations sources allocation and sizing in distribution systems. In: IEEE proceedings of Lausanne power tech, Tehran, pp 555–560
56. Wang L, Singh C (2008) Reliability-constrained optimum placement of reclosers and distributed generators in distribution networks using an ant colony system algorithm. IEEE Trans Syst Man Cybern Appl Rev 38(6):757–764
57. Abu-Mouti FS, El-Hawary ME (2011) Optimal distributed generation allocation and sizing in distribution systems via artificial bee colony algorithm. IEEE Trans Power Delivery 26 (4):2090–2101
58. El-Zonkoly AM (2013) Multistage expansion planning for distribution networks including unit commitment. IET Gen Trans Distrib 7(7):766–778
59. Nekooei K, Farsangi MM, Nezamabadi-pour H, Lee KY (2013) An improved multi-objective harmony search for optimal placement of DGs in distribution systems. IEEE Trans Smart Grid 4(1):557–567
60. Banerje B, Islam SM (2011) Reliability based optimum location of distributed generation. Int J Electr Power Energy Syst 3(8):1470–1478
61. Hemdan NGA, Kurrat M (2011) Efficient integration of distributed generation for meeting the increased load demand. Int J Electr Power Energy Syst 33(9):1572–1583
62. Celli G, Ghiani E, Soma GG, Pilo F (2012) Planning of reliable active distribution systems. In: Proceedings of CIGRE
63. Millar RJ, Kazemi S, Lehtonen M, Saarijarvi M (2012) Impact of MV connected micro grids on MV distribution planning. IEEE Trans Smart Grid 3(4):2100–2108

64. Rotaru F, Chicco G, Grigoras G, Cartina G (2012) Two-stage distributed generation optimal sizing with clustering-based node selection. Int J Electr Power Energy Syst 40(1):120–129
65. Humayd ASB, Bhattacharya K (2013) Comprehensive multi-year distribution system planning using back-propagation approach. IET Gen Trans Distrib 7(12):1415–1425
66. Bayat A, Bagheri A, Noroozian R (2016) Optimal siting and sizing of distributed generation accompanied by reconfiguration of distribution networks for maximum loss reduction by using a new UVDA-based heuristic method. Electr Power Energy Syst 77:360–371
67. Zeinalzadeh A, Mohammadi Y, Moradi MH (2015) Optimal multi objective placement and sizing of multiple DGs and shunt capacitor banks simultaneously considering load uncertainty via MOPSO approach. Electr Power Energy Syst 67:336–349
68. Vahidinasab V (2014) Optimal distributed energy resources planning in a competitive electricity market: multiobjective optimization and probabilistic design. Renew Energy 66:354–363
69. Kai Z, Agalgaonkar AP, Muttaqi KM, Perera S (2012) Distribution system planning with incorporating DG reactive capability and system uncertainties. IEEE Trans Sustain Energy 3:112–123
70. Brown RE, Freeman LAA (2001) Analyzing the reliability impact of distributed generation". Power Eng Soc Sum Meet 2(1):1013–1018
71. Borges CLT, Falcao DM (2006) Optimal distributed generation allocation for reliability, losses, and voltage improvement. Int J Electr Power Energy Syst 28:413–420
72. Kumar M, Kumar A, Sandhu KS (2018) Optimal location of WT based distributed generation in pool based electricity market using mixed integer non linear programming. Mat Today Proc 5(1 Part 1):445–457
73. Uniyal A, Kumar A (2018) Optimal distributed generation placement with multiple objectives considering probabilistic load. Proc Comp Sci 125:382–388
74. Doagou-Mojarrad H, Gharehpetian GB, Rastegar H, Olamaei J (2013) Optimal placement and sizing of DG (distributed generation) units in distribution networks by novel hybrid evolutionary algorithm. Energy 54:129–138
75. Viana MS, Manassero G, Udaeta MEM (2018) Analysis of demand response and photovoltaic distributed generation as resources for power utility planning. Appl Energy 217(1):456–466
76. Hejeejo R, Qiu J (2017) Probabilistic transmission expansion planning considering distributed generation and demand response programs. IET Renew Power Gen 11(5):650–658
77. Tanaka I, Yuge H, Ohmori H (2017) Formulation and evaluation of long-term allocation problem for renewable distributed generations. IET Renew Power Gen 11(12):1584–1596

Bat Search Algorithm for Solving Multi-objective Optimal Power Flow Problem

Saket Gupta, Narendra Kumar and Laxmi Srivastava

Abstract This work presents bat search (BS) algorithm to solve optimal power flow problem. BS algorithm is a population-based random search technique that mimics bats' behavior. The main motive of solving an optimal power flow (OPF) problem is to obtain the optimal setting of control variables in a power system that minimizes or maximizes one or more objective functions. The power system equality and inequality constraints such as generator constraints, transformer constraints, shunt VAR constraints, line flows, and bus voltage constraints are effectively handled in OPF problem by implementing penalty factor approach. The proposed bat search algorithm is applied to find optimal setting of the power system control variables like generators real power outputs except slack bus, generator bus voltages, transformer tap settings and other sources of reactive power such as shunt capacitor or some shunt FACTS controller. The objective functions to carry out OPF are fuel cost minimization, improvement voltage profile, and enhancement of voltage stability under normal condition as well as during line outage contingency. Effectiveness of the proposed bat search algorithm has been demonstrated by applying BS algorithm to solve OPF problem in the standard IEEE 30-bus system with the above-mentioned objectives. The results obtained using BS algorithm are compared with the results obtained using other evolutionary computing techniques reported in the literature. The comparison of results clearly shows that the proposed bat search algorithm provides better and feasible solution when solving the OPF problem.

S. Gupta (✉) · N. Kumar
Electrical Engineering Department, Delhi Technological University (DTU),
Shahbad Daulatpur Bawana Road, Delhi 110042, India
e-mail: sguptamits@gmail.com

N. Kumar
e-mail: dnk_1963@yahoo.com

L. Srivastava
Electrical Engineering Department, MITS, Gwalior, India
e-mail: laxmigwl@gmail.com

1 Introduction

The main aim of solving an OPF problem is to find optimal setting of control variables that optimizes a certain objective function such as minimization of generators fuel cost, improvement of voltage profile, and enhancement of voltage stability under normal and contingency condition, etc., subject to satisfying various operating constraints and power balance equation. OPF problem formulation yields a highly nonlinear, multimodal, non-convex, non-differential objective function having continuous and discrete control variables, and it has been introduced by Carpentier in the early 1960s [1].

Nowadays, voltage instability problem is being faced, because generation and transmission capability expansion is unable to meet the load demand. At the same time, lack of reactive power sources in power system leads to bulk power losses in transmission lines. So, it is very important to consider voltage profile improvement and voltage stability improvement as the objectives of OPF problem.

To solve optimal power flow problem, several conventional optimization techniques like mixed integer programming, linear programming, nonlinear programming, interior point method, quadratic programming, and Newton-based methods were used. Because of the nonlinear, non-differential, multimodal, non-smooth, and non-convex nature of the problem, the traditional optimization techniques are not appropriate for solving optimal power flow problem [2, 3]. On the other hand, evolutionary computing (EC)-based techniques [4] do not have any such restrictions of objective functions and are able to solve any type of the optimization problem. These population-based random search optimization techniques are heuristic in nature which, though not assuring global optimality, are able to offer good near-optimal solutions within acceptable computation time.

In recent years, various EC-based techniques have been implemented to solve OPF problem. Some of these techniques are Dragonfly algorithm (DA) [5], genetic algorithm (GA) [6], linear adaptive genetic algorithm (LAGA) [6], particle swarm optimization [7], quasi-oppositional biogeography-based optimization (QOBBO) [8], chaotic krill herd algorithm (CKHA) [9], refined genetic algorithm (RGA) [10], glowworm swarm optimization (GSO) [11], league championship algorithm (LCA) [12], improved differential evolution-based approach (IDE) [13], modified differential evolution algorithm (MDE) [14], and many others.

The BS algorithm developed by Xin She Yang in 2010, is a heuristic algorithm, and has been inspired by echolocation characteristics of bats. Most of the bats species use a type of sonar called echolocation that guides them in their flying as well as in hunting even in complete darkness [15]. Bat search algorithm has been applied in this paper for solving OPF problem with the objectives of minimizing

fuel cost and improving voltage profile and voltage stability. Effectiveness of the BS algorithm is tested on IEEE 30-bus system.

2   Problem Formulation

The optimal power flow problem considered in this paper is for minimizing fuel cost and improving voltage profile and voltage stability subject to various equality and inequality constraints [16] as discussed below.

2.1   *Objective Function*

In this paper, four different objective functions are considered for solving OPF problem. The objective functions are as follows:

(a) **Minimization of Generators' Fuel cost**

The first objective function, namely generators' fuel cost minimization, can be expressed as:

$$F_1(x, u) = \sum_{i=1}^{\text{NGN}} f_i\left(P_{g_i}\right) (\$/\text{h}) \tag{1}$$

The fuel cost equation can be written as:

$$f_i\left(P_{g_i}\right) = A_i + B_i P_{g_i} + C_i P_{g_i}^2 (\$/\text{h}) \tag{2}$$

where A_i, B_i, and C_i are the quadratic fuel cost coefficients of the ith generator.

(b) **Voltage profile improvement**

The second objective function deals with minimization of voltage deviations at all the load (PQ) bus voltage from 1.0 p.u.

In Case 1, considering only fuel cost may provide feasible solution but poor voltage profile. So, in this case (Case 2) simultaneous minimization of fuel cost and improvement of voltage profile has been considered using twofold objective function as:

$$F_2(x, u) = \sum_{i=1}^{\text{NGN}} f_i(.)\$/\text{h} + \alpha_{\text{VD}} \sum_{i \in \text{NL}} |V_i - 1| \tag{3}$$

where α_{VD} is a weight factor, and it is to be selected by the user.

(c) **Enhancement of Voltage Stability**

It is very important to maintain load bus voltage within acceptable operating limit under normal condition, as well as under increased or decreased loading condition or changed system configuration condition. Voltage stability can be assessed by determining voltage stability indicator, L-index at every load bus of a power system. The value of L-index varies from 0 at no load condition to 1 at voltage collapse condition of a power system. The bus or node with the highest value of L-index will be the most vulnerable bus in a power system. Voltage stability of a power system can be enhanced by moving far from the voltage collapse point through minimization of the overall power system L-Index [16]. The objective function in this case (Case 4) can be written as follows:

$$F_3(x, u) = \sum_{i=1}^{NGN} f_i(.)\$/h + \alpha_L L_{\max} \tag{4}$$

where α_L as α_{VD} is a scaling factor and is decided by the user.

(d) **Voltage stability improvement during contingency**

In this case (Case 4), single line outage contingency is considered in a power system. Thus, in this case, the objective function is enhancement of voltage stability under the condition of single line outage.

2.2 Constraints

The optimal power flow problem has two types of constraints, namely equality and inequality constraints, as given below.

(a) **Equality Constraints**

These constraints are the power balance equations and can be divided into real power and reactive power static load flow equations as:

$$0 = P_{gi} - P_{di} - V_i \sum_{j=1}^{NB} V_j \left[G_{ij} \cos\left(\theta_{ij}\right) + B_{ij} \sin\left(\theta_{ij}\right) \right] \tag{5}$$

$$0 = Q_{gi} - Q_{di} - V_i \sum_{j=1}^{NB} V_j \left[G_{ij} \sin\left(\theta_{ij}\right) - B_{ij} \cos\left(\theta_{ij}\right) \right] \tag{6}$$

where $\theta_{ij} = \theta_i - \theta_j$, the voltage magnitudes of bus i and bus j are V_i and V_j, respectively, NB is the number of buses, P_{gi} and Q_{gi} are the active and reactive power generation, respectively, at bus i, P_{di} and Q_{di} are the active and reactive load demand at bus i, and G_{ij} and B_{ij} are the elements of the admittance matrix

$\left(Y_{ij} = -G_{ij} + jB_{ij}\right)$ representing the conductance and susceptance between bus i and bus j, respectively.

(b) Inequality Constraints

These constraints can be categorized into four types, namely generation constraints, shunt VAR compensation constraints, transformer constraints, and security constraints.

- Generator Constraints:

$$V_{g_k}^{\min} \leq V_{g_k} \leq V_{g_k}^{\max}, \quad k = 1 \ldots \text{NGN} \tag{7}$$

$$P_{g_k}^{\min} \leq P_{g_k} \leq P_{g_k}^{\max}, \quad k = 1 \ldots \text{NGN} \tag{8}$$

$$Q_{g_k}^{\min} \leq Q_{g_k} \leq Q_{g_k}^{\max}, \quad k = 1 \ldots \text{NGN} \tag{9}$$

- Transformer Constraints:

$$T_k^{\min} \leq T_k \leq T_k^{\max} \quad k = 1 \ldots \text{NTR} \tag{10}$$

- Shunt VAR compensator constraints:

$$Q_{C_k}^{\min} \leq Q_{C_k} \leq Q_{C_k}^{\max} \quad k = 1 \ldots \text{NC} \tag{11}$$

- Security Constraints:

$$V_{L_k}^{\min} \leq V_{L_k} \leq V_{L_k}^{\max} \quad k = 1 \ldots \text{NLB} \tag{12}$$

$$S_{l_k} \leq S_{l_k}^{\max} \quad k = 1 \ldots \text{ntl} \tag{13}$$

Aggregating above equations, optimal power flow problem can be written in general form as:

$$\text{Minimize } F(x, u) \tag{14}$$

Subject to;

$$\text{Equality constraint } g(x, u) = 0 \tag{15}$$

and

$$\text{Inequality constraint } h(x, u) \leq 0 \tag{16}$$

and

$$\text{Variable bounds} \quad u_k^{(L)} \leq u_k \leq u_k^{(U)}, \ k = 1, 2, \ldots, n \tag{17}$$

where x is set of dependent variables, u is set of control variables, and $u_k^{(L)}, u_k^{(U)}$ are lower and upper bounds, respectively, of kth decision variable

Here, x can be expressed as

$$x^{\mathrm{T}} = \left[P_{g_1}, V_1 \ldots V_{\mathrm{NLB}}, Q_{g1}, \ldots Q_{\mathrm{gNG}}, S_1, \ldots S_{\mathrm{ntl}} \right] \tag{18}$$

while u can be expressed as

$$u^{\mathrm{T}} = \left[P_{g_2} \ldots P_{g\mathrm{NGN}}, V_{g_1} \ldots V_{g\mathrm{NGN}}, Q_{C_1} \ldots Q_{C_{\mathrm{NC}}}, T_1 \ldots T_{\mathrm{NTR}} \right] \tag{19}$$

where NLB is the number of load buses; ntl is the number of transmission lines; NGN, NC, and NTR are the numbers of generators, numbers of VAR compensation units, and numbers of regulating transformers, respectively.

2.3 Incorporation of Constraints

To obtain feasible solution, the inequalities are included into the objective function and the extended objective function can be formulated as:

$$F_{\mathrm{aug}} = F + C_1.h(x_i) + C_2 \sum_{i=1}^{\mathrm{NGN}} h(Q_{\mathrm{G}_i}) + C_3 \sum_{i=1}^{\mathrm{NLB}} h(V_{\mathrm{L}_i}) + C_4 \sum_{i=1}^{\mathrm{ntl}} h(S_{\mathrm{l}_i}) \tag{20}$$

where C_1, C_2, C_3, and C_4 are the penalty factors corresponding to limit violations and selected by the user.

Bat search algorithm has been applied for this optimal power flow problem, which is a combinatorial optimization problem having nonlinear and multi-extremism property. In this paper, the OPF problem has been solved by optimizing real power output and voltages of the generators, tap settings of regulating transformers, and settings of shunt VAR compensations, and these optimization variables are considered as continuous values.

3 Bat Search Algorithm

Bat search algorithm is a nature-inspired optimization technique, developed by Xin She Yang in the year 2010. This algorithm is based on the echolocation capability of bats responsible for their unique foraging behavior. Most of the bats are using

sonar echoes to recognize, detect, or sense different types of obstacles. The species including bats using sonar echoes ability emit some sound pulses of frequencies in the range of 10–200 kHz. These pulses when hitting the objects or the prey around a bat produce echoes. The bats listen to the echo and then analyze and evaluate the distance of prey from them. Yang developed basic BS algorithm considering following approximation and ideal rules [17]:

- Echolocation is used by all the bats to sense the distance, and the difference between food/prey and background barriers is also known to bats.
- The bats have a random flying velocity v_k at position X_k with a frequency $f^{\min}$, changing wavelength or frequency, and loudness L^O to find prey.
- Bats have capability to regulate automatically the frequency (or wavelength) of their emitted pulses and to regulate the pulse emission rate $R \in [0, 1]$, according to the proximity of the object.
- Even though the loudness of the emitted pulses can vary in various ways, it is assumed to lie within a large positive value L^O to some minimum value $A^{\min}$.

The basic steps used in bat search algorithm can be summarized as follows [18]:

3.1 Initialization of Bats

The initial population of bats N is randomly generated with dimension d by taking into account upper and lower boundaries. The jth component x_{kj} of position vector X_k can be written as:

$$x_{kj} = X_j^{\min} + \varphi\left(X_j^{\max} - X_j^{\min}\right) \tag{21}$$

where $k = 1, 2 \ldots N$, $j = 1, 2 \ldots d$, and $X_j^{\min}$ and $X_j^{\max}$ are the lower and upper boundaries for dimension j, respectively. φ is a randomly generated number, and it lies within range of 0–1.

3.2 Movement of Bats

The frequency, velocity, and position of the bat are updated according to Eqs. (22)–(24).

$$f_k = f^{\min} + \beta\left(f^{\max} - f^{\min}\right) \tag{22}$$

$$v_k^t = v_k^{t-1} + \left(X_k^t - X_*\right)f_k \tag{23}$$

$$X_k^t = X_k^{t-1} + v_k^t \tag{24}$$

where $f^{\max}$ and $f^{\min}$ are the maximum and minimum values of frequency, f_k represents the frequency of the kth bat; β is a number that is randomly generated between 0 to 1; vector X_* is present global best location or solution obtained on comparison of all the N number of solutions; and v_k^t and X_k^t are the velocity and position of the kth bat at tth time step.

BS algorithm uses the benefit of the local search for maintaining the solutions' diversity of the population. The local search follows the random walk strategy to generate a new solution.

$$X_{\text{new}} = X_{\text{old}} + \epsilon A^t \tag{25}$$

where ϵ is a random number uniformly distributed ranging from -1 to 1 and A^t is average loudness value of all bats at tth time step.

3.3 Loudness and Pulse Emission Rate

The loudness L and pulse emission rate r can be updated according to Eqs. (26) and (27), respectively.

$$L_k^{t+1} = \alpha L_k^t \tag{26}$$

$$r_k^{t+1} = r_k^0(1 - e^{-\gamma t}) \tag{27}$$

where γ and α are constants, and r_k^0 is the initial pulse emission rate value of the kth bat.

4 Implementation of BS Algorithm for OPF

The solution algorithm for solving OPF using BS algorithm can be summarized in following steps:

(i)   Set the bat population size (N), loudness (L), pulse emission rate r^o, the maximum number of iteration (iter$_{\max}$), and the number of decision variables (d). Initialize the load flow data.

(ii) Initialize bat position X_k of N individuals randomly in the feasible area and their velocities v_k.

(iii) For each virtual bat, run load flow (e.g., NRLF) program, to find the fitness for each individual as per the objective functions of various cases mentioned above.

(iv) Adjust the frequency, and update velocities and position using Eqs. (22)–(24) to produce new solutions.

(v) If *rand* is greater than r_k, select the best solution among various solutions and generate new solution using local search. Otherwise, create a new solution randomly.

(vi) If *rand* is less than L_k and $f(X_i)$ is less than $f(X_*)$, accept the created new solution. Increase the value of r_k, and decrease the loudness L_k.

(vii) Perform the ranking of bats (solutions), and find the present best solution.

(viii) If iter < $iter_{max}$, increase *iter* by 1, i.e., iter = iter+ 1 and go to step (iv), Otherwise, go to step (iii).

ix) Best solution obtained. Stop.

Flowchart of BS algorithm has been shown in Fig. 1.

5 Result and Discussion

In order to assess the superiority of the proposed bat search algorithm, it has been implemented for solving OPF problem in IEEE 30-bus system [19]. This system has following characteristics: six generators at bus nos. 1, 2, 5, 8, 11, and 13; four transformers with off-nominal tap settings in line nos. 6–9, 6–10, 4–12, and 27–28; and shunt VAR compensation at buses 10, 12, 15, 17, 20, 21, 23, 24, and 29.

The standard IEEE 30-bus system bus data, line data, generator data, and their control variable maximum and minimum limits are taken from [19]. As many as, 30 trials were taken using BS algorithm for solving the optimal power flow problem, and the best results are given here.

5.1 Case 1: Total Fuel Cost Minimization

In this case, total fuel cost minimization was considered as objective function as defined in Eq. (1). Here, cost characteristics of all the generators were assumed to be quadratic in nature. The total fuel cost obtained using BS algorithm is compared with those of other methods reported in Table 1, while the optimal setting of decision or control variable yielded by the proposed algorithm is given in Table 2. This demonstrates the potential of the proposed approach to solve OPF problem. Figure 2 shows the convergence characteristic of BS algorithm for minimization of total fuel cost. It has been observed that the methods reported in [20–22] provided lesser minimum fuel cost than the proposed algorithm. However, as reported in [23, 24], the best solutions obtained in [20–22] are infeasible solutions. Due to limited space, only few result are compared in Table 1 and the result marked with '*' is actually infeasible.
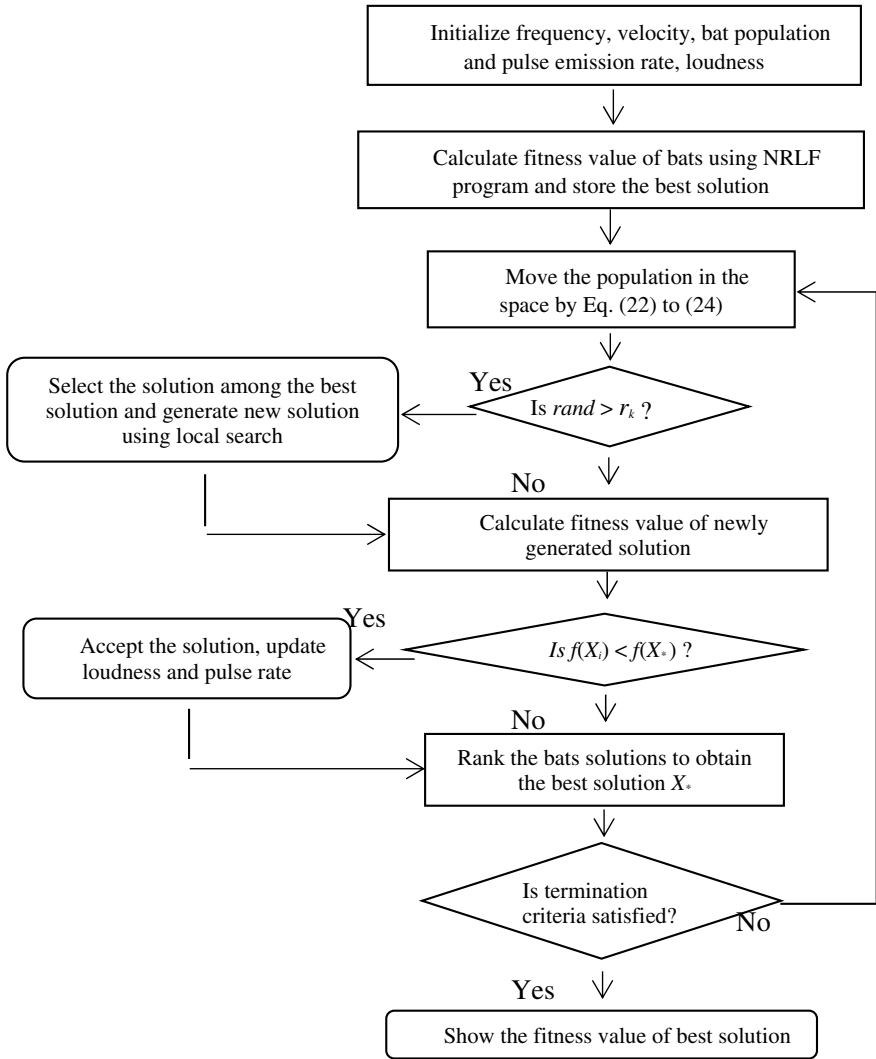
Fig. 1 Flowchart of bat search algorithm

5.2 Case 2: Voltage Profile Improvement

The objective function chosen in Case 2 was the minimization of total fuel cost and improvement of voltage profile simultaneously as defined in Eq. (3). The value of minimum total fuel cost and voltage deviation obtained by the BS algorithm were 807.3128 $/h and 0.0789, respectively. The optimal setting of control variables is given in third column of Table 2. It is clear that the voltage profile is significantly

Table 1 Comparison of Case 1 result

Method	Fuel cost
BSA	**800.5087**
MSA [25]	800.5099
MPSO [25]	800.5164
MDE [25]	800.8399
MFO [25]	800.6863
FPA [25]	802.7983
ARCBBO [26]	800.5159
RCBBO [26]	800.8703
BBO [26]	801.0562
GWO [27]	801.41
DE [27]	801.23
HSFLA-SA [28]	801.79
MSFLA [29]	802.287
SFLA [29]	802.5092
GPU-PSO [23]	800.53
ABC [24]	800.66
PSO [20]	800.41[a]
DE [21]	799.1116[a]
BH [22]	799.92[a]

[a]Infeasible solution

improved as compared to that of Case 1, as the total voltage deviation is reduced from 0.8871 in Case 1 to 0.0789 in Case 2. The voltage at various buses of IEEE 30-bus system in Case 1 and Case 2 is compared in Fig. 3. The results attained using bat search algorithm have been compared with reported results using other algorithms in Table 3. However, the best solutions reported in [20, 21] are indeed infeasible solutions.

5.3 Case 3: Voltage Stability Enhancement

The objective function for minimization of the total fuel cost and enhancement of voltage stability simultaneously as defined in Eq. (4) was selected in Case 3. The value of minimum total fuel cost and L-index as obtained by the BS algorithm were 825.2849 \$/h and 0.1237, respectively. The optimal setting of control variables is given fourth column of Table 2. The result attained using BS algorithm is compared with the reported results obtained using other algorithms in Table 4. As depicted in Table 4, BS algorithm has provided better results as compared to other meta-heuristic optimization algorithms. In this case also, it has been observed that result marked with '*' in Table 4 is the infeasible solution indeed [24].

Table 2 Optimum value of control variable for different cases

Control variable	Case 1	Case 2	Case 3	Case 4
P_{G2}	0.4879	0.44996	0.54837	0.57500
P_{G5}	0.2146	0.24237	0.31404	0.32490
P_{G8}	0.2110	0.19675	0.23718	0.24840
P_{G11}	0.1198	0.15665	0.20289	0.20060
P_{G13}	0.1110	0.18293	0.26395	0.27160
V_{G1}	1.0838	1.02797	1.05157	1.05340
V_{G2}	1.0643	1.01575	1.04665	1.04600
V_{G5}	1.0323	1.02002	1.04264	1.03070
V_{G8}	1.0374	1.00380	1.05333	1.04420
V_{G11}	1.0473	0.99693	1.05091	1.06510
V_{G13}	1.0506	1.00151	1.04487	1.04370
T_{6-9}	1.0019	1.00520	1.02555	1.01610
T_{6-10}	0.9900	0.97555	1.03177	1.03510
T_{4-12}	0.9862	0.97858	1.03296	1.00680
T_{28-27}	0.9823	0.97664	0.98819	1.00400
Q_{C10}	0.0279	0.02881	0.05000	0.04980
Q_{C12}	0.0275	0.01543	0.04977	0.04310
Q_{C15}	0.0251	0.02839	0.04395	0.04560
Q_{C17}	0.0353	0.01531	0.04987	0.04860
Q_{C20}	0.0248	0.04603	0.05000	0.05000
Q_{C21}	0.0474	0.04631	0.05000	0.05000
Q_{C23}	0.0111	0.01714	0.03718	0.04920
Q_{C24}	0.0414	0.05000	0.05000	0.05000
Q_{C29}	0.0154	0.01773	0.01622	0.03110
Fuel cost($/h)	**800.5087**	807.3128	825.2849	833.1631
V.D (p.u)	0.8871	**0.0789**	1.0390	0.8850
L-index	0.1289	0.1378	**0.1237**	**0.1348**

5.4 Case 4: Improvement of Voltage Stability During Contingency

In practical power system operation, there might be various types of contingencies occurring such as transmission line outage and generator unit outage. It is necessary to have enough stability margins in normal operating condition of a power system as well as under contingency conditions. So, objective function of Case 4 is minimization of the total fuel cost and enhancement of voltage stability of the power system simultaneously under $(N-1)$ contingency, which is simulated as outage of the line connected between bus no. 2 and bus no. 6. The optimum setting of decision variables is given in Table 2, and comparison of the results obtained using the proposed BS algorithm and reported results using other algorithms are given in
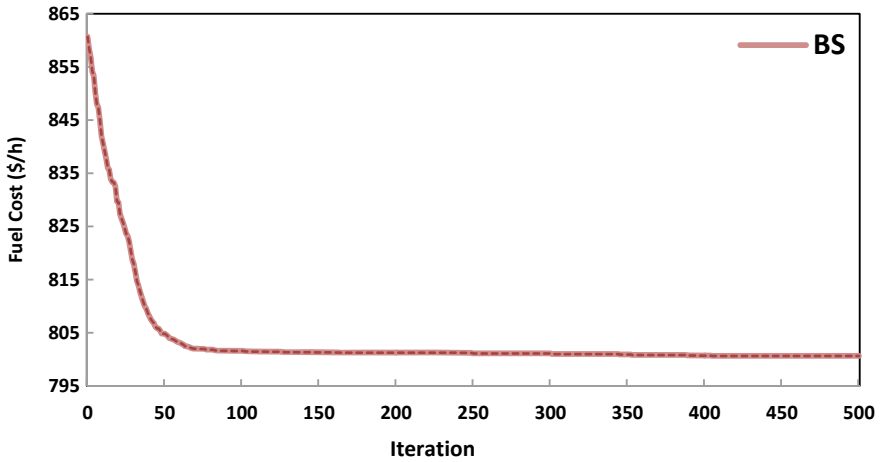
Fig. 2 Convergence for fuel cost minimization
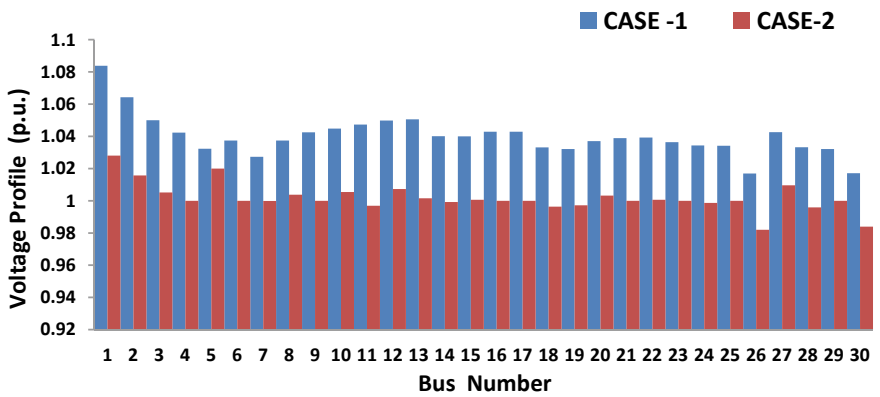
Fig. 3 System voltage profile improvement

Table 3 Comparison of Case 2 results

Method	Fuel cost	Voltage deviation
BSA	807.3128	**0.0789**
MSA [25]	803.3125	0.10842
MPSO [25]	803.9787	0.1202
MDE [25]	803.2122	0.12646
MFO [25]	803.7911	0.10563
FPA [25]	803.6638	0.13659
DE [21]	805.2619	0.1357[a]
PSO [20]	806.3800	0.0891[a]

[a]Infeasible solution

Table 4 Comparison of Case 3 result

Method	Fuel cost	L-index
BSA	825.2872	**0.1237**
MSA [25]	801.2248	0.13713
MPSO [25]	801.6966	0.13748
MDE [25]	802.0991	0.13744
MFO [25]	801.668	0.13759
FPA [25]	801.1487	0.13758
BBO [30]	805.7252	0.1104
ABC [24]	801.6650	0.1379
PSO [20]	801.1600	0.1246[a]
DE [21]	807.5272	0.1219[a]
GSA [31]	806.6013	0.1162[a]

[a]Infeasible solution

Table 5 Comparison of Case 4 result

Method	Fuel cost	L-index
BS	**833.1631**	**0.1348**
MSA [25]	804.4838	0.13917
MPSO [25]	807.6519	0.14051
MDE [25]	806.6668	0.13982
MFO [25]	804.556	0.13935
FPA [25]	805.5446	0.14149
ABC [24]	809.0112	0.1474
DE [21]	810.2661	0.1347[a]
GSA [31]	801.1834	0.0930[a]

[a]Infeasible solution

Table 5. From Table 5, it is clear that the bat search algorithm has provided better optimization results as compared to other reported algorithms. Further, it has been reported in [24] that the best solutions provided by DE algorithm [21] and GS algorithm [31] are infeasible.

6 Conclusion

In this paper, a recently developed Bat Search algorithm has been applied to solve optimal power flow problem with the objectives as minimization of total fuel cost, improvement of voltage profile, and enhancement of voltage stability under normal condition as well as during contingency.

The proposed bat search algorithm has been applied to solve OPF problem in the standard IEEE 30-bus system. The results obtained using BS algorithm were compared with the reported results obtained using other meta-heuristic algorithms.

On comparison, this has been clearly observed that the BS algorithm provides better results than those reported in literature. This confirms the superiority and effectiveness of BS algorithm over other EC-based techniques to solve different cases of OPF problem with feasible results.

References

1. El-Hana Bouchekara HR, Abido MA, Chaib AE (2016) Optimal power flow using an improved electromagnetism-like mechanism method. Electr Power Compon Syst 44(4):434–449
2. Niu M, Wan C, Xu Z (2014) A review on applications of heuristic optimization algorithms for optimal power flow in modern power systems. J Mod Power Syst Clean Energy 2(4):289–297
3. Momoh JA, El-hawary ME, Adapa R (1999) A review of selected optimal power flow Literature. IEEE Trans Power Syst 14(1); Power 14(1):96–104
4. AlRashidi MR, El-Hawary ME (2009) Applications of computational intelligence techniques for solving the revived optimal power flow problem. Electr Power Syst Res 79(4):694–702
5. Bashishtha TK, Srivastava L (2016) Nature inspired meta-heuristic dragonfly algorithms for solving optimal power flow problem. Int J Electron Electr Comput Syst 5(5):111–120
6. Abusorrah AM (2014) The application of the linear adaptive genetic algorithm to optimal power flow problem. Arab J Sci Eng 39(6):4901–4909
7. Sharma B (2012) Security constrained optimal power flow employing particle swarm optimization, pp 2–5
8. Roy PK, Mandal D (2011) Quasi-oppositional biogeography-based optimization for multi-objective optimal power flow. Electr Power Compon Syst 40(2):236–256
9. Mukherjee A, Mukherjee V (2015) Solution of optimal power flow using chaotic krill herd algorithm. Chaos, Solitons Fractals 78:10–21
10. Paranjothi SR, Paranjothi K (2002) Optimal power flow using refined genetic algorithm. Electr Power Compon Syst 30(10):1055–1063
11. Surender RS, Srinivasa RC (2016) Optimal power flow using glowworm swarm optimization. Int J Electr Power Energy Syst 80:128–139
12. Bouchekara HREH, Abido MA, Chaib AE, Mehasni R (2014) Optimal power flow using the league championship algorithm: a case study of the Algerian power system. Energy Convers Manag 87:58–70
13. Suganthi D (2013) An improved differential evolution based approach for emission constrained optimal power flow. IEEE 2013:1308–1314
14. Sayah S, Zehar K (2008) Modified differential evolution algorithm for optimal power flow with non-smooth cost function. Energy Convers Manage 49:3036–3042
15. Yang XS (2011) Bat algorithm for multi-objective optimization. Int J Bio-Inspired Comput 3(5):267–274
16. Kessel P, Glavitsch H (1986) Estimating the voltage stability of a power system. IEEE Trans Power Delivery 1(3):346–354
17. Yang XS (2013) Bat algorithm: literature review and applications. Int J Bio-Inspired Comput 5(3):141
18. Biswal S, Barisal AK, Behera A, Prakash T (2013) Optimal power dispatch using BAT algorithm. In: International conference on energy efficient technologies for sustainability, pp 1018–1023
19. Lee KY, Park YM, Ortiz JL (1985) A united approach to optimal real and reactive power dispatch. IEEE Power Eng. Rev PER-5(5):42–43
20. Abido MA (2002) Optimal power flow using particle swarm optimization 24:563–571

21. El Ela AAA, Abido MA, Spea SR (2010) Optimal power flow using differential evolution algorithm. Electr Power Syst Res 80(7):878–885
22. Bouchekara HREH (2014) Optimal power flow using black-hole-based optimization approach. Appl Soft Comput J 24:879–888
23. Roberge V, Tarbouchi M, Okou F (2016) Optimal power flow based on parallel metaheuristics for graphics processing units. Electr Power Syst Res 140:344–353
24. Adaryani MR, Karami A (2013) Artificial bee colony algorithm for solving multi-objective optimal power flow problem. Int J Electr Power Energy Syst 53(1):219–230
25. Mohamed AAA, Mohamed YS, El-Gaafary AAM, Hemeida AM (2017) Optimal power flow using moth swarm algorithm. Electr Power Syst Res 142:190–206
26. Kumar AR, Premalatha L (2015) Electrical power and energy systems optimal power flow for a deregulated power system using adaptive real coded biogeography-based optimization. Int J Electr Power Energy Syst 73:393–399
27. El-Fergany AA, Hasanien HM (2015) Single and multi-objective optimal power flow using grey wolf optimizer and differential evolution algorithms. Electr Power Compon Syst 43 (13):1548–1559
28. Niknam T, Narimani MR, Azizipanah-Abarghooee R (2012) A new hybrid algorithm for optimal power flow considering prohibited zones and valve point effect. Energy Convers Manage 58:197–206
29. Niknam T, Rasoul Narimani M, Jabbari M, Malekpour AR (2011) A modified shuffle frog leaping algorithm for multi-objective optimal power flow. Energy 36(11):6420–6432
30. Bhattacharya A, Chattopadhyay PK (2011) Application of biogeography-based optimisation to solve different optimal power flow problems. IET Gener Transm Distrib 5(1):70
31. Duman S, Güvenc U, Sönmez Y, Yörükeren N (2012) Optimal power flow using gravitational search algorithm. Energy Convers Manag 59:86–95

BIJLI: A Hyperledger-Based Blockchain-Powered Application for Decentralized Power Management and Electricity Distribution

Rachna Pathak, Neha Gupta, Poras Khetarpal and Shubham Jain

Abstract We present in this article—BIJLI: a peer-to-peer-based power management system built on blockchain technology. BIJLI is a platform where renewable energy consumers and producers can unite, and producers can directly sell renewable energy to consumers. It is built on the Angular framework. The use of blockchain aids in increasing the security and robustness of the whole transaction process, thus introducing transparency into the system. This, in turn, helps in fraud prevention and enables each member of the community to view past transaction records, without letting any member to manipulate the authentic records. We believe that innumerable threats can be avoided with the introduction of blockchain technology in power management systems. Consumers can make informed decisions about from where and from whom do they want to purchase energy resources according to their requirements. Depleting levels of non-renewable energy resources pose a major challenge faced all over the world. Consequently, the substitution of a significant part of present-day conventional power generation techniques by techniques like wind energy and solar energy is being planned by nations and is being implemented in progressive stages. Thus, developing a power management platform that can be integrated into power grids, where exchanges could take place effectively and transparently, is something we believed to be necessary and of high importance.

R. Pathak (✉) · N. Gupta · P. Khetarpal · S. Jain
Bharati Vidyapeeth's College of Engineering, New Delhi 110063, India
e-mail: pathak.rachna04@gmail.com

1   Introduction

Considering the widespread generation and consumption of renewable energy, there arises a need to monitor and control its production and distribution. We believe this to be a vital issue that needs to be addressed during the integration of renewable energy into electricity grids in smart cities on a wide scale. While the sources of renewable energy can be spread over large areas, the conventional sources of energy are restricted only to certain regions. Subject to advancements in computational powers of software and hardware, creating dedicated systems that provide foolproof and fraud-free management facilities has become convenient. In this research, we propose a specialized software system as a user-friendly Web application having a powerful and robust back-end built on the Hyperledger fabric-based blockchain.

The development and adoption of blockchain-based applications in energy market are a young topic among researchers and the businesses. Earlier, we saw that in their research, Imbault et al. [1] proposed the idea of exploring the implementation of blockchain into an industrial OS that would help develop new applications to advance the distributed energy systems of future. They believe that there is a lot of scope for the research on the topics revolving around blockchain technology and the growth of corresponding business implementations and integrations. They also felt the need of suitable experimental setups to figure out how real-time data from smart sensors integrated into the Internet of things-based devices can be used to build better applications. In another research, Kenji Tanaka et al. [2] proposed the usage of blockchain-powered trading system for electricity with digital grid router being its underlying platform. They believe electricity grids must be bidirectional systems that are connected using distributed energy management software, and that providing safe, decentralized control to independent exchanges between peers is a significant challenge. Digital grid router provides bidirectional digital inverters controlled via software, thus enabling reliable power transfers.

Some researchers [3, 4] analyzed the ways in which blockchain can enable energy management in distribution grids and within residential micro-grids—with the help of integration of the distributed RES. Furthermore, Mihaylov et al. [5] introduced a very interesting concept of integration of digital currencies into management systems, which allowed the energy producers on a grid to basically sell the energy they produced to consumers who are in need. In another research, Tai et al. [6] studied the corresponding concept of congestion management that arises during blockchain-based transactions of energy. The academic research around the concept of blockchain explains how it is being used to solve issues in the energy market, but is not really contributing directly to businesses and is not creating potential organizational opportunities. This introduces a gap regarding software systems and business models that revolve around blockchain technology in the electricity market.

Decentralized cryptocurrencies, for example, bitcoin, has gained attention and has been highly successful as compared to prior attempts at the development of

concepts and models related to electronic cash. In the research industry, this rise is sometimes believed to be of vital importance since it creates opportunities for defining applications that integrate smart contracts. Smart contracts are based on the assumption that the cryptocurrency, on which they are based, is highly secure. These contracts can be visualized as programs created by users, which specify sets of rules for the transactions. A network of peers enforces these programs. Smart contracts involve comparatively lesser transactional and legal costs, as compared to classic finance world contracts. On similar grounds, we introduce, via this research, the concept of "BijliCoin" (abbreviated BIC), as a payment/reward system that is used like a commodity for trading renewable energy in our proposed ecosystem of BIJLI.

2 Application Design and Implementation

2.1 Blockchains

Blockchains help in eradication of the requirement of a controlling authority allows organization, structuring and storage data. Blockchains contain databases that host records that are shared over the network. Instead of maintaining the data in a single file, the database here maintains records in the form of blocks. These blocks are maintained and updated in chronological and linear order; i.e., each new incoming block is appended to the existing chain of blocks, using a cryptographic hash. Thus, the records cannot be revised, and any efforts made in order to introduce changes would be directly visible to all the network participants. This in turn enables the usable of blockchains as ledgers that can be shared and used by any person/ organization who possesses appropriate permissions. These can then be spread across multiple sites, institutions, and geographic locations. This makes blockchain a potentially powerful tool.

2.2 Angular Framework

Angular allows the development of single-page Web apps. It is a front-end JavaScript system. It is available and used usually a JavaScript file, which users can add on their Web page. Being completely front-end Angular in itself does not have involvement with /relation to the backend/servers. The server just needs to deliver JSON data in order to communicate with Angular. Being a data binding framework that makes use of a model view controller pattern, it enables its users to keep values in a model, for example, an item that is being kept in a shopping cart. It keeps that value in sync with a view, which is an HTML page in the Angular environment. The view thus updates along with the model. Being just a JSON object, the model can be taken from anywhere over the Internet.

2.3 Rest Api

REST is the short form for representational state transfer. Roy Fielding introduced it in his famous dissertation in 2000. It separates user interface from data storage. On the other hand, APIs can be visualized as sets of protocols or tools, which can be used to develop various application/software. APIs are basically sets of predefined protocols for communication and interaction between software applications and other systems. The requests from a client to a back-end have to contain all the information that is necessary to process the request at server. It cannot take any context-based help from the server. The data within every response to a request must be labeled as cacheable or not, according to the requirements of the cache constraints. REST is primarily defined by four interface constraints: identification of resources; manipulation of resources through representations; self-descriptive messages; and hypermedia as the engine of application state. Because of the layered system, the architecture is composed of layers, having constraints on the component behavior—in a way that every component is unable to see beyond the immediate layer with which it is interacting [7]. Getting and executing the code in form of scripts are a way in which REST allows the extension of client functionality.

2.4 GET Calls

The GET method is basically used to retrieve the representation of a resource. In the case of the non-error path, i.e., upon a successful and fault-free call, a JSON format representation and an HTTP response code of 200 (that indicates an OK) are returned. In an erroneous case, it usually returns a 404 or 400 error. According to HTTP specifications, GET requests are used in order to read data. They do not modify the data. Thus, they are considered safe to use; i.e., they can be called without any fear of data being modified or corrupted, and also, calling it one time is equivalent to calling it multiple times, or not calling it at all, i.e., 0 times. This makes GET idempotent, i.e., making more than one, i.e., multiple identical requests —finally end up generating the same results as a single request.

2.5 Proposed Model

Unlike the blockchain-based peer-to-peer networks, the existing power market is centralized and the authority of deciding prices for energy lies in the hands of a central utility. Consumers do not get to choose the kind/type of energy they want to use. Our model revolves around the idea of providing an open and secure platform for energy transaction. It concentrates on peer-to-peer transaction of solar energy. It

ensures the eradication of any third party and makes the transaction process simple, fast, and transparent. The peer nodes on the blockchain would be responsible for hosting, updating, and validating the transactions.

We built the model upon Hyperledger fabric. Its architecture has three main components, viz. Hyperledger blockchain, REST server, and a UI communicating with the blockchain via the server, with which the user interacts. The UI can be deployed as a Web application or a mobile application. The participants can register themselves, and in return, a smart contract would provide them with their login credentials. The user can log in and make transactions via the UI. Since there is no central authority to govern the transactions, the users can bid for the price of energy they want to buy at from other residents. If Resident 1 has generated solar energy more than what he/she requires to power up his house, they can sell the excess of energy to Resident 2. In return of selling the energy, Resident 1 would receive BIC as per the standard rate, i.e., 1 BIC per 1KWh. However, if the demand goes higher than a generation, the bidding process would decide the price at which energy will be sold. All the potential buyers of the energy will bid the prices for buying the energy, and the seller would have the authority of making the final decision after analyzing all the bids.

The BIC received can be used with other utility companies on the blockchain network. It can be exchanged with banks to get equivalent monetary funds. Further, ICO motivates people to participate in the generation and usage of renewable energy resources. After every transaction, the state of the blockchain is updated. A new transaction would first be validated with the help of consensus. More than half of the adjacent nodes would have to be confirmed for the addition of the new block in the chain.

2.6 Layout and Working of the Web App

As mentioned, users can interact with the BIJLI management system via a Web-based application. The application's UI is built on Angular framework, providing the user with a friendly and easy-to-use interface. The administrator interacts with distributed energy economy UI comprising of the Angular framework. Firstly, the administrator needs to set the Fabric version to 1.0, after terminating and removing all the running containers and all previous chaincode images. This allows the user to start the fabric and generate peer admin card and the business network archive in order to deploy the network to the fabric. A peer requires installed Hyperledger Fabric and the business network archive in order to add new participants, identities, etc., to serve as admins. After importing the network admin business network card for use, the network response can be checked via pings. In the case of positive response, the business network can be deployed and the network admin ID can be imported as a usable business network card. The Web app

processes the user requests to the network through a REST API. It processes requests to blockchain state database on Hyperledger fabric. To retrieve the state of database, the REST API is used. Angular framework gets data through GET calls to the REST API. The application hence shows energy sharing over a network involving 'residents' of an economy. In order to make this possible, real smart meters will have to be linked with the blockchain. Solar energy would be generated by photovoltaic cells placed on the roof of the buildings of residents. The information about generation and usage of solar power would be logged onto the cloud with the help of smart meters. The users can then interact with the Web app to directly transfer power to someone else in exchange of BIC. The actual price (in rupees) of BIC changes dynamically based on the demand and supply fundamentals; i.e., when the demand is more than supply, the coin will be worth higher; thus, the producers will be paid more, and in the case when the supply exceeds the demand of renewable energy, the consequent value of BIC falls. The users can choose from whom do they want to purchase the energy, thus providing them a fair and equal say in deciding the distribution authority for himself or herself, hence eradicating the unnecessary price hikes faced in the case of present-day monopoly-prone ecosystems (Figs. 1, 2, and 3).

Fig. 1 Snippet from the Web app displaying a transaction between two residents of the ecosystem. Producer and consumer are uniquely identified on the basis of their IDs. Producer having ID 222 is about to send 22 kWh to consumer having ID 12342, at the rate of 1 BIC/kWh

Fig. 2 Depicting the successful transaction and the generated ID for record
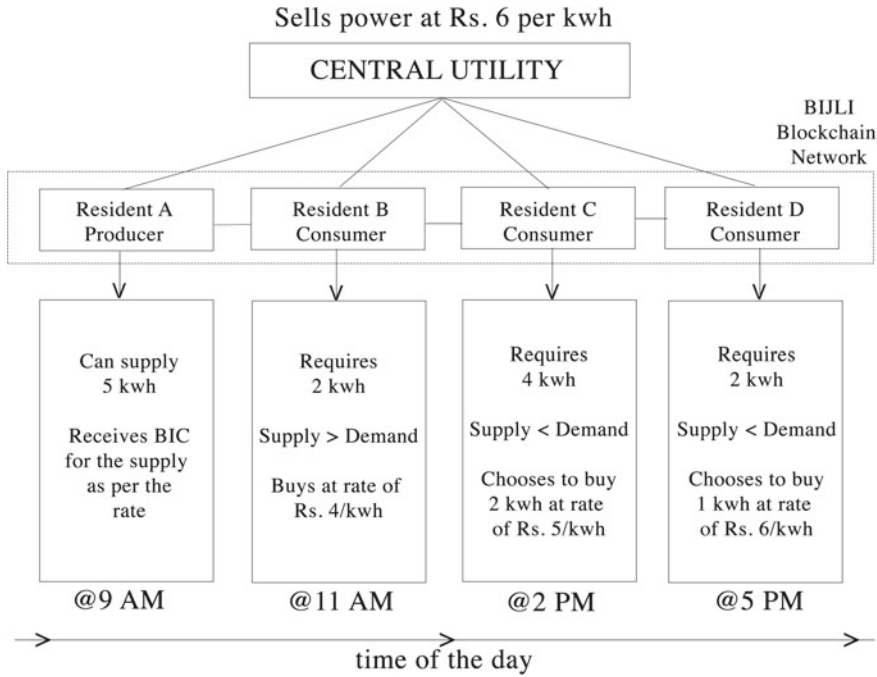
Fig. 3 An example depicting the concept of change in price of energy, based on the demand and supply factors, between four residents, where A is the producer and B, C, D are consumers at a given day. Based on the demand, A can set the price at which he wants to sell the energy. This introduces dynamicity in price of BIC

2.7 Model Code Snippets

The following JS code depicts the exchange of energy with BIC:

```
function Energy2Coins(Update_Values)

{//determine change in coin's value from rate

var coins_Change=
(Update_Values.energy_Rate*Update_Values.energy_Value);

//update values of the assets

Update_Values.coinsInc.value =
Update_Values.coinsInc.value + coins_Change;

Update_Values.coinsDec.value =
Update_Values.coinsDec.value - coins_Change;

Update_Values.energyInc.value=Update_Values.energyInc.val
ue + Update_Values.energy_Value;

Update_Values.energyDec.value=Update_Values.energyDec.val
ue - Update_Values.energy_Value;

return
getAsset_Registry('org.decentralized.energy.network.Coins
')

.then(function (asset_Registry) {return
asset_Registry.updateAll([Update_Values.coinsInc,Update_V
alues.coinsDec]);})

.then(function () {return
getAsset_Registry('org.decentralized.energy.network.Energ
y')

            .then(function (asset_Registry) {return
asset_Registry.updateAll([Update_Values.energyInc,Update_
Values.energyDec]);

            });

    });

}
```

The following JS code depicts the exchange of cash with BIC:

```javascript
function Cash2Coins(Update_Values)

{

//determining change in coin's value from rate

var coins_Change =
(Update_Values.cash_Rate * Update_Values.cash_Value);

//update values of the assets

Update_Values.coinsInc.value =
Update_Values.coinsInc.value + coins_Change;

Update_Values.coinsDec.value =
Update_Values.coinsDec.value - coins_Change;

Update_Values.cashInc.value = Update_Values.cashInc.value
+ Update_Values.cash_Value;

Update_Values.cashDec.value = Update_Values.cashDec.value
- Update_Values.cash_Value;

return
getAsset_Registry('org.decentralized.energy.network.Coins
')

.then(function (asset_Registry) {return
asset_Registry.updateAll([Update_Values.coinsInc,Update_V
alues.coinsDec]);})

.then(function () { return
getAsset_Registry('org.decentralized.energy.network.Cash'
)

            .then(function (asset_Registry) {return
  asset_Registry.updateAll([Update_Values.cashInc,Update_
  Values.cashDec]);

            });

      });

}
```

3   Conclusion of This Research

We believe that blockchain is a highly promising innovation for the trusted esti-
mation and monitoring of energy-related resources, which are required to be more
decentralized as self-generation and small-scale business scenarios are spreading
widely, both amongst people in general, governmental and private divisions. Our
application, BIJLI, can be incorporated into electricity grids at a large scale in urban
cities, where users have access to the latest advancements in technologies. We
believe that the need for such a system to exist will become inevitable in the coming
time due to a rise in wide-scale generation and adoption of renewable energy. There
will be a need to govern the consumption, production, management, and storage of
such energy, and it would be best done without monopoly of single parties at
power. The users would ultimately benefit more if they would directly be involved
in deciding the sources of their power needs from a variety of producers.

BIJLI application demonstrates a basic idea of a decentralized energy network
using blockchain and can be ameliorated in certain ways, some of which include the
addition of specific permissions and participant access; setting up of real-time
transactions among participants; integration with IoT to read from power meter; and
distribution of energy accordingly according to needs.

This model does have certain disadvantages; e.g., the model assumes that all the
residents are willing to participate in the generation and usage of renewable energy.
Also, if the majority of the people become producers, the prices of solar energy on
the blockchain would go down. But we firmly believe that the advantages provided
by our model far outweigh such disadvantages.

References

1. Imbault F, Swiatek M, de Beaufort R, Plana R (2017) The green blockchain managing
   decentralized energy production and consumption. In: IEEE international conference on
   environment and electrical engineering and IEEE industrial and commercial power systems
   Europe (EEEIC/ I&CPS Europe)
2. Tanaka K, Nagakubo K, Abe R (2017) Blockchain-based electricity trading with Digitalgrid
   router. In: IEEE international conference on consumer electronics—Taiwan (ICCE-TW)
3. Danzi P, Angjelichinoski M, Stefanović C, Popovski P (2017) Distributed proportional-fairness
   control in microgrids via blockchain smart contracts. arXiv:1705.01453
4. Horta J, Kofman D, Menga D (2017) Novel paradigms for advanced distribution grid energy
   management. arXiv:1712.05841
5. Mihaylov M, Razo-Zapata I, Rădulescu R, Jurado S, Avellana N, Nowé A (2016) Smart grid
   demonstration platform for renewable energy exchange. Lecture notes in computer science:
   advances in practical applications of scalable multi-agent systems, vol 9662, pp 277–280.
   https://doi.org/10.1007/978-3-319-39324-7_30
6. Tai X, Sun H, Guo Q (2016) Electricity transactions and congestion management based on
   blockchain in energy internet
7. Fielding RT (2000) Architectural styles and the design of network-based software architec-
   tures. University of California, Irvine

Fractal Geometry with Enhanced Bandwidth Using Periodically Capacitive Loading Structure

Shashi Bhushan Kumar and Pramod Kumar Singhal

Abstract The proposed paper emphasizes on multiband characteristics of fractal geometry of Sierpinski's carpet antenna, as there is great demand of multiband antenna in many applications like wireless, WiMax, defense, and secure communication. The proposed fractal patch antenna of second iteration with and without electromagnetic band gap (EBG) structure is presented. In this paper, simulated and fabricated results are investigated and both results show multiband application. Electromagnetic simulator software IE3D was used to design presented antenna, which is based on method of moment. The presented antenna is suitable for multiband applications. Enhancement in the bandwidth helps enhancement channel capacity and reduction in intersymbol interference (ISI). As the physical size of antenna is reduced, hence requirement of embedding is less.

Keywords Fractal antenna · EBG · Bandwidth

1 Introduction

Antenna is a very important component for the wireless communication systems using radio frequency and microwaves. By definition, an antenna is a device used to transform an RF signal, traveling on a conductor, into an electromagnetic wave in free space. Fractal is irregular geometric shape that can be fragmented into parts, each of which is a reduced-size copy of the original one. Fractal geometry follows either self-similarity or self-affinity properties. A self-similar [1, 2] set is one that consists of scaled-down copies of itself, i.e., a contraction which reduces an image by same factors horizontally and vertically. This letter examines a novel antenna design,

S. B. Kumar (✉)
Dept of Electronics & Communication, Bharati Vidyapeeth's College of Engineering, New Delhi, India
e-mail: Sbkumar2010@gmail.com

P. K. Singhal
Dept of Electronics, Madhav Institute of Technology & Science, Gwalior, MP, India

which is based on the self-affinity property of fractals and evaluates its suitability for multiband usage. It is a mathematical construction that is self-similar, which means that you can cut out a piece of a fractal and it would look the same as the original figure. Fractals are used to design antennas, such as Sierpinski's gasket and Sierpinski's carpet because it helps to make the antenna smaller and work in a multiband mode. Each geometry has unique attributes. It has excellent performance at different frequencies simultaneously. They are extremely low profile, lightweight, simple, and inexpensive to fabricate using modern-day printed circuit board technology [3–5], compatible with microwave and millimeter-wave integrated circuit (MMIC), and have the ability to conform to planar and non-planar surfaces. A self-affine structure is a contraction which reduces an image by different factors, horizontally and vertically [6–10]. Thus, it can provide additional flexibility in the antenna design, since by selecting the scale factors appropriately; resonances can be spaced by different factors. A conventional patch antenna gives a maximum directive gain of around 4–6 dBi. It is relatively easy to print an array of patches on a single substrate using lithographic techniques. Patch arrays can be used to achieve high gain than a conventional patch at less cost. Matching and phase adjustment can be done for printed microstrip feed structures [6, 11–13]. The ability to create high-gain arrays in a low-profile antenna is one reason that patch arrays are common on airplanes, and in other military applications this makes the fractal antenna excellent. As the microstrip antennas has been more demanding as par manufacturer demand for wideband and multiband applications, inexpensive to manufacture. They are very much useful at ultra-high frequency and higher frequencies because of its size. Antenna is applicable to the wavelength at the resonance frequency [14–16]. Electromagnetic band gap structures [17] can be called as periodic or few non-periodic objects that prevent and assist the propagation of electromagnetic waves in a specified band of frequency [18]. The paper has shown only simulated result and shows multiband behavior. To validate simulated result, proposed antenna was fabricated, tested and compared with measured result. It was found good agreement between them.

2 Specification Design Parameter and Antenna Geometry

Dielectric constant of substrate is 4.4, height of substrate is 1.588 mm, loss tangent is 0.0001, frequency of operation (f_o) is 6.74 GHz, length of patch antenna (L) is 10 mm, and width of patch antenna (W) is 13.54 mm.

Fractal antenna is excellent for wideband and multiband applications. The resonant frequency of proposed antenna has been kept at 6.74 GHz. This has place in the tri-band of microwave bands of electromagnetic spectrum [16, 19]. Enhancement in the bandwidth helps enhancement in the channel capacity [20, 21], which is the requirement for transmission media. As the physical size of antenna is kept small, hence requirement of embedding space would be less. It will find applications where the limitation of space is more stringent like wireless device, amateur radio [22].

3 Simulated and Measured Result

In the present work, the proposed antenna design starts with the second iteration of Sierpinski's carpet fractal antenna with and without EBG structure as shown in Figs. 1 and 2. Simulated results of antennas are shown in Figs. 5 and 6. Fabrication of the same antenna was done and is shown in Figs. 3 and 4. Fabricated antenna was tested using network analyzer, and result of return loss is shown in Figs. 7 and 8. Comparable result was achieved. Some deviation is due to inaccuracy in fabrication process. Design specifications are mentioned above. Using IE3D software, proposed antenna was designed. Table 1 shows the comparable results of bandwidth of Figs. 1 and 2.
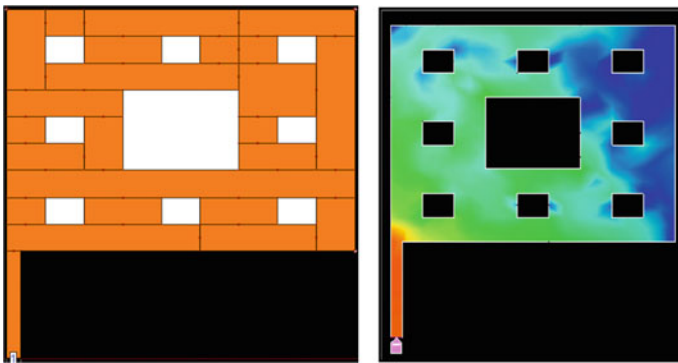
Fig. 1 Proposed fractal antenna of second iteration
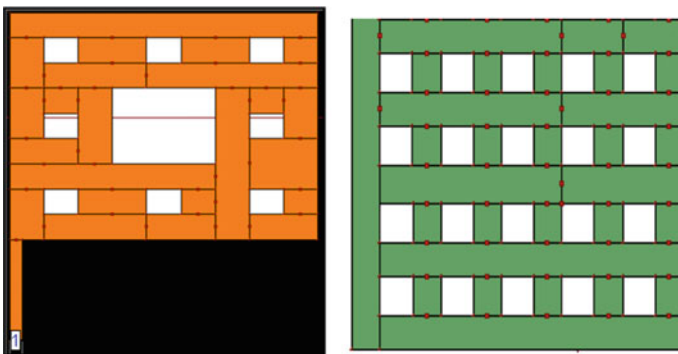
Fig. 2 Antenna with EBG geometry of ground plane with hole dimension 1 mm × 1 mm hole's spacing is 0.875 mm

Fig. 3 Fabricated antenna
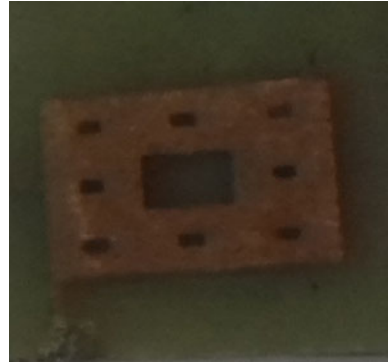
Fig. 4 Fabricated antenna
with EBG

Fabricated antenna was measured in the anechoic chamber with the help of network analyzer in the frequency range of 5–12 GHz, and three resonance points were achieved in both cases.

4   Conclusion

A Sierpinski's carpet fractal antenna with and without EBG structure was proposed and investigated the effect of EBG structure. Measured and simulated result was of both design was compared and had almost good agreement between them. Simulated and measured result shows good return loss at different resonance frequencies. It is seen that iteration of antenna tends to multiband operation. From the result analysis, it was seen that there was great enhancement in the bandwidth. Hence, using EBG structure, bandwidth can be enhanced and this plays vital role in current technology. Enhancement in the bandwidth helps enhancement channel capacity and reduction in ISI. In addition, with reduced physical size of proposed antenna, requirement of embedding space would be reduced for any kind of wireless device and device will be small, light, and handy.
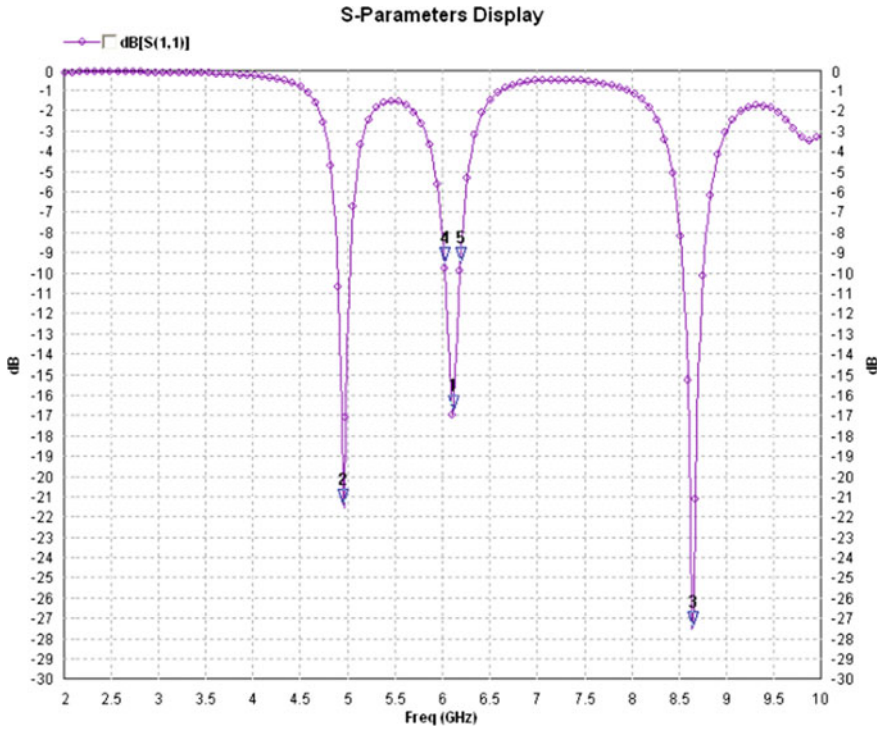
Fig. 5 S_{11}—parameter plot of proposed geometry
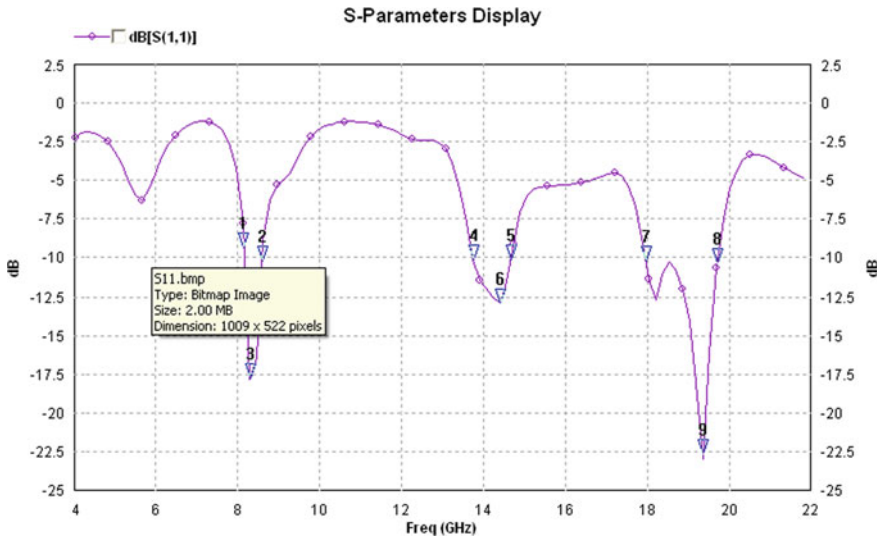
Fig. 6 S_{11}—parameter of antenna with EBG structure
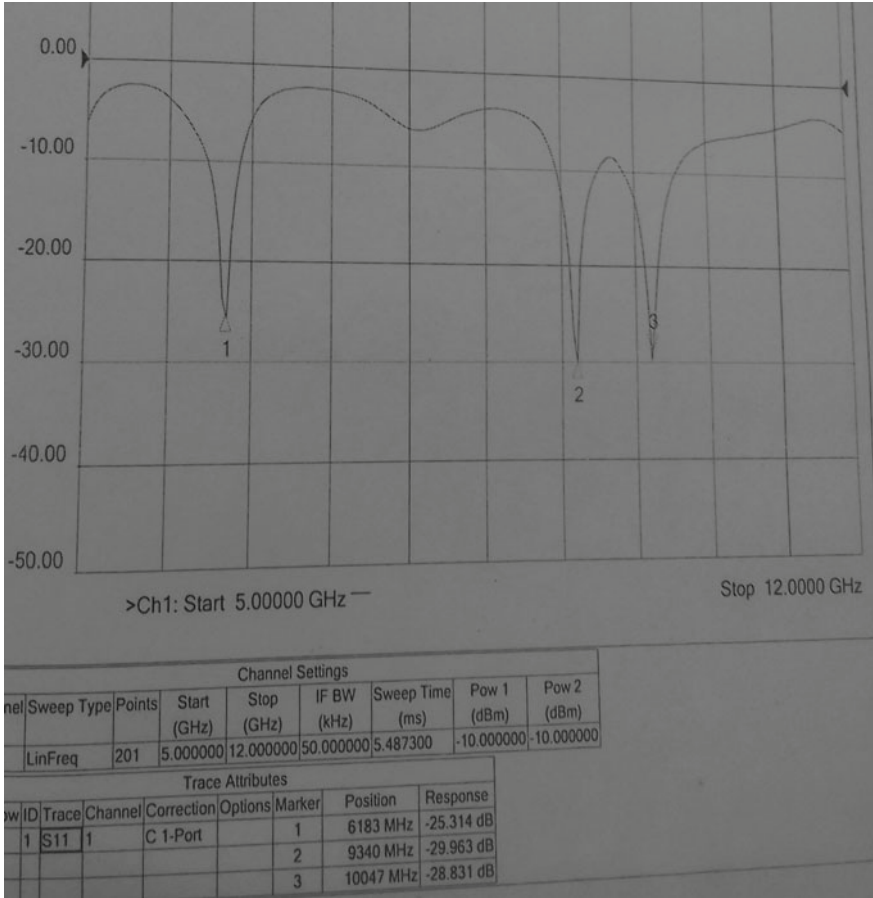
Fig. 7 Measured return loss parameter without EBG

Channel Settings							
Sweep Type	Points	Start (GHz)	Stop (GHz)	IF BW (kHz)	Sweep Time (ms)	Pow 1 (dBm)	Pow 2 (dBm)
LinFreq	201	5.000000	12.000000	50.000000	5.487300	-10.000000	-10.000000

Trace Attributes						
Trace	Channel	Correction	Options	Marker	Position	Response
S11	1	C 1-Port		1	5917 MHz	-26.224 dB
				2	9116 MHz	-25.003 dB
				3	9725 MHz	-37.029 dB
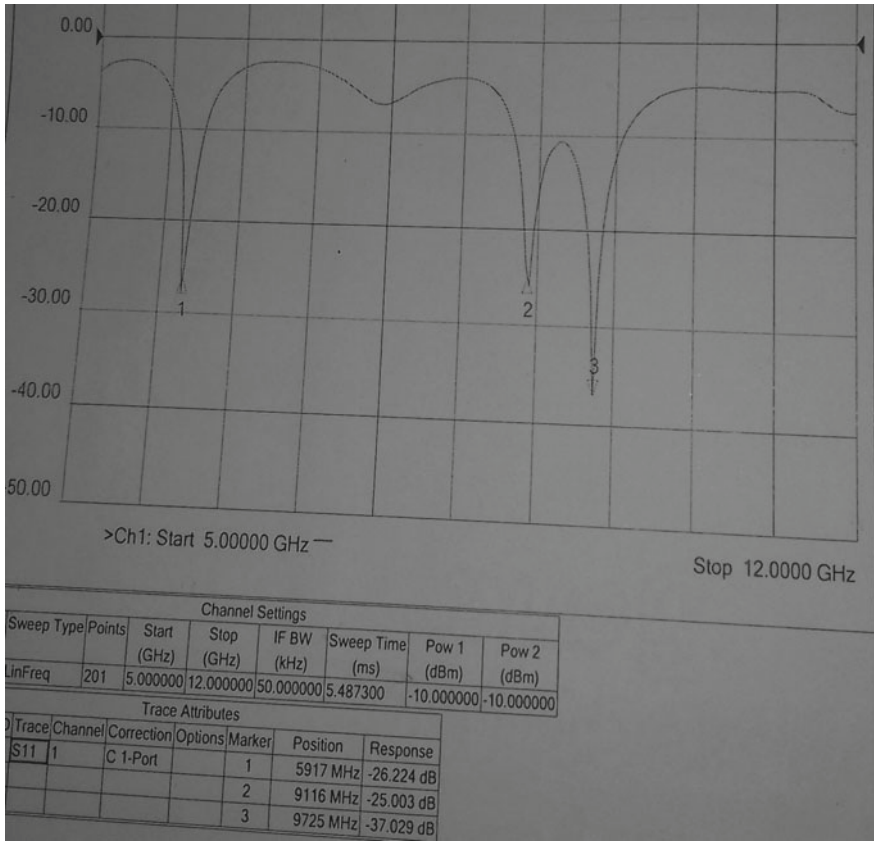
Fig. 8 Measured return loss parameter with EBG

Table 1 Bandwidth of proposed antenna	Proposed antenna design	Bandwidth (MHz)
	Without EBG	170.21
	With EBG	1145.7

References

1. Abd Kadir MF, Ja'afar MS, Abd Aziz MZA (2007) Sierpinski carpet fractal antenna. In: Asia-Pacific conference on applied electromagnetic, 2007. APACE 2007. Issue Date: 4–6-Dec-2007, pp 1–4, Location: Melaka, Print ISBN: 978-1-4244-1434-5, INSPEC Accession Number: 10183847
2. Werner DH, Ganguly S (2003) An overview of fractal antenna engineering research. IEEE Antennas Propag Mag 45(I):38–57
3. Islam MT, Shakib MN, Misran N (2009) Multi-slotted microstrip patch antenna for wireless communication. Prog Electromagnet Res Lett 10:11–18
4. Qian ZH, Chen R-S, Leung KW, Yang HW (2005) FDTD analysis of microstrip patch antenna covered by plasma sheath. In: Progress in electromagnetics research, PIER-52, pp 173–183
5. Wang YJ, Lee CK (2002) Design of dual-frequency microstrip patch antennas and application for IMT-2000 mobile handsets. In: Progress in electromagnetic research, PIER 36, pp 265–278
6. Li X, Yin XX, Cui TJ, Hong W (2004) A new version of printed sierpinski multiband fractal antenna. In: Antennas and propagation society international symposium, 2004, vol 4, pp 3457–3460. (IEEE Issue Date: 20–25 June 2004)
7. Chakravarty T, Roy SM, Sanyal SK, De A (2005) A novel microstrip patch antenna with large impedance bandwidth in VHF/UHF rang. In: Progress in electromagnetic research, PIER54, pp 83–93
8. Garg R, Bahl I (2001) Microstrip antenna design handbook. Arcade House Publication, YOP: 2001, pp 1–68
9. Balanis CA (1997) Antenna theory, 2nd edn. Wiley, pp 28–79
10. Falconer K (1990) Fractal geometry mathematical foundations and application. Wiley
11. Zhang K (2008) Analysis of conformal sierpinski fractal microstrip antenna. In: International conference on microwave and millimeter wave technology, ICMMT2008, vol 3, pp 21–24, pp 1106–1109
12. Cakir G, Sevgi L (2005) Design, simulation and tests of a low-cost microstrip patch antenna arrays. Turk J Elec Engine 13(1):1–3
13. Werne DH, Haup RL, Werne PL (1999) Fractal antenna engineering the theory and design of fractal antenna arrays. IEEE Antennas Propag Mag 41:37–58. (Issue Date: Oct 1999)
14. Rahim MKA, Ph.D. thesis design titled "Design and development of fractal antenna for ultra band high frequency" from Jabatan Kejuruteraan Perhubungan Radio, Universiti Teknologi Malaysia, dated 04 Apr 2005, pp 1–19
15. Ja'afar ASB (2005) Masters of engineering thesis titled "Sierpinski gasket patch and monopole fractal antenna", from Universiti Teknoloi Malaysia, dated 04 Apr 2005, pp 1–31 and 48–57
16. Chen ZN, Chia MYW (2005) Broadband planar antennas. University of Infocom Research, Singapore. Wiley, pp 17–31
17. Yang F (2008) Electromagnetic band gap structures in antenna engineering. University of Mississippi and Yahya Rahmatt Samii, University of California, Los Angeles
18. Kumar SB, Singhal PK (2017) Bandwidth enhancement using electromagnetic band gap fractal antenna for mobile app. In: International conference on innovative entrepreneurship and startup, KNIT, Sultanpur, UP, 03–04 Mar 2017
19. Stutzman WL, Thiele GA (1984) Antenna theory and design, 2nd edn. Wiley, pp 210–218
20. Han K, Harackiewicz FJ (2003) Stacked multiband fractal patch antenna. In: Department of electrical and computer engineering conference proceedings, pp 38–43. (Issue Date: Sep 2003)

21. Abdel-Rahman (2008) A Design and development of high gain wideband micro strip antenna and DGS filters. Ph.D. student at Microwave and Communication Engineering Department, University of Magdeburg, Germany, pp 17–31
22. Pozar DM (1998) Microwave engineering, 2nd edn. Wiley, pp 655–672

Krill Herd Algorithm for Solution of Economic Dispatch with Valve-Point Loading Effect

Harish Pulluri, N. Goutham Kumar, U. Mohan Rao, Preeti and Mekala Girish Kumar

Abstract The article presents a novel bio-inspired Krill Herd (KH) algorithm to solve economic dispatch problems. KH algorithm is based on crowding behavior of the krill individuals and achieves a near global optimum solution by using three main actives. The proposed algorithm is tested by considering three and six generating unit systems on different loads on objective function. The attained results have proved that the KH algorithm provides remarkable results as compared with the other optimization algorithms reported in the literature.

Keywords Krill Herd algorithm · Evolutionary algorithm · Economic dispatch · Valve-point effect

H. Pulluri
Department of EEE, Geethanjali College of Engineering
and Technology, Hyderabad, Telangana, India
e-mail: harishpulluri@gmail.com

N. Goutham Kumar
Department of EEE, V R Siddhartha Engineering College,
Vijaywada, Andhra Pradesh, India
e-mail: gowthamkumar218@gmail.com

U. Mohan Rao
Department of EEE, Lendi Institute of Engineering and Technology,
Vizianagaram, Andhra Pradesh, India
e-mail: mohan13.nith@gmail.com

Preeti (✉)
Department of EEE, ABES Engineering College, Ghaziabad, Uttar Pradesh, India
e-mail: preetieednith@gmail.com

M. G. Kumar
Department of ECE, Vidya Jyothi Institute of Technology,
Hyderabad, Telangana, India
e-mail: giri.frds@gmail.com

1 Introduction

During recent times, the increase in load demand and power system security issues has raised the complexity in power system operations. Economic dispatch (ED) is one of the basic tools for optimal operation and control in modern energy management system. The idea of economic operation is to schedule the power outputs of all the committed generating units to minimize the total fuel cost by satisfying several constraints.

ED is a nonlinear, non-convex, large-scale optimization problem. Therefore, several mathematical methods are applied to solve the ED problems such as quadratic programming (QP) [1], Lagrangian relaxation [2], Branch and bound (BB) [3], and linear programming (LP) [4, 5]. All these methods are excellent convergence characteristics to solve convex ED problems. Nevertheless, these methods are difficult to find an optimal solution due to non-convex nature of ED problem. Therefore, to defeat shortcomings the above methods and to get a near global optimal solution evolutionary algorithms, namely genetic algorithm (GA) [6], particle swarm optimization (PSO) [7], tabu search (TS) [8], differential evolution (DE) [9], evolutionary programming (EP) [10], evolution strategy (ES) [11], artificial bee colony (ABC) [12], harmony search (HS) [13], firefly (FF) [14], and symbiosis optimization search (SOS) [15] algorithms are developed to solve ED problems.

Recently, Gadnomi and Alavi [16] developed a new bio-inspired Krill Herd (KH) algorithm to solve the continuous optimization problems. KH method is based on the simulation of the herding behavior of krill individuals. The minimum distances of each individual krill from food source and the highest density of the herd is considered as an objective function. KH contains two local and two global strategies and these are working parallel that makes KH a powerful algorithm and it has been applied to many real-world problems [17–19]. The achieved results have confirmed that the KH is an efficient method to solve optimization problems. Here, KH has been applied to find solution ED problem by considering different test systems.

2 Mathematical Formulation

In general, the aim of ED problem is to optimize a given objective function by adjusting some of control variables to satisfy several constraints and is given below:

$$\min f(x, u) \tag{1}$$

$$\text{Subjected to} \begin{cases} g(x, u) = 0 \\ h(x, u) \leq 0 \end{cases} \tag{2}$$

where f is an objective function to be minimized; x denotes set of dependent variables, u represents set of independent variables. In this study, total fuel cost with valve-point loading effect is considered to verify the performance of KH algorithm. The objective function and related constrained can be expressed below [15]:

2.1 Objective Functions

(a) *Minimization of total fuel cost (TFC)*: The total fuel cost (TFC) in terms of real power outputs is given as [15]:

$$\min f_1 = \sum_{k=1}^{N_g} a_k + b_k P_{gk} + C_k P_{gk}^2 \tag{3}$$

where f_1 gives total fuel cost of all the thermal generators; P_{gk} denotes real power generation at k^{th} generator; N_g denotes number of thermal generators.

(b) *Minimization of total fuel cost with valve-point loading effect (TFCV)*: The TFCV of each thermal generator is expressed as the sum of a quadratic TFC and a sinusoidal function, which is expressed as follows:

$$\min f_2 = \sum_{k=1}^{N_g} a_k + b_k P_{gk} + C_k P_{gk}^2 + \left| d_k * \sin\left(e_k * \left(P_{gk}^{min} - P_{gk}\right)\right)\right| \tag{4}$$

where f_2 denotes TFCV of all the thermal generators; a_k, b_k, c_k, d_k and e_k denote cost coefficients k^{th} generating unit. P_{gk}^{min} represents the lower real power generation limit of the kth generator.

2.2 Constraints

During the minimization of TFC, various equality and inequality are considered, which are given below [15]:

(a) *Equality constraints*: The equality constraints $g(x, u)$ are defined real power balance constraint, which is given below

$$\sum_{k=1}^{N_g} P_{gk} = P_D \tag{5}$$

where P_D denotes total load demand

(b) *Inequality constraints*: The inequality constraints $h(x, u)$ are defined between their prescribed limits that are articulated as below:

$$P_{\text{gk}}^{\min} \le P_{\text{gk}} \le P_{\text{gk}}^{\max} \quad k = 1, 2, \ldots, N_{\text{g}} \tag{6}$$

3 Krill Herd Algorithm

The concept of increasing the densities of krill individuals and attain the areas of food absorption is the basis of Krill Herd (KH) algorithm. Every krill revolves in a multi-dimensional search space and its position is updated by three movements in a repetition process [16] and those are described below:

3.1 *Motion Induced by Other Krill Individuals*

The krill continuously try to maintain the highest density and rotates in a search space with a velocity due to other krills. The velocity of each krill is influenced with local, repulsive and target effects, the velocity of ith krill is defined as

$$N_i^{k+1} = N^{\max}\left(\sum_{j=1}^{\text{NN}} \hat{F}_{ij}\hat{X}_{ij} + 2(rand + I/I_{\max})\hat{X}_{i,\text{best}}\hat{F}_{i,\text{best}}\right) + \omega_n N_i^k \tag{7}$$

where $N^{\max}$ gives maximum speed; NN denotes neighbor krill individuals, here sensing distance (d_{s}) is evaluated to identify the number of neighbors to each krill. The sensing distance for ith krill is evaluated as below

$$d_{\text{s},i} = \frac{1}{5P}\left(\sum_{m=1}^{\text{NK}} \|X_i - X_j\|\right) \tag{8}$$

3.2 *Foraging Motion*

The foraging motion comprises two parts, the current and past experience about the food location. For ith krill, the foraging motion is evaluated as below

$$F_i^{k+1} = V_f\left(2(1 - I/I_{\max})\hat{F}_{i,\text{best}}\hat{X}_{i,\text{best}} + \hat{F}_{i,\text{food}}\hat{X}_{i,\text{food}}\right) + \omega_f F_i^k \tag{9}$$

where the center of food location (X_{food}) and it is calculated as

$$X^{food} = \frac{\sum_{j=1}^{P} X_j/F_j}{\sum_{j=1}^{P} 1/F_j} \tag{10}$$

3.3 Physical Diffusion

The Physical diffusion of ith krill is evaluated as below

$$D_i = (1 - I/I_{max})D^{max}\delta \tag{11}$$

3.4 Positions Update

After calculating the fitness value, position of every krill is modified as

$$X_i(t + \Delta t) = X_i(t) + C_t \sum_{j=1}^{CV} (UL_j - LL_j)(N_i + F_i + D_i) \tag{12}$$

3.5 Detailed Procedure of the Proposed KH Algorithm

Step 1: Define KH algorithm parameters and create initial population as given below.

$$X_k = \begin{bmatrix} X_{k,1} & X_{k,2} & \cdots & X_{k,m} & \cdots & X_{k,N_g} \end{bmatrix} \tag{13}$$

The complete search space for KH algorithm with NK krill individuals is given below:

$$X = \begin{bmatrix} X_1 \\ X_2 \\ \vdots \\ X_k \\ \vdots \\ X_{NK} \end{bmatrix} = \begin{bmatrix} P_{g1,1} & P_{g1,2} & \cdots & P_{g1,m} & \cdots & P_{g1,N_g} \\ P_{g2,1} & P_{g2,2} & \cdots & P_{g2,m} & \cdots & P_{g2,N_g} \\ \vdots & \vdots & \vdots & \vdots & \vdots & \vdots \\ P_{gk,1} & P_{gk,2} & \cdots & P_{gk,m} & \cdots & P_{gk,N_g} \\ \vdots & \vdots & \vdots & \vdots & \vdots & \vdots \\ P_{gNK,1} & P_{gNK,2} & \cdots & P_{gNK,m} & \cdots & P_{gNK,N_g} \end{bmatrix} \tag{14}$$

Step 2: Evaluate the fitness each krill using below equation [15].

$$|F| = f + w_\mathrm{P}\big(|P_{G1} - P_{G1}^{\lim}|\big)^2 \tag{15}$$

where f denotes minimization of TFCV objective, w_P denotes penalty coefficient of slack bus real power output.

Step 3: We need to arrange all the fitness values in ascending order.

Step 4: Modified the positions of each krill using (7)–(11).

Step 5: If any control variable is violated its limits, set it to respective boundary value.

Step 6: Update each krill using (15).

Step 7: If generations are reached to the maximum value, then stop the procedure, consider the best solution from the last iteration as an optimal solution. Else, move to step 2.

4 Simulation Results

The efficacy of KH algorithm is verified on two systems three- and six-unit systems with one objective function, namely minimization of TFC with valve-point loading effect (TFCV). The number of krill individuals and stopping criterion, i.e., total number of generations are taken as 30 and 400, respectively, for both the systems.

4.1 Three-Unit System

It comprises three generators and load demand is 850 MW. The low and high values of real power outputs and cost coefficients of generators are referred from [10]. The optimal set of real powers obtained in three-unit system with KH algorithm are compared with GA [6], improved EP (IEP) [10], modified PSO (MPSO) [7], CPSO-SQP [15], firefly algorithm (FA) [14], novel direct search (NDS) [15] and the respective results are delineated in Table 1 and it identified that the TFCV attained with KH is least in comparison with GA [6], IEP [10], NSD [15], FA [14] and similar TFCV is provided as compared to MPSO [17], CPSO-SQP [15], GAAPI [15], SOS [15] methods. The convergence characteristics obtained with KH algorithm in the present case are shown in Fig. 1 and it is understood that the KH algorithm provided smooth convergence characteristics.

Table 1 Comparison of optimal real power output attained in three-unit system with the other methods

Unit/methods	1	2	3	TFCV ($/h)
GA [6]	300.00	400.00	150.00	8234.60
IEP [10]	300.23	400.00	149.77	8234.09
MPSO [7]	300.27	400.00	149.74	8234.07
CPSO-SQP [15]	300.27	400.00	147.73	8234.07
FA [14]	300.27	400.00	149.73	8234.074
NDS [15]	300.27	400.000	149.73	8234.0724
GAAPI [15]	300.25	399.98	149.77	8234.07
SOS [15]	300.27	400.00	149.73	8234.07
KH	**300.27**	**399.99**	**149.73**	**8234.071**

The bold values indicating the optimal values achieved by the porposed alogirthm

Fig. 1 Convergence characteristics obtained in three-unit system
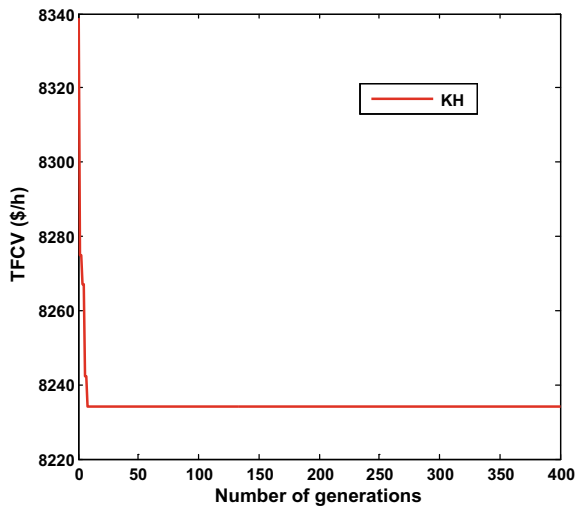
4.2 Six-Unit System

To check the effectiveness of the poroposed alogrithm in case of medum systems, six unit bus system is considered. This system comprises six generators and three different load demands are considered here such as 1200, 1400, and 1600 MW, respectively. The TFCV achieved in different loads are compared with Quadratic PSO (QPSO) [15], G-best guided ABC (GABC) [15] and these are depicted in Table 2, and it is perceived that the KH algorithm is worth to optimize the TFCV for all the load demands taken above. The convergence characteristics attained for 1200 MW with KH algorithm is depicted in Fig. 2, and it is identified that the proposed algorithm provided smooth convergence characteristics. In comparison with other methods, the minimum, average, maximum and standard

Table 2 Comparison of optimal real power output obtained in six-unit system with the other methods for different loads

Different loads (MW)	Units	QPSO [15]	GABC [15]	KH
1200	1	107.73	98.65	98.54
	2	99.92	99.89	98.54
	3	582.54	592.14	591.24
	4	259.03	259.32	261.68
	5	110.42	110.00	110.00
	6	40.36	40.00	40.00
	TFCV ($/h)	291,555.7	29,147.0	**29,109.67**
1400	1	108.60	99.09	98.54
	2	99.63	98.76	98.54
	3	588.73	591.46	591.24
	4	416.16	419.24	424.16
	5	146.86	151.45	147.52
	6	40.01	40.00	40.00
	TFCV ($/h)	33,686.80	33,187.0	**33,132.85**
1600	1	109.94	110.00	100.44
	2	99.34	100.00	98.54
	3	578.78	599.93	591.24
	4	509.34	477.11	424.16
	5	259.72	272.96	345.62
	6	42.88	40.00	40.00
	TFCV ($/h)	37,841.88	37,502.0	**37,443.58**

The bold values indicating the optimal values achieved by the porposed alogirthm

Fig. 2 Convergence characteristics in six-unit system of 1200 MW load
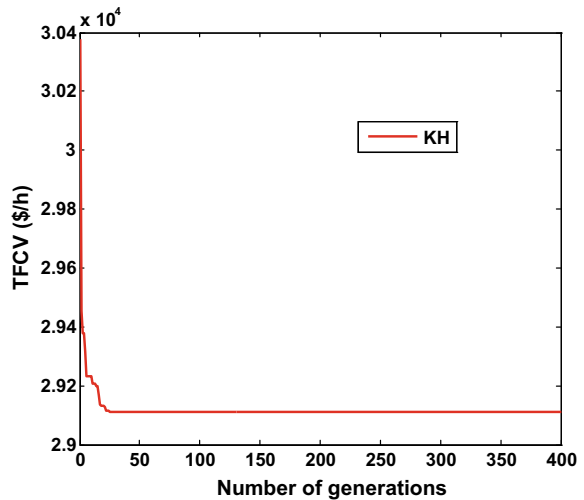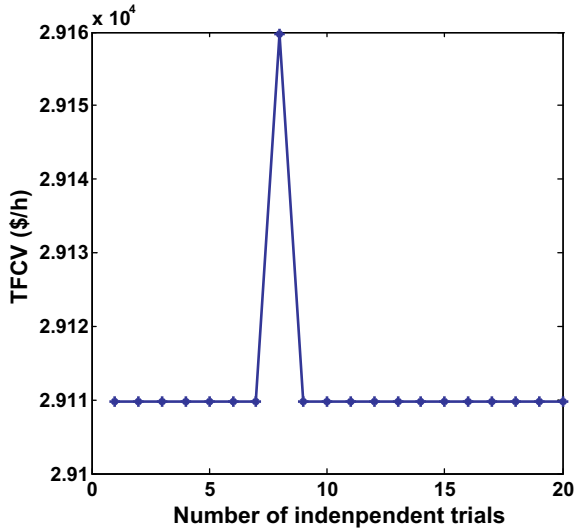
Fig. 3 Deviation of optimal cost of six-unit system for 1200 MW with 20 trials

Table 3 Statistical results attained for different loads of six-unit system

Different loads	Minimum ($/h)	Average ($/h)	Maximum ($/h)	SD
1200	29,109.67	29,112.17	29,159.65	11.17
1400	33,132.85	331,379.24	33,234.24	22.67
1600	37,443.58	37,447.42	37,453.44	3.71

deviation (SD) obtained for 20 independent trials in this case proved that the suggested technique provided better statistical results. Further, Fig. 3 shows that the minimum TFCV achieved in 1200 MW load with 40 independent trials and it is observed that the KH algorithm provided optimal or near optimal value for 19 trials. All these results proved that the KH algorithm is efficient and reliable to solve the ED problem for small and medium test systems (Table 3).

5 Conclusion

In the present article, a new Krill Herd (KH) algorithm is proposed to solve the ED problem. Due to the introduction of three essential parameters such as movement induced by the other krill's, foraging motion, and random diffusion in KH, it is capable to identify the better solutions. The feasibility and efficacy of KH are examined on three and six test systems with minimization of TFCV objective function. In comparison with the techniques reported in the literature, the presented method shows to have promising efficiency and improved statistical results.

References

1. Reid GF, Hasdorff L (1973) Economic dispatch using quadratic programming. IEEE Trans Power Syst 92:2015–2023
2. El-Keib J, Ma H, Hart JL (1994) Environmentally constrained economic dispatch using the Lagrangian relaxation method. IEEE Trans Power Syst 30(4):1723–1729
3. Chen CL, Wang S (1993) Branch-and-bound scheduling for thermal generating units. IEEE Trans Energy Convers 8(2):184–189
4. Fanshel S, Lynes ES (1964) Economic power generation using linear programming. IEEE Trans Power Apparatus Syst 83(4):347–356
5. Wood J, Wollenberg BF (1984) Power generation, operation, and control, 2nd edn. Wiley
6. Walters DE, Sheble GB (1993) Genetic algorithm solution of economic dispatch with valve point loading. IEEE Trans Power Syst 8(3):1352–1332
7. Jong Bae P, Song LK, Rin SJ, Lee KY (2005) A particle swarm optimization for economic dispatch with non-smooth cost functions. IEEE Trans Power Syst 20(1):34–42
8. Pothiya S, Ngamroo S, Kongprawechnon W (2008) Application of multiple tabu search algorithm to solve dynamic economic dispatch considering generator constraints. Energy Convers Manage 49(4):506–516
9. Coelho LDC, Mariani VC (2006) Combining of chaotic differential evolution and quadratic programming for economic dispatch optimization with valve point effect. IEEE Trans Power Syst 21(3):989–996
10. Nidul S, Chakrabarti R, Chattopadhyay PK (2003) Evolutionary programming techniques for economic load dispatch. IEEE Trans Evol Comput 7(1):83–94
11. Pereira-Neto A, Unsihuay C, Saavedra OR (2005) Efficient evolutionary strategy optimization procedure to solve the nonconvex economic dispatch problem with generator constraints. IET Gener Transm Distrib 152(5):653–660
12. Abro AG, Mohamad-Saleh J (2013) Enhanced probability-selection artificial bee colony algorithm for economic load dispatch: a comprehensive analysis. Eng Optim 46(10):1315–1330
13. Coelho LDS, Mariani VC (2009) An improved harmony search algorithm for power economic load dispatch. Energy Convers Manage 50(10):2522–2526
14. Yang XS, Hosseinib SSS, Gandomic AH (2012) Firefly algorithm for solving non-convex economic dispatch problems with valve loading effect. Appl Soft Comput 12(3):1180–1186
15. Naveen P, Chandel AK, Vedik B, Topwal T (2016) Economic dispatch with valve point effect using symbiotic organisms search algorithm. In: Proceedings of international conference on energy efficient technologies for sustainability (ICEETS), pp 430–435
16. Gandomi AH, Alavi AH (2012) Krill herd: a new bio-inspired optimization algorithm. Commun Nonlinear Sci Numer Simul 17(12):4831–4845
17. Pulluri H, Naresh R, Sharma V (2017) Application of stud krill herd algorithm for solution of optimal power problems. Int Trans Electr Energy Syst 27(6). https://doi.org/10.1002/etep.2316
18. Pulluri H, Naresh R, Sharma V (2017) A solution network based on stud krill herd algorithm for optimal power flow problems. Soft Comput 22(1). https://doi.org/10.1007/s00500-016-2319-3
19. Gai-Ge W, Amir HG, Amir HA, Guo-Sheng H (2014) Hybrid krill herd algorithm with differential evolution for global numerical optimization. Neural Comput Appl 25:297–308

Improvement of Power Quality Using Hybrid Active Filter with Artificial Intelligence Techniques

Soumya Ranjan Das, Prakash K. Ray and Asit Mohanty

Abstract In this paper, a shunt hybrid active filter (SHAF) is utilised for the improvement of power quality. Hybrid filters avail advantage of both passive filters and active filters by maintaining reactive power management and compensating harmonics related to different source and load conditions. In modern days, different artificial intelligence (AI) techniques are widely adapted for harmonics compensation. Here, a new intelligence technique, radial basis function neural network (RBFNN), is implemented along with conventional instantaneous power theory (p–q theory) for compensating harmonics and computing reference currents. The system performance is analysed using MATLAB/SIMULINK tool. The simulated results of the new technique are compared with those of the conventional neural controller with p–q theory. Results outcome indicates that the proposed techniques have better performance in improving power quality by reducing total harmonic reduction (THD) below IEEE standard.

Keywords Artificial intelligence · Instantaneous power theory · Radial basis function neural network · Shunt hybrid active filter · Total harmonic distortion

1 Introduction

This power electronics equipment is widely used in recent days. This equipment consistently deteriorates power quality by generating unwanted signals called harmonics in the utility network. A power system network is said to be having

S. R. Das · P. K. Ray
IIIT Bhubaneswar, Bhubaneswar, India
e-mail: srdas1984@gmail.com

P. K. Ray
e-mail: pkrayiiit@gmail.com

A. Mohanty (✉)
CET Bhubaneswar, Bhubaneswar, India
e-mail: asithimansu@gmail.com

healthy power quality if the voltage waveform is having purely sinusoidal and in phase with purely sinusoidal current waveform. Deterioration of power quality occurs if any of the parameters (like voltage, current or frequency) deviates from sinusoidal waveform. Hence, the essential part is to suppress the harmonics and to control total harmonic distortion (THD) less than 5% as identified in IEEE 519 standard and reduce reactive power [1]. In recent times, custom power devices are designed to compensate harmonics and reactive power and to improve the quality of power by reducing the THD. In this paper, a shunt hybrid active filter (SHAF) is employed for getting the advantages of both the passive and active filters [2]. SHAF is helpful in compensating the voltage or current harmonics under different source and load conditions. The performance of SHAF depends on extraction of harmonic current and calculation of reference current. Nowadays, it has been seen that the application of artificial intelligence (AI) techniques are widely used for estimating the harmonics currents. Among different AI techniques, the artificial neural network (ANN) controller found active participation in estimating the harmonics current and also helpful in computing reference current generation along with other conventional techniques. Many other examples also made ANN to utilise widely in different fields. AI possesses robustness, high speed and better efficiency with reduced switching frequency. ANN controller generates sinusoidal component from nonlinear supply voltage. The extracted fundamental currents are then subtracted from source current to evaluate the reference signal, i.e. harmonic current. In this paper, RBFNN controller [3–5] is used to control SHAF. This controller along with traditional p–q theory [6–8] is implemented for calculating reference current generation. RBFNN controller offers self-learning with large accurateness and is utilised in harmonic filtering under different load conditions. The RBFNN is suitable for relating highly nonlinear functions, and constructional characteristics simplify the training process. As the training is carried out in a serial way, practice of local calculation provides better simplification abilities. The proposed method is analysed using MATLAB/SIMULINK tool, and the simulated results are compared with those of conventional ANN with p–q theory.

2 System Configuration

In Fig. 1, the proposed model is represented using SHAF with RBFNN controllers. The SHAF implemented in this paper uses three-phase three-wire system which is used to compensate the current in opposite phase. A voltage-source inverter-based IGBT is attached in the configuration with DC link capacitor for compensating nonlinear unbalanced and balanced loads. Usually, SHAF operates in two stages. In one stage, it is controlled by using neural network controllers which are helpful for the calculation of reference currents, and the other is PI controller for maintaining DC bus voltage. The design of RBFNN constitutes three layers: input layer with inputs $(i_1, i_2, \ldots, i_N)$, hidden layer with K neurons and eventually output layer with outputs $(y_1, y_2, \ldots, y_m)$. The input–output relation constitutes different transformations.
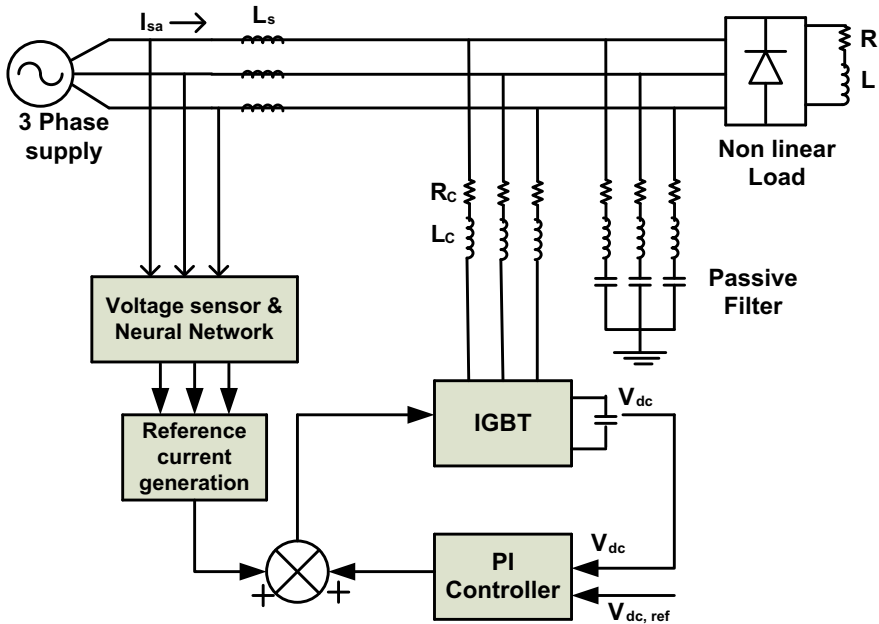
Fig. 1 Configuration of the proposed model using SHAF with RBFNN controllers

Transformations from input to hidden layer are called nonlinear transformations, and other from hidden to output layer is called linear transformation. The mapping among input and hidden layers is termed centres, and mapping among hidden and output layers is termed weights. The configuration circuit of RBFNN is shown in Fig. 2. Response of the RBFNN is expressed in Eq. (1)

$$F_{xy} = \sum_{i=1}^{n} w_i \varnothing \left(\| y - c_i \|^2 / \sigma_i \right) \tag{1}$$

where n, c, σ and w are respectively number of computing units, RBF centre, width of the units and weight.

The weights matrix w is given by

$$w = A^{-1} \varnothing^{\mathrm{T}} D \tag{2}$$

where D is output value during 1 training period. The summation of the outputs is similar to reference signal $r(k)$. Here, error $e(k)$ is equal to zero and there is no variation in RBFNN weight
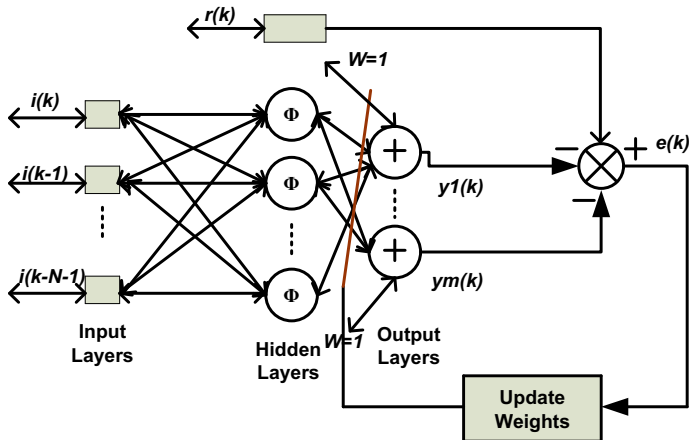
Fig. 2 Configuration of the proposed RBFNN controllers

$$e(k) = r(k) - [y_1(k) + y_2(k) + \cdots + y_n(k)] \tag{3}$$

$e(k)$ is utilised to update the weights depending on least mean square algorithm.

$$
\begin{aligned}
w_{1\mathrm{new}} &= w_{1\mathrm{old}} + \eta_1 \phi(k) e(k) \\
w_{m\mathrm{new}} &= w_{m\mathrm{old}} + \eta_n \phi(k) e(k)
\end{aligned}
\tag{4}
$$

where η_j is the regulation factor for the jth output node. The process of updating weight will remain until $e(k)$ equals to zero again.

3 Control Strategy

3.1 p–q Theory

This theory usually deals with three-phase supply voltage and load currents. Initially, the three-phase source voltages and currents are transformed to $\alpha\beta0$ coordinates with the help of Park transformation technique. The transformed value is again converted to p, q coordinates where the DC and AC parts are separated with help of low-pass filters. Similarly, reference currents are calculated from filtered p, q to $\alpha\beta0$ and then to *abc* coordinate system by inverse transformation. The detail computations are expressed in the following equations:

$$\begin{bmatrix} v_\alpha \\ v_\beta \end{bmatrix} = [A] \begin{bmatrix} v_a \\ v_b \\ v_c \end{bmatrix}, \quad \begin{bmatrix} i_\alpha \\ i_\beta \end{bmatrix} = [A] \begin{bmatrix} i_a \\ i_b \\ i_c \end{bmatrix} \tag{5}$$

$$[A] = \begin{bmatrix} 1 & -1/2 & -1/2 \\ 0 & \sqrt{3}/2 & -\sqrt{3}/2 \end{bmatrix} \tag{6}$$

where A is the transformation matrix

$$\begin{bmatrix} i_{c\alpha}^* \\ i_{c\beta}^* \end{bmatrix} = \frac{1}{v_\alpha^2 + v_\beta^2} \begin{bmatrix} v_\alpha & v_\beta \\ v_\beta & -v_\alpha \end{bmatrix} \begin{bmatrix} \tilde{p} \\ \tilde{q} \end{bmatrix} \tag{7}$$

$$\begin{bmatrix} i_{ca}^* \\ i_{cb}^* \\ i_{cc}^* \end{bmatrix} = \sqrt{\frac{2}{3}} \begin{bmatrix} 1 & 0 \\ -1/2 & \sqrt{3}/2 \\ -1/2 & -\sqrt{3}/2 \end{bmatrix} \begin{bmatrix} i_{c\alpha}^* \\ i_{c\beta}^* \end{bmatrix} \tag{8}$$

where $\tilde{p}$ and $\tilde{q}$ are respectively the AC part of instantaneous active and reactive power.

3.2 RBFNN with p–q Theory

Initially, a delay buffer is designed in which the instantaneous real power gets sampled at a fixed rate and delivered over a first-input first-output (FIFO) buffer as such to build a delayed vector by length N and is equivalent to the input vector length of RBFNN. The training data samples are expressed in Eq. (9)

$$X = |x_1 \quad x_2 \quad \ldots \quad x_k| = \begin{vmatrix} p_{11} & p_{12} & \cdots & p_{1k} \\ p_{21} & p_{22} & \cdots & p_{2k} \\ \cdot & \cdot & \cdots & \cdot \\ p_{N1} & p_{N2} & \cdots & p_{Nk} \end{vmatrix} \tag{9}$$

Fast Fourier transform (FFT) is implemented for each and every x_k to calculate DC part of instantaneous real power. After implementing FFT on x, the reference current calculation shown in Eq. (10) is given as

$$\text{FFT}[x_k] = d_i^{\text{DC}} \tag{10}$$

Finally for sequence current calculations, three-phase currents are considered as the input and its corresponding output values. In this technique, initially the input currents are subjected to zero and subsequently increase in steps. In a cycle, thousands of samples are chosen and are arranged in three individual rows. The data training data is created for different load conditions.
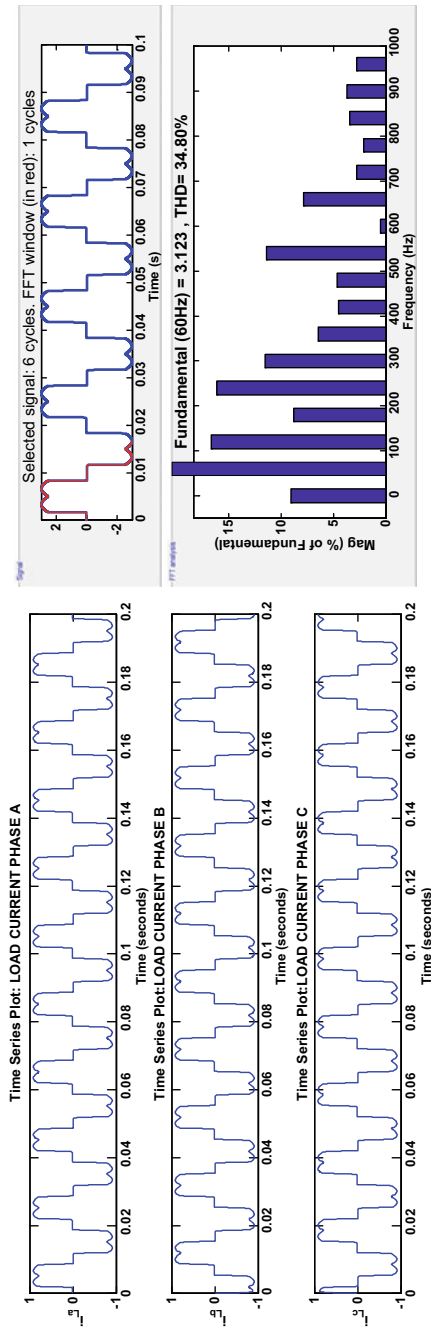
Fig. 3 Load currents and THD without filters
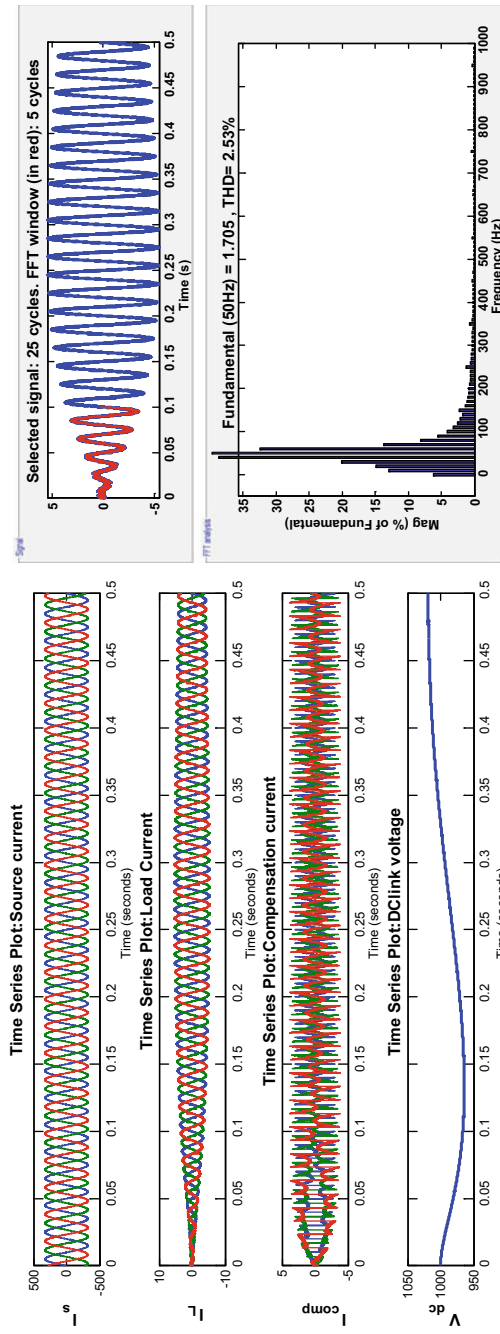
Fig. 4 Load currents and THD with SHAF using ANN-p–q theory
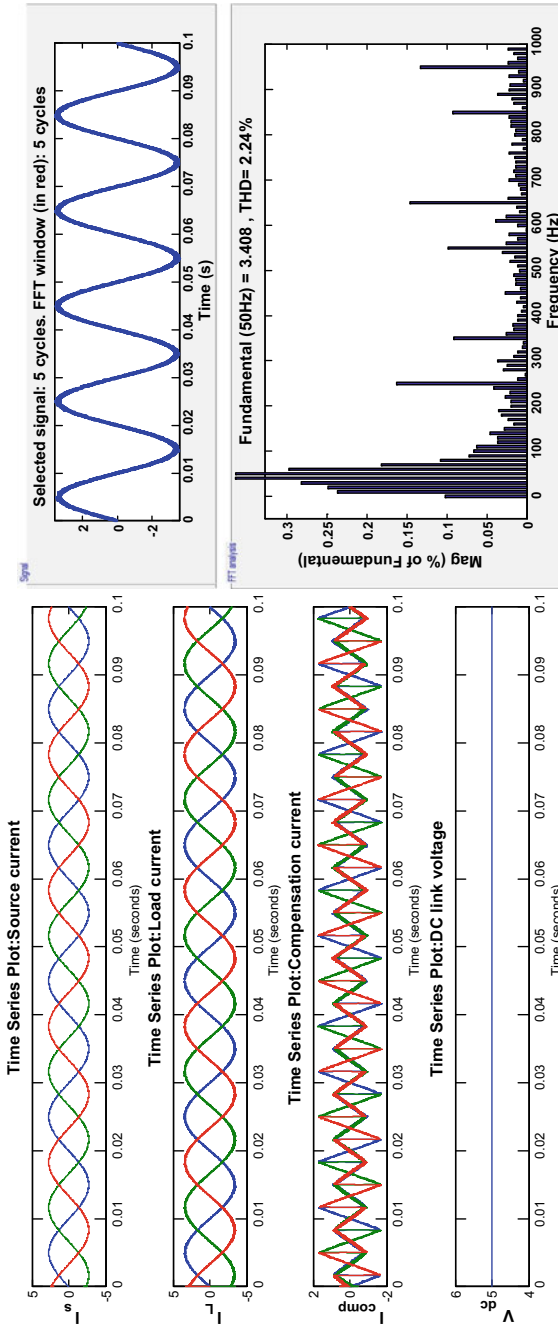
Fig. 5 Load currents and THD with SHAF using RBFNN-p–q theory

Table 1 Different parameters' value of the model

Parameters	Value
Line voltage and frequency	415 V, 50 Hz
Line and load impedance	LC = 0.15 mH, RC = 60 Ω,
Tuned passive filter	Cf = 50 μF, Lf = 8.10 mH, Rf = 10 Ω
Ripple filter	CRF = 50 μF, LRF = 0.68 mH
DC link parameters	C = 1200 μF, CVD = 800 V
Filter coupling inductance (mH)	2.25
Controller gain	KP = 24, KI = 1.2, for shunt PF
Hysteresis band limit (A)	0.5
Sampling time (s)	2e

4 Simulation Results and Analysis

This section explains the comparison of total harmonic distortion (THD) of load current by employing SHAF using p–q theory, conventional neural network with p–q theory and RBFNN with p–q theory. The simulated outputs of source current, load current, compensation current and DC link bus voltage of different controllers are also shown in this section. Initially, before connecting SHAF, the THD value across the load is found to be 34.80%. The simulated waveform and its corresponding THD are shown in Fig. 3. It has been investigated that after connecting SHAF using AI techniques, the power quality gets improved by reducing THD value. At first, the model is performed under unbalanced nonlinear load. The resultant figures are shown in Fig. 4. It has been seen that THD value gets improved to 2.53%. On latter stage, the model is performed using RBFNN with p–q theory. The resultant of simulated waveforms is shown in Fig. 5. It is evident from the simulations that THD value gets upgraded to 2.24% using RBFNN with p–q technique. The different parameters values of the model are shown in Table 1.

5 Conclusions

In this paper, the work offered makes a major influence on detection and control strategies to develop the efficiency of SHAF. The proposed technique is based on AI techniques. A comparative study between p–q, ANN with p–q and RBFNN with p–q controllers is presented. It is realised that RBFNN with p–q has better improvement in power quality and control of reactive power management compared to other controllers. The performance of the proposed technique was verified through simulation studies with MATLAB/SIMULINK tool.

References

1. Haugan PTS, Tedeschi E (2015) Reactive and harmonic compensation using the conservative power theory. In: International conference on ecological vehicles and renewable energies (EVER)
2. Mahela OP, Shaik AG (2016) Topological aspects of power quality improvement techniques: a comprehensive overview. Renew Sustain Energy Rev 58
3. Chang GW, Chen C-I, Teng YF (2010) Radial-basis-function-based neural network for harmonic detection. IEEE Trans Ind Electron 57:2171–2179
4. Zouidi A, Fnaiech F, Haddad KA, Rahmani S (2008) Adaptive linear combiners a robust neural network technique for on line harmonic tracking. In: 34th annual conference of IEEE industrial electronics, 2008. IECON 2008, pp 530–534
5. Tah PC, Panda AK, Panigrahi BP (2017) Shunt active filter based on radial basis function neural network and p-q power theory. Int J Power Electron Drive Syst (IJPEDS) 8
6. Thirumoorthi P, Yadaiah N (2015) Design of current source hybrid power filter for harmonic current compensation. Simul Model Pract Theory 52
7. Singh B, Dube SK, Arya SR (2015) An improved control algorithm of DSTATCOM for power quality improvement. Electr Power Energy Syst 64
8. Lam S, Wong MC, Choi WH, Cui XX, Mei HM, Liu ZJ (2014) Design and performance of an adaptive low-DC-voltage-controlled LC-hybrid active power filter with a neutral inductor in three-phase four-wire power systems. IEEE Trans Ind Electron 61

Prioritization of Transmission Lines in Expansion Planning Using Data Mining Techniques

Smita Shandilya, Shishir Kumar Shandilya and Tripta Thakur

Abstract In transmission expansion planning phase, a clear and multifacet understanding of proposed transmission lines and their respective associations in transmission expansion plans is crucial to analyze and compare similar expansion plans. It is also equally important to analyze that how many transmission lines are fully or partially frequent with other transmission lines to chalk down the progression pathway. While the related researches are focusing on the refinement of transmission expansion plan under different scenarios, only few researchers have observed the importance of finding the associative correlations between the expanded plans and the lines based on different scenarios. This paper attempts to discover the associative correlations among the transmission lines of different proposed plans to facilitate the effective execution during the implementation phase. This paper presents the applicability of the existing data mining approaches on this power system problem to make the transmission system more reliable and robust, while analyzing the future scenarios in expansion planning.

Keywords Transmission expansion planning problem · Deregulated environment · Independent system operator · Data mining · H-Mine · ECLAT

S. Shandilya (✉)
Sagar Institute of Research, Technology & Science, Bhopal, India
e-mail: smita.sam27@gmail.com

S. K. Shandilya
VIT Bhopal University, Bhopal, India
e-mail: shishir.sam@gmail.com

T. Thakur
Maulana Azad National Institute of Technology, Bhopal, India
e-mail: tripta_thakur@yahoo.co.in

1   Introduction

With the growing need of transmission expansion planning, there is an increasing demand of clear understanding of proposed expansion plan and its elements at more granular level. These elements are generally the transmission lines in expansion plan which are proposed to be expanded. It is important to reveal the characteristics of proposed transmission lines in order to carefully prepare an implementation plan for proposed expansion. A thorough analysis of transmission lines is therefore an important area of research in transmission expansion planning problem (TEPP).

Most of the researches that are carried out for transmission expansion focuses either on the application of soft computing techniques for expansion or on the implementation of any practical condition to the traditional objective of cost minimization [1]. However, the problem has many more constraints and several practical scenarios like contingency analysis, expansion during congestion, considering various load scenarios, expansion in market-based scenario, and many others. Finding the correct expansion plan under all these conditions is a very complex task. We have attempted to explore the possibility of application of data mining algorithms to this power system problem to find the association among the new candidates (lines) that are to be added to the existing system. This is important in deregulated environment as there are n numbers of players and each player has its own preferences and choices toward the expansion. If a particular line is beneficial to one player, it may or may not be beneficial for other players in the same domain, which results conflicts between the players. But, if that particular line is improving the overall system power flow scenario, then it should be added to the system by independent system operator (ISO), instead of considering the individual preferences.

Among the various baselines of analysis, we are concentrating on the frequency of specific transmission line in almost all the qualifying expansion plans. This would prioritize the transmission lines as per its importance and need and will also reveal the fact that specific transmission lines should be added even if there are multiple plans to propose.

2   Data Mining

Data mining is a powerful computational tool to discover the hidden knowledge strategically from huge amount of data. Data mining has been applied on several interdisciplinary and diverse fields like market analysis, bioinformatics, network attack detection, Web mining, and several decision-support systems. There are various well-explored and well-experimented techniques which come under the span of data mining like association rule mining, frequent pattern mining, clustering, and classification [2, 3].

Association rule mining attempts to reveal the hidden relationships among the given set of data items or database. The prime objective of association rule mining

is to find frequent item set and then to generate association rules based on the obtained frequent item sets. It follows a two-step procedure for the same; firstly, it performs the frequent item set mining, and thereafter, it derives association rules on the resultant data.

Formally, given

$$I = \{I_1, I_2, \ldots, I_m\}$$
$$D = \{t_1, t_2, \ldots, t_n\}$$

$$\text{where } t_i = \{I_{i1}, I_{i2}, \ldots, I_{ik}\}$$
$$\text{and } I_{ij} \in I$$

I is a set of items, D is a database of transactions, and X and Y are set of items.

The association rule problem is to identify all association rules $X \rightarrow Y$ with a minimum support and confidence where support of association rule $X \rightarrow Y$ is the percentage of transactions in the database that contain $X \cup Y$ and confidence is the ratio of support of $X \cup Y$ to support of X [4]. Some popular association rule mining algorithms are given in [5–7].

These association rules are based on '*support*' and '*confidence*' values which are larger than some user-specified thresholds. These user-specified minimum support threshold is denoted by '*min-sup*' which means if the support of a given item set is larger than '*min-sup*', the respective item set will be called '*frequent*' and will appear in output, else not. However, the selection of exact value for '*min-sup*' to get desired results is a problem because a very small value for '*min-sup*' will lead to more number of frequent item sets and a large value for '*min-sup*' will disqualify potentially good results.

3 Background

There are many variations of association rule mining algorithm to mine frequent item sets and association rules based on certain criteria or developed for various application areas. Following are some of the most important association rule mining algorithms.

3.1 Apriori Algorithm

It is one of the most popular algorithms for association rule mining. It states that if any item set of k length is not frequent in the database, then the superset of that item of length $k + 1$ cannot be frequent [7]. Therefore, it generates a set of item sets of

$k + 1$ length and analyzes the respective frequency counts in the given database through breadth-first search algorithm to ensure that the support value of all the subset is to be known in advance.

3.2 FP-Growth Algorithm

The task of finding frequent pattern in very large databases is computationally expensive and time-consuming. FP-Tree is an efficient and scalable method for mining the complete set of frequent patterns by pattern fragment growth [8, 9]. It proposes a novel frequent item set tree structure called '*FP-Tree*' which is basically a prefix-tree structure for storing information of frequent item sets. Each node of FP-Tree has three fields (*item set, count,* and *link*). '*FP-Growth*' is based on a partition-based, divide-and-conquer method. It reduces the search space by dividing the mining task into task subsets [5].

3.3 ECLAT—Equivalence Class Clustering and Bottom-Up Lattice Traversal

ECLAT is the pioneer work in vertical data processing. It is an efficient algorithm which performs depth-first search for identification of frequent item sets. The same authors suggested few more algorithms in their work, namely MAXECLAT, CLIQUE, MAXCLIQUE, APRCLIQUE, and top-down; however, ECLAT received more attention by the researchers. ECLAT uses prefix-based equivalence relation with bottom-up search to enumerate all frequent item sets.

3.4 H-Mine Algorithm

H-Mine works over a hyperlinked data structure known as '*H-Struct*'. H-Mine algorithm dynamically adjusts these links with an objective for mining the frequent rules. The main advantage of H-Mine is its low-memory utilization even for very large databases, its execution time is less, and the results are remarkable. It bears the scalability aspect of real-time databases through partitioning and creating FP-Trees dynamically when needed.

There are various algorithms which are efficient and capable in mining frequent and associative item sets in the large database. However, our focus is more on the results achieved through these algorithms; therefore, detailed explanation on working methodology of these algorithms is avoided.

4 Transmission Expansion Planning

Transmission expansion planning is a process to propose a new line and/or upgrading existing transmission line, to adequately satisfy the loads for a foreseen future. With the growing investments in electricity markets, the need of having better and long-term expansion plans is growing rapidly. This makes it necessary for a planner to perform more rigorous analysis of all the feasible expansion plans and compare them before the proposal.

The traditional model considers only the investment cost for expansion of the transmission system. But, as the present market demands, this model needs to be modified to make it compatible with new scenario. The model should not only deal with investment cost but also the operational cost, subjected to various load scenarios for multiple numbers of years. Complete load scenario with load levels, operating hours, and the participation factors for Garver 6-bus system [10] are considered in this paper. For multiyear planning, it is assumed that generation and load both are increasing every year by a factor of 0.05 and 0.03, respectively.

The objective function for the reference network subproblem is

$$C = \sum_k C_k(D_k) L_k n_{ij} + \sum_{p=1}^{dp} T_p \sum_{g=1}^{ng} \mathrm{mp}_g P_{pg} \tag{1}$$

The first part of this objective function represents the investment cost, and the second part represents the operational cost at various load levels for one year.

Here,

dp = number of load levels p
T_p = operating hours of load level p
ng = number of generators g
mp_g = marginal cost of generation
P_{pg} = output of generator during demand period.
The constraints in this formulation are:

$$P_L = bAXP \tag{2}$$

$$AP_L + P_G - P_D = 0 \tag{3}$$

$$|P_L| \leq \left(n_{ij}^0 + n_{ij}\right) S_{\max} \tag{4}$$

$$\left|P_L^{Co}\right| \leq \left(n_{ij}^0 + n_{ij}\right)^m S_{\max} \tag{5}$$

$$\sum_{j=1}^{N} B_{ij}^{m}\left(\theta_i^m - \theta_j^m\right) = P_{\text{G}i}^m - P_{\text{D}i} \tag{6}$$

$$\sum_{j=1}^{N} B_{ij}\left(\theta_i - \theta_j\right) = P_{\text{G}i} - P_{\text{D}i} \tag{7}$$

$$P_{\min} \leq P \leq P_{\max} \tag{8}$$

$$0 \leq n_{ij} \leq n_{ij}^{max} \tag{9}$$

n_{ij} = number of lines to be added in corridor ij, i.e., total lines between corridor ij minus existing lines in the same corridor
n_{ij}^0 = already existing branches
$S_{\max}$ = maximum possible power flow in the branch, transmission line capacity
S = power flow calculated on the basis of load flow
P_L = branch flow vector during demand period p
$b = (b_{kk})$ equal to susceptance of line k, having non-diagonal elements as zero
A = branch bus incidence matrix
X = admittance matrix with $R = 0$
P = bus active power injection
P_D = demand at the bus for demand period p
P_G = generation at a bus during demand period p
B_{ij} = susceptance of branch ij (X_{ij})
θ_i = voltage phase angle of bus i
θ_j = voltage phase angle of bus j
k = line between buses i and j
m = contingency parameters.

In the above formulation, Eq. (3) represents Kirchhoff's law constraint; i.e., power flowing to a node is equal to the power flowing out of a node. Equations (4) and (5) represent the thermal constraints; i.e., transmission line flows should not exceed its capacity during normal and contingency conditions. Equations (5) and (6) represent the constraints under contingency condition. Equation (8) represents the limits on the output of the generators, and Eq. (9) represents the limit on the number of lines. All the constraints should be met during each demand period, i.e., 1—dp.

Various methods like heuristic and meta-heuristic approaches can be used to solve the TEPP as formulated above.

The focus of this paper is on the effective utilization of existing data mining approaches for achieving the best expansion plan. The methods are applied to

Fig. 1 Garver 6-bus system
[10]
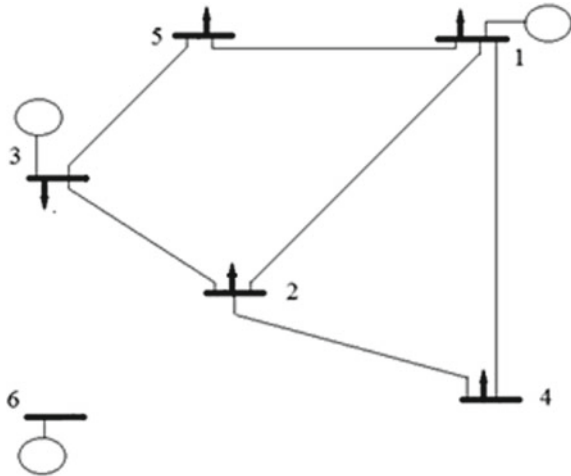
Table 1 Results under different load scenarios using forward search on Garver system

Year	Corridor
1	3–5, 3–4, 4–6, 2–6
2	3–5
3	3–5
4	2–3
5	3–5

Garver 6-bus system as shown in Fig. 1, and the sample results using simple heuristics (forward search) on Garver system under normal condition are shown in Table 1.

5 Analysis

In any transmission plan, some lines are closely associated with each other. Together, these lines lead to better results after expansion. If closely associated lines are partially expanded (any one or some of them), their associability benefits may not be gained. To identify such associated transmission lines, we have used frequent item set mining for analyzing the frequency and associations among the proposed transmission lines of the expansion plans generated using Frog Leap Optimization algorithm. To make the transaction database, we have generated expansion plans by recursively introducing the increase in load growth (by 5%) from 0 to 150%. This process has generated 31 transmission expansion plans, and each plan contains the suggested transmission lines to expand. Then, we focused on finding those sets of transmission lines that have minimum support value (externally supplied). This

process assisted the identification of associated transmission lines (to expand critical and combinational transmission lines).

We have then used sequential pattern mining framework (SPMF), which is an open-source data mining platform written in Java. It is distributed under the GPLv3 license. We have experimented with H-Mine and ECLAT algorithms available in SPMF (Tables 2 and 3).

Here, 9, 11, 14, and 15 are the serial numbers given to the candidate lines of the transmission system. Each number represents a specific transmission line that is added to the existing system. The results are validated as both the algorithms are giving the same results.

The prime objective of this analysis is to find the most frequent and associated transmission lines. The results shows that the line numbers 9 and 14 (3–5 and 2–6) are to be added simultaneously to the existing system, which means that if line number 9 is added, then line number 14 should also be added to the system to make the system more efficient. Also, the 'support' value between line number 9 and 14 is 100% which signifies their strong association that serves the basic necessity of expansion planning at the implementation phase.

After carefully examining the TEPP problem and its solution, we may conclude the following:

1. Till now, very less work is reported to find out the transmission lines which are associated with each other. This is important in deregulated environment as the expansion plan involves the market players, and the associated lines may not be beneficial to all the individual players, but it may be beneficial for the system as a whole.
2. Prioritization of these associated transmission lines in proposed expansion plan.
3. Analysis of 'support' values of various transmission lines proposed in expansion plan along with their dependency values.

Table 2 Results of association between lines using H-Mine

Candidate line no.	Support
9, 11, 14, 15	26/31 = 0.83
9, 11, 14	30/31 = 0.96
9, 11, 15	26/31 = 0.83
9, 11	30/31 = 0.96
9, 14, 15	27/31 = 0.87
9, 14	31/31 = 1
9, 15	27/31 = 0.87
11, 14, 15	26/31 = 0.83
11, 14	30/31 = 0.96
11, 15	26/31 = 0.83
11	30/31 = 0.96
14, 15	27/31 = 0.87

Table 3 Results of association between lines using ECLAT

Candidate line no.	Support
9, 11	30
9, 11, 14	30
9, 11, 14, 15	26
9, 11, 15	26
9, 14	31
9, 14, 15	27
9, 15	27
11, 14	30
11, 14, 15	26
11, 15	26
14, 15	27

6 Conclusions

In this paper, data mining algorithms are applied to the results, i.e., expansion plans obtained for the transmission expansion planning problem. This is done in order to find the association between the new or upgrading lines, which are to be added to the system. In deregulated market environment, the expansion planning phase involves the current market players also. They all may have their own expansion plan, but the final expansion plan is to be coordinated among all the individual players. This is important because, if a line is added with its closely associated line, it would help market players not only reduce investment cost but also their operational cost. This application of data mining to the outcome of different expansion plans helps not only in finding the associative correlation between lines but also in prioritizing the lines based on the *support* and *confidence* values. In this paper, a single objective function is used and the dataset is generated by varying the load and the generation. The results can be more refined further by considering different varieties of objective functions and generation expansion plans recursively to find the association between the lines while prioritizing the lines to be added to the system.

References

1. Shandilya SK, Shandilya S, Deep K, Nagar AK Handbook of research on soft computing and nature-inspired algorithms. IGI Global
2. Cios KJ (2007) Data mining: a knowledge discovery approach. Springer
3. Witten IH, Frank E (2005) Data mining: practical machine learning tools and techniques. Elsevier
4. Bariş Y (2010) Impacts of frequent itemset hiding algorithms on privacy preserving data mining. Master's thesis

5. Han J, Pei J, Yin Y (2000) Mining frequent patterns without candidate generation. In: Proceeding of the ACM SIGMOD international conference on management of data
6. Zaki MJ, Parthasarathy S, Ogihara M, Li W (1997) New algorithms for fast discovery of association rules. In: Proceedings of the 3rd ACM SIGKDD international conference on knowledge discovery and data. AAAI Press, Menlo Park, CA, USA
7. Agrawal R, Srikant R (1994) Fast algorithms for mining association rules. In: Proceedings of the 20th VLDB conference Santiago, Chile
8. Dubey AK, Shandilya SK (2010) Exploiting need of data mining services in mobile computing environments. In: Proceedings of international conference on computational intelligence and communication networks
9. Dubey AK, Shandilya SK (2010) A novel J2ME service for mining incremental patterns in mobile computing. In: Communications in computer and information science
10. Garver LL (1970) Transmission network estimation using linear programming. IEEE Trans Power Apparatus Syst PAS-89:1688–1697

Development of Charging System for Multiple Electric Vehicle Using Bidirectional DC–DC Buck–Boost Converter

**A. Dominic Savio, A. Vimala Juliet, C. Bharatiraja,
R. K. Pongiannan, Mohd Tariq and Abdul Azeem**

Abstract Electric vehicle (EV) charging system integrated with DC microgrid and nonconventional energy sources will give a way for the envisioned future of EV charging infrastructure. In this paper, mobile charging station (MCS) to charge multiple electric vehicles has been designed and developed. The MCS is integrated with DC microgrid and is operating in four different modes. The charging terminals of grid-connected MCS are developed with DC/DC bidirectional buck–boost converter. The charging station is modelled using MATLAB–Simulink, and the system operation has been verified for the different operating modes. A laboratory prototype has been developed, and the results show the practical possibility of the MCS.

A. Dominic Savio · A. Vimala Juliet · C. Bharatiraja · R. K. Pongiannan
School of Electrical Engineering, SRM Institute of Science
and Technology (formerly known as SRM University),
Kattankulathur Campus, Chennai 603203, India
e-mail: agdominicsavio@gmail.com

A. Vimala Juliet
e-mail: vimlala@yahoo.co.in

C. Bharatiraja
e-mail: bharatiraja@gmail.com

R. K. Pongiannan
e-mail: rkp.annan@gmail.com

M. Tariq (✉) · A. Azeem
Department of Electrical Engineering, Aligarh Muslim University,
Aligarh 202002, India
e-mail: tariq.iitkgp@gmail.com

A. Azeem
e-mail: azeem.abdul25@gmail.com

1   Introduction

Electric vehicle (EV) technology is highly beneficial in terms of emission-free environment, economy and comfortable as well as noiseless operation and requires very less maintenance [1]. Environmental pollution is increasing due to the usage of internal combustion engine (ICE) vehicle technology. Current road transportation mostly based on ICE vehicle technology is creating more CO_2 emission [2]. The use of fossil fuel is to be reduced and alternative solution to be introduced for transportation to reduce the emission. Due to the advantages, the EV technology is growing in a faster way. In the research, the EV developments are in high volume in terms of the development of motor drive, efficient control technique, hybrid vehicles, protection and suitable charging stations. The EV has matured in the domains like controllers and drive motors to some extent, but still, intensive research is going on in the fast charge charging system development [3–5].

From the charging performance available, the significant glitches very long charging time and lack of charging facilities [6]. Due to these issues, the driving range is very limited. The need of the day is a fast-charging infrastructure. Even though some slow-charging systems are available with a power rating of few kW, it is difficult to utilize in a large number of charging stations since they affect the reliability of existing power system grid regarding power quality aspects. The problems associated with EV charging station are voltage fluctuations, increase in peak load and requirement of the upgradation in the existing power system which is also highly expensive [7].

An alternate is fast-charging system for charging. Even though the fast chargers are available up to 50 kW rating with a charging period of one hour, it difficult the install in home applications which affects the power to a great extent.

In the literature, energy storage systems and renewable energy sources (RESs) have been integrated into the charging system, which can be made available in public charging stations [8, 9]. The power electronic convert along with a suitable PWM control provides an efficient charging system performance [10, 11]. In this context, many literatures were presented using the topologies like DC–DC boost converter, DC–DC buck converter, hybrid DC–DC converters, and so on [12]. In this paper a mobile charging system is designed using battery storage, bidirectional dc–dc buck–boost parallel converter is designed and developed [13, 14]. The paper is organized as follows: Sect. 2 elaborates the function of proposed mobile charging point for multiple electric vehicles and the operating modes of charging station; the simulation study and experimental validation are presented in Sect. 3. The conclusions are drawn in Sect. 4.

2 The Function of the Proposed Charging System for Multiple Electric Vehicles

The charging station consists of a bidirectional DC–DC buck–boost converter which enables the power flow from the grid to vehicle and vehicle to grid and three charging terminals [15, 16]. The charging system structure is shown in Fig. 1. In the charging system, the energy storage unit is directly connected to the microgrid to provide peak load charging. The DC microgrid is connected to charging unit through conventional charge controllers. The DC microgrid is connected to three charging terminals through buck converters. Additionally, a standby input terminal is provided by the buck–boost converter which provides the charging from a vehicle to grid.

The system operates in four different modes depending on the voltage levels of the microgrid in the vehicle during charging. The performance of bidirectional buck–boost converter used in the system is shown in Fig. 2.
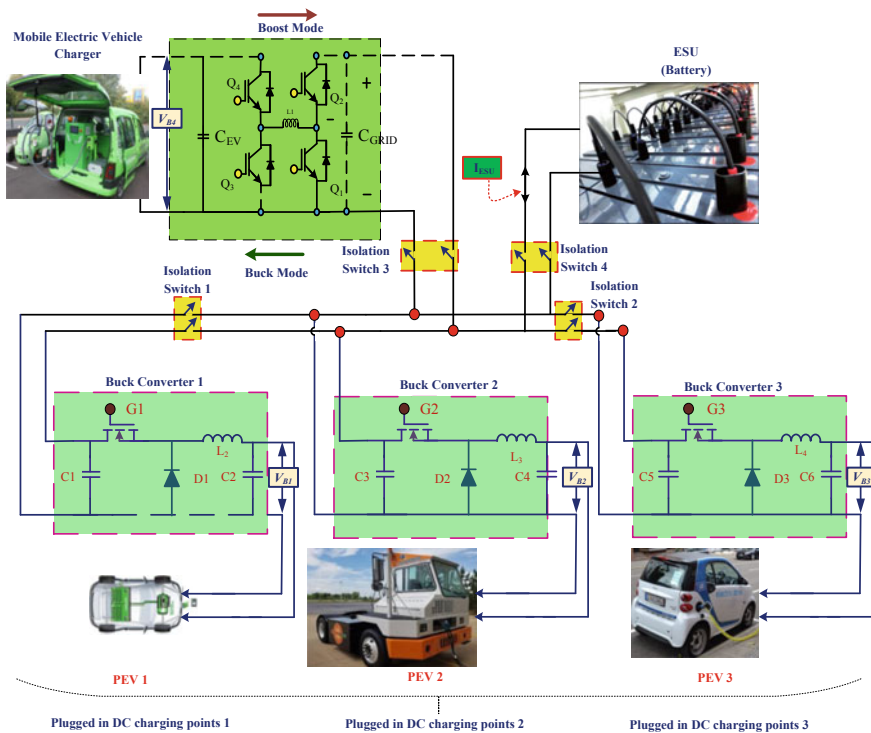
Fig. 1 Typical charging station architecture station

Fig. 2 Efficiency and operation time ratio
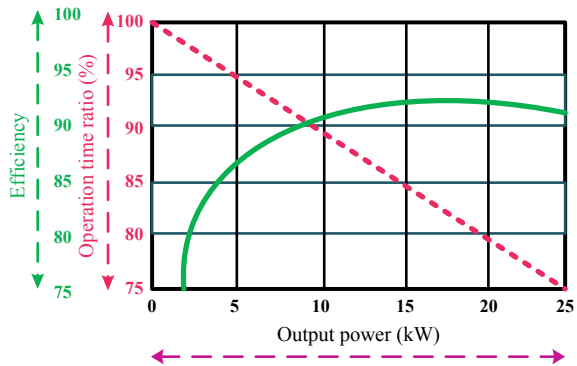
A. Operating Modes of Charging Station

The operating modes of the charging stations are defined based on the supply level in DC microgrid and PEVs available at the charging station. When the mobile charging unit is present in the charging station with a fully charged condition, BDC can operate in boost mode; otherwise, it can operate in buck mode. The vehicle-to-vehicle charging is enabled during the absence of power supply from other PEVs and mobile charging point. The following variables are taken into consideration: V_{B1}–V_{B4}, I_{L1} and $V_{DC\text{-}BUS}$. V_{B1} to V_{B3} are the PEV battery voltages, and V_{B4} is the mobile charging point voltage. The DC–DC bidirectional converter consists of four controllable MOSFET switches. The bidirectional power switches exhibit four quadrant operations and are used to control the power flow between the electric vehicles and ESU maintained at low voltage and the DC link maintained at the higher power level. In order to control the power flow as per requirement, it is necessary to control the duty cycle and phase delay of the MOSFET switches. The gate signals are needed to carry out charge operation, i.e., the power transfer from high power DC link to low power dual battery of PEVs. Based on the SOC of the vehicle, the operating modes of the charging station are decided. The functional flow of four modes of operation of the charging system is shown in Fig. 3. The operating modes of the charging station are as follows:

Mode 1: Mobile EV charging ($SOC_{MEVC} > 80\%$)
Mode 2: Mobile EV discharging ($SOC_{MEVC} < 80\%$)
Mode 3: V2V charging (MEVC not present, $SOC_{PEV1} > 80\%$ and $SOC_{PEV2} < 60\%$)
Mode 4: ESU charging (MEVC not present, $SOC_{PEV1\text{-}PEV3} < 70\%$)

Mode 1: Mobile EV charging ($SOC_{MEVC} > 80\%$)

In this mode, MEV has the maximum power which is identified by measuring V_{B4} voltage. Assuming that all the vehicles are ready to charge, the total power is fed from MEVC to the PEVs as shown in Fig. 4.
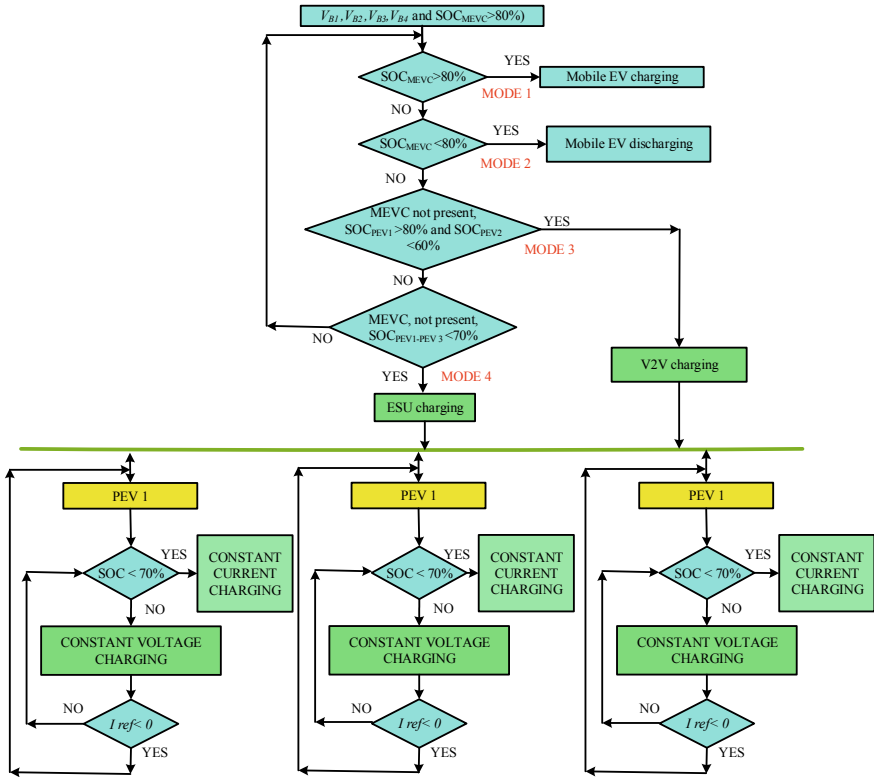
Fig. 3 Functional flow diagram of four modes of the operation of the charging system

Fig. 4 Mobile EV charging
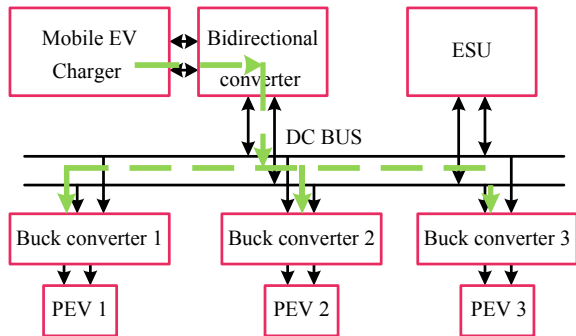
Mode 2: Mobile EV discharging ($SOC_{MEVC} < 80\%$)

In this mode, MEV has the minimum power and is identified by measuring V_{B4} voltage. Assuming that all the vehicles are fully charged, the MEVC charged from the PEVs as shown in Fig. 5.

Fig. 5 Mobile EV discharging
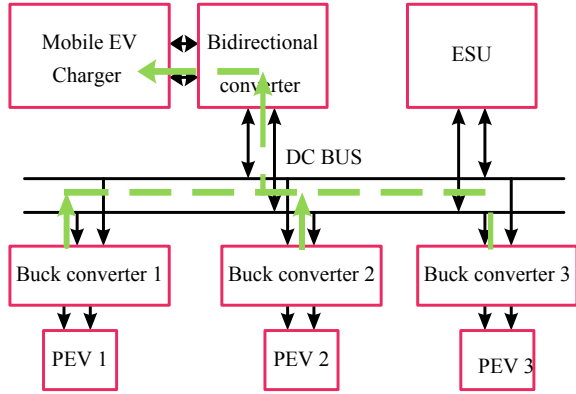
Mode 3: V2V charging (MEVC not present, $SOC_{PEV1} > 80\%$ and $SOC_{PEV2} < 60\%$)

In this mode, MEVC has the minimum power and is identified by measuring V_{B4} voltage. Assuming that the status of SOC PEV1, PEV2 and PEV3 is less than the predetermined level, PEV1 and PEV2 supply the power to PEV3 as shown in Fig. 6.

Mode 4: ESU charging

Assumed that MEVC has minimum power and is identified by measuring V_{B4} voltage. Assuming that the status of SOC PEV1, PEV2 and PEV3 is less than the predetermined level, ESU supplies the power to the PEV1, PEV2 and PEV3 as shown in Fig. 7.

Fig. 6 V2V charging
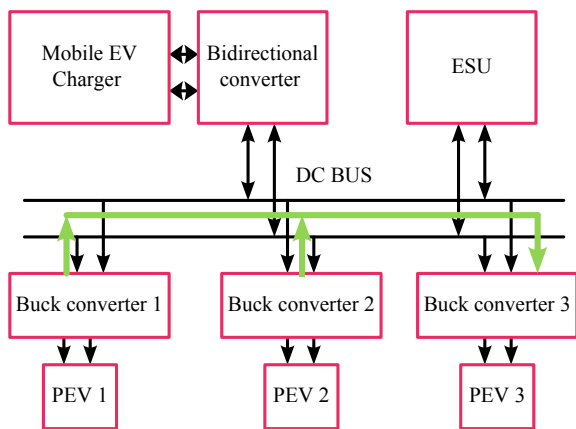
Fig. 7 ESU charging
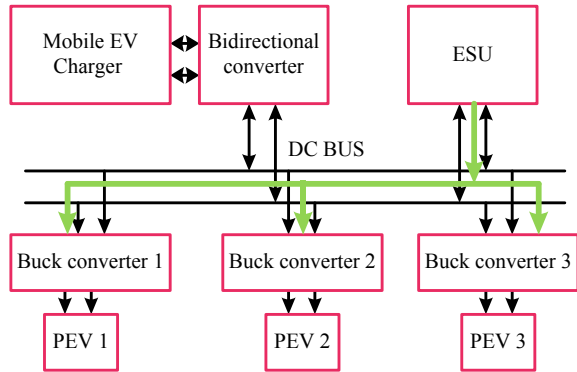
3   Design of Charging System for Multiple Electric Vehicles

The electrical vehicle charging system with multiple charging terminals has been designed using DC grid, DC–DC boost converters, bidirectional DC–DC buck–boost converter. The system performance has been studied using simulation and experimental verification.

A. Simulation Study

The simulation model developed using MATLAB–Simulink consist of DC–DC power converters, DC grid and a digital controller. Three PEVs (PEV1, PEV2 and PEV3) are connected to the microgrid through DC–DC buck converter assuming that all the PEVs at different power levels of SOC, and the maximum DC bus voltage is 320 V. The power rating of the PEVs is: PEV1 and PEV2 = 480 W and PEV3 = 240 W. The corresponding SOC of all the PEVs at the time of connecting to the charging station is 80, 70 and 60%, respectively. Consider all three PEVs are connected to the microgrid at different time intervals, PEV1 is connected at a time of 0 s, and PEV2 is connected after 30 s. Then, PEV3 is connected after 60 s. After 75 s, PEV1 reaches the SOC of 81%, operating under a constant voltage charging mode with the reference voltage (48 V). The SOC variations of PEV1, PEV2 and PEV3 under G2V mode are shown in Fig. 10. The experimental results are presented for different operating conditions of the charging system such as grid to vehicle (G2V) and vehicle to grid (V2G).

During V2V charging, PEV1 is PEV2 connected to the charging station with 100% of SOC and voltage of 50 V, and then it transfers the power to the next available PEV or the MEVC. During this mode, the PEV1 charging converter works in the constant current discharge mode, and PEV3 charging converter operates in the constant current charging mode which are shown in Figs. 8, 9, 10 and 11.
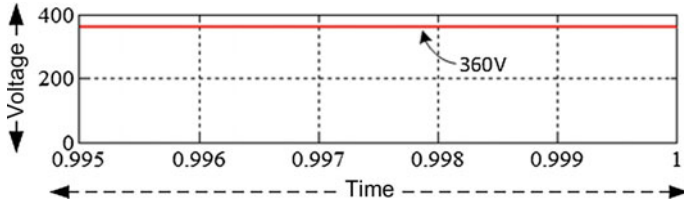
Fig. 8 DC link voltage
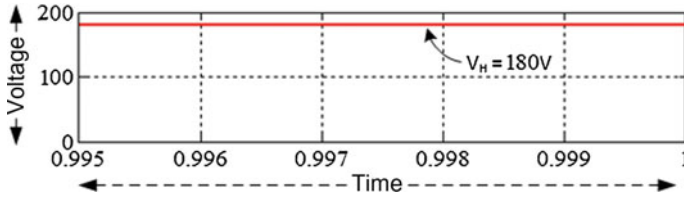
Fig. 9 MEVC voltage
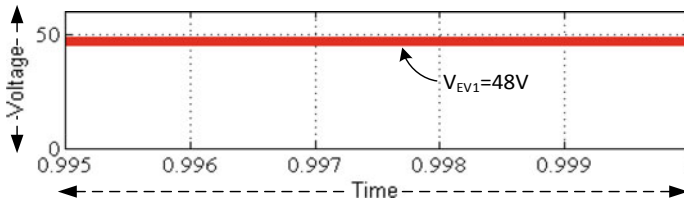
Fig. 10 PEV1 voltage
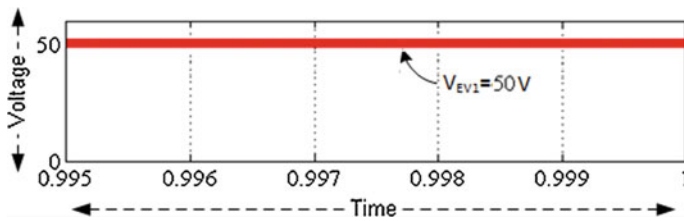
Fig. 11 PEV2 voltage
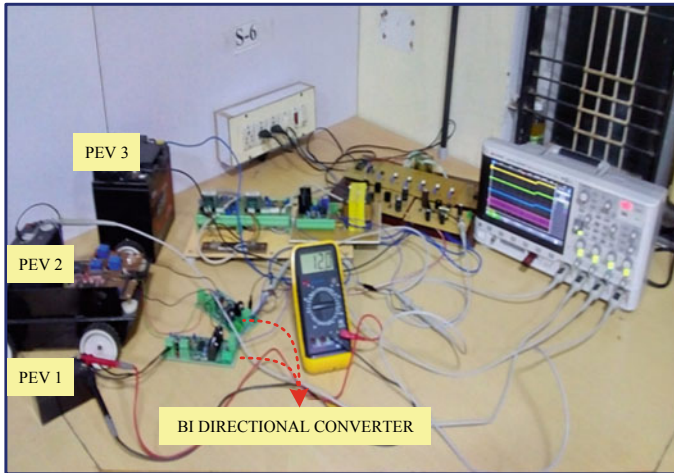
Fig. 12 Photograph of the experimental set-up

B. **Experimental Verification**

The laboratory prototype of 1 kW EV charging system consists of a digital controller, DC grid, charging terminals and battery storage. The photograph of the experimental set-up is shown in Fig. 12. The control signals for the power electronics converters are generated by a digital controller. The control algorithm has been developed using code composer studio and implemented in a digital signal controller form microchip.

The experimentation has been carried out for the following settings, namely grid to vehicle 1, grid to vehicle 2, grid to vehicle 3, battery storage to vehicle 1, battery
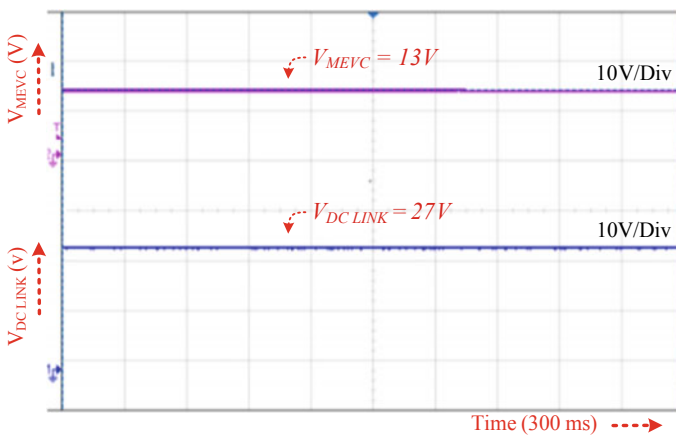
Fig. 13 DC link voltage and charging voltage level in mode 1
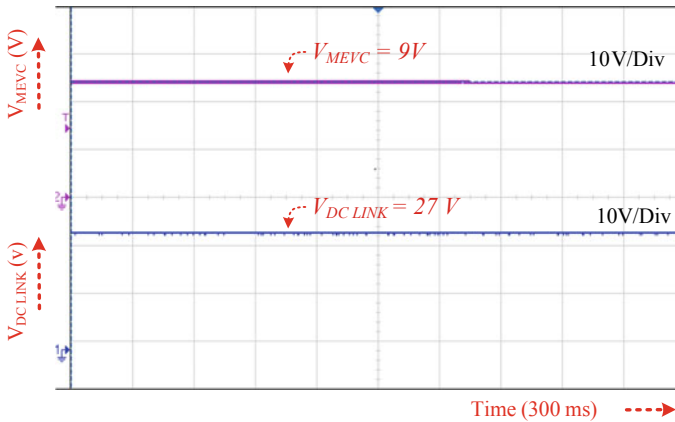
Fig. 14 DC link voltage and charging voltage level in mode 2

storage to vehicle 2, battery storage to vehicle 3. The experimental result for Mode 1 and Mode 2 operation of the system is shown in Figs. 13 and 14, respectively. From the results, it is observed that the EV charging system is functioning satisfactorily in all four modes.

4 Conclusion

In this paper, electric vehicle (EV) charging system integrated with DC microgrid and nonconventional energy sources has been designed and developed. The EV charging system has been modelled using MATLAB–Simulink environment. The laboratory prototype of 1 kW power rating has been developed, and the experimentation is carried out for the four modes of operation. The fast charging is achieved in one hour which is acceptable for practical cases.

References

1. Jehlikl F et al (2015) Fuel consumption effects of a diesel hybrid electric vehicle across a range of driving styles and ambient conditions. In: Proceedings of IEEE conference KBEI 2015, pp 978–982
2. Hajimiragha A, Cañizares CA, Fowler MW, Elkamel A (2010) Optimal transition to plug-in hybrid electric vehicles in Ontario, Canada, considering the electricity-grid limitations. IEEE Trans Ind Electron 57:690–701
3. Ahmadi M, Mithulananthan N, Sharma R (2016) A review on topologies for fast charging stations for electric vehicles. In: Proceedings of IEEE conference 2016, pp 1–6
4. Bharatiraja C, Sanjeevikumar P, Pierluigi S, Ramesh K, Raghu S (2017) Real time forecasting of EV charging station scheduling for smart energy system. Energies 10(377):1–14

5. Varghese AS et al (2017) An efficient voltage control strategy for fast charging of plug-in electric vehicle. In: IEEE conference proceedings i-PACT 2017, pp 1–4
6. Behzadpour A, Eliasi H (2015) Fuzzy based controller design for parallel hybrid EV. In: Proceedings of IEEE conference KBEI 2015, pp 640–650
7. Ruba M, Fodorea D (2016) Development of a complete motor-drive solution for light EV based on a SRM. In: Proceedings of IEEE conference EPE 2016, pp 197–205
8. Bharatiraja C et al (2018) Energy management strategy for rural communities' DC micro grid power system structure with maximum penetration of renewable energy sources. Appl Sci 8 (4):585
9. Sechilariu M, Wang B, Locment F (2013) Building integrated photovoltaic system with energy storage and smart grid communication. IEEE Trans Ind Electron 60:1607–1618
10. Bharatiraja C, Jeevananthan S, Latha R (2014) FPGA based practical implementation of NPC-MLI with SVPWM for an autonomous operation PV system with capacitor balancing. Int J Electr Power Energy Syst 61:489–509
11. Bharatiraja C, Babu S, Krishnakumar V, Sanjeevikumar P, George N (2017) Investigation of slim type BLDC motor drive with torque ripple minimization using abridged space-vector PWM control method. Int J Power Electron Drive Syst 8(2):593–600
12. He JW, Li YW, Munir MS (2012) A flexible harmonic control approach through voltage-controlled DG-grid interfacing converters. IEEE Trans Ind Electron 59:444–455
13. Bharatiraja C, Ravi A, Banerjee S, Chakraborty A (2017) A hybrid cascaded multilevel inverter with diode assisted boosting network. In: First international conference on power engineering, computing and control, PECCON 2017, Chennai, India, 2–4 Mar 2017
14. Chung HSH, Chow WC (2000) Development of a switched-capacitor DC/DC converter with bidirectional power flow. IEEE Trans Circuits Syst I Fundam Theory Appl 47(9):1383–1389
15. Bharatiraja C, Shabin M (2013) A novel reduced switch single source MLI topology with variable input overvoltage control. In: IConDM 2013: international conference on design and manufacturing, IIITDM Kancheepuram, Chennai, India, 18–20 July 2013
16. Veeraraghavan A et al (2017) Driving scenario recognition for advanced hybrid electric vehicle control. In: Proceedings of IEEE conference ITEC, pp 978–985

Analysis of Stator Current MRAS for Speed Estimation of Induction Motor Aided with ANN

Trishla Goyal and Bhavnesh Kumar

Abstract In this paper, a detailed study of stator current-based MRAS speed estimator is presented. Here, in this research work, a two-layer offline-trained feedforward neural network-based flux estimator is designed. The network proposed in this network is trained using Levenberg–Marquardt back-propagation learning algorithm using 5000 input–output samples obtained from the conventional simulation model. And the drive performance is tested for various criterions with the conventional model and neural network-based model including in low speed region and regenerative mode of operation. MATLAB/Simulink is used for experimentation purpose.

Keywords Induction motor · MRAS speed estimator · Stator current-based MRAS · Neural networks

1 Introduction

Squirrel-cage-type induction motors are most widely used in electric drives due to their better performance, high robustness, less cost, good efficiency and less maintenance. In many applications, induction motor drives have taken over dc motor drives as it does not require mechanical commutator. Furthermore, the fine control during transient as well as in steady state can be obtained from these drives by employing control schemes such as vector control and direct torque control [1].

Vector-controlled drive requires speed information, traditionally, which is collected by mounting a speed encoder on its shaft, but the use of encoder makes drive expensive, and also, it requires shaft of sufficient length. Because of the limitations imposed by speed encoder in drive, the research is nowadays more focused towards

T. Goyal (✉) · B. Kumar
NSIT, New Delhi, India
e-mail: goyaltrishla12@gmail.com

B. Kumar
e-mail: kumar_bhavnesh@yahoo.co.in

sensorless drives [2]. These sensorless drives employ speed estimators for gathering speed information. Speed estimation can be done by various methods, but model-based speed estimation methods such as Kalman filtering, adaptive observers, sliding-mode observers, artificial intelligence-based methods, MRAS-based speed estimator are more often used [3]. Among these techniques, model reference adaptive scheme (MRAS) is mostly used due to its easy implementation and its well-known structure, and also, it does not require any hardware modifications [4].

MRAS speed estimators can be subdivided into four main categories based on the parameters used for estimation such as rotor flux-based, stator current-based, back emf-based and reactive power-based. Despite various efforts, speed estimation becomes a tedious task at low speed due to almost zero back emf and drift problems. However, back emf-based estimation method eliminates this issue due to the use of back emf as variable instead of rotor flux, but this method has a deficiency as it is prone to stator resistance variation and parameter mismatch in reference model, whereas stator current method is robust to these parameter variations. Speed estimation using stator current-based MRAS requires the estimation of rotor flux, which can be estimated using either current model-based flux estimator or voltage model-based flux estimator. Both of these conventional models have their own issues in exact flux estimation [5–7].

Voltage model has a problem of pure integration which makes it sensitive towards parameter variations such as stator and rotor resistance variations and unstable for low-speed operations, but it shows good performance in regenerative mode of operation, whereas the current model performs flux estimation using synchronous reference frame stator currents and estimated speed which makes it unstable in regenerative mode of operation. So both the conventional flux estimators have complications in estimating flux precisely and hence in the estimation of speed [5].

In order to overcome these drawbacks of the conventional schemes discussed, many artificial intelligence techniques have been applied so far, where neural network and fuzzy are mostly used. Various architectures of neural networks as feedforward, linear network, radial function basis neural network and recurrent structure have been used in the literature (Fig. 1).

In this paper, stator current-based MRAS scheme is used for study purposes which is explained in detail in Sect. 2. A comparative assessment of drive performance with the conventional stator current speed estimator and stator current-based estimator with the conventional flux estimator replaced by feedforward neural network is presented. In Sect. 3, the proposed scheme is discussed, and in Sect. 4, results are presented and discussed.
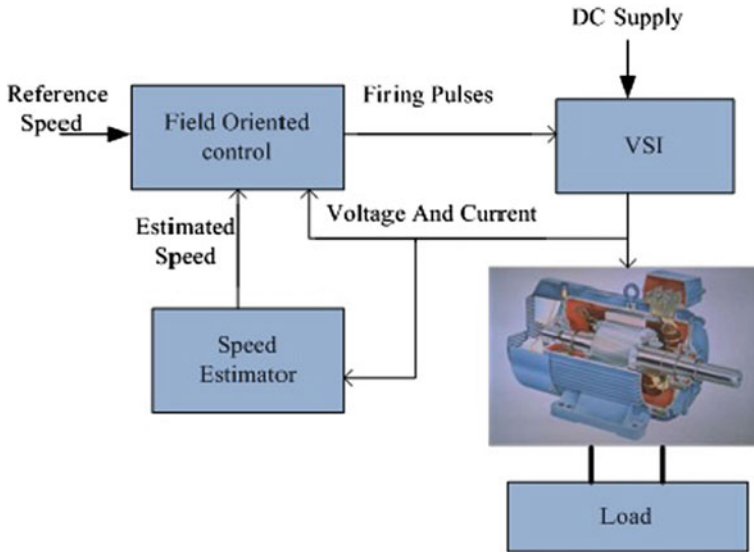
Fig. 1 Basic block diagram of induction motor drive with speed estimator

2 Stator Current-Based MRAS

Basic MRAS structure comprises of the reference model, adaptive model and adaptation mechanism. In stator current-based MRAS, adaptive model itself has two segments, i.e., flux estimator and current estimator. In this method, error function used in adaptation mechanism is a function of estimated flux linkage and estimated currents. The adaptation mechanism generally has a PI controller, gains of which K_p, K_i have to be chosen. In this work, these values are selected on trial and error basis. Based on stator voltage of d- and q-axis in synchronous reference frame [4], modelling of flux estimator can be done as follows (Fig. 2):

2.1 Modelling of Flux Estimator Based on Voltage Model

The following equations are obtained for flux estimation by rearranging the above stator voltage equations.

$$p\psi_{\mathrm{qr}}^{e*} = \frac{L_{\mathrm{m}}}{L_{\mathrm{r}}}\left(V_{\mathrm{qs}} - R_s i_{\mathrm{qs}} - \sigma L_s p i_{\mathrm{qs}}\right) \tag{1}$$

$$p\psi_{\mathrm{dr}}^{e*} = \frac{L_{\mathrm{m}}}{L_{\mathrm{r}}}\left(V_{\mathrm{ds}} - R_s i_{\mathrm{ds}} - \sigma L_s p i_{\mathrm{ds}}\right) \tag{2}$$
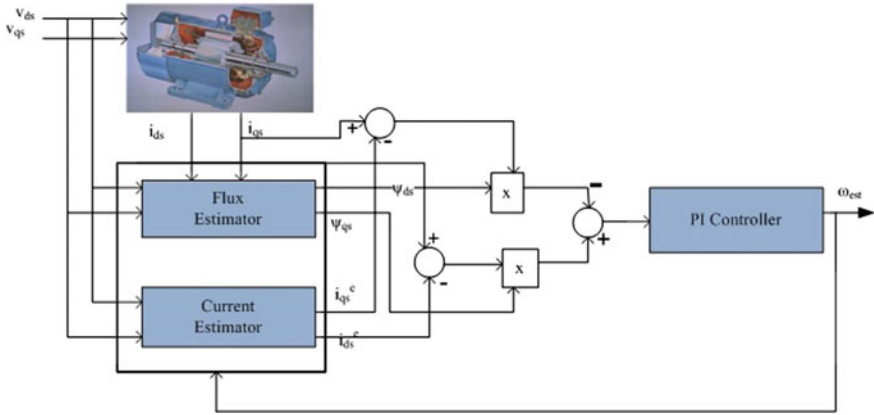
Fig. 2 Stator current-based MRAS scheme

2.2 Modelling of Current Estimator

Current estimator is based on the current model only. Current estimation is done using estimated flux, stator voltages and speed estimated by the estimator as feedback. All these parameters are taken in synchronous reference frame. It is explained by the figure and equations shown below:

$$p\psi_{qr}^e = \frac{L_m}{T_r} i_{qs} - \frac{1}{T_r} \psi_{qr}^e - \omega_r^e \psi_{dr}^e \tag{3}$$

$$p\psi_{dr}^e = \frac{L_m}{T_r} i_{ds} - \frac{1}{T_r} \psi_{dr}^e + \omega_r^e \psi_{qr}^e \tag{4}$$

Substituting above equations into Eqs. (1) and (2), respectively, and rearranging them:

$$pi_{qs}^e = \frac{1}{\sigma L_s} \left(V_{qs} - \left(R_s + \frac{L_m^2}{L_s L_r} \right) i_{qs}^e + \frac{L_m}{T_r L_r} \psi_{qr}^e + \frac{L_m}{L_r} \omega_r^e \psi_{dr}^e \right) \tag{5}$$

$$pi_{ds}^e = \frac{1}{\sigma L_s} \left(V_{ds} - \left(R_s + \frac{L_m^2}{L_s L_r} \right) i_{ds}^e + \frac{L_m}{T_r L_r} \psi_{dr}^e - \frac{L_m}{L_r} \omega_r^e \psi_{qr}^e \right) \tag{6}$$

where ω_r, T_r and $\sigma = \left(1 - L_m^2/L_s L_r\right)$ are rotor speed, rotor time constant and leakage factor, respectively. Error function is derived using estimated and actual parameters in adaptation mechanism as follows:

$$\varepsilon = \psi_{dr}^{e}\left(i_{qs} - i_{qs}^{e}\right) - \psi_{qr}^{e}\left(i_{ds} - i_{ds}^{e}\right) \tag{7}$$

3 Neural Network-Based Flux Estimation

Artificial neural network is a model of human brain, and its fundamental unit is known as neuron, which has the capability of learning and generalization. Each neuron acts as an information processing unit. Architecture and number of neurons in each layer (in case of multilayer neural networks) may be chosen according to the criterion of the drive performance required for the application of the drive. Mostly used neural architecture is feedforward neural network in MRAS-based speed estimators.

In the literature, various neural architectures have been used which are classified as feedforward, linear, radial basis and recurrent. In this research work, an artificial neural network-based flux estimator is proposed. An offline-trained feedforward multilayer neural network with 3–30–2 structure as shown in Fig. 3 is used to estimate rotor flux in stationary reference frame, wherein a number of hidden layer neurons are chosen on trial and error basis. The inputs of the neural network having three neurons have stator currents of stationary reference frame and estimated speed, and the output layer has two neurons giving flux estimated components.

Tan-sigmoid activation function is used in hidden layer and Purelin function for output layer. For training of network, the proposed data is obtained from simulation of the conventional model. Input data is extracted from conventional current model, and the target is set as the flux estimated from the conventional voltage model. For obtaining training data, the conventional model is simulated with speed varying

Fig. 3 Neural network architecture proposed
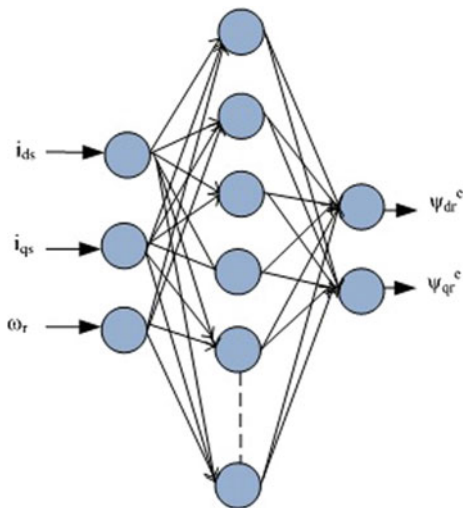
between −50 and 50 rad/s including zero speed operation with torque in the range of 25% of rated load making drive to operate in all modes of operation possible which makes it adaptable for all kind of variations.

Since target data is the output of voltage model which is independent of speed estimated, the response becomes stable in regenerative mode of operation. And as input data is from current model and operation of current model is insensitive towards parameter variation, so the output of NN becomes insensitive towards parameter variations. Levenberg–Marquardt training algorithm is used for training. Five thousand input–output samples are taken for training, testing and validation. Sampling time of the simulation model is kept to be 2×10^{-6} s. Mean square error between targets and NN output decays to 1×10^{-6} after training the network for about 2500 epochs.

4 Results and Discussion

In this section, the results obtained after applying above the proposed scheme are presented and discussed. A 4 kW, 400 V, 1430 RPM, 50 Hz squirrel-cage induction motor drive having parameters mentioned in Appendix is taken to perform various tests.

4.1 Speed Tracking

In this test, the motor is driven for speed varying from 5 rad/s initially and at $t = 1$ s. Speed is changed to 50 rad/s. The test is performed both at no load and at 25% of rated load. The response of speed tracking is shown for 2 s as shown below (Fig. 4).

4.2 Speed Reversal

In this test, the drive is operated at 5 rad/s initially at $t = 0$ s, and then, speed is changed from 5 to −5 at $t = 1$ s at no load and 25% of rated load (Fig. 5).

Fig. 4 **a** Speed tracking at no load with NN flux estimator; **b** speed tracking at 25% of rated load with NN flux estimator
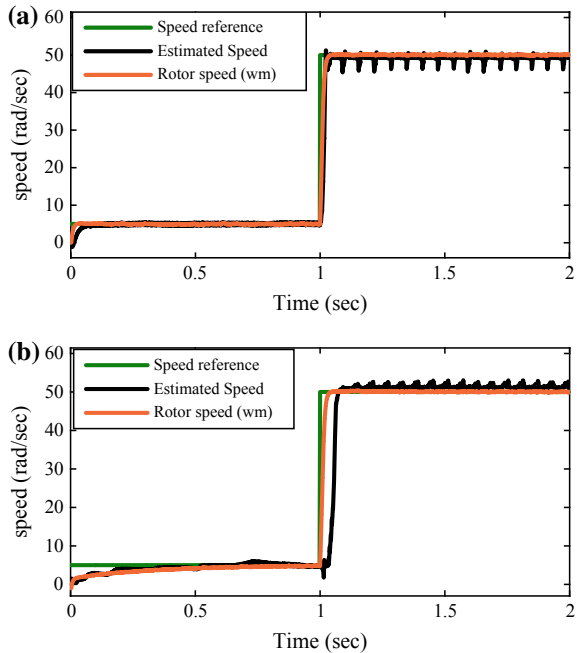
4.3 Regenerative Mode of Operation

In this test, the efficiency of drive in regenerative mode of operation with neural-based speed estimator is shown compared to the conventional current model-based speed estimator. NN-based speed estimator has improved performance comparatively as shown (Fig. 6).

4.4 Parameter Sensitivity

A. Rotor Resistance Sensitivity:

As discussed above that the conventional voltage model-based flux estimator is sensitive towards rotor resistance variations, so here the performance of drive with the conventional VM and with NN-based Flux estimators is compared at no load condition. The drive is operated at 5 rad/s initially and then at $t = 1$ s; speed is changed to 50 rad/s speed. Rotor resistance of drive is changed in 25% range of actual value. The response below shows that NN-based flux estimator has better performance (Fig. 7).
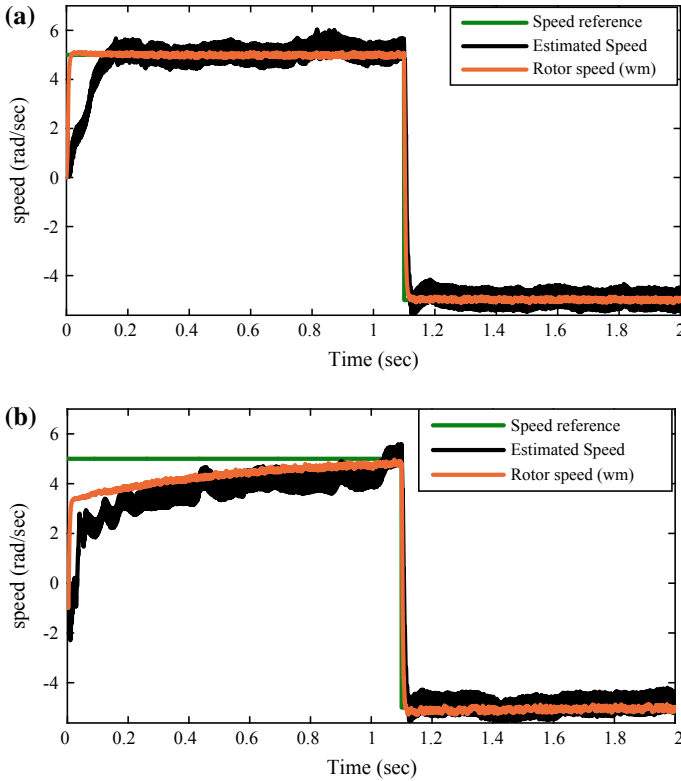
Fig. 5 a Speed reversal at no load; **b** speed reversal at 25% rated load

B. **Stator Resistance Variation**:

In this test, the drive is tested with stator resistance mismatch of 25% of actual value. Drive is again operated without load having the conventional VM and NN-based flux estimator with the same 5–50 rad/s speed variation from initial to $t = 1$ s (Fig. 8).

5 Conclusion

This paper has shown investigations for various rotor flux observers. Voltage model-based flux estimator gives poor performance for parameter variations at low speeds. And current model deteriorates drive performance in regenerative mode. In order to provide a decent solution of the problem discussed, a multilayer neural

Fig. 6 **a** Regenerative mode of operation with CM flux estimator; **b** regenerative mode of operation with NN flux estimator proposed
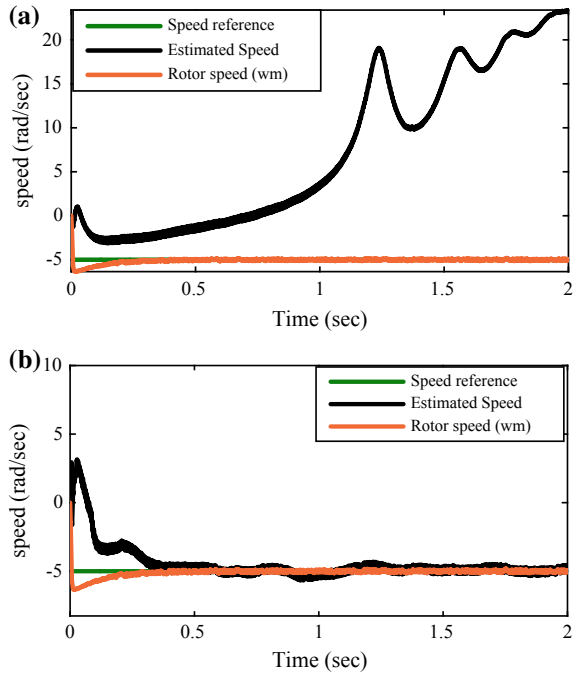
Fig. 7 **a** Performance of drive with VM at rotor resistance variation; **b** performance of drive with NN at rotor resistance variation
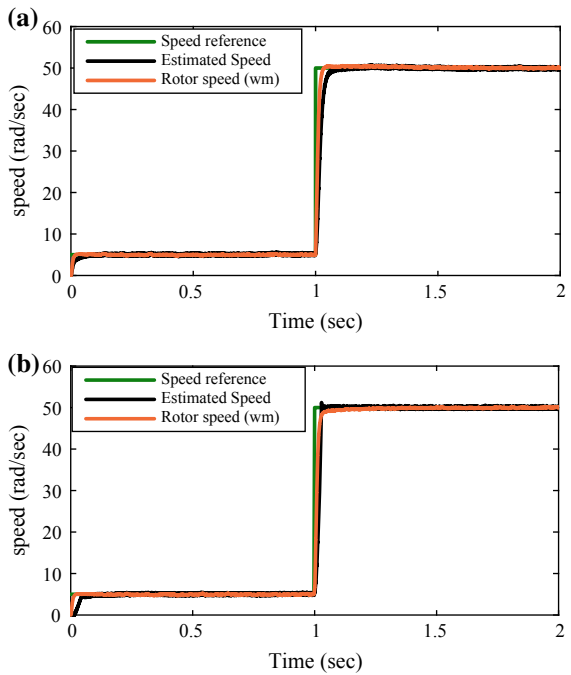
Fig. 8 **a** Stator resistance variation drive performance for VM; **b** stator resistance variation drive performance for NN-based flux estimator
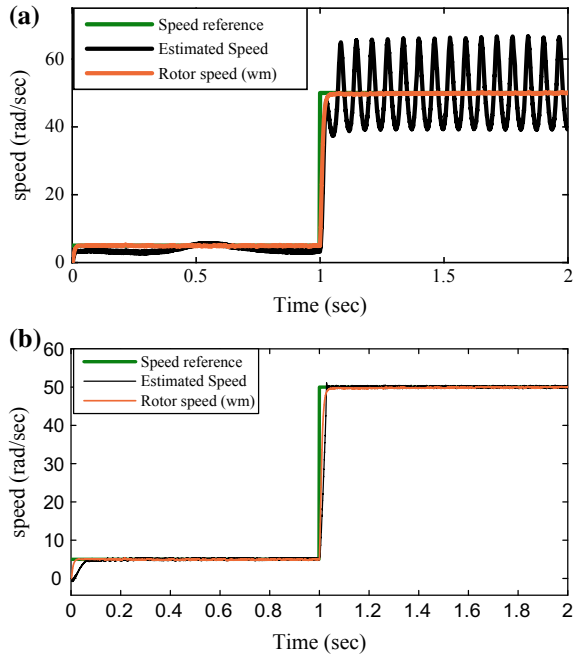
network 3–30–2 structure is proposed and its performance for various tests is represented, which enhances drive performance comparatively. The proposed scheme may be enhanced by proposing even more complex networks which will increase the authenticity and accuracy of the drives compared to traditional drives.

Appendix

Motor parameters

Parameter	Value
Stator resistance (R_s)	1.405 Ω
Rotor resistance (R_r)	1.395 Ω
Stator inductance (L_s)	0.005839 H
Rotor inductance (L_r)	0.005839 H
Mutual inductance (L_m)	0.1722 H
Inertia (J)	0.0131 kg m^2
Pole pair (P)	2
Friction factor (F)	0.002985 Nm s

References

1. Menghal PM, Laxmi AJ (2014) Dynamic modeling, simulation & analysis of induction motor drives. In: 2014 international conference on science engineering and management research (ICSEMR), Chennai, pp 1–7
2. Zhang Y, Zhao Z, Lu T, Yuan L, Xu W, Zhu J (2009) A comparative study of Luenberger observer, sliding mode observer and extended Kalman filter for sensorless vector control of induction motor drives. In: 2009 IEEE energy conversion congress and exposition, San Jose, CA, pp 2466–2473
3. Keshavarz M, Mojran A, Toosi KN (2015) Dynamic modeling of breast tissue with application of model reference adaptive system identification technique based on clinical robot-assisted palpation. J Mech Behav Biomed Mater 51:269–278
4. Bose BK (2007) Neural network applications in power electronics and motor drives—an introduction and perspective. IEEE Trans Ind Electron 54(1):14–33
5. Gadoue SM, Giaouris D, Finch JW (2009) Sensorless control of induction motor drives at very low and zero speeds using neural network flux observers. IEEE Trans Ind Electron 56(8):3029–3039
6. Gadoue SM, Giaouris D, Finch JW (2011) An experimental assessment of a stator current MRAS based on neural networks for sensorless control of induction machines. In: 2011 symposium on sensorless control for electrical drives, Birmingham, pp 102–106
7. Gadoue SM, Giaouris D, Finch JW (2013) Stator current model reference adaptive systems speed estimator for regenerating-mode low-speed operation of sensorless induction motor drives. IET Electr Power Appl 7(7):597–606

Performance Analysis of Diode-Clamped Inverter-Fed Three-Phase Induction Motor Drive Using SVPWM Technique

Ashish Srivastava, Deepak Pandey, Anurag Chauhan and Ashish Tripathi

Abstract The multilevel diode-clamped inverter is widely used in industries due to its various advantages over conventional voltage source inverter (VSI). For diode-clamped multilevel inverter (DCMLI)-fed induction motor, a space vector pulse width modulation (SVPWM) algorithm has been proposed in this paper and is applied to three-level and five-level inverters. The memory of the controller is saved through determining the switching sequence without using lookup tables. The switching time of voltage vector of multilevel inverter has been computed based on the same pattern as followed in two-level inverter. The suggested method can also be applied to any level inverter. The simulation has been performed for five-level inverter-fed induction motor in this paper using the proposed method.

Keywords Induction motor drive · Space vector pulse width modulation · Five-level inverter

1 Introduction

In the present context, the adjustable speed drives (AC motor) are the most widely used in industrial automation. The desired motor control system is essential for the best performance of automated sectors that can enhance the production rate. Generally, the operations of an automated system are defined in terms of accuracy,

A. Srivastava (✉) · A. Chauhan · A. Tripathi
Rajkiya Engineering College, Banda 210201, Uttar Pradesh, India
e-mail: iitrashish220@gmail.com

A. Chauhan
e-mail: anurag.chauhan36@gmail.com

A. Tripathi
e-mail: ashish11ucer@gmail.com

D. Pandey
Kanpur Institute of Technology, Kanpur 208001, Uttar Pradesh, India
e-mail: d.pandey2906@gmail.com

smoothness, and efficiency of motor control scheme. Induction motor is widely used in electromechanical drive in industries due to its features of robustness, low cost, high speed, and less maintenance. The control of AC motor is a challenging task due to its fast motor dynamics and nonlinear models. The control strategies for AC motor include direct torque control and field-oriented control [1–4].

Traditional two-level inverter is generally used for low-voltage magnitude applications. Therefore, these inverters face the difficulty in meeting the high-power requirements. However, multilevel inverter can be used for medium and high power or voltage applications. The multilevel inverters give output voltage with low harmonic distortion at low switching frequency. Also, multilevel inverter requires low blocking voltage switches for its operation [5–9].

Tamasas et al. [10] developed a technique to assess three different control techniques using multicarrier level-shifted PWM to improve the voltage characteristics of five-level diode-clamped inverter. Tan et al. [11] analyzed a space vector pulse width modulation (SVPWM) strategy of the five-level diode-clamped inverter. They developed a strategy to combine 125 space vectors by 96 triangles in the seven-segment vector synthesis method. Hasegawa et al. [12] presented a new DC-voltage-balancing circuit for a five-level inverter to analyze the operating conditions of a medium voltage drive. Namballa et al. [13] investigated the sinusoidal PWM scheme for five-level neutral-point-clamped inverters.

The present paper is focused on the speed control and performance investigation of induction motor drive. A five-level neutral-point-clamped (NPC) inverter is used here in place of VSI. The harmonic content minimizes with the increase in numbers of level of output voltage. Multilevel inverters offer good electromagnetic compatibility and power quality, high-voltage capabilities, and low switching losses. Active rectifiers and the FACTS controller use these inverters. The *n*-level inverters require various levels of the DC input for synthesis of several voltage levels in the output.

2 System Description

The block diagram of suggested control scheme of IM drive is displayed in Fig. 1. The basic *V/f* control technique is used to control the machine with good starting torque and steady state. The PI controller is used to convert speed error into slip speed, and by adding a rotor speed with the slip speed we get synchronous speed. The space vector modulation is performed in SVM generator block. SVM generator gives the eight switching pulses for each leg in three-phase five-level inverter.
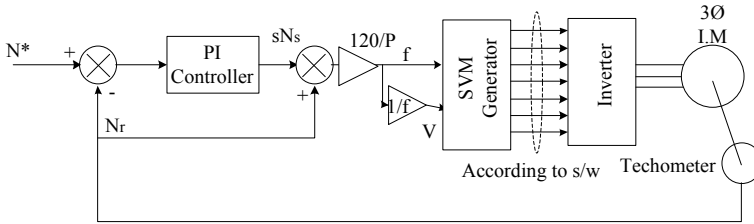
Fig. 1 Block diagram of the proposed control scheme of IM drive

3   Modulation Technique

In neutral-point-clamped inverter, the two main modulation strategies are given as follows:

(1) Sinusoidal pulse width modulation technique
(2) Space vector modulation technique.

The various space vector modulations are available, and they are differed in terms of computational requirement and ease of implementation. The high switching frequency inverter switches additionally reduce the total harmonic distortion in generated output voltage.

In space vector modulation (SVM), stator voltage vectors can directly transform from α–β coordinate system to PWM signals. An inverse Clarke transformation technique has been used for the generation of three-phase output voltage. Using these values of phase voltages, the duty cycles required to control the power switches are then calculated.

The SVPWM algorithm based on fractal hexagon structure is used to generate switching signals for five-level inverter. In this algorithm, the complete hexagon is broken into small triangles and its location and the switching states can be calculated using the following steps:

1. Transformation of three-phase (a, b, and c) system to two-phase (d and q) system.
2. Identification of triangle where tip of the reference vector is located.
3. Determination of three nearby voltage vectors.
4. To implement the triangularization algorithm.
5. Calculation and comparison of cancroids of each triangulated segment with reference vector.
6. For higher-level execution of fractal structure, this algorithm is performed until the reference vector comes nearby the centroid of respective triangle on which triangularization has to be executed using Eqs. (1)–(6).
   Coordinates of Δ_{11} are:

$$\alpha_{11} = \frac{1}{2}(\alpha_{00} + \alpha_{01}) \tag{1}$$

$$\beta_{11} = \frac{1}{2}(\beta_{00} + \beta_{01}) \tag{2}$$

Coordinates of Δ_{12} are:

$$\alpha_{12} = \frac{1}{2}(\alpha_{00} + \alpha_{02}) \tag{3}$$

$$\beta_{12} = \frac{1}{2}(\beta_{00} + \beta_{02}) \tag{4}$$

Coordinates of Δ_{13} are:

$$\alpha_{13} = \frac{1}{2}(\alpha_{01} + \alpha_{02}) \tag{5}$$

$$\beta_{13} = \frac{1}{2}(\beta_{01} + \beta_{02}) \tag{6}$$

where vertices α_{00}, α_{01}, and α_{02} are used to form the region-I of the two-level inverter. The coordinates of these three vertices are $(\alpha_{00}, \beta_{00})$, $(\alpha_{01}, \beta_{01})$, and $(\alpha_{02}, \beta_{02})$ respectively.

The coordinates of new voltage space vectors set at Δ_{11}, Δ_{12}, and Δ_{13} are represented in Fig. 2 and are obtained through coordinates of α_{00}, α_{01}, and α_{02}.

7. Equations (7)–(9) are used to obtain switching states.

$$S_3 = \frac{1}{2}(S_0 + S_1) \tag{7}$$

$$S_4 = \frac{1}{2}(S_0 + S_2) \tag{8}$$

$$S_5 = \frac{1}{2}(S_2 + S_1) \tag{9}$$

8. The basic two-level timings are used to calculate the switching time duration.
9. For calculation of optimized switching sequence, these steps can be considered as:

   (a) The virtual zero vectors are considered as zero.
   (b) The redundant switching states are to be eliminated.
   (c) Acknowledge the favorable switching where only one switching is involved when inverter changes its state.
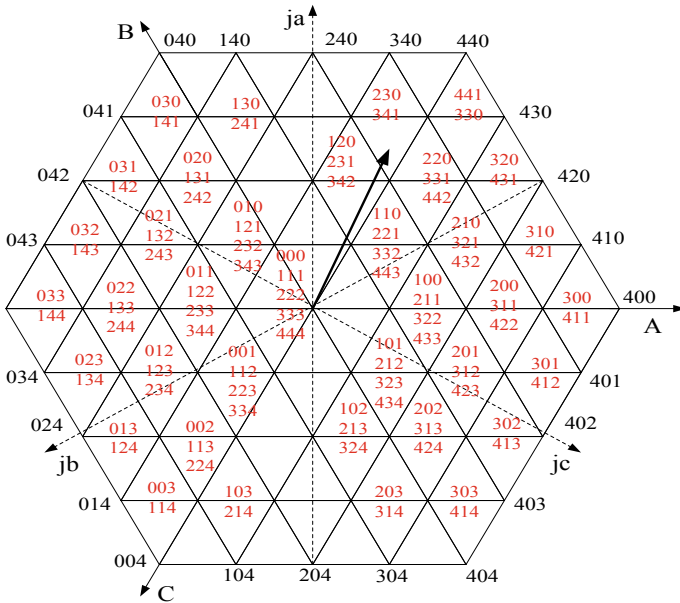
Fig. 2 Space vector diagram of the five-level diode-clamped converter

4 Results and Discussion

The MATLAB/Simulink model of five-level NPC-fed PI-controlled closed-loop induction motor drive is shown in Fig. 3. The space vector pulse width modulation technique is used in the simulation. The drive is tested on various test conditions in which load and speed reference both are variable.

The performance of IM drive at various test conditions is discussed as follows:

Case 1. Response of the Induction Motor Drive for Start-Up (0–1000 rpm) at No Load Condition:

The response of the drive under this condition is shown in Fig. 4a–c, which shows the response of the (a) stator current, (b) rotor speed, and (c) electromagnetic torque. Drive starts from its standstill condition (0 rpm) up to a speed 1000 rpm under no load. During the starting of the motor drive, starting current and torque have high value with oscillating behavior. After 0.65 s, motor attains a desired reference speed with an overshoot of 3%. After some oscillations, its speed settled down in 0.3 s. Hence, the settling time of the drive under such case is 0.3 s.

Case 2. Response of the Induction Motor Drive for Constant Speed (1000 rpm) at Increasing Load (0–11.8 Nm) Condition:

In this case, performance of the drive under constant speed of 1000 rpm and varying load (from no load to rated load of 11.8 Nm) has been investigated as
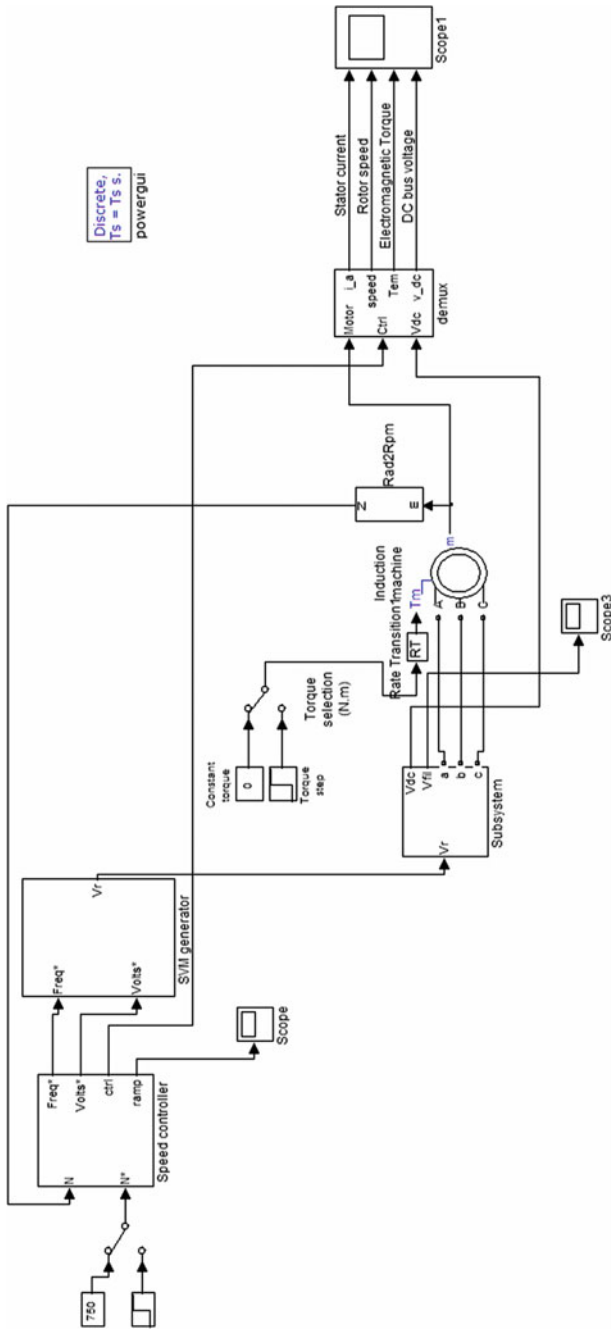
Fig. 3 MATLAB/Simulink model of drive system
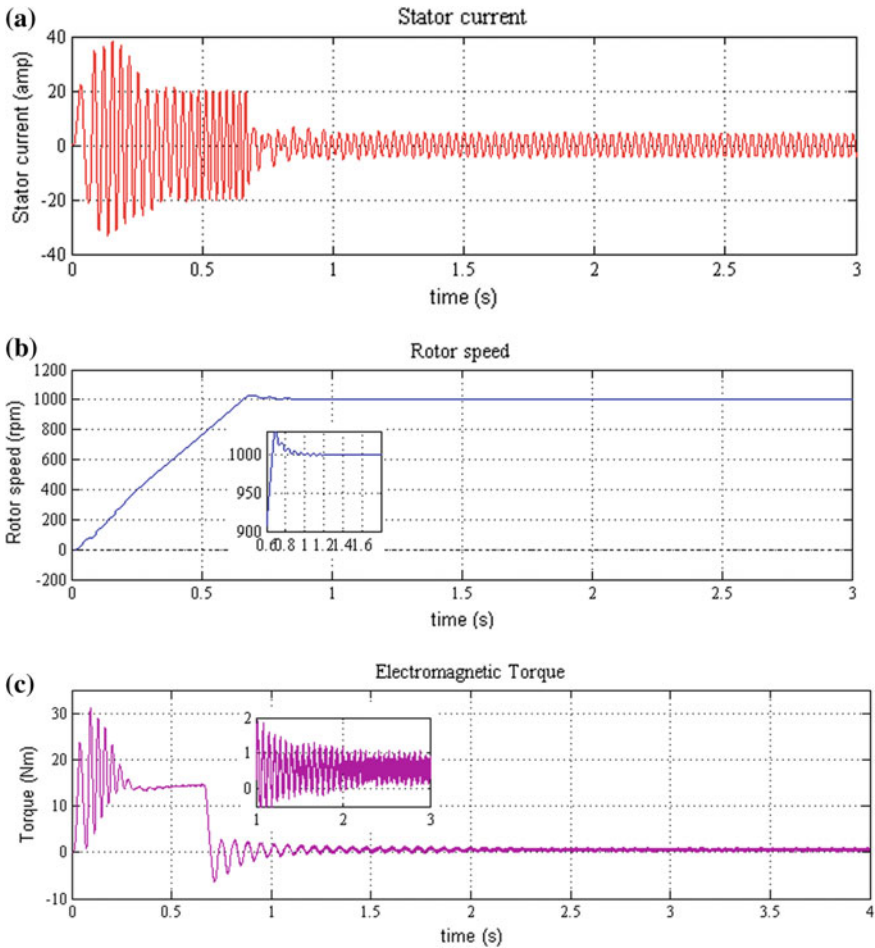
Fig. 4 **a** Stator current response of drive for increasing speed (0–1000 rpm) at no load condition, **b** rotor speed response of drive for increasing speed (0–1000 rpm) at no load condition, and **c** torque response of drive for increasing speed (0–1000 rpm) at no load condition

shown in Fig. 5a–c. Due to the increase in torque, the speed of the drive decreases with an undershoot of 2.2%. After some fluctuations, the speed of rotor settled down with settling time of 0.25 s.

Case 3. Response of the Induction Motor Drive for Increases in Speed (1200–1400 rpm) with Constant Load (6 Nm):

In this case, the drive was tested under variable speed and constant torque condition and simulation results are shown in Fig. 6a–c. Speed varied from 1200 to 1400 rpm, and load is kept constant at half load (6 Nm). In such condition, motor took comparatively more time to settle down.
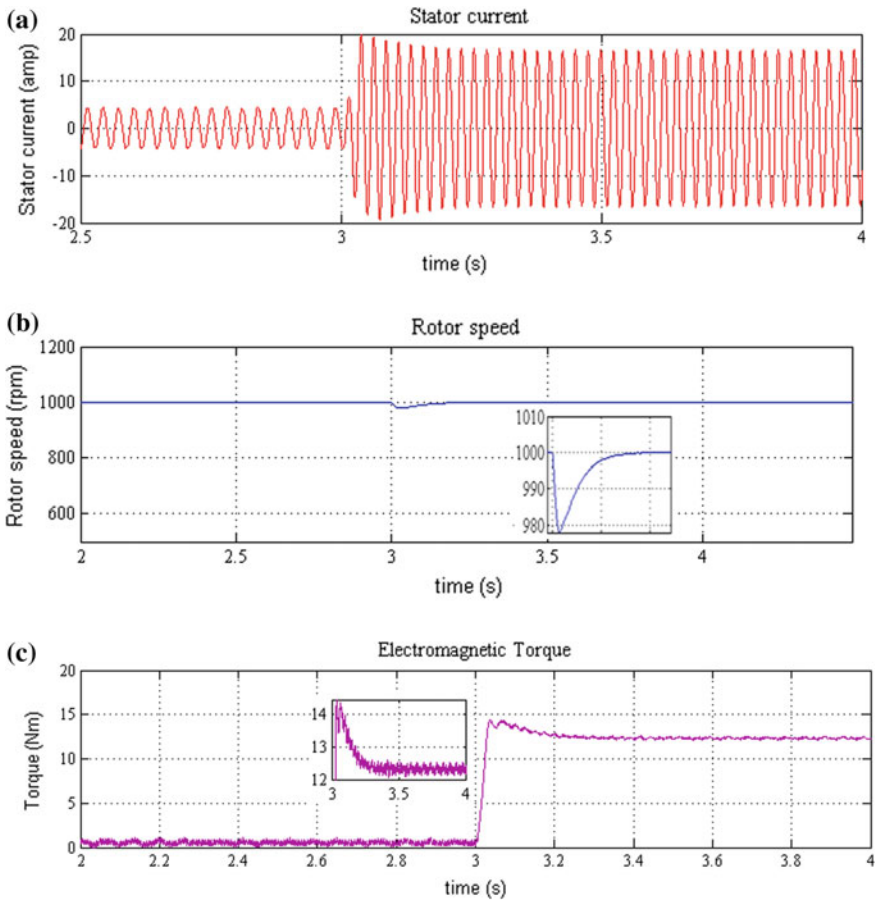
Fig. 5 **a** Stator current response of drive for constant speed (1000 rpm) at increasing load (0–11.8 Nm) condition, **b** rotor speed response of drive for constant speed (1000 rpm) at increasing load (0–11.8 Nm) condition, and **c** torque response of drive for constant speed (1000 rpm) at increasing load (0–11.8 Nm) condition

Case 4. Response of the Induction Motor Drive for Speed Decrease (1400–1200 rpm) at Constant Load (14 Nm)

In this case, the motor's performance is tested at overload torque condition as shown in Fig. 7a–c. It has been found that initially motor torque falls and then rises to meet the equilibrium point and during this time motor speed falls and settles to the reference speed of 1200 rpm.
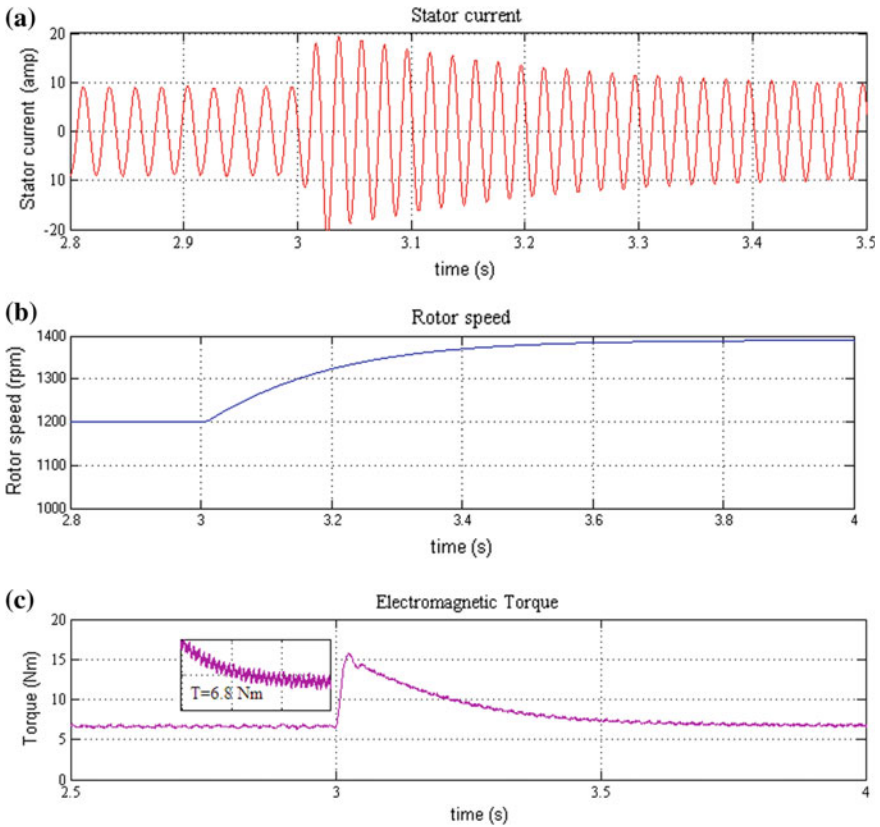
Fig. 6 a Stator current response of drive for increasing speed (1200–1400 rpm) at constant load (6 Nm) condition, **b** rotor speed response of drive for increasing speed (1200–1400 rpm) at constant load (6 Nm), and **c** torque response of drive for increasing speed (1200–1400 rpm) at constant load (6 Nm)

5 Conclusion

A MATLAB-/Simulink-based model of the IM drive has been studied for different load and speed conditions. A comparative chart on the performance of the closed-loop induction motor drive fed by SVPWM-controlled five-level inverter is given in Table 1. It has been found that the proposed control scheme gives the least steady-state error at high speed and at rated load torque. At steady state, a considerable amount of overshoot of less than 3% is observed below the rated speed. At half load, settling time and steady-state error are found to be higher compared to full load condition. The simulation results obtained in this paper may be helpful for the performance enhancement of medium voltage induction motor drive for industrial applications.

(a)

(b)

(c)
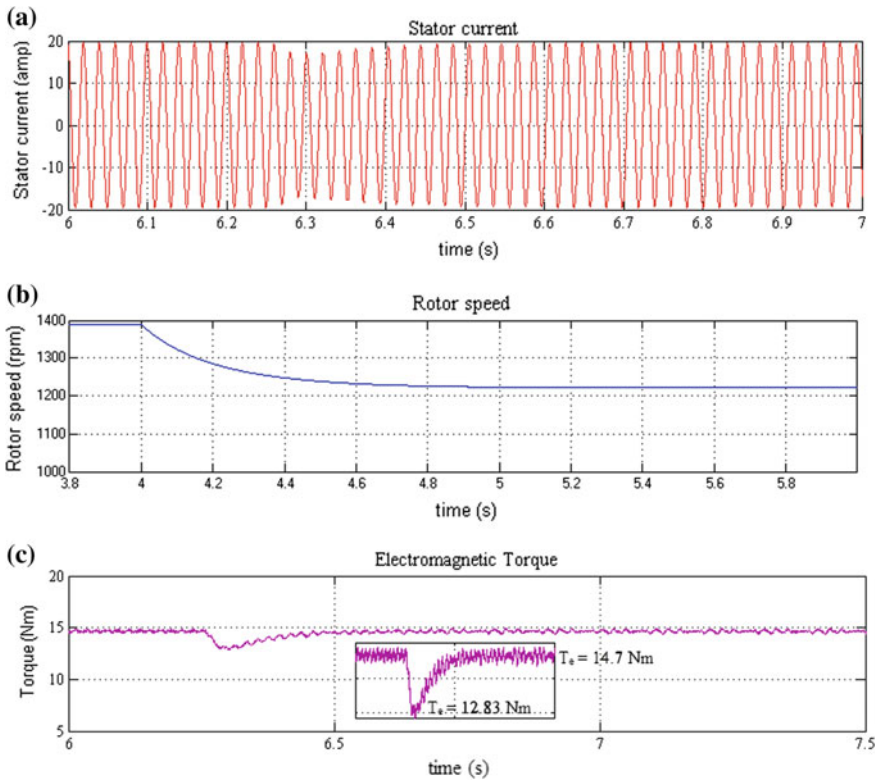
Fig. 7 **a** Stator current response for speed decreases (1400–1200 rpm) at constant load (14 Nm), **b** response of rotor speed for speed decreases (1400–1200 rpm) at constant load (14 Nm), and **c** response of torque for speed decreases (1400–1200 rpm) at constant load (14 Nm)

Table 1 Performance analysis of motor drive

Case	Step change in reference speed (rpm)		Step change in load torque (Nm)		Settling time (s)	Speed overshoot (%)	e_{ss} (%)
	Initial	Final	Initial	Final			
1.	0	1000	0		0.3	3	0.02
2.	1000		0	11.8	0.25	–	0.07
3.	1200	1400	6		0.41	–	0.135
4.	1400	1200	14		0.36	–	0.06

Appendix

Specifications of the induction motor considered in the simulation study are as follows:

Type	Squirrel cage
Rotor speed	1440
Pole pairs	2
Nominal power	2238 VA
Stator resistance (R_s)	0.435 Ω
Stator inductance (L_s)	0.02 H
Rotor resistance (R_r)	0.816
Rotor inductance (L_r)	0.002
Mutual inductance (L_m)	69.31 mH
Inertia (J)	0.089 kg m^2

References

1. Holmes G, Lipo TA (2002) Pulse width modulation for power converters, principle and practice. IEEE Press, Wiley
2. Sen PC (1989) Principle of electric machine and power electronics. Wiley
3. Lai J, Peng FZ (1996) Multilevel converters-a new breed of power converters. IEEE Trans Ind Appl 32(3):509–517
4. Yuan X, Barbi I (2000) Fundamentals of a new diode clamping multilevel inverter. IEEE Trans Ind Appl 15(4)
5. Krause PC, Wasynczuk O, Sudhoff SD (2013) Analysis of electrical machinery and drive systems. IEEE Power Engineering Series, Wiley Student Edition
6. Hatti N, Kondo Y, Akagi H (2008) Five-level diode-clamped PWM converter connected back-to-back for motor drives. IEEE Trans Ind Appl 44(4):1268–1276
7. Akagi H, Hatada T (2009) Voltage balancing control for a three-level diode-clamped converter in a medium-voltage transformerless hybrid active filter. IEEE Trans Power Electron 24(3):571–579
8. Singh GK (2002) Multiphase induction motor drive research—a survey. Electr Power Syst Res 61:139–147
9. Iqbal A, Levi E (2006) Space vector PWM techniques for sinusoidal output voltage generation with a five-phase voltage source inverter. Electr Power Compon Syst 34(2):119–140
10. Tamasas M, Saleh M, Shaker M, Hommoda A (2014) Evaluation of modulation techniques for 5-level inverter based on multilevel shift PWM. In: 17th IEEE Mediterranean electrotechnical conference, Beirut, Lebanon, 13–16 April 2014
11. Tan G, Deng Q, Liu Z (2014) An optimized SVPWM strategy for five-level active NPC (5L-ANPC) converter. IEEE Trans Ind Appl 29(1)
12. Hasegawa K, Akagi H (2011) A new DC-voltage-balancing circuit including a single coupled inductor for a five-level diode-clamped PWM inverter. IEEE Trans Ind Appl 47(2)
13. Namballa S (2003) A sinusoidal PWM scheme for neutral point clamped five level inverter. Int Electr Eng J 4(1):918–925

Automatic Generation Control and Load Frequency Control: A Comprehensive Review

Krishan Arora, Ashok Kumar and Vikram Kumar Kamboj

Abstract In this paper, a comprehensive literature survey has been done on various control techniques of load frequency control (LFC). This research paper reveals the basic studies of the control techniques used in load frequency control to generate and hand over an electric power in an interconnected power system as effectively and accurately as possible while supporting the voltage and frequency inside the acceptable boundaries. The survey consists of both single-area and multi-area power system and various control approaches of conventional power system and modern soft computing strategies which can be applicable to the load frequency approach.

1 Introduction

Restructuring in power system brings considerable revolution in the power sector and governing of power enterprise has turned into simpler by eradicating the ownership of vertically unified service. However, the cooperation of several power

K. Arora (✉)
M.M University, Mullana, Ambala, India
e-mail: vikram.23687@lpu.co.in

K. Arora
School of Electronics and Electrical Engineering, Lovely Professional University, Phagwara, Punjab, India

A. Kumar
Department of Electrical Engineering, M.M University, Mullana, Ambala, India

V. K. Kamboj
Domain of Power Systems, School of Electronics and Electrical Engineering, Lovely Professional University, Phagwara, Punjab, India

manufacturers along with autonomous power manufacturers (APM) and numerous traders have also made the operation of power system more complicated. The periodically dynamic load and inadequacy of superb arrangements among numerous collaborators are a big threat, and any immediate fluctuation in the load will produce sudden alterations in frequency and tie-line power faults. Therefore, it is mandatory to manage the frequency and tie-line power transfer of any area inside permissible limits followed by alteration in the load. It can be accomplished by automatic generation control (AGC) which will balance the frequency and power variation in the interconnected power system and manage the net difference by reducing the unbalance of various areas.

In realistic interconnected power system, the total generation constitutes of different sources like thermal, nuclear hydro, wind, and solar gas. However, the nuclear power plants are operated as base load plants near to its maximum operating range and gas power generation is also a viable option for meeting the variable load demand during peak hours. Thus, the reasonable preference for automatic generation control (AGC) goes with either thermal or hydro generating units. The major targets of automatic generation control are:

1. Influence the system frequency at or very near to titular amount.
2. Retain the generation of each unit at the most productive value.
3. To hold tie-line power flow inside some pre-specified tolerance.

2 Control Techniques

2.1 Load Frequency Control Techniques Can Be Classified as Conventional Control Techniques and Modern Soft Computing Techniques

A. **Conventional Control Techniques**

  1. Linear quadratic regulator-based controlling technique
  2. Integral controlling technique
  3. Proportional integral (PI) controlling technique
  4. Proportional integral derivative (PID) controlling technique

B. **Modern Soft Computing Techniques**

  1. Fuzzy logic-based techniques
  2. Artificial neural network-based techniques
  3. Genetic algorithm-based techniques
  4. Particle swarm-based techniques

Discussion on various load frequency techniques is described by different researchers in their pioneer work.

A. **Conventional Control Techniques**

1. **Linear Quadratic Regulator-Based Controlling Technique**: The precisely control of any system is generally associated with running an effective system with at least possible expenditure. A situation where the system dynamics are characterized by a group of linear differential equations and the expenditure is represented by a quadratic functional equation is termed as the LQ problem. One of the most frequent problems in linear system theory is to precisely control the linear multi-variable system with the quadratic benchmark function.

2. **Integral Controlling Technique**: By observing frequency deviations, the speed changer settings can be adjusted naturally and after modification of system parameters, the value of steady state error should be zero.

3. **Proportional Integral (PI) Controlling Technique**: The proportional integral controller is universally used strategy for LFC system design. The main influencing factor of the PI control technique is to diminish the steady-state error to zero by feeding the unknown faults in the past forward to the system.

4. **Proportional Integral Derivative (PID) Controlling Technique**: The various variables involved in PID controller are the proportional, integral, and derivative values. The proportional value regulates the feedback to present faults, the integral regulates feedback on the basis of new faults, and the derivative resolves the reaction based on the rate by which the fault has been varying.

2.2 Modern Soft Computing Techniques

1. **Fuzzy Logic-Based Techniques**: Fuzzy logic controller-based techniques are basically drafted to diminish the inconstancy of the system productivity. In FLC-based strategies, there is no need of operator for regular checking and all parameters are adjusted automatically with respect to the reference value.

2. **Artificial Neural Network (ANN)-Based Techniques**: The PID controller can find the optimal solution by fixing the values of parameters for proportional, integral, and derivative term. But in transient state, the controller cannot perform better until or unless by varying the values of above-said parameters. The variation in parameter's value can only be achieved by ANN controller. ANN controller is quite competent with the set of inputs to find a better solution.

3. **Genetic Algorithm (GA)-Based Techniques**: The genetic algorithm-based technique is dependent on the process of natural genetics and draws in a survival of the fittest about analytical behavior data network. The GAs have been universally used to solve complicated nonlinear incremental issues.

4. **Particle Swarm-Based Techniques**: The particle swarm-based strategies are distinguished into three basic groups which are evolutionary, physics-based, and swarm intelligence (SI) algorithm. EA is those techniques which are inspired by the concept of evolution in nature. Examples of EAs are differential evolution (DE) and evolutionary programming (EP), etc. The second category is physics-based techniques which are also considered as main branch of the metaheuristic strategies. The main difference between these techniques from EA-based techniques is an arbitrary set of search agents which convey and move all over according to physics rule. Examples of physics-based techniques are gravitational local search algorithm (GLSA), gravitational search algorithm (GSA), and charged system search (CSS), etc. SI techniques are the third main category of metaheuristic techniques. These strategies generally pursue the communal performance of herds, swarms, and fish schooling.

S. No.	Author name	Objective	Methodology used
1	Asma Aziz, G. M. Shafiullah, M. T. O. Amanullah and Alex Stojcevski; December 2016 [1]	Development of momentary unpredictability of inexhaustible power system output as well as reduction of momentary impacts due to volatile generation forecast error	PID controller
2	Chaturvedi Ratnesh and Dwivedi Bharti; May 2014 [2]	Compared the sensitivity of LFC by PI controller and fuzzy logic controller	PI controller Fuzzy logic controller
3	Parmar K. P. Singh; February 2014 [3]	Dynamic response like frequency and tie-line power alterations was settled instantly with zero error by varying the step load perturbation from 1 to 3%	Particle swarm optimization
4	Kumari Reena and Avtar Ram; May 2013 [4]	Designed different membership functions to balance the load and generation of automatic generation control (AGC) of multi-area	Fuzzy logic controller
5	Panda Gayadhar; February 2013 [5]	Consideration of nonlinearities in multi-area reheat thermal system	Modified genetic algorithm
6	Modi Neha, Khare Manju and Chaturvedi Kanchan; February 2013 [6]	Performance of PI controller compared to determine optimal solution in single-area power system	Genetic algorithm method (GA) Particle swarm optimization (PSO)
7	Prakash Surya and Sinha Sunil Kumar; May 2013 [7]	Evaluation of performance is compared for multi-area with electric governor	Adaptive neuro-fuzzy inference system (ANFIS)

(continued)

S. No.	Author name	Objective	Methodology used
8	Lathwal Deepika, Malik Priyanka and Kumar Sunil; April 2013 [8]	Analyzed the voltage and frequency deviation of decentralized thermal and hydro plant	ANN Genetic algorithm
9	Verma Rishabh, Pal Shalini and Sathans; April 2013 [9]	Implementation of intelligent controllers in two-area power system	ANN Fuzzy logic
10	Verma Rishabh, Pal Shalini and Sathans; May 2013 [10]	Investigated the dynamic response by considering over- and undershoot of frequency	Fuzzy gain-scheduled proportional derivative (FGSPD) controller
11	Shankar Ravi, Chatterjee K. and Chatterjee T. K.; December 2012 [11]	Analyze the behavior of LFC under consideration of thyristor-controlled phase shifter connected in series with tie line	Genetic algorithm
12	Sharma Akanksha, Parmar K. P. Singh and Gupta Dr. S. K.; March 2012 [12]	Examined the steady-state error in five-area power system with thermal reheat	Artificial neural network
13	Biswas S. and Bera P.; April 2012 [13]	Controlled the area control error by battery energy storage system	Genetic algorithm
14	Garg Isha; May 2012 [14]	Two-area LFC are compared with deregulated power system	Artificial neural network
15	Prakash Surya, Bhardwaj A. K. and Sinha S. K.; October 2012 [15]	Analyzed the dynamic response of four-area interconnected power system	Hybrid neuro-fuzzy (HNF) approach
16	Khuntia Swasti R. and Panda Sidhartha; June 2011 [16]	Investigated the frequency deviation of interconnected power system by considering generation rate constraints	Artificial neural network
17	Parmar K. P. Singh, Majhi S. and Kothari D. P; January 2011 [17]	Dynamical response of LFC is considered with designing of output feedback controller	Fuzzy logic
18	Sathans and Swarup A.; March 2011 [18]	Formulation of area control error in multi-area system with and without superconducting magnetic energy storage unit	Fuzzy gain-scheduled proportional integral (FGSPI) controller
19	Prakash Surya and Sinha S. K.; December 2010 [19]	Reduction of steady-state error with the development of artificial intelligent control methodologies	Artificial neural network (ANN) Fuzzy logic controller (FLC)

(continued)

S. No.	Author name	Objective	Methodology used
20	Sreenath A., Atre Y. R. and Patil D. R.; May 2008 [20]	Management of fuzzy gain-scheduled proportional and integral controller for the improvement of frequency deviation in electrical power system	Fuzzy logic controller (FLC)
21	Fikret, Caliskan and Istemihan, Genc; July 2008 [21]	With the usage of robust sensors and actuators, various unknown faults associated with load frequency control can be detected	Fuzzy logic controller (FLC)
22	Bjorn H. Bakken and Ove S. Grande; November 1998 [22]	Observed two LFC systems by handling faults, system deviations, and HVDC ramping	Artificial neural network
23	Kumar, Jayant, Kah-Hoe Ng and Sheble, G; May 1997 [23]	Examined AGC model for price-based operation in deregulated environment	PI controller
24	Noureddine Bekhouche and Ali Feliachi; July 1992 [24]	Solved the LFC problem by varying the frequency and tie-line power of electrical system	Genetic algorithm
25	Kothari, M. L., Kaul, B. L. and J. Nanda; October 1980 [25]	Optimized the controller gain by selecting proper value of speed regulator for multi-area system	Genetic algorithm

3 Conclusion

From a review of literature regarding load frequency control, it has been investigated that lots of exercise have been made in the field of load frequency control of single-area and multi-area power system to enhance the controller gain followed by discussion about various methods like conventional and modern soft computing techniques. Concluding that load frequency control can be controlled better by different optimization algorithms used in modern soft computing techniques.

References

1. Aziz A, Shafiullah GM, Amanullah MTO, Stojcevski A (2016 Dec) Automatic generation control in wind integrated power system: new perspectives and challenges. Int Assoc Sharing Knowl Sustain 12(1)
2. Chaturvedi R, Dwivedi B (2014 May) Fuzzy and PI controller based load frequency control of thermal-hydro power system. Int J Innov Sci Eng Technol 1(3)
3. Parmar KPS (2014 Feb) PSO based PI controller for the LFC system of an interconnected power system. Int J Comput Appl (0975–8887) 88(7)
4. Kumari R, Avtar MR (2013 May) Frequency stabilization of two area interconnected power system using fuzzy logic controller and PID controller. IJETT 4(5)
5. Panda G (2013) Automatic generation control of multi-area electric energy systems using modified GA. World Academy of Science, Engineering and Technology. Int J Electr, Robot, Electron Commun Eng 7(5)
6. Modi N, Khare M, Chaturvedi K (2013) Performance analysis of load frequency control in single area power system using GA and PSO based PID controller. IJEECE 2(1):108–114
7. Prakash S, Sinha SK (2013 May 26) Performance evaluation of hybrid intelligent controllers in load frequency control of multi area interconnected power systems. World Academy of Science, Engineering and Technology, vol 7
8. Lathwal D, Malik P, Kumar S (2013) Analysis of Automatic generation control two area network using ANN and genetic algorithm. IJSR, India Online 7(4). ISSN: 2319-7064
9. Verma R, Pal S, Sathans (2013) Intelligent automatic generation control of two-area hydrothermal power system using ANN and fuzzy logic. 9780-7695-4958 3/13/$26.00@2013 IEEE
10. Verma R, Pal S, Sathans (2013) Fuzzy gain scheduled automatic generation control of two area multi unit power system. 978-1-4673-3630-5/13/$31.00@2013 IEEE
11. Shankar R, Chatterjee K, Chatterjee TK (2012) Genetic algorithm based controller for load frequency control of interconnected systems. In: 1st international conference on recent advances in information technology RAIT-2012. 978-1-4577-0697-4/12, $26.00, ©2012 IEEE
12. Sharma A, Parmar KPS, Gupta SK (2012 Mar) Automatic generation control of multi area power system using ANN controller. IJCST 3(3)
13. Biswas S, Bera P (2012) ga application to optimization of AGC in two area power system using battery energy storage. 978-1-4673-4700-6/12/$31.00@ 2012 IEEE
14. Garg I (2012 May) Multi-area load frequency control implementation in deregulated power system. Int J Soft Comput Eng (IJSCE) 2(2). ISSN: 2231-2307
15. Prakash S, Bhardwaj AK, Sinha SK (2012) Neuro fuzzy hybrid intelligent approach for four area load frequency control of interconnected power system. 978-1-4673-1049-9/12/ $31.00@2012 IEEE
16. Khuntia SR, Panda S (2011) A novel approach for automatic generation control of a multi-area power system. In: CCECE, Niagara Falls, Canada. 978-1-4244-9789-8/11/ $26@2011 IEEE
17. Parmar KPS, Majhi S, Kothari DP (2011 Jan) Optimal load frequency control of an interconnected power system. IJEIE 1
18. Sathans, Swarup A (2011) Intelligent automatic generation control of two area interconnected power system using hybrid neuro fuzzy controller. World Academy of Science, Engineering and Technology 60
19. Prakash S, Sinha SK (2010 Dec) Artificial intelligent & PI in load frequency control of interconnected power system. Int J Comput Sci Emerg Technol 1(4). E-ISSN: 2044-6004
20. Sreenath A, Atre YR, Patil DR (2008) Two area load frequency control with fuzzy gain scheduling of PI controller. 978-0-7695-3267-7/08, $25, ©2008 IEEE
21. Caliskan F, Genc I (2008 July) A robust fault detection and isolation method in load frequency control loops. IEEE Trans Power Syst 23(4):1756–1767

22. Bakken BH, Grande OS (1998 Nov) Automatic generation control in a deregulated power system. IEEE Trans Power Syst 13(4):1401–1406
23. Kumar J, Ng KH, Sheble G (1997 May) AGC simulator for price-based operation: Part I. IEEE Trans Power Syst l2(2):527–532
24. Bekhouche N, Feliachi A (1992 July) Decentralized estimation for the automatic generation control problem in power systems, vol 3, pp 621–632
25. Kothari ML, Kaul BL, Nanda J (1980 Oct) Automatic generation control of hydro-thermal system. J Inst Eng (India) 61:85–9, pt. EL-2

Performance Analysis of Classical Controllers Tuned Using Heuristic Approaches for Frequency Regulation

Preeti Dahiya, Sandeep Dogra, Veena Sharma, Harish Pulluri, N. Gouthamkumar and U. Mohan Rao

Abstract This paper presents the performance analysis of classical controllers tuned using heuristic approaches for frequency regulation. The system under study comprises of two areas each having one thermal turbine in each control area. The frequency regulation is achieved using different classical controllers whose controller gains have been optimized using heuristic techniques namely genetic algorithm (GA) and gravitational search algorithm (GSA). To overcome the concerns of local trapping in local minima, hybridized GSA incorporating the concept of opposition learning and disruption, i.e., disrupted oppositional learned gravitational search algorithm (DOGSA) has also been used for optimization of controller gains.

P. Dahiya
Department of Electrical and Electronics Engineering, ABES Engineering College,
Ghaziabad, Uttar Pradesh, India
e-mail: preetieednith@gmail.com

S. Dogra
Gurugram, India
e-mail: dogra.sandeep1589@gmail.com

V. Sharma
Department of Electrical Engineering, National Institute of Technology,
Hamirpur, Himachal Pradesh, India
e-mail: veenanaresh@gmail.com

H. Pulluri (✉)
Department of Electrical and Electronics Engineering, Geethanjali College
of Engineering and Technology, Hyderabad, Telangana, India
e-mail: harishpulluri@gmail.com

N. Gouthamkumar
Department of Electrical and Electronics Engineering, V R Siddhartha Engineering College,
Vijaywada, Andhra Pradesh, India
e-mail: gowthamkumar218@gmail.com

U. Mohan Rao
Department of Electrical and Electronics Engineering, Lendi Institute of Engineering
and Technology, Vizianagaram, Andhra Pradesh, India
e-mail: mohan13.nith@gmail.com

The simulation results in terms of fitness value, settling time, and peak overshoot/undershoot depict the superiority of the DOGSA-optimized controllers under load perturbations in the system.

Keywords Frequency regulation · Proportional integral derivative controller · Gravitational search algorithm · Disruption operator · Opposition learning

1 Introduction

The load demanded by the consumers changes continuously due to which deviations occurs in the interconnected power system frequency and tie-line power. To solve this problem, generation should be changed accordingly with the load demand. The automatic generation control also said to be as secondary control helps in accomplishing the power balance between generation and demand of electrical power. In order to secure this objective, the area control error (ACE) which is the combination of frequency and tie-line power is observed unceasingly and used as an objective function for heuristic techniques.

The state-of-the-art of frequency regulation in conventional interconnected power systems given in [1–3] discloses that the researchers have used and implemented several controllers and optimization methods to find the optimal gains of the controller parameters. The conventional controllers such as integral (I), proportional integral (PI) and proportional integral derivative (PID) controllers have been used to solve AGC problem, but has the limitation of optimal tuning of controller gains. This limitation is overcome by using the heuristic techniques such as genetic algorithm (GA) [4], firefly algorithm (FA) [5] and imperialist competitive algorithm (ICA) [6], etc., for tuning of controller parameters. Sometimes, the limitations posed by these algorithms are getting trapped in local minima and converging after a long time to optimal solution. This arises the need of a more efficient optimization technique for obtaining the optimal controller. Based on the Newton's law of motion, GSA introduced in [7] shows promising efficacy over the other algorithms. However, it lacks the features of exploration and exploitation of the search space.

In the present work, to incorporate these capabilities of exploration and exploitation, opposition learning [8] and disruption operator [9] have been added and the hybridized stochastic practices specifically oppositional learned gravitational search algorithm (OGSA), disrupted gravitational search algorithm (DGSA), and disrupted oppositional learned gravitational search algorithm (DOGSA) [9–11]; GA and gravitational search algorithm (GSA) have been employed for the resolution of AGC problem by optimizing the classical controllers namely integral (I), proportional integral (PI), and proportional integral derivative (PID) controllers for optimum performance of the two-area system under load perturbations. The performance of these optimal controllers is validated on two-area interconnected power system by analyzing performance indices like fitness value, settling time, and overshoot/undershoot.

2 Modeling of System Under Investigation

The system under study comprises of two areas each having one thermal turbine in each control area as shown in Fig. 1. The variables used for mathematical analysis of system under study are:

state variables:

$$X = \left[\Delta f_1 \ \Delta f_2 \ \Delta P_{\text{tie}12} \ \Delta P_{m1} \ \Delta P_{v1} \ \int \text{ACE}_1 \ \Delta P_{m2} \ \Delta P_{v2} \ \int \text{ACE}_2 \right]$$

control inputs: $u_1 \ u_2$ and disturbance inputs: $d_1 = \Delta P_{D1} \quad d_2 = \Delta P_{D2}$

The I, PI, and PID controllers have been used for simulation in the present research article [9].

3 Optimization of Controller Gains

In the present work, the fitness function given as follows has been used as an objective function for frequency regulation problem:

$$FF = \sum_{\substack{i,j=1 \\ i \neq j}}^{n} \int \left(\Delta f_j^2 + \Delta P_{\text{tie}ij}^2 \right) \mathrm{d}t. \tag{1}$$
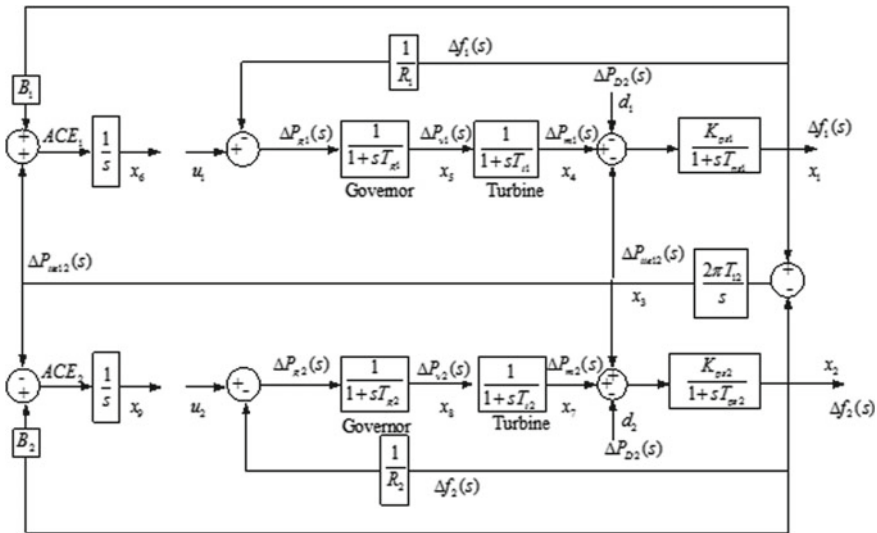
Fig. 1 Block diagram of two-area interconnected power system
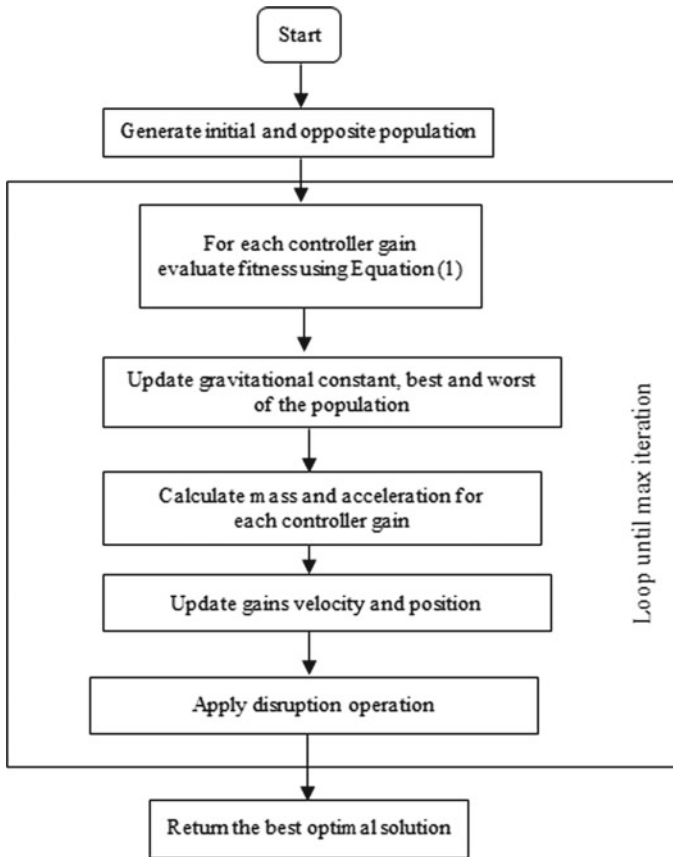
Fig. 2 Flowchart of DOGSA algorithm

where n is the total number of areas in the system. The mathematical expressions and detailed algorithms of GSA, OGSA, DGSA, and DOGSA can be referred from [9, 11]. The flowchart of DOGSA is shown in Fig. 2.

4   Simulation Results and Discussion

A two-area interconnected system with thermal turbines shown in Fig. 1 has been used to illustrate the behavior of I-, PI-, and PID-optimized controllers. The same data as in [10] is used for carrying out the simulations. The parameters of GA, GSA, and its variant algorithms taken in the present work are given in Table 1.

   The objective function FF in Eq. (1) has been used to obtain the optimal values of I, PI, and PID controller parameters and the fitness values of these controllers are depicted in Figs. 3, 4, and 5 and their values are given in Table 2. It is depicted

Table 1 Parameters of optimization algorithms

Algorithm	Parameters
GA	Population size = 30 Maximum number of iterations = 30 Probability of crossover = 0.8 Probability of mutation = 0.001
GSA and its variants	Population size = 20 Decaying constant = 20 Gravitational constant = 150 Disruption constant = 100
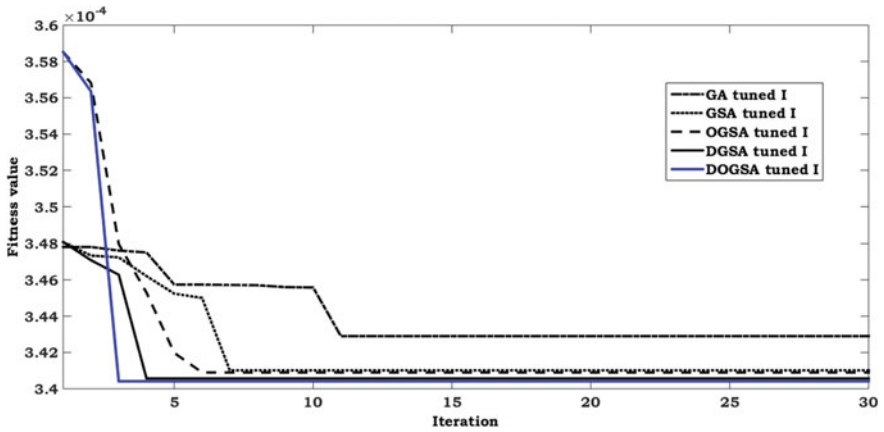
Fig. 3 Fitness value of FF with integral controller
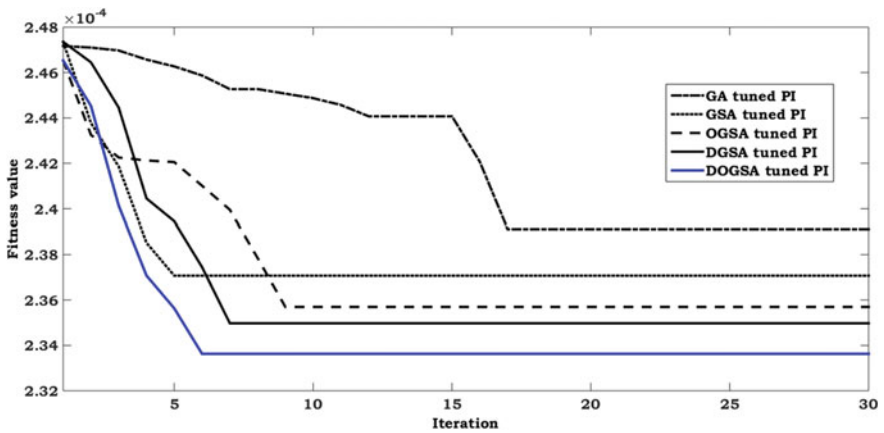
Fig. 4 Fitness value of FF with proportional integral controller
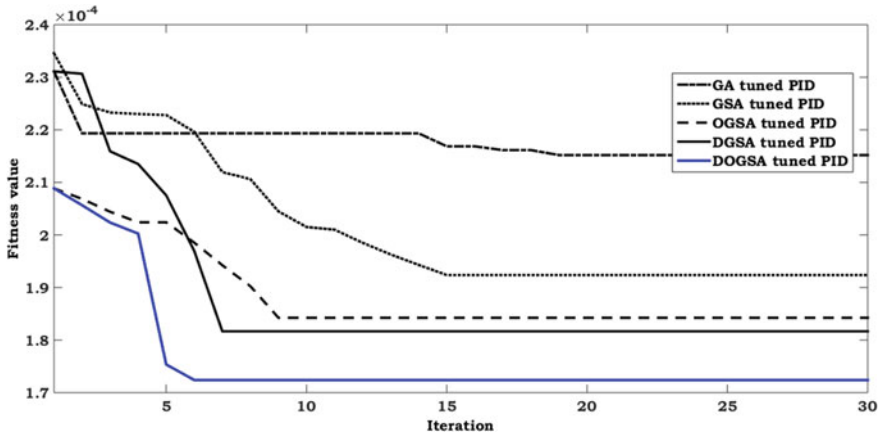
Fig. 5 Fitness value of FF with proportional integral derivative controller

Table 2 Parameters of two-area system with optimal controllers

Parameters		GA	GSA	OGSA	DGSA	DOGSA
I controller						
Δf_1	OS	0.00555	0.005016	0.003484	0.001957	0.0001013
	US	−0.02199	−0.02194	−0.02169	−0.02158	−0.02148
	ST	23.14	19.77	16.87	15.64	12.92
Δf_2	OS	0.007546	0.007473	0.005823	0.003621	0.000015
	US	−0.01781	−0.01749	−0.01698	−0.01695	−0.01681
	ST	22.73	17.77	15.91	14.85	13.31
$\Delta P\mathrm{tie}_{12}$	OS	0.001285	0.000887	0.0003911	0.0004828	0.0000034
	US	−0.005703	−0.006036	−0.005853	−0.005758	−0.005702
	ST	25.75	19.41	15.62	15.22	14.68
Obj	FF	0.0003429	0.000341014	0.000340899	0.000340572	0.000340414
PI controller						
Δf_1	OS	0.002114	0.001199	0.0007406	0.0001817	0.0001817
	US	−0.02107	−0.02001	−0.01961	−0.01958	−0.01956
	ST	21.33	15.34	14.89	14.83	14.81
Δf_2	OS	0.001926	0.000171	0.00001	0.00001	0.000592
	US	−0.01613	−0.0145	−0.01445	−0.01439	−0.0143
	ST	22.13	19.79	19.76	19.23	18.06
$\Delta P\mathrm{tie}_{12}$	OS	0.0002123	0.00000031	0.0000	0.0000	0.0000
	US	−0.005614	−0.005201	−0.005033	−0.00497	−0.004898
	ST	22.93	20.45	20.38	20.34	20.32
Obj	FF	0.00024457	0.00023852	0.000235696	0.00023497	0.00023363

(continued)

Table 2 (continued)

Parameters		GA	GSA	OGSA	DGSA	DOGSA
PID controller						
Δf_1	OS	0.0000	0.0000	0.0000	0.0000	0.0000
	US	−0.01401	−0.01352	−0.01216	−0.01014	−0.009583
	ST	15.06	9.91	9.62	9.47	9.06
Δf_2	OS	0.0000	0.0000	0.0000	0.0000	0.0000
	US	−0.01032	−0.00997	−0.007955	−0.007843	−0.006977
	ST	15.86	12.32	10.66	10.28	9.86
$\Delta P\text{tie}_{12}$	OS	0.0000	0.0000	0.0000	0.0000	0.0000
	US	−0.003459	−0.003418	−0.002982	−0.002896	−0.002896
	ST	16.66	12.01	11.46	11.21	10.66
Obj	FF	0.00021933	0.00020101	0.00018424	0.00018166	0.00017239

from Figs. 3, 4, and 5 that the hybridized DOGSA due to the opposition learning and disruption operator gives the faster convergence in comparison to other algorithms.

The simulation responses of heuristic approaches tuned I-, PI-, and PID-controlled system under investigation in the present work are presented in Figs. 6, 7, and 8, respectively, and its parameter values, i.e., overshoot (OS)/undershoot (US), settling time (ST), and fitness values (FF) are given in Table 2.
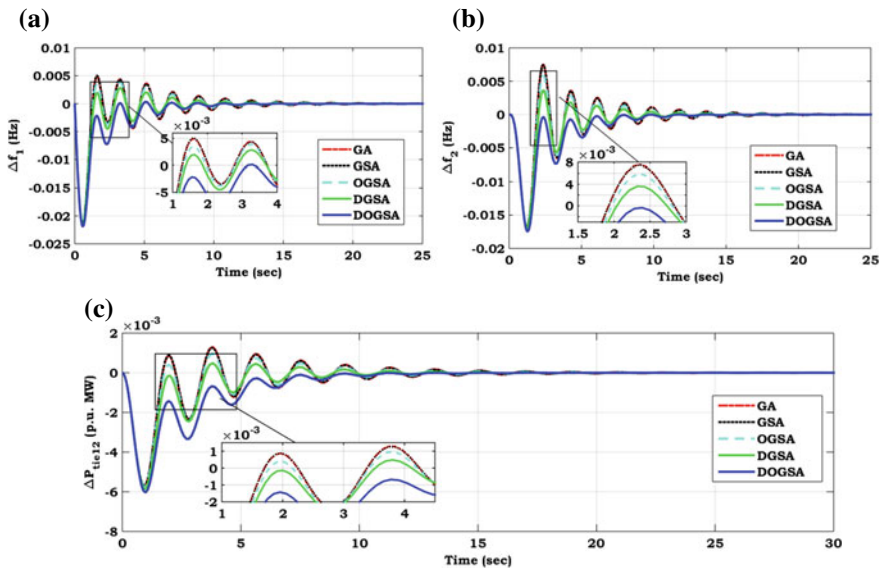
Fig. 6 Transient response of system under study with I controller
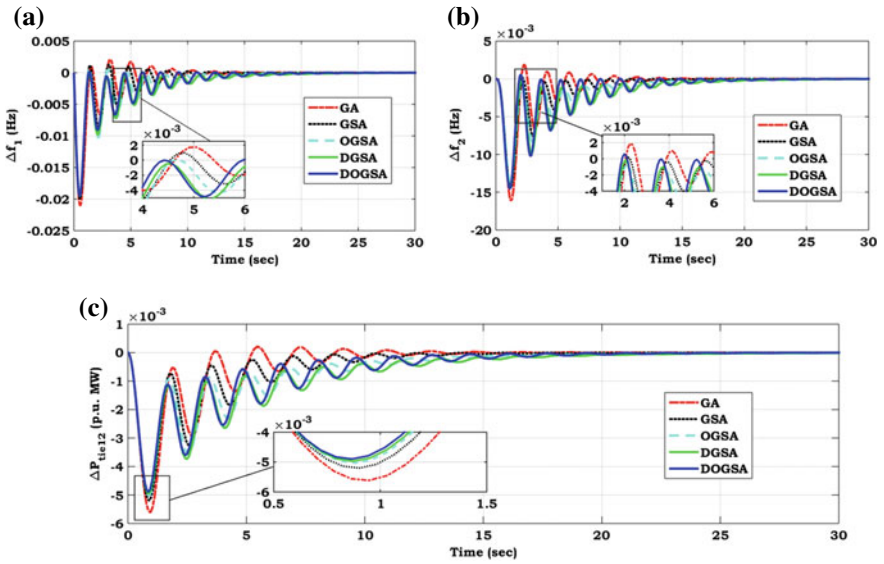
Fig. 7 Transient response of system under study with PI controller
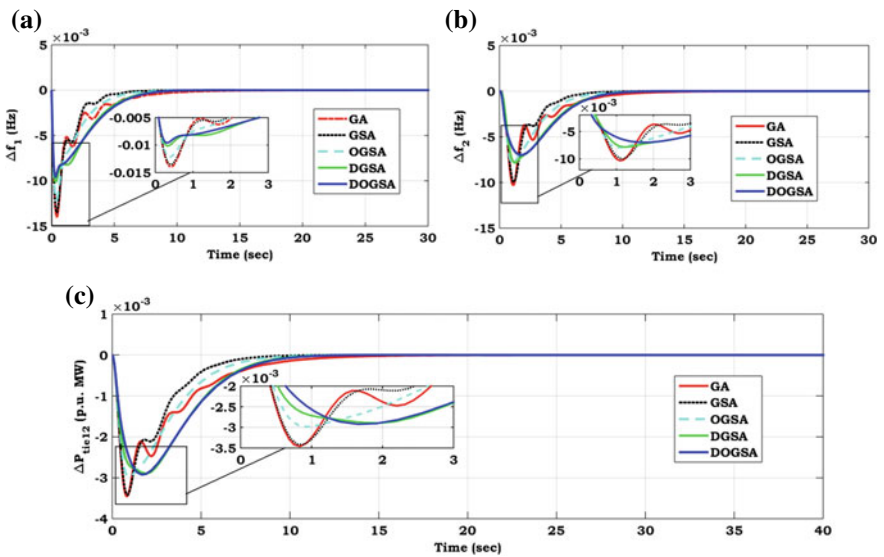
Fig. 8 Transient response of system under study with PID controller

5 Conclusion

In the present article, the frequency regulation of two-area power system has been accomplished using I, PI, and PID controllers which are fine-tuned using heuristic methods namely GA; GSA, and its hybridized variations namely OGSA, DGSA, and DOGSA. The superiority of the hybridized DOGSA-tuned PID controller is proved by simulation results in terms of settling time, peak overshoot, peak undershoot, and fitness function values in comparison to other controllers.

References

1. Ibraheem, Kumar P, Kothari DP (2005) Recent philosophies of automatic generation control strategies in power systems. IEEE Trans Power Syst 20:346–357
2. Shayeghi H, Shayanfar HA, Jalili A (2009) Load frequency control strategies: a state-of-the-art survey for the researcher. Energy Convers Manage 50:344–353
3. Pandey SK, Mohanty SR, Kishor N (2013) A literature survey on load-frequency control for conventional and distribution generation power systems. Renew Sustain Energy Rev 25:318–334
4. Golpira H, Bevrani H, Golpira H (2011) Application of GA optimization for automatic generation control design in an interconnected power system. Energy Convers Manage 52:2247–2255
5. Debbarma S, Saikia LC, Sinha N (2014) Solution to automatic generation control problem using firefly algorithm optimized $I^\lambda D^m$ controller. ISA Trans 53:358–366
6. Shabani H, Vahidi B, Ebrahimpour M (2013) A robust PID controller based on imperialist competitive algorithm for load-frequency control of power systems. ISA Trans 52:88–95
7. Rashedi E, Nezamabadi-pour H, Saryazdi S (2009) GSA: a gravitational search algorithm. Inf Sci 179:2232–2248
8. Rahnamayan S, Tizhoosh HR, Salama MMA (2007) A novel population initialization method for accelerating evolutionary algorithms. Comput Math Appl 53:1605–1614
9. Dahiya P, Sharma V, Naresh R (2015) Solution approach to automatic generation control problem using hybridized gravitational search algorithm optimized PID and FOPID controllers. Adv Electr Comp Eng 15:23–34
10. Dahiya P, Sharma V, Naresh R (2017) Hybridized gravitational search algorithm tuned sliding mode controller design for LFC system with DFIG wind turbine. In: Optimal control applications and methods, Wiley. https://doi.org/10.1002/oca.2305
11. Dahiya P, Sharma V, Naresh R (2016) Automatic generation control using disrupted oppositional based gravitational search algorithm optimized sliding mode controller under deregulated environment. IET Gener Transm Distrib 10:3995–4005

Review, Design and Mathematical Modeling of Packed U-Cell Multilevel Inverter

Abdul Azeem, Mohd Tariq, Mahetab Alam and C. Bharatiraja

Abstract Mathematical modeling also gives the information about designing of controller. The analysis and different application of PUC inverter such as inverter, rectifier, STATCOM and voltage controllers are given here. A brief review on PUC inverter for single phase operation, mathematical modeling and switching scheme is also presented. It has been shown that PUC inverter topology is preferable than the conventional multilevel inverter in terms of device counts.

Keywords Packed U-cell (PUC) inverter · Multilevel inverters (MLIs) · Power quality · Mathematical modeling

1 Introduction

Nowadays, multilevel inverters are gaining more popularity due to high quality of power and feasibility of its operation for high power with medium- and high-voltage drive applications. The conventional inverter was able to produce two-level square wave output with low quality of power and not applicable for high-power applications [1, 2]. Multilevel inverters are fulfilling the above problem.

A. Azeem · M. Tariq (✉) · M. Alam
Department of Electrical Engineering, Aligarh Muslim University,
202002 Aligarh, India
e-mail: tariq.iitkgp@gmail.com

A. Azeem
e-mail: azeem.abdul25@gmail.com

M. Alam
e-mail: mahetab_alam@zhcet.ac.in

C. Bharatiraja
School of Electrical Engineering, SRM Institute of Science and Technology
(formerly known as SRM University), Kattankulathur Campus, Chennai 603203, India
e-mail: bharatiraja@gmail.com

Continuous research is going on in the development of multilevel inverter to get more optimization and enhancing its reliability. Multilevel output is obtained by synthesizing the various small DC level combining at output [3]. The output of multilevel is closer to the sine wave as number of output level increases. Hence, requirement of the large filter is eliminated [4, 5].

Neutral-point clamped (NPC) for three levels is the most using multilevel inverter in industrial and commercial drive application [6]. The main attracting feature of the NPC inverter is the requirement of the single DC source for all three legs. But for more than three levels, a big problem of capacitor voltage balancing is there and also for a higher number of level, inverter becomes complex due to the requirement of large device counts [7]. Flying capacitor (FC) multilevel inverter have same structure than the NPC inverter except that the clamping diode is replaced by the flying capacitor. Similar to the NPC for three levels, this inverter has no issue, but for a higher number of output voltage, it encounters the same problem of capacitor voltage balancing [8]. Cascaded H-bridge (CHB) has advantage of modularity, but it needed isolated DC sources which limit its application [9].

Regarding the above issues, PUC inverter was invented in 2008 as a deduction of cascaded H-bridge inverter, wherein two lower switches were removed and two U-cells are connected directly by modifying upper two switches [10]. PUC inverter comprises least device counts among all multilevel for particular output levels. Up to now, a number of papers have been published on its designing, modeling, and applications [11–13]. In this paper, author has discussed about the study of the PUC topology and its mathematical modeling in details. Application of PUC inverter in a different area is also discussed in brief.

2 PUC Inverter Topology and Its Operation

PUC inverter is topology is shown in Fig. 1. It comprises six active switches in three pairs, and each pair of switches (T_1 and T_4, T_2 and T_5, and T_3 and T_6) is working complementarily. The secondary DC source is the capacitor which has to be controlled at a particular value to get desired levels at output waveform.

Table 1 shows the switching table for PUC inverter. It contains the eight switching states which give the different operating states. For seven-level output, capacitor voltage has to be balanced at 1/3 of the main DC-link voltage. Assuming $V_1 = 3V_2 = 3$ V, seven-level output can be generated as $0, \pm E, 2 \pm E$ and $\pm 3E$. Similarly for five-level operation assuming $V_1 = 2V_2 = 2$ V, the five-level output can be $0, \pm E, \pm 2E$. For three-phase operation, three similar modules of PUC inverter as shown in Fig. 1 are connected to get three-phase output. The eight possible operating states are shown in Fig. 2. The red lines show the current flowing path through the switches depending on the switching schemes.

Switching Tables 2 and 3 shows the seven-level and five-level output generation.

Fig. 1 PUC inverter topology
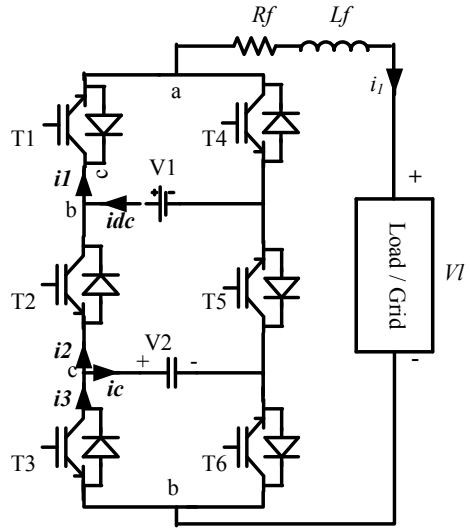
Table 1 Switching table

States	Van	T_1	T_2	T_3
1	V_1	1	0	0
2	V_1-V_2	1	0	1
3	V_2	1	1	0
4	0	0	0	0
5	0	1	1	1
6	$-V_2$	0	0	1
7	V_2-V_1	0	1	0
8	$-V_1$	0	1	1

3 Modeling of PUC Inverter

The PUC inverter due to its configuration structure called packed U-cell inverter. Figure 3 shows a single U-cell (Table 4 shows no. of levels versus capacitor voltage).

The switching function of the PUC inverter is defined as:

$$T_i = \left. \begin{matrix} 0 & \text{if } T_i \text{ is off} \\ 1 & \text{if } T_i \text{ is on} \end{matrix} \right\} \tag{1}$$

The inverter output voltage can be written as Eq. (2), from the circuit diagram (Fig. 1)
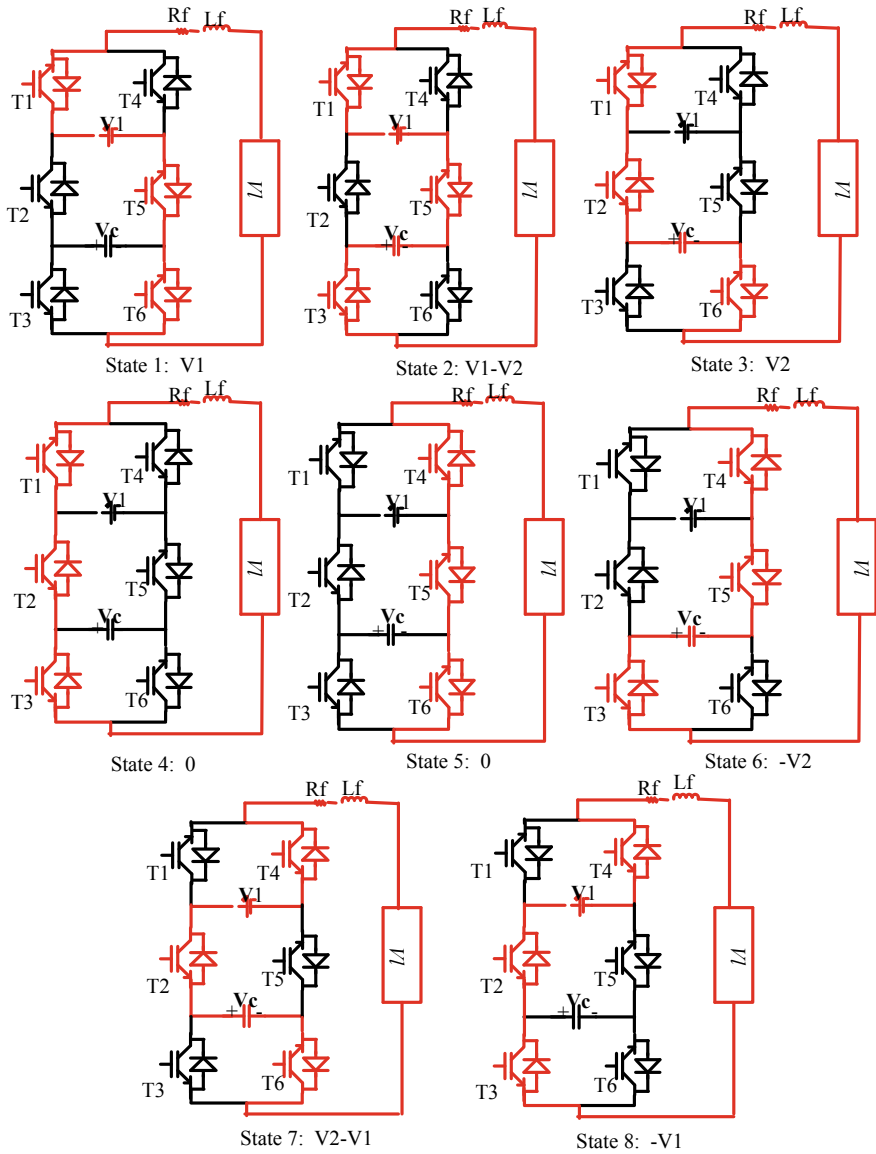
Fig. 2 Operating states of PUC inverter

$$Vad = Vab + Vbc + Vcd \qquad (2)$$

where the nodes *a*, *b*, *c*, and *d* are shown in Fig. 1, and voltage across the point can be calculated according to switching function:

Table 2 Switching table for seven-level inverter

States	S_1	S_2	S_3	Output	Vad
1	1	0	0	V_1	+3E
2	1	0	1	$V_1 - V_2$	+2E
3	1	1	0	V_2	+E
4	1	1	1	0	0
5	0	0	0	0	0
6	0	0	1	$-V_2$	−E
7	0	1	0	$V_2 - V_1$	−2E
8	0	1	1	$-V_1$	−3E

Table 3 Switching table for five-level inverter

States	S_1	S_2	S_3	Output	Vad
1	1	0	0	V_1	+2E
2	1	0	1	$V_1 - V_2$	+E
3	1	1	0	V_2	+E
4	1	1	1	0	0
5	0	0	0	0	0
6	0	0	1	$-V_2$	−E
7	0	1	0	$V_2 - V_1$	−E
8	0	1	1	$-V_1$	−2E

Fig. 3 A single U-cell
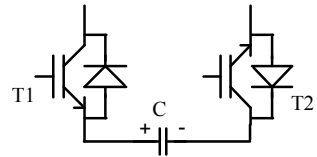
Table 4 No. of levels versus capacitor voltage

No. of output levels	Capacitor voltage (V)
Three levels	Equal to main DC-link voltage
Five levels	Half of main DC-link voltage
Seven levels	One-third of main DC-link voltage

$$\left. \begin{aligned} Vab &= (T_1 - 1)V_1 \\ Vbc &= (1 - T_2)(V_1 - V_2) \\ Vcd &= (1 - T_3)V_2 \end{aligned} \right\} \qquad (3)$$

where V_1 and V_2 are the main DC-link voltage and capacitor voltage, respectively.

By substituting Eq. (3) into Eq. (2), we get Eq. (4) as:

$$
\begin{aligned}
Vad &= (T_1 - 1)V_1 + (1 - T_2)(V_1 - V_2) + (1 - T_3)V_2 \\
&= V_1 T_1 - V_1 + V_1 - V_2 - V_1 T_2 + V_2 T_2 + V_2 - V_2 T_3 \\
&= (T_1 - T_2)V_1 + (T_2 - T_3)V_2
\end{aligned}
\tag{4}
$$

Since one of the switches in pairs of T_1 and T_4, T_2 and T_5, and T_3 and T_6 is turned ON, the current in the switches can be expressed with respect to the current in the load as:

$$
\left.
\begin{aligned}
i_1 &= T_1 i_1 \\
i_2 &= T_2 i_1 \\
i_3 &= T_3 i_1
\end{aligned}
\right\}
\tag{5}
$$

By applying KCL at node c, we get the following:

$$
i_3 = i_c + i_2
\tag{6}
$$

and

$$
i_c = (T_3 - T_2)i_1
\tag{7}
$$

$$
C \frac{dV_2}{dt} = (T_3 - T_2)i_1
\tag{8}
$$

We can write Eq. (8) as:

$$
\frac{dV_2}{dt} = \frac{(T_3 - T_2)i_1}{C} = -\frac{i_1}{C}T_2 + \frac{i_1}{C}T_3
\tag{9}
$$

For the current (in the load) and the voltage, the Kirchhoff voltage law is expressed as follows:

$$
V_1 = Vad - i_1 R_f - L_f \frac{di_1}{dt}
\tag{10}
$$

where R_f and L_f be the filter resistance and inductance, respectively. Calculating Eq. (10) with the help of Eq. (4), the following relation will be obtained:

$$
\frac{di_1}{dt} = \frac{V_1}{L_f}T_1 + \frac{V_1 - V_2}{L_f}T_2 - \frac{V_2}{L_f}T_3 - \frac{R_f}{L_f}i_1 - \frac{V_L}{L_f}
\tag{11}
$$

The average model of the packed U-cell inverter may be obtained using the expression given by (9) and (11).

$$\frac{dX}{dt} = A(x,t) + B(x,t)U + C(t) \tag{12}$$

Assuming the state variables as $x_1 = i_1$ and $x_2 = V_2$ and using duty cycles (d_1, d_2, d_3) of switch (T_1, T_2, T_3) as input matrix, the state-space average model of the packed U-cell inverter may be obtained as follows.

$$A(x,t) = \begin{bmatrix} \frac{-R_f}{L_f} \\ 0 \end{bmatrix}$$

$$B(x,t) = \begin{bmatrix} \frac{-V_1}{L_f} & -\frac{V_1 - V_2}{L_f} & \frac{-V_2}{L_f} \\ 0 & \frac{-i_1}{C} & \frac{i_1}{C} \end{bmatrix}$$

$$d = \begin{bmatrix} d_1 \\ d_2 \\ d_3 \end{bmatrix}, \quad \text{and} \quad C(t) = \begin{bmatrix} \frac{-V_1}{L_f} \\ 0 \end{bmatrix}$$

The above state-space model can be used to design the controller to regulate the capacitor voltage to a particular value to get the desired multilevel output voltage. This state-space model has been used to design the voltage controller in seven-level and fifteen-level PUC inverter [14, 15]. In spite from inverter, PUC inverter can also be used as rectifier [16]. A hysteresis band current controller for seven-level and fifteen-level PUC inverter has been implemented for standalone operation in [12, 17]. Based on the modeling, a PR controller also introduces the five-level PUC inverter for harmonic compensation in grid-connected operation [18]. For grid-connected operation, inverter injected current should be in phase with the grid voltage to ensure the unity power operation and DC component being injected into grid by inverter should be less than the 0.5% of the rated value [19]. A seven-level PUC inverter based on solar PV system is connected to the grid [20].

4 Five-Level PUC Inverter Self-balancing Capacitor Voltage Feature

For five-level operation, the capacitor voltage has to be maintained at ½ of the main DC-link voltage, but fortunately five-level PUC has self-balancing capacitor voltage feature. This balancing phenomenon can be proved by energy storing in positive and negative cycle of PUC inverter operation. Five-level PUC has more redundant switching states. It can be seen in Table 3. Redundancy in the PUC-5 inverter is more than the PUC-7 inverter, and this redundancy helps to maintain charging and discharging of capacitor evenly in a complete cycle [16, 21]. Based on Fig. 2, it can be seen that when the capacitor is connected to the load it get

charging, the capacitor is charged (states 2 and 7). When the capacitor is connected to the load, it feeds the power which means it is discharging (states 3 and 6) (Table 5).

Figure 4 shows one cycle of the output voltage of PUC-5 waveform. V_E is a part of output voltage generated by the capacitor ($+E$ or $-E$) whether connected to load with series of main DC-link voltage in charging or alone with the capacitor with load in discharging. It is assumed that output voltage and current are a sine function:

$$V_1 = V_m \sin(\omega t) \tag{13}$$

$$i_1 = I_m \sin(\omega t) \tag{14}$$

$$I = \frac{dq}{dt}$$
$$dU = Vdq = VIdt \tag{15}$$

where, I, q, V and U shows the current flowing through capacitor, electronic charge voltage and energy stored by capacitor, respectively, substituting Eqs. (13) and (14) into Eq. (15), energy stored in positive half cycle we get,

Table 5 Capacitor operating states

States	Capacitor voltage
1	No change
2	Capacitor charging
3	Capacitor discharging
4	No change
5	No change
6	Capacitor discharging
7	Capacitor charging
8	No change

Fig. 4 Output voltage wave for PUC-5 inverter
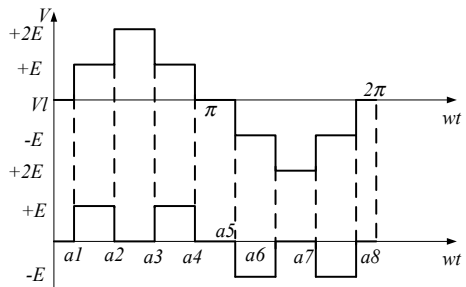
$$U^+ = \int_0^\pi V_E I_m \sin(\omega t - \theta_0) d(\omega t)$$

$$= I_m \int_0^\pi V_E \sin(\omega t - \theta_0) d(\omega t)$$

$$= I_m \left[\int_0^{a1} 0 * \sin(\omega t - \theta_0) d(\omega t) + \int_{a1}^{a2} E * \sin(\omega t - \theta_0) d(\omega t) \right.$$

$$\left. + \int_{a2}^{a3} 0 * \sin(\omega t - \theta_0) d(\omega t) + \int_{a3}^{a4} E * \sin(\omega t - \theta_0) d(\omega t) + \int_{a4}^{\pi} 0 * \sin(\omega t - \theta_0) d(\omega t) \right]$$

$$= -E I_m \cos(\omega t - \theta_0) \left\{ \begin{matrix} a2 \\ a1 \end{matrix} - E I_m \cos(\omega t - \theta_0) I \begin{matrix} a2 \\ a3 \end{matrix} \right.$$

$$= E I_m [\cos(a_1 - \theta_0) - \cos(a_2 - \theta_0) + \cos(a_3 - \theta_0) - \cos(a_4 - \theta_0)]$$

$$(16)$$

Similarly in negative half cycle,

$$U^- = \int_\pi^{2\pi} V_E I_m \sin(\omega t - \theta_0) d(\omega t)$$

$$= I_m \int_\pi^{2\pi} V_E \sin(\omega t - \theta_0) d(\omega t) \qquad (17)$$

$$= E I_m \cos(\omega t - \theta_0) I \begin{matrix} a6 \\ a5 \end{matrix} + E I_m \cos(\omega t - \theta_0) I \begin{matrix} a8 \\ a7 \end{matrix}$$

$$= [\cos(a_6 - \theta_0) - \cos(a_5 - \theta_0) + \cos(a_8 - \theta_0) + \cos(a_8 - \theta_0)]$$

It is cleared from Eqs. (16) and (17) that both equations are same but have opposite sign; this means in positive and negative cycle storing and releasing energy are same.

$$\left. \begin{matrix} a_5 = \pi + a_1 \\ a_6 = \pi + a_2 \\ a_7 = \pi + a_3 \\ a_8 = \pi + a_4 \end{matrix} \right\} \qquad (18)$$

Hence,

$$U^+ = U^- \qquad (19)$$

5 PUC Inverter Application in Different Areas

In the literature, PUC inverter has been found in various applications in power electronics as well as power system. Due to its features, PUC inverter attracted the researchers to extend its application on different areas. A brief review of application of PUC inverter is presented below.

5.1 Grid-Connected and Standalone Solar-Based Inverter

The application of PUC inverter for solar PV application in grid-connected mode is found in [21–24] in which grid-connected as well as standalone operation of the PUC-5 inverter is successfully implemented. A solar PV-based isolated PUC fifteen-level inverter is implemented in [14]. A model predictive control grid connected seven-level PUC inverter is reported in [20].

5.2 PUC Inverter in Power System

A modified form of PUC-5 inverter is designed as an active power filter to power factor correction in [16]. In this paper, a single-phase-modified PUC-5 inverter is implemented; this modified form of PUC inverter was able to boosting the voltage. A three-phase PUC-5 inverter is using as STATCOM to inject the reactive power to grid with regulating the DC-link capacitor voltage [21].

5.3 PUC Inverter as Rectifier

PUC inverter can also be used in rectifier mode operation a seven level, nine level and fifteen level PUC rectifier is designed in [17]. This dual operation of the PUC inverter opened the new door for electric vehicle application. In this mode of operation, upper DC link is connected to the load and DC-link capacitor is operation at no load condition.

6 Conclusion

The aim of this paper was to study and analyze the operation of the PUC inverter. PUC inverter was able to generate a different number of the output levels by regulating the capacitor voltage. The main attracting features are of the requirement

of single DC-link voltage. PUC inverter also can be operated in rectifier mode simultaneously that leads it toward the electric vehicle operation. Like CHB, modified PUC inverter can operate in boost and buck mode. PUC inverter can be easily integrated with solar PV system, active filters, electric vehicle battery chargers, etc.

References

1. Rodríguez J et al (2007) Multilevel voltage-source-converter topologies for industrial medium-voltage drives. IEEE Trans Ind Electron 54(6):2930–2945
2. Tariq M, Bhattacharya TK, Varshney N, Rajapan D (2016) Fast response Antiwindup PI speed controller of brushless DC motor drive: modeling, simulation and implementation on DSP. J Electr Syst Inf Technol 3(1):1–13
3. Gadalla S, Yan X, Altahir SY, Hasabelrasul H (2017) Evaluating the capacity of power and energy balance for cascaded H-bridge multilevel inverter using different PWM techniques. J Eng 2017(13):1713–1718
4. Rohner S, Bernet S, Hiller M, Sommer R (2010) Modulation, losses, and semiconductor requirements of modular multilevel converters. IEEE Trans Ind Electron 57(8):2633–2642
5. Rodríguez J, Lai JS, Peng FZ (2002) Multilevel inverters: a survey of topologies, controls, and applications. IEEE Trans Ind Electron 49(4):724–738
6. Rodríguez J, Leon JI, Kouro S, Portillo R, Prats MAM (2008 June) The age of multilevel converters arrives 28–39
7. Lopez et al (2016) Modulation strategy for multiphase neutral-point-clamped converters. IEEE Trans Power Electron 31(2):928–941
8. Qashqai P, Sheikholeslami A, Vahedi H, Al-Haddad K (2015) A review on multilevel converter topologies for electric transportation applications. In: 2015 IEEE vehicle power and propulsion conference (VPPC)—proceedings
9. Shehu GS, Kunya AB, Shanono IH, Yalcinoz T (2016) A review of multilevel inverter topology and control techniques 4(3):233–241
10. Bharatiraja C, Munda JL, Bayindir R, Tariq M (2016) A common-mode leakage current mitigation for PV-grid connected three-phase three-level transformerless T-type-NPC-MLI. In: 2016 IEEE international conference on renewable energy research and applications (ICRERA), Birmingham, pp 578–583
11. Ounejjar Y, Al-Haddad K, Gregoire L-A (2011) Packed U cells multilevel converter topology: theoretical study and experimental validation. IEEE Trans Ind Electron 58(4):1294–1306
12. Vahedi H, Al-Haddad K (2016) Real-time implementation of a seven-level packed U-cell inverter with a low-switching-frequency voltage regulator. IEEE Trans Power Electron 31(8):5967–5973
13. Ounejjar Y, Al-Haddad K (2010) Fourteen-band hysteresis controller of the fifteen-level packed U cells converter. In: IECON proceedings (Industrial electronics conference), pp 475–480
14. Ounejjar Y, Al-Haddad K, Alolah AI (2011) Averaged model of the 31-level packed U cells converter. In: Proceedings—ISIE 2011 (IEEE international symposium on industrial electronics), pp 1831–1836
15. Ounejjar Y, Al-Haddad K, Vahedi H (2015) An advanced photovoltaic system based on the fifteen-Level PUC inverter. In: IEEE international symposium on industrial electronics, vol 2015, pp 1056–1061

16. Vahedi H, Al-Haddad K, Kanaan HY (2014) A new voltage balancing controller applied on 7-level PUC inverter. In: IECON proceedings (Industrial electronics conference), pp 5082–5087
17. Vahedi H, Shojaei AA, Dessaint L, Al-Haddad K (2017) Reduced DC link voltage active power filter using modified PUC5 converter. IEEE Trans Power Electron PP(99)
18. Ounejjar Y, Al-Haddad K (2009) A new high power efficiency cascaded U cells multilevel converter. In: IEEE international symposium industrial electronics, no. ISlE, pp 483–488
19. Tariq M, Iqbal MT, Meraj M, Iqbal A, Maswood AI, Bharatiraja C (2016) Design of a proportional resonant controller for packed U cell 5 level inverter for grid-connected applications, pp 3–8
20. Cheng J, CEng, CEM, CEA, and CMVP (2014) IEEE standard 519-2014. In: Schneider Electric, p 50
21. Metri J, Vahedi H, Kanaan HY, Member S, Al-Haddad K (2016) Solar energy processor based on packed U-cells 7-level inverter for grid applications, pp 6528–6533
22. Vahedi H, Labbé PA, Al-Haddad K (2016) Sensor-less five-level packed U-cell (PUC5) inverter operating in stand-alone and grid-connected modes. IEEE Trans Ind Inf 12(1): 361–370
23. Tariq M, Iqbal MT, Iqbal A, Meraj M, Roomi MM, Khan MSU (2016) Comparative analysis of carrier schemes for PWM in multilevel PUC inverter for PV applications. In: 2016 4th international conference on the development in the in renewable energy technology (ICDRET), Dhaka, pp 1–6
24. Tariq M, Meraj M, Azeem A, Maswood AI, Iqbal A, Bharatiraja C (2018) Evaluation of level-shifted and phase-shifted PWM schemes for seven level single-phase packed U cell inverter. CPSS Trans Power Electron Appl

Mathematical Analysis of Various Modulation Strategies Used for Multilevel Inverter

Abdul Azeem, Mohd Tariq, Adil Sarwar, Ahmed Riyaz and C. BharatiRaja

Abstract The concept of multilevel inverter arrived from the conventional two-level inverter. Two-level inverter is not suitable for the high-power, medium-voltage, and high-voltage industrial and commercial application. Multilevel inverters fulfill the above requirement. Control of multilevel inverter is done by adjusting the time average of their voltage levels. Generally, this is performed by pulse-width modulation (PWM) techniques. Output performance in terms of the power quality, common mode voltage, etc., greatly depends on the types of the modulation schemes applied. The aim of this paper is to present the different carrier-based modulation schemes that are available in the literature for five-level inverter. The detailed mathematical analysis of modulation techniques is presented to better understand the five-level inverter.

Keywords Modulation strategies · Multilevel inverters (MLIs) ·
Total harmonic distortion (THD) · Pulse-width modulation (PWM)

A. Azeem · M. Tariq (✉) · A. Sarwar
Department of Electrical Engineering, Aligarh Muslim University, Aligarh, India
e-mail: tariq.iitkgp@gmail.com

A. Azeem
e-mail: azeem.abdul25@gmail.com

A. Sarwar
e-mail: adilsarwar123@gmail.com

A. Riyaz
Department of Electrical and Renewable Energy Engineering,
BGSB University, Rajouri, J&K, India

C. BharatiRaja
School of Electrical Engineering, SRM Institute of Science and Technology
(formerly known as SRM University), Kattankulathur Campus, Chennai 603203, India
e-mail: bharatiraja@gmail.com

1 Introduction

In the industrial electrical drive application, output voltage and frequency have to be controlled/maintained for achieving the required power characteristics from drives. To get the regulated output, generally pulse-width modulation (PWM) strategies are used. Various modulation strategies are reported in the literature; each strategy has own advantages compared to other strategies [1–3]. The modulation strategies for multilevel inverters are evolved from two-level inverter. Same modulation strategies are applied with modification of multiple carrier wave which is vertically spaced.

In this paper, modulation scheme which is based on carrier signals and implemented for five-level inverter is studied and discussed. Mainly four types of multilevel inverter are available in the literature. They are (1) diode-clamped, (2) flying capacitor (FC), (3) cascaded H-bridge (CHB), and (4) packed U cell (PUC). Among these multilevel inverters, PUC inverter is recently introduced and comprises least device count which provides high reliability, easy control, compact size, and cost-effectiveness than the other multilevel inverters [4, 5]. Diode-clamped multilevel inverter required complex control algorithm for DC-link capacitor voltage; flying capacitor multilevel inverter suffers the same problem, but it has both active and reactive power supply capability, when it is being used in reactive power supply compensation. Cascaded H-bridge required separate DC source for each module which limits its operation. PUC inverter is overcoming issues and becomes a good supplement for these three conventional multilevel inverters [4, 6]. Modulation index also plays a vital role in all schemes; modulation index may be under and over depending on modulation ratio. With the modulation index, output voltage and total harmonic distortion (THD) vary accordingly. There are some definitions which make more understanding of the modulation techniques:

Amplitude modulation index (A) can be expressed as:

$$m = \frac{A_r}{(N-1)A_c}$$

where A_r and A_c be the amplitude of the reference and carrier waves, respectively. And N is the number of levels.

Frequency modulation index is:

$$A = \frac{f_c}{f_r}$$

where f_c and f_r be the frequency of carrier wave and reference wave, respectively.

2 Classifications of Various Carrier-Based Modulation Strategies

Figure 1 shows the carrier-based PWM schemes for the multilevel inverter for single-phase as well as for three-phase system.

In multicarrier pulse-width modulation scheme, several vertically spaced carrier signals are compared with sinusoidal reference of desired frequency. For N level output waveform, $N - 1$ carrier waves have same amplitude and frequency, but they are disposed in such a way the occupied band is continuous. The modulating reference wave has 50 or 60 Hz frequency. At each point of crossing of carrier and modulating reference waves, a switching pulse is generated.

3 Description of Various Modulation Signals

Carrier frequency may be the sawtooth or triangle in shape. And output signal is generated on comparing the sine and carrier waves on the basis of which one is larger or smaller in magnitude.

Fig. 1 Carrier-based modulation strategies for multilevel inverters
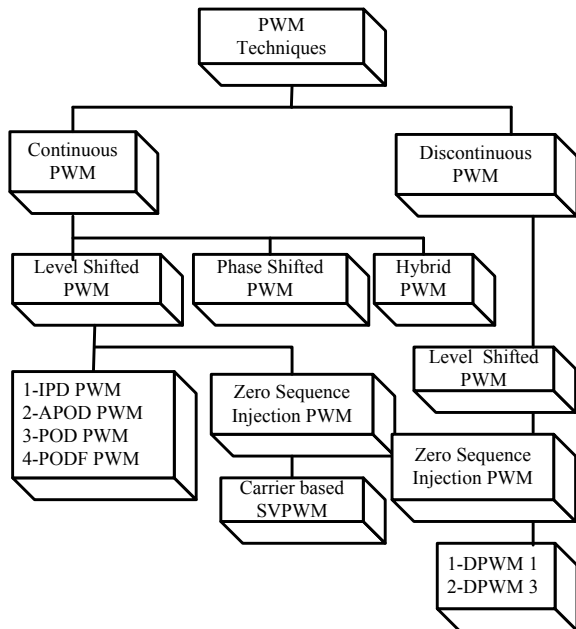
3.1 General Mathematical Expression for Carrier-Based Modulation Techniques

The main attractive feature of the PWM is the harmonic contents in the output wave. It can be solved either by analytical method or Fourier transformation. Each periodic function features infinite set of sine and cosine functions, i.e., the Fourier series:

$$f(wt) = \frac{a_0}{2} + \sum_{v=1}^{\infty} (a_v \cos vwt + b_v \sin vwt) \tag{1}$$

where v is the harmonic order and

$$a_0 = \frac{1}{2\pi} \int_{-\pi}^{\pi} f(wt)\, dwt; \quad v = 0, 1, 2\ldots\infty \tag{2}$$

$$a_v = \frac{1}{\pi} \int_{-\pi}^{\pi} f(wt) \cos vwt\, dwt; \quad v = 0, 1, 2\ldots\infty \tag{3}$$

$$b_v = \frac{1}{\pi} \int_{-\pi}^{\pi} f(wt) \sin vwt\, dwt; \quad v = 1, 2\ldots\infty \tag{4}$$

The PWM signal comprises of periodic function of two variables with different angular frequencies and phase shifts $f(wt)$ and $z(wt)$ as:

$$w(t) = w_c t + \theta_c \tag{5}$$

$$z(t) = w_t t + \theta_t \tag{6}$$

where ω_c is the angular frequency of the carrier signal, θ_c is its phase shift, wt is the angular frequency of reference signal, and θ_t is phase shift. Even function of two variables can be comprises by Fourier series:

$$f(w, z) = \frac{a_{00}}{2} + \sum_{v=1}^{\infty} (a_{0v} \cos vz + b_{0v} \sin vz) + \sum_{u=1}^{\infty} (a_{u0} \cos uw + b_{u0} \sin uw)$$
$$+ \sum_{u=1}^{\infty} \sum_{v=-\infty}^{\infty} [a_{uv} \cos(uw + vz) + b_{uv} \sin(uw + vz)] \tag{7}$$

where

$$a_{uv} = \frac{1}{2\pi^2} \int_{-\pi}^{\pi} \int_{-\pi}^{\pi} f(w, z) \cos(uw + vz)\, dw\, dz \tag{8}$$

$$b_{uv} = \frac{1}{2\pi^2} \int\limits_{-\pi}^{\pi} \int\limits_{-\pi}^{\pi} f(w,z)\sin(uw+vz)\,dwdz \qquad (9)$$

By the substitution of Eqs. (5) and (6) into Eq. (7), we get Eq. (10):

$$
\begin{aligned}
f(t) = \frac{a_{00}}{2} &+ \sum_{v=1}^{\infty}[a_{0v}\cos(vw_t t + v\theta_t) + b_{0v}\sin(vw_t t + v\theta_t)] \\
&+ \sum_{u=1}^{\infty}[a_{u0}\cos(uw_c t + u\theta_c) + b_{u0}\sin(uw_c t + u\theta_c)] \\
&+ \sum_{u=1}^{\infty}\sum_{\substack{v=-1}}^{\infty} \begin{aligned}&[a_{uv}\cos(uw_c t + u\theta_c + vw_t t + v\theta_t) \\ &+ b_{uv}\sin(uw_c t + u\theta_c + vw_t t + v\theta_t)]\end{aligned} \\
&(v \neq 0)
\end{aligned} \qquad (10)
$$

where first term represents the DC offset value, second term represents the fundamental components of output, third term represents the harmonics in the carrier signal, and last term represents the sideband harmonics. Equation (10) expresses all switched patterns of carrier-based PWM. The constant v determines the order of sideband harmonics in total harmonic set that are around the uth carrier harmonic waves.

3.2 Triangular PWM Scheme

In two-level pulse-width modulation using triangular carrier as a carrier signal, the expression for the phase voltage is given as [7]:

$$
\begin{aligned}
F(t) = \frac{MV}{2}\cos(\omega_F t) &+ \frac{2V}{\pi}\sum_{m=1}^{\infty} J_0\left(mM\frac{\pi}{2}\right)\sin\left(m\frac{\pi}{2}\right)\cos(m\omega_c t) \\
&+ \frac{2V}{\pi}\sum_{m=1}^{\infty}\sum_{n=1}^{\pm\infty} \frac{J_n\frac{mM\pi}{2}}{m} * \sin\left((m+n)\frac{\pi}{2}\right)\cos(m\omega_c + n\omega_F t)
\end{aligned}
$$

ω_F = fundamental frequency in rad/s
ω_c = carrier signal frequency in rad/s
M = index (modulation)
V = dc supply voltage
J_0 = Bessel functions of the first kind.

Term 1 in the above expression shows the fundamental value which is directly related to the index (modulation). Term 2 is due to $\sin[(m\pi)/2]$, which states that

the there is zero existence of harmonics at multiples (even) of the carrier frequency. Term 3 expresses the amplitudes of the harmonics in the sidebands around each multiple of the carrier frequency. According to the $\sin[(m+n)\pi/2]$ proportional in this term:

(1) There is only even-order sidebands existence for odd harmonics of the carrier.
(2) There is only odd-order sidebands existence for even harmonics of the carrier.

Triangular carrier-based pulse-width modulation can be classified as:

1. In-phase disposition PWM (IPD-PWM)
2. Phase opposition disposition PWM (POD-PWM)
3. Alternate phase opposition disposition PWM (APOD-PWM)
4. Triangular phase-shifted PWM
5. Third harmonic injection PWM.

1. **In-phase disposition PWM scheme**

In IPD-PWM scheme, all carrier wave has same peak–peak amplitude and frequency as shown in Fig. 2. The IPD-PWM gives odd harmonics for odd m_f and odd and even harmonics for even m_f [8]

2. **Phase opposition deposition PWM scheme**

In the phase opposition disposition PWM scheme, the carrier waves above and below zero reference line are in phase with each other, but the carriers above and below zero reference are in 180° out of phase. Figure 3 shows the POD-PWM scheme and the resulting output waveform.

3. **Alternate phase opposition disposition PWM (APOD-PWM)**

In this scheme, the carrier wave has phase displacement by 180° alternatively with same frequency as shown in Fig. 4. The APOD-PWM scheme does not

Fig. 2 IPD-PWM scheme and output waveform

IPD-PWM scheme

Five level output waveform

Fig. 3 POD-PWM scheme
and output waveform

POD-PWM scheme

Five level output voltage
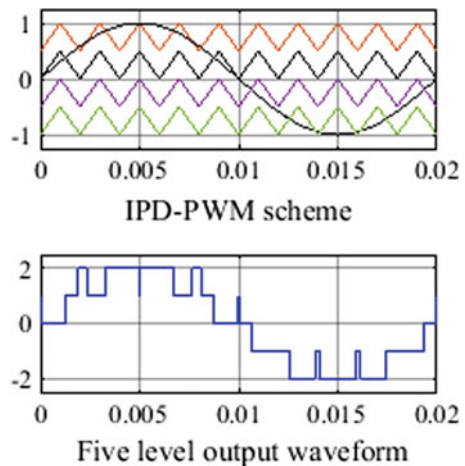
Fig. 4 APOD-PWM scheme
and output waveform
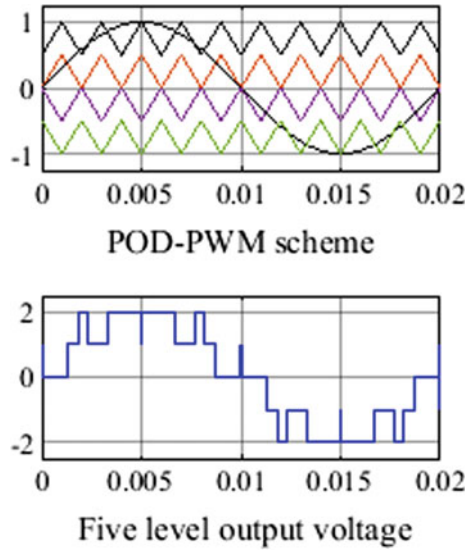
APOD-PWM scheme

Five level output waveform
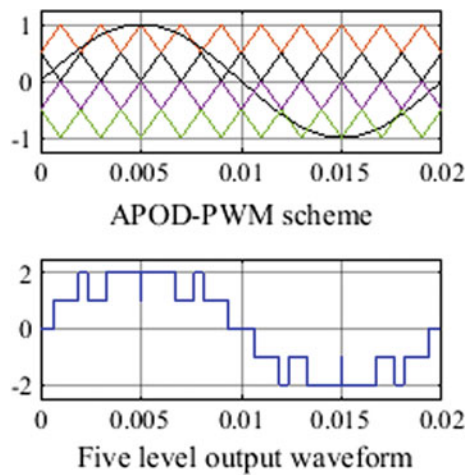
produce the first carrier harmonics, but sideband harmonics are around the first carrier harmonics. APOD-PWM scheme contains a considerable amount of energy (harmonic) in the output when frequency modulation index is even. If frequency modulation index is odd, then the output waveform has odd symmetry [9].

4. Triangular phase-shifted PWM

In the triangular phase-shifted PWM scheme, the carrier waves have the same frequency and peak-to-peak amplitude, but there exists a phase shift between two adjacent carrier waves which is represented as [10]:

Fig. 5 Phase-shifted PWM
scheme and output waveform

Phase shift PWM

Five level output waveform
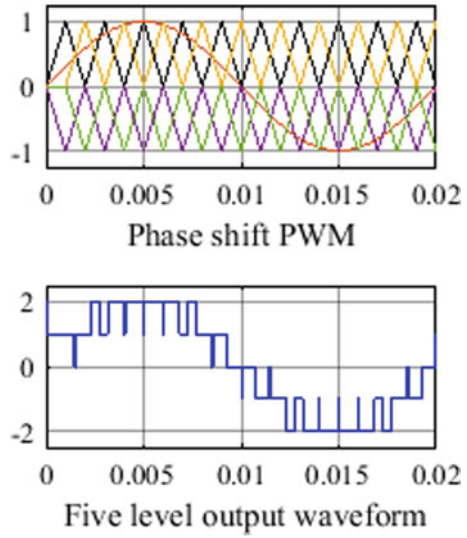
$$\varnothing_{cr} = \frac{360°}{N - 1}$$

where N be the number of output voltage levels.

For the five-level inverter, the required phase shift is 90°. Figure 5 shows the triangular phase-shifted PWM scheme and output waveform in p.u.

5. Third harmonic injection PWM

Third harmonic injection PWM has an advantage to achieve the 15.5% more output in linear range of modulation range. The optimum value of third harmonic component amplitude can be calculated as:

Assume a phase waveform of the type of

$$x = \sin\theta + a\sin3\theta \tag{11}$$

where $\theta = \omega t$ and a is the parameter to be determined. We locate the turning point of this function by differentiating x with respect to θ and equating that with zero,

$$\frac{dx}{d\theta} = \cos\theta + 3a\cos3\theta = 0 \tag{12}$$

Maxima and minima of the waveform occur at

$$\cos\theta = 0 \tag{13}$$

And

$$\cos\theta = \left(\frac{9a - 1}{12a}\right)^{1/2} \tag{14}$$

From Eq. (13), we get

$$\sin\theta = 1 \tag{15}$$

And from Eq. (14), we have,

$$\sin\theta = \left(\frac{1 + 3a}{12a}\right)^{1/2} \tag{16}$$

We know that $\sin\theta = (1 - \cos^2\theta)^{1/2}$; by using this identity, the peak value of x can be found by substituting the value obtained for $\sin\theta$ in Eqs. (15) and (16) into Eq. (11). This can be facilitated by manipulating Eq. (14), and we get

$$\sin 3\theta = 3\sin\theta - 4\sin^3\theta \tag{17}$$

Thus, Eq. (11) becomes

$$x = (1 + 3a)\sin\theta - 4a\sin^3\theta \tag{18}$$

Substituting for $\sin\theta$ the values obtained in Eqs. (15) and (16), we get

$$x^\neg = 1 - a \tag{19}$$

$$x^\neg = 8a\left(\frac{1 + 3a}{12a}\right)^{3/2} \tag{20}$$

where $x^\neg$ is the peak value of x.

The optimum value for a is that value which minimizes $x^\neg$. The optimum value of a can be found by differentiating Eq. (20) and equating with zero

$$\frac{dx^\neg}{da} = \left(\frac{1 + 3a}{12a}\right)^{\frac{1}{2}}\left(2 - \frac{1}{3a}\right) = 0 \tag{21}$$

Form Eq. (21), we can get

$$a = \frac{-1}{3}, \quad a = \frac{1}{6} \tag{22}$$

From Eq. (22), it is observed that the (−ve) value of a given "$x^\neg$" which is greater than the unity is therefore rejected. The accepted value of "a" is hence 1/6th, and the desired waveform is:

$$x = \sin\theta + \frac{1}{6}\sin 3\theta \tag{23}$$

To establish that no further decrease in "$x^\neg$" is achievable by the insertion of other triplen harmonics, the values of θ at which the peak of $x^\neg$ occurs are achieved by substituting for a in Eqs. (13) and (14). As desired, Eq. (14) gives $\theta = \pi/2$, independent of a, but (15) gives

$$\cos\theta = 1/2 \tag{24}$$

i.e.,

$$\theta = \frac{\pi}{3}, \frac{2\pi}{3}, \text{etc.} \tag{25}$$

On substituting the value of $\theta(= n\pi/3)$ in Eq. (23), the peak values of $x^\neg$ are:

$$x = \pm\sqrt{3}/2 \quad \text{and} \quad x^\neg = \pm 0.866 \tag{26}$$

The output voltage amplitude of this modulating wave can be increased by a factor of K, in order to achieve/utilize full output range of inverter. Thus,

$$x = K\left(\sin\theta + \frac{1}{6}\sin 3\theta\right) \tag{27}$$

From Eq. (26), we get

$$1 = K \times 0.866$$

$$K = 1.155$$

By third harmonic injection, output voltage can be increased by 15.5% in linear range of modulation [11] (Figs. 6, 7). Similarly, space vector modulation techniques and other techniques given in [12] can be implemented.

Fig. 6 Principle of third harmonic injection

Third harmonic injection PWM
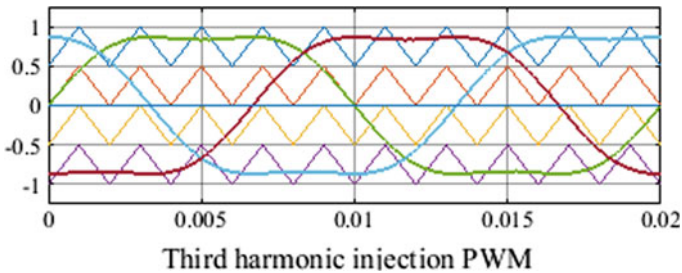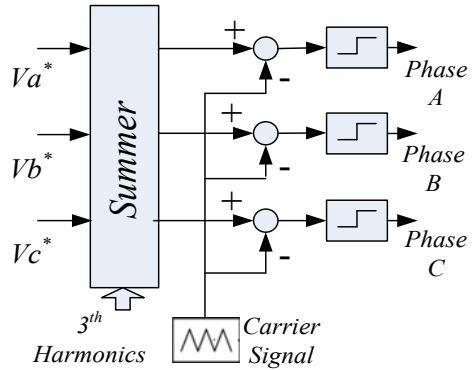
Fig. 7 Principle of third harmonic injection PWM

4 Conclusion

The objective of this work was to discuss the mathematical analysis of triangular carrier-based modulation techniques for single-phase and three-phase multilevel inverter. This equation shows that output of the inverter is mainly dependent on the modulation index, and Fourier transform shows that what kind of the harmonics is present in the output waveform.

References

1. Rushiraj J, Kapi1 PN (2016) Analysis of different modulation techniques for multilevel inverters
2. Tariq M, Meraj M, Azeem A, Maswood AI, Iqbal A, Bharatiraja C (2018) Evaluation of level-shifted and phase-shifted PWM schemes for seven level single-phase packed U cell inverter. CPSS Trans Power Electron Appl
3. Tariq M, Iqbal MT, Iqbal A, Meraj M, Roomi MM, Khan MSU (2016) Comparative analysis of carrier schemes for PWM in multilevel PUC inverter for PV applications. In: 2016 4th

international conference on the development in the in renewable energy technology (ICDRET), Dhaka, pp 1–6

4. Vahedi H, Kanaan HY, Al-Haddad K (2015) PUC converter review: topology, control and applications. In: IECON 2015—41st annual conference of the IEEE industrial electronics society, pp 4334–4339

5. Tariq M, Iqbal MT, Meraj M, Iqbal A, Maswood AI, Bharatiraja C (2016) Design of a proportional resonant controller for packed U cell 5 level inverter for grid-connected applications, pp 3–8

6. Iqbal A, Tariq M, Rahman K, Al-qahtani A (2014) Control of packed U-cell multilevel five-phase voltage source inverter. In: Qatar foundation annual research conference, ITPP0493

7. Hamman J, van der Merwe FS (1988) Voltage harmonics generated by voltage-fed inverters using PWM natural sampling. IEEE Trans Power Electron 3(3):297–302

8. Houldsworth JA, Grant DA (1984) The use of harmonic distortion to increase the output voltage of a three-phase PWM inverter. IEEE Trans Ind Appl IA-20(5):1224–1228

9. Zhou K, Wang D (2002) Relationship between space-vector modulation and three-phase carrier-based PWM: a comprehensive analysis. IEEE Trans Ind Electron 49(1):186–196

10. Bin W (2006) High power converters and AC drives

11. Iqbal A, Levi E, Jones M, Vukosavic SN (2006) Generalised sinusoidal PWM with harmonic injection for multi-phase VSIs. In: PESC—IEEE annual power electronics specialists conference

12. Bharatiraja C, Munda JL, Bayindir R, Tariq M (2016) A common-mode leakage current mitigation for PV-grid connected three-phase three-level transformerless T-type-NPC-MLI. In: 2016 IEEE international conference on renewable energy research and applications (ICRERA), Birmingham, pp 578–583

Hybrid Improved Teaching Learning-Based Optimization and Differential Evolution (hITLBO-DE)-Based Optimization of Multi-area Thermal Power System with Automatic Generation Control

Aurobindo Behera, Tapas Kumar Panigrahi and Arun Kumar Sahoo

Abstract Stability and integrity of the power system being a major concern requires the system parameters to be monitored. The problem considered in the paper is an improvement in functioning of automatic generation control (AGC) in a cross-connected power system with different approaches. The objective of the paper is facilitating an approach to design a fast and precise controller for the power system with unequal areas, and tuning the response of AGC is a multi-objective function with constraints. The initial approach requires verifying the conventional objective function to be implemented for the formation of the proposed approach. This paper deals with exploration of a proportional integral derivative (PID) controller with a hybrid improved teaching learning-based optimization and differential evolution (hITLBO-DE) being studied for controlling system response. The major focus in the hybrid is to improve the learning process and achieve a faster and effective learning. Various cases of load variation are considered for the analysis such as 10% change in area-1 (Case-1), 10% change in area-2 (Case-2), and 10% change in both the areas simultaneously (Case-3). The analysis of results for all the 3 cases confirms the effectiveness of the proposed scheme. Also, a significant improvement in the response time of the system is observed.

A. Behera (✉) · A. K. Sahoo
Department of Electrical Engineering, International Institute
of Information Technology Bhubaneswar, Bhubaneswar,
Odisha 751003, India
e-mail: abehera2205@gmail.com

A. K. Sahoo
e-mail: C116003@iiit-bh.ac.in

T. K. Panigrahi
Department of Electrical Engineering, Parala Maharaja
Engineering College, Berhampur, Odisha 761003, India
e-mail: tkpanigrahi.ee@pmec.ac.in

1 Introduction

Of many essential ancillary services being provided, automatic generation control (AGC) [2, 5] is foremost required. The system frequency should be maintained close to the nominal value to maintain the system equilibrium. The system frequency and tie line power are continuously monitored, and the net change in generation is evaluated. The set points of the individual generators are varied based on the net change evaluated to maintain low values of time average of area control error (ACE) [10]. ACE is adjusted to make the deviation in frequency (Δf_i) and the error in tie line power (ΔP_{tie}) zero, in case of a multi-area power system [22]. The controlled output of the AGC is termed as area control error (ACE).

Several control strategies have been discussed over the past epoch in this area of research by researcher as revealed by the study literature . The effort is being put forth to understand the response of the system to these strategies and their ability to sustain nominal frequency and retain the tie line power at nominal limit, both during standard operating condition and under minor perturbations [9]. Many governing and optimization methods such as orthodox methods [12], "genetic algorithm (GA)," by Mühlenbein [11], optimum control [7, 14], "PSO (particle swarm optimization)," by Gozde [8], "bacteria foraging optimization algorithm (BFOA)," by [1, 13], "fuzzy logic controller (FLC)," by Chandrakala [3], "artificial neural network (ANN)," by Saikia [21], and "differential evolution algorithm (DE)," by Rout [18]. "Chaotic optimization algorithm (COA)" by Farahani [6] and "teaching learning-based optimization (TLBO)" by Sahu [19] have been proposed for AGC. In [18], use of an "integral of multiple of time and absolute value of error" (ITAE) with a modified function consisting also of dominant eigenvalue's damping ratio with settling time has been presented. In [15], a controller is proposed with hybrid neuro-fuzzy (HNF)-based capability of handling the non-linearities and provides quicker response as compared to orthodox controllers. Gains of a fuzzy PI controller in a non-reheat thermal system with two areas are enhanced using a hybrid PSO and PS (hPSO-PS) optimization method, in [20]. In [16], "non-dominated shorting genetic algorithm-II (NSGA-II)," by Panda, a multi-objective technique is discussed for designing a proportional integral (PI) and a proportional integral derivative (PID) controller for automatic generation control (AGC) of an interconnected system.

As seen from the study of literature, the optimization technique has high influence on the operation of the controller and thus the interconnected system. It basically has two major governing factors such as the objective function and the variable parameters (i.e., *teaching factor*, *student learning factor*, *crossover ratio*, *scaling factor*, *sampling time*, *nos of students*, *max nos of iteration*, etc.), which

decide the rate and degree of convergence of the system response when subjected to a perturbation. For a particular system under study, the variable parameters are assumed to be constant. Thus, the objective function is mainly responsible for the optimal response of the controller. Thus, many objective functions have been proposed and implemented by researchers. Any heuristic technique may converge very fast, but is adversely affected by local minima, and the adverse effect can be overcome by evaluating numerous vectors concurrently. This is the primary technique used in the differential evolution (DE) algorithm [10]. And in the improved TLBO, the use of teacher and student phases improves the effectiveness of the algorithm. Researchers have used different objective functions "*ITAE* (integral time absolute error), *IAE* (integral absolute error), *ITSE* (integral time square error), *ISE* (integral square error)" to optimize the controller parameter as minimization of these functions tend to minimize the error in the output signal and a desired output could be achieved.

In this discussion, a hybrid improved teaching learning-based optimization and differential evolution (hITLBO-DE) is proposed and applied for tuning of controller in an AGC system. As the response parameters are highly conflicting to each other, minimization of this function would definitely ensure the optimization of the response. This hybrid of the two highly effective techniques, which can provide faster yet a better response, is the key motivation for the paper. As for a smooth operation of the system, variance between demand and generated power is to be nullified within the least possible interval.

In the application of the hITLBO-DE, a maiden attempt has been made to optimize the control parameters of the simple PID in an unequal area scenario. The improvement in the optimization of the system response can vividly be observed by the comparison of the obtained output to some newly available methodologies such as chaotic optimization algorithm [6], teaching learning-based optimization (TLBO) [19], and improved TLBO [4, 17] for a 2-area thermal power system with non-reheat and interconnection among the areas. In [4], the ITLBO technique proposed is claimed to be producing a global optimal solution and avoiding local minima for some complex problems. However, in [10], the application of DE by Mohanty et al. reveals the ability of the technique to encounter the issue of local minima by crossover and mutation stages. This phenomenon ensures that each population is updated by three randomly selected populations. These steps of DE are incorporated into ITLBO for making it more effective and enhance the learning process of the individual populations. In the mentioned setup of ITLBO, the learning takes place between two distinct individuals, but in the proposed technique, every individual would learn from another group of individuals by the application of crossover and mutation states of DE. This process, when implemented to teacher and student phases of ITLBO, boosts the rate of learning hence leading to faster convergence.
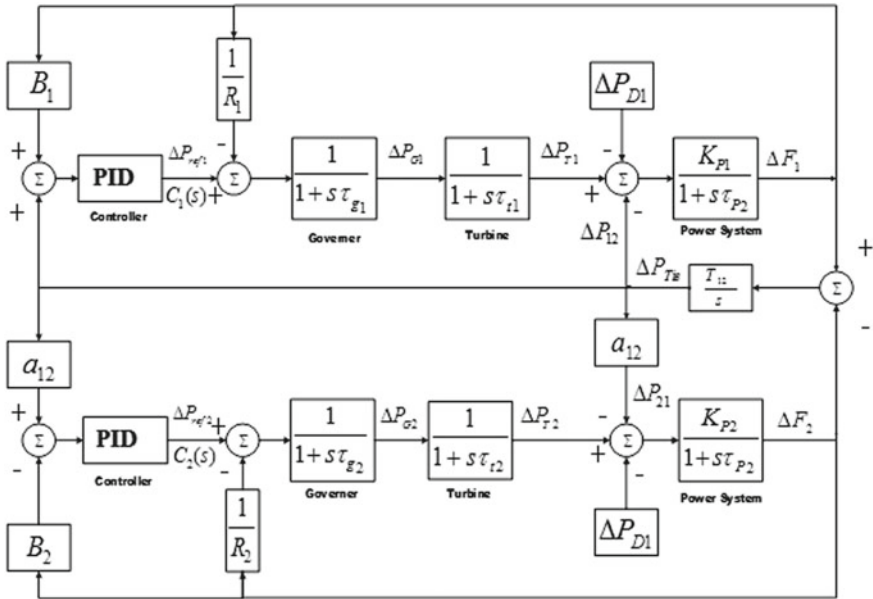
Fig. 1 Model for two-area thermal systems with simple PID

2 Modeling and Methodologies

The power system model in Fig. 1 considers an unequal area for the system analysis, and a simple PID controller is applied for control action. The result obtained by the hITLBO-DE algorithm is compared to the previously used and preferred techniques by various researchers.

2.1 Controller Modeling

A controller being an essential component for the stable operation of an AGC system, the choice made should be effective for improvement of transient as well as steady-state stability. The purpose of selection of proportional integral derivative (PID) controller for the application to the system is its proficiency of refining the overall system stability. The simple structural and operational design of PID controller and exhibitions of a reliable response under prevalent variation operational circumstances makes it a desirable choice for the operation. The elementary mathematical depiction of t-domain PID controller:

$$u(t) = \frac{c(t)}{r(t)} = K_\mathrm{p}e(t) + K_\mathrm{i} \int_0^t e(\tau).\mathrm{d}\tau + K_\mathrm{d} \frac{\mathrm{d}e(\tau)}{\mathrm{d}\tau} \tag{1}$$

In Laplace domain:

$$U(s) = \frac{C(s)}{R(s)} = K_\mathrm{p} + \frac{K_\mathrm{i}}{s} + K_\mathrm{d}s \tag{2}$$

2.2 Objective Function

The problem considered in the paper is to make the system response faster and less prone to instability during perturbation. To optimize the system response parameters (i.e., *rise time* (T_r), *peak time* (T_p), *overshoot/undershoot* (*OS/US*), *settling time* (T_s), *steady-state error* (e_ss)), an objective function is to be considered which can converge the response faster to its equilibrium point. Many different objective functions have been implemented by scholars in the past few years to obtain optimum solution for discussed problem. Some frequently preferred functions for optimization in Eqs. (3)–(6), as revealed by research work [20], are ITSE, ISE, ITAE, and IAE.

$$\mathrm{ITAE} = \int_0^t t.(\Delta f_1 + \Delta f_2 + \Delta P_\mathrm{tie}) \, \mathrm{d}t \tag{3}$$

$$\mathrm{IAE} = \int_0^t (\Delta f_1 + \Delta f_2 + \Delta P_\mathrm{tie}) \, \mathrm{d}t \tag{4}$$

$$\mathrm{ITSE} = \int_0^t t.(\Delta f_1 + \Delta f_2 + \Delta P_\mathrm{tie})^2 \, \mathrm{d}t \tag{5}$$

$$\mathrm{ISE} = \int_0^t (\Delta f_1 + \Delta f_2 + \Delta P_\mathrm{tie})^2 \mathrm{d}t \tag{6}$$

All the functions have been analyzed for different values of crossover ratio (CR) and scaling factor (F) and a fixed value T_f, L_f. Comparison in Table 1 shows that the *ITAE* is having least objective function value, so of all the available functions, ITAE is included in the modified objective function when applied for the two-area model. The crossover ratio (CR) is 0.2 and the scaling factor (F) is 0.7

Table 1 System response parameter for different error functions

Error functions	Rise time (T_r) (s)	Peak time (T_p) (s)	Maximum overshoot (OS) $\times 10^{-3}$	Settling time (T_s) (s)	Objective function value
IAE	0.29316	0.91	0.740	0.837	0.004
ITAE	0.21759	0.88	1.298	0.543	0.0028
ISE	0.29316	0.89	1.481	0.954	0.218
ITSE	0.29316	0.98	0.652	0.622	0.0361

considering the number of population (NP) to be 20, and dimension of the parameter (D) to be 6 is found to produce the optimized result for ITAE.

The system parameters being contradicting to each other are difficult to minimize simultaneously; thus, instead these are optimized to get the best possible response. The objective function includes the best of the above functions and the weighted system parameters and is given by "M".

$$M = m_r T_r + m_p T_p + m_{us} US + m_{ss} e_{ss} + \text{ITAE} \tag{7}$$

Here m_r, m_p, m_{us}, m_{ss} are scaled weight for each parameter as per their impact on the response of the system.

3 Hybrid Differential Evolution and Improved Teaching Learning-Based Optimization (hITLBO-DE) Algorithm

Intrinsic worth of DE [10] and improved TLBO [4] algorithms are combined to provide an approach with better optimization capability. TLBO has two phases for the search of optimized value, i.e., the teacher and student phases. Since there are limits in the ability of learners, it can learn from the neighbors. Learners phase can get improved location search via self-learning based on historical understandings. Under the circumstances of learner not getting improved value, it can go for a different location within a constricted dominion. Here, the DE technique is applied for the formation of new test domain where more probable best solutions may be available. The flowchart shown in Fig. 2 describes the proposal of hITLBO-DE process. The productivity of the proposed methodology has been demonstrated by implementation to three distinct cases of operation of 2-unequal area model which has been discussed briefly in Sect. 4.

The hybrid is created by modification of both the phases. The initial stage is the teacher stage, and teacher is highly responsible for the improvement of the student results, and the self-studying ability of the student also greatly influences the improvement in the result of the student. Thus, the crossover process of differential evolution is implemented to the ITLBO at the teacher learning stage and student
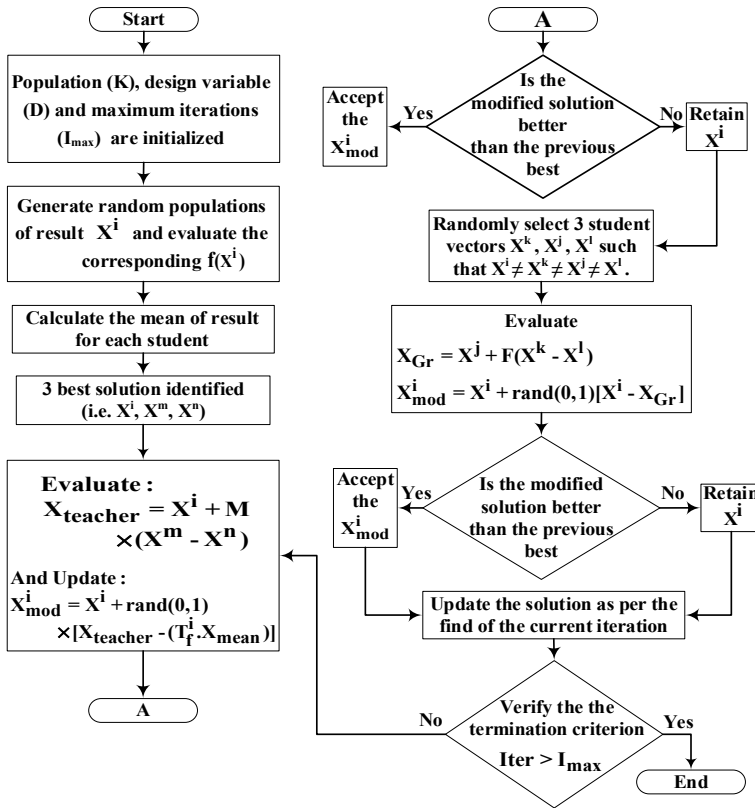
Fig. 2 Flowchart of the hITLBO-DE algorithm

self-learning stage. Equations (8)–(11) describe the procedure to formulate the hybrid technique, and the same is presented in the form of a flowchart in Fig. 2 for better understanding. The subsequent Eqs. (8)–(9) are realized for the modification in X_{teacher} of teacher phase as per the proposal.

$$X_{\text{mod}}^i = X^i + \text{rand}(0, 1)\left[X_{\text{teacher}} - \left(T_{\text{f}}^i.X_{\text{mean}}\right)\right] \tag{8}$$

$$X_{\text{teacher}} = X^i + M(X^m - X^n) \tag{9}$$

where X_{teacher} is formulated by the concept of DE. Earlier, the best solution was "X_{teacher}" and was responsible for the improvement of the results of the other student vectors. But in the present concept, the three best solutions (i.e., X_i, X_m, and X_n) would be responsible for the self-learning stage of the teacher vector. It improves the teacher's ability to reach a global best solution, and the students get better guidance.

In the student phase as per Eqs. (10)–(11), the student vector learns from the other students one by one, instead they can improve their learning speed by learning from a group of students. So, three students are nominated arbitrarily such that $X_i \neq X_k \neq X_j \neq X_l$. Here, X_i is the learner vector and others are picked arbitrarily for assisting X_i as a group and reach a point of higher knowledge by many to one learning process.

$$X_{\text{Gr}} = X^j + F(X^k - X^l) \tag{10}$$

$$X^i_{\text{mod}} = X^i + \text{rand}(0,1)\left[X^i - X_{\text{Gr}}\right] \tag{11}$$

The crossover operation when incorporated to hITLBO-DE inherits the benefit of not getting confined by local minima from DE by group learning involving three students simultaneously and thereby having a faster and reliable converging toward a global minimum point.

4   Result and Discussion

The hybrid technique developed and discussed in the above section is put to work for testing of three different cases of load variation. Each is done on the same system with the same parameters of the controller (i.e., K_p, K_i, K_d). But proportional, integral, and derivative coefficients of both the controllers installed in either area are chosen differently as 2-unequal area is considered. The proposed hybrid of improved TLBO and DE algorithms is used for the optimization process of parameters for the controller, and the optimum values for the same have been presented in Table 2.

Table 2 Controller parameter for the unequal area with simple PID controller

S. No.	Optimization technique/controller	Parameter type		Parameter value	
1	hITLBO-DE/PID	K_{p1}	K_{p2}	1.9040	0.1374
		K_{i1}	K_{i2}	1.9500	0.8265
		K_{d1}	K_{d2}	1.9210	0.9299
2	Chaotic optimization/PID	K_{p1}	K_{p2}	1.9800	0.1451
		K_{i1}	K_{i2}	1.9999	0.4294
		K_{d1}	K_{d2}	1.9999	0.9633
3	TLBO [17]/PID	K_{p1}	K_{p2}	0.9048	0.7425
		K_{i1}	K_{i2}	0.2412	0.2431
		K_{d1}	K_{d2}	0.5910	0.4241
4	ITLBO/PID	K_{p1}	K_{p2}	0.8016	0.9961
		K_{i1}	K_{i2}	0.8595	0.2170
		K_{d1}	K_{d2}	0.6896	0.5143

Table 3 System response parameters with different optimization techniques for the unequal area with simple PID controller with step load surge of 10% in area-1

Parameters		hITLBO-DE	ITLBO	TLBO	COA	DE
Overshoot/undershoot	Δf_1 (10^{-3})	−1.08	−1.27	−2.33	−2.63	−2.46
	Δf_2 (10^{-4})	−1.51	−2.87	−4.26	−3.59	−4.74
	ΔP_{tie} (10^{-3})	−2.16	−4.23	−6.89	−4.52	−7.93
Settling time (2%)	Δf_1	6.75	8.46	9.32	8.76	12.67
	Δf_2	9.42	10.97	11.07	12.42	20.31
	ΔP_{tie}	9.78	10.54	16.79	11.85	20.24
Steady-state error	Δf_1 (10^{-6})	1.04	11.09	1.04	1.15	2.61
	Δf_2 (10^{-6})	−0.01	−0.40	−1.99	−0.02	−0.04
	ΔP_{tie} (10^{-8})	−0.25	−6.26	−29.07	0.31	−0.31

Table 3 holds the mathematical results for Case-1 where a power demand deviation of 10% in area-1 is applied. Figure 3 shows the frequency alteration of area-1 and area-2 and power exchange deviation, for Case-1, with the result compared to that of DE, COA, TLBO, and ITLBO. Here, it is distinctly observed that the response of the system with the proposed controller can reduce the overshoot and settling time significantly.

Table 4 and Fig. 4 hold the mathematical and graphical results for the Case-2, where a power demand deviation of 10% in area-2 is considered and the result is compared to that of DE, COA, TLBO, and ITLBO. The response of the system for Case-2 shows a significant reduction in interoscillation, thus improving the stability.

Table 5 and Fig. 5 hold the mathematical and graphical results for the Case-3, where a power demand deviation of 10% in area-1 and area-2 is considered and the result is compared with that of DE, COA, TLBO, and ITLBO. This case study depicts the response of the system when subjected to simultaneous load variation in both the areas. The transient and steady-state parameters having utmost significance are observed to be irresponsive to the perturbation. Thus, minimum overshoot and better settling time are obtained by implementation of PID controller and tuned by the proposed optimization technique.

5 Conclusion

In this study, the focus is made on the hybrid optimization technique used in optimizing the performance of the system by tuning the controller parameters. It can be concluded that the hITLBO-DE is functioning well as observed in Tables 3, 4, and 5 and Figs. 3, 4, and 5 where the comparison of some recent optimization techniques is provided. The comparison is done for the three different operating conditions. In the first case, the perturbation is applied to area-1 only, second is the

(a)

(b)

(c)
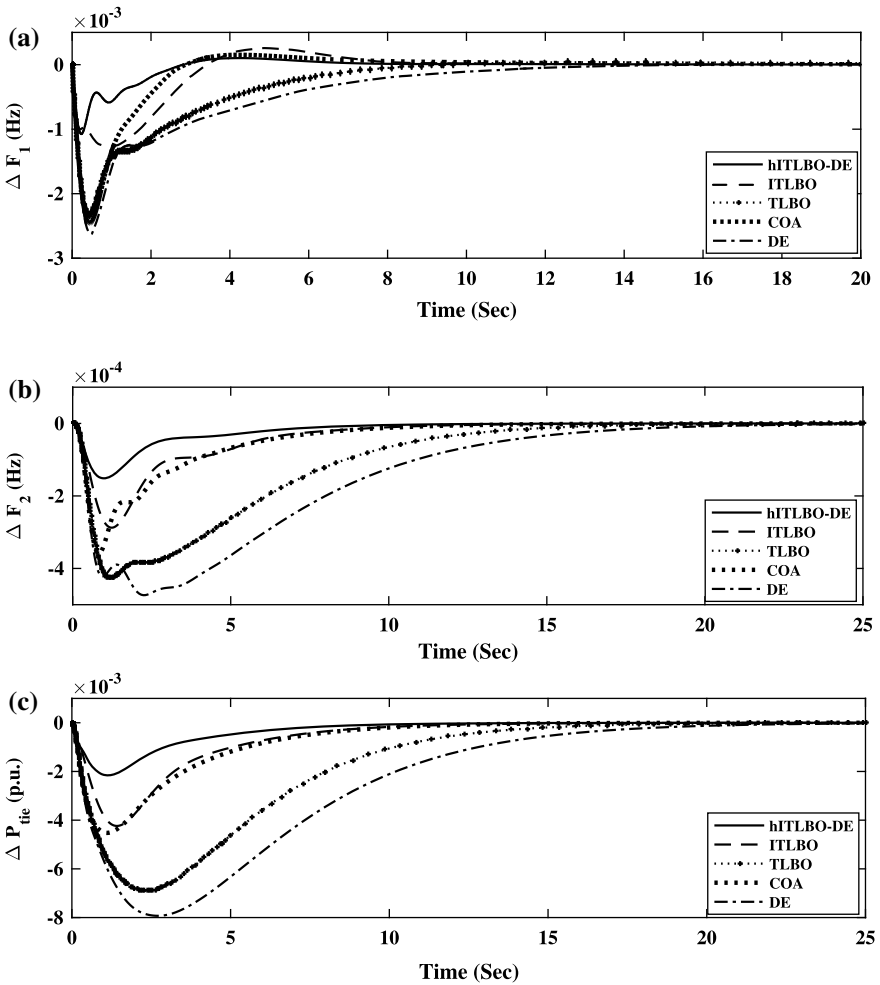
Fig. 3 Variation in frequency for **a** area-1, **b** area-2, **c** tie line exchange power for step load surge of 10% in area-1

application of perturbation to area-2 only, and final case is the application of perturbation to both the areas. In the analysis of all the cases, we can conclude that the damping ratio, for the thermal power system in the both the areas with local as well as inter-area fluctuation, is improved. The improvement is not only in the peak undershoot of the response but also the settling time has significant improvement proving the response to be faster than the controllers with other optimization techniques concurrently. Thus, the application of a crossover in both the phases of ITLBO provided promising improvement in the performance of the metaheuristic technique.

Table 4 System response parameters with different optimization techniques for the unequal area with simple PID controller with step load surge of 10% in area-1 as well as area-2

Parameters		hITLBO-DE	ITLBO	TLBO	COA	DE
Overshoot/undershoot	Δf_1 (10^{-3})	−0.46	−0.581	−0.60	−0.51	−0.81
	Δf_2 (10^{-3})	−4.62	−4.682	−5.76	−5.30	−6.91
	ΔP_{tie} (10^{-3})	12.76	16.90	15.74	15.41	20.31
Settling time (2%)	Δf_1	10.45	12.92	21.70	22.48	13.85
	Δf_2	8.31	16.17	16.84	13.71	22.26
	ΔP_{tie}	11.53	13.79	22.79	24.66	15.93
Steady-state error	Δf_1 (10^{-6})	−0.10	−0.23	−4.54	−14.17	−0.50
	Δf_2 (10^{-6})	3.55	8.67	58.25	51.03	21.67
	ΔP_{tie} (10^{-6})	1.53	3.30	11.87	27.60	12.68
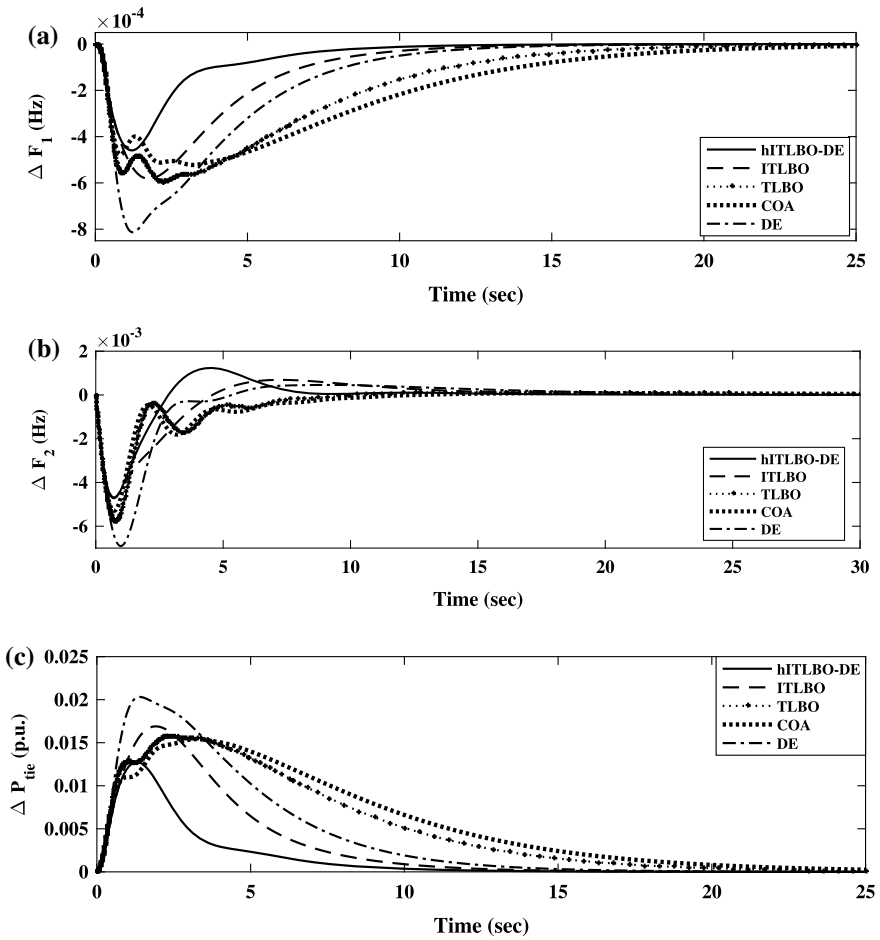
Fig. 4 Variation in frequency for **a** area-1, **b** area-2, **c** tie line exchange power for step load surge of 10% in area-2

Table 5 System response parameters with different optimization techniques for the unequal area with simple PID controller with step load surge of 10% in area-1 as well as area-2

Parameters		hITLBO-DE	ITLBO	TLBO	COA	DE
Overshoot/undershoot	$\Delta f_1 \ (10^{-3})$	−1.38	−3.77	−2.68	−2.50	−2.37
	$\Delta f_2 \ (10^{-3})$	−7.28	−7.27	−5.91	−5.42	−7.10
	$\Delta P_{\text{tie}} \ (10^{-3})$	10.58	15.26	7.32	13.35	14.26
Settling time (2%)	Δf_1	13.45	13.92	25.70	28.48	17.85
	Δf_2	8.17	14.57	16.84	12.71	15.26
	ΔP_{tie}	11.53	13.79	22.79	26.85	13.93
Steady-state error	$\Delta f_1 \ (10^{-6})$	−1.34	0.91	−35.54	−78.23	−3.48
	$\Delta f_2 \ (10^{-6})$	2.70	7.61	0.24	0.48	8.55
	$\Delta P_{\text{tie}} \ (10^{-8})$	6.29	13.96	209.90	794.50	11.14
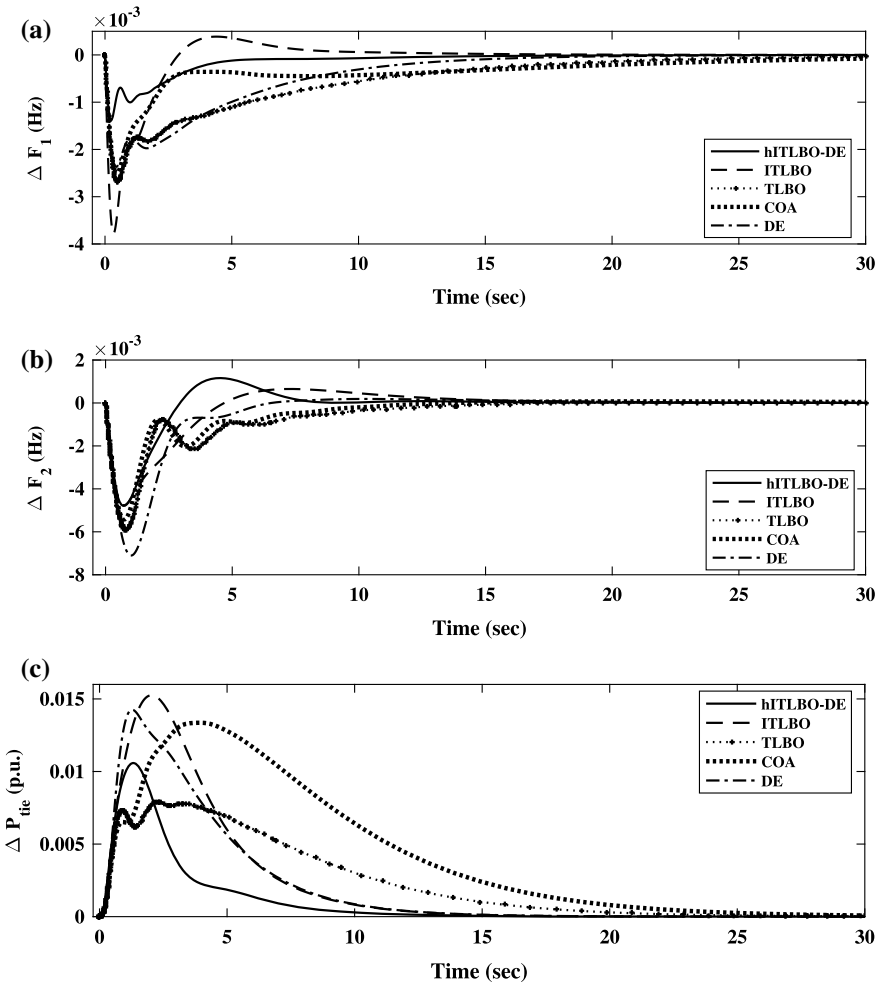
Fig. 5 Variation in frequency for **a** area-1, **b** area-2, **c** tie line exchange power for step load surge of 10% in area-1 as well as area-2

Appendix

Governor gain: $\tau_{g1} = 0.2$, $\tau_{g1} = 0.3$;
Turbine gain: $\tau_{t1} = 0.5$, $\tau_{t2} = 0.6$;
Power system gain: $H_1 = 5$, $D_1 = 0.6$, $H_2 = 4$, $D_2 = 0.9$;
Droop characteristics: $R_1 = 0.05$, $R_2 = 0.0625$;
Feedback gain: $B_1 = 29.6$, $B_2 = 16.9$;
Tie line gain: $a_{12} = -1$, $T_{12} = 0.545$.

References

1. Ali E, Abd-Elazim S (2011) Bacteria foraging optimization algorithm based load frequency controller for interconnected power system. Int J Electr Power Energy Syst 33(3):633–638
2. Bevrani H (2009) Robust power system frequency control. Springer
3. Chandrakala KV, Balamurugan S, Sankaranarayanan K (2013) Variable structure fuzzy gain scheduling based load frequency controller for multi-source multi area hydro thermal system. Int J Electr Power Energy Syst 53:375–381
4. Chen D, Zou F, Li Z, Wang J, Li S (2015) An improved teaching–learning-based optimization algorithm for solving global optimization problem. Inf Sci 297:171–190
5. Elgerd OI (2000) Electric energy systems theory an introduction. McGraw-Hill Book Company, New York, NY
6. Farahani M, Ganjefar S, Alizadeh M (2012) PID controller adjustment using chaotic optimisation algorithm for multi-area load frequency control. IET Control Theory Appl 6 (13):1984–1992
7. Ghoshal SP (2004) Application of GA/GA-SA based fuzzy automatic generation control of a multi-area thermal generating system. Electr Power Syst Res 70(2):115–127
8. Gozde H, Taplamacioglu MC (2011) Automatic generation control application with craziness based particle swarm optimization in a thermal power system. Int J Electr Power Energy Syst 33(1):8–16
9. Kumar P, Kothari DP et al (2005) Recent philosophies of automatic generation control strategies in power systems. IEEE Trans Power Syst 20(1):346–357
10. Mohanty B, Panda S, Hota PK (2014) Controller parameters tuning of differential evolution algorithm and its application to load frequency control of multi-source power system. Int J Electr Power Energy Syst 54:77–85
11. Mühlenbein H, Schomisch M, Born J (1991) The parallel genetic algorithm as function optimizer. Parallel Comput 17(6–7):619–632
12. Nanda J, Mangla A, Suri S (2006) Some new findings on automatic generation control of an interconnected hydrothermal system with conventional controllers. IEEE Trans Energy Convers 21(1):187–194
13. Nanda J, Mishra S, Saikia LC (2009) Maiden application of bacterial foraging-based optimization technique in multi-area automatic generation control. IEEE Trans Power Syst 24 (2):602–609
14. Parmar KS, Majhi S, Kothari DP (2012) Load frequency control of a realistic power system with multi-source power generation. Int J Electr Power Energy Syst 42(1):426–433
15. Panda G, Panda S, Ardil C (2009) Hybrid neuro fuzzy approach for automatic generation control of two–area interconnected power system. Int J Comput Intell 5(1):80–84

16. Panda S, Yegireddy NK (2013) Automatic generation control of multi-area power system using multi-objective non-dominated sorting genetic algorithm-II. Int J Electr Power Energy Syst 53:54–63
17. Rao RV, Patel V (2013) An improved teaching-learning-based optimization algorithm for solving unconstrained optimization problems. Scientia Iranica 20(3):710–720
18. Rout UK, Sahu RK, Panda S (2013) Design and analysis of differential evolution algorithm based automatic generation control for interconnected power system. Ain Shams Eng J 4 (3):409–421
19. Sahu BK, Pati S, Mohanty PK, Panda S (2015) Teaching learning based optimization algorithm based fuzzy-PID controller for automatic generation control of multi-area power system. Appl Soft Comput 27(Supplement C):240–249
20. Sahu RK, Panda S, Sekhar GC (2015) A novel hybrid PSO-PS optimized fuzzy PI controller for AGC in multi area interconnected power systems. Int J Electr Power Energy Syst 64:880–893
21. Saikia LC, Mishra S, Sinha N, Nanda J (2011) Automatic generation control of a multi-area hydrothermal system using reinforced learning neural network controller. Int J Electr Power Energy Syst 33(4):1101–1108
22. Tan W (2011) Decentralized load frequency controller analysis and tuning for multi-area power systems. Energy Convers Manage 52(5):2015–2023

Grid Integration of Fuzzy-Based Solar Photovoltaic with Battery Storage System for Conditioning the Electrical Power

Ravi Dharavath and I. Jacob Raglend

Abstract In the present trend, the grid-connected solar photovoltaic systems are playing a major role in supporting the utility peak power and providing the quality of power supply. The installation of solar photovoltaic system is reasonable cost for producing the power. But the solar power may not meet the utility peak demand continuously due to the intermittent nature of solar power. To make continuous supply, the battery storage system is proposed with the bidirectional convert using PI controller. In this work, the grid integration of solar photovoltaic with battery storage system is proposed using the hysteresis current controller for conditioning the electrical power. The solar power is extracted using fuzzy-based maximum power point tracking methods under dynamic variations in the irradiance and temperature. The extracted power is integrate with DC link, and the voltage at DC link is stabilized with the help of battery storage system. The DC link is integrated with the grid through the inverter using a hysteresis current control technique with the PI controller. The inverter and battery storage controllers are used for providing quality of power supply and can meet the necessary peak demand. The performance of the grid-connected solar photovoltaic and battery storage systems is simulated in MATLAB–Simulink software under the dynamic irradiance and the temperature variations.

R. Dharavath (✉) · I. Jacob Raglend
Vellore Institute of Technology, Vellore, Tamil Nadu, India
e-mail: rv.dharavath@gmail.com

I. Jacob Raglend
e-mail: jacobraglend.i@vit.ac.in

1 Introduction

The tremendous use of power due to high invention in technology, population growth, industries and this challenging issue leads to attention on clean power generation. In Indian, the total installed renewable capacity is 57,260.23 GW as of March 31, 2017 [1]. Still Indian has the peak demand with a capacity of 2192 MW as of 24th Jan 3 2018 [2]. The shortage of power for last three years is shown in Table 1. The every year necessary supply required for the peak demand is improved due to installation of multi-renewable energy sources.

Solar power generation is the green economy and pollution-free which makes the motivation for installing solar photovoltaic (PV) systems. The installed renewable energy sources with the grid integration are again a challenging task for conditioning the electrical power. The solar PV system integrated with the grid at a point of common coupling (PCC) through the inverter is to meet the peak demand and providing continuous power supply.

Due to solar intermittent nature and dynamic variation in climate cause power quality problem as voltage and frequency variations [3]. These variations in sources influence at the PCC in the grid-connected system. This effect can be reduced with the appropriate controller. The grid-connected system may include some other small-scale energy sources like wind and diesel generation, and gas engine-based generation [4] majorly causes the variations in the supply, and this can lead to influence the sensitive load. Finally, reduce the life span of the load. Diesel-based generation causes the global warming. To reduce the effect of global warming, to make continuity supply, providing the necessary peak power and for conditioning the electrical power solar PV is integrated with battery storage system.

In this paper, the novel structure of grid-connected solar photovoltaic system is fed to the DC link, DC load, and AC load through the converter. Solar power is extracted using fuzzy-based maximum power point tracking method. The DC-link system is integrated with the grid through the two-level three-phase voltage source inverter. In solar PV systems, grids are providing continuous power to the AC and DC sensitive load. The grid-connected solar photovoltaic system is simulated with and without battery storage system using MATLAB–Simulink software. The proposed system performance is simulated under dynamic condition of the source. The following sections deal with the proposed grid-connected solar photovoltaic systems.

Table 1 The shortage of electricity during the peak demand [2]

S. No.	Month and years	Power peak demand and shortage (MW)	Energy shortage (MU)
1	January 2018	2192	14
2	January 2017	2171	17
3	January 2016	2707	54

2 Modules of Grid-Connected Solar Photovoltaic Systems

The single line diagram of grid integration of solar photovoltaic (PV) and battery storage system with grid control units are shown in Fig. 1. The major requirements for the proposed hybrid system are:

(1) Solar photovoltaic system
(2) Boost converter
(3) Battery storage systems with bidirectional converter
(4) Three-phase voltage source converter.

2.1 Solar Photovoltaic (PV) System

The solar PV system works on the principle of photoelectric effect. It converts solar energy into electrical energy due to an incident of sunlight on the PV array. Figure 2 shows the basic model of the solar PV equivalent circuit. To provide flexible voltage and current, these PV cells are framed in PV array configuration. Equations (1) and (2) give the behavior of solar PV array voltage and current characteristics

$$V_{\mathrm{PV}} == \frac{nKT}{q} \ln\left(\frac{I_{\mathrm{sc}}}{I_{\mathrm{pv}}} + 1\right) \tag{1}$$
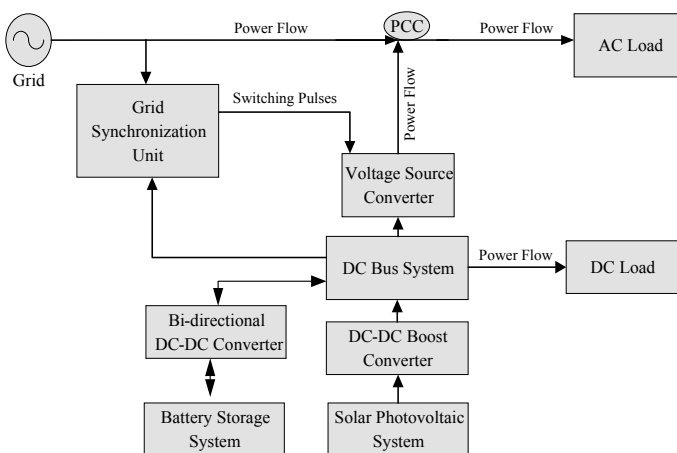
Fig. 1 Grid integration of solar PV, battery storage systems

Fig. 2 Solar photovoltaic
equivalent circuit [5]
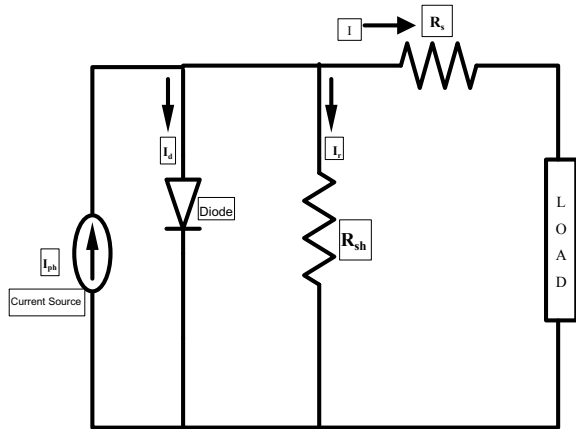
$$I_{pv} = I_{sc} - I_{pvo}\left[\exp\left(\frac{q\left(V_{pv} + I_{pv}R_s\right)}{N_s KTn}\right) - 1\right] - \frac{V_{pv} + R_s I_{sc}}{R_{sh}} \tag{2}$$

Power from a photovoltaic system is given by Eq. (3)

$$P_{PV} = V_{pv} \times I_{pv} \tag{3}$$

where I_{pv}—photovoltaic current (A), V_{pv}—photovoltaic voltage (V), K—Boltzmann constant, T—cell reference temperature. The basic characteristic of 100-kW solar photovoltaic is shown in Fig. 3 under different irradiances. The solar PV maximum power is tracked with fuzzy-based maximum power point tracking (MPPT).
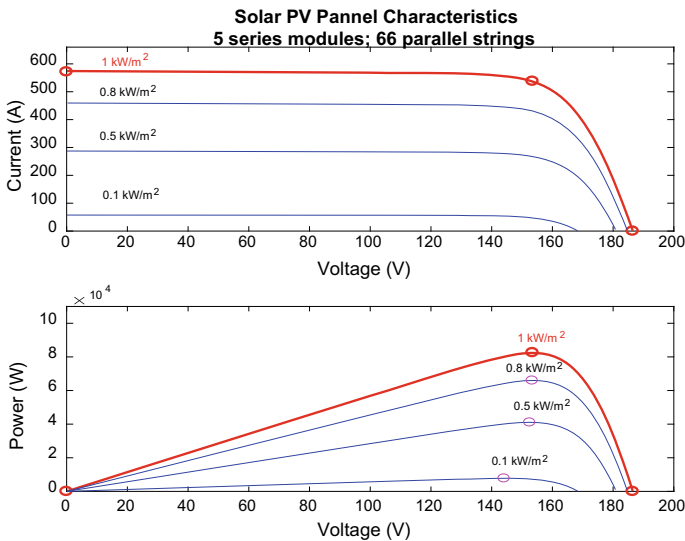
Fig. 3 Solar PV characteristics

2.2 Boost Converter

The boost converter is used between the solar PV and DC link to step up the solar photovoltaic voltage into 600 V DC. Figure 4 shows schematic of boost converter, and it is operated based on the switching pulses generated by the fuzzy controller-based MPPT technique.

The boost converter output voltage is calculated using Eq. (4)

$$V_o = \frac{V_{in}}{1 - D} \tag{4}$$

where V_o—the boost converter output voltage (V), V_{in}—the boost converter input voltage (V), D—duty ratio. The boost converter [5] is model based on Eqs. (5) and (6).

$$\Delta V_c = \frac{I_o * D}{C * F} \tag{5}$$

$$\Delta I = \frac{V_s * D}{L * F} \tag{6}$$

L (mH) and C (μF) are boost converter inductor and capacitor which are calculated based on the output voltage and current rating. F is thetemperature in $°C$, ΔV_c and ΔI are tolerable voltage and current limits, and V_s is input voltage of the boost converter (V).

2.3 Voltage Source Converter

The proposed voltage source converter is a three-phase two-level voltage source inverter. It will convert DC bus voltage into AC with a specified voltage, frequency

Fig. 4 Basic diagram of boost converter
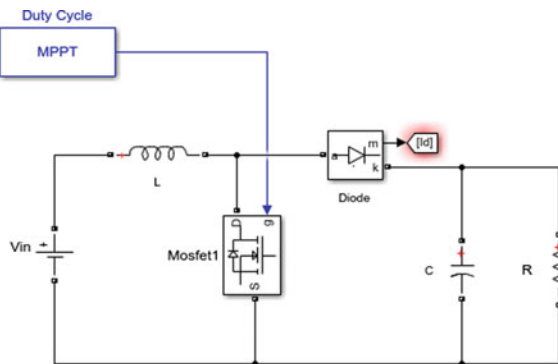
Fig. 5 Fuzzy logic control circuits [5]
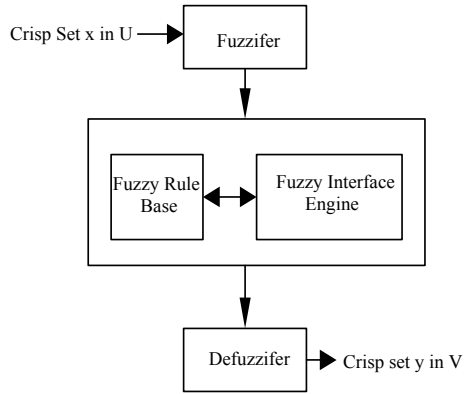
Fig. 6 Fuzzy-based MPPT control of solar PV
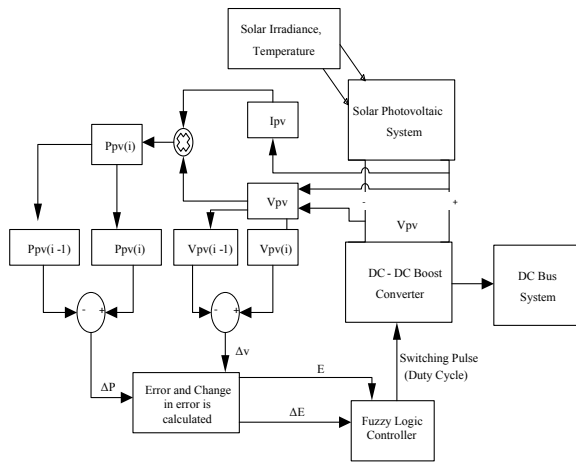
based on the switching pulses generated from the grid synchronization unit as shown in Fig. 7.

2.4 Control Algorithm

In the proposed hybrid system, control techniques can be divided into three parts, namely:

1. Maximum power point tracking-based fuzzy controller
2. PI controller-based hysteresis current controller for voltage source inverter
3. Battery bidirectional power flow controller.

Each controller description is given in the following section.

Fig. 7 Error input
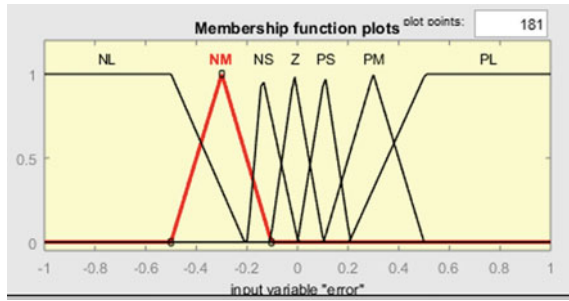
2.4.1 Fuzzy-Based Maximum Power Point Tracking Technique (MPPT)

In the proposed systems, the fuzzy controller is used to get the flexible output for taking smooth decision. The fuzzy logic controller mainly consists of four processes such as fuzzifier, fuzzy interface, rule base, and de-fuzzification as shown in Fig. 5 [6]. Fuzzy controller is implemented to get the maximum power from the solar PV as shown in Fig. 6. In the maximum power point-based fuzzy controller, the error signal can be distinct as the ratio of small change in the power to change in voltage ($\frac{\Delta P}{\Delta V}$ called as fuzzy factor).

At the maximum power point, the error signal E_o is zero. For the desired response, the fuzzy inputs are the error and the change in error signals obtained using the following equations.

$$E(i) = \frac{P_\mathrm{pv}(i) - P_\mathrm{pv}(i-1)}{V_\mathrm{pv}(i) - V_\mathrm{pv}(i-1)} \tag{7}$$

$$\Delta E(i) = E(i) - E(i-1) \tag{8}$$

The boost converter duty cycle is regulated using the fuzzy factor to get the maximum power from the solar photovoltaic system. The input and output variable of fuzzy rule are segmented in seven logistic variables such as negative large (NL), negative medium (NM), negative small (NS), zero (Z), positive large (PL), positive medium (PM), and positive small (PS), and it is presented as shown in Table 1. If the E and ΔE are NL, then the duty cycle is positive large. The membership functions of fuzzy logic controller are modulated as shown in Figs. 7, 8, and 9, respectively (Table 2).

2.4.2 Control Technique for Two-Level Voltage Source Inverter

Two-level voltage source converter is connected between the DC link and PCC point of the grid. The three-phase two-level voltage source converter controller is
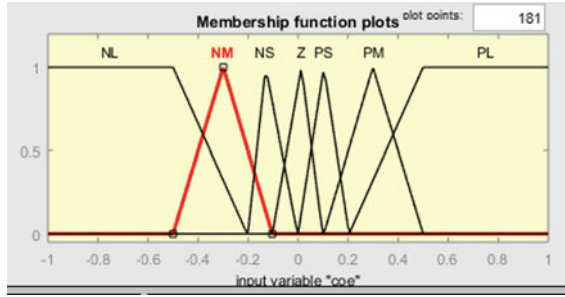
Fig. 8 Change in error input
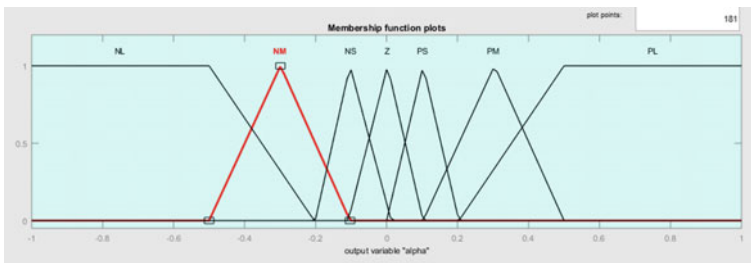
Fig. 9 Fuzzy output variable

Table 2 Rule-based fuzzy information table [5]

$\frac{E}{\Delta E}$	NL	NM	NS	Z	PS	PM	PL
NL	PL	PL	PL	PL	NM	Z	PL
NM	PL	PL	PM	PL	PS	Z	Z
NS	PL	PM	PS	PS	PS	Z	Z
Z	PL	PM	PS	Z	NS	NM	NL
PS	Z	Z	NM	NS	NS	NM	NL
M	Z	Z	NS	NM	NL	NL	NL
PL	Z	Z	NM	NL	NL	NL	NL

shown in Fig. 10 [7]. The switching pulses of the converter are controlled using a hysteresis current controller-based PWM generator, and it is regulated by the control of DC bus voltage and measured alternating current (AC) output voltages.

2.4.3 Battery Bidirectional Power Flow Controller

The battery storage is interface with the DC link through the bidirectional converter [7, 8]. The bidirectional converter operated based on the battery state of the charge and DC-link voltage. The battery charge controller is implemented with the
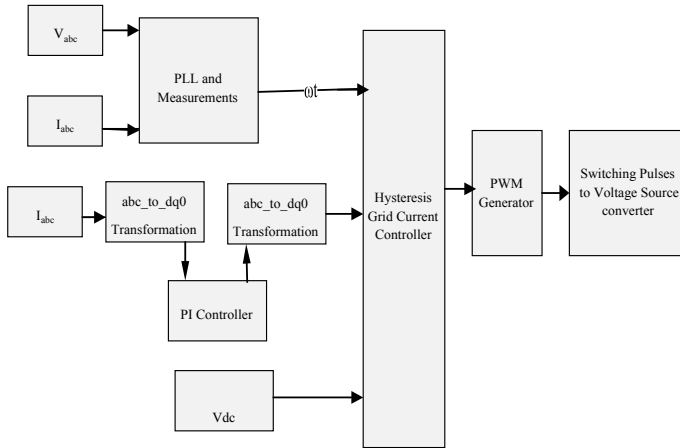
Fig. 10 Grid synchronization control unit

proportional and integral (PI) controller as shown in Fig. 11. The battery charge controllers are used to stabilize the DC-link voltage.

3 Simulation Results of Proposed System

The proposed system is simulated at 25 °C, 1000 W/m^2 standard test conditions. The 100-kW grid-connected solar photovoltaic system is simulated under dynamic irradiances, Temperature is shown in Fig. 12. At $t = 0.5$ s, the irradiance 500 W/m^2 and at $t = 1$ s varied from 500 to 1000 W/m^2. The temperature varies between $t = 1.5$ s and $t = 2$ s. The dynamic behavior of solar PV system is simulated with fuzzy controller. The boost converter output is obtained by regulating the duty cycle using fuzzy controller-based maximum power tracking method. The boost converter output is connected to the DC-link voltages. Under dynamic irradiance causes the interruption in the dc link Voltages as shown in Fig. 13. The harmonics
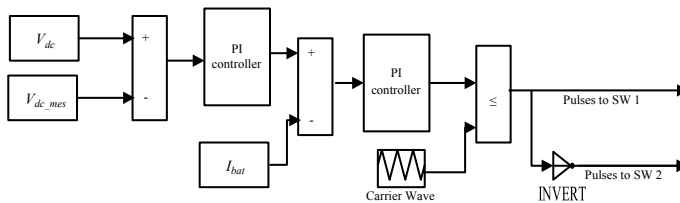
Fig. 11 Bidirectional controller

solarhysterisisswithbattery/Irradiance Temp : Ramp-up/down Irradiance
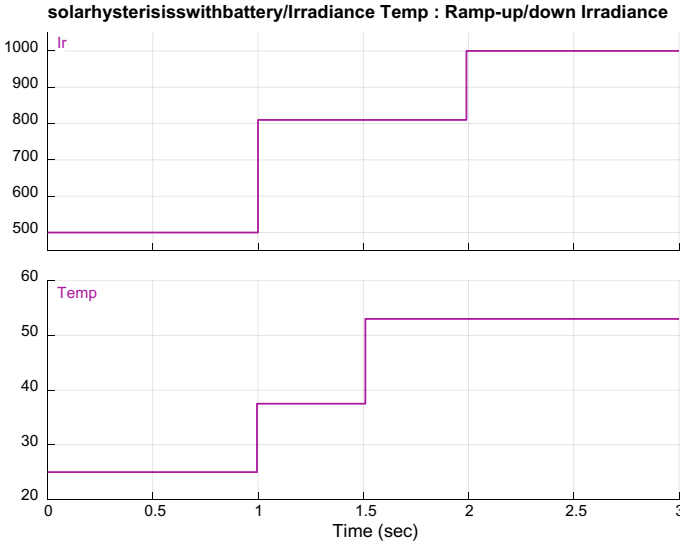
Fig. 12 Dynamic changes of irradiance and temperature

and oscillations are the presences in the grid system. This will affect the disturbance on the grid. This may lead to collapse the grid, and it will reduce the life span of the sensitive load. The power quality problem arises in the system due to changes in the DC-link voltage. The temperature also varied from 25 to 50 °C at $t = 0.5$ s. Initially, voltage source converter and the boost converter are in operation, but the voltage source inverter output and grid voltage are not in synchronism.

Two-level voltage source converter responses without filter and without battery are shown in Fig. 15. The line-to-line voltage of inverter with filter and without battery is shown in Fig. 16. The DC-link voltage with battery maintained 600-V constant voltage as shown in Fig. 14 and the corresponding inverter output
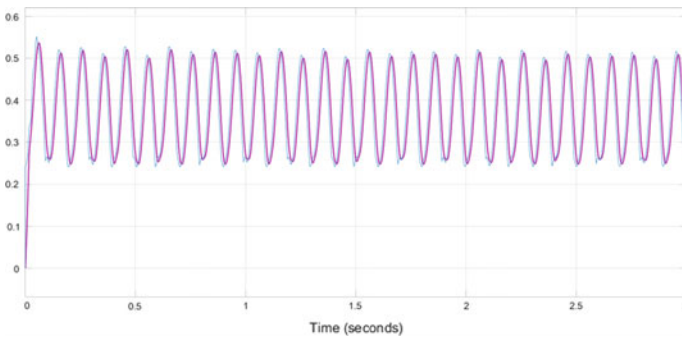
Fig. 13 DC-link voltage without battery charge current controller
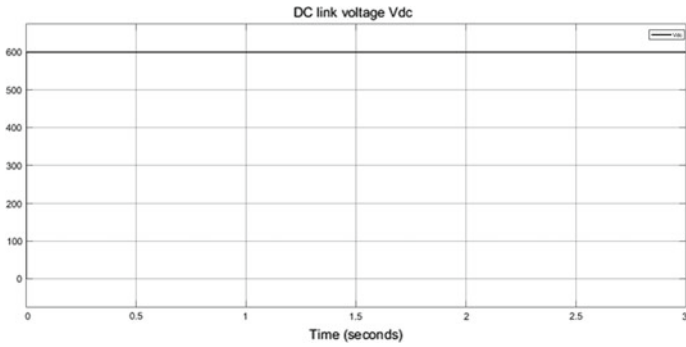
Fig. 14 DC-link voltage with battery charge controller
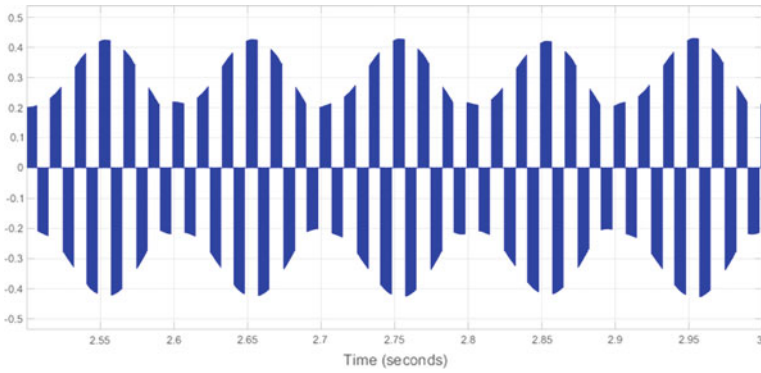
Fig. 15 Voltage source converter output without filter and battery

line-to-line voltage is shown in Fig. 17. The power quality problem can be avoided by using a PI controller-based hysteresis current control technique as shown in Figs. 18, 19, 20, and 21.
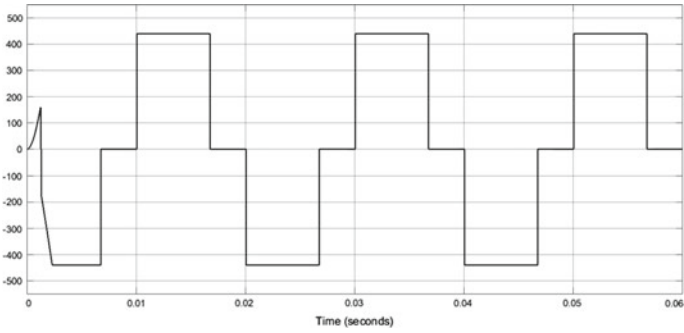
Fig. 16 Inverter line-to-line output voltages without battery controller
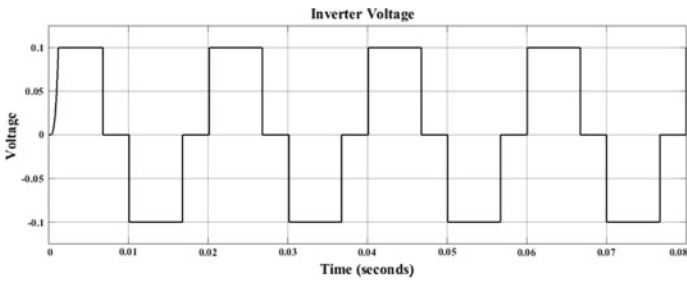
Fig. 17 Inverter line-to-line output voltages with battery controller
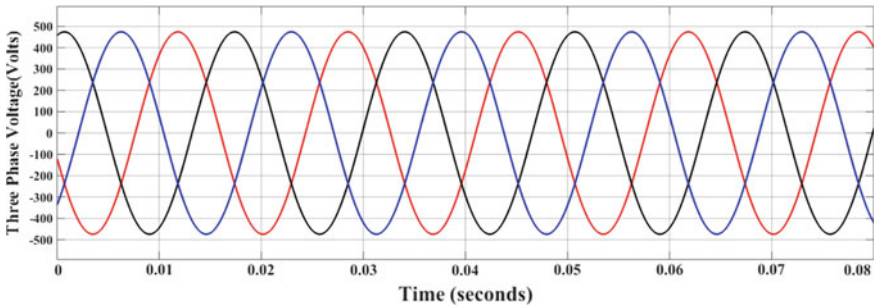
Fig. 18 Grid synchronization voltages with filter
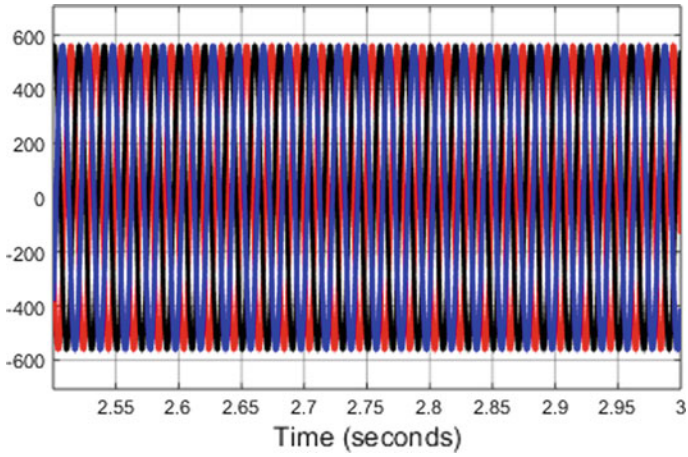
Fig. 19 Grid synchronization voltages with battery
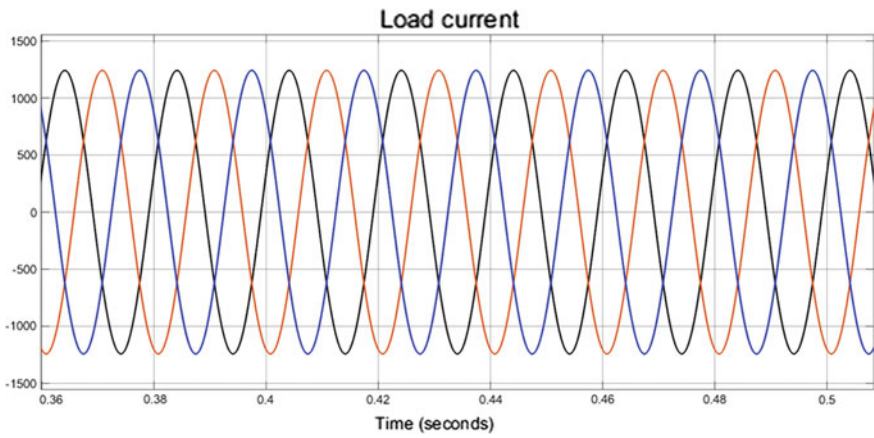
Fig. 20 Load with current controller
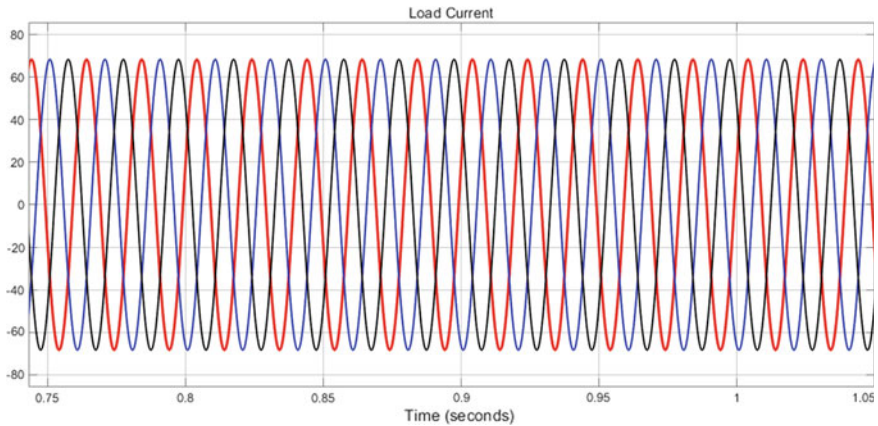
Fig. 21 Grid current with current controller

4   Conclusion

The proposed grid-connected solar PV with battery storage system is simulated under different load and source conditions. The solar PV and battery are maintaining the necessary power. The maximum power is extracted from the solar PV using fuzzy controller. The battery is stabilized with constant DC-link voltage even under dynamic irradiance and temperature. At the load end, the voltage is stabilized under grid-connected mode. The necessary smoothening power is met continuously by maintaining the appropriate DC-link voltage. The inverter and grid voltage are synchronized using a PI controller-based hysteresis current controller.

References

1. https://en.wikipedia.org/wiki/Electricity_sector_in_India#cite_note-capacity-4; June 7 2017
2. http://vidyutpravah.in/; June 9 2017
3. Liang X (2017 Mar) Emerging power quality challenges due to integration of renewable energy sources. IEEE Trans Ind Appl, 855–866
4. Chung YH, Kim HJ, Kim KS, Choe JW, Choi J (2008 Dec) Power quality control center for the microgri system. In: IEEE 2nd international power and energy conference PECon, pp 942–947
5. Sumathi S, Kumar LA, Surekha P (2015 Apr) Solar PV and wind energy conversion systems: an introduction to theory, modeling with MATLAB/SIMULINK, and the role of soft computing techniques. Springer, Berlin
6. Reddy D, Ramasamy S (2017) A fuzzy logic MPPT controller based three phase grid-tied solar PV system with improved CPI voltage. In: 2017 innovations in power and advanced computing technologies (i-PACT), pp 1–6
7. Meshram S, Agnihotri G, Gupta S (2012) An efficient constant current controller for PV solar power generator integrated with the grid. In: IEEE fifth power India conference, pp 1–6

8. Dharavath R, Raglend IJ, Manmohan A (2017) Implementation of solar PV—battery storage with DVR for power quality improvement. In: 2017 innovations in power and advanced computing technologies (i-PACT), pp 1–5

9. Saxena N, Singh B, Vyas AL (2017 Jan) Single-phase solar PV system with battery and exchange of power in grid-connected and standalone modes. IET renewable power generation, pp 325–333

Active Foreground Neural Network

Ayush Aggarwal and Subhash Chand Gupta

Abstract Active Foreground Neural Network (AFNN) is a revolutionary neural network which aims at bridging the computation, learning, and application's implementation gap across conventional neural networks and cognitive learning processes with dual-band training and application layers. The aim is to perform asynchronous and parallel training of cross-interface Artificial Intelligence models with simultaneous implementation of the same. Therefore, the user may or may not need to implement the learning model.

Keywords Active Foreground Neural Network (AFNN) · Artificial neural network (ANN) · Tensor processing unit (TPU) · OpenCL (Open Computation Library) · Compute Unified Device Architecture (CUDA) · Graphical processing unit (GPU)

1 Introduction

Artificial Neural Networks (ANNs) or simply neural networks are machine computational models based on the biological neural networks which function cognitively and approximate surrounding events [1]. Some ANNs are adaptive systems and are used to model populations and environments (or weather systems), which constantly change. Neural networks can be hardware-based peripherals and devices, or they can be software based such as computational models and use a variety of topologies and learning algorithms [2].

The computer being used here uses an Intel Core i7 8700K chipset, LPDDR4 ECC 64 GB RAM, and AORUS XTREME OC NVIDIA GEFORCE

A. Aggarwal (✉) · S. C. Gupta
Amity School of Engineering and Technology, Amity University, Noida, Uttar Pradesh, India
e-mail: highestage@gmail.com

S. C. Gupta
e-mail: scgupta@amity.edu

GTX 1080ti for trying to achieve the computational performance of a tensor processing unit (or TPU) [3]. The chipset is used for the mathematical computations of basic BODMAS strategy (Bracket, Of, Division, Multiplication, Addition, Subtraction in order) as a neuro-linguistic learning model for the learning set, instead of a Natural Learning Language, since the project is in its early stages [4]. The ECC (Error Correcting Code) RAM is used for automatically determining run-time errors in the storage for the learnt processing models [5]. Since only the machine knows in which format and how the learning model is 'learnt', ECC memory aids the computer to correct its own learnt modules. The Graphical Processing Unit (GPU) used here is for running the neural network's neurons, computation for floor and ceil functions for multi-threaded compilations and is programmed using CUDA programming (Compute Unified Device Architecture) for the NVIDIA Maxwell/Pascal Architecture [6] and in OpenCL programming (Open Core Library) for the AMD Polaris Architecture of GPUs [7]. NVIDIA Turing architecture of GPUs should be supported, since the Turing cores can be used as simplified SIMD processors.

The test environment used here uses a NVIDIA GPU. Hence, the test program is coded in CUDA programming architecture and only targets Maxwell/Pascal GPU architecture. The algorithm can be reprogrammed to support AMD Polaris GPUs as well.

This neural network can at the time only output values in the form of 0 or 1 (false or true). So, the decision specifier has to perform the function. Thus, it can tell whether a particular function has to be performed or not.

Being a completely new model for the ANN, active foreground model can perform up to two times the work a normal ANN model, for instance, how feed-forward or recurrent machine learning model work, while still being processed at the same speed and time, on the same platform. Since the format has to adapt first by the machine itself, the starting compilations are 2.5 ns slower than the other two models. But, by using ECC memory, the machine can itself make the algorithm better with every computation cycle.

2   Paper Preparation

Dependence on computers has been growing at the same pace as the computational power of the computers and development of support technologies, i.e., software, connectivity, and cross-platform communication. However, computers have never been able to make decisions or detect complex applications like speech recognition and handwriting recognition. To do this, a fairly recent field in computer science was developed, called Artificial Intelligence (or AI). Artificial Intelligence is the intelligence demonstrated by machines. An AI-enabled computer or machine can mimic "cognitive" functions which are exhibited by any human brain, like remembering and learning. AI research and development is subdivided into many, yet specific problems, and is utilized for solving particular problems. There are four different models of artificial intelligence, one of them being neural network-enabled

AI systems. Over the years, artificial intelligence has grown immensely and has been contributing to the growth of new industries, such as drones and self-driving cars, becoming the biggest creator for autonomous and automotive industries. The world has always depended upon computers and with the advent of artificial intelligence, is likely to underpin further development as it offers possibility of mimicking humans.

In this research paper, we try to create a new type of neural network model, which can perform the same type of predictions as a recurrent, or a feedforward neural network, but at a reduced number of neurons (or hidden layers), thus reducing the learning time, compilation time, and the executing time for the same amount of input nodes. The device peripherals used for the project are Intel Core i7 8700K 4.2 GHz, LPDDR4 ECC 64 GB RAM, and AORUS XTREME OC NVIDIA GEFORCE GTX 1080ti.

3   Active Foreground Neural Network

Active foreground neural network (AFNN) means a neural network which can actively perform data calculations, predictions, and compilations while executing data in the background because of HYPER-V (or hyper virtualization technique) threading, which can turbo boost the CPU or the GPU for a limited time (1–100 ms) [8]. Thus using multithreading, this ANN model can outperform any other neural network model when running off the same platform.

The ideal test environment includes even number of input nodes and requires only 1 neuron to start computations. The program is designed in such a manner that if the machine feels it needs more than one neuron, it can create as many as it wants. In this experiment, the program maxed out at 128 input nodes and 4 neurons to perform 2860 computations and still be able to do live calculations faster than feedforward and recurrent models.

The test program here is an Unreal Engine 4 [9] game which uses bot system to fight against the human players and against computer bots as well. The codebase is purely written using C++, Vulkan (Windows Operating Systems) and Metal (macOS) APIs, CUDA, OpenCL and OpenAL (Open Audio Library) APIs. The textures and shaders are created in blender. The entire game is created on a Windows machine with the aforementioned specifications. The neural network algorithm was created using MATLAB and then ported to C++.

The neural network is capable of deciding which parts of the human player to hit to injure the player the most, while also being able to compute which parts of the bot to be saved when the human player is firing the bullets at the bot. Thus, the game learns how the players are playing and has the capability to access Amazon Web Servers (AWS) servers for storing the learnt models for different players, if the game is being played remotely. If the player is creating a server on his/her computer, the RAM on the computer will be used for storing the learnt model.

To preserve the learnt models once the PC is shut down, the models are converted to binary code and saved as a non-accessible file in the hard storage bays (usually RAID 0).

There are 5–8 different parts of the player where the computer bot can hit, namely hands, legs, torso, lower body, backbone, and the head. To decide among these, the network first looks at which parts affect the health least, and start reducing the input vector down the number where the bot can actually hit. The computation is done for every 10 rounds fired, out of which usually 2–3 are entered into the input vector. The elements of the input vector are then put into the input nodes for the computation to start. The length of the vector has to be an even number, or the neurons will create problems in the calculation of the exponential error function.

The neuron or the "hidden layer" performs the calculations by recurring the value through another exponential function, and then, it gives the output as a single value of either 0 or 1. 0 means the computer bot should not hit the targeted location, and 1 means the computer bot can hit the targeted location.

This neural network model can be tailored for any purpose in the future and will not be limited to only 0 and 1 (or false and truth). For example, the network can make approximations such as finding out the real image from an edited one, given that the second vector is either the rasterized pixel values of the filter or the same edited image with different editions. Similarly, the machine would be able to suggest new kinds of filters depending upon how the person edits a photograph.

The hidden layer consists of perceptrons and neurons, much like the conventional neural system of the human body. Perceptrons are the "think" center of the neural network, which reduces its errors depending upon the computation cycle, computation count, and the value of regression error. The output which comes in the form of 0 or 1 is what defines the output of the bot system. Since the controls of the bot system include firing, movement, path tracing, shortest distance retrieval and most vulnerable place for the bot to fire on the user, the perceptron output is the final stage for the decisions made by the bot. Neurons are the connection systems, much like the spinal cord and nerves of the human body. A single neuron controls four different axons, which are the learning centers of the neural network. Once the model gets accepted completely by the axons, the data is sent to the perceptrons using regression. The learnt model is saved in the RAID 0 and 1 division of the hard drive, since there is no immediate need to access the data.

4   Implementation

The neural network's mathematical module is created in MATLAB, and the initial learning protocols were implemented as MATLAB simulations. The algorithm is then rewritten in C++ (using Vulcan and Metal APIs), and the implementation is done in CUDA (for NVIDIA GPUs) and OpenCL (for AMD GPUs). The entire algorithm-oriented codebase is then ported to Unreal Engine 4. The game, being

Table 1 Hamming distance relations for input and output bipolar vectors

S. No.	Hamming distance relations		
	Input set-bipolar vector	Output set-bipolar vector	Hamming distance
1	0	0	0.1230840234
2	500	1000	0.149924798
3	1000	2000	0.159244938
4	1500	3000	0.183928499
5	2000	4000	0.292849289
6	2500	5000	0.402040023
7	3000	6000	0.5839398
8	3500	7000	0.739483
9	4000	8000	0.918439498
10	4500	9000	0.8018449

developed in this game engine, uses the ported codebase. The bots use the output from the neural network and act as a plug into the entire game. Therefore, the AI of the game gets developed and the bots can communicate in real time with the neural network.

The difficulty of the game rises with the passage of time. Therefore, the amount of time spent on playing the game is directly proportional to the amount learnt about the way the player plays (Table 1).

Figure 1 shows the curve of hamming distance between input bipolar vector and its corresponding output bipolar vector. The logarithmic curve shows the stability of fuzzy set calculation for the neural network.
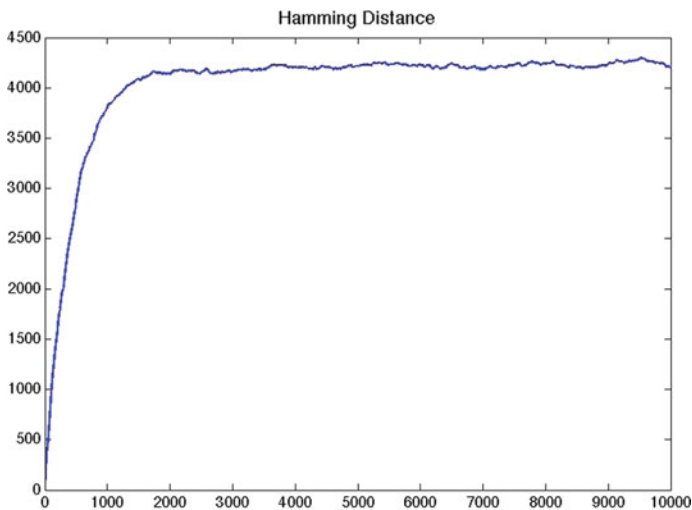
Fig. 1 Hamming distance relation between input and output bipolar vectors
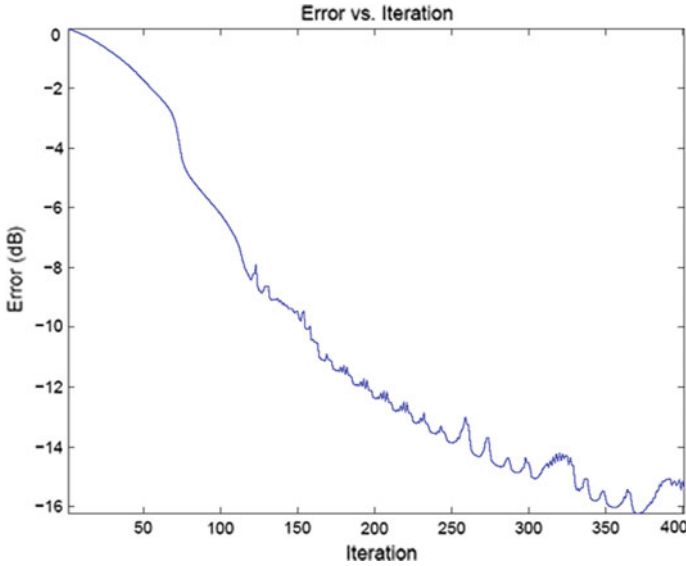
Fig. 2 Graph of error to iteration

Figure 2 is a graph comparing error (in dB) in detection to iteration count. Iteration ranges from 0 to 400 on the *X*-axis, and the error ranges from 0 to 16 dB on the *Y*-axis.

AFNN is currently under development and can thus give output of only 0 and 1. But with further elaborations and work, this neural network can outperform all other models while running active calculations on a TPU (Fig. 3).

5 Equations

The equations for execution of the neural network are:

- $O(x) = \frac{1}{1025} \cdot \int e^{\frac{-x}{dt}} dt$

$O(x)$ function is for the forward regression of values from the input nodes to the hidden nodes for the forward regression algorithm. These values include a range from (0, 1), where 0 and 1 are not included. This is to prevent any direct interjection for the output nodes as the computation of values depends upon the cycles per second.
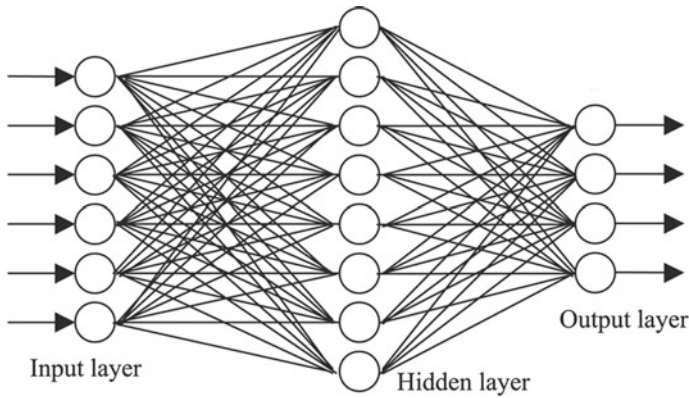
Fig. 3 Visual demonstration for a common application of Active Foreground Neural Network

- $\phi(x) = 1 + \frac{e^{-0.174x}}{e^{-0.43}} + \beta$

  $\phi(x)$ is the function which determines which regression cycle value has to go where in the four-node hidden layer system.

- $\beta = \frac{1}{e^{-0.3}} \int (e^{\frac{-x}{dt}} \cdot \log x)dt$

  β is the constant which derives its values from the CPU cores operating frequency to bring the value close to 12 float point average to maintain a standard 17.8 TFLOPS output when the calculation is going on in the background and the game is being rendered in the foreground.

- $\theta(x, y, z) = \frac{[\{(x,y) \times (y,z)\} - \{x,y,z\}]}{[e^{-x} + e^{-y} + e^{-z}]}$

  $\theta(x, y, z)$ takes three parameters, where each parameter is the input taken from the forward regression cycle.

- $\alpha(y) = 0.194 \cdot \log(\theta(x, y, z))$

  $\alpha(y)$ takes the third input vector as the input for the function α. The returned value is a constant which is then used in the calculation of regression error

- $\mathrm{Err}(x, y) = \frac{[\alpha(y) \cdot e^{\phi(x)} \cdot O(x)]}{1 + e^{-O(x)}} - Err(x, y)$

  $\mathrm{Err}(x, y)$ function is for finding the error during the back tracing or recurrence of the computation values from hidden layers to input nodes.

- $\omega(x, y, z) = \left[\frac{\omega(x,y,z)}{\alpha(y)} - Err(x, y)\right] \cdot 0.192$

$\omega(x, y, z)$ is the function which gets the reverse values from last hidden layer to the input layer for value of range (0, 1).

- $\rho(x, y) = \left[\frac{\log(x)}{e^{-0.5x}}\right] + [\phi(x) \cdot \omega(x, y, z)]$
- $\psi(z) = \rho(x, y) \cdot \alpha(y) \cdot \left[\frac{\theta(x,y,z)}{\beta - Err(x,y)}\right] \cdot Err(x, y)$
- $\gamma(x, y) = [\psi(z) - \alpha(y)] \cdot \frac{\omega(x,y,z)}{\theta(x,y,z)}$

$\rho(x, y), \psi(z)$ and $\gamma(x, y)$ are foreground and background constants which reduce the regression error generated by the $Err(x, y)$ function and help close the gap between the projected value and the real value.

6 Testing

When the game is launched from the Unreal Engine Editor, in debugging mode, the output can be seen in the console. The test bench is an Alienware 17 with Intel Core i7 8700K 4.2 GHz, LPDDR4 ECC 64 GB RAM, AORUS XTREME OC NVIDIA GEFORCE GTX 1080ti, and Windows 10 Creator's Update with Vulcan API beta running in the background for the dedicated GPUs. The game is a server-based session, which can be started on the computer, with the bots enabled. The GPU gets switched automatically from integrated to dedicated. But since the graphical requirements of the game are very high, the game can run at the lowest setting on a single GTX 960m with LPDDR3 8 GB RAM.

7 Uses

This neural network, being like all other AI models, can perform image recognition, video comparison, handwriting recognition, and natural language processing. The advantage of using this model over others is that it can reduce the number of layers, thus reducing the computation cycles required to do the same job, has higher efficiency per unit time, and has higher performance output per unit watt, so it is lighter on the computational requirements. These changes are most noticeable on very high-performance machines such as gaming computers, server rigs, and data farms. Since the network is in its developmental stage, it can only answer yes or no and determine real images from edited ones. But with further development, this neural network model can outperform many other neural network models.

8 Conclusions

AFNN is a very young artificial intelligence model, which is a very niche area in the field of computer science. Currently about 40% of all computers in the world are using artificial intelligence in some form. But with the advancement of both hardware and software technologies, artificial intelligence will someday be used throughout the world. AFNN is an attempt to refine the process which bridges the gap between developers and the general consumers by being both lightweight and fast.

References

1. Butler S (1863 June 13) Darwin among the machines. Letters to the editor. *The Press*. Christchurch, New Zealand. Retrieved 16 October 2014, via Victoria University of Wellington
2. Hochreiter S (1991) Untersuchungen zu dynamischen neuronalen Netzen. Diploma thesis. Institut f. Informatik, Technische Univ. Munich. Advisor: J. Schmidhuber
3. Hochreiter S et al (2001 Jan 15) Gradient flow in recurrent nets: the difficulty of learning long-term dependencies. In: Kolen JF, Kremer SC (eds) A field guide to dynamical recurrent networks. Wiley, New York. ISBN 978-0-7803-5369-5
4. McCulloch W, Walter P (1943) A logical calculus of ideas immanent in nervous activity. Bull Math Biophys
5. Werbos PJ (1975) Beyond regression: new tools for prediction and analysis in the behavioral sciences
6. Jouppi N (2016 May 18) Google supercharges machine learning tasks with TPU custom chip. Google Cloud Platform Blog. Google
7. Christopher H, Paul W (2010 Dec 21) Social engineering. Wiley, New York. ISBN 978-0-470-63953-5
8. ACM (1998) ACM computing classification system: artificial intelligence. Retrieved 30 Aug 2007
9. Serenko A (2010) The development of an AI journal ranking based on the revealed preference approach (PDF). J Informetr 4(4):447–459

A Skywatch on the Challenging Gradual Progression of Scheduling in Cloud Computing

Ashish Tiwari and R. M. Sharma

Abstract The continuing innovation across new and existing wireless technologies presents challenges in designing and testing of features, modules, and devices that makes the connected world possible. In computing system, the end users have to follow the basic idea of cloud computing, i.e., pay and use. The most vital continues to be at the forefront offering a full portfolio of test and designing ways that defines the overall process of the computing and its simulation. According to research and development teams, the overall view is verified and issued with all the computing service level agreements. The concept of scheduling is being achieved by the high-performance computing and efficient throughput. Computing system is a heterogeneous view, and the increasing speed of the computer systems and services is increasing rapidly. Cloud computing is the best viral technology which is increasing drastically. The best effective working of cloud computing for the job scheduling is to provide maximum profit to cloud service providers. This algorithm is the future proof, making it easier to evolve with changing technologies and stay on the leading edge. This algorithm efficiency design and test are available to advise, assist, and augment cloud computing all around the world. Fundamentally, the arrangement of standards works for the extraordinary bolstered booking between cloud benefit bearers and cloud clients. The cloud brokers are betting a basic part inside the offerings outfitted by methods for the CSPs.

Keywords High-performance dynamic computing · Cloud providers · Scheduling algorithms · Rough set theory · Datacenters · Users · Parameters · Cloud simulator

A. Tiwari (✉) · R. M. Sharma
Department of Computer Engineering, NIT Kurukshetra, Kurukshetra, Haryana, India
e-mail: ashishtiwari_6160081@nitkkr.ac.in

R. M. Sharma
e-mail: rmsharma123@rediffmail.com

531

1   Introduction

In recent world, the foremost issues to examine here are that it plays a very important role in businesses. The development in business style users wishes to avoid wasting lots of their money, time, performance, etc. Basic demand required for this technology is web. Cloud computing could be a combination of computation, software and knowledge access and additionally provides storage services [1–4]. In cloud, the major issue is the storage data and its management does not seem to be glorious to the user. It gets the features which are being provided by the providers such as IaaS, PaaS, SaaS, virtualization, resource provisioning, and data security. The cloud has a lot of benefits and is straightforward to implement with any business logics. Cloud delivers services from totally completely different knowledge sources and servers set on different geographical locations; however, the user gets single purpose of read from the cloud service. The computing service suppliers are to blame for delivering end users requirements as a service with the efficient cost and time. The topmost cloud service providers are as follows AWS, Google, Sale Force, Oracle, etc. [5]. Each CSP has its own method of providing services [4, 6]. The research of the artifacts provided by varied cloud customary generating suppliers that things providing the assorted agreements and security shows that each and every coming requirement is being classified on the basis of various parameters (Fig. 1).
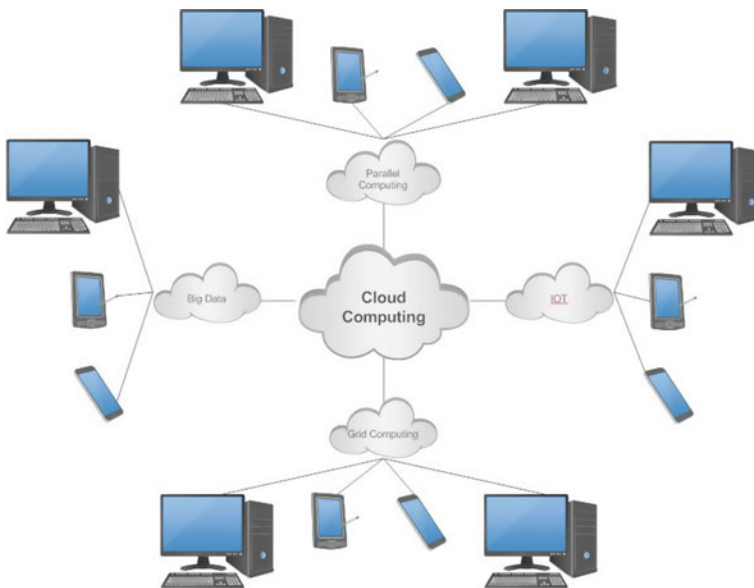
Fig. 1 Basic cloud services

The purpose of framework for estimating price and verify have the benefit of computing is one of the best traditional advanced technology infrastructure, like in private in hand and managed advanced technology hardware. The research in this field provides the most motivated by the rapid increase of advanced computing suppliers so that the industry is moving towards the hardware resources in the advanced computing technology [6, 7]. Cloud is that the delivery of IT services through the web. Cloud service suppliers host applications and supply computing power from its information centers, cashing in on huge economies of scale and dramatically lowering the prices of IT. Virtualization could be a key feature of cloud.

2 Problem Statements

Customers may need that their applications area unit hosted on hardware that's specific to them, instead of on shared hardware. There ought to be Associate in nursing access privileges between cloud suppliers and cloud customers. This may defend the unauthorized access, authentication procedure area unit followed for permitting user to access their information in cloud. The technology is growing rather like net use to grow in its time. The way of collecting the providers among the big database of the advanced computing technology with the concept of which Cloud Provider Provides What type of service to which extend. So, the major questions come in the mind of the researchers that:

1. How much big data will be safe with the cloud?
2. Can anyone tell the best security aspects provided by the provider are sufficient?
3. What is the ways by which any one trust to cloud?
4. What are the key aspects of open source software?
5. What is the concept of datacenters in cloud technology?

3 Literature Survey

The literature deals the major area of computing technology and analysis the things with their values and model best applications wherever information collected throughout the survey would be accustomed infer results. A group of parameter necessities and pointers area unit devised for cloud platform and repair. As per analysis, when undefeated implementation of algorithmic program at the broker aspect, it is operating pretty much as good as different projected algorithms. In our algorithmic program tend to area unit handling the Rough Set and Fuzzy pure mathematics at broker aspect [8–10]. By the utilization of such properties tend to have gotten higher results as compared to antecedently developed algorithmic program.

3.1 Cloud Utilities

The cloud utilities are the most important and are divided into three major parts; i.e., infrastructure as a service (IaaS) gives the best and efficient use of data storage, resource providing systems, computing network technology for the end users. IaaS users can deploy the best technological application, system software, the operational systems on the infrastructure that is capable of scaling dynamical change. Platform as a service (PaaS) provides the most dynamic and recent integrated technological environment to develop, run, and simulate with the host customer designed or congenital technological applications. Software as a service (SaaS) may well be a package delivery model throughout those technological applications given by the providers in an efficient way. The end users need not be the part of anyone provider [11, 12]. In all the most effective renowned is that the answer for its client Relationship Management (CRM) (Fig. 2).

3.2 Cloud Service Providers

Amazon Cloud Drive: Its space for storing is often accessed from up to eight specific devices. The devices are often mobile devices, completely different computers, and completely different browsers on identical PC. The device limit is often

Fig. 2 Connectivity in cloud computing

reached if applications' programmed cookies do not seem to be keep or area unit deleted. The Google technology in computing platform could be a portfolio of advanced computing services provided by the Google service providers, that's giving hosting on identical the best advanced infrastructure which should be provided by the Google will be provided to the end users. It absolutely was supported and supported open supply technologies like Solaris ten, Sun Grid Engine, and also the Java platform [11].

3.3 Cloud Parameters

There are several programming parameter algorithms projected at the broker facet as well as A Brokerage-Based system is the most advanced computing system to the selecting the best and efficient services. The following could be a straightforward framework system that identifies the best-suited parameters that facilitate to gauge initial cloud risk and inform security selections in programming [10, 11, 13]. Commerce Systems and their Safety Features: It deals with the problems that however processes and procedures area unit outlined to implement Commerce Systems and safety ways. Technological Application with Advanced Security system: It deals with the factors and risks that could prevail in securing application software for a cloud. How the end users are sure? What should be the major steps take to sure the data of users? How the end users become trusted fully to a provider while providing his personal details?

Advanced Key Management System: It deals with the proper identified measures for scalable key management. How one can believe the given agreements? How much such agreements are being trusted? What should be the key trust value to the end users? Advanced Virtualization System: It is the main works with the foremost problems like AVM isolation, AVM co-residence, multi-tenancy Systems; Advanced hypervisor vulnerability etc. The foremost part of advanced virtualization in cloud is relating to the protection problems. How the user has proper information about the AVM? Is end user able to use the concept of AVM? There are a lot of questions on which the researcher have gone thought parameters and how these should be solved.

3.4 Cloud Broker

A broker in computing is applicable between the providers and the end users who play a vital role in providing the most efficient services. The brokers take care of end users and the provider so that there should be no issues in providing the efficient services [14, 15]. The broker's view is always different by saving lots of the user's efficient time by researching suitable services from overall world compression to the suppliers and providing to the end users with data concerning a way

to use cloud computing to support business goals. In such a state of system, brokers are the middle man so the attacks are mostly done in this section, and the broker works with the end users to grasp work processes, data provisioning, budgeting and advanced data system management needs.

3.5 Cloud Scheduling

Scheduling implies that defined for the resources services so that the resource should be provided to the end users over time so as that service on demands should be met throughout a timely and worth effective way. The economical efficient utilization in resources should be vital and for that programming plays a significant role to urge most have the benefit of the resources [14, 16, 17]. There have been varied forms of scheduling formula existing in distributed automatic data processing system. There are a lot of classification algorithms and job scheduling algorithms in the advanced computing algorithm [18–20].

4   Proposed Technique

The method of exploitation differing kinds of programming algorithms to execute in services and also the method by that the resources are being provided by the supplier's are being studied in massive views. During this space, plenty of labor goes on like task in associate ordered method and also the knowledge arrival of the services on the premise of competition. Currently, the research workers are attending to touch upon the conception of rough set theory technique; as per the conception of RST, the analysis says that it is an organized method of dealing the data within which the worth of data is to be seen. The values of data with the set of various objects are being thought about. The objects are being known on the premise of some characteristics. The method by that the information is to be employed in several algorithms to seek out unallocated characteristics, to spot the methodology of reduction of information's, to spot the worth of information that however necessary is that the information, to spot the numerous place wherever and by that ways that the data is being employed, to spot the foundations by that data sets are going to be maintained and the way to get the economical results on the premise of knowledge. The RST is employed by the algorithms to support the mathematical methodology that supports the conception of data processing and multiprogramming. The fundamental issue that the RST deals is that the extensions and equally that is being found in numerous applications within the world [21]. The RST deals with the conception of approximation, the higher approximation, and also the lower approximation; these two ideas are currently being employed in developing the model that is providing the economical values. Rough sets cannot be outlined in victimization supported data. That the sets are being created on the

premise of approximation that is offended paired with the crisp sets that is claimed to be the lower and higher approximation. This approximation conjointly deals with some boundary values that are terribly effective in several places. Once applying the algorithmic program, the data table is being received and also the information table is the base table of all values. The columns of knowledge table offer elaborate description of attributes and rows for objects of the table. Such table's square measure is stated as data systems, attribute-value tables, or knowledge tables. The tendency to square measure proposing a consistent quite approach but to tier over that of job coming up with [21]. In cloud techniques, the providers of the cloud services have taken care of efficiency of the services so that the broker which is working as a middle ware gives the best service provider to the end users. The broker works for both the people (CSP and end users). The cloud broker works on the algorithms with the help of RST in which the service will be best. The RST handles objects and its characteristics. In this, information table services provided by the provider are the objects like information operation system, legal problem issues, the risk management system, interoperability and immovability of the datacenters, information center operations and their techniques, the key management system, the identity, protection, virtualization, and security of information. In the protocol, there are a unit variety of cloud services provided by the providers in which can contain the quantity of datacenters where the information is being stored. The rule elaborates, however, a tendency to maintain the services using RST in the cloud broker where the efficient service will be provided [21].

5 Result and Simulation

In the simulation, it is viewed that the results that but revised ROSP are providing the efficiency become higher than the ROSP algorithm. The time it got to boot examine some interface graphs that are compared with the previous algorithm. The interfaces results are plenty of clearly delineate but the results are over ROSP algorithm. The computing technique forms thanks to the advancement of technological world to induce economical, sure, well-established correct, minimum price and time. Moreover, these services are additionally offered in private datacenters (private clouds) and additionally commercially offered for purchasers (public clouds), or all the same it's come-at-able that every public and private clouds are combined in hybrid clouds.

5.1 Cloud Simulator

The cloud machine is employed to simulate the high speed of many events of advanced application provisioning algorithms within the technological computing.

Cloud machine is also a toolkit that is capable of simulating the system in cloud. The initial base for describing the datacenters, VM, advanced applications, resource provisioning and also the rules of managements in numerous ways that [12, 22]. The aim of cloud simulation is to produce a well-outlined structure of the performed algorithms underneath the implication of machine. The cloud computing permits the users to specify the services that are being needed by the users and to simulate the service with the suppliers. Within the initial work of analysis in RST within the broker the analysis was developed is ROSP algorithm, in Simulation it got used some existing packages of CloudSim to create Cloud Service suppliers, Datacenters, Network etc. The initial packages are being employed within the Internet beans of the cloud machine [22].

5.2 Results

The main goal of the analysis is to use the foundations within the RROSP algorithms; as per rule, the eight parameters have taken total time and economical processor utilization of the algorithm for mounted values. The graph represents the full time taken in unit of time denoted with ms to execute the algorithm by altogether completely different CSPs with increasing variety of users. From the rear of the portrayed graph, it is seen that, however, the rise within the quality and execution of algorithmic program is being performed. By increasing vary of Datacenters put together affects in sight of graph. The calculated for fifty datacenters. The full time taken by the CSP is directly proportional to the quantity of cloud advanced parameters [23, 24].

(1) Result 1: inside the viewed graph its tendency to face live representing the economical processor Utilization proportion to execute the algorithmic program by completely different CSPs with increasing variety of users. The economical processor utilization conjointly will increase exponentially to lot of users and however decrease with increasing number of CSPs. It is clearly ended that if there is increase in the resources in a very system, the economical processor utilization decreases. The increasing variety of datacenters conjointly affects the ensuing graph. The calculated for fifty datacenters. The economical processor utilization by the CSP is directly proportional to the quantity of cloud parameters. It's taken eight Parameters the system Configuration affects the economical processor Utilization. The below graph shows the processor utilization running on Windows Ten, Intel Core i7 Processor, Ram 4 GB, disk (1 TB) (Fig. 3).

(2) Result 2: The full time taken by the CSP is directly proportional to the quantity of cloud advanced parameters which is being calculated. The time of arrival and also the time taken by the supplier to produce the service are being calculated and being known between CSPs and also the finish users. The graph shows the time taken by the algorithmic program higher than configuration system (Fig. 4).
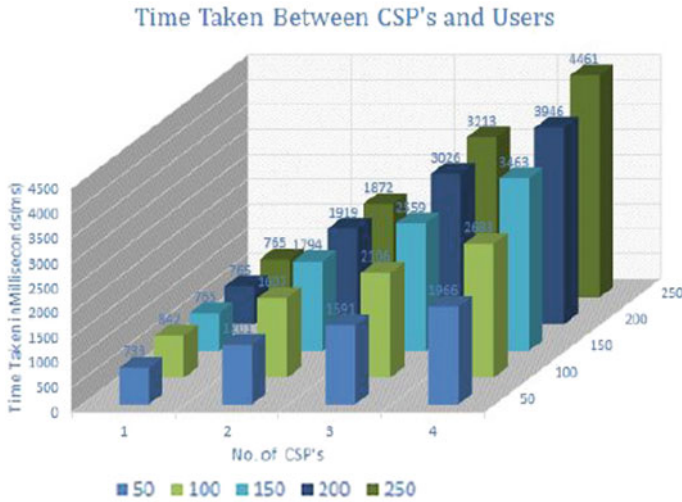
Fig. 3 Time taken between CSPs and users
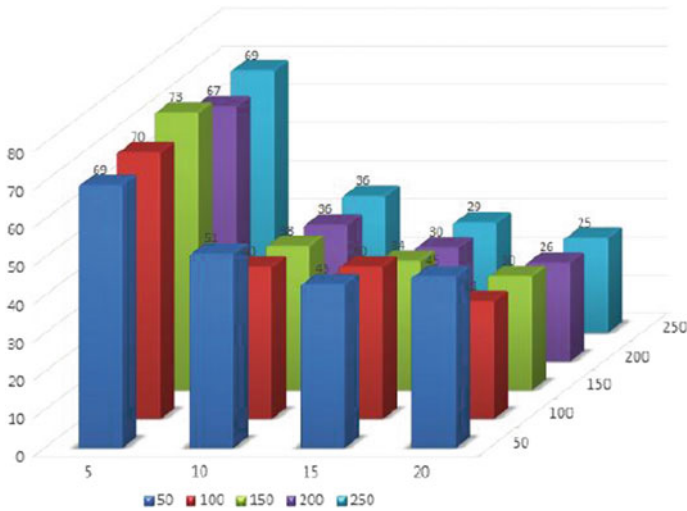
Fig. 4 CPU utilization between CSPs and users

6 Conclusion and Future Work

The planned system touch upon the conception of RST conception employed in the computing service within the cloud machine. There is plenty of computing service that is being taken into thought so there ought to be straightforward to spot the

acceptable parameters. There are completely different datacenters, CSPs, end users, cloud brokers that play an important role. The tenant desires to not determine the service needs before submitting their job to the cloud. The work of the center ware is incredibly necessary and is taken in thought with correct approximations. The algorithms are managing the time situation wherever the research worker show the experimental read of the data table. If needed, the top users are capable of obtaining the simplest services on the algorithmic program productive. The conception of ontologies is to be superimposed that the performance might increase. The analysis is additionally being needed to spot the value supporting the capabilities of the service and also the suppliers.

References

1. Armbrust M et al (2009) Above the clouds: a Berkeley view of cloud computing, vol 4. Technical Report UCB/EECS-2009-28, EECS Department, University of California, Berkeley
2. Weiss A (2007) Computing in the clouds. networker 11(4):16–25
3. Buyya R et al Cloud computing and emerging IT platforms: vision, hype, and reality for delivering computing as the 5th utility. Fut Gener Comput Syst 25(6):599–616
4. Mell P, Tim G (2011) The NIST definition of cloud computing
5. Klems M, Jens N, Stefan T (2008) Do clouds compute? A framework for estimating the value of cloud computing. Workshop on e-business. Springer, Berlin
6. Tiwari A, Sah MK, Gupta S (2015) Efficient service utilization in cloud computing exploitation victimization as revised rough set optimization service parameters. Procedia Comput Sci 70:610–617
7. Calheiros RN et al (2011) CloudSim: a toolkit for modeling and simulation of cloud computing environments and evaluation of resource provisioning algorithms. Softw Pract Exp 41(1):23–50
8. Heilig L, Voß S (2014) A scientometric analysis of cloud computing literature. IEEE Trans Cloud Comput 2(3):266–278
9. Van den Bossche R, Vanmechelen K, Broeckhove J (2011) Cost-efficient scheduling heuristics for deadline constrained workloads on hybrid clouds. In: 2011 IEEE third international conference on cloud computing technology and science (CloudCom). IEEE, New York
10. Nair TRG, Sharma V (2012) A pragmatic scheduling approach for creating optimal priority of jobs with business values in cloud computing. In: ACC 2012
11. Gutierrez-Garcia JO, Sim KM (2013) A family of heuristics for agent-based elastic cloud bag-of-tasks concurrent scheduling. Fut Gener Comput Syst 29(7):1682–1699
12. Ergu D et al (2013) The analytic hierarchy process: task scheduling and resource allocation in cloud computing environment. J Supercomput 64(3):835–848
13. Younge AJ et al (2010) Efficient resource management for cloud computing environments. In: 2010 international green computing conference. IEEE, New York
14. Chhetri MB et al (2013) Smart cloud broker: finding your home in the clouds. In: 2013 IEEE/ACM 28th international conference on automated software engineering (ASE). IEEE, New York
15. Nair TRG, Sharma V (2012) A pragmatic scheduling approach for creating optimal periority of jobs with business values in cloud computing. In: ACC 2012s
16. Tiwari A et al (2013) A cloud computing using rough set theory for cloud service parameters through ontology in cloud simulator. In: ACITY-2013 conference at Chennai, in CS and IT proceedings

17. Komorowski J et al (1999) Rough sets: a tutorial. In: Rough fuzzy hybridization: a new trend in decision-making, pp 3–98
18. Yan-hua Z, Lei F, Zhi Y (2011) Optimization of cloud database route scheduling based on combination of genetic algorithm and ant colony algorithm. Procedia Eng 15:3341–3345
19. Mahrishi M, Shrotriya A, Sharma DK (2012) Globally recorded binary encoded domain compression algorithm in column oriented databases. Glob J Comput Sci Technol (2012)
20. Liu H, Xu D, Miao HK (2011) Ant colony optimization based service flow scheduling with various QoS requirements in cloud computing. In: 2011 First ACIS international symposium on software and network engineering (SSNE). IEEE, New York
21. Q Z, Lu C, Raouf B (2010) Cloud computing: state-of-the-art and research challenges. J Internet Serv Appl 1(1):7–18
22. Buyya R, Yeo CS, Venugopal S (2008) Market-oriented cloud computing: vision, hype, and reality for delivering it services as computing utilities. In: 10th IEEE international conference on high performance computing and communications, 2008. HPCC'08. IEEE, New York
23. Tiwari A, Nagaraju A, Mahrishi M (2013) An optimized scheduling algorithm for cloud broker using adaptive cost model. In: 2013 IEEE 3rd international advance computing conference (IACC). IEEE, New York
24. Mahrishi M, Nagaraju A, Rating based formulation for scheduling of cloud service providers. National Conference on emerging treands in IT
25. Tiwari A, Sharma RM (2016) Potent cloud services utilization with efficient revised rough set optimization service parameters. In: Proceedings of the international conference on advances in information communication technology & computing. ACM, New York
26. Pawlak Z (2012) Rough sets: theoretical aspects of reasoning about data, vol 9. Springer Science & Business Media

DCHD-3T: Early Diagnosis of Congenital Heart Diseases in WBAN-Cloud Using Three-Tier Network Architecture—an Efficient Solution

Sonal, S. R. N. Reddy and Dinesh Kumar

Abstract Most of the state-of-the-art research papers have discussed only common abnormality detection. This proposed work aims to diagnose congenital heart defect (CHD) in new-born babies. By monitoring different physiological parameters in neonates, CHD in neonates is detected in early stage. The designed WBAN environment is **three-tier architecture**. This three-tier architecture is comprised of entities as body sensor, hub, base station, and diagnosing server. Each of the processes is segregated in each tier such as data aggregation, authentication, channel selection, and classification. IEEE 802.15.6 standard is used in WBAN by which identification of the criticality and allocation of high priority will be done. Then, hub prefers the best channel to transmit the sensed reports without any packet loss. The sensed data reaches diagnosing server from the base station. Diagnosing server is responsible to classify the sensed data according to its severity (normal and critical). Early diagnosis of CHD in neonates using WBAN is not addressed in any of the previous works; so, this paper presents an efficient solution for diagnosing CHD.

Sonal (✉)
Indira Gandhi Delhi Technical University for Women, New Delhi, India
e-mail: sonal.gahlot14@gmail.com

S. R. N. Reddy · D. Kumar
Dr. Ram Manohar Lohia Hospital and Post Graduate Institute
of Medical Education and Research, New Delhi, India
e-mail: rammallik@yahoo.com

D. Kumar
e-mail: dineshkumar169@yahoo.co.in

543

1   Introduction

Wireless body area network (WBAN) is an emerging network which is enabled to offer ubiquitous health-based monitoring environment. WBAN is applicable for both real-time and non-real-time applications. Security also exists in this type of network to break the confidentiality. WBAN is enabled to work with the Internet of Things and Cloud for aggregating information and to make use of it [1, 2, 3].

WBAN-IOT is the reliable approach through which various limitations of previous work can be removed. This paper presents an efficient solution of this approach for early diagnosis of congenital heart disease (CHD). Early diagnosis of CHD in neonates using WBAN is not addressed in any of the previous works; hence, this is the first work to present WBAN for early diagnosis of CHD.

2   Related Works

A four-tier architecture was designed in a previous work [4] which involves classifying, scheduling, and abnormality diagnosis. The four-tier architecture is proposed for remote monitoring system (RMS) which carries over the following process such as classification, scheduling, and vertical handover decision. The classified packets are scheduled based on priority-weighted round robin, in which the data are mapped to its priority and segregated into four classes and scheduled. QoS guaranteed vertical handover is supported by taking into account of the following two parameters such as latency and reliability. This overall network architecture aims to minimize delay and increase throughput. Classification needs to be performed faster to provide immediate actions. Previously, IEEE 802.15.6 standard used Slotted Aloha for data transmission which results in higher collision [5].

Channel allocation was also proposed in some of the previous research works for achieving better performance results [6, 7]. This process of efficient channel selection leads to increase in resource allocation. A prioritized resource allocation algorithm was proposed, in which a channel is chosen and shared by two users that causes collision and packet loss. This paper [6] designed with a prioritized resource allocation algorithm for increasing quality of services in medical services. This work uses IEEE 802.15.6 standard to achieve compatibility with other devices. This work considers master WBAN who has received active superframe and slave WBAN who is in need of an active superframe. The master WBAN computes service rate from minimum service rate, peak service rate, maximum delay, and slack. Then, a flexible channel selection was used to select a channel on the basis of channel stability. This paper [7] discusses the flexible channel selection for transferring the sensed data via channels. According to this work, cognitive radio module is fed into each WBAN coordinator for the purpose of sensing the channel. In this work, the coordinator searches for a channel; if no channel is available, then

the cognitive radio module performs sequential sensing for determining an idle and usable channel. A channel is chosen only when it satisfies the formulated stability condition. Here, the channel stability is defined from received noise power.

Data transmission was performed by a preferred route [8]. In this paper [8], a novel data classification scheme is proposed for separating sensor information into urgent, semi-urgent, and non-urgent packets. Semi-urgent packets are buffered in sensor nodes for certain time period; in case, if the next packet is also under semi-urgent category, then it will be either transmitted to gateway or packet is dropped. The main aim of this work is to achieve energy-efficient WBAN. Two routes are involved for data transmission, the second route is preferred only when gateway failure occurs. According to this work, two routes are chosen for data transmission but this was effective only for a single sensor node. Data aggregation was performed by using the design of inter-BAN scheduling and aggregation mechanism that involves many mathematical formulations and makes the system complex [9].

The information from the sensor is considered to be in the form of the image, but the major problem here is space complexity [10]. The authors of this paper [10] designed a chaotic compressive sensing (CSS) for providing security and saving storage space. For the providence of security, confusion and mask are the two encryption mechanisms involved in this paper. A sensor is enabled to transfer the data on the basis of images to its end server.

Data classification was performed using particle swarm optimization (PSO) algorithm [11]. In this paper, the authors have illustrated a classification of normal and abnormal data by using particle swarm optimization algorithm. In this work, some rules are provided for segregating ECG and blood sugar into two categories as normal and abnormal. But traditionally, only a single output is obtained from PSO algorithm. This work is evaluated based on a certain set of data that is already stored in the database.

PSO resulted in the slow performance for classifying more than one sensing result since it was capable only to classify one sensing result at a time. Prior data classification in WBAN leads to higher energy consumption [12]. This paper [12] work focuses on improvising reliability of the system, by using reliable Ad hoc On-demand Distance Vector (RelAODV) protocol. The data from sensor nodes are classified into critical and non-critical messages. On the basis of the measured values, the messages are classified into two categories. After classification, the messages are encrypted for the purpose of security which is performed before data transmission.

2.1 Existing Limitations of Previous Work and Their Proposed Solution

See Table 1.

Table 1 Limitations and their solutions

Ref.	Existing limitations	Solution
7	• Transmission failure may occur due to collision • A new incoming packet needs to wait until the first allocated slot is completed • Larger back off time for emergency data due to large 'CP*max*'	CSMA/CA is used by which collision is avoided
12	Higher energy consumption in sensor node since it analyzes the measured value for classification	Energy consumption is lesser than the previous work since classification is performed in diagnosing server
4	Sharing of the same channel for two communications is not effective, it leads to collision or packet loss	Channels are not shared
10	Sensed signal in the form of images are transmitted which consumes higher space and also if any critical data is sensed then it consumes longer time for delivery after compression	Sensed data are transmitted in the form of values and not in images, hence space complexity is minimized
11	PSO is not able to support processing of two different sensing reports (blood sugar and ECG) at the same time, hence it consumes higher time	For faster processing neural network is used
5	Channel stability is estimated only from a single parameter, i.e., noise power	Best channel is selected based on three significant parameters as RSRQ, SNR, and channel capacity which is applied over BSA algorithm
8	• Evaluated only with a single sensor node, use of multiple sensor nodes causes congestion during data transmission • Sensors are capable only with short-range communications so preference of the second route in case of gateway failure is not appropriate. If the patient is far from an access point, then data transmission is not possible. • Direct communication of sensor to access point consumes the higher power of sensor nodes	• More than one sensor nodes are deployed on each Baby • The static route is followed for all communication
9	Delay is the only metric taken into account to guarantee Quality of Service	Other parameters taken into account along with delay

3 Efficient Three-Layered Network Architecture Approach

To resolve all the limitations existed in previous research work, our research is focused on cloud-based WBAN environment. Most of the state-of-the-art research papers have discussed only common abnormality detection. In this proposed work, the aim is to diagnose **Congenital Heart Defect** (CHD) in new-born babies. This CHD in neonates is identified early by symptoms as changes in *oxygen level, heart rate, and respiratory rate*. By monitoring these symptoms, CHD in neonates is detected in early stage. The designed WBAN environment is **three-tier archi-tecture**. This three-tier architecture is comprised of entities as body sensor, hub (mobile phone), base station, and diagnosing server. It is segregated each process in each tier such as

- **TIERI: Data Aggregation**
- **TIERII: Channel Selection**
- **TIER III: Classification.**

Figure 1 shows the elaborated tiered architecture which shows the main focusing area.

1. **TIER I: Data Aggregation**

IEEE 802.15.6 standard is used in WBAN by which we identify the criticality and provided high priority. A new field "Data type" is additionally included in MAC header for providing priority. The priority is given based on Table 2.

If the measured data is critical, then it is given high priority and transmitted to other data. Data from the sensor is collected by the hub in **Time Division Multiple Access** slots.
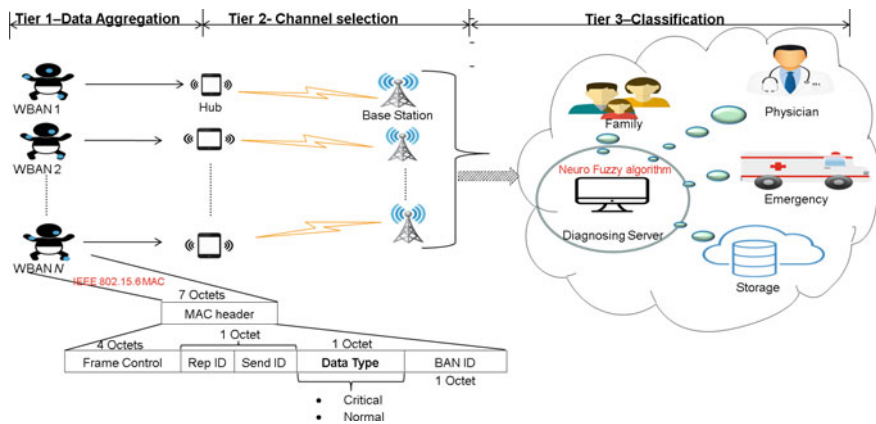
Fig. 1 Three-tier architecture of proposed framework

Table 2 Priority in data type field

data type	Binary representation	Priority
Normal	00	Low
Critical	01	High

2. **TIER II: Channel Selection**

The aggregated time slots are transferred to the server via the base station. Then, hub prefers the best channel to transmit the sensed reports without any packet loss. The best channel is chosen by involving **Bird Swarm Algorithm** in which fitness is computed from *Reference Signal Received Quality (RSRQ), Signal to Noise Ratio (SNR) and channel capacity.*

3. **TIER III: Classification**

The sensed data are transmitted via the chosen best channel, then the data reaches diagnosing server from the base station. Diagnosing server is responsible to classify the sensed data according to its severity (normal and critical). Classification is performed using **Neuro-Fuzzy** (NF) algorithm. Here, fuzzy is integrated with neural network for achieving faster results and take actions immediately. CHD in new-born babies is detected in an early stage by screening their **Pulse Oximetry** measurements periodically. However, for babies, the oxygen level may be low, but it can not be assured that CHD is being detected. Therefore, heart rate is also diagnosed, based on these measurements, early CHD is detected in newborn babies.

4   Conclusion

The three-tier network architecture is proposed in order to remove the existing limitations. By adopting various techniques as mentioned in the proposal, the architecture can improve various quality of service (QoS) parameters and can show better performances in terms of,

- **Delay**
- **Average Delay**
- **Power Consumption**
- **The Probability of Available Channels**

The neonates suffering from CHD can be early diagnosed which is the present need of today's world. And, the real-time remote monitoring can be done along with transmission of suggestions to the caretaker on remote side in an efficient manner by using this architecture.

References

1. Punj R, Kumar R (2018) Technological aspects of WBANs for health monitoring: a comprehensive review. Wirel Netw, 1–33
2. Ahmed S, Saqib M, Adil M, Ali T, Ishtiaq A (2018) Integration of cloud computing with internet of things and wireless body area network for effective healthcare. In: International symposium on wireless systems and networks
3. Aktas F, Ceken C, Erdemli YE (2017) IoT-based healthcare framework for biomedical application. J Med Biol Eng, 1–14
4. Manirabona A, Fourati LC (2017) A 4-tiers architecture for mobile WBAN based health remote monitoring system. Wirel Netw, 1–12
5. Orozco-Barbosa L (2016) Performance study of the IEEE 802.15.6 slotted aloha mechanism with power control in a multiuser environment. Ad Hoc Netw, 27–37
6. Kim S, Song BK (2017) A prioritized resource allocation algorithm for multiple wireless body area networks. Wirel Netw 23(3):727–735
7. Jaafar Ali M, Mougla H, Younis M, Mehaoua A (2017) IoT-enabled channel selection approach for WBANs. In: International conference wireless communications and mobile computing
8. Abiodun AS, Anisi MH, Ali I, Akhunzada A, Khan MK (2017) Reducing power consumption in wireless body area networks: a novel data segregation and classification technique. IEEE Consum Electron Mag 6(4):38–47
9. Omala AA, Kibiwott KP, Li F (2017) An efficient remote authentication scheme for wireless body area network. J Med Syst
10. Peng H, Tian Y, Kurths J, Li L, Yang Y, Wang D (2017) Secure and energy-efficient data transmission system based on chaotic compressive sensing in body-to-body networks. IEEE Trans Biomed Circuits Syst 11(3):558–573
11. Mohnani P, Jabeen F (2016) Opportunistic diagnosis using particle swarm optimization in wireless body area network. Int J Comput Sci Inf Secur 14(1):153–160
12. Raja KS, Kiruthika U (2015) An energy efficient method for secure and reliable data transmission in wireless body area networks using RelAODV. Wirel Pers Commun 83 (4):2975–2997

Cryptography and Optimization-Driven Support Vector Neural Network to Mitigate DoS Attacks in E-Commerce

Javed R. Shaikh, Ravinder Beniwal and Georgi Iliev

Abstract Nowadays, cloud computing has become a significant area for the business due to the high demand of people engaging in E-commerce. E-commerce applications are very popular for conducting business via the Internet which includes online banking, bill payment, and purchasing goods, etc. E-commerce is said to be more straightforward, easier to use, intuitive, and less threatening. The rapid development of the Internet over the past decade appeared to have facilitated an increase in the incidents of online attacks. One such powerful and harmful attack is the denial-of-service (DoS) attack, and hence, protecting the entities from such attacks is essential. Therefore, an effective DoS attack detection technique is required in the E-commerce transactions to offer security in this platform. Accordingly, in this paper, a technique is developed for DoS attack detection in the E-commerce transactions by proposing glowworm swarm optimization-based support vector neural network (GSO-SVNN)-based authorization. The security will be provided with elliptic-curve cryptography (ECC) and hashing function to show the strength of the security protocol against a DoS attacks. The performance of the proposed technique is evaluated using four metrics, like accuracy, precision, recall, and false positive rate (FPR).

Keywords DoS · ECC · E-commerce · GSO · SVNN

J. R. Shaikh (✉) · R. Beniwal · G. Iliev
Technical University of Sofia, Sofia, Bulgaria
e-mail: javedsheikh1987@gmail.com

R. Beniwal
e-mail: ravin.beniwal29@gmail.com

G. Iliev
e-mail: gli@tu-sofia.bg

1   Introduction

The use of cloud computing is increasing rapidly as an attractive model for computing, for the reason that it offers comparatively unlimited computing and network resources. The increasing demand for computing model allows providers to achieve improved resource utilization with statistical multiplexing and evade the costs of the resource over-provisioning with dynamic scaling [1]. On the other side, the economic case for cloud computing is irresistible, and the available security challenges are equally prominent [2]. Trust and trustworthiness of participating entities are the main concern for consumers doing business over Internet [3]. Due to this concern, robust security and trust mechanisms should be implemented to provide protection to communicating entities against malicious ones. Protection using well-known security services, such as authentication, is known as hard security [4] and is not capable of finding entities that will act dishonestly or provide ambiguous information. For that reason, additional robust control mechanisms should be designed to protect the system against such threats.

In a cloud computing environment, various resources such as computation power, network resources, and storage space are shared, because this opponent may take benefit of this sharing environment to launch attacks on the confidentiality, availability, accountability, and integrity of the service. Out of many attacks on these services, DoS attack is a foremost security risk in cloud computing. It is a type of attack where a malicious client (attacker) prevents legitimate clients partially or entirely from gaining service from a server (victim). Another form of DoS attack is distributed denial-of-service (DDoS) attack, which slowdowns the server in responding to the legitimate client or refuses the client request. The main goal of such attack is to exhaust server resources such as CPU, I/O bandwidth, sockets, and memory. As a result, the resources available to other normal users/clients get limited or sometimes may not be available. As per the report of cloud security alliance, DoS attack ranks fifth among cloud threats [2, 5]. DoS attacks are common and can cause significant losses [6].

2   Literature Survey

Trust and reputation management systems play very important role in promoting trust between unknown parties in online environments. In order to develop trust and reputation management techniques, many authors have proposed various computational models of trust [7, 8]. The reason behind this is to increase the number of functional interactions between agents, evade bad interactions, and reduce the risk involved in transactions. There are many open problems associated with trust and reputation management systems, out of which the existence of unfair ratings in E-commerce systems is most important [9, 10]. Unfair ratings are the fundamental problem because an entity in an E-commerce system computes trust based on the

ratings from other entities, of which it cannot control the honesty. The assessed trust value is misleading if false ratings from other entities are taken into the trust computation. It is clearly seen that the problem of unfair ratings should be resolved and is of great importance for E-commerce systems [11]. Table 1 shows the literature of a variety of trust and reputation models proposed by the researchers.

Table 1 Literature survey

Authors	Contribution	Advantages	Disadvantages
Jiuxin et al. [2]	Cloud DoS attack detection architecture	The detection system can rapidly and precisely response to DoS attacks	Difficult to avoid all kind of attack flow
Eva and Denis [11]	Innovative (qualitative assessment dynamics extended) trust model	In order to correct the agent's trust attitude, it provides effective filtering of unfair ratings	Could not handle time-related issues
Al-Haidari et al. [12]	An analytical model based on Cloud Web Service Architecture	Scalability and availability of the cloud services, also suitable for other similarly behaving attacks such as DoS attacks	Computation cost is high
Gaik-Yee et al. [13]	Predictive fuzzy associative rule model (FARM)	Adaptive, dynamic, predictive, sensitive, scalable, and accurate in detection rate and prediction accuracy	Not suitable for bigger data sets on different data types
Prasad et al. [14]	Bio-inspired anomaly-based app-DDoS detection model	Significantly minimized the computational overhead and retains the maximal prediction accuracy	Unable to identify the other significant attacks like Flash crowd
Guojun et al. [15]	Sybil identification algorithm	Duplicated Sybil attack peers can be known as the neighbor peers become familiar and hence more trusted to each other	Unable to implement Sybil trust inside the context of peers which is there in many groups
Mukhopadhyay et al. [16]	Cyber-risk assessment and mitigation (CRAM) framework	Improve information security, and effectively minimize security breaches to a particular level	The small size of the dataset makes it a bit difficult to train and test
Karoui [17]	Bit alternation method was developed	Ensures the reversibility of the likelihood and impact metrics, diagnosing the cause of high risks	Unable to stop all kinds of threats, and processing time is high

3 Proposed DoS Detection Technique

The main objective of this paper is to design and develop a technique for DoS attack detection in the E-commerce applications based on two mechanisms, namely authentication and authorization. In the authentication phase, mutual authentication between user and server will be performed using several security parameters, such as session password and number of cache access. Initially, the user and the server have to be registered under Authorization Center (AC) for the authentication. Then, to authenticate the users, various levels of verification will be performed through different messages.

The security will be offered using the hashing function and ECC to prove the strength of the security protocol against DoS attacks. Once the authentication of the user and the server is over, the authorization will be performed to mitigate the DoS attack during the E-commerce transactions. Here, the user behavior will be recorded based on several parameters, such as duration, service, flag, verification status, num_access_files, wrong_fragment, number of bytes sent from source to destination, number of bytes sent from destination to source, logged_in, number of connections to the same service as the current connection in the last two seconds, and number of connections to the same host as the current connection in the last two seconds, in the Web log file. Then, the important features will be selected from the Web log file in the feature extraction process. Once the features are extracted, it will be fed as input to the proposed model of glowworm swarm optimization
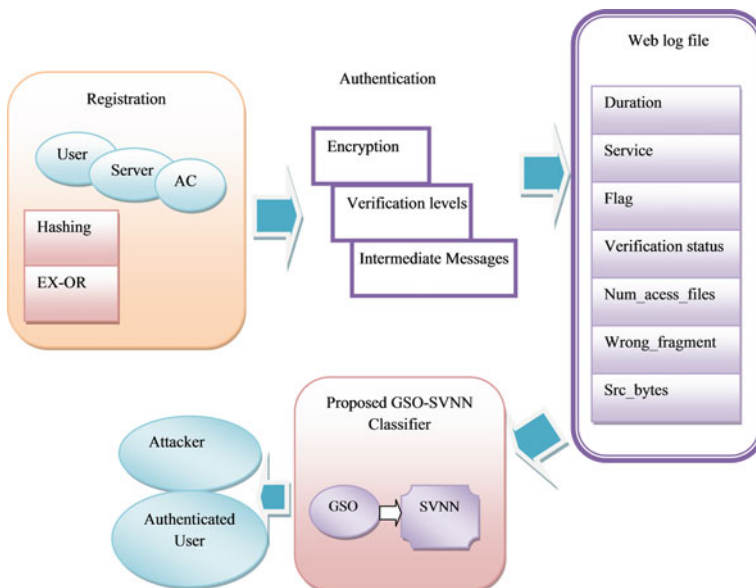
Fig. 1 Block diagram of a proposed system model

(GSO)-based support vector neural network (GSO-SVNN), to detect the DoS attack. The proposed GSO-SVNN will be designed by training the SVNN using GSO [18]. Figure 1 shows the block diagram of the proposed system model. The performance of the proposed design will be evaluated in terms of accuracy, precision, recall, and FPR and will be compared with that of existing works [10, 11, 15]. Moreover, an attack analysis will be performed to demonstrate the effectiveness of the proposed technique.

4   Registration of User and Server

The registration procedure designed in the proposed technique follows ECC approach. Before the authentication of the user, it is mandatory that the user and the server have to be registered. The proposed DoS attack detection in the E-commerce transactions includes three entities, namely the user, the server, and the AC. The registration between the user and the server is done based on the hashing operation and the EX-OR operation with the password, the private keys, and the identity of the three entities. The procedure involved in the registration process is given as follows:

(1) Initially, the server has its identity, I^S and password, P^S, which are stored in the AC as I_+^S and P_+^S, to register in the cloud for the transaction.

(2) Then, the private key of the server is computed in the AC by taking the EX-OR of P_+^S and the private key of the AC, and the resulting value is concatenated with I_+^S, as given below,

$$K^S = h\left(I_+^S \,||\, \left(P_+^S \oplus K^A\right)\right) \tag{1}$$

where P_+^S is the stored password of the server, $\oplus$ is the EX-OR operation, and K^A private key of the AC.

(3) Using the computed K^S, K^A and the public key, the AC finds the data profile of the server as,

$$D^S = \left(h\left(K^S \oplus K^A\right) \Theta K^P\right) \tag{2}$$

where K^P is the public key, $h(.)$ is the hashing function, and Θ is the element-wise multiplication.

(4) The private key and the data profile of the server computed in the AC are transferred to the server, where it stores K^S and D^S as K_+^S and D_+^S. Also, the user identity, I^U, and the password, P^U that the user holds are stored in the server as I_+^U and P_+^U.

(5) Then, the server computes the user private key by hashing the I_+^U that is concatenated with the EX-ORed P_+^U and K^S.

$$K^U = h\big(I^U_+ ||\big(P^U_+ \oplus K^S\big)\big) \tag{3}$$

where I^U_+ and P^U_+ are the stored user identity and password, and K^S is the private key of the server.

(6) Moreover, the server computes the data profile of the user, similar to that of the server, as

$$D^U = \big(h\big(K^U \oplus K^S\big)\Theta K^P\big) \tag{4}$$

(7) Finally, K^U and D^U calculated by the server is received by the user and are stored as K^U_+ and D^U_+.

5 Authentication Using ECC

Followed by the registration of the user and the server, authentication is performed using ECC. ECC [19, 20] is one of the methods based on public key encryption that encrypts the data with the keys using the concept of elliptic curve. The reduced size of the key and the high security offered make ECC a promising approach for the encryption. In ECC, an elliptic curve, often a plane curve is chosen and the key generation is done based on the points mapped on the curve. Then, the key is exchanged following Diffie–Hellman key exchange procedure, and finally, the encryption is performed. The proposed DoS attack detection technique performs several levels of verification by forwarding various intermediate messages, represented as S. Here, four messages and four verification levels are considered for the authentication. The authentication process is given below.

(1) At first, the user concatenates I^U and P^U and encrypts the result using the stored private key of the user. The encrypted result is again concatenated with the user identity to create the message S_1.

$$S_1 = \Big(E_{K^U_+}\big(I^U||P^U\big)||I^U\Big) \tag{5}$$

where $E_{K^U_+}$ represents the encryption using ECC with K^U_+.

(2) The message generated by the user is verified at the server using the stored I^U and P^U, as

$$S^*_1 = \big(E_{K^U}\big(I^U||P^U_+\big)||I^U_+\big) \tag{6}$$

where E_{K^U} is the encryption using ECC with K^U. If $S_1 = S_1^*$, it is considered as the first level of verification, V_1.

(3) Then, the server constructs another intermediate message by encrypting the server identity and the password as follows,

$$S_2 = \left(E_{K_+^S} \left(I^S || P^S || I^S \right) \right) \tag{7}$$

where $E_{K_+^S}$ is the encryption using ECC with private key of the server K_+^S.

(4) Then, the same message is verified at the AC using the stored key and identity of the server as,

$$S_2^* = E_{K^S} \left(I^S || P_+^S \right) || P_+^S \tag{8}$$

where E_{K^S} is the ECC encryption using K^S. If $S_2 = S_2^*$, it is the level 2 verification, V_2.

(5) For the third level of verification, a message is created in the AC by EX-ORing the hashed public key and the data profile of the server, as

$$S_3 = D^S \oplus h \left(K^P \right) \tag{9}$$

where D^S and $h(K^P)$ indicate the data profile of the server and the hashing function of the public key.

(6) Then, the message is verified at the server using the stored D^S as,

$$S_3^* = D_+^S \oplus h \left(K^P \right) \tag{10}$$

where D_+^S is the stored data profile of the server. Thus, the level 3 verification, V_3, is complete if $S_3 = S_3^*$.

(7) The fourth message is generated at the server similar to S_3, but with the data profile of the user, instead of D_+^S,

$$S_4 = D^U \oplus h \left(K^P \right) \tag{11}$$

where D^U is the data profile of the user.

(8) Then, the user, with the message S_4, finds the data profile of the user as,

$$D_*^U = h \left(K^P \right) \oplus S_4 \tag{12}$$

If the condition $D_*^U = D_+^U$ is satisfied, it is the level 4 verification, V_4. Thus, from the four levels of verification, the user can be authenticated when the verification condition is satisfied. If not, the user is meant to be an attacker.

6   Proposed GSO-SVNN Classifier for Authorization

In this section, the proposed GSO-SVNN is developed for the authorization of the user and the server in the E-commerce Web is elaborated. SVNN [21] is comprised of three layers, namely input layer, hidden layer, and output layer. Based on the information attained during the authentication phase, the SVNN classifies the user either as an intruder or an authenticated user. Hence, the input fed to the input layer of the SVNN is the user information. The proposed GSO-SVNN is developed by training the SVNN with the GSO, rather than the genetic algorithm (GA) such that the performance of the classifier is improved due to the ability of GSO in solving problems of multimodal functions. The output of the proposed GSO-SVNN is given by a function,

$$O = w_1 \cdot \log \text{sig} \left[\left(\sum_{f=1}^{7} u_f * w_2^l \right) + b_1 \right] + b_2 \tag{13}$$

where w_1 and w_2 indicate the weights between the hidden and the output layers and between the input and the hidden layers, and b_1 and b_2 represent the biases at the hidden and the output layers, respectively.

7   Results and Discussion

This section deals with the results of the proposed method. The performance of the proposed method is evaluated with the setup given below in terms of four metrics, such as accuracy, precision, recall, and FPR [22].

   The proposed method is implemented in MATLAB tool using the PC installed with Windows 10 OS and Intel(R) i3 processor with 64-bit operating system and 4 GB RAM. The experiment is done using simulation setup where 100 users and 10 attackers are considered. Figure 2 shows the simulation setup where 100 users and 10 attackers are participating in the E-commerce system.

   The techniques taken for the comparison of the performance with the proposed technique are neighbor similarity trust [15], QADE [11], ECC + SVM (Applied SVM instead of GSO-SVNN in the proposed technique), BARTD [14], ECC + SVNN (Applied SVNN instead of GSO-SVNN in the proposed technique). For each technique, the results of simulation are considered for detecting the accuracy, precision, recall, and FPR. Figure 3a illustrates the accuracy metric with the varying training dataset denoted by k. For 80% training data, the corresponding accuracy measured by neighbor similarity trust, QADE, ECC + SVM, BARTD, ECC + SVNN, and proposed ECC + GSO-SVNN is 0.784, 0.818, 0.827, 0.871,
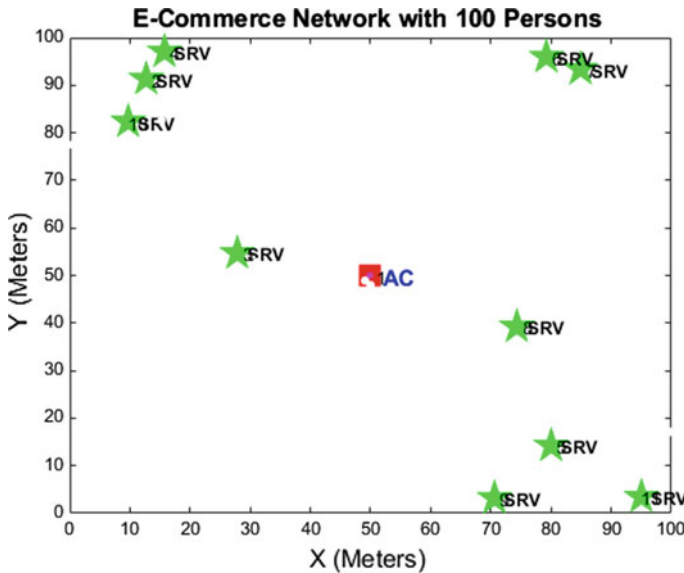
Fig. 2 Simulation setup showing 100 users and 10 attackers

0.885, and 0.921, whereas for 60% training data, the accuracy measured by neighbor similarity trust, QADE, ECC + SVM, BARTD, ECC + SVNN, and proposed ECC + GSO-SVNN is 0.769, 0.814, 0.824, 0.828, 0.882, 0.919, respectively. Hence, the proposed method predicts result with highest accuracy.

Figure 3b shows the precision values based on training data varying from 0.3 to 0.8. When the data is 80%, the precision measured by neighbor similarity trust, QADE, ECC + SVM, BARTD, ECC + SVNN, and proposed ECC + GSO-SVNN is 0.889, 0.893, 0.894, 0.894, 0.955, and 0.969. Figure 3c shows the recall value calculated the comparative techniques. For 80% data, the recall values measured by neighbor similarity trust, QADE, ECC + SVM, BARTD, ECC + SVNN, and proposed ECC + GSO-SVNN are 0.864, 0.896, 0.915, 0.924, 0.93, and 0.952, respectively. In Fig. 3d, the FPR analysis is given, where the minimum FPR measured by neighbor similarity trust, QADE, ECC + SVM, BARTD, ECC + SVNN, and proposed ECC+ GSO-SVNN is 0.4, 0.4, 0.4, 0.315, 0.05, and 0.05, respectively. It is concluded that the proposed method shows outstanding results than existing methods.
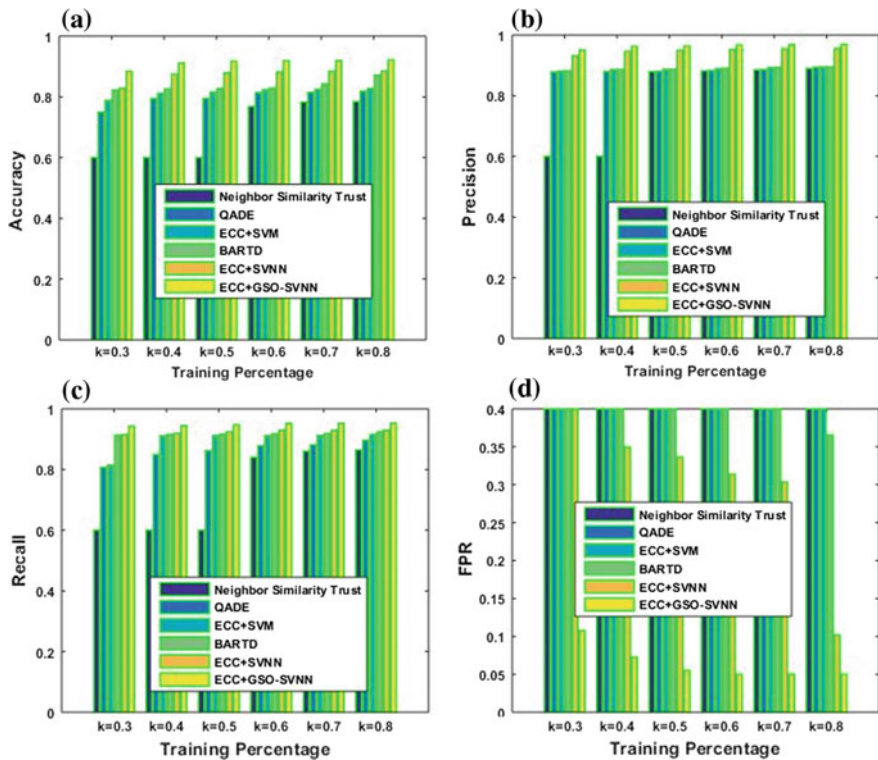
Fig. 3 **a** Analysis of simulation setup based on accuracy. **b** Analysis of simulation setup based on precision. **c** Analysis of simulation setup based on recall. **d** Analysis of simulation setup based on FPR

8 Conclusion

In this paper, the design of ECC-based authentication and glowworm swarm optimization-based support vector neural network (GSO-SVNN) authorization for DoS attack detection is proposed. The design consists of the two mechanisms, namely authentication and authorization. The proposed design will overcome all the drawbacks mentioned in the literature survey. As ECC is used instead of other cryptography mechanisms, it provides the benefits of less storage requirement, fast computation, and high security level with less key size.

The proposed GSO-SVNN classifies the user as authenticated user or attacker based on the information extracted. The experimentation is carried out using four metrics, like accuracy, precision, recall, and FPR, to evaluate the performance of the proposed technique. The results suggest that the proposed technique of DoS attack detection is effective in attack detection in the E-commerce transactions with 95.1% accuracy.

References

1. Yanpei C, Vern P, Randy HK (2010) What's new about cloud computing security. University of California, Berkeley Report No. UCB/EECS-2010-5, pp 2010-5
2. Jiuxin C, Bin Y, Fang D, Xiangying Z, Shuai X (2015) Entropy-based denial-of-service attack detection in cloud data center. Concurr Comput Pract Exp 27(18):5623–5639
3. Estrella G, Bertin M, Geomina T (2014) The drivers and impediments for cross-border E-commerce in the EU. Inf Econ Policy 28:83–96
4. Lars R, Sverker J (1996) Simulated social control for secure Internet commerce. In: Proceedings of the 1996 ACM workshop on new security paradigms, 18–25
5. TTW Group: The notorious nine: cloud computing top threats in 2013. Report Cloud Security Alliance (2013)
6. Jose B (2002) Protecting electronic commerce from distributed denial-of-service attacks. In: Proceedings of the 11th ACM international conference on World Wide Web, 553–561
7. Isaac P, Jordi S (2013) Computational trust and reputation models for open multi-agent systems: a review. Artif Intell Rev 40(1):1–25
8. Audun J, Roslan I, Colin B (2007) A survey of trust and reputation systems for online service provision. Decis Support Syst 43(2):618–644
9. Kevin H, David Z, Cristina N (2007) A survey of attacks on reputation systems, 1–17
10. Ya-Fei Y, Qin-Yuan F, Yan LS, Ya-Fei D (2009) Dishonest behaviors in online rating systems: cyber competition, attack models, and attack generator. J Comput Sci Technol 24 (5):855–867
11. Eva Z, Denis T (2017) QADE: a novel trust and reputation model for handling false trust values in e–commerce environments with subjectivity consideration. Technol Econ Dev Econ 23(1):81–110
12. Al-Haidari F, Sqalli M, Salah K (2015) Evaluation of the impact of EDoS attacks against cloud computing services. Arab J Sci Eng 40(3):773–785
13. Gaik-Yee C, Chien-Sing L, Swee-Huay H (2014) Defending against XML-related attacks in E-commerce applications with predictive fuzzy associative rules. Appl Soft Comput 24:142–157
14. Prasad KM, Reddy ARM, Rao KV (2017) BARTD: bio-inspired anomaly based real time detection of under rated App-DDoS attack on web. J King Saud Univ Comput Inf Sci, 1–15
15. Guojun W, Felix M, Song G, Muhammad BA (2015) Neighbor similarity trust against sybil attack in P2P E-commerce. IEEE Trans Parallel Distrib Syst 26(3):824–833
16. Mukhopadhyay A, Chatterjee S, Bagchi KK, Kirs PJ, Shukla GK (2017) Cyber risk assessment and mitigation (CRAM) framework using logit and probit models for cyber insurance. Inf Syst Front, 1–22
17. Karoui K (2016) Security novel risk assessment framework based on reversible metrics: a case study of DDoS attacks on an E-commerce web server. Int J Netw Manag 26(6):553–578
18. Kaipa KN, Ghose D (2017) Glowworm swarm optimization: algorithm development. Glowworm swarm optimization. Springer International Publishing, 21–56
19. Seroussi G (1999) Elliptic curve cryptography. In: Information theory and networking workshop (Cat. No. 99EX371), Metsovo, 41
20. Hankerson D, Alfred JM, Scott V (2006) Guide to elliptic curve cryptography. Springer Science & Business Media
21. Oswaldo L, Urbano N, Rui A (2014) Eigen value decay: a new method for neural network regularization. Neurocomputing 124:33–42
22. Samal S, Bandopdhaya S, Dora S, Poulkov V (2017) Coverage analysis of heterogeneous wireless network with n-interacted transmission nodes. Int J Interdiscip Telecommun Netw (IJITN) 9(4):49–58

Fusion of IoT and Machine Learning Approach to Prevent Confidential Data from Digital Crimes and Cyber Mugging for Covert Transmission

Amit Kumar Shakya, Ayushman Ramola, Hemant Singh Pokhariya and Akhilesh Kandwal

Abstract We are aware of the scenario of the twenty-first century where each and every nation of the world wants to progress at a rapid rate, weaker nations are destabilized by adopting policies like state-sponsored terrorism and online hacking which are part of the government official agenda. In this situation, there is strong need for policies to prevent data from online hacking and cyber mugging. Every nation wants to secure its data in terms of future plans, satellite images, new military setups, new river linkage plans, etc. Here, we have developed a new model advanced private content-based image retrieval (APCBIR) of data privacy based on content-based image query and retrieval (CBIQ/R). In this approach, data is smartly encrypted with only 10% of the original data, features of the original and newly encrypted images are matched by statistical parameters, and finally, the transmission of the data is done in a manner so that no one is able to reveal the identity of the original data. The efficiency of this system becomes more effective as IoT is attached to the model; data of usefulness is automatically selected and encrypted accordingly. Finally, the data gets secured from various types of malware attacks.

Keywords Online hacking · Cyber mugging · Advanced private content-based image retrieval · Encryption · Random permutation · IoT · Malware

1 Introduction

Cybercrimes are among one the new crimes which are increasing rapidly day by day as the country like India is moving towards digitalization there is an exponential increase in the online crimes, scams and frauds. In the era of the twenty-first century, if a country, state, organization, etc., want to progress at a rapid rate,

A. K. Shakya (✉) · A. Ramola · H. S. Pokhariya · A. Kandwal
Department of Electronics and Communication Engineering,
Graphic Era (Deemed to be University), 566/6 Bell Road Clement Town,
Dehradun, Uttarakhand, India
e-mail: xlamitshakya.gate2014@gmail.com

then they have change their conventional approach of business and trade and adopt the policy of online transactions, but here comes the biggest hurdle of development, i.e., privacy and data theft. Digital crimes are related directly to social, personal, and national data theft [1]. Recently, Facebook is facing issues related to the data robbery and online personal information leakage problems [2]. This situation of digital crimes becomes more tenacious when two nations get involved with each other in cyber warfare, recently U.S.A. and Russia were involved in such activities as during the U.S. Presidential election America was claiming that group of Russia based hackers are influencing American elections [3]. So, such types of situations are becoming common in day-to-day life. There are several types of cyberattacks such as indiscriminate attacks [4], destructive attacks [5], cyber warfare [6], government espionage [7], cooperate espionage [8], stole email and login credentials [9], stole medical data [10], stole credit card data [11], stole financial data [12], etc.; these attacks can be directed from a personal hacking groups or directly supported from some nation. The first step of these cyberattacks involved the use of various types of malware on the personal or the professional data of the person, company, or organization [13]. This type of malware includes remote access [14], Trojan [15], adware [16], worm [17], spyware [18], root kit [19], exploit kit [20], blended threat [21], etc. So, all these malwares are destroying the capabilities of the computer system by hacking, stealing, and manipulating the data, so it becomes quite important to use some encryption schemes based on the image statistical parameters to prevent the data from getting hacked to stolen. Most of these suspicious activities happen during the transmission of the data using an external device, so for secure transmission, it becomes quite important to use encryption schemes for the data of extreme importance. In this context, machine learning is considered as an important approach of training the data that uses statistical properties to give computer systems the ability to learn from the data without being explicitly programmed. Arthur Samuel was the person who gave this technique the name of machine learning [22, 23]. In the machine learning approach, system is trained with the dataset followed by supervised and unsupervised classifications; finally, the classified images in our case encrypted images/data are transferred to their desired locations. The Internet of thing (IoT) is a network of devices which when linked with the Internet-based computer systems enables these systems to connect and exchange data [24]. IoT can play a very important role in the classification of the image dataset; here, we have trained our system to call the dataset directly from the Internet and classify them and finally present the result of our encryption schema. So, here a novel approach to connect machine learning-based system with IoT is developed, through which Internet-based images are directly transmitted to the computer systems where proposed algorithm automatically classifies the images and encrypts them. Finally, the encrypted images are transmitted to desired location where a reverse operational algorithm instantly becomes active and decrypts the encrypted images to obtain original image providing secure transmission free from hacking and cyber mugging.

2   Mathematical Imitation of the Proposed APCBIR System

A digital image contains DN (digital numbers) or pixel values which represent intensity values of the particular element. These pixels are arranged in a matrix format to represent an image which can be optically explained; i.e., pixels must be located at a specific position to represent a useful image. Let an image I_{org} contain m numbers of rows and n number of columns, then the total pixel contained in the image is $m \times n$. These $m \times n$ pixels need to be arranged in a specific position to represent a meaningful image (Fig. 1).

Now, all the DN values are randomly arranged in vector of single row, and from them, only 10% of the pixels are selected through random permutation from which new creep images are formed. These creep images contain m_{new} number of rows and n_{new} number of columns. Now, these 10% pixels are arranged in single vector which are converted to the matrix notation.

$$v = \left[p_{1,n} p_{2,m} p_{77} p_{m,n} \cdots \cdots \cdots \cdots \cdots p_{62,89} \right] \tag{1}$$

Here, $p_{1,n}$ to $p_{62,89}$ represents the pixel intensity of the 10% pixels which are selected in a random manner from the vector v. The newly created image contains total of $m_{new} \times n_{new}$ numbers of DNs. The newly created image matrix contains DN arrangement as shown in Fig. 2.

In the proposed system, general normal distribution model is used, and the domain is stretched by a factor σ (standard deviation) and peaked by the μ (mean value). The normal distribution of the APCBIR model is thus expressed as

$$I(org) = \begin{bmatrix} (1,1) & (1,2) & (1,3) & & (1,n-2) & (1,n-1) & (1,n) \\ (2,1) & (2,2) & (2,3) & \cdots & (2,n-2) & (2,n-1) & (2,n) \\ (3,1) & (3,2) & (3,3) & & (3,n-3) & (3,n-1) & (3,n) \\ \vdots & & & \ddots & & & \vdots \\ (m-2,1) & (m-2,2) & (m-2,3) & & (m-2,n-2) & (m-2,n-1) & (m-2,n) \\ (m-1,1) & (m-1,2) & (m-1,3) & \cdots & (m-1,n-2) & (m-1,n-1) & (m-1,n) \\ (m,1) & (m,2) & (m,3) & & (m,n-2) & (m,n-1) & (m,n) \end{bmatrix}$$

Fig. 1 Matrix representation of the original image

$$Creep\,(I) = \begin{bmatrix} (m,n) & (5,n-3) & & (1,8) & (m-1,n-6) \\ (m-2,n-8) & (3,2) & \cdots & (m-2,n-3) & (8,n-1) \\ \vdots & & \ddots & & \vdots \\ (8,n-2) & (1,1) & \cdots & (5,2) & (66,22) \\ (m-7,n-5) & (1,2) & & (1,n) & (1,1) \end{bmatrix}$$

Fig. 2 Matrix representation of the encrypted image with random permutation of the image pixels

$$p(\text{DN}/\mu, \sigma^2) = \frac{1}{\sigma} Z\left(\frac{\text{DN} - \mu}{\sigma}\right) \tag{2}$$

Here, DN is the digital number or the pixel value and the probability density function Z is scaled by $1/\sigma$. Now, the first-order image statistics, i.e., mean, variance, and standard deviation of the image, are obtained from probability density function (pdf). The probability of the occurrence of the specific intensity value in the original image is expressed as

$$p(\text{org}) = \left\{\frac{n(i(\text{org}))}{m \times n}\right\} \tag{3}$$

where $n\,(i(\text{org}))$ is the occurrence time of the intensity value in the original image.

$$\text{Mean } \mu_\circ = \sum_{\text{first pixel}}^{\text{last pixel}} i(\text{org}) \times p(\text{org}) \tag{4}$$

$$\text{Variance } \sigma_\circ^2 = \sum_{\text{first pixel}}^{\text{last pixel}} (i(\text{org}) - \mu_0)^2 \times p(\text{org}) \tag{5}$$

$$\text{Standard deviation} = \sqrt{\text{Variance } \sigma_\circ^2} \tag{6}$$

Now, for the creep images, first-order statistical parameters are computed, and finally, they are compared with the original image statistical parameters.

$$\text{Mean } \mu_{\text{creep}} = \sum_{\text{first pixel}}^{\text{last pixel}} i(\text{creep}) \times p(\text{creep}) \tag{7}$$

$$\text{Variance } \sigma_{\text{creep}}^2 = \sum_{\text{first pixel}}^{\text{last pixel}} \left(i(\text{creep}) - \mu_{\text{creep}}\right)^2 \times p(\text{creep}) \tag{8}$$

$$\text{Standard deviation} = \sqrt{\text{Variance } \sigma_{\text{creep}}^2} \tag{9}$$

Finally through our APCBIR system mean of the original image $\cong$ mean of the creep image, i.e., Eq. (4) $\cong$ Eq. (7), variance of the original image $\cong$ variance of the creep image, i.e., Eq. (5) $\cong$ Eq. (8), and finally, the standard deviation of the original image $\cong$ the standard deviation of the creep image, i.e., Eq. (6) $\cong$ Eq. (9).

3 Proposed Algorithm

The proposed algorithm contains the following steps.

a. Input an image of $m \times n$ dimension.
b. Randomly arrange the image pixels through random permutation.
c. Select the minimum number of pixels from randomly arranged image pixels.
d. Store the obtained pixels in a new matrix of dimension $m_{new} \times n_{new}$ dimension.
e. Calculate the statistical parameters for original image.
f. Calculate the statistical parameters for encrypted image.
g. Obtain the histogram signature plot of the both original and encrypted images.
h. Transmit the encrypted image to its desired location.
i. Finally, compare the statistical parameters from desired location of the both original and encrypted images to recover the original images.

4 Experiment

In the experiment, we have taken observations on various datasets which contain several categories of images broadly classified as satellite images, textures samples of various surfaces, documents formats, handwritten book notes, etc.; every dataset has shown satisfactory result from our encryption model. Here, we are presenting some samples of the popular McGill texture dataset, Mars hand lens image dataset, Tobacco 800 dataset, and ICFHR text dataset (Fig. 3).

Now, the first-order image statistical parameters for the original images, i.e., mean, variance, and the standard deviation for the original datasets, are evaluated. These statistical parameters' values are represented for the original dimension of the image dataset which is shown in Table 1.

Datasets (Mars hand lens, Mc Gill texture, Tobacco 800 documents, ICFHR 2016)

(a) (b) (c) (d) (e) (f) (g) (h) (i) (j)

(k) (l) (m) (n) (o) (p) (q) (r) (s) (t)

(u) (v) (w) (x) (y)
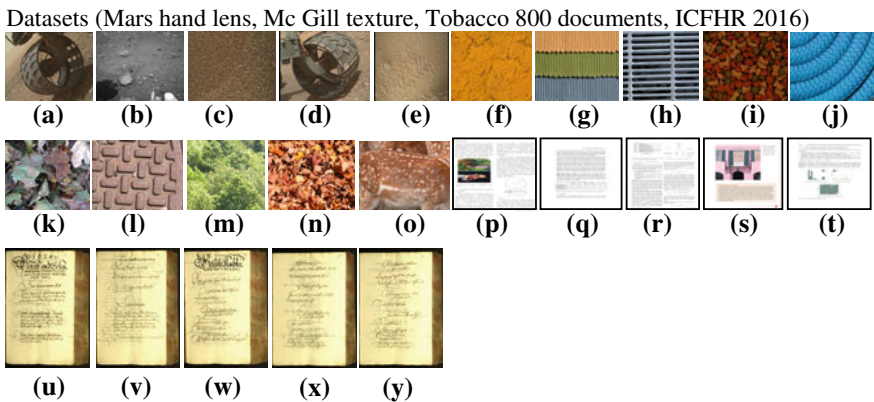
Fig. 3 a 2030 MH 25, b NLB EDR, c 2027 MH, d 2030 MH 26, e 2017 MD, f PP 0042, g PP 0223, h Punistrt 024, i PP RS Yacht, j RVH texture 016, k PP peal 096, l Mex 07, m PP peal 037, n Merymt 107_029, o PP pare Safari 050, p RAW 02, q RAW 03, r RAW 04, s RAW 47, t RAW 118, u Seite 0001, v Seite 0003, w Seite 0007, x Seite 0011, y Seite 0013

Table 1 First-order statistical parameters for the original dataset

S. no.	Dataset	Sample no.	Original dimension	Total pixels	Mean	Variance	Standard deviation
1	Mars hand lens dataset	2030 MH 25	1632 × 1200	1,958,400	83.6555	9.88774	3.1444
2		NLB EDR	1024 × 1024	1,048,576	71.6894	6.5471	2.5587
3		2027 MH	1632 × 1200	1,958,400	85.7742	9.24966	3.0413
4		2030MH 26	1584 × 1184	1,875,456	96.7638	10.4196	3.2279
5		2030MH	1648 × 1200	1,977,600	124.685	10.1172	3.1807
6	McGill texture	PP 0042	768 × 576	442,368	118.83	11.5903	3.4044
7		PP 0223	768 × 576	442,368	120.956	10.0445	3.1693
8		Punistrt 024	768 × 576	442,368	100.4	11.0333	3.3216
9		PP RS Yacht	768 × 576	442,368	47.4121	9.31035	3.0512
10		RVH texture 016	768 × 576	442,368	114.271	11.5367	3.3965
11		PP peal 096	768 × 576	442,368	114.891	10.3981	3.2246
12		Mex 07	768 × 576	442,368	140.169	10.4391	3.2309
13		PP peal 037	768 × 576	442,368	134.524	10.1508	3.1860
14		Merymt 107_029	768 × 576	442,368	115.501	10.4838	3.2378
15		PP pare Safari 050	768 × 576	442,368	124.168	10.3454	3.2164
16	Marmot math dataset	Raw 02	2133 × 3200	6,825,600	221.007	13.8213	3.7177
17		Raw 03	2479 × 3508	8,696,332	244.419	10.2941	3.2084
18		Raw 04	2550 × 3300	8,415,000	239.479	14.4252	3.7980
19		Raw 47	1800 × 2700	4,860,000	217.272	12.9021	3.5919
20		Raw 118	2008 × 2385	4,789,080	242.272	12.1952	3.4921
21	ICFHR 2016	Seite 0001	2538 × 3551	9,012,438	165.015	11.3834	3.3739
22		Seite 0003	2538 × 3551	9,012,438	175.594	11.5737	3.4020
23		Seite 0007	2562 × 3567	9,138,654	168.283	11.3992	3.3762
24		Seite 0011	2490 × 3567	8,881,830	179.571	11.8444	3.4415
25		Seite 0013	2482 × 3567	8,853,294	181.003	11.8431	3.4414
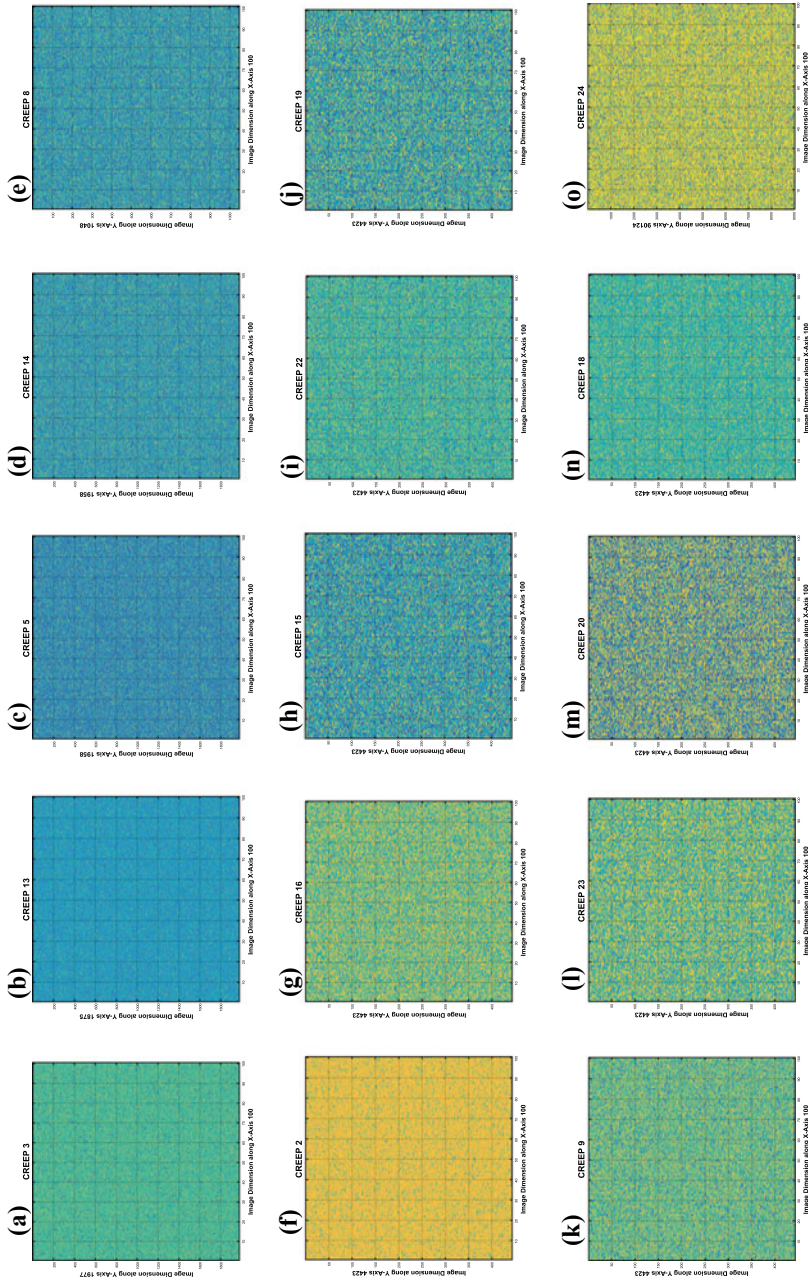
Fig. 4 **a** Creep 3, **b** Creep 13, **c** Creep 5, **d** Creep 14, **e** Creep 8, **f** Creep 2, **g** Creep 16, **h** Creep 10, **i** Creep 15, **j** Creep 22, **k** Creep 9, **l** Creep 19, **m** Creep 23, **n** Creep 20, **o** Creep 18, **p** Creep 24, **q** Creep 21, **r** Creep 11, **s** Creep 17, **t** Creep 12, **u** Creep 1, **v** Creep 4, **w** Creep 6, **x** Creep 25, **y** Creep 7
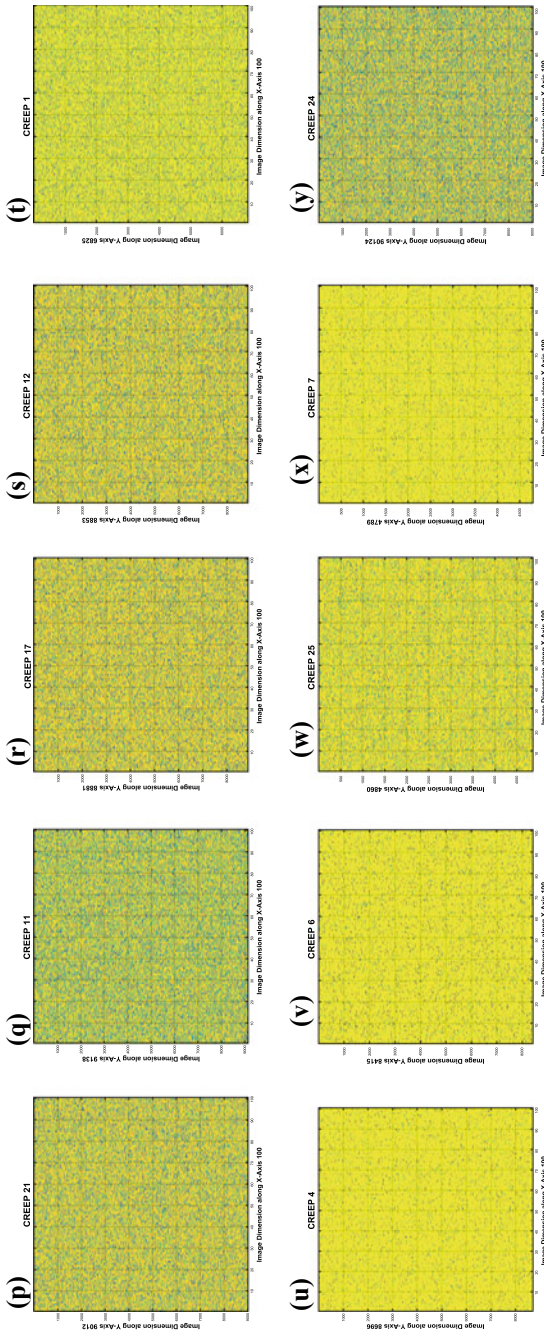
Fig. 4 (continued)

Table 2 First-order statistical parameters for the creep images

S. no.	Dataset	Sample no.	Total pixels	10% of total pixels	Mean	Variance	Standard deviation
1	Mars hand lens dataset	2030 MH 25	1,958,400	195,840	83.6469	9.8875	3.1444
2		NLB EDR	1,048,576	104,858	71.5812	6.1254	2.4749
3		2027 MH	1,958,400	195,840	85.7711	9.2966	3.0489
4		2030MH 26	1,875,456	187,547	96.7534	10.3983	3.2246
5		2030MH	1,977,600	197,760	124.68	10.1163	3.1806
6	McGill texture	PP 0042	442,368	44,237	118.815	11.5875	3.4041
7		PP 0223	442,368	44,237	120.956	10.0529	3.1706
8		Punistrt 024	442,368	44,237	100.399	11.0335	3.3216
9		PP RS Yacht	442,368	44,237	47.3929	9.3145	3.0519
10		RVH texture 016	442,368	44,237	114.269	11.5365	3.3965
11		PP peal 096	442,368	44,237	114.892	10.3987	3.2247
12		Mex 07	442,368	44,237	140.169	10.4323	3.2299
13		PP peal 037	442,368	44,237	134.537	10.1147	3.1803
14		Merymt 107_029	442,368	44,237	115.501	10.4961	3.2397
15		PP pare Safari 050	442,368	44,237	124.168	10.3507	3.2172
16	Marmot math dataset	Raw 02	6,825,600	682,560	221.452	14.3726	3.3808
17		Raw 03	8,696,332	869,633	244.831	9.71625	3.4039
18		Raw 04	8,415,000	841,500	240.020	14.3612	3.3825
19		Raw 47	4,860,000	486,000	217.291	13.0005	3.4431
20		Raw 118	4,789,080	478,908	242.611	11.5695	3.4427
21	ICFHR 2016	Seite 0001	9,012,438	901,243	165.018	11.4301	3.7911
22		Seite 0003	9,012,438	901,244	175.596	11.5868	3.1170
23		Seite 0007	9,138,654	9,013,866	168.285	11.4418	3.7896
24		Seite 0011	8,881,830	888,183	179.572	11.8553	3.6056
25		Seite 0013	8,853,294	885,323	181.003	11.8525	3.4013
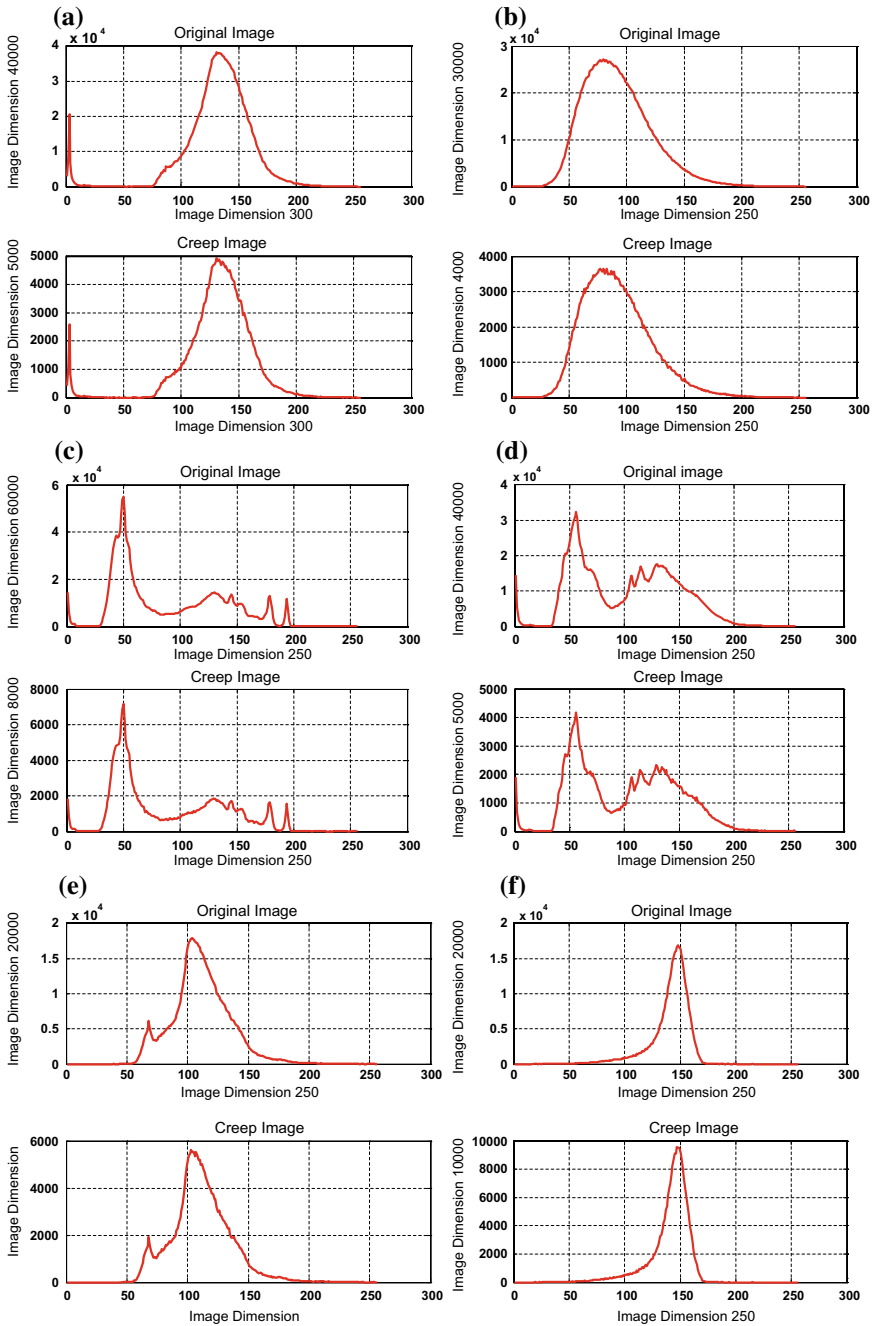
Fig. 5 **a** H 4, **b** H 11, **c** H 5, **d** H 12, **e** H 6, **f** H 13, **g** H 23, **h** H 25, **i** H 24, **j** H 1, **k** H 16, **l** H 2, **m** H 14, **n** H 3, **o** H 15, **p** H 20, **q** H 21, **r** H 17, **s** H 7, **t** H 8, **u** H 22, **v** H 19, **w** H 18, **x** H 9, **y** H 10
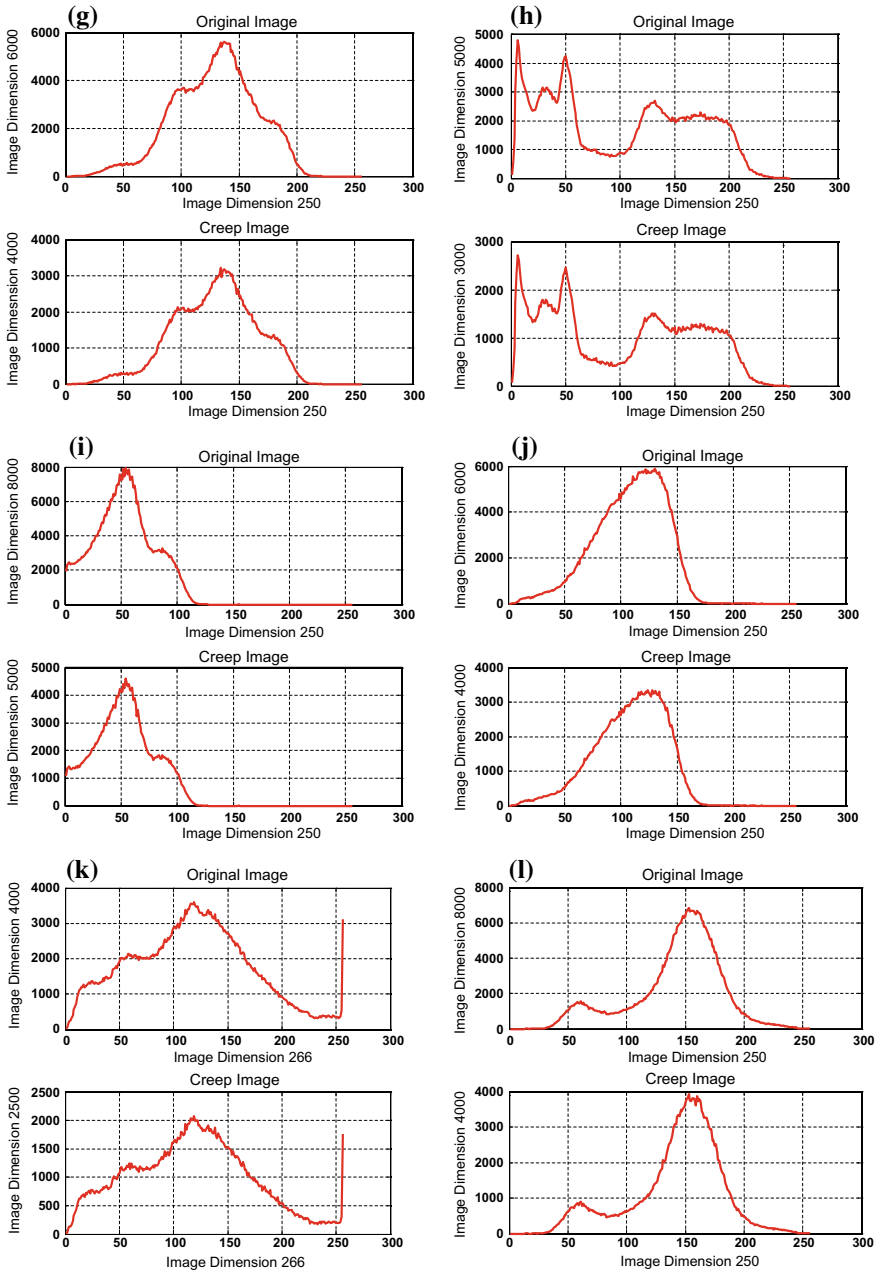
Fig. 5 (continued)
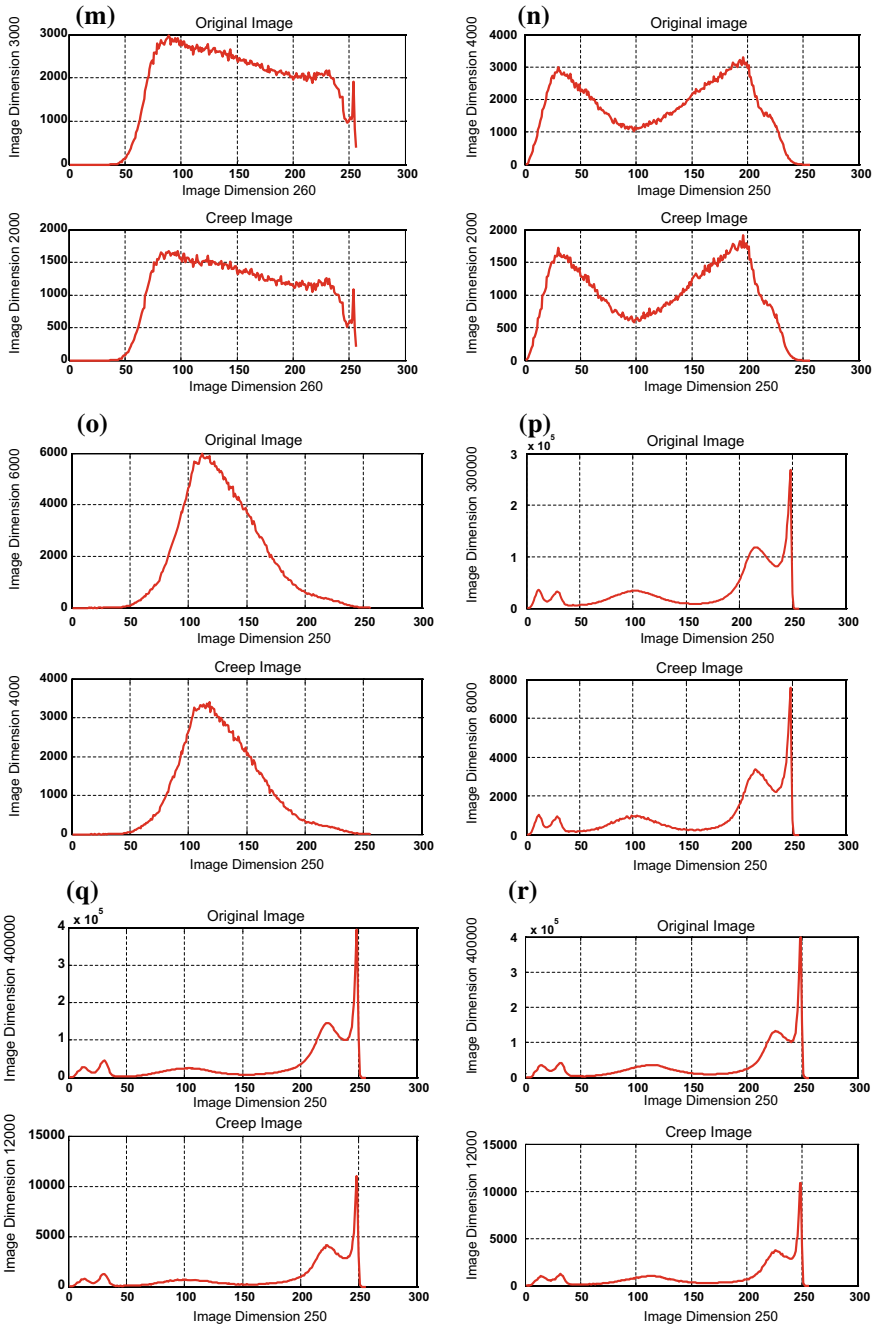
Fig. 5 (continued)
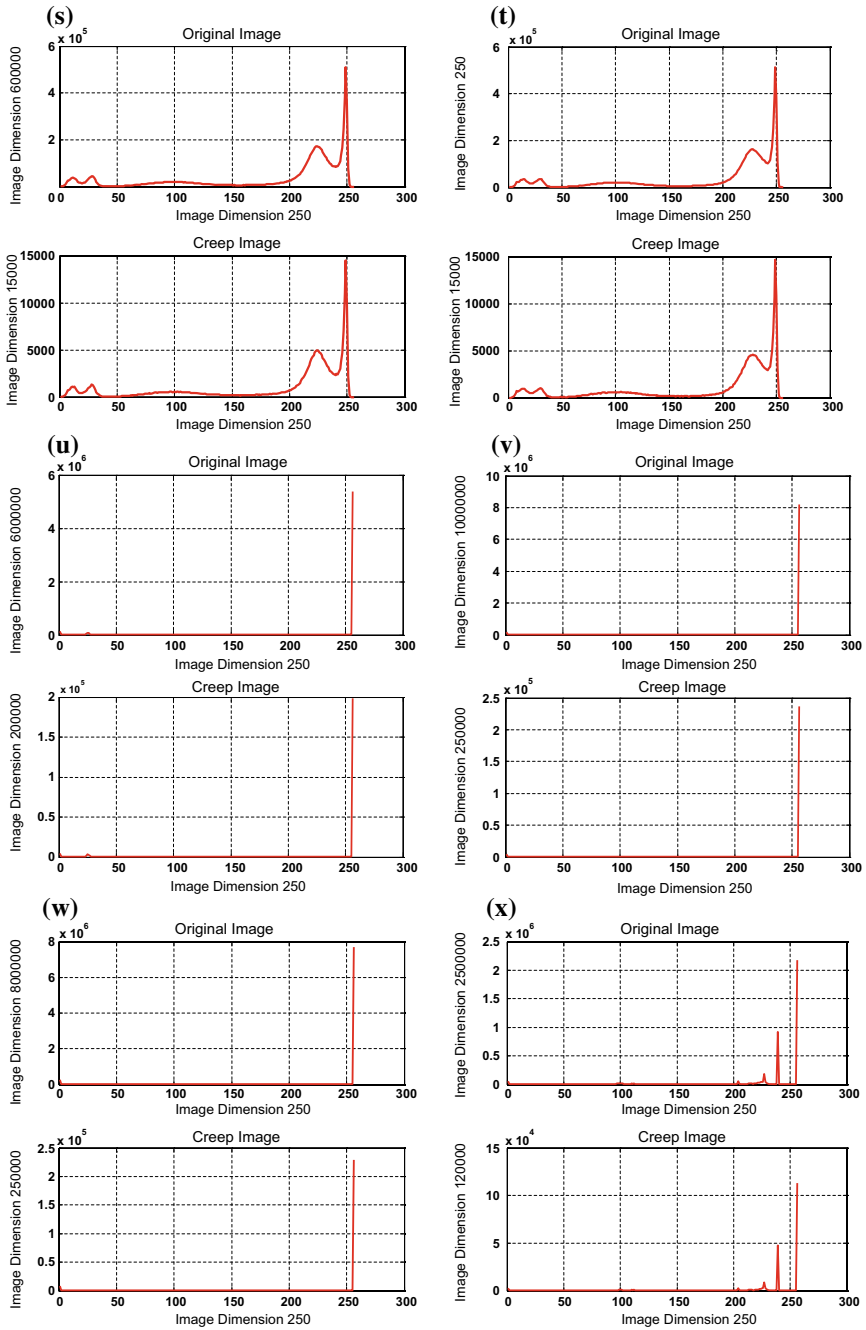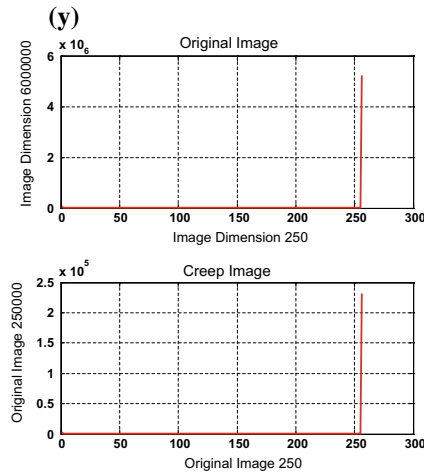
Fig. 5 (continued)

Fig. 5 (continued)

Now, the dataset image pixels are arranged in a random manner, and finally, the encrypted images are obtained. These pixels carry specific properties as their original images. We will reveal the identity of the original image and its encrypted version in final stage. We have obtained the statistical parameters for the encrypted image also, which are matched with the statistical parameters of the original images to identify the original images. Later, histogram signature plots of the original and encrypted images are plotted together which reveal the visual similarity between the original and encrypted images (Fig. 4).

Now, the statistical parameters for these creep images are obtained which reflect the similarity in the features with the original images (Table 2).

Now, for the visual interpretation histogram signatures (HS) of both original and encrypted images are plotted together which present the similarity between original and encrypted images. We have randomly arranged these HS plots, and in the final section, we will reveal the identity of the original image, its creep version, and HS plot (Fig. 5).

Now, here we have observed that like statistical parameters the HS plots have also obtained the same visual similarity. The HS rectifies that creep images can be used in place of original image for secure transmission purpose (Table 3).

Now, the overlay plotting of the obtained statistical parameters suggests that both first-order statistical parameters have obtained same numerical values, and Fig. 6a and b suggests that statistical parameter mean has obtained approximately same value for 100% cases, whereas statistical parameters standard deviation has obtained same value for 96% cases.

Table 3 Image identification on the basis of the statistical parameter and HS plots

S. no.	Dataset	Sample no.	Creep version no.	Histogram signature no.
1	Mars hand lens dataset	2030 MH 25	Creep 5	HS 5
2		NLB EDR	Creep 8	HS 6
3		2027 MH	Creep 13	HS 11
4		2030MH 26	Creep 14	HS 12
5		2030MH	Creep 3	HS 4
6	McGill texture	PP 0042	Creep 2	HS 13
7		PP 0223	Creep 16	HS 23
8		Punistrt 024	Creep 10	HS 25
9		PP RS Yacht	Creep 15	HS 24
10		RVH texture 016	Creep 22	HS 1
11		PP peal 096	Creep 19	HS 16
12		Mex 07	Creep 9	HS 2
13		PP peal 037	Creep 23	HS 14
14		Merymt 107_029	Creep 20	HS 13
15		PP pare Safari 050	Creep 18	HS 15
16	Marmot math dataset	Raw 02	Creep 24	HS 20
17		Raw 03	Creep 21	HS 21
18		Raw 04	Creep 11	HS 17
19		Raw 47	Creep 17	HS 7
20		Raw 118	Creep 12	HS 8
21	ICFHR 2016	Seite 0001	Creep 1	HS 22
22		Seite 0003	Creep 4	HS 19
23		Seite 0007	Creep 6	HS 18
24		Seite 0011	Creep 25	HS 9
25		Seite 0013	Creep 7	HS 10
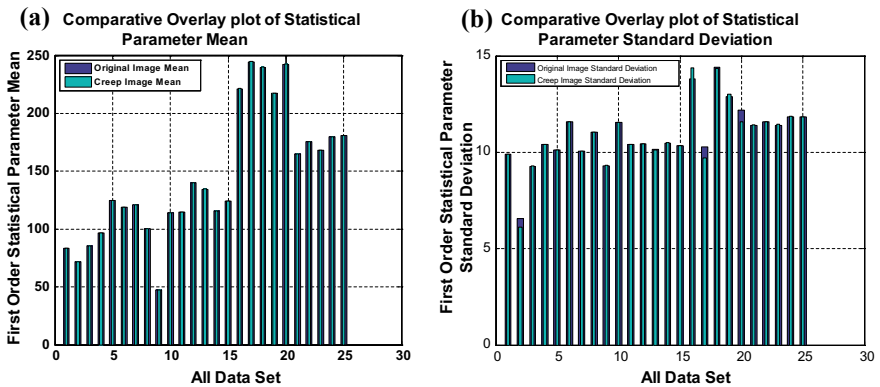
Fig. 6 **a** Comparative overlay plot of the first-order statistical parameter 'mean.' **b** Comparative overlay plot of the first-order statistical parameter 'standard deviation'

5   Conclusion

The proposed encryption scheme is a quite effective approach of image and document encryption through statistical parameters. The fusion of IoT and machine learning is explored a lot in this research; the most important advantage of this system is computer system will quickly classify images and encrypt them and send them through secure transmission. One of the areas under investigation can be if two images develop same statistical features, i.e., same numerical values for mean and standard deviation, then it is a possibility that computer can transmit that encrypted image or data to some unauthorized location or person. An attempt to reduce such technical faults can be inclusion of some more statistical features like skewness and kurtosis in the experiment process.

References

1. Gilbert K, Stephenson P (2013) Investigating computer-related crime, 2nd edn. Taylor and Francis Group, Boca Raton
2. Times of India. Over half a million Indian Facebook users may have been affected in data breach
3. The New York Times. Russian hacking and influence in the U.S. election
4. Dinstein Y (2012) The principle of distinction and cyber war in international armed conflicts. J Confl Secur Law 17(2):261–277
5. Gervais M (2012) Cyber attacks and the laws of war. Berkeley J Int Law 30(2):525–579
6. Farwell J, Rohozinski R (2011) Stuxnet and the future of cyber war. Survival 53(1):23–40
7. Landau S (2013) Making sense from Snowden: what's significant in the NSA surveillance revelations. IEEE Comput Reliab Soc 11(4):54–63
8. Hyman P (2013) Cybercrime: it's serious but exactly how serious? Commun ACM 56(3): 18–20
9. Thomas K, Li F, Zand A, Barrett J, Ranieri J (2017) Data breaches, phishing, or malware? Understanding the risks of stolen credentials. In: Proceedings of the 2017 ACM SIGSAC conference on computer and communications security, vol I, Dallas, Texas, USA, Nov 2017, pp 1421–1434
10. Ameen M, Liu J, Kwak K (2012) Security and privacy issues in wireless sensor networks for healthcare applications. J Med Syst 36(1):93–101
11. Akhilomen J (2013) Data mining application for cyber credit-card fraud detection system. In: Advances in data mining. Applications and theoretical aspects, vol III, London, pp 218–228
12. Gai K, Qiu M, Thuraisingham B (2015) Proactive attribute-based secure data schema for mobile cloud in financial industry. In: IEEE high performance computing and communications (HPCC), New York, NY, USA, pp 1332–1337

13. Ben-Asher N, Gonzalez C (2015) Effects of cyber security knowledge on attack detection. Comput Hum Behav 48(1):51–61
14. Faruki P, Bharmal A, Laxmi V, Ganmoor V, Gaur M, Conti M (2014) Android security: a survey of issues, malware penetration and defenses. IEEE Commun Surv Tutor 17(2): 998–1022
15. Faghani M, Nguyen U (2017) Modeling the propagation of Trojan malware in online social networks. IEEE Trans Dependable Secure Comput 15:1–18
16. Roy S, DeLoach J, Li Y, Herndon N (2015) Experimental study with real-world data for android app security analysis using machine learning. In: ACM proceedings of the 31st annual computer security applications conference, vol I, Los Angeles, CA, USA, pp 81–90
17. Ahmad M, Woodhead S, Gan D (2016) Early containment of fast network worm malware. In: IEEE information and computer science (NICS), vol I, Danang, Vietnam
18. He D, Chan S, Guizani M (2015) Mobile application security: malware threats and defenses. IEEE Wirel Commun 22(1):138–144
19. Muthumanickam K, Ilavarasan E (2015) Optimization of rootkit revealing system resources— a game theoretic approach. J King Saud Univ Comput Inform Sci 27(4):386–392
20. Eshete B, Alhuzali A, Monshizadeh M, Porras P, Venkatakrishnan VN, Yegneswaran V (2015) EKHUNTER: a counter-offensive toolkit for exploit kit infiltration. In: NDSS internet society I, pp 1–15
21. Chandra J, Challa N, Pasupul S (2015) Intelligence based defense system to protect from advanced persistent threat by means of social engineering on social cloud platform. Indian J Sci Technol 8(28):1–9
22. Carrasquilla J, Melko R (2017) Machine learning phases of matter. Nat Phys 13(1):431–434
23. Lee K, Lam M, Pedarsani R, Papailiopoulos D, Ramchandran K (2016) Speeding up distributed machine learning using codes. In: IEEE information theory (ISIT), vol I, Barcelona, Spain, pp 1143–1147
24. Conti M, Dehghatanha A, Franke K, Watson S (2017) Internet of Things security and forensics: challenges and opportunities. Future Gener Comput Syst 78:544–546

Drishti—Artificial Vision

Sneh Rathore, Sahil Sharma and Lisha Singh

Abstract Drishti is a computer vision and deep learning-based application developed using Python programming language for the sole purpose of envisioning the real-time environment by generating the natural language description of the real-time captured scenes. The primary objective of this project is to enable a visually impaired person to know about his or her environment in real time. In this, digital image processing is used to generate the annotations about the surroundings. To express the features, Python has been selected as an interacting language. For the ease of a user, GUI has been provided for their usage. Though the GUI has been operated and guided by Python script, there is no need for a person to know the language, for general usage.

Keywords Natural language description · Digital image processing · Image annotation · GUI

1 Introduction

"Drishti" is an intelligent and interactive artificial intelligence-based application that provides the users with the facility to generate a natural language description of the scene of his or her surroundings which is of utmost importance to the blind people. This involves generating a caption of the surrounding by capturing an image and generating the description of the scene which is human understandable. The challenge is to generate a correct description within a time frame for which

S. Rathore (✉) · S. Sharma · L. Singh
Department of Information Technology, HMR Institute of Technology, New Delhi, India
e-mail: sneh.rathore96@gmail.com

S. Sharma
e-mail: sahil8sharma8@gmail.com

L. Singh
e-mail: lisha.engg@gmail.com

various techniques such as convolution neural network and recurrent neural network are used along with long short-term memory (LSTM) network. It also incorporates the existing and well-established techniques such as computer vision and natural language processing.

The goal is to provide blind people with an application which he or she could in her daily life do daily chores of their life. This application generates a description of the image as well as the audio of the generated text so that blind can hear that out. This is achieved with the work based on deep learning techniques to generate the description of the scene. Image from the camera is fed into the pre-trained convolution neural network to create a feature vector which consists of the features in the image such as objects and motions. Then the feature vector is fed into encoder which is recurrent neural network to create encoding information which is later on used by the decoder to generate a natural language description [1]. This encoded information is fed into a long short-term memory (LSTM) decoder which generates the natural language sentence from the words fed into the network. It follows top-down approach in which the system first understands the image completely, and then it generates related words that appropriately define the image. These generated words are then used to create a meaningful sentence which can be easily understood by a human.

In Drishti, we implement our application as a single combined architecture that works on both the models. Firstly, the feature extraction through visual understandings of the provided input image and secondly a language model that generates some semantically correct and meaningful description or a natural language description for the images. We further explore the possibilities of utilizing the generated description in the form of content filtering, i.e., the image is classified as safe or unsafe, and based on this classification, the access to such images is restricted. This application can very well describe the road signs which can help not only the visually impaired but anyone to walk around. It also provides short verbal information about the surrounding or the scene on the request of the user. This information along with the image description and the image itself is saved and can be shared through e-mails. The interactive interface of the application makes it easy for anyone to access it.

2 Workflow

The Drishti application developed here is for the use of providing a low cost with high-quality vision-based assurance specifically to the visually impaired. In this, the user gets the results in the form of an audio and the application also provides voice control in the form of a Chatbot. When the user starts the application, he gets the option to either capture a real-time image or use some stored image from his/her system. This selected image enters into the backend of the application as the input where it is analyzed and classified on the basis of the features in that image. These extracted features are then provided a natural language description which is

presented in both textual and audio formats. The results can later be shared in the form of e-mail where the image along with the audio file is attached into it. With this working, Drishti provides various features by automatically describing the contents of the given input image. From humans to signboards, food, and animals everything can be classified into a natural language description for the image, thus helping the blind or visually impaired to recognize and get familiar with their surroundings. Apart from just providing the description, Drishti also makes sure of the content which is appropriate for certain age-groups. Access to the images with adulterated content is denied and restricted before it can be displayed to others. As the instructions and results are also provided in audio format, this makes it easier for anyone to access and control the application from anywhere.

Further to make the application easily available to all, an executable file has been created. The .exe file is to be installed in the system and thus can be used for required purpose. The advantage of this software is that it is platform independent and there is no restriction to OS. The use of python makes the developers more comfortable, as the open community language for it makes the project worthier. The graphical user interface here used is Tkinter. For mobile users, Drishti is also available in the form of a Chatbot. This makes it even more convenient to access the application and know about the real-time surroundings.

2.1 Flowchart

The flow of control begins with the initiation of the application, Drishti. Here the user is provided with two options:

1. Capture some real-time image
2. Use some stored image

Based on the option chosen by the user, the application performs accordingly. If the service chosen is 'Capture Image', the following set of processes take place one after the other.

1. First the camera module is called using the computer vision where real-time frames are displayed.
2. As soon as the user selects a particular frame, it is taken as the input image which is further processed for feature extraction and natural language generation.

When the user selects stored image as the working service, the following set of processes take place:

1. The user is asked to select an image from the stored images on the device through the application.
2. This selected image is taken as the input and is processed further within the natural language description module.

On successful generation of the natural language description with the help of computer vision and artificial intelligence, the result is presented to the user in the form of text and audio with the help of display module. This result can also be shared in the form of e-mail to the user for the future reference and report generation. The above-explained flow of control can be pictorially depicted as in Fig. 1.
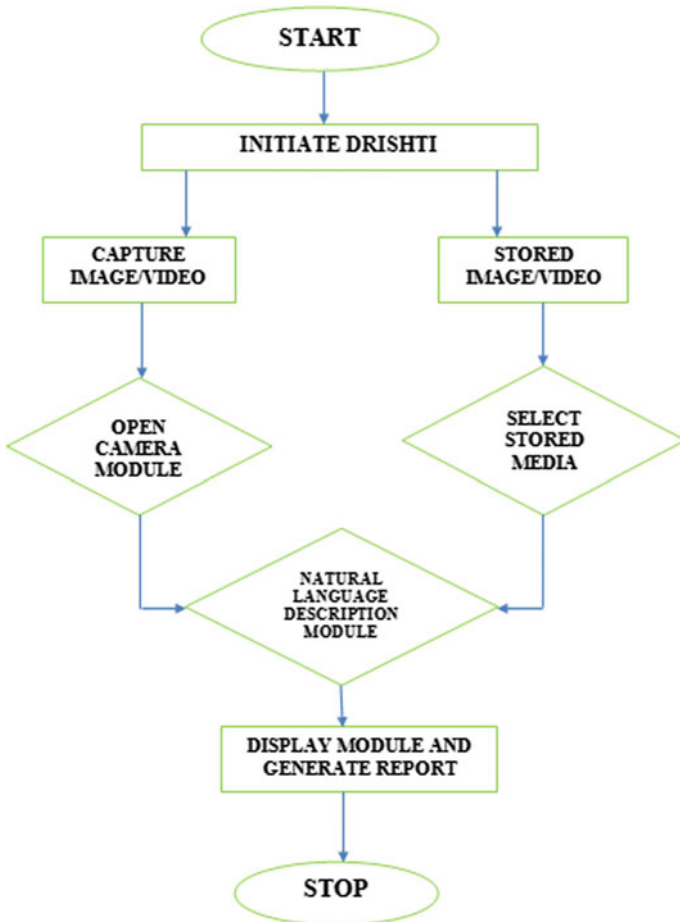
Fig. 1 Drishti—flow of control

3 Implementation

The extraction of visual features is challenging as it requires the classification of not only the objects, but also other visual features like motion and details. The next step is to generate a meaningful description of the same. This implementation focuses on the translation of the source image pixels into a semantically correct target English language description. The process to approach from the source input image to target English description is as follows.

3.1 Preprocessing

For the automatic generation of natural language description of any image or scene, preprocessing of the dataset is done and for that we build a vocabulary about the dataset, and we clean the dataset by resizing the images [2]. These steps are as follows:

1. **Building the Vocabulary**: Vocabulary is the dictionary of words which is created by using the captions present in the training dataset. This dictionary of words is then used to generate a description of the scene. The words in the dictionary are given as the input to the long short-term memory (LSTM) network. To build the vocabulary, captions from the training dataset are taken and are tokenized, and each word is given an ID. Also special tokens such as start, end, pad, and unk (unknown) are also added to the vocabulary. These words work as the starting word and ending word while generating the caption.
2. **Resize**: Images in the training dataset are of different dimensions, so it is required to resize the images to a common dimension. Although there is loss of information while resizing the images, it is acceptable since the images are then easier to process and less error occurs.

3.2 Training

This phase of Drishti is associated with the training of the dataset on the basis of which the annotations regarding the selected image are generated. First, we extract the image feature vector from the input image. The feature vector is extracted using the pre-trained convolution neural network (CNN). It is then linearly transformed to the dimension required by the LSTM network. Then decoding is done by creating the LSTM model which is used to predict words to generate the sentence. Words are predicted in steps in which each new word is dependent on the previous word and on the image feature vector. Initially, image feature vector is fed into the network only once, and then each memory cell generates a new image vector which

is used to guess the word. Then this newly generated feature vector is fed into the next memory cell as an input to predict next words.

3.3   Technical Implementation

Our Approach

Automatic generation of the image description is a difficult task. It involves the identification of the objects, their attributes, actions, and motion all together and finally the generation of a meaningful English sentence that describes all the objects and the related actions correctly. For this, it requires a detailed understanding of the image or scene which is provided by the user and further a fluent description in natural language [3]. In order to achieve this, we have chosen Python as the programming language and PyTorch for the development of the system. For the accuracy in the image description, certain set of images are pre-trained in the form of the dataset being used. The system is trained using this dataset of images with the implementation of neural networks.

3.4   Neural Network Used

1. **Convolution Neural Network (CNN)**
   When an image is provided as an input to the system, first step is the feature extraction of that image. This requires the implementation of neural network. Convolutional neural network or CNN is used for this purpose. It is used as the encoder for the extraction of the feature vector. Here, we have used ResNet-152 as the residual framework which makes the training of the network less complex than the deeper neural networks [4]. The last layer of the encoder module enters the decoder part as the input which works on LSTM [5].
2. **Long Short-Term Memory (LSTM)**
   Long short-term memory or LSTM is a special version of recurrent neural network (RNN) which reduces the complexity and tough long-sequence training done by RNN. LSTM uses a gating mechanism, and the semantic representation of the input image generated by the convolution neural network is decoded by the LSTM model [6].

3.5   Dataset Used and Training Dataset

For the accuracy and correctness of the natural language generation of the provided image/video, training of the system is necessary. For the ease of training the deeper
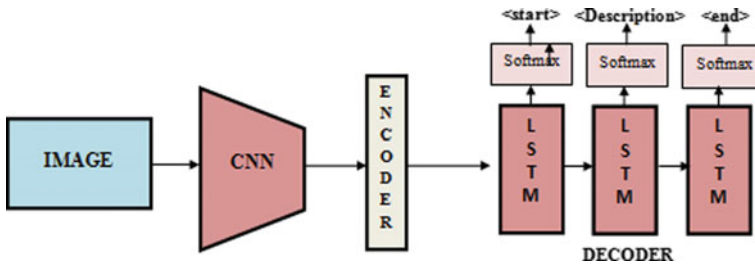
Fig. 2 Technical implementation

neural network, residual learning framework is used here. The goal of converting the given input image or a video into a natural language description is done by the encoder–decoder framework. The image encoder is a CNN, while the decoder works as LSTM [7]. This can be explained as in Fig. 2.

When the input image is selected, the CNN module receives this image and extracts the descriptive part that is the feature vector which enters into the encoder module of the application. This feature vector is then linearly transformed into the dimensions similar to the provided input dimension of the long short-term memory network [8]. The last layer of the encoder part enters the decoder part as an input. For the decoder part, LSTM decoder is used as a special type of RNN which uses the gates and is trained as a language model that provides the description of semantic features extracted by the CNN [9].

The training of the dataset involves the use of LSTM which predicts the next word on the basis of the previous word and the visual features that are extracted by the convolution neural network. This also requires the use of keywords that indicate the source and target for the decoder to work efficiently. The source is initialized by the keyword <start>, while the target is the ending of the phrase with the keyword <end> [10]. Between the source and the target comes the visual description in English language.

3.6 Software Implementation

Drishti is software which is implemented as a desktop application as well as a Chatbot for the mobile users. It provides the feature of generating the natural language description of the images or videos either stored or captured in real time. The GUI is designed using the Tkinter, which is a Python-based tool for designing interfaces. Drishti has two modules that work independently of each other. These modules are called from a common interface to provide the functionality to the user.

First module is for capturing the real time image; this can be used for recording a video and analyzing it frame by frame where the user receives the description both textually and verbally. The application can also be controlled through voice using

the Chatbot which provides the visually impaired to control the application as and when required. In this, the application first calls a capture module which shows the current view of the camera where the user can select the current frame which then goes to the analyzer part of the application where the real-time frame is classified based on the feature vectors and then results into the natural language description of the features.

Second module is for using the stored images. Similar to the captured images, stored images are also analyzed for its features that are further presented in the form of a human language textually as well as verbally. This can be used for content filtering in the form of parental control over the visuals that can or cannot be presented to the children. These two modules are combined as a whole to provide artificial vision features using digital image processing.

Software is implemented as a desktop application with the help of scripts. Application is called using the main script which imports the required packages and loads the interface. All the modules are accessible through the main script. The application is compatible with all the operating systems, i.e., Linux, Windows, Mac OS, etc. This can also be used on mobile phones that have a camera and support Internet in the form of a Chatbot with all the operating systems, i.e., iOS and Android.

4   Snapshots

The application snapshots are as follows in Fig. 3.

5   Conclusion and Future Scope

In current work, we developed the system that provides a description about the user's surrounding using digital image processing and natural language description. This system is developed in Python and has an interactive GUI for the ease of the user in the form of a desktop application and a Chatbot for mobile users. Drishti provides a description in verbal as well as in audio form. The user can get to know about the different traffic signboards, real-time images, videos, and textual content. This can also be used for filtering the content for the selected categories. Also the warnings can be generated for the images or visuals that are not safe for children or any other age-group. The user also receives an e-mail along with the image and audio files for later usage. With the help of the Drishti Chatbot, the user can take the advantage of this application from anywhere.

Thus, the provided features in the above-discussed software give it long scope in the future as

a) Application Interface   b) Usage of a Stored Image   c) Real time Image

d) Content Filtering   e) Chat bot in Android   f) Chat bot in Ios

Fig. 3 **a–f** Drishti—artificial vision

1. Implementation of the application on Raspberry Pi to make it portable and flexible for usage.
2. Live coverage of the environment under surveillance on the mobile phone of the owner. This requires the development of the mobile app.
3. It can be implemented for traffic management.
4. The generated description can be used as a recommendation system on the basis of the extracted features.

Further to these, there are many more aspects where the development of the application can be extended.

References

1. Pan P, Xu Z, Yang Y, Wu F, Zhuang Y (2015) Hierarchical recurrent neural encoder for video representation with application to captioning. CoRR, abs/1511.03476
2. Chen X, Zitnick CL (2014) Learning a recurrent visual representation for image caption generation. CoRR, abs/1411.5654
3. Farhadi A, Hejrati M, Sadeghi MA, Young P, Rashtchian C, Hockenmaier J, Forsyth D (2010) Every picture tells a story: generating sentences from images. In: Proceedings of the 11th European conference on computer vision: part IV, ECCV'10. Springer-Verlag, Berlin, Heidelberg, pp 15–29
4. He K, Zhang X, Ren S, Sun J (2015) Deep residual learning for image recognition. CoRR, abs/1512.03385
5. Krizhevsky A, Sutskever I, Hinton GE (2012) Imagenet classification with deep convolutional neural networks. In: Bartlett PL, Pereira FCN, Burges CJC, Bottou L, Weinberger KQ (eds) NIPS, pp 1106–1114
6. Hochreiter S, Schmidhuber J (1997) Long short-term memory. Neural Comput 9:1735–1780
7. Venugopalan S, Rohrbach M, Donahue J, Mooney R, Darrell T, Saenko K (2015) Sequence to sequence—video to text. CoRR, abs/1505.00487
8. Venugopalan S, Xu H, Donahue J, Rohrbach M, Mooney R, Saenko K (2014) Translating videos to natural language using deep recurrent neural networks. CoRR, abs/1412.4729
9. Karpathy A, Johnson J, Fei-Fei L (2015) Visualizing and understanding recurrent networks. CoRR, abs/1506.02078
10. Ng JY, Hausknecht MJ, Vijayanarasimhan S, Vinyals O, Monga R, Toderici G (2015) Beyond short snippets: deep networks for video classification. CoRR, abs/1503.08909

A Comprehensive Study on Virtual Machine Migration Techniques of Cloud Computing

Gurpreet Singh, Manisha Malhotra and Ajay Sharma

Abstract Cloud computing emergence is based on virtualization technologies which comes out with more opportunities without investing any cost on infrastructure. Every cloud data center comprises of heterogeneous servers which are hosting different VMs with different specifications and instances. It may cause the imbalance of resources. This paper exemplifies the concept of virtualization in cloud environment with virtual machine (VM) migration techniques. It also presents the survey and comparative analysis of VM migration algorithms given by eminent researchers in this field.

1 Introduction

The term cloud stands for **C**ommon **L**ocation-independent **O**nline **U**tility service, available on-**D**emand. It is virtualized environment which provides computing resources like storage, platforms, and application with user interactive interface. Cloud computing offers online resources, offline access, flexibility, savings, etc., that can overcome the limitations of traditional computing. Initially, Amazon

G. Singh · A. Sharma
Department of Computer Science and Engineering, SRM University,
Delhi-NCR, Sonepat, Sonipat, India
e-mail: gps.srm@gmail.com

A. Sharma
e-mail: ajay.s@srmuniversity.ac.in

M. Malhotra (✉)
Chandigarh University, Mohali, India
e-mail: mmanishamalhotra@gmail.com

introduced Elastic Compute Cloud (EC2) in 2006, and then, the term cloud computing came in limelight [1]. Although it becomes more popular in 2007 and increases its demand because of flexible and dynamic infrastructures, computing environments and configurable quality of software services.

Earlier there was a computing technology known as mainframe computing which provided resources on large scale. It was very intense, reliable, and specific for large information developments and enormous I/O tasks. They were for the most part utilized by immense associations for large amount of data handling. This technology adopted batch processing. After this and supercomputers, cluster computing industrialized in 1980. For processing of parallel and high computing, the size of supercomputers was reduced and also the cost. Attributable to headways in innovation, grid computing evolved in 1990s. It had the ability to get the massive computational power and different kinds of tasks. All the clusters that have been distributed geographically together make a grid. These clusters have associated with different organizations and shared computational power. Clusters were limited to regular assets prompting advancement of networks. Cloud computing is frequently considered as the successor of grid computing. Basically, it provides three kinds of services: Software as a service (SaaS), platform as a service (PaaS), Infrastructure as a service (IaaS). Every layer has its own inherent issues. Cloud computing is one of the most recent domains of research interests; however, at center it is not something new truly. It might be contrasted, post-paid cell phones where client may profit the bought in administrations and pays in light of the utilization. Client is unconscious of the specialized points of interest of setting up system and administration provisioning. Each one of those points of interest is taken care of by the organization or service provider. Comparative idea is center of the innovation in center where client now appreciates boundless administrations on computer system without really owning them. Consequently, an essential result is benefit provisioning at the service provider's end without overburdening the node in a safe manner [2]. It can be done by successful migration of virtual machines with in the data centers. Moreover, cloud computing revolves around many issues like resource scheduling, load balancing, scalability, virtual machine replacement, energy efficiency, etc. This paper focuses on virtual machine migration techniques in an optimized manner so that user will get quality of services. Before proceeding further, the concept of virtualization should be clear.

This paper is organized in some different sections. Section 2 will elaborate the concept of virtualization and its types. Then, virtual machine migration and its process are described in Sect. 3. Section 4 depicts the literature survey available on VM migration techniques in cloud computing. After that, a comparative study follows the literature survey based on some parameters. Finally, the last section will conclude this paper and describe some issues still prevailing and scope of further research in this field.

2 Virtualization

Before proceeding further on virtual machine migration, the concept of virtualization must be clear. Therefore, this section describes the virtualization and its types in detail.

As it is already known, virtualization has been started in 1960. But it becomes a staple with the advent of cloud computing. To optimize the cost of operating system and improve the efficiency of infrastructure's services, it is rapidly used in cloud computing. It allows running multiple operating system and applications on a single server which is logically separated [3]. It is the process to create a different virtual environment which performs different tasks without interrupting each other on a single server. It can be a single instance or combination of networks. The main benefits of virtualization are as follows:

- Reduction in cost
- Optimized resource utilization
- Accessibility
- Risk optimization.

There is a firmware available known as hypervisor which is responsible for interaction between virtual machine and host machine or with server. Figure 1 represents the scenario of virtualization.
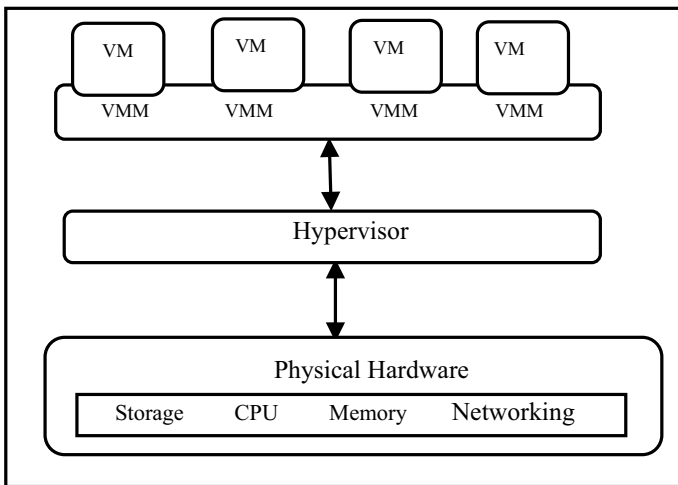
Fig. 1 Scenario of virtualization

2.1 Types of Virtualization

Different types of virtualization are available and are shown in figure. It is quite difficult to say that which one is better and which one in worse. It totally depends upon the usage of resources, type of computing task, and operating system.

2.1.1 Hardware Virtualization

Whenever the virtual machine is installed on hardware system, it acts like a real operating system which is known as hardware virtualization. For example, a system contains Windows operating system and installs Linux operating system as virtual machine, and then, Windows acts as host and Linux operating system acts as guest. The main aim of virtual machine manager (VMM) is to control and monitor processor, memory, and hardware resources. It actually improves the overall efficiency of system along with cost. Because all operating systems run parallel on a single CPU, it is easy for companies to manage the updates and instant changes in operating system and various applications without interference of user.

The hardware virtualization further is categorized into two parts:

Full Virtualization: In this virtualization, the guest operating system does not require any modifications, because hardware is simulated.
Para Virtualization: The guest operating system requires modification because hardware is not simulated.

2.1.2 Software Virtualization

It creates multiple virtual environments on a single machine. For example, android is running on Windows machine and .net is also running on same machine, which is known as software virtualization.

2.1.3 Memory Virtualization

For providing shared, distributed, and network function, memory virtualization is introduced by decoupling memory from server. It is directly related to end user and focused on application performance. It plays an important role in strategic decisions for any enterprises. It provides different storage resources built on a single storage device which is known as storage virtualization. It has the capability to use resources more efficiently. It is actually required in both environment cloud and virtual. Generally, it is of two types: *Block*: It takes place at disk level before the file system exists. *File*: For file level usage, software must be installed on it.

2.1.4 Data Virtualization

Without any efforts, the user can easily manipulate the data. Users can easily scale up and scale down data storage as when they needed. It decreases the workload and data errors.

2.1.5 Network Virtualization

It is defined as the ability to create virtual network having decoupled from underlying network hardware. It ensures the integrate network that can provide better support in virtual environment. It also intends to provide network optimization for different parameters like security, reliability, and flexibility.

2.1.6 Desktop Virtualization

It is the process to isolate instance of logical operating system from client which is used to access it. It also provides flexibility to users by accessing data of PC from any location. It also supports security of the data.

All types of virtualization depict that it is an easy way to create the virtual server in cloud so that provider and users do not have to manage so many things. It keeps the data and can be access from everywhere. Therefore, it increases the productivity, efficiency, and security and decreases the cost and overhead of provider. The next section describes the virtual machine migration techniques in cloud computing.

3 Virtual Machine Migration in Cloud Computing

This section provides the technologies of virtual machine migration with its execution procedures. Basically, it is the process of migrating a virtual machine from one host to another. It also has the capability to move workload of multiple running virtual machines on a single physical machine. The main difference between virtualization and virtual machine migration is that only migration module is inculcated with hypervisor. The architecture of virtual machine migration virtualized platform is shown in Fig. 2.

Although the process of migration has been initiated in 1980, it was used often, due to its main limitation, i.e., how to handle interaction between various modules of operating system. But it overcomes in virtual machine migration because it moves the whole operating system along with running processes. VM migration becomes this process simplified and efficient. It also takes care of load balancing, energy consumption, workload consolidation, etc. Henceforth, it becomes more popular and widely adopted in industry. Table 1 describes the types of VM migrations.
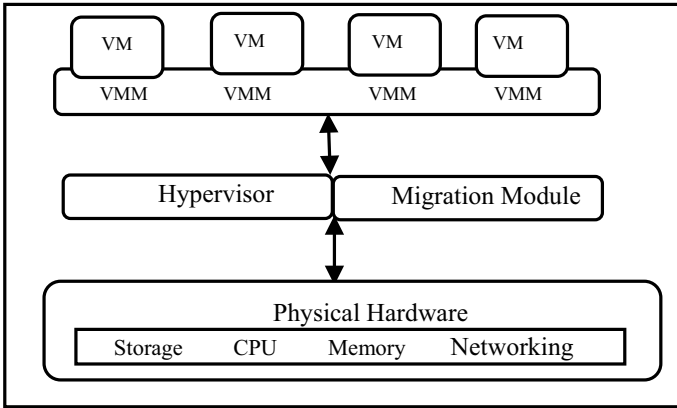
Fig. 2 Migration—virtualization architecture

Table 1 VM migration type

VM migration type	Description
Cold migration	Before migration, the virtual machine must be powered off, after doing this task. The old one should be deleted from source host. Moreover, the virtual machine need not to be on shared storage
Warm migration	While transferring OS and any application, there is no need to suspend the source host. Basically, it has high demand in public cloud
Live migration	It is the process of moving a running virtual machine without stopping the OS and other applications from source host to destination host

3.1 Techniques of VM Migration

This section describes the types of virtual machine migration techniques. It is basically of two types:

- Pre-copy migration
- Post-copy migration

3.1.1 Pre-copy Migration

In this migration, the hypervisor copies all memory page from source machine to destination machine, while the virtual machine is running. It has two phases: warm-up phase and stop-and-copy phase.

Warm-Up Phase: During copying all memory pages from source to destination, some memory pages changed because source machine CPU is active. All the

changed memory pages are known as dirty pages. All these dirty pages are required to be recopied on destination machine; this phase is called as warm-up phase.

Stop-and-Copy Phase: Warm-up phase is repeated until all the dirty pages recopied on destination machine. This time CPU of source machine is deactivated till all memory pages will transfer another machine. Ultimately, at this time CPUs of both source and destination are suspended; this is known as downtime phase. This is the main thing that has to explore in migration for its optimization.

3.1.2 Post-copy Migration

In this technique, VM at the source is suspended to start post-copy VM migration. When VM is suspended, execution state of the VM (i.e., CPU state, registers, non-pageable memory) is transferred to the target. In parallel, the sources actively send the remaining memory pages of the VM to the target. This process is known as pre-paging. At the target, if the VM tries to access a page that has not been transferred yet, it generates a page fault, also known as network faults. These faults are redirected to the source, which respond with the faulted pages. Due to this, the performance of applications is degrading with number of network faults. To overcome this, pre-paging scheme is used to push pages after the last fault by dynamically using page transmission order. Figures 3 and 4 shows the pre-copy and post-copy migration technique, respectively.

The upcoming section will describe the existing VM replacement algorithms by different academia and industries followed by the comparative analysis of algorithms.

4 Comparative Analysis of VM Migration Algorithms

This section presents the brief view of some existing algorithms on VM migration. Live migration techniques are used for efficient utilization of cloud data centers. Few of the mechanisms of eminent researchers are explained as follows.

The authors [4] proposed an agent-based migration algorithm for load balancing dynamically in high-level applications. The main objective of this algorithm is to migrate the load between different federations and reduce the communication cost. It has the capability to identify the overloaded VM on prior basis. It also applies the live migration and selects the destination VM as least in cost. Hence, it reduced the number of overloaded hosts. Ni et al. [5] proposed the algorithm of concurrent users. These users might have acquired same resources from same data center which may lead to degradation in performance of VM. The authors have proposed multiple resources with its weights. Every VM contains score which is inversely proportionate to its utilization. It reduces the standard deviation of used nodes. It also concentrates on placement of VM at initial stage rather than running stage.

Fig. 3 Pre-copy migration technique
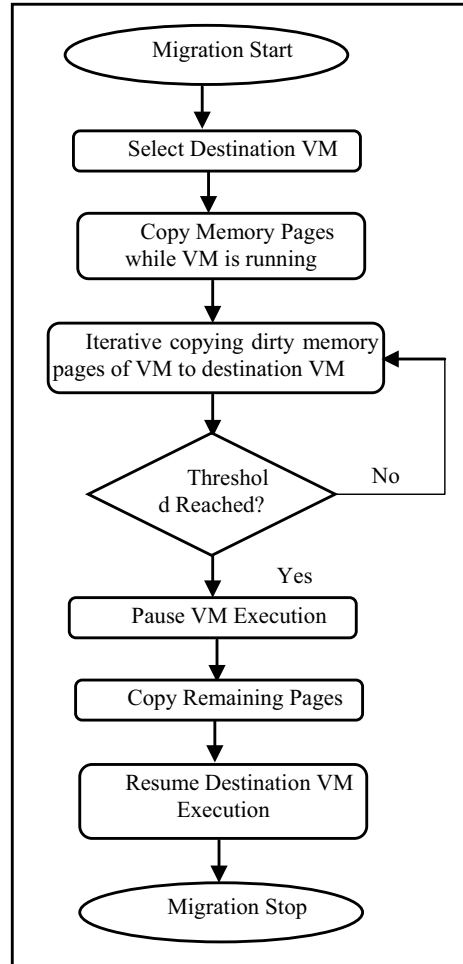
Tordsson et al. [6] solution is based on multi-objective VM placement algorithm. To reduce the user's efforts, the authors proposed an optimized algorithm which is based on integer programming and assignment problem with different parameters like makespan, throughput, and network bandwidth. Zhao and Huang [7] presented adaptive live migration of VMs. It was designed for eucalyptus enhancement by implementing load balancing mechanism. Individually, it calculates the function value of each host. To calculate the cost between two different VMs, firstly build a connection and then select it randomly. It applied Nash equilibrium which is used for load balancing.

Yang et al. [8] presented a mechanism to avoid unnecessary migration and reduction in number of overloaded hosts. This mechanism adopted weighted function with multiple types of resources. To evaluate the load of a VM, this

Fig. 4 Post-copy migration technique
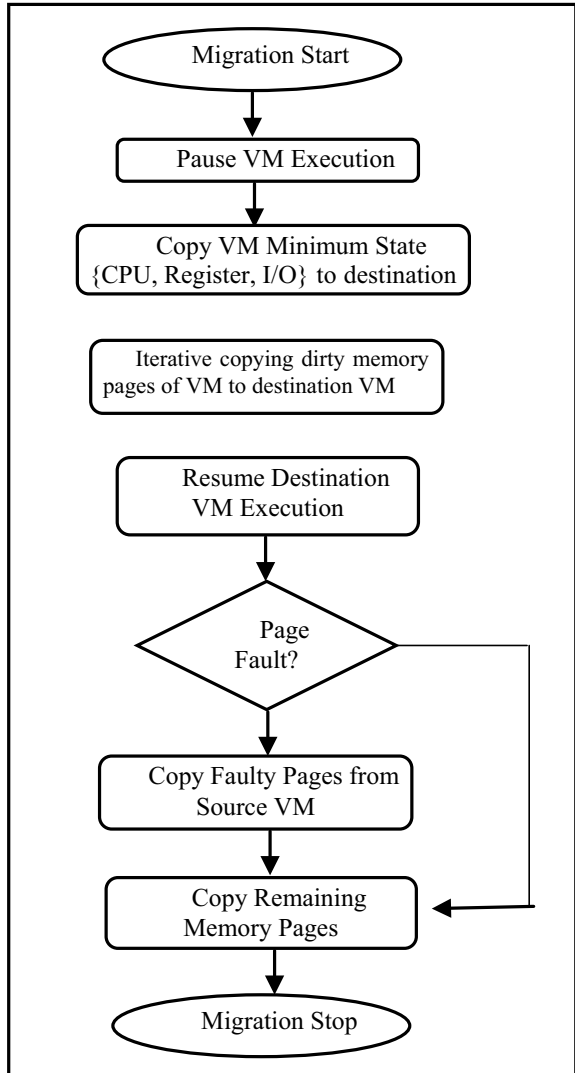
algorithm is categorized into four main domains: light load, optimal, warning, and overloaded. Every domain has its different migration strategies. In addition to this, three times handshaking protocol is used to avoid multiple migrations with in the same host. The main objective of this paper [9] is to minimize the response time and throughput. Firstly, it generated low overhead; secondly, load information is collected periodically; finally, it minimizes the downtime which is the main cause of live migration.

Rouzaud-Cornabas [10] presented peer-to-peer architecture. Its main objective is to reduce load on single host. The authors have selected dynamic scheduling due to

VM behaviors that cannot be predicted as it is non-deterministic in nature. It also ensures the system scalability. Gao et al. [11] proposed VM placement algorithm by modifying ant colony system. It proposed multi-objective algorithm named as virtual machine placement ant colony system (VMPACS).

Tian et al. [12] proposed integrated environment for VM scheduling along with weights of CPU and network bandwidth. To evaluate the performance, the authors have taken average imbalance level as a new metric for all hosts. In this paper, the authors have not considered the VM communication cost. Thiruvenkadam and Kamalakkannan [13] proposed hybrid genetic algorithm. Its main objective is to minimize the number of migration. It has twofold. Firstly, VM packing which is done by checking the load of host and heuristic approach then optimize VM replacement based on fitness function.

From Table 2, it has been observed that most of the algorithms have focused on communication cost, response time, and throughput by inculcating optimization techniques. Few of the researchers have used agent technology to address this issue. In future, software or mobile agents can deploy for getting more effective and optimized results.

Table 2 Comparative analysis of VM migration algorithms

Authors/Years	Migration cost	Optimization strategy	Live migration	Environment	Performance evaluation
Deshpande and Keahey (2017) [14]	×	Heuristic	√	Simulated with private cloud	Reduced migration time and VM traffic
Desai and Patel (2016) [15]	×	Heuristic	√	Simulated cloud using CloudSim	Improved total migration time and downtime
Tao et al. (2016) [16]	×	Heuristic	×	Simulated with private cloud	Reduced energy consumption
Song et al. (2015) [4]	√	Heuristic	√	Real with public cloud	Reduced execution time
Thiruvenkadam and Kamalakkannan (2015) [13]	√	Hybrid	√	Simulated with private cloud	Lower load imbalance as compared to round robin
Cho et al. (2015) [17]	×	Meta-heuristic	√	Simulated with private cloud	Reduced makespan
Wen et al. (2015) [18]	√	Meta-heuristic	√	Simulated with private cloud	Reduced load variance

Table 2 (continued)

Authors/Years	Migration cost	Optimization strategy	Live migration	Environment	Performance evaluation
Tian et al. (2014) [19]	√	Heuristic	√	Simulated with public cloud	Processing time fast
Gao et al. (2013) [11]	√	Meta-heuristic	√	Simulated with public cloud	Increased computation time
Tordsson et al. (2012) [6]	√	Meta-heuristic	×	Real with hybrid cloud	Optimized cost
Ni et al. (2011) [5]	×	Heuristic	×	Real with private cloud	Reduced imbalance effects
Tian et al. (2011) [12]	√	Heuristic	√	Simulated with public cloud	Reduced average imbalance value
Yang et al. (2011) [8]	√	Heuristic	√	Simulated with private cloud	Low standard deviation
Bhadani and Chaudhary (2010) [9]	×	Heuristic	√	Real with public cloud	Reduced overloaded hosts
Rouzaud-Cornabas (2010) [10]	×	Heuristic	√	Simulated with public cloud	Improved throughput
Hu et al. (2010) [20]	×	Meta-heuristic	√	Real with private cloud	Overcome load balancing

5 Conclusion and Future Scope

The comprehensive study and survey of this paper throws light on virtualization, its types, VM migration techniques, and its types to come up with solution of prevailing issues during VM replacement. This paper mainly focuses on survey of various migration algorithms. Every algorithm has its specific strength and weakness. From this survey, it has been observed that many of algorithms are based on resource scheduling and load balancing while migration. Few of work has been done using agents. In future, agents can inculcate and will get more efficient and reliable results. Moreover, service-level agreement (SLA) violations are neglected in most of the proposed solutions. Hence in future, it can also be taken into consideration.

References

1. Armbrust M, Fox A, Griffith R, Joseph AD, Katz RH, Konwinski A, Lee G, Patterson DA, Rabkin A, Stoica I, Zaharia M (2009) Above the clouds: a Berkeley view of cloud computing. UC Berkeley Reliable Adaptive Distributed Systems Laboratory, pp 1–23
2. Yang H, Tate M (2009) Where are we at cloud computing?: A descriptive literature survey. In: Association for information system, pp 807–819
3. Kejiang Y, Xiaohong J, Dawei H, Jianhai C, Bei W (2011) Live migration of multiple virtual machines with resource reservation in cloud computing environments. In: IEEE 4th international conference on cloud computing, pp 267–274
4. Song X, Ma Y, Teng D (2015) A load balancing scheme using federate migration based on virtual machines for cloud simulations. Math Probl Eng 1–11
5. Ni J, Huang Y, Luan Z, Zhang J, Qian D (2011) Virtual machine mapping policy based on load balancing in private cloud environment. In: International conference on cloud and service computing (CSC), IEEE, pp 292–295
6. Tordsson J, Montero RS, Moreno-Vozmediano R, Llorente IM (2012) Cloud brokering mechanisms for optimized placement of virtual machines across multiple providers. Future Gener Comput Syst 28:358–367
7. Zhao Y, Huang W (2009) Adaptive distributed load balancing algorithm based on live migration of virtual machines in cloud. In: 5th international joint conference on INC, IMS and IDC, pp 170–175. IEEE, USA
8. Yang K, Gu J, Zhao T, Sun G (2011) An optimized control strategy for load balancing based on live migration of virtual machine. In: 6th annual China grid conference, pp 141–146. IEEE, Dalian, China
9. Bhadani A, Chaudhary S (2010) Performance evaluation of web servers using central load balancing policy over virtual machines on cloud. In: 3rd annual ACM Bangalore conference, ACM, pp 1–4
10. Rouzaud-Cornabas J (2010) A distributed and collaborative dynamic load balancer for virtual machine. In: European conference on parallel processing, Ischia, pp 641–648
11. Gao Y, Guan H, Qi Z, Hou Y, Liu L (2013) A multi-objective ant colony system algorithm for virtual machine placement in cloud computing. J Comput Syst Sci 79:1230–1242
12. Tian W, Zhao Y, Zhong Y, Xu M, Jing C (2011) A dynamic and integrated load-balancing scheduling algorithm for cloud datacenters. In: IEEE international conference on cloud computing and intelligence systems, pp 311–315
13. Thiruvenkadam T, Kamalakkannan P (2015) Energy efficient multi-dimensional host load aware algorithm for virtual machine placement and optimization in cloud environment. Indian J Sci Technol 8:1–11
14. Deshpande U, Keahey K (2017) Traffic sensitive live migration of virtual machines. Future Gener Comput Syst 72:118–128
15. Desai MR, Patel HB (2016) Performance measurement of virtual machine based migration using pre-copy approach in cloud computing. In: 2nd international conference on information and communication technology for competitive strategies, ACM, pp 1–4
16. Tao F, Li C, Liao T, Laili Y (2016) BGM-BLA: a new algorithm for dynamic migration of virtual machines in cloud computing. IEEE Trans Serv Comput 9:910–925
17. Cho KM, Tsai PW, Tsai CW, Yang CS (2015) A hybrid meta-heuristic algorithm for VM scheduling with load balancing in cloud computing. Neural Comput Appl 26:1297–1309
18. Wen WT, Wang CD, Wu DS, Xie YY (2015) An ACO-based scheduling strategy on load balancing in cloud computing environment. In: 9th international conference on frontier of computer science and technology, pp 364–369

19. Tian W, Xu M, Chen Y, Zhao Y (2014) Prepartition: a new paradigm for the load balance of virtual machine reservations in data centers. In: IEEE international conference on communications (ICC), pp 4017–4022
20. Hu J, Gu J, Sun G, Zhao T (2010) A scheduling strategy on load balancing of virtual machine resources in cloud computing environment. In: 3rd international symposium on parallel architectures, algorithms and programming, pp 89–96

Genetic-Algorithm-Optimized Artificial Neural Network for Short-Term Load Forecasting: An Indian Scenario

Dhruv Upadhaya, Ritula Thakur and Navneet Kumar Singh

Abstract Power system planning (PSP) plays a path-decider role for power engineers, during power system operation/expansion or establishing an entirely new plant. Accurate load forecasting (LF) is a mandatory need for good PSP. Short-term LF is one of the vital tools, to support short-term planning issue. There is a rich literature exhibiting artificial-neural-network-(ANN)-based forecasting models. These models have certain limitations like slow and convergence in local optima, and low accuracy, especially when dealing with recent power system load profiles. This paper proposes the implementation of genetic algorithm and ant colony (AC) as weight optimizer for ANN-based LF model. It is hence established from the obtained results that GA-optimized ANN model outperforms, comparing to AC-optimized ANN model as well as Levenberg–Marquardt trained ANN model. While developing these models meteorological parameters, viz temperature, precipitation, and wind speed besides the electric load belonging to Shimla, Himachal Pradesh is considered.

Keywords Genetic algorithm (GA) · Feedforward neural network (FFNN) · Ant colony optimization (ACO) · Short-term load forecasting (STLF)

D. Upadhaya (✉) · R. Thakur
National Institute of Technical Teachers' Training and Research, Chandigarh, India
e-mail: dhruv.upadhaya1994@gmail.com

R. Thakur
e-mail: ritula.thakur@gmail.com

N. K. Singh
Motilal Nehru National Institute of Technology Allahabad, Allahabad, India
e-mail: nvnt.kmr.sngh@gmail.com

1   Introduction

The importance to gathering the power consumption and generating information increases with the steep increase in power consumption. Having prior information about the energy consumption can help in proper scheduling of generators [1]. This lowers down the operating cost of power system. It also saves the maintenance and thus increases the reliability of power system, so that an uninterruptable supply is available at the consumer end [2, 3]. An accurate forecast leads to economic scheduling, maintenance, tariff rates adjustment, and contract evaluation in a convenient way [4, 5]. Effective planning can save a huge amount of money from draining and can lead a pivotal role in economic growth of the developing countries like India.

Factors affecting energy consumption are.

- Weather variables like temperature, dew point, dry bulb temperature, wind speed, cloud cover, and relative humidity.
- Demographic factors like human body index and population growth.
- Economic factors like GDP, average income, standard of living, and quality of life.
- Other factor like day of week.

In this technological era, an accurate forecast can help in implementation of concept of smart buildings and smart grids [6]. Depending upon the time span, the LF can be divided into three categories, i.e., short-term LF, medium-term LF and long-term LF [7]. But due to a wide range of application of STLF, it has been on the prime focus of the researchers [8]. With the ability of the ANN to identify the nonlinear relationship between the input and the output, ANN is always preferred when the load profile is nonlinear. Three models proposed in the paper are Feedforward neural network (FFNN), AC-optimized FFNN, and GA-optimized FFNN. FFNN is the simplest ANN structure which uses Levenberg–Marquardt for its training. But it has slow learning rate as well as it easily gets trapped in the local minima, so its usage is generally discouraged for load forecasting. The global minima of the weights are found out, so that the error between the actual load and the forecasted load can be minimized. Intended for finding the global minima, the ant colony ANN and GA-ANN are used. Hidden and output neurons have to be activated by a function. Transfer function for the hidden and the output neuron is hyperbolic tangent sigmoid.

In this paper, STLF for Himachal Pradesh is done. Input parameters taken are historical load, temperature, wind speed, and precipitation. Shimla is taken for the weather variables. Load forecast is done for six days, and the accuracy is determined by calculating mean absolute percentage error (MAPE), mean absolute error (MAE), mean square error (MSE), and root mean square error (RMSE).

2 Load Data Analysis

A proper data is required for training of ANN. So after acquiring the data, some modifications have to be done to the data. This section deals with the procedure for the proper utilization of the data.

2.1 Case Study

To develop the STLF model, the load for Himachal Pradesh is acquired from 1 October, 2016 to 31 October, 2017, i.e., 365 days. A total of 359 days are used for the training of the model, and the load forecast for the next six days is done, i.e., from 26 October to 31 October, 2017.

2.2 Load Profile Analysis

To analyze the data on week of November is taken, and the analysis shows that the load peak is in the morning from 8 a.m. to 9 a.m. It faces a decrease in the noon time as the temperature increases. Again the load rises during the sundown. Figure 1 shows the normal load profile for the first week of November.

2.3 Pattern of Input–Output for Training of ANN

The input–output pattern used for the model constructed is shown as follows. Day type is taken as the input and the rest of the inputs are shown in Table 1.
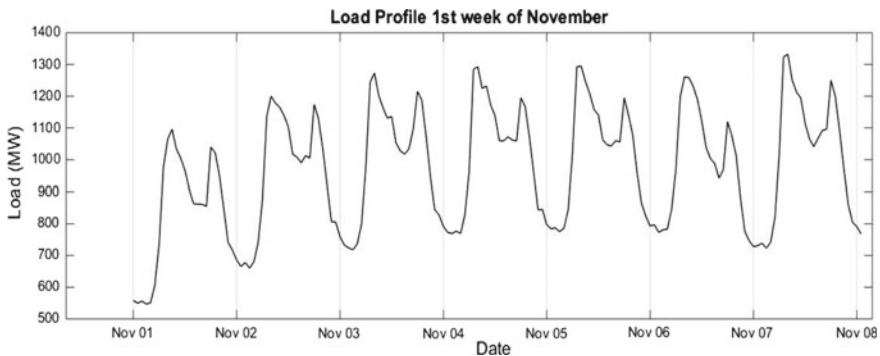
Fig. 1 Load profile of Himachal Pradesh from 1 November to 7 November, 2016

Table 1 Neural input/output configuration

Input neurons	9
Hidden neurons	10
Output neurons	1
Load values taken as input	$L(t-1)$, $L(t-168)$
Temperature values as input	$T(t-1)$, $T(t-168)$
Precipitation values as input	$P(t-1)$, $P(t-168)$
Wind speed values as input	$W(t-1)$, $W(t-168)$

3 ANN Models

In this section, the basic idea of the feedforward neural network is discussed.

Feedforward Neural Network

The basic FFNN is shown in Fig. 2. The number of the input neurons and output neurons is selected on the basis of the application for which the forecast has to be done. For the processing, hyperbolic tangent sigmoid transfer function is used for both the hidden as well as the output neuron. The output of the nth layer is given by the equation.

$$Y_p^N = f\left(\sum_{i=1}^{n} Y_i^{N-1} \times w_{pk} + b_{p0}w_{p0}\right) \tag{1}$$

where, Y_p^{N-1} = sum of inputs of the pth neuron of the $N-1$ layer, w_{qk} is the weight between the pth neuron of the nth layer and kth neuron of the $(n-1)$th layer, and z is the number of neurons in the nth layer. b_{p0} is the bias for the pth neuron.
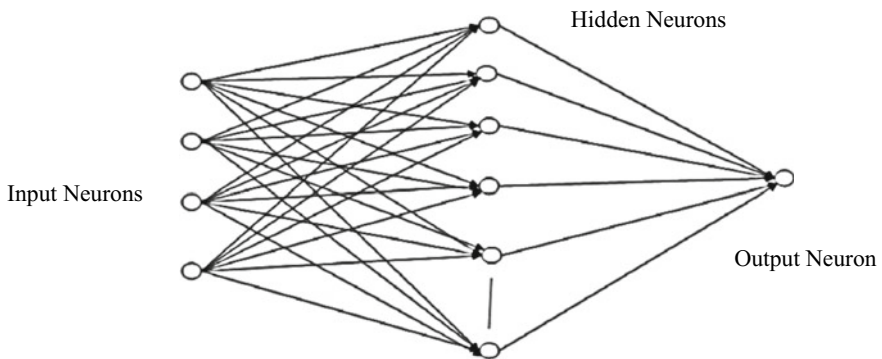
Fig. 2 Feedforward neural network

4 Proposed GA-ANN Model

As discussed in the previous sections that the existing forecasting systems with FFNN with conventional back propagation do not optimizes the weights for proper training; thus, it is not able to generate an accurate load forecast. Therefore for the proper calculation of the forecasted load, its parameters, i.e., biases and weights are optimized by GA and thus sustainability of the model is increased.

4.1 Genetic Algorithm

The main principle on which genetic algorithm based is the "survival of the fittest." It is driven by the principle of biological evolution. The population of the individuals or current population is modified for each solution. The highest fitted individuals are used for the next generation or off springs.

The general flowchart of genetic algorithm is shown in Fig. 3.

4.2 Fitness Functions and Proposed Process

The weights and the biases of the FFNN are optimized by using GA for decreasing the MAPE. The process is summarized below:

1. Generation of the values for the weights and biases randomly and initialization of the generation count to 1.
2. Assessment of the generated population is done by evaluating the MAPE between the actual and the forecasted load for the fitness.
3. The maximum errors individuals are discarded.
4. Recombination and mutations of the present population is done so that better fitness new generations can be created.
5. Repeat the step 2.
6. Substitute the parents with newly generated variables depending on the amount of error, i.e., replace the population with new population having less error.
7. Raise the generation quantity by 1 and then repeat the steps from 3 to 7 until the maximum number of generation is reached.
8. Criteria for stopping may be defined by either the maximum number of generations or the minimum error threshold. Termination of algorithm is done in agreement to the stopping criteria.
9. The individuals with least error are then chosen and the weights are updated in accordance with that and final MAPE is found.
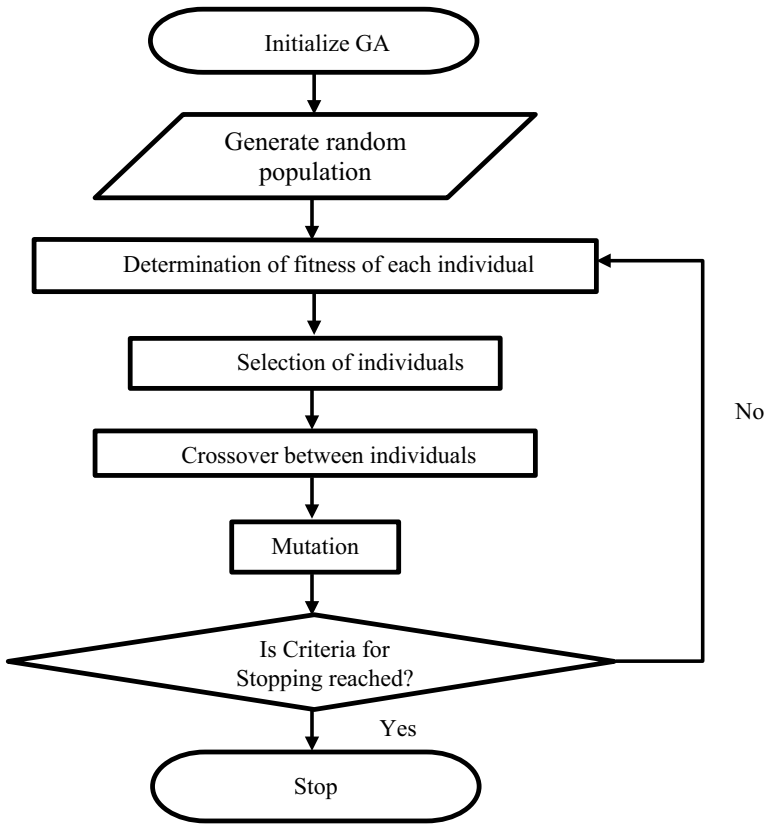
Fig. 3 Flowchart of GA

5 Proposed ACO-ANN Model

5.1 Ant Colony Optimization

Ant colony optimization was first proposed by Marco Dorigo in 1992. ACO is a probabilistic technique which can be used to search an optimal path between the ant colony and the food source in a graph. The distance travelled by the ants from their colony to the food source should be minimum, and the selection of this depends upon the pheromone accumulation. The minimum distance path has maximum pheromone as maximum number of ants follows that path.

5.2 Fitness Functions and Proposed Process

1. Construct a random ant solution of the weights and initialize the iteration to 1.
2. The generated solution is evaluated by calculating the MAPE between the forecasted and the actual load.
3. Generate the new solutions by calculating the probability of the ants to take another path and move on that path. In proposed model, Gaussian kernel is selected using roulette wheel selection and Gaussian random variable is generated for the generation of new solutions.
4. Update the pheromone and the ant solution and discard the solutions with the maximum errors.
5. Increment the iteration and repeat step 2 until the maximum iteration is reached.
6. The least error ant path solution is then selected and the weights are updated according to best solution and final MAPE is found.

The general coding for finding the new solution is shown below.

```
% Solution Weights
w=1/(sqrt(2*pi)*q*nPop)*exp(-0.5*(((1:nPop)-1)/(q*nPop)).^2);
p=w/sum(w);% Selection Probabilities
l=RouletteWheelSelection(p); % Select Gaussian Kernel
% Generate Gaussian Random Variable
newpop(t).Position(i)=s(l,i)+sigma(l,i)*randn;
```

6 Results and Discussion

The suggested hybrid model is tested for the load forecasting of the Himachal Pradesh, India. For training and testing of the model, the data of 359 days are taken and the load is forecasted for six days. The results of the proposed model are compared with artificial neural network with Levenberg–Marquardt and ANN optimized by ant colony optimization. The results of GA-ANN were better than the other models as shown in Fig. 4.

The results of the forecasted load are carried out by measuring the MAPE, MAE, MSE, and RMSE between the actual load and the forecasted load. The results are summarized in Table 2.

7 Conclusion

In this paper, the three models of STLF, i.e., ANN with Levenberg–Marquardt, AC-ANN, and GA-ANN are used to develop model for Himachal Pradesh, India for focusing on Indian scenario. It can be deduced that ANN with Levenberg–
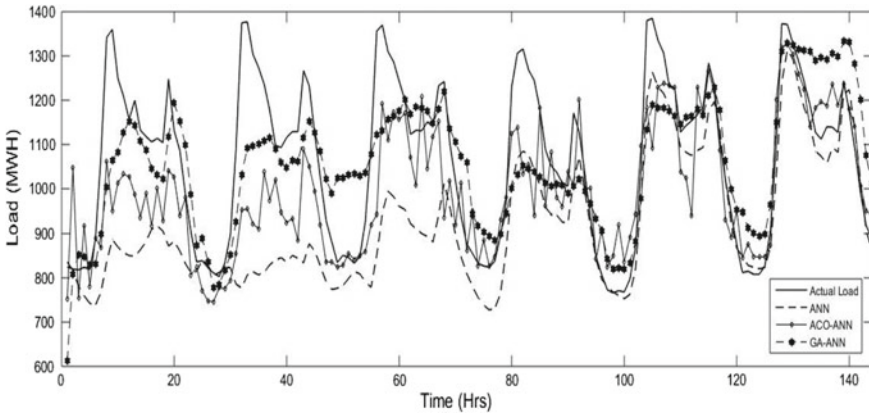
Fig. 4 Comparison of results for proposed algorithm

Table 2 Results comparison

Model	ANN-BP	ACO-ANN	GA-ANN
MAPE (%)	12.8367	9.4050	8.800
MAE (MWh)	148.3550	105.6340	95.8263
MSE (MWh)	4.131×10^4	2.045×10^4	1.5022×10^4
RMSE (MWh)	203.2486	142.9869	122.5659

Marquardt and ACO-ANN gets trapped to a local minima and does not give proper results. The load is forecasted from 26 October, 2017 to 31 October, 2017 with a satisfactory and considerable limit of accuracy. The proposed GA-ANN gives much accurate results when compared with other two models.

References

1. Amjady N (2001) Short-term hourly load forecasting using time-series modeling with peak load estimation capability. IEEE Trans Power Syst 16(4):798–805
2. Saksornchai T, Lee W-J, Methaprayoon K, Liao J, Ross R (2004) Improve the unit commitment scheduling by using the neural network based short term load forecasting. In: 2004 IEEE industrial and commercial power systems technical conference, no 3, pp 33–39
3. Ruzic S, Vuckovic A, Nikolic N (2003) Weather sensitive method for short term load forecasting in electric power utility of Serbia. IEEE Trans Power Syst 18(4):1581–1586

4. Borges CE, Penya YK, Ferńandez I, Prieto J, Bretos O (2013) Assessing tolerance-based robust short-term load forecasting in buildings. Energies 6(4):2110–2129
5. Shenoy S, Gorinevsky D, Boyd S (2015) Non-parametric regression modeling for stochastic optimization of power grid load forecast. In: Proceedings of American control conference, no 1, July 2015, pp 1010–1015
6. Moghram I, Rahman S (1989) Analysis and evaluation of five short-term load forecasting techniques. IEEE Trans Power Syst 4(4):1484–1491
7. Xia C, Wang J, McMenemy K (2010) Short, medium and long term load forecasting model and virtual load forecaster based on radial basis function neural networks. Int J Electr Power Energy Syst 32(7):743–750
8. Huang SJ, Shih KR (2003) Short-term load forecasting via ARMA model identification including non-Gaussian process considerations. IEEE Trans Power Syst 18(2):673–679

PSO-Optimized ANN for Short-Term Load Forecasting: An Indian Scenario

Dhruv Upadhaya, Ritula Thakur and Navneet Kumar Singh

Abstract Short-term load forecasting is always important for the power engineers and policy-makers for understanding the prevailing energy marketing style and for effective planning of expansion of power systems. The load forecasting has always been a primal focus of the researchers. A huge literature is present in load forecasting from ANN, but with modern power system profile, it suffers some limitations like trapping into local minima and inaccurate load forecast. This work proposes a new method of optimizing the biases and weights of ANN by using particle swarm optimization (PSO), the predetermination of load for Himachal Pradesh, India. It can be deduced that the forecasted results of PSO-optimized ANN are much better than ant colony (AC)-optimized ANN as well as ANN model trained by Levenberg–Marquardt.

Keywords Artificial neural network (ANN) · Particle swarm optimization · Short-term load forecasting (STLF) · Ant colony optimization

1 Introduction

Load forecasting (LF) is a process of predetermining the future load with respect to the historical load and weather variables. STLF has a huge influence on the efficiency of the electrical utilities and taking the important decisions like economic scheduling of generators, buying and selling of power, management of load, load dispatch, unit commitment, and short-term maintenance scheduling [1],

D. Upadhaya (✉) · R. Thakur
National Institute of Technical Teachers' Training and Research, Chandigarh, India
e-mail: dhruv.upadhaya1994@gmail.com

R. Thakur
e-mail: ritula.thakur@gmail.com

N. K. Singh
Motilal Nehru National Institute of Technology Allahabad, Allahabad, India
e-mail: nvnt.kmr.sngh@gmail.com

thus improving overall reliability and reducing operating costs of power system [2, 3]. Inaccurate load forecasting affects the power system and increases the operating costs of the power system.

With the increasing nonlinearity in the load profile, artificial intelligent methods are anticipated to give better results. The inputs given to the model can be historical load in addition to meteorological variables like temperature, wind precipitation, etc., and demographic variables like population of area, population growth rate, etc., and economic variables like average income, standard of life, etc.

In this study, the LF for Himachal Pradesh is done for six days. PSO is used as an optimizer for the biases and weights of the ANN. The results of the proposed method PSO-optimized ANN are compared with ANN-BP and ACO-optimized ANN. Mean absolute percentage error (MAPE), mean absolute error (MAE), mean square error (MSE), and root mean square error (RMSE) between the actual and forecasted loads are calculated for performance evaluation of the proposed model.

2 Load Profile Analysis

Load profile and other inputs which are given to the ANN model do not follow linear relationship with its output. This nonlinear relationship can only be easily learned by the ANN model if the input data is properly preprocessed and analyzed and arranged in a proper manner. The case study of Himachal Pradesh and the analysis of the load profile are shown in this section.

2.1 Case Study

In this paper, the real-time hourly data of Himachal Pradesh, India, is referred. To develop the load model from October 26, 2017 to October 31, 2017, the load data is considered. For training and testing of ANN model, data of 359 days is used to predict the load.

Figure 1 shows the typical load profile of the first week of the months of November 2016, March 2017, and July 2017. In time series, each load starts from 00 h of the first day. Intentionally, the first day for the load profile is taken as Tuesday and weeks are decided as such. It can be seen with the load profile that the peaks are achieved during Fridays. March shows the maximum peak of loads. Consequently, it can be deduced that the load is maximum during the weekends. Mostly, it can be seen that during the morning the peak load of a day is found and the demand decreases for noon which again increases as the sun sets.

There is a great significance of the input variables which are given to the network. There are two methods of selection of inputs which are either statistical or
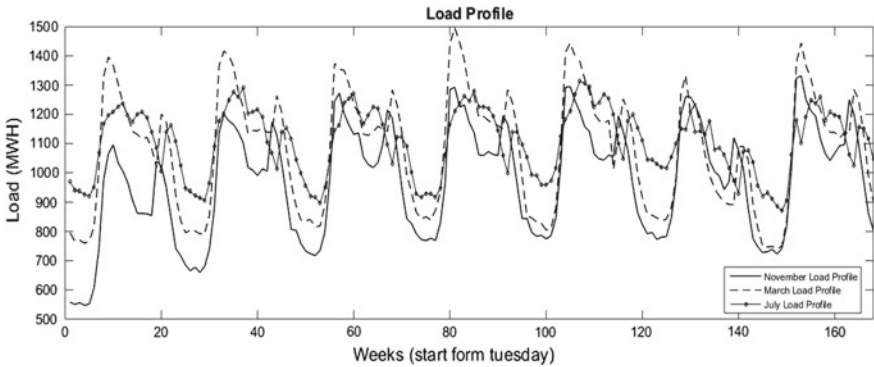
Fig. 1 Load profile for three months

by experience. The inputs which can be given to the model are historical load in addition to meteorological data which can be given as inputs such as temperature, rainfall, wind speed, relative humidity, cloud cover, and type of the day [4].

2.2 Pattern of Input Output for ANN Model

The data acquired is not in proper form and is needed to be normalized so that a fast learning can be achieved [5]. In this model, the numbers of input, hidden, and output neurons are 9, 10, and 1, respectively. Day type, historical load (L(t-1) and L (t-168)), is given as input in addition to temperature (T(t-1) and T(t-168)), pre-cipitation (P(t), P(t-168)), and wind speed (W(t-1) and W(t-168)).

3 Artificial Model

Biological neuron is taken as an inspiration for ANN which provides an alternative computational approach for nonlinear data [6]. Due to its ability to handle complex systems and adaptability, it is used to recognize the pattern in a nonlinear data [7].

3.1 Feedforward Neural Network

Feedforward neural network (FFNN) is the most basic and widely used neural network form for the engineering applications. The basic structure is shown in Fig. 2.
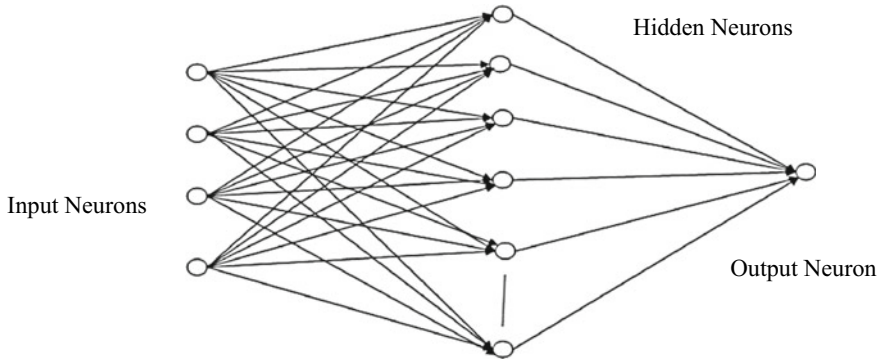
Fig. 2 Feedforward neural network

The hidden and output neurons have hyperbolic tangent sigmoid as their activation function. The output of FFNN with the nth layer is given by the equation.

$$Y_p^N = f\left(\sum_{i=1}^{n} Y_i^{N-1} \times w_{pk} + b_{p0}w_{p0}\right)$$

where Y_p^{N-1} = sum of inputs of the pth neuron of the $N-1$ layer, w_{pk} is the weight between the pth neuron of the nth layer and kth neuron of the $(n-1)$th layer, and z is the number of neurons in the nth layer. b_{p0} is the bias for the pth neuron.

The proposed ANN for which PSO optimization is done is shown in Fig. 3.

4   Proposed PSO-ANN

Particle swarm optimization is used as an optimizer of weights and biases of FFNN. PSO is evolutionary algorithm which optimizes to a global solution and is inspired by the movement of swarm, i.e., bird flock or school of fish. The general PSO-ANN is shown in Fig. 4. The velocities of particles are updated by the formula
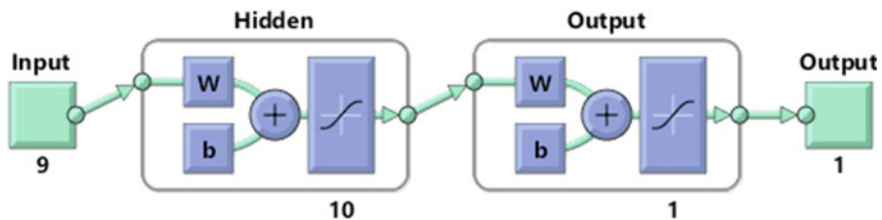
Fig. 3 Proposed ANN
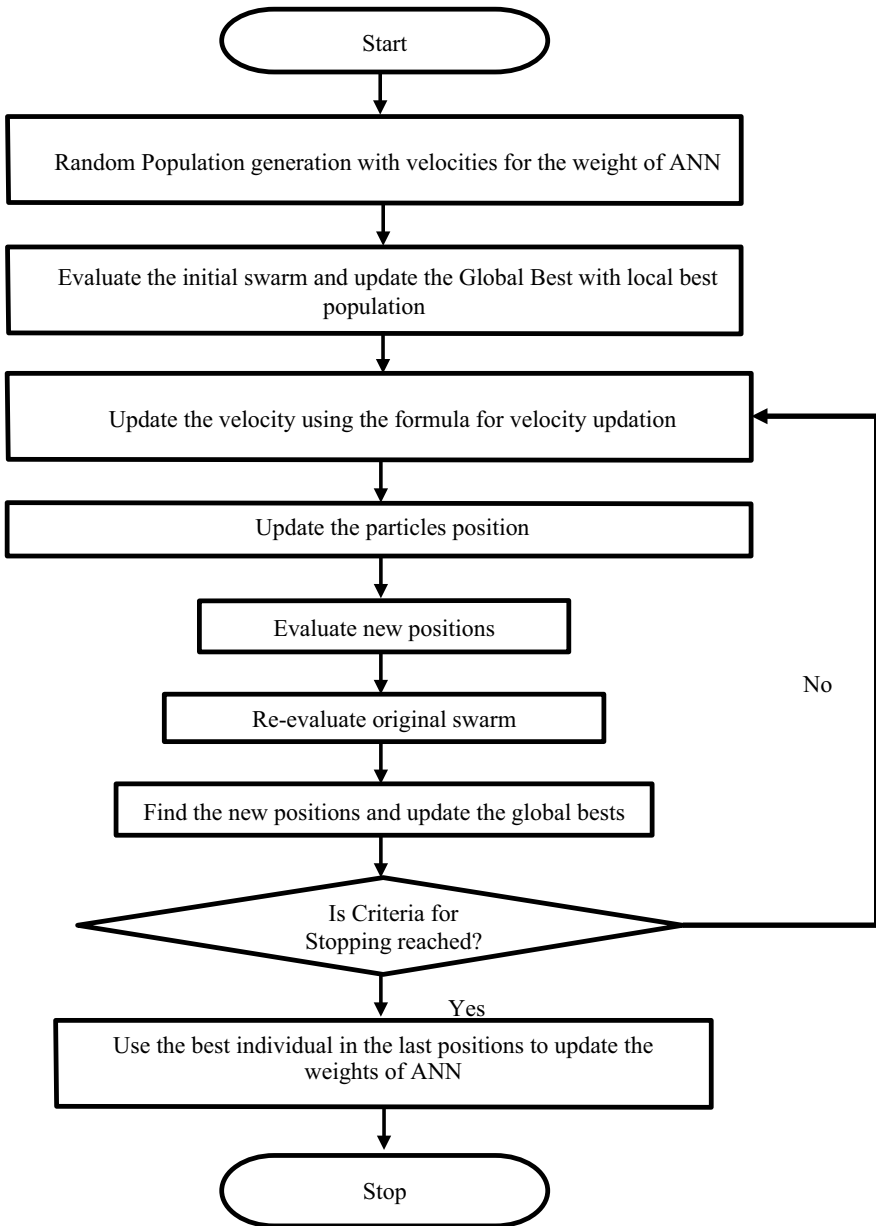
Fig. 4 PSO-ANN flowchart

$$V_{t+1} = W \times V_t + C_1 R_1 (\text{LBP} - \text{CP}) + C_2 R_2 (\text{GBP} - \text{CP})$$

where R_1, R_2 are the randomly generated, C_1, C_2 are the accelerations coefficients, CP is the current position, LBP is the local best position, and GBP is the global best position of the particles.

5   Proposed ACO-ANN

Ant Colony Optimization

Ant colony optimization is a population-established metaheuristic technique which is utilized to find an approximate solution to a complex optimization problem first proposed by Marco Dorigo in 1992. It is inspired by the behavior of ants to follow the minimum distance path from their colony to the food source. From different path, the probability of ants to follow a selected path is dependent on the pheromone accumulation on that path. Pheromone is updated with the number of ants following the path, i.e., if more ants follow the same path, the pheromone accumulation on that path would be more and vice versa. Pheromone evaporation also takes place with time due to which the larger distance paths are forgotten by the ants.

In proposed model, a random solution is generated and its fitness is calculated by calculating the MAPE between the actual and forecasted load. The probability of paths is defined by selection of Gaussian random variables which are generated by using Gaussian kernel. The values of Gaussian kernel are selected with the help of roulette wheel selection. The coding shown for updating the positions is shown below.

```
% Solution Weights
w=1/(sqrt(2*pi)*q*nPop)*exp(-0.5*(((1:nPop)-
1)/(q*nPop)).^2);

% Selection Probabilities
p=w/sum(w);

% Select Gaussian Kernel
l=RouletteWheelSelection(p);

% Generate Gaussian Random Variable
newpop(t).Position(i)=s(l,i)+sigma(l,i)*randn;
```

The new solution is evaluated for minimum errors, and the better solutions are only selected for next solution. On the last iteration, the weights are updated according to the best solution and MAPE is calculated.
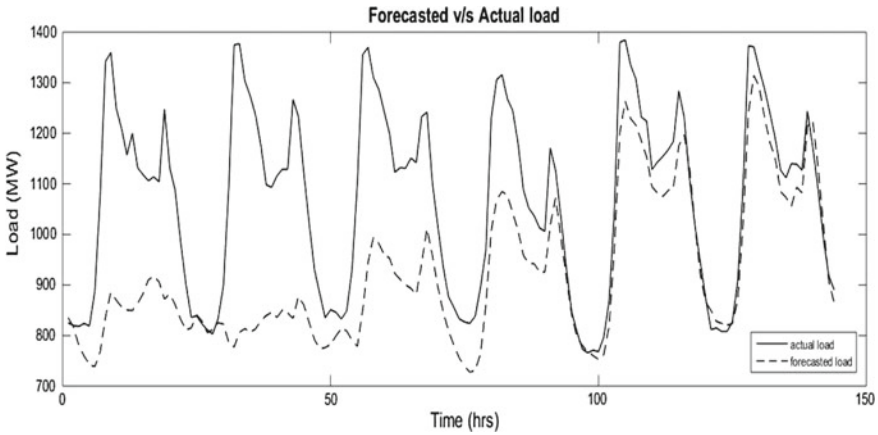
Fig. 5 Actual versus forecasted load for FFNN-BP
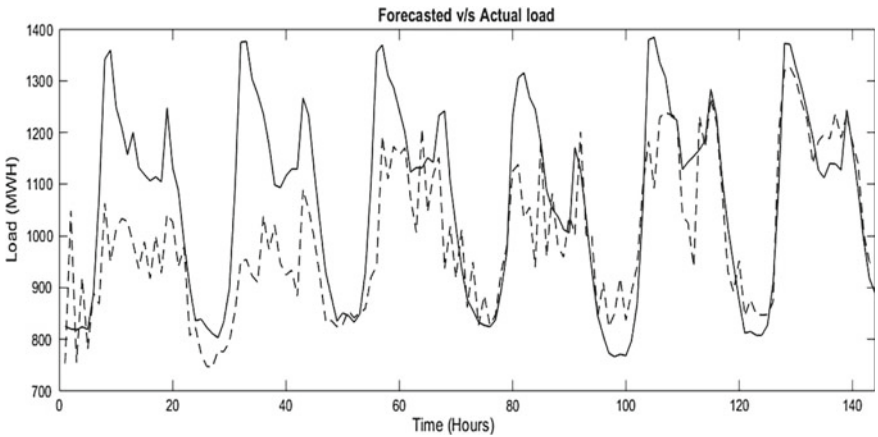
Fig. 6 Actual versus forecasted load for ACO-ANN

6 Results and Discussion

The forecasted results for the proposed model PSO-ANN were the best with swarm size three times of the dimension of the problem. Results were better than compared to ANN with Levenberg–Marquardt and AC-ANN (ACO-ANN). The forecasted load curves for ANN-BP, ACO-ANN, and proposed PSO-ANN are shown in Figs. 5, 6, and 7.

The performance of the proposed method is calculated using MAPE as the performance indices. MAE, MSE, and RMSE between the actual and forecasted load are also calculated. The results are summarized in Table 1.
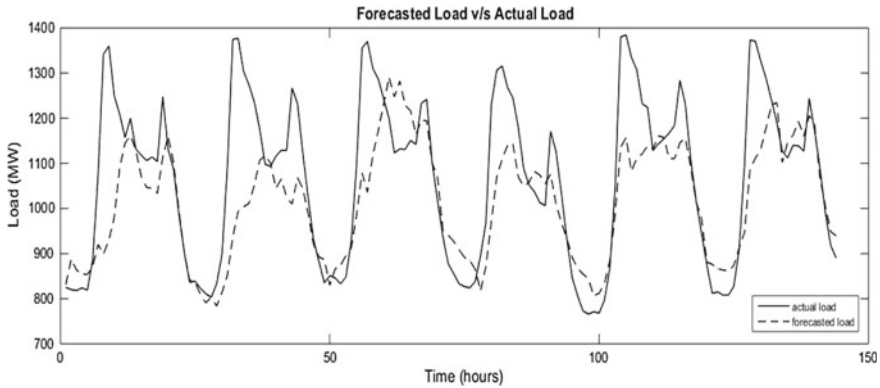
Fig. 7 Actual versus forecasted load for PSO-ANN

Table 1 Comparison of results

Model	ANN-BP	ACO-ANN	PSO-ANN
MAPE (%)	12.8367	9.4050	7.5708
MAE (MWh)	148.3550	105.6340	87.8903
MSE (MWh)	4.131×10^4	2.045×10^4	1.6782×10^4
RMSE (MWh)	203.2486	142.9869	129.5465

7 Conclusion

Accurate load forecast is always needed for proper operation of the power system and has always been in the focus of researchers. Evolutionary algorithm-optimized ANN has many benefits over ANN with Levenberg–Marquardt training. Unlikely, it takes less memory and does not get trapped in local minima. This paper explores PSO-ANN which has shown much better results than AC-ANN and ANN with Levenberg–Marquardt training.

References

1. Singh NK, Tripathy M, Singh AK (2011) A radial basis function neural network approach for multi-hour short term load-price forecasting with type of day parameter. In: 2011 6th international conference on industrial and information systems, ICIIS 2011, Sri Lanka, pp 316–321

2. Xia C, Wang J, McMenemy K (2010) Short, medium and long term load forecasting model and virtual load forecaster based on radial basis function neural networks. Int J Electr Pow Energy Syst 32(7):743–750
3. Riva F, Tognollo A, Gardumi F, Colombo EA (2018) Long-term energy planning and demand forecast in remote areas of developing countries: classification of case studies and insights from a modelling perspective. Energy Strateg Rev 20:71–89
4. Kandil N, Wamkeue R, Saad M, Georges S (2006) An efficient approach for short term load forecasting using artificial neural networks. Int J Electr Pow Energy Syst 28(8):525–530
5. Raza MQ, Khosravi A (2015) A review on artificial intelligence based load demand forecasting techniques for smart grid and buildings. Renew Sustain Energy Rev 50:1352–1372
6. McCulloch WS, Pitts WH (1943) A logical calculus of ideas imminent in nervous activity. Bull Math Biophys 5:115–133
7. Lee C-M, Ko C-N (2009) Time series prediction using RBF neural networks with a nonlinear time-varying evolution PSO algorithm. Neurocomputing 73(1–3):449–460

Delayed Replication Algorithm with Dynamic Threshold for Cloud Datacenters

Chetna Dabas and Juhi Aggarwal

Abstract Cloud computing offers a large amount of services as well as storage space over the Internet to a large number of customers. One of the services offered by the cloud is data as a service. Often, cloud computing is dealt with the challenge of managing data and also improving the availability of data. To ensure data availability and manage storage space, the concept of data replication has been used in this work. With the help of data replication technique, multiple copies of a data are created and distributed over geographically distributed sites. In this work, a delayed replica creation scheme based on dynamic threshold is designed and employed for creating replicas. Replication is done for the data based on its relative importance with other data. With the help of this work, the authors are able to improve the response time of accessing the data from a particular site and also reduce the cost involved in data access.

Keywords Cloud · Data storage · Replica · Response time

1 Introduction

Cloud computing is a contemporary technology which provides a virtual environment for sharing a number of resources while using the Internet as a medium to communicate. The number of users and the amount of data stored in the cloud is ever increasing making cloud an expandable domain. Cloud computing provides its customers with certain services. The commonly available services are infrastructure as a service (IaaS) [1], software as a service (SaaS) [2], and platform as a service (PaaS) [3]. There are many cloud service providers (CSPs) responsible for providing these services to the clients on a pay-per-use basis. The clients enter into a

C. Dabas (✉) · J. Aggarwal
Jaypee Institute of Information Technology, Noida, India
e-mail: chetna.dabas@gmail.com

J. Aggarwal
e-mail: aggjuhi28@gmail.com

service-level agreement (SLA) with their service provides and sign an agreement as to what services will be provided keeping in consideration factors like cost, bandwidth, and security policy [4].

There are a lot of factors determining the cost of storing the data. The customer is charged on the basis of amount of the data he wishes to store on the cloud and also for the time duration for which data is held on the cloud. The cost also varies depending on the quality of service requirements which vary for each individual as someone may require data which gives higher response time and can compromise with the quality of data but for some other customer quality should not be compromised at all. The cost of service also varies according to privacy policies. As we have seen that cloud computing is a costly affair, therefore, it becomes evident that there is a need to manage its resources wisely and deal with the challenges faced.

In cloud computing, data is stored at datacenters which are geographically distributed over the world. Each CSP has its own center which may be at more than one location. At every datacenter location, data is stored on some physical device having many servers to handle the request. The storage mediums have hardware associated with it having certain properties. Each user has to pay for the amount of space they have occupied on the storage device. The storage space is not unlimited, therefore, should be utilized optimally [5]. For efficient utilization of storage space, different CSP seek different approaches. Some handle the issue by data partitioning, i.e., by dividing a data unit into chunks and then storing them onto different storage nodes. On the other hand, some CSP decide whether to maintain a data on its storage node or not based on its importance. Such is the approach followed in this work.

Ensuring data availability is an important challenge faced by cloud computing [6, 7]. It means to make sure that data is available to the users and applications as and when required without having to cause a miss or a delay. It not only concerns with the presence of data at a particular site but also insists upon ensuring that it is ready for use by the client. Since cloud storage contains data which is critical to its users, therefore unavailability may cause huge amount of loss to an organization or may lead to an application failure as well. Fault tolerance is another challenge faced in any distributed computing. Fault may occur because of different reasons such as a physical node failure, link failure, data unavailable, poor connectivity, natural calamity. The CSP needs to make sure they have a mechanism designed to deal with this scenario. In order to manage data in such a way that it's available to its customer as per their needs even in case of any failure, we move toward the approach of data replication.

The concept of data replication is applied to make multiple copies of a data which can be anything a file, photo, email, etc., and store it either in the same site as the original data or across multiple sites [8]. The benefit of using this scheme lays in the fact that failure of a single copy of the data or a data hosting site will not lead the customer dangling midair in need of their data. The customer can always reach out to an alternate copy of the original file or to an alternate location in search of data. Also, the availability of data is improved as with data replication more than

one copy of the data exists and the user can access whichever copy is nearer to him and easy for him to access without experiencing any delay.

In this work, data replication is studied with the motive of masking its effect with respect to relative importance of the data. It is assumed that each data has different importance. With this approach, replicas are created based on how important the data is at present and what will be its likelihood in near future. Importance of a data is judged by how frequently a data is accessed. In Sect. 4, we discuss the details of this approach.

The rest of this paper is organized as follows. Related work is presented in Sect. 2. In Sect. 3, system model is described. In Sect. 4, we give detailed explanation of our proposed work. Section 5 gives the implementation details of our work and show experimental results. Finally, in Sect. 6, conclusions of the work and future scope are discussed.

2 Related Work

Replication is the process of creating a copy of an original thing. In reference to data to it means producing multiple copies of a data unit and storing it somewhere for future use. It can be observed in day-to-day life also we tend to make copies of important data such as pictures, documents, and files and copy them from our phones to say a computer, or on an external storage device such as hard disk, pen drive, or a CD. Data replication is most commonly used as backup mechanism by data providers, business organizations as well as by individuals. Apart from providing as a backup in case of a failure, it is also used to improve the availability and reliability of the overall system. Data replication improves data availability and performance of the cloud storage system by serving data request by various replicas placed at different locations either at the same site or different sites [9]. Replicating data onto different sites also provides as a means for fault tolerance. Failures can be of the type disk failure, site failure, or node failure. Data replication provides the benefit that there is more access to the shared data. Since availability is improved, therefore the waiting times are reduced, and hence, the latency is also reduced.

Mansouri et al. [10] proposed an adaptive data replication scheme which takes into account various parameters while designing their replica creation and replacement strategy. The replica creation is based on the time required to service a request, the probability with which a file may fail, load on a site, amount of storage space available and already in use and the delay in answering a request. By calculating a function value based on the above-mentioned parameters, it is decided on which site to place a data for a particular file. The second phase of this algorithm is replica replacement. In this step, it is determined if there is enough space on the storage device in a site to store a new replica. For making this decision, parameters like availability of the file, size of file, last access time, and the number of access are considered. Based on these, a factor is calculated. The value of this factor is compared for each replica and the one with least value is placed in the site. This

work focuses on creating replicas for the most important data. Through the results of the experiment, it is observed that it provides with balanced load on the sites and gives better result with the increase in the number of jobs. Adaptive replication techniques have also been discussed in [11, 12].

In [13], a location-based technique for replication is approached. The works aim at targeting the users who are constantly moving and traveling such that their location can be monitored for applying their replication algorithm. By tracking the current location, the next destination of the user is estimated and efforts are made to move the replica of the data to that location such that data is always available. This work also emphasizes on the importance of data in terms of number of times it is accessed. The data which is most accessed will be replicated to the location which is predicted to be the next possible location of the mobile users. This way not the entire data is replicated but only the important one is. For location prediction, some information about the user such as their interests, activities, and schedules [13] are gathered by using artificial neural network and analyzed. This technique gives better results in terms of response time, storage space, and execution when compared with full replication.

In [13], a popularity-based scheme is proposed for catering to simultaneous failure of machines. For their scheme, the data is divided into three categories, i.e., hot, warm, cold which in common terms mean very important data, moderately important data, and less important data. They have extended the principle of traditional three-way replication to their model in such a way that two copies of each type of the data are put on a primary storage, and the third replica of most important data, moderately important and less important data is stored at remote location as backup. The aim is to ultimately reduce the cost of storing data and the amount of bandwidth used. For that compression, strategies are used to remove redundant data. The hot data is most frequently used and should be available at all times to the user, therefore; primary replicas are stored on storage devices which are fast to access. To deal with correlated failures, the number of failure tolerant sets is reduced.

Many authors have explored the QoS for replication in data clouds like the works of [14, 15]. The authors of [15] have proposed a data replication strategy which takes into account the physical adjacency property of the blocks of the storage disk for managing the replicas. For the purpose of achieving the QoS requirements of the users, ensuring greater availability and reducing the response time a unit called locality replica manager (LRM) is employed. With this approach, a fully connected graph is constructed based on the requests coming from the user for each data block. There is a catalog which stores information about these graphs and the number of access to each graph. For constructing the algorithm, certain values have been calculated. Firstly, since in cloud systems the availability of blocks is a very important factor; therefore, the probability with which a block is available is calculated. Next, the delay caused in accessing the graphs is calculated. Finally, a function value is calculated to determine on which node a graph can be hosted for enquiry. For the replication process, the copy of original data needs to be selected. As we have mentioned before that the blocks are stored in the form of

blocks therefore for each request of the user, it is checked if the requested graph is a subgraph of any of the existing graphs. If a graph already exists, then that request can be met otherwise a new graph is created to host the request. While selecting the nodes for hosting the request, it should be checked that QoS requirements are met. In case, the QoS requirement which in this work is the delay in system is not met then an algorithm is invoked which uses genetic algorithm for reorganizing the graph inquires on the nodes.

Many works consider data-intensive applications like the work of [16, 17]. In the work of [17], the authors have proposed two schemes for ensuring the quality of service (QoS) requirements of the users of an application in the event of failure or data distortion. The aim is also to do this job while incurring a low cost. The two algorithms used to solve different purposes. One of the algorithms called the HQFR is used to maintain the QoS of the application and the second MCMF algorithm is used to produce the optimized results thus bringing it to polynomial time only. The QoS can be expressed in different ways depending upon the requirement of the user. It can be defined in terms of storage space required by a user, bandwidth that should be provisioned, response time as well as access time. In this work, QoS is defined in terms of access time. In this work, the HDFS architecture is followed where the major components are the name node which is responsible for looking after the position of data blocks and the other one being data blocks responsible for holding data with respect to the applications. In the HQFR algorithm, the parameter for QoS is considered to be access time required to access a file from a data node. It is a greedy technique, therefore; a request with higher QoS requirement gets priority over the one with lower value. To qualify as QoS nodes, two conditions should be met:

1. The requested node and the node on which data is to be placed should not be in the same rack so as to avoid any possible rack failure, and
2. The time to access a node $q_{j,}$ for a requested node $r_{i,}$ should be less than the time required to access a QoS requested node.

With only HQFR, it is not possible to achieve minimum cost; therefore, a maximum flow minimum cost algorithm is applied for cost optimization. To make the system scalable to requests, a node combination technique is applied in which nodes having similar CPU time and disk access time can be grouped together.

3 System Model

In cloud computing, a large amount of data and services are involved which can be accessed from anywhere around the world. In different approaches, architectures like HDFS [18] and Google file systems have been used to express their model. In this paper, our model considers that there are N datacenters DC_1, DC_2, …, DC_n distributed across different regions of the world. In every region, there is one or

more user base which accounts for the number of users requesting a data. To communicate between the datacenters and the user base, there is a service broker. We explain below the components of our model with their functioning. Figure 1 depicts the architecture of our model.

(1) *Datacenter*—it is a unit which can be present anywhere in the world and acts majorly as an infrastructure providing storage and computing capabilities. It consists of nodes which store data and process the data according to user requirements.
(2) *User base*—it is an entity which is a representative of the number of users in a particular region. The user base more often than not is collection of users requesting services from a service provider for meeting their requirements. Each user base has a user count which is the peak number of users present in a user base at given time. The request generated by them is considered to be a job request.
(3) *Service broker*—it is a component which acts as a coordinator between the datacenter and the users. Whenever a request for replica is generated by a user, the service broker checks from which datacenter the request can be fulfilled and fetches data from that site. It employs different strategies for selecting from which datacenter to bring the replica to address to the user needs. Our algorithm uses the nearest first policy to fetch the data.
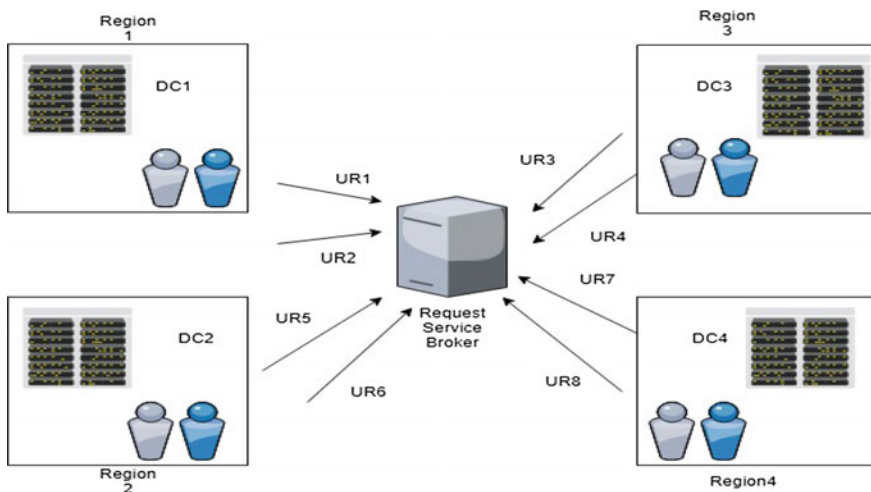
Fig. 1 System model

4 Proposed Work

The authors proposed a replication scheme to deal with issues in storing and managing the less frequently used data. It is assumed that not all the data present in a storage node at a datacenter of any service provider is of equal importance. While some data is more important and therefore used more frequently, there are also certain data entities which are not so important and used less frequently. With this work, we aim to minimize the time and effort required to manage such a data. First we explain a few example scenarios in which our algorithm can be applied, and next we explain the workflow of our algorithm.

4.1 Example Scenarios of Application of Algorithm

Here the authors explain through a few examples the difference between a hot data and cold data, more precisely most frequently used and least frequently used data.

- For instance, suppose a person was working on a technology 'A' and had study material for it stored on his personal cloud. Later, he switched to a new technology 'B' and did not use technology 'A' for the longest time. Now, after some years, the same person has again switched to technology 'A' and wants to access data that he stored previously. So we conclude from this, what was supposed to be an obsolete data some time ago has now become an important data.
- Consider another scenario in which a Gmail user has some mails which he has not excessed for years but Google does not have the right to delete that data as well. It will rather put it on a remote storage site such that space on a local site can be saved for a more recent mail. Now suppose if the user wants to access the mail which is five years old, then that data may be considered less important for some while until it becomes frequently accessed by the user again.
- Another interesting example of this scenario is all business organizations keep a record of their employees in their DB. During the stay of an employee in that organization, his data is frequently accessed. Once an employee leaves the company, the company does not delete his data but moves it to a secondary storage location. For this period, the data has become a least important data. Now, suppose that the same employee has joined again then again his data becomes important.

4.2 Workflow of the Algorithm

In this section, we define the process of our algorithm which creates delayed replicas based on a dynamic threshold value. Initially, only the data currently or frequently in use is stored in a local site. The data which is less frequently used is

stored at a remote location with respect to the current request location. For a less important data to become important, it has to earn a value and then eventually a place in the local site.

The procedure of the algorithm is explained below.

Algorithm: Delayed replica creation with dynamic threshold

```
Input: A set of user requests= {UR₁, UR₂, . . . .,URₘ}

1. Start
2. For each user request URᵢ do
3.        If a file does not exist in the storage DCᵢ then
4.             for each file in the remote site do
5.
Calculate delayed replica creation   factor DRCFᵢ using equation (1)
6.             for each site do
7.                  Calculate the threshold value THᵢ using equation (3)
8.               endfor
9.             while DRCFᵢ <= THᵢ do
10.               fetch the file from the remote site
11.            else
12.                  Create a replica of Fᵢ and store locally
13.           end while
14.       end for
15.       else
16.        fetch the file from local site
17.end for
```

The functioning of our algorithm can be explained in two major components.

(1) *Calculating the delayed replica creation factor*

When the request for a data file is generated, if the request can be met locally, then the corresponding resources are allocated to that particular job. If the job cannot be met locally, then the job broker will redirect the request to the remote site and the request will be served from there. Since the data in question is not a frequently used data, therefore when it called for the first time no new replica for it will be created. A dynamic replica creation factor (DRCF) will be calculated each time a file in the remote site is accessed. This factor is nothing but the access frequency of a particular file. It is calculated as in (1).

$$\text{DRCF} = w_i * \text{Access frequency} \tag{1}$$

where w_i is a weight which can be defined according to own requirements. The access frequency is defined as the number of users requesting a data file at a particular time and is given as in (2).

$$\text{Access frequency} = \text{Number of users accessing the file}/\text{total time} \qquad (2)$$

(2) *Replica placement*

After calculating the value of DRCF each time, the data is accessed it is checked with the threshold value for a particular site. Till the time DRCF value for a file is less than the threshold value, the request is met from the remote site. When the value exceeds threshold value, then a copy of the original data is placed in the local site. The threshold value is also dynamic and is incrementally calculated by considering the number of peak users present in all the sites at a given point. It is calculated as below

$$\text{TH} = \sum_{i=1}^{n} \text{User count}\,[\text{DC}_i] \qquad (3)$$

5 Experimental Setup and Results

In this section, the first discussion about experimental setup and the assumptions made while executing the algorithm is done and then the results are displayed and compared with an existing strategy.

In this work, simulation environment is created in Visual Studio 2017 using ASP.NET framework 4.0. For simulating the configuration, we have divided the entire world into four regions horizontally. The simulation results are shown for four datacenters residing in four different regions and having four different user bases. Each datacenter storage node has one of the four types of file: low-priority type-1, low-priority type-2, high-priority type-1, and high-priority type-2. While implementing the following assumptions are made:

- Each region has only one datacenter.
- In each region, one user base is present.
- Each datacenter has a file type of its own already existing in its storage.
- Each user base can have any number of peak users at a given time.

For evaluating the performance, we have considered two metrics response time for accessing a file from a datacenter location and the cost involved in accessing the data. The calculation of response time is dependent on the number of users accessing a file during a period, the amount of bandwidth used by them and the threshold value depending upon the type of scenario. If the requested file type is already available at a datacenter, then the response time is calculated as in Eq. (4).

$$\text{Response time} = \text{No. users accessing a datacenter storage/bandwidth} \quad (4)$$

If the request cannot be fulfilled from the datacenter in a region from where the request originated, then the service broker fetches the result from some other datacenter. The response time in such a scenario is calculated as in (5)

$$\text{Response time} = \text{threshold/bandwidth} \quad (5)$$

The overall cost of execution is calculated as

$$\text{Cost} = \text{cost} + (\text{No. of hops required to fetch data} + 1) * \text{threshold} \quad (6)$$

5.1   Results Assessment

The assessment of results begins by comparing the results of our algorithm with the exhaustive strategy in terms of the cost incurred for the scenario in which only one user base request is being met within its own datacenter and rest three user base requests are fulfilled by other datacenters. In Fig. 2, the overall cost of both our algorithm and the exhaustive strategy are depicted. Here a plot of the cost of both the strategies is plotted by varying the number of peak users from 50 to 250. It is observed as the number of users increase there is an increase in the cost. But the cost for our strategy is comparatively very less from the exhaustive strategy because in our strategy only till the time data is accessed from the remote site the cost of accessing from that site is included but once it has become local, the rest of the users can access it from local site. In Fig. 2a, an instance of only one request being fetched from local site is shown, whereas Fig. 2b shows an instance of two requests being fetched from local site. It is observed that when three files are accessed from remote site the cost is more as compared to the cost incurred when two requests are satisfied from the remote site.

In Fig. 3a, b, we depict the response time with respect to each datacenter averaged over a total of five peak user instances. It is observed that the user base present in DC_1 got its data from the same region; therefore, its response time is the least and same as that of exhaustive strategy. All the other users have to access data from a datacenter other than that to which they belong; therefore, the response time increases. The response time for exhaustive strategy is more because for each request they fetch the data from the remote site thus increasing the response time.
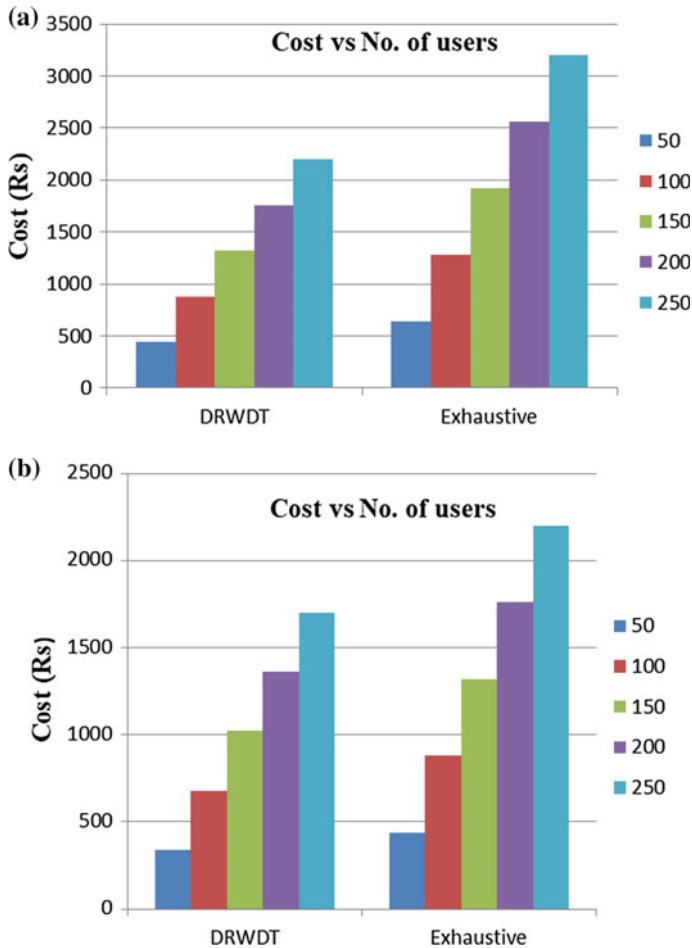
Fig. 2 **a** Cost comparison between DRWDT and exhaustive strategy for one request satisfaction from local site. **b** Cost comparison between DRWDT and exhaustive strategy for two requests satisfaction from local site

6 Conclusion

This paper deals with the issue of replication of relatively less important and less frequently used data in the cloud data storage units. It is argued that some data is not always in use and may be accessed sometime in a month, year, or even more time. Storing such a data in local storage always can cause access skew on the storage unit; therefore, our strategy works by bringing a replica of the data from the remote location to the local site only when the factor or replication has reached a certain threshold value. By doing so, the overall effort applied in storing the replica at each
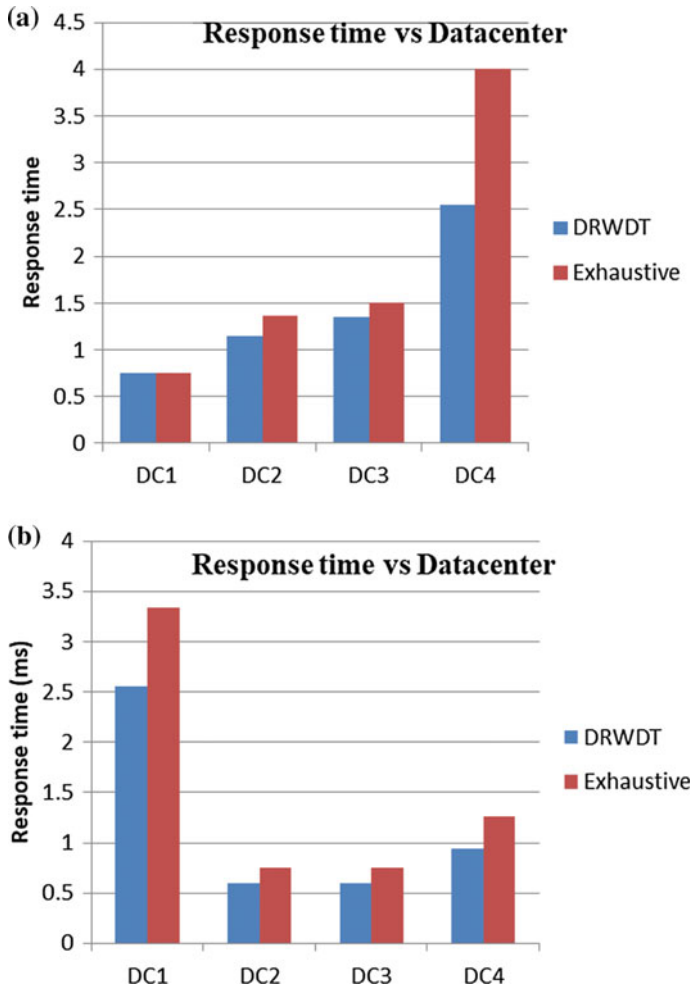
Fig. 3 **a** Response time of datacenter averaged over five user instances for one request satisfaction from the local site. **b** Response time of datacenter averaged over five user instance for two request satisfaction from local site

site for each data is reduced. With the help of this work, it can be established at any point of time the number of replicas of any data is no more than two as replica is brought in only when the threshold value is reached. The parameters involved in evaluating the performance are the user count and the access frequency. Evaluation of cost is dependent on availability of a file in particular site, the bandwidth available at a datacenter and the distance between two datacenters. Also we have compared our algorithm with an exhaustive strategy in which data is accessed from the remote location always and found that our algorithm gives up to 32–36% better response time. With this work, the overall cost of accessing the data can be reduced

up to 31% as compared to the exhaustive strategy. In the future, we wish toward extending the approach in a real environment and consider load balancing at all the sites.

References

1. Moreno-Vozmediano R, Montero RS, Llorente IM (2012) Iaas cloud architecture: from virtualized datacenters to federated cloud infrastructures. Computer 45(12):65–72
2. Tsai W, Bai X, Huang Y (2014) Software-as-a-service (SaaS): perspectives and challenges. Sci China Inf Sci 57(5):1–15
3. Teixeira C, Pinto JS, Azevedo R, Batista T, Monteiro A (2014) The building blocks of a PaaS. J Netw Syst Manage 22(1):75–99
4. Zhu J (2010) Cloud computing technologies and applications. In: Handbook of cloud computing, pp 21–45. Springer, Boston, MA
5. Tos U, Mokadem R, Hameurlain A, Ayav T, Bora S (2017) Ensuring performance and provider profit through data replication in cloud systems. Cluster Comput 1–14
6. Zhang Q, Cheng L, Boutaba R (2010) Cloud computing: state-of-the-art and research challenges. J Internet Serv Appl 1(1):7–18
7. Al-Dhuraibi Y, Paraiso F, Djarallah N, Merle P (2018) Elasticity in cloud computing: state of the art and research challenges. IEEE Trans Serv Comput 11(2):430–447
8. Mohamed MF (2016) Service replication taxonomy in distributed environments. SOCA 10 (3):317–336
9. Malik SUR, Khan SU, Ewen SJ, Tziritas N, Kolodziej J, Zomaya AY, Madani SA, Min-Allah N, Wang L, Xu CZ, Malluhi QM (2016) Performance analysis of data intensive cloud systems based on data management and replication: a survey. Distrib Parallel Dat 34(2):179–215
10. Mansouri N (2016) Adaptive data replication strategy in cloud computing for performance improvement. Front Comput Sci 10(5):925–935
11. Wei Q, Veeravalli B, Gong B, Zeng L, Feng D (September 2010) CDRM: a cost-effective dynamic replication management scheme for cloud storage cluster. In: 2010 IEEE international conference on cluster computing (CLUSTER), pp 188–196. IEEE
12. Rajalakshmi A, Vijayakumar D, Srinivasagan KG (April 2014) An improved dynamic data replica selection and placement in cloud. In: 2014 international conference on recent trends in information technology (ICRTIT), pp 1–6. IEEE
13. Al Ridhawi I, Mostafa N, Masri W (October 2015) Location-aware data replication in cloud computing systems. In: 2015 IEEE 11th international conference on wireless and mobile computing, networking and communications (WiMob), pp 20–27. IEEE
14. Ramanan M, Vivekanandan P (2018) Efficient data integrity and data replication in cloud using stochastic diffusion method. Cluster Comput 1–8
15. Sookhtsaraei R, Artin J, Ghorbani A, Faraahi A, Adineh H (2016) A locality-based replication manager for data cloud. Front Inform Technol Electron Eng 17(12):1275–1286
16. Shamsi J, Khojaye MA, Qasmi MA (2013) Data-intensive cloud computing: requirements, expectations, challenges, and solutions. J Grid Comput 11(2):281–310
17. Lin JW, Chen CH, Chang JM (2013) QoS-aware data replication for data-intensive applications in cloud computing systems. IEEE Trans Cloud Comput 1(1):101–115
18. Shvachko K, Kuang H, Radia S, Chansler R (May 2010) The hadoop distributed file system. In: 2010 IEEE 26th symposium on mass storage systems and technologies (MSST), pp 1–10. IEEE

PV Emulator Modeling and Design Using Buck Converter

Dheeraj Joshi and Simmi Sharma

Abstract Electricity generated from the photovoltaic (PV) system plays an important role as renewable energy source due to zero green house gas emission and no fossil fuel consumption. Sunshine is accessible for longer hours per day and with high intensity in India due to location of its southern half in the torrid zone. Solar energy is thus one of the abundant renewable forms of energy available in India. This paper uses buck converter for PV emulator modeling and designing. This will reduce the time-space requirements, dependence of output on weather conditions, and overall cost incurred for PV system designing, testing, and maintenance. The purpose is to get the current–voltage (*I–V*) characteristics close to the real PV module.

Nomenclature

V_{in}	Input voltage
V_o	Output voltage
I_o	Output current
f_c	PWM switching frequency
G	Irradiance
T	Temperature
STC	Standard test conditions, i.e., $T = 25$ °C and $G = 1000$ W/m^2
i_L	Current through inductor
v_c	Voltage across capacitor
R	Load resistance

D. Joshi · S. Sharma (✉)
DTU, Delhi, India
e-mail: simnit08@gmail.com

D. Joshi
e-mail: ee.dheeraj@gmail.com

1   Introduction

Power projects utilizing renewable energy forms such as wind, biomass, hydro-, and hybrid systems are the prime focus of researchers to meet the energy requirements of far-off communities and areas that seem to be non-electrified in coming years. Renewable energy sector of India is one of the world's most active players in renewable sector, especially for solar and wind electricity generation. The aim of the Ministry of New and Renewable Energy (MNRE) is to expand and employ new and renewable energy for fulfilling the energy requirements of the country. In May 2017, a record of low solar tariff of Rs. 2.44/unit was achieved in Bhadla, Rajasthan, having 250 MW plant capacity [1]. The solar capacity is increased by 370% in the last 3 years from around 2.6 GW to more than 12.2 GW. The equivalent energy potential of India is about 6000 million GWh of energy per year. India ranked 7th with a capacity of 9.01 GW in 2016 [2]. As per reports, India and China in June 2017 have emerged as the leading developers of large-scale solar projects. The top five largest power plants of the world are Tengger Desert Solar Park-1500 MW China, Datong Solar Power Runner Base-1000 MW China, Kurnool Ultra Mega Solar Park-900 MW India, Longyangxia Dam Solar Park-850 MW China, Kamuthi Solar Power Project-648 MW India. As per reports till date, the world's largest solar power park is located in the Kamuthi, Tamil Nadu, India. Governments around the world have recognized the need of sustainable sources for electrical energy production, and PV technology is gaining parity with the incentives provided by them. The introduction of regulatory policies has broadened the research area of PV solar interconnection [3–5]. So, solar energy has a great scope as future energy source and is highly encouraged in many countries. Large interest in solar energy has made PV systems the best alternative to conventional energy sources [6, 7]. PV systems are interfaced with power electronic inverters to enable its interconnection to the power system network [8] and are explored due to the factors contributing toward lower carbon emissions and decreasing capital investment [9–13]. Research conducted on them encountered sensitive issues related to high price coated [10, 13, 14] for purchasing photovoltaic panels. PV emulators have emerged as a solution to these issues. They produce current–voltage (I–V) characteristics similar to that of real PV generator. Research conducted on emulating the I–V characteristics of PV systems has focused on different power converter topologies [15–19]. PV emulator is required to study new PV inverters and MPPT tracking algorithms [20–31] in the laboratory to improve their performance under varying conditions. However, few prominent problems [32, 33] faced by existing PV panels include the following:

1. Requirement of large space for installation.
2. Dependence on weather conditions.
3. Big budget requirement for onsite testing process.
4. Selection of panel among large variety of available choices of solar panels.

The nonlinear and explicit equations defining solar cell characteristics are described [11, 12, 21, 33–43], and the effect of dependent factors [20, 31, 40, 41, 44] is described.

There are three widely used approaches for designing PV emulators:

1. Use of the equivalent circuit of PV generator: It comprises of power devices, resistors, and diodes. The performance of diode is badly affected due to dissipated power, thereby requiring an efficient cooling system [32, 33, 44].
2. Practically exposing photovoltaic cell to a source of light under adequate conditions of temperature and irradiation: It is efficient for low power levels for factors such as heat dissipation, and the size of testing setup results in difficulties at high power applications [6, 7, 44, 45].
3. Utilizing the modern power electronic components: The power supplies are based on converter controllable power such as various DC–DC converters [13, 18, 22, 46], which is the most efficient way among all approaches [11, 20, 33, 35–41, 44].

Different converter topologies [16, 18, 19, 47, 48] used in literature include Buck, Boost [49–51], Buck-Boost, Cuk, Sepic, and Zeta converters. PWM with P, PI, PID performs good for constant switching frequency and small signals.

2 Classification of Emulator Based on Converter Used

a. **Buck Converter**:

It is a power converter providing output voltage less than input voltage. It is simplest among all the converters in construction. As it is a switching converter, the power losses are low and it has small size. To achieve a crossover frequency (say 1 kHz), a 10 times (10 kHz) switching frequency is to be chosen. This is a general criterion when applying a linear control of buck converter as the linear small signal models of switching converters are valid till half the switching frequency [52]. By considering switching frequency, the chosen power transistor for the buck converter is a MOSFET, as other transistors such as IGBT offer high switching power losses above 50 kHz and 520 V input [53]. In continuous conduction mode, the ratio of output to the input voltage is termed as duty cycle. A low pass filter is added to limit ripples in output current and voltage. The minimum values of inductor and capacitor [33, 37] are selected using the following formula:

$$L = \frac{V_{\text{in}}d(1-d)}{\Delta I_0 f_c}$$
$$C = \frac{(1-d)v_o}{8Lf_c^2 \Delta v_o}$$

The output voltage and the output current of the converter are sensed and fed to the controller, which in turn controls the gate signal of the converter to behave like a PV emulator and provide the desired *I–V* characteristics. In order to include the dynamic effect (due to changing *G* and *T* and varying loads), the controller can be fed *G*, *T*, and varying load values.

3   Modeling Buck Converter

The equations obtained by considering ideal nature of elements [54] and applying KVL and KCL are as follows: ON STATE (t_{on})

$$\frac{v_{in}}{dt} = L di_L + v_c \tag{1}$$

Or

$$\frac{di_L}{dt} = \frac{v_{in}}{L} - \frac{v_c}{L} = \dot{x}1$$

$$iL = \frac{C dv_c}{dt} + \frac{v_c}{R}$$

Or

$$\frac{dv_c}{dt} = \frac{i_L}{C} - \frac{v_c}{R} = \dot{x}2 \tag{2}$$

Off state (t_{off})

$$\frac{di_L}{dt} = \frac{-v_c}{L} = \dot{x}1 \tag{3}$$

$$\frac{dv_c}{dt} = \frac{i_L}{L} \frac{-v_c}{RC} = \dot{x}2 \tag{4}$$

Output current to Control transfer function is derived as:

$$\frac{i_L(s)}{d(s)} = \frac{V_{in}}{R\left[1 + s^2 LC + s\frac{L}{R}\right]} \tag{5}$$

The diode and switch ratings can be evaluated from peak inverse voltage and average current of both components. For the diode, the peak inverse voltage occurs at ON state. This value will be equal to the input voltage, and the current through the diode will be equal to the maximum output current.

b. **State Space Averaging**

State space averaging is known as an approximation technique which for high switching frequencies allows a continuous time signal frequency analysis to be carried out separately from the switching frequency analysis [55, 56]. It can be used to describe the input and output relations of a switching converter having different switching modes of operation. The original system is generally linear, but the resulting system is nonlinear.

If the duty cycle is d and $d = f(x, u)$
where x = state vector
u = source vector
$d = t_{on}/T$
where $T = t_{on} + t_{off}$
By formula

$$A = A_{on}d + A_{off}(1 - d) \tag{6}$$

$$B = B_{on}d + B_{off}(1 - d) \tag{7}$$

By substituting value of A_{on}, A_{off}, B_{on}, B_{off}
In Eqs. (6) and (7), we get:
$A = [0 - 1/L; 1/C - 1/RC]$
$B = [d/L\ 0]$
After setting the value of duty cycle, d the controllability and observability of the system can be easily calculated using Simulink in MATLAB.

c. **Buck converter as PV emulator**

A buck converter can be implemented to obtain PV emulator. In PV emulator, a controller is required to get $I–V$ characteristics with lesser deviation from actual characteristics. Figure 1 shows Simulink model of PV emulator employing PID controller.

Input voltage is 24 V, and output voltage varies with variation in load resistance from 5 to 100 Ω. The advantage of using PID controller is its simplicity of implementation, but the tuning of PID is time-consuming process (Fig. 2).

Although PID controller provides satisfactory results close to real PV but the process can be made more efficient and fast by the use of other control schemes like

Fig. 1 Buck converter
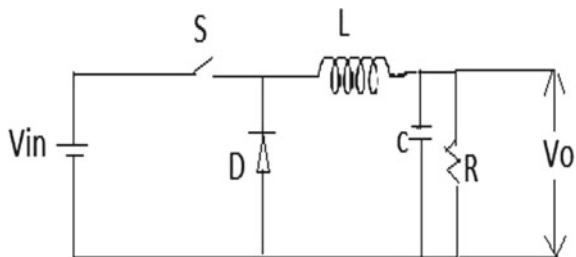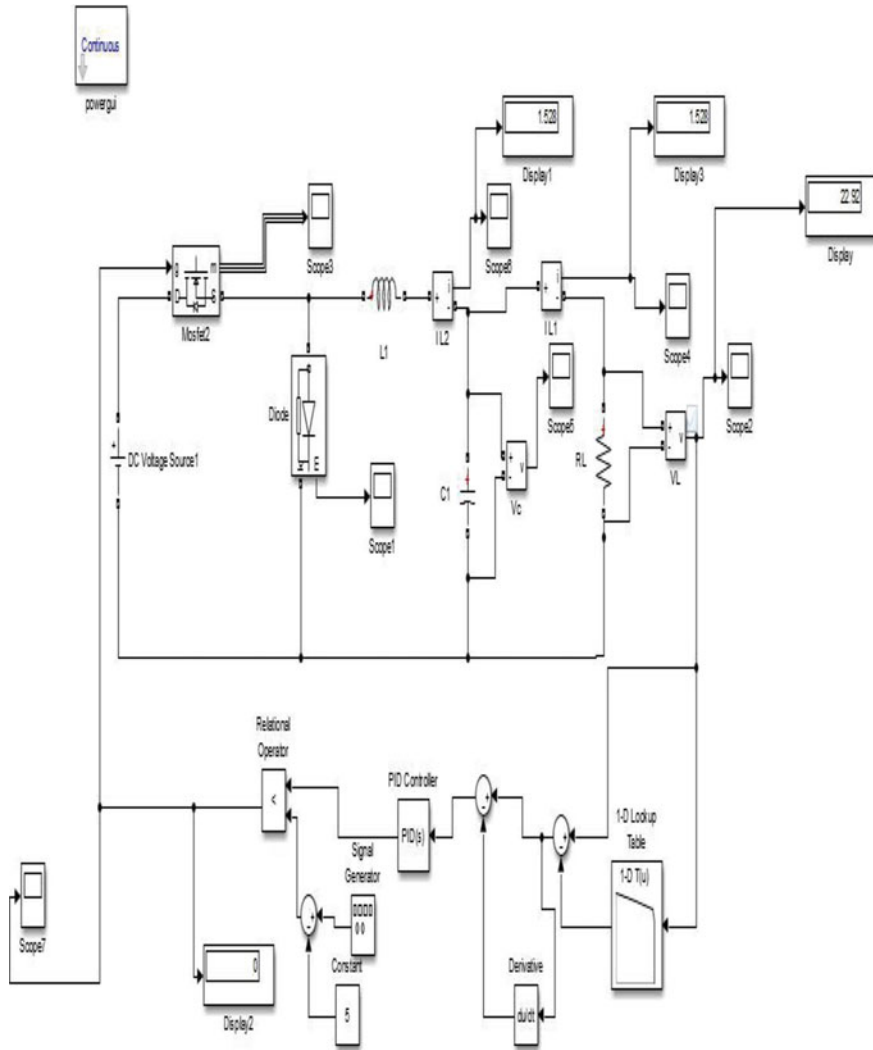
Fig. 2 Simulink model of designed PV emulator

fuzzy logic control which is best suited for obtaining the imprecise nature of the real world, it is helpful in multi-objective and robust control realization. Voltage mode control and current mode control are simple and old techniques which have limitation of the controller design particularly for higher order converter topologies. Lyapunov based controller [57] avoids the use of inductor current so noise due to current sensor is reduced. Sliding mode control scheme has the capability to respond suddenly to transient condition and provide robustness.

Fig. 3 *I–V* characteristics of designed PV emulator
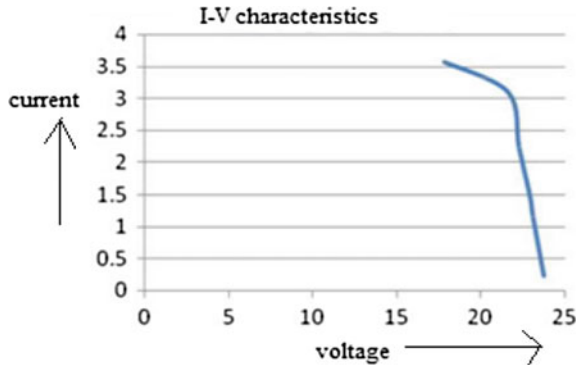
4 Result and Conclusion

The designed PV emulator shows *I–V* characteristics (Fig. 3) close to real PV panel at different resistive loads, but the open circuit voltage and short circuit current values are not obtained after simulation at varying load. So in future, the work can be carried out on designing the converter or the control scheme to get V_{oc} and I_{sc} values.

References

1. Available online: http://www.mnre.gov.in/
2. Available online: https://www.solarinsure.com/largest-solar-power-plants
3. Available: http://apps1.eere.energy.gov/state_energy_program/Green Energy DC program. District of Columbia, Washington DC, USA. Available: http://www.green.dc.gov
4. The California solar initiative program, California, USA. Available: http://www.gosolarcalifornia.ca.gov/csi/index.html
5. IEEE Standards Association (2014) IEEE 1547 Standard for interconnecting distributed resources with electric power systems. Available: http://grouper.ieee.org/groups/scc21/1547/1547_index.html. Accessed 4, 2014
6. Zghal W, Kantchdev G, Kchaou, H (2012) Determination of the exploitable solar energy for electricity generation using the photovoltaic systems. In: IEEE 1st international conference on renewable energies and vehicular technology, pp 43–48
7. Matos FB, Camacho JR (2007) A model for semiconductor photovoltaic (PV) solar cells: the physics of the energy conversion from the solar spectrum to DC electric power. IEEE international conference on clean electrical power (ICCEP), May 2007
8. Benson CL, Magee CL (2014) On improvement rates for renewable energy technologies: solar PV, wind turbines, capacitors and batteries. Renew Energy 68:745–751
9. Atmaja TD (2012) Façade and rooftop PV installation strategy for building integrated photo voltaic application. In: Energy procedia international conference on sustainable energy engineering and application [ICSEEA 2012], pp 105–114, Mar 2014. Available online at www.sciencedirect.com

10. de Brito MAG, Sampaio LP, Junior LG, Canesin CA (2011) Research on photovoltaics: review, trends and perspectives. In: IEEE conference on power electronics (COBEP), pp 531–537, Sept 2011
11. Binduhewa PJ, Barnes M (2013) Photovoltaic emulator. In: IEEE 8th international conference on industrial and informatics systems (ICIIS), pp 519–524, Aug 2013
12. Rana A, Patel H (2013) Current controlled buck converter based PV emulator. J Ind Intell Inf 1(2)
13. Thale S, Wandhare R, Agarwal V (2014) A novel low cost portable integrated solar PV, fuel cell and battery emulator with fast tracking algorithm. In: IEEE conference on photovoltaic specialist, pp 3138–3143
14. Raja R, Udhaya Kumar L, Rakesh Kumar S (2013) Fuzzy logic controller for photovoltaic array simulator. Int J Eng Technol (IJET) 5(2):1625–1630
15. Mandal K, Banerjee S, Chakraborty C (2014) A new algorithm for small signal analysis of DC–DC converters. IEEE Trans Ind Inf 10(1):1–9
16. Tauquir Iqbal M, Tariq M (2015) Analytical study of different DC-DC converter topologies for photovoltaic emulator. J Autom Syst Eng (JASE), 245–254. Available online: jase. esrgroups.org
17. Abdel-Gawad H, Sood VK (2014) Small-signal analysis of boost converter, including parasitics, operating in CCM. In: 6th IEEE power India international conference (PIICON), pp 1–5
18. Bansal S, Saini LM, Joshi D (2013) Design of PI and fuzzy controller for high efficiency and tightly regulated full bridge DC-DC converter. Int J Electr Comput Energ Electr Commun Eng 7:446–452
19. Reatu A, Kazimierczuk MK (2000) Current controlled current source model for a PWM DC-DC converters operated in discontinuous current mode. In: IEEE international symposium circuits and systems, ISCAS, vol 3, pp 239–242, May 2000
20. Agrawal J, Aware M (2012) Photovoltaic system emulator. In: IEEE international conference on power electronics, drives and energy systems (PEDES), pp 1–6
21. Singh MD, Shine VJ, Janamala V (2014) Application of artificial neural networks in optimizing MPPT control for standalone solar PV system. International conference on contemporary computing and informatics (IC3I), pp 162–166, Nov 2014
22. Miloudi L, Acheli D (2015) Prediction global solar radiation and modeling photovoltaic module based on artificial neural networks. In: IEEE 3rd international conference on control, engineering and information technology (CEIT), pp 1–6
23. Messalti S, Harrag AG, Loukriz AE (2015) A new neural networks MPPT controller for PV systems. In: IEEE 6th international conference on renewable energy congress (IREC), pp 1–6, Mar 2015
24. Hua C, Lin J, Shen C (1998) Implementation of a DSP-controlled photovoltaic system with peak power tracking. IEEE Trans Ind Electr 45(1)
25. AI Nabulsi A, Dhaouadi R (2012) Efficiency optimization of a DSP-based standalone PV system using fuzzy logic and dual-MPPT control. IEEE Trans Ind Inf 8(3):573–583
26. Enrique JM, Duran E, Sidrach-de-Cardona M, Andujar JM (2007) Theoretical assessment of the maximum power point tracking efficiency of photovoltaic facilities with different converter topologies. Sci Direct Solar Energy 81:31–38
27. Esram T, Chapman PL (2007) Comparison of photovoltaic array maximum power point tracking techniques. IEEE Trans Energy Convers 22(2):439–449
28. Madani V, Novosel D, Zhang P, Meliopoulos S, King R (2006) Vision in protection and control area meeting the challenges of 21st century. In: IEEE conference on PES power system conference and exposition, Oct 2006
29. Shiau J-K, Li M-Y, Wei YC, Chen B-C (2014) Circuit simulation for solar power maximum power point tracking with different buck boost converter topologies. In: IEEE 1st international e-conference on energies, pp 1–17, Mar 2014

30. Kamejima T, Phimmasone V, Konda Y, Miyatake M (2011) The optimization of control parameters of PSO based MPPT for photovoltaic. In: IEEE conference PEDS, pp 881–884, Dec 2011

31. Verma D, Nema S, Shandilya AM, Dash SK (2015) Comprehensive analysis of maximum power point tracking techniques in solar photovoltaic systems under uniform irradiation and partial shaded condition. J Renew Sustain Energy 7. Available online: http://dx.doi.org/10.1063/1.4926844, July 2015

32. Cazzaniga R, Rosa-Clot M, Rosa-Clot P, Tina GM (2012) Floating tracking cooling concentrator (FTCC) systems. In: 38th IEEE photovoltaic specialists conference, pp 000514–000519

33. Ajaamoum M, Kourchi M, Bouachrine B, Ihlal A, Bouhouch L (2014) Modeling an emulator of photovoltaic panels. Int J Enhanc Res Sci Technol Eng 3(10):163–171

34. Altas IH, Sharaf AM (2007) A photovoltaic array simulation model for matlab-simulating GUI environment. In: IEEE international conference on clean electrical power, pp 341–345

35. Savita N, Nema RK, Agnihotri G (2010) MATLAB/Simulink based study of photovoltaic cells/modules/array and their experimental verification. Int J Energy Environ 3:487–500

36. Adbulkadir M, Samosir AS, Yatim AHM (2012) Modeling and simulation based approach of Photovoltaic system in simulink model. ARPN J Eng Appl Sci 7(5):616–623

37. Dolan D, Durago J, Crowfoot J, Taufik T (2010) Simulation of a photovoltaic emulator. IEEE North American power symposium (NAPS), pp 1–7, Sept 2010

38. Gonzalez-Llorente J, Rambal-Vecino A, Garcia-Rodriguez LA, Balda JC, Ortiz-Rivera EI (2016) Simple and efficient low power photovoltaic emulator for evolution of power conditioning systems. In: IEEE conference on applied power electronics and exposition (APEC), pp 3712–3716

39. Vijaykumari A, Devarajan AT, Devarajan N (2012) Design and development of a model-based hardware simulator for photovoltaic array. Electr Power Energy Syst 43:40–46. Available online at ScI-Verse Science Direct, homepage: www.elsevier.com/locate/ijepes

40. Samosir AS (2015) Modeling and evaluation of solar photovoltaic emulator based on simulink model. ARPN J Eng Appl Sci 10(22):10288–10295

41. Pelin D, Jukic Antolovic J, Rapcan V (2014) PV emulator. Int J Electr Comput Eng Syst 5(1):21–26

42. Nema RK, Nema S, Agnihotri G (2009) Computer simulation based study of photovoltaic cells/modules and their experimental verification. Int J Recent Trends Eng 1(3):151–156

43. Raveendhra D, Thakur P, Narasimha Raju BL (2013) Design and small signal analysis of solar PV fed FPGA based closed loop control bi-directional DC-DC converter. In: IEEE international conference on circuits, power and computing technologies (ICCPCT), pp 283–288

44. Elyaqouti M, Bouhouch L, Ihlal A (2016) Modeling and simulation of an emulator of photovoltaic generator. J Commun Appl Electr (CAE) 5(8). Available online: www.caeaccess.org

45. Shinde UK, Kadwana SG, Gawande SP, Keshri R (2016) Solar PV emulator for realizing PV characteristics under rapidly varying environmental conditions. In: IEEE international conference on power electronics, drives and energy systems (PEDES), pp 1–4

46. Bangia S, Jain S, Neha (2015) DC motor control system using model predictive controller. Int Res J Eng Technol (IRJET) 2:1010–1014

47. Salimi M, Soltani J, Zakipour A, Hajbani V (2013) Two-loop adaptive and non-linear control of the DC-DC boost converter in discontinuous conduction mode. In: IEEE conference on 4th power electronics, drive systems & technologies (PEDSTC 2013), pp 164–169, Feb 2013

48. Bhardwaj M (2015) Modeling bi-directional buck-boost converter for digital control using C2000 microcontrollers. Application Report Texas Instruments SPRABX5, p 11, Jan 2015

49. Middlebrook RD, Cuk S (1976) A general unified approach to modeling switching-converter power stages. In: IEEE power electronics specialists conference, pp 18–34

50. Solaiman HM, Hasan MM, Mohammad A, Kawsar SR, Hassan MA (2015) Performance analysis of DC to DC Boost convertor using different control methods. In: IEEE international conference on electrical, computer and communication technologies (ICECCT), pp 1–3
51. Haripriya T, Parimi AM, Rao UM (2013) Modeling of DC-DC boost converter using fuzzy logic controller for solar energy system applications. IEEE Asia Pacific conference on postgraduate research in microelectronics and electronics, pp 147–152
52. Vorperian V (1990) Simplified analysis of PWM converters using model of PWM switch, continuous conduction mode. IEEE Trans Aerosp Electron Syst 26:490–496
53. Gonzalez-Medina R, Patrao I, Garcera G, Figures E (2014) A low cost photovoltaic emulator for static and dynamic evaluation of photovoltaic power converters and facilities. Prog Photovolt Res Appl 227–241
54. Mahesh Gowda NM, Kiran Y, Parthasarthy SS (2014) Modeling of buck DC-DC converter using simulink. Int J Innov Res Sci Eng Technol 3(7):14965–14975
55. Modabberenia MR (2013) The state space average model of buck-boost switching regulator including all of the system uncertainties. Int J Comput Sci Eng (IJCSE) 5(2):120–132
56. Rim CT, Joung GB, Cho GH (1988) A state-space modeling of non-ideal converters. IEEE PESC 943–948
57. Panda RK, Mohapatra A, Srivastava SC (2016) A Lyapunov based controller for boost converter to integrate solar photovoltaic source. In: IEEE conference on innovative smart grid technologies-Asia (ISGT-Asia), pp 599–604, Nov 2016

Fault Detection in Single-Phase Inverters Using Wavelet Transform-Based Feature Extraction and Classification Techniques

Varaha Satya Bharath Kurukuru, Ahteshamul Haque and Mohammed Ali Khan

Abstract A fault classification and identification system for prognosis of single-phase inverters was presented in this paper. This concept involves the resolution and analysis of different technical constraints associated with the operation and integration of the inverters. The work presented is centered on fault identification for single-phase inverters by developing a suitable technique utilizing signal processing and machine learning techniques. This task is approached by observing the behavior of inverters under various faults and the factors affecting them. Thereafter, the output voltage under both normal and faulted operation was subjected to signal processing techniques to observe the features. The obtained features are trained for classification and identification of faults using support vector machines. Simulation was carried out for operation of inverter under different events of a fault. By combining output voltages and their features with wavelet transforms and feature detection, the developed algorithms are capable of capturing the key features of inverters. The results depicted how to perform numerical fault analysis calculations using MATLAB classification learner by adapting the trained data for identifying the fault.

Keywords Discrete wavelet transform (DWT) · Feature detection · Feature extraction · Support vector machine (SVM)

V. S. B. Kurukuru (✉) · A. Haque · M. A. Khan
Department of Electrical Engineering, Faculty of Engineering and Technology,
Jamia Millia Islamia, New Delhi 110025, Delhi, India
e-mail: kvsb272@gmail.com

A. Haque
e-mail: ahaque@jmi.ac.in

M. A. Khan
e-mail: mak1791@gmail.com

1 Introduction

The voltage source inverters are widely utilized in the applications such as PV systems, wind energy conversion systems, and dynamic voltage restores [1]. Ensuring optimal voltage input when integrated with optimized systems [2, 3] extends the life and improves the performance characters of inverters. Speaking about reliability, this is a very vital aspect since many kinds of unexpected faults in inverter may influence the operation of the whole system. Among all the components in the inverter, switching devices are the most vulnerable. In general, faults occurring on them can be broadly categorized as short- and open-circuit faults [4]. The open-circuit faults may not create a major problem for the system but may remain undetected for a larger period, resulting in the inverter or drive component failure [5]. Research has been carried up to a great extent for addressing the different types of faults and their diagnosis problems for inverters [6–10]. Unfortunately, these fault detection techniques tend to be highly unreliable under different operating conditions, such as light load and fast transients. It was also observed that these methods also have some drawbacks such as large detection time, higher complexity, and time-delay values which must be precisely defined. In response to these concerns, a diagnostic method for different types of faults in the inverter is proposed in this paper. Unlike the traditional methods that are based on the voltage or current sensors, the proposed method uses the voltage across the output filter inverter as the diagnostic criterion. Since the voltage across the output filter inductor can be easily obtained by applying an auxiliary winding across the inductor [11] or fixing a magnetic near field probe near the inductor [12], no external sensors are needed and the isolation is realized naturally. In order to observe the operation of inverter during various faults, a sample of four faults like triggering failure, IGBT short circuit, IGBT open circuit, and harmonics due to filter failure were simulated, and the output voltages were measured as shown in Fig. 1. Further sections of this paper deal with conventional fault diagnosis methods associated with various applications. With reference to theoretical analysis, the diagnostic algorithm is designed using wavelet transforms and classification learner systems. The feature detection and extraction procedure and their results were elaborated, and the extracted features were tabulated for classification. The final results thought process implementation and validation were depicted along with the conclusion and future work.

2 Literature Survey

Overall, faults can be detected visually or with the help of more advanced methods that rely on computational power.
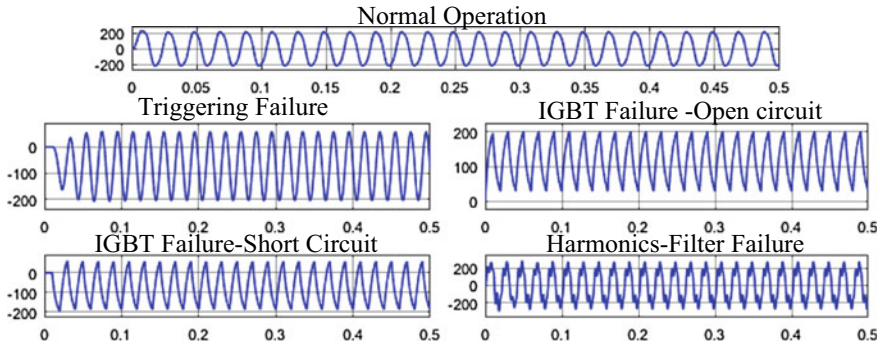
Fig. 1 Voltage outputs of inverter operation under simulated faults

2.1 Visual Inspection

Visual inspection is one of the simplest and yet most practical methods for detecting a multitude of different faults. Despite its simplicity, it is still an effective way of fault detection. It is the most commonly used method for some of the previously mentioned faults. It is also a method for confirming suspicions that the system operator/installer could have after looking at the results shown by other fault detection methods. Some failures, however, do not manifest physically and should be inspected with the help of more sophisticated tools.

2.2 Electrical and Data Analytics Methods

The trend for developing new and efficient electrical fault detection methods has been increasing in recent years. This interest is reflected in the literature, which has been visibly expanding on this particular subject. This following section contains a general overview of the most acknowledged methods in the literature. To begin with, in [13] a method was proposed which relies on satellite-based systems to acquire meteorological data of the desired location. This method allows the detection of constant and variable energy losses caused by inverter's limitations and switching failures. While this method cuts down on simulation and computational costs, it can also lead to high costs for communication systems and data loggers. A monitoring circuit built to measure the voltage and current of inverters under various operating conditions was developed in [14]. Finally, a statistical method developed in [15] utilizing analysis of variance and Kruskal–Wallis (KW) tests shows high levels of accuracy and speed in locating maloperations and forecasting faults. A technique based on expert systems was developed in [16] and allows the identification of two fault types (failures due to shading effects and inverter failures). An effective technique based on artificial neural networks (ANN) was

proposed in [17]. Finally, [18, 19] are two separate Takagi Sugeno fuzzy rule-based methods. The results shown in these methods point out that these systems can recognize more than 90% of fault conditions. A technique based on decision trees (DT) was used in [20] to determine faults using an over-current protection device (OCPD).

3 Wavelet

Wavelet is a rapidly decaying wave-like oscillation with zero mean, best suited for localizing frequency content in real-world signals. Availability of a wide variety of wavelets is a key strength of wavelet analysis.

3.1 Discrete Wavelet Transform

DWT deals with decomposition of a signal with orthonormal basis $\psi_{m,n}(x)$. It is known as the mother wavelet, and signal is obtained through translation and dilation of the basic functions. Fourier transform uses sines and cosines for basis which are localized in only frequency domain but not in time, where wavelets transform is represented by different types of basic functions taking the advantage over Fourier transforms both in time and frequency domain. Any minor change in frequency of Fourier transform will affect everywhere in the time domain, but for wavelets, both frequency and time are in local domain. This is the advantage of wavelet transform. The coefficients of wavelet transform for a signal $f(x)$ can be written as follows because of the orthogonality property:

$$C_{m,n} = \int_{-\infty}^{+\infty} f(x)\psi_{m,n}(x)\mathrm{d}x \tag{1}$$

and following formula will be used to obtain $f(x)$ from wavelet coefficients:

$$f(x) = \sum_{m,n} C_{m,n}\psi_{m,n}(x) \tag{2}$$

Before construction of mother wavelet, scaling function—(x) should be determined with satisfying following two equations:

$$\phi(x) = \sqrt{2}\sum_{k} h(k)\phi(2x - k) \tag{3}$$

And

$$\psi(x) = \sqrt{2} \sum_k g(k)\phi(2x - k) \tag{4}$$

where

$$g(k) = (-1)^k h(1 - k) \tag{5}$$

The coefficients of $h(k)$ given in Eq. 3 need to satisfy some conditions. There are a lot of sets of coefficients $h(k)$ satisfying the above conditions in the literature like Haar, Daubechies, Fejer-Korovkin, Lagrange, etc. wavelet filter [12, 21–23]. In our work, we adapted a multilevel DWT filter bank using wavelet Symlets 7 (sym7) to obtain the wavelet coefficients.

4 Feature Detection and Extraction

Wavelet analysis compliments signal processing techniques to identify and extract features in real-world signals. The voltage output of the inverter system was used to identify important features and extract them and perform downstream processing. The output variation in the voltage signal due to different faults carries a lot of meaning and one needs to use appropriate techniques to analyze the signal.

4.1 Feature Detection

The signals are loaded from the simulation and preprocessed to remove the artifacts. The preprocessed signals are explored to identify the features. A time–frequency analysis using wavelets was adapted to carry the above process. To visualize the signal, we use analyzer application from MATLAB. A general signal contains two types of components, slowly varying components and rapidly varying components. To preprocess the signal, we need to observe the frequency domain representation. In MATLAB with the help of spectrum graph in signal analyzer, we can observe the power of the signal as a function of frequency. In case of any harmonics, we can eliminate them by using wavelet, due to their advantage of eliminating the harmonics without introducing the spike, or any abrupt spike in the spectrum. To quantify the spectral nature of the signal, we adopt a time–frequency technique. A spectrogram can be used as shown in Fig. 2, to obtain the time–frequency visualization. The output of the spectrogram is a joint time–frequency visualization along with power information which is denoted using various colors.
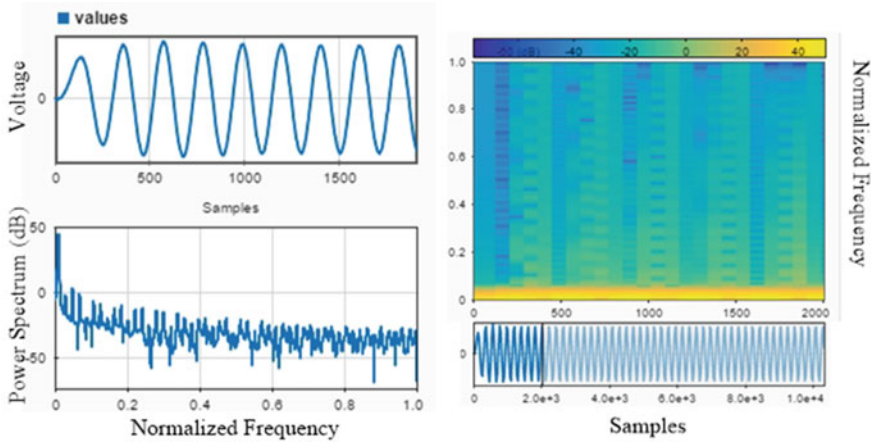
Fig. 2 Feature detection using signal analyzer

By analyzing the spectrogram at high levels, we can observe the time and frequency dilation of the signal. The slowly varying components of signal are interspersed with rapidly varying events. To analyze this event, we adapt wavelet transform.

4.2 Feature Extraction

In order to extract the features of signal, we have to decompose the signal to obtain the coefficients of the signal (Fig. 3) as discussed in Sect. 4.1. By decomposing a signal into various sub-bands, we isolate the noise inside the signal.

Energy. First, we observe the energy features of the signal using the obtained coefficients. The energy of the signal is given by:

$$E_x = \int\limits_{-\infty}^{\infty} |x(t)^2| \, dt \tag{6}$$

where $x(t)$ is the continuous time complex signal.

The equation when applied to one-dimensional wavelet decomposition gives percentage of error corresponding to approximation and vector of percentage of error corresponding to the details of the signal.

Power Spectral Density. Power spectral density as shown in Fig. 4 characterizes a stationary random process in the frequency domain. Power spectrum $s(\omega)$ is defined as the discrete time Fourier transform of the correlation sequence $r[k]$.
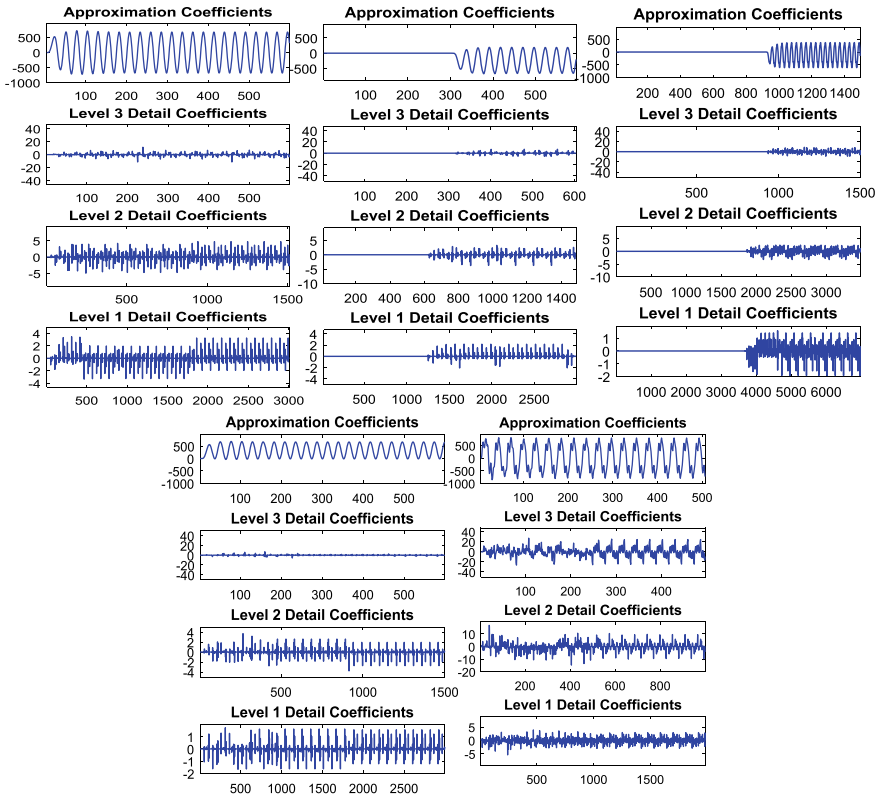
Fig. 3 Coefficients of decomposed signals

$$s(\omega) \overset{\text{DTFT}}{\leftrightarrow} r[k] \tag{7}$$

where $s(\omega)$ is given by

$$s(\omega) = \sum_{k=-\infty}^{\infty} r[k]e^{-jk\omega} \tag{8}$$

And $r[k]$ is given by

$$r[k] = \frac{1}{2\pi} \int_{-\pi}^{\pi} s(\omega)e^{jk\omega}d\omega \tag{9}$$
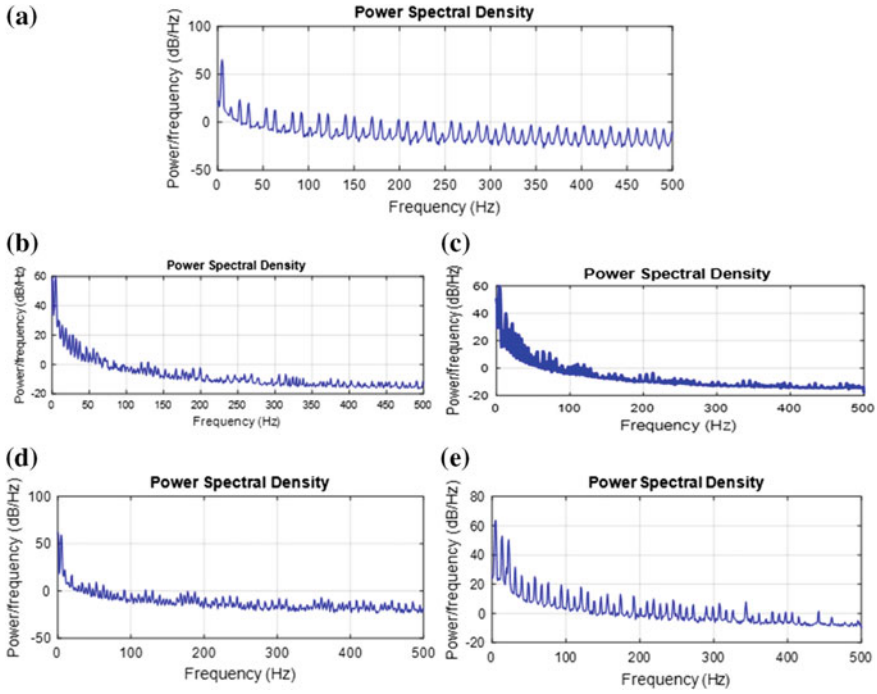
Fig. 4 Power spectral density of reconstructed output voltage signals

For the purpose of interpretation, we integrate the power spectral density from ω_a to ω_b and normalize it by 2π.

$$P_{ab} = \frac{1}{2\pi} \int\limits_{\omega_a}^{\omega_b} s(\omega) d\omega \tag{10}$$

P_{ab} is defined as the average contribution to the total power (variance) that is due to the components of the random process between ω_a and ω_b. The power spectrum $s(\omega)$ may be normalized on [0, π] rather than [$-\pi$, π].

Peak Analysis. Peaks of a signal are most noticeable and useful features. Peaks can determine the period of a signal by measuring the distance between the peaks. For the above reasons, peak analysis is an important area of feature extraction. Figure 5 shows the peak analysis of reconstructed signal of an inverter under various operating conditions.

Total Harmonic Distortion. The measure of distortion present in a waveform due to harmonics is known as total harmonic distortion. In general terms, the power of a signal is P_1 and f_1 as fundamental frequency, whereas for harmonics i, f_i and P_i are its value, respectively, the THD then comes out to be,
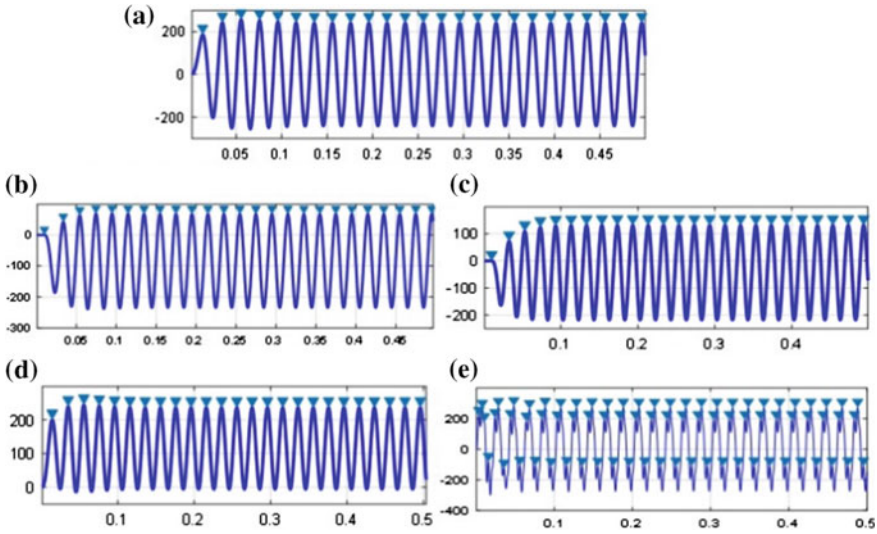
Fig. 5 Peak analysis of reconstructed voltage signals

$$\text{THD} = \frac{\sum_{i>1} P_i}{P_1} = \frac{P_{\text{total}} - P_1}{P_1} \tag{11}$$

where P_{total} denotes the total power for waveform (harmonics included). THD can also be denoted as ratio of the power of all the harmonics and total power in the fundamental frequency.

THD equation can also replace the squared RMS voltages which is equivalent to power:

$$\text{THD} = \frac{\sum_{i>1} V_i^2}{V_1^2} = \frac{V_{\text{total}}^2 - V_1^2}{V_1^2} \tag{12}$$

THD is also defined as power ratio instead of amplitude ratio in some of the cases:

$$\text{THD} = \frac{\sqrt{\sum_{i>1} V_i^2}}{V_1} = \frac{\sqrt{V_{\text{total}}^2 - V_1^2}}{V_1} = \sqrt{\text{THD}} \tag{13}$$

It may lead to a value square root time of other functions.

Measurement of THD can be done by waveform sample setup and by computation of frequency spectrum using Fourier analysis. And from that, the harmonic power sum is divided by the power in fundamental frequency.

Signal-to-Noise Ratio. The measure of signal strength to that of the noise is known as signal–noise ratio (SNR). Some amount of noise is present in every signal. A higher signal-to-noise ratio is desirable. signal–noise ratio can be calculated by:

$$SNR = 10 \log\left(\frac{P_{\text{signal}}}{P_{\text{noise}}}\right)(\text{dB}) \tag{14}$$

or in case of amplitudes related to signal and noise

$$SNR = 10 \log\left(\left(\frac{A_{\text{signal}}}{A_{\text{noise}}}\right)^2\right) = 20 \log\left(\frac{A_{\text{signal}}}{A_{\text{noise}}}\right)(\text{dB}) \tag{15}$$

For SNR measurement, it is necessary to measure value and RMS and noise separately by using true RMS meter and oscilloscope. In most of the cases, noise is already present in the signal and by implementing SNR formula results can be obtained.

5   Classification and Identification

Classification is a process of statistics and machine learning that lets you train models to classify data using supervised machine learning. This performs a common machine learning tasks by specifying validation schemes, interactively explaining data, selecting features, training models, and assessing model performance. The validation schemes are used to examine the predictive accuracy of the fitted models. There were multiple classification types like decision trees, support vector machines, nearest neighbor, and ensemble classifiers. The classifier is chosen based on the type of data and requirement of the user. Here, we choose support vector machines after performing a brief assessment on all the classifiers as they provide better training accuracy for the tabulated data. In this experiment, all the extracted features for various operating conditions were tabulated as predictors, and the type of operation was tabulated as response for the purpose of classification using support vector machines.

6   Support Vector Machines

SVMs are also referred to as supervised machine learning algorithms used for classification as well as regression problems. They are based on the concept of decision planes that separate between a set of objects having different class memberships. MATLAB classification learner application is used for implementation of SVM.
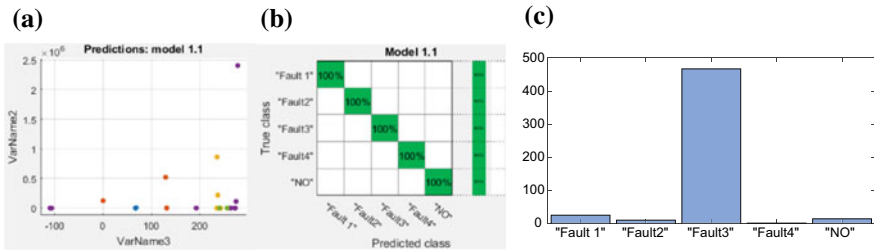
Fig. 6 Classification learner. **a** scatter plot, **b** confusion matrix, and **c** predicted fault from the trained data

The basic illustration of SVMs deals with observations, where it will differentiate between the objects or data in the observation in the most optimal way. There are several ways to split or differentiate the data, but the goal is to arrive at the optimal hyperplane which segments the data so that there is widest margin between the hyperplane and the observations. The inputs to the SVM are a matrix of predictors and responses, where the responses correspond to an array of class defined with labels and predictors correspond to the features extracted from various operating conditions of inverter. The data were used to train SVM, and then, the classifier is cross-validated. The trained data are used to classify or predict new data. For better accuracy with SVM, various SVM kernel functions can be used by training the parameters and kernel functions. After training the data for a particular classifier, we can observe the scatter plots as shown in Fig. 6a which explore the data for important predictors, outliners, and visual patterns. A confusion matrix is also observed as shown in Fig. 6b which helps in assessing how currently selected classifier performs in each class. A dominantly diagonal confusion matrix indicates a good classifier since all the predictor levels match the actual levels. The classified models obtained are used to generate predictions on a new set of data. Once the data are predicted using the obtained trained model, we can identify the fault type on the basis of how the new data fit with the trained data as shown in Fig. 6c.

7 Conclusion

This paper presents a diagnostic approach for faults in single-phase inverters using discrete wavelet transform and classification learner by using the output voltage as a diagnostic norm. Discrete wavelet transform along with feature detection and extraction techniques were used to develop the algorithm which is further combined with support vector machines to classify and identify the faults. The fault diagnostic time is about a fundamental period. The diagnostic system is simple and can be implemented at a low cost. It is noticed that the diagnostic system is more precise, and the fault identification can be easily performed. Further, the algorithm can be extended for locating and isolating the fault.

References

1. Wan X (2011) Electrical power systems and computers : selected papers from the 2011 international conference on electric and electronics (EEIC 2011) in Nanching, China on June 20–22, 2011, vol 3. Springer, Berlin
2. Haque A (2014) Maximum power point tracking (MPPT) scheme for solar photovoltaic system. Energy Technol Policy 1:115–122
3. Zaheeruddin, Mishra S, Haque A (2016) Performance evaluation of modified perturb & observe maximum power point tracker for solar PV system. Int J Syst Assur Eng Manag 7:229–238
4. Klima J, Schreier L (2004) Investigation and control of an induction motor drive under inverter fault conditions. IFAC Proc 37:489–494
5. Sobanski P, Orlowska-Kowalska T (2016) Application of open-circuit IGBT faults diagnostic method in DTC-SVM induction motor drive. Autom J Control Meas Electron Comput Commun 57:387–395
6. Zhang J, Zhao J, Zhou D, Huang C (2014) High-performance fault diagnosis in PWM voltage-source inverters for vector-controlled induction motor drives. IEEE Trans Power Electron 29:6087–6099
7. Dhumale RB, Lokhande SD (2017) Comparative study of fault diagnostic methods in voltage source inverter fed three phase induction motor drive. In: IOP conference series: materials science and engineering, vol 197
8. Meinguet F, Sandulescu P, Aslan B, Lu L, Nguyen N, Kestelyn X, Semail E (2013) A Signal-based technique for fault detection and isolation of inverter faults in multi-phase drives
9. Zidani F, Diallo D, Benbouzid MEH, Naït-Saïd R (2008) A fuzzy-based approach for the diagnosis of fault modes in a voltage-fed PWM inverter induction motor drive. IEEE Trans Ind Electron 55:586–593
10. Raj N, Mathew J, Jagadanand G, George S (2016) Open-transistor fault detection and diagnosis based on current trajectory in a two-level voltage source inverter. Procedia Technol 25:669–675
11. Nie S, Chen Y, Pei X, Wang H, Kang Y (2011) Fault diagnosis of a single-phase inverter using the magnetic field waveform near the output inductor. In: Conference proceedings—IEEE applied power electronics conference and exposition—APEC, pp 1648–1655
12. Yun S, Sobelman GE, Zhou X (2018) Adaptive directional lifting wavelet transform VLSI architecture
13. Drews A, de Keizer AC, Beyer HG, Lorenz E, Betcke J, van Sark WGJHM, Heydenreich W, Wiemken E, Stettler S, Toggweiler P, Bofinger S, Schneider M, Heilscher G, Heinemann D (2007) Monitoring and remote failure detection of grid-connected PV systems based on satellite observations. Sol Energy 81:548–564
14. Guerriero P, D'Alessandro V, Petrazzuoli L, Vallone G, Daliento S (2013) Effective real-time performance monitoring and diagnostics of individual panels in PV plants. In: 4th international conference on clean electrical power: Renewable energy resources impact, ICCEP 2013, pp 14–19 (2013)
15. Vergura S, Acciani G, Amoruso V, Patrono GE, Vacca F (2009) Descriptive and inferential statistics for supervising and monitoring the operation of PV plants. IEEE Trans Ind Electron 56:4456–4464
16. Yagi Y, Kishi H, Hagihara R, Tanaka T, Kozuma S, Ishida T, Waki M, Tanaka M, Kiyama S (2003) Diagnostic technology and an expert system for photovoltaic systems using the learning method. Sol Energy Mater Sol Cells 75:655–663
17. Wu Y, Lan Q, Sun Y (2009) Application of BP neural network fault diagnosis in solar photovoltaic system. In: 2009 International conference on Mechatronics and Automation, pp 2581–2585

18. Ducange P, Fazzolari M, Lazzerini B, Marcelloni F (2011) An intelligent system for detecting faults in photovoltaic fields. In: International conference on intelligent systems design and applications, ISDA, pp 1341–1346
19. Bonsignore L, Davarifar M, Rabhi A, Tina GM, Elhajjaji A (2014) Neuro-Fuzzy fault detection method for photovoltaic systems. Energy Procedia 62:431–441
20. Zhao Y, Yang L, Lehman B, de Palma JF, Mosesian J, Lyons R (2012) Decision tree-based fault detection and classification in solar photovoltaic arrays. In: 2012 Twenty-seventh annual IEEE applied power electronics conference and exposition, pp 93–99
21. Wang Zhi-Zhong, Yong Jun-Hai (2008) Texture analysis and classification with linear regression model based on wavelet transform. IEEE Trans Image Process 17:1421–1430
22. Salerno E, Cetin AE, Salvetti O (2012) Computational intelligence for multimedia understanding : international workshop, MUSCLE 2011, Pisa, Italy, 13–15 Dec 2011. Revised selected papers. Springer, Berlin
23. Gerek ÖN, Çetin AE (2000) Adaptive polyphase subband decomposition structures for image compression. IEEE Trans Image Process 9:1649–1660

Voltage-Balancing Control for Stand-Alone H5 Transformerless Inverters

**Mohammed Ali Khan, Ahteshamul Haque
and Varaha Satya Bharath Kurukuru**

Abstract In photovoltaic inverters, transformerless inverter has been emerging trend in recent years. Control of transformerless inverter keeping all other parameters in consideration is a major concern. This paper presents proportional–integral–derivative (PID) and fuzzy-based control strategies for H5 inverter topologies describing their principal functions are uses. Voltage balancing of H5 inverters under various load conditions was observed with the use of PID, fuzzy and fuzzy-PID controllers. Several specific requirements are taken into consideration and subsequently analysed, the simulation model and the results defined effectiveness of the system for various controllers in terms of stability, settling time and harmonic distortions. At the end, the experimental results are introduced, and they confirm the accuracy of propounded control strategies.

Keywords H5 transformerless inverter · Control system · Fuzzy · Proportional–integral–derivative (PID)

1 Introduction

Constant decrease in non-renewable resource and increase in demand of power have made sustainable power generation which is one of the most important issues. With emerging technology, attempts are being made to obtain the most out of the renewable source. Research is taking place to limit the losses in conversion process. One of the recently growing researches in field of inverters is Transformerless

M. A. Khan (✉) · A. Haque · V. S. B. Kurukuru
Department of Electrical Engineering, Faculty of Engineering and Technology,
Jamia Millia Islamia, New Delhi 110025, Delhi, India
e-mail: mak1791@gmail.com

A. Haque
e-mail: ahaque@jmi.acin

V. S. B. Kurukuru
e-mail: kvsb272@gmail.com

inverter topology. The focus of these inverters is to reduce the transformer losses and constraint such as size and cost. Only concern in transformerless inverter is leakage current which exist because of the absence of isolation between the AC and DC half of the inverters.

In the work done by Gubia et al. [1] presented an in-depth analysis of ground current concept in transformerless inverter and proposed a new topology to reduce the leakage current also. For maximum power extraction, research by Haque [2] provides a modified approach towards maximum power point tracking implemented at DC–DC converter. Work by Sukumar and Ahteshamul [3] builds upon the previous proposal and performance parameter of P&O is improved. Xiao et al. [4] presented a full-bridge structure which was designed considering the advantages and disadvantages of the existing structures. Patrao et al. [5] reviewed different transformerless topologies and compared it with the conventional topologies. Whereas in Islam et al. [6], work performance analysis and classification of different transformerless topologies have been done. Li et al. [7] modified H5 topology of transformerless inverter for the elimination of common mode current. Ahmad and Singh [8] presented a detailed analysis on different transformerless inverters with its main focus on common mode voltage and method to reduce leakage current.

Control of the inverter being one of the major aspects. Shen et al. [9] proposed a feedback using proportional and resonant controller for current control. Balaguer et al. [10] discussed about control strategy for grid connected as well as islanding condition operation of the microgrid. Sefa et al. [11] studied regarding implementation of fuzzy PI controller for maintaining a steady active and reactive power in the grid-connected inverter. Chakraborty et al. [12] presented a comparison of various inverter topologies and its response to different filter circuits. Rajeev and Agarwal [13] research presented a study of closed loop transformerless inverter with the aim of synchronization of grid and controlling active and reactive power.

2 Transformerless Inverter H5 Topology

Most transformerless inverters use H5 topology, for generation of unipolar output voltage, and this idea adapted when zero-voltage vector disconnects the PV array from the grid. From Fig. 1, the operation of H5 topology can be observed. In this topology, five switches are arranged to operate in four different modes and periods. While operating in active mode, because of the presence of S5 in the DC side, the current flows through three switches. While operating in freewheeling mode, the current flows through two switches.

Mode 1—Switch S1 operates at switching frequency and is ON continuously during positive half cycle. To obtain a positive-voltage vector, a high-frequency switching is observed simultaneously amid S5 and S4 switches. During the ON time of Switch S1, the current flow is held through S5–S1 and returned through S4.
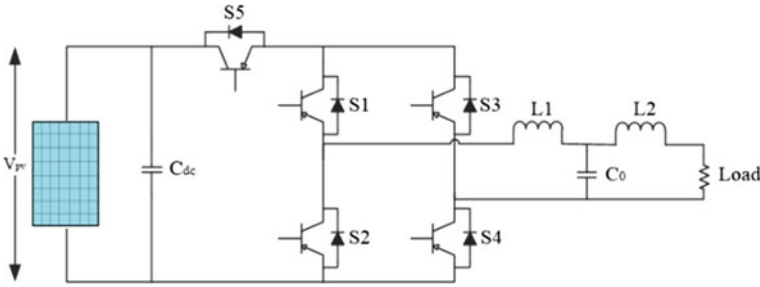
Fig. 1 H5 topology representation

Mode 2—Switches S5 and S4 are turned OFF during the zero-voltage vector, providing a path to the freewheeling current through S1–S3.

Mode 3—Switch S3 operates at switching frequency and is ON continuously during positive half cycle. To obtain a positive-voltage vector, a high-frequency switching is observed simultaneously amid S5 and S2 switches. During the ON time of Switch S3, the current flow is held through S5–S3 and returned through S2.

Mode 4—Switches S5 and S4 are turned OFF during the zero-voltage vector, providing a path to the freewheeling current through S1–S3.

3 Control Algorithm

Different controllers are tested with the inverter topology for obtaining voltage stability and better performance. Different control algorithms are explained below.

3.1 PID Controller

PID controller is one of the conventional and most convenient control strategies. The difference gain of proportional (K_p), integral (K_i) and differentiator (K_d) of the PID controller are calculated for the system to obtain a balanced output voltage under various load and ambient conditions.

The transfer function of PID controller is given by:

$$\text{T.F.} = K_p \left[1 + \frac{1}{T_i s} + T_d s \right] \tag{1}$$

where, K_p = proportional gain, T_i = time constant of the integral and T_d = time constant of the derivative. For the control output, following equation is considered.

$$U_n = r_{\mathrm{p}}e + r_{\mathrm{i}} \int_0^t e\mathrm{d}t + r_{\mathrm{d}}e' \qquad (2)$$

where $r_{\mathrm{p}} = K_{\mathrm{p}}$, $r_{\mathrm{i}} = \frac{K_{\mathrm{p}}}{T_{\mathrm{i}}s}$ and $r_{\mathrm{d}} = K_{\mathrm{p}}T_{\mathrm{d}}$

$$e = U_{\mathrm{ref}} - U_{\mathrm{out}} \qquad (3)$$

where U_{ref} = desire gain value and U_{out} = Output gain value.

In order to reduce the system error, the proportional gain is increased, whereas to minimize the offset value of controller integrator gain is controlled. Values of present gain determine the proportional gain, whereas integrator is determined by past error value.

The inverter topologies discussed in previous sections were integrated with PID controller where the error between output voltage and reference voltage was fed as input to the system and the output of PID controller is fed to PWM so that the feedback PID control signal can control the switching of the different inverter switches.

3.2 Fuzzy Logic Controller

Fuzzy logic control or fuzzy inference system deals with permutation, combinations, probability and statistics utilizing datasets as linguistic variables. The process of training a dataset mainly depends on specified inputs, outputs and membership functions. The functionality of fuzzy inference system was classified as fuzzification, rule set and training and defuzzification. Conversion of crisp value input in terms of linguistic variables is carried out in fuzzification process. In further stage, the linguistic variables are assisted with membership functions of different types to train the rule base. Once the rule base is established, based on the inputs being fed to the fuzzy system, the output is obtained. In defuzzification process, the result obtained in terms of linguistic variables is converted either to crisp value or in terms of binary codes as per the user interface. The fuzzy structure and the membership function are illustrated in Fig. 2.
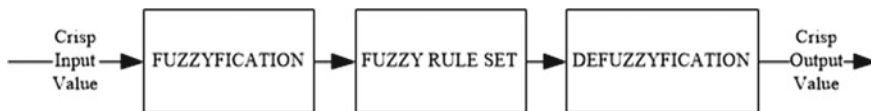
Fig. 2 Fuzzy analysis structural breakdown
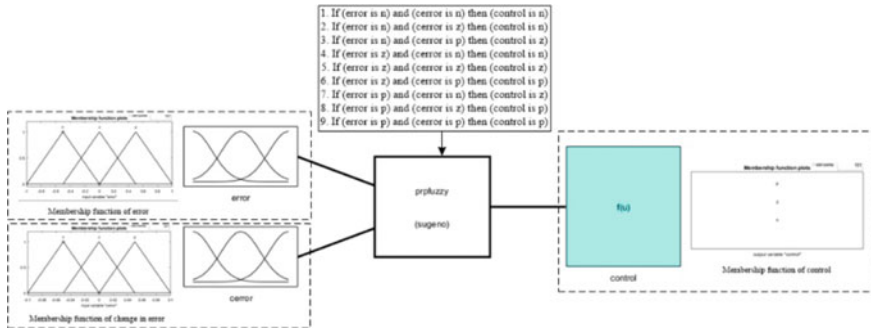
Fig. 3 Fuzzy membership function and rules execution of inverter

In this research, fuzzy inference system was integrated with different transformerless inverter topologies to achieve balanced voltage under various load and ambient conditions. The rule set with fuzzy membership function is shown in Fig. 3.

The output voltage of the inverter is compared with a generated reference voltage and the error and rate of change of error were fed to the fuzzy block. The fuzzy block which has an integration with the fuzzy graphical user interface in MATLAB/Simulink trains the given set of inputs for a defined output using membership functions and linguistic variables. Depending on the relationship between the inputs and outputs, a set of rules were determined as depicted above. The fuzzy system output is fed to the two-level discrete pulse width modulation generator which generates pulses for controlled switching of power electronics switches in inverter.

3.3   Fuzzy-PID Controller

Fuzzy-PID control is a supervisory control technique in which the fuzzy inference system is trained to tune the PID controller. This type of supervisory control helps in improving the stability of the system and enhances the performance characteristics like accuracy and reliability. The error and change in error are provided as inputs for the fuzzy inference system, and the rules were trained in perspective of controlling the gain values for PID controller as per the closed loop requirement. The supervisory control for PID tuning is depicted in Fig. 4.

The defuzzied output of the fuzzy system acts as inputs for the PID controller. The output signal of PID controller is fed to the discrete PWM generator where the signal is compared with carrier wave for triggering of the power electronic switches in the inverter.
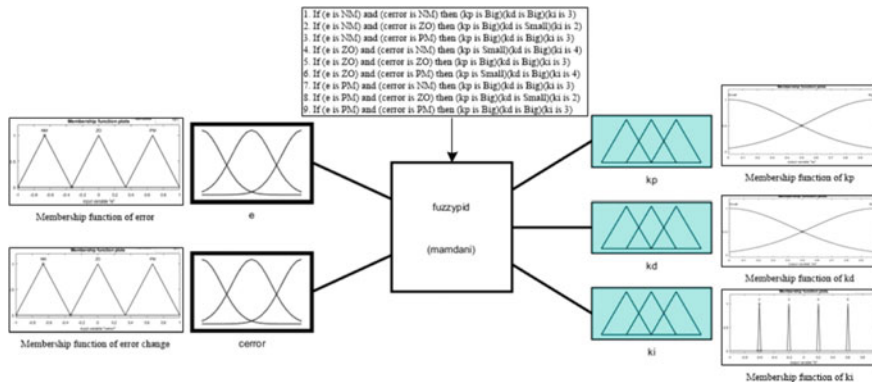
Fig. 4 Fuzzy-PID Membership function and rules execution of inverter

4 Simulation and Discussion

The aim of the experiment was to study the response of different controllers on H5 transformerless inverter topology. Simulation was performed on MATLAB 2017a and designing for various components such as filter, PV panel and control loop was performed. Components designing are explained in the section below.

4.1 Solar Panel Designing

A 2 kW solar panel is modelled taking Sanyo (HIP-210HKHA6) datasheet into consideration. Range for different components such as irradiance and temperature is set to 1000 W/m^2 and 25 °C, respectively. Parameters needed for designing are presented in Table 1.

4.2 Filter Designing

At the output end of the inverter, filter is implemented for reducing the effect of harmonics in the result. In work presented, a T-LCL filter is employed which

Table 1 Solar panel design parameters

Specification	Value
Short-circuit current (I_{Short})	5.57 A
Maximum power (P_{max})	210 W
Open-circuit voltage (V_{open})	50.0 V

consist of a capacitor and two inductors arranged in the form of T shape. Following formulas are used for the calculation of filter components.

$$c = \frac{1}{2X\pi XfXZ} \tag{4}$$

$$L = CZ^2 \tag{5}$$

where,
  f = cut-off frequency
  Z = impedance

4.3 Feedback Stability Analysis

For understanding the system stability transfer function needed to be analysed. Different components such as filter, inverter and pulse width modulator are modelled using control block. In the block representation in Fig. 5 illustrated system control unit.

The transfer function for determining the stability is as follows,

$$L.T = \frac{G_{inverter}G_{lcl}}{1 + (G_{inverter}G_{lcl})G_{control}G_{gain}G_{PWM}H(s)} \tag{6}$$

where,

$G_{inverter}$ = gain of inverter
G_{lcl} = gain of filter = $\frac{1}{s(L_1 + L_2) + s^3(C_f L_1 L_2)}$
$G_{control}$ = gain of PI controller = $K_p + \frac{K_p}{sT}$
G_{gain} = overall gain
G_{PWM} = pulse width modulation gain = $\frac{1}{1 + 1.5Ts}$
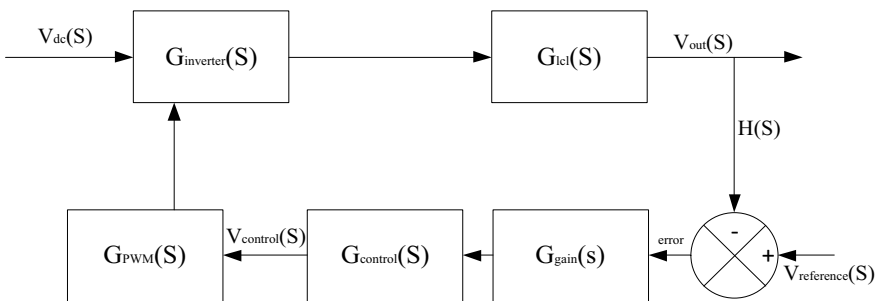
Fig. 5 Control block representation of the system

5 Results

The expected output of the inverter designed is to give a constant 230 V output even when there is a change in load and ambient conditions. A 6% error range is acceptable as for voltage as per National electrical code which is published by Bureau of Indian standards [14]. Run-time load variation was also carried out for making sure that system becomes stable and response time is also lower. THD study was also focused on and kept under the acceptable range of 5% as per EN 50160 [15]. For different controllers, common mode voltage analysis was done. Control parameters are analysed using bode plot, and different characteristics of bode plot are checked to make sure system is stable.

5.1 Load Variation

Inverter response to variation in load is depicted in the Fig. 6. It can be well illustrated that the range remains under the acceptable error value as discussed above.

The error value at different loads with respect to 230 V is depicted in Table 2. All the values are well under the range as per criteria.

Load keeps varying while an inverter is under operation; hence, it is required that the inverter gain its stability back fast when load variation takes place. In Table 3, settling time of the inverter on load variation is depicted and at higher load settling time is very small and it just disrupts one half cycle of operations.

In Fig. 7, a complete analysis of H5 topology is presented. Their response to load variation with different control algorithms is described in the figure.

From the figure, it can be concluded that the highest variation takes place when operation is taking place between 25 and 50% load. At higher load, inverter gets stable faster.
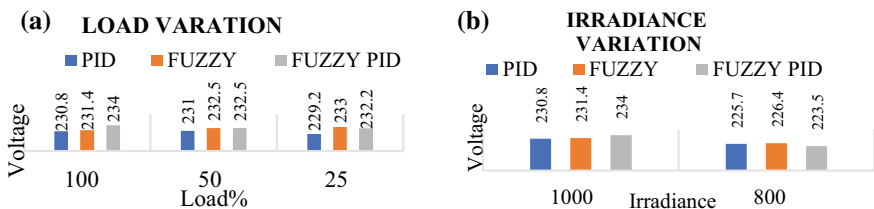
Fig. 6 Voltage at different. **a** Load, **b** irradiance for H5

Table 2 H5 topology error calculation

Load %	Topologies		
	H5		
	PID (%)	Fuzzy (%)	Fuzzy-PID (%)
100	0.3	0.6	1.7
50	0.4	1.0	1
25	0.3	1.3	1.1

Table 3 Settling time during operating condition (in seconds)

Control	Load%			
	H5 topology			
	0–25%	25–50%	50–75%	75–100%
PID	0.17	0.034	0.024	0.001
Fuzzy	0.05	0.037	0.024	0.02
ANFIS	0.06	0.04	0.037	0.032
Fuzzy-PID	0.114	0.037	0.02	0.001
ANFIS-PID	0.15	0.03	0.025	0.004
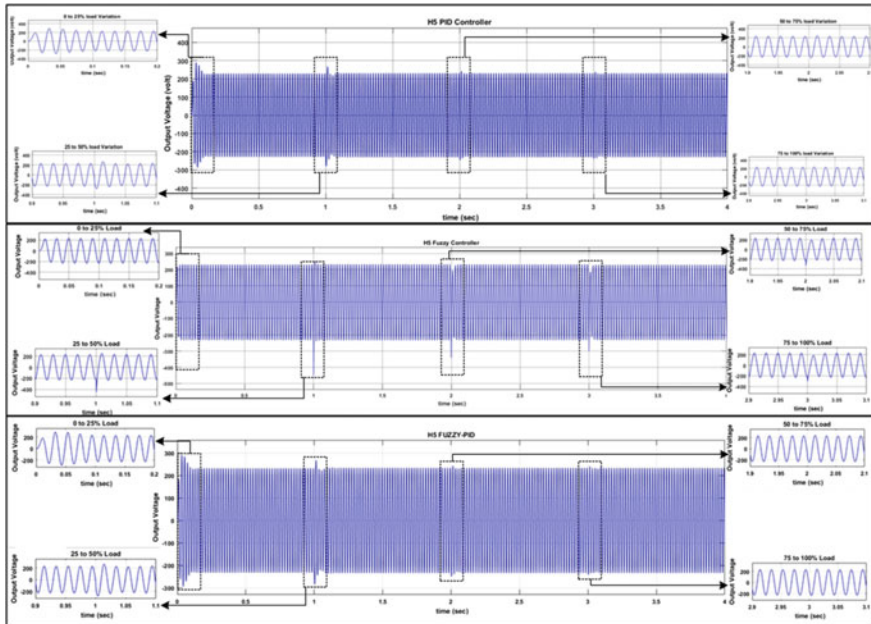
Fig. 7 Load variation under operation for different control algorithms implemented in H5 topology

5.2 Common Mode Voltage

Common mode voltage aids in determining the leakage current present in transformerless inverter. Common mode voltage can be calculated by using voltages between output and reference and finding out the average.

$$V_{\text{cmv}} = (V_a + V_b)/2 \tag{6}$$

V_a and V_b are the values of voltage between the neutral point and the converter's output voltage.

From Fig. 8, it can be well established that fuzzy-PID has the least common mode voltage fluctuations and is best when it comes to reduced leakage current operation.

5.3 Total Harmonic Distortion

Computational efficiency is a factor because of which a fast Fourier transformation (FFT) is implemented for harmonic analysis. Fundamental and other components are isolated for calculation purpose. Sum of RMS value along with other component of harmonics is squared and divided by fundamental component.
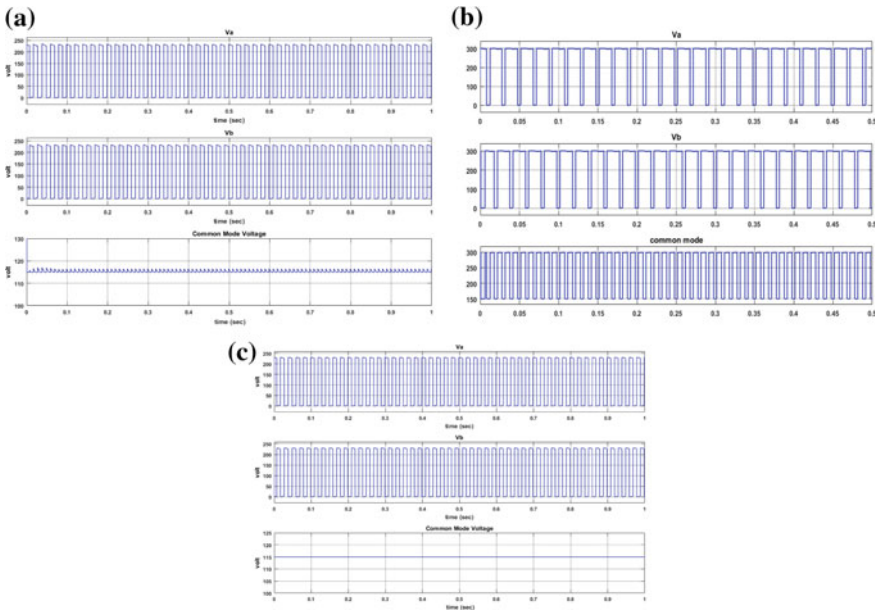
Fig. 8 V_a, V_b and common voltage for H5 under **a** PID, **b** fuzzy and **c** fuzzy-PID

Table 4 THD and FFT analysis of different topologies using various algorithms
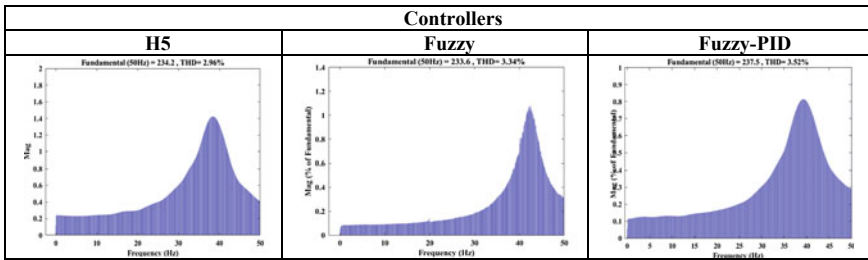
$$\text{THD\% of fundamental} = \frac{Q_{\text{rmsdistorted}}}{Q_{\text{fundamental}}} \times 100$$

As per the international standards of IEEE 516 [16] allowed range of voltage distortion in THD is up to 5%. In Table 4, THD value is well under the range and THD analysis is done using FFT.

5.4 Stability Analysis of Inverter

Stability analysis is carried out by bode plot of the system. MATLAB linearization tool was implemented in the research for studying the different controller's stability analysis. In Table 5, it is represented that for H5 topology of transformerless inverter when operating in various control algorithms, the system remains stable as by studying the bode plot, and it was found that gain margin and phase margin of all the topologies are in same half [17]. The gain crossover frequency and phase crossover frequency are found by the plot illustrated in Fig. 9.

Table 5 Bode plot characteristics of H5 topology with different control algorithms

	H5 topology		
	PID	Fuzzy	Fuzzy-PID
Gain margin (G_{m})	0.6003	1.4167	2.4342
Phase margin (P_{m})	60.8492	46.2738	24.9995
Gain crossover frequency (W_{gm})	0.001	0.001	0.001
Phase crossover frequency (W_{pm})	0.0328	0.00714	0.0892
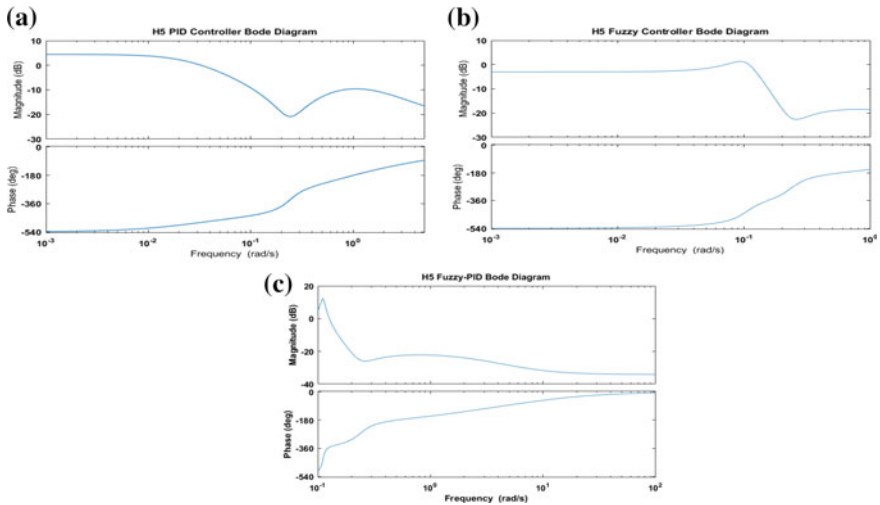
Fig. 9 H5 topologies bode plot on different control algorithms

6 Conclusion

The research depicted the functionality of H5 inverter topology and their control strategies. The popular switching strategies are summarized with the emphasis on two-level discrete PWM. The topic of voltage balancing without any auxiliary power circuit is explained as well as various control strategies were compared for implementation with H5 topologies. Furthermore, the dynamic model of the H5 was developed and both the closed loop control and load balancing have been realized in MATLAB/Simulink. The control strategies have been designed regarding their subsequent implementation into the real-time control system. Both the balancing algorithm and the performed analysis on all the topologies using various control techniques like PID, FUZZY and FUZZY-PID have been verified using simulation results that have also been presented. The results show that, according to our expectations, the switching process with the intelligent control strategies improves the voltage-balancing inverter.

References

1. Gubia E, Sanchis P, Ursua A (2007) Ground currents in single phase transformerless photovoltaic system. J Optoelectron Adv Mater 15:326–334. https://doi.org/10.1002/pip
2. Haque A (2014) Maximum power point tracking (MPPT) scheme for solar photovoltaic system. Energy Technol Policy 1:115–122

3. Sukumar Z, Ahteshamul M (2015) Performance evaluation of modified perturb & observe maximum power point tracker for solar PV system. Int J Syst Assur Eng Manag 7:229–238. https://doi.org/10.1007/s13198-015-0369-z

4. Xiao H, Xie S, Chen Y, Huang R (2011) An optimized transformerless photovoltaic grid-connected inverter. IEEE Trans Ind Electron 58:1887–1895. https://doi.org/10.1109/TIE.2010.2054056

5. Patrao I, Figueres E, González-Espín F, Garcerá G (2011) Transformerless topologies for grid-connected single-phase photovoltaic inverters. Renew Sustain Energy Rev 15:3423–3431. https://doi.org/10.1016/j.rser.2011.03.034

6. Islam M, Mekhilef S, Hasan M (2015) Single phase transformerless inverter topologies for grid-tied photovoltaic system: a review. Renew Sustain Energy Rev 45:69–86. https://doi.org/10.1016/j.rser.2015.01.009

7. Li H, Zeng Y, Zheng TQ (2016) A novel H5-D topology for transformerless photovoltaic grid-connected inverter application. In: IEEE 8th international power electronics and motion control conference (2016)

8. Ahmad Z, Singh SN (2017) Comparative analysis of single phase transformerless inverter topologies for grid connected PV system. Sol Energy 149:245–271. https://doi.org/10.1016/j.solener.2017.03.080

9. Shen G, Zhu X, Zhang J, Xu D (2010) A new feedback method for PR current control of LCL filter-based Grid connected inverter. IEEE Trans Ind Electron 57:2033–2041

10. Balaguer IJ, Lei Q, Yang S, Supatti U, Peng FZ (2011) Control for grid-connected and intentional islanding operations of distributed power generation. IEEE Trans Ind Electron 58:2005–2008. https://doi.org/10.1109/tie.2010.2049709

11. Sefa I, Altin N, Ozdemir S, Kaplan O (2015) Fuzzy PI controlled inverter for grid interactive renewable energy systems. IET Renew Power Gener 9:729–738. https://doi.org/10.1049/iet-rpg.2014.0404

12. Chakraborty S, Mahedi M, Razzak MA (2016) Transformerless single phase grid tie photovoltaic inverter topologies for residential application with various filter circuits. Renew Sustain Energy Rev 0–1. https://doi.org/10.1016/j.rser.2016.10.032

13. Rajeev M, Agarwal V (2016) Closed loop control of novel transformer-less inverter topology for single phase grid connected photovoltaic system. In: Power and energy conference, Urbana, IL, USA

14. National Electrical Code (2011)

15. Markiewicz H, Klajn A (2004) Power quality application guide—voltage disturbances standard EN 50160. Copp Dev Assoc 5.4.2:4–11

16. IEEE Guide for Maintenance Methods on Energized Power Lines (2003) IEEE Std 516-2003 (Revision IEEE Std 516-1995)

17. Nagrath IJ, Gopal M (2012) Control system engineering

Comprehensive Analysis of Modulation Techniques for Two-Level Inverter

Abdul Azeem, Shafia Abida, Mohammad Ali, Mohd Tariq, Charu Gupta, Mohd. Owais and Mohd. Anzeb

Abstract Three (3)-phase voltage source inverters are extensively used for different applications requiring high power. A three (3)-phase voltage source inverter circuit changes DC input voltage into a three (3)-phase AC voltage having variable frequency. The fundamental output voltage can be controlled by controlling the width of the pulses. This is done by pulse width modulation. The sinusoidal pulse width modulation (SPWM) technique is one of the most popular PWM techniques for harmonic reduction of inverters. Third-harmonic injection technique is also used to reduce harmonic contents of the output voltage and to enhance the utilization of the DC bus that is being unused in sine PWM technique. 120° and 180° conduction of two-level inverter are also done in this paper. This concept has been verified in MATLAB®/Simulink environment and also validated experimentally.

Keywords Two-level inverter · Pulse width modulation (PWM) · Third-harmonic injection PWM · Total harmonic distortion (THD)

1 Introduction

In the AC motor drives application, output voltage and frequency have to be controlled in order to achieve the required/desired power characteristics from drives. Generally, pulse width modulation (PWM) techniques are used to get the controllable output. In the literature, various classifications of the modulation techniques are available, and each has its own merits and demerits [1–4].

The common modulation techniques that are employed for two-level inverter and have been discussed in this paper are:

A. Azeem · S. Abida · M. Ali · M. Tariq (✉) · C. Gupta ·
Mohd. Owais · Mohd. Anzeb
Department of Electrical Engineering,
Aligarh Muslim University, Aligarh 202002, India
e-mail: tariq.iitkgp@gmail.com
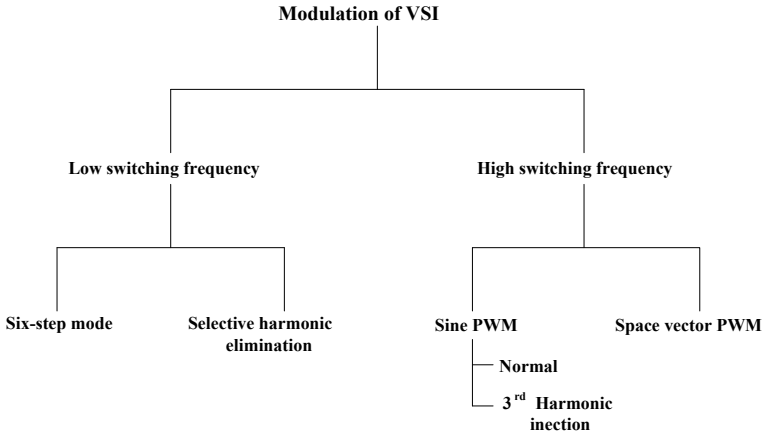
Fig. 1 Classification of VSI based on modulation techniques

1. Sine PWM technique
2. Third-harmonic injection PWM
3. 120° conduction mode
4. 180° conduction mode

   Among above modulation techniques, sine PWM and third-harmonic injection PWM are mostly common techniques, and 120°, 180° are the quasi-square-wave modulation techniques having significant lower-order harmonics than the PWM scheme, hence not preferable in practice [5].

   Figure 1 shows the basic classification of the modulation techniques for two-level VSI. Low-switching-frequency-based techniques are suitable for high-power application, and high-switching-frequency-based techniques are preferable for low power applications [6] (Fig. 2).

2 Circuit Modeling

The output of the two-level inverter can be given by from Eq. (1).

$$
\begin{aligned}
V_{an} &= \sum_{n=1,3,5..}^{\infty} \frac{2V_{dc}}{n\pi} \cos\left(\frac{n\pi}{6}\right) \sin n\left(\omega t + \frac{\pi}{6}\right) \\
V_{bn} &= \sum_{n=1,3,5..}^{\infty} \frac{2V_{dc}}{n\pi} \cos\left(\frac{n\pi}{6}\right) \sin n\left(\omega t + \frac{\pi}{2}\right) \\
V_{cn} &= \sum_{n=1,3,5..}^{\infty} \frac{2V_{dc}}{n\pi} \cos\left(\frac{n\pi}{6}\right) \sin n\left(\omega t + \frac{\pi}{6}\right)
\end{aligned}
\tag{1}
$$

Fig. 2 Two-level voltage source inverter topology
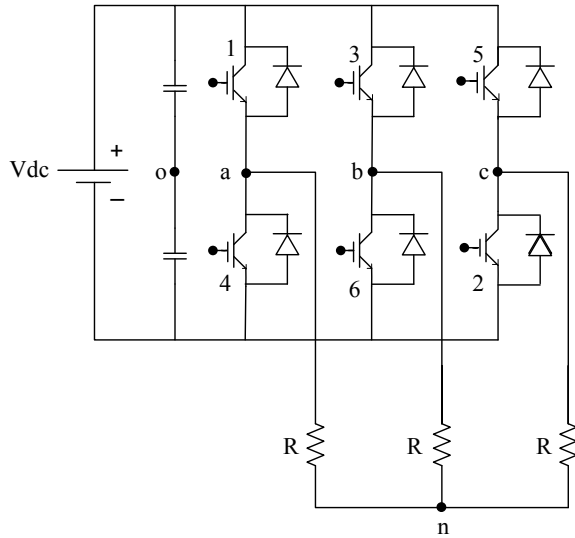
3 Modulation Techniques

3.1 Sine PWM Scheme

In the pulse width modulation (PWM) technique, the pulse duration is modulated to generate a constant amplitude pulse. The basic purpose of PWM is to reduce harmonic voltages and their harmful effects. PWM control requires the generation of both reference and carrier signals that are fed into the comparator, and based on some logic, the final output is generated [7]. The reference signal or modulating signal is the desired signal which can be a sinusoidal/square wave, whereas the carrier signal is either a triangular/sawtooth having a frequency of ten (10) times (minimum) with respect to the reference signal. There are various PWM techniques, but sinusoidal pulse width modulation (SPWM) is most widely used among them. The advantages of PWM are high-energy efficiency (90%), less power consumption, compatible with digital microprocessors, and easy to implement and control [8]. Figure 3 shows the sinusoidal PWM generation principle.

Amplitude modulation index (A) can be defined as:

$$m = \frac{A_\mathrm{r}}{A_\mathrm{c}}$$

where A_r and A_c be the amplitude of the reference and carrier wave respectively. Frequency modulation index:
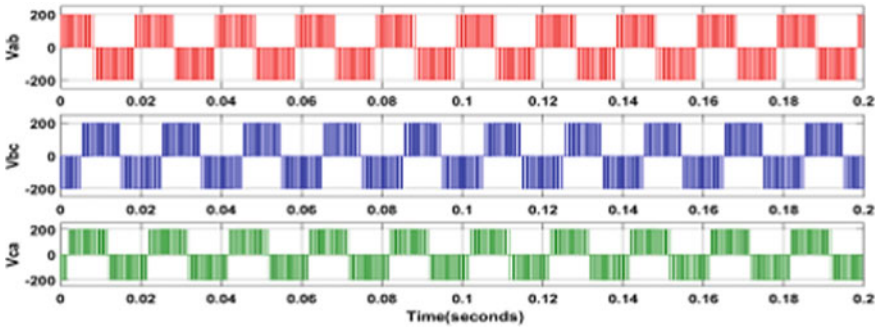
Fig. 3 Simulation result for line voltage in sine PWM scheme
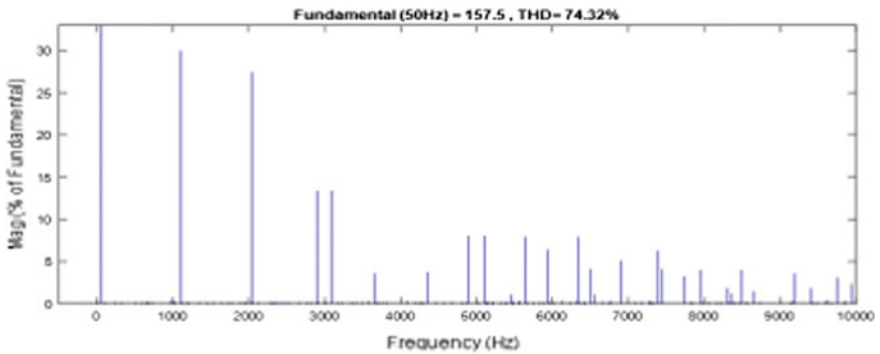
Fig. 4 FFT analysis for line voltage in SPWM scheme

$$A = \frac{f_c}{f_r}$$

where f_c and f_r be the frequency of carrier wave and reference wave, respectively (Fig. 4).

3.2 Third-Harmonic Injection PWM

The sine PWM is one of the simplest modulation schemes to understand/implement, and however, it is not able to enhance the utilization of DC bus voltage [9]. To overcome this problem, the third (3rd)-harmonic injection PWM (THIPWM) technique was originated/developed for improving the performance of the inverter and DC bus utilization, and hence, by simply adding a third-harmonic signal to each of the phases with 1/6 amplitude of its fundamental [10].

Assuming a phase waveform given as

$$x = \sin\theta + a\sin 3\theta \tag{2}$$

where $\theta = \omega t$ and a are the parameters which need to be determined. Locating the turning point of the given function by differentiating x with respect to θ and equating that with zero,

$$\frac{dx}{d\theta} = \cos\theta + 3a\cos 3\theta = 0 \tag{3}$$

Minima and maxima of the waveform occur at

$$\cos\theta = 0 \tag{4}$$

And

$$\cos\theta = \left(\frac{9a-1}{12a}\right)^{1/2} \tag{5}$$

From Eq. (4), we get

$$sin\theta = 1 \tag{6}$$

And from Eq. (5), we have,

$$\sin\theta = \left(\frac{1+3a}{12a}\right)^{1/2} \tag{7}$$

We know that $\sin\theta = (1 - \cos^2\theta)^{1/2}$ by using this identity the peak value of x can be found by substituting the value obtained for $\sin\theta$ in Eqs. (6) and (7) into Eq. (2). This can be facilitated by manipulating Eq. (5), we get

$$\sin 3\theta = 3\sin\theta - 4\sin^3\theta \tag{8}$$

Thus, Eq. (2) becomes

$$x = (1+3a)\sin\theta - 4a\sin^3\theta \tag{9}$$

Substituting for $\sin\theta$, the values obtained in Eqs. (6) and (7), we get

$$x^\neg = 1 - a \tag{10}$$

$$x^\neg = 8a\left(\frac{1+3a}{12a}\right)^{3/2} \tag{11}$$

where $x^\neg$ is the peak value of x.

The optimum value for a is that value which minimizes $x^\neg$. The optimum value of a can be found by differentiating Eq. (11) and equating with zero

$$\frac{\mathrm{d}x^\neg}{\mathrm{d}a} = \left(\frac{1+3a}{12a}\right)^{\frac{1}{2}}\left(2 - \frac{1}{3a}\right) = 0 \tag{12}$$

From Eq. (12), we can get

$$a = \frac{-1}{3}, \quad a = \frac{1}{6} \tag{13}$$

From Eq. (13), we can see that negative value of a given the $x^\neg$ greater than unity therefore discarded. The accepted value of a is therefore 1/6, and the required waveform is:

$$x = \sin\theta + \frac{1}{6}\sin 3\theta \tag{14}$$

3.3   120° Conduction Mode

Each switch conducts for 120°. At a given time, two (2) switches are conducting simultaneously, one from the upper group and one from the lower group. After every 60°, one of the conducting switches is turned off, and other switch starts conducting. The conduction sequence of switches is 61, 12, 23, 34, 45, and 56. It is clear that in mode 1, two switches are in conducting positions, i.e., S6 and S1. Switch S1 conducts for 120° (from $\omega t = 0°$ to at $\omega t = 120°$). After a gap of 60° that is the onset of mode 2($\omega t = 60°$), S1 still conducts, whereas S6 turns off and switch S2 comes into 'On' state. Now S2 conducts for 120° (from $\omega t = 60°$ to at $\omega t = 180°$). Again after 60° that is at $\omega t = 120°$, mode 3 starts and two switches S2 and S3 conduct. In a similar way, two switches conduct at the same time but from different leg.

3.4   180° Conduction Mode

In this scheme, the switch is conducting for 180° or π radians. At a given time, three (3) switches are conducting simultaneously, and the combination is such as that two are from one group (lower or upper) and the third one is from the other group. After every 60°, one of the conducting switches is turned off and next switch will start conducting. If the upper switch of the leg turns off and at the same time lower switch of the same leg will be turned on, there is no time delay between the turnings off and turning on of upper and lower switches of same leg and there is a possibility

of short circuiting of DC supply through upper and lower switches of same leg, this is avoided by introducing a dead time. The conduction sequences of switches are 651, 621, 123, 243, 345, and 456. In this manner, the pattern of firing the six switch is given as S5, S6, and S1 should be gated for mode 1; S6, S1, S2 for mode 2; S1, S2, S3 for mode 3 and so on.

4 Simulation and Experimental Results

4.1 Sine PWM Scheme

Simulation is performed in MATLAB®/Simulink. Power quality is measured using the qualities discussed in [11]. Figure 3 shows the simulation results for line voltage in SPWM scheme. Figure 5 shows the FFT and its analysis, and THD found in this scheme is 74.32%. Figure 5 shows the experimental result for line voltage in SPWM scheme, and the peak magnitude of voltage is 13 V. Figure 6 shows the experimental setup which is developed following the paper in [12] of three-phase
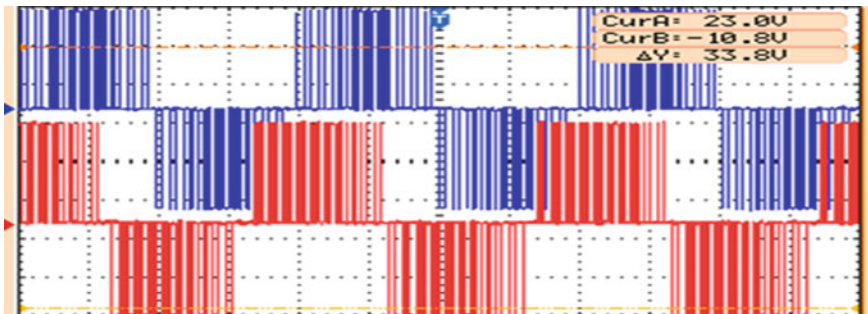
Fig. 5 Experimental result for line voltage V_{ab} and V_{bc} in SPWM scheme
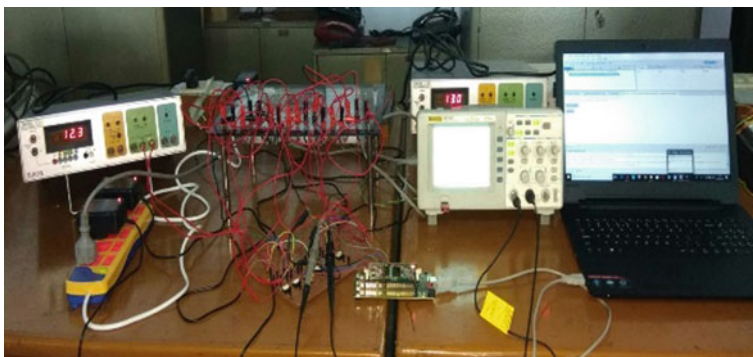
Fig. 6 Experimental setup of three-phase two-level inverter
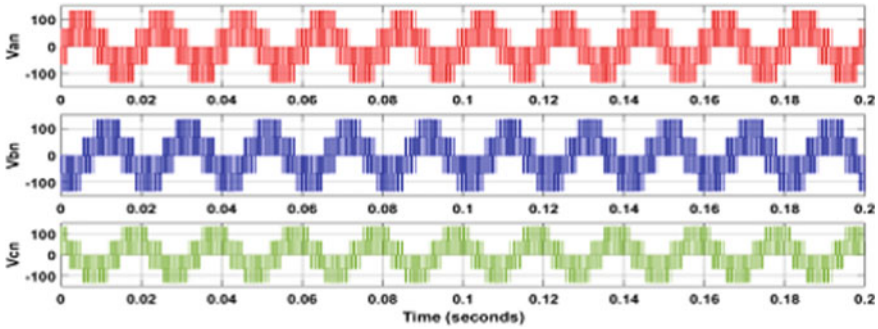
Fig. 7 Simulation result for phase voltage in SPWM scheme
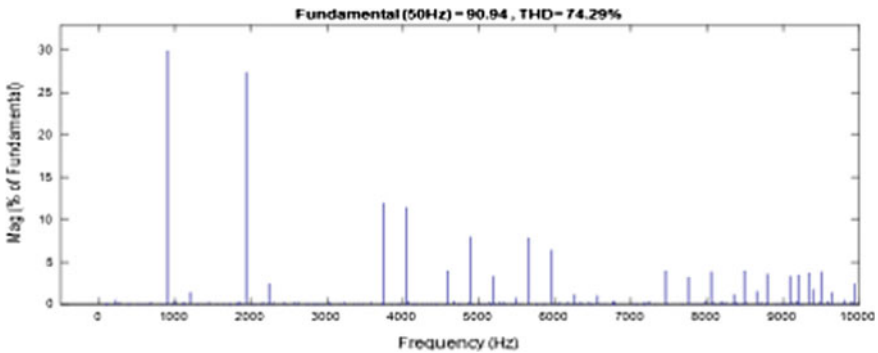
Fig. 8 FFT analysis of the phase voltage in SPWM scheme

two-level inverter. Phase voltage is presented in Fig. 7which shows that THD in this case is 74.29% as shown in Fig. 8. Experimental result of phase voltage is shown in Fig. 9, wherein peak amplitude of output wave is 13 V.

Figure 7 shows the simulation result for phase voltage in two-level VSI. FFT analysis of the phase voltage is presented in Fig. 8 which shows that THD in this case is 74.29%. Experimental result of phase voltage is shown in Fig. 9, wherein peak amplitude of output wave is 13 V.

4.2 Third-Harmonic Injection PWM Scheme

Figure 10 shows the simulation result for line voltage in third-harmonic injection PWM scheme, and the simulation DC voltage is chosen as 200 V. FFT analysis of this scheme is presented in Fig. 11. THD in this scheme is found is 63.73%. Figure 12 shows the experimental result for line voltage in third-harmonic injection PWM scheme.
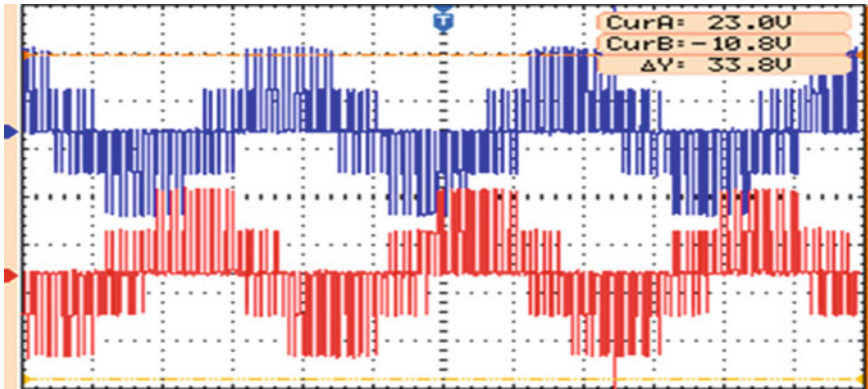
Fig. 9 Experimental result for phase voltage in SPWM scheme
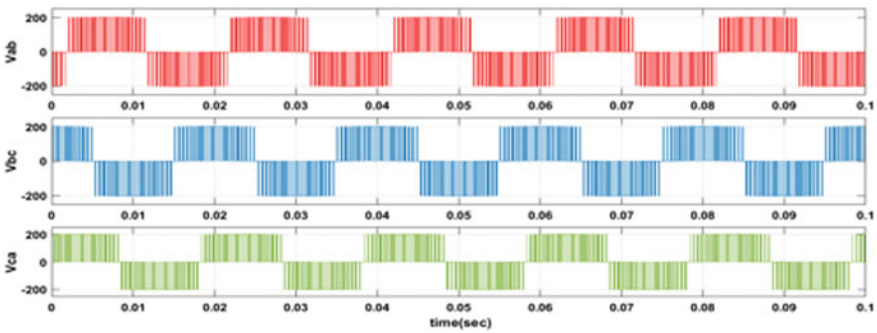
Fig. 10 Simulation result for line voltage in third-harmonic injection PWM scheme
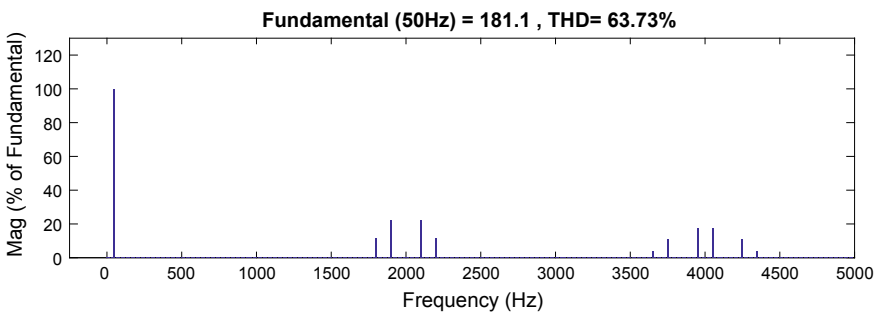
Fig. 11 FFT analysis for line voltage in third-harmonic injection PWM scheme
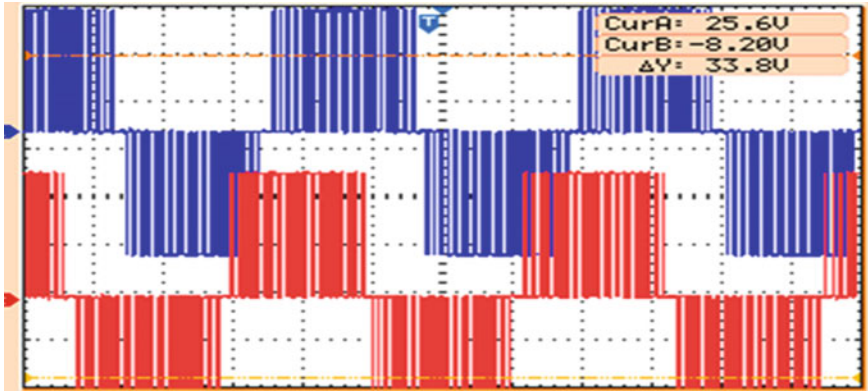
Fig. 12 Experimental result for line voltage in third-harmonic injection PWM scheme
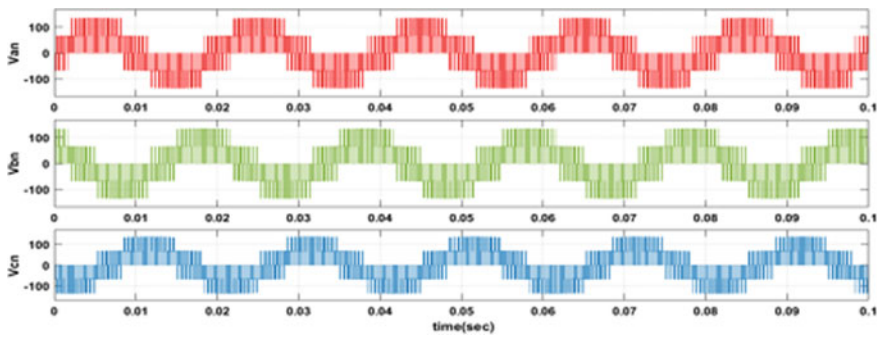
Fig. 13 Simulation result for phase voltage in third-harmonic injection PWM scheme

Figure 13 shows the simulation result for phase voltage in third-harmonic injection PWM scheme, and its FFT analysis is shown in Fig. 14, which shows that THD is 63.71%. Figure 15 shows the experimental result for phase voltage in third-harmonic injection PWM scheme.
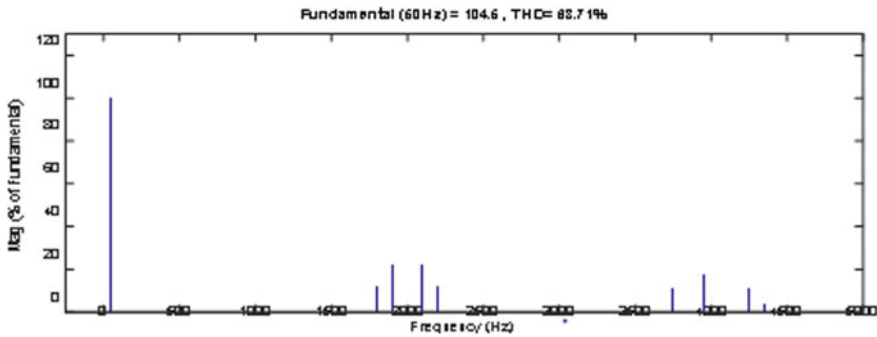
Fig. 14 FFT analysis for phase voltage in third-harmonic injection PWM scheme
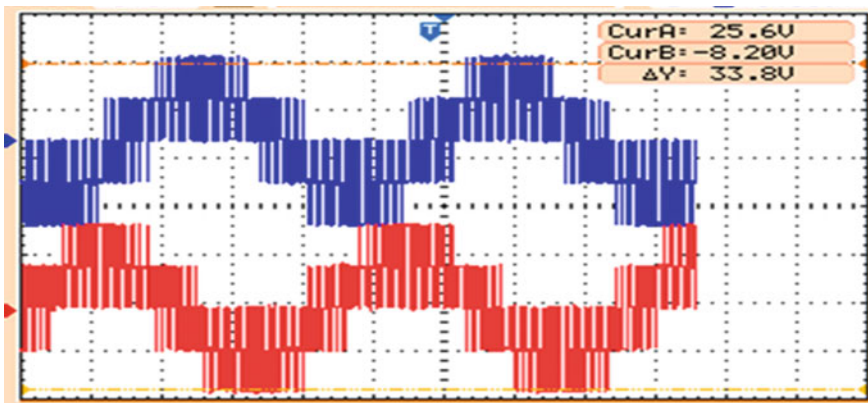
Fig. 15 Experimental result for phase voltage in third-harmonic injection PWM scheme

5 Conclusion

The aim of this paper was to analyze the performance of two-level VSI in sinusoidal and third-harmonic injection PWM scheme. The THD in SPWM was 74.39 and 74.32% in line and phase voltage, respectively, but in case of THIPWM scheme, it was 63.73 and 63.71% in line and phase voltage, respectively.

References

1. Tariq A, Husain MA, Ahmad M, Tariq M (2011) Simulation and study of a grid connected multilevel converter (MLC) with varying DC input. In: 2011 10th international conference on environment and electrical engineering, Rome, pp 1–4

2. Dordevic O, Jones M, Levi E (2013) A comparison of carrier-based and space vector PWM techniques for three-level five-phase voltage source inverters. IEEE Trans Ind Inf 9(2): 609–618

3. Bharatiraja C, Munda JL, Bayindir R, Tariq M (2016) A common-mode leakage current mitigation for PV-grid connected three-phase three-level transformerless T-type-NPC-MLI. In: 2016 IEEE international conference on renewable energy research and applications (ICRERA), Birmingham, pp 578–583

4. Tariq M, Bhardwaj S, Rashid M (2013) Effective battery charging system by solar energy using C programming and microcontroller. Am J Electr Power Energy Syst 2(2):41–43

5. Bin W (2006) High power converters and AC drives

6. Engg E (2017) Inverter using modified multicarrier PWM technique. In: International conference on innovative mechanisms for industry applications (ICIMIA 2017), pp 50–55

7. Subsingha W (2016) A Comparative study of sinusoidal PWM and third harmonic injected PWM reference signal on five level diode clamp inverter. Energy Procedia 89:137–148

8. Tan C, Xiao D, Fletcher JE, Rahman MF (2016) Analytical and experimental comparison of carrier-based PWM methods for the five-phase coupled-inductor inverter. IEEE Trans Ind Electron 63(12):7328–7338

9. Rushiraj J, Kapil PN (2016) Analysis of different modulation techniques for multilevel inverters.

10. Houldsworth JA, Grant DA (1984) The use of harmonic distortion to increase the output voltage of a three-phase PWM inverter. IEEE Trans Ind Appl IA-20(5):1224–1228

11. Tariq M, Iqbal MT (2014) Power quality improvement by using multi-pulse AC-DC converters for DC drives: modeling, simulation and its digital implementation. J Electr Syst Inf Technol 1(3):255–265

12. Tariq M, Bhattacharya TK, Varshney N, Rajapan D (2016) Fast response Antiwindup PI speed controller of brushless DC motor drive: modeling, simulation and implementation on DSP. J Electr Syst Inf Technol 3(1):1–13

Analysis and Modelling of Two-Phase Interleaved DC to DC Boost Converter with Lifting Capacitor for Fuel Cell Hybrid Electric Vehicle

Deepak Ravi, S. L. Shimi, Bandi Mallikarjuna Reddy and Paulson Samuel

Abstract Full cells are the popular choice as source of energy in many applications like hybrid electric vehicle as they have many advantages over other sources besides the fact that they do not discharge any pollutants. The interleaved dc to dc boost converters are used with fuel cells to match the demand of load voltage as the output of one fuel cell is approximately 0.6–0.7 V. The conventional dc converters produce higher input current ripple as well as higher output voltage ripple. In order to overcome these, a unidirectional interleaved dc to dc boost converter is used because interleaving helps in reducing the input current ripple, output voltage ripple and also cuts the voltage stress on switches. Several topologies of interleaved dc to dc converters are explored in recent years such as conventional two-phase and double-dual boost two-phase interleaved converter topology. This paper proposes a modified high voltage gain two-phase interleaved boost converter and compares this topology with conventional two-phase and double-dual boost two-phase interleaved converters. The topologies are simulated in MATLAB and results are compared on the basis of output voltage gain, ripple content in input current and output voltage.

D. Ravi (✉) · S. L. Shimi
National Institute of Technical Teachers Training and Research, Chandigarh, India
e-mail: dpsngh990@gmail.com

S. L. Shimi
e-mail: shimi.reji@gmail.com

B. M. Reddy · P. Samuel
Motilal Nehru National Institute of Technology Allahabad, Allahabad, India
e-mail: ree1505@mnnit.ac.in

P. Samuel
e-mail: paul@mnnit.ac.in

689

1 Introduction

Fuel cell has become a very popular source of energy as its output does not depend on the atmospheric conditions unlike wind energy turbines and solar PV arrays. Moreover, fuel cell contains high energy density and emits only water as by-product without any pollutants [1]. However, the output of fuel cell is typically 0.6–0.7 V per cell [2]. Hence, more cells have to be connected in either series or in parallel to get a considerable amount of output voltage. But using higher number of cells in a single fuel cell system increases the total price of the system. Hence, dc to dc boost converter is used to step up the output voltage of fuel cell system according to the demand of load [3]. Generally, a fuel cell system encompasses ripples in the input current as well as in the output voltage. Ripples in the input current effects the operation of the fuel cell itself and ripples in the output voltage effects the performance of load. Hence, IDBC is used in fuel cell system as a power conditioning circuit for stepping up the output voltage and to diminish the ripple contents in input and output voltage [4]. Interleaving of dc converters is also helpful to cut the voltage stress as well as current stress from the power semiconductor switches due to the division of current in the parallel paths. Figure 1 shows the fuel cell powered electric vehicle system. Bidirectional dc to dc converters are employed to interface energy storage system between the load and dc bus to make the system reliable and capture the regenerative braking power [5, 6].

This paper is presented in the following manner: in Sect. 2 circuit of conventional two-phase IDBC and its working principle is discussed. In Sect. 3, double-dual-boost high voltage gain two-phase IDBC topology is discussed. In Sect. 4, the modified high voltage gain two-phase IDBC is discussed. In Sect. 5, results of MATLAB simulation of all the three topologies are discussed and in Sect. 6, all the results are compared with each other on the basis of number of passive component, output voltage gain, output voltage ripple and ripples in input
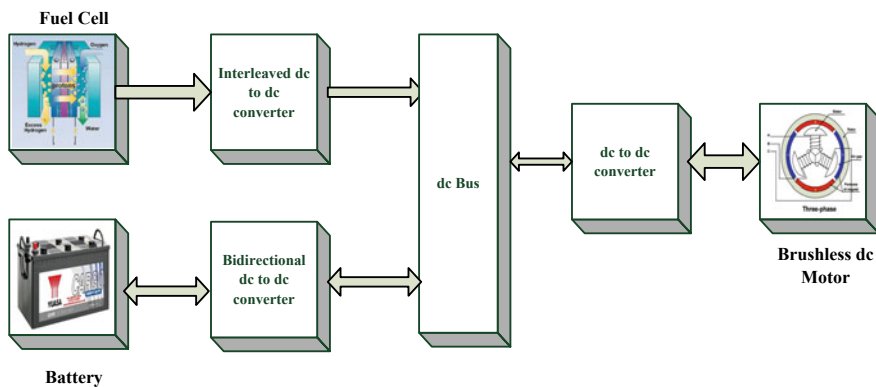
Fig. 1 Fuel cell powered electric vehicle

current which shows that the proposed topology has high voltage gain ratio as well as low ripple content in input current as well as in output voltage.

2   Conventional Interleaved DC to DC Boost Converter

Interleaving is a procedure in which more than one converters are connected parallelly with a phase shift of $360/n$ (n = number of converters in parallel) in their switching. IDBCs help to diminish ripple content in the input current and output voltage since the ripple in each phase becomes phase shifted. Moreover, the current stress and voltage stress reduce from the power semiconductor switches because the current divides in the parallel paths [7].

Figure 2 shows the conventional two-phase IDBC. By increasing the number of phases in interleaving, the ripple contents in input current as well as in the output voltage reduce, but the size and complexity of the circuit also increase because number of passive components per phase increases.

Input voltage is correlated with output voltage with the help of voltage-second balance because the average voltage across an inductor over a period of complete cycle is zero [8].

$$\frac{V_{\mathrm{o}}}{V_{\mathrm{in}}} = \frac{1}{1 - D} \tag{1}$$

To reduce the input current ripples, the following correlation is used.

$$\frac{\Delta I_{\mathrm{in}}}{I_{\mathrm{in}}} = \frac{(1 - D)^2 * D * T_s}{\frac{L_{\mathrm{eq}}}{R_{\mathrm{o}}}} \tag{2}$$

D = duty cycle.
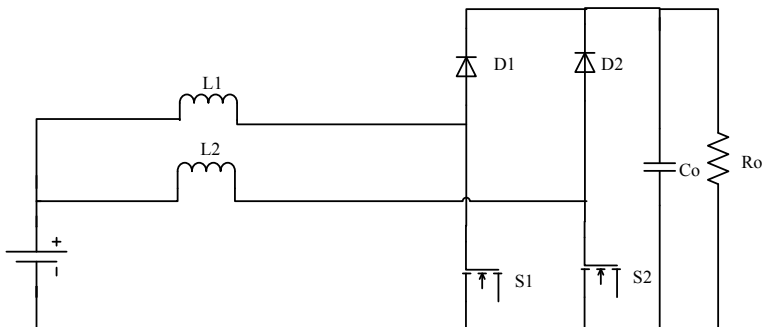
Fig. 2   Conventional two-phase IDBC

Equation (2) shows that for keeping the low ripple content in input current, switching period T_s must be less than time constant (L/R) i.e.

$$T_s \ll \frac{L_{eq}}{R_o} \tag{3}$$

Similarly, to reduce the output voltage ripple following correlation is followed.

$$\frac{\Delta V_o}{V_o} = \frac{D * T_s}{R_o * C_o} \tag{4}$$

D = duty cycle.

Equation (4) shows that ripples in output voltage ripple can be reduced by keeping switching period less than the time constant ($R * C$), i.e.

$$T_s \ll R_o * C_o \tag{5}$$

3 Double-Dual Boost Two-Phase Interleaved Boost Converter

Garcia et al. [9] proposed double-dual boost topology for IDBC which gave a high output voltage gain. Figure 4 shows the double-dual boost topology. In this topology, two boost converters are connected parallelly but in opposite manner to get the high output voltage by summing the voltage across the capacitors C_{o1} and C_{o2}. In contrast to classical boost converter topology, this topology gave a higher output voltage gain (Fig. 3).

The relational between V_{in} and V_o is the same as given in Eq. (1) and the conditions to reduce the input current ripple is the same as discussed in Eq. (3) and output voltage ripple are the same as discussed in Eq. (5) in the conventional IDBC.

4 The Proposed Topology: Two-Phase Interleaved Boost Converter with Lifting Capacitor

This offered topology is a simple two-phase IDBC having a lifting capacitor C_1 in its input side as shown in Fig. 4. This lifting capacitor C_1 utilized in the input side helps to get high voltage gain in the output voltage.

The offered topology has only two phases, and then the switching is provided a phase difference of $\frac{360}{2} = 180$; i.e., both the phases are 180° out of phase as shown in Fig. 5. Phase-shifted switching technique makes the current ripple out of phase, hence, total ripple in input current decreases.
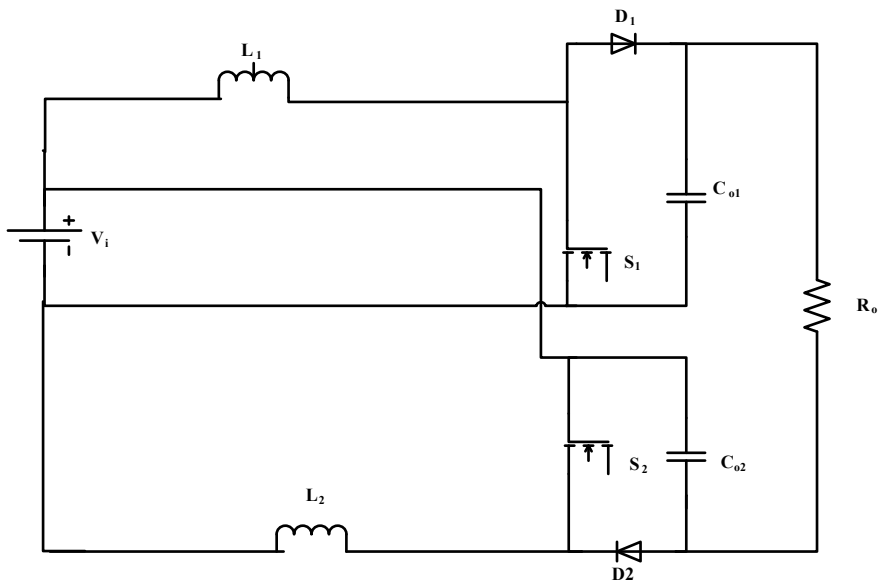
Fig. 3 Two-phase double-dual boost interleaved boost converter
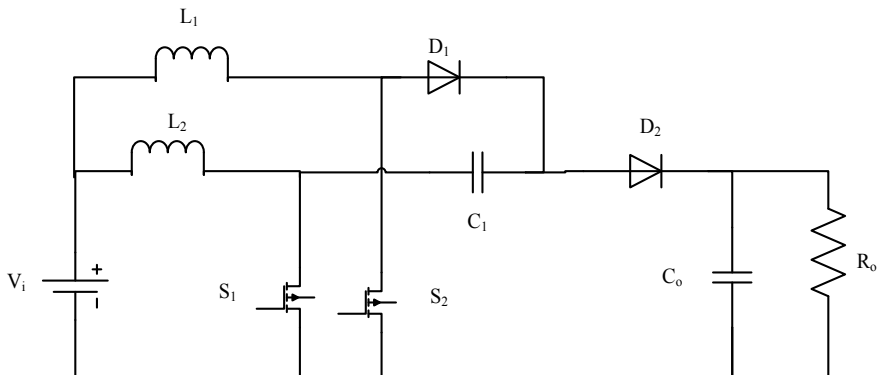
Fig. 4 Two-phase interleaved boost converter with lifting capacitor

The relation between V_{in} and V_o is shown in Eq. (1), i.e., $\frac{V_o}{V_{in}} = \frac{1}{1-D}$ and the conditions to reduce the ripple content in input current and output voltage are the same as discussed in Eqs. (3) and (5) for the conventional IDBC, i.e., $T_s \ll \frac{L_{eq}}{R_o}$ and $T_s \ll R_o * C_o$, respectively.
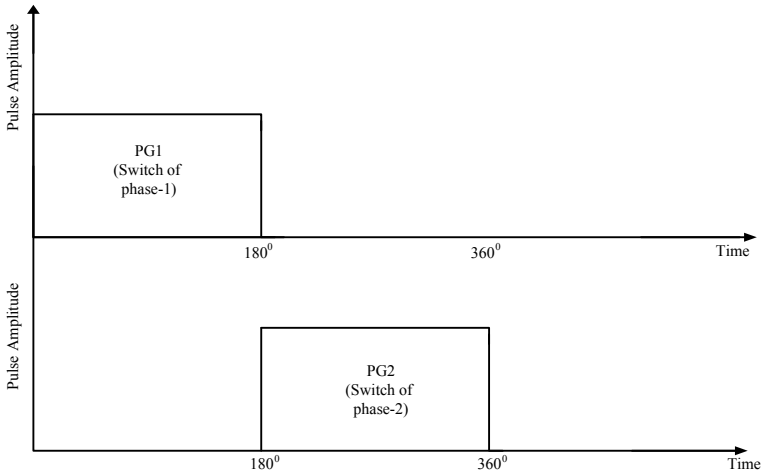
Fig. 5 Switching pattern for switches in interleaved converter

5　MATLAB Simulation Results

All three topologies are simulated with circuit parameters as given in Table 1.

　　All three discussed topologies are simulated on the above parameter shown in the table. The parameters are the same for all three discussed topologies and the comparison of results has been discussed in section No. 6.

Table 1 Design parameters of discussed topologies

Parameter	Conventional two-phase IDBC	Double-dual boost two-phase IDBC	Two-phase IDBC with lifting capacitor
Input voltage (V_{in})	24 V	24 V	24 V
Input inductors (IL_1 and IL_2)	999 μH	999 μH	999 μH
Output capacitor (C_o)	470 μf	470 μf	470 μf
Load (R_o)	60 Ω	60 Ω	60 Ω
Time period (T_s)	9.8 μs	9.8 μs	9.8 μs
Duty cycle (D)	50	50	50
Lifting capacitor (C_1)	0	0	470 μf

5.1 Conventional Two-Phase IDBC

Figures 6, 7 and 8 are the input current, output current and output voltage, respectively. The input current ripple must be less than or equal to 5% but in Fig. 6, it can be seen that the ripple content in the input current waveform is 25% which is very high and will affect the performance of fuel cell.

5.2 Double-Dual Boost Two-Phase IDBC

Figures 9, 10 and 11 are the input current, output current and output voltage, respectively. In Fig. 9, input current waveform shows that the ripple content is 17% which is more than 5%. The output voltage gain is 3.4 times the input voltage. The ripple in output voltage is 0.04%.
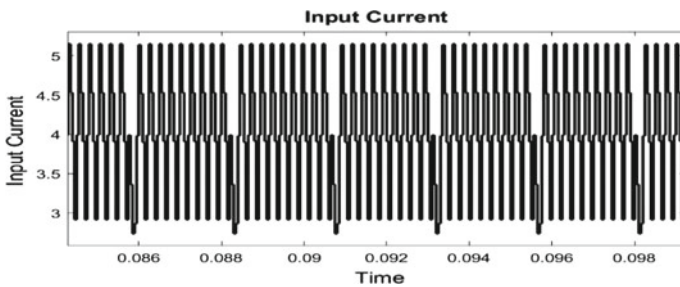
Fig. 6 Input current waveform of the conventional two-phase IDBC
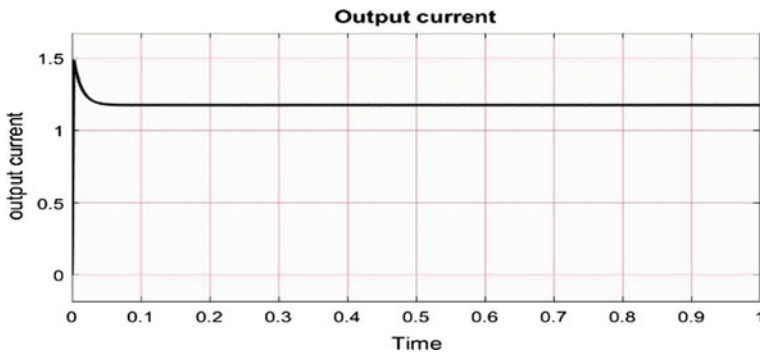
Fig. 7 Output current waveform the conventional two-phase IDBC
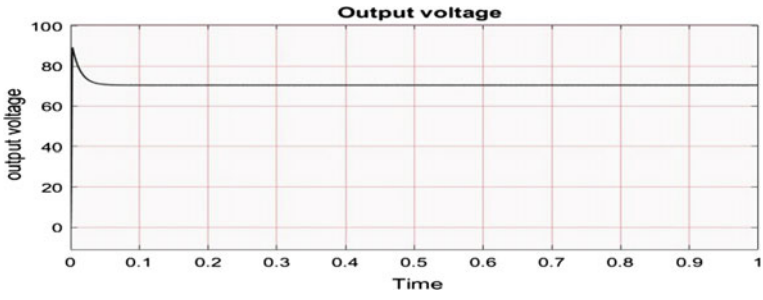
Fig. 8 Output voltage waveform the conventional two-phase IDBC
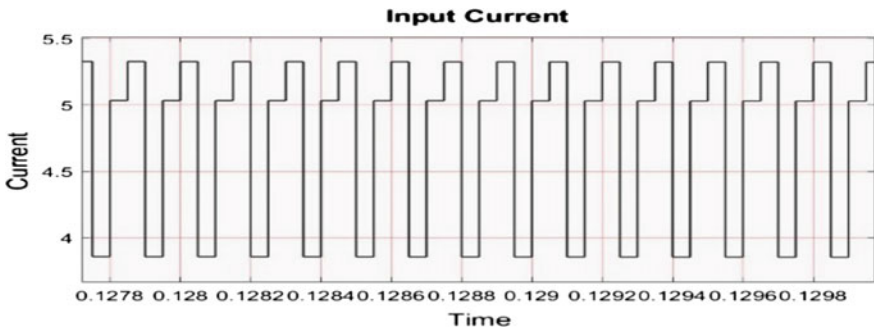
Fig. 9 Input current waveform of the double-dual boost two-phase IDBC
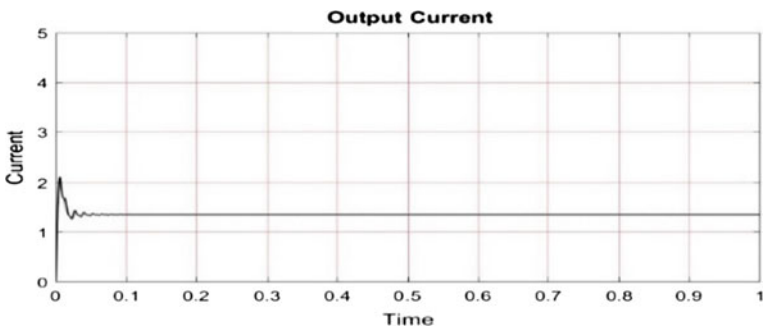
Fig. 10 Output current waveform the double-dual boost two-phase IDBC
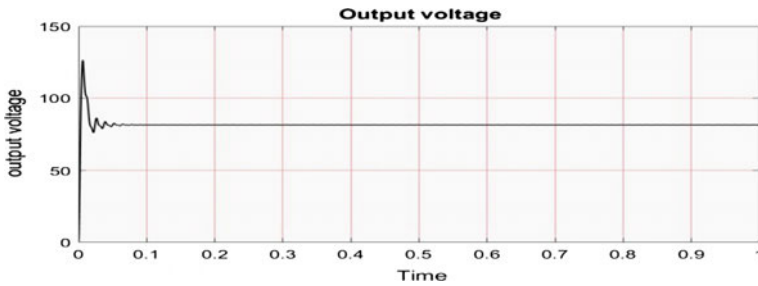
Fig. 11 Output voltage waveform the double-dual boost two-phase IDBC

5.3 Two-Phase IDBC with Lifting Capacitor

Figures 12, 13 and 14 are the output current, input current and output voltage, respectively for the proposed converter. In Fig. 13, input current waveform shows that the ripple content is 2.4% which is less than 5%. The output voltage gain is 3.9 times the input voltage. The output voltage is 0.55%. Hence, the offered topology shows better results than other two discussed topologies.
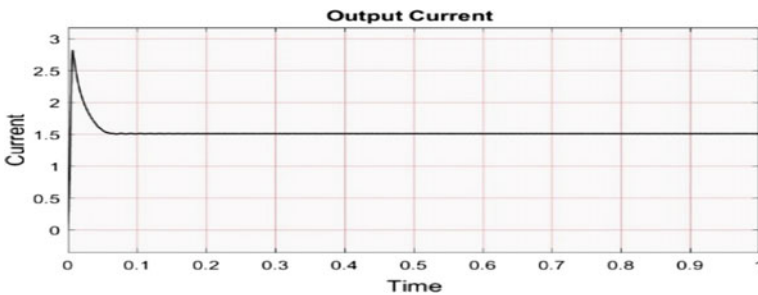
Fig. 12 Output current waveform of the two-phase IDBC with lifting capacitor
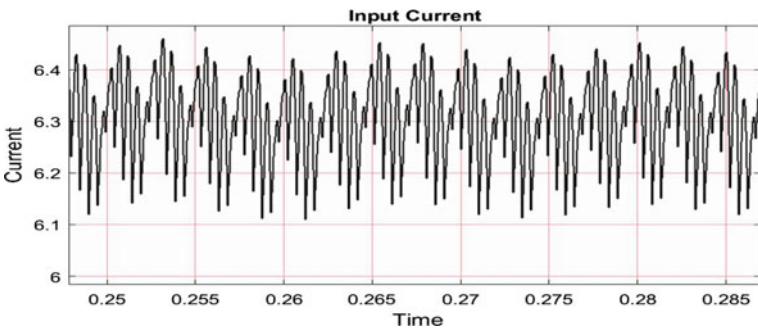
Fig. 13 Input current waveform of the two-phase IDBC with lifting capacitor
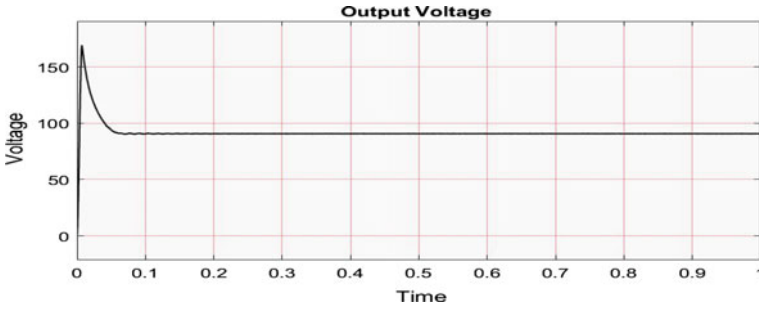
Fig. 14 Output voltage waveform of the two-phase IDBC with lifting capacitor

6   Comparison of Simulation Results

See Table 2.

Table 2 Results comparison of discussed topologies

Topology	Input voltage (V_{in}, V)	Output voltage (V_o, V)	Output voltage ripple ($\Delta V_o/V_o$, %)	Input current (I_{in}, A)	Input current ripple ($\Delta I_{in}/I_{in}$, %)	No. of passive component
Conventional two-phase IDBC	24	70.4	0.14	4	25	4
Double-boost two-phase IDBC [9]	24	81.2	0.04	4.6	17.4	4
Two-phase IDBC with lifting capacitor	24	94	0.55	6.30	2.4	5

7   Conclusion

After comparing the simulation results of all three discussed topologies, it is shown that the proposed two-phase IDBC with boosting capacitor shows better results than other two topologies because the input current ripple is 2.4% which is less than other two topologies as shown in Fig. 8a. The voltage gain ratio is 3.9; i.e., output voltage is 3.9 times the input voltage in two-phase IDBC with boosting capacitor

than other two topologies as compared in Table 2. Although the output voltage ripple is marginally higher, it is well within the required limits.

Two-phase IDBC with boosting capacitor has one disadvantage that it has one extra passive component than other two topologies but its lower ripple content compensates this disadvantage. Hence, the proposed two-phase IDBC with boosting capacitor will prove to be a better selection for fuel cell powered electric vehicle due to its simplicity, high voltage gain, low ripple content input current as well as low ripple content in output voltage.

References

1. Reddy BM, Samuel P, Reddy NSM (218) Government policies help promote clean transportation in India: proton-exchange membrane fuel cells for vehicles. IEEE Electrif Mag 6(1):26–36
2. Reddy BM, Samuel P (2017) Technology advancements and trends in development of proton exchange membrane fuel cell hybrid electric vehicles in India: a review. J Green Eng 7(3)
3. Hegazy O, Mierlo JV, Lataire P (2012) Analysis, modeling, and implementation of a multidevice interleaved DC/DC converter for fuel cell hybrid electric vehicles. IEEE Trans Power Electron 27(11):4445–4458
4. Kong X, Khambadkone AM (2007) Analysis and implementation of a high efficiency, interleaved current-fed full bridge converter for fuel cell system. IEEE Trans Power Electron 22 (2):543–550
5. Chiu HJ, Lin LW (2006) A bidirectional DC–DC converter for fuel cell electric vehicle driving system. IEEE Trans Power Electron 21(4):950–958
6. Phattanasak M, Gavagsaz-Ghoachani R, Martin JP, Nahid-Mobarakeh B, Pierfederici S, Davat B (2015) Control of a hybrid energy source comprising a fuel cell and two storage devices using isolated three-port bidirectional DC–DC converters. IEEE Trans Ind Appl 51 (1):491–497
7. Slah F, Mansour A, Hajer M, Faouzi B (2017) Analysis, modeling and implementation of an interleaved boost DC-DC converter for fuel cell used in electric vehicle. Int J Hydrog Energy 42(48)
8. Reddy BM, Samuel P (2016) A comparative analysis of non-isolated bi-directional dc-dc converters. In: 2016 IEEE 1st international conference on power electronics, intelligent control and energy systems, Delhi, 2016, pp 1–6
9. Garcia FS, Pomilio JA, Spiazzi G (2013) Modeling and control design of the interleaved double dual boost converter. IEEE Trans Industr Electron 60(8):3283–3290

Comparative Explication of Flyback and SEPIC Converter Topologies

Sandeep Gupta, Tarun Varshney and Shekhar Gehlaut

Abstract In this paper, the flyback converter and single-ended primary induction converter (SEPIC) based two different converter topologies are examined. For comparison, both topologies are designed with similar operating conditions and simulated using MATLAB simulink. Here, the comparison constraints are taken such as input–output relation, component stresses, harmonics, and effect of a snubber circuit. The comparison outcomes show that the flyback converter is the preferred topology when considering the basic topologies, but the SEPIC converter is very promising with some adaptations to the topology. Basic operating principle, design and modeling of flyback, and SEPIC converters are also described in this paper.

Keywords DC–DC power conversion · Flyback · SEPIC converter · Snubber circuit and THD

1 Introduction

The flyback and the SEPIC converter are two DC-to-DC converters with uses in similar applications. Both topologies are derived from the traditional buck–boost converter and hence are capable of both buck and boost conversion [1, 2]. The main advantage of the flyback topology is the transformer that acts as a coupled inductor and assures a galvanic separation of the input and output [3]. The classic SEPIC topology uses two inductors, thereby increasing the complexity and size of the circuit [4, 5].

S. Gupta (✉)
JECRC University, Jaipur 303905, Rajasthan, India
e-mail: jecsandeep@gmail.com

T. Varshney · S. Gehlaut
Surendera Group of Institutions, Sri Ganganagar, India
e-mail: t_varshney@yahoo.com

S. Gehlaut
e-mail: gehlaut.shekhar@gmail.com

However, in recent years, SEPIC converters with coupled inductors have become available on the market for only a slight extra cost and the use of the SEPIC converter has risen. Nevertheless, the flyback converter is still the most widely used because of its simplicity and the familiarity many designers have with it [6].

This paper aims to give a comparative study of the two topologies (flyback and SEPIC converters) in the same operating conditions. Section 2 explains the structure of these two topologies. Design and modeling of flyback and SEPIC converters are presented in Sect. 3. In Sect. 4, the output results of these converter topologies with same initial conditions are clearly explained for comparison. Finally, Sect. 5 concludes this paper.

2 Operating Principle

2.1 Flyback Converter

Figure 1 shows the basic topology of the flyback converter. When the switch S is on, the input voltage source is connected to the primary winding of the transformer. The diode is reverse biased and blocks the current path of the secondary winding. Energy from the voltage source is stored in the magnetic field in the transformer's core with a percentage of losses due to the leakage inductance of the primary winding. At the same time, the output capacitor discharges over the load and maintains a steady output voltage. When the switch S is turned off, the current path through the primary winding is blocked. The diode is forward biased, and the energy stored in the magnetic field will discharge over the load and the output capacitor. Neglecting the
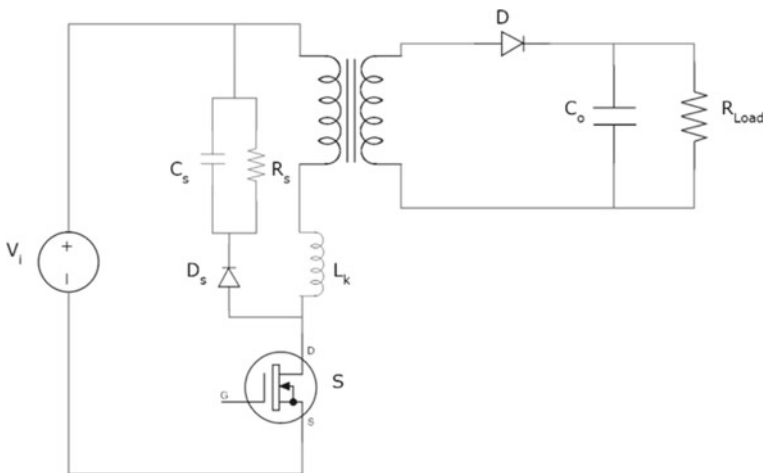
Fig. 1 Basic flyback converter topology
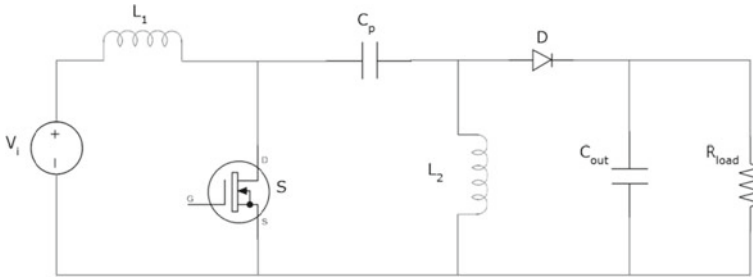
Fig. 2 Basic SEPIC converter topology

losses and the diode-forward voltage, the output voltage is determined by the input voltage, the duty ratio D and the transformer winding ratio N [7]:

$$V_0 = \frac{D}{1-D} \times N \times V_i \tag{1}$$

2.2 SEPIC Converter

Figure 2 shows the basic topology of the SEPIC converter. When the switch S is on, the input voltage source charges the inductor L_1 and the capacitor C_p charges the inductor L_2. The diode is reverse biased and the output capacitor discharges over the load, maintaining a constant output voltage. When the switch S is off, the inductors will discharge through the diode over the load and charge the capacitors. Neglecting the losses and the diode-forward voltage, the output voltage is determined by the input voltage and the duty ratio D [8]:

$$V_0 = \frac{D}{1-D} V_i \tag{2}$$

3 Design and Modeling

The design of both converters is carried out for the same operating conditions. The input is a 150 V/50 Hz rectified AC voltage source. Due to the relatively constant input, the output capacitors can maintain the output voltage stability and eliminate the need for a feedback loop. The design output voltage is 15 V DC. The flyback transformer has a leakage inductance of 3% of the magnetizing inductance, which entails the need of a snubber circuit. The modeling of both topologies is done using MATLAB simulink. Figures 3 and 4 show the simulation modeling of different converters.
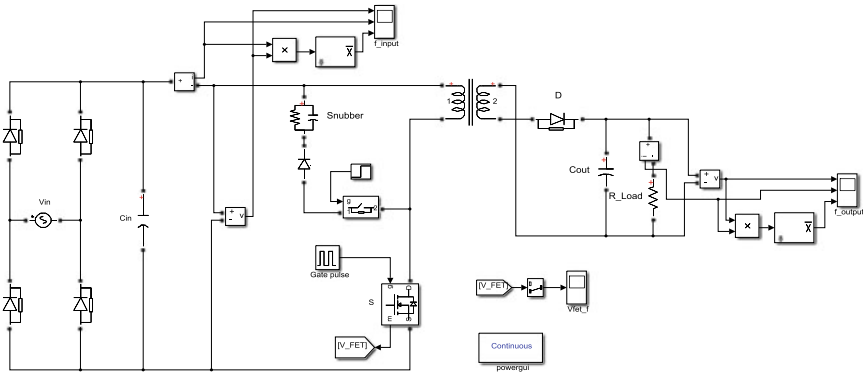
Fig. 3 Simulink model of the flyback converter
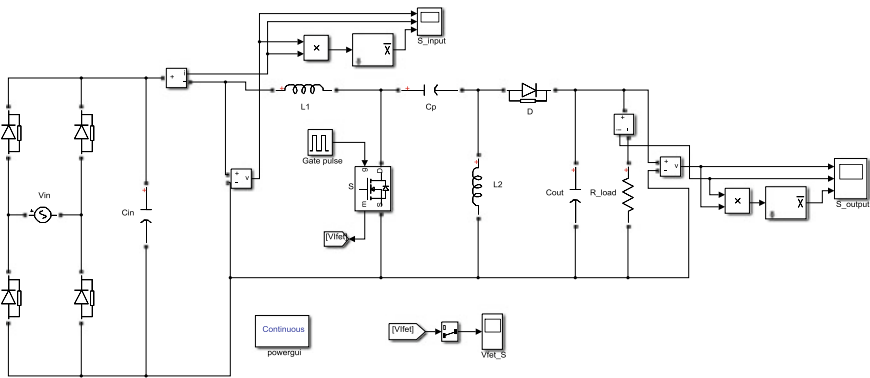
Fig. 4 Simulink model of the SEPIC converter

4 Simulation Results

Both topologies are simulated with a *R* load to compare the input–output relations. The switching voltage of the MOSFETs is examined to compare the component stresses. After that, the harmonics in the outputs and the required snubber circuit of the flyback converter are examined to determine its effect. For comparison between flyback and SEPIC converter topologies, following constraints are taken.

4.1 Converter with a **R** *Load*

Figures 5 and 6 show the result of the simulation of both topologies with a load of 10 Ω. In view of the output voltage, current, and power, the results are similar.
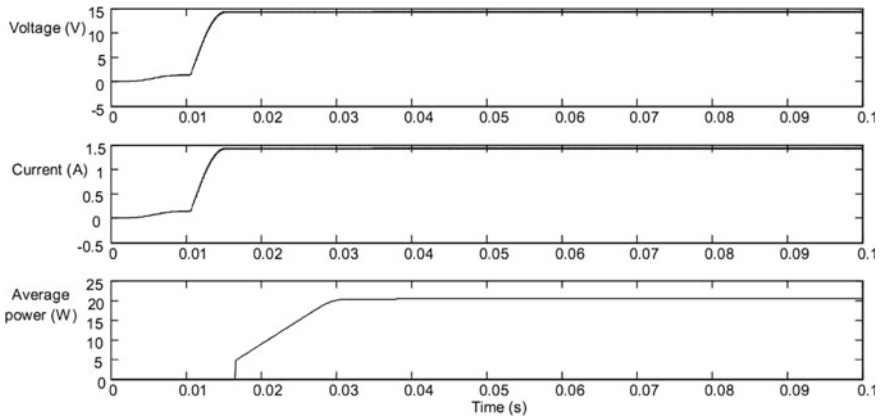
Fig. 5 Voltage, current, and power output of the flyback converter with a 10 Ω load
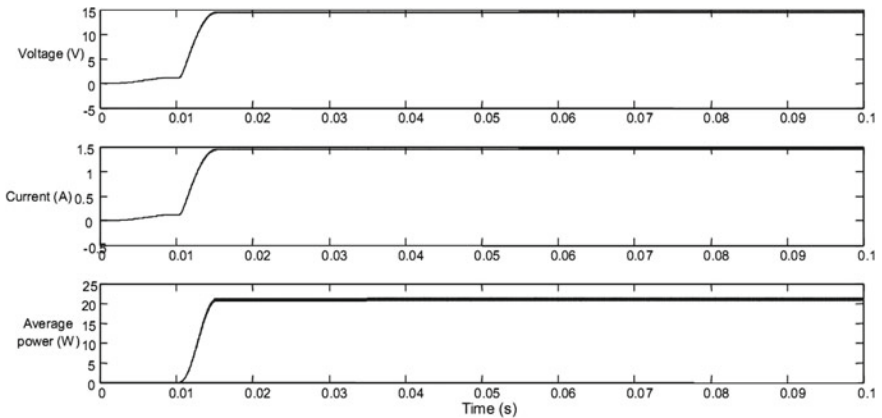
Fig. 6 Voltage, current, and power output of the SEPIC converter with a 10 Ω load

The SEPIC converter reaches an output voltage of 14.4 V (average), slightly closer to the design output of 15 V than the flyback converter that reaches 14.3 V. Both voltages have a ripple within the design limit of 0.1 V. However, the flyback converter requires an output capacitor of 22 μF for this versus 2.7 μF for the SEPIC converter. The bigger output capacitor incorporates an extra cost. The settling time of both topologies is almost equal and is mainly due to the settling time of the full-wave rectifier. The efficiency of the flyback topology is 81.2%. The SEPIC converter reaches 78.3%. Although the SEPIC converter has a better output, the input current and therefore the input power is higher than that of the flyback converter. This results in the lower efficiency.

4.2   MOSFET Switching Voltage

Figures 7 and 8 show the MOSFET drain-source voltage of both the flyback and
SEPIC converters, respectively. In the SEPIC topology, the capacitor C_p clamps the
MOSFET drain-source voltage, so no voltage spikes occur. In the flyback topology,
the transformer leakage inductance induces voltage peaks over the MOSFET. This
causes voltage stresses that are much higher compared to the SEPIC converter, thus
requiring a higher rated and more expensive switching device.
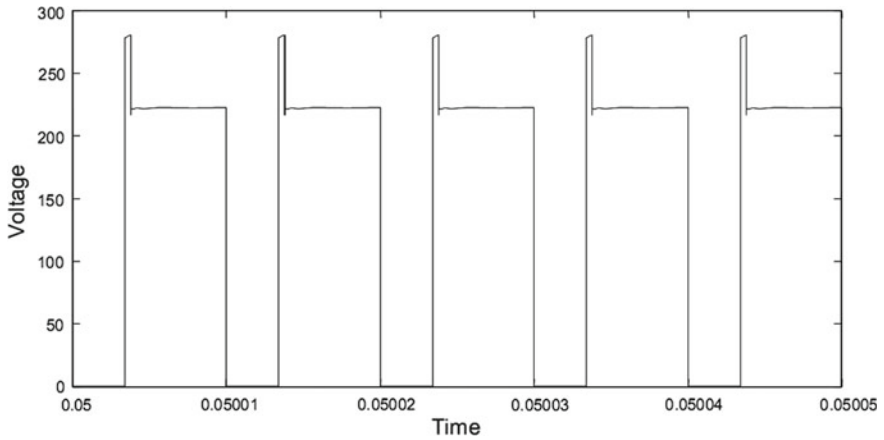
Fig. 7 Drain-source voltage of the flyback converter
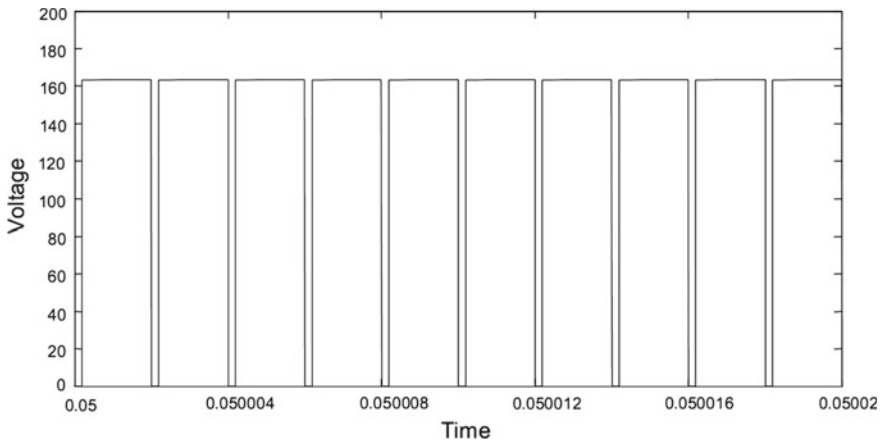
Fig. 8 Drain-source voltage of the SEPIC converter

4.3 Output Harmonics

Figures 9 and 10 show the FFT analysis of the output voltages for both topologies. The harmonic content is similar in both cases, with the SEPIC converter slightly over performing the flyback converter due to its lower THD.
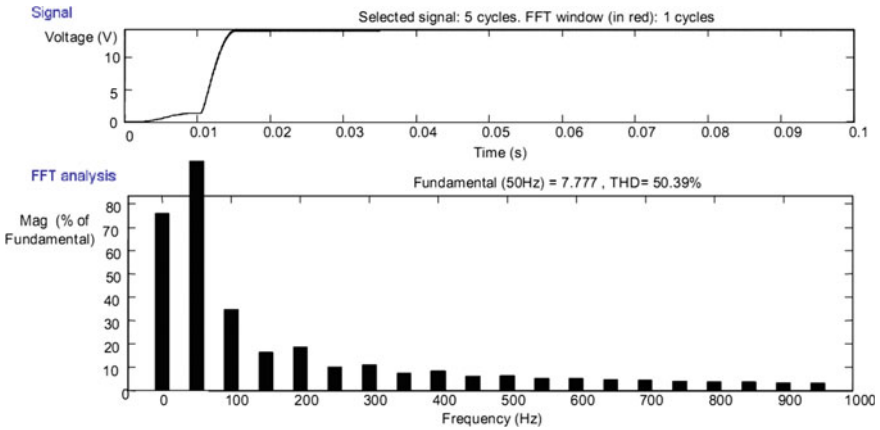
Fig. 9 FFT analysis of the output voltage of the flyback converter
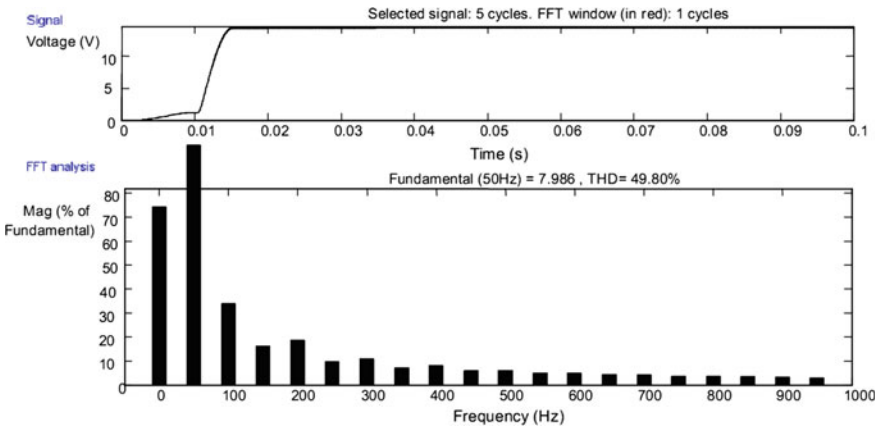
Fig. 10 FFT analysis of the output voltage of the SEPIC converter
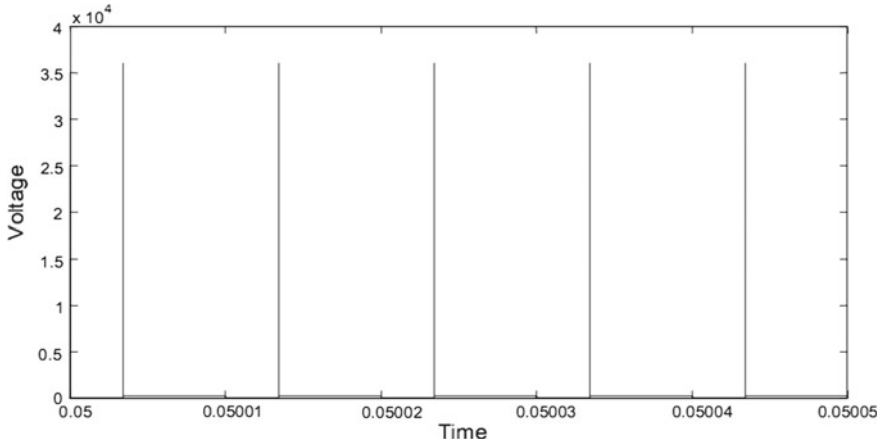
Fig. 11 Drain-source voltage of the flyback converter without the RCD snubber circuit

4.4 Snubber Circuit Effect

In the SEPIC topology, the clamping of the MOSFET drain-source voltage by the capacitor C_p omits the requirement of a snubber circuit. As observed in previous section, the leakage inductance induces voltage peaks and high voltage stresses on the MOSFET in the flyback topology. The snubber circuit is required here to dissipate the energy stored in the parasitic inductor during every cycle and clamp the voltage over the MOSFET [9]. Figures 7 and 11 show the MOSFET voltage with and without snubber circuit, respectively. Without the snubber circuit, the voltage stress over the MOSFET reaches unacceptable values. The snubber circuit also affects the total efficiency of the system. When the snubber circuit is removed, the efficiency of the converter is 84.2%. As in previous section, the efficiency of the total system with the snubber circuit drops to 81.2%. An ultra-fast diode in the RCD snubber circuit limits the efficiency loss, but incorporates an extra cost [10].

5 Conclusion

This paper presents the comparative analysis between two different power-electronic-based topologies such as flyback and SEPIC converters. In the flyback topology, the transformer leakage inductance induces voltage peaks over the MOSFET. This causes voltage stresses that are much higher compared to the SEPIC converter, thus requiring a higher rated and more expensive switching device. From outcome results, it can be said that the bigger MOSFET and output capacitor of the flyback converter combined with the RCD snubber circuit do not outweigh the higher cost and larger area of the basic SEPIC topology. As in

practice, the results of the flyback and the SEPIC converter are similar, with the flyback converter coming out as the first choice. The better efficiency of the flyback converter is also a main advantage of this topology. However, as research on SEPIC converters has increased in recent years, adaptations to the basic topology have been proposed that solve the major issues and make it an alternative to compete with the flyback converter.

References

1. Wei H, Batarseh I (1998) Comparison of basic converter topologies for power factor correction. In: IEEE proceedings in Southeastcon'98, pp 348–353
2. Erickson R, Madigan M, Singer S (1990) Design of a simple high-power-factor rectifier based on the flyback converter. In: Proceedings of IEEE APEC, vol 90, Mar 1990, pp 792–801
3. Li Y (2017) A new single-phase single-stage AC-DC stacked flyback converter with active clamp ZVS. Ph.D. dissertation, The University of Western Ontario
4. Rosa AH, de Souza TM, Morais LM, Seleme SI (2018) Adaptive and nonlinear control techniques applied to SEPIC converter in DC-DC, PFC, CCM and DCM modes using HIL simulation. Energies 11(3):602–610
5. Gupta S, Tripathi RK, Shukla RD (2010) Voltage stability improvement in power systems using facts controllers: state-of-the-art review. In: IEEE international conference on power, control and embedded systems (ICPCES), pp 1–8
6. Betten J, Kollman R (2006) No need to fear: SEPIC outperforms the flyback. EE Times Mag 1–7
7. Chang KM, Chen L, Huang Q (2018) Zero voltage switching flyback converter for primary switch turn-off transitions. U.S. Patent No. 9,899,931. 20 Feb 2018
8. Kommukuri VS et al (2018) Modified bridgeless SEPIC rectifier for power factor correction with reduced switch stress operating in continuous conduction mode. J Circuits Syst Comput 27(08):18 p
9. Mohanty PK, Dalai RP (2014) Observation and calculation of different harmonics in fly back converter. Int J Recent Dev Eng Technol 2:90–97
10. Gao K, Goerke UB (2015) Choosing standard recovery diode or ultra-fast diode in snubber. Texas Instruments Application, Report No. SNVA744, Oct 2015

Localization and Impulse Analysis of Experimental Bot Using eZ430-Chronos

Rohit Mittal, Vibhakar Pathak, Nidhi Mishra and Amit Mithal

Abstract The paper examines the effect of forces on bot working in indoor environment. The effects of forces are needed for localization of bot, which is one of the important parameters for SLAM (simultaneous localization and mapping). The forces give a physical overview of surface, which is a vital parameter for localization. The experiments are carried out with the help of remote system based on Bluetooth 4.0. For impulse analysis, real-time data acquisition is done with the help of eZ430-Chronos and TI control center software. In eZ430-Chronos, only 3-axis accelerometer is used. Here, authors conclude that bots' data required for localization can remotely be acquired with some time real-time devices at finer level which determines geophysical characteristics used in localization. The experimental results demonstrate friction, surface parameter reported by bot when it is moving inside the experimental arenas.

R. Mittal (✉) · N. Mishra
Poornima University, Jaipur, India
e-mail: rohit18mittal@yahoo.com

N. Mishra
e-mail: nidhi.mishra@poornima.edu.in

V. Pathak
Arya College of Engineering & I.T, Jaipur, India
e-mail: vibhakarp@rediffmail.com

A. Mithal
JECRC, Jaipur, India
e-mail: amit.mithal81@gmail.com

1 Introduction

For navigation purposes, simultaneous localization and mapping (SLAM) system is required in many robotic applications [1]. SLAM is divided into two parts viz localization and mapping, where localization is an important attribute of mapping. SLAM was generally implemented with visual sensors and can navigate in indoor or outdoor environment [2, 3], but in this paper, authors examine the effect of motion and forces due to surface or terrain in which experimental bot is stimulated. The bot is equipped with multisensory system in both visual and non-visual mode acquisitions of attribute used in localization.

The bot contains visual and non-visual sensors such as accelerometer gyroscope, temperature, sonar sensors, camera, which are used for localization data. In this paper, authors present acceleration data which are captured through TI Chronos series eZ430. It is a multisensory system having 3-axis accelerometer, heart rate, and temperature sensor. Only accelerometer is used in the experiment for capturing localization data as a base point to start design of multisensory SLAM as localization of environment requires the use of external sensors for obtaining real-time data and can get bot's position in navigation. For autonomous navigation in an area given, the bot needs a map of that arena and localizes itself on the map. Various models are used which are based on some sensors to capture various localization parameters in either 2D or 3D.

Next section describes the previous work which had been done in probabilistic robotics using filters, after which authors discuss experimental arena used in research laboratory combining plane surface, moderate steep surface, and inclined surface with various types of fixed obstacles. Next sections describe the sensing effects of various forces 3-axis accelerometer; sensors taken using eZ430-Chronos watch with its specifications have been discussed. The Chronos was assembled at the centre of gravity of the bot to examine the effect of acceleration and force over it. Finally, in the last section, results were discussed which are captured by Bluetooth control center running on smartphone.

2 Previous Work

In the past, most of the researchers have implemented techniques for probabilistic robotics like extended Kalman filtering (Gaussian noise is added for movement of robot on circular trajectory) and particle filters for providing a reliable estimation of camera poses [4, 5]. Some projects making use of both RGB-D data and graph optimization, this RGB and depth information provided by camera use 6-DOF through Kinect developed by PrimeSense [6]. Kinect uses OpenNI framework which offers gesture recognition and motion tracking, and for feature extraction, Harris Corner [7], SIFT [8], and SURF [9] methods were used. These methods were used to detect not only corner points but also invariant feature keypoints.

In [10], researchers talked about various algorithms for dispensing number of robots in indoor environment, and they should maintain network connectivity and allowing robots for communication purposes, and for that, robots need unique identification, light sensors, camera, modem, etc. In [11], robots are spread throughout an enclosed space quickly and uniformly, while keeping each robot connected to the network. The optimal running time occurs when each robot moves from a central start location to its final position along the shortest possible path at maximum velocity. Researchers have talked about visual sensors only. But they had not tried to evaluate any other sensory system; they simply combined the data set of different sensors with the help of large computational system. Also geophysical information and its parameters were also missing in previous research works.

After analyzing the above works, authors conclude that previous authors have not tried an independent sensory system with different control centers which were examined in this paper.

3   Tools and Hardware Used

The Chronos watch has various sensors which are shown in Fig. 1. Here, authors have used 3D accelerometer only.

The eZ430-Chronos is developed by Texas Instrument which is a wireless integrated system that provides a complete reference design for developers creating wireless smart watch applications shown in Fig. 2, and deployment of watch with bot is shown in Fig. 3.

Fig. 1   eZ430-Chronos [12]
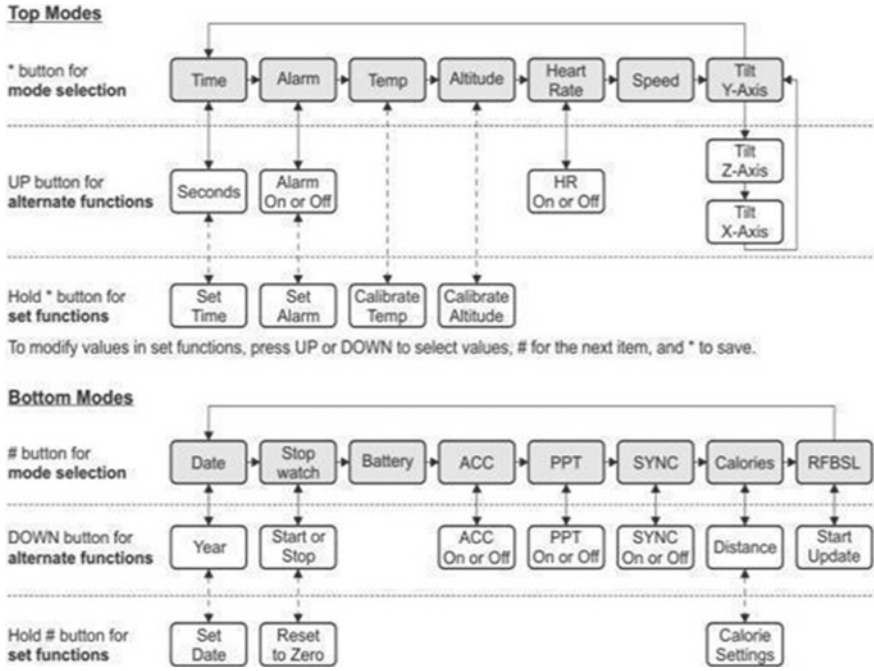
Fig. 2 eZ430 sensory array [13]

Fig. 3 Deployment of watch
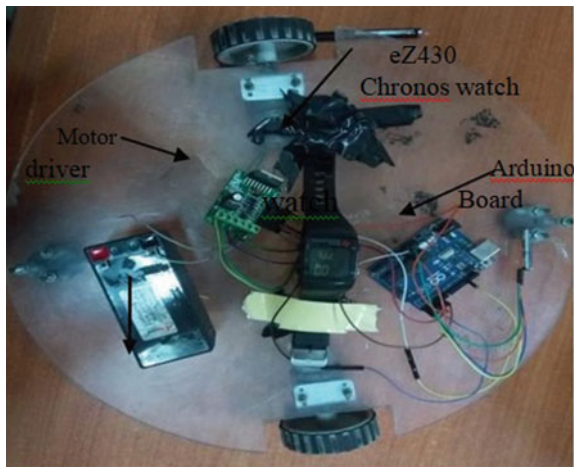
4   Implementation Mechanism

In previous work, authors discussed localization based on preexisting map and acquired real-time data. For navigation of bot, some preexisting map is needed, combined with some sensors reading of 3D cameras, sonar, etc. SLAM faces several problems like:

- Known map, known localization
- Known map, unknown localization
- Unknown map, unknown localization

The work discussed in this research paper comes under the third category.

In this paper, the work based on geophysical data captured by bot is discussed, which is one of the novel approaches. Several parameters of mechanics have been calculated like force, impulse, friction, momentum (not analyzed). After getting the geophysical information, bot can more accurately localize itself, after which third-category problem may be resolved. Next section discusses experiments carried out on bot by navigating on various surfaces and their geophysical information with analysis.

5   Experimental Work

In the experiment, authors navigate bot in robotics research laboratory, and the bot runs up to 17 m in 48 s using remote area network (RAN), i.e., Bluetooth, on various surface types like marble flooring, glaze tile, rough tile, and boulder tile at different time intervals starting from 1 s and with a total of 50 runs. In this paper, 13 optimized runs will be taken. Following tables show specifications of bot and navigation data for RAN (Tables 1 and 2).

The bot was navigated on one of the surfaces with the help of Arduino RC app which is shown in Fig. 4.

Data sensed by Chronos was acquired by the control center using Bluetooth RF access point connected to control center PC by RF USB emulator provided by Texas Instrument (Table 3).

In this experiment, accelerometer mode of eZ430-Chronos watch was used which has following modes:

- Temperature mode
- Altimeter mode
- Acceleration mode

The Chronos control center software is a multitasking system capable of providing real-time data over air to Windows Operating System. The control center provides:

Table 1 Specifications of bot

Area covered	2 × 5 m
Distance	Max = 73 cm
	Min = −102 cm
Speed	Max = 91.78 cm/s
	Min = 2.8 cm/s
Type of force	X, Y and Z direction
2 wheels	Diameter = 7.5 cm
	Width = 1.8 cm
Arduino UNO board	Microcontroller
	ATmega328P
	Operating voltage 5 V
	14 pins
Motor type	D.C. (sync)
Motor driver	L298
Battery	12 V, 1.3 A
Bluetooth module	HC-06
Connecting wires	8
Bot weight	2.5 kg

Table 2 Connecting navigation data

Android mobile phone	Gionee S Plus
Bluetooth mobile phone	4.0
Arduino RC app	

Fig. 4 Movement of bot via Gionee S Plus

Table 3 Data acquisition ez430-Chronos watch specifications	Microcontroller	MSP 430
	Sensors	3 axes
		Accelerometer
		Pressure sensor
		Temperature sensor
		Battery voltage sensor
	LCD display	96 segment
	Operating frequency	433 MHz
	RF USB emulator	1

- 3D acceleration graph with PC mouse control
- Time, date, and calibration data synchronization tool

Acceleration mode of eZ430-Chronos watch requires control center software. For this experiment, accelerometer mode of eZ430-Chronos is used. It transmits real-time acceleration data to the control centre in all X, Y, and Z coordinates. Authors use 3D acceleration graph to calculate impulse, that is, the overall effect of force acting over time. The control center describes the data monitoring in accelerometer mode which is received during movement of bot (Fig. 5).

Here, F is resultant force applied from different time intervals. A resultant force causes acceleration and a change in velocity of body for as long as it acts. A resultant force applied for a longer time therefore produces bigger change in linear momentum. The term impulse is also used to refer to a fast acting force or impact.

$$\text{Force} = \text{Mass} \times \text{Acceleration} \tag{1}$$

Flowchart in Fig. 6 shows the navigation of bot and its effect received by control center. Impulse is calculated by the force applied over the time interval "t" to move the bot inside experiment area, and readings are shown in Figs. 7 and 8.

Fig. 5 Battery connected with Arduino board
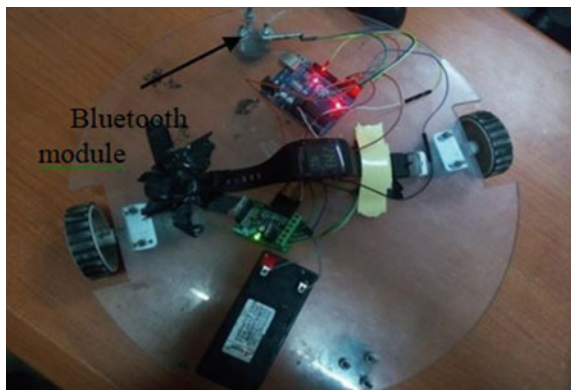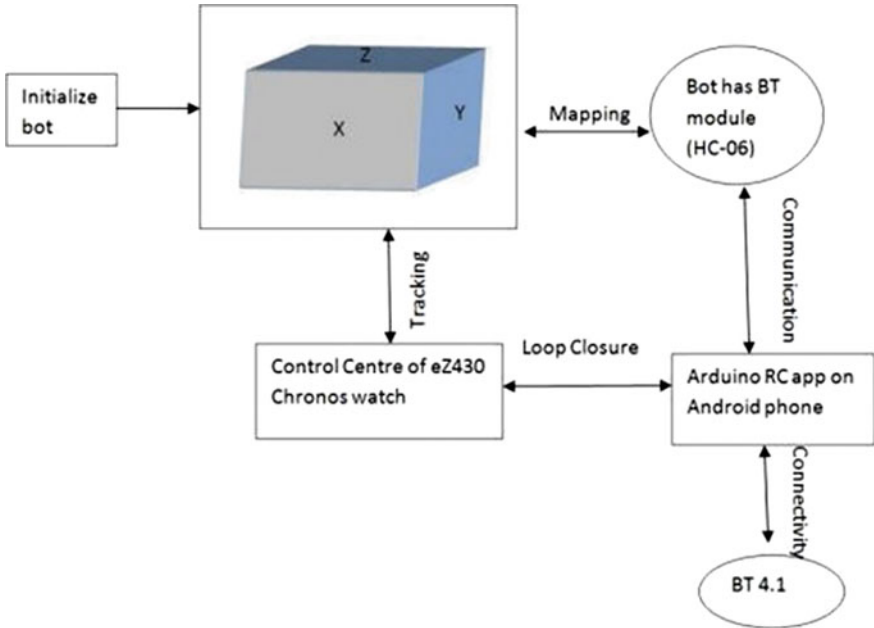
Fig. 6 Navigation of bot using control center

Fig. 7 eZ430-Chronos
control center
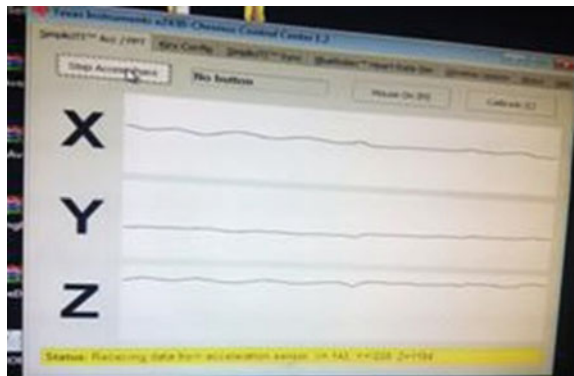
6 Final Results and Discussion

Experiments were conducted on various types of surfaces and the bot was run up to
17 m for more than a dozen times. The bot was moved from initial position and
impulse was calculated on different time intervals starting from 1 to 48 s at varying
distances. Results obtained are shown in Tables 4, 5, 6, and 7.

Fig. 8 RF USB emulator on PC

Table 4 Results analyzed after movement of bot on marble flooring

S. No.	Time (s)	X (cm)	Y (cm)	Z (cm)	Time * Z (N s)	$H^2 = X^2 + Y^2$
1	1	18	90	1227	1227	91.78235
2	2	11	80	1224	2448	80.75271
3	3	−17	80	1227	3681	81.78631
4	3.8	−22	−122	1206	4582.8	123.9677
5	4	−15	90	1011	4044	91.24144
6	4.48	−27	107	1209	5416.32	110.354
7	5	−20	−107	1213	6065	108.8531
8	5.8	−11	−103	1218	7064.4	103.5857
9	7.38	73	198	1335	9852.3	211.0284
10	9.3	−102	−207	1232	11457.6	230.7661
11	22.5	−12	−123	1197	26932.5	123.584
12	26.6	−35	−133	1192	31707.2	137.5282
13	48	−3	−133	1192	57216	133.0338

When the bot starts moving, it observes a drop in friction; after few time seconds, it observes a steep high friction due to obstacles found on the surface of the arena which obstructs the treads in the movement. Then a drop in friction is observed by the bot for a few steps; after taking a lower dip, a linear raise in friction is observed by the bot with respect to resultant force applied: acceleration force on X, Y direction. After running the bot from 3.8 to 9.3 s, it observes that first friction linearly increases then linearly decreases, and then due to change in surface texture, bot's friction gets constant and moves in linear direction.

Results were generated on MS-Excel simulator and concluded using graph shown in Fig. 9 between impulse and friction shown in graph. It can be seen that

Table 5 Results analyzed after movement of bot on glaze tile

S. No.	Time (s)	X (cm)	Y (cm)	Z (cm)	Time * Z (N s)	$H^2 = X^2 + Y^2$
1	1	18.36	91.8	1251.54	1251.54	93.618
2	2	11.22	81.6	1248.48	2496.96	82.36776
3	3	−17.34	81.6	1251.54	3754.62	83.42204
4	3.8	−22.44	−124.44	1230.12	4674.456	126.4471
5	4	−15.3	91.8	1031.22	4124.88	93.06627
6	4.48	−27.54	109.14	1233.18	5524.646	112.5611
7	5	−20.4	−109.14	1237.26	6186.3	111.0302
8	5.8	−11.22	−105.06	1242.36	7205.688	105.6574
9	7.38	74.46	201.96	1361.7	10049.35	215.249
10	9.3	−104.04	−211.14	1256.64	11686.75	235.3814
11	22.5	−12.24	−125.46	1220.94	27471.15	126.0557
12	26.6	−35.7	−135.66	1215.84	32341.34	140.2788
13	48	−3.06	−135.66	1215.84	58360.32	135.6945

Table 6 Results analyzed after movement of bot on rough tile

S. No.	Time (s)	X (cm)	Y (cm)	Z (cm)	Time * Z (N s)	$H^2 = X^2 + Y^2$
1	1	18.9	94.5	1288.35	1288.35	96.37147
2	2	11.55	84	1285.2	2570.4	84.79035
3	3	−17.85	84	1288.35	3865.05	85.87563
4	3.8	−23.1	−128.1	1266.3	4811.94	130.1661
5	4	−15.75	94.5	1061.55	4246.2	95.80351
6	4.48	−28.35	112.35	1269.45	5687.136	115.8717
7	5	−21	−112.35	1273.65	6368.25	114.2958
8	5.8	−11.55	−108.15	1278.9	7417.62	108.765
9	7.38	76.65	207.9	1401.75	10344.92	221.5798
10	9.3	−107.1	−217.35	1293.6	12030.48	242.3044
11	22.5	−12.6	−129.15	1256.85	28279.13	129.7632
12	26.6	−36.75	−139.65	1251.6	33292.56	144.4046
13	48	−3.15	−139.65	1251.6	60076.8	139.6855

there are distinct values of friction and impulse when bot runs on rough tile, glaze tile, boulder tile, and marble flooring, due to geophysical parameters used, hence localize identification of bot problem has been resolved.

Impulse uses force and time as variables and friction uses X and Y variables, i.e., distance from origin to destination, and converts it into H. Here impulse is used because time is also a factor that is considered in our test results.

Table 7 Results analyzed after movement of bot on boulder tile

S. No.	Time (s)	X (cm)	Y (cm)	Z (cm)	Time * Z (N s)	$H^2 = X^2 + Y^2$
1	1	19.8	99	1349.7	1349.7	100.9606
2	2	12.1	88	1346.4	2692.8	88.82798
3	3	3	−18.7	88	1349.7	4049.1
4	3.8	−24.2	−134.2	1326.6	5041.08	136.3645
5	4	−16.5	99	1112.1	4448.4	100.3656
6	4.48	−29.7	117.7	1329.9	5957.952	121.3894
7	5	−22	−117.7	1334.3	6671.5	119.7384
8	5.8	−12.1	−113.3	1339.8	7770.84	113.9443
9	7.38	80.3	217.8	1468.5	10837.53	232.1312
10	9.3	−112.2	−227.7	1355.2	12603.36	253.8427
11	22.5	13.2	−135.3	1316.7	29625.75	135.9424
12	26.6	−38.5	−146.3	1311.2	34877.92	151.281
13	48	−3.3	−146.3	1311.2	62937.6	146.3372
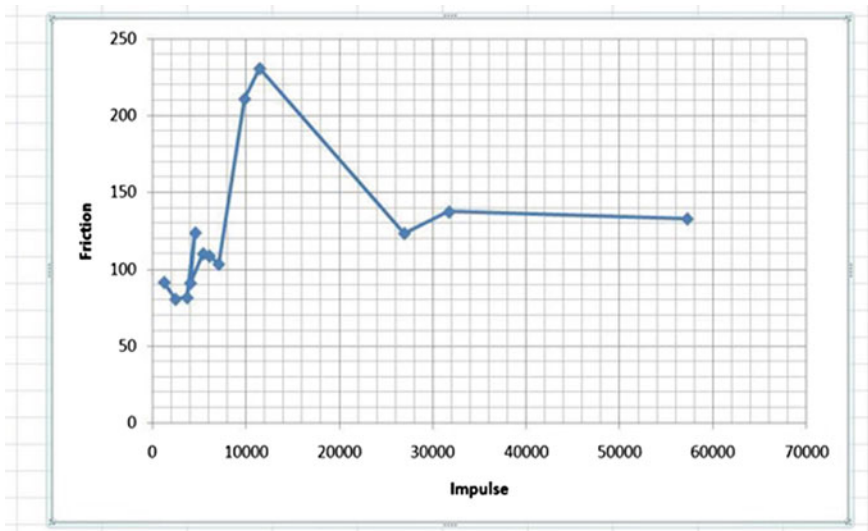
Fig. 9 Results generated

7 Conclusion and Future Work

From the above discussion, we conclude that the surface type and small obstacles on surface can be observed with the help of accelerometer as sensor from our array of sensors used in multisensory SLAM. The observation concludes the efficacy of our independent accelerometer working as a component of multisensory array in

combination with control center based on RC-USB emulator. For further work, one can explore battery voltage mode, temperature mode of eZ430-Chronos watch of Texas Instrument, and can go up to 9D or 12D by adding sonars, gyro/IMU in bot.

References

1. Li S, Lee D (2017) RGB-D SLAM in dynamic environments using static point weighting. IEEE Robot Automat
2. Kerl C, Sturm J, Cremers D (2013) Dense visual slam for RGB-D cameras. In: Proceedings of IEEE/RSJ international conference on intelligent robots systems, pp 2100–2106
3. Gutierrez-Gomez D, Mayol-Cuevas W, Guerrero J (2015) Inverse depth for accurate photometric and geometric error minimisation in RGB-D dense visual odometry. In: Proceedings of IEEE international conference on robotics and automations, pp 83–89
4. Thrun S, Burgard W, Fox D (2005) Probabilistic robotics. Intelligent robotics and autonomous agents series. The MIT Press
5. Deans M, Hebert M (2000) Invariant filtering for simultaneous localization and mapping. In: Proceedings of the IEEE international conference on robotics and automation (ICRA), pp 1042–1047, San Francisco, CA. IEEE
6. Brooks R (1986) A robust layered control system for a mobile robot. IEEE J Robot Autom RA-2:14–23
7. Harris C, Stephens M (1988) A combined corner and edge detector. In: Proceedings of the 4th Alvey vision conference, pp 147–151
8. Lowe DG (2004) Distinctive image features from scale-invariant key points. Int J Comput Vis 60(2):91–110
9. Bay H, Ess A, Tuytelaars T, Van Gool L (2008) Speeded-up robust features (SURF). Comput Vis Image Underst 110:346–359
10. McLurkin J, Smith J (2007) Distributed algorithms for dispersion in indoor environments using a swarm of autonomous mobile robots. In: Distributed autonomous robotic systems, pp 399–408
11. www.csc.kth.se/∼aydemir/thesis_virgile_hogman.pdf
12. www.itopen.it
13. www.ti.com

A Nine-Level Cascaded Multilevel Inverter with Reduced Switch Count and Lower Harmonics

Adil Sarwar, Md Irfan Sarwar, Md Shahbaz Alam, Seerin Ahmad and Mohd Tariq

Abstract Multilevel inverters (MLI) have numerous applications in industrial drives. In the last two decades, there is a tremendous increase in the application of MLI in the industrial drives. The modular nature of MLI is utilized to upgrade the power handling capability without the need for new converters. This paper presents a reduced switch count cascaded H-bridge (CHB) converter utilizing a lone stiff DC source (battery) to obtain a nine-level output. The mathematical analysis is presented which is verified by simulation and experimental results. Variation of total harmonic distortion (THD) with modulation index is also analyzed and shown.

Keywords Multilevel inverter (MLI) · Cascaded H-bridge (CHB) converter · Pulse width modulation · Phase opposition disposition (POD) · Total harmonic distortion (THD) · MATLAB

A. Sarwar · M. I. Sarwar · M. S. Alam · M. Tariq (✉)
Department of Electrical Engineering, Aligarh Muslim University,
Aligarh 202002, India
e-mail: tariq.iitkgp@gmail.com

A. Sarwar
e-mail: adilsarwar123@gmail.com

M. I. Sarwar
e-mail: irfanamu97@gmail.com

M. S. Alam
e-mail: shahbazalam6205@gmail.com

S. Ahmad
Department of Electric Power Engineering, Budapest University
of Technology and Economics, Budapest, Hungary
e-mail: Seerin.amu@gmail.com

1 Introduction

The idea of multilevel inverter was evolved in 1981 [1, 2]. These converters have a stepped output voltage resembling a sinusoidal wave produced from several DC voltage sources [2–4]. The power electronics inverters are widely used in industrial application because of low harmonic distortion in the output. The area of application includes static VAR generation, flexible AC transmission system (FACTS) [5], solar photovoltaic system [6, 7], and battery-based application such as charging batteries [8]. MLI are also used in traction drive as a rectifier in the vehicle for regenerative braking [9]. The complexity in circuitry due to substantial number of switches and utilization of many DC sources in multilevel inverter has opened up avenues for research to reduce them. There has been rigorous research ongoing to decrease the number of power electronic switches and DC power supply used in MLI without compromising with the number of output levels [10, 11]. The research endeavor can be broadly divided into finding newer topologies for achieving the above objective and devising suitable control algorithms for it. Conventional multilevel converters are classified as (a) diode clamped (b) flying capacitor, and (c) cascaded multilevel converters. The cascaded multilevel converter topology is considered to be simple, reliable, and modular. Cascaded multilevel converter could further be classified as symmetrical CHB converter and asymmetrical CHB converter [12]. Symmetrical CHB converter uses equal DC voltage source, while asymmetrical counterpart uses unequal voltage sources. Least THD with less complex control is obtained in comparison with different control techniques presented in [13–16]. In this paper, cascaded H-bridge asymmetrical multilevel inverter is analyzed to produce the output of nine levels with the switch count of eight. More the number of levels are, the better is the shape of the output waveform [17]. The switching strategy employed ensures that nine-level output is generated which is regulated using multicarrier phase opposition disposition modulation strategy. A simulation model for the proposed nine-level CHB converter is developed in MATLAB®/Simulink environment. Results for the performance of the converter are also shown in the paper.

1.1 Operation of Multilevel Cascaded H-Bridge Inverter

In general, n-level output in a cascaded H-bridge inverter can be generated from $2(n-1)$ switches and $(n-1)/2$ DC sources. So, to generate nine-level output 16 switches, 4 DC sources are required. Employing asymmetric-cascaded CHB will reduce the switch count drastically, but this is at the cost of reduction in redundant states. Moreover, there will be asymmetry in output voltage with any of the modulation strategy. But the cost benefits with reduced switch count and DC voltage sources are the important factors to look into these types of inverter configuration for their possible application. Figure 1 shows the circuit diagram of two cascaded H-bridge converters. Various possible output levels that could be generated with

Fig. 1 Cascaded H-bridge
converter
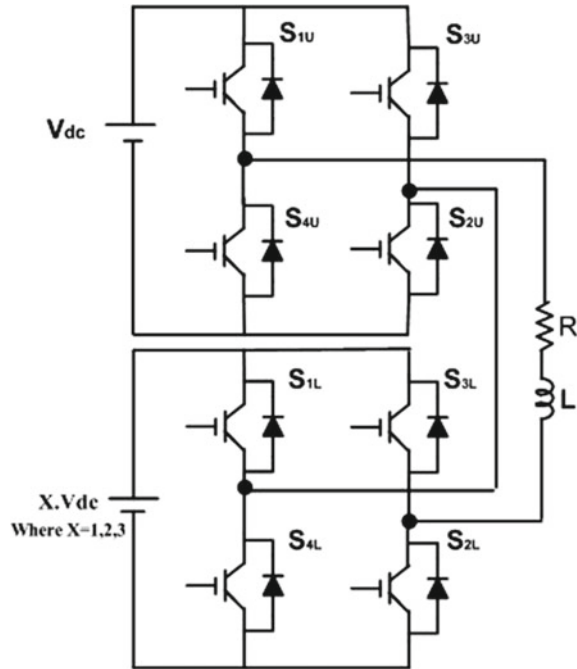
asymmetric-cascaded CHB with different DC source combination are presented
along with their switching scheme from Figs. 2 and 3. It could be seen that nine-level
output could be generated with battery voltage combination of $3V_{dc}$ and V_{dc}. Table 1
compares the various MLI topology with respect to the element count.

1.2 Generation of Multilevel Output Using Cascaded H-Bridge Converter

Multilevel output can be generated by cascading two or more H-bridge converters.
In general, $(2n + 1)$ level could be generated from cascaded converter using n equal
DC source. The number of level increases by choosing unequal DC source.
Figure 1 shows two cascaded H-bridge converter.

The switching scheme for generation of various multilevel outputs from two
cascaded H-bridge converters with unequal DC voltage levels along with the output
has been shown in Tables 2, 3, and 4.

1.3 (A) Five-Level Output

For generating five-level output, the switching scheme is given in Table 2.
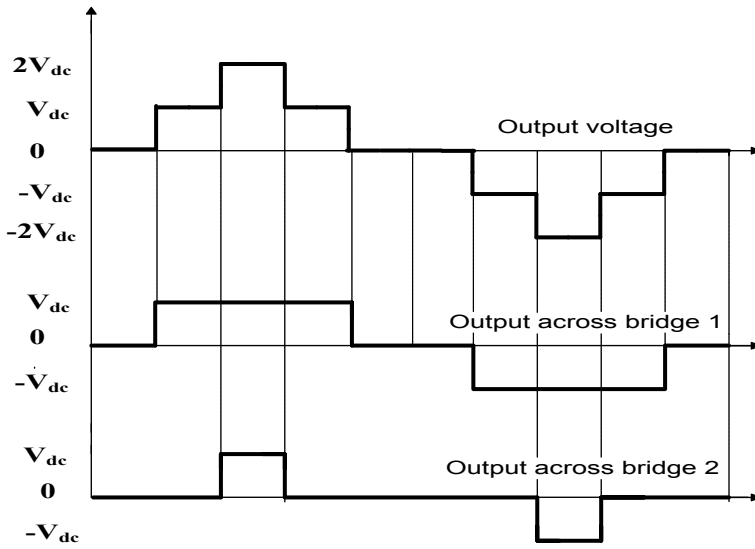
Fig. 2 Output across each H-bridge for five levels

Fig. 3 Output across each H-bridge for five levels
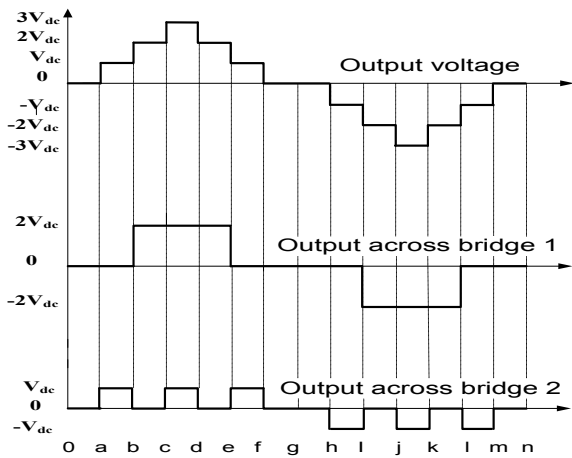
Table 1 Switch count

Multilevel inverter structure	Diode clamped	Cascaded H-bridge	Flying capacitor	Investigated asymmetric CHB
DC sources	1	4	1	2
Clamping capacitors	–	–	6	–
DC split capacitors	4	–	4	–
Clamping diodes	12	–	–	–
Main switches	16	16	16	8
Total component count	33	27	27	10

Table 2 Five-level output

S_{1U}	S_{2U}	S_{3U}	S_{4U}	V_1	S_{1L}	S_{2L}	S_{3L}	S_{4L}	V_2	V_O
On	On	–	–	V_{dc}	On	On	–	–	V_{dc}	$2V_{dc}$
On	On	–	–	V_{dc}	On	–	On	–	0	V_{dc}
–	–	–	–	0	–	–	–	–	0	0
–	–	On	On	$-V_{dc}$	–	On	–	On	–	$-V_{dc}$
–	–	On	On	$-V_{dc}$	–	–	On	On	$-V_{dc}$	$-2V_{dc}$

Table 3 Seven-level output

S_{1U}	S_{2U}	S_{3U}	S_{4U}	V_1	S_{1L}	S_{2L}	S_{3L}	S_{4L}	V_2	V_O
On	On	–	–	$2V_{dc}$	On	On	–	–	V_{dc}	$3V_{dc}$
On	On	–	–	$2V_{dc}$	On	–	On	–	0	$2V_{dc}$
On	–	On	–	0	On	On	–	–	V_{dc}	V_{dc}
–	–	–	–	0	–	–	–	–	0	0
–	On	–	On	0	–	–	On	On	$-V_{dc}$	$-V_{dc}$
–	–	On	On	$-2V_{dc}$	–	On	–	On	0	$-2V_{dc}$
–	–	On	On	$-2V_{dc}$	–	–	On	On	$-V_{dc}$	$-3V_{dc}$

Table 4 Nine-level output

S_{1U}	S_{2U}	S_{3U}	S_{4U}	V_1	S_{1L}	S_{2L}	S_{3L}	S_{4L}	V_2	V_O
On	On	–	–	$3V_{dc}$	On	On	–	–	V_{dc}	$4V_{dc}$
On	On	–	–	$3V_{dc}$	On	–	On	–	–	$3V_{dc}$
On	On	–	–	$3V_{dc}$	–	–	On	On	$-V_{dc}$	$2V_{dc}$
On	–	On	–	–	On	On	–	–	V_{dc}	V_{dc}
–	–	–	–	–	–	–	–	–	–	0 V
–	On	–	On	–	–	–	On	On	$-V_{dc}$	$-V_{dc}$
–	–	On	On	$-3V_{dc}$	On	On	–	–	V_{dc}	$-2V_{dc}$
–	–	On	On	$-3V_{dc}$	On	–	On	–	–	$-3V_{dc}$
–	–	On	On	$-3V_{dc}$	–	–	On	On	$-V_{dc}$	$-4V_{dc}$

1.4 (B) Seven-Level Output

For generating seven-level output, the switching scheme given in Table 3.

1.5 (C) Nine-Level Output

For generating nine-level output, the switching scheme is given in Table 4. The switching circuit diagrams for the various conduction states are shown in Fig. 4a–i. There are multiple redundant switching states for zero output voltage. The combinations of two sources are added or subtracted in such a manner so that they form the stepped output waveform. In this switching scheme discussed here, the time interval for each switching mode has been taken to be the same. The total Harmonic Distortion (THD) of the output voltage wave is quite high as shown in Fig. 6 (Fig. 5).

2 Comparison of Nine-Level Inverter Output with the Sine Wave

For reducing the THD in the output of the nine-level CHB converter, a comparison with sine wave is made. The nine-level output is redrawn with equal subsequent level amplitude. The instant of switching mode changeover is done instantly, when next level V_{dc} touches the sinusoidal wave as shown in Fig. 7.

2.1 Calculation of Switching Instants

Assume a sinusoidal wave in Eq. (1)

$$v = V_m \sin(\omega t) \tag{1}$$

where V_m is the peak amplitude of sine wave and V_{dc} is the amplitude of each levels.

Calculation of the instants of switching,

$$V_{dc} = V_m \sin(\omega t) \tag{2}$$

$$t = \frac{1}{\omega} \sin^{-1}\left(\frac{V_{dc}}{V_m}\right) \tag{3}$$
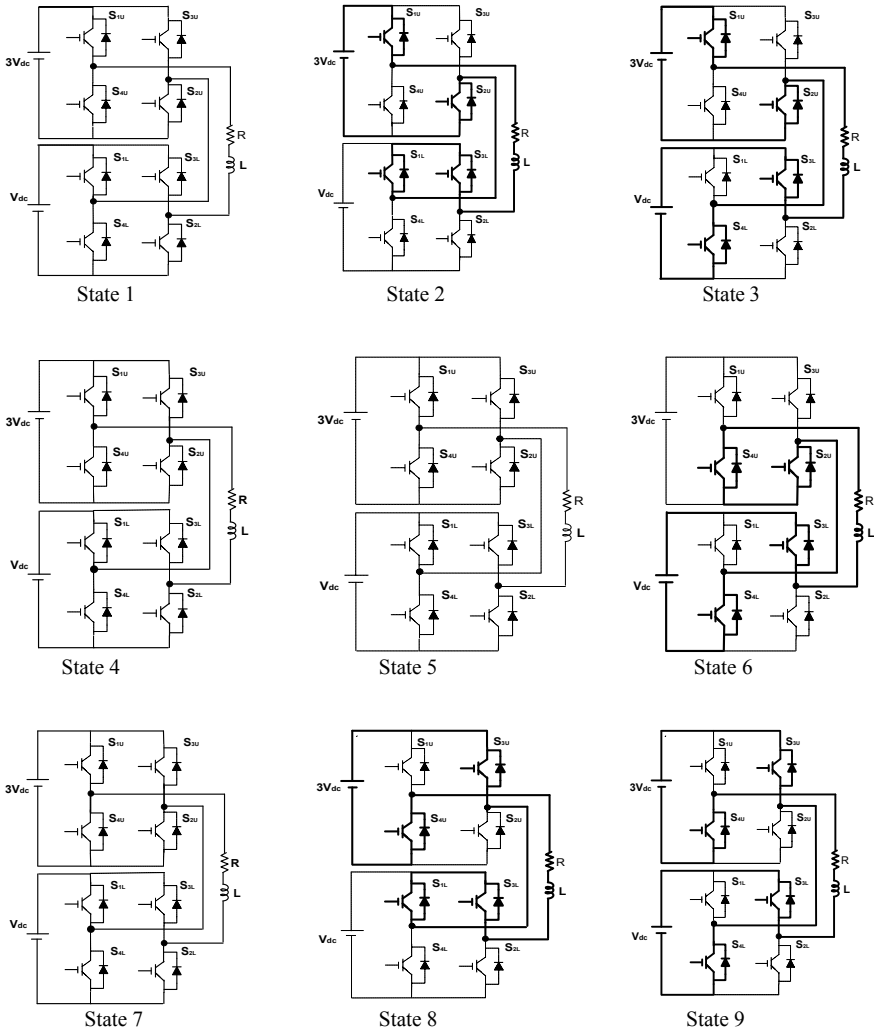
Fig. 4 **a** State 1 **b** state 2 **c** state 3 **d** state 4 **e** state 5 **f** state 6 **g** state 7 **h** state 8 **i** state 9

$$\text{Assume} \quad t = \frac{1}{\omega} \sin^{-1}\left(\frac{V_{dc}}{V_m}\right) \tag{4}$$

where $\omega = 2\pi f$.

Values for different instants have been calculated from Eqs. (2) and (4) (Fig. 8).
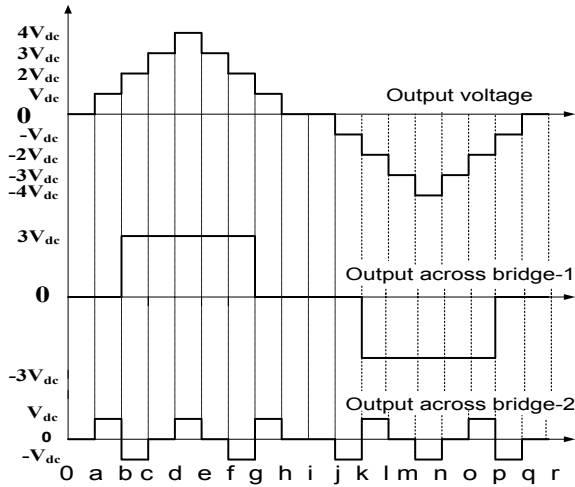
Fig. 5 Output across each H-bridge for nine levels
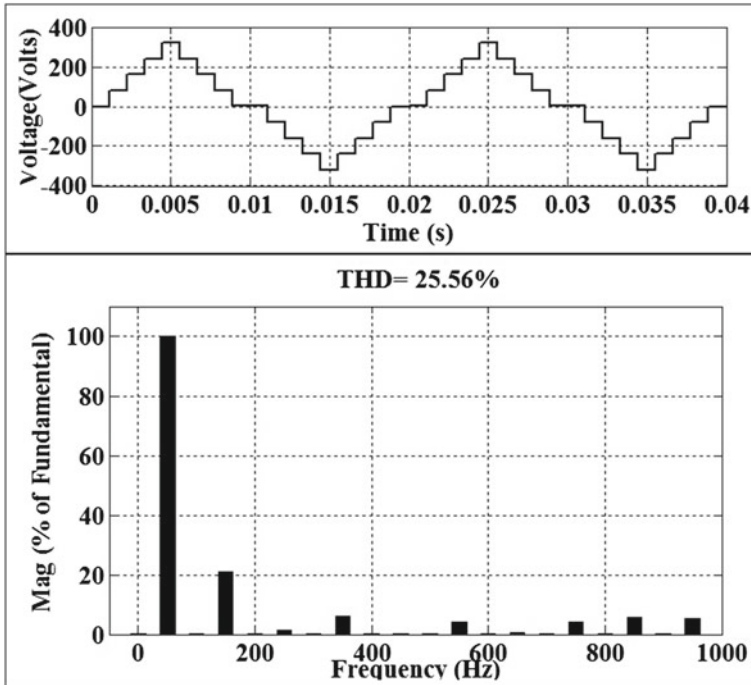
Fig. 6 Output voltage waveform along with THD for equal switching state
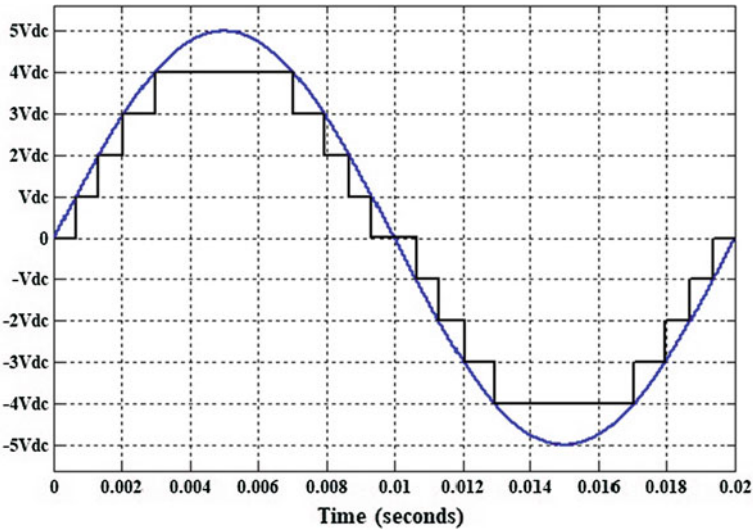
Fig. 7 Stepped output voltage waveform and its comparison with the sine wave

2.2 Development of Simulation Model

The repeating sequence block gives out a periodic scalar signal. Its dialog box has two parameters: a time value and the output value. This is done by changing the time value parameter of repeating sequence (Fig. 9).

3 Control of the Output Voltage

For the H-Bridge topology, two carriers waves are employed. There are two conventional pulse width modulation (PWM) schemes for MLI, i.e., phase-shifted modulation and level-shifted modulation. Level-shifted modulation generates output with lower THD [7]. It is further classified into three types.

(a) In-phase disposition (IPD): All the carrier waves are in the same phase but are level shifted with respect to one another.
(b) Alternate phase opposition disposition (APOD): All the adjacent carrier waves are out of phase by 150°.
(c) Phase opposition disposition (POD): All the carrier waves above zero level are out of phase by 180° with that of carrier wave below zero level.

Level-shifted modulation with in-phase opposition disposition (IPOD) shows better output with lower THD [7]. In all the multicarrier sinusoidal pulse width modulation schemes, sine wave is compared with reference triangular carrier wave.

Fig. 8 Output voltage waveform and its THD

(a) Switching Pulses for Bridge 1   (b) Switching Pulses for Bridge 2
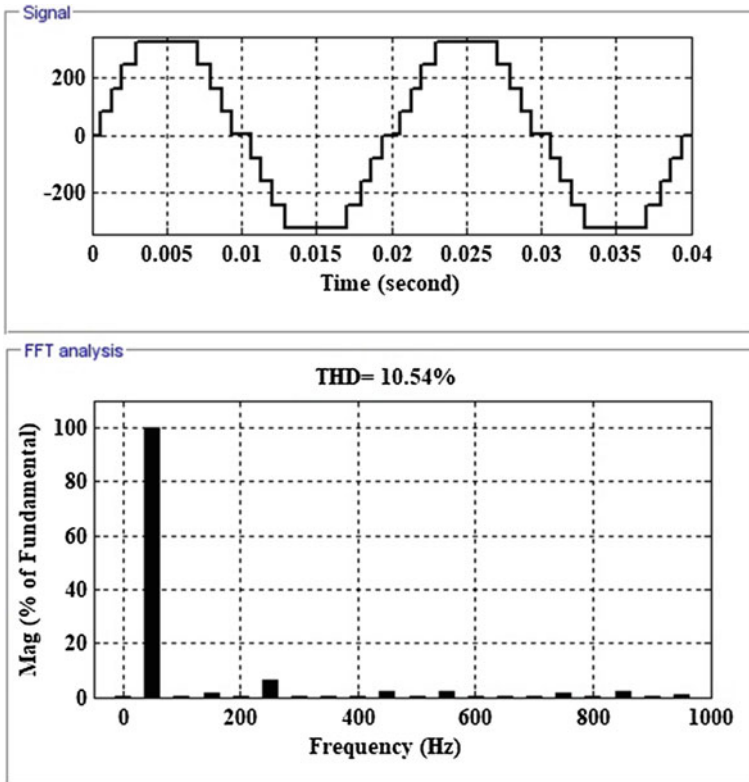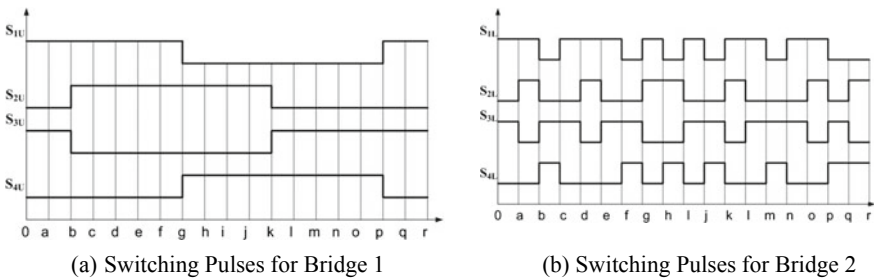
Fig. 9 **a** Switching pulses for bridge 1 **b** switching pulses for bridge 2

The instant when carrier wave becomes greater than the sine wave, the output of the comparator goes high. In simulation, the triangular wave or a carrier wave shown in Fig. 11 are generated using repeating sequence block and sine wave is generated using sine block available in the SIMULINK library browser. The frequency of sine
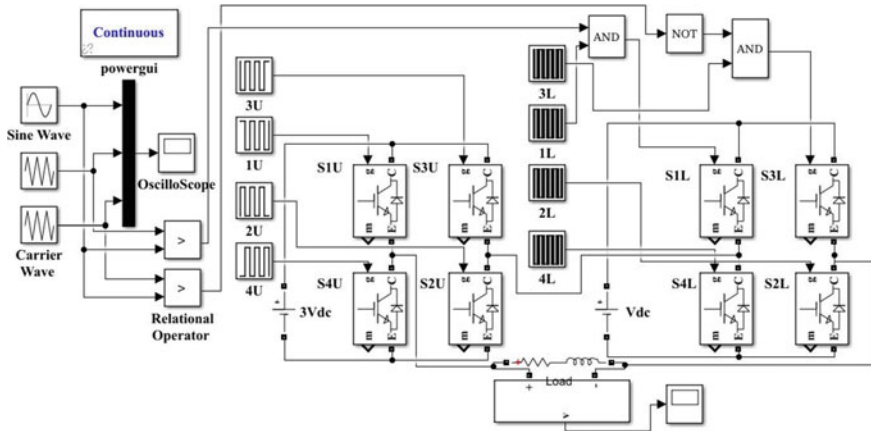
Fig. 10 Simulation model
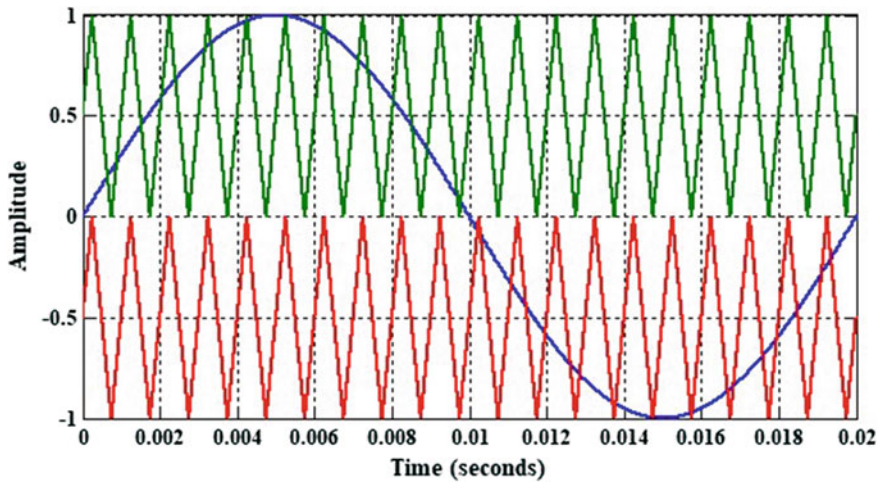
Fig. 11 Level shifted carrier wave

wave is taken 50 Hz and that of carrier wave is 1 kHz. Comparisons are made using a logical operator block, and by comparing the amplitude of sine wave and triangular wave the gating pulse is generated. The two-triangular carrier waves V_{cr1} and V_{cr2} are used to provide the gating pulse for the two IGBT switches S_{1U} and S_{3U} of H-Bridge (H1). The gate signal for the lower switches in H-bridge (H2) is complementary to their corresponding upper switches. The complete MATLAB®/ Simulink model of the proposed converter scheme is shown in Fig. 10. The modulated output voltage wave form is shown in Fig. 12. The THD of the output voltage and current wave form is shown in Figs. 13 and 14 respectively, with the
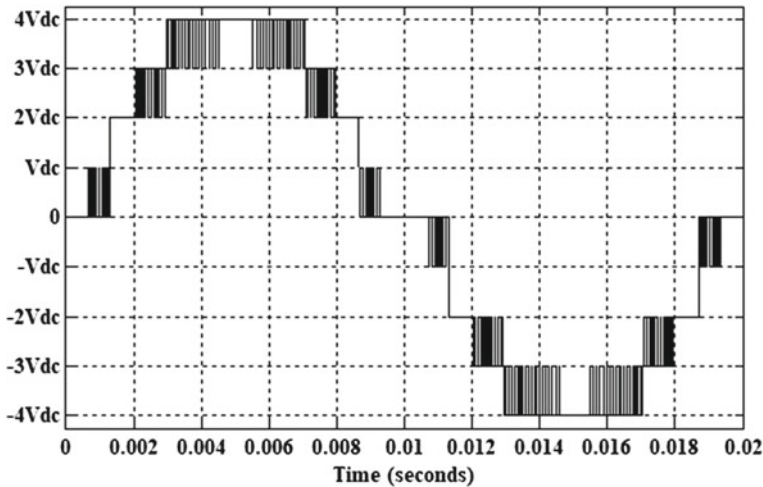
Fig. 12 Modulated output voltage

fundamental frequency of 50 Hz for two cycles. The variation of THD along with modulation index is shown in Fig. 15.

4   Hardware Implementations

The hardware implementation of the topology was performed to validate the proposed switching technique. Eight IGBTs with voltage and current ratings 1200 V, 50 A was used in the experiment. The switching technique was applied using DSP TMS320F28335 controller. Two DC power supplies of 45, 15 V provided the required voltages to the two H-bridges. Table 5 lists the specification of the equipment's used. Figure 18 shows the laboratory experimental setup. Figure 16a, b shows the switching pulses for upper and lower H-bridges, respectively.

Figure 17 shows the load voltage across the rheostat (400 Ω). The experimental results conform to the result obtained in the simulation.
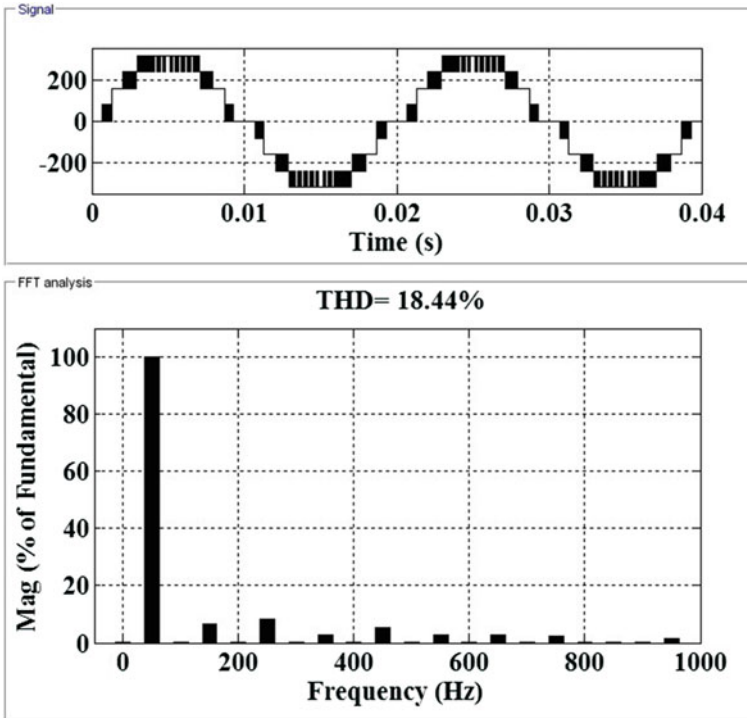
Fig. 13 THD of output voltage
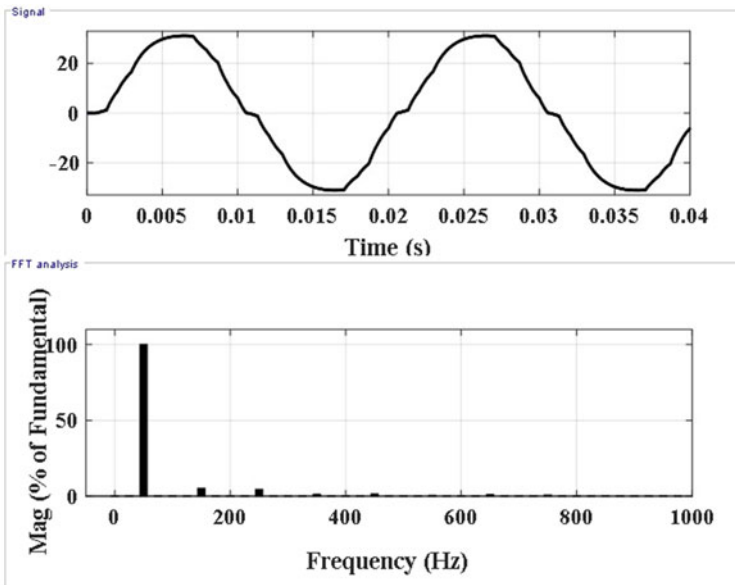
Fig. 14 THD of output current
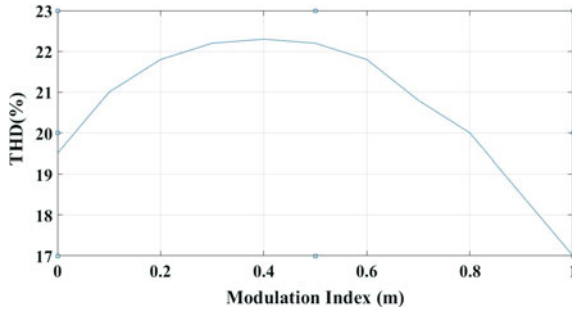
Fig. 15 Plot between THD versus *m*

(a). Switching pulse for H-bridge 1   (b). Switching pulse for H-bridge 2
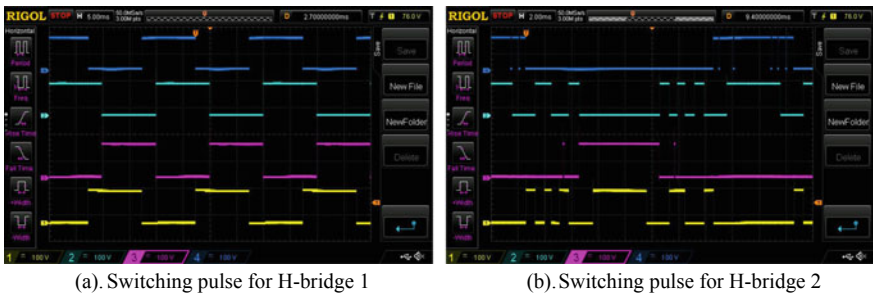
Fig. 16 a Switching pulse for H-bridge 1 **b** switching pulse for H-bridge 2

Fig. 17 Output voltage across the load

Table 5 Specification of the hardware implementation

S. No.	Parameters/components	Specifications
1.	Two DC supplies	15, 45 V
2.	Fundamental frequency	50 Hz
3.	Switching frequency	1 kHz
4.	Resistive load	400 Ω
5.	Eight IGBT	SKM75GB063D
6.	IGBTs driver circuit	TLP 250, ±12 V, 1 A
7.	DSP	TMS320F28335

Fig. 18 Laboratory experimental setup
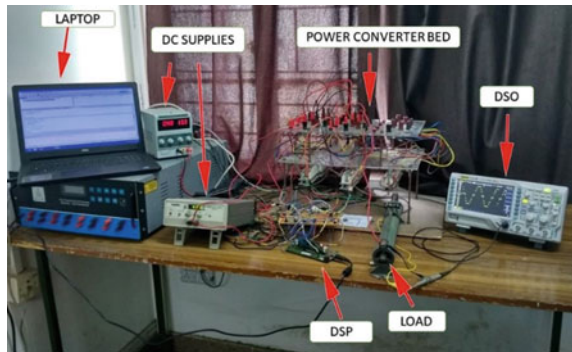
5 Conclusions

This paper investigated a new strategy to obtain nine-level output from a cascaded H-bridge multilevel inverter with reduced number of switches and sources. A strategy of overlapping the stepped output with a sinusoidal wave was successfully implemented to reduce the THD of the output voltage. The strategy has been validated with the experimental results.

References

1. Nabae, Takahashi I, Akagi H (1981) A new neutral-point-clamped PWM inverter. IEEE Trans Ind Appl IA-17(5):518–523
2. Tariq, Husain MA, Ahmad M, Tariq M (2011) Simulation and study of a grid connected multilevel converter (MLC) with varying DC input. In: 2011 10th international conference on environment and electrical engineering, Rome, pp 1–4
3. Lai J-S, Peng FZ (1996) Multilevel converters-a new breed of power converters. In: IAS '95 conference record of the 1995 IEEE industry applications conference thirtieth IAS annual meeting, vol 3, no 3, pp 2348–2356

4. Bharatiraja, Munda JL, Bayindir R, Tariq M (2016) A common-mode leakage current mitigation for PV-grid connected three-phase three-level transformerless T-type-NPC-MLI. In: 2016 IEEE international conference on renewable energy research and applications (ICRERA), Birmingham, pp 578–583
5. Rathore S, Kirar MK, Bhardwaj SK (2015) Simulation of cascaded H-bridge multilevel inverter using PD, POD, APOD techniques. Electr Comput Eng Int J 4(3):27–41
6. Sarwar A, Asghar MSJ (2010) Multilevel converter topology for solar PV based grid-tie inverters. In: 2010 IEEE international energy conference exhibition (ENERGYCON), pp 501–506
7. Tariq M, Bhardwaj S, Rashid M (2013) Effective battery charging system by solar energy using C programming and microcontroller. Am J Electr Power Energy Syst 2(2):41–43
8. Rodriguez-Rodríguez J, Venegas-Rebollar V, Moreno-Goytia E (2015) Single DC-sourced 9-level DC/AC topology as transformerless power interface for renewable sources. Energies 8 (2):1273–1290
9. Du Z, Ozpineci B, Tolbert LM, Chiasson JN (2009) DC–AC cascaded H-bridge multilevel boost inverter with no inductors for electric/hybrid electric vehicle applications. IEEE Trans Ind Appl 45(3):963–970
10. Tariq M, Iqbal MT, Meraj M, Iqbal A, Maswood AI, Bharatiraja C (2016) Design of a proportional resonant controller for packed U cell 5 level inverter for grid-connected applications. In: 2016 IEEE international conference on power electronics, drives and energy systems (PEDES), Trivandrum, pp 1–6
11. Tariq M, Iqbal MT, Iqbal A, Meraj M, Roomi MM, Khan MSU (2016) Comparative analysis of carrier schemes for PWM in multilevel PUC inverter for PV applications. In: 2016 4th international conference on the development in the in renewable energy technology (ICDRET), Dhaka
12. Wu (2006) High power converters and AC drives. IEEE press, Wiley, New Jersey, USA
13. Kavitha M, Arunkumar A, Gokulnath N, Arun S (2013) New cascaded multilevel inverter topology with reduced number of switches and sources. In: 2013 8th international conference on electrical and electronics engineering (ELECO), vol 2, no 6, pp 97–101
14. Kumar PS, Natarajan SP, Nachiappan A, Shanthi B (2013) Performance evaluation of nine level modified CHB multilevel inverter for various PWM strategies. Int J Mod Eng Res 3 (5):2758–2766
15. Murali Krishna T (2015) Matlab simulink modeling of hybrid cascaded five level inverter. Int J Sci Res 4(12):834–837
16. Kumar V, Mittal A, Saifee AH (2014) A new model of H-bridge multilevel inverter for reduced harmonics distortion. Int J Eng Res Appl 4(12):30–35
17. Tariq M, Iqbal MT (2014) Power quality improvement by using multi-pulse AC-DC converters for DC drives: modeling, simulation and its digital implementation. J Electr Syst Inform Technol 1(3):255–265

Performance Comparison of MCML and CMOS Inverters at High Operation Frequencies

Antriksh Sharma and Dileep Dwivedi

Abstract This paper presents a comparative study between the conventional CMOS technique and the MOS current mode logic. The basic inverter logic gate designed by both the styles has been analyzed by varying the power supply voltage as well as the frequency of operation. Power dissipation and delay generated by both the circuits have been investigated. A close inspection reveals that MCML technique proves to be far more superior to the currently existing CMOS style at higher frequencies of operation as its power dissipation is minimal when compared with CMOS. Results show that at high frequencies such as 9 GHz, the dissipation of power by MCML inverter is only 5.54 μW as compared to a much higher value of 13.612 μW that is dissipated by CMOS inverter.

Keywords CMOS · MOS current mode logic · Frequency · Power dissipation

1 Introduction

MOS current mode logic is seen as a substitute technique to the conventional CMOS style. A literature survey of the MOS current mode logic circuits was performed to develop a better understanding regarding the technique. In [1], a detailed design guideline has been presented emphasizing on the parameters which can be included while studying MCML. Also, an analytical formulation for the design parameters such as delay, DC voltage gain, noise margin, voltage swing ratio, signal slope ratio, power dissipation, current, voltage swing, and transistor sizes has been discussed. Testing has been performed on various test benches such as ring oscillators and clock distribution networks. An MCML exclusive OR gate

A. Sharma (✉) · D. Dwivedi
Guru Gobind Singh Indraprastha University, Sector 16 C, Dwarka 110078, Delhi, India
e-mail: antrikshsharma05@gmail.com

D. Dwivedi
e-mail: dileep.gcet@gmail.com

using triple cells and multi-threshold triple cells has been designed in [2]. It proposes a new low-voltage MCML XOR gate consisting of two triple-tail cells biased by separate current sources. This is an improvement over the traditional MCML XOR gate which consists of two levels of source coupled transistor pairs to implement the logic function along with a constant current source. A performance optimization of the MCML inverter circuit has been done in [3] by considering parameters such as figure of merit, load resistance, biasing voltage source, and the aspect ratio of the transistors. It also explains the trade-offs among the different parameters. A shallow-depth multiple-tail current mode logic style is highlighted in [4]. The overhead of tail current proves to be a prohibiting factor on circuit designs requiring low V_{DD}. The triple-tail cell technique is employed to combat this problem. This technique utilizes an active load in addition to a differential pair. Besides a single tail current, it employs three common-emitter transistors. This allows a minimization in the pair of transistors being used which further ensures a low supply voltage for low-voltage applications. The implementation of tristate buffers using the MOS current mode logic is explained in [5–10]. These buffers consist of three states of operation, namely high, low, and a high impedance state. An enable signal acts as a control signal which allows the buffer to function as a regular gate when disabled and enters a high impedance state when enabled. Existing buffer designs such as the switch-based, voltage follower-based, and low-power tristate buffers, have been presented along with their functionalities. A comparison between MCML and CMOS techniques is exhibited in [11] for low-power applications. The various parameters of MCML are studied and compared with those of CMOS. The changes in propagation delay with respect to supply voltage are seen for different current bias values of 1 mA, 1 μA, and 1 nA for MCML inverter and static inverter. The power delay product variations with the supply voltage have also been studied at 90 nm technology. The effects of length size for PMOS load and NMOS differential transistors are also taken into account. Variations in width size for PMOS load are also presented here. The newly designed D-latch, XOR/XNOR, and NAND/AND circuits are further optimized for applications requiring low-power and high-speed operations in [11].

2   Inverter Architecture

The conventional CMOS inverter is illustrated in Fig. 1, where P1 and N1 are the PMOS and NMOS transistors, respectively. A is provided as the input, and its complement A_bar is obtained as the output. The two merits of CMOS inverter stated in the literature are that, firstly, its power dissipation in steady state is almost negligible, except for that which occurs due to leakage currents. Secondly, a full voltage swing between 0 V and V_{DD} is exhibited by its voltage transfer characteristic (VTC), and this transition is very sharp quite often. Hence, this VTC shows a resemblance to that of an ideal inverter. MCML is a style of differential nature; i.e., differential inputs are provided to obtain differential outputs. As illustrated in

Fig. 1 CMOS inverter
schematic
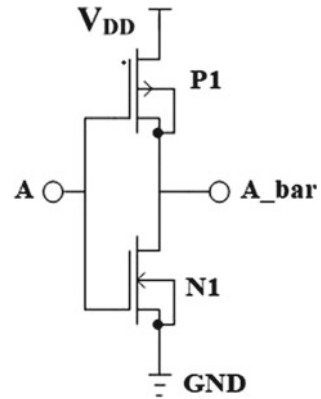
Fig. 2, an MCML inverter circuit consists of three major parts, namely the current
source Ns, the differential pair pull-down network N1, N2, and the load resistance.
The circuit outputs along with the inputs to the pull-down network are fully dif-
ferential. Properly biased PMOS devices such as P1 and P2 or linear resistors can
be used as the load. An NMOS device like Ns can be used to represent the constant
tail current source. Further, two NMOS devices namely N1 and N2 can also be used
as switches in the MCML circuit. The goal of the NMOS differential pair provides
the goal of switching the current provided by the current source from one side to the
other. The differential nature of the MCML circuit allows it to have an ON and OFF
branch. Ideal MCML circuits are perfect current switches in which all the current
I supplied by the current source traverses through the ON branch. Although, in
practice, a portion of current I flows through the OFF branch, thus causing a
reduction in the output voltage swing of the circuit. Transistor Ns operating in the
saturation region is responsible for controlling the tail current I_{ss}. The voltage levels
at the output are $V_H = V_{DD}$ at logic high and $V_L = V_{DD} - \Delta V$ at logic low where
$\Delta V = I_{ss} \times R$ is the logic swing. The biasing voltages of PMOS load P1, P2 and
NMOS current source Ns are V_{rp} and V_{rn}, respectively, in Fig. 2. The supply voltage
V_{DD} is kept as 1 V. V_{rp} is kept as 0.4 V, and V_{rn} can be varied to obtain optimum
results. V_{rp} is chosen such that PMOS pair operates in the triode region, whereas V_{rn}
is selected such that NMOS current source operates in the saturation region.

3   Results and Discussions

3.1   Variable Operating Frequency

A comparison between the MCML and CMOS inverters at different operating
frequencies reveals that at higher frequencies, MCML is better than CMOS in terms
of power dissipation as displayed in Table 1. It can be observed that the power

dissipated by CMOS at 0.5 GHz is a meager 1.27 μW, while that of MCML at the
same frequency is 5.57 μW. This indicates that at lower frequencies, CMOS is a
suitable candidate for designing. However, the MCML inverter shows promise in
terms of delay at lower operating frequencies. At 0.5 GHz, MCML displays a delay
of 534.6 ps which is far lower than the CMOS delay of 783.27 ps. Thus, it can be
deduced that although MCML is agile at lower frequencies, it tends to dissipate
more power in comparison with CMOS. Up to a certain frequency, CMOS seems to
have supremacy over MCML. However, as the frequency is further increased, a
change in trend is detected at around 2.5 GHz. At this frequency, it is discovered
that the CMOS power dissipation starts to escalate, while that of MCML dimin-
ishes. To balance this out, an increase in delay is perceived for MCML, whereas
CMOS delay now starts decrementing. After 2.5 GHz, MCML starts displaying
better statistics for power dissipation and a moderate performance in delay.
As the frequency is further increased, it is seen that at 9 GHz, the CMOS power
dissipation becomes extreme around 13.61292 μW, while MCML dissipates only
5.540349 μW at this frequency. Moreover, the MCML shows an almost constant
dissipation from 2.5 to 9 GHz. To maintain a constant power delay product, the
propagation delay of MCML is higher than CMOS at this frequency. However, the
delay is in picoseconds and hence can be considered for optimal circuit operation.
This behavior can be attributed to the fact that the dynamic power dissipation of

Table 1 Power and delay comparisons between CMOS and MCML inverters at different operating frequencies

Frequency (GHz)	Power (µW)		Delay (ps)	
	CMOS	MCML	CMOS	MCML
0.5	1.27	5.57	783.27	534.6
1.0	2.51	4.67	283.27	535.95
2.0	4.71	5.63	33.26	159.6
2.1	4.98	5.64	13.26	149.6
2.2	5.02	5.647	10.26	148.1
2.3	5.421	5.655	1.38	143.1
2.4	5.62	5.663	3.15	138.6
2.5	5.840	5.671	7.19	134.6
2.6	6.015	5.680	11.24	130.6
2.7	6.192	5.689	14.77	127.1
2.8	6.426	5.701	18.31	123.6
2.9	6.638	5.710	21.34	120.6
3.0	6.828	5.723	23.86	118.1
3.5	7.904	5.806	36.46	105.6
3.6	8.165	5.827	38.46	103.6
3.8	8.637	5.872	41.95	100.1
3.9	8.107	5.896	43.42	98.6
4.0	11.080	5.277	57.97	103.68
6.0	15.679	6.324	6.27	51.6
7.0	16.008	6.104	12.137	45.8
8.0	12.12	5.537	3.77	26.99
9.0	13.612	5.540	7.51	23.24

MCML is lower at higher frequencies since only the static power dissipation is dominant for MCML. CMOS on the other hand dissipates dynamic power due to switching events of the load capacitor. The power and delay comparisons between the CMOS and MCML inverters are illustrated in Figs. 3 and 4, respectively.

3.2 Variable Power Supply Voltage

Process limits place an upper bound on the power supply voltage. However, for a reduced power consumption, it is required that V_{DD} be kept as low as possible for proper circuit operation. A direct relation exists between the power supply voltage and power consumption. Power consumption increases linearly as the supply voltage is increased. In MCML circuits, the NMOS current source provides a crucial lower limit on the power supply voltage. If V_{DD} is decreased too much, the output impedance of current source is affected and it gets pushed beyond saturation region. This leads to deterioration in the current matching ratio (CMR) which further diminishes the gate current. Concurrently, a decrement is also observed in
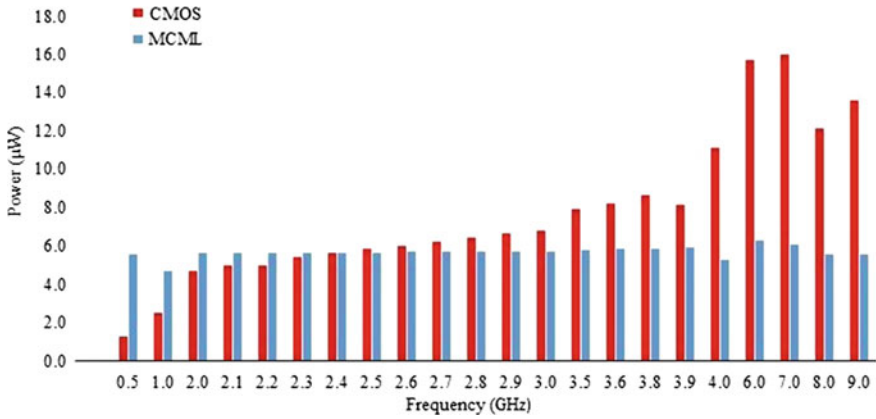
Fig. 3 Power comparison at different operating frequencies
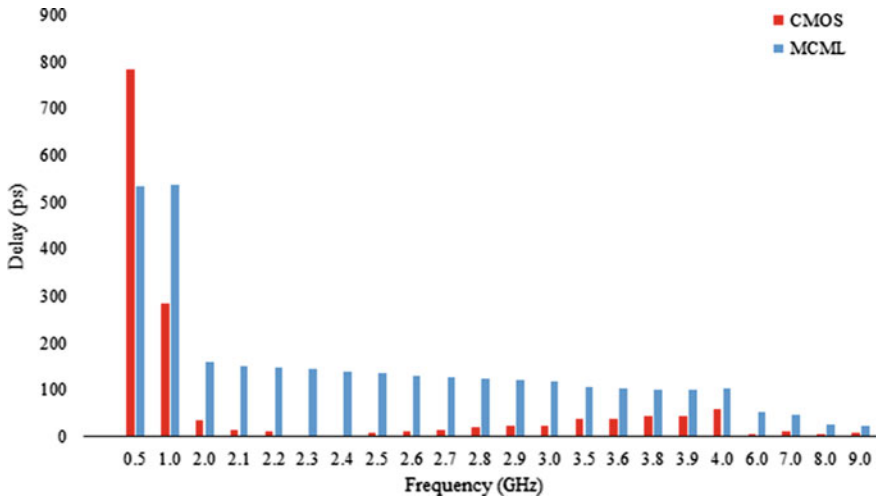
Fig. 4 Delay comparison at different operating frequencies

the DC voltage gain (A_V). Table 2 represents the inverter circuit behavior when different supply voltages are applied. The range of supply voltage is taken from 0.6 to 5 V. As can be seen, the power dissipated by MCML inverter is fairly low in comparison with the CMOS inverter at each supplied voltage. MCML delay is higher than CMOS in order to maintain the constant power delay product. Figure 5 illustrates the power comparison between MCML and CMOS inverters at a frequency of 2.5 GHz graphically. As can be seen, the power dissipated by CMOS is higher than MCML as the supply voltage is increased, keeping the frequency of operation constant at 2.5 GHz. Figure 6 represents the delay comparison between

Table 2 Power and delay comparisons between CMOS and MCML inverters at different supply voltages

V_{DD} (V)	Power (μW)		Delay (ps)	
	CMOS	MCML	CMOS	MCML
0.6	2.104	2.04	6.380	134.00
1.0	5.84	5.67	7.199	134.60
1.5	15.33	13.89	4.140	134.92
1.8	24.57	20.69	12.309	134.92
2.5	57.72	44.87	48.490	132.51
3.0	95.15	68.37	48.800	132.25
4.0	196.4	131.11	50.6	132.07
5.0	359.9	211.63	55.7	120.8
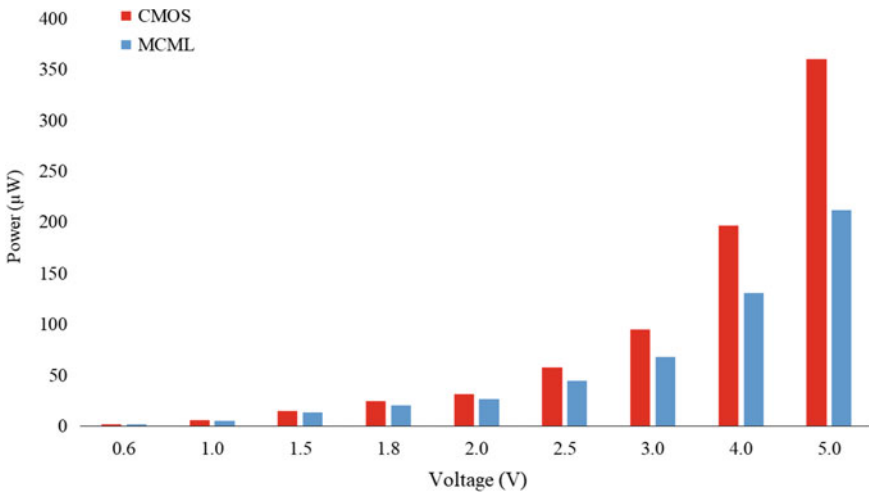
Fig. 5 Power comparison at 2.5 GHz for different supply voltages

CMOS and MCML inverters at 2.5 GHz. It can be observed that the delay of MCML inverter is higher than CMOS. The delay of CMOS inverter keeps on escalating as the supply voltage is increased, whereas at high power supply a decrease in MCML delay is observed.

4 Conclusion

An elaborate comparison between the MCML and CMOS inverters was presented in this work. Variable supply voltage and operating frequency were taken as the parameters under observation. The power dissipation and delay generated for each
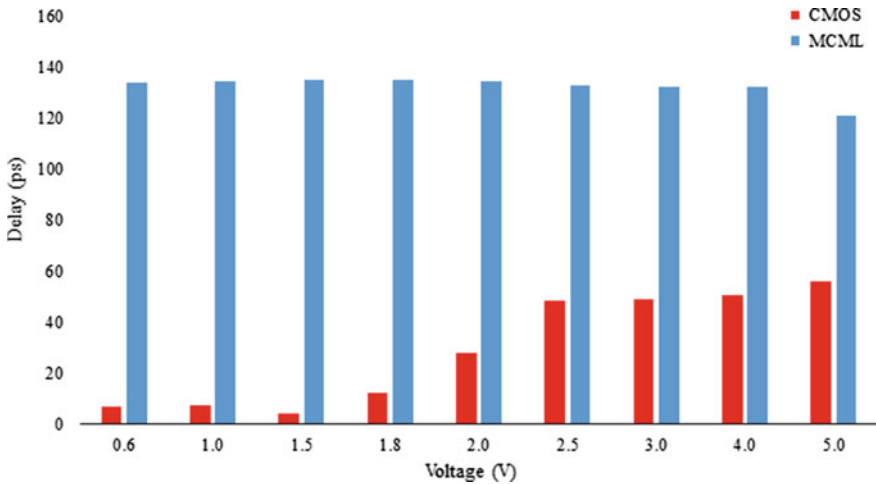
Fig. 6 Delay comparison at 2.5 GHz for different supply voltages

of the inverter design was attained. It is deduced that at high frequency of operation, MCML is the better candidate for circuit design. The MCML advantages and disadvantages in comparison with the CMOS. The literature survey performed depicts the various advances that have been made with the MCML logic style till date. The basic MCML functioning was also studied which has led to the belief that MCML is a technique of differential nature which allows the inputs as well as outputs to be differential. The study also reveals that at high frequencies the power dissipated by MCML is negligible as static power dissipation is dominant in MCML due to the presence of a constant current source, whereas CMOS dissipates more power and has larger dynamic power dissipation because of faster switching required by the load capacitance to charge and discharge at higher frequencies.

References

1. Hassan H, Anis M, Elmasry M (2005) Design and optimization of MOS current mode logic for parameter variations. Integr VLSI J 38(3):417–437
2. Gupta K, Pandey N, Gupta M (2013) Analysis and design of MOS current mode logic exclusive-OR gate using triple-tail cells. Microelectron J 44(6):561–567
3. Sharroush SM (2016) Performance optimization of MOS current-mode logic. In: International conference on electrical, electronics, and optimization techniques (ICEEOT). IEEE, Mar 2016, pp 2915–2920
4. Ghaznavi-Ghoushchi MB, Ejtahed SAH (2017) MTCML: analysis, design and optimization of an alternative shallow-depth multiple-tail current mode logic. Microelectron J 67:57–70
5. Badel S, Leblebici Y (2007) Tri-state buffer/bus driver circuits in MOS current-mode logic. In: Research in microelectronics and electronics conference, 2007. PRIME 2007, Ph.D. IEEE, July 2007, pp 237–240

6. Golshan R, Haroun B (1994) A novel reduced swing CMOS BUS interface circuit for high speed low power VLSI systems. In: 1994 IEEE international symposium on circuits and systems ISCAS '94, vol 4. IEEE, May 1994, pp 351–354
7. Louis L (1999) A self-sensing tri-state pad driver for control signals of multiple bus controller. In: Proceedings of the IEEE international symposium on circuits and systems, pp 447–450
8. Chao HJ, Johnston CA, Smoot LS (1989) A packet video/audio system using the asynchronous transfer mode technique. IEEE Trans Consum Electron 35(2):97–105
9. Gupta K, Pandey N, Gupta M (2013) Low-power tri-state buffer in MOS current mode logic. Analog Integr Circ Sig Process 75(1):157–160
10. Pandey N, Choudhary B (2015) Improved tri-state buffer in MOS current mode logic and its application. Analog Integr Circ Sig Process 84(2):333–340
11. Ali LS, Mahmod ZR (2013) Comparison between MCML and CMOS digital circuits for using ADS simulation. Al-Rafadain Eng J 21(1)

Performance Analysis of Sierpinski Carpet Fractal Antenna for Wireless Communication

Pawan Bhutani, Shweta Sagar and Abhijeet Kumar

Abstract The proposed multiband Sierpinski carpet fractal antenna is designed, modeled, simulated, and fabricated for the radiation characteristics up to 10 GHz for wireless communication system applications. Different aspects of design, fabrication, and analysis have been discussed in the paper. Sierpinski carpet antenna is simulated and fabricated up to third iterations simulated using Ansoft's HFSS v 13 fabricated using FR-4 epoxy ($\varepsilon = 4.4$) as substrate. The simulated results can be optimized to operate in multiple bands between 2 and 10 GHz and are matched with the experimental results. The graph for return loss demonstrates the multiband characteristics of antenna in the desired frequency range. The VSWR is approximately 1.03. Also, radiation and gain graphs show minimum loss in side lobes. The efficiency of the antenna is roughly 60%.

Keywords Multiband · Carpet fractal antenna · Return loss · VSWR · Efficiency

1 Introduction

There is an ever-surging demand for concise and mobile communication devices in the current world of wireless communication. There is also a need to evolve antenna design to minimize the size and other tangible parameters. There is also a need to evolve antenna designs to minimize the size just as the size of circuitry has evolved to transceivers on a single chip. A number of mobile devices utilize the concept of simple monopole using the matching circuit design. If monopoles were very short

P. Bhutani (✉)
School of Engineering, Noida International University, Greater Noida 203201, UP, India
e-mail: pvbhutani@gmail.com

S. Sagar · A. Kumar
ECE Department, HMRITM, Hamidpur, Delhi, India
e-mail: shweta.hmritm@gmail.com

A. Kumar
e-mail: abhijeetkmr07@gmail.com

compared to the wavelength, the radiation resistance would decrease and stored reactive energy increases and the radiation efficiency would decrease. Resultantly, matching circuitry tends to be complicated. Fractal antenna can be tested as a solution by minimizing antenna dimensions. It has a large effective length as well as the perimeter of its shape can generate a capacitance or inductance which can be used to improvise the antenna with the circuit design. They can demonstrate a number of shapes and sizes. The prime goal of the analysis of fractal antenna arrays is to obtain the special antenna traits by the use of fractal distribution of elements. Generally, the conventional antenna array system designs are band-limited because the array spacing depends on the operational frequency. A better control of side lobes can be obtained by the use of random fractals which reduce the fractal dimension. It has also been found that the current distribution on the array affects the fractal dimension of the radiation pattern. In short, it can be drawn that fractal properties such as self-similarity and dimension play a key role in the design of such arrays.

Fractal shapes have unique mathematically geometrical have unique geometrical traits naturally present in the nature. The same theory can be used to explain branching of tree leaves, coastal lines, rough surfaces, etc. The fractal antennas have been used as an effective technique to design and fabricate generally antennas with multiband characteristics. They show unique features due to their geometrical shapes. Generally, an increase in number of iterations can lead to improvement in various performance parameters of a fractal antenna. The microstrip antenna is cost-effective, easy integration with RF-enabled devices and systems, etc. A fractal geometrical shape is a rough one that can be divided into parts that is basically is the copy of the parent shape. It is an antenna which can utilize the same to maximize perimeter of the material which can transmit or receive electromagnetic waves within a specific surface area. The example of the same can be fractal electrodynamics. Fractal antenna has numerous traits like it can operate as multiband or wideband, frequency independence, compact size, etc. It also has a unique feature of fractal loading which adds capacitance and inductance.

2   Carpet Antenna Design

In today's world, there is an ever-evolving requirement of concise, compact, and mobile communication systems. There is also a need to evolve antenna design to minimize the size, etc. Sierpinski carpet fractal antenna is simulated and fabricated up to third iterations simulated using Ansoft's HFSS v 13 fabricated using FR-4 epoxy ($\varepsilon = 4.4$) as substrate. The one of the most important advantages of the antennas is its multiband behavior at reduced size. Increased bandwidth and multiband characteristics leading to improved one can be obtained leading to improved voltage standing-wave ratio (VSWR) and return losses on the basic shape on performing. Fractal antennas take various forms and shapes. In first iteration, the equally spaced squares are placed on the substrate, and the basic square patch is

segmented by removing the middle square from it, by taking scale factor 1/3. For second iteration, same procedure is done by taking scale factor 1/3 and same done for third iteration also. There is also an intimate relationship between antenna dimensions (shapes) and the wavelength. It says that if the size of an antenna is less than $\lambda/4$, then an antenna does not perform as desired due to some loss in gain and bandwidth. Fractal antennas are feed through microstrip feeding technique. The location of microstrip feed to the patch is adjusted to match with its input impedance (usually 50 Ω) with perfect matching as per requirements. The electromagnetic (EM) waves propagate through the lateral side of the antenna.

First Iteration

See Figs. 1 and 2.

Second Iteration

See Figs. 3 and 4.

Third Iteration

See Figs. 5, 6, and Table 1.

Return loss for various iterating loops had been achieved. With increase in iterative loops, the resonant frequency shifts to higher side. The return loss achieved in third function is best among all, and the bandwidth requirement is less in third iterative loop. The multiband nature is achieved, and the efficiency is best among all. The antenna is designed on HFSS and simulated at a frequency of 2.364 GHz.

Voltage Wave Standing Ratio (VWSR) is a performance parameter of the reflection coefficient that measures the power reflected from an antenna. It is a
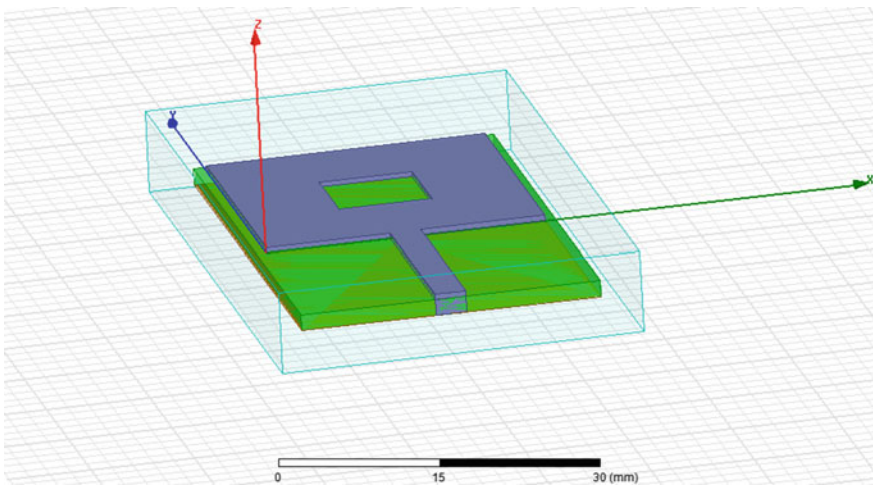
Fig. 1 Sierpinski carpet antenna screenshot for first iteration
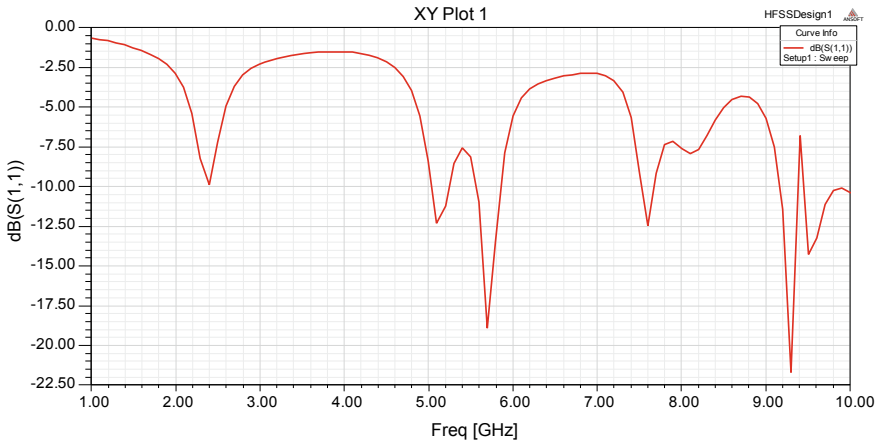
Fig. 2 Return loss of first iteration
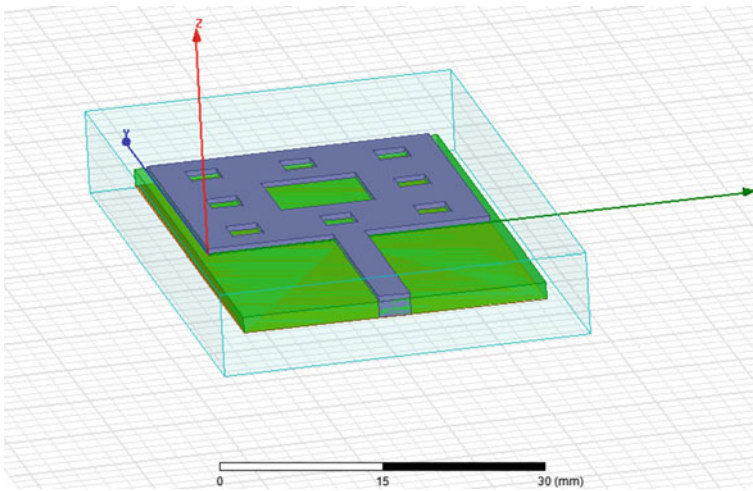
Fig. 3 Sierpinski carpet antenna screenshot for second iteration

quantity which deals with impedance matching of an antenna. It describes power reflected from an antenna (Fig. 7).

Gain is a parameter that estimates the degree of directivity of radiation pattern of an antenna. The gain of an antenna is the ratio of maximum radiation intensity in a particular direction to the maximum radiation intensity from a referenced antenna generated in the same direction with same power input. The third iteration having the maximum gain with increasing the iteration gain of the antenna increases (Fig. 8).
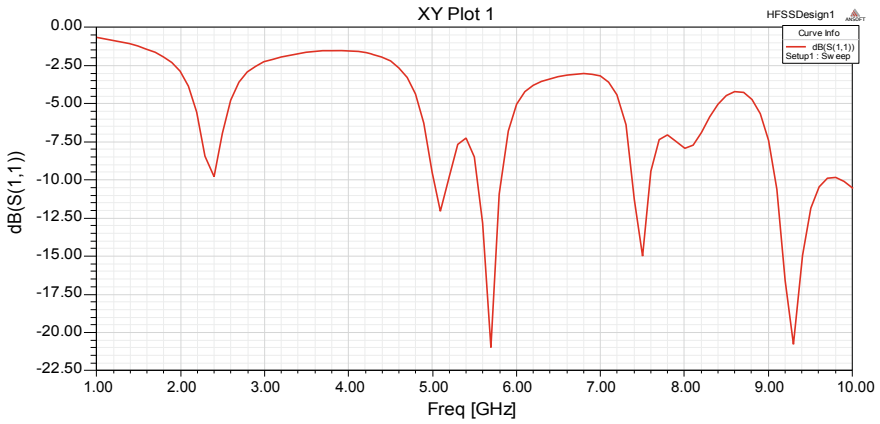
Fig. 4 Return loss of second iteration
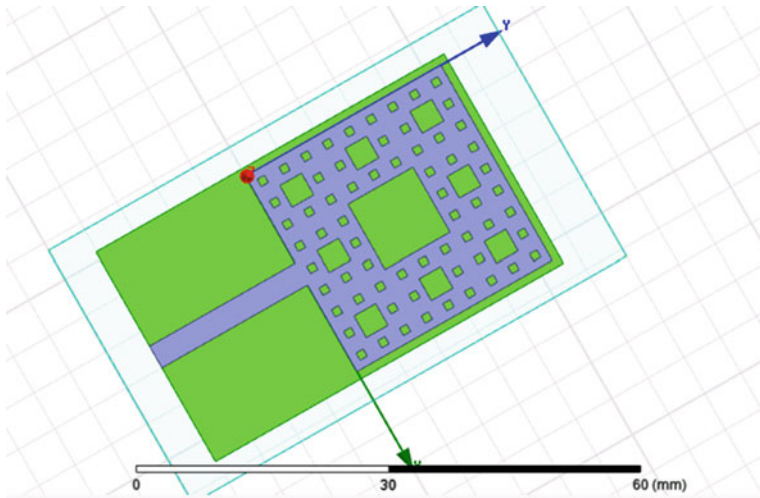
Fig. 5 Sierpinski carpet antenna screenshot for third iteration

3 Results and Analyses

Simulated results are obtained by simulating the antenna at a frequency of 2.364 GHz. The graph for return loss demonstrates the multiband characteristics of antenna in the desired frequency range. The VSWR is approximately 1.03. Also, radiation and gain graphs show minimum loss in side lobes. The efficiency of the antenna is roughly 60%. The feature of self-similarity feature definitely helps in improving multiband and Ultra Wide Band (UWB) properties of the antennas (Fig. 9).
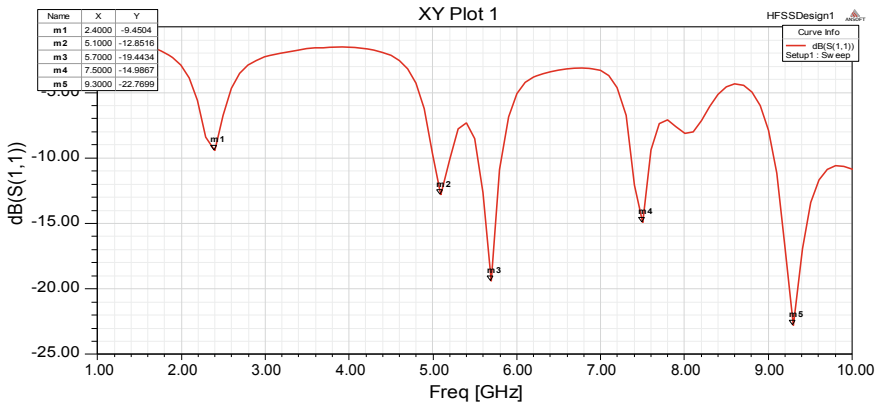
Fig. 6 Return loss of third iteration

Table 1 Antenna specification

Length of patch (mm)	Width of patch (mm)	Permittivity of substrate (FR-4)	Height of substrate (mm)
27	27	4.4	1.6
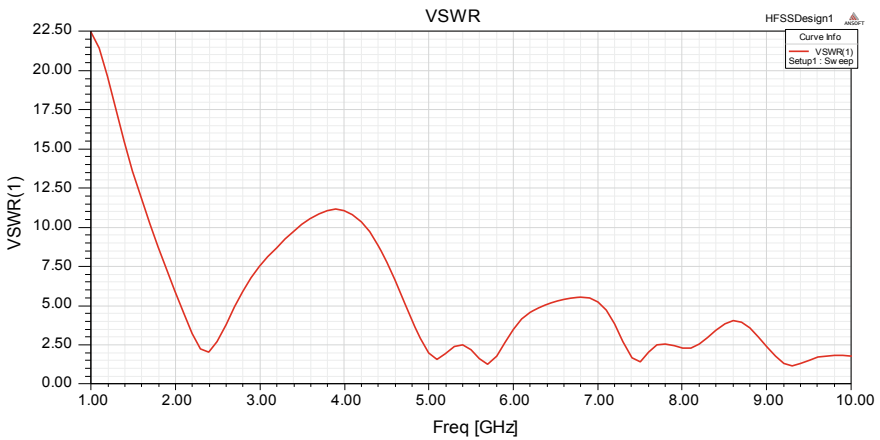
Fig. 7 VSWR for third iteration

A network analyzer is a device which can be used to measure the response of electronic at RF and microwave frequencies. It is basically used to devices, components, and circuits. It contains multiple receivers that demonstrate amplitude and phase normally in a format of ratio. It generally works on the principle of a
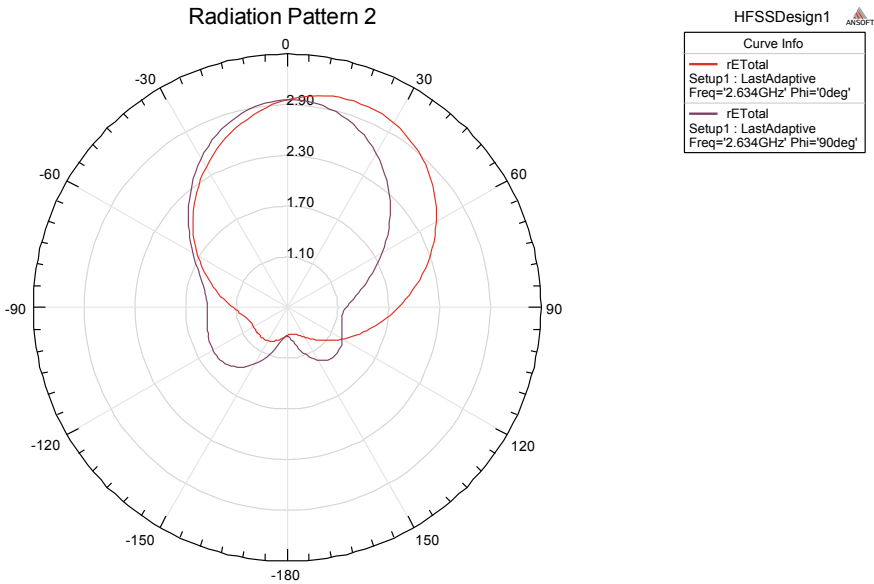
Fig. 8 Gain of the carpet antenna
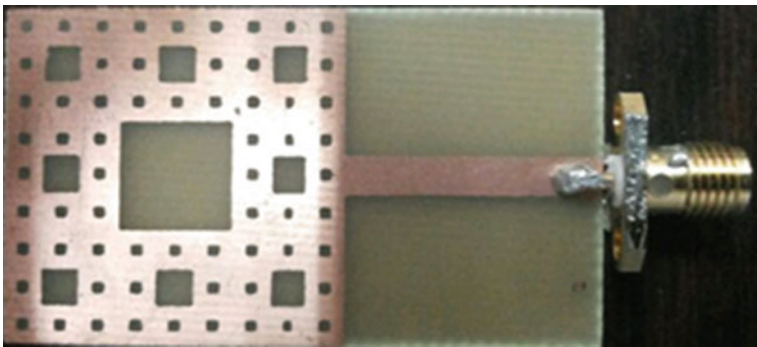
Fig. 9 Fabricated antenna with SMA connector

predetermined frequency as it is a stimulus–response system at the output of the device under test. Last but not least, it shows greater measurement precision with its vector error correction feature.

The results are obtained by connecting antenna to network analyzer using SMA connector. The return loss obtained on network analyzer demonstrates that antenna has the characteristics of multiband behavior. This vividly shows the return loss achieved at multiple frequencies is below −10 dB, and thus, it has wideband features.

4 Future Work

The design of the antenna can be further improved with different parameters such as thickness, dielectric constant, and type of the substrate. In the future, possibilities in designing microstrip antenna with different patch shapes and sizes are crucial. A study can be carried out in iteration and array of carpet antennas for better results and all. These antennas can be utilized to identify geological faults, natural resource location, etc. (Figs. 10 and 11).

5 Conclusion

Different aspects of design, fabrication, and analysis have been discussed in the paper. The Sierpinski carpet antenna has been simulated and fabricated up to third iterations simulated using Ansoft's HFSS v 13 fabricated using FR-4 epoxy ($\varepsilon = 4.4$) as substrate. The proposed multiband Sierpinski carpet fractal antenna is designed, modeled, simulated, and fabricated for the radiation characteristics from 1 to 10 GHz for the wireless communication applications. However, an optimum selection of position of the feed is crucial for better results. It is vividly noted that with an increase in the number of iterations, bandwidth of the antenna also increases and the antenna begins to demonstrate multiband behavior on second and third iterations. The antenna too exhibits very good matching and radiation efficiencies.

Fig. 10 Antenna connected to network spectrum analyzer

Fig. 11 Result using network analyzer

It is noticed that the increase in the number of iterations has led to overall improvement in the VSWR and the return loss. Finally, these types of antennas find various applications in wireless communication system designs where size reduction and shape variations are one of the key factors.

References

1. Balanis C (1997) Antenna theory analysis and design, 2nd edn. Wiley, New York
2. Jibrael FJ, Hammed MH (2010) A new multiband patch microstrip plusses fractal antenna for wireless applications. ARPN J Eng Appl Sci 5(8):155–158
3. Aggarwal A, Kartikayen MV (2010) Design of Sierpinski carpet antenna using two different feeding mechanism for WLAN applications. IEEE
4. Kumar R, Malathi P (2010) Design of CPW-fed ultra wide band fractal antenna and backscattering reduction. J Microw Optoelectron Electromagnet Appl 9(1):10–19
5. Lizzi L, Oliveri G (2010) Hybrid design of a fractal shaped GSM/UTMS antenna. Microw Opt Technol Lett 50(3):825–829
6. Vinoy KJ, Jose KA, Vardan VK, Vardan VV (2001) Hibert curve fractal antenna: a small resonant antenna for VHF/UHF applications. Microw Opt Technol Lett 29:215–219
7. Blairada CP, Romeu J, Pous R, Cardama A (1998) On the behaviour of the Sierpinski multiband fractal antenna. IEEE Trans Antennas Propag 46(4):517–524
8. Shanmuganathan T, Mohanmurli R (2012) Sierpinski carpet fractal antenna for multiband applications. Int J Comput Appl (0975-8887) 39(14):19–23

9. Naghshvarian-Jahromi M (2008) Novel wideband planar fractal monopole antenna. IEEE Trans Antennas Propag 56(12):3844–3849
10. Qiu J, Lin S, Yang C, You Q (2005) A novel printed fractal log-periodic dipole antenna. In: International IEEE proceedings, pp 50–53
11. Wang B, Chen A, Su D (2008) An improved fractal tree log-periodic dipole antenna. In: IEEE proceedings, pp 831–834
12. Moallemizadeh A, Hassani HR, Nezhad SMA (2013) Wide bandwidth and small size LPDA antenna. In: International IEEE proceedings, pp 1–3
13. Werner DH, Werner PL, Ferraro AJ (2006) Frequency independent features of self-similar fractal antennas. In: IEEE proceedings, vol 3, pp 2050–2053
14. Karim MNA, Rahim MKA, Majid HA, Ayop O, Zubair et al (2010) Log periodic fractal koch antenna for UHF band applications. PIER 100:201–218
15. Werner DH, Ganguly S An overview of fractal antenna engineering research. IEEE antennas
16. Khan SN, Hu J, Xiong J, He S (2008) Circular fractal monopole antenna for low VSWR UWB applications. Progress Electromagnet Res Lett 1:19–25

Design and Performance Analysis of Round Micro-Strip Patch Antennae 2 × 4 Array for 2.40 GHz Wireless Demands

Anurag Verma, Arun Kumar and Saptarshi Gupta

Abstract This paper introduces the plan and reproduction of roundabout-shaped micro-strip-plotted antennae showing wideband working frequencies for different remote applications. This micro-strip antenna will provide the wide transmission capacity or bandwidth (BW) which is required in different applications like satellite, SiriusXM Radio, Wi-Fi, Bluetooth, mobile phones, remote correspondence etc. The coaxial feeding method is used to excite the antenna structure. The execution of the composed antennae was dissected as far as return loss; Gain, BW, VSWR, and radiation pattern. The outline is streamlined to meet the most ideal outcome. A substrate of low dielectric steady is chosen to acquire a smaller transmitting structure that meets the requesting BW capacity. The proposed antenna is planned by Fr4_epoxy substrate which has a dielectric consistency of 4.40. The outcomes demonstrate that the antenna structure can work from 1.7 to 3.3 GHz band with optimum frequency at 2.40 GHz. The reflection coefficient at the contribution of the improved roundabout-formed micro-strip antenna is underneath—10 dB over the whole recurrence L- and S-bands. The outcomes of proposed design are in great concurrence with the HFSSv15.0 simulation outcomes.

Keywords Circular-shaped patch antenna array · Fr4_epoxy substrate · HFSSv15 software · Wireless communication

A. Verma · A. Kumar (✉) · S. Gupta
Department of Electronics and Communication Engineering,
SRM Institute of Science & Technology, NCR Campus, Modinagar,
Ghaziabad, UP, India
e-mail: arunvlsi83@gmail.com

A. Verma
e-mail: anurag1091994@gmail.com

S. Gupta
e-mail: ece.saptarshi@gmail.com

1   Introduction

At a present scenario cell phone or portable wireless device are become daily need
in society and all of these equipments requires antenna for proper transmission
(Tx) and reception (Rx) of the signal.

In the current years, there is an extraordinary need for lightweight and
low-profile antenna prepared to do great execution over an extensive variety of
frequencies. Use of single element antenna most of the times can not produce
required pattern (radiation) and the desired gain so, in this context array can be
utilize to overcome the above said shortcommings.

The radio waves emanated by every individual reception apparatus to join and
superpose. Array structure improves the overall antenna gain as well as directivity.
Large and sufficient amount of antenna gain can be achieved with the increase in the
quantity of antenna element in an array. Some extreme example of antenna array
can be seen in defence application where one complete array can be the combi-
nation of some hundred to thousand individual antenna element. Design of antenna
arrays can increase the gain or directivity of the antenna structure which can be
useful for direction finding application in a particular direction.

The patch antenna is normally made of driving materials, for instance,
Fr4_epoxy and the geometrical structure of the patch can be of any possible
shape (rectangular, circular, triangular etc.). The transmitting patch and coaxial
support are photoscratched on the dielectric substrate. The patch could be
empowered by various ways, for instance, micro-strip line feed, coaxial wire feed,
aperture coupling feed, and proximity coupling feed. The coaxial cable feed is easy
to manufacture and very popular because this technique exhibit good radiation
pattern and provide moderate amount of spurious radiation.

2   Related Work

Keshtkar et al. [1] proposed an antenna array which is examine and tested with the
simulation software and the results of the proposed antenna is satisfactory as
requirements. The purpose of this antenna design was to get a gain of 12 dB, a
satisfactory case, and a sensible estimation of SWR for altimeter system applica-
tion. The reception apparatus has been intended to be utilized as a part of altimeter
framework application, in the C-band. This antenna was intended to work for
4.3 GHz and 12 dB gain. The array design which is used for the specific application
contains the four circular elements and these elements are placed in an equal
spacing. Planned reception apparatus has been demonstrated great execution
regarding return loss and radiation (a model has been manufactured and tested).

Upadhyay et al. [2] suggested an array of antenna which is suitable for the
S-band applications. The shape of the antenna is round about. The extensive
number of antenna component, the better gain of reception apparatus exhibit is

accomplished. In this paper, sustaining component and power divider are utilized to outline the 4×1 small-scale strip patch antenna cluster. Smaller scale strip line sustains and power dividers are utilized to configuration parallel micro-strip patch reception apparatus exhibit. The deliberate radiation example and return loss of 4×1 component antenna cluster are exhibited. In this paper, 4-component parallel micro-strip patch antenna exhibits by gap sustain stacked at S-band are displayed. They accomplish higher gain and better data transmission with down-to-earth innovation and hypothetical examination. In this paper, S-band micro-strip patch antenna clusters might be utilized in correspondence connections, searchers, and recognition exhibits. In the proposed antenna design the increased thickness of the substrate is responsible for increment of the impedance bandwidth.

Vasujadevi Midasala et al. [3] proposed a 3×3 antenna array which consisting of 6 individual rectangular shaped antenna elements, which is proposed to work at Ku-band. The suggested antenna has been design with the array of patches (six numbers). All the elements in the antenna are placed in a such manner that the cross polarization and the side lobe level fulfill the requirements. The working frequency of groups are shaped into 12.0–18.0 GHz. The major parameters of the designed antenna has been found in good agreement. With the help of HFSS 14.0 the design has been simulated. The simulator software works based on Finite Element Methods (FEM) and all the parameters are simulated and tested using FEM. The main shortcoming of this paper is that they do not analyze the design with network analyzer.

Kwaha et al. [4] developed the FORTRAN programs to reenact fundamental parameter of microwaves round antenna. These parameters are the genuine radius and effective radius of patch, conductance because of radiation, conductance because of conduction, conductance because of dielectric loss and resistance—input side and quality factors (QF) because of conductions, dielectric loss, and radiation. In this designed antenna the power handling capacity is more or improved due to the substrate selection. Radius of the patch is reduced while the frequency of operation increase (patch radius 0.2374 and 0.05079 cm and the operating frequency are 10 and 45 GHz respectively). The outcomes acquired in this outline contrast positively with the results are obtained from manual calculation of similar parameters.

3   Design Methodology

The HFSS software v15.0 of circular patch antenna array design for 2.40 GHz is used.

3.1 Examination of Antenna Method

The full wave show is the most mind-boggling. It is extremely exact in the plan of limited and unbounded exhibits or stacked structures.

$$S = E \times H$$

where S = Poynting vector
E = electric field intensity
H = magnetic field intensity

The intricate fields E and H are related to their counterparts (instantaneous) [5, 6].

$$\left.\begin{array}{l} E(x, y, z, t) = \mathrm{Re}[E(x, y, z)\mathrm{e}^{iwt}] \\ H(x, y, z, t) = \mathrm{Re}[H(x, y, z)\mathrm{e}^{iwt}] \end{array}\right\}$$

Use this equation $\mathrm{Re}[X\mathrm{e}^{iwt}] = \tfrac{1}{2}[X\mathrm{e}^{iwt} + X^*\mathrm{e}^{iwt}]$ than upper equations as:

$$S = 1/2\,\mathrm{Re}[E \times H] + 1/2\,\mathrm{Re}\left[E \times H\mathrm{e}^{iwt}\right]$$

Thus, the time normal Poynting vector can be composed as:

$$\mathrm{Sav} = 1/2\,\mathrm{Re}[E \times H]\ \mathrm{W\,m}^{-2}$$

The factor ½ shows up in light of the fact that the E- and H-fields are crest esteems and not rms.

3.2 Design Analysis of 2 × 4 Round Patch Antennae Arrangement

See Fig. 1 and Table 1.

3.2.1 Circular Patch Radius and Effective Antenna Radius

The measurement of the patch is dealt with a round circle; the real range of the patch is given by [7]:
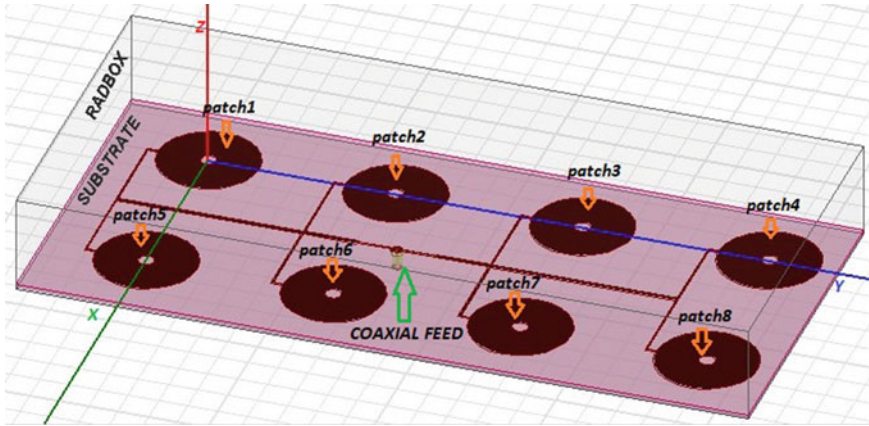
Fig. 1 Circular patch antenna 2 × 4 array design

Table 1 Calculated values for the proposed antenna array

Substrate material	Fr4_epoxy, $\varepsilon_r = 4.4$
Substrate width (S_w)	115.7 mm
Substrate length (S_l)	244.4 mm
Substrate height (S_h)	1.6 mm
Circular patch (All)	
Patch radius (a)	17 mm
Patch mid-cut radius (a_r)	2.6 mm
Radbox material	Vacuum, $\varepsilon_r = 1$
Radbox width (R_w)	115.7 mm
Radbox length (R_l)	244.4 mm
Radbox height (R_h)	32.85 mm
Coaxial feed	
Probe material	Pec, $\varepsilon_r = 1$
Probe radius	0.35 mm
Probe height	1.6 mm
Pin material	Pec, $\varepsilon_r = 1$
Pin radius	0.7 mm
Pin height	5 mm
Coax material	Teflon, $\varepsilon_r = 2.1$
Coax radius	1.6 mm
Coax height	5 mm
Source radius	1.6 mm
Ground width (G_w)	115.7 mm
Ground length (G_l)	244.4 mm

$$a = \frac{F}{\left\{1 + \frac{2h}{\pi \varepsilon_r F}\left[\ln\left(\frac{\pi F}{2h}\right) + 1.7726\right]\right\}^{\frac{1}{2}}}$$

where a = Patch radius
h = Substrate height
ε_r = Substrate material dielectric constant.

Range of the patch condition does not contemplate the bordering impact. Since bordering makes the patch electrically bigger, the viable span of patch is utilized. The patch effective radius is calculated by [8]:

$$a_e = a\left\{1 + \frac{2h}{\pi \varepsilon_r a}\left[\ln\left(\frac{\pi a}{2h}\right) + 1.7726\right]\right\}^{\frac{1}{2}}$$

where a_e = Patch effective radius.

Then, the thunderous recurrence for the predominant mode is TM_{110}^Z. Resonant frequency is [9]:

$$(f_r)_{110} = \frac{1.8412 v_0}{2\pi a_e \sqrt{\varepsilon_r}}$$

where f_r = Resonant frequency of substrate
v_0 = Light speed (free space).

3.2.2 Ohmic Resistance

The speculation of most outrageous power trade communicates that for the trading of most noteworthy power from a source with settled inward impedance to the store, the impedance of the stack must be the same of the source.

$$Z_0 = \left\{\begin{array}{ll} \frac{60}{\sqrt{\varepsilon_{\text{eff}}}}\ln\left[\frac{8h}{W_0} + \frac{W_0}{4h}\right], & \frac{W_0}{h} \leq 1 \\ \frac{120\pi}{\sqrt{\varepsilon_{\text{eff}}}\left[\frac{W_0}{h} + 1.393 + 0.667\ln\left(\frac{W_0}{h} + 1.444\right)\right]}, & \frac{W_0}{h} > 1 \end{array}\right\}$$

3.2.3 Resonant Input Impedance

The info impedance of a round patch at reverberation is genuine, and the infor-mation control is free of sustain spot area on this loop. Taking reference of nourish point at $\emptyset' = 0°$ information protection at any spiral separation $\rho' = \rho_0$ from the focal point of the patch can be composed as [7]:

$$R_{\text{in}}(\rho' = \rho_0) = \frac{1}{G_t} \frac{J_m^2(k\rho_0)}{J_m^2(ka_e)}$$

For roundabout patch reception apparatus, the thunderous information protection with an inset nourish is:

$$R_{\text{in}}(\rho' = \rho_0) = R_{\text{in}}(\rho' = a_e) \frac{J_m^2(k\rho_0)}{J_m^2(ka_e)}$$

where

$$R_{\text{in}}(\rho' = a_e) = \frac{1}{G_t}$$

3.2.4 Strip Line Connector

Each of the patches is connected to 100 Ω feedline. The equivalent of the junction of the two 100 Ω lines is 50 Ω. Feedline is connected to coaxial cable feed. Inter-element spacing should be between $\frac{\lambda}{2}$ and λ.

$$\text{Lambda}\,(\lambda) = \frac{C}{f}$$

4 Model Design and Simulation

4.1 Dielectric substrate: Fr4_epoxy

Substrate length $(S_l) = (6h) + P_l = 24.44\,\text{cm}$
Substrate width $(S_w) = (6h) + P_w = 11.57\,\text{cm}$
Substrate height $(h) = 0.16$ cm
where P_l = Patch length
P_w = Patch width.

4.2 Patch

4.2.1 Creation of Array

Given: f_r = resonant frequency = 2.4 GHz
ε_r = dielectric constant = 4.40

h = substrate height = 0.16 cm

$$F = \frac{8.791 \times 10^9}{f_r \sqrt{\varepsilon_r}} = 1.746227$$

Given: $F = 1.746227$

$\pi = \frac{22}{7}$

$$a = \frac{F}{\left\{1 + \frac{2h}{\pi \varepsilon_r F}\left[\ln\left(\frac{\pi F}{2h}\right) + 1.7726\right]\right\}^{\frac{1}{2}}} = 1.70 \text{ cm}$$

4.2.2 Cut of Mid-radius of Array Patch

Mid-radius of patch array $(a_r) = \left(\frac{a}{4h \text{ or } 5h}\right)$.

4.3 Ground

Ground length $(G_l) = (6h) + P_l = 24.44$ cm.
Ground width $(G_w) = (6h) + P_w = 11.57$ cm.

4.4 Radiation Box

Radbox length $(R_l) = (6h) + P_l = 24.44$ cm.
Radbox width $(R_w) = (6h) + P_w = 11.57$ cm
Radbox height $(R_h) = \left(\frac{\lambda}{4}\right) + h = 3.285$ cm.

5   Result and Discussion

5.1   S11 Response and Bandwidth

S_{11} is return loss as characterized as transmission capacity. From the figure, obviously the arrival loss at the resounding recurrence 2.40 GHz is −27.0727 dB. The bandwidth achieved is 137.80 MHz (Fig. 2).

5.2   VSWR

The VSWR (Voltage Standing Wave Ratio) is a measure that depicts how well the gathering mechanical assembly is impedance facilitated to the radio or transmission line it is related to VSWR. For a good designed antenna this parameter value must be lies between 1–2. VSWR value 1 indicates no mismatch between feed line and antenna. For Proposed design VSWR value is 1.1098 (Fig. 3).

5.3   Fresnel Pattern

Radiation design is identified with the radiation of the antenna exhibit. In the field of antenna plan, the term radiation suggests the directional dependence of the nature of the radio waves from the antenna or other sources (Fig. 4).
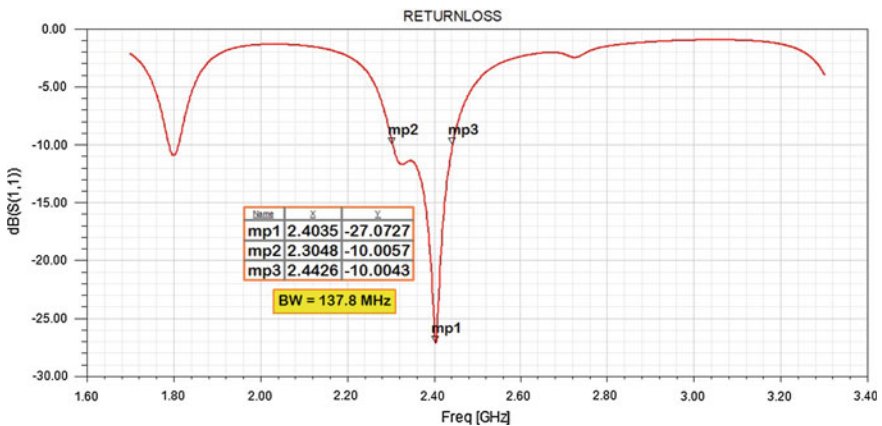
Fig. 2 S_{11} response of 2 × 4 array (circular patch)
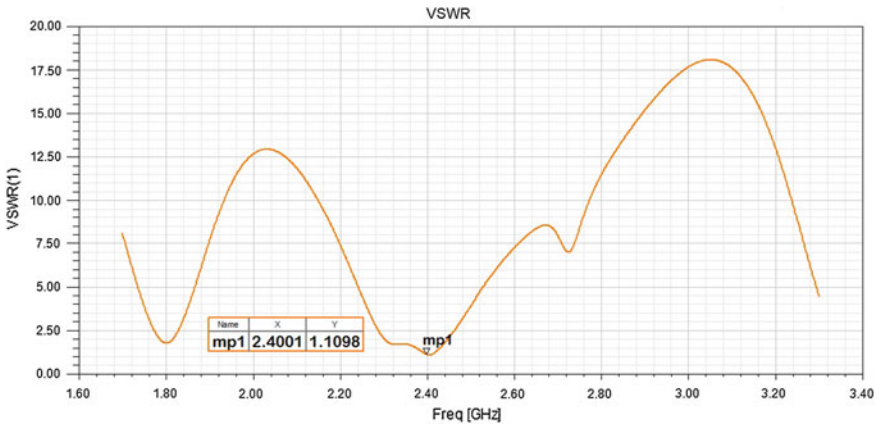
Fig. 3 VSWR

Fig. 4 Radiation pattern
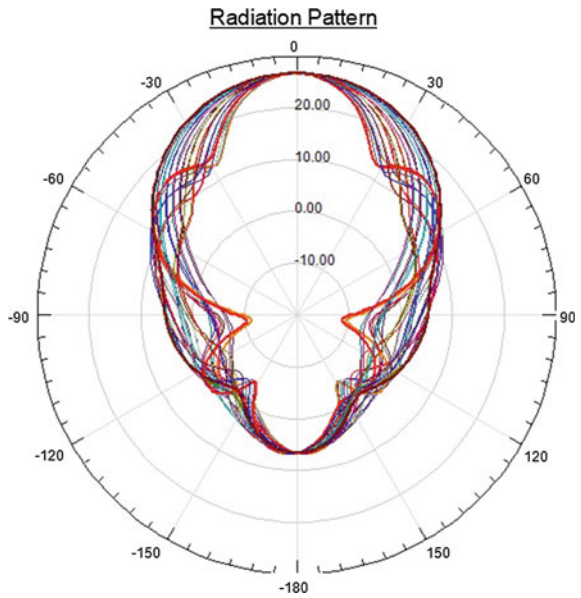
5.4 Antenna Gain

In spite of the fact that the gain of the antenna is firmly identified with the directivity, it is a measure that considers the effectiveness of the reception apparatus and additionally its directional abilities. Proposed antenna exhibits 8.9 dB gain, that is, the indication of a good design antenna (Fig. 5).
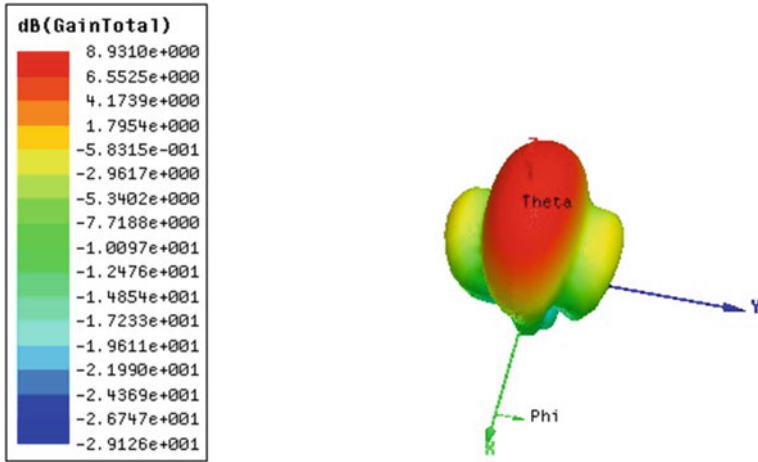
Fig. 5 Antenna gain

5.5   *E-field* $(\phi = 0°)$

This is lies between $\phi = 0°$ and $\theta = -180° < 0° < 180°$ (Fig. 6).

5.6   *Field Overlays*

Field overlays are two parts of the antenna design of the wireless communication. *E*- and *H*-field overlays find (mag_E, vector_E) and (mag_H, vector_H) (Fig. 7).

Fig. 6 E-field

(a) mag_E-field overlay

(b) vector_E-field overlay

(c) mag_H-field overlay

(d) vector_H-field overlay
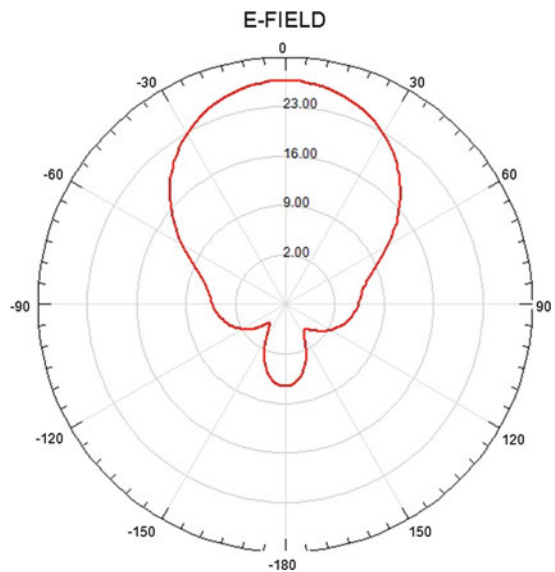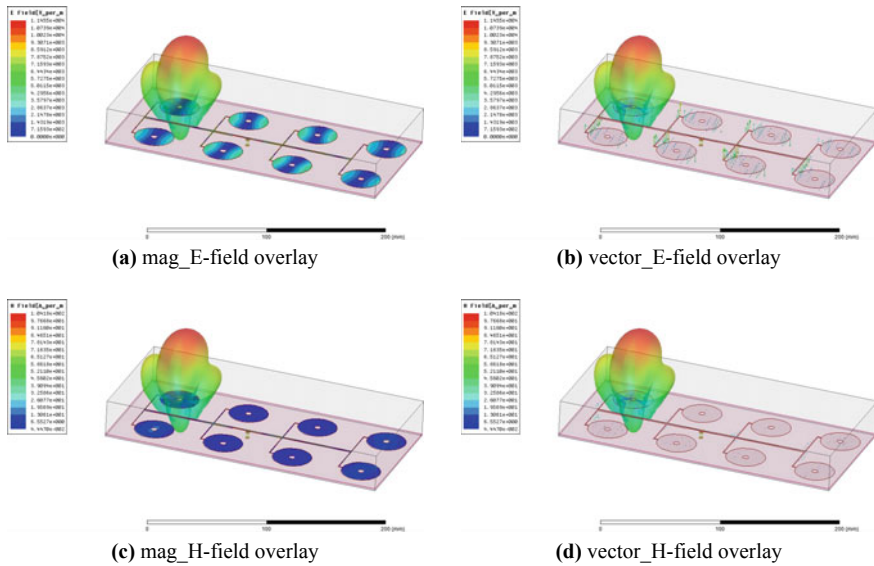
Fig. 7 **a** mag_E-field overlay, **b** vector_E-field overlay, **c** mag_H-field overlay, **d** vector_H-field overlay

6 Conclusion

This paper proposes a 2×4 array of circular micro-strip patch antenna in the ground plane to enhance the gain and bandwidth. In one way, this 2×4 array of circular micro-strip patch antenna acts as defected ground structure and allows antenna to resonate at additional bands. This causes enhancement in the bandwidth and gains with 2.4 GHz at operating band. The antenna model occupies compact size with stable radiation pattern and gains over the better operating band. An average gain of 8.9 dB is the feature of this proposed antenna. The prototyped antenna on Fr4 substrate provides excellent correlation with simulation results obtained from commercial HFSS tool. The 2×4 array of circular micro-strip patch antenna etched on the ground plane provides path for additional resonant frequencies and enhancement in the bandwidth. This model can be extended with multiple-split-ring resonator in the ground plane as well as can be enhanced by the impedance bandwidth. Conformal structure of this antenna model is also one of the challenging tasks to attempt for vehicular applications.

References

1. Keshtkar A, Keshtkar A, Dastkhosh AR (2008) Circular microstrip patch array antenna for C-band altimeter system. Int J Antennas Propag 2008:1–7
2. Upadhyay P, Sharma V, Sharma R (2012) Design of microstrip patch antenna array for WLAN application. IJEIT 2(1):2008–2010
3. Midasala V, Siddaiah P (2016) Microstrip patch antenna array design to improve better gains. Procedia Comput Sci 85:401–409
4. Kwaha B, Inyang ON, Amalu P (2011) The circular microstrip patch antenna-design and implementation. IJRRAS 8(1):86–95
5. Richards WF (1988) Microstrip antennas. Theory, application and design. Van Reinhold Co., New York
6. Gonca C (2005) Design, simulation and tests of low-cost microstrip patch antenna arrays for the wireless communication. Turk J Elect Engin 13(1):93–103
7. Balanis CA (2016) Antenna theory analysis and design. Wiley
8. Shen L, Long S, Allerding M, Walton M (1977) Resonant frequency of a circular disc, printed-circuit antenna. IEEE Trans Antennas Propag 25(4):595–596
9. Watkins J (1969) Circular resonant structures in microstrip. Electron Lett 5(21):524

Comparative Evaluation of Cluster-Head Selection Algorithms for Wireless Sensor Networks

Tanvi Sood and Kanika Sharma

Abstract The self-organizing wireless sensor networks (WSNs) have become an important research area in the emerging technologies. For several years, these remotely deployed WSNs have laid many unparalleled challenges to the researchers like overall energy efficiency, network lifetime, secure data transmission and aggregation of the collected data. Depending on the network orientation, WSN may either have a flat architecture or a clustered architecture. Over the years, clustering has become an essential research area as clustered WSN has been observed to have an advantage of several features like better lifetime, energy efficiency and throughput over flat WSN. Clustering has become an efficient criterion for a better data transmission through the network using relevant cluster-head selection algorithms. The prime objective of this paper is to survey and evaluate several cluster-head selection algorithms on various clustering strategies. Based on these clustering strategies, comparison of the clustering algorithms has been done.

Keywords Clustering algorithms · Cluster-head selection strategies · Wireless sensor network · Clustering · Clustering analysis · Comparative analysis · Survey

1 Introduction

In recent years, many technological advancements are being made in low-powered miniaturized designs of battery-operated motes (or sensor nodes) in WSNs [1]. Since the basic component of a sensor network, i.e. sensor nodes, can detect ambient data of real-time environment, they are being increasingly employed for many critical applications like monitoring of the environmental conditions, home

T. Sood (✉) · K. Sharma
Department of Electronics and Communication Engineering,
Panjab University, Chandigarh 160019, India
e-mail: ece.tanvisood@gmail.com

K. Sharma
e-mail: kanikasharma80@yahoo.com

applications, socio-economic areas, military applications and many more commercial applications [2, 3]. The WSN may sometimes be deployed in a natural harsh phenomenon or in any disastrous environment or even in emergency-based operations where the applications demand sensor networks to hold an efficient fault-tolerant capability for a high quality response. Since, sensor network is a collection of randomly deployed hundreds or thousands of motes, it is necessary that when a WSN is faced with any atrocious environment that demands a quick efficient response, failure of any one mote should not lead to the network failure. Failure is incurred only if the central monitoring system does not have a complete or a partial global knowledge of the network in question as every sensor node has its own function to perform [4].

The sensor nodes are dropped randomly by a chopper at the application-affected areas and have a short lifespan since they are battery-powered and their energies cannot be replenished. These sensor nodes cover a very large area and may even be redundant in number since they are dropped in hundreds/thousands of number (see Fig. 1). Hence, it is essential that energy-efficient algorithms/protocols be defined for prolonging the sensor network lifespan [5–7].

Given the immense area to be dealt with these sensor nodes of the network, out of the hundreds or thousands of nodes deployed, some may be redundant for the network while some essential nodes may get damaged. Envisioning the loss that these nodes may incur, lead to the designing of energy-aware algorithms which became an important factor for increasing the network's lifespan [8]. Hence, development of clustering-based energy-aware algorithms became the prime research issue as a clustered architecture was found the most energy-efficient solution to the failed connectivity of the nodes comprising the WSN [9].
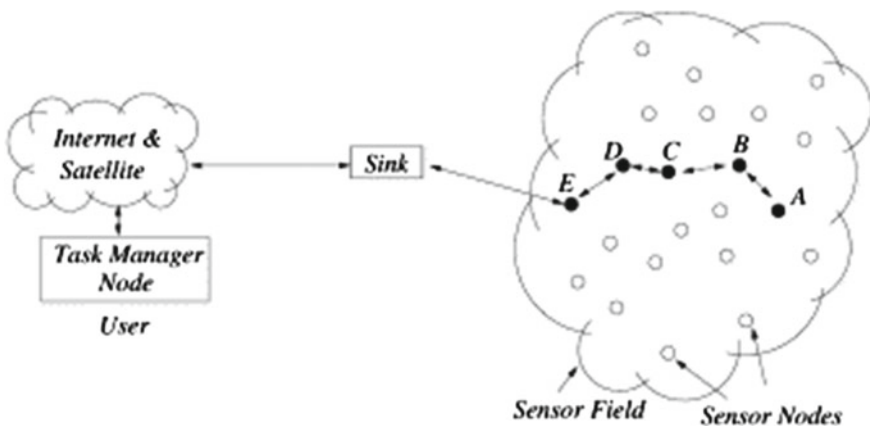
Fig. 1 Wireless sensor network [10]

2 Clustering

In a network of plurality of sensor nodes, where each node engages itself in data transmission, it is essential that the network does not experience congestion or collisions. To make sure the network does not run out of its limited energy source, it is important that the central monitoring unit of the network has partial or complete global knowledge of the network to fend off the unnecessary failure of the network. Clustering plays a vital part in averting this failure while also maintaining scalability, efficient resource usage and load balancing in the WSN.

A WSN has two basic components, i.e. a Base Station (BS)/Sink (see Fig. 2) and motes (see Fig. 3). The motes interact amongst themselves and with the BS which may either be laid locally or remotely. Grouping these motes, which have limited capacity and irreplaceable power source, into clusters has become a prime objective in the research community [1].

Efficient organization of nodes into clusters reduces the energy dissipation of the WSN to a large extent. The clustering technique involves segregating the network of thousands of nodes into clusters which are each governed by a single cluster head (CH) (see Fig. 4). These CHs are either pre-assigned by the central monitoring unit or elected by the sensor nodes of the network. These CHs are either fixed for the lifetime of the network or variable depending upon few parameters defined by the central monitoring unit. WSN can either be homogeneous in nature where all nodes all the same resources and have the same functions to perform or can be heterogeneous in nature where nodes vary in terms of the resources they have and the functions they perform. Therefore, CHs can either be any one of the nodes like in homogeneous WSN or be the one with higher resources in heterogeneous WSN [14, 15].

To generate stable clusters in WSN, several clustering algorithms were proposed but the clustering technique was introduced in LEACH protocol. In LEACH protocol, hierarchical clustering was done based on the data obtained by the sink node. The clustering technique involved a set-up phase and a steady phase. In set-up phase, CHs are elected based on a random probability parameter after which the remaining sensor nodes correspondingly select their respective CHs. After the clusters are made, and CHs and their corresponding member sensor nodes are defined, the CHs transmit the TDMA schedule with different time-slots assigned to their member sensor nodes. In steady phase, the member sensor nodes transmit their data in their defined slots to their CHs where henceforth, the data is aggregated, redundant data is

Fig. 2 A base station node [11]
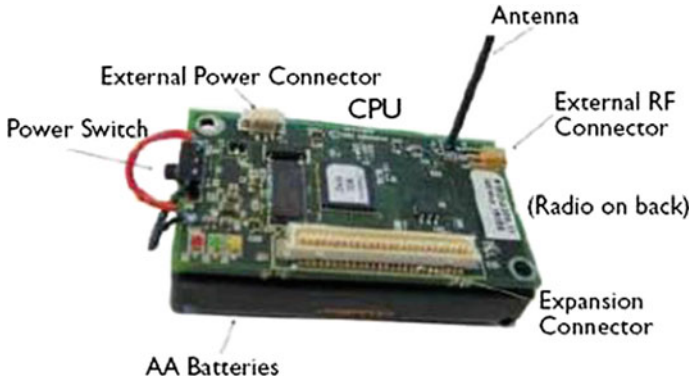
Fig. 3 A sensor node [12]

Fig. 4 An example of clustered WSN [13]
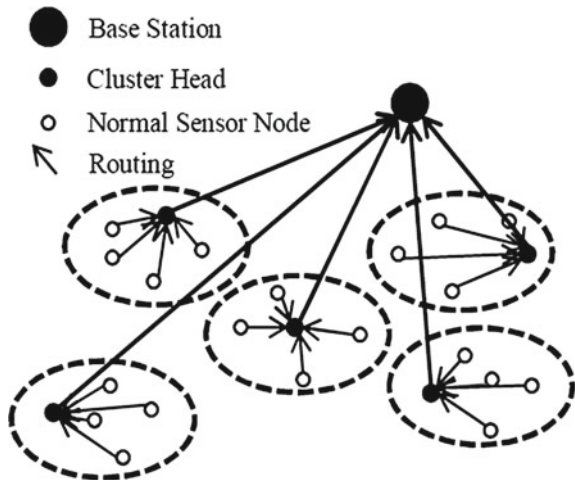
removed and finally the processed aggregated data is forwarded to the sink node or the base station. Hence, clustering also allows data aggregation which not only saves the channel bandwidth but also saves energy as lesser redundant packets will be forwarded to the sink node [14, 16]. This feature also makes the clustered WSN effective in query-based applications where the query can be broadcasted and only the data from the interested nodes can be forwarded by the CH [17]. Since different tiers are introduced in the network with clustering, stabilized clusters lessen the data overhead of the topology maintenance as the member sensor nodes have a direct connection only with their CH in the network and not with the other nodes [18].

3   Cluster-Head Selection Strategies

LEACH protocol had many limitations like improper area coverage as network may somewhere have large clusters while in other regions may have small clusters, sometimes also since the location of the motes is not taken into consideration,

CH-selection is based only on a single parameter, i.e. random probabilistic value [19]. To overcome the limitations of LEACH protocol, many improvements have been done and hence many clustering algorithms have been proposed. The clustering algorithms, which have so far been proposed, introduced different CH-selection strategies based on the parameters which define the sensor nodes. In order to elect CH, the different strategies that were followed by the researchers were deterministic, adaptive and combined metric (hybrid) strategies.

3.1 Deterministic Strategies

When motes are deployed in a region, they are given a unique ID and also their locations are fixed in static WSN. Since the locations are fixed, the number of neighbours (node degree/weight value) is fixed for every node. If either the BS pre-assigns the CH nodes or the election of CHs is based on these fixed parameters, it is known as deterministic CH-selection strategy [20]. It is also known as non-probabilistic strategy where the output of the selection criteria is a stable value and does not change over the rounds of network lifetime [21].

3.2 Adaptive Strategies

Certain mote attributes like residual energy, energy dissipation in transmitting a packet (which varies with the packet size which needs to be transmitted), a random number which is to be chosen by the mote and average energy of the network change over the course of network lifetime, and hence associate with the adaptive CH-selection strategies [21]. These CH-selection algorithms may either be initiated by the BS or by the sensor nodes themselves. The BS-assisted clustering algorithms (alternatively known as centralized algorithms) require BS to have global knowledge of the network and failure of BS may lead to the complete protocol failure [19, 22]. However, self-assisted clustering algorithms (alternatively known as distributed algorithms/localized algorithms) operate on fewer sections of nodes making the network more scalable and robust. Since such algorithms operate within the clusters and do not require additional overhead messages, they are preferred for large-scale networks [23–25].

3.3 Hybrid Strategies

With more advancements, many clustering algorithms have been reported which consider attributes of deterministic and adaptive CH-selection strategies [26, 27]. It is alternatively known as combined metric strategies.

A few Cluster-Head selection strategies have been evaluated in Table 1.

Table 1 Comparative evaluation of cluster-head selection strategies

Authors	Year	CH-selection strategy (Deterministic—D, Adaptive—A, Hybrid—H)	Heterogeneity (Y/N)	Parameters for CH-selection	Advantage	Evaluation tool (MATLAB—M, NS2—N, Test Bed—T)
Ye et al. [28]	2005	A	N	Residual Energy	Efficient load Balancing	M
Ding et al. [29]	2005	D	N	Weight value	Balanced clustering and efficient energy consumption	T
Lin et al. [30]	2006	A	N	Residual energy and communication cost	Lengthened network lifetime and optimized resource usage	T
Qing et al. [23]	2006	A	Y	Node's residual energy and Network's average energy's ratio-based probability	Prolonged stability period and better throughput	M
Deng et al. [31]	2007	A	N	Random selection(for level-1 CH); residual energy(for level-2 CH)	Lengthened lifetime and improved energy distribution	M
Hoang et al. [26]	2010	H	N	Distance from the cluster centre (for the CH of the first round); residual energy and distance from the cluster centre(for the respective CHs)	Uniform cluster formation and improved network lifetime	M
Nam et al. [32]	2013	A	N	Energy-consumption-based threshold value	Better distribution of energy usage and network lifetime	N
Xie et al. [33]	2013	D	N	Minimized distance from all nodes in the cluster	Optimum cluster size and minimum data transmissions	T

Table 1 (continued)

Authors	Year	CH-selection strategy (Deterministic—D, Adaptive—A, Hybrid—H)	Heterogeneity (Y/N)	Parameters for CH-selection	Advantage	Evaluation tool (MATLAB—M, NS2—N, Test Bed—T)
Chauhan et al. [24]	2014	A	Y	Residual energy	Better communication approach, high stability and prolonged lifetime	M
Kuila et al. [34]	2014	D	Y	Pre-assigned CHs with high initial energy than the other sensor nodes	Extended network lifetime and efficient energy usage	M
Azharuddin et al. [35]	2015	D	Y	Pre-assigned CHs with less energy constraints	Efficient fault tolerance and better lifetime	M
Gherbi et al. [36]	2015	H	N	Function of distance of nodes from the BS, residual energy and node weight	Evenly distributed energy usage, better throughput, longer lifetime	N
Sert et al. [37]	2015	H	N	Distance from BS, residual energy and competition radius based on fuzzy logic	More energy efficient	M
Bouyer et al. [38]	2015	D	N	Fuzzy probability vector	Lengthened network lifetime	M
Elhoseny et al. [39]	2015	D	Y	Fitness function and neighbour density	Extended network life	T
Khan et al. [40]	2016	D	N	Pre-assigned mobile actor nodes as CH nodes	High throughput and improved PDR with minimized packet transmissions	N
Batra et al. [41]	2016	H	N	Total advertisement lifespan and residual energy	Stable CH count and improved lifetime	N

Table 1 (continued)

Authors	Year	CH-selection strategy (Deterministic—D, Adaptive—A, Hybrid—H)	Heterogeneity (Y/N)	Parameters for CH-selection	Advantage	Evaluation tool (MATLAB—M, NS2—N, Test Bed—T)
Jia et al. [42]	2016	A	Y	Redundancy (stage 1); energy heterogeneity (stage 2)	Reduced redundancy, energy usage and better lifetime	M
Ammar et al. [25]	2016	A	N	Conventional LEACH probabilistic method	Successful data delivery and better lifetime	M
Lee et al. [19]	2016	A	N	FCM approach (level 2); random (level 1)	Longer lifetime and energy conservation	N
Rao et al. [27]	2017	H	N	Distance parameters (intra-cluster and BS distance) and residual energy	Improved lifetime and throughput at the BS	M
Merabtineet al. [22]	2017	H	N	New weight function based on residual energy and communication cost to transmit data to BS	Better throughput, reduced energy consumption and improved lifetime	N
Zhang [43]	2017	H	Y	Residual energy and its degree, its neighbour's residual energy	Load-balancing problem solved, prolonged average lifetime, energy-efficient network	M
Mirzaie et al. [44]	2017	H	N	Residual energy and node degree	Energy efficient	M
Mittal et al. [45]	2017	A	N	Residual energy	Load balancing achieved, increased stability period	M
Pradhan et al. [46]	2018	A	N	Residual energy, initial energy and signal quality	Efficient coverage area, energy efficient	Castalia simulator

(continued)

Table 1 (continued)

Authors	Year	CH-selection strategy (Deterministic—D, Adaptive—A, Hybrid—H)	Heterogeneity (Y/N)	Parameters for CH-selection	Advantage	Evaluation tool (MATLAB—M, NS2—N, Test Bed—T)
Krishna et al. [47]	2018	A	N	Residual energy	Lesser delay and higher PDR	N
Patil et al. [48]	2018	H	N	Average number of CHs, normalized distance from overlapped region	Better energy and lifespan efficiency	Sensoria simulator

4 Conclusion

Clustering is an important aspect of an ever-growing technology, i.e. wireless sensor networks (WSN). Efficient clustering solely depends upon the right choice of the cluster-head selection strategy for the WSN. Cluster-head selection strategies have been categorized as deterministic strategies, adaptive strategies and hybrid strategies. Many clustering algorithms based on these cluster-head selection strategies have been introduced over the past years. Depending upon the application, these strategies have their own pros and cons. This paper presents an evaluation of the CH-selection strategy-based clustering algorithms. From the comparative evaluation, we observe that the focus of the clustering strategies is diverting towards using the adaptive or hybrid strategies for electing CHs as it reduces the message overhead which is caused due to network management packets.

References

1. Abbasi AA, Younis M (2007) A survey on clustering algorithms for wireless sensor networks. Comput Commun 30:2826–2841
2. Yu Y, Krishnamachari B, Kumar VP (2006) Information processing and routing in wireless sensor networks. World Scientific Publishing Co. Pte. Ltd
3. Boujelben M, Youssef H, Abid M (2008) Survey on pre shared key in WSN. In: International conference on wireless and mobile computing, pp 532–537
4. Chan H, Perrig A (2004) ACE: an emergent algorithm for highly uniform cluster formation. In: European workshop on wireless sensor networks, pp 154–171
5. Krishna P, Vaidya NH, Chatterjee M, Pradhan DK (1997) A cluster-based approach for routing in dynamic networks. ACM SIGCOMM Comput Commun Rev 27:49–64
6. Min R, Bhardwaj M, Cho SH, Shih E, Sinha A, Wang A, Chandrakasan A (2001) Low-power wireless sensor networks. In: Fourteenth international conference on VLSI design, vol 1, pp 205–210
7. Sohrabi K, Gao J, Ailawadhi V, Pottie GJ (2000) Protocols for self-organization of a wireless sensor network. IEEE Pers Commun 7(5):16–27
8. Boyinbode O, Le H, Takizawa M (2011) A survey on clustering algorithms for wireless sensor networks. Int J Space-Based Situated Comput 1(2–3):130–136
9. Younis O, Krunz M, Ramasubramanian S (2006) Node clustering in wireless sensor networks: recent developments and deployment challenges. IEEE Netw 20(3):20–25
10. Akyildiz IF, Su W, Sankarasubramaniam Y, Cayirci E (2002) Wireless sensor networks: a survey. Comput Netw 38(4):393–422
11. Deeter Electronics: deeternet® Wireless Sensor System Base Station. http://www.deeter.co.uk/products/wireless-sensor-system/multi-channel-base-station
12. Stavrou E Wireless sensor networks pt1: introduction. http://webhosting.devshed.com/c/a/Web-Hosting-Articles/Wireless-Sensor-Networks-pt-1-Introduction/1/
13. Park GY, Kim H, Jeong HW, Youn HY (2013) A novel cluster head selection method based on K-means algorithm for energy efficient wireless sensor network. In: 2013 27th International conference on advanced information networking and applications workshops, pp 910–915

14. Heinzelman WB, Chandrakasan AP, Balakrishnan H (2002) An application-specific protocol architecture for wireless microsensor networks. IEEE Trans Wirel Commun 1(4):660–670
15. Duarte-Melo EJ, Liu M (2014) Analysis of energy consumption and lifetime of heterogeneous wireless sensor networks. In: Global telecommunications conference 2002, GLOBECOM'02. IEEE, vol 1, pp 21–25
16. Mhatre V, Rosenberg C, Kofman D, Mazumdar R, Shroff N (2004) Design of surveillance sensor grids with a lifetime constraint. In: European workshop on wireless sensor networks. Lectures notes computer science, pp 263–275
17. Estrin D, Govindan R, Heidemann J, Kumar S (1999) Next century challenges: scalable coordination in sensor networks. In: Proceedings of the 5th annual ACM/IEEE international conference on mobile computing and networking, pp 263–270
18. Hou YT, Shi Y, Sherali HD, Midkiff SF (2005) On energy provisioning and relay node placement for wireless sensor networks. IEEE Trans Wirel Commun 4(5):2579–2590
19. Lee JS, Kao TY (2016) An improved three-layer low-energy adaptive clustering hierarchy for wireless sensor networks. IEEE Internet Things J 3(6):951–958
20. Ramesh K, Somasundaram DK (2012) A comparative study of clusterhead selection algorithms in wireless sensor networks. Int J Comput Sci Eng Surv 2:153–164
21. Jain N, Gupta SK, Sinha P (2013) Clustering protocols in wireless sensor networks: a survey. Int J Appl Inf Syst 5(2):41–50
22. Merabtine N, Djenouri D, Zegour DE, Lamini E, Bellal R, Ghaoui I, Dahlal N (2017) One-step clustering protocol for periodic traffic wireless sensor networks. In: 2017 26th Wireless and optical communication conference WOCC 2017, pp 1–6
23. Qing L, Zhu Q, Wang M (2006) Design of a distributed energy-efficient clustering algorithm for heterogeneous wireless sensor networks 29(12):2230–2237
24. Chauhan A, Kaushik A (2014) TADEEC: threshold sensitive advanced distributed energy efficient clustering routing protocol for wireless sensor networks. Int J Comput Appl 96 (23):26–31
25. Ammar AB, Dziri A, Terre M, Youssef H (2016) Multi-hop LEACH based cross-layer design for large scale wireless sensor networks. In: 2016 International wireless communications and mobile computing conference (IWCMC). IEEE, pp 763–768
26. Hoang DC, Kumar R, Panda SK (2010) Fuzzy C-Means clustering protocol for Wireless Sensor Networks. In: 2010 IEEE international symposium on industrial electronics, pp 3477–3482
27. Rao PCS, Jana PK, Banka H (2017) A particle swarm optimization based energy efficient cluster head selection algorithm for wireless sensor networks. Wirel Netw 23(7):2005–2020
28. Ye M, Li C, Chen G, Wu J (2005) EECS: an energy efficient clustering scheme in wireless sensor networks. In: IPCCC 2005. 24th IEEE international performance, computing, and communications conference, 2005, pp 535–540
29. Ding P, Holliday J, Celik A (2005) Distributed energy-efficient hierarchical clustering for wireless sensor networks. In: International conference on distributed computing in sensor systems, pp 322–339
30. Younis O, Fahmy S (2004) HEED: a hybrid, energy-efficient, distributed clustering approach for ad hoc sensor networks. IEEE Trans Mob Comput 3(4):366–379
31. Zhixiang D, Bensheng Q (2007) Three-layered routing protocol for WSN based on LEACH algorithm. In: 2007 IET Conference on Wireless, Mobile and Sensor Networks (CCWMSN07), pp 72–75
32. Nam CS, Han YS, Shin DR (2013) The cluster-heads selection method considering energy balancing for wireless sensor networks. Int J Dist Sens Netw 9(11)
33. Xie R, Jia X (2014) Transmission efficient clustering method for wireless sensor networks using compressive sensing. IEEE Trans Parallel Distrib Syst 25(3):806–815
34. Kuila P, Jana PK (2014) A novel differential evolution based clustering algorithm for wireless sensor networks. Appl Soft Comput J 25:414–425
35. Azharuddin M, Jana PK (2015) A distributed algorithm for energy efficient and fault tolerant routing in wireless sensor networks. Wirel Netw 21(1):251–267

36. Gherbi C, Aliouat Z, Benmohammed M (2015) Distributed energy efficient adaptive clustering protocol with data gathering for large scale wireless sensor networks. In: 12th International Symposium on Programming and Systems, pp 1–7
37. Sert SA, Bagci H, Yazici A (2015) MOFCA: Multi-objective fuzzy clustering algorithm for wireless sensor networks. Appl Soft Comput J 30:151–165
38. Bouyer A, Hatamlou A, Masdari M (2015) A new approach for decreasing energy in wireless sensor networks with hybrid LEACH protocol and fuzzy C-means algorithm. Int J Commun Netw Distrib Syst 14(4):400–412
39. Elhoseny M, Yuan X, Yu Z, Mao C, El-Minir HK, Riad AM (2015) Balancing energy consumption in heterogeneous wireless sensor networks using genetic algorithm. IEEE Commun Lett 19(12):2194–2197
40. Khan S, Khan F, Fahim Arif Q, Jan MA, Khan SA (2016) Performance improvement in wireless sensor and actor networks based on actor repositioning. J Appl Environ Biol Sci 6: 1–200
41. Batra PK, Kant K (2016) LEACH-MAC: a new cluster head selection algorithm for Wireless Sensor Networks. Wirel. Netw 22(1):49–60
42. Jia D, Zhu H, Zou S, Hu P (2016) Dynamic cluster head selection method for wireless sensor network. IEEE Sens J 16(8):2746–2754
43. Zhang Y, Wang J, Han D, Wu H, Zhou R (2017) Fuzzy-logic based distributed energy-efficient clustering algorithm for wireless sensor networks. Sensors 17(7):1554
44. Mirzaie M, Mazinani SM (2017) Adaptive MCFL: An adaptive multi-clustering algorithm using fuzzy logic in wireless sensor network. Comput Commun 111:56–67
45. Mittal N, Singh U, Sohi BS (2017) A stable energy efficient clustering protocol for wireless sensor networks. Wirel Networks. 23(6):1809–1821
46. Pradhan N, Sharma K, Singh VK, Tamang ND (2018) TEECS: a time-based energy efficient clustering scheme in wireless sensor networks. Adv Electron. Commun. Comput 443: 263–272
47. Krishna RK, Ramanjaneyulu BS (2018) A strategic node placement and communication method for energy efficient wireless sensor network. In: Proceedings of 2nd international conference on micro-electronics, electromagnetics and telecommunications, pp 434, 95–103 (**2018**)
48. Patil M, Sharma C (2018) Energy-efficient packet routing model for wireless sensor network. Adv Electron Commun Comput 443:341–350

Structural and Statistical Feature-Processed PST for Angle Robust Iris Recognition

Kapil Juneja and **Chhavi Rana**

Abstract Iris is one such biometric feature that cannot be altered by the individual. In this paper, an improved structural and statistical feature-based iris authentication system is investigated. The model first used the Fisher face approach to generate the structural features. These structural features are processed on block-specific N PST divisions to achieve the directional and geometric variations. The statistical contrast, correlation, energy, and homogeneity features are extracted for each PST block. N-angle-specific M features acquisition method has provided the wider and descriptive feature set for iris images. This statistical transformed dataset is processed by SVM classifier to recognize the iris accurately. The proposed novel model is applied on CASIA-Iris-V3 dataset. The implementation results are applied on angle-variant samplesets. The implementation results identified that the model has achieved the higher accuracy gain for angle robust iris recognition.

Keywords Iris recognition · Statistical · Structural · PST · SVM

1 Introduction

Iris [1–3] can identify the individual distinctly by applying effective feature encoding and classification methods. The iris is basically identified as the pupil region of the eye which is used by authentication systems, medical systems, and behavior identification systems. Each of the application domains is having various integrated sub-applications and environment in which the iris recognition is having scope as online or offline system. Iris images can be characterized well if they are acquired through specialized technology and devices. The camera quality, distance from the camera, and the environmental conditions can affect the reliability of iris

K. Juneja (✉) · C. Rana
Department of Computer Science and Engineering, University Institute
of Engineering and Technology, Maharshi Dayanand University,
Rohtak 124001, Haryana, India
e-mail: kapil.juneja81@gmail.com; kapil.juneja.1981@ieee.org

recognition system. The iris recognition is considered one of the most technical and reliable aspect of biometric verification system. The researchers have provided the work to improve the characterization of the iris image. In unconstrained [4] and complex situations and environments, the iris images can be degraded in terms of illumination, blur, and defocusing [5–7]. The characterization of eye elements such as pupil position, wetness of eye, contact lenses, and degree of eye-openness also affects the characterization of iris and individuals [8, 9]. The improvement at the preprocessing and feature generation stages can be done to tackle these unconstrained phenomena and situations. The accuracy and performance of iris recognition system depend on the accurate extraction of pupil region and iris features. The various segmentation models are available that extract the circular-, elliptical-, and boundary [10]-driven extraction of pupil region. The differential operators, decomposition methods, and various derivatives are available to acquire the effective region even in unconstraint conditions. The model fitting methods are available to improve the classification rate under the variant visible spectrum.

The adaptive segmentation methods are able to exploit the iris features [11–13], effective pupil and sclera regions. The structural and textural features can be acquired by applying the active contour methods robust to the sparse gradient information. The iris feature pattern [14] in raw form is containing hundred of visual aspects and pigments. The cornea and vein's features can be exploited to enhance the effectiveness of any recognition system. The template mapping and the clustering methods can be applied to obtain the designed region from eye image. More roughly, an image it captures, more effective the segmentation method is required to acquire the contributing region and features. The camera direction and the head orientation also affect the reliability of the recognition system. The non-visibility of the iris pattern is another challenge to the iris recognition system. This situation occurs by iris region occlusion by eyelashes or eye-glasses. The degree of missing information or occlusion degrades the strengths of the recognition system. The qualitative adaptation is required to transform the raw-captured iris image to normalized form. This form is more robust against illumination, lighting, physical, behavioral, and environmental aspects [6, 7, 13, 15].

In this paper, a more robust and reliable iris recognition model is provided. This model is robust against the directional and lighting effects. The structural and statistical features are combined to improve the performance of iris recognition system. PST is applied to improve the robustness against structural and camera out-of-focus issues. In this section, the characteristics of iris recognition system are provided with relative challenges. The environmental and physical issues that can affect the performance of iris recognition system are discussed in this section. In Sect. 2, the PST and Fisher face-based proposed model is provided with integrated process stages. The exploration of each functional stage is defined in this section. In Sect. 3, the comparative results of proposed model are provided on CASIA dataset against PCA, neural network, and SVM method. The conclusion of the work is provided in Sect. 4.

2   Research Methodology

Iris recognition is adopted as the advanced biometric in various online and offline applications. The availability of high-resolution cameras has increased the scope and diversity of iris recognition systems. But these self captured images also have the basic issues of real-time challenges. Researchers have defined various generic and application-specific models to improve the performance and accuracy of individual identification based on iris features. In this paper, an angle robust model is provided to improve the accuracy of iris recognition for real-time capturing. The proposed model as shown in Fig. 1 is processed on normalized real-time images. These images are either acquired in normalized environment such as indoor capturing. Even then, the image can be affected by some contrast and illumination change. The proposed model is able to handle the deficiencies in terms of angle change, lighting variation, and alignment issue. The acquired normalized iris image is processed by Fisher face method to generate the structural and textural feature face. The Fisher face-acquired structural features are then processed by PST [16] (polar sine transformation) to generate the rotation adaptive structural featureset. In this stage, the iris image is divided into smaller blocks of 9 × 9. For each block, PST is applied at 12 different angles to generate a wider and angle robust feature space. This variant angle-based structural feature space is generated for both training and testing datasets. In the final stage, the statistical feature for each PST adaptive block is generated to represent the various aspects of structural and rotation-specific iris images. This statistical featureset includes contrast, energy, homogeneity, and correlation features. Once the training and testing sets are transformed into statistical featureset, the SVM classifier is applied to recognize the iris image. The proposed model is capable to handle the rotational difference or positional jerks existing in the unlabeled real-time iris image. In this section, descriptive formulation of each of the integrated work stage is provided. The implementation results on angle-variant samplesets are provided in the next section of this paper.
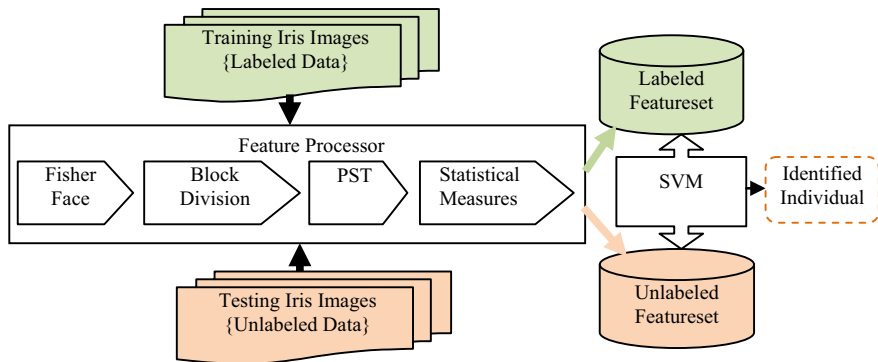
Fig. 1 Proposed classification model

2.1   Fisher Face

LDA (linear discriminate analysis) or Fisher face are able to project the image in higher dimension to increase the ratio of determinants. The Fisher face method generates the scatter matrix to generate the linear subspace to project the iris image. To generate the Fisher face, the class-specific evaluation is performed on labeled iris images. The mean of each class-specific iris images is obtained and represented in Eq. (1)

$$\text{Mean}_c = \frac{1}{N_c} \sum_{i=1}^{N_c} \text{CTr}(i) \tag{1}$$

where N_c is the number of iris images of specific class c in training set. CTr is the labeled set with class specification.

Once the mean iris image is obtained, the Fisher face is generated for each training and testing iris image. The Fisher face (Ff) generation for training set is provided in Eq. (2) and for testing it is provided in Eq. (3).

$$\text{Ff}_{\text{Tr}} = \sum_{c=1}^{C} \sum_{i=1}^{N_c} (\text{CTr}_i - \text{Mean}_c)(\text{CTr}_i - \text{Mean}_c)^T \tag{2}$$

and,

$$\text{Ff}_{\text{Ts}} = \sum_{i=1}^{N} (\text{Ts}_i - \text{Mean})(\text{Ts}_i - \text{Mean})^T \tag{3}$$

The Fisher face is able to explore the structural features and generate the effective face region as the class distance vector from mean face. The PST is applied on block adaptive Fisher face to generate the rotation robust structural features.

2.2   PST

The polar sine transformation (PST) is the process applied on image to generate the expected angular variation at earlier phase. This method increases the robustness of any recognition system against rotational change. The PST is defined with specification of angle on which rotation is performed and it is defined within radial kernel, i.e., $\{0, \pi\}$. Equation (4) represents the standard PST with specification or radial coefficient r and number of coordinate points n

$$\text{PST}_n^C(r) = \sin\left(\pi n r^2\right) \tag{4}$$

This rotation function is applied on each Fisher block to generate the robust wider feature set. In this research to improve the scalability and scope, feature space is generated for 12 equally spaced angled. For each angle space, the structural feature space is generated called fPST.

2.3 Statistical Measures

The N-acquired fPST blocks of iris image are processed by statistical measure to acquire the textural and structural features. This featureset is informative against the variations, and deficiencies exist in the real-time capturing of iris images. The illumination and lighting difference is identified by contrast (Cnt) feature represented by Eq. (5).

$$\text{Cnt} = \sum_{x,y} |x - y|^2 \text{FFBlk}(x, y) \tag{5}$$

After dealing with illumination variation existing in individual block, the relational evaluation on two consecutive blocks is done. The correlation (Corr) vector provided in Eq. (6) defines the similarity existing between these blocks.

$$\text{Corr} = \sum_{x,y} \frac{(x - \mu_x)(y - \mu_y)\text{FFBlk}(x, y)}{\sigma_x \sigma_y} \tag{6}$$

The energy (En) is the content-representative feature existing within the block. The spatial difference is identified by the energy feature. The structural information in the form variation existing within the block can be represented by energy feature. Higher the energy value for a block is, more representatives a block can be considered.

$$\text{En} = \sum_{x,y} \text{FFBlk}(x, y)^2 \tag{7}$$

Homogeneity (Hm) identifies the similarity that exists within the block. Higher the smoothening or blurness exists within the block, more homogeneity identifies within the block. The homogeneity is also taken in this research as a part of statistical featureset.

$$\text{Hm} = \sum_{x,y} \frac{\text{FFBlk}(x, y)}{1 + |[x - y|} \tag{8}$$

These four feature vectors are obtained for each PST-angle-variant Fisher face block. A wider statistical dataset is generated to represent the training and testing sets to represent the structural and textural features. The SVM classifier is applied to statistical transformed featureset to recognize the iris accurately.

2.4 SVM

Support vector machine (SVM) is the learning method defined based on several functions including radial basis function, polynomial function, etc. The labeled training set of iris images is taken as input in this research. The SVM is more adaptive to statistical features and is able to handle the situation of noise and scalability. In this research, the radial basis function is defined as kernel to control the learning process. The radial basis function is provided in Eq. (9)

$$\text{rbf}(x, z) = \exp\left\{-\frac{||x - z||^2}{2\sigma^2}\right\} \tag{9}$$

where x and z are the feature weights of training and testing datasets, and σ is width of function.

Basic of the kernel function, the supervised learning is applied to train the label data and generate the classification rules. The high-dimensional feature space is processed to identify the class specific rules. The mapping of testing features is done on these rules to recognize the iris class.

The proposed model is implemented on multiple sets of CASIA iris dataset. The analysis results of implementation are provided in the next section with comparative evaluation.

3 Results

The proposed angle robust iris recognition model is tested on standard CASIA-IrisV3-Interval [17] dataset. The dataset is having 2639 iris images of 249 subjects. The images are captured in indoor environment in two sessions with a good resolution of 320×280. The proposed model is robust against angular variation and lighting effect. To test the results for angular change, capturing jerks and misposition of camera, the five test sets are generated. The normal iris testset is a testset with angular variation of 15°, 30°, −15°, and 30°. The comparative evaluation of this proposed fPST-SVM method is generated against PCA, LDA, and SVM methods. The accuracy is computed on each sampleset by generating the training set with and without inclusion of angle-variant iris images. Figure 2 has

provided the comparative analysis on five different sets of 30 images each with angular variations. The training set is composed of 300 normal dataset images.

Form Fig. 2, the results identified that the proposed fPST-SVM model has achieved a higher accuracy of 93.33% for normal test images, whereas the existing PCA, LDA, and SVM methods achieved the accuracy of 70, 76.67, and 80%, respectively. For the angle-variant testsets, the accuracy of existing methods decreased with an increase in angle. The accuracy of PCA method drops to 50 and 56.67% for the testsets taken at angle 15° and −15°. For angle 30° and −30°, the recognition rate drops to 40 and 36.36%. The recognition rate of existing LDA and SVM methods also drop in the same ratio as the angle variation is identified in the testsets. The proposed feature face and PST-based method is more robust against angular and structural variations. The higher accuracy of 90, 93.33, 86.67, and 90% is maintained for the samplesets taken at angle 15°, −15°, 30°, and −30°.

Figure 3 has provided the analysis results by learning the training set with 600 angle-variant iris images. Five testsets with 30 images are generated for different angles. The results identified that the angle variation-based training improved the slight improvement in accuracy for proposed fPST-SVM model. The proposed model maintained a higher accuracy over 90% for each testset. The inclusion of angle-variant images in training set improved the capability of existing PCA, LDA, and SVM methods, and a higher gain is accuracy is observed. For the angle 30°, the accuracy of 56, 62, and 58% is achieved for PCA, LDA, and SVM classifiers. For testset of angle −30°, the PCA, LDA, and SVM classifiers achieved the 64, 66, and 62% of accuracy.
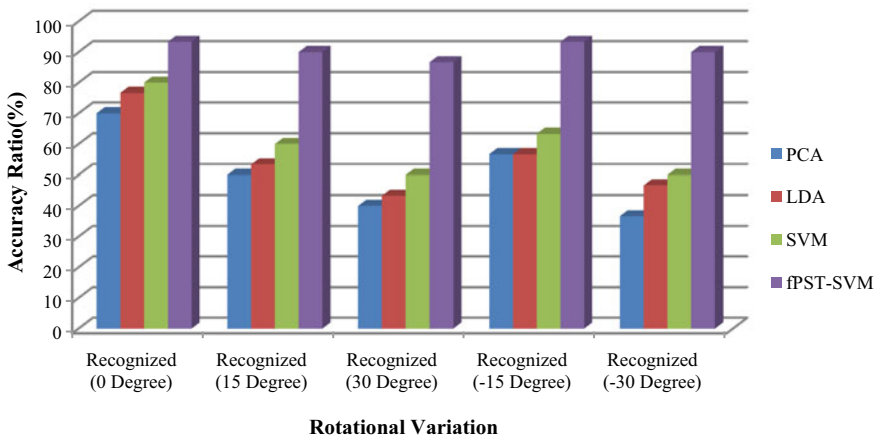
Fig. 2 Accuracy ratio analysis with rotational variant
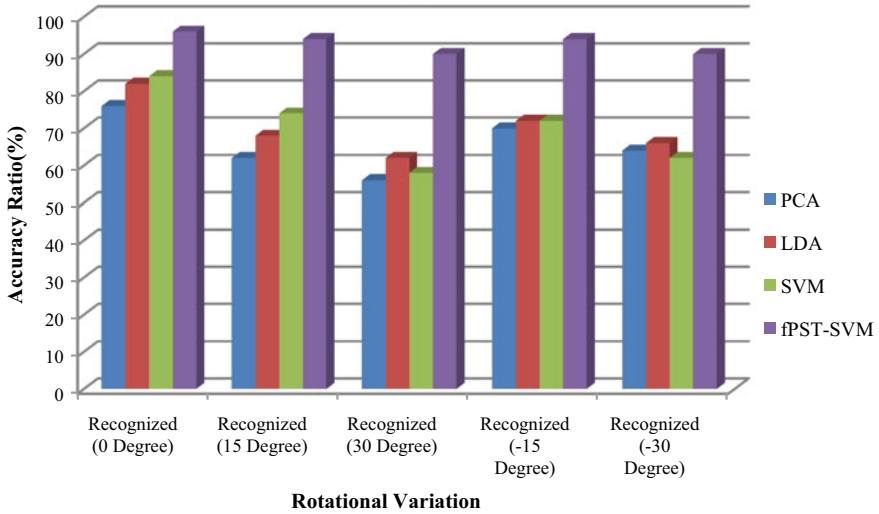
Fig. 3 Accuracy Ratio analysis with rotational variant (rotation variant training set)

4 Conclusion

Iris recognition systems are adopted by many online and offline applications to verify the individual's presence. The availability of high-quality cameras has improved their capability to capture the low-level features of eye. But capturing the images in an unprofessional way can affect the alignment of image. In this paper, the angular invariant iris recognition model is provided. The model has acquired the Fisher face to acquire the structural feature and applied the PST to generate the angle robust features. The block adaptive structural and textural features are generated for each angle-variant iris image. The SVM classifier is applied to statistical transformed featureset to recognize the individual. The implementation of the model is applied on angle-variant samplesets of Casia-V3 dataset. The comparative results identified that the proposed fPST-SVM model is more adaptive to angle variation than the existing PCA, LDA, and SVM classifiers.

References

1. Aleem A, Togneri R, Bennamoun M, Naseem I (2017) Iris recognition using class-specific dictionaries. Comput Electr Eng 62:178–193
2. Tao B, Wang Y, Li X, Li J (2012) Research and implementation of iris recognition algorithm. Proc Eng 29:3353–3358
3. Petrosino A, Ricciardi S, De Marsico M (2016) Iris recognition through machine learning techniques: a survey. Pattern Recogn Lett 82(2):106–115

4. Juneja K (2017) Multiple feature descriptors based model for individual identification in group photos. J King Saud Univ Comput Inf Sci

5. Pavaloi I, Ignat A (2017) Iris recognition using statistics on pixel position. In: E-health and bioengineering conference (EHB), Sinaia, pp 422–425

6. Dehkordi AB, Abu-Bakar SAR (2015) Noise reduction for iris recognition using adaptive fuzzy filtering. In: IEEE international conference on signal and image processing applications (ICSIPA), Kuala Lumpur, pp 399–403

7. Nam GP, Jeong DS, Cho DH, Kang BJ, Park KR, Kim J, Shin KY (2012) New iris recognition method for noisy iris images. Pattern Recogn Lett 33(8):991–999

8. Mohamed E, Magdi F, El-Samie FEA, AbdElnaby M, F. Soliman NF (2017) Efficient iris localization and recognition. Optik—Int J Light Electron Opt 140:469–475

9. Nappi M, Riccio D, di Baja GS, Frucci M (2016) WIRE: watershed based iris recognition. Pattern Recogn 52:148–159

10. Gill NS, Juneja K (2015) Tied multi-rubber band model for camera distance, shape and head movement robust facial recognitio. In: International conference on applied and theoretical computing and communication technology (iCATccT), pp 218–223

11. Budik N, Ivanushkina N, Ivanko K (2017) Feature selection for biometric iris recognition. In: 5th IEEE workshop on advances in information, electronic and electrical engineering (AIEEE), pp 1–5

12. Nurhadi R, Suryanto Y, Presekal A, Ramli K (2017) Performance analysis on iris recognition based on half polar iris localization and normalization method using modified low cost camera. In: 15th international conference on quality in research (QiR): international symposium on electrical and computer engineering, pp 1–4

13. Li Z (2017) An iris recognition algorithm based on coarse and fine location. In: IEEE 2nd international conference on big data analysis (ICBDA), Beijing, pp 744–747

14. Suciati N et al (2016) Feature extraction using statistical moments of wavelet transform for iris recognition. In: International conference on information & communication technology and systems (ICTS), Surabaya, pp 193–198

15. Aouat S, Hamouchene I (2014) A new texture analysis approach for iris recognition. AASRI Proc 9:2–7

16. Juneja K, Gill NS (2015) A PCT/PST improved HMM-PCA model for pose robust facial recognition. In: International conference on applied and theoretical computing and communication technology (iCATccT), pp 131–136

17. CASIA-IrisV3 Database [Online]. http://www.cbsr.ia.ac.cn. [Online]. http://www.cbsr.ia.ac.cn/english/IrisDatabase.asp

LBP Pattern-Processed Log-Gabor Filter for Expression and Illumination Robust Facial Recognition

Kapil Juneja and **Chhavi Rana**

Abstract In this paper, an illumination and expression robust feature face is generated to improve the accuracy of facial recognition system. In the pre-processing stage, the median filter is applied to heal the noise impact and to extract the structural features. The weighted LBP filter is applied on smoothen face to generate the pattern region. This frequency and angle-based Log-Gabor filter is applied on LBP-weighted face to generate the expression and illumination robust pattern-feature set. The PCA-based rules are generated on pattern-feature-based training set to recognize the input face image. The proposed model is applied on three samplesets of expression and illumination-affected images of ORL dataset. The comparative results against PCA, Gabor PCA, Log-Gabor PCA, and LBP-PCA methods have observed a significant gain in accuracy ratio of face recognition.

Keywords Face recognition · Illumination · Expression robust · Gabor · LBP

1 Introduction

Face is the most common biometric information used by many online and offline authentication systems and other applications. Various classification and recognition algorithms are suggested by the researchers to improve the accuracy of facial recognition in complex environments and constraints. These constraints can be specific to application requirement, device specification, or the scene characterization. Researchers defined the contribution to improve the pre-processing, feature generation, and classification stages to reduce the error in face identification.

Facial recognition on normalized and front view faces are considered most adaptive. But the complex environmental situation such as brightness and contrast can disturb the facial features. A probabilistic neural network (PNN) [1] method

K. Juneja (✉) · C. Rana
Department of Computer Science and Engineering, University Institute of Engineering and Technology, Maharshi Dayanand University, 124001 Rohtak, Haryana, India
e-mail: kapil.juneja81@gmail.com; kapil.juneja.1981@ieee.org

with Delaunay tessellation and template machine was defined for effective facial recognition. The edge gradient analysis was used to compute the matching score respective to referenced images. Gillan et al. [2] used the Mexican Hat wavelet method for locating and generating the effective facial features to improve the accuracy of facial recognition.

The captured faces can be affected by different kind of variations such as pose, expression, and contrast. Researchers defined methods to handle one or more kind of irregularity or the challenge. The orientation and scale specific facial variation were handled by Dai and Zhou [3] using Gabor wavelet-based feature processor. Author also combined the KPCA and SVM methods to provide expression and pose robust facial recognition. Chen and Zhang [4] used the energy and entropy-processed wavelet decomposition for facial pose and expression robust feature extraction.

The quality of facial recognition depends on accurate acquisition of facial region. Various pre-processing methods, filters, and tools are investigated by the researchers for effective face localization. One such FaceScry [5] tool was defined to extract the facial region for mobile devices. The tool is robust against the size and real-time illumination conditions. Rani et al. [6] have defined a two-step method for facial recognition using integral normalized gradient image (INGI) and discrete orthogonal moment method. The method is able to handle the noise, rotation, and illumination variations. Gao et al. [7] has used the Gabor features to handle the challenges associated with facial localization, scalability, and orientation. Goel and Agarwal [8] have defined an illumination robust facial region extraction, feature generation, and facial recognition method.

In more advanced biometrics system, multiple biometric elements, multiple feature processing methods, and multiple classifiers are processed collectively to avoid the chances of mistaken identity. A nonlinear feature fusion [9] method based on kernel Fisher discriminant analysis (KFDA) was used to generate the combined rules for face and ear recognition. The hybridization on feature generation and classification was proposed by Panda and Naik [10] using linear discriminant analysis (LDA) and genetic algorithms. The optimal feature components were identified using E-coli bacterial foraging strategy (EBFS). An effective facial recognition method using Hybrid Fourier feature was proposed by Hwang et al. [11] in uncontrolled illumination variations. The feature fusion was used by the author to improve the robustness for realistic environment. Another hybridization on feature selection was provided by Azzawi and Al-Saedi [12] using multiwavelet and particle swarm optimization (PSO) methods. This more selective and relevant feature set improved the efficiency and effectiveness of facial recognition. A discriminant feature set was utilized by Mallipeddi and Lee [13] using PCA and differential devolution (DE) methods. The ensemble learning method was applied on extracted feature set to identify the difference between classes. Valuvanathorn et al. [14] have used the PCA, histogram, and 2D-PCA methods for effective feature generation. Author applied the SVM- and PSO-based hybrid classifier to process the features and to recognize the face effectively. The local and global facial

features were processed by Nazari and Moin [15] using KNN and SVM classifiers. The feature fusion with hybrid classifiers improved the recognition rate.

2　Research Methodology

The real-time face images are affected by real-time challenges of lighting change, environment impact, and camera quality. These changes can be identified as the noise inclusion, illumination unbalancing, etc. Other than these, the expression can change the physical appearance of an individual. In this paper, the expression, illumination, and noise robust face recognition method is provided. These challenges are handled by the proposed model at pre-processing and feature generation stages. The selective pattern-based feature processor is provided in this research to generate the expression and illumination robust feature face. The proposed pattern-feature face model is shown in Fig. 1.

The model provided in Fig. 1 is processed on raw face image submitted to the application. The captured face is processed earlier by the nonlinear median filter in pre-processing stage to remove the noise. The filter preserved the structural features and smoothed the pixels of sliding window of 9 × 9. This filtered feature image is then processed by LBP filter to generate the weighted binary pattern. This frequency and direction-based Log-Gabor filter is applied on LBP-extracted pattern to generate the illumination and expression robust textural feature. The pattern-based feature is extracted on available database images as well as on input real-time face image. Algorithm I has provided the functional behaviour to transform any of input or database image to illumination, noise, and expression robust feature image.

```
Algorithm I : PatternFeatureFace(fImage)
/*fImage is the input facial Image taken from real environ-
ment with illumination, noise and expression variant*/
Begin
```

1. `BfImage = GenerateBlks(fImage,size)/*Divide the image in blocks of size 9×9*/`
2. `SfImage = MedianFilter(BfImage)/*Smooten    the    facial image*/`
3. `PfImage = LBPFilter(SfImage,Th)/*Generate   the   pattern region for facial image*/`
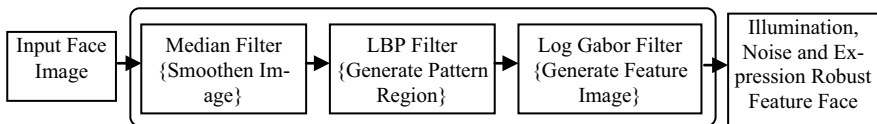
Fig. 1 LBP pattern-based Log-Gabor filter face

4. GMap = ConfigureLGabor(f0,θ)/*Configure   radial   feature
   mapper based on center frequency and direction vectors*/
5. LGfImage = ApplyLGabor(PfImage,   GMaps)/*Generate   log
   gabor adaptive illumination, noise and expression robust
   feature face is generated*/

Return LGfImage
End

   The functional stages of algorithm I are applied to each training and testing image. The PCA qualifier is applied to pattern-feature images to generate the training rules and to recognize the face accurately. In this section, the equational and procedural description of each of integrated work stage is provided.

2.1 LBP Filter

Local binary pattern (LBP) performs the region texture analysis based on the variance existing in neighbourhood pixels. The threshold limit is applied on mean value of intensity of neighbour pixels within the region to transform the region block to binary code. In this work, the medial-filtered facial image is divided in smaller blocks of 3×3 pixels. The intensity of neighbour (NPx) eight pixels is evaluated for binary code (BPx) conversion using Eq. (1)

$$BPx_i = \begin{cases} 0 & \text{if } NPx_i < NPx_c \\ 1 & \text{Otherwise} \end{cases} \tag{1}$$

where NPx_c is the centre pixel of region block

   Once the grey-level values are computed for neighbour pixels, the binary weights are computed to generate the LBP-computed pattern. The LBP weight computation is evaluated from neighbour pixel evaluation as shown in Eq. (2)

$$Weights_{LBP} = \sum_{i=0}^{N-1} NPx_i * 2^{i-1} \tag{2}$$

   The weighted LBP pattern is generated on the region blocks for neighbour pixel evaluation. In this research, N is 8 for the generation of weights to generate the encoded pattern region for the face images. The Log-Gabor features are extracted only for the LBP-weighted pattern. This pattern feature is processed by PCA to recognize the individual. The feature generator and classification method are defined in Sects. 2.2 and 2.3.

2.2 Log-Gabor Filter

The extracted LBP pattern is processed by Log-Gabor filter to generate the expression and polar robust textural features. This filter uses the frequency features with radial Gb(fr) and Gb(θ) constraints to explore the radial angle robust texture. The constraint controlled Log-Gabor filter is provided in Eq. (3)

$$\text{Gb}(\text{fr}, \theta) = \exp\left\{ -\frac{\left(\log\frac{\text{fr}}{\text{fr}_0}\right)^2}{2\log\left(\frac{\sigma_{\text{fr}}}{\text{fr}_0}\right)^2} \right\} \exp\left\{ -\frac{(\theta - \theta_0)^2}{2\sigma_\theta^2} \right\} \tag{3}$$

where fr_0 is the frequency of centre pixel of block, θ_0 is direction of filter, σ_{fr} is the radial bandwidth, σ_θ is the angle bandwidth.

The Log-Gabor filter pattern is applied on the LBP-weighted pattern face (LBPface) to generate the direction, illumination, and expression robust face image. The generation of pattern-filter face is given in provided in Eq. (4)

$$\text{LBPGface}(\text{fr}, \theta) = \text{LBPface}(x, y) * \text{Gb}(\text{fr}, \theta) \tag{4}$$

The training and testing faces are transformed into LBP pattern faces to improve the robustness of face recognition against illumination and expression difference. The PCA-based method is applied on these pattern-feature faces to recognize the individuals accurately.

2.3 PCA

PCA (principal component analysis) is the linear transformation-based method to reduce the feature space and dimension effectively. PCA generates the Eigenspace for training set images using covariance metrics-based eigenvectors. The LBP pattern adaptive Log-Gabor faces of training set (TrfFaces) are processed to project the feature vectors. The mean feature face is computed using Eq. (5)

$$\text{mTrFace} = \frac{1}{N}\sum_{i=1}^{N} \text{TrfFaces}(i) \tag{5}$$

The covariance matrix is generated by differencing the TrfFace (training feature faces) and mTrFace (mean training face) image. The computation method for covariance matrix is provided in Eq. (6)

$$C = \frac{1}{N} \sum_{i=1}^{N} (\text{TrfFaces}(i) - \text{mTrFace})(\text{TrfFaces}(i) - \text{mTrFace})^T \qquad (6)$$

Based on this covariance matrix, the eigenvalues (eval_i) and eigenvectors (evec_i) are generated and are provided in Eq. (7).

$$\frac{1}{N} \sum_{i=1}^{N} (\text{TrfFaces}(i) - \text{mTrFace})(\text{TrfFaces}(i) - \text{mTrFace})^T \text{eval}_i = \text{eval}_i \text{evec}_i \quad (7)$$

The covariance matrix and eigenvectors are generated for the training set. The test eigenfeature image is compared with each vector image, and the image with maximum match is considered as the identified face image. The proposed model is implemented on illumination and expression variant ORL dataset. The comparative implementation results of this proposed model are provided in the next section.

3 Results and Discussion

The proposed LBP pattern and Log-Gabor feature-based model is implied on ORL [16] face database. The database is originally generated by AT & T Laboratories. The database contains 400 facial instances of 40 distinct people. Each subject is represented by 10 variant images in terms of lighting, facial expression, and facial details. Each image exists in PGM format and 92×112 pixels in size. The face images are captured through frontal and upright camera positions and with the same background. The proposed model is analysed on three samplesets with different training–testing set combinations. Different ratio combinations are taken to generate these sample sets. The sampleset I (50%Tr-50%Ts), sampleset II (40%Tr-40%Ts), and sampleset III (70%Tr-30%Ts) are generated for generation of analytical results. The samplesets are generated separately for three different trails. In first trail, the random images are selected for training and testing set. In second trail, the illumination variant images are taken in the test set. In third analysis trail, the samplesets are generated with expression variant images. The comparative results are generated against PCA, Gabor + PCA, Log-Gabor PCA, and LBP-PCA methods. The comparative results for first trail of randomly selected test images are provided in Fig. 2.

Figure 2 has provided the comparative evaluation of accuracy rate for three samplesets generated with random face images. In sampleset I, the individual instances are equally split as training and test images. A total of 30 images are tested in this sampleset, and the proposed pattern-feature-based method has gained the accuracy of 90% which is comparatively higher then Log-Gabor + PCA method which achieved 86.67% accuracy. All accuracy of other methods is quite lower than these two feature classifiers. In sampleset II, as the number of training images are
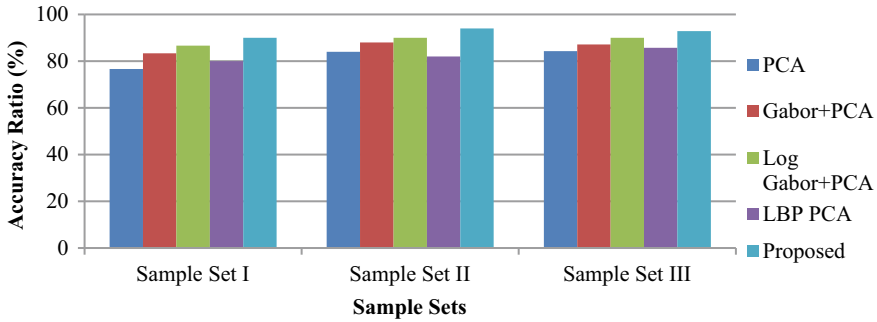
Fig. 2 Accuracy analysis (trail I-random face images)

increased, a significant accuracy gain is achieved by each of recognition method. Even then, the proposed method is the leading model with higher accuracy rate. The third test set is generated with 70 face images with 3 or lesser instances of an individual. A lesser difference in accuracy rate is identified for each classification method.

The proposed pattern-feature-based model is defined to improve the facial recognition on complex illumination and expression variant images. The results of second trail are generated for illumination variant images and are shown in Fig. 3. To handle the lightening difference, more number of training images are required. The sampleset I with lesser training instances gives the lesser accuracy rate for all the existing methods. The maximum accuracy obtained for existing methods is 73.33%, whereas the proposed pattern-feature-based method achieved the 86.67% of accuracy. It identified that the proposed model is eligible even for the smaller training set. The increase in the training set instances has given an effective improvement in performance of existing and proposed methods. In sampleset II and III, the Log-Gabor method achieved the accuracy rate of 78 and 80%, respectively. The maximum improvement is achieved for LBP-PCA method with an increase in training set size. The proposed model achieved the accuracy rate of 88 and 90% for samplesets II and III. It identified that the model is robust against the illumination variant with higher scalability support.

In third trail provided in Fig. 4, the expression variant samplesets are generated and analysed. The existing PCA and Gabor PCA methods provided the least performance against expression variation. The PCA, Gabor PCA, and LBP-PCA methods have achieved the accuracy of 65.7, 70, and 67.14% even for sampleset III with larger training sets. Even for the Log-Gabor PCA method, the accurate rate between 72 and 73% is achieved for different samplesets. Whereas the proposed model healed the expression effect using median and log-Gabor filter. The selective and relevant feature processed method has achieved a higher accuracy of 86.66, 88, and 87.14% for all three samplesets. The results identified that the proposed pattern-feature model is robust against expression variation and scalability vector.
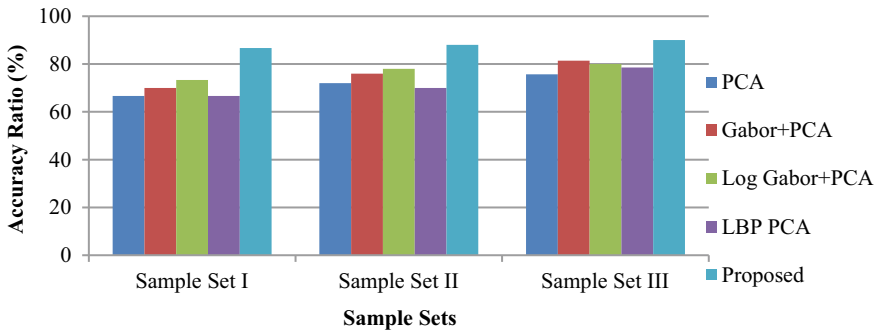
Fig. 3 Accuracy analysis (trail II-illumination variant faces)
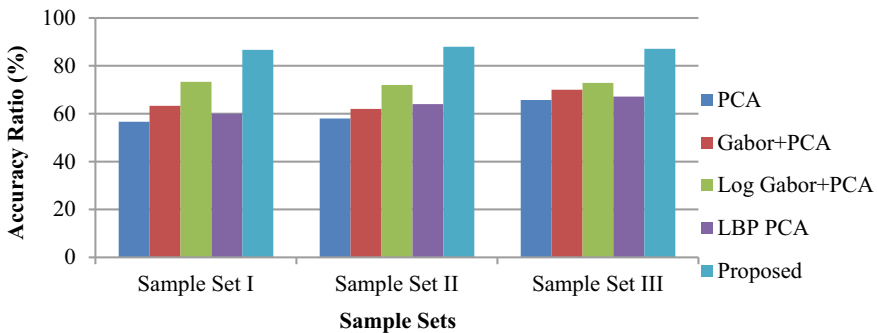
Fig. 4 Accuracy analysis (trail III-expression variant faces)

4   Conclusion

This research work is focused to improve the facial recognition in existence of illumination and expression variations. The proposed model applied the smoothen filter to resolve the noise impact. The illumination and expression deficiencies are handled by generating the LBP pattern-based Log-Gabor Feature face. The PCA is implied to train the pattern-feature face and to recognize the illumination and expression variant faces. The analytical results taken for expression variant and illumination variant datasets identified the significant improvement in facial recognition. The proposed model outperformed the existing PCA-based classifiers.

References

1. Vinitha KV, Kumar GS (2009) Face recognition using probabilistic neural networks. In: World congress on nature & biologically inspired computing, pp 1388–1393
2. Gillan S, Agathoklis P, Yasein MS (2009) A feature based technique for face recognition using mexican hat wavelets. In: IEEE Pacific rim conference on communications, computers and signal processing, pp 792–797
3. Dai G, Zhou C (2003) Face recognition using support vector machines with the robust feature. In: 12th international workshop on robot and human interactive communication, ROMAN, pp 49–53
4. Chen C, Zhang J (2007) Wavelet energy entropy as a new feature extractor for face recognition. In: Fourth international conference on image and graphics, pp 616–619
5. Schneider C, Esau N, Kleinjohann L, Kleinjohann B (2006) Feature based face localization and recognition on mobile devices. In: 9th International conference on control, automation, robotics and vision, pp 1–6
6. Rani JS, Devaraj D, Sukanesh R (2007) A novel feature extraction technique for face recognition. In: International conference on computational intelligence and multimedia applications, vol 2, pp 428–435
7. Gao JB, Li JP, Xia Q (2008) Slowly feature analysis of gabor feature for face recognition. In: International conference on apperceiving computing and intelligence analysis, pp 177–180
8. Goel P, Agarwal S (2012) An illumination invariant robust and fast face detection, feature extraction based face recognition system. In: Third international conference on computer and communication technology (ICCCT), pp 110–115
9. Xu XN, Mu ZC, Yuan L (2007) Feature-level fusion method based on KFDA for multimodal recognition fusing ear and profile face. In: International conference on wavelet analysis and pattern recognition, vol 3, pp 1306–1310
10. Panda R, Naik MK (2009) EBFS-fisher: an efficient algorithm for LDA-based face recognition. In World congress on nature & biologically inspired computing, pp 1041–1046
11. Hwang W, Wang H, Kim H, Kee SC, Kim J (2011) Face recognition system using multiple face model of hybrid Fourier feature under uncontrolled illumination variation. IEEE Trans Image Process 20(4):1152–1165
12. Azzawi AAG, Al-Saedi MAH (2010) Face recognition based on mixed between selected feature by multiwavelet and particle swarm optimization. In: Developments in e-systems engineering (DESE), pp 199–204
13. Mallipeddi R, Lee M (2012) Ensemble based face recognition using discriminant PCA features. In: IEEE congress on evolutionary computation (CEC), pp 1–7
14. Valuvanathorn S, Nitsuwat S, Huang ML (2012) Multi-feature face recognition based on PSO-SVM. In: 10th international conference on ICT and knowledge engineering (ICT & knowledge engineering), pp 140–145
15. Nazari S, Moin MS (2013) Face recognition using global and local gabor features. In: 21st Iranian conference on electrical engineering (ICEE), pp 1–4
16. Samaria FS, Harter AC (1994) Parameterisation of a stochastic model for human face identification. In: 2nd IEEE workshop on applications of computer vision. http://www.face-rec.org/databases

A Dimension-Based Database Reduction Approach to Optimize the Facial Recognition on Large Dataset

Kapil Juneja and **Chhavi Rana**

Abstract As the facial recognition model is used on an outsized dataset, the efficiency and trustworthiness of recognition method become more challenging. In this paper, a dataset diminution framework is offered to improve the reliability and competence of face recognition scheme. The facial parameters considered in this work are age, gender, and the feature-based classification. Each parameter is observed first on facial dataset under distance-level investigation to discover the qualified class. Each parameter is utilized to a dataset as a sequential observation to deduct the data set size as quantification vector. The paper also presented the experimentation to identify the performance in different sequences of factors applicability. The concluded observation signifies that the model has enhanced the efficiency of a recognition system for larger facial datasets.

Keywords Iris recognition · Statistical · Structural · PST · SVM

1 Introduction

The major applications of face recognition [1–3] are the process of identification or recognition of a person based on facial feature analysis, such as a criminal identification system. Such kind of systems is used by the intelligence department or the crime department of a country. When a user performs the identification process for a person or the criminal, it must search the database of all the history criminals, and such kind of database is obviously very large. It can have thousands or maybe lakhs of database images on which the recognition process will be performed. Even if we consider the smallest database that represents the country-wide data, then thousands of images is the minimum number of images in the database. In an identification-based application, the number of images decides the efficiency of

K. Juneja (✉) · C. Rana
Department of Computer Science and Engineering, University Institute of Engineering and Technology, Maharshi Dayanand University, Rohtak, Haryana 124001, India
e-mail: kapil.juneja81@gmail.com; kapil.juneja.1981@ieee.org

images. For each image, an individual comparison is performed. Because of this, there is the requirement of such an approach that can reduce the database size dynamically. In this present work, such an approach is presented to reduce the database size based on some parametric decisions. In this work, three main parameters are being considered to perform the classification of database in smaller sub-databases. With each level, the size of the database will be reduced. These parameters are represented by three parametric classification approaches called gender-based classification, age-based classification, and feature-based classification [2–5]. Here, the deductive parametric model is presented to reduce the database size based on these parameters in different combinations, and each combination is analyzed with a set of example with mixed type of images.

Figure 1 shows the overview of the proposed model. As we can see, the first four steps of the model are very generic and implemented by all the biometric applications for the recognition process, and the rest of the three steps are the actual part of the presented deductive model. Here, the description of all the stages of the recognition process is given.

1.1 Dataset Generation

The presented system will give better results for the heterogeneous large dataset. The large dataset here signifies that the number of images should be above 1000. The heterogeneity is required in gender and age of the person. The independent parameters of the dataset can be size of image, resolution, noise over the image, image type, etc. These parameters are defined in Table 1.
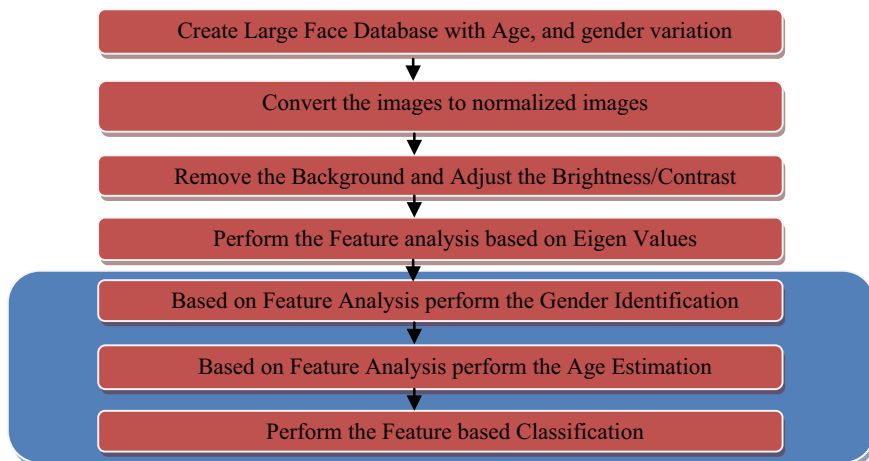
Fig. 1 Flow of proposed model

Table 1 Required parameter for facial database

Parameter	Values
Number of image	>1000
Age	15–60 recommended
Gender	Male and female
Image type	Jpg, gif, bmp, or png
Resolution	Any high resolution image
Physical size	100×100 recommended
Background	Does not matter
Noise	Does not matter

1.2 Normalization

Normalization is the process to convert the images respective to some defined parametric values. As the database is generally collected from different sources, because of this, the image set can differ in its physical and external characteristics. The normalization process will analyze all these parameters and convert all the images according to standardized parametric values. In this stage, the noise reduction, contrast, and illumination balancing are done to explore the image features.

1.3 Background Removal and Contrast Adjustment

In a general face image, the focus is on the face area, and this area is called region of interest (ROI). The actual feature analysis will be done. For the extraction of face area, the first task is to perform the brightness and contrast adjustment. For this adjustment, some mathematical operations can be implemented. Here the morphological mathematical model is suggested to perform the contrast adjustment. Now on this image, the background elimination will be performed to get the face area. Two morphological operators "OPEN" and "CLOSE" are suggested to extract the face area from the facial image. The open is the combined operation of erosion and dilatation, and these operations are performed in a sequence on same structure elements. This operation is used to preserve the global shape of the object. Open operation can expand the image and remove the background peaks. If closing operation occurs, the dilation process is followed by erosion performed on the same structural elements. It performs the hole and gap filling and gives the smoothness in object extraction.

1.4 Feature Extraction

Once the face area derives from the face image, the next work is to perform the feature extraction. In this work, the eigenvalues-based approach is suggested to

perform the feature extraction. In this PCA-based approach, the facial part of the image is represented by a vector of size n. We must identify this facial vector all N images over the database. Let each face vector is represented by Img_i to represent the ith face image [6, 7]. Then, the eigenvalue and the eigenvector for the image will be extracted by using Eq. (1)

$$C = \sum_{i=1}^{N} \frac{1}{N} \text{Img}_i \text{Img}_i^T \tag{1}$$

Here, N represents the number of face images, Img is for face image vector, and C for co-variance of images.

Now on C, the eigenvalue and eigenvector will be calculated for all the images. The calculated eigenvalues will store in a vector form. This eigenvector form is represented by Eig_i, where i lies between 1 and N for N images. These eigenvalues will work as the third parameter of classification.

2 Classification Process

The classification is the process to categorize the dataset in sub-classes or the categories, respectively, to different parameters. These parameters can be facial components, gender, etc. There are several dedicated applications in which the classification of dataset is required. Such as the many customer-based product recommender system does the gender identification to avail the required products to the customers [8]. In this present work, a three-layered classification approach is suggested based on three parameters shown in Fig. 2.

Fig. 2 Facial-database classification parameters
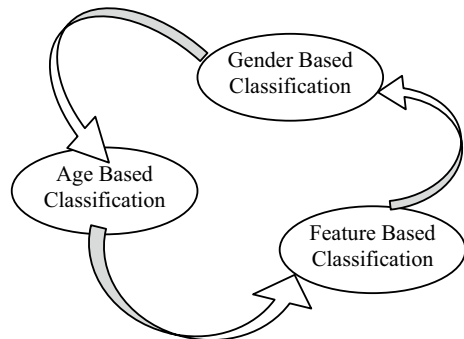
2.1 Gender-Based Classification

Gender is the most associated parameter that divides the available dataset in two major subsets called male and female. This categorization will divide the database into two almost equal halves, and because of this the classification will double the efficiency of the recognition process. There are several approaches available for the gender-based classification such as PCA [9], neural network, and KNN. In this present work, the KNN [10] is being implemented for the gender recognition. KNN is the vector quantization-based approach to perform the feature extraction and analysis. In this image, the minimum distance is from the featured image. Here, the distance parameter can be defined under different factors such as block distance [10] and Euclidean distance [10]. The equation of the block distance is given as

$$\text{Distance}(x, y) = \sum_{i=1}^{N} |xi - yi| \tag{2}$$

Here, xi and yi are the block pixels of two blocks x and y. Here, N is the scalar vector distance of the block.

The equation of the Euclidean distance is given as

$$\text{Distance}(x, y) = \sum_{i=1}^{N} \sqrt{|xi - yi|} \tag{3}$$

Here, xi and yi are the pixels of two blocks of size N and distance is representing the Euclidean distance between two blocks.

2.2 Age-Based Classification

In a face recognition process, one major problem is the aging. Designing an age-invariant system is one of the complex tasks during the identification process [11, 12]. In this present work, the age is another factor for the classification of the face database [13]. To perform the age estimation, internal features are extracted from the image. A lot of work already done in analyzing the person age based on facial analysis. Number of applications are available that require the age restriction. These applications perform the estimation of age group. More the age ranges will be decided, more efforts are required for the estimation. In most of the application, the considered age set is between 15 and 60 years. In this present work, the face images are divided into three main age groups as shown in Table 2.

In this present work, PCA with Markov model [14] is suggested to analyze the age group of a person, and on this basis the classification will be performed.

Age range	Class name
15–25	Young
26–40	Middle
41–60	Old

Table 2 Age-based classification

2.3 Feature-Based Classification

In this present work, the major criteria for the face recognition will be performed based on PCA [15]. It is one of the most effective mathematical and statistical models to identify useful information from an image. In this work, the eigenvalue and eigenvector will be calculated on the face area represented as the region of interest (ROI). In this work, we will first identify the eigenvalues for N images and maintained those in a scalar array of size N called $Eigen_{1,\ 2,\ 3\ldots N}$. In this present work, we have divided the eigenvalues into three main classes by setting up the two partitions $P1$ and $P2$ between the minimum and the maximum eigenvalues as shown in Fig. 3.

Here $M1$ = Minimum (Eigen)
$M2$ = Maximum (Eigen)
$P1 = (M2 - M1)/3$
$P2 = (2 * (M2 - M1))/3$

Based on the extracted features, three classes are defined at equal distance within the extracted eigenvalues. These classes are defined in Table 3.

3 Experimental Analysis

In Sect. 2, all the classification parameters are defined that are being used in this proposed work. Once the image dataset is normalized, then the classification process is done to divide the dataset into smaller sets. In this classification process, the above-defined parameters are used in a sequence. In this presented model, these three parameters will be used collectively irrespective to the order in which these

Fig. 3 Eigenvalue partitions for classification

Range	Classes
$M1$ to $P1$	Class A
$P1$ to $P2$	Class B
$P2$ to $M2$	Class C

Table 3 Feature-based classes

Table 4 Assumptions regarding presented model

Parameters	Assumed values	Parameters	Assumed values
Number of images	1500	Middle age	500
Number of males	750	Old age	500
Number of females	750	Class A images	500
Young persons	500	Class B images	500

parameters will be applied. After the classification process, smaller image sets will be generated. Now recognition process will be performed only on a small subset. Different models based on the order of parametric classification are defined in this section. To present the experimental analysis in a mathematical way, we are taking some assumptions. These assumptions are taken regarding the dataset on which the model will be implemented. In this experimental analysis, we are giving equal weightage to all the parameters. These assumptions are defined in Table 4.

Based on these assumptions, three models are presented to reduce the dataset. Here the comparative analysis is defined under some parameters. The time taken to perform the comparison on one image is represented by x. It means if y is the number of images been processed for the comparison, then total time taken will be $x * y$. Here, the analysis will be performed to find the number of image processing under different models. The other comparative parameter is the number of sub-data sets generated. These proposed models with comparative analysis are shown as below.

3.1 Model 1: Gender => Age => Feature

In this model, the face database classification and segmentation is performed under three parameters. At first, the dataset will be categorized based on the gender of persons. These two sub-datasets will be categorized again under the age parameter. This will further divide each imageset into three subsets under the age categorization. Finally, the feature-based categorization will be performed. The presented model is shown in Fig. 4.

As shown in Fig. 4, a total of 18 small datasets are generated, and the size of each db is approximate to 85 images. When user will pass an image for the recognition, at the first level, it be selected for the male or the female images set. If the input image is a male image, then the second categorization will check for the age factor and select the dataset with same age group as of an input source image. Finally, the small dataset will be generated based on eigenvalue analysis. The final statistics calculated is

Number of Imageset Generated: 18
The number of Images compared for recognition: 85.
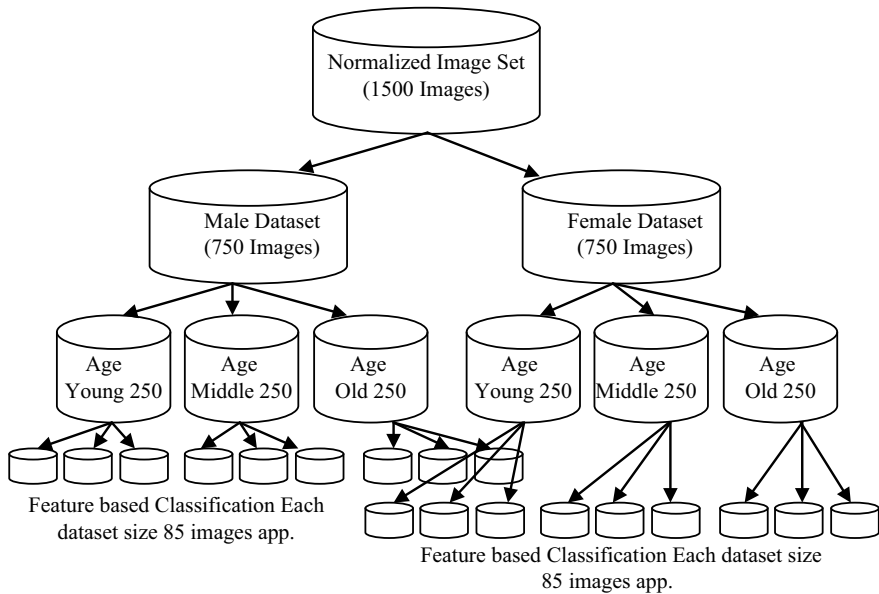
Fig. 4 Classification model 1

3.2 Model 2: Age =>Gender => Feature

The model in Sect. 3.1 is effectively efficient, but by changing the order of parametric classification a new model is generated. In this model, at first the age-based classification is performed. This classification process divides the dataset into a group of three sub-imagesets. Now each subset will be divided further based on the gender. Finally, the feature-based classification is performed based on eigenvalue. With each level, the size of the imageset is being reduced. Figure 5 shows the graphical representation of the proposed model.

The outcome driven from the second model is the same as the previous. It means the change of the classification parameter age and gender will not affect the efficiency of the recognition process. In this model, the total imagesets generated are 18. The number of images processed for the recognition is 85 approximately. The final statistics calculated is

Number of Imageset Generated: 18
The number of Images compared for recognition: 85.
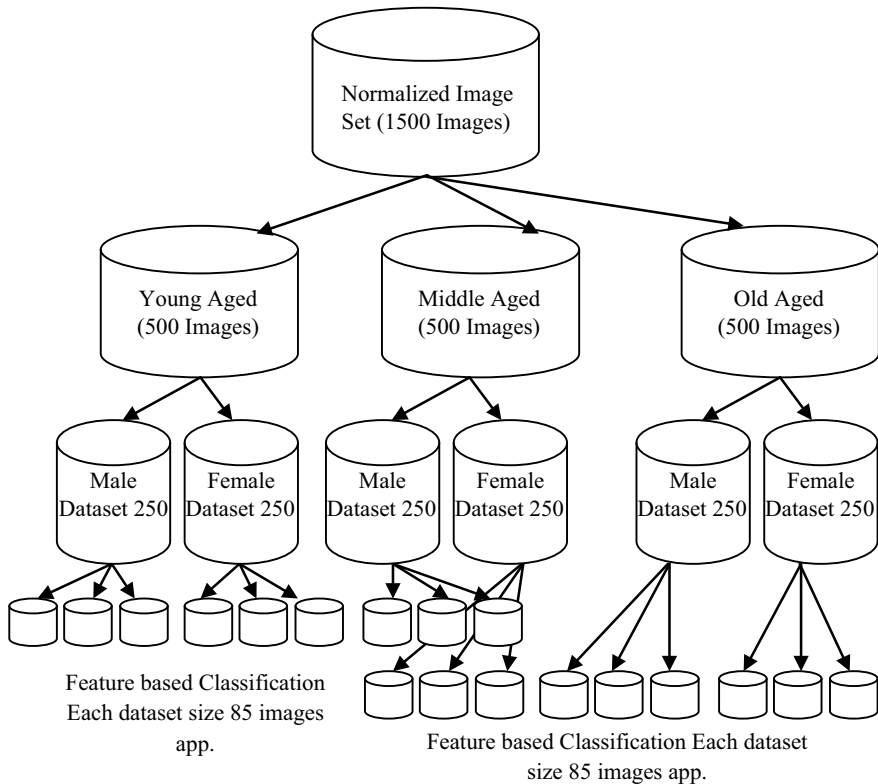
Fig. 5 Classification model 2

3.3 Model 3: Age => Feature =>Gender

The model in Sects. 3.1 and 3.2 are very efficient to reduce the dataset size and to improve the efficiency of recognition process. In this model, the first-level classification will be performed based on age parameter. On this classified imageset, the second-level classification will be performed based on eigenvalues-based feature extraction and finally the gender-based classification will be performed. The model is shown in Fig. 6.

The output driven from this model is the same as the all parametric values are constant. The number of image sets is 18, and the comparison required for the face image is about 83.

From these all analyses, we obtain the results with constant vector. But all these models show that the maximum number comparison after this model will be around 85, and if general approach occurs about 1500 comparisons are required.

Feature based Classification Each dataset size 83 images app.
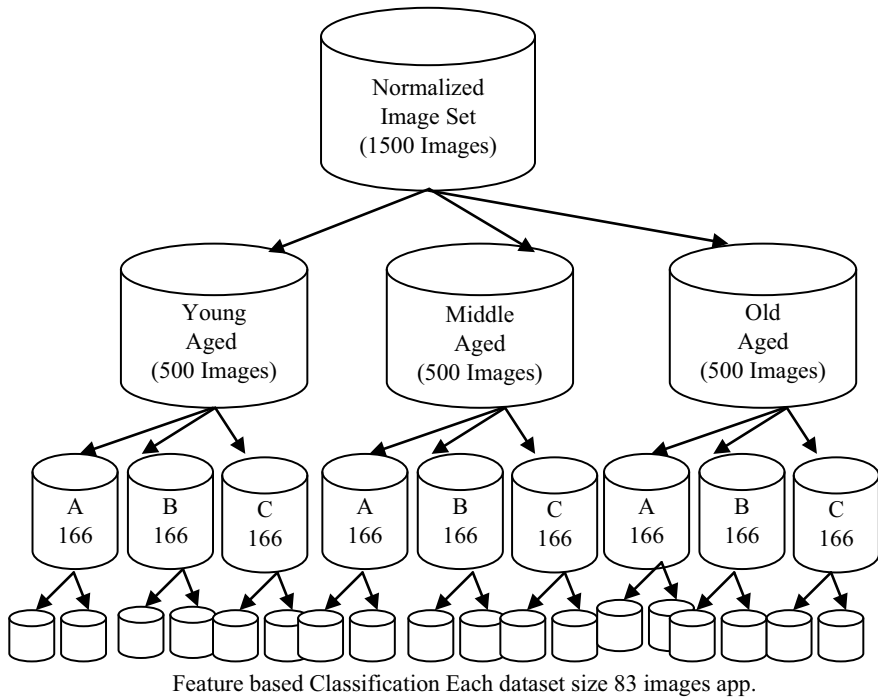
Fig. 6 Classification model 3

4 Conclusion

In this present work, a three-layered classification approach is presented to reduce the comparison imageset for the recognition process. The parameters suggested in this work are gender-based, feature-based, and age-based comparison. The experimental analysis shows the order of these parameters will remain the same if all classification parameters divide the dataset into equal parts. But with actual dataset, these models will return the high-performance results. The presented model can improve the efficiency of the system up to 90%.

References

1. Juneja K, Gill NS (2015) Tied multi-rubber band model for camera distance, shape and head movement robust facial recognition. In: International conference on applied and theoretical computing and communication technology (iCATccT), Davangere, pp 218–223
2. Juneja K (2015) Generalized and constraint specific composite facial search model for effective web image mining. In: International conference on computing and network communications (CoCoNet), Trivandrum, pp 353–361

3. Juneja K, Gill NS (2015) A hybrid mathematical model for face localization over multi-person images and videos. In: 2015 4th international conference on reliability, infocom technologies and optimization (ICRITO) (trends and future directions), Noida, pp 1–6
4. Juneja K (2015) MFAST processing model for occlusion and illumination invariant facial recognition. In: Advanced computing and communication technologies: proceedings of the 9th ICACCT, pp 161–170
5. Juneja K (2017) Multiple feature descriptors based model for individual identification in group photos. J King Saud Univ Comput Inf Sci. Computer and Information Sciences.
6. Chellappa R, Rajagopalan AN (2005) Background learning for robust face recognition with PCA in the presence of clutter. IEEE Trans Image Process 14(6):832–843
7. Su G (2002) MMP-PCA face recognition method. Electron Lett 38(25):1654–1656
8. Lian X-C, Li B (2011) Gender classification by combining clothing, hair and facial component classifiers. Neurocomputing 76(1):18–27
9. Boiser J (2009) Classifying gender with eigenfaces. Climate Informatics Laboratory, San Diego State University
10. Kouzani A, Ebrahimpour H (2007) Face recognition using bagging KNN. In: International conference on signal processing and communication systems (ICSPCS'2007), pp 17–19
11. Li Z (2011) A discriminative model for age invariant face recognition. IEEE Trans Inf Forensics Secur 6(3):1028–1037
12. Tin HHK (2011) Robust method of age dependent face recognition. In: 2011 4th international conference on intelligent networks and intelligent systems (ICINIS), pp 77–80
13. Fu Y (2010) Age synthesis and estimation via faces: a survey. IEEE Trans Pattern Anal Mach Intell 32(11):1955–1976
14. Zhuang X (2008) Face age estimation using patch-based hidden markov model supervectors. In: 2008 19th international conference on pattern recognition (ICPR 2008), pp 1–4
15. Bartlett MS (2002) Face recognition by independent component analysis. IEEE Trans Neural Net 13(6)

Human Emotion Recognition from Speech in Audio Physical Features

Akshay Chatterjee and Ghazaala Yasmin

Abstract Emotion is the part of human life which highly influences decision making compared to other things. The human emotion is not only conveyed by the body language but also through speech. Speech delivers the maximum information regarding the feelings of human. Nowadays, still there are many scenarios that these emotions are not being recognized properly. This is why this area has taken the attention of the researcher to explore. This fact has motivated us to propose a methodology to discriminate human emotions precisely. The proposed methodology has selected a set of features which carry more information about emotional feelings. The audio files database has been preprocessed. Physical features means both time-domain and frequency-domain features have been extracted from the preprocessed data. The files have been classified based on the feature. Some well-known classifier has been adopted for classification to achieve better outcome.

1 Introduction

Emotion recognition through speech has taken the center of interest among the researchers because of its ambiguous nature. As a result, it is difficult to achieve efficient accuracy while implementing the techniques for the emotion recognition system. Emotion is the most natural activity of human which can be expressive in gesture. Speech is the most expressive way to carry out the human emotions. This fact has motivated researchers to choose speech for exploring the domain of emotion recognition. Emotion detection is required in many applications. It is an

A. Chatterjee (✉) · G. Yasmin
Department of Computer Science and Engineering, St Thomas' College
of Engineering and Technology, Kolkata 700023, India
e-mail: akshay.chatterjee2015vit@gmail.com

G. Yasmin
e-mail: me.ghazaalayasmin@gmail.com

important factor of the human–computer interaction field. Our proposed work is to detect the emotion from an audio speech. An efficient human emotion recognition system will lead to more natural and friendly interaction between the human and digital computer.

1.1 Related Work

Numerous approaches on emotion recognition have been proposed to achieve better result. Nanavare and Jagtap [1] have been suggested recognition of human emotions from speech processing through hidden Markov model by means of dynamic programming. Wanare and Dandare [2] have proposed human emotion recognition from speech through neural network and support vector machine. Karpagavalli and Chandra [3] have given a review of different speech recognition techniques. Zeng et al. [4] have summarized a survey of affect recognition methods in audio, visual, and spontaneous expressions. Ververidis and Kotropoulos [5] have proposed emotional speech recognition through different audio features. Neiberg et al. [6] has propounded emotion recognition in spontaneous speech using Gaussian mixture model. Song et al. [7] have suggested audio–visual-based emotion recognition through hidden Markov model. Ramakrishnan [8] has highlighted algorithm and application of enhancement, modeling and recognition for speech. Vogt et al. [9] have given a review on automatic recognition of emotions from speech. Pokorny et al. [10] proposed an efficient technique for the detection of negative emotions in speech signals using bags-of-audio-words. Zhongzhe [11] have analyzed recognition of emotions in audio signals through different techniques. Pawar [12] has suggested recognition and classification of human emotion from audio. Kamińska and Pelikant [13] have proposed a technique for the recognition of human emotion from a speech signal based on Plutchik's model.

2 Proposed Methodology

Emotion can be categorized into different groups based on the various features of speech. They are discriminative in nature. While observing the various characteristics of speech, it has been observed that each kind of emotion has different features. The proposed work has aim to extract those features from the input speech. Then, we have used some dimensionality reduction principle to reduce the size of features. We have classified the speech according to the features. From the past works, it has been found that spectral flux and MFCC are one of the essential features for emotion classification. We have used four types of classifiers in our proposed work. And we have also depicted a clear comparison between them. Figure 1 gives a clear view of the proposed work.
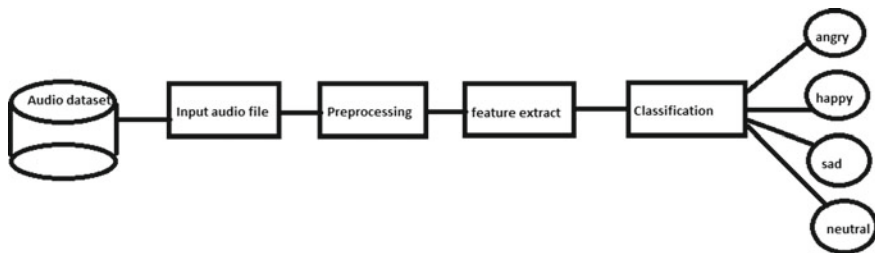
Fig. 1 Schematic block diagram for emotion recognition system

2.1 Feature Extraction

There are two kinds of features in audio. They are clip-level and frame-level features. The features are again divided into physical features and perceptual features. Physical features are of two types. Perceptual features contain pitch, tempo, etc. Time-domain features include zero-crossing rate (ZCR) and energy. Frequency-domain features include spectral flux. In our proposed work, we have used ZCR, energy, spectral flux, and MFCC.

2.1.1 Zero-crossing Rate (ZCR)

It is a time-domain feature. The audio signal changes the sign from positive to negative and back. The rate of change of sign along a signal is called zero-crossing rate. It is always a key feature to classify sounds. ZCR is defined in Eq. (1)

$$z = \sum_{p=1}^{n-1} \mathrm{sign}[x(p-1) * x(p)] \tag{1}$$

Here, n indicates the number of samples present in the rth frame and

$$\mathrm{sign}[x] = \begin{cases} 1, & \text{if } x > 0 \\ 0, & \text{otherwise} \end{cases} \tag{1.1}$$

It has been found that during different emotions the sign change is an important factor. So, we have considered the rate of sign change feature for our classification of emotions. Mean and standard deviation has been calculated from ZCR.

2.1.2 Energy

Short-time energy (STE) is a simple but effective time-domain feature, which is widely calculated for finding the variation in the emotion of a person. The energy of the pth frame is defined in Eq. (2).

$$Ep = \sum_{n=1}^{r} [xp(n)]^2 \qquad (2)$$

2.1.3　Mel Frequency Cepstral Coefficients (MFCC)

It is Mel Frequency Cepstral Coefficient. In audio, frequency bands are not linear and arranged by their mel scale. In other words, it is a scale of melody and calculates the difference in level. The first 13 coefficients of MFCC are highly discriminative in nature in terms of classification. So, we have used MFCC as a feature. In Fig. 2, *X*-axis denotes the audio dataset number and *Y*-axis denotes the MFCC value of the corresponding audio file. Figure 2 shows the 13 coefficients of MFCC in the plot.

$f_n = 2595 * \log_{10} (1 + f)$; f is the frequency of the given speech signal.

2.1.4　Spectral Flux

It is also a frame-level feature and a frequency-domain feature. It is the squared difference between the normalized magnitudes of the spectra of the two successive frames. The mean and standard deviation has been calculated from the spectral flux with respect to all frames. It has been noticed that the spectral flux changes precisely as the human emotion changes in their speech. Figure 3 shows the plot for spectral flux. The mathematical expression for spectral is given in Eq. (3). *N* is the
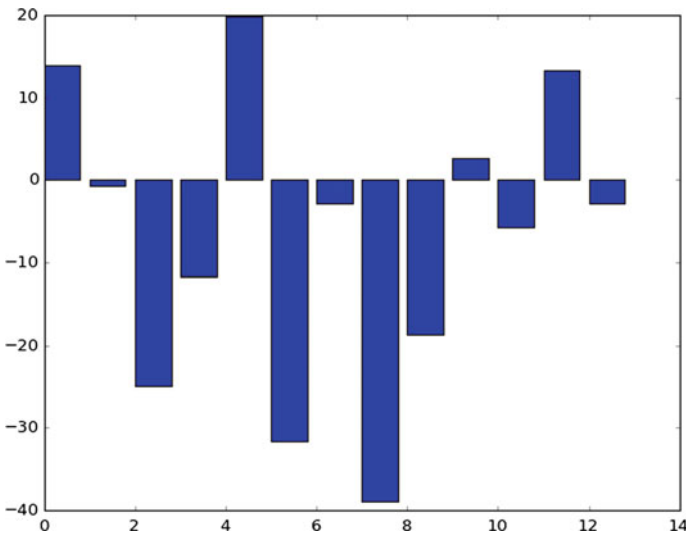
Fig. 2 MFCC plot for speech
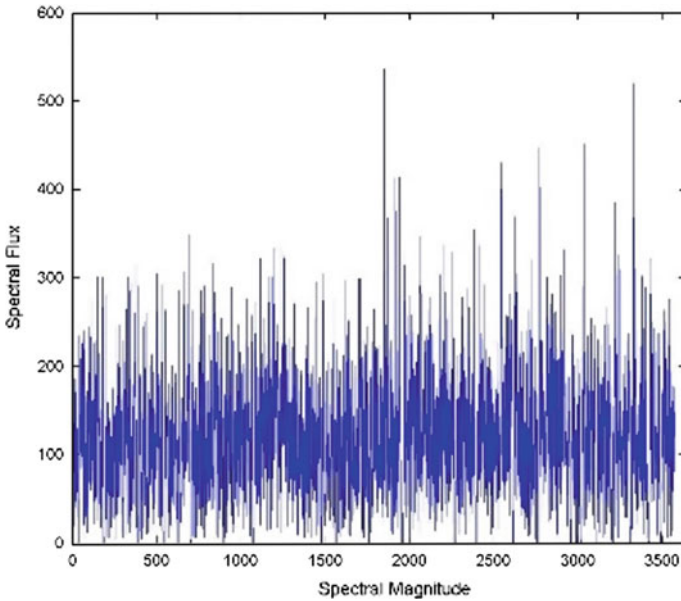
Fig. 3 Spectral flux of sample speech file

total number of frames. The square of the difference of sample value of frame $t-1$ and t for sample has been computed. Henceforth, mean and standard deviation has been calculated.

$$\sum_{x=1}^{n} \{Nt(x) - Nt - 1(x)\}^2 \tag{3}$$

2.2 Classification

Classification is defined as the process of grouping the given observation into a set of categories. This term involves two types of learning process; one is supervised learning where the set of class for identification is mentioned. Another is unsupervised learning also termed as clustering which categorizes the data based on some inherent similarity. The classification algorithm is known as classifier. For classification, weka tool [14] has been used to check the accuracy of the proposed work. Classifiers like Naïve Bayes and multilayer perceptron have been taken into account. Furthermore, random forest has been chosen as it has been noticed that this classifier gives the better result among all decision tree algorithm for the proposed system. For each classifier ten folds cross validation has been done.

2.2.1 Random Forest Classifier

It is a supervised learning technique. It creates a subset of decision trees from a set of training variables. Then, it takes feedback from the trees and creates a voting system and finds the maximum efficient set. From the past outcome, it has been found that random forest is one of the powerful classifiers.

2.2.2 Support Vector Machine

This is a supervised model that helps in classification and regression. Given a set of different data as an input, it will just find out what are the various types are there and classify them in non-probabilistic and binary form. It is a path from the artificial neural network which was unable to give the same accuracy to the functions what SVM performs. Only follows not obeys algorithms like support vector classification and support vector clustering. Classification algorithm is solved using some kernel functions like: linear, polynomial, and radial basis function. It helps in classifying different classes.

2.2.3 Multilayer Perceptron

This also comes under supervised learning technique. It is a feedforward neural network which contains at least three layers of nodes. Every layer of node except the input one uses nonlinear activation function. It can classify nonlinear datasets. That is why it is appropriate for classification in case of our dataset.

2.2.4 Naïve Bayes Classifier

This is scalable and class-probabilistic classifiers and is based on Bayes theorem. It requires parameters linear in the number of variables. It is a supervised model that trains the features and classifies by labeling each class. This consists of a group of algorithms like GaussianNB and multinomialNB. Gaussian Naïve Bayes has been used for the proposed methodology.

3 Experimental Result

The verification for the suggested method has been tested for wide range of heterogeneity in speech dataset. These datasets have been made up with 400 files having duration of each file is 120 s. These datasets have been collected from recording of different speakers, and some files have been downloaded from the

Table 1 Classification accuracy (in %) for proposed work

Classification of scheme	Happy	Angry	Sad	Neutral
Random forest	91.5	92.4	93.7	91.9
Support vector machine	81	80.6	80.4	80.3
Multilayer perceptron	96	95.3	92.6	94.9
Naïve Bayes'	90.4	90.3	91.6	90.7

Internet. To determine the feature more precisely, each speech signal has been broken into multiple frames consisting 8 s each. The sound has been preprocessed through noise removal to achieve better accuracy. In Table 1, the accuracy of proposed work has been shown which has been classified by different types of classifiers. Here, the accuracy has been summarized based on the classifier which has given better accuracy compared to other classifiers. A total of 18 features (13 MFCC + 2 ZCR + 2 Spectral flux + 1 Energy) have been subjected for classification. Since the feature set is small, feature selection algorithm has not applied on the extracted features.

3.1 Comparative Analysis

The proposed methodology has been compared with the work of Nanavare and Jagtap [1] on the sample data collected for the proposed work. The same has also been tested on the technique proposed by Song et al. [7] and Kamińska and Pelikant [13]. Nanavare et al. has proposed the methodology based on hidden Markov model. The same technique has been used by Song et al. [7]. Kamińska and Pelikant [13] have adopted audio features from speech. Table 2 shows the result achieved by the proposed technique is coming up with better result compared to the other techniques.

Table 2 Comparative study (in %) for the substantial work

Precedent approach	Happy	Angry	Sad	Neutral
Nanavare and Jagtap [1]	88.5	86.7	85.1	86
Song et al. [7]	87	84.2	83	82.8
Kamińska and Pelikant [13]	90.02	89.4	88.3	87.3
Proposed work	96	95.3	92.6	92.5

4   Conclusion

The proposed system has developed to discriminate different types of human emotion more precisely. The novelty of the system is achieving better result by extracting small set of feature. The proposed method can be explored more with new features in the future. New feature selection algorithm will be implemented. The proposed system will be tested with different indiscriminative emotions. Furthermore, the system will be tested with some benchmark data. The method classifies the emotion into four groups; it can be extended for more classes of emotion which can be used for worldwide human–computer interaction fields.

References

1. Nanavare VV, Jagtap SK (2015) Recognition of human emotions from speech processing. Procedia Comput Sci 49:24–32
2. Wanare MAP, Dandare SN (2014) Human emotion recognition from speech. System 6
3. Karpagavalli S, Chandra E (2016) A review on automatic speech recognition architecture and approaches. Int J Signal Process Image Process Pattern Recogn 9(4):393–404
4. Zeng Z et al (2009) A survey of affect recognition methods: audio, visual, and spontaneous expressions. IEEE Trans Pattern Anal Mach Intell 31(1):39–58
5. Ververidis D, Kotropoulos C (2006) Emotional speech recognition: resources, features, and methods. Speech Commun 48(9):1162–1181
6. Neiberg D, Elenius K, Laskowski K (2006) Emotion recognition in spontaneous speech using GMMs. In: Ninth international conference on spoken language processing
7. Song M et al (2004) Audio-visual based emotion recognition—a new approach. In: Proceedings of the 2004 IEEE computer society conference on computer vision and pattern recognition, 2004, CVPR 2004, vol 2. IEEE
8. Ramakrishnan S (2012) Recognition of emotion from speech: a review. In: Speech enhancement, modeling and recognition-algorithms and applications. InTech
9. Vogt T, André E, Wagner J (2008) Automatic recognition of emotions from speech: a review of the literature and recommendations for practical realisation. In: Affect and emotion in human-computer interaction. Springer, Berlin, Heidelberg, pp 75–91
10. Pokorny FB et al (2015) Detection of negative emotions in speech signals using bags-of-audio-words. In: 2015 international conference on affective computing and intelligent interaction (ACII). IEEE
11. Zhongzhe XIAO (2008) Recognition of emotions in audio signals. Dissertation thesis, Google Scholar
12. Pawar A, Student ME (2017) Recognition and classification of human emotion from audio. Int J Eng Sci 13790
13. Kamińska D, Pelikant A (2012) Recognition of human emotion from a speech signal based on Plutchik's model. Int J Electron Telecommun 58(2):165–170
14. Srivastava S (2014) Weka: a tool for data preprocessing, classification, ensemble, clustering and association rule mining. Int J Comput Appl 88(10)

A Critical Analysis of Present Net Metering Regulatory Framework and Identification of Potential Barriers in the Growth of Rooftop Market

Hansika Dhankhar and Naqui Anwer

Abstract Rooftop solar in Indian market has seen a tremendous growth all these years, especially in industrial and commercial segments, increasingly in the OPEX model. Considerable efforts have been put up to develop the rooftop solar sector (40 GW targeted, out of 100 GW of grid-connected solar energy) by the government, regulatory commissions, and concerned agencies. One aspect of growth can be attributed to net metering, which is being adopted at a larger scale. Net metering with an objective to meet the self-demand of electricity by the consumers is essentially a billing mechanism which enables the consumers export the excess power into the grid. Excess power is banked with the local utility and adjusted in the bill of the consumers. This paper provides a thorough analysis of the state-wise regulatory framework for net metering and the intricacies involved in implementation.

1 Introduction

If a solar energy-generating system makes more electricity than is consumed, the consumer has an option to export the excess power back to the grid and in return get credited or paid for it. This net metering-based system offers numerous benefits to the consumer and society.

Almost all the states have come up with different net metering regulations, and their implementation has been a momentous success. This paper will highlight various parameters involved in the analysis of state net metering and stress on

H. Dhankhar (✉)
Amplus Energy Solutions Pvt Ltd, Gurgaon, India
e-mail: hansikadhankhar@gmail.com

N. Anwer
TERI School of Advanced Studies, New Delhi, India
e-mail: naqui.anwer@terisas.ac.in

state-specific issues at the policy implementation front. An analysis between different states has been carried out to understand the slow progress on the implementation front. A set of case studies will also be taken into consideration to get a clear picture on the ground implementation of it. The final goal is the importance of analyzing net metering in the context of more comprehensive energy policies.

2 State-Wise Comparative Analysis of Net Metering

A comparative analysis is required to understand the working model for different state net metering regulations. We have here considered all major states, i.e., Andhra Pradesh, Delhi, Gujarat, Haryana, Karnataka, Maharashtra, Madhya Pradesh, Punjab, Rajasthan, and Tamil Nadu.

The basis of our analysis will be different parameters (mentioned below) to help us bring clarity on the regulations and its implementation.

2.1 Parameters Considered

1. Definition of premises
2. Capacity cap
3. Cap as per sanctioned load
4. Cap as per distribution transformer
5. Multiple interconnection allowance
6. Solar generation meter specification
7. Meter class for net meter
8. Check meter requirement
9. Settlement

2.1.1 Andhra Pradesh [1]

Andhra Pradesh came out with the net metering regulations in the year 2015.

Definition of premises	Rooftops or/and elevated areas on land, building, or infrastructure or part or combination in respect of which a separate metering arrangement have been made by the license
Capacity cap	1000 kWp
Cap as per sanctioned load	The cap can exceed the sanctioned load
Cap as per distribution transformer rating	60% of the distribution transformer (DT) rating

<div align="right">(continued)</div>

(continued)

Multiple interconnection allowance	Allowed in the state
Solar generation meter specifications	Class: 0.5 s LT meter
Meter class for net meter	Class: 0.2 s
Check meter requirement	Required to be installed with main meter; accuracy class of the meter to be the same as that of meter with which it must be installed
Settlement	Monthly settlement at average cost of supply (ACoS) at the end of settlement period

2.1.2 Delhi [2]

Delhi came out with the net metering regulations in the year 2014.

Definition of premises	Rooftops or/and elevated areas on land, building, or infrastructure or part or combination in respect of which a separate metering arrangement have been made by the license
Capacity cap	No cap
Cap as per sanctioned load	The cap can exceed the sanctioned load
Cap as per distribution transformer rating	20% of the distribution transformer (DT) rating
Multiple interconnection allowance	Allowed in the state
Solar generation meter specifications	Class: 0.5 s LT meter
Meter class for net meter	Class: 0.2 s or 0.5 s
Check meter requirement	Check meter not required
Settlement	Yearly settlement In the case of TOD, settlement will be in the same time block as of generation Settlement at average power purchase cost (APPC) at the end of settlement period

2.1.3   Gujarat [3]

Gujarat came out with the net metering regulations in the year 2016.

Definition of premises	Rooftops or/and elevated areas on land, building, or infrastructure or part or combination in respect of which a separate metering arrangement have been made by the license
Capacity cap	1000 kW
Cap as per sanctioned load	Cap of 50% of the sanctioned load
Cap as per distribution transformer rating	65% of the distribution transformer (DT) rating
Multiple interconnection allowance	The state has not given any clarity on it
Solar generation meter specifications	Class: 0.5 s LT meter
Meter class for net meter	Class: 0.2 s with or without ABT
Check meter requirement	Required to be installed with main meter; accuracy class of the meter to be the same as that of meter with which it has to be installed
Settlement	Monthly settlement at average power purchase cost (APPC) at the end of settlement period

2.1.4   Haryana [4]

Haryana came out with the net metering regulations in the year 2014.

Definition of premises	Rooftops or/and elevated areas on land, building, or infrastructure or part or combination in respect of which a separate metering arrangement have been made by the license
Capacity cap	1000 kWp
Cap as per sanctioned load	The cap is 100% of the sanctioned load
Cap as per distribution transformer rating	15% of the distribution transformer (DT) rating
Multiple interconnection allowance	Allowed in the state
Solar generation meter specifications	Class: 0.5 s LT meter
Meter class for net meter	Class: 0.2 s
Check meter requirement	Check meter not required
Settlement	Yearly settlement In the case of TOD, settlement will be in the same time block as of generation No payment of excess energy at end of settlement period

2.1.5   Karnataka [5]

Karnataka came out with the net metering regulations in the year 2016.

Definition of premises	The definition of premises includes rooftops
Capacity cap	1000 kWp
Cap as per sanctioned load	The cap is 100% of the sanctioned load
Cap as per distribution transformer rating	80% of the distribution transformer (DT) rating
Multiple interconnection allowance	Allowed in the state
Solar generation meter specifications	Class: 0.5 s LT meter
Meter class for net meter	Class: 0.2 s
Check meter requirement	Required to be installed with main meter; accuracy class of the meter to be the same as that of meter with which it has to be installed
Settlement	Monthly settlement The settlement rate will be as follows for different plant capacities: 50–100 kW: INR 6.14 per unit 100–500 kW: INR 5.67 per unit 500–1000 kW: INR 5.2 per unit

2.1.6   Maharashtra [6]

Maharashtra came out with the net metering regulations in the year 2015.

Definition of premises	Rooftops or/and elevated areas on land, building, or infrastructure or part or combination in respect of which a separate metering arrangement have been made by the license
Capacity cap	1000 kW
Cap as per sanctioned load	The cap is 100% of the sanctioned load
Cap as per distribution transformer rating	40% of the distribution transformer (DT) rating
Multiple interconnection allowance	Allowed in the state
Solar generation meter specifications	Class: 0.5 s LT meter
Meter class for net meter	0.5 s/0.2 s (0.5 s if sanctioned load < 1000 kVA and 0.2 s if sanctioned load > 1000 kVA)
Check meter requirement	Check meter mandatory, if load is more than 1000 kVA
Settlement	Yearly settlement at APPC at the end of settlement period In case of TOD, settlement will be in same time block as of generation

2.1.7   Madhya Pradesh [7]

Madhya Pradesh came out with the net metering regulations in the year 2015, and then amended in the year 2017.

Definition of premises	Rooftops or/and elevated areas on land, building, or infrastructure or part or combination in respect of which a separate metering arrangement have been made by the license
Capacity cap	2000 kW
Cap as per sanctioned load	The cap cannot exceed the sanctioned load
Cap as per distribution transformer rating	30% of the distribution transformer (DT) rating
Multiple interconnection allowance	Allowed in the state
Solar generation meter specifications	Class: 0.5 s LT meter
Meter class for net meter	0.5 s, 5 A up to 132 kV 0.2 s, 1 A 132 kV and above
Check meter requirement	Required to be installed with main meter for plants above 250 kW; accuracy class of the meter to be the same as that of meter with which it must be installed
Settlement	Yearly settlement at APPC at the end of settlement period In case of TOD, settlement will be in same time block as of generation

2.1.8   Punjab [8]

Punjab came out with the net metering regulation in the year 2015.

Definition of premises	Rooftops or/and elevated areas on land, building, or infrastructure or part or combination in respect of which a separate metering arrangement have been made by the license
Capacity cap	1000 kW
Cap as per sanctioned load	The cap is 80% of the sanctioned load
Cap as per distribution transformer rating	30% of the distribution transformer (DT) rating
Multiple interconnection allowance	Allowed in the state
Solar generation meter specifications	Class: 0.5 s LT meter
Meter class for net meter	Class: 0.2 s
Check meter requirement	No check meter required
Settlement	Yearly (Oct to Sept) settlement

(continued)

	Electricity generation capped at 90% of energy consumed
	In the case of TOD, settlement will be in same time block as of generation
	No payment of excess energy at end of settlement period

2.1.9 Rajasthan [9]

Rajasthan came out with the net metering regulations in the year 2015.

Definition of premises	Rooftops or/and elevated areas on land, building, or infrastructure or part or combination in respect of which a separate metering arrangement have been made by the license
Capacity cap	1000 kWp
Cap as per sanctioned load	The cap is 80% of the sanctioned load
Cap as per distribution transformer rating	30% of the distribution transformer (DT) rating
Multiple interconnection allowance	Allowed in the state
Solar generation meter specifications	Class: 0.5 s LT meter
Meter class for net meter	Class: 0.2 s
Check meter requirement	Required to be installed with main meter; accuracy class of the meter to be the same as that of meter with which it has to be installed
Settlement	Monthly settlement at feed in tariff (FiT) if excess units exceed 50 units, otherwise the excess units are carried forward to next billing cycle
	In the case of TOD, settlement will be in same time block as of generation
	No payment of excess energy at end of settlement period

2.1.10 Tamil Nadu [10]

Tamil Nadu came out with the net metering regulation in the year 2014.

Definition of premises	Rooftops or/and elevated areas on land, building, or infrastructure or part or combination in respect of which a separate metering arrangement have been made by the license
Capacity cap	No capacity cap
Cap as per sanctioned load	The cap is 100% of the sanctioned load

(continued)

(continued)

Cap as per distribution transformer rating	30% of the distribution transformer (DT) rating
Multiple interconnection allowance	No clarity on the multiple interconnection allowance
Solar generation meter specifications	Mandatory for availing GBI (solar generation check meter above 20 kW in the case of GBI) Class: 0.5 s LT meter
Meter class for net meter	Class: 0.2 s ABT above 112 kW
Check meter requirement	No requirement for check meter
Settlement	Yearly settlement Electricity generation capped at 90% of energy consumed from DISCOM No payment of excess energy at end of settlement period

3 State Specific Major Challenges in Net Metering

It is observed that the slow progress on the net metering policy front is attributed largely, but not limited to:

- Inadequate regulatory framework.
- Passive opposition from DISCOMs.
- Lack of appropriate training and process protocol at the local utility level.

Some of the major hurdles are:

3.1 Capacity Cap

Currently, the capacity of solar plant can reach up to 100% of sanctioned load but is limited to 1 MWp for net metering. This creates a bottleneck in utilization of large rooftops available with the commercial and industrial consumers. We feel that restricting the project capacity with contracted load is a rational approach and same should be adopted across states.

States such as Karnataka, Uttar Pradesh, Andhra Pradesh, and Telangana have allowed higher capacity and restricted it with contracted load.

Also, the capacity cap according to the distribution transformer (DT) should be increased. Currently, the capacity allowed in the area of a particular distribution transformer is capped at 15% of the rated capacity of the DT in Uttar Pradesh, whereas Karnataka has allowed a cap of 80% in the area of the distribution transformer.

3.2 Asymmetricity Between the Government Policies and Regulations

Government encourages developers by announcing incentives and exemptions; however, unless adopted by the state regulators, benefits are not made available by the DISCOMs to developers.

To name a few:

- Delhi Govt. has provisioned the concept of virtual net metering and group net metering in solar policy. However, regulatory framework for both is awaited. Therefore, implementation is yet to appear and practice.
- In Haryana Govt. has provisioned several incentives such as exemption from electricity duty, wheeling charges, and transmission charges, but regulators have not adopted them regulations, and hence benefits are not available to the developers.

3.3 Inconsistence Policy Framework Across the States

There is a lack of consistency in the way net metering is dealt with in various states. Implementation is not improving with more experience or years of policy in operation.

Examples:

- Gujarat and Chhattisgarh do not allow net metering to third-party-owned rooftop plants.
- West Bengal has not recognized third-party sale under net metering.
- Tamil Nadu has allowed net metering to commercial and industrial consumers.
- Haryana does not allow net metering to open access consumers—Central Electricity Authority (CEA) has exempted the inspection of Chief Electrical Inspector General (CEIG) for renewable energy plant up to 500 kW. However, states have taken individual approaches on it.

3.4 Unawareness of Authorities Regarding the Implementation Process

The installers have varying experiences presumably because of different policy interpretation by local implementation authorities. The authorities mostly are unaware of the process, and this leads to further delay in implementation.

An example:

- In Uttar Pradesh, according to the current regulation, consumer has to intimate Uttar Pradesh New and Renewable Energy Development Agency (UPNEDA) about the installation of solar plant. But it is interpreted by DISCOMs that consumer has to provide a NOC from UPNEDA which takes time and delays the process of net metering by at least 30 days.

We feel, if the plant is not under any Govt. scheme, then the customer should not have any liability to inform UPNEDA, instead UPNEDA shall take the information directly from DISCOM or UPNEDA can have an online portal where details of the solar plant can be uploaded and that too after completion of installation.

3.5 Procedural Challenges

Procedural/operational challenges have been controlling execution in an undesired direction by forming delays. Since procedures have important consequences on operational efficiency, it prohibits the seamless implementation of net metering.

For instance:

- Uttar Pradesh: DISCOMs insist on a no-objection certificate (NOC) from State Nodal Agency (SNA) before accepting the applications for net metering. SNA takes minimum 20 days in issuing NOC. It causes the delay in processing the application and consumes time and efforts. It is to be noted that the role of SNA is insignificant in the whole process and not required by the regulations.
- Haryana: DISCOMs process the application only after receiving the project completion report (PCR) from SNA. PCR is relevant for projects allocated under state program/tender/subsidy and has no significance for projects installed under a direct arrangement between developer and consumer. PCR as a pre-requisite leads to an undesirable delay in last mile implementation and forces generators to run only the partial capacity of plant and keep rest in "Off" mode for at least two months from the commissioning.

4 Conclusion

Implementation of net metering has to be improved, and the process should be smoothened in order to overcome the barriers to drive the growth of the sector. All the efforts taken by the government will not be able to provide the desired results until net metering policy framework is urgently reformed.

References

1. Andhra Pradesh Electricity Regulatory Commission. Available at: http://www.aperc.gov.in/
2. Delhi Electricity Regulatory Commission. Available at: http://www.derc.gov.in/
3. Gujarat Electricity Regulatory Commission. Available at: http://www.gercin.org/
4. Haryana Electricity Regulatory Commission. Available at: http://herc.gov.in/
5. Karnataka Electricity Regulatory Commission. Available at: http://www.karnataka.gov.in/kerc/Pages/home.aspx
6. Maharashtra Electricity Regulatory Commission. Available at: http://www.mercindia.org.in/
7. Madhya Pradesh Electricity Regulatory Commission. Available at: http://www.mperc.nic.in/index.htm
8. Punjab Electricity Regulatory Commission. Available at: http://www.pserc.nic.in/
9. Rajasthan Electricity Regulatory Commission. Available at: http://rerc.rajasthan.gov.in/
10. Tamil Nadu Electricity Regulatory Commission. Available at: http://www.tnerc.gov.in/

Impact on Performance of Bundled SWCNT Interconnects Surrounded with Semiconductor Shielding Materials

V. Sulochana, Sunil Agrawal and Balwinder Singh

Abstract In this paper, a technique of shielding the bundled single-walled carbon nanotube (SWCNT) interconnects is discussed to reduce the crosstalk interference in adjacent CNT networks. An aggressor–victim test structure is formed to examine the effect of aggressor on victim line with/without shielding. Simulations are carried for the aforementioned test structures, and the performance of SWCNT bundle is analyzed in terms of potential distribution, drain current, crosstalk current gain, and power dissipation in the test structure. Because the proposed test structure reduces the effect of electromagnetic interference in adjacent CNT interconnects due to shielding, the structure with shielding material (silicon and aluminum gallium arsenide) exhibits an even potential distribution and constant crosstalk current gain nearly equal to zero in victim CNT line when compared to without shielding. Further, Si displays better shielding characteristics than AlGaAs against power dissipation. Therefore, it can be concluded that a considerable reduction the in induced cross talk can be achieved by employing the proposed shielding technique.

Keywords Carbon nanotube (CNT) · Single-walled CNT (SWCNT) · Propagation delay · Crosstalk noise · Interconnects · Shielding · Aluminum gallium arsenide (AlGaAs)

V. Sulochana (✉) · B. Singh
Centre for Development of Advanced Computing (C-DAC), Mohali, India
e-mail: vemus@cdac.in

B. Singh
e-mail: balwinder@cdac.in

S. Agrawal
Department of Electronics & Communication, University Institute of Engineering & Technology, Panjab University, Chandigarh, India
e-mail: s.agrawal@hotmail.com

1 Introduction

Carbon nanotubes (CNTs) have unique properties, which make them vital for nanotechnology and other electronic and material science fields. One of the major applications of CNTs is as interconnects. Interconnects are widely in the operation for transmission of clock, power supply, data, and ground throughout an integrated circuit. Earlier metals such as aluminum and copper were preferred, but they suffer from electromigration which in turn reduces their reliability. CNTs can be acknowledged as encouraging candidate in comparison to copper, as they have higher reliability and better performance. Another variation is in the formation technique as interconnect developed from copper is formed using a traditional top-down approach and for CNT bottom-up (developed on substrate and then adjusted according to the need) approach is used [1]. Formerly, it was pretended that single-walled CNTs (SWCNTs) do not devote in conduction and hence overlooked [2, 3], but SWCNTs reduce coupling capacitance when shielded by semiconducting CNTs [4]. Therefore, in [4], a test structure where metallic CNTs are at core and semiconducting CNTs are at periphery of CNT bundle is used to analyze the crosstalk effect. Generally, a single SWCNT possesses a higher quantum resistance and hence is not suitable for interconnect applications. Therefore, a bundle of SWCNTs is preferred for the high-speed interconnect applications. A bundled SWCNT can achieve better performance than Cu interconnects in current IC technology [5–7].

In [8], multiequivalent, single-conductor model is developed to reduce cross talk in bundled CNTs and with the reduced delay. In this paper, the simulation-based result is shown, but cross talk can also be examined with RLC model, and by RLC model, it can be shown that cross talk is affected by diameter of CNTs and spacing between them. With proper geometry of RLC network, 59% reduction in crosstalk-induced delay and 81% reduction in crosstalk-induced peak voltage can be obtained [9, 10]. It is shown that along with single-walled nanotubes and multiwalled nanotubes, mixed carbon nanotube bundles can also be used which showed an improvement by 80% (compared to SWCNTs and MWCNTs) [11]. In recent studies, it is found that as compared to copper interconnects, CNTs are also beneficial in increasing the gate oxide reliability [12]. In [13], 4H-silicon carbide-based CNTs have been used as it is directly available in ATLAS library and it requires only few modifications (recombination and band parameters) to make it work as a metallic SWCNT with a sheet resistance of 128 Ω. In earlier work, it is shown that polypropylene composite plates and cellulose fibers can also be used as a shielding material which decreases the effect of electromagnetic interference (EMI), where cellulose paper works in a very effective way for frequency range 15–40 GHz [14–16].

In the present research paper, the reduction of cross talk with proper shielding techniques and a comparison has been done for drain current, crosstalk current gain, and power dissipation with and without shielding technique. Semiconducting materials such as silicon (Si) and aluminum gallium arsenide (AlGaAs) are used in

shielding technique as they show potential for EMI shielding in CNT interconnects. The rest of the paper is organized as follows: The design of bundled SWCNT interconnect with/without shielding test structures are presented in Sect. 2. The shielding effect on bundled SWCNT performance parameters is discussed in Sect. 3. Finally, in Sect. 4, the findings of this paper are concluded.

2 Test Structure of Bundled SWCNT Interconnect

To analyze the effect of cross talk in parallel CNT interconnects of a bundled SWCNT, a test structure for SWCNT bundle is formed in this section to model the interconnects with different parameters like material and its composition, thickness, and length. To analyze the effect of cross talk in current on adjacent interconnects, in the proposed structure, two SWCNT bundle interconnects are considered as shown in Fig. 1. In order to model CNT interconnect, the material properties of 4H–SiC were modified to give the material metallic characteristics [13].

The wire that is the source of cross talk is termed as aggressor, whereas the wire that is affected by the cross talk is termed as victim. The length of aggressor CNT bundle interconnect is fixed at 55 nm and width at 5 nm, while the length of victim
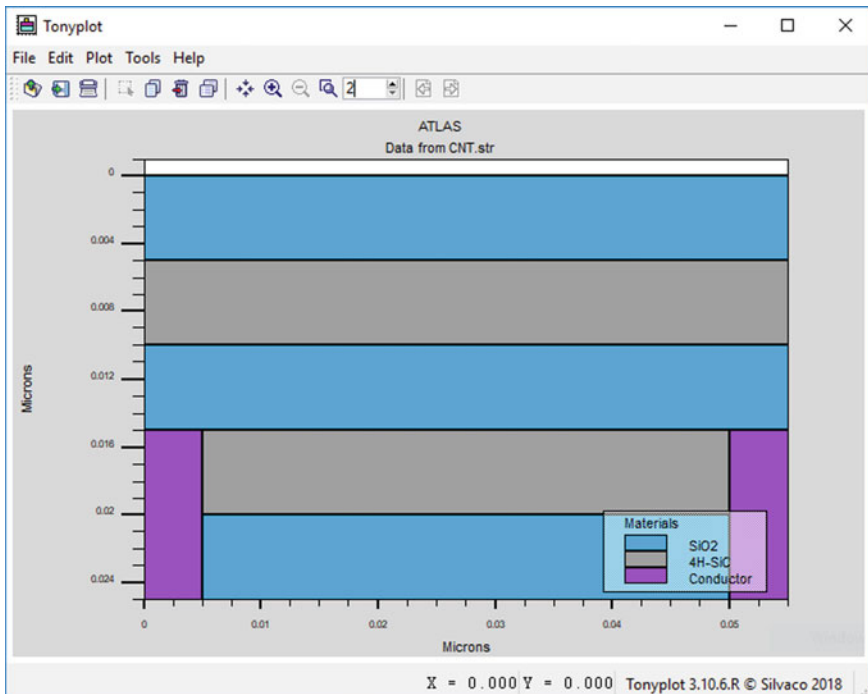
Fig. 1 Basic structure of SWCNT bundle interconnect model

CNT bundle interconnect is fixed at 45 nm and width at 5 nm. The electrodes of length 5 nm and width 10 nm are formed on both the ends of victim CNT bundle, termed as drain and source. Both CNT bundles are separated by an insulating layer SiO_2 of length 55 nm and width 5 nm. Further to analyze the shielding effect and to reduce crosstalk current gain, two layers of shielding material—silicon (Si) and aluminum gallium arsenide (AlGaAs)—of length 43 nm and width 2 nm are used across the victim CNT bundle as shown in Fig. 2.

3 Results and Discussions

To analyze the effect of shielding on crosstalk reduction, the proposed aggressor–victim test structure of SWCNT bundled interconnect was first simulated without shielding material and then with shielding material on ATLAS. Simulations were carried for two fixed electrode voltages across victim CNT interconnect, termed as drain voltage (V_d) for 0.05 and 1.2 V. Further, the voltage provided at aggressor CNT interconnect, termed as gate voltage (V_g), was varied from −0.5 to 1.5 V. By analyzing the variations in potential, electric field, and current between both CNT interconnects, induced crosstalk was deducted in the form of crosstalk current gain [17] and power dissipation across the victim CNT interconnect. It is found that the introduction of shielding material around the victim CNT line inhibits the interference due to electromagnetic coupling of adjacent CNT lines. Following parameters further explain the effect of induced cross talk between two CNTs in a bundled SWCNT interconnect.

3.1 Potential Distribution

Repercussions of cross talk can be inferred from the potential distribution throughout the structure including CNT interconnects, shielding material, electrode, and insulating layer. In this section, for an applied drain voltage V_d = 1.2 V and gate voltage V_g = 1.2 V, crosstalk effect is analyzed for three cases: without shielding, shielding with silicon, and shielding with aluminum gallium arsenide. From the structure without shielding as shown in Fig. 3a, uneven distribution of potential especially in the victim CNT wire near the drain electrode is observed. This results in an anomaly in overall current measured across victim CNT interconnect.

The abnormality induced in victim CNT interconnect can be minimized by inserting a layer of silicon around the victim line as a shielding material as shown in Fig. 3b. This enclosing of silicon results in an even distribution of potential over the victim CNT interconnect and less impact on victim CNT due to aggressor CNT. Furthermore, when (Si) is replaced by (AlGaAs) as a shielding material, it is inferred from Fig. 3c that with an even potential distribution in victim CNT line, the intensity of potential has increased. This implies a lesser effect of aggressor line on victim line.
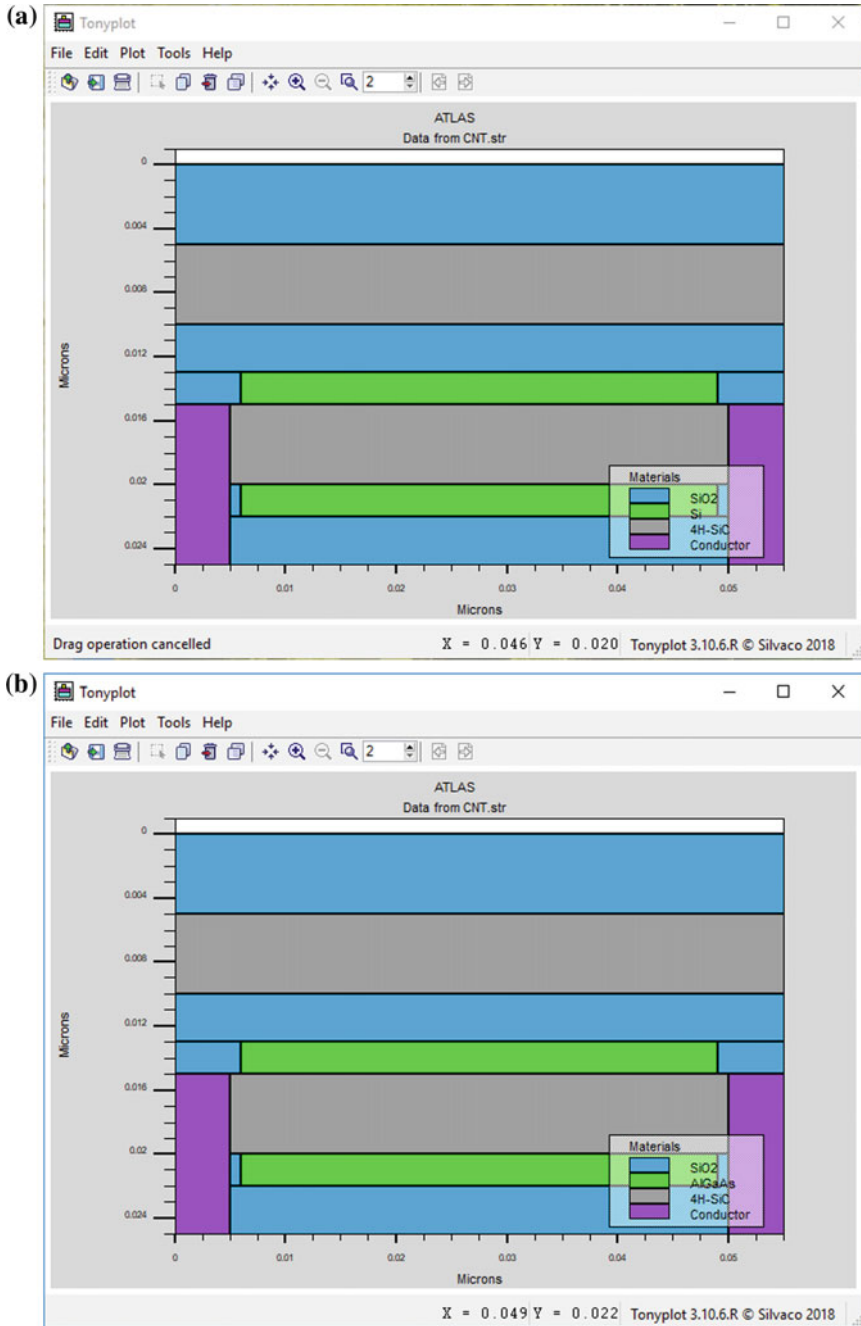
Fig. 2 CNT interconnect model with **a** Si, **b** AlGaAs as shielding materials
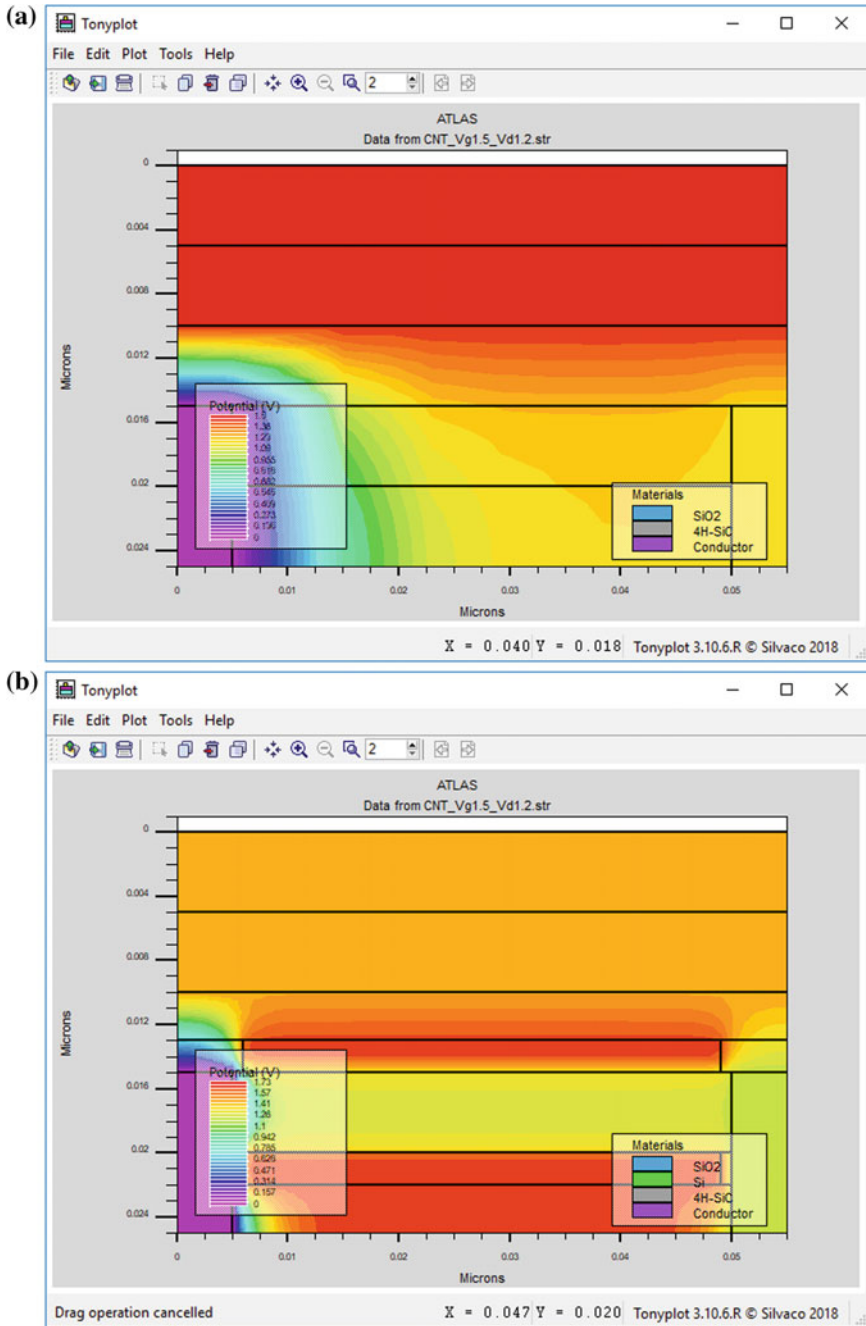
Fig. 3 Potential distribution in **a** basic structure without shielding, **b** with shielding by Si, **c** with shielding by AlGaAs
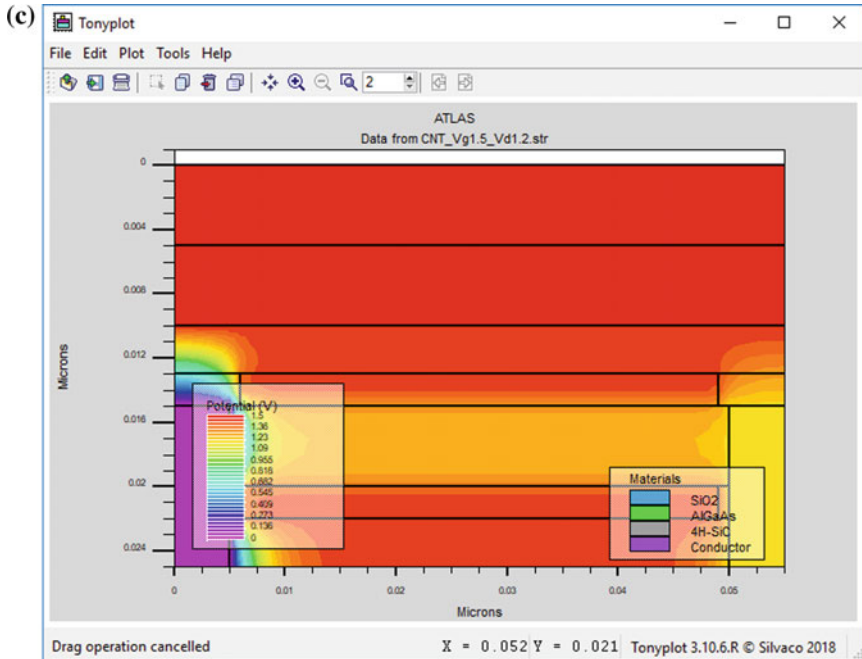
Fig. 3 (continued)

3.2 Drain Current

The drain current (I_d) variation in victim line by the aggressor line gate voltage (V_g) change is shown in Fig. 4a and b for fixed values of drain voltage 0.05 and 1.2 V, respectively. From the I_d–V_g plot, it can be inferred that the shielding of victim CNT line results in a constant value of drain current (I_d) irrespective of gate voltage (V_g), while the current get reduced in shielding technique as compared to without shielding.

Tables 1 and 2 show the drain current (I_d) variation for different test structures with change in V_g, at fixed drain voltage of 0.05 and 1.2 V, respectively.

This data shows that the drain current fluctuates for every value of gate voltage in case of without shielding, whereas in case of shielding, drain current remains consistent with respect to gate voltage. It is also inferred that shielding with AlGaAs results in marginally higher drain current as compared to shielding with Si, because electron mobility of AlGaAs is greater than silicon.

(a)

(b)
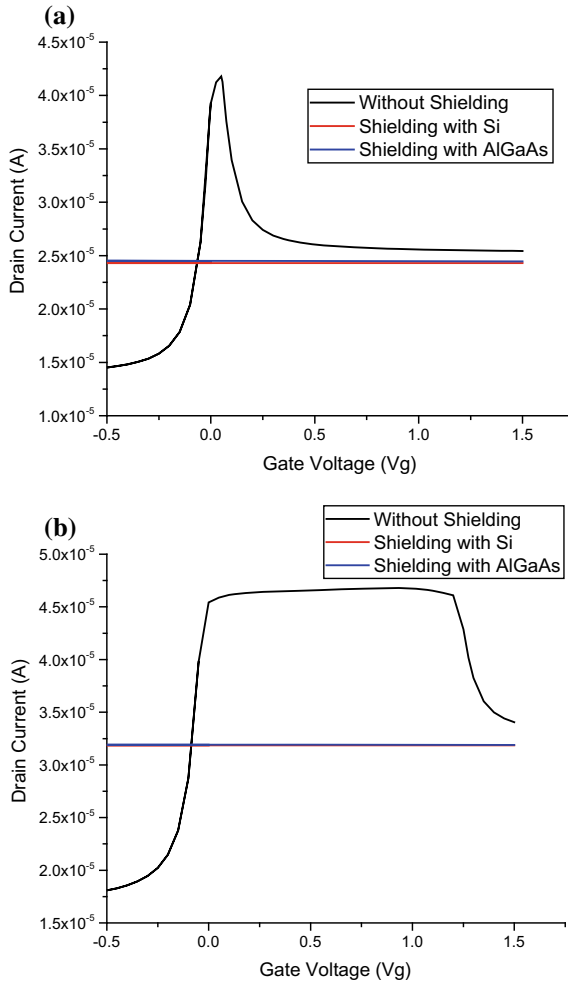
Fig. 4 Effect of V_g on I_d at **a** $V_d = 0.05$ V, **b** $V_d = 1.2$ V

Table 1 Comparison of drain current for different structures at $V_d = 0.05$ V

Gate voltage (V_g) in V	Drain current (I_d) in A		
	Without shielding	Shielding with Si	Shielding with AlGaAs
−0.5	1.45×10^{-5}	2.43×10^{-5}	2.45×10^{-5}
0.0	3.93×10^{-5}	2.43×10^{-5}	2.45×10^{-5}
0.5	2.60×10^{-5}	2.43×10^{-5}	2.45×10^{-5}
1.0	2.56×10^{-5}	2.43×10^{-5}	2.45×10^{-5}
1.5	2.54×10^{-5}	2.43×10^{-5}	2.45×10^{-5}

Table 2 Comparison of drain current for different structures at $V_d = 1.2$ V

Gate voltage (V_g) in V	Drain current (I_d) in A		
	Without shielding	Shielding with Si	Shielding with AlGaAs
−0.5	1.81×10^{-5}	3.18×10^{-5}	3.19×10^{-5}
0.0	4.54×10^{-5}	3.18×10^{-5}	3.19×10^{-5}
0.5	4.66×10^{-5}	3.18×10^{-5}	3.19×10^{-5}
1.0	4.67×10^{-5}	3.18×10^{-5}	3.19×10^{-5}
1.5	3.41×10^{-5}	3.18×10^{-5}	3.19×10^{-5}

3.3 Crosstalk Current Gain

Crosstalk current gain has deducted by the variation in drain current (I_d) with respect to maximum drain current for different values of gate voltage (V_g). Figure 5a and b shows the variation in crosstalk current gain with change in V_g. For shielded victim CNT line, crosstalk current gain remains constant and nearly equal to zero, but for the unshielded victim CNT, crosstalk current gain varies with V_g. Further, as shown in Fig. 5c, increasing the scale size of crosstalk current gain, with respect to gate voltage, exhibits better perception of the dependence of crosstalk gain on gate voltage in case of shielding with Si and AlGaAs. From Fig. 5c, silicon exhibits better shielding properties than that of AlGaAs, and also, the crosstalk interference get reduced with increase in drain voltage.

3.4 Power Dissipation

From Fig. 6a and b, a considerable variation in power dissipation for different values of gate voltage is observed for unshielded CNT line, whereas there is negligible variation in power dissipation and equivalent to zero in case of shielded CNT line. To analyze the variation in power dissipation with respect to gate voltage in case of shielding with Si and AlGaAs, the above plots are further scaled up as shown in Fig. 6c. It is inferred that silicon performs better than AlGaAs as shielding material against power dissipation, but the difference between them is negligibly small.
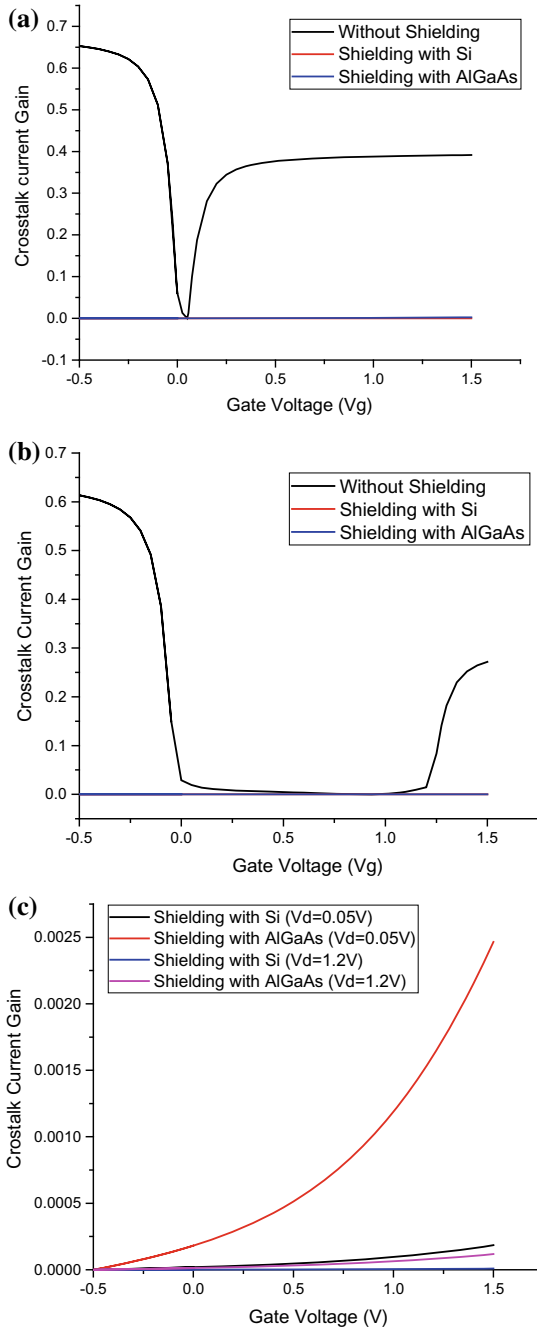
Fig. 5 Effect of V_g on crosstalk current gain at **a** $V_d = 0.05$ V, **b** $V_d = 1.2$ V, **c** comparison of crosstalk current gain for shielding with Si and AlGaAs
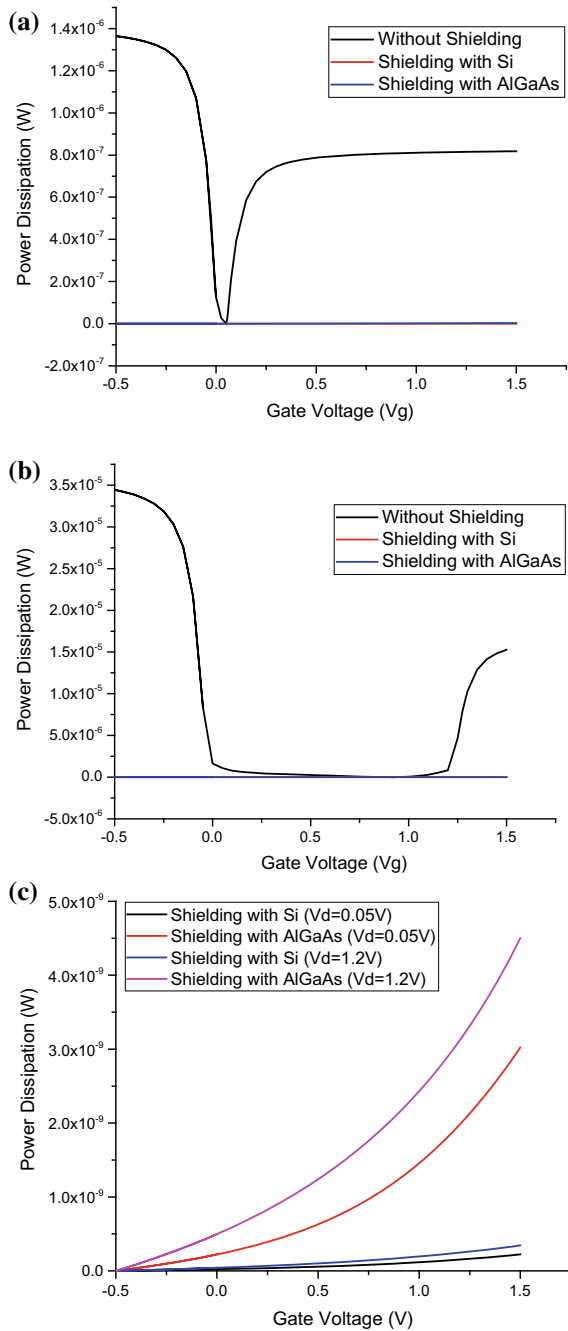
Fig. 6 Effect of V_g on power dissipation at **a** $V_d = 0.05$ V, **b** $V_d = 1.2$ V, **c** comparison of power dissipation for shielding with Si and AlGaAs

4 Conclusion

The proposed test structures have shown a considerable reduction in cross talk which can be achieved by inserting a layer of shielding material (silicon and aluminum gallium arsenide) around bundled SWCNT interconnect. The test structure without shielding has displayed an uneven distribution of potential, especially in the victim CNT wire near the drain electrode. The test structure with shielding material (Si/AlGaAs) exhibited an even potential distribution in victim CNT line, and the intensity of potential has increased, which implies lesser effect of aggressor line on victim line. For different test structures with a change in gate voltage (V_g), at a fixed drain voltage (V_d), the drain current fluctuates for every value of V_g in case of without shielding, and with shielding, it remains consistent. It is also inferred that shielding with AlGaAs results in marginally higher drain current as compared to Si, because electron mobility of AlGaAs is greater than silicon. For shielded victim CNT line, crosstalk current gain remains constant and nearly equal to zero, but for the unshielded victim CNT, crosstalk current gain varies with V_g. Moreover, Si performs better than AlGaAs as shielding material against power dissipation, but the difference between them is negligibly small. Therefore, it is concluded that the effect of cross talk has considerably reduced by enclosing bundled SWCNT interconnect with a semiconducting material Si and AlGaAs as a shielding material.

References

1. Ceyhan A, Naeemi A (2013) Cu interconnect limitations and opportunities for SWNT interconnects at the end of the roadmap. IEEE Trans Electron Devices 60:374–382
2. Srivastava N, Li H, Kreupl F, Banerjee K (2009) On the applicability of single-walled carbon nanotubes as VLSI interconnects. IEEE Trans Nanotechnol 8:542–559
3. Giustiniani A, Tucci V, Zamboni W (2011) Carbon nanotubes bundled interconnects: design hints based on frequency and time-domain crosstalk analyses. IEEE Trans Electron Devices 58:2702–2711
4. Uma SP, Karthikeyan A, Mallick PS (2013) Role of semiconducting carbon nanotubes in crosstalk reduction of CNT interconnects. IEEE Trans Nanotechnol 12(5):662–664
5. Li H, Xu C, Srivastava N, Banerjee K (2009) Carbon nanomaterials for next-generation interconnects and passives: physics, status, and prospects. IEEE Trans Electron Devices 56 (9):1799–1821
6. Naeemi A, Meindl JD (2009) Carbon nanotube interconnects. Annu Rev Mater Res 39:255–275
7. Rutherglen C, Burke PJ (2009) Nanoelectromagnetics: circuit and electromagnetic properties of carbon nanotubes. Small 5(8):884–906
8. Uma SP, Karthikeyan A, Kavish RJ, Mallick PS (2014) Reduction of crosstalk in mixed CNT bundle interconnects for high frequency 3D ICs and SoCs. In: IEEE conference on advances in electrical engineering, Vellore, India
9. Majumder MK, Pandya ND, Kaushik BK, Manhas SK (2012) Analysis of crosstalk delay and area for MWNT and bundled SWNT in global VLSI interconnects. In: IEEE symposium on quality electronic design, Santa Clara, CA, USA

10. Rossi D, Cazeaux J, Metra C, Lombardi F (2007) Modeling crosstalk effects in CNT bus architectures. IEEE Trans Nanotechnol 6(2):133–145
11. Majumder MK, Manhas SK (2012) Analysis of delay and dynamic crosstalk in bundled carbon nanotube interconnects. IEEE Trans Electromagn Compat 56(6):1666–1673
12. Das D, Rahaman H (2011) Analysis of crosstalk in single- and multiwall carbon nanotube interconnects and its impact on gate oxide reliability. IEEE Trans Nanotechnol 10(6)
13. Singh KJ, Singh TJ, Chettri D, Sarkar SK (2017) A thin layer of CNT as semi-transparent charge collector that improve the performance of the GaAs solar cell. Optik 135:256–270
14. Rochefort A, Ventra MD, Avouris P (2001) Switching behavior of semiconducting carbon nanotubes under an external electric field. Appl Phys Lett 78:2521–2524
15. Al-Saleh MH, Sundararaj U (2009) Electromagnetic interference shielding mechanisms of CNT/polymer composites. Carbon 1738–1746
16. Fugetsu B, Sano E, Sunada M, Wang X, Hiraki T (2008) Electrical conductivity and electromagnetic shielding efficiency of CNT/cellulose composite paper. Carbon 1253–1269
17. Zhang K, Tian B, Zhu X, Wang F, Wei J (2012) Crosstalk analysis of carbon nanotube bundle interconnects. Nanoscale Res Lett 7(1):138

Analysis and Impact of Electrode Related Parameters in Cochlear Implant

Deepti Gupta, Pratistha Mathur and Peeyush Tewari

Abstract In Cochlear Implant electrode stimulation plays an immense role in respect of providing hearing sensation to the user. Thus electrode working is a most precise thing in the cochlear implant. This paper describes the difference between different kinds of electrodes stimulation according to different situations. These situations affect the performances. The size, shape, depth of insertion, and different measurements of electrodes affects the performance of Cochlear Implant (CI) users. Exactly up to what extent electrode roles matters in terms of good performance for CI users.

Keywords Cochlear Implant (CI) · Hearing preservation · Round window · Electrode length · Electrode insertion · Electric acoustic simulation (EAS)

1 Introduction

Cochlear Implant (CI) is the best miracle for the deaf or partially deaf person from the medical science with multiple disciplines in the world. The main work of CI is to utilize left over hair cells to generate hearing sensation to the brain through the neurons. CI has two parts internal and external. Internal part of CI consist the array of electrodes. Electrodes are responsible for giving hearing sensation in the form electric stimulation to the brain [1].

D. Gupta (✉)
Banasthali Vidyapith University, Tonk, Rajasthan, India
e-mail: 29.deepti@gmail.com

P. Mathur
Manipal University, Jaipur, Rajasthan, India

P. Tewari
Birla Institute of Technology, Noida, India

2   Background

In first experiment of the electrical stimulation which has been done by Alessandro Volta, he got the sound like when some thick material is jerking, bubbling, or crackling. After that many experiments happened but didn't get success. Later on in 1961 Dr. House get success in cochlear implant implantation with his team. The patient is able to discriminate few frequency or some words. But later on due to infection this work becomes unsuccessful. Thus House restarts his work with different team and finally gets success in terms of biocompatibility of the implant.

Initially all manufacturing company made circular electrode based on theory that electrode should be closer to modiolus. According to theory when electrode remains closer to modiolus it increases battery life and loudness of sound. The normal length of cochlea is between 20 and 30 mm. Therefore electrodes of different lengths are available 25 and 30 mm initially. There are two kinds of stimulation mode is present monopolar and bipolar. In monopolar one electrode is active and another electrode is known as ground or return electrode. Stimulation happens when current flows between these two. In bipolar two adjacent electrodes in the electrode array worked as active and return electrode [1, 2].

3   The Electrode Insertion

In the cochlea electrode insertion can be done in two ways either through scala tympani or through round window. The maximum deep insertion of electrode can be up to the 30 mm in the cochlea. For getting the lower frequency contact speech should lie in the range of 200–1200 Hz and insertion should be through round window at the depth of 1.5 turns [3, 8].

Each channel is associated with each electrode through which user perceived an only one of its kind of pitch. The electrodes which are inserted into cochlea able to 1.25 turns are Nucleus Contour Advance 24, the Advanced Bionics HiFocus 1J, and the MED-EL FLEX[24]. This kind of insertion can provide characteristics frequency of 500 Hz in a normal hearing. The longest electrode array which is available now with the size of 31.5 mm is launched by ME-DEL company in two variation MED-EL STANDARD and MEDELFLEX[SOFT]. These long arrays allow insertion up to 1.75 or 2 turns in the cochlea while other allows insertion up to 1.25 turn only. Due to deep insertion it allows lower frequency stimulation also. There are some benefits related to long electrode array like it provides stimulation like normal hearing. Due to long electrode it provides more contacts which reduce the mismatching of frequency. The long electrode can provide less interference between channels because it increase the distance between channels if number of channels are fixed. In the same way if want to increase the number of channels with very less interference by fixing the distance between the channels.

But electrode insertion depends upon two things cochlea length and electrode length. Electrode array full insertion cannot be feasible due to many reasons like cochlea anatomy, the angle of round window, due to disease. But the main focus should be proper insertion of electrode array without damage of cochlea.

There are multiple factors which collectively give best results in terms of user performance. First and most important is choose the correct electrode array according to user need because user cochlea is malfunctioned. Due to this reason there is a need to choose electrode which work perfectly in user situation. Other factors are electrode insertion which matches perfectly tonotopic position of hair cells (Fig. 1).

Spiral ganglion (SG) cells also play a major role in terms of electrode placement. If spiral ganglion cells are absent then electrode stimulation is not possible. Such areas are also called dead regions due to this reason. Due to this reason in case of post-lingual CI user frequency mismatch can occur because total coverage of stimulation is not possible. An electrode part where all contacts are working correctly known as active area and its length is different from the complete length of electrode. For a perfect electrode design many factors need to be considered.
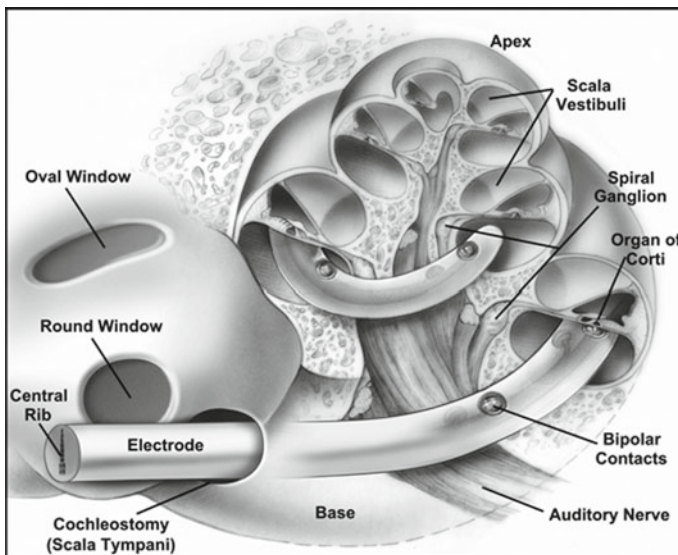
Fig. 1 Drawing of implanted cochlea with electrode

4 Matching Neuro-Tonotopicity

In terms of frequency function allow frequency map in two ways either at Organ of Corti or at Spiral ganglion cells. Although Organ of Corti covers the entire length of cochlea and Spiral ganglion cells covers only 1.75–1.85 turns of the cochlea. This shows that SG cells go middle turn of the cochlea and the modiolus trunk diameter in the second turn becomes extremely small in the range. Thus it is better not going up to that range that is highly sophisticated. To achieve neuro-tonotopic matching the first 3–4 mm from round window should not consider for any electrical stimulation for the highest frequency.

5 Atraumatic Electrode Array Insertion

Electrode insertion should be like that there should be no damage in the inner part of the cochlea. Still it's not possible to do insertion without trauma. So according to trauma few categories has been defined. In category 0: there is no trauma in electrode insertion; category 1: there is a lift in basilar membrane; category 2: there is a damage of spiral ligament; category 3: there is a translocation from the scala tympani (ST) to the scala vestibuli (SV); category 4: worst injury because electrode array fracture the spiral lamina. Due to category 3 pre-operative residual hearing loss can occur and this kind of loss is not curable. Thus in this kind insertion should be more careful [4, 5].

6 Effects of Round Window Opening Size

When round window opening happens in cochlear implant then different sizes of round window create different kinds of intracochlear fluid pressure which is an important factor in terms of hearing preservation. It happens because when electrode goes in the cochlea it displaced the fluid present in the cochlea. From different kinds of experiments it is found that wide opening of the round window is giving the best result in terms of pressure to retain hearing [6].

7 Electrode Length Difference on Speech Between CI and EAS

EAS is used for persons who have some residual hearing in low frequencies with severe hearing loss at high frequencies. EAS provides both facilities CI plus hearing aid. At low frequencies it works as hearing aid and at high frequencies it works at

CI. Based on lengths of electrode FLEX[20], FLEX[24], FLEX[28] one experiment has been done between CI and EAS in terms of speech perception in quiet and noise for the durations of 3 and 6 months. From the results it is clear that in case of CI FLEX[28] is giving best results in respect of speech perception for both the durations of 3 and 6 months. In the case of EAS short length electrodes FLEX[20], FLEX[24] giving good results for both durations [7].

Fig. 2 First: Med-El Combi 40+™′ Second: Advanced Bionics Helix™; Third: Cochlear Contour™ electrode arrays
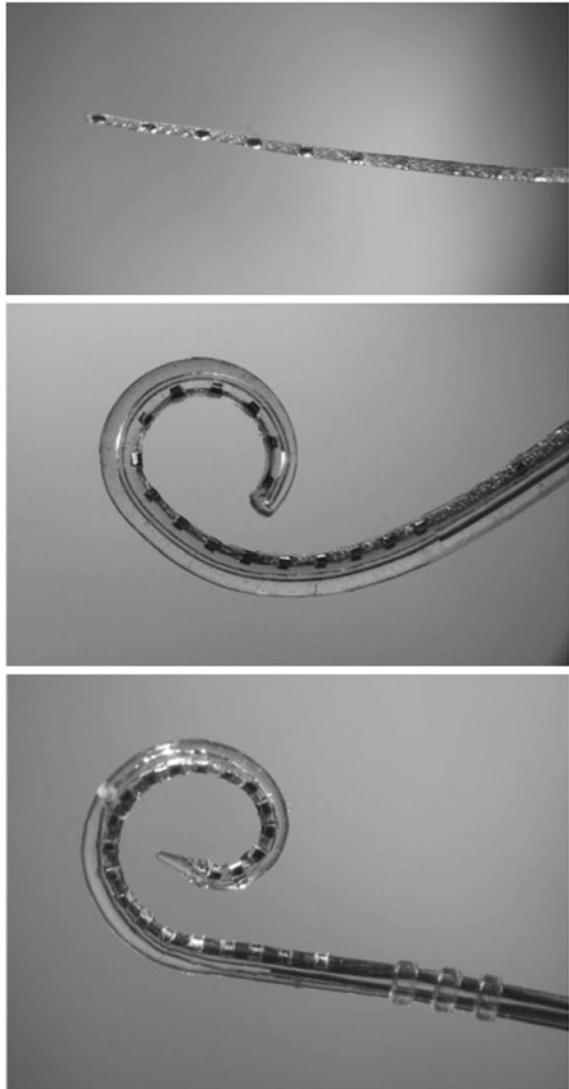
8 Power Consumption

The correct utilization of power is very important factor because there is no internal battery available in the CI. Thus the distance between electrode and nerve should be less for less power consumption. In this way try to insert electrode near the modiolus.

For the further improvements in terms of safety many changes happens like increased number of channels which either work pair wise or work virtually. For more clarity in speech deeper insertion is suitable and for user point of view decrement in the manufacturing cost also provided. In terms of mechanical characteristics the stiffness of array and the shape of the tip of array all are important points which are considered for the best performance. Here some types of electrodes are showing in the Fig. 2 [8].

9 Number of Electrodes

Many experiments happened still there is no perfect answer related to how many number of electrodes are perfect. Every company which is present in the market has different perspective related to it. There should be minimum 8 numbers of electrodes for good performance according to all. But if talks about maximum then some are saying 12 and few are saying 22 number of electrodes.

If used bilateral CI. In bilateral CI in both ears CI is used. The user is able to locate from which direction sound is coming if used bilateral CI. On the other hand if user is using Bilateral EAS then music perception also possible. Because in the case of EAS low frequency also present for the user so it provide better music perception for the user as compared to the only CI [9].

10 Conclusion

Although today Cochlear Implant is a remarkable technology. In which electrodes play a major role. Still there are many gaps available like no one can define the perfect number of electrodes for best performance for all users. Some are talking about virtual channels where there is no limit of number of channels and some are saying 22 are best.

Except number of channels many other things are equally important for good performance like correct placement, in which deep insertion and a place where maximum contacts should be present. Insertion of electrode should not provide any trauma to the cochlea. Still some points are there whose answer should be found out like why few users' performance is remarkable through same electrode array and few users' performance is too bad. Some user's performance is growing after proper training and some user's performance has no change.

References

1. Eshraghi AA, Nazarian R, Telischi FF, Rajguru SM, Truy E, Gupta C (2012) The cochlear implant: historical aspects and future prospects. Anat Rec 295:1967–1980
2. Namasivayam A (2004) Cochlear implant technical issues: electrodes, channels, stimulation mode and more. Audiology Online. https://www.audiologyonline.com/articles/cochlear-implant-technical-issues-electrodes-1081
3. Wilson BS, Dorman MF (2008) Cochlear implants: current designs and future possibilities. J Rehabil Res Develop (JRRD) 45(5):695–730
4. Landsberger DM (2014) Perceptual changes in place of stimulation with long cochlear implant electrode arrays. Acoust Soc Am. http://dx.doi.org/10.1121/1.4862875
5. Dhanasingh A, Jolly C (2017) An overview of cochlear implant electrode array designs. Elsevier. http://creativecommons.org/licenses/by/4.0/
6. Todt I, Ernst A, Mittmann P Effects of round window opening size and moisturized electrodes on intracochlear pressure related to the insertion of a cochlear implant electrode. S. Karger AG, Basel, 1664–5537/16/0061–0001
7. Büchner A, Illg A, Majdani O, Lenarz T (2017) Investigation of the effect of cochlear implant electrode length on speech comprehension in quiet and noise compared with the results with users of electro-acoustic-stimulation, a retrospective analysis. Plos One. https://doi.org/10.1371/journal.pone.0174900
8. Zeng F-G, Rebscher S, Harrison WV, Sun X, Feng H (2009) Cochlear implants: system design, integration and evaluation. NIH-PA, PMC
9. Wilson BS (2017) The cochlear implant and possibilities for narrowing the remaining gaps between prosthetic and normal hearing. World J Otorhinolaryngol-Head Neck Surg. Available online at www.sciencedirect.com

Assessment of Cutting Forces in Machining with Novel Neem Oil-Based Cutting Fluid

Narayan Agrawal and Rahul Katna

Abstract Current manufacturing industries use a high amount of cutting fluids in order to increase the machining rates and achieve higher productivity. A huge amount of cutting fluid is used in the manufacturing processes involving metal removal processes. But the negative impacts also increase with the increased amount the utilization of cutting fluids. Occupational diseases also increase when workers work in close contact with the cutting fluid. The workers are the worst affected because they are prone to inhale the mist generated. A new cutting fluid was developed from vegetable oils and was tested for emulsion stability. After that, the performance was compared with two different conventional fluids at a varying flow rate of cutting fluid.

Keywords Cutting force · Biodegradable · Feed force · Thrust · Emulsion stability

1 Introduction

Metalworking fluids have been used in the manufacturing industries for a long time. Cutting fluids are essential for reducing heat generation and also provide lubrication. Heat is generated in machining due to friction [1]. It is well known that whenever a surface slides over another surface, friction comes into play, and it causes temperature rise due to friction. The use of vegetable oil-based cutting fluids increases the performance of machining. This also increases the productivity, and the increased machining rates can be achieved [1, 2].

In fact, the use of water alone without any lubricant increases the machining performance [3].

N. Agrawal (✉) · R. Katna
Delhi Institute of Tool Engineering, New Delhi, India
e-mail: narayan.dite@gmail.com

Vegetable oils have inherent good properties which can be used for developing a cutting fluid which performs better than the conventional mineral oil-based cutting fluids.

Using petroleum and mineral oil-based cutting fluids has a huge negative impact on the ecosystem [1, 3]. It causes diseases in human, and its disposal causes water pollution. So in order to save the environment and to have increased productivity simultaneously, it is important to develop a cutting fluid which will perform equivalent to the conventional mineral oil cutting fluid. Many researches have been done using vegetable oils. The experiments have been carried out mainly with edible oils. The researches report that use of vegetable oil-based cutting fluids performs better than the conventional mineral oil-based cutting fluids [4–6]. They are effective in reducing cutting forces during machining [7–9]. They have also shown to improve the surface characteristics of the machined surface. Better surface finish is obtained. Also, they have shown to increase the tool life by reducing the rate of tool wear. When a cutting fluid performs better in all these parameters like reduction in cutting forces, tool wear, surface roughness [10–12] it indicates that this is a good cutting fluid and can be used for machining because they perform at par with the mineral oil-based cutting fluid. The development of cutting fluid from vegetable oils needs to be done with an emulsifier which is non-petroleum-based and is thus non-toxic and non-carcinogenic.

2 Materials and Methods

In this work, unedible neem oil was procured and was blended in different concentrations with an emulsifier which is food grade. The concentrations were varied from 5, 10, 15 and 20%. The oil and emulsifier blends were then diluted in the ratio of 1:9. Maintaining a constant flow rate for every set of machining, cutting forces, feed force and thrust force were recorded throughout the experiment and their average was taken. The material chosen was unhardened EN8 steel (AISI 1045) because of its wide range application in the automotive sector. Indexable inserts of WIDIA were procured from market, and the configuration of the inserts was CNMG120408 and a compatible tool holder. The machining was done at varying cutting fluid flow rate of 0.5 litre/min, 1 litre/min and 1.5 litre/min. A submersible pump was used to maintain the flow rates of cutting fluids.

3 Results and Discussions

Machining was carried out with different cutting fluids under constant cutting conditions. The abbreviations MIN, NE5, NE10, NE15 and NE20 mean mineral oil-based cutting fluid, neem oil having 5% emulsifier, neem oil having 10% emulsifier, neem oil having 15% emulsifier and neem oil having 20% emulsifier.

Cutting Force Average cutting force, feed force, thrust force and resultant force were measured for all the flow rates.

Figure 1 shows the variation of cutting force, feed force, thrust force and resultant force at 1.5 litre per minute flow rate different with different cutting fluids and at constant cutting condition. As can be seen from the results, the neem oil-based cutting fluids perform at par with the mineral oil-based cutting fluid. Also, feed force and thrust force have performed at par with the mineral oil-based cutting fluid. On decreasing the flow rate to 1 litre per minute, the cutting force increased for all the cutting fluids, but even then, the neem oil-based cutting fluids performed better than the mineral oil-based cutting fluid and even better than mineral oil-based cutting fluid in some cases. Similar results can be observed for feed force reduction and thrust force reduction by using neem oil-based cutting fluid.

On further reduction of fluid flow rate to 0.5 litre per minute, the cutting force and thrust force increased. But in this case, also the neem oil-based cutting fluids performed better than the mineral oil-based cutting fluid. Thus, we see that neem oil-based cutting fluid performs better than the mineral oil-based cutting fluid. Thus, neem oil-based cutting fluid can be a suitable substitute and replacement to the mineral oil-based cutting fluid. Also, there are no other performance boosters added in the formulated cutting fluid, and this is totally biodegradable and non-toxic (Figs. 2 and 3).
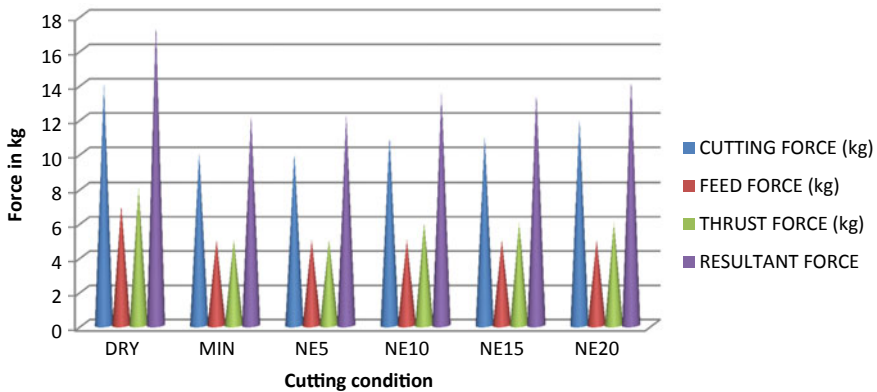
Fig. 1 Cutting forces with different cutting fluids at 1.5 LPM flow rate
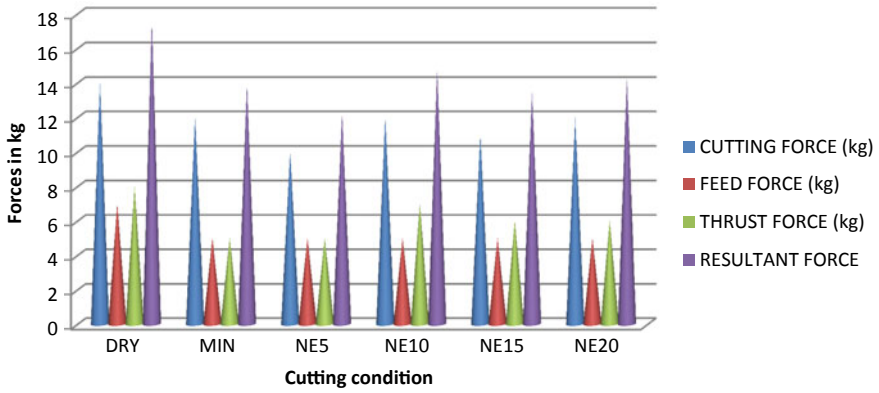
Fig. 2 Cutting forces with different cutting fluids at 1.0 LPM flow rate
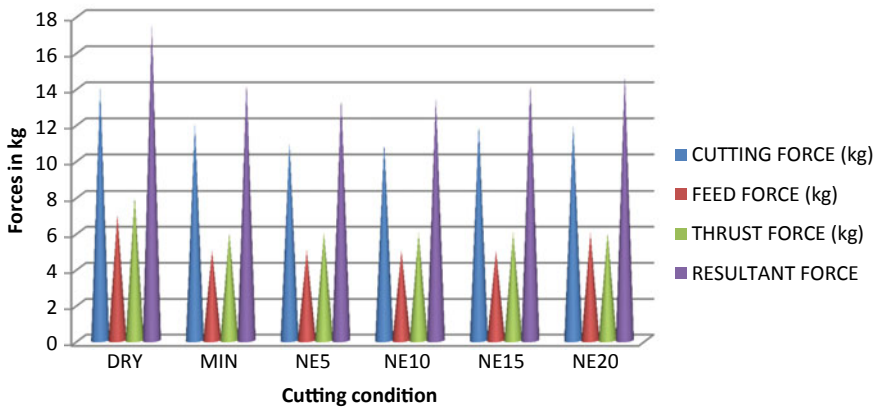
Fig. 3 Cutting forces with different cutting fluids at 0.5 LPM flow rate

4 Conclusion

The results indicate that the newly formulated cutting fluids can be used as an alternative to the conventional mineral oil-based cutting fluid as these perform at par and in some cases even better than the mineral oil-based cutting fluid in reducing the cutting forces. Also, these are without any other additive—only oil and emulsifier. So these can be a substitute for mineral oil cutting fluids.

References

1. Brinksmeier E, Meyer D, Huesmann-Cordes AG, Herrmann C (2015) Metalworking fluids—mechanisms and performance. CIRP Ann Manuf Technol 64(2):605–628
2. Isik Y (2010) An experimental investigation on effect of cutting fluids in turning with coated carbides tool. J Mech Eng 56(3):195–201
3. Anthony Xavior M, Adithan M (2009) Determining the influence of cutting fluids on tool wear and surface roughness during turning of AISI 304 austenitic stainless steel. J Mater Process Technol 209:900–909
4. Debnath S, Reddy MM, Yi QS (2014) Environmental friendly cutting fluids and cooling techniques in machining: a review. J Clean Product 83:33–47
5. Hamdan A, Sarhan AA, Hamdi M (2012) An optimization method of the machining parameters in high-speed machining of stainless steel using coated carbide tool for best surface finish. Int J Adv Manuf Technol 58(1):81–91
6. Lawal SA, Abolarin MS, Ugheoke BI, Onche EO (2007) Performance evaluation of cutting fluids developed from fixed oils. Leonardo Electron J Pract Technol 10:137–144
7. Prabhu MV, Ponnusamy P, Kumar, JS, Performance of various cutting fluids by estimating surface roughness of mild steel in turning
8. Onuoha OJ, Abu JO, Lawal SA, Mudiare E, Adeyemi MB (2016) Determining the effect of cutting fluids on surface roughness in turning AISI 1330 alloy steel using Taguchi method. Mod Mech Eng 5(2):51–59
9. Shashidhara YM, Jayaram SR (2012) Tribological studies on AISI 1040 with raw and modified versions of Pongam and Jatropha vegetable oils as lubricants. Adv Tribol
10. Elmunafi MH, Kurniawan D, Noordin MY (2015) Use of castor oil as cutting fluid in machining of hardened stainless steel with minimum quantity of lubricant. Procedia CIRP 26:408–411
11. Khan MMA, Mithu MAH, Dhar NR (2009) Effects of minimum quantity lubrication on turning AISI 9310 alloy steel using vegetable oil-based cutting fluid. J Mater Process Technol 209(15):5573–5583
12. Paul PS, Varadarajan AS, Gnanadurai RR (2016) Study on the influence of fluid application parameters on tool vibration and cutting performance during turning of hardened steel. Eng Sci Technol Int J 19(1):241–253

Fault Detection and Correction in Omni Bundle Robot Using EKF

Rohit Rana, Vijyant Agarwal, Prerna Gaur and Harish Parthasarathy

Abstract In this paper, the entire focus is on fault detection and correction using extended Kalman filter (EKF) on industrially used omni bundle robot. Here, the authors considered a problem where a robot does monotonous job and repetitively traverse the same trajectory every time. Due to wear and tear or any fluctuation in input signals, the robot may not track the desired trajectory. Faults may arise at various levels in robots, for example, in actuator, encoder, and dynamical parameters. Actuator fault detection using encoder sensor will be the main focus in this research paper. The dynamics of robotic arm link is modeled using a DC motor attached with the link, and the encoder attached with the motor will provide position feedback. The fault is detected using EKF state estimation, and the fault is corrected using a PID controller feedback into the motor input torque.

Keywords Omni bundle · Fault detection · EKF · PID

R. Rana (✉) · P. Gaur
Instrumentation and Control Engineering Division, Netaji Subhas Institute
of Technology, Sec-03, Dwarka 110078, India
e-mail: rohitrana982007@gmail.com; rohitrana@nsit.ac.in

P. Gaur
e-mail: prernagaur@yahoo.com

V. Agarwal
Manufacturing Process and Automation Engineering Division, Netaji Subhas Institute
of Technology, Sec-03, Dwarka 110078, India
e-mail: vijaynt.agarwal@gmail.com

H. Parthasarathy
Electronics and Communication Engineering Division, Netaji Subhas Institute
of Technology, Sec-03, Dwarka 110078, India
e-mail: harisignal@yahoo.com

1   Introduction

In industrial applications, many robots do monotonous jobs like assembly line car painting work and pick and place materials in manufacturing plant assembly line. These kinds of heavy jobs lead to very early wear and tear of the robot's electrical and mechanical parts. This may create the difference in the desired and actual trajectory of the robot. Any change in the trajectory will also change the joint angles in a proportional way.

The parameters of the omni bundle are sufficiently provided in [1]. The robotic arm model is taken as per [2]. In [3–9], the importance of fault is highlighted. In [7], the authors used EKF as a disturbance observer and detected the fault in a generalized model of electric motor. Till date, most of the authors use filters (EKF, UKF) as state estimators to find faults in the system. In [10], the authors used sensorless fault detection by using a sensorless voltage inverter fed squirrel cage induction motor with LC filter. Further, in light of the above contributions, it can be concluded that in robotics the fault detection must be investigated and a model should be developed for the robotic links. Therefore, one-link robotic arm model is the first step to further investigate in multi-link robotic systems.

This paper presents an overall view and implementation of fault detection and correction in robotic arm model. A simple robotic arm model is investigated in this paper, and mathematical modeling is done for the same with EKF. Further, fault correction is also discussed and implemented on Phantom Omni.

2   Problem Formulation

The block diagram implemented is provided in Fig. 1. It shows the overall connection between the blocks and feedback from encoder sensor to fault detection and correction block. Later, the output from the correction block is fed into the motor along with input torque. The mechanical working of motor with link is shown in Fig. 2.
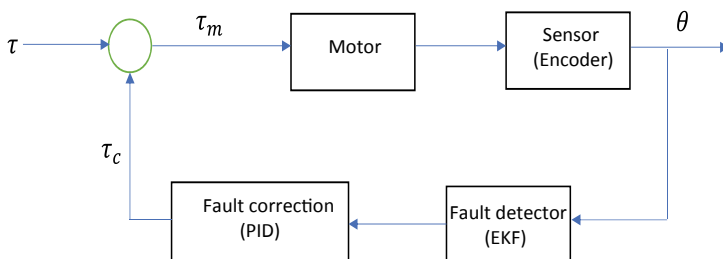
Fig. 1 Overall logical block diagram of 1-DOF link fault detection and correction

Fig. 2 Motor and link model used in problem formulation
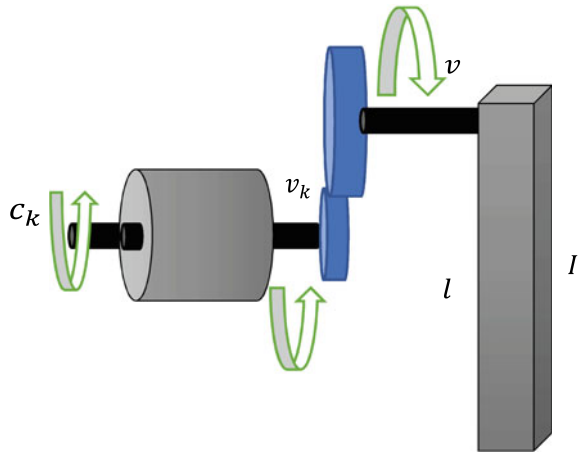
Figure 2 shows that the motor is connected to the link via the gear assembly, which is an absolute representation of nearly all industrial robots.

From Fig. 2, robot arm model, the link shown is actuated by the torque fr to load axis. The equations of dynamics in this case are written as follows:

$$c_k = I_k \dot{\omega}_k + F_k \omega_k + fr_k \tag{1}$$

and

$$fr = I\dot{\omega} + F\omega + P \tag{2}$$

where $P = mgl * \sin(v)$ is the reaction torque given on load axis and I is the moment of inertia. F is the viscous force coefficient and K_r is the reduction factor. The equation can be written as follows:

$$c_k = I_d \dot{\omega}_k + F_d \omega_k + \frac{P}{K_r} \tag{3}$$

here $v = \frac{v_m}{K_r}$ in Eq. 3 can be written as follows:

$$\dot{\omega}_k = \frac{\left(c_k - F_d \omega_k - \frac{P}{K_r}\right)}{I_d} \tag{4}$$

Thus with constant torque, the state space model of above is given as follows:

$$\begin{bmatrix} \dot{\omega}_k \\ \dot{c}_k \end{bmatrix} = \begin{bmatrix} \frac{\left(c_k - F_d \omega_k - \frac{P}{K_r}\right)}{I_d} \\ 0 \end{bmatrix} \tag{5}$$

and the measurement equation is as follows:

$$y = \begin{bmatrix} \omega \\ \frac{\left(c_k - F_d\omega_k - \frac{P}{K_r}\right)}{I_d} \end{bmatrix} \tag{6}$$

Eq. (6) is converted into the discrete time and can be written as follows:

$$\begin{bmatrix} \omega_{z+1} \\ c_{z+1} \end{bmatrix} = \begin{bmatrix} \omega_z + \frac{\left(c_z - F_d\omega_z - \frac{P}{K_r}\right)}{I_d} \\ c_z \end{bmatrix} \tag{7}$$

$$y_z = \begin{bmatrix} \omega_z \\ \frac{\left(c_z - F_d\omega_z - \frac{P}{K_r}\right)}{I_d} \end{bmatrix} \tag{8}$$

where $k + n = z$ and the discretization step size is unity. We also consider the high process noise disturbance due to friction and measurement noise disturbance with zero mean and covariance $Q = E(qq')$ and $R = E(rr')$. Therefore,

$$\begin{bmatrix} \omega_{z+1} \\ c_{z+1} \end{bmatrix} = \begin{bmatrix} \omega_z + \frac{\left(c_z - F_d\omega_z - \frac{P}{K_r}\right)}{I_d} \\ c_z \end{bmatrix} + q \tag{9}$$

$$y_z = \begin{bmatrix} \omega_z \\ \frac{\left(c_z - F_d\omega_z - \frac{P}{K_r}\right)}{I_d} \end{bmatrix} + r \tag{10}$$

The above state equations are evolved with EKF to estimate $\hat{c}$ and $\hat{\omega}$. The generalized EKF equations are as follows:

$$x_{k+1} = f(x_k, u_k, t) + w_k \tag{11}$$

$$z_k = h(x_k, t) + v_k \tag{12}$$

where x_k is the state, f( ) is the state transition function, and w_k random noise perturbations. z_k is the measurement equation, and v_k is the measurement noise. The prediction and update state can be finally derived. Also, the Jacobian measurement equation is calculated and is represented in the form given below:

$$\frac{\partial f}{\partial x} = \begin{bmatrix} \frac{1 - T_s c_k}{I_d} & -\frac{1 - T_s c_k}{I_d} \\ 0 & 1 \end{bmatrix} \tag{13}$$

$$\frac{\partial h}{\partial x} = \begin{bmatrix} 1 & 0 \\ \frac{-c_k}{I_d} & -\frac{\omega_k}{I_d} \end{bmatrix} \tag{14}$$

The estimated $\hat{\theta}$ is then compared to the actual θ, and the fault is located. Also the magnitude of the fault is calculated. The difference between both $\hat{\theta}$ and θ is calculated and converted into torque using inverse dynamics of robotic arm model. This converted error torque is applied to the PID controller to generate correction torque τ_c. τ_c is applied to the motor with desired torque τ. Thus, the error is minimized.

3 Implementation and Results

3.1 Fault Detection

The implementation is done on the Omni bundle robot as shown in Fig. 4. It is a 6-DOF robot controlled through computer with Quanser software installed. Second link of omni bundle is used to implement Fig. 1 model in MATLAB simulink. Desired torque signal τ is generated with signal builder and saved in workspace. Then this signal is fed into omni bundle block. The output of omni bundle block is configured such that it gives encoder values as an output. This encoder output is then converted into the joint angle q_1 using gear and gain parameters. The process

noise and measurement noise with zero mean and process covariance $Q = \begin{bmatrix} 1e-6 & 0 \\ 0 & 1e-2 \end{bmatrix}$ and measurement noise covariance $R = \begin{bmatrix} 1e-4 & 0 \\ 0 & 1e-4 \end{bmatrix}$ are provided. Then, the EKF is configured in the simulink. The EKF provides the estimated $\hat{q}_1$ as an output.

3.2 Fault Correction

Estimated $\hat{q}_1$ is then converted back to torque using inverse dynamics of omni bundle and then the converted torque is fed into the PID controller. The PID controller generates the compensating torque τ_c. The τ_c is then combined with τ to minimize the error. Figure 3 shows the output of the above simulation in terms of desired joint angle q_1, estimated joint angle $\hat{q}_1$, and measured joint angle with measurement noise. Figure 5 shows the error graph between desired and estimated joint angles.
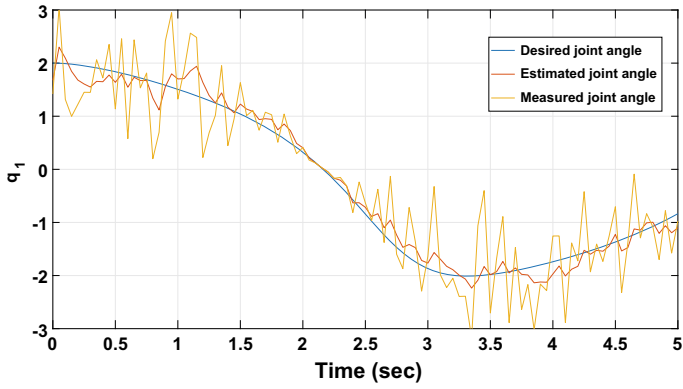
Fig. 3 Graph showing comparison between desired, estimated, and measured joint angle

Fig. 4 Picture of omni bundle
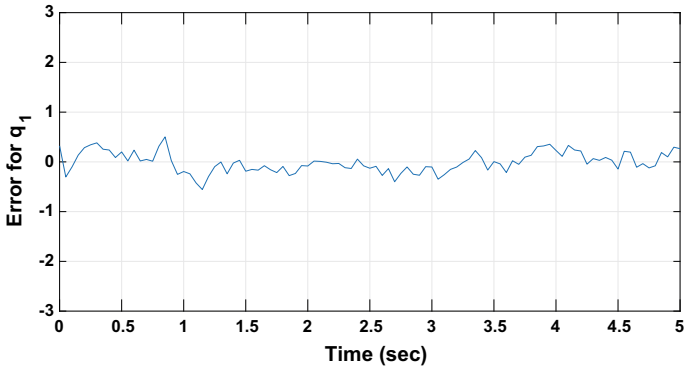
Fig. 5 Graph showing error between actual and desired joint angles

4 Conclusion

The fault detection in omni bundle robot is successfully investigated and implemented. The results were satisfactory and may be improved using different control techniques. Similarly, the model may be extended to multi-link robotic system.

References

1. Agarwal V (2016) An extended Kalman filter for real-time estimation and control of Omni® robot with stochastic noise. In: 2016 3rd international conference on computing for sustainable global development (INDIACom), New Delhi, pp 2456–2460
2. Siciliano B, Sciavicco L, Villani L, Oriolo G (2009) Robotics modelling, planning and control, 1st edn. Springer, London. https://doi.org/10.1007/978-1-84628-642-1
3. Isermann R (2006) Fault-diagnosis systems, 1st edn. Springer, Berlin. https://doi.org/10.1007/3-540-30368-5
4. Goel P, Dedeoglu G, Roumeliotis SI, Sukhatme GS (2000) Fault detection and identification in a mobile robot using multiple model estimation and neural network. In: Proceedings 2000 ICRA. Millennium conference. IEEE international conference on robotics and automation. Symposia proceedings (Cat. No.00CH37065), vol 3, San Francisco, CA, pp 2302–2309. https://doi.org/10.1109/robot.2000.846370
5. Visinsky ML, Cavallaro JR, Walker ID (1994) Robotic fault detection and fault tolerance: a survey, reliability engineering & system safety 46(2):9–158. ISSN 0951-8320, https://doi.org/10.1016/0951-8320(94)90132-5. http://www.sciencedirect.com/science/article/pii/0951832094901325
6. Surwase DA, Jalit AS, Chavan MD (2017) Fault detection and protection of induction motor using fuzzy logic. In: 2017 international conference on innovations in electrical, electronics, instrumentation and media technology (ICEEIMT), Coimbatore, pp 66–70. https://doi.org/10.1109/icieeimt.2017.8116807

7. Fernandez Gomez AJ, Jaramillo VH, Ottewill JR (2014) Fault detection in electric motors by means of the extended Kalman Filter as disturbance estimator. In: 2014 UKACC international conference on control (CONTROL), Loughborough, pp 432–437. https://doi.org/10.1109/control.2014.6915179

8. Muenchhof M, Beck M, Isermann R (2009) Fault tolerant actuators and drives and structures, fault detection principles and applications. In: IFAC proceedings volumes, vol 42, issue 8, pp 1294–1305. ISSN 1474-6670, ISBN 9783902661463, https://doi.org/10.3182/20090630-4-ES-2003.00211. (http://www.sciencedirect.com/science/article/pii/S1474667016359547) Keywords: Sensor and actuator faults; structural analysis; aerospace applications; automotive applications; electro-mechanical applications; other applications

9. Rana R, Agarwal V, Parthasarthy H (2015) Wavelet transformation based tremor removal. In: 2015 international conference on computer, communication and control (IC4), Indore, pp 1–3. https://doi.org/10.1109/ic4.2015.7375544

10. Strankowski P, GuziÅski J (2016) Sensorless fault detection of induction motor with inverter output filter. In: 2016 Progress in applied electrical engineering (PAEE), Koscielisko-Zakopane, pp 1–6. https://doi.org/10.1109/paee.2016.7605104

Comparative Study of Convolution Neural Network's Relu and Leaky-Relu Activation Functions

Arun Kumar Dubey and Vanita Jain

Abstract Convolutional neural networks refer to a collection of feed-forward artificial neural networks. These networks have been implemented successfully on visual imagery. It uses a variety of perceptrons. These perceptrons are multilayered, that need very little preprocessing. Shift invariant or space invariant NN are alias for CNN, because of their architecture which is based on shared weights. It is also established on translation invariance features. In this paper, we have used rectified linear unit (Relu) and Leaky-Relu activation for inner CNN layer and softmax activation function for output layer to analyze its effect on MNIST dataset.

Keywords Activation function · Relu · Leaky-Relu · CNN

1 Introduction

Deep learning is a machine learning method that has made extraordinary progress in fields like picture acknowledgment and discourse acknowledgment. There are four kinds of deep learning models [1]. Different models are as follows:

- Stacked autoencoder [2]: This model is generally built by stacking a few autoencoders. It consists of two phases, i.e., encoding and decoding stages. An autoencoder figures out how to pack information from the info layer into a short code and after that uncompress that code into something that intently coordinates the first information.
- Deep belief network (DBN) [3]: DBN is a generative graphical model, or on the other hand, a class of profound neural systems, made out of numerous layers of

A. K. Dubey
University School of Information, Communication and Technology, GGSIPU New Delhi,
Delhi 110078, India
e-mail: arudubey@gmail.com

V. Jain (✉)
Bharati Vidyapeeth's College of Engineering New Delhi, Delhi, India
e-mail: Vanita.jain@bharatividyapeeth.edu

inert factors, with associations between the layers and not between units inside each layer. At the point when prepared on an arrangement of cases without supervision, a DBN can figure out how to probabilistically remake its sources of information. After this learning step, a DBN can be additionally prepared with supervision to perform arrangement. It is stacked with numerous confined Boltzman machines that use Gibbs inspection to prepare the illustrations.

- Convolutional neural network [4]: This is the most commonly utilized deep learning method for large-scale picture characterization. This model consists of an input layer and an output layer along with many hidden layers. The hidden layers of CNN model mainly consist of convolutional layer, pooling layer, and fully connected layer. **Convolutional layer** applies a convolution operation to the input and then passes the result to the next layer. **Pooling layer** combines the output of neuron cluster at one layer into another single neuron in the subsequent layer. **Fully connected layer** is the interface between each neuron in one layer and each neuron in another layer.
- Recurrent neural network [5]: It is another type of deep learning model where associations between units shape a coordinated diagram along an arrangement. It is learned to highlight the arrangement of information by memory of past data sources that are put away in the inner condition of neural systems.

Deep learning has been used in all the aspects of research work and significantly used in computer vision [6].

CNN [7] was initially inspired by biological processes as compared to the patterns of links of neurons. This pattern resembles the origin of visual cortex of animals. This is built on the response of stimuli and their restricted regions, called receptive field, which partially overlap to gain the entire coverage area.

2 Role of Activation Function in Analysis

Activation functions have very important role in analysis. Both linear unit, not good for complex dataset, and nonlinear unit, mostly used for multiple features, have different effects on different situations.

These functions can capture complex nonlinear relationship. Apart from learning from continuous data, it has a capability to learn from categorical data. Functions are important for biases and weights in the artificial neural network to perform in nonlinear function. With the activation function, the back propagation has become possible since the gradients can update the weights and biases on the basis of error values they have. These functions are monotonic; therefore, error surface associated with the model is guaranteed to be convex.

We cannot say that all activation functions can handle all situations; for example: Sigmoid has slow convergence rate and also kills gradients; Tanh has a problem called vanishing gradient; Relu: Some gradients may be soft/fragile while training the data and may die. In other words, it can result in dead neurons. Binary step: This
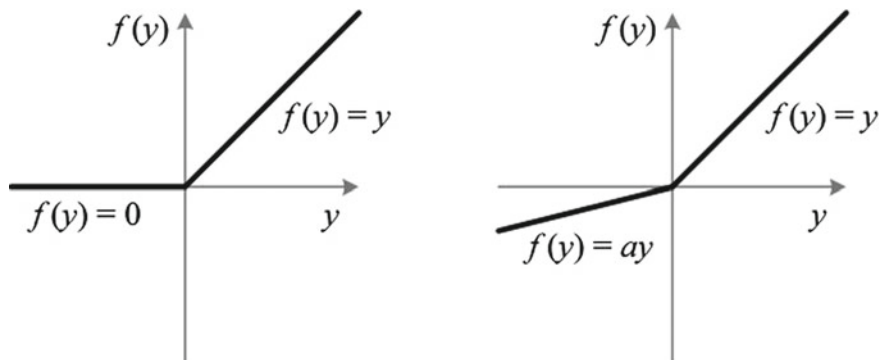
Fig. 1 Comparison between Relu and Leaky-Relu [9]

Table 1 Mathematical expression of Relu and Leaky-Relu

	Relu	Leaky-Relu
Function	$F(z) = \begin{cases} 0, & z<0 \\ z, & z \geq 0 \end{cases}$	$F(z) = \begin{cases} 0.01z, & z<0 \\ z, & z \geq 0 \end{cases}$
Derivative	$F'(z) = \begin{cases} 0, & z<0 \\ 1, & z \geq 0 \end{cases}$	$F'(z) = \begin{cases} 0.01, & z<0 \\ 1, & z \geq 0 \end{cases}$

function is not continuously differentiable (at 0), therefore not suitable for gradient-based optimization. Leaky-Relu: It suffers from exploding gradient problem during front propagation problem if rate of learning is set too high.

Rectified linear unit (Relu) [8] and Leaky-Relu are very popular activations in current era, but there is some difference between these two. It is shown in Fig. 1. Both are monotonic and their differentiation is also shown in Table 1.

Softmax is a type of regression technique, specifically logistic regression technique, where we consider multiple classes at the same time instead of binary classes, so the output label y can take on K different values, rather than only two. Thus, we have our training set given as below:

$$\{(x(1), y(1)), \ldots, (x(m), y(m))\}\{(x(1), y(1)), \ldots, (x(m), y(m))\},$$

For this particular training set, we have our label having values as below:

$$y(i)\{1, 2, \ldots, K\} y(i) \in \{1, 2, \ldots, K\}$$

One example of softmax regression is digit recognition through MNIST in which images of digits along with their corresponding labels are stored.

3   Experimental Results

We have used simple CNN on hand-written MNIST dataset which is part of NIST and used Relu and Leaky-Relu activation functions and softmax activation function for output layer. Figure 2 shows this dataset.

Fig. 2 MNIST dataset

Problem Type: Multi-class classification (Supervised learning)	
Image size:	28 × 28
Samples:	60,000
Input size:	60,000 × 1 × 28 × 28
Convolutional network configuration	
Number of RGB channels:	1
Layers of CNN:	1 (simple CNN)
Number of filters:	32
Size of filters:	8 × 8
Polling method used:	Max-Polling
Polling size:	2 × 2
Layers of MLP:	2
Number of nodes in input MLP layer:	128
Number of nodes in output MLP layer:	10
Dropout percent:	40% (Purpose: To avoid overfitting)
Number of epochs:	5
Batch size:	32

Model summary

```
Layer (type)                    Output Shape              Param #
=================================================================
conv2d_3 (Conv2D)               (None, 32, 21, 21)        2080

leaky_re_lu_3 (LeakyReLU)       (None, 32, 21, 21)        0

max_pooling2d_3 (MaxPooling2    (None, 32, 10, 10)        0

dropout_3 (Dropout)             (None, 32, 10, 10)        0

flatten_3 (Flatten)             (None, 3200)              0

dense_5 (Dense)                 (None, 128)               409728

dense_6 (Dense)                 (None, 10)                1290
=================================================================
Total params: 413,098
Trainable params: 413,098
Non-trainable params: 0
```

(a) **Learning Curve**:

Training and testing curves are approaching each other; therefore, CNN model used is not affected by the problem of overfitting and underfitting. As per following results of learning curve, digit model accuracy and model loss on Relu are better than Leaky-Relu (Fig. 3).

(b) **Top K categorical accuracy**:

It is a metric function to calculate accuracy on dataset which shows accurate prediction of model. After using both activation functions, it is found that epoch Relu constantly performed better than Leaky-Relu. Keras function has the following format:

top_k_categorical_accuracy(Q_true,Q_pred,k) here Q_true represents True label and Q_pred shows prediction. best result we get on $k = 5$ value.

Figure 4 depicts the accuracy curve for top three most accurately recognizable classes. It shows that there exist the classes which are more easily recognizable than other classes with an accuracy of nearly 100%. Therefore, it means that the test score might be misleading sometimes, and there is a need for other metrics such as F-score and confusion metrics. Misleading accuracy due to existing simple examples can be avoided by using stratified k-fold cross-validation.
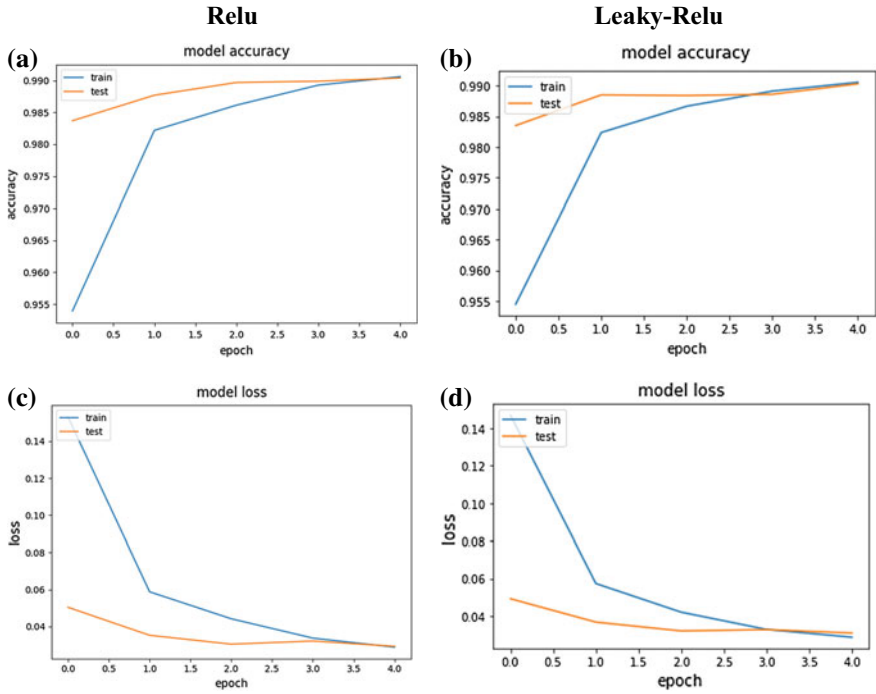
Relu **Leaky-Relu**

Fig. 3 Model accuracy and model loss
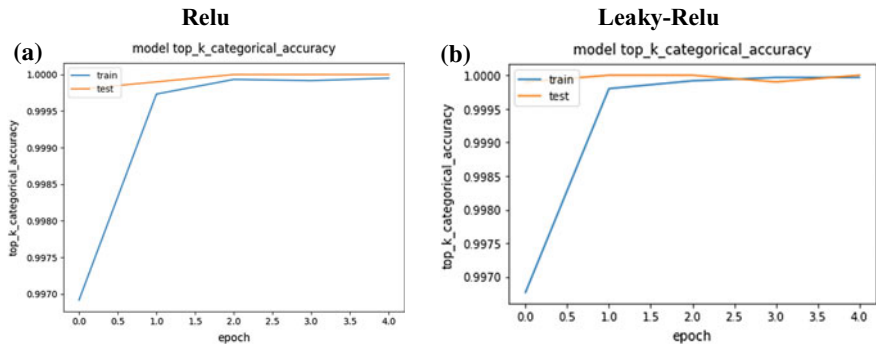
Relu **Leaky-Relu**

Fig. 4 Metric function for accuracy

(c) **Recall**:

It shows that fraction of positive predictions out of positive samples is increasing, i.e., false negative is decreasing (Fig. 5).
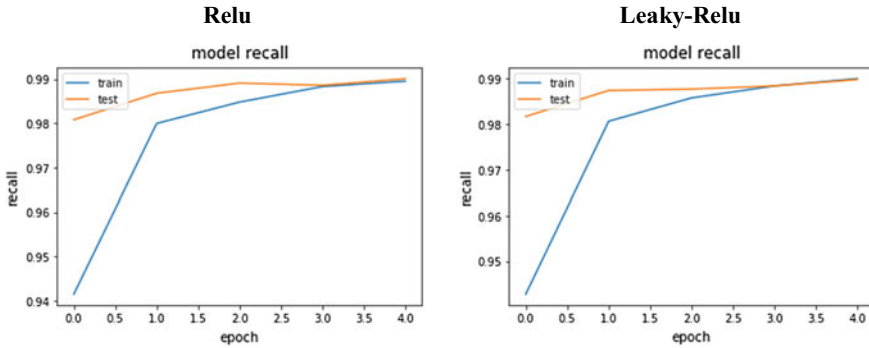
Fig. 5 Recall of Relu and Leaky-Relu

$$\mathrm{Recall} = \frac{\text{digits correctly identified}}{\text{digits correctly identified} + \text{individuals incorrectly identifed as not digit}}$$

(d) **FMeasure**:

Curve shows the progress in F-score with increasing number of epochs. Increasing F-score shows that the model is better than models making most frequent prediction and making random prediction; it is weighted harmonic mean (HM) of precision and recall. Figure 6 shows that increasing epoch value leads to equivalent F-score.

P : Precision

$$P = \frac{\text{digits correctly identified}}{\text{digits correctly identified} + \text{individuals incorrectly identifed as digit}}$$
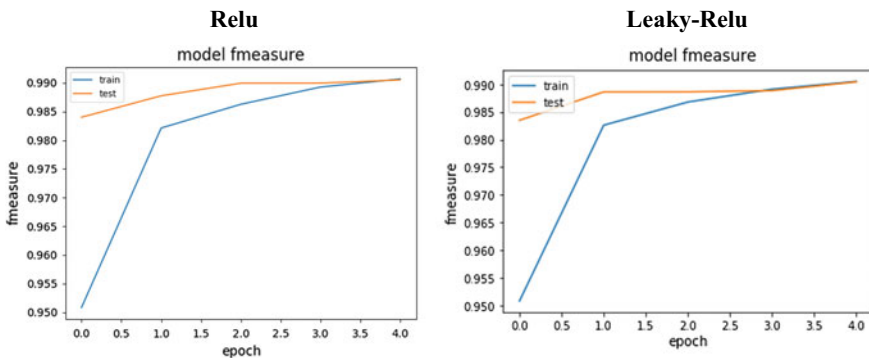
Fig. 6 F-Score of Relu- and Leaky-Relu-based activation function modes

$$F - \text{score} = 2\frac{\text{Precision} * \text{Recal}}{\text{Precision} + \text{Recal}}$$

4   Conclusion

Convolution neural network for deep learning is highly and effectively used in this world, and rectified linear unit and Leaky-Relu are famous activation functions. Digit recognition in MNIST, hand-written digit dataset, using these functions has delivered good result. Model accuracy and model loss on Relu are better than Leaky-Relu, but on comparison of Recall and F-score, Leaky-Relu works effectively and gives better accuracy. Top k category metric function is used to calculate accuracy on dataset which shows accurate prediction of model. This metric performed better on k value at five. This paper has shown the comparative results on activation functions, while CNN layer had not been changed for MNIST dataset.

References

1. Gheisari M, Wang G, Bhuiyan MZA (2017) A survey on deep learning in big data. In: 2017 IEEE international conference on computational science and engineering (CSE) and IEEE international conference on embedded and ubiquitous computing (EUC), Guangzhou, pp 173–180
2. Du B, Xiong W, Wu J, Zhang L, Zhang L, Tao D (2017) Stacked convolutional denoising auto-encoders for feature representation. IEEE Trans. Cybern 47(4):1017–1027
3. Kamada S, Ichimura T (2016) An adaptive learning method of Deep Belief Network by layer generation algorithm. In: 2016 IEEE region 10 conference (TENCON), Singapore, pp 2967–2970
4. Manana M, Tu C, Owolawi PA (2017) A survey on vehicle detection based on convolution neural networks. In: 2017 3rd IEEE international conference on computer and communications (ICCC), Chengdu, pp 1751–1755
5. Shukla P, Biswas KK, Kalra PK (2017) Recurrent neural network based action recognition from 3D skeleton data. In: 2017 13th international conference on signal-image technology & internet-based systems (SITIS), Jaipur, pp 339–345
6. Koohzadi M, Charkari NM (2017) Survey on deep learning methods in human action recognition. IET Comput. Vis 11(8):623–632
7. Takahashi N, Gygli M, Pfister B, Van Gool L (2016) Deep convolutional neural networks and data augmentation for acoustic event recognition. In: Proceedings of interspeech, Sept 2016
8. Hang ST, Aono M (2016) Open world plant image identification based on convolutional neural network. In: 2016 Asia-Pacific signal and information processing association annual summit and conference (APSIPA), Jeju, pp 1–4
9. Xu B, Wang N, Chen T, Li M (2015) Empirical evaluation of rectified activations in convolutional network. ICML deep learning workshop, Lille, France, 06–11 July 2015

Correlation Between Poincare Plot Indices and Linear–Nonlinear Heart Rate Variability During Fasting and Postprandial States

Jitendra Kumar Jain and Ranjan Maheshwari

Abstract The beat-to-beat fluctuations in the electrocardiogram (ECG) are called heart rate variability (HRV). There are various linear and nonlinear methods for measurement of the HRV. Poincare plot is one of the nonlinear methods to evaluate HRV. Previous studies have shown strong correlation between Poincare plot descriptors SD1 and SD2 with linear and nonlinear HRV measures. The present study is aimed to verify the correlation during fasting and postprandial states. A total of 46 young adults participated in the study. 10 min of ECG lead II was recorded in supine position with minimum 8 h of fasting. The subjects were then given 75 gm of glucose. The ECG was again recorded after postprandial 1 h (PP1H) and postprandial 2 h (PP2H) intervals. The linear and nonlinear HRV indices were calculated. The correlation coefficient was obtained by Spearman's correlation test and regression analysis. The strong correlation was verified for SD1 and SD2 with linear HRV measures; however, the degree of correlation was changing during fasting and postprandial states. SD1/SD2 was strongly correlated with LF/HF ratio, Detrended Fluctuation Analysis (DFA) ($\alpha1$, $\alpha2$), suggesting nonlinear characteristics of the parameters. The entropy measures were not statistically significant with any index of Poincare plot. It can be concluded that the correlations exist between linear and nonlinear HRV measures and degree of correlation changes during fasting and postprandial states. Therefore, in studies correlating linear and nonlinear HRV, the fasting and postprandial states must be specifically identified.

Keywords Poincare plot · Heart rate variability · Fasting · Postprandial

J. K. Jain (✉)
Government Engineering College, Bikaner, Rajasthan, India
e-mail: jitendra.ecb@gmail.com

R. Maheshwari
Rajasthan Technical University, Kota, Rajasthan, India
e-mail: ranjan.alpi@gmail.com

1   Introduction

Heart rate is the number of cardiac cycles per minute. It can be computed from successive RR intervals from the recorded electrocardiogram (ECG) over a time period [1]. The RR interval has spontaneous fluctuations about the mean value which is defined as heart rate variability (HRV) [2]. The beat-to-beat fluctuations in the heart rate are predominated regularly by the autonomic nervous system (ANS). Thus, HRV is considered as a powerful noninvasive tool for the assessment of autonomic activity [3, 4].

To quantify the beat-to-beat variability, time domain and frequency domain methods are used. The time domain method uses statistical or geometrical approaches in evaluating HRV parameters, but they provide information only about total variability. To get detailed information about specific components of the variability, frequency domain methods are used [5]. These time domain and frequency domain methods are considered as linear HRV indices.

Since the heart rate is influenced by various factors, e.g., blood pressure, respiration, baroreflex activity, mental activity, their synergistic effect makes the system nonlinear and complex. Therefore, nonlinear dynamics have been applied for the classification of the HRV. Poincare plot, Approximate Entropy (ApEn), Sample Entropy (SampEn), and Detrended Fluctuation Analysis (DFA) are the examples of nonlinear HRV methods [6].

The researchers have investigated the relationship between linear and nonlinear HRV indices. Brennan et al. [7] characterized the Poincare plot geometry and found that the existing measures of the Poincare plot were associated with linear aspect of the variability. Mourot et al. [8] carried out the quantitative analysis of Poincare plots to study effectiveness of endurance training. They also reported significant correlation between SD1 and SD2 with time domain and frequency domain HRV indices. The relationship was further explored by Hoshi et al. [9] in healthy and subjects with coronary artery disease. They reported a strong relation between Hurst exponent (HE) and DFA (α1) with SD1/SD2 ratio, whereas individual SD1 and SD2 indices were related to linear HRV parameters.

Contreras et al. [10] correlated the Poincare plot width with frequency domain HRV indices in healthy and diabetic subjects. They reported stronger correlation in the diabetic group between SD1 and LF-HF power as compared to healthy group. Since the diabetic subjects have higher blood glucose level (BGL), it could be an influencing factor in the correlation. Furthermore, the food intake causes BGL to increase which further results into increased muscle nerve sympathetic activity, thus affecting the autonomic function [11, 12]. In support to this, Rothberg et al. [13] found significant correlation between BGL and HRV parameters in type 2 diabetes mellitus subjects.

Therefore, the present study was carried out to identify the correlation between Poincare plot indices with linear–non linear HRV measures during fasting and postprandial states.

2 Materials and Methods

2.1 Study Population

Forty-six healthy young individuals participated in the study. Subjects were invited for data acquisition whenever they had minimum of 8 h of fasting. Details of the study, procedure, and objectives were given to all subjects, and written consent was obtained. ECG lead II was recorded in supine position for 10 min of duration with a PowerLab26$^{®}$ data acquisition system (M/s ADInstruments Pvt. Ltd., Australia). Subjects were then given 75 gm of glucose with 300 mL of water orally. The ECG signal was again recorded at postprandial 1 h (PP1H) and postprandial 2 h (PP2H) intervals.

2.2 Data Processing

ECG recording of 5-min duration was selected for short-term HRV analysis [5]. The RR interval data was extracted with excluding ectopic beats by the aid of HRV module of the LabChart8.0$^{®}$ software. Time domain HRV indices, e.g., SDNN (standard deviation of normal RR intervals), RMSSD (root mean squared differences of normal RR intervals), PRR50 count (number of adjacent RR intervals differ by more than 50 ms), were obtained from HRV module of the LabChart8.0$^{®}$ software. Frequency domain HRV indices, e.g., low frequency (LF), high frequency (HF), total power (TP), and LF/HF ratio, were obtained by fast Fourier transformation technique [14]. Nonlinear HRV indices, e.g., Poincare plot descriptors (SD1, SD2, SD1/SD2), Approximate Entropy (ApEn), Sample Entropy (SampEn), short-term Detrended Fluctuation Analysis (DFA(α1)) and long-term scaling component DFA (α2), were calculated with the aid of Kubios HRV analysis software [15].

2.3 Nonlinear HRV Indices

Poincare Plot—It represents the nonlinear dynamics of the HRV visually. In this plot, RR intervals are plotted against successive RR intervals. The plot appears as a cloud along the line of identity. The cloud is assumed to be influenced by parasympathetic and sympathetic activities. Thus, beat-to-beat fluctuations provide the information about the behavior of the heart. For characterization of the shape of the clouds, an ellipse is fitted whose center is representing the mean RR interval. Standard deviation of the inter-beat variability along minor axis is represented by the SD1, whereas inter-beat variability along major axis of the ellipse is represented by SD2 [16]. The dispersion of point in the plot along minor and major axes is given by Eqs. (1) and (2), respectively.

$$D_{i(\text{minor})} = \frac{\text{RR}_i - \text{RR}_{i+1}}{\sqrt{2}} \tag{1}$$

$$D_{i(\text{major})} = \frac{\text{RR}_i + \text{RR}_{i+1} - 2\overline{\text{RR}}}{\sqrt{2}} \tag{2}$$

SD1 and SD2 are calculated by Eqs. (3) and (4)

$$\text{SD1} = \sqrt{\frac{1}{N-1} \sum_{i=1}^{N-1} D_{i(\text{minor})}^2} \tag{3}$$

$$\text{SD2} = \sqrt{\frac{1}{N-1} \sum_{i=1}^{N-1} D_{i(\text{major})}^2} \tag{4}$$

where

$\overline{\text{RR}}$ mean RR interval

N number of RR intervals.

Approximate Entropy—It is used to measure the complexity and regularity of RR interval time series data by quantification of the unpredictable fluctuations. ApEn reflects the likelihood that similar patterns in the time series will not be followed by additional similar patterns. Higher values of ApEn indicate more irregular data (high complexity), whereas lower values indicate repetitive patterns in data (less complex) [17].

Sample Entropy—It also measures the complexity of the physiological time series data. It has slight modification from ApEn where template vector is compared with the rest of the vectors excluding self match. Thus, it is a less biased estimation of the signal complexity within short time segments [18]. It is defined as the negative natural logarithm of conditional probability that a series of data points at distance m would repeat itself at $m + 1$. Thus similar to ApEn, data point with similar distances would result in lower SampEn, whereas larger distances produce higher values of SampEn.

Detrended Fluctuation Analysis (DFA)—DFA is used to find out the statistical self-affinity of a signal. The time series of N samples is integrated. The integrated time series $y(k)$ is divided into boxes of equal length n. A trend line is fitted to the data in each box. The $y(k)$ is detrended by subtracting the local trend $y_n(k)$ in each box. The fluctuation which is the root mean square deviations from the trend is calculated by Eq. (5).

$$F(n) = \sqrt{\frac{1}{N} \sum_{k=1}^{N} [y(k) - y_n(k)]^2} \tag{5}$$

The double-logarithmic plot [$\log F(n)/\log(n)$] describes $\alpha 1$ as short-range scaling exponent and $\alpha 2$ as long-range scaling exponent [19]. The values of $\alpha < 0.5$ correspond to anti-correlated signal, whereas $\alpha > 0.5$ is an indication of positive autocorrelation in the signal.

Statistical Analysis

The linear and nonlinear HRV measures were tested for the strength of the relationship by Spearman's correlation coefficient and regression analysis in the Microsoft Excel®. In regression analysis, $p < 0.0001$ was considered a significant level. The correlation coefficient r_s varies from -1 to $+1$ and is given by Eq. (6) [20].

$$r_s = 1 - \frac{6 \sum_{i=1}^{n} d_i^2}{n(n^2 - 1)} \tag{6}$$

where

d_i difference between two rankings
n number of observations.

3 Results

The absolute value of correlation coefficient r_s from 0.80 to 1.0 indicates very strong correlation, and values from 0.60 to 0.79 are considered as strong correlation. The r_s and p values obtained for fasting, PP1H and PP2H cases, are presented in Tables 1, 2, and 3.

Table 1 Spearman's correlation coefficients between linear and nonlinear HRV indices during fasting

Linear–nonlinear HRV indices	Poincare HRV indices		
	SD1 (r_s, p)	SD2 (r_s, p)	SD1/SD2 (r_s, p)
LF	0.69, < 0.0001	0.88, < 0.0001	0.19, 0.2662
HF	0.95, < 0.0001	0.94, < 0.0001	0.63, 0.0002
LF/HF	−0.77, < 0.0001	−0.55, 0.0005	−0.80, < 0.0001
TP	0.88, < 0.0001	0.98, < 0.0001	0.46, 0.0057
SDNN	0.95, < 0.0001	0.99, < 0.0001	0.59, < 0.0001
RMSSD	0.99, < 0.0001	0.89, < 0.0001	0.80, < 0.0001
pRR50	0.97, < 0.0001	0.84, < 0.0001	0.83, < 0.0001
ApEn	−0.61, 0.0038	−0.65, 0.0059	−0.37, 0.1289
SampEn	0.29, 0.2142	0.06, 0.6985	0.50, 0.0023
DF (α_1)	−0.75, < 0.0001	−0.45, 0.0066	−0.91, < 0.0001
DF (α_2)	−0.72, < 0.0001	−0.67, < 0.0001	−0.56, < 0.0001

Table 2 Spearman's correlation coefficients between linear and nonlinear HRV indices during PP1H

Linear–nonlinear HRV indices	Poincare HRV indices		
	SD1 (r_s, p)	SD2 (r_s, p)	SD1/SD2 (r_s, p)
LF	0.83, < 0.0001	0.94, < 0.0001	0.28, 0.0756
HF	0.93, < 0.0001	0.96, < 0.0001	0.51, 0.0002
LF/HF	−0.53, 0.0002	−0.42, 0.0010	−0.58, < 0.0001
TP	0.92, < 0.0001	0.99, < 0.0001	0.43, 0.0008
SDNN	0.96, < 0.0001	0.99, < 0.0001	0.52, < 0.0001
RMSSD	0.99, < 0.0001	0.93, < 0.0001	0.70, < 0.0001
pRR50	0.97, < 0.0001	0.93, < 0.0001	0.62, < 0.0001
ApEn	−0.53, 0.0129	−0.60, 0.0071	−0.15, 0.1059
SampEn	0.24, 0.2056	0.06, 0.4342	0.48, 0.0521
DF (α_1)	−0.63, < 0.0001	−0.38, 0.0011	−0.92, < 0.0001
DF (α_2)	−0.74, < 0.0001	−0.65, < 0.0001	−0.56, < 0.0001

Table 3 Spearman's correlation coefficients between linear and nonlinear HRV indices during PP2H

Linear–nonlinear HRV indices	Poincare HRV indices		
	SD1 (r_s, p)	SD2 (r_s, p)	SD1/SD2 (r_s, p)
LF	0.73, < 0.0001	0.88, < 0.0001	0.21, 0.3605
HF	0.92, < 0.0001	0.93, < 0.0001	0.56, 0.0038
LF/HF	−0.67, < 0.0001	−0.54, 0.0012	−0.67, < 0.0001
TP	0.91, < 0.0001	0.97, < 0.0001	0.45, 0.0396
SDNN	0.95, < 0.0001	0.99, < 0.0001	0.51, 0.0019
RMSSD	1, < 0.0001	0.92, < 0.0001	0.73, < 0.0001
pRR50	0.93, < 0.0001	0.87, < 0.0001	0.67, < 0.0001
ApEn	−0.48, 0.0267	−0.39, 0.2685	−0.32, 0.0051
SampEn	0.24, 0.9174	0.18, 0.8979	0.37, 0.4077
DF (α_1)	−0.68, < 0.0001	−0.43, 0.0493	−0.89, < 0.0001
DF (α_2)	−0.80, < 0.0001	−0.65, < 0.0001	−0.76, < 0.0001

The width of the Poincare plot SD1 had very strong correlation ($r_s > 0.90$) with short-term variability indices, e.g., HF power, RMSSD, and pRR50. The correlation decreases slightly with HF power in PP1H and PP2H states. This may be due to dominance of sympathetic activity with glucose ingestion. The length of Poincare plot SD2 had a very strong correlation with linear time and frequency domain HRV indices. The correlation increased during PP1H and PP2H states. This may be due to increased sympathetic nerve activity with glucose ingestion. The SD1 and SD2 presented a weaker correlation with nonlinear HRV indices. The SD1/SD2 ratio presented a weaker correlation with linear HRV indices, whereas strong correlation

($r_s > 0.89$) was obtained with nonlinear index DF ($\alpha 1$). The correlation between LF/HF and SD1/SD2 was also significant ($p < 0.0001$) during fasting and postprandial states. The approximate entropy and sample entropy presented weaker correlation ($r_s < 0.65$, $r_s < 0.50$, respectively, $p > 0.001$) with all Poincare plot indices.

4 Discussion

In this study, the results verify that the Poincare plot indices SD1 and SD2 have linear features of HRV. Since the SD1 is a measure of the dispersion of points perpendicular to the line of identity representing short-term variability, it had strong correlation with parasympathetic measures of linear HRV.

The length of Poincare plot SD2 representing overall variability of the HRV, therefore it had very strong correlations ($r_s > 0.80$) with LF power, HP power, Total power, SDNN, RMMSD, pRR50. The correlation becomes stronger during postprandial states as compared to fasting. This may be due to increased muscle nerve sympathetic activity with glucose ingestion. These findings corroborate the study of Otzenberger et al. [21] who reported the correlation of Poincare plot length with SDNN, LF power, and HF power. These results are also in support with the study carried out by Brennan et al. [7] who found a strong correlation between width of Poincare plot and short-term HRV measures, whereas length was correlated with long-term variability. Karmakar et al. [16] also presented the SD1 and SD2 of Poincare plot with basic statistical measures of HRV.

The LF/HF ratio had statistically significant correlation ($p < 0.0001$) with SD1/SD2 during both fasting and postprandial states, suggesting that sympathovagal balance contains nonlinear features of the HRV.

Acharya et al. [22] stated that the entropy measures reflect the unpredictability of fluctuations in the heart signals. In our results, the entropy measures had weak correlations with Poincare indices during both fasting and postprandial states, suggesting that the Poincare plot indices do not have the features of presenting unpredictability of fluctuations in the RR time series.

The DFA ($\alpha 1$) presented a strong correlation with SD1/SD2 ratio during fasting and postprandial states, suggesting that the ratio can be used to represent the fractal scaling properties of the heart rate signal. Hoshi et al. [9] also observed a strong correlation between DFA ($\alpha 1$) and SD1/SD2 ratio and suggested that the ratio can be used as a surrogate nonlinear variable.

5 Conclusion

The study results show that the SD1 and SD2 have linear features of the HRV, while the SD1/SD2 ratio has nonlinear features of the HRV. Sample entropy and approximate entropy measures are not having significant correlation with Poincare

plot indices. The study outcomes can be concluded that the Poincare plot indices have significant correlation with linear and nonlinear HRV measures and degree of correlation changes during fasting and postprandial states. Therefore, in studies correlating Poincare indices with linear and nonlinear HRV, the fasting and post-prandial states must be specifically identified.

References

1. Mansier P, Clairambault J, Charlotte N, Medigue C, Vermeiren C, Lepape G et al (1996) Linear and nonlinear analyses of heart rate variability: a mini review. Cardiovasc Res 31:371–379
2. Frank A, Belokopytov M, Moran D, Shapiro Y, Epstein Y (2001) Changes in heart rate variability following acclimation to heart. J Basic Clin Physiol Pharmacol 12:19–32
3. Berntson GG, Bigger JT, Eckberg DL, Grossman P, Kaufmann PG, Malik M et al (1997) Heart rate variability: origin, methods and interpretive caveats. Psychophysiology 34:623–648
4. Nitzan M, Boer H, Turivnenko S, Babchenko A, Sapoznikov D (1994) Power spectrum analysis of spontaneous fluctuations in the photoplethysmographic signal. J Basic Clin Physiol Pharmacol 5:269–276
5. Malik M (1996) Task force of the European society of cardiology and the North American society of pacing and electrophysiology. Heart rate variability: standards of measurement, physiological interpretation and clinical use. Eur Heart J 17:354–381
6. Acharya UR, Joseph KP, Kannathal N, Lim CM, Suri JS (2006) Heart rate variability: a review. Med Bio Eng Comput 44:1031–1051
7. Brennan M, Palaniswami M, Kamen P (2001) Do existing measures of poincare plot geometry reflect nonlinear features of heart rate variability? IEEE Trans Biomed Eng 48:1342–1347
8. Mourot L, Bouhaddi M, Perry S, Rouillon JD, Regnard J (2004) Quantitative Poincare plot analysis of heart rate variability: effect of endurance training. Eur J Appl Physiol 91:79–87
9. Hoshi RA, Pastre CM, Marques Vanderlei LC, Godoy MF (2013) Poincare plot indexes of heart rate variability: relationship with other nonlinear variables. Auton Neurosci 177:271–274
10. Contreras P, Canetti R, Migliaro ER (2007) Correlations between frequency domain HRV indices and lagged Poincare plot width in healthy and diabetic subjects. Physiol Meas 28:85–94
11. Rowe JW, Young JB, Minaker KL, Stevens AL, Pallotta J, Landsberg L (1981) Effect of insulin and glucose infusion on sympathetic nerve system activity in normal man. Diabetes 30:219–225
12. Spraul M, Anderson EA, Bogardus C, Ravussin E (1994) Muscle sympathetic nerve activity in response to glucose ingestion. Diabetes 43:191–196
13. Rothberg LJ, Lees T, Bligh RC (2016) Association between heart rate variability measures and blood glucose levels: implications for noninvasive glucose monitoring for diabetes. Diabetes Technol Ther 18:366–374
14. Johncy SS, Karthik CS, Bondade SY, Jayalakshmi MK (2015) Altered cardiovascular autonomic function in young normotensive offspring of hypertensive parents—is obesity an additional risk factor. J Basic Clin Physiol Pharmacol 26:531–537

15. Sharma VK, Subramanian SK, Radhakrishnan K, Rajendran R, Ravindran BS, Arunachalam V (2017) Comparison of structured and unstructured physical activity training on predicted VO2max and heart rate variability in adolescents—a randomized control trial. J Basic Clin Physiol Pharmacol 28:225–238
16. Karmakar CK, Khandoker AH, Gubbi J, Palaniswami M (2009) Complex correlation measure: a novel descriptor for Poincare plot. Biomed Eng Online 8:17
17. Pincus SM (1991) Approximate entropy as a measure of system complexity. Proc Natl Acad Sci 88:2297–2301
18. Lewis MJ, Short AL (2007) Sample entropy of electrocardiographic RR and QT time series data during rest and exercise. Physiol Meas 28:731–744
19. Acharya UR, Lim CM, Joseph P (2002) Heart rate variability analysis using correlation dimension and detrended fluctuation analysis. ITBM-RBM 23:333–339
20. Mukaka MM (2012) Statistics corner: a guide to appropriate use of correlation coefficient in medical research. Malawi Med J 24:69–71
21. Otzenberger H, Gronfier C, Simon C, Charloux A, Ehrhart J, Piquard F et al (1998) Dynamic heart rate variability: a tool for exploring sympathovagal balance continuously during sleep in men. Am J Physiol 275:H946–H950
22. Acharya UR, Kannathal N, Sing OW, Ping LY, Chua T (2004) Heart rate analysis in normal subjects of various age groups. Biomed Eng Online 3:24–31

An Extensive Review on Organic Light-Emitting Diode for Energy-Saving and Eco-friendly Technology

Rita Rana, Akanksha Jetly and Rajesh Mehra

Abstract OLEDs have turned out to be the boon in the field of display technology and solid-state lighting because of compelling characteristics. They have remarkably emerged as an energy-saving technology to cope up with the increased demand for electricity and its generation. OLEDs are solid-state devices which consume very less power and have very low driving voltage. LEDs have grabbed so much of attention because of minuscule energy consumption, but this even newer technology is intriguing the interest of both manufacturers and consumers. OLED displays offer startling vivid pictures of high-definition resolution with vibrant and radiant colors and highly efficient illumination. Companies are investing significant financial resources for the development of future technology. So, there is a need of the hour to study in depth the milestones and challenges of this emerging technology. The critical areas on which the enormous valuable improvements are being carried out involve efficient current injection, light extraction techniques, efficiency, lifetime issues, and power consumption. The central idea of the review is to make the reader familiar with the structural and the operational details of the device, types of OLED and their drawbacks, material science, and important parameters governing the huge success of the OLED technology.

Keywords Organic light-emitting diodes · Electroluminescence · Organic compounds · Excitons · Device parameters

R. Rana (✉) · A. Jetly · R. Mehra
National Institute of Technical Teachers Training and Research,
Chandigarh 160019, India
e-mail: er.ritarana@gmail.com

A. Jetly
e-mail: akankshajetly@gmail.com

R. Mehra
e-mail: rajeshmehra@yahoo.com

1 Introduction

OLEDs are going to be the most promising technology for lighting as well as display applications in upcoming future era. It will dominate the world in a way nothing else would do. Presently, OLEDs are still a young area of technology but sooner they are going to be the razzle-dazzle of the future world. They have rapidly progressed over the years and managed to create a place in the market because of its huge commercial success. OLEDs being an energy-saving device have revolutionized the recent trends in display and lighting technology. About one-third of the total electricity generated is used for lighting applications [1]. With OLEDs, it will cut the cost of lighting to a great extent. This review is intended to showcase the significant attainment in the field of OLEDs display. This paper aspires to throw the light on the various aspects of the OLED technology. Display technology future shows great potential of fascinating the world with its unbelievable advantages. Moving from inorganic to organic explains itself that how dedicatedly we are transforming to the eco-friendly generations. They are very thin, lightweight, flexible, varying in shapes and sizes. They are self-illuminating, i.e., does not require backlighting, have wide viewing angle, a low operating voltage, light emission throughout the visible region, small production cost, fast response time, high efficiency, and high contrast ratio. These significant merits of OLEDs outnumber the challenges faced by the technology [2–10]. An OLED is a light-emitting diode which emits light when current is passed through it. This emissive electroluminescent device is composed of several layers made of organic compounds which are sandwiched between two electrodes out of which one electrode is transparent. OLEDs are based on the principle of efficient injection and transportation of the charge carriers, i.e., the electrons and the holes. A major research direction is the improvement of light outcoupling efficiency, stability, and lifetime issues [11–13]. Power consumption and temperature analysis are also the key factors which impact the overall performance of the device. Power consumed by the device and temperature are interrelated parameters. Research is concentrated on the enhancements of the OLED architecture and electrode structures so as to improve the device parameters. The scope of this review is to enlighten the impressive technological progress in the domain of OLEDs. This paper discusses the structure, working principle, classification, materials, and device parameters of OLEDs. After reading this paper, the audience will gain thorough knowledge about the OLED technology.

1.1 *Basic Light Phenomenons*

The Law of Conservation of Energy states that 'Energy can neither be created nor be destroyed; it can only be converted from one form of energy to another.' Light is a form of energy too. So, to produce light, some form of energy must be provided to

get it converted into light energy. There are two phenomenons through which light is generated, and they are stated as below:

Incandescence

It converts the heat energy into the light energy. It is concerned with the high-level agitation of the atoms in the material that excite the electrons to higher electronic states. As a result, atom agitation raises the temperature of the body or material to such an extent that it starts glowing. It is observed in heavenly bodies like star and sun. Filament lamps also make use of same phenomenon to glow.

Luminescence

Luminescence pertains to the emission of light below the room temperature. Therefore, it is also called the cold light. It converts the invisible form of energy to the visible light. The material absorbs energy, and this energy excites the electrons to higher energy states, thus causing luminescence with the transition of excited electrons from the unstable (excited state) to stable state (ground state). The energy absorbed can be in the form of ultraviolet rays, X-rays, electron beams, or chemical reactions. It can further be of many types but we will only study about photoluminescence and electroluminescence.

Photoluminescence

In this, the energy absorbed is the photon energy. It can occur by the virtue of electromagnetic radiations. The emitted light has wavelength which is equal or greater than the incident light. The phenomenon is governed by the optical properties of material. It is further classified into two types—fluorescence and phosphorescence. Fluorescence occurs as soon as the energy is supplied to the material and stops immediately after the removal of source of excitation with luminescence lasting upto less than 10^{-8} s. The transition occurs from ground state to the singlet excited state (excited electron spin is still paired with the ground state electron, i.e., spins are anti-parallel) as shown in Fig. 1. In phosphorescence, material continues

Fig. 1 Showing transitions in fluorescence and phosphorescence
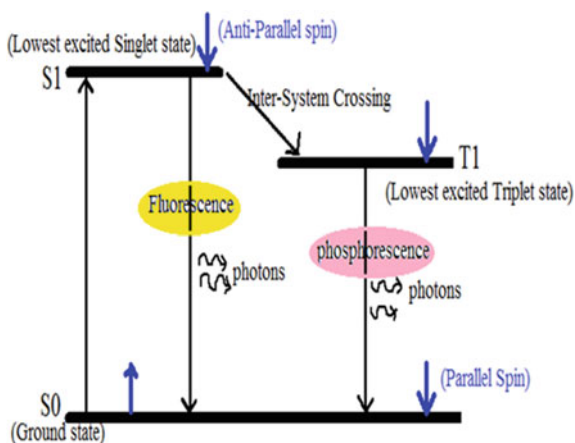
to radiate for some time even after the removal of radiation with luminescence lasting upto more than 10^{-8} s. The transition occurs from ground state to the triplet state (excited electron spin is not paired with the ground state electron, i.e., spins are parallel) as shown in Fig. 1.

Electroluminescence

It is the phenomenon in which light is emitted from the material in response to the flow of electricity through it. This phenomenon is governed by the optical properties of the active layers, physical device structure, electrical properties of the conductive layer and contacts. Prior to the recombination, electrons are separated either by doping the material or through carrier injection by applying voltage. Then, these separated electrons recombine either by singlet/singlet transition or singlet/triplet transition releasing their energy as photons. Certain organic materials exhibit electroluminescence which is being exploited in OLEDs devices [14, 15].

2 Why OLEDS?

Before the emergence of OLED, many lightning and display technologies were used. But all these technologies were having their own flaws and limitations which eventually led to the development of OLEDs. Some of the display technologies that were used prior to the OLEDs are as follows.

2.1 Incandescent Lamps

These were the earliest source of the electrical light. They produce light by glowing wire or filament whenever external power was supplied. It was developed in 1879 by Edison. The main disadvantage of using incandescent lamps was their large size. Moreover, they were very energy inefficient [16].

2.2 Cathode Ray Tube (CRT)

The first CRT was developed by John B. Johnson in 1922. CRTs were mainly used for image displays, waveform and for signals synthesis, analysis, and monitoring. Therefore, all the above advantages of CRT contributed to the development of CRT television that was invented by Telefunken in 1934 in Germany. The big problem that arose during that era was to move from small-scale to large scale production of CRT Televisions. For that purpose, many structures and new technologies were employed by the different manufacturers. But all those structures were eventually based on the idea of placing the electrodes on the insulating bars and then

assembling the entire structure precisely in a chamber [17]. However, the recent development over these structures is the use of cold cathode fluorescent lamps (CCFLs) as backlight in LCDs [18]. The main disadvantage of using CRT was the small lifetime, high production cost, very bulky and heavy structure, slow starting and response time [19].

2.3 Fluorescent Lamps

They were developed in 1930. They were manufactured in a glass chamber filled with inert gases and mercury with a phosphor coating over it. In addition to this, a current regulator with integrated electronic ballasts was employed to control the energy of the fluorescent lamps [20]. The ultraviolet light generated by vaporizing the mercury within the chamber usually combined with the phosphor to generate the visible light. The main disadvantage of using these lamps was the small lifetime and very small lumen output of the lamps. Then, in 1970s, CFL came into existence but due to their high production cost, they were made available in the market from the late 1990s. They were not environmentally friendly since mercury was used and moreover, they were known to catch the fire easily as electronic ballasts were used. They also suffered from the problem of small lifetime and response time.

2.4 Inorganic LEDs

Inorganic LEDs are usually manufactured with the inorganic materials, i.e., the combination of group III and group V elements of the periodic table. Few examples are aluminum gallium arsenide, gallium arsenide phosphide, etc. They were invented by Distriau in 1936 and got available in the market since 1960s. At first, red LED was developed. Then between 1970 and 1990, green, yellow, orange, and blue LEDs were introduced but they were used only as a small indicator of light, i.e., to lighten up only a small area. Then in 1990, white LEDs were introduced which were then used as a traditional light source commercially and in homes. The inorganic LEDs are used mainly for lightning purposes and advanced displays. These days, quantum dot (QD)-based LEDs are particularly in use for the radiant and high-resolution displays.

Quantum dot-based LEDs hold excellent quantum and photoluminescence efficiency and possess very high color intensity [21, 22]. The quantum-dot particles used in LEDs convert the backlight to produce RGB colors, thereby improving the brightness along with producing excellent color saturation. QDs have a tiny semiconductor core and have a large band gap [23]. In the recent trends, inorganic LEDs are deposited on the non-epitaxial substrates, so as to make ultrathin, flexible, very lightweight LEDs for advanced display purposes [24]. The main disadvantage of using inorganic LEDs is that they suffer from the self-quenching phenomenon,

i.e., their fluorescence intensity decreases with time without using any external circuit [25]. They also suffer from the problem of quenching in photoluminescence especially in QD-based inorganic LEDs.

2.5 High-Intensity Discharge (HID) Lamps

HID lamps had longer lifetime and greater efficiency than the incandescent and fluorescent lamps. They came into the existence after the development of the mercury vapor (MV) lamps. These mercury vapor lamps had high efficacy and produced more vibrant colors by adjusting the electronic ballasts and using more complex compounds. But they suffered from the problem of small life which led to the introduction of SON lamps. They were most suited for the outdoor applications and had longer lifetime than the MV lamps, but they produced only yellow-colored light. They could be used in the applications where the color of the light was not of a big concern. Nowadays, modern induction lamps are being used which have a long lifetime and require very small temperatures than fluorescent lamps to start.

2.6 Liquid Crystal Display (LCD)

In 1962, LCD showing an electro-optic property was first developed by Richard Williams. Friedrich Reinitzer in 1988 discovered a liquid crystal material that has an intermediate state between solid and liquid states. The liquid crystal material has an excellent display performance and has been used in various technologies and applications like television, calculators, mobile phones, watches, etc. This has increased the market contribution of LCD devices. The LCDs basically are of two types—active-matrix-based LCDs and direct-multiplexed LCDs—which differ from one another in the structure. The direct-multiplexed LCD consists of electrodes placed on the non-epitaxial substrates usually glass, whereas the active-matrix-based LCDs use semiconductor technology and produce radiant displays while their cost of production is very much higher than that of the direct-multiplexed LCDs [26].

Active-matrix-based LCDs are the most widely used LCD technology for the large screen displays. The main problem encountered in the LCDs for a long time was the small viewing angle and very slow response to the signals. To overcome this problem, wide-view film LCD instead of the optical twisted-nematic (NM) mode LCD was used. The main advantage of using wide-view film was that even at the oblique angle of incidence also, a very good contrast ratio was obtained. Therefore, LCDs can now be used in big and high-resolution monitor displays [27]. Nowadays, to increase the color performance and light efficiency of LCDs, quantum dot-based backlight is greatly used. Quantum dots have many merits over the other technologies like large photoluminescence efficiency, peak

wavelength, etc. The main disadvantage of LCDs over OLEDs is that they are less flexible, broader, heavy in weight, have large response time and small viewing angle than OLEDs [28].

2.7 OLEDs Emergence

OLED is based on the phenomenon of the electroluminescence, i.e., whenever an external electric field is applied to the matter in the condensed form, the electromagnetic radiations are emitted. The OLED emergence is explained as follows. The electroluminescence phenomenon was demonstrated in early 1953 by Andre Bernanos in France [29]. He connected a very high external voltage to the organic material acridine and observed the emission of blue color from the LED. In the year 1963, Pope et al. proposed the AC-driven electroluminescent cells using doped anthracene [30]. Kalinowski in the year 1976 observed the electroluminescence phenomenon in tetracene crystals. In 1983, electroluminescence phenomenon was observed in polymers by Roger Partridge at National Physical Laboratory [31]. Using this phenomenon, Kodak in 1987 introduced the first OLED. In beginning, OLED was composed with the small molecules [32]. This OLED is a double-layer OLED consisting of conductive and emissive layer sandwiched between the anode and the cathode which emit light in the emissive layer. These OLEDs were produced with the help of vacuum deposition technique. Although OLEDs produced with this technique emit very bright light, it was a costly manufacturing technique.

Then in 1990, OLEDs using organic polymer were introduced by Cambridge University researchers for the better light generation and large displays. This research led to the development of single-layer polymer LED which proved to be more efficient than the OLED made up from small polymers by vacuum deposition process. By using about 100-nm-thick organic film of poly (*p*-phenylenevinylene) polymer, a commercial polymer green OLED was manufactured [33]. First, commercial application of OLED was a small display for a car radio launched in the year 1997. Now, the focus of OLEDs has shifted to lightning applications, i.e., toward white OLEDs since 2000. The first OLED lightning product came into the market in 2009 named 'Luni Blade' by Philips with a thickness of 2.1 mm and area of 100 cm square which was later scaled successfully to 25 cm square by Panasonic. The introduction of flexible OLEDs by the researchers of Pacific Northwest Laboratory has revolutionized the commercial market since 2000. They were named as flexible as these OLEDs were made on flexible glass substrates and generally Barix film coating was used to protect the displays from the hazardous effect of the air and the moisture [34]. Flexible OLEDs are used in smart phones and high-resolution television screens. Then, the two types of OLEDs—PMOLED and AMOLED—that differ from one another in the addressing of pixels were invented. PMOLEDs can be fabricated easily but generally consumes more power

which led to the development of AMOLED. The flexible AMOLED is used widely in military and defense applications as they are more eco-friendly, portable, lightweight, consumes low power, and requires no backlight [35].

3 OLED Structure

Based on the number of organic layers between the anode and the cathode, OLEDs structures are classified into single-layer, two-layer, three-layer, and multilayer OLED structures. The single-layer structure comprises of a single organic layer inserted between the positively charged anode and the negatively charged cathode. In two-layer structure, the conducting layer and the emitting layer are placed in between the two electrodes [36]. Three-layer structure also consists of the conducting and emitting layers between the two electrodes. However, electron transport layer (ETL) and the hole transport layer (HTL) replace the conducting layer in the structure. Multilayer structure comprises various functionally different organic layers between the anode and the cathode as shown in Fig. 2. The multilayer OLED mainly consists of the following layers, and the materials that can be used for various layers are discussed in Table 1.
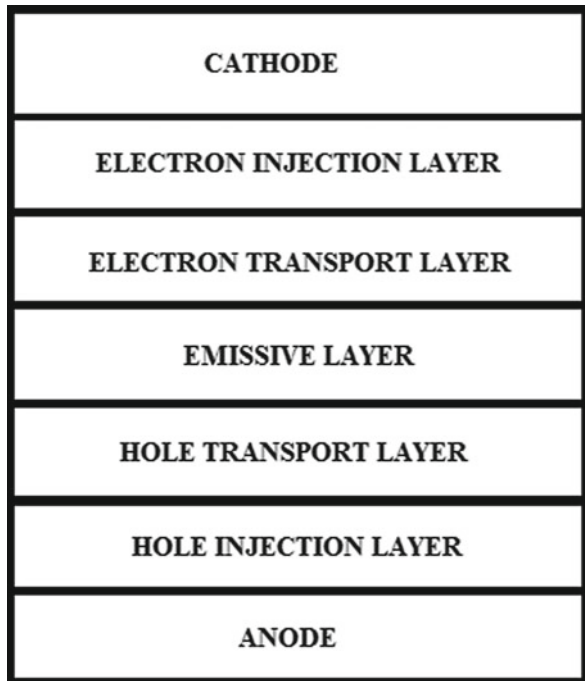
Fig. 2 Multilayer OLED

Table 1 Materials used for OLED

Layers	Materials
Substrate	Made up of materials having high work function like plastic, foil, glass materials
Anode	Indium tin oxide; indium zinc oxide; aluminum oxide; silicon oxide; PEDOT:PSS, etc.
Cathode	Magnesium: silver; lithium: calcium; calcium: thin insulator; LiF; magnesium oxide
Hole transport layer	HOMO level; Spiro-TAD; NPB; TPD; dendrimer
Electron transport layer	LUMO level; Alq_3; TPBI; BCP, etc.
Emissive layer	Polyfluore; rare earth complexes; rubrene; quinacridone, etc.

Starting with the substrate, it is the base on which all other layers are deposited and is generally composed of glass materials but sometimes, metal foils, semiconductor or plastic materials can also be employed. The work function of substrates should be high, i.e., near about 5 eV. Anode is a positively charged electrode that generally comprises materials like ITO. Nowadays, research is being carried out to replace the ITO material. It should have high work function, and should be highly conductive and transparent. HTL main function is to transport the holes and stop the electrons from arriving at the opposite. ETL transports the electrons and stops the holes from arriving at the opposite electrode. The role of emitting layer is to emit the light in the visible spectrum when electricity is supplied to it. This layer consists of materials that have high efficiency and longer life span. The materials used for the emissive layer decide the light coupling efficiency, quantum efficiency, and overall life span of the device. Cathode is a negatively charged electrode. It generally has low work function and comprises materials like calcium and magnesium. By making adjustments in the layer's thickness and increasing the doping concentrations of the different layers in the multilayer architecture, the efficiency of OLEDs can be enhanced [37, 38].

4 OLED Working

First of all, to produce light a small positive voltage of about 2.5–20 V is applied to OLED in a way such that the anode is at higher positive potential relative to that of cathode [39]. As the electricity starts flowing, the two kinds of electric charges are injected by the oppositely charged electrodes, i.e., holes from the anode and electrons from the cathode. The electrons are forced into the LUMO of ETL at the cathode and are withdrawn from the HOMO of HTL at anode followed by the injection of holes into HOMO of HTL and withdrawal from the LUMO of ETL. Therefore, these injected holes and electrons move toward the oppositely charged electrodes following a series of 'hops' from the molecule to molecule. Holes are generally much more mobile than the negatively charged electrons. The holes and

the electrons follow the hopping mechanism to gather near the same heterojunction [40, 41], i.e., near the emissive layer, the electrons and holes are electrostatically so close to one another that they get localize on the same molecule and then recombine forming an exciton which is the bounded state of electron and hole. Now, these excitons relax radiatively to the ground state (stable state) by the spontaneous emission.

This process is followed by the release of photons (packet of light energy) whose frequency falls within the visible region. The frequency of the emitted photons generally depends on the energy difference between the conduction and the emission band. The electrons and the holes are generally half-integer spin. Depending upon the combination of spins of electrons and the holes, an exciton can be in singlet state or in the triplet state. By using the spin–orbit interactions between the singlet and triplet states, phosphorescent OLEDs are thus obtained from the photon emission of both the singlet and the triplet states. The efficiency of these OLEDs is high. The other mechanisms which are non-radiative may also take place but those mechanisms do not interfere in the light production. Thus, recombination of the electrons and the holes produce light and results in very radiant display whose power consumption is very less than that of the other devices [36].

5   OLED Classification

OLEDs enable the manufacturing of solid thin-film, highly emissive, bright, less power consumable, wide viewing angle, flexible, and efficient displays. They can be classified into different categories on the basis of as follows.

5.1   Addressing of Pixels

Based on the addressing of pixels, OLEDs are classified as active-matrix OLEDs and passive-matrix OLEDs:

Passive-matrix OLEDS
Passive stands for the way how a pixel is driven in an OLED display. Basically, it is a control mechanism through which each row is sequentially controlled. PMOLED displays are structured mainly in the form of rows and column and consist of strips of organic cathode material, organic layers, and anode material. The intersection of a row and column makes up a pixel through which light is emitted when a voltage is applied through the driving circuitry to a particular row and column lines. However, they are easy to fabricate but at the same time require complicated driving circuitry because current is limited for each pixel and varies as the number of rows increases. The intensity of each pixel emission is directly proportional to the applied voltage magnitude. So, high voltage is required to make the passive displays glow at a

higher intensity. The magnitude of the voltage applied to each pixel generally increases with the resolution and size of the display.

Over the eras, OLEDs have evolved greatly but still challenges exist regarding the device stability in both storage and operation. There are various aspects that govern the stability of the device such as device structures, organic materials, electrode material, processing conditions, fabrication techniques, driving circuits, and so on. Driving circuits play a major role in the device stability as they account for the critical power consumption, thereby improving the overall device performance. An important issue that is the matter of concern in PMOLED is the crosstalk between the pixels due to the close proximity of electrodes. A driving circuit for passive matrix addressing which decreases the problem of crosstalk had been demonstrated in Ref. [42]. A lot of power is consumed in passively driven circuit which is a setback in this control mechanism. OLED technology has moved to a more efficient active-matrix OLED display.

Active-matrix OLEDS

It consists of a thin-film transistor (TFT) array which acts as a storage capacitor making the pixel glow all the time. All the other layers are same as are in PMOLED except a TFT matrix is placed in between the substrate and the OLED pixels. Each individual pixel consisting of red, green, and blue organic materials is driven by two TFTs. Therefore, they need less power as no backlighting is required. The problem of increase in the drive current for each pixel as the number of pixels increases in passive-matrix OLEDs was overcome by AMOLED. Generally, a polysilicon TFT was used to provide a constant current to each pixel. The design issue which comes into the picture is the uniformity of pixel to pixel luminance. The uniformity in luminance is achieved by supplying constant current to each pixel. The threshold variations can be removed by connecting OLED to the drain of the drive transistor as it will provide a constant current to the OLED in saturation region.

The simple driving circuitry uses two-TFT model. One transistor acts as a drive transistor which provides constant current and other acts as a switch for sample and hold of the voltage at drive transistor's gate. The main source of non-uniformity is threshold variations of drive transistor which can be improved by the process refinements in patterning polysilicon. Later, a four-TFT model was proposed to diminish the effect of non-uniformity. TFTs form the basis for AMOLED displays and play a vital role in stability and performance of the device. Amorphous indium gallium zinc oxide (a-IGZO) TFTs are promising candidates for AMOLED. They offer high resolution and refresh rates of 100,000 Hz. They offer comparatively greater contrast ratio and larger displays than PMOLED. But the only drawback is their expensive manufacturing process as fabrication of substrate and TFT matrix production is complex [43–45].

5.2 OLED Architecture

The various OLEDs architectures include:

Top- and Bottom-emitting OLED
With the coalition of backplane-thin-film transistors and high resolution, top-emitting OLEDs (TEOLED) and bottom-emitting OLEDs (BEOLEDs) are nowadays extensively used in TV screens and mobile screens' display. TEOLEDs are constructed by ejecting the light via the top electrode which can be either transparent or semi-transparent, whereas BEOLEDs are constructed by ejecting the light via the bottom electrode [46]. TEOLEDs are extensively used in active-matrix OLEDs. TEOLEDs have comparatively large aperture ratio because they are not influenced by the use of TFTs as they are usually built on the opaque substrate. So, it is viable to cover the TFTs beneath the metallic anode [47, 48]. As a result, they require small driving current, low operational voltage, and have a comparatively long life span.

Transparent OLED
Transparent OLED technology is a breakthrough in the display technology that permits interactive information to be projected on it alongside with the capability of viewing through it. All the components of this type of OLED, i.e., anode, cathode, and substrate, are transparent, and transparency of their substrates is nearly about 85%. Each pixel of transparent OLED consists of four subpixels, namely red, green, blue and a clear pixel. The clear pixel is responsible for the transparency in this type of OLED. They have the tendency of getting easily integrable with the organic TFTs in AMOLEDs [49, 50].

Transparent conductive oxides and thin metal films are being studied for transparent electrodes. Deposition of these materials takes place through different techniques. Thickness of electrode layers also plays a crucial role in governing electrical and optical properties of the OLED [51]. Selection of different electrode materials yields trade-off between optical transparency and electrical conductivity. Later, metal–dielectric composite electrode was proposed which offers good transparency, large-area film uniformity, and electrical conductivity. But it suffers from the problem of surface plasmonic losses and microcavity effect. To eliminate these effects, quasi-periodic nanostructure was incorporated along with the organic emitter and metal–dielectric composite top electrode [52].

Stack OLED
It is basically a pixel architecture that is used for full-color displays in which a pixel comprising of red, green, and blue subpixels are placed one above the other, i.e., stacked vertically. Therefore, this architecture leads to the minimum pixel size, maximum fill factor, increased color gamut, increased color depth with a good resolution [53–55]. A multistacked architecture provides high efficiency, high device, and color stability.

Inverted OLED

Conventional OLEDs are generally built on the bottom electrode. In the conventional OLED, bottom anode is generally connected to the driving TFT source end that affects the stability of the source voltage which further depends on the voltage drop across OLED materials. To solve this problem, inverted OLED were introduced [56]. Inverted OLED uses a bottom cathode so that it can be connected to n-channel TFT drain end. Amorphous silicon is generally used as n-channel TFTs and are main contenders for AMOLEDs display backplane because they offer high uniformity in terms of mobility and threshold voltages as compared to polycrystalline Si TFT. The next generation of TFTs, i.e., amorphous oxides, are also n-channel TFTs which make the realization of AMOLED displays easier. The a-IGZO TFT provides better uniformity and conduction properties [57]. The drawback of inverted OLEDs is that the bottom cathode is not able to inject electrons efficiently [58]. So, another EIL layer has to be introduced. Efficient OLEDs with low driving voltage and high luminescent efficiency can be built with inverted structure [59].

5.3 State of the Art

Based on need of current scenario, new advancements are taking place in OLEDs. Some of them are listed below:

White OLED

WOLED is a promising future technology for lighting applications which are finding way to market. Various architectures are being studied for improving the performance of WOLEDs. Most recently, two-stack (blue–yellow) and three-stack (blue–blue–yellow) architectures are proposed for efficient WOLEDs that are able to meet the standard white CIE coordinates and result in high quantum efficiency [60]. Blue-emitting materials are crucial in generation of white light. Balanced combination of fluorescent blue and phosphorescent yellow-emitting materials yields perfect white CIE coordinates. This is the current area of research in the domain of WOLEDs in which fluorescence and phosphorescence are combined to achieve very long life span and higher efficiency. The light outcoupling efficiency can be enhanced by adjusting the refractive indices of internal light extraction structure (IES) and external light extraction structure (EES) which form graded refractive index substrate [61].

Flexible OLED

Flexible OLEDs are OLEDs in which organic layers are deposited on flexible substrate. The various aspects of concern in which the advancements are made for the development of flexible OLEDs are flexible transparent conducting electrodes (TCE), device fabrication, light extraction technologies, and encapsulation techniques. The alluring feature of flexible OLEDs is its mechanical flexibility. The tensile strength of the device depends on the substrate and transparent conducting

electrodes. Flexible OLEDs make use of highly flexible substrates. High optical transparency, good mechanical bending capability, low electrical resistance, and low oxygen/moisture permeability are the traits of the flexible substrate. Flexible TCE, light extraction schemes, and device encapsulation are three parameters that wholly solely determine the performance of the OLED device. Transmittance and sheet resistance are the two important parameters which are kept in mind while selecting the materials for flexible TCEs.

Various techniques have been proposed for flexible TCEs like conduction polymers, graphene, hybrid composites, single-walled carbon nanotubes, and metal networks. Finding of polyacetylene was the milestone in the field of conducting polymers. After that various polymers such as polyaniline (PANI), polythiophene, poly (N-vinylcarbazole), and polypyrrole were developed which marked the beginning toward flexible foldable OLEDs. Polythiophene-based PEDOT:PSS is currently the widely used polymer material for making the flexible transparent electrodes. Various encapsulation techniques such as multibarrier structure which makes use of inorganic/organic layers have been proposed to protect the OLED from being damaged by the penetration of oxygen/moisture. The recent advances involve the devices being manufactured for biological implants and wearable electronics [62, 63].

6 OLED Fabrication Techniques

These techniques are simple and provide a cost-effective solution. The common fabrication techniques are as follows.

6.1 Physical Vapor Deposition

The various steps involved in the physical vapor deposition technique are: (i) formation of vapors of the solid organic materials, (ii) transfer of the vapors from the source over to the substrates, and (iii) deposition of thin films of the vapors over the substrates by condensing the vapors. The merit of using this technique is that the thickness of the films can be easily controlled and deposited over the substrates without damaging the surface. But the disadvantage is that this process is not economical.

6.2 Vacuum Thermal Deposition

In this, the solid material is heated to change it to the gaseous form. In this method, the small organic molecules are first heated in a vacuum chamber or an electron beam evaporator can also be used. In the vacuum chamber, the organic material is

melted by the resistance heater so as to increase its vapor pressure. An electron gun firing a high-energy beam in the electron beam evaporator can also be used to heat the organic molecules. This process is followed by the condensation of molecules as thin films which are then employed on the substrates [64].

6.3 Sputtering

In this technique, the high-energy ions imparted by the plasma that are produced in the sputtering equipment are used to change the atoms of the solid material to the gaseous phase. In other words, the collision of solid material with the high-energy ions takes place in this process. The plasma is produced from the group 18 elements of the periodic table, i.e., noble gases such as argon and helium [65].

6.4 Shadow Masking

A shadow mask having holes for red, blue, and green subpixels is placed above the vapors. Then the substrate over which thin film is to be deposited is placed above this shadow mask. After the deposition of pixels of one color, the mask is moved ahead by one pixel so as to deposit the other color pixels over the substrates. Different shadow masks can be employed for these different materials. But the main problem is that these different emitting materials have different lifetimes, and this can lead to the color imbalance.

6.5 Ink-jet Printing

The technique is used to deposit the polymer molecules over the substrates. The polymer molecules should be dissolvable in some solvent. In this method, an ink-jet printer or ink-jet nozzle is used to sprinkle the organic solution over the substrates. The ink-jet nozzles to be used depend upon the colors to be printed. This technique allows several organic layers to be deposited over the substrates simultaneously. The OLEDs fabricated with this technique are used for large displays like TV and computer screens with very high resolution. This technique is very economical. The main advantage of this technique is that no physical contact with the surface is required as ink is sprayed over the substrates. As a result, there is no chance of contagion [66].

7 OLED Metrics

The various parameters that govern the performance of OLEDs are listed below. They characterize the overall behavior of the OLED. These design parameters should be taken into account during the fabrication of OLEDs.

7.1 Internal Quantum Efficiency (IQE)

It is defined as the proportion of electron–hole pairs that recombine through radiative recombination process. IQE is given as follows in Eq. (1):

$$\eta_{int} = \gamma \eta_s \phi_f \tag{1}$$

where γ is the charge balance factor, η_s is the single exciton factor, and ϕ_f is the fluorescence quantum efficiency [67, 68]. $\gamma \leq 1$ gives measure of the fraction of the electrons and holes that recombine to form an exciton. It can be improvised by varying the composition and the thickness of the charge injection layer and the charge transport layer to balance the electrons and holes injection into the device as excessive charges can lead to unbalanced injection and joule heating. The factor η_s gives the fraction of exciton that takes part in the radiative recombination, it is 25% for fluorescent OLEDs, but for electro phosphorescent OLED it can reach up to 100% [69, 70]. ϕ_f depends on the material design and synthesis. Therefore, to improve ϕ_f, efficient emitting systems are used. Thus, internal quantum efficiency can be enhanced by improvising the factors on which it depends.

7.2 External Quantum Efficiency (EQE)

It is defined as the total number of photons emitted from the device to the total number of charge carriers injected into the device, i.e., how efficiently a device converts injected electrons to the photons. It is important to increase the external quantum efficiency as enhancement in the device efficiency not only deals with energy issues but also increases the lifetime of the device. Hence, there are requirements for low driving voltage for the same output power as it reduces the heating losses and increases energy efficiency [67, 68].

EQE is given by Eq. (2) as:

$$\eta_{ext} = \xi \eta_{int} \tag{2}$$

where ξ is the extraction efficiency which gives the number of photons emitted exterior to the OLED to the number of internally generated photons. External quantum efficiency is ξ times the internal quantum efficiency.

7.3 Outcoupling Efficiency

Light outcoupling efficiency is the proportion of photons that actually manage to escape the device out of the total generated photons. Outcoupling efficiency depends on the refractive index of all the layers involved in the device structure particularly emitting layers, electrodes, and substrate. Light generated in the device gets trapped at the barrier between the two layers due to reflection or refraction occurring at the interface. Total internal reflection phenomenon traps the light inside the panel, thus lowering the extraction efficiency of the device. Excited molecules in the device can couple to undesirable optical modes. There are four modes among which light produced by the emitters is distributed. The air mode, the substrate mode, the organic/ITO mode, and the mode '4' light account for surface plasmon polaritons (SPPs), light absorbed in the structure and for other losses.

Approximately about $1/2n^2$ of the generated light come out of the device where n is the refractive index of the layers. Therefore, IES and EES are applied to enhance the light outcoupling efficiency. IES are applied inside the device structure, i.e., between the electrodes or between substrate and the transparent electrode. These schemes are able to extract organic/ITO mode of light and mode-4 light. EES are applied over the OLED device mainly outside the substrate surface and includes schemes like microlens, roughened substrate surfaces, and scattering films to avoid reflection of light from the substrate. The distance between the emitting layer and the electrodes, layer thicknesses, and the refractive index are the important design parameters that must be kept in mind to increase the extraction efficiency of the OLED [71–73].

7.4 Efficacy

The efficacy of the light source is defined as the ratio of the total photonic output of the device to the total power applied, i.e., the amount of light we get for the amount of power we put in. It is given by Eq. (3) as:

$$E = \frac{L}{V * I} \tag{3}$$

where L is the luminous output of the device weighted by the color sensitivity of the human eye, V is the voltage applied, and I is the operating current. It is measured in cd/W. The theoretical limit of efficacy is the ratio of maximum light output to the minimum operating voltage [6]. The color quality of the OLED lighting and efficacy is highly correlated. The better the quality of the color (achieving standard CIE coordinates), the better is the efficacy number. The efficacy of the device can be enhanced by improving the structure of the emissive layer allowing each individual color to emit at the maximum efficiency.

7.5   Lifetime Issues

Lifetime is defined as the average number of life hours in which device brightness decreases to 50% or 70% of its initial value under constant current operation [74, 75]. The operational lifetime is directly proportional to the operating current and is given in Eq. (4):

$$I^n Tx = \text{const.} \tag{4}$$

where I represents the operating current and Tx is the operational lifetime in which x represents the value to which decrease in brightness is acceptable. x is generally 50 or 70. T50 is the total time in which the brightness decreases to 50% of its initial output value, and T70 is the total time in which the brightness decreases to 30% of its initial output value [70]. Enhancing charge transport properties and using the mixed host structure and more stable host material are certain modifications which should be incorporated in the design to enhance the life hours of the device. OLED lifetime can be analyzed in two aspects—operational lifetime and shelf life. The operational lifetime refers to the gradual degradation in the performance of the device when current is passed constantly through it. The shelf life is defined as the total time period for which device can be kept safely without disruption from its normal behavior. Intrinsic and extrinsic factors are the two broad categories that cover the entire range of causes strongly responsible for lifetime reduction of the device. Chemical degradation of the organic materials, device architecture, charge imbalance, temperature dependency, unstable host, improper electrodes are the causes related to intrinsic factors, whereas the operating conditions of the device come under the extrinsic category. Although a lot of work has been done on the advancements of this most competitive display technology, the operational lifetime of the device still remained a problem. Dark spot formation and degradation in the performance because of the passage of current through the device are the two main causes that results in decrease in the brightness of the OLED. Dark spot formation occurs due to exposure of the device to the atmospheric oxidants such as oxygen and moisture. Thin encapsulation techniques have been devised that almost eliminate the permeation of oxygen/moisture into the device.

8   Conclusion

This review gives a bird's-eye view on the emerging OLED technology. After the discovery of electroluminescence in organic materials, OLEDs have evolved out of scientific curiosity. Advancements are being carried out in these areas to enhance the OLED performance and increase its efficiency. OLEDs striking features have lured its use in lighting and display applications. The intensification in OLED technology will tend to accelerate with the full exploitation of the technology

potential. Considerable efforts are being carried out for improving the electrical and optical properties of the OLED device. Better materials and manufacturing processes are required for further advancement in the OLED field. As natural resources are rapidly depleting, energy crisis has hit the backbone of all the economies. So, there is a major concern for energy conservation which can only be enforced with the existing technology up gradation. OLED technology is the key solution to this problem. In the coming future years, OLEDs will provide cost-effective and elegant solution for energy efficient and environmentally friendly lighting and display applications.

References

1. Kalyani NT, Dhoble SJ (2012) Organic light emitting diodes: energy saving lighting technology—a review. Renew Sustain Energy Rev 16(5):2696–2723
2. Bagher AM (2014) OLED display technology. Amer J Opt Photon 2(3):32–36
3. Khazanchi A, Kanwar A, Saluja L, Damara A, Damara V (2012) OLED: a new display technology. Int J Eng Comp Sci 1(2):75–84
4. Schmidt TD, Scholz BJ, Mayr C, Brutting W (2013) Efficiency analysis of organic light-emitting diodes based on optical simulations. IEEE J Sel Topics Quant Elect 19(5):1–12
5. Patel BN, Prajapati MM (2014) OLED: a modern display technology. Int J Sci Res Pubs 4(6):1–5
6. Dhyani G, Bisht N (2016) A review paper on: study of organic light emitting diode. Int Res J Eng Tech 3(6):55–57
7. Singh A, Vishwakarma HL (2014) Organic light emitting diodes: materials, fabrications and applications. Int J Sci Res 3(6):557–581
8. Batool F (2016) A review paper on: organic light-emitting diode (OLED) technology and applications. Int J Adv Res Comput Commun Eng 5(11):152–156
9. Ijeaku AM, Chidubem MH, Chukwunonyerem EK, Obioma NU (2015) Organic light emitting diode (OLED). Amer J Eng Res 4(9):153–159
10. Pope M, Kallmann HP, Magnante P (1963) Electroluminescence in organic crystals. J Chem Phys 38(8):2042–2043
11. Meerheim R, Lüssem B, Leo K (2009) Efficiency and stability of p-i-n type organic light emitting diodes for display and lighting applications. Proc IEEE 97(9):1606–1626
12. Saxena K, Jain VK, Mehta D (2009) A review on the light extraction techniques in organic electroluminescent devices. J Opt Mater 32:1221–1233
13. Choudhary S, Qureshi S (2008) Life time issues in organic light emitting diodes. In: IEEE Conference of Proceedings TENCON, Hyderabad, India, pp 1–4
14. Kalinowski J (1999) Electroluminescence in organics LEDs. J Phys D Appl Phys 32(24):179–250
15. Godlewski J, Obarowska M (2007) Organic light emitting devices. J Opto-Elect Rev 15(4):179–183
16. Cole M (2013) The lighting revolution: if we were experts before, we're novices now. IEEE Trans Ind Appl 50(2):1509–1520
17. Broadway LF (1951) Cathode-ray tubes-a review of progress. Proc IEEE Part I Gen 98(114):316–320

18. Alberts IL, Barratt DS, Ray AK (2010) Hollow cathode effect in cold cathode fluorescent lamps: a review. J Disp Tech 6(2):52–59
19. Langmuir DB (1937) Theoretical limitations of cathode-ray tubes. Proc Inst Radio Eng 25 (8):977–991
20. Ho YKE, Lee STS, Chung HSH, Hui SYR (2001) A comparative study on dimming control methods for electronic ballasts. IEEE Trans Power Electron 16(6):828–836
21. Colvin VL, Schlamp MC, Allvisators AP (1994) Light-emitting-diodes made from cadmium selenidenanocrystals and a semiconducting polymer. Lett Nat 370(6488):354–357
22. Kim S, Im SH, Kim SW (2013) Performance of light-emitting-diode based on quantum dots. J Nanosci 5(12)
23. Amini P, Dolatyari M, Rostami A, Rostami G, Mathur S, Torabi P (2015) High-performance solution processed inorganic quantum-dot LEDS. IEEE Trans Nanotech 14(5):911–917
24. Kim T, Kim RH, Rogers JA (2012) Microscale inorganic light-emitting diodes on flexible and stretchable substrates. IEEE Photon J 4(2):607–612
25. Shirasaki Y, Supran GJ, Bawendi MG, Bulovic V (2013) Emergence of colloidal quantum-dot light-emitting technologies. J Nat Photon 7:13–23
26. Ishii Y, Awane K (1995) Technology advances in liquid-ciystal display. In: IEEE international conference solid-state circuits, San Francisco, USA, pp 64–65
27. Mori H (2005) The wide view (WV) film for enhancing the field of view of LCDs. J Disp Tech 1(2):179–186
28. Luo Z, Xu D, Wu ST (2014) Emerging quantum-dots-enhanced LCDs. J Disp Tech 10 (7):526–539
29. Chen Z, Yu J, Ogino K, Miyata S (2002) Blue emission from light-emitting diodes based on lithium complex. J Phys D Appl Phys 35(11):1099–1102
30. Pope M, Kallmann H, Mangnate P (1963) Electroluminescence in organic crystals. J Chem Phys 43(8):2620–2621
31. Partrige RH (1983) Electroluminescence from Polyvinylcarbazole Films: 2. Polyvinylcarbazole films containing antimony pentachloride. J Polym 24(6):733–762
32. Tang CW, Slyke SAV (1998) Organic electroluminescent diodes. Appl Phys Lett 51(12):913–915
33. Kaur P, Singh H (2016) New era in solid state lighting: organic light emitting diode (OLED). Int J Core Eng Manage 3(2):37–46
34. Hack M, Hewitt R, Urbanik K, Chwang A, Brown JJ (2006) Full colour top emission AMOLED displays on flexible metal foil. In: Proceedings of international Meeting on Information Display Conference, Daegu, South Korea, pp 305–308
35. Sarma KR, Roush J, Schmidt J, Chanley C, Dodd S (2006) Flexible active matrix organic light emitting diode (AMOLED) displays. In: Proceedings of 9th Asian symposium information display, New Delhi, India, pp 337–342
36. Karzazi Y (2014) Organic light emitting diodes: devices and applications. J Mater Environ Sci 5(1):1–12
37. Jordan RH, Dodabalapur A, Strukelj M, Miller TM (1996) White organic electroluminescence devices. Appl Phys Lett 68(9):1192–1194
38. Andrade BWD, Brooks J, Adamovich V, Thompson ME, Forrest SR (2002) White light emission using triplet excimers in electrophosphorescent organic light-emitting devices. J Adv Mater 14(15):1032–1036
39. Dhyani G, Bisht N (2016) Review paper on: study of organic light emitting diode. Int Res J Eng Tech 3(6):1155–1157
40. Shire A, Jawarkar U, Arbat A (2015) A review paper on: organic light emitting diode over conventional LED. Int J Adv Res Comp Sci Soft Eng 5(1):178–181
41. Pandey RK, Kumar S, Kumar P, Kumar A, Rathore GS, Sharma C (2014) Organic light emitting diode: a new era in display techniques. Appl Phys Lett 1(1):26–29
42. Bu-xin Z, Zhi-lin Z, Wen-qing Z, Xue-yin J, Shao-hong X (2001) Organic thin film electroluminescent passive matrix display. J Shang Univ 5(2):151–155

43. Kuo A, Won TK, Kanicki J (2008) Advanced amorphous silicon thin-film transistors for AM-OLEDs: electrical performance and stability. IEEE Trans Electron Devices 55(7):1621–1629

44. Baek G, Abe K, Kuo A, Kumomi H, Kanicki J (2011) Electrical properties and stability of dual-gate coplanar homojunction DC sputtered amorphous indium–gallium–zinc–oxide thin-film transistors and its application to AM-OLEDs. IEEE Trans Electron Devices 58(12):4344–4353

45. Purohit V, Banu T, Daiya K (2012) AMOLED: an emerging trends in LED. Int J Sci Eng Res 3(10):1–4

46. Park WY, Cheong HW, Lee C, Whang KW (2016) Design of highly efficient RGB top-emitting organic light-emitting diodes using finite element method simulations. Opt Express 24(21):18–31

47. Chen S, Deng L, Xie J, Peng L, Xie L, Fan Q, Huang W (2010) Recent developments in top emitting organic light emitting diodes. J Adv Mater 22(46):5227–5239

48. Huang Q, Walzer K, Pfeiffer M, Lyssenko V, He G, Leo K (2006) Highly efficient top emitting organic light-emitting diodes with organic outcoupling enhancement layers. Appl Phys Lett 88(11):51–53

49. Bulovic V, Gu G, Burrows PE, Forrest SR, Thompson ME (1996) Transparent light-emitting devices. Int J Nat Sci 380:29

50. Parthasarathy G, Adachi C, Burrows P, Forrest SR (2000) High-efficiency transparent organic light-emitting devices. Appl Phys Lett 76(15):28–30

51. Raychaudhuri P, Madathil J, Shore JD, Slyke SAV (2012) Performance enhancement of top-and bottom-emitting organic light-emitting devices using microcavity structures. J Soc Info Disp 12(3):315–321

52. Zhang YB, Ou QD, Li YQ, Chen JD, Zhao XD, Wien J, Xie ZZ, Tang JX (2017) Transparent organic light-emitting diodes with balanced white emission by minimizing waveguide and surface plasmonic loss. Opt Express 25(14):62–75

53. Sun H, Chen Y, Chen J, Ma D (2015) Interconnectors in tandem organic light emitting diodes and their influence on device performance. IEEE J Sel Topics Quantum Electron 22(1):154–163

54. Forrest SR, Burrows PE, Shen Z, Gu G, Bulovic V, Thompson ME (1997) The stacked OLED (SOLED): a new type of organic device for achieving high-resolution full-color displays. J Synt Met 91(1–3):9–13

55. Stephen GG, Forrest R (1998) Design of flat-panel displays based on organic light-emitting devices. IEEE J Sel Topics Quantum Electron 4(1):83–99

56. Jeong JK, Chung HJ, Mo YG, Kim HD (2008) Comprehensive study on the transport mechanism of amorphous indium-gallium-zinc oxide transistors. J Electrochem Soc 155(11):873–877

57. Noh JK, Kang MS, Kim JS, Lee JH, Ham YH, Kim JB, Son S (2012) Inverted OLED. J Soc Info Disp 39(1):212–214

58. Wu C, Ho M, Su S, Chen CH (2012) Flexible inverted bottom-emitting organic light-emitting devices with a semi-transparent metal-assisted electron-injection layer. J Soc Inf Disp 18(1):76–80

59. Springer R, Kang BY, Lampande R, Ahn DH, Lenk S, Reineke S, Kwon JH (2016) Cool white light-emitting three stack OLED structures for AMOLED display applications. Opt Express 24(24):28131–28142

60. Chang CH, Chang T, Lo Y, Liang YH, Wu YJ, Chang HH (2015) Improving the efficiency of white OLEDs based on a gradient refractive index substrate. In: 22nd international conference on active-matrix flat panel display, devices, Kyoto, Japan, pp 73–76

61. Xu RP, Li YQ, Tang JX (2016) Recent advances in flexible organic light-emitting diodes. J Mater Chem C 4(39):9116–9142

62. Lee SM, Kwon JH, Kwon S, Choi KC (2017) A review of flexible OLEDs toward highly durable unusual displays. IEEE Trans Electron Devices 64(5):1922–1931

63. Yamamura T, Kitamura M, Kuribayashi K, Arakawa Y, Takeuchi S (2007) Flexible organic LEDs with parylene thin films for biological implants. In: 20th international conference on micro electro mechanical system, Hyogo, Japan, pp 739–742
64. Katsuki K, Kawakami A, Ogino K, Tanaka K, Usui H (2005) Preparation of carbazole polymer thin films by electron-assisted deposition of 3-(n-carbazolyl) propyl acrylate. Jpn J Appl Phys 44(6A):4182–4186
65. Usui H (2009) Formation of polymer thin films and interface control by physical vapor deposition. Proc SPIE 7404:1–12
66. Tekin E, Smith PJ, Schubert US (2008) Inkjet printing as a deposition and patterning tool for polymers and inorganic particles. J Soft Matter 4(4):703–713
67. Salleh M, Hasnan T, Azis T, Sepeai S, Yahaya M (2007) Fabrication of organic light emitting diodes (OLEDs) for flat panel displays. BerkalaIlmiah MIPA 17(3):9–14
68. Hong K, Lee JL (2011) Review paper: recent developments in light extraction technologies of organic light emitting diodes. J Electron Mater Lett 7(2):77–91
69. Lim TB, Cho KH, Kim YH, Jeong YC (2016) Enhanced light extraction efficiency of OLEDs with quasi periodic diffraction grating layer. Opt Express 24(16):50–59
70. Lamansky S, Djurovich P, Murphy D, Razzaq FA, Lee HE, Adachi C, Burrows PE, Forrest SR, Thompson ME (2001) Highly phosphorescent bis-cyclometalated iridium complexes: synthesis, photophysical characterization, and use in organic light emitting diodes. J Am Chem Soc 123(18):4304–4312
71. Adachi C, Baldo MA, Forrest SR, Thompson ME (2001) High efficiency red electrophosphorescence devices. Appl Phys Lett 78(11):1622–1624
72. Tyan YS (2011) Organic light-emitting-diode lighting overview. J Photon Energy 1(1):1–15
73. Brutting W, Frischeisen J, Schmidt TD, Scholz BJ, Mayr C (2013) Device efficiency of organic light-emitting diodes: progress by improved light outcoupling. J Phys Status Solid A 210(1)
74. Mehta DS, Saxena K (2006) Light out-coupling strategies in organic light emitting devices. In: Proceedings of Asian symposium information display, New Delhi, India, pp 198–201
75. Lee ST, Gao ZQ, Hung LS (1999) Metal diffusion from electrodes in organic light-emitting diodes. J Appl Phys Lett 75(10):1404–1406

Distraction-Free Car Dashboard Control Through Gesture Recognition

Aneesh D. Joshi, Chinmayee D. Joshi, Abhishek M. Karambelkar and S. B. Somani

Abstract In this paper, a gesture recognition-based human–vehicle interaction system has been developed which primarily aims to reduce driver distraction while operating dashboard controls in an automobile. This is achieved through simple gestures and camera positioning which ensures the driver keeps his eyes on the road and hands on the wheel. This method is also compared with other types of inputs which aim to achieve better ergonomics. These inputs include voice commands, physical inputs like steering-mounted controls and also existing gesture recognition methods. This method overcomes the limitations of the aforementioned input techniques by providing a simpler and effective alternative. Said system is found to be superior compared to existing dashboard control media on grounds of operability, execution time and ease of operation.

Keywords Automotive electronics · Car dashboard · Driver distraction · Hand gesture recognition · Human–vehicle interaction

1 Introduction

The modern automobile has a plethora of technologies integrated into its every single system. The top-most priority of today's vehicles is safety. The primary purpose of these systems is to ensure the occupants' comfort and safety.

The number of features in a car has been ever increasing. As new interactive technology is introduced in cars, driver distraction has become an increasing threat due to cluttered dashboards. Accidents have occurred where the driver had taken his or her hand off the steering wheel to interact with the dashboard. To counter the above-mentioned issue, voice commands and ergonomic facilities like steering-mounted controls have been introduced. But these methods did not address

A. D. Joshi (✉) · C. D. Joshi · A. M. Karambelkar · S. B. Somani
MAEER's MIT College of Engineering, Ex-Servicemen Colony,
Paud Road, Pune 411038, India
e-mail: aneesh.270596.joshi@gmail.com

the root cause that was making the driver shifts his focus from the much more important task of driving to a menial task of operating dashboard controls.

This system employs a human–dashboard interaction which addresses the above-mentioned issue. This is done through real-time gesture recognition. Here, the driver's hand gestures are captured by a camera and accordingly, a function on the dashboard is executed while the driver's hands remain on the steering wheel and eyesight on the road. The gestures are based on the number of fingers raised by the driver on steering wheel.

Each combination will be responsible for a specific function on the dashboard. For now, the focus is on climate control. Based on the gestures, the fan speeds, air distribution and climate modes will be controlled. This will be extended to other dashboard facilities like infotainment system, where radio stations can be toggled or call feature, where calls can be accepted or rejected based on gestures. Also, this project provides customizable gestures which can be set according to the driver's preference.

The primary aim of this project is to maintain the driver's vision on the road and hands on the steering wheel. Through our system, we introduce an innovative, simple and safe alternative for operation of dashboard functions.

1.1 Driver Distraction and Safety

Driver distraction is a major cause in accidents [1]. In a vehicle, comfort, convenience and safety go hand in hand. If interacting with the vehicle is comfortable and convenient, it ensures that the system is non-intrusive and reduces visual load on the driver. While cognitive distraction is something an automobile manufacturer cannot have control over, visual and manual distractions solely depend on the layout of the dashboard controls.

This system aims to eliminate two out of the three types of distractions, that is, visual and manual. This can be done by ensuring that the gesture input is in the driver's binocular field of vision and also ensuring that the gesture input can be given without taking the hands off the steering wheel.

1.2 Existing Human–Vehicle Interfaces

The existing human–vehicle interfaces incorporated onto the dashboard have been studied extensively. This study includes existing gesture recognition technology.

1.2.1 Physical Inputs' Examples

(1) **Knobs and buttons**

Physical knobs and buttons are the basic components of a car's dashboard. Although they are very intuitive and simple, there are some glaring issues when it comes to their operation during driving. There is a vast array of functions that are available on the dashboard, because of which the number of buttons and knobs increases, making it cumbersome to operate. Also, during driving, it becomes even more difficult to operate since the driver needs to concentrate on the road.

(2) **Touch screen control**

Touch screens were introduced as a futuristic method for the driver to interact with the car. They reduced the number of physical knobs and buttons, but the underlying issue of operating them by taking eyes off the road is still present. Also, the sensitivity of touch screens varies, which might compromise the comfort of operation. Hence, it does not necessarily improve the situation.

(3) **Steering-mounted control**

To improve ergonomics, steering-mounted controls were introduced by migrating some key functions from the dashboard to the steering wheel. This helped to keep the driver's hands on the wheel, which was an improvement.

But, due to very limited space, there is a limitation on how many controls that can be ported to the steering wheel. Also, controls on the steering wheel are not customizable. Priority levels of controls are set solely by the manufacturer.

1.2.2 Voice Commands

With the recent introduction of Bluetooth connectivity in cars, it enabled a smartphone to be paired with the infotainment system. This allowed the smartphone's voice command system to be integrated with the car's infotainment system.

Voice command is a very popular feature in cars, especially when it is compatible with Google's Android Auto or Apple Car Play. Basic dashboard commands are executed using voice, like changing radio stations, calling a person or playing a particular song.

Despite its popularity, it has significant restrictions imposed on the driver on the grounds of language, clarity, accent [2], volume, etc. Also, there are limited commands which are not customizable by the driver. Its performance capabilities vary for different manufacturers [3]. If the car manufacturer requires an independent voice command system, it requires extensive development process in machine learning.

1.2.3 Existing Gesture Commands

To introduce a superior method of interacting with cars, gesture recognition was developed. It was also aimed at being less distractive than other input methods. The gestures that are currently being used are complex and non-intuitive hand movements. The region of interaction is situated at the centre of the dashboard, which could be a cause for distraction [4].

Ultimately, it involves taking the hands off the steering wheel and performing a particular gesture, making it difficult for the driver.

2 Architecture

In order to enhance system performance without compromising on safety and ease of operation, a new architecture has been developed as shown in Fig. 1. The system consists of the camera, Raspberry Pi and MCP2515 CAN Controller. The CAN messages are sent to the car's electronic control unit through which the dashboard controls are operated.

2.1 System Block Diagram

This vision-based gesture recognition system consists of a camera for visual input and an image processor (Raspberry Pi using OpenCV in Python). This system communicates to the car's electronic control unit (ECU) using CAN protocol. This is executed through the MCP2515 CAN bus module because the Raspberry Pi does not support direct CAN communication. Figure 1 illustrates the proposed system. Functioning of the system using these modules is explained below.
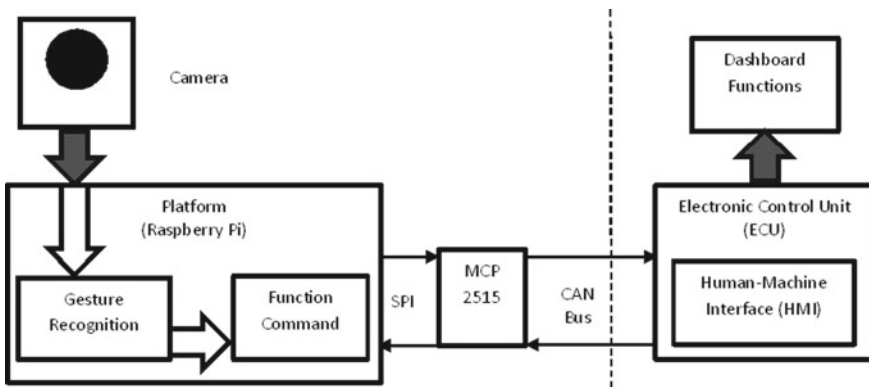

Fig. 1 Block diagram of proposed system

(1) Camera

The Raspberry Pi Cam v1.3 is a compact and customizable module dedicated to Raspberry Pi. It comes with a flat ribbon cable which is connected to a dedicated camera port on the Raspberry Pi. The specifications are as follows:

- Sensor still resolution: 5 megapixel (2592 × 1944 resolution)
- Video: Recording 1080p@30fps, 720p@60fps and 640 × 480p 60/90
- Size: 20 × 25 × 9 mm and lightweight (10 gm)
- IR sensitive: Optional motorized IR cut filter for detecting gestures at night.

(2) Raspberry Pi

The Raspberry Pi is a compact yet powerful single-board computer. It is a very effective and proficient platform when it comes to computer vision applications. Execution of image processing algorithms is done smoothly and seamlessly. The specifications are as follows:

- CPU: 1.2 GHZ quad-core ARM Cortex A53
- Memory: 1 GB LPDDR2-900 SDRAM
- Network: 10/100 MBps Ethernet, 802.11n
- Wireless LAN.

(3) MCP2515

All electronic communications in cars take place using the CAN protocol. The Raspberry Pi does not have a CAN bus. It has an SPI interface. Hence, we use the MCP2515 CAN controller which converts the SPI signals from the Pi to CAN. MCP2515 is a cheap and effective solution for proper CAN communication. This CAN controller board consists of two main ICs: The MCP2515 Standalone CAN controller with SPI interface and the TJA1050 CAN transceiver.

- Supports CAN V2.0B specification
- Communication speed: 1 Mb/s
- Data Field: 0–8 Byte
- Three frames—standard, expand the frame and remote
- Power supply: DC 5 V module and SPI interface protocol control.

(4) Electronic control unit (ECU)

The electronic control unit is an embedded system in the automobile which controls different electrical sub-systems in an automobile. It communicates with these sub-systems via the Controller Area Network (CAN) protocol. In the proposed system, the gestures that are captured will execute a function on the dashboard.

(5) Dashboard Functions

These are basically the various sub-systems in a car which control various features in a car. These functions include the infotainment unit, the climate control, driving modes, etc.

3   Methodology

Proposed system primarily focuses on accurate positioning of system components. It ensures the driver does not take his or her hands off the steering wheel or his vision off the road.

3.1   Positioning of System Components

Camera is placed behind the steering wheel without obstructing driver's vision. The upper curve of the wheel is the target area, which is covered in the camera's entire field of vision. The driver places his or her hands on the steering wheel and points his or her fingers without leaving the grip of the wheel. This way, the fingers are protruding above the upper curve of the wheel. The camera counts the number of fingers protruding above the steering wheel.

Camera positioning is illustrated in Figs. 2 and 3. The camera's compact size ensures that it does not become an obstruction in the driver's field of vision. Since the driver's eyes are also in the camera's field of view, they can also be monitored for a drowsiness detection system.
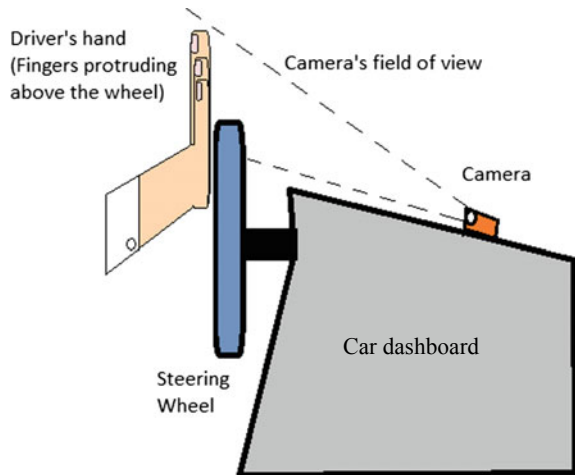

Fig. 2 Positioning of camera

Driver's hand
(Fingers protruding
above the wheel)

Camera's field of view

Camera

Car dashboard

Steering
Wheel

Fig. 3 Positioning of driver's hands in region of interaction

3.2 Image Acquisition and Gesture Extraction

Figure 4 shows the flow of the entire image processing algorithm, right from capturing the image to obtaining a particular gesture. The camera captures an RGB image of the fingers protruding above the steering wheel. Since the gesture requires a still position of the fingers, the acquired image is a single still frame and not a series of frames. Hence, the acquired image does not need to be of high resolution

Fig. 4 Flow chart for image processing algorithm
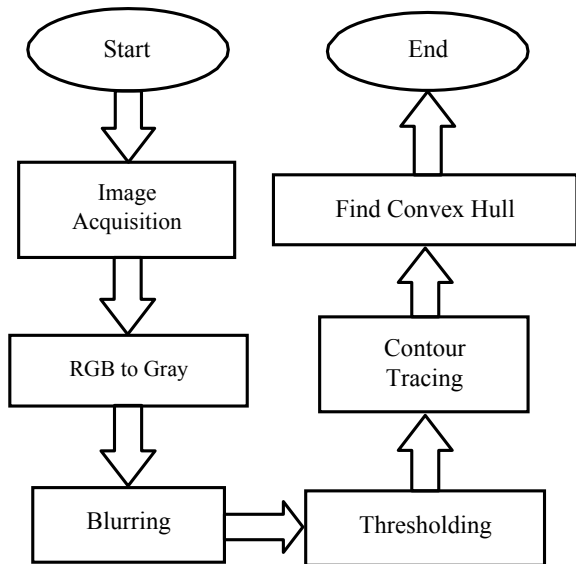
or a high frame rate. Therefore, this system uses a low resolution of 640 × 480 and six frames per second. A higher resolution and a better frame rate for higher quality can be considered, but this increases processor usage. For optimum performance, the above resolution and frame rate have been used. The stepwise representation of algorithm is represented in Fig. 5 (greyscale image), Fig. 6 (blurred image), Fig. 7 (thresholded image), Fig. 8 (traced contours).

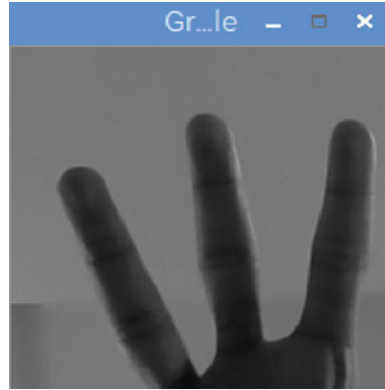

Fig. 5 Grey image after conversion of RGB image

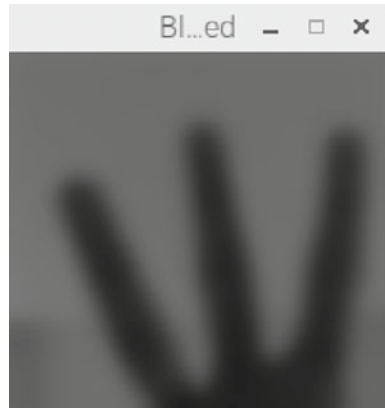**Fig. 6** Image after Gaussian blurring

Fig. 7 Otsu's binarization
thresholding
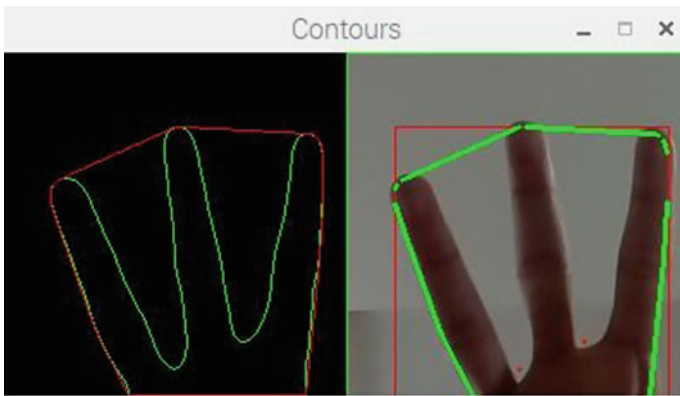
Fig. 8 Tracing of contours and detection of convexity defects

3.3 Pre-processing

The image is converted from RGB to grey since the system does not require colour.
This also enables the system to work on a single colour level, thus making pro-
cessing simpler.

In order to eliminate any noise, Gaussian blurring is done which basically means
low-pass filtering. Mask size is kept (35×35) for best results.

$$G(x, y) = \frac{1}{2\pi\sigma^2} e^{-\frac{x^2+y^2}{2\sigma^2}} \tag{1}$$

The image needs to be threshold according to specific grey levels. This is done
through Otsu's binarization method.

$$\sigma_\omega^2(t) = \omega_0(t)\sigma_0^2(t) + w_1(t)\sigma_1^2(t). \tag{2}$$

After thresholding, unnecessary details in the background are filtered out and the entire focus is on fingers of driver. It works similar to binary logic (white and black). Black is the area of interest while white is eliminated.

The driver places his or her hands on the upper curve of the steering wheel such that the fingers protrude in the region of interaction. For efficient capture of the driver's gesture, focus is required on particular areas in the frame. The acquired frame is split into two regions of interaction, one for each hand, by using the simple crop function. Therefore, rectangles of optimum dimensions have been set in frame for both hands of driver. The dimensions and the placement of these rectangles are such that the gesture is captured easily with minimum effort from driver. These two regions are then processed individually.

3.4 Gesture Identification

The gestures that are being used are finger based. Meaning, the gesture is based on the number of fingers that the driver is pointing. For this, the interest area is acquired through contouring. Contour is a virtual boundary of our interest area which is the driver's hand. So *findContour* function is used. It considers continuous shapes and finds their areas. The biggest contour includes the largest area, in this case, the driver's hand. After finding the *maxContour*, the entire focus now is only on the largest contour. The exact counting is done by the process of finding convex hulls and convexity defects.

A hand has fingers and cavities in between two consecutive fingers. The finger tips are convex hulls, and the cavities in between fingers are convexity defects. Counting either one of the above-mentioned parameters will yield the number of fingers pointed. Here, convexity defects are counted. This has been done based on the angle in between the fingers. If the angle between two consecutive fingers is less than 90°, then that is considered as a convexity defect. Cosine rule is applied for this purpose.

Once the angles are found, we draw a triangle such that it joins the two lower convexity defects and above convex hull. *drawContour* function is used for this purpose.

$$a^2 = b^2 + c^2 - 2bc \cos A. \tag{3}$$

After the triangles are constructed, all the upper points (convex hulls) are joined.

Finally, the total number of fingers is one more than total convexity defects detected. Hence, the gesture is identified.

4 Evaluation

Experiments were conducted inside a car to evaluate the performance of the system's gesture recognition capabilities. Different combinations of fingers of both hands in dark and bright environments were tested. Table 1 illustrates the combinations of fingers and corresponding functions on the dashboard.

Customizable commands in Table 1 can be infotainment control (volume/channels on radio), call feature (accept/reject calls), etc.

4.1 Results

Few examples of the captured gestures and their corresponding function from Table 1 are shown below. Figure 11 shows 'four-four' gesture indicating 'customizable command 3'. Similarly, Fig. 14 indicates 'two-three' meaning 'Defogger Mode' activation. Fingers are pointed by both hands in the region of interaction as shown in Figs. 9, 10, 11, 12, 13 and 14. Using thresholding, the fingers are represented by the white area. The convex hulls and convexity defects are found out.

Table 1 Matrix of gestures and the corresponding dashboard functions

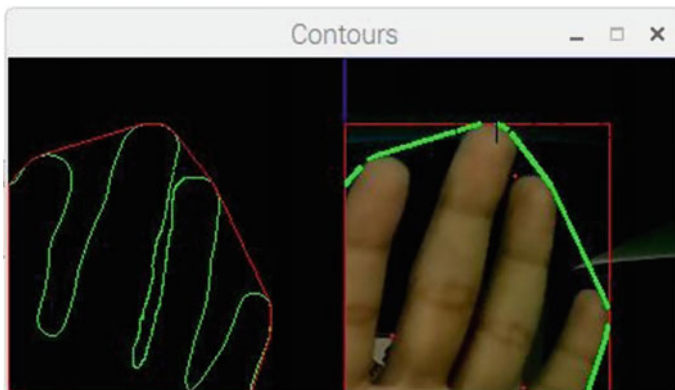| Left hand ↓	Right hand →	2 fingers	3 fingers	4 Fingers
2 fingers		Fan speed 1	Fan speed 2	Fan speed 3
3 fingers		Defogger mode	Air conditioner	Recirculation mode
4 fingers		Customizable command 1	Customizable command 2	Customizable command 3

Fig. 9 Contours and convexity defects

Fig. 10 Image thresholded

Fig. 11 Captured gesture 'four-four'
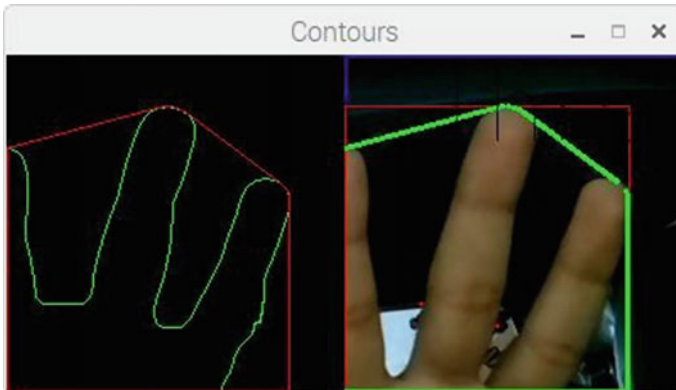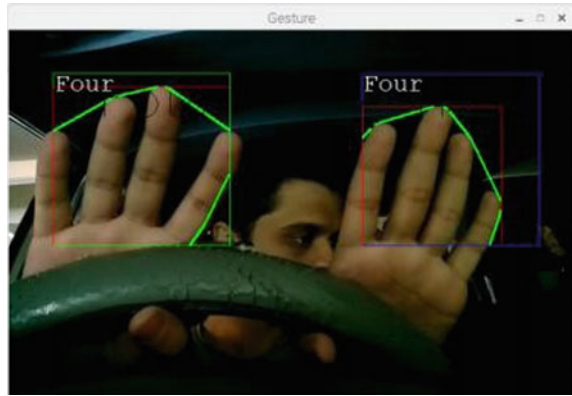

Fig. 12 Contours and convexity defects

Fig. 13 Image thresholded

Fig. 14 Captured gesture 'two-three'
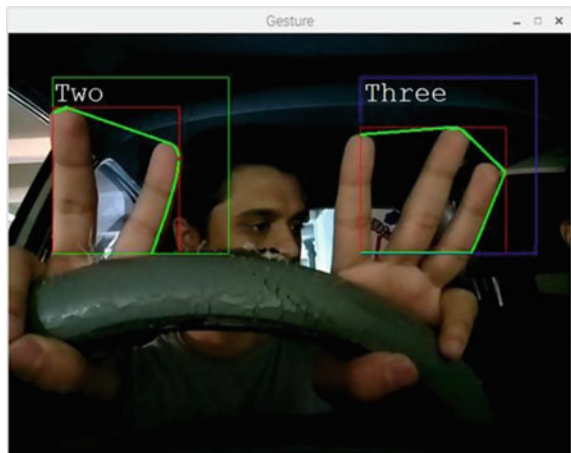
5 Conclusion

This system is developed to provide a refined and safe assistance to the driver. It introduces a method to control a car's dashboard functions using gesture recognition. The type of gestures in this project enabled the driver to keep his/her hands on the steering wheel and eyes on the road. For accurate gesture detection in a variety of environments, accurate thresholding, boundary conditions and tolerances were maintained. The testing was carried out in different environments, and accurate results were obtained.

These gestures were processed in real time without incurring any lags with the help of optimizing techniques like lowering the resolution, reducing the frame rate and processing greyscale images. Ultimately, the desired output was acquired.

References

1. Gonzalez R, Woods R (2016) Digital image processing. Pearson Prentice-Hall, Delhi, Chennai
2. Chowdary P, Babu M, Subbareddy T, Reddy B, Elamaran V (2014) Image processing algorithms for gesture recognition using MATLAB. In: 2014 IEEE international conference on advanced communications, control and computing technologies
3. Seppa N (2013) Impactful distraction: talking while driving poses dangers that people seem unable to see. Sci News 184(4):20–24
4. Chant I (2014) Study shows voice-controlled devices distract drivers. IEEE Spectrum. Available: https://spectrum.ieee.org/cars-that-think/transportation/safety/in-car-infotainment-can-distract-drivers

Neural Network Data Fusion
for Cognitive Radio Network

Reena Rathee Jaglan, Rashid Mustafa and Sunil Agrawal

Abstract Cognitive radio network practices dynamic spectrum access for efficient spectrum utilization. Sensing being the utmost task involves cooperation of different secondary users contributing to cooperative network. Thus, fusion rules play an important role for decision making. In this paper, we considered a scenario of cooperative spectrum sensing and analyzed the performance of fusion schemes implanted at fusion center for decision making. We have also proposed a learning-based neural network fusion scheme for reliable decision. Further, we have analyzed the performance of proposed scheme under different fading channels. The proposed scheme outperforms conventional schemes accomplishing substantial enhancement in detection probability and decline in probability of false alarm.

Keywords Cooperative spectrum sensing · Fusion scheme · Neural network

1 Introduction

The wireless network moves in a new segment of growth where more devices are connected and demand for sharing richer data is increasing with each passing day. The upsurge demand for frequency bands with increasing wireless services and applications leads to spectrum scarcity issue. Cognitive radio (CR) holds significance in the literature for spectrum underutilization problem by exploiting dynamic spectrum access (DSA) [1, 2].

In cognitive radio network (CRN), secondary users (SUs) which are unlicensed users are permissible to access the licensed frequency band if primary user (PU) is not using it. The SUs have to periodically check the availability of vacant spectrum band for the efficient functioning of this technology and if the band is found to be empty, SUs can use it. Further, they need to vacate the band as soon as they analyze the PU's activity in that particular frequency band. Thus, spectrum sensing (SS) is

R. R. Jaglan (✉) · R. Mustafa · S. Agrawal
Department of Electronics & Communication, UIET, Panjab University, Chandigarh, India
e-mail: reenarathee5@gmail.com

the utmost task in cognition cycle. Prolific SS techniques are discussed in the literature but energy detection (ED) has gained popularity due to its ease in implementation and no requirement for any prior information regarding PU [3].

However, SS reliability is enhanced in fading and shadowing conditions by cooperative spectrum sensing (CSS). Here, each SU searches for vacant spectrum band and observation of each SU contributes in inferring a final verdict about PU's existence/non-existence. Fusion rules discussed in the literature can broadly be categorized in three categories based on involvement of number of bits in making decision, i.e. soft, quantized, and hard. Involvement of multiple bits in sensing information contributes to soft fusion rules, e.g., equal gain combining (EGC), mean cumulative sum (MCS), and weighted gain combining (WGC). Involvement of two-bit sensing information contributes to quantized or soft–hard rule. This contributes to reduced reporting time and overhead. The third category involves one-bit sensing information, i.e., AND, OR, and majority (k-out-of-N) fusion schemes [4–7]. Considering these factors into account, we proposed a neural network-based fusion scheme which learns from its previous datasets. At fusion center, we used scaled conjugate back-propagation training algorithm. The prominent features of our proposed scheme are simplicity and computationally less complex.

Remaining paper is structured as follows: System model along with fusion schemes and the details of proposed scheme's algorithm are given in Sect. 2. Simulation results and analysis are clearly demonstrated in Sect. 3. The paper is concluded in Sect. 4 with remarkable comments.

2 System Model

We considered a CRN with centralized cooperative topology consisting of 'M' SUs, '1' PU, and a central entity, i.e., fusion center (FC) as shown in Fig. 1. SNR of each SU depends on its location with respect to base station, i.e., lesser the distance between these two entities, higher will be the SNR value or vice versa.

Each SU performs the sensing operation independently using any appropriate SS technique. It checks the status of PU activity in the licensed band using the following two hypotheses:

$$y_k = h_k m_k + n_k; \quad k \in \{1, 2 \ldots M\} : \quad H_1 \tag{1}$$

$$y_k = n_k; \quad k \in \{1, 2. \ldots . M\} : \quad H_0 \tag{2}$$

where y_k is the received signal at FC by kth SU, h_k is the channel gain, n_k is noise while m_k is transmitted PU signal. Here hypothesis H_1 corresponds to PU presence, while the alternative hypothesis depicts absence of PU in the licensed band.

Energy detector (local detector) detects the PU's status using energy or test statistics and sends their local decision of sensing to the central entity, i.e., FC for
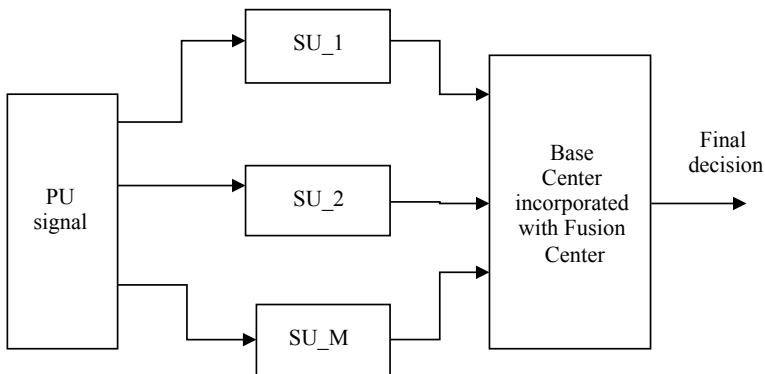
Fig. 1 System model

final decision making [8, 9]. The energy received by kth SU can be given by following test statistics:

$$E_k(Y) = \frac{1}{k}\sum_{m=1}^{M}(Y_k[n])^2 \tag{3}$$

where k (sample size) $= \tau f_s$, τ is sampling time while f_s is sampling frequency. The test statistics [10, 11] is compared with threshold (λ) concluding local sensing verdict (d_k).

Detection probability, i.e., probability of algorithm correctly determining the presence of PU in the licensed band under hypothesis H_1, can be mathematically formulated as:

$$P_d = \Pr\{d_k = H_1|H_1\} \tag{4}$$

$$P_d = \Pr\{E_k(Y) > \lambda|H_1\} \tag{5}$$

False alarm probability, i.e., probability of falsely determining the presence of PU under hypothesis H_0 when in actual PU is present. Mathematically, it can be formulated as:

$$P_f = \Pr\{d_k = H_1|H_0\} \tag{6}$$

$$P_f = \Pr\{E_k(Y) > \lambda|H_0\} \tag{7}$$

Missed detection probability, i.e., probability of algorithm falsely determining the PU's absence in the licensed band while in actual PU is present. It can be more clearly explained by the following mathematical expression:

$$P_{\mathrm{m}} = \Pr\{d_k = H_0|H_1\} \tag{8}$$

$$P_{\mathrm{m}} = \Pr\{E_k(Y) > \lambda|H_1\} \tag{9}$$

In CSS, individual decision made by each SU is reported to FC which combines or fuses all the received sensing information (based on implemented fusion rule) to conclude final verdict of decision regarding PU's status in the licensed band. Considering bandwidth efficiency, hard fusion rules are discussed and analyzed for decision-making task [12–14]. AND, OR, and majority rules can be articulated based on involvement of number of users for decision making at FC.

- AND: When all the users support hypothesis H_1, this rule indicates PU's presence otherwise absence. It can be mathematically formulated as:

$$\text{Decision (AND)} = \begin{cases} H1; & \text{if } \sum_{k=1}^{M} d_k = M \\ H0; & \text{if } \sum_{k=1}^{M} d_k < M \end{cases} \tag{10}$$

- OR: When any one user indicates PU's presence, this rule favors hypothesis H_1 otherwise H_0. It can be mathematically formulated as:

$$\text{Decision (OR)} = \begin{cases} H1; & \text{if } \sum_{k=1}^{M} d_k \geq 1 \\ H0; & \text{if } \sum_{k=1}^{M} d_k < 1 \end{cases} \tag{11}$$

- Majority: When the number of users supporting hypothesis $H1$ exceeds or is equal to half of the total decisions made, then this rule favors hypothesis H_1 otherwise H_0. Mathematically, it can be formulated as:

$$\text{Decision (Majority)} = \begin{cases} H1; & \text{if } \sum_{k=1}^{M} d_k \geq \frac{M}{2} \\ H0; & \text{if } \sum_{k=1}^{M} d_k < \frac{M}{2} \end{cases} \tag{12}$$

To make the system more effective, we introduced neural network at FC considering feed-forward network where each stratum of node receives data from former stratum for learning. The network is trained using neural pattern recognition classifying inputs into target categories, and the performance is evaluated based on confusion matrix. The neural network-based data fusion for CSS can be explained effectively by the following algorithm.

Algorithm: Neural Network-based Data Fusion for CSS model

Step 1: Calculate energy E_k at FC using Eq. (3).

Step 2: Compare with threshold λ to get one-bit sensing information.

Step 3: Steps 1 and 2 are repeated for M number of SUs which are involved in cooperative environment.

Step 4: Sensing information by each SU is transmitted to FC.

Step 5: Obtain training and target dataset from workspace.

Step 6: Select hidden layer's neuron (quantity) of patternet (pattern recognition neural network).

Step 7: Formulate decision-making algorithm using trainscg training algorithm.

Step 8: Randomly divide input datasets as training: 70%, validation: 15%, and testing: 15%.

Step 9: Evaluate performance using confusion matrix.

3 Result

We designed a CSS environment in MATLAB/Simulink considering $M = 15$ SUs, 1 PU. The SNR received at each SU depends upon its distance from the base station, i.e., larger the distance between them, lower will the received SNR or vice versa. Here, we considered SNR in the range of −20–10 dB. All simulations are carried out in MATLAB version 2015a. Table 1 demonstrates the significant parameters involved in the proposed neural network-based data fusion CSS model.

The performance of the system model is analyzed in terms of missed detection, false alarm, and accuracy. False alarm is an important parameter as any wrong information forwarded regarding PU can cause interference thus defoliating system performance. Ideally, false alarm should be close to 0. In Fig. 2 and Table 2, performance of proposed neural network (NN)-based scheme is compared with conventional fusion schemes.

Table 1 Network parameters involved in proposed algorithm

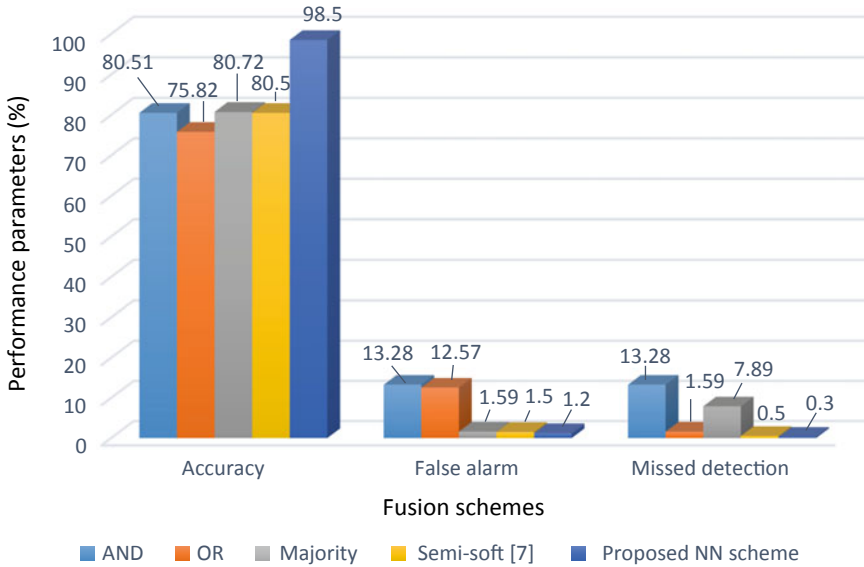| Parameters	Description
Network type	Feed-forward network
Training algorithm	Trainscg
Learning rate	0.01
Output neuron function	Softmax
Hidden layer function	Sigmoid
Number of hidden neurons	10
Modulation scheme	PSK

Fig. 2 Comparative performance analysis of proposed NN scheme

Table 2 Performance analysis of different fusion schemes

Performance evaluation parameters (%)	Fusion schemes				
	AND	OR	Majority	Semi-soft	Proposed NN scheme
Accuracy	80.51	75.82	80.72	80.59	98.5
False alarm	13.28	22.57	7.89	1.5	1.2
Missed detection	13.28	1.59	12.38	0.5	0.3

Figure 2 clearly shows that the accuracy of proposed NN scheme is increased by 22.68, 17.99, 17.78, and 18% when compared with conventional fusion schemes OR, AND, majority, and semi-soft [7] schemes, respectively.

Further, the proposed scheme shows a remarkable decrease in false alarm by 21.37, 12.08, 0.29, and 0.3%, while the decrease in missed detection is by 1.21, 12.98, 7.59, and 0.2% for OR, AND, majority, and semi-soft schemes, respectively. It is most desirable and holds great significance for CRN as reduced false alarm and missed detection with increased accuracy lead to overall system improvement.

We further tested the trained system model considering SNR values along with PU's status as input or test dataset. The SNR value is captured at the local decision-making process and stored in test dataset for further analysis.
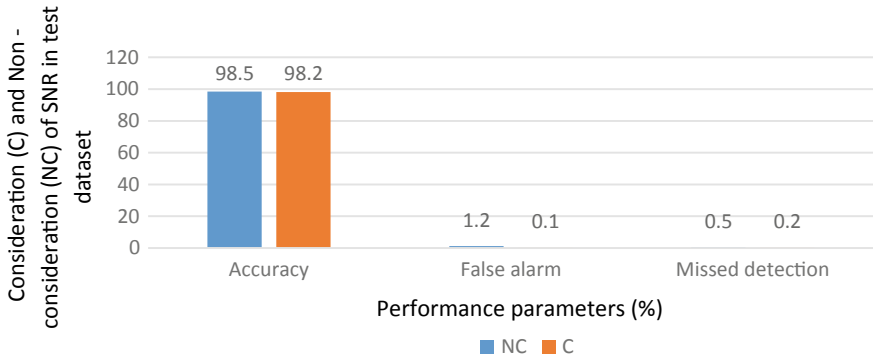
Fig. 3 Consideration and non-consideration of SNR in test dataset performance analysis

Figure 3 clearly demonstrates decline of 8.33% in false alarm when SNR along with local decision is apprehended in test dataset for further analysis, while the detection performance remains almost same. Hence, it can be clinched that SNR contemplation along with decision is one of the significant factors.

4 Conclusion

In CRN, PU activity is the utmost concern. In any case, PU's communication should not be disturbed. On arrival of PU in the licensed band, the SU has to immediately vacate the band and search for another vacant frequency band. The performance of the system is measured in terms of accuracy, false alarm, and missed detection. Achieving reduced false alarm and missed detection with improved detection performance achieves a remarkable importance in this field. It has been observed that the proposed NN scheme is increased by 22.68, 17.99, 17.78, and 18% when compared with conventional fusion schemes OR, AND, majority, and semi-soft [7] schemes, respectively. Further, the proposed scheme shows a remarkable decrease in false alarm by 21.37, 12.08, 0.29, and 0.3%, while the decrease in missed detection is by 1.21, 12.98, 7.59, and 0.2% for OR, AND, majority, and semi-soft schemes, respectively. This can be concluded that the proposed scheme outperforms the existing fusion schemes that are available in the literature. Thus, clinching SNR contemplation along with decision is one of the vital factors. The proposed scheme can further be tested considering more SUs among network.

References

1. Federal Communications Commission: Spectrum policy task force report (2002), pp 02–155
2. Mitola J, Maguire GQ (1999) Cognitive radio: making software radios more personal. IEEE Pers Commun 6:13–18
3. Garhwal A, Bhattacharya PP (2011) A survey on spectrum sensing techniques in cognitive radio. Int J Comput Sci Commun Netw 1:196–206
4. Bouraoui R, Besbes H (2016) Cooperative spectrum sensing for cognitive radio networks: fusion rules performance analysis. In: Proceedings IEEE conference on wireless communication & mobile computing (IWCMC), vol 1, pp 1–6
5. Lu Y, Wang D, Fattouche M (2016) Cooperative spectrum-sensing algorithm in cognitive radio by simultaneous sensing and BER measurements. EURASIP J Wirel Commun Netw 136:1–22
6. Farag HM, Mohamed EM (2017) Soft decision cooperative spectrum sensing with noise uncertainty reduction. Pervasive Mob Comput 35:146–164
7. Verma P, Singh B (2016) On the decision fusion for cooperative spectrum sensing in cognitive radio networks. Wireless Netw 16:1–10
8. Jaglan RR, Mustafa R, Sarowa S, Agrawal S (2016) Performance evaluation of energy detection based cooperative spectrum sensing in cognitive radio networks. In: Springer smart innovation, systems and technologies (SIST), vol 51, pp 585–593
9. Sriharipriya KC, Baskaran K (2014) Collaborative spectrum sensing of cognitive radio networks with simple and effective fusion scheme. Circ Syst Signal Process 33:2851–2865
10. Lavanis N, Jalihal D (2017) Performance of p-Norm detector in cognitive radio networks with cooperative spectrum sensing in presence of malicious users. Wireless Commun Mob Comput 17:1–8
11. Jaglan RR, Mustafa R, Agrawal S (2018) Scalable and robust ANN based cooperative spectrum sensing scheme for cognitive radio network. Wireless Pers Commun 99:1141–1157
12. Alkheir AA, Ibnkahla M (2016) A selective decision-fusion rule for cooperative spectrum sensing using energy detection. Wireless Commun Mob Comput 16:1603–1611
13. Chen X, Chen H-H, Meng W (2014) Cooperative communications for cognitive radio networks-from theory to applications. IEEE Commun Surv Tutorials 16:1180–1192
14. Kay SM (1998) Fundamentals of statistical signal processing: detection theory, vol 2. Prentice-Hall PTR

Novel Secured Image Scrambling Technique Using Chaotic Sequence Shuffling and Pixel Value Modification Through Random Grid Map and Its Performance Analysis

Rama Kishore Reddlapalli and Sunesh Malik

Abstract Images are scrambled generally for different purposes like information hiding and communicating data in secret manner so that even unauthenticated persons hack the data not be able to understand as it is not true data. A novel and secured image scrambling technique is being proposed here in which the original image values are shuffled through a specific chaotic sequence order which will act as key and pixel values which are also manipulated through created random grid map which acts as another key. Person with both correct keys can only unscramble the image to reveal the original image. This method is implemented on different bitmap and grayscale images. Performance of proposed algorithm is also done by performing certain tests and it is found to be proposed method which is giving very convincing, and scrambled image is not at all perceptible to the human eye.

Keywords Chaotic sequence shuffling · Random grid map · Image scrambling

1 Introduction

The rapid technological advancement has made the Internet an excellent application for transfer and processing of digital images because of its interesting features like fast, inexpensive, efficient, and easy to handle. With this, security and protection of digital images have become a challenging issue. In this context, different methods

R. K. Reddlapalli
USICT, Guru Gobind Singh Indraprastha University, Sector-16,
Dwarka, New Delhi, India
e-mail: ram_kish@yahoo.com

S. Malik (✉)
USICT,Guru Gobind Singh Indraprastha Uuniversity, Sector-16, Dwarka, India
e-mail: Suneshmlk@gmail.com

S. Malik
Maharaja Surajmal Institute of Technology, Janakpuri, New Delhi, India

were developed in the literature to deal with these problems. Digital image scrambling method seems one of the solutions for ensuring security of digital image. Digital image scrambling is an encryption method that can be utilized in different applications like preprocessing of watermark in watermarking and information hiding [1]. Digital image scrambling is a technique that reforms a new image from the original image by readjusting pixels of image in such a way that original image becomes unrecognizable, loses its meaning, and unsymmetrical.

In history, many scrambling algorithms were proposed by using different techniques in different manner [1–20]. Arnold transform and chaos sequence is one of the popular techniques used for achieving image scrambling. The techniques other than Arnold and chaos sequence used in implementation of image scrambling are random number, matrix transformation [18], Fibonacci series, chaotic map, R-Prime shuffle, and Hilbert curve. Arnold transform scheme is invertible without information loss and area preserving [18].

Another important technique used with scrambling is chaotic system. Chaotic system contains significant properties like aperiodic, sensitive dependence, system parameters, topological transitivity, and density of set of periodic points that offer new approaches in cryptography. The digital image scrambling scheme based on chaos can execute both grayscale substitution on image by means of chaotic key sequence and position permutation.

In this paper, a digital image scrambling method based on combination of chaos sequence and random grid is presented. Proposed method is highly secured as it requires two keys for unscrambling process. On the one hand, pixel positions are shuffled by using Key1. On the other hand, Key2 is used for modifying pixel values.

The rest of paper is organized as follows: Sect. 2 reviews image scrambling techniques reported in the literature. In Sect. 3, digital image scrambling and unscrambling methods are proposed. Security of proposed method is tested and analyzed in Sect. 4. Finally, Sect. 5 illustrates concluding remarks.

2   Related Work

This section reviews work stated to traditional digital image scrambling scheme in the literature. In history, concept of Arnold transform, baker transformation, Hilbert curve, magic transform, gray code transform, chaos, Fibonacci number, R-Prime shuffle, etc. are utilized for implementation of image scrambling scheme [1–15, 21, 22]. Here, some of scrambling schemes based on concept of Arnold transformation, chaos, Fibonacci numbers, and R-Prime shuffle are discussed [3–6, 13–15, 23].

In 2004, Zou et al. [15] introduced a new digital image scrambling scheme by exploiting concept of Fibonacci numbers. In this, the author also throws some light on uniformity and periodicity of scrambling information. In 2008, Qin et al. [3] proposed scrambling scheme based on random shuffling that scrambles non-equilateral image and builds coordinate shifting path with low cost, whereas

Sang et al. [13] reported block location scrambling method by deploying Arnold transformation and logistic map. Logistic map is used to generate sequence, and this sequence is utilized on different Arnold transformed blocks.

Concept of chaos is utilized by Liu et al., Wang et al., and Ye in [1, 5, 6]. In 2006, Ye also reported [6] image scrambling scheme that is drastically transforming statistical traits of original image through chaos map. Single chaos map is used once to implement scrambling. In 2011, Liu et al. [1] presented another image scrambling method based on space bit-plane and chaos by the way of shuffling the positions and modifying gray pixel values of image simultaneously. This scheme can be used for information hiding area. In this sequel, Wang et al. [5] also reported image scrambling scheme based on chaos sequence that scrambles and changes pixel values by means of decomposition and recombination of pixel values.

In 2014, Kekre et al. [14] presented digital image scrambling scheme by utilizing traits of R-Prime shuffle on different block size in image. Also, Kekre et al. [7] reported study of perfect shuffling for image scrambling method. In this, different factors are discussed like down-sampling effect, the effect of perfect shuffle with different factors of image size, and number of iteration required to get back original image which has a relation to the power of 2.

In 2015, Aziz et al. [4] proposed simple scrambling method by employing random number generation. In this scheme, image encryption is implemented by modifying the position of pixel in image without changing pixel value. Later, Waghulde et al. reported a brief review of digital image scrambling encryption techniques based on Arnold transformation, R-Prime shuffle, and random number generation [24].

On basis of above discussion, chaos sequence and random grid-based digital image scrambling method is proposed. Proposed image scrambling method utilizes chaos sequence for pixel position shuffling and random grid map for pixel value modification.

3 Proposed Scrambling Scheme

In this section, an image scrambling scheme based on double secured process is presented. This scrambling scheme utilizes concept of pixel position shuffling and pixel value modification. Pixel modification is achieved by means of random grid. The proposed scheme is given below steps.

3.1 Pixel Positions Shuffling Details

In pixel position shuffling concept, Input_vector elements are shuffled into shuffled_vector. This method of order will act as a Key1 and used while unscrambling the image. In this shuffle phenomenon, input image of size $[m1, m2]$

is converted into l-D vector of n elements. Then, shuffling is performed on these n elements. This shuffling process starts by reaching the center of the input vector and pick the elements, i.e., $n/2$th and $(n/2 + 1)$th and place them into the first and second element positions of the shuffled vector. After that pickup, the elements from the input vector immediate right and immediate left elements are placed as the next elements in the shuffled vector. This process is repeated till we reach the extreme ends (first and last elements) of the input vector. The process for one iteration is explained as below.

```
j = 1;
shuffled_vect (j) = input_vect((n/2));
j = j+1;
shuffled_vect (j) = input_vect((n/2) + 1);
j = j+1;
for i = 1:((n/2)-1)
temp = input_vect((((n/2) + 1)) + i);
shuffled_vect(j) = temp;
j = j+1;
temp = input_vect(((n/2))-i);
 shuffled_vect(j) = temp;
j = j+1;
end
```

3.2   Proposed Image Scrambling Method

Step1   Input: Read the input image and convert it into grayscale format.
Step2   Convert the image pixels in one-dimensional vector of n elements.
Step3   Pixel position shuffling: The pixels in the input array are shuffled using the method explained in Sect. 3.1 and converted again into two-dimensional array.
Step3   Chaotic random grid: Produce a chaotic random grid of the same size of input image.
Step4   Pixel modification: Modify the pixel values based on the created grid values which act as a key while unscrambling.
Step5   Scrambled image: Display the scrambled image.

The above steps can be repeated till degree of the scrambling is meeting the requirement.

3.3 Proposed Image Unscrambling Method

In unscrambling process, original input image is extracted. Unscrambling process almost follows reverse steps of image scrambling method. Detailed unscrambled process is as follows:

Step1 Input: Read the scrambled image.

Step2 Pixel modification: Using the Key2 that is the same chaotic grid two-dimensional array values remodify to get the original pixel values with shuffled order.

Step3 Pixel position shuffling: Convert them into one-dimensional vector of *n* elements. Reorder the element again into the original order using the same concept in reverse as explained in (Sect. 3.1) of pixel position shuffling details.

Step4 Conversion into 1D: Convert again into two-dimensional array of matrix from reordered one-dimensional vector.

Step5 Unscrambled image: Display the unscrambled image.

The above steps are repeated depending upon the number of times scrambling process is implemented.

4 Experimental Results

The proposed method is tested on different bitmap images as well as grayscale images. Experiments are performed on Core i5 processor, 4 GB RAM and MATLAB 113.a platform. In order to evaluate the performance of scrambling scheme, five measures are applied, i.e., BER(bit error rate), MSE (mean square error), time taken for scrambling and unscrambling, NPCR (number of pixels change rate), UACI (unified average changing intensity) and entropy. The proposed method is evaluated in terms of perception of the unscrambled image by measuring imperceptibility. Firstly, BER (bit error rate) and MSE (mean square error) values are calculated using unscrambled output image and the original image. Bit error rate can be defined as counts ratio of number of differing pixels between input and unscrambled images to total number of pixels in the image.

$$\text{BER} = \sum_{i=1}^{m1} \sum_{j=1}^{m2} \frac{\text{Io}(i,j) \neq \text{Is}(i,j)}{m1 * m2} \tag{1}$$

I_o is intensity of the original image, and I_s is intensity of the scrambled image [25].

MSE is computed which represents the cumulative squared error between original image and unscrambled image. Mean squared error is defined as follows:

$$\text{MSE} = \frac{\sum_{MN} \left[I_{1(m,n)} - I_2(m,n) \right]^2}{M * N} \tag{2}$$

here M and N are representing the size of the given input image, [25] $I(m, n)$ represents the pixel intensity at coordinate (i, j).

Secondly, number of pixels change rate (NPCR) test is conducted to measure the influence of one-pixel position change in the original and scrambled image using following formula [25]

$$\text{NPCR} = \sum_{i=1}^{m1} \sum_{j=1}^{m2} (D(i,j) * 100)/(m1 * m2) \tag{3}$$

$$\text{where } D(i,j) = \{D(i,j) = 0 \text{ if } I_o(i,j) == I_S(i,j)\} \tag{4}$$

I_o is intensity of the original image, and I_s is intensity of the scrambled image.

Thirdly, unified average changing intensity (UACI) test is also conducted to measure the average change in intensity between original and scrambled image and is calculated using following equation [25]

$$\text{UACI} = \sum_{i=1}^{m1} \sum_{j=1}^{m2} \frac{(I_o(i,j) - I_s(i,j) * 100)/(m1 * m2)}{255} \tag{5}$$

Lastly, entropy is evaluated. Entropy measures randomness statistically that can be used to depict the texture of the image. Entropy of the unscrambled image is measured to find the performance of the scrambling method.

$$\text{Entropy } H(x) = -\sum_{i=1}^{n} P(x_i)\log_2 P((x_i)) \tag{6}$$

where p is the normalized histogram counts obtained from image histogram [25]. Proposed algorithm is implemented on the input image for two iterations. Output
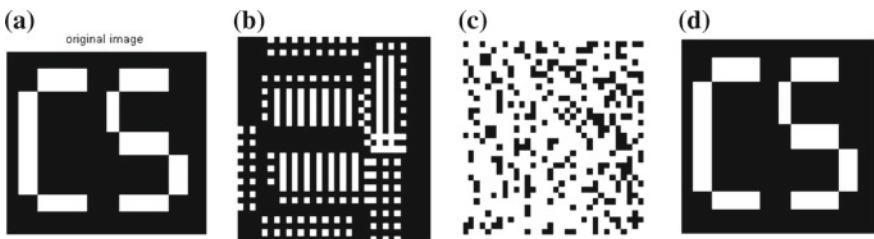

Fig. 1 **a** Original image of bitmap CS, **b** first-level scrambled image CS, **c** second level of scrambled image CS, and **d** unscrambled image of CS

results of the first-level scrambled image and second-level scrambled image are shown in the following Figs. 1, 2, 3, and 4.

The above figures show that first iteration of scrambling gives reasonable scrambling and second iteration gives scrambling image such that it is not at all revealing details of the original image. The method is also implemented on Lena, cameraman, baboon, and pepper grayscale images. The same is shown in Figs. 5, 6, 7, and 8.

Results of performance analysis of the proposed methods on different parameters are shown below in Table 1.
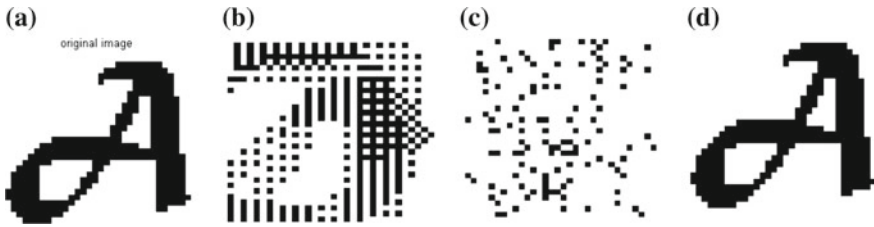
Fig. 2 **a** Original image of bitmap *A*, **b** first-level scrambled image *A*, **c** second level of scrambled image *A*, and **d** unscrambled image of *A*
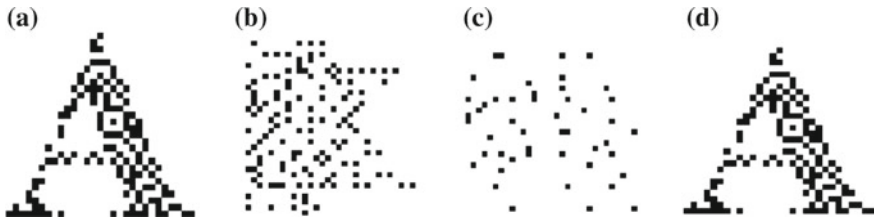
Fig. 3 **a** Original image of bitmap **A**, **b** first-level scrambled image **A**, **c** second level of scrambled image **A**, and **d** unscrambled image of **A**
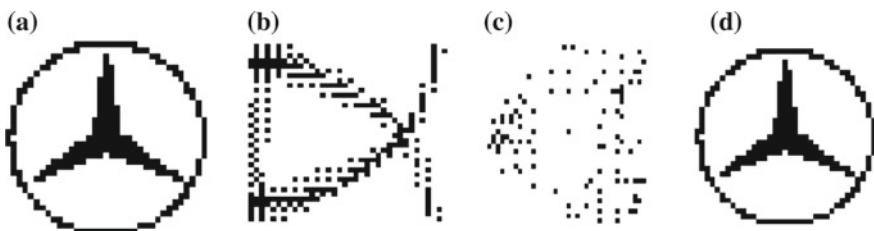
Fig. 4 **a** Original image of Bitmap **Logo**, **b** first-level scrambled image **Logo**, **c** second level of scrambled image **Logo**, and **d** unscrambled image of **Logo**

Fig. 5 **a** Original image of bitmap *Lena*, **b** first-level scrambled image *Lena*, **c** second level of scrambled image *Lena*, and **d** unscrambled image of *Lena*

Fig. 6 **a** Original image of bitmap *Cameraman*, **b** first-level scrambled image *Cameraman*, **c** second level of scrambled image *Cameraman*, and **d** unscrambled image of *Cameraman*

Fig. 7 **a** Original image of bitmap *Baboon*, **b** first-level scrambled image *Baboon*, **c** second level of scrambled image *Baboon*, and **d** unscrambled image of *Baboon*
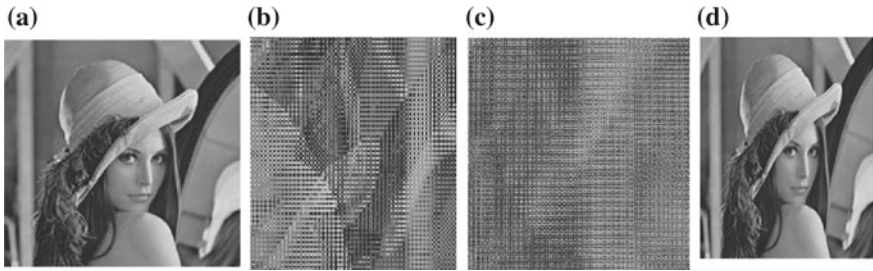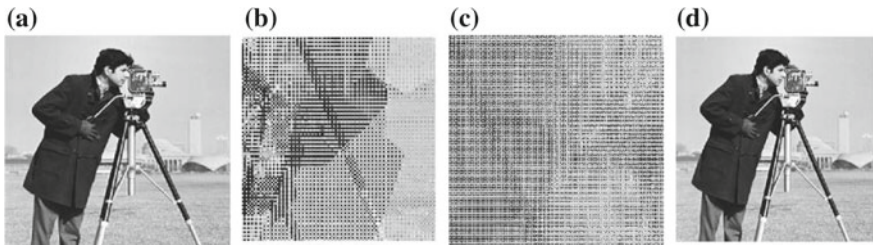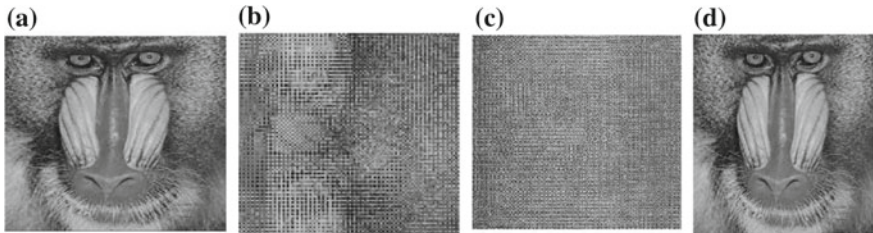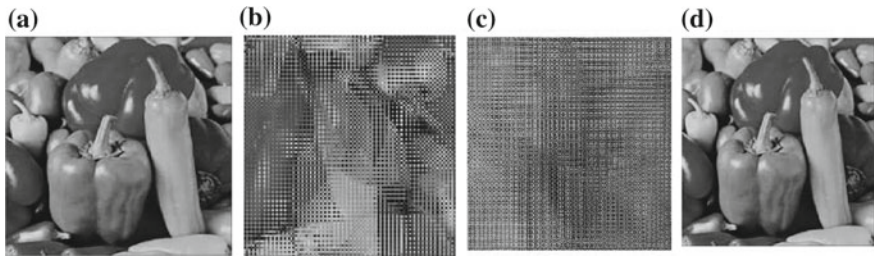
Fig. 8 **a** Original image of bitmap *Pepper*, **b** first-level scrambled image *Pepper*, **c** second level of scrambled image *Pepper*, and **d** unscrambled image of *Pepper*

Table 1 Performance analysis of the proposed method through different parameters

S. No.	Image	BER	MSE	Time taken for scrambling and unscrambling in (s)	NPCR	UACI	Entropy
1	Lena	8.3923×10^{-4}	0.1426	6.868	99.35	0	7.47
2	Cameraman	0.0223	4.914	6.608	98.95	0	7.159
3	Baboon	11.7166×10^{-4}	0.0312	6.614	99.24	0	7.3123
4	Pepper	5.798×10^{-4}	0.1233	6.313	99.46	0	7.6806

5 Conclusions

The performance analysis of the proposed technique is shown in Table 1 and found to be very convincing results in terms of being able to retrieve or unscramble the true image after the unscrambling process with very low MSE and BER values. BER values are almost nearer to zero. Entropy values are also almost in the range of 7.159–7.6806, and it is very nearer to theoretical limit of 8-bit plane image. This proves that probability of pixel values in the input image and scrambled image is very close. The proposed method is faster and powerful as the results are very convincing in the second iteration itself. The results show that proposed method is able to scramble the image in a faster and be able to hide the original information of input image successfully.

References

1. Liu R, Tian X (2011) A space-bit-plane scrambling algorithm for image based on chaos. J Multimedia 6:458–466
2. Han F, Hu J, Yu X (2006) A biometric encryption approach incorporating fingerprint indexing in key generation. In: International conference on intelligent computing, pp 342–351
3. Liping S, ZhengQ, Bo L, Jun Q, Huan L (2008) Image scrambling algorithm based on random shuffling strategy. In: 3rd IEEE conference on industrial electronics and applications, ICIEA 2008, pp 2278–2283

4. Aziz MM, Ahmed DR (2015) Simple image scrambling algorithm based on random numbers generation. Int J 5
5. Wang D, Chang C-C, Liu Y, Song G, Liu Y (2015) Digital image scrambling algorithm based on chaotic sequence and decomposition and recombination of pixel values. Int J Netw Secur 17:322–327
6. Ye G (2010) Image scrambling encryption algorithm of pixel bit based on chaos map. Pattern Recogn Lett 31:347–354
7. Kekre HB, Sarode T, Halarnkar PN (2014) Study of perfect shuffle for image scrambling. Int J Sci Res Publ 227
8. Li B, Xu J (2005) Period of arnold transformation and its application in image scrambling. J Central S Univ Technol 12:278–282
9. Lin X-H, Cai L-D (2004) Scrambling research of digital image based on Hilbert curve. Chin J Stereol Image Anal 9:224–227
10. Shen J, Jin X, Zhou C (2005) A color image encryption algorithm based on magic cube transformation and modular arithmetic operation. In: Pacific-Rim conference on multimedia, pp 270–280
11. Tang Z, Zhang X (2011) Secure image encryption without size limitation using Arnold transform and random strategies. J Multimedia 6:202–206
12. Wang D, Jin Y (2005) Semi-period of doubly even order magic square transformed digital image. J Zhejiang Univ Sci Ed 32:273
13. Shang Z, Ren H, Zhang J (2008) A block location scrambling algorithm of digital image based on Arnold transformation. In: The 9th international conference for young computer scientists, ICYCS 2008, pp 2942–2947
14. Kekre HB, Sarode T, Halarnkar P (2014) Image scrambling using r-prime shuffle on image and image blocks. Int J Adv Res Comput Commun Eng 3
15. Zou J, Ward RK, Qi D (2004) A new digital image scrambling method based on Fibonacci numbers. In: Proceedings of the 2004 international symposium on circuits and systems, ISCAS'04, pp III–965
16. Amin M, Faragallah OS, El-Latif AAA (2010) A chaotic block cipher algorithm for image cryptosystems. Commun Nonlinear Sci Numer Simul 15:3484–3497
17. El-Latif AAA, Li L, Wang N, Niu X (2011) Image encryption scheme of pixel bit based on combination of chaotic systems. In: 2011 seventh international conference on intelligent information hiding and multimedia signal processing (IIH-MSP), pp 369–373
18. Zhang S, Chen Y (2004) Digital image scrambling technology based on matrix transformation. J Fujian Normal Univ (Nat Sci Ed) 22:1–5
19. Wang Y, Wong K-W, Liao X, Chen G (2011) A new chaos-based fast image encryption algorithm. Appl Soft Comput 11:514–522
20. Yanling W (2009) Image scrambling method based on chaotic sequences and mapping. In: First international workshop on education technology and computer science, ETCS'09, pp 453–457
21. Ding W (2001) Digital image scrambling technology based on Arnold transformation. J Comput Aid Des Comput Graph 13:338–341
22. Zou W, Huang J, Zhou C (2010) Digital image scrambling technology based on two dimension Fibonacci transformation and its periodicity. In: 2010 international symposium on information science and engineering (ISISE), pp 415–418
23. Zhang H, Cai R (2010) Image encryption algorithm based on bit-plane scrambling and multiple chaotic systems combination. In: 2010 international conference on intelligent computing and integrated systems (ICISS), pp 113–117
24. Dhananjay Santosh Waghulde DPMM (2017) A review on digital image scrambling encryption techniques. Int J Res Appl Sci Eng Technol 5
25. Somaraj S, Hussain MA (2015) Performance and security analysis for image encryption using key image. Indian J Sci Technol 8

A Feature Fusion Method for Effective Face Recognition Under Variant Illumination and Noisy Conditions

Kapil Juneja and **Chhavi Rana**

Abstract Faces extracted in bad light are affected in terms of unequal contrast, noise, and variant illumination. These kinds of disruptions decrease the accuracy of facial authentication real and complex environments. In this paper, a feature fusion method is provided to achieve illumination-robust face recognition. In this model, the Gaussian filter and Gabor filters are applied on facial image to generate the illumination-variant features. Each of the Gaussian and Gabor face is processed by LBP filter to generate the effective visual description for face. A block-level feature fusion is applied on Gaussian-LBP and Gabor-LBP faces to generate the composite feature pattern. This most relevant and adaptive feature patterns are processed on SVM classifier to recognize the face accurately. The proposed feature fusion model is applied on illumination, noise, and contrast-variant sample sets of extended Yale databases. The comparative results against SVM, KNN, and ANN methods verified the significant gain in accuracy of facial identification in complex environmental conditions.

Keywords Face recognition · Complex environment · Illumination · Gabor · LBP · SVM

1 Introduction

Facial capturing in unconstraint [1, 2] environment affects the facial quality and disrupts the facial features. The common uncontrolled behavior identified in such environment is the lighting condition, fog or smog effect, camera quality, partial occlusion, etc. The lighting conditions are one such environmental feature that can affect the facial appearance and content information in different ways. The facial capturing can be done in natural light, artificial light, multi-light environment.

K. Juneja (✉) · C. Rana
Department of Computer Science and Engineering, University Institute of Engineering and Technology, Maharshi Dayanand University, Rohtak 124001, Haryana, India
e-mail: kapil.juneja81@gmail.com; kapil.juneja.1981@ieee.org

Table 1 Characterization of lighting on facial images

Properties	Description	Behavior impact
Source	The direction of camera, distance, orientation, number of sources	Intensity of lighting, degree of contrast, shadowing direction, mix light impact
Type of lighting	Natural light (sun, moon), artificial lighting (camera light, room light, strength of lighting)	Degree of brightness and contrast, noise
Location	Indoor or outdoor	Shadowing, lighting, and contrast issue
Time of capturing	Night capturing without specialized camera or fog or smog environment capturing	Noisy and content-disturbed capturing

The lighting behavior affects the facial information in diverse aspects and forms. The characterization of source, behavior, and impact of lighting is provided in Table 1.

The lighting source, conditions, and environmental factors affect the visibility of facial features. Various features [3–5] of lighting and environmental condition and its impact on facial features are provided in Table 1. The lighting or environmental variant constraints affect the facial images in terms of noise, unequal contrast, and illumination unbalancing. Other than these, the technical factors such as camera resolution, camera-man experience, and camera orientation also affect the quality of facial images. There is the requirement of some normalization methods at the preprocessing [6] stage to balance the image or extract the features that are not affected by the illumination or lighting behavior.

In this paper, a structural feature adaptive fusion model is recommended to improve the facial recognition in unconstraint conditions. The proposed model is adaptive to noise, contrast, and illumination variances. A composite feature fusion set is generated using Gabor-LBP and Gaussian-LBP faces. In this section, descriptive studies on various challenges in facial recognition system are described. The impact of illumination and noise disruption is also discussed in this chapter. In Sect. 2, various feature generation methods and face recognition methods are provided. In Sect. 3, the proposed composite-feature-fusion-based model is provided with integrated work stages. In Sect. 4, the comparative results obtained for each constraint situation are provided against different classifiers. In Sect. 5, the conclusion of this research work is provided.

2 Related Work

The facial capturing in extreme conditions affects its visual and information adaptive features. Researchers have provided the feature generator methods and classifiers to improve the facial recognition for noisy, illumination-variant, pose-variant, and expression-variant faces. A comparative study on region level and statistical modeling methods for facial recognition was provided by Smeets [7]. The feature evaluation and classification methods were explored by the author for class-specific matching.

Various feature descriptors were investigated by the researchers to improve the robustness against different environmental challenges. The textural, geometrical, region-specific, and point-specific features were generated and processed by the researchers. A geometric [8] tool was defined as a noise-robust feature descriptor. Author applied the kernel-specific convolutional analysis for adaptive subspace modeling of face. A normal facial point [9] evaluation with coordinate specification was provided to reduce the error rate to improve the facial recognition. Distance-level evaluation on feature points was provided to improve robustness of unconstraint face recognition. The shape [10] structural-map model was provided for dense mapping of pose-robust faces. The fiducial [11] points were generated as the landmark descriptors to achieve holistic facial recognition under constraint and unconstraint conditions. The pattern prior evaluation method was provided for misaligned and partial face recognition. The differential [12] facial components were extracted to recognize the degraded and illumination-variant faces accurately. The fusion-score-based evaluation was implied to achieve accuracy gain. The demographic [13] features were processed on role-based analysis to achieve higher accuracy in facial recognition. A comprehensive evaluation on photometric stereo [14] features were applied to recognize the pose-variant faces. The bur faces were identified accurately by generating the local phase pattern [15]. Author combined the Fourier transformation with local binary patterns (LBPs) to improve the effectiveness of facial recognition. Bonnen et al. [16] has provided an evidence-based component extraction method to obtain the structural alignment. The shape modeling was also included to match the individual misaligned components and to improve the overall facial recognition. The probabilistic Markov [17] model was applied to reconstruct the face to handle the pose-variant challenges. The normalized reconstructed face was propagated on Fourier wrapping to improve the recognition on gallery images.

The independent, compositional, and modified classification frameworks were also investigated by the researchers to generate adaptive facial mapping using distinct feature forms. A composition of principal component analysis (PCA) with linear regression [3] was provided to improve the facial recognition in illumination-variant conditions. A dictionary-[18] based recognition method with constraint adaptation was provided to match the pose- and light-variant faces. Lee et al. [12] has applied the hidden Markov model (HMM) with Adaboost-weighted approach for improving the facial feature classification. The distance-level mapping

algorithm was also integrated to recognize the faces with variant poses. A quantitative [18] measure for quality assessment was integrated with support vector machine (SVM), principal component analysis (PCA), and linear discriminant analysis (LDA) classifiers. The uncontrolled pose and illumination problem was addressed by the researcher through composite framework.

The facial occlusion is another real-time challenge that hides or disrupts the partial information of face images. The structural, selective, and adaptive feature measures were defined by the researchers to utilize the limited information for effective face recognition. The curve- and key-point-based saliency features were extracted by De Marsico [19] to recognize the partial faces. The Markov-integrated grammatical [20] model was provided to isolate the structural and spatial features to recognize the occluded faces.

3 Research Methodology

The environmental constraints such as bad light, multi-light, fog, and smog can affect the quality of facial image. In real-time facial recognition system, the quality of image affects the extracted features and increases the error rate in facial verification. In this paper, an illumination- and noise-robust method is provided to improve the accuracy of facial recognition. The feature fusion method is introduced in this work to generate the most relevant and decision-driven features. The main contribution of this research is to generate most adaptive and relevant feature set. To cover these real-time issues, a fusion persist model is provided in this research. At the earlier phase of this model, the high-level contrast and brightness balancing is done using histogram equalization. The block-based dynamic thresholding is combined to improve the effectiveness of histogram equalization. This rectified and normalized facial image is taken as input to the feature generation stage. In this feature fusion phase, the rectified facial image is divided in smaller blocks. The Gaussian filter and Gabor filter are applied at this stage to generate the illumination and contrast-robust features. These textural features are able to represent the particular block in terms of textural aspect. At earlier fusion level, the LBP filter is applied on Gaussian and Gabor faces to generate the effective Gaussian-LBP and Gabor-LBP features. At the second fusion level, the patterns of Gaussian-LBP and Gabor-LBP are fused together at block level to generate the composite feature pattern. The feature fusion model defined in this research is provided in Fig. 2. This composite fusion feature set is generated for both the training and test face images. This fusion features are later on processed under the SVM classifier to recognize the face accurately. In this section, each of the integrated stage with algorithmic method and procedural aspects are provided.
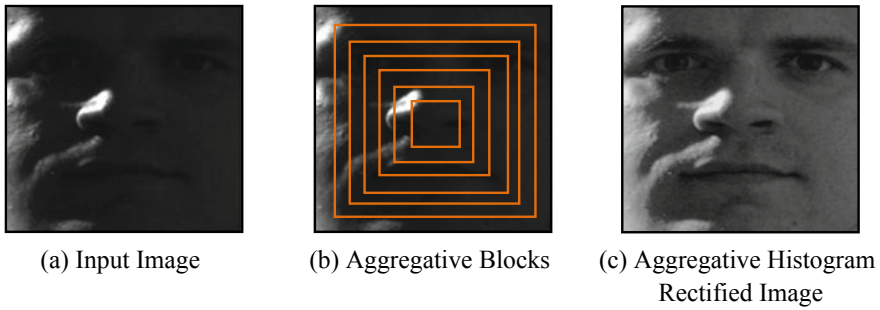
(a) Input Image	(b) Aggregative Blocks	(c) Aggregative Histogram Rectified Image

Fig. 1 Facial rectification

3.1 Facial Rectification

The facial acquisition in real environment also suffers from real-time challenges including unequal lighting, contrast and noise inclusion. Some high-level filter at preprocessing stage can be implied to repair the image against these quality issues. In this research, the dynamic threshold-controlled histogram equalization is applied on each aggregative and wider block. The average intensity ranges on these aggregative blocks are computed to control the histogram equalization. The histogram equalization is applied on each aggregative block. The aggregative-block-based histogram equalization results for facial normalization are provided in Fig. 1.

Figure 1a shows the sample image taken from extended Yale [21] database taken in bad light and affected by unequal brightness. Figure 1b shows the aggregative blocks generated over the image, and the histogram equalization is applied on each block. The dynamic threshold-controlled histogram has rectified the image effectively. Figure 1c shows the outcome of high-level rectification applied in the preprocessing stage on each input image to the system.
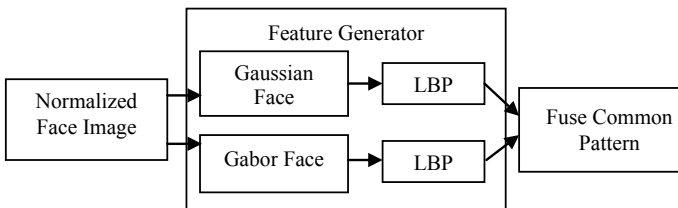

Fig. 2 Feature fusion model

3.2 Feature Fusion

The rectified and normalized facial image is processed by feature fusion model to extract the noise- and illumination-robust features. Figure 2 shows the proposed feature fusion model applied in this stage to extract more adaptive and relevant facial features. A three-stage collaborative task is defined in this stage to acquire the illumination- and noise-robust features. In first stage, the image is divided into smaller rectangular blocks of size 9×9. In this stage, the Gaussian and Gabor filters are applied to generate the corresponding noise and illumination-robust textural features.

The LBP is applied on illumination- and noise-robust feature faces. The LBP is able to handle the textural changes exist within the facial region. After applying the LBP filter, the Gabor-LBP, and Gaussian-LBP are obtained for each facial image. In third phase of this feature fusion model, the composition of these Gabor-LBP and Gaussian-LBP is done to identify the most relevant and problem-focused information pattern. This composite-fused feature pattern is processed by SVM classifier to recognize the face accurately. In this section, each of the feature descriptor and fusion method is explained with functional behavior.

3.2.1 Gaussian Face

The Gaussian filter is defined to smooth the face image by applying the mathematical filter. The convolutional filter with persistive structural exploration is applied to smooth the noisy region over the face image. Let $F(i, j)$ is the facial image which is processed by the Gaussian filter G; then, resultant Gaussian face (GF) image is obtained.

$$GF(i,j) = G * F(i,j) \tag{1}$$

The filter has performed intensity-driven evaluation to highlight the structural edge features. The directional gradient-based Sobel filter is applied to smooth the image and highlight the edges. x- and y-direction-based convolved mask defined in this work is given as

$$\text{Maskx} = \begin{bmatrix} -1 & 0 & 1 \\ -2 & 0 & 2 \\ -1 & 0 & 1 \end{bmatrix} \text{ and Masky} = \begin{bmatrix} 1 & 2 & 1 \\ -2 & 0 & 2 \\ -1 & -2 & -1 \end{bmatrix}$$

These masks are convolved on image blocks to smoothen the image by applying the directional filter. The structural persist Gaussian filter is provided in Eq. (2)

$$\mathrm{GFx}(i,j) = \mathrm{Maskx} * \mathrm{GF}(i,j) \text{ and } \mathrm{GFy}(i,j) = \mathrm{Masky} * \mathrm{GF}(i,j) \qquad (2)$$

The compositional filtered image obtained after directional filters is obtained using Eq. (3). The compositional block-processed GF is obtained from this composition

$$\mathrm{GF} = \sqrt{\mathrm{GFx}^2 + \mathrm{GFy}^2} \qquad (3)$$

The Gaussian face is dominant to noise and contrast unbalancing. This filtered face is later on processed by LBP filter to generate the fused feature pattern.

3.2.2 Gabor Face

The Gabor filter acquires the immense textural filter respective to intensity deviation and extracted at different orientations and frequencies. The spatial evaluation on adjacent pixels is performed by this filter to characterize the illumination-robust feature. It is the improved form of Gaussian function with frequency- and orientation-specific modulations. The illustration of Gabor mask is shown in Eq. (4)

$$\mathrm{GbMask}(x, y) = \exp\left(-\frac{x'^2 + \gamma^2 y'^2}{2\sigma^2}\right) \cos\left(2\pi \frac{x'}{\lambda} + \psi\right) \qquad (4)$$

where

$$x' = x \cos(\theta) + y \sin(\theta) \text{ and } y' = y \cos(\theta) + x \sin(\theta)$$

λ is wavelength of cosine vector
θ is orientation angle to perform the Gabor function
ψ is the phase offset in degree, γ is the spatial aspect ratio

The Gabor face is generated by applying the spatial frequency-driven mask on each block of facial image. The Gabor filter provided the localization-point-based solution to retain the structural information. The structural information is preserved under the computational efficiency analysis. In this work, the evaluation is performed at eight different orientations to obtain more adaptive and computed solution.

3.2.3 LBP Pattern Descriptor

The noise- and illumination-robust Gabor and Gaussian faces are generated at first level of this fusion model. The LBP filter is applied on Gaussian and Gabor faces to identify the most concerned features. The composition of Gaussian, Gabor, and LBP filter unifies the structural and statistical features to generate adaptive textural features. The LBP-adaptive feature descriptor is here applied to obtain the texture

information under information change analysis under computational efficiency. This thresholding is here applied based on feature adaptive analysis. This compositional feature form has evaluated the neighborhood features. This model is based on the central pixel analysis, and based on this analysis the computational feature is obtained under thresholding approach. This model is defined under high-intensity descriptor to obtain the effective intensity block pixel, so that the effective descriptor will be gained. The equation form of feature extraction is shown in Eq. (5)

$$\text{LBP pattern} = \sum_{i=1}^{N} \text{Face}(\text{px}_i - \text{px}_c)2^i \tag{5}$$

where face is either Gaussian face or Gabor face image

px   are the block pixels on which the pattern weight evaluation is performed
c is the center pixel of that block
i represents the other corresponding pixels available within block
N is the number of pixels within block

Based on this evaluation, the weights for Gaussian-LBP and Gabor-LBP are generated. The threshold-specific evaluation is provided in Eq. (6)

$$\text{LBP selected} = \begin{cases} 1, & \text{If } \text{px}_i - \text{px}_c \geq 0 \\ 0, & \text{otherwise} \end{cases} \tag{6}$$

Based on the evaluation, the effective-information-preserved Gabor-LBP and Gaussian-LBP are obtained. These pattern faces are finally processed on second-level fusion to generate the composite feature set. The algorithm to generate the feature fusion pattern is provided in next subsection.

3.2.4   Fusion Model

The first-level fusion has generated the Gaussian-LBP and Gabor-LBP to obtain the noise- and illumination-robust descriptors. In second-level fusion, these binary patterns are combined with relative weights. The common pattern blocks of both pattern-faces are defined with higher weights. The blocks that lie either within Gaussian-LBP or Gabor-LBP are assigned with lower weight. The OR operator is applied to generate the composite pattern. The Algorithm 1 has provided functional description of the two-level fusion model used in this research.

```
Algorithm 1: Algorithmic Model
FusionAlgorithm(FImg)
/*FImg is the normalized face image on which the fusion fea-
ture model is applied to generate the robust feature
pattern*/
Begin
```

1. Define the Block Size Respective to which the feature
   Extraction is performed.
2. NoofBlocks=Image.Size/BlockSize
   [Identify the Number of Blocks over the Image]
3. For i=1 to NoofBlocks
   [Get the Image Blocks from the image]
   Begin
4. Block=GetBlock(Image,i)
   [Get the Image block on which feature extraction and pro-
   cess will be done]
5. GF=GetGaussian(Block)
   [Generate the Gaussian Face for each image block]
6. G_LBP=GenerateLBPPattern(GF)
   [Generate Gaussian–LBP Pattern Face)
7. GbF=GetGabor(Block)
   [Generate the Gabor Face for each image block]
8. Gb_LBP=GenerateLBPPattern(GF)
   [Generate Gabor–LBP Pattern Face)
9. FuseFeaturePattern=HighWeightFuseFeature(G_LBP,
   Gb_LBP,AND)
   [Generate the composition and fused high weight feature
   pattern]
10. FuseFeaturePattern= FuseFeaturePattern   U
    LowWeightFuseFeature(G_LBP, Gb_LBP, OR)
    [Combine the low weight feature pattern to fuse feature
    pattern]
    End
    Return FuseFeaturePattern
    End

Algorithm 1 has provided the two-phase fusion model implied in this research to generate the illumination- and noise-robust feature pattern. To attain the features, the facial region is divided into smaller blocks of size 9×9. Each block is processed one by one, and the Gaussian and Gabor faces are generated for each block. The threshold constraint LBP filter is applied successively on Gabor and Gaussian faces. This first-phase fusion has generated the Gabor-LBP and Gaussian-LBP. In second fusion phase, the composition of these pattern faces is generated by applying the AND/OR operators. The higher weights are assigned to AND-acquired region and the lower weight to OR-acquired region. After this compositional stage, the most effective and decision-driven feature pattern is generated. The SVM classifier described in the next subsection is applied on this weighted pattern to recognize the face accurately.

3.3 SVM Classifier

SVM is the supervised model applied in this research on weighted fused feature pattern. SVM is integrated with polynomial function to recognize the test face image. SVM is also able to handle the variant feature values that occur because of noise or other behavioral disruptions. To apply the SVM classifier, a larger labeled set is trained with margin and weight specification. The feature space is analyzed by the nonlinear basis function to generate the decision rules. The non-stationary kernel applied in this work to generate the normalized and intelligent decision is provided in Eq. (7).

$$\text{Kernel}(x, z) = \left(\alpha x^{\mathrm{T}} z + c \right)^{d} \tag{7}$$

where c is constant, d is degree, and α is the slope vector.

The condition-controlled learning process is defined by this classifier to recognize the face accurately and effectively. The SVM classifier is applied under tenfold cross-validation on multiple sample sets infected by noise and unequal illumination. The results obtained on these sample sets are provided in the next section.

4 Results and Discussion

In this section, the experimentation results of proposed feature fusion model are provided on extended Yale dataset. To verify the robustness of proposed model, four different test sets are generated in each environmental condition of unbalanced illumination, contrast, and noise. Each of the test set is generated with 30, 50, 80, and 100 unconstraint face images. The comparative results are generated separately on each issue against Kth nearest neighbor (KNN), SVM, and artificial neural network (ANN).

The test sets are generated with variant lighting effects to verify the robustness of proposed model against illumination factor. Figure 3 has provided the analytical
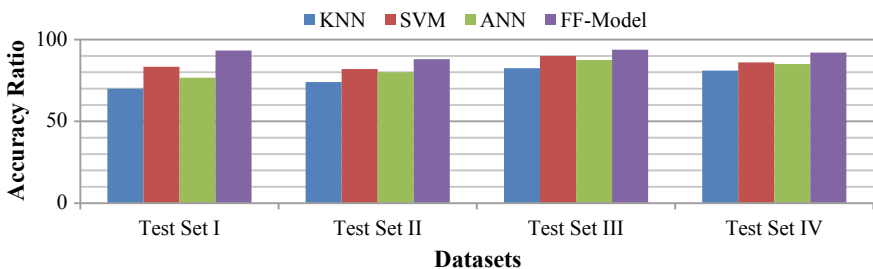

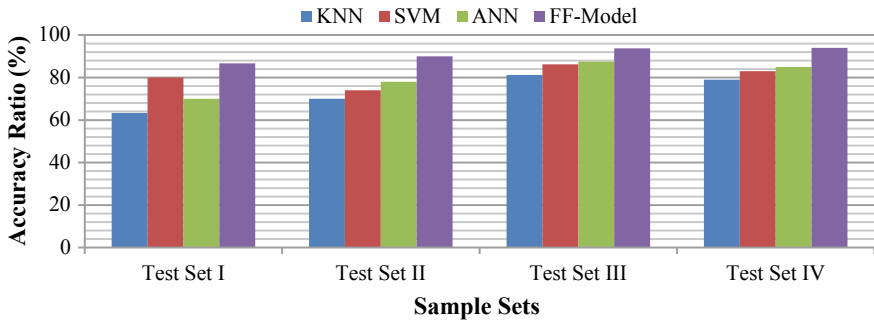**Fig. 3** Comparative evaluation (variant illumination)

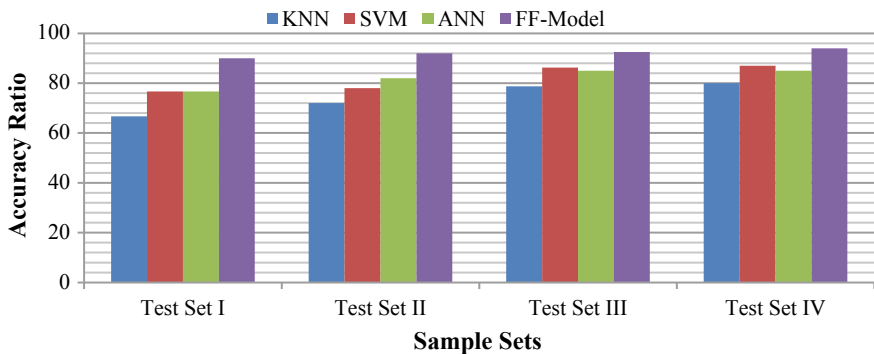**Fig. 4** Comparative analysis (variant contrast)

Fig. 5 Comparative analysis (random noise)

results for all four test sets. The observations identified that the proposed feature fusion model is more robust than existing approaches. For each dataset, the proposed model has achieved the significant enhancement in accuracy. The minimum accuracy achieved is 88% for test set II, and the maximum accuracy achieved by proposed model is 93.75%. Whereas, no existing method has gained the accuracy over 90%. Other challenges tackled in this proposed research are contrast and noise. The verification of the effectiveness of proposed feature fusion model is provided in Figs. 4 and 5.

Figure 4 has provided the evaluation of proposed feature fusion model in the existence of different levels of contrast. The contrast-variant test sets are processed by existing and proposed classification models. The comparative results identified that the proposed model achieved the minimum accuracy of 86.67% for the smaller sample set. As the size of test increased, the accuracy rate is improved and the highest accuracy of 94% is achieved for test set IV. Whereas, the maximum accuracy achieved by the existing ANN approach is 87.5%. All other existing methods also provided the lesser accuracy rate on different-samplesets of variant

size. The results ensure that the proposed model has achieved a significant improvement to recognize the contrast-variant faces.

Noise is another vector that disturbs the quality of facial image because of device or environment factors. The comparative observations shown in Fig. 5 identified that the proposed feature fusion model has achieved the higher accuracy rate of 94% for larger test set IV and the minimum accuracy rate achieved is 90%. The existing SVM classifier achieved the highest accuracy rate of 87% for test set IV. It identified that the proposed model is more robust against random noise and pixel-level disruptions.

5 Conclusion

The facial capturing in real time suffers from unbalanced illumination, contrast, and noise. The environmental, situational, and device-specific factors can affect the quality of face image. In this paper, a feature fusion model is provided to improve the face recognition against these real-time challenges. The Gaussian and Gabor faces are generated as the noise- and illumination-robust descriptors. The LBP filter is applied on these feature faces to acquire the information persist patterns. In the second phase of fusion, the composition of Gabor-LBP and Gaussian-LBP is done using AND/OR operators. This composite-fused feature pattern is finally trained on SVM classifier to recognize the face accurately. The proposed model is applied in noisy, contrast-variant, and illumination-variant sample sets of extended Yale dataset. The comparative results against SVM, KNN, and ANN classifiers have identified the effective gain in accuracy.

References

1. Juneja K (2017) A noise robust VDD composed PCA-LDA model for face recognition. In: International conference on information, communication and computing technology, pp 216–229
2. Juneja K (2016) MFAST processing model for occlusion and illumination invariant facial recognition. In: Advanced computing and communication technologies, pp 161–170
3. Huang S-M, Yang J-F (2012) Improved principal component regression for face recognition under illumination variations. IEEE Sig Process Lett 19(4):179–182
4. Juneja K (2017) Ring segmented and block analysis based multi-feature evaluation model for contrast balancing. In: International conference on information, communication and computing technology, pp 181–193
5. Juneja K (2017) Multiple feature descriptors based model for individual identification in group photos. J King Saud Univ Comput Inf Sci
6. Juneja K, Gill NS (2015) A hybrid mathematical model for face localization over multi-person images and videos. In: 2015 4th international conference on reliability, Infocom technologies and optimization (ICRITO) (trends and future directions), pp 1–6

7. Smeets DP (2012) A comparative study of 3-D face recognition under expression variations. IEEE Trans Syst Man Cybern Part C (Appl Rev) 42(5):710–727
8. Gopalan RS (2012) A blur-robust descriptor with applications to face recognition. IEEE Trans Pattern Anal Mach Intell 34(6):1220–1226
9. Mohammadzade H, Hatzinakos D (2013) Iterative closest normal point for 3D face recognition. IEEE Trans Pattern Anal Mach Intell 35(2):381–397
10. Ding LX (2012) Continuous pose normalization for pose-robust face recognition. IEEE Sig Process Lett 19(11):721–724
11. Liao SA (2013) Partial face recognition: alignment-free approach. IEEE Trans Pattern Anal Mach Intell 35(5):1193–1205
12. Lee P-H, Hsu G-S, Wang Y-W, Hung Y-P (2012) Subject-specific and pose-oriented facial features for face recognition across poses. IEEE Trans Syst Man Cybern Part B (Cybern) 42(5):1357–1368
13. Klare BF (2012) Face recognition performance: role of demographic information. IEEE Trans Inf Forensics Secur 7(6):1789–1801
14. Zafeiriou SG (2013) Face recognition and verification using photometric stereo: the photoface database and a comprehensive evaluation. IEEE Trans Inf Forensics Secur 8(1):121–135
15. Wang WW (2012) Recognition of blurred faces using local phase pattern. Electron Lett 48(20):1269–1271
16. Bonnen K, Klare BF, Jain AK (2013) Component-based representation in automated face recognition. IEEE Trans Inf Forensics Secur 8(1):239–253
17. Ho HT (2013) Pose-invariant face recognition using Markov random fields. IEEE Trans Image Process 22(4):1573–1584
18. Patel VM (2012) Dictionary-based face recognition under variable lighting and pose. IEEE Trans Inf Forensics Secur 7(3):954–965
19. De Marsico MM (2013) Robust face recognition for uncontrolled pose and illumination changes. IEEE Trans Syst Man Cybern Syst 43(1):149–163
20. Berretti SA (2013) Sparse matching of salient facial curves for recognition of 3-D faces with missing parts. IEEE Trans Inf Forensics Secur 8(2):374–389
21. Lee K-CJ (2005) Acquiring linear subspaces for face recognition under variable lighting. IEEE Trans Pattern Anal Mach Intell 27(5):684–698

Reduction of Discrete Systems Using Hybrid Method

Aswant Kumar Sharma and Dhanesh Kumar Sambariya

Abstract This paper contains the hybrid method for reduction of higher order. The proposed method uses the balanced truncation of time domain and mode selection method. The balanced truncation used for the reduction of numerator coefficient and the denominator part is reduced by the mode selection method. The obtained result is compared with the result available in the literature by using the step response characteristics as settling time, rise time, peak, peak time, settling max, and settling min of the system and response indices. The step response characteristics are compared with a reason that the reduced order must retain the important characteristics of the original order.

Keywords Discrete order reduction · Hybrid method · Balanced truncation · Mode selection method · Time domain · Response indices

1 Introduction

The order reduction of higher order is the mathematical and optimization technical area in the field of engineering, where the higher order of a model gets reduced with systematic mathematical procedures. The techniques applied in the continuous and discrete systems. The higher-order systems get reduced with time domain and frequency-domain methods to analyze and design the complex systems. For effortless simulation and designing lower-order controllers, reduced order minimizes computational work. The order reduction techniques have important property that obtained a reduced order to preserve important characteristics of the original order of the system. This manuscript used the mode selection method and balanced truncation method.

A. K. Sharma (✉) · D. K. Sambariya
Rajasthan Technical University, Akelgarh, Kota, India
e-mail: aswantksharma@gmail.com

D. K. Sambariya
e-mail: Dsambariya_2003@yahoo.com

In this paper, time domain methods are used to develop the hybrid method for the reduction. The numerator part is reduced order of the balanced truncation (BT) method. The BT introduced by Moore [1] for continues system reduction, where controllability and observability lead to a coordinate system in which the "internally balanced" model has special properties. The frequency-weighted balanced truncation obtains the stable lower order with the situation of weighted function located any in input or in output [2]. The parallel computing based on BT requires the calculation of Gramians of linear time invariant system given in [3]. The method of error bounds for BT linear time-varying discrete time system is obtained in [4]. The BT in discrete time bilinear system (DTBS) is with sufficient conditions for DTBS. Leading the bounded outputs for some bounded inputs the property of reach ability and observability Gramians by [5]. The denominator part in the proposed system is reduced by using the mode selection method (MSM). In MSM, the method is derived by using a consistent expansion of the crossing point displacement in terms of frequency-dependent small parameters. The reduced order is selected between the lower bound frequency and upper bound frequency [6].

The concept of mixed method combining the dominant eigenvalue and matrix continued fraction approach is available in [7]. The Pade method has the property that is applied in mixed method. However, if separately applied, it will mostly destabilize the system in the reduced form. The use of Pade method develops the mixed method and available in [8]. For linear multivariable systems, order reduction of a denominator is done by preserving the dynamic modes with dominant energy contributions, and numerators are found by using the continued fractions [9]. The large order is reduced in [10], where a combination of eigenvalue spectrum analysis for the denominator with Cauer second form for the numerator commented guarantees the stability of the obtained order.

The latest hybrid techniques applied in order reduction based on the soft computing. The big-bang, big-crunch optimization technique is used for the numerator part reduction, and the stability equation (SE) is used for the denominator part. The method proposed in [11] is for the linear continues single input and single output. The firefly algorithm with the SE is used in [12]. In another mixed method for order reduction in [13] where the Routh approximation is used for the reduction of denominator coefficients, upper part is reduced by Cuckoo Search.

This paper is well-planned and is divided into six sections; the first is of introduction. Section 2 is of the problem formulation, and Sect. 3 is of methodology applied, which is divided into two Subsects. 3.1 and 3.2 for the two types of methodology. The next section is followed by example for the proposed methods. The result of the example is discussed in Sect. 5 named as Discussion. The last section is of the Conclusion followed by the References.

2 Problem Formulations

Consider a discrete higher-order system of order η, and representation is as follows

$$G(z) = \frac{N(z)}{D(z)} = \frac{a_1 z^{\eta-1} + a_2 z^{\eta-2} + \cdots + a_n}{z^\eta + b_1 z^{\eta-1} + b_2 z^{\eta-2} + \cdots + b_n} \tag{1}$$

Here a_i and b_i are the constants for $i = 1, 2, 3, 4, 5, \ldots$.
The reduced order of the above system is represented as follows:

$$G_r(z) = \frac{N_r(z)}{D_r(z)} = \frac{g_1 z^{r-1} + g_2 z^{r-2} + \cdots + g_r}{z^r + h_1 z^{r-1} + h_2 z^{r-2} + \cdots + h_r} \tag{2}$$

Here g_r is the unknown constant of the reduced order in numerator part and is calculated by the BT, and h_r is the unknown constant of the denominator and is obtained by MSM.

3 Methodologies

The hybrid method is developed by using the balanced truncation and mode selection method. The methods are given in Subsects. 3.1 and 3.2.

3.1 Balanced Truncation Method

The two Lyapunov equations give the relation to the system matrices A, B and C for balanced realization is given in Eq. (3)

$$A \sum + \sum A^{\mathrm{T}} + BB^{\mathrm{T}} = 0$$
$$\sum A + A^{\mathrm{T}} \sum + CC^{\mathrm{T}} = 0 \tag{3}$$

Hence, $\sum = \mathrm{diag}[\rho_\iota]$ and $\rho_1 < \rho_2 < \rho_3 \cdots \rho_n$. The ρ_ι is well known as the Hankel singular values of the original system. Suppose $\mathbb{R}$ and $\mathbb{Q}$ are the controllability, and observe ability Gramians associated with an arbitrary minimal realization $[A, B, C]$ of the stable transfer function which is as follows in Eq. (4)

$$\mathbb{R} = U_C \mathbb{S}_C U_T$$
$$Q = U_O \mathbb{S}_O U_T \tag{4}$$

The $\mathbb{S}_O$ and $\mathbb{S}_c$ are diagonal matrices. The matrix given as in Eq. (5)

$$H = \mathbb{S}_0^{1/2} U_O^{\mathrm{T}} U_C \mathbb{S}_C^{1/2} \tag{5}$$

is constructed, and singular value decomposition is obtained from Eq. (6)

$$H = U_H \mathbb{S}_H V_H^{\mathrm{T}} \tag{6}$$

Using these matrices, the balancing transformation is given by Eq. (7)

$$T = U_O^{1/2} \mathbb{S}_O^{-1/2} U_H \mathbb{S}_H^{1/2} \tag{7}$$

The balanced realization is in Eq. (8)

$$\begin{bmatrix} A & B \\ C & D \end{bmatrix} = \begin{bmatrix} T^{-1}AT & T^{-1}B \\ TC & D \end{bmatrix} \tag{8}$$

Through the simple calculation obtained Eq. (9)

$$T^{\mathrm{T}} \mathbb{Q} T = T^{-1} \mathbb{R} (T^{\mathrm{T}})^{-1} = \mathbb{S}_H \tag{9}$$

Consider a stable system $G \in RH\infty$ available in Eq. (10)

$$G = \begin{bmatrix} \bar{A} & \bar{B} \\ \bar{C} & \bar{D} \end{bmatrix} \tag{10}$$

In balanced realization denoting the balanced Gramians by $\sum$, we have Eq. (11)

$$\bar{A} \sum + \sum \bar{A}* + \bar{B}\bar{B}* = 0$$
$$\sum \bar{A} + \bar{A}* \sum + \bar{C}*\bar{C} = 0 \tag{11}$$

Partition of the balanced Gramian as in Eq. (12)

$$\sum = \begin{bmatrix} \sum_1 & 0 \\ 0 & \sum_2 \end{bmatrix} \tag{12}$$

Partition of the system accordingly to Eq. (13)

$$G(z) = \begin{bmatrix} \begin{bmatrix} A_{11} & \overline{A_{12}} \\ \underline{A_{21}} & A_{22} \end{bmatrix} & B_1 \\ C_1 \quad C_2 & \boxed{D} \end{bmatrix} \tag{13}$$

The most energetic modes of the systems are in $\sum_1$ and the less energetic are in $\sum_2$. The system with $\sum_1$ is balanced Gramians would be a good approximation of

the original system. The procedure to obtain the reduced-order model would as follows:

(1) Obtain the balanced realization of the system.
(2) Choose appropriate reduced order.

The reduced-order model obtained is in Eq. (14)

$$G_r(z) = \begin{bmatrix} \bar{A}_{11} & \bar{B}_1 \\ C_1 & D \end{bmatrix} \tag{14}$$

The form of transfer function is available in Eq. (15)

$$G_r(z) = \frac{\mu_{12}z + \mu_{11}}{z^2 + \mu_{21}z + \mu_{22}} \tag{15}$$

3.2 Mode Selection Method

Considering a discrete time SISO system given in Eq. (16)

$$\dot{X} = Ax + Bu$$
$$y = Cx + D \tag{16}$$

Presume that $\chi_1, \chi_2, \chi_3, \dots, \chi_\eta$ are part, negative real eigenvalues and $\chi_1, \chi_2, \chi_3, \dots, \chi_\mu$ may be retained in the reduced-order model as given in Eq. (17)

$$y = CKT = \sum_{int=1}^{\eta} \frac{Er_{int}c_{int}}{\chi_{int}}[e^{\chi_{int}t} - 1] \tag{17}$$

K represents the model matrix of the reduced system T denote the transformed matrix $(X = KT)Er_{int}$ Element of row vector $Er = CK c_{int}$ Elements of column vector $c = K^{-1}B$. The reduced-order model can be obtained as represented in the Eq. (18)

$$Z_1 = (F^{\Upsilon_1 t} - I)\Upsilon_1^{-1}N_1$$
$$Z_2 = -\Upsilon_2^{-1}N_2 \tag{18}$$

Using $y = CX = CKT, \bar{y}$, the output of the reduced model is represented in Eq. (19)

$$\bar{y} = \sum_{int=1}^{o} \frac{Er_{int}c_{int}}{\chi_{int}}[e^{\chi_{int}t} - 1] - \sum_{int=o+1}^{n} \frac{Er_{int}c_{int}}{\chi_{int}} \tag{19}$$

The reduced order in second-order from is available in Eq. (20)

$$A_{2r} = \begin{bmatrix} a_{11} & a_{12} \\ a_{21} & a_{22} \end{bmatrix}, \ B_{2r} = \begin{bmatrix} b_{11} \\ b_{21} \end{bmatrix}, \ C_{2r} = \begin{bmatrix} c_{11} & c_{12} \end{bmatrix}, \ D_r = \begin{bmatrix} 0 \end{bmatrix}$$

By applying the state space to transfer function technique, the obtained reduced transfer function in discrete form is given as in Eq. (20)

$$R_{2byMSM} = \frac{\eta_{21} + \eta_{22}z}{1 + \lambda_{11}z + \lambda_{12}z^2} \tag{20}$$

The hybrid method obtained is given in Eq. (21)

$$G_{rhm}(s) \frac{\mu_{12}z + \mu_{11}}{1 + \lambda_{11}z + \lambda_{12}z^2} \tag{21}$$

4 Higher-Order System Reductions

4.1 Example 1

Consider a discrete system higher-order transfer function from [14]

$$G_8(z) = \frac{\begin{array}{l} 0.4209z^7 + 0.2793z^6 - 0.0526z^5 + 0.038z^4 \\ -0.1291z^3 - 0.0656z^2 - 0.011z - 0.0015 \end{array}}{\begin{array}{l} z^8 - 0.4209z^7 - 0.2793z^6 + 0.0526z^5 - 0.038z^4 \\ + 0.1291z^3 + 0.0656z^2 - 0.011z + 0.0015 \end{array}} \tag{22}$$

Discrete time state-space model of the chosen transfer function is in Eq. (23)

$$A_{EX1} = \begin{bmatrix} 0.4209 & 0.2793 & -0.0526 & 0.0380 & -0.1291 & -0.0656 & 0.0110 & -0.0015 \\ 1.0000 & 0 & 0 & 0 & 0 & 00 & 0 & 0 \\ 0 & 1.0000 & 0 & 0 & 0 & 0 & 0 & 0 \\ 0 & 0 & 1.0000 & 0 & 0 & 0 & 0 & 0 \\ 0 & 0 & 0 & 1.0000 & 0 & 0 & 0 & 0 \\ 0 & 0 & 0 & 0 & 1.0000 & 0 & 0 & 0 \\ 0 & 0 & 0 & 0 & 0 & 1.0000 & 0 & 0 \\ 0 & 0 & 0 & 0 & 0 & 0 & 0 & 0 \end{bmatrix} \tag{23}$$

$$B_{EX1} = \begin{bmatrix} 1 & 0 & 0 & 0 & 0 & 0 & 0 & 0 \end{bmatrix}^T$$
$$C_{EX1} = \begin{bmatrix} 0.4209 & 0.2793 & -0.0526 & 0.0380 & -0.1291 & -0.0656 & -0.0110 & -0.0015 \end{bmatrix}$$
$$D_{EX1} = \begin{bmatrix} 0 \end{bmatrix}$$

The reduced order obtained from balanced truncation method is in Eq. (24)

$$A_{\mathrm{BTr}} = \begin{bmatrix} 0.7551 & 0.2191 \\ -0.4291 & 0.7474 \end{bmatrix}, \ B_{\mathrm{BTr}} = \begin{bmatrix} -0.8465 \\ -0.2698 \end{bmatrix},$$
$$C_{\mathrm{BTr}} = \begin{bmatrix} -0.6987 & -0.1437 \end{bmatrix}, \ D_{\mathrm{BTr}} = [0] \tag{24}$$

The second-order transfer function obtained from the discrete state-space values is as follows in Eq. (25)

$$G_{\mathrm{BTr}}(z) = \frac{0.6302z - 0.4822}{z^2 - 1.503z + 0.6584} \tag{25}$$

The reduced order obtained from the mode selection method in state-space form is as follows in Eq. (26)

$$A_{\mathrm{MSMr}} = \begin{bmatrix} 0.7512 & -0.219 \\ 0.4297 & 0.7572 \end{bmatrix}, \ B_{\mathrm{MSMr}} = \begin{bmatrix} 0.8513 \\ -0.2541 \end{bmatrix}$$
$$C_{\mathrm{MSMr}} = \begin{bmatrix} -0.6989 & -0.001498 \end{bmatrix}, \ D_{\mathrm{MSMr}} = [0] \tag{26}$$

The obtained reduced transfer function from reduced state-space form is as follows in Eq. (27)

$$G_{\mathrm{MSMr}}(z) = \frac{0.5954z - 0.4125}{z^2 - 1.508z + 0.6629} \tag{27}$$

The hybrid method is combination of balanced truncation numerator and mode selection method denominator given as in Eq. (28)

$$G_{\mathrm{rHybrid}}(z) = \frac{0.6302z - 0.4822}{z^2 - 1.508z + 0.6629} \tag{28}$$

The step response in the Fig. 1 clearly shows the proposed second order is following the important characteristics of the original system. The proposed system is indicated in red-dotted line following the original system indicated in blue. The rise time, settling min, and peak with comparison are shown in Table 1.

The response indices Integral Square Error (ISE), Integral Absolute Error (IAE), and Integral Time Absolute Error (ITAE) are given as

Integral Square Error (ISE) is given in Eq. (29)

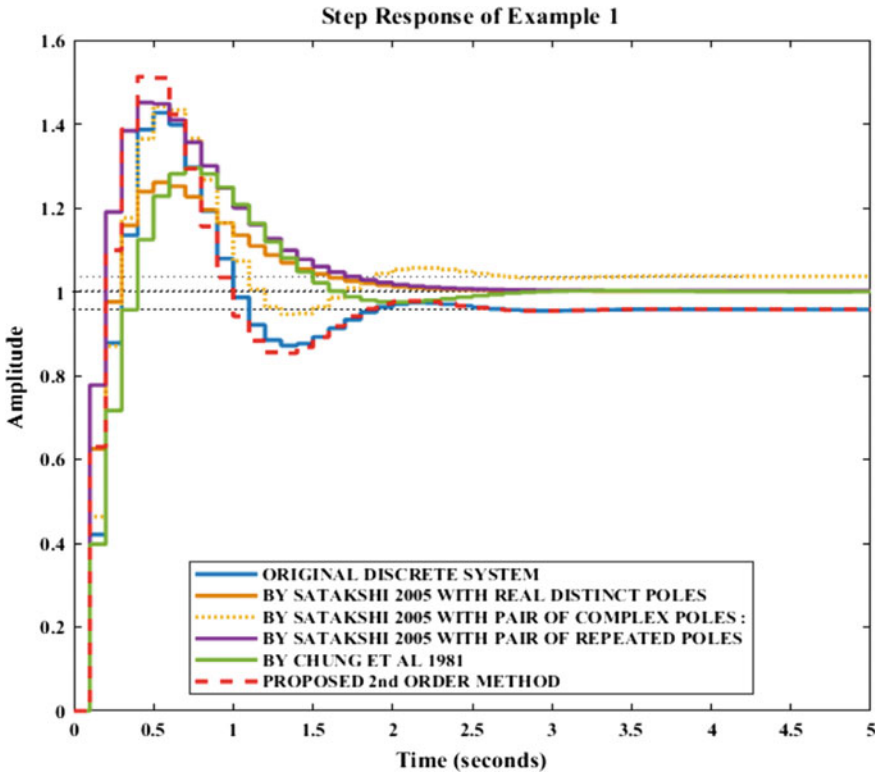$$\mathrm{ISE} = \int_{0}^{\infty} [G_c(t) - G_{cr}(t)]^2 \mathrm{d}t \tag{29}$$

Fig. 1 Step response of the Example 1 proposed second order with original discrete system and second order from the literature

Table 1 Step response characteristics of the proposed system with original and second order from literature

Sr. No.	Model	Rise time	Settling min	Peak time
1	Original	0.1000	0.8714	0.5000
2	Proposed	0.1000	0.8530	0.400
3	Satakshi [14]	0.1000	0.9759	0.5000
4	Satakshi [14]	0.2000	0.9461	0.5000
5	Satakshi [14]	0.10000	1.0024	0.4000
6	Chung [15]	0.2000	0.9566	0.7000

Integral Absolute Error (IAE) is given in Eq. (30)

$$IAE = \int_0^\infty |G_c(t) - G_{cr}(t)| \, dt \tag{30}$$

Table 2 Response indices of the proposed with the methods from the literature

Sr. No.	Model	ITAE	IAE	ISE
1	Proposed	0.3354	0.2508	0.0378
2	Satakshi [14]	2.793	0.7268	0.08249
3	Satakshi [14]	3.892	0.7096	0.05448
4	Satakshi [14]	3.308	0.871	0.1427
5	Chung [15]	2.638	0.7389	0.1051

Integral Time Absolute Error (ITAE) is given in Eq. (31)

$$\text{ITAE} = \int_0^\infty t \cdot |G_c(t) - G_{cr}(t)| \mathrm{d}t \tag{31}$$

In response indices, Eqs. (29)–(31) $G_c(t)$ is the step response of the higher order and $G_{cr}(t)$ is the response of the lower order.

The obtained ITAE, IAE, and ISE are given in Table 2 on next page. The comparative analysis of the obtained second order proposed is done with the other second order available in the literature.

5 Discussions

The proposed order rise time is 0.1, and settling min is 0.8530 with peak time 0.400. The comparison of the step response characteristics of original system represented in Ex 1 and the reduced order system form literature Satakshi [14] with real, distinct poles is on the sr. no. 2, with a pair of complex poles is in sr. no. 3, repeated poles is in sr. no. 4 and 5 Chung et al [15] is on sr. no. 6 in Table 1. The response indices available in Table 2 of the proposed system are ITAE 0.3354, IAE 0.2508, and ISE 0.0378.

6 Conclusions

The mixed method obtained from balanced truncation as the numerator part and mode selection method as the denominator part leads to a good result in the discrete system. The comparative step response characteristics of the proposed are in Table 1, and response indices available in Table 2 clearly indicates that the results are better than the result available in the literature for the same discrete higher-order system.

References

1. Moore B (1981) Principal component analysis in linear systems: controllability, observability, and model reduction. IEEE Trans Autom Control 26:17–32
2. Zhou K, Zheng Y, Lu T (1993) Stability and error bounds for discrete time frequency weighted balanced truncation. In: Proceedings of 32nd IEEE conference on decision and control, vol 2923, 15–17 Dec 1993, pp 2927–2928
3. Benner P, Quintana-Ortí ES, Quintana-Ortí G (2000) Balanced truncation model reduction of large-scale dense systems on parallel computers. Math Comput Model Dyn Syst 6:383–405
4. Sandberg H, Rantzer A (2002) Error bounds for balanced truncation of linear time-varying systems. In: Proceedings of the 41st IEEE conference on decision and control, vol 2893, 10–13 Dec 2002, pp 2892–2897
5. Zhang L, Lam J, Huang B, Yang G-H (2003) On gramians and balanced truncation of discrete-time bilinear systems. Int J Control 76:414–427
6. Kim SM, Kim J-G, Park KC, Chae S-W (2018) A component mode selection method based on a consistent perturbation expansion of interface displacement. Comput Methods Appl Mech Eng 330:578–597
7. Shieh L, Wei Y (1975) A mixed method for multivariable system reduction. IEEE Trans Autom Control 20:429–432
8. Shamash Y (1978) Mixed method for reducing discrete-time multivariable systems. Int J Syst Sci 9:237–239
9. Liaw CM (1989) Mixed method of model reduction for linear multivariable systems. Int J Syst Sci 20:2029–2041
10. Parmar G, Prasad R, Mukherjee S (2007) A mixed method for large-scale systems modelling using eigen spectrum analysis and Cauer second form. IETE J Res 53:93–102
11. Desai S, Prasad R (2013) A new approach to order reduction using stability equation and big bang big crunch optimization. Syst Sci Control Eng Open Access J 1:20–27
12. Sambariya D, Arvind G (2016) Reduced order modelling of SMIB power system using stability equation method and firefly algorithm. In: 2016 IEEE 6th international conference on power systems (ICPS), IEEE, pp 1–6
13. Sambariya D, Sharma O (2016) Model order reduction using Routh approximation and cuckoo search algorithm. J Autom Control 4:1–9
14. Satakshi, Mukherjee S, Mittal RC (2005) Order reduction of linear discrete systems using a genetic algorithm. Appl Math Model 29:565–578
15. Chung CG, Han KW, Yeh HH (1981) Simplification and identification of discrete transfer function via step-response matching. J Franklin Inst 311:231–241

Analysis of the Effect of Bias Current on the Performance of MOS Current-Mode Logic Circuits

Antriksh Sharma and Dileep Dwivedi

Abstract This paper highlights the effect of the constant current source employed in the MOS current-mode logic. This bias current plays a significant role in the functionality of MCML circuits as it gets steered to the different branches present in the circuit. In addition to the variations in the power dissipation and delay generated, this paper also investigates the changes in the swing of the output voltage as the tail current is varied. Simulations are performed for three current values, namely 10 µA, 10 nA, and 10 pA, and their effect on numerous parameters has been discussed. A comparison between CMOS and MCML inverters for these different current values proves the efficiency of MCML at high supply voltages.

Keywords MCML · CMOS · Current source · Voltage swing

1 Introduction

The traditional CMOS technology is now witnessing an alternative in the form of MOS current-mode logic. Its differential nature provides significant merits to its topology. Primarily, a differential behavior supports high noise immunity especially to common-mode noise. It is elaborated in the literature that a common-mode rejection ratio (CMRR) of 20 is appropriate for the desired MCML operation [1]. The complementary type of inputs and outputs also results in protection against inductive and capacitive glitches that get induced in the circuit. Secondly, the effective voltage swing which has a fundamental association with noise margin improves because of the differential signaling. This enhancement observed in noise margin and noise immunity sets a trade-off between noise margin and voltage

A. Sharma (✉) · D. Dwivedi
Guru Gobind Singh Indraprastha University, Sector 16 C,
Dwarka 110078, Delhi, India
e-mail: antrikshsharma05@gmail.com

D. Dwivedi
e-mail: dileep.gcet@gmail.com

swing. A better voltage swing can be accomplished at the expense of poor noise margin. Conversely, an upgraded noise margin can be attained by decrementing the voltage swing. A direct relation exists between delay and voltage swing. A low output voltage swing yields an enhanced delay according to the following equation:

$$D = \frac{C\Delta V}{I_{ss}}.$$

(1.1)

where C is the capacitance seen at the output, ΔV is the voltage swing, and I_{ss} is the constant current provided by the tail current source. The sudden and extreme change of current traversing the supply lines forms a critical source of switching noise. However, the provision of a steady-state current in MCML gates, regardless of the switching activity, can be attributed to the presence of a current sink which ensures that MCML can be operated efficiently in mixed-signal applications. Thus, MCML provides numerous features such as high noise immunity because of its differential nature, low output voltage swing, a constant power dissipation due to the usage of a constant current source, and the need to include a reference voltage for biasing the current source device [2]. Many contradictions and trade-offs have been encountered while designing the MCML circuits. Firstly, on increasing the load resistance, there is an increase in the required chip area as well as the propagation delay. However, the voltage swing obtained at the output also increases along with the voltage gain. The noise immunity of the circuit also improves. Secondly, more area and power are required when the size of the MOS tail current source device is increased. However, this also leads to a decrease in the high-to-low propagation delay and an increase in the voltage swing. Thirdly, the area is increased on increasing the size of either of the two input transistors. But, this also lowers the high-to-low propagation delay and increases the voltage gain. Lastly, on increasing the biasing voltage of the MOS tail current source, an increase in the tail current is also observed. However, this leads to an elevation in the power consumed as well as a reduction in the headroom of the input voltage. Moreover, the design of an MCML circuit is a complex and challenging problem. The design time required is very long, leading to a further increase in the total design cost [3]. It appears that the most crucial merit of MOS current-mode logic tends to be its worst demerit. The noiseless operation of MCML because of the static DC current also compels the gate to leak excess power even in an idle condition. On the other hand, this static power acts as the only source of power dissipation in MCML gates and can be expressed as:

$$P_{MCML} = I_{SS} \times V_{DD}.$$

(1.2)

Static power in CMOS is dissipated because of charge leakage, while the dynamic power dissipation occurs due to switching events. During such events, the output load capacitance gets alternatively charged and discharged and hence power is inevitably dissipated by CMOS. This static leakage acts as a hindrance when the

feature sizes tend to diminish. The expression for dynamic power dissipation in CMOS is obtained as:

$$P_{\text{CMOS}} = \alpha f_c C_L V_{\text{DD}}^2 \tag{1.3}$$

where α is the switching activity, f_c is the clock frequency, and C_L is the capacitance seen at the output node [4]. Thus, a direct relation can be seen between power dissipation and frequency of operation. The literature shows that the frequency at which MCML gates dissipate less power than their CMOS counterparts lies in the GHz range. It is reported in [5] that at a frequency of 300 MHz, the MCML implementation of a pipelined CORDIC DSP unit shows 30% less power dissipation than its CMOS counterpart implementation. Thus, power dissipation can be minimized significantly by designing the MCML gates properly.

2 Effect of Bias Current

The effect of bias current on power dissipation, delay, voltage drop, and voltage swing obtained by an MCML inverter when a constant current source is applied is displayed in Table 1. The current in the circuit is varied by changing the value of the current source. A current variation of 10–100 µA is performed. It is seen that as the current is increased, the power dissipation as well as the delay rises. At low current values such as those of 10 µA, the voltage drop is extremely high (around 968.1 mV) resulting in poor output swing (31.98 mV only), whereas at larger current values such as 100 µA, the voltage swing improves (788.21 mV) considerably leading to a decrement in the voltage drop (210.27 mV). Since an ideal MCML circuit operates as a perfect current switch by steering the entire current generated by the tail current source through the ON branch. However, in reality, some portion of current I traverses the OFF branch. This diminishes the output

Table 1 MCML parameter variation at different current source

Current (µA)	Power (µW)	Delay (ns)	Voltage drop (mV)	Output swing (mV)
10	10.00347	5.3646	968.10	31.98
20	20.00362	5.3823	942.52	57.56
30	30.00390	5.3854	918.54	81.54
40	40.00415	5.3864	884.97	115.11
50	50.00443	5.3870	852.99	147.09
60	60.00520	5.4500	813.02	187.06
70	70.00506	5.4811	741.08	259.01
80	79.99970	5.4856	614.77	385.31
90	89.99934	5.4863	432.51	567.57
100	99.98086	5.5445	210.27	788.21

voltage swing of the circuit. Thus, higher the current applied, higher will be the voltage swing and more the voltage swing, more will be the delay generated as presented in Eq. (1.1).

Figure 1 illustrates that as the current is increased from 10 to 100 µA, the drop in voltage continuously diminishes from 968.1 to 210.27 mV while the output swing keeps on increasing from 31.98 to 788.21 mV. Thus, MCML circuits work well at higher values of current provided by a constant current source. The power dissipated by the MCML inverter is directly proportional to the current supplied via the current source as shown in Fig. 2. As the amount of current is incremented, the
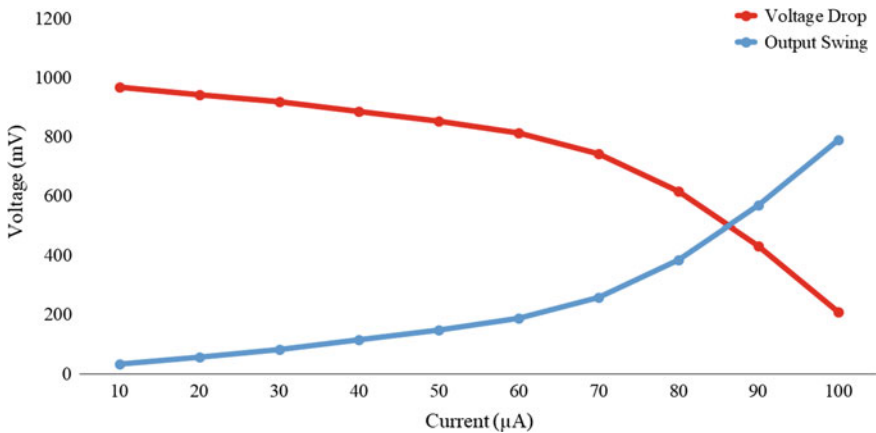
Fig. 1 Variation of MCML voltage drop and voltage swing with current source
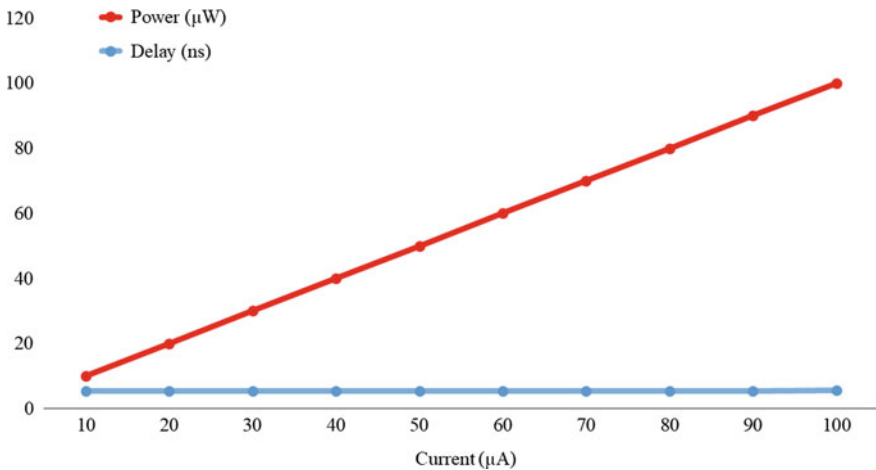
Fig. 2 Comparison of power and delay at different current source

dissipation of power also increases according to Eq. (1.1) [6]. A constant delay is observed at lower current values, whereas delay keeps on increasing as the current is further increased.

2.1   Bias Current Versus Supply Voltage

In Table 2, the supply voltage is varied from 1 to 5 V to observe the variations in the power dissipation attained by the MCML and CMOS inverters [7]. Simulations indicate that as the voltage is increased, power dissipated also shows an upsurge for both MCML and CMOS inverters. However, this escalation in power of MCML is less as compared to the power for static CMOS inverter. Also, it is revealed that when current bias for MCML inverter decreases, the power dissipation also diminishes at a given supply voltage. At a maximum of 5 V, CMOS inverter demonstrates a power dissipation of 182.3163 μW, whereas for the same supply voltage, the power dissipated by MCML inverter is only 50.00161 μW at a current bias of 10 μA, 50.17484 nW at a current bias of 10 nA, and 247.7949 pW at a current bias of 10 pA. Thus, the constant current source plays a significant role in the dissipation of power and is seen to be beneficial than CMOS when the power supply voltage is varied. MCML consumes static power because it employs a constant current source [8]. However, the dynamic power dissipation of MCML is ignorable with respect to static power because of the smaller output swings. The power dissipation for MCML is given by the product of supply voltage and current

Table 2 Power comparison between CMOS and MCML inverters at different supply voltages

| Voltage (V)	Power (μW)		Power (nW)	Power (pW)
	CMOS	At 10 μA	At 10 nA	At 10 pA
1.0	0.6988764	10.00003	9.995879	12.87103
1.2	1.65898	12.00001	11.99777	15.98653
1.4	3.085193	14.00008	14.00043	19.15334
1.6	5.140805	16.00016	16.00428	22.44356
1.8	7.883763	18.00026	18.01375	42.52275
2.0	11.01169	20.00036	20.01534	45.82491
2.2	14.82335	22.00081	22.01794	50.28615
2.4	19.26208	24.00101	24.02146	55.75443
2.6	24.37544	26.00135	26.02586	62.19222
2.8	30.43105	28.00151	28.03119	69.62589
3.0	37.26494	30.00176	30.03751	78.11832
3.5	57.8874	35.00110	35.05700	104.5977
4.0	86.40456	40.00129	40.08490	140.0922
4.5	126.306	45.00146	45.12303	186.9348
5.0	182.3163	50.00161	50.17484	247.7949
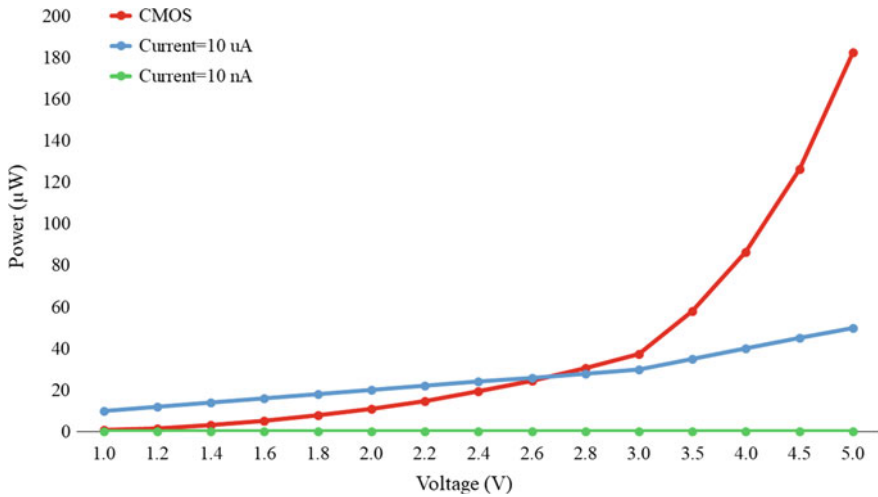
Fig. 3 Power comparisons at different supply voltages

applied. Hence, lower the current source, minimal will be the power dissipated. It can be ascertained that power dissipation in MCML is constant with frequency and faster switching occurs as the frequency of operation is increased, unlike CMOS where power dissipation varies directly in proportion to the frequency as the load capacitance is required to switch ON and OFF at a faster rate at higher frequencies. Figure 3 highlights the power dissipation by the MCML and CMOS inverters as the supply voltage is varied. For the MCML case, current biasing of 10 μA and 10 nA is plotted for comparison with the CMOS scenario. The graph clearly indicates that the power dissipation of CMOS is far greater than that of MCML as the supply voltage is increased.
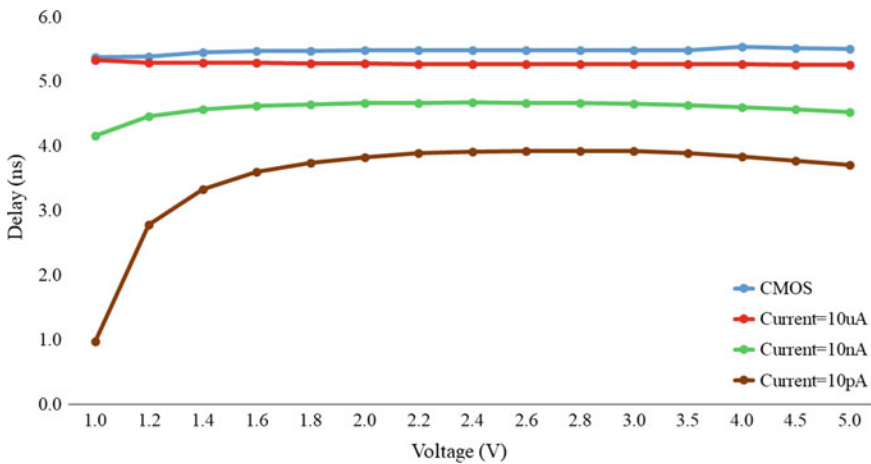
As the supply voltage is increased, it is revealed that the delay for MCML inverter increases at first and then gradually starts to decrease as the voltage is increased further as shown in Table 3. However, it is observed for CMOS inverter that the delay increases continuously as the supply voltage is elevated. The delay obtained for CMOS is higher than that of MCML inverter. Moreover, as the current in MCML is increased, the delay also increases [3]. Thus, the delay for current bias 10 μA is greater than that for 10 nA, which further exceeds the delay due to 10 pA current bias.

Figure 4 represents the delay of MCML and CMOS inverters as the supply voltage is varied from 1 to 5 V. It is discerned that CMOS has the maximum delay when compared to MCML inverter with current bias of 10 μA, 10 nA, and 10 pA. With a current bias of 10 μA, the delay starts to diminish from 1 V itself and continues reducing up to 5 V. However, for the current bias of 10 nA and 10 pA, the delay first increases and then gradually shows a decrease as the supply voltage is further scaled up. It is also perceived that as the current bias is decreased, the delay tends to scale down as well at a given supply voltage. As the supply voltage is

Table 3 Delay comparison between CMOS and MCML inverters at different supply voltages

Voltage (V)	Delay (ns)			
	CMOS	At 10 μA	At 10 nA	At 10 pA
1.0	5.3807	5.3351	4.1619	0.96859
1.2	5.3863	5.2864	4.4645	2.7800
1.4	5.4532	5.285	4.5711	3.3297
1.6	5.4716	5.2842	4.6186	3.5981
1.8	5.4772	5.2837	4.6450	3.7419
2.0	5.4796	5.2834	4.6614	3.8270
2.2	5.4809	5.2649	4.6696	3.8878
2.4	5.4817	5.2664	4.6713	3.9085
2.6	5.4823	5.2683	4.6682	3.9203
2.8	5.4828	5.2676	4.6616	3.9232
3.0	5.4832	5.2668	4.6529	3.9192
3.5	5.4837	5.2651	4.6275	3.8932
4.0	5.5334	5.2636	4.6024	3.8329
4.5	5.5164	5.2623	4.5706	3.7759
5.0	5.5059	5.2612	4.5298	3.7027

Fig. 4 Delay comparisons at different supply voltages

increased, it is revealed that the delay for MCML inverter increases at first and then gradually starts to decrease as the voltage is increased further. Keeping the supply voltage fixed, an increase in current bias from 10 pA to 10 nA and further to 10 μA results in higher delays because more the current supplied, more will be the output swing. This leads to a slower rise time and fall time, hence increasing the delay. This can be seen on comparing the rows of Table 3. Keeping the current bias fixed,
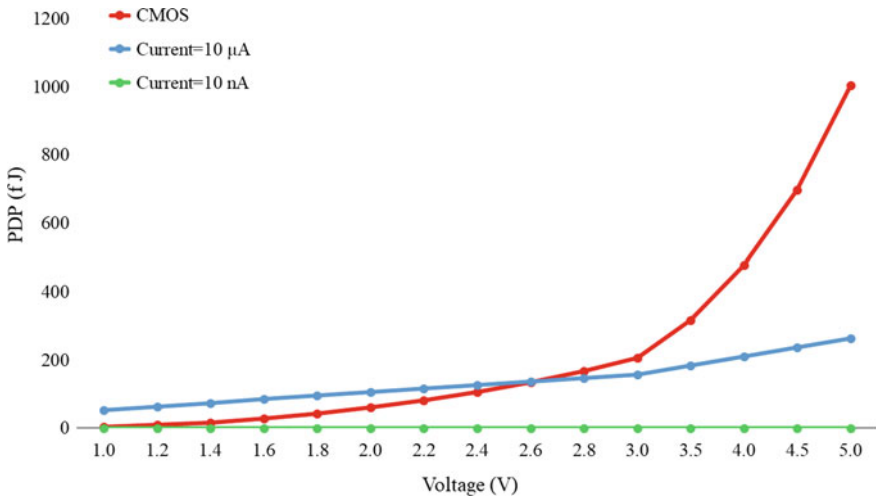
Fig. 5 PDP comparisons at different supply voltages

an increase in the supply voltage leads to an increase in delay for CMOS while for MCML, an initial increase in delay is followed by a decrease after a particular supply voltage [9].

Power delay product (PDP) is the product of power dissipation and the delay of a circuit. Figure 5 illustrates a comparison of power delay product for CMOS and MCML inverters. The graph indicates that with a current bias of 10 nA, the PDP is very low for MCML inverter as compared to the current bias of 10 μA. While the PDP of CMOS inverter is maximum at high supply voltages, it is comparable to the PDP of MCML at 10 μA current bias for lower supply voltages. It gives a fair idea about the variations in the power delay product on varying the supply voltage.

Moreover, Table 4 explains the relation between PDP and the power supply voltage (V_{DD}). It is observed that on scaling up the supply voltage, the PDP increases for both MCML and CMOS inverters. A decrease in PDP is observed when the current bias is reduced in case of MCML inverter. Initially, the PDP of CMOS inverter is lower than that of the MCML inverter with current bias of 10 μA. However, as the supply voltage is increased, an increase in PDP for CMOS inverter is seen because the power dissipation at high supply voltage comes into play. At 5 V, it is found that CMOS has a greater PDP than that of MCML. Another observation that can be made from Table 4 is that PDP of MCML is less for current bias of 10 nA and 10 pA. The current bias of 10 pA shows the minimum PDP out of all the cases. Thus, as the current bias decreases, a diminished PDP is obtained for MCML inverter. For lower current bias values, a low PDP is obtained even at higher supply voltage. As the supply voltage increases, the PDP also shows an increase for both CMOS and MCML inverters. At 5 V, CMOS inverter shows an astounding PDP of 10003.8153 fJ which is far superior to that of the MCML with a

Table 4 PDP comparison between CMOS and MCML inverters at different supply voltages

Voltage (V)	PDP CMOS (10^{-15} J)	PDP MCML (10 µA) (10^{-15} J)	PDP MCML (10 nA) (10^{-15} J)	PDP MCML (10 pA) (10^{-21} J)
1.0	3.7604	53.3511	0.0416018	12.4667
1.2	8.9357	63.4368	0.053564	44.4425
1.4	16.8241	73.9904	0.0639973	63.7748
1.6	28.0338	84.5472	0.0739173	80.7541
1.8	43.1809	95.1079	0.0836738	159.1158
2.0	60.3396	105.6699	0.0932997	175.3719
2.2	81.2452	115.832	0.1028149	195.5024
2.4	105.5889	126.3989	0.1122111	217.9161
2.6	133.6334	136.9829	0.1214939	243.8121
2.8	166.8473	147.5007	0.1306701	273.1562
3.0	205.976	158.0132	0.1397615	306.1613
3.5	317.4371	184.2842	0.1622262	407.2197
4.0	478.1109	210.5507	0.1844867	536.9593
4.5	696.7544	236.8111	0.2062393	705.8471
5.0	1003.8153	263.0684	0.2272819	917.5101

current bias of 10 µA (263.0684 fJ), 10 nA (0.2272819 fJ), and 10 pA (917.5101×10^{-21} J). MCML proves to be more PDP efficient in comparison to the CMOS logic design.

3   Conclusion

The effect of bias current on MCML inverter was studied in this paper. The constant current source also known as the tail current source plays an important role in the performance of the MOS current-mode logic. It affects parameters such as the voltage swing, voltage drop, delay, and power dissipation. At lower current values, reduced voltage swing results in decremented delays and hence faster switching activities. It is also discovered that as the supply voltage increases, the delay gradually decreases. MCML proves to be a better substitute for CMOS at high supply voltages as well as high frequencies of operation.

References

1. Hassan H, Anis M, Elmasry M (2005) Design and optimization of MOS current mode logic for parameter variations. Integr VLSI J 38(3):417–437

2. Gupta K, Pandey N, Gupta M (2013) Analysis and design of MOS current mode logic exclusive-OR gate using triple-tail cells. Microelectron J 44(6):561–567
3. Sharroush SM (2016) Performance optimization of MOS current-mode logic. In: International conference on electrical, electronics, and optimization techniques (ICEEOT), IEEE, Mar 2016, pp 2915–2920
4. Kang SM, Leblebici Y (2003) CMOS digital integrated circuits. Tata McGraw-Hill Education
5. Musicer JM, Rabaey J (2000) MOS current mode logic for low power, low noise CORDIC computation in mixed-signal environments. In: Proceedings of the 2000 international symposium on low power electronics and design, ACM, Aug 2000, pp 102–107
6. Badel S, Leblebici Y (2007) Breaking the power-delay tradeoff: design of low-power high-speed MOS current-mode logic circuits operating with reduced supply voltage. In: IEEE international symposium on circuits and systems (ISCAS), May 2007, pp 1871–1874
7. Vyas K, Jain G, Maurya VK, Mathur R (2015) Illustrative comparison of MCML and CMOS design techniques using tanner EDA. Int J Comput Appl 118(4)
8. Jain G, Vyas K, Maurya VK, Mathur R (2015) Comparative analysis of universal gates using MCML and CMOS technique. Int J Comput Appl 118(5)
9. Ali LS, Mahmod ZR (2013) Comparison between MCML and CMOS digital circuits for using ADS simulation. Al-Rafadain Eng J 21(1)

Handling the Energy-Delay Trade-off in Wireless Sensor Networks: State-of-the-Art

Nikita Shandil, Suniti Dutt and Sunil Agrawal

Abstract WSN (wireless sensor network) is the most researched field these days which has finite advancements every year. It aggregates the MEMS (micro-electrical mechanical system) technology with wireless communication and digital electronics for sensor processing operations. WSN has many objectives such as enhanced network lifetime, energy utilization, reliability, stability, throughput, security, and less delay. But this paper considers the contradiction that the wireless sensor network faces in its own two objectives which are maximum energy utilization and less delay. There is always some trade-off between energy and delay parameters to achieve better results especially in the case of enhanced lifetime and time-critical applications. This paper provides the brief review of approaches taken by the researchers to achieve the balance between energy and delay parameters.

Keywords Delay · Energy · Wireless sensor networks

1 Introduction

Wireless sensor network (WSN) is the most popular and emerging field these days because of its wide range of applications such as scientific, medical, defense, forest fire detection, chemical hazard detection, home automation, and disaster management [1–4]. It is an ad hoc network of nodes which aims to sense an event, collect data readings, and then forward that data to its base station (BS). The deployment of nodes in the network is application-specific. The operation of WSN can also be

N. Shandil (✉) · S. Dutt · S. Agrawal
University Institute of Engineering and Technology,
Panjab University, Chandigarh, India
e-mail: nikita.shandil3107@gmail.com

S. Dutt
e-mail: sunitidutt@gmail.com

S. Agrawal
e-mail: s.agrawal@hotmail.com

Fig. 1 Categorization of operation of WSN [5]

categorized into five stages as shown in Fig. 1. Planning refers to the objective for which WSN is to be employed. The deployment denotes establishment of nodes, post-deployment mentions neighborhood discovery mechanisms, operation can be assumed as clustering in hierarchical WSN, and post-operation is additional operations on packet received like removal of redundancy.

The sensor nodes are provided with limited battery, storage, computation, and communication capabilities [5]. So there is a need to design various techniques or routing protocols for efficient use of energy of sensor nodes to maximize the lifetime of network. But WSN usually compromises with delay for more energy-efficient network. There are also various issues prevalent in WSN such as localization issue [6], energy-reliability trade-off [7], energy-throughput trade-off [8], and energy-delay trade-off [9].

This paper focuses on energy-delay trade-off. Energy consumption usually depends on the transmission energy which is directly proportional to the distance between transmitter and receiver. While delay depends on the number of intermediate nodes or forwarding nodes between sender and receiver, i.e., multihop increases the delay while it reduces the energy consumption. So energy efficiency and delay are the contradicting parameters with having inverse relation. So there is a requirement of the balanced value of energy-delay trade-off which gives desired results. Our contribution for this work is review of some approaches for balancing of this trade-off parameter, their evolution from the specified time interval and the improvement provided by them for handling delay in packet propagation with lifetime maximization which would be beneficial for the researchers who are willing to do advancement in this parameter contradiction for achieving the desired objectives of WSN.

This paper is organized into four sections. First section provides the introduction, second gives a brief review of approaches selected by the researchers, third deals with the categorization of that approaches along with tabular representation, and fourth represents the conclusion of all this review work.

2 Literature Review

This section provides detailed study of approaches taken by the researchers to balance the compromise in energy consumption and delay parameters.

Zorzi and Rao [10] presented geographical random forwarding (GRF) technique along with semi-Markov model which gave accurate performance evaluation. In

this approach, it was assumed that all nodes can get positional information of other nodes. Positional information was inserted along with message. So nodes who hears the message decides whether they can be relay node to the message or not. This method worked on getting best relay node. No routing table or topology information was needed, just positional information. For collision avoidance, two channels were used: one for data traffic and another for wakeup signals. CSMA (carrier sense multiple access) was also used to sense the channel frequencies before sending data to avoid collision.

Yu et al. [11] gave the idea of modulation scaling (MoS) which was based on efficient utilization of energy present in the network. The authors presented the paper on the basis of scheduled packet transmission over the data aggregation tree under the particular value of latency. The proposed technique was applicable to any data aggregation function. This also analyzed the variation either by varying packet size with different values of delay parameters which showed the adaptability of this protocol. They assumed non-monotonic energy model, where transmission energy increases with transmission time after reaching certain threshold. Interference was handled through packet scheduling.

Yang et al. [12] show how pipeline-toned wakeup scheme (PTWS) can be used to handle energy-delay trade-off in the WSN. Here, asynchronous wakeup scheme is used where all nodes had no need to wake up at particular time. The nodes activate only at the reception of wakeup beacon signal. Here, the main gist is to overlap the packet transmission time with the wakeup time to save energy. As wakeup signal has no identity about destination, so it is sent over a particular transmission range. Here, the use of wakeup tone avoids much delay at each hop. The drawback observed here was that all the burden was on sender to wake up all the nodes in its transmission range so it could be adjusted to achieve better performance.

Yu and Prasanna [13] claimed the first work on task allocation (EBTA) on WSN to balance energy-delay trade-off. Here, the dynamic voltage scaling technique was used where each task was scaled with voltage values. To handle latency, epoch is set and all the tasks have to be completed within the time period of that epoch. Either the task of computation or communication was allotted to the sensor nodes in an area. So during certain activity in the network, epoch is released and all sensor nodes do their allotted tasks within the time limit of that epoch. Task allocation comprises of these steps. (1) Allocation of tasks to sensor nodes in the network. (2) Voltage scaling of the tasks. (3) Channels were assigned to communication activities. (4) Scheduling of computation and communication activities. The network assumed was cluster of homogeneous nodes with single hop.

Borghini et al. [14] presented the paper where they balanced energy-delay trade-off in data aggregation process and showed the improvement in sequence. The authors combined the concept of data aggregation with rerouting (DAR) based on residual energy and scheduling to achieve the desired trade-off. First, they started with static routing where the path did not change aggregation with time and each sensor node was not supposed to do data so here by LP (Linear Programing) optimization. This showed equalized energy consumption over the network with each node having multihops up to two nodes: one close for transmitter and other for

sink. Here, the incremental approach of complexity was followed. Then the authors increased the complexity by introducing dynamic rerouting and scheduling for balancing energy and delay in data delivery. It provides better results due to dynamic routes.

Durresi et al. [15] proposed a scalable and distributive routing protocol, delay energy aware routing protocol (DEAP) for heterogeneous sensor and actor networks. It provides flexible energy-delay trade-off. It combines the forwarding of nodes criteria with asynchronous wakeup of nodes. Wakeup cycle of node is so adjusted that any node in a particular area acquires a fixed time slot. Energy consumption was managed by introducing threshold in the distance for avoiding single hop for larger distance and by the use of actor nodes instead of sensor nodes. For delay-specific applications, there was adjustment in the wakeup cycle of nodes. The scheme of energy management used was adaptive.

Moscibroda et al. [16] described the energy-delay trade-off by adjustment in non-operational phase (ANOP) of WSN. Non-operational phase was divided into deployment and notification. Usually, the length of deployment phase is larger than notification time. Here, the approach chosen was to divide the node states into listen, transmit, and sleep. There is time taken by node to go back from sleep state to transmit state. So the concept of launching point was introduced here which is basically a signal who upon completion of deployment phase notifies all nodes in network by multihop way. Either one or two nodes are triggered by launching point, and then triggered nodes notify their neighbors and so on. Here three algorithms, birthday algorithm, uniform algorithm, and cluster algorithm, were analyzed by the presented model.

Huynh and Hong [17] proposed a routing scheme called cluster and chain-based energy and delay-efficient routing scheme ($\mathbf{C}^2\mathbf{E}^2\mathbf{S}$). It was limited to 3-hop as for greater than three it required large delay and complexity. It was the hybrid of inter-cluster and intra-cluster communication along with chain- and cluster-based protocols, respectively. Chain approach for cluster heads ensures high energy efficiency. To form chain and cluster, central approach was used which results in large communication overhead. To handle this, passive-BS-based routing was used where nodes do piggyback of their information such as residual energy and distance. ID along with data and send it to the base station. It was not necessary at every step. Here, the assumption used was that base station had enough energy to communicate with every node of network.

Ammari and Das [18] presented data dissemination protocol which involves the division of transmission range of sensor nodes (DTRS) into three concentric circular bands where one closer to source has high degree of interest in energy, middle one balanced degree of interest in energy and delay, and farther one having high degree of interest in delay. The assumptions in this protocol were that source is located in dense network of nodes and are uniformly distributed, transmission range of sink is greater than source, only one sink is available, for position information location approximation techniques are used and nodes piggyback their residual energy information to their neighbor only at the beginning and by local means source estimates the residual energy of its neighbors.

Minhas et al. [19] proposed the idea of fuzzy multiobjective routing algorithm for maximum lifetime and minimum delay (FMOLD) by using fuzzy cost function for both energy and delay and fuzzy membership function for aggregating their cost functions. This algorithm was used to compute the efficient route selected for packet transmission from source to sink which balances energy-delay trade-off. Here, WSN network was assumed to be directed graph of sensor nodes. Edge is defined between two sensor nodes whose transmission range was within specified range. This protocol uses centralized approach which results in large control overhead. It was online routing algorithm that means here route selection was based on current situation of network not on future requests for route selection. It was not fully implemented in real conditions of sensor network.

Shahraki et al. [20] presented an intra-cluster routing algorithm (ICRA) to manage energy-delay trade-off. To determine the end-to-end delay, queue theory was used. Here, the focus was on intra-cluster routing as there is direct transmission between member nodes and cluster head by TDMA (time division multiple access). This is not a problem in the case of smaller geographical region but in the case of larger geographical region, it will deteriorate the lifetime of network and enhance the energy depletion. So cost function was used for determining either direct transmission or indirect transmission. This cost function uses energy and delay as its parameters.

Cheng et al. [21] claimed that their proposed multiobjective framework would provide non dominated solutions for the energy-delay trade-off which are not possible from other clustering approaches. It used NSGA-II (non-dominated sorting of genetic algorithm). Here, it deals with Pareto frontier for finding non-dominating solution for multiobjective optimization. The advantage of this approach based on Pareto front is that it did not depend on weight combinations whose slight change shifted the solution from one critical point to another. As this technique was free to select any optimum number of cluster head, it resulted in less value of delay, because large value of cluster heads leads toward high delay and lesser value toward higher energy consumption. So they deal with optimum value which provides balanced energy-delay trade-off.

Li et al. [22] studied the energy-delay trade-off during data aggregation under physical interference model by considering the technique of successive interference reduction (DASIR) done by the receiver in the case of multiple senders. Successive interference reduction is a technique which breaks the ideology of one sender at one time slot as it belongs to multiple packet reception categories. It reduces delay as the cluster member nodes send their data to their head at one time slot instead of separate. So here the technique is to select the strongest signal and then by applying estimation, regeneration, and subtraction of unwanted components up to last signal. To handle enhanced energy consumption, approximation algorithm was used to determine the lower bounds and optimum value of this trade-off and proved that their algorithm provides lower delay in aggregation and also balancing the energy consumption at its best.

Ammari [23] presented the TED (trade off energy with delay) algorithm to solve the multiobjective problem of minimum energy consumption, uniformity in power

depletion and minimum delay. It sliced the communication range into concentric circular bands, and each band was applied some weightage with the particular objective. For weightage, it used weighted scale-uniform-unit sum approach and the obtained the solution for getting best route by TED. Basically, its aim is to find the optimum route for forwarding node selection which completes this multiobjective optimization problem. Effectiveness of TED was supported by various numerical results and they extended its application in real-world scenario.

Huyang et al. [24] proposed the routing protocol CAR (correlation aware opportunistic routing). Opportunistic routing was considered because of its advantages in lossy and realistic scenario of WSN. Entropy coding was used here for data correlation. Data in the node were divided into two categories, i.e., aggregated data from other nodes and its own generated data locally. For routing, opportunistic routing was used which consists of three steps which were next hop forwarder selection, their prioritization and acknowledgment Energy-delay trade-off was handled as data were divided, correlated and sent by the two routes according to their type as aggregated or locally generated and by using the advantages of opportunistic routing.

3   Review Extract

From all above briefly discussed approaches from the literature, the authors classified the solution of this parameter contradiction into adjustment in the duty cycle of nodes, data aggregation techniques, forward node selection, topology management, and scheduling of packets, as depicted in Table 1.

Table 1 Categorization of approaches

Protocol	Duty cycle	Data aggregation	Routing/forward node selection	Cluster/topology Management	Scheduling
GRF	✓		✓	✓	
MS		✓		✓	✓
PTWS	✓				✓
EBTA				✓	✓
DEAP	✓		✓		✓
ANOP	✓		✓	✓	
C^2E^2S			✓	✓	✓
DTRS			✓	✓	
FMOLD			✓	✓	
ICRA			✓	✓	
NSGA-II			✓	✓	
DASIR		✓		✓	✓
TED			✓	✓	
CAR		✓	✓		

4 Conclusion

The approaches mentioned here were considered by the researchers for handling energy-delay trade-off, and its review extract is that this trade-off usually depends on the efficient techniques from the deployment of nodes, organization of network, type of nodes, duty cycle of nodes, multiple access schemes whether it is TDMA (time division multiple access), CDMA (code division multiple access), CSMA (carrier sense multiple access), etc., cluster head selection, routing between member nodes and cluster head, data aggregation and correlation to handle redundant information and route for packet transmission, etc. It just needs the balancing of the parameters involved in the WSN organization to achieve better trade-off. WSN has a lot of applicability in almost every field because of its vast advantages. So there is a need for further improvement in this field to attain its objectives and maximization of its performance up to the optimum level.

References

1. Alkhatib AAA (2014) A review on forest fire detection techniques. Int J Distrib Sens Netw
2. Durisic MP, Tafa Z, Dimić G, Milutinović V (2012) A survey of military applications of wireless sensor networks. In: Mediterranean conference on embedded computing MECO (2012)
3. Nirmal Kumar K, Sarma Dhulipala VR, Prabakaran R, Ranjith P (2011) Future sensors and utilization of sensors in chemical industries with control of environmental hazards. In: 2nd international conference on environmental science and development, IPCBEE, vol 4
4. Devasena A, Sowmya B (2015) Wireless sensor network in disaster management. Indian J Sci Technol 8(15)
5. Sohraby K, Minoli D, Znati T (2007) Wireless sensor networks: technology, protocols, and applications. Wiley, New York, pp 42–57
6. Singh P, Agrawal S (2013) TDOA based node localization in WSN using neural networks. In: International conference on communication systems and network technologies (CSNT). IEEE, pp 400–404
7. Dutt S, Agrawal S, Vig R (2018) Cluster-head restricted energy efficient protocol (CREEP) for routing in heterogeneous wireless sensor networks. Wirel Pers Commun. https://doi.org/10.1007/s11277-018-5649-x
8. Dutt S, Kaur G, Agrawal S (2018) Energy-efficient sector-based clustering protocol for heterogeneous WSN. In: 2nd international conference on communication, computing and networking (ICCCN), Chandigarh. Springer LNNS series (2018)
9. Akkaya Kemal, Younis Mohamed (2005) A survey on routing protocols for wireless sensor networks. Ad Hoc Netw 3:325–349
10. Zorzi M, Rao RR (2003) Geographic random forwarding (GeRaF) for ad hoc and sensor networks: energy and latency performance. IEEE Trans Mobile Comput 2(4)
11. Yu Y, Krishnamachari B, Prasanna VK (2004) Energy-latency tradeoff for data gathering in wireless sensor networks. In: IEEE international conference on computer communications, China (2004)
12. Yang X, Vaidya N (2004) A wakeup scheme for sensor networks: achieving balance between energy saving and end-to-end delay. In: IEEE real-time and embedded technology and applications symposium, Toronto, Canada (2004)

13. Yu Y, Prasanna VK (2005) Energy-balanced task allocation for collaborative processing in wireless sensor networks. Mobile Netw Appl 10(1):115–131
14. Borghini M, Cuomo F, Melodia T, Monaco U, Ricciato F (2005) Optimal data delivery in wireless sensor networks in the energy and latency domains. In: IEEE international conference on wireless internet, Budapest, Hungary
15. Durresi A, Paruchuri V, Barolli L (2005) Delay-energy aware routing protocol for sensor and actor networks. In: IEEE 11th international conference on parallel and distributed systems
16. Moscibroda T, Rickenbach PV, Wattenhofer R (2006) Analysing the energy-latency trade-off during the deployment of sensor networks. In: IEEE international conference on computer communications (INFOCOM'06), Barcelona, Spain (2006)
17. Huynh TT, Hong CS (2006) An energy-delay efficient multi-hop routing scheme for wireless sensor networks. IEICE Trans Inf Syst 89(5):1654–1661
18. Ammari Habib M, Das Sajal K (2008) A trade-off between energy and delay in data dissemination for wireless sensor networks using transmission range slicing. Comput Commun 31:1687–1704
19. Minhas MR, Gopalakrishnan S, Leung V (2009) Multiobjective routing for simultaneously optimizing system lifetime and source-to-sink delay in wireless sensor networks. In: IEEE international conference on distributed computing systems workshops, Canada (2009)
20. Shahraki A, Rafsanjani MK, Saeid AB (2011) A new approach for energy and delay trade-off intra-clustering routing in WSNs. Comput Math Appl 62:1670–1676
21. Cheng CT, Leung H (2012) A multi-objective optimization framework for cluster-based wireless sensor networks. In: IEEE international conference on cyber-enabled distributed computing and knowledge discovery, China
22. Li H, Wu C, Yu D, Hua Q-S, Lau F (2013) Aggregation latency energy tradeoff in wireless sensor networks with successive interference cancellation. IEEE Trans Parallel Distrib Syst 24 (1):2160–2170
23. Ammari HM (2013) On the energy-delay trade-off in geographic forwarding in always-on wireless sensor networks: a multi-objective optimization problem. Comput Netw 57: 1913–1935
24. Huang G, Zhang B, Yao Z (2017) Data correlation aware opportunistic routing protocol for wireless sensor networks. In: IEEE ICC ad-hoc and sensor networking symposium

Analysis and Reduction of Fiber Non-linearity in Optical Communication System

Rukhsana Kouser and Supreet Singh

Abstract In this paper, the effect of nonlinearity has been investigated with different techniques such as non-return-to-zero (NRZ), return-to-zero (RZ), duo-binary return-to-zero (DRZ), and modified duo-binary return-to-zero (MDRZ) modulations. We have explored the fiber nonlinearities by taking dispersion of single-mode optical fiber at 2.5 Gbps communication system with various transmission lengths; i.e., 72–132 km is evaluated with respect to the nonlinearity in fibers. The evaluation is done in terms of Q factor and BER with the 0 dBm input launched power. Along with this pre-compensation, post-compensation and symmetrical compensation techniques are also applied, and it is observed that the Q factor in symmetrical compensation is higher in comparison to the pre-compensation and post-compensation techniques. Therefore, it is examined that nonlinearity effects are less effective in symmetrical compensation instead of pre-compensation and post-compensation.

Keywords Non-linearity · Dispersion compensation · Modulations · Bit error rate and Q factor

1 Introduction

The term "nonlinearity" refers to the intensity dependent and intensity in-dependent phenomena. The variations in the refractive index of the communication medium and inelastic scattering are the major reasons behind the occurrence of nonlinearity in optical fiber. Nonlinear effects hinder bit rate along with limiting propagation distances in systems. The power dependence characteristic of refractive index is

R. Kouser (✉) · S. Singh
Department of Electronics and Communication Engineering,
Chandigarh University, Gharuan, Chandigarh, India
e-mail: rukhsana4536@gmail.com

S. Singh
e-mail: uic.supreet@gmail.com

Table 1 Comparison of nonlinear effect

Characteristics	SPM	XPM	FWM
Bit rate	Dependent	Dependent	Independent
Origin	Nonlinear susceptibility $(X)^3$	Nonlinear susceptibility $(X)^3$	Nonlinear susceptibility $(X)^3$
Effects of $(X)^3$	Phase shifts due to pulse itself only	Phase shift is alone due to co-propagating signals	New signals are generated
Shape of broadening	Symmetrical	Symmetrical	–
Energy transfer between medium and optical pulse	No	No	No
Channel spacing	No effect	Increases on reducing the spacing	Increases on reducing the spacing

accountable for Kerr's effect. Further, the Kerr effect is manifested in three various effects such as four-wave mixing (FWM), self-phase modulation (SPM), and cross-phase modulation (XPM).

The combined effects of group velocity dispersion, Kerr nonlinearity effects, and accumulated amplified emission result in signal degradation. Thus, dispersion and nonlinearities serve as major concerns in WDM systems [2] (Table 1).

2 The Effect of Dispersion

The dispersion is defined as distortion or scattering of signals or pulse due to inconsistent frequency and light pulse mode leading to certain errors in networks. Chromatic dispersion (CD) which occurs due to multiplexing of distinct colors corresponding to different colors of different wavelengths affect the efficiency of single-mode fiber optic WDM. The quality of signal is further degraded by Polarization which is involved even in single-mode fiber which is associated with two different Polarizations. The propagation velocity for each polarization may get introduced by certain variations caused by fiber distortions. This entire process of polarized dispersion is referred as Birefringence which is given by the following equation:

$$B_m = \frac{|B_x - B_y|}{k_0} = n_x - n_y \tag{1}$$

where

B_m denote birefringence;
n_x and n_y denote the refractive index of two orthogonal polarizations.

The phase difference of light propagation over L km for the specified value of B_m is evaluated by the equation given below:

$$\phi = k_0 B_m L = \frac{2\pi}{\lambda}(N_x - N_y)L = (\beta_x - \beta_y)L \tag{2}$$

The difference between slow and fast is repeated periodically in case the value of B_m remains constant for entire light transmission process. The periodic power exchange is called polarization beat length which is obtained from the following equation:

$$L_B = \frac{2\pi}{|\beta_x - \beta_y|} = \frac{\lambda}{B_m} \tag{3}$$

In case of single mode fiber (SMF) occurred dispersion major type is various spectral components associated different group velocities results in waveguide or material dispersion comprised Group velocity Dispersion (GVD). The negative dispersion-type special designed fiber are dispersion-compensating fiber (DCF) that have −70 to −90 ps/nm km negative dispersion. The fiber inside nonlinear effect is negligible if the value of average optical power is low; then, GVD fiber can be compensated by DCF. Out of two fiber segmented optical pulse propagation, the second one is DCF.

$$A(L,t) = \frac{1}{2\pi}\int_{-\infty}^{\infty} A(0,w)\exp\left(\frac{i}{2}w^2(\beta_{21}L_1 + \beta_{22}L_2) - iwt\right)dw \tag{4}$$

In which $L = L_1 + L_2$ and L_1 length fiber segment GVD parameter is represented by β_{21}. The original shape can be recover if the pulse is vanished by w^2, and the value of DCF should be according to it.

$$\beta_{21}L_1 + \beta_{22}L_2 = 0 \tag{5}$$

Or

$$D_1 L_1 + D_2 L_2 = 0 \tag{6}$$

It is a DCF using dispersion compensation best condition.

$D_1 > 0$ in case of standard Eq. 6 that shows a negative value of D_2 DCF for dispersion compensation.

Mohan [10] proposed the concept of chromatic dispersion which occurred in optical communication systems leading to signal degradation. The signal dispersion rate increased with the increase in data transmission rate.

3   Simulation Setup

The proposed work implements the optical fiber communication system and analyzed it by using three different compensation techniques and various modulation techniques. The used compensation techniques are pre-compensation, post-compensation, and symmetrical compensation. The proposed communication system is designed by using the data source, electrical driver, and laser source and amplitude modulator at transmitter's end. The data source generates the digital signal at 2.5 Gbps in the desired data transmission formats. Then electrical pulse generator converts the digital input signals to electrical signals. After generating the electrical pulse, the signal is transmitted to the modulator along with the laser beam. The modulator used is NRZ, RZ, and DRZ, and after that, pre-, post-, and symmetric compensation techniques are applied. On receiver end, there is a photo detector and low-pass filter, and a BER analyzer are installed. The role of photo detector is to detect the light by analyzing the effect of each photon. While transmitting the signal from sender to receiver, the noise enters to the signal and leads to the corruption of data; therefore, the low-pass filter is applied at the receiver end to filter the signal and to remove the effect of noise from it. The role of the BER is to analyze the effect of bit-wise error rate in the final received signal.

4   Proposed Work

After having a review to the problem that has been discussed in previous section of this study, it is decided to develop a communication system with reduced fiber non linearity. As the major objective of this work is to decrease the effect of fiber non-linearity, thus the different modulation techniques such as NRZ, DRZ, and RZ are used with DCF and SMF mechanisms. For the purpose of simulation, different lengths of fiber are considered. The post-, pre-, and symmetrical dispersion compensation methods are also implemented to analyze the effects of dispersion compensation.

Figures 1, 2, and 3 delineate the proposed system with pre-, post-, and symmetrical compensation techniques by using DCF for different modulation techniques. Along with DCF, the SMF and EDFA are used for compensating the power loss. The length of SMF varies from 72 to 132 km.

5   Results

The graph in Fig. 4 depicts the Q factor analyzed in the proposed system by using three of the compensation schemes and NR generator. From the observations, it is manifested that the Q factor was higher when the transmission distance was less and a sudden fall has been seen in the Q factor with the increment in the transmission
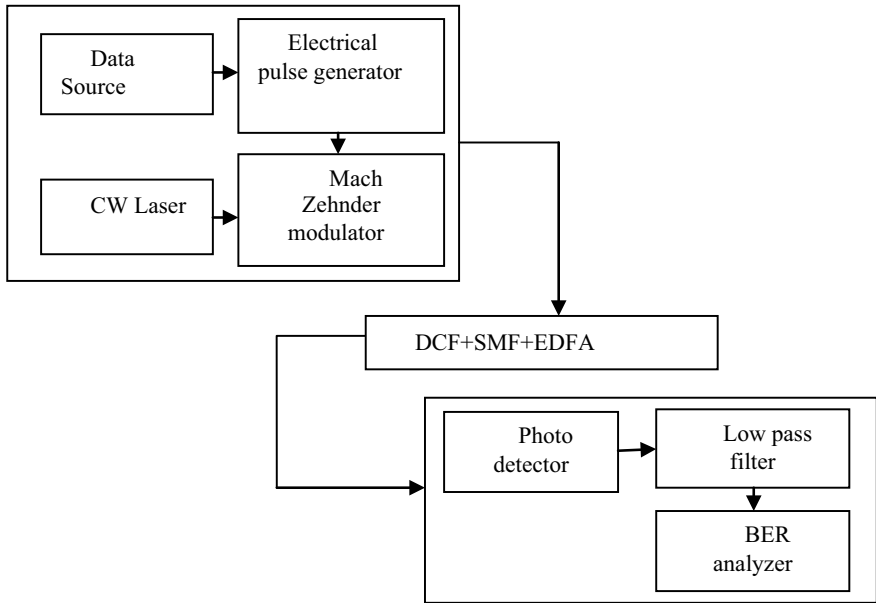
Fig. 1 pre-compensation
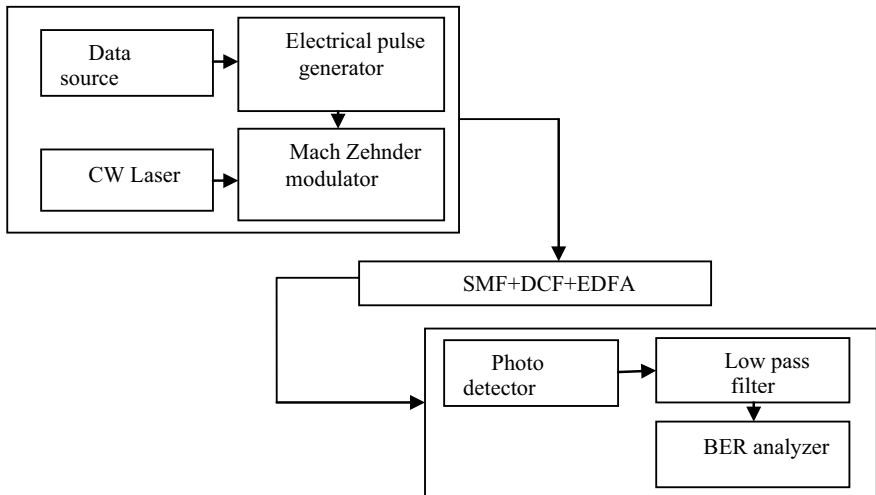
Fig. 2 post-compensation

distance. Initially, the *Q* factor of symmetrical compensation is observed to be 37.69, post-compensation is 242.60, and pre compensation is 37. Then, it falls to the 61.77 for post-compensation, 53.74 for pre-compensation, and 41.16 for symmetrical compensation.
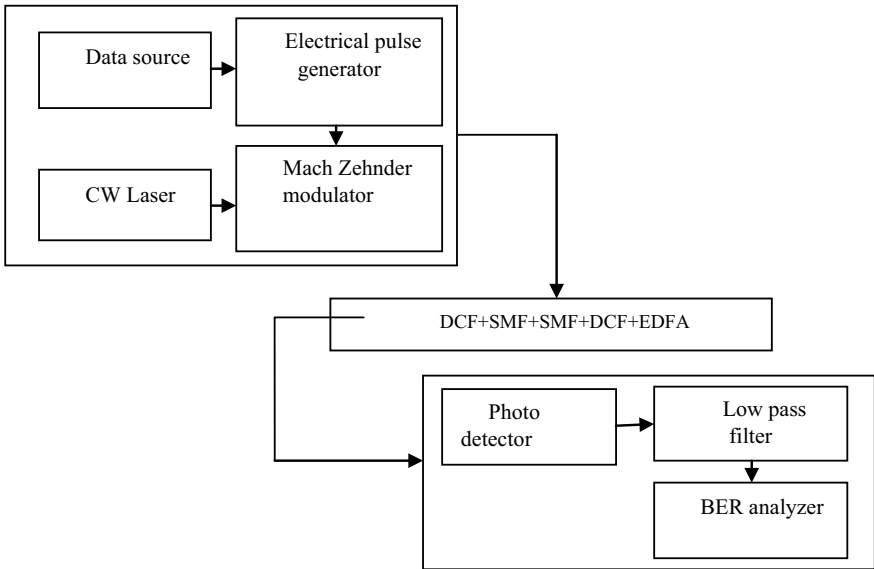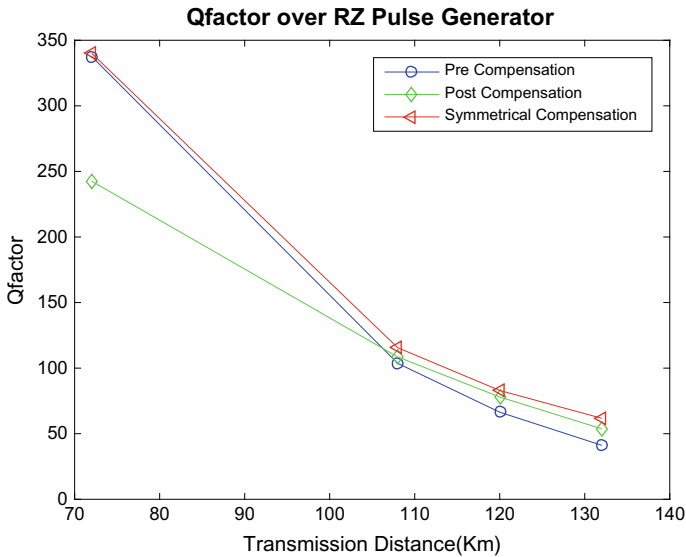
Fig. 3 Symmetrical compensation

Fig. 4 *Q* factor of RZ modulation

The comparison of compensation scheme on the basis of the NRZ generator. The graph proves that the initial Q factor of pre-compensation is high, i.e., 185.81 than post-compensation (235.05) and symmetrical compensation (281.47) (Fig. 5).
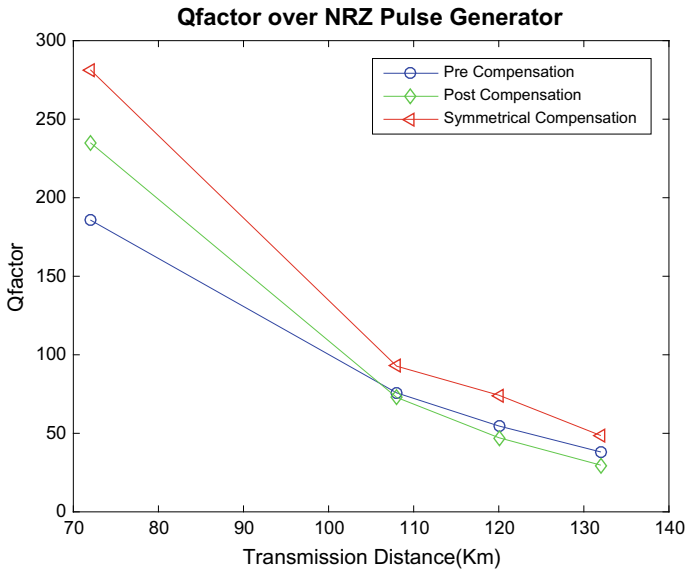
Fig. 5 Q factor of NRZ modulation
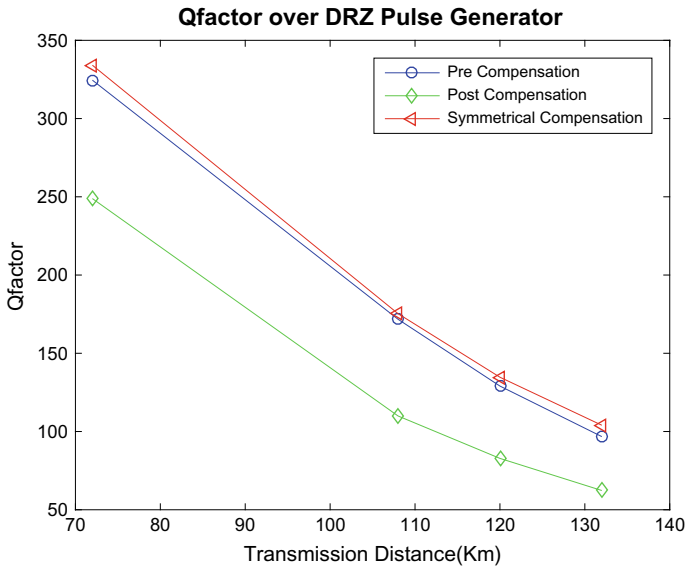
Fig. 6 Q factor of DRZ modulation

The comparison graph in Fig. 6 explains the Q factor of pre-compensation, post-compensation, and symmetric compensation with respect to the DRZ modulation. The graph manifested that initially the Q factor of pre-compensation is

Table 2 BER of proposed work is as follows

Modulation technique	Compensation scheme		
	pre-compensation	post-compensation	Symmetrical compensation
RZ	0	0	0
NRZ	1.39e−19	1.70e−319	2.55e−060
DRZ	0	0	0

higher than the Q factor of other two compensation techniques and it remains higher till the higher transmission distance in case of DRZ, whereas in case of NRZ and RZ, it has been seen that the compensation technique with higher Q factor initially fails to remain same at the end.

6   Conclusions

To sum up, it can be said that the value of Q factor relies on the transmission distance. As from the graph it is sequel that when we increase the transmission distance, the value of Q factor decreases and reveals that the effect of fiber non-linearity occurred at higher distance. By using the different compensation techniques, pre, post, and symmetrical, we have observed that the value of Q factor is higher in case of DRZ modulation in comparison to the NRZ and RZ modulations. BER (Table 2) of DRZ is evaluated to be lower ones in each compensation scheme. Thus, it is concluded that DRZ is a better modulation mechanism which can outperform in the case of all compensation schemes. In future, more amendments can be done in the present work by amending the electronic dispersion compensation (EDC) mechanism with DCF compensation mechanism to obtain better results.

References

1. Agrawal GP (1997) Fiber-optic communication systems. Wiley, pp 1–530
2. Senior JM (2009) Optical fiber communications. Prentice Hall, pp 1–1023
3. Xiao X, Gao S, Tian Y, Yang C (2007) Optimization of the net residual dispersion for self-phase modulation-impaired systems by perturbation theory. J Light Wave Techno 25(3): 929–937
4. Xiao X, Yang C, Shum P (2008) Analytical design of SPM-limited systems with optical phase conjugation. IEEE Photonics Techno Lett 20(7):472–474
5. Wang HM, Taga H (2010) An experimental study of XPM and SPM upon a long-haul RZ-DSPK transmission system with a block-type dispersion map. J Light Wave Techno 28(22):3220–3225
6. Udalcovs A, Bobrovs V Porins J (2012) Evaluation of SPM-induced optical signal distortions in ultra-dense mixed-WDM system. IEEE Institute of Telecommunications

7. Jindal PK, Kaur B, Bansal N (2013) Self phase modulation reduction for WDM transmission using EDFA. Int J Appl Eng Manag 2(12):36–40
8. Srivastava M, Kapoor V (2014) Analysis and compensation of self phase modulation in wavelength division multiplexing system. In: IEEE Engineering and System Conference, pp 1–4, 28–30 May 2014
9. Neheeda P (2016) Analysis of WDM system with dispersion compensation schemes. Procedia Comput Sci 93:647–654
10. Mohan A (2014) Compensation of dispersion in 5 Gbps WDM system by using DCF. IEEE
11. Soni G (2015) Performance analysis of WDM link using dispersion compensating fiber at different wavelengths. IEEE
12. Kumar V (2014) Design and performance analysis of optical transmission system. IOSR J Eng (IOSRJEN) 04(05):22–26
13. Qi X (2010) Fiber dispersion and nonlinearity influences on transmissions of AM and FM data modulation signals in radio-over-fiber system. IEEE J Q Electron 46(8):1170–1177
14. Sultana N, Islam MS (2012) Analysis of XPM effect with SPM and GVD in WDM fiber optic transmission system. ICCCE 2012, 3–5 July 2012
15. Bobrovs V (2012) Comparison of chromatic dispersion compensation techniques for WDM-PON solution. IEEE, pp 64–68

Low-Power High Output Impedance-Improved Bandwidth Current Mirror Using FGMOS and QFGMOS

Bhaskar Prakash, Urvashi Bansal and Maneesha Gupta

Abstract This work presents two novel circuits of current mirror offering high output impedance and improved bandwidth using floating gate MOSFET (FGMOS) and quasi-floating gate MOSFET (QFGMOS). These circuits are very useful in current amplification, biasing, active loading, and level shifting. The performance of current mirror is judged on the basis of current copying capability, noise, sensitivity, and bandwidth. In this work, it is tried to improve output impedance and bandwidth at cost of very low power consumption. The circuits presented here are implemented on SPICE with 0.18 µm TSMC BSIM3 and level 49 technology. All simulations have been carried out with the power supply of 0.65 V. These proposed circuits offer very low input resistance and very high output resistance. The 3-dB bandwidth with compensation technique is observed to improve by a high factor. Both circuits offer high linearity and fulfill the requirements for high-performance current mirror.

Keywords Current mirror · High output impedance · FGMOS · QFGMOS

1 Introduction

Low-voltage, low-power devices have become more popular due to demand for portability and for a long-lasting battery. In analog integrated circuits, current mirror is the basic building block to provide active loading and biasing. Hence, the

B. Prakash (✉) · U. Bansal · M. Gupta
Department of Electronics and Communication, NSIT, New Delhi 110059, India
e-mail: bhaskarprakash94@gmail.com

U. Bansal
e-mail: urvashi.bansal@gmail.com

M. Gupta
e-mail: maneeshapub@gmail.com

optimum design of current mirror is very crucial for high performance of the overall circuit. There are certain parameters such as high output impedance, low input impedance, and the constant output current regardless of the loading [1] which are useful to judge the efficiency of any mirror circuit.

However, limitations like channel length modulation and mismatch in aspect ratio of current mirror cause variation in the drain-to-source voltages which affect the current copying capability. These limitations can be overcome in cascode current mirror [2], but it requires higher power supply. It is also evident that cutting-edge technology demands for compact devices with small power consumption. In this direction, standard MOSFETs are tried to implement applications suitable for low-voltage, low-power VLSI, but it is found that circuits designed with conventional technique suffer from many disadvantages when power supply voltage is reduced like threshold voltage variation and degradation of dynamic range [3].

Recently, many solutions have been proposed by researchers useful for low-voltage and low-power applications [4] such as FGMOS [5, 6], QFGMOS [7], FVF [8], self-cascode [9], and body-driven techniques [10].

In this work, a novel low-voltage current mirror is presented using FGMOS and QFGMOS. Both ways, the proposed circuits offer high output impedance and enhanced bandwidth. Section 2 gives working and device structure of FGMOS and QFGMOS. Section 3 contains a circuit description, Sect. 4 presents the simulation results of the proposed circuit, and Sect. 5 concludes the paper.

2 Low-Voltage Technique

The supply requirement of a circuit can be minimized using FGMOS and QFGMOS.

2.1 Review of FGMOS

The FGMOS transistor has two types of gate, out of which one is floating gate and other one is controlling gate. As the name suggests, the floating gate is electrically isolated and it has no direct connection with controlling gate and MOSFET body.

The controlling gates are located over the floating gate separated by oxide. Multiple inputs are connected to them. Thus, the floating gate is capacitively coupled with controlling gate. FGMOS is suitable for low-voltage, low-power application because its threshold voltage can be programmed and reduced against its conventional value. The basic structure of multi-input, two-channel FGMOS is shown in Fig. 1a and b.
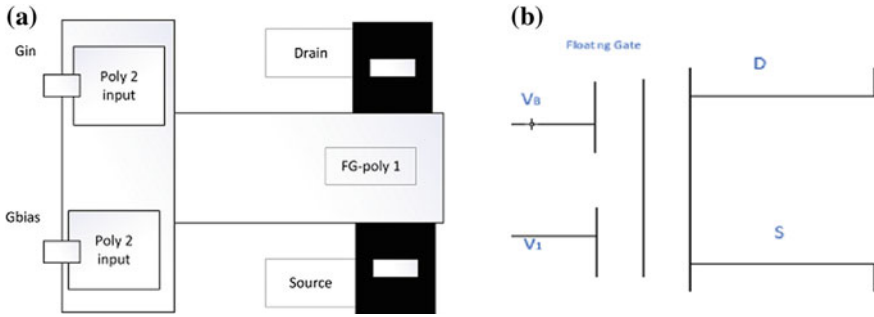
Fig. 1 **a** Layout of two-input FGMOS, **b** symbol of two-input FGMOS

The drain current of n-type FGMOS is following [11]:

$$I_D = \frac{\beta}{2}(V_{FGS} - V_{TH})^2 \tag{1}$$

in which V_{FGS} and β are the effective floating gate voltage and transconductance of FGMOS, respectively.

$$V_{FGS} = \frac{C_A V_{BS} + C_B V_{2S} + C_{FGD} V_{DS} + C_{FGB} V_{BS} + Q_{FG}}{C_{eff}} \tag{2}$$

Total capacitance at the gate terminal of FGMOS is C_{eff}, and it is equivalent to

$$C_{eff} = C_A + C_B + C_{FGD} + C_{FGB} + C_{FGS} \tag{3}$$

in which C_A and C_B are the capacitance between controlling gate and floating gate. C_{FGD}, C_{FGB}, and C_{FGS} are the parasitic capacitances of FGMOS, and amount of charge trapped in the floating gate during fabrication is Q_{FG}. This unwanted Q_{FG} in the floating gate causes the difference between the identical devices. The trapped charge can be removed using ultraviolet light (UV), hot electron injection, and tunnel effect.

For N-input FGMOS, if $(C_A + C_B) \gg C_{FGD}, C_{FGB}, C_{FGS}$, then Eq. (3) can be written as:

$$C_{eff} = C_A + C_B. \tag{4}$$

Equation (1) can be modified as:

$$I_D = \frac{\beta}{2}\left[\frac{(C_A V_{BS} + C_B V_{2S})}{C_{eff}} - V_{TH}\right]^2 \tag{5}$$

Equation ([5](#)) is rewritten as follow:

$$I_D = \frac{\beta}{2}\left(\frac{C_B}{C_{eff}}\right)\left[V_{2S} + \left(\frac{C_A}{C_B}\right)V_{BS} - \frac{C_{eff}}{C_B}V_{TH}\right]^2 \tag{6}$$

Equation ([6](#)) can be simplified as follows:

$$I_D = \frac{\beta}{2}\left(\frac{C_B}{C_{eff}}\right)[V_{2S} - V_{TFG}]^2 \tag{7}$$

From Eq. ([6](#)), the effective threshold voltage V_{TFG} is as follows:

$$V_{TFG} = \left(\frac{c_{eff}}{c_B}\right)\left[V_{TH} - \left(\frac{C_A}{C_{eff}}\right)V_{BS}\right] \tag{8}$$

where $\alpha_1 = \left(\frac{C_A}{C_{eff}}\right)$ and $\alpha_2 = \left(\frac{C_B}{C_{eff}}\right)$.

By Eq. ([7](#)), FGMOS transistor's threshold voltage (V_{TFG}) can be controlled by varying the voltage at the controlling gate and capacitance ratios α_1 and α_2. By adjusting the input voltage, threshold voltage can be minimized till zero. With this advantage, FGMOS is preferable for low-voltage and tunable circuits.

2.2 Quasi-floating Gate Technique

FGMOS have some drawbacks like high bias capacitance which causes reduction in transconductance and gain–bandwidth product, and it also increases the silicon area on the chip. Besides, FGMOS has initial trapped charge in floating gate. All these drawbacks are improved with QFGMOS, which requires less silicon area and does not have problem of trapped charges and offers high output resistance. In QFGMOS, floating gate is connected to biasing voltage with a high resistance. This high resistance is realized with conventional MOSFET working in cutoff. In N-type QFGMOS, the biasing resistor is realized using P-type MOSFET in cutoff region. Figure [2](#)a and b shows the basic two-input QFGMOS and the layout of QFGMOS, respectively.

3 Circuit Description

The conventional current mirror [4] is modified using two low-voltage techniques, namely FGMOS and QFGMOS. The schematic diagrams of proposed circuits are shown in Figs. [3](#) and [4](#), respectively. However, the basic circuit topology is same. To reduce the input resistance and the input voltage of the current mirror, the circuit
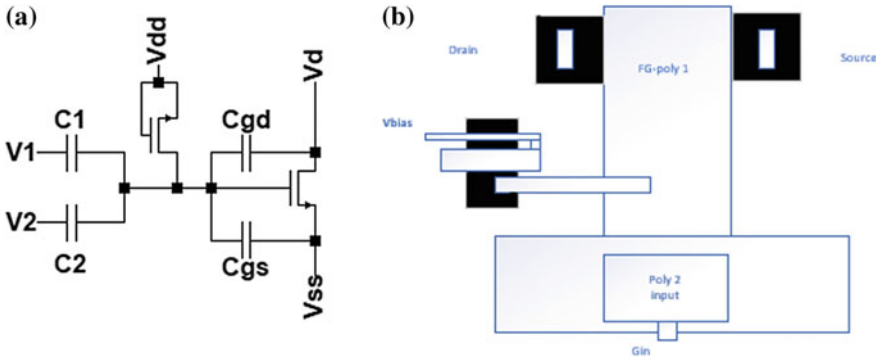
Fig. 2 a Two-input QFGMOS, b layout of two-input QFGMOS
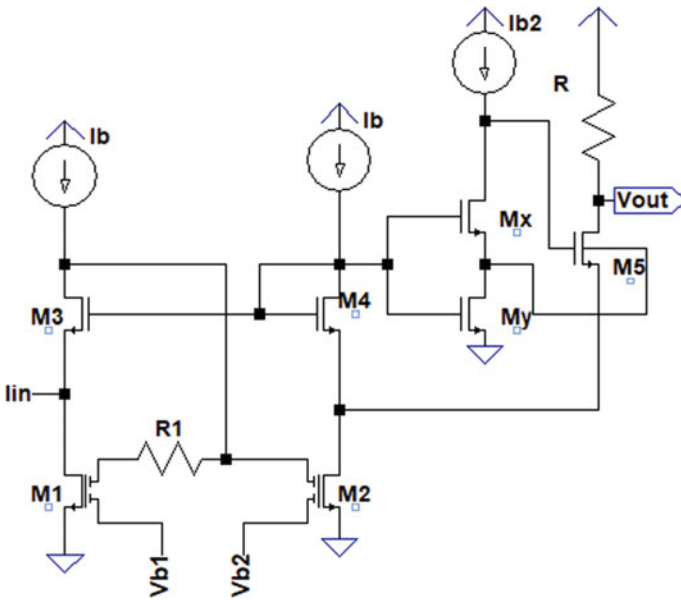
Fig. 3 Proposed current mirror using FGMOS

employs a FVF current sensor. Transistors M_1, M_2, M_3 are connected for this purpose. A self-cascode structure with transistors M_x, M_y is connected at the output end for high output impedance. As aspect ratio of M_x transistor is m times greater than M_y, self-cascode has gain of M. The output of self-cascode circuit is applied at the gate terminal of M_5 transistor; besides, M_5 is a bulk driven transistor which increases the transconductance g_{mb} as well as changes some parameters like output impedance and output voltage.
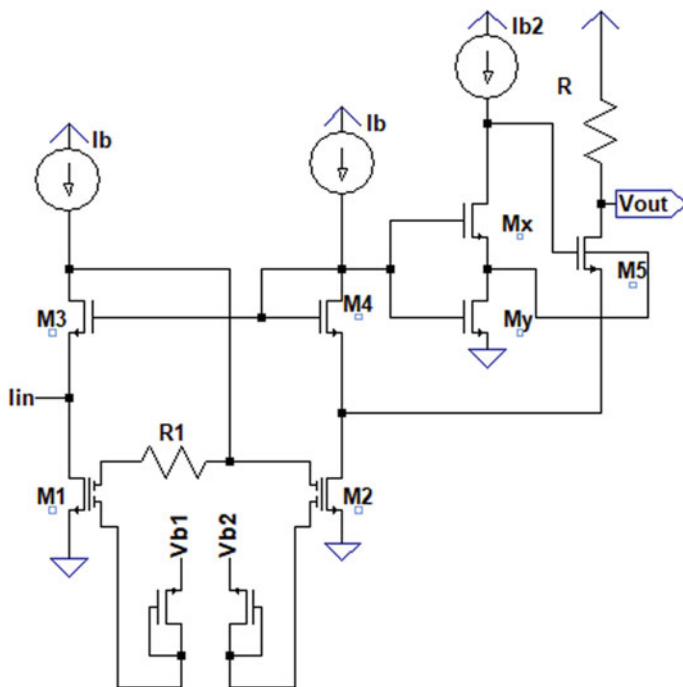
Fig. 4 Proposed current mirror using QFGMOS

Transistors M_1–M_4 are forming a high swing current mirror, in which M_1, M_2 transistors are FGMOS or QFGMOS. They reduce the power supply voltage to a very low level by adjusting bias voltage. Current sources I_{b1} and I_{b2} are for biasing of the high swing current mirror. The both biasing currents are kept same, so transistors M_4 and M_3 have same V_{ds} ($V_{ds4} = V_{ds3}$); hence, the channel length modulation is very less. It is evident from standard conventional equation that if $V_{ds} < V_{gs} - V_{th}$,, then transistor will be in linear region which causes the significant reduction in output resistance.

The speed of the current mirror bank on bandwidth. To increase the bandwidth, gate capacitance and transconductance of transistor should be reduced. Thus, resistive compensation technique [1] is applied in this circuit by connecting a resistor between gate terminals of the transistor making the current mirror. A pole and zero get introduced because of this technique in the transfer function of the current mirror. The dominant pole will be canceled with newly created zero by adjusting the value of compensating resistor. The proposed circuit shows significant improvement in bandwidth using this technique.

4　Simulation Results

The circuit presented here is implemented on SPICE with 180 nm TSMC BSIM3 and level 49 technology. All simulations have been carried out with the power supply of 0.65 V and load resistance of 1 kΩ. Biasing currents in circuit are $I_{b1} = I_{b2} = 15$ μA and $I_{b3} = 12.5$ μA and I_{in} is 15 μA. The aspect ratio of all transistors is given below in Table 1.

Figure 5a shows the output impedance of FGMOS current mirror. The observed value is around 37 GΩ. When same curve is plotted for QFGMOS-based current mirror, then it is noticed that output resistance increases further and reaches to 48 GΩ.

Figure 6 shows the plot current transfer ratio which is found similar for both types of current mirror. The input current is varied in the range of 1–500 μA, and the slope is close to unity which shows high performance of the proposed circuit.

Figure 7a and b represent the input resistance of the proposed FGMOS current mirror and QFGMOS current mirror which is quite low around 10.5 and 20.7 Ω, respectively.

Table 1 Aspect ratio of various transistors

Transistor	Aspect ratio (μm)
M_1	(55/0.54)
M_2	(55/0.54)
M_3	(5.5/0.27)
M_4	(5.5/0.27)
M_5	(36/0.18)
M_x	(0.9/0.18)
M_y	(0.55/0.35)
M_6	(0.25/0.25)
M_7	(0.25/0.25)
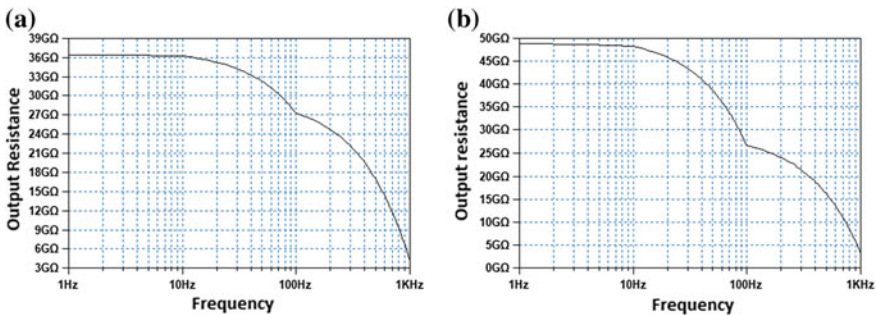
Fig. 5　a Output resistance with FGMOS current mirror, **b** output resistance with QFGMOS current mirror
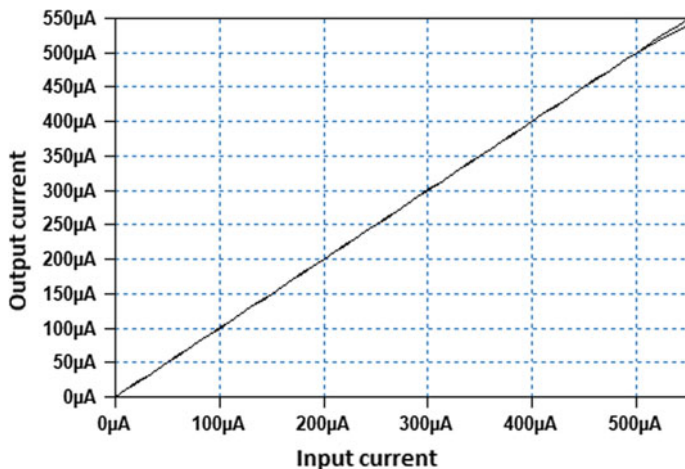
Fig. 6 DC response of proposed current mirror
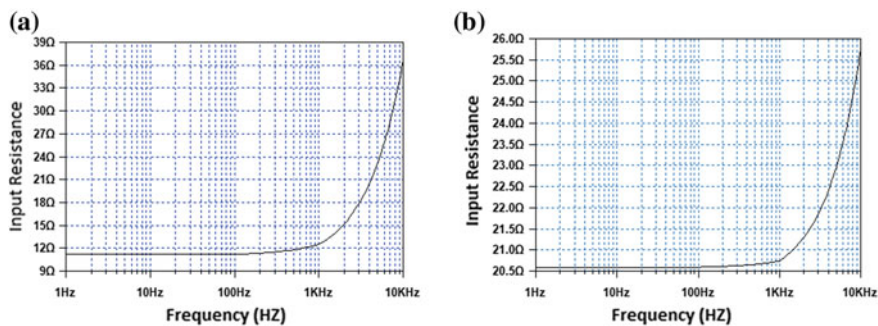
Fig. 7 **a** Input resistance with FGMOS current mirror, **b** input resistance with QFGMOS current mirror
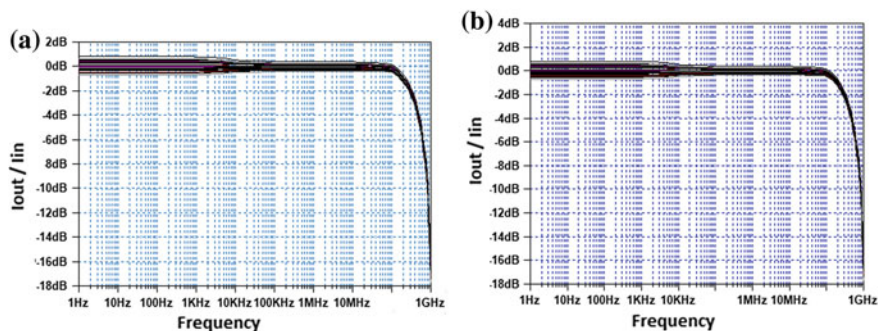
Fig. 8 **a** Monte Carlo analysis of bandwidth of FGMOS current mirror, **b** Monte Carlo analysis of bandwidth of QFGMOS current mirror
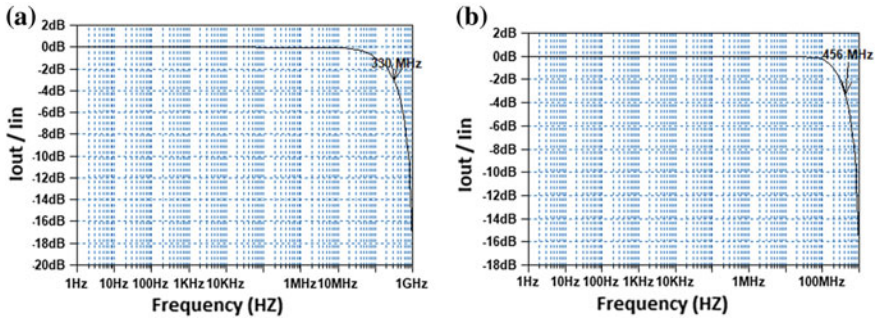
Fig. 9 a Bandwidth of the proposed circuit with FGMOS current mirror, **b** bandwidth of the proposed circuit with QFGMOS current mirror

Table 2 Performance comparison of the various conventional and proposed current mirror

Reference	[12]	[13]	FGMOS (cm) [1]	[14]	Proposed circuit with FGMOS	Proposed circuit with QFGMOS
Power supply	1.8	1.8	1	1	0.65	0.65
I_{in} (μA)	50	110	10	15	15	15
I_b (μA)	110	50	15	15	15	10
R_{in} (Ω)	0.75	0.012	8.5 k	13.3	10.8	20.7
R_{out} (Ω)	200 M	2.3 G	30 M	34.3 G	37 G	45 G
BW (MHz)	620	220	7.8	210	398	456
P (μW)	NA	NA	39.2	42.5	45.5	49

The Monte Carlo analysis for AC response of the proposed circuit has been illustrated in Fig. 8a and b. It is worth noting that results do not deviate more than ±10%.

The bandwidth of FGMOS circuit (Fig. 9a) is 330 MHz, and with QFGMOS circuit (Fig. 9b), the bandwidth has been increased up to 456 MHz.

To illustrate high performance of the proposed current mirror, a state of the art is included as Table 2. It is clear that output impedance and bandwidth are very high as compared to [1, 12–14].

5 Conclusion

In this paper, a low-voltage, low-power high output impedance-improved bandwidth current mirror using FGMOS and QFGMOS is presented. The proposed current mirror works with very low voltage, consumes less power, and also has bandwidth improvement. The simulation results with 0.65 V power supply shows

an improvement in the bandwidth. And the proposed circuits also have low input resistance and very high output resistance, the power consumption is 49 µW, and the current copying capability is also highly accurate. These results shows that these proposed current mirrors are good for low-power application, and the use of FGMOS and QFGMOS is a suitable way to improve the performance of current mirror.

References

1. Aggarwal B, Gupta M, Gupta AK (2016) A comparative study of various current mirror configurations: topologies and characteristics
2. Rajput SS, Jamuar SS (2002) Low voltage analog circuit design techniques. IEEE Circuits Syst Mag
3. Vittoz EA (1994) Analog VLSI signal processing: why, where, and how? Analog Integr Circuits Signal Process
4. Azhari S, Baghtash H, Monfaredi K (2011) A novel ultra-high compliance, high output impedance low power very accurate high performance current mirror. Microelectron J 42:432–439
5. Rodriguez-Villegas E (2006) Low power and low voltage circuit design with the FGMOS transistor
6. Bansal U, Gupta M (2018) High bandwidth transimpedance amplifier using FGMOS for low voltage operation. Integr VLSI J 60:153–159
7. Aggarwal B, Gupta M (2015) QFGMOS based very low voltage wide bandwidth high performance CMOS current mirror. In: 2015 annual IEEE India conference (INDICON)
8. Carvajal, Ramirez, Lopez-Martin, Torralba (2015) The flipped voltage follower: a useful cell for low voltage, low power circuit design. IEEE Trans Circuits Syst 52(7):1276–1291
9. Zhu Z, Mo J, Yang Y (2008) A low voltage bulk-driving NMOS cascade current mirror. In: 9th international conference on solid-state and integrated-circuit technology
10. Yani L, Yintang Y, Zhangming Z (2010) A novel low-voltage low-power bulk-driven cascade current mirror. In: Proceedings of the 3rd international conference on advanced computer theory and engineering (ICACTE), vol 3, Chengdu, pp 78–83
11. Srivastava R, Gupta M, Singh U (2015) Low voltage FGMOS squarer/divider-based analog building blocks. Int J Electron 102:4
12. Garimella A et al (2005) Low voltage high performance compact all cascode CMOS current mirror. Electron Lett 41(25):1359–1360
13. Sawant MS (2005) New compact implementation of a very high performance MOS current mirror. In: 48th midwest symposium on IEEE, circuits and systems, vol 1, pp 840–842
14. Bastan Y, Hamzehil E, Amiri P (2016) Output impedance improvement of a low voltage low power current mirror-based technique 56

Memory-Based FIR Digital Filter Using Modified OMS-LUT Design

Dhruv Sharma, Justin Johnson, Neeraj and Anirudh Sharma

Abstract In this paper, a modified optimization of look-up table (LUT) used in memory-based multipliers is used for the implementation of FIR digital filter. Modified odd multiple scheme (OMS) is being proposed for the implementation of FIR filter, and the comparison results have been carried out between the conventional multiplier-based FIR filter design and the modified OMS multiplier-based FIR filter design in which we see that the modified OMS multiplier-based FIR filter requires less memory in comparison to conventional multiplier-based FIR filter. The filter structure is simulated using Verilog code and implemented in Xilinx Virtex device, and its performance characteristics are discussed.

1 Introduction

Signal processing deals with analysis, synthesis, and modification of signals in which FIR digital filter is primarily used [1]. The filters of higher order play a very important role in many applications; hence, a number of techniques are devised and

D. Sharma · J. Johnson (✉) · Neeraj · A. Sharma
HMR Institute of Technology and Management, Delhi, India
e-mail: justinseena1@gmail.com

D. Sharma
e-mail: dhruv.0906@yahoo.in

Neeraj
e-mail: neerajkhola@gmail.com

A. Sharma
e-mail: anisharma71@gmail.com

developed for the real-time analysis of higher-order filters. Multiplication operation is a major arithmetic operation involved in signal processing, and the number of operations required in multiply-accumulate (MAC) increases with the increase in filter order; therefore, several attempts are being made to develop dedicated VLSI systems with low-complexity considerations for higher-order filters. The implementation of these circuits are done using sequential circuits. The design techniques used for the designing and implementation of high-speed and higher-order FIR filters is done in a very careful manner as the critical path computation time (CPCT) should not get affected by techniques devised.

The memory-based structures have become very popular due to the advancement in technology of VLSI. The main advantages of VLSI technology includes lower cost, smaller size, higher speed, and more ease of use which provides wide advantages to the system designers. By using this technique, we are able to take the advantage of VLSI memory technology and decrease the complexity of the design which in turn reduces the area of the system.

In this, the term memory-based systems have been used for memory elements like ROM or RAM [2]. Memory-based structures are more accurate and advantageous in comparison to MAC structures. It offers high throughput, reduced latency, and less dynamic power consumption, and also memory-based structures are best suited for many algorithms of digital signal processing as it involves multiplication with fixed set of coefficients. In this paper, a new modified approach of LUT design is proposed which is the OMS scheme that optimally uses the registers in the memory. The phrase LUT is used in synonymous to register in memory unit.

Conventional multiplier in Fig. 1 shows the basic principle of LUT-based multiplication. Let F be a fixed coefficient and input word be X which is multiplied with the fixed coefficient F. If X is a binary number (unsigned) whose word length is L, the possible values of X are 2^L and also possible values for product $P = F \cdot X$ will be 2^L. For the conventional multiplier analysis of memory-based implementation, a memory unit with 2^L words is required to be used as LUT which consists of precomputed values of products corresponding to all possible values of F [3].

The paper is organized as, in Sect. 2, conventional multiplier. In Sect. 3 which is divided into two subsections which deals with the proposed LUT-multiplier for 4-bit and its modified form for the 8-bit respectively. Section 4 gives the simulation results and the comparison for the conventional and the proposed technique, whereas in Sect. 5, the conclusions are presented.

Fig. 1 Conventional multiplier
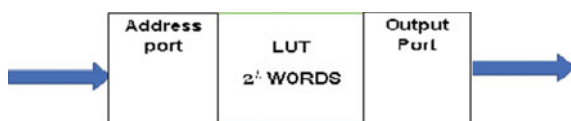
2   Modified OMS 8-Bit LUT Multiplier and Its Dual-Port Implementation

Many techniques have been devised for the memory-based computations; at first, an odd multiple storage scheme was proposed for an input of four bits; in this compilation, the modified odd multiple storage technique has been proposed for eight-bit input which is used in the proper implementation of proposed OMS-LUT multiplier, and also, its dual-port implementation is carried out for the memory-based realization of FIR filter.

Figure 2 shows the proposed modified LUT design for multiplication of a W-bit fixed coefficient F with the input. The proposed design which is based on the OMS scheme and only the odd multiples of the product terms are stored in the memory. The even multiples are derived from the odd terms using appropriate shifters. Thus, the required memory storage is reduced to half. All the other multiples of F are odd. This is illustrated in Table 2 at 127 memory locations, 127 odd multiples are stored and the even multiples are derived by the left shift operations. The address $A = (00000000)$ gives the product value $(F \cdot A) = 0$, which can be obtained by resetting the output. Based on the above illustration, an LUT is designed by the following strategies:

- Encoder is used for the mapping of L-bit input to $(L - 1)$-bit LUT address.
- A barrel shifter is required for producing $(L - 1)$ left shifts which derives all even multiples of F.
- Memory unit is used for the storage of odd multiples of F.
- The control bits are generated by the control circuit and fed to barrel shifter to perform necessary shifts of output.
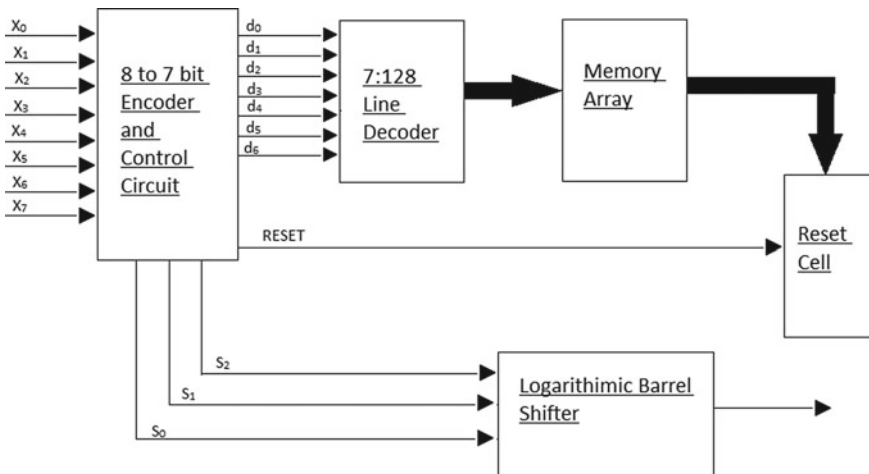
Fig. 2 Modified OMS-LUT multiplier (proposed) [4]

Table 1 shows the truth table for the OMS-LUT multiplier for eight-bit input (which shows only few input stages only); in this, we see that the maximum number of shifts required are seven; therefore, we can say that a three-stage logarithmic barrel shifter is used for the multiplier.

Figure 3 shows memory-based multiplier with dual-port which can perform multiplication of a fixed-bit coefficient with a 16-bit input using a memory with dual-port memory unit which consists of 16 words (or two single-port memory units) which also consists of a pair of barrel shifters, encoder, decoder, and NOR cells. In this, the left-shift operation is performed by shift adder which is the output produced by the barrel shifter corresponding to the most significant half of input and is added to the output generated by the other second barrel shifters.

Table 1 Product values and LUT words for $L = 8$

Word symbol	Value stored in memory	Input data of 8-bit	Product obtained	Shifts required
$P0$	F	00000001	F	0
		00000010	$F \times 2^1$	1
		00000100	$F \times 2^2$	2
		00001000	$F \times 2^3$	3
		00010000	$F \times 2^4$	4
		00100000	$F \times 2^5$	5
		01000000	$F \times 2^6$	6
		10000000	$F \times 2^7$	7
$P1$	$3F$	00000011	$3F$	0
		00000110	$3F \times 2^1$	1
		00001100	$3F \times 2^2$	2
		00011000	$3F \times 2^3$	3
		00110000	$3F \times 2^4$	4
		01100000	$3F \times 2^5$	5
		11000000	$3F \times 2^6$	6
$P2$	$5F$	00000101	$5F$	0
		00001010	$5F \times 2^1$	1
		00010100	$5F \times 2^2$	2
		00101000	$5F \times 2^3$	3
		01010000	$5F \times 2^4$	4
		10100000	$5F \times 2^5$	5
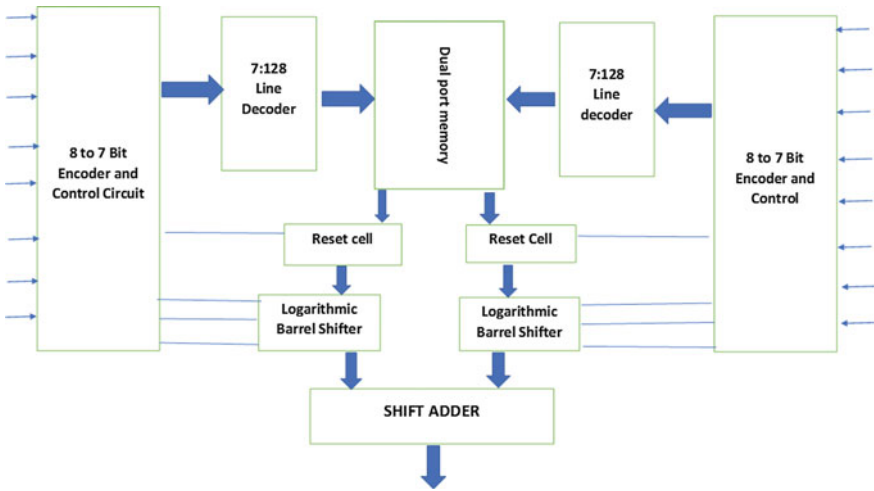
Fig. 3 Proposed OMS-LUT multiplier with dual-port memory [5]

3 Realization of FIR Filter (Memory-Based) LUT Design Using OMS Technique

The memory-based structure of FIR filter (for 16-bit input) using proposed LUT design is shown in figure. The design of FIR digital filter (for eight-bit input) with the implementation of proposed EMS-LUT design is depicted in Fig. 3a which is different from conventional design in two aspects:

- All N LUT multipliers uses same pair of adder words; therefore, instead of using N memory modules for N segments, only one memory module can be used which reduces the hardware complexity for two $(N - 1)$ decoder circuits which could be eliminated.
- Odd multiple storage is used in place of conventional design, so that multiplication using a dual-port memory segment could be implemented by $(2^{L/2})/2$ words in LUT.

Figure 4a, b, and c shows the structure of Nth order FIR filter using the proposed OMS-LUT multiplier for 16-bit input, its dual-port memory segment, and LUT multiplier-based FIR filter structure. As shown in the figure, the compiled representation of FIR filter has a dual-port segmented memory core, a delay register, and an array of N shift-add (SA) cells, $(N - 1)$ AS cells. The compiled figure consists of control circuits, a pair of 8-to-7-bit encoders and a pair of 7-to-128 line decoders to carry out the necessary control signals and word-select signals for the dual-port memory core (which consists $[128 \times (W + 8)] \times N$ array of bit-level is devised in 128 rows of $[(W + 8) \times N]$-bit width). The conventional multiplier structure for FIR filter uses more memory requirements as compared to the proposed design of FIR filter [6]. The comparison results for the two are given in Table 2.
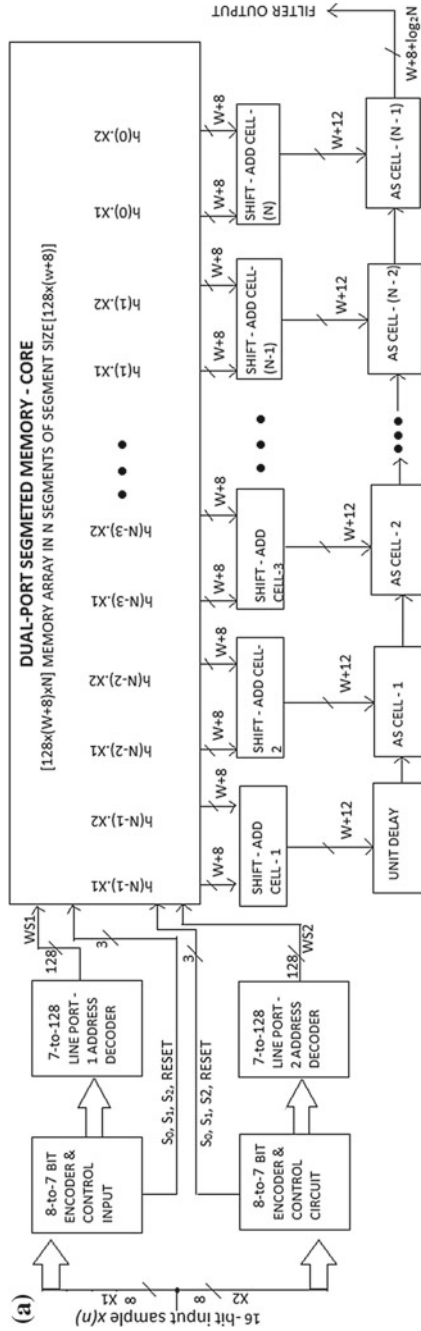
Fig. 4 **a** Structure of Nth order FIR filter using proposed OMS-LUT multiplier for 16-bit input. **b** Dual-port segmented memory core for Nth order filter. **c** LUT multiplier-based structure of an N-tap FIR filter by transposed form realization using segmented memory core using 16-bit input
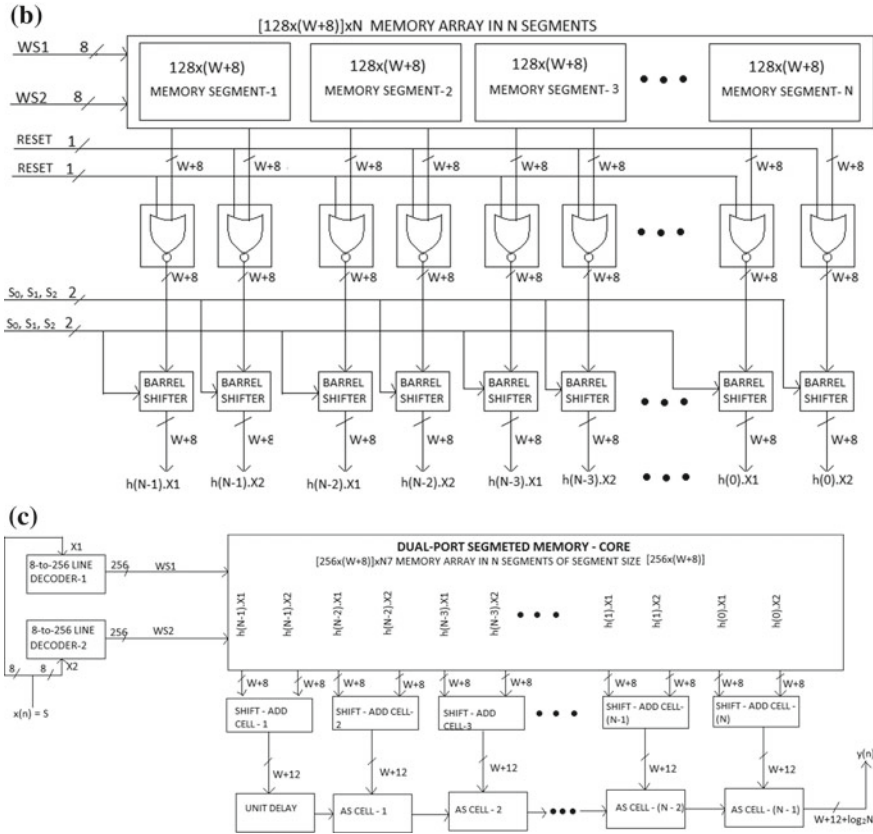
Fig. 4 (continued)

4 Result and Discussion

Digital filters play a very important role in the field of electrical and electronics engineering which includes various signal processing applications. In this paper, a memory-based FIR digital filter is designed using the modified OMS-LUT technique which requires less power requirements and lesser area which also reduces the complexity for higher-order and higher input systems. The transposed structure of filter is designed using the dual-port memory-based multiplier for OMS-LUT design. The simulations are carried out for the proposed work on Xilinx ISE Design Suite 14.5 and Altera Model-Sim 6.4a (Figs. 5 and 6).

Table 2 Comparison of FIR filter of order N with conventional design and modified OMS-LUT multiplier-based FIR filter with 16-bit input

Designs	Conventional LUT multiplier	LUT multiplier for address-length 16 based design
Memory	$[256 \times (W + 8) \times N]$-bit memory	$[128 \times (W + 8) \times N]$-bit memory
Decoders	2(8:256 decoders)	2(7:128 decoders)
Registers	49,224 (1-bit registers)	39,208(1-bit registers)
Throughput	1 per cycle	1 per cycle
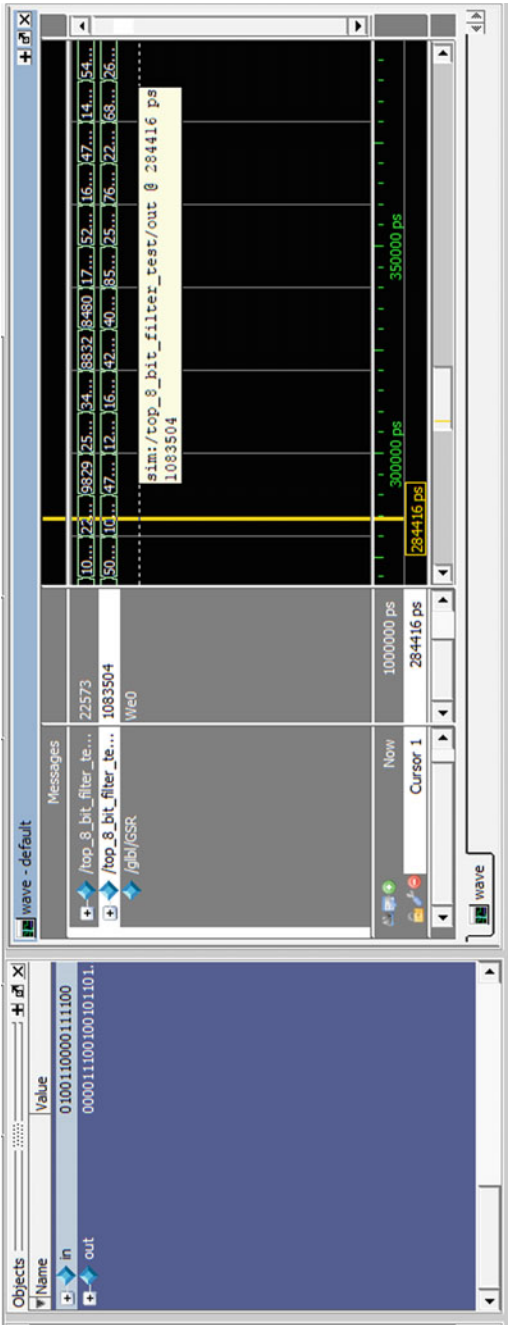
Fig. 5 Simulation result for transposed form FIR filter for 16-bit filter input using OMS-LUT multiplier using dual-port multiplier
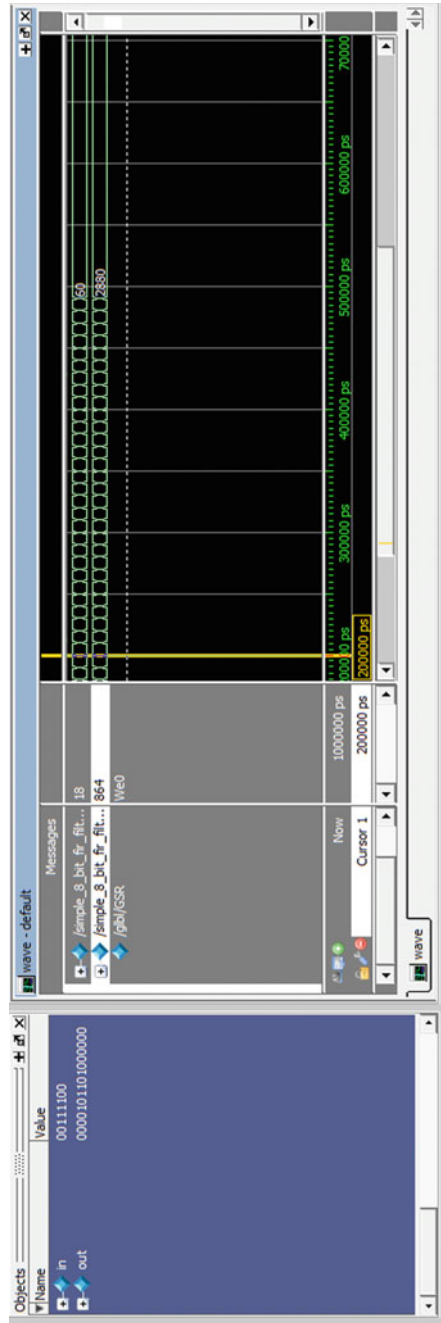
Fig. 6 Simulation result for conventional transposed form FIR filter for 16-bit filter input

5 Conclusion

In this paper, modified proposed OMS-LUT technique is presented which is used for the representation of memory-based multiplier which is further used in the implementation of digital FIR filter. Comparing the proposed filter design with the conventional design, we see that the memory requirement for the proposed design is less in comparison to the conventional design. The complexity for the higher-order and higher input is reduced by the usage of proposed FIR filter design. The proposed filter design can be used in many application of electrical and electronics.

References

1. Proakis JG, Manolakis DG (1996) Digital signal processing: principle algorithms and applications. Prentice-Hall, Upper Saddle River, NJ
2. Parhi KK (1999) VLSI digital signal processing systems: design and implementation. Wiley, New York
3. Meher PK (2010) New approach to Look-Up-Table design and memory-based realization of FIR digital filter. IEEE Trans Circuit Syst-1 57(3)
4. Meher PK, Senior member IEEE (2010) LUT optimization for memory-based computation. IEEE Trans Circuit Syst-2 57(04)
5. Sharma D, Vinitha CS, Kandari R, Neeraj, Modified OMS-LUT design for memory-based multiplication. In: IEEE proceedings, Computing for sustainable global development, Conference ID: 42835
6. Sharma D, Sharma S, Payal S, Vinitha CS A new pipelined memory-based FIR Filter. In: IEEE proceedings, computing for sustainable global development, Conference ID: 42835

Comparative Performance Analysis of Different High-Speed Buffer Drivers Using BiCMOS Technology and MVL Logic

Pankaj Kumar, V. Sulochana and Balwinder Singh

Abstract In complementary metal–oxide–semiconductor (CMOS) high-speed buffer design, leakage power dissipation, complex routing area, and low-power consumption are the most common challenges. To overcome these challenges, the BiCMOS technology and CMOS multi-valued logic (MVL) are used to maintain the yield and the performance of the high-speed buffers. In this paper, performance comparison of different types of buffers: Schmitt trigger, tristate and bidirectional buffer with BiCMOS and CMOS MVL logic are presented. Cadence virtuoso editor and ADE spectre simulator at gpdk 180 nm technology node are used for simulation setup. The results show that CMOS MVL logic delay, power dissipation, low and high noise margin are better than BiCMOS by 20, 43, 19, and 39%, respectively. Based on these results, CMOS MVL logic outperforms BiCMOS for low-power applications at comparable speed.

1 Introduction

In digital circuits, the buffer is the most prevailing element [1, 2]. It is vastly used for the reduction of delay, noise, and crosstalk and for signal cleaning. It also plays a very important role in the VLSI interconnect [1, 3]. In a logic gate design, the buffer drives large fan out so that it is capable to drive high current for high speed. The buffer can also restore the parasitic effected signal in placement and routing and

P. Kumar (✉) · V. Sulochana · B. Singh
Centre for Development of Advanced Computing (C-DAC), Mohali, India
e-mail: pankaj.kumar370@gmail.com

V. Sulochana
e-mail: vemus@cdac.in

B. Singh
e-mail: balwinder@cdac.in

maintain the performance of the chain of inverters. The buffer can be designed by cascading two inverter gates in which the output of the first inverter fed into the input of the second inverter. The two inversion functions of the circuit cancel each other, and the final output of the circuit is the same as the input. Important parameters of the buffer are the delay, power dissipation, and noise margin for analysis of the digital circuit. According to Moore's law, complementary metal–oxide–semiconductor (CMOS) transistor's size has been scaled down for high-speed buffer [2]. Due to the shrinking of CMOS transistor size, the problems like leakage current, power dissipation, and complex routing area get raised in high-speed buffer design. To reduce this problem and maintain the yield and performance of high-speed buffer by CMOS (multi-valued logic) MVL and BiCMOS technology. Nowadays, BiCMOS technology [4] is more significant, that integrate with bipolar and CMOS devices on a single chip area. In BiCMOS, the bipolar transistor increases the speed and the low power dissipation is maintained by the CMOS transistor. BiCMOS buffer gives the optimum system performance on VLSI constraints (speed, power, and area). This technology has secured the best position in fast switching speed, low power dissipation; high packing density, and large load drive capabilities.

A digital integrated circuit uses binary logic (0 or 1) switching activity as an input signal. Drawbacks of binary logic are routing (interconnection) and pin-out. Binary VLSI circuit uses approximately 70% of the area for routing, 20% to insulation, and 10% to devices [5]. Interconnect is consuming large area on a VLSI chip. The binary logic performance is limited due to complex routing. The effective solution of this drawback is higher radices multiple-valued logic (MVL) [6, 7]. CMOS MVL logic plays a very important role to overcome the more interconnect and pin-out problem, and it also decreases the noise margin, power consumption, and power dissipation. MVL logic has more than two inputs like zero, $V_{dd}/2$, and V_{dd}. MVL logic defines the inverter in a three-way positive ternary inverter (PTI), negative ternary inverter (NTI), and standard ternary inverter (STI) [8].

This paper proposes the Schmitt trigger buffer, tristate buffer, and bidirectional buffer circuit design using CMOS MVL Logic (ternary). The design of buffers using BiCMOS binary logic is performed in Sect. 2, and the design of buffers using CMOS MVL logic (ternary) is performed in Sect. 3. The simulation results and the comparison of parameters between BiCMOS binary logic and CMOS MVL logic (ternary) are provided in Sect. 4, and finally, the conclusion is provided in Sect. 5.

2 Buffering in BiCMOS Environment

In this work, the three types of buffer circuits are designed using a BiCMOS technology: BiCMOS buffer, Schmitt trigger buffer, tristate buffer, and bidirectional buffer.

2.1 BiCMOS Buffer

In IC design, BiCMOS technology [9] is very useful. Many researchers have worked on BiCMOS circuit design. Most important parameters of BiCMOS circuit design are power, delay, overshoot, and power delay product. BiCMOS circuit design mainly focuses on low-power circuit design. The circuit operation of Fig. 1 describes as following the transistor Q1 is ON when supply input voltage is "low" because of that V_{out} is logic high "1", then the N3 transistor is ON, and Q2 is OFF and capacitor C1 gets start charging. When the input voltage equals to V_{dd}, the transistor Q1 is OFF and N3 is also OFF. Consequently, transistor Q2 is ON, V_{out} is logic "0", and capacitor C1 gets start discharging.

As shown in Fig. 2, the buffer can be designed by cascading two BiCMOS inverter gates in which the output of the BiCMOS first inverter fed into the input of the second BiCMOS inverter [10]. The two inversion functions of the circuit cancel each other, the final output of the circuit is same as the input, and a capacitor C1 has connected to the output V_{out}. Charging and discharging of capacitor C1 depend on the input voltage Vin.
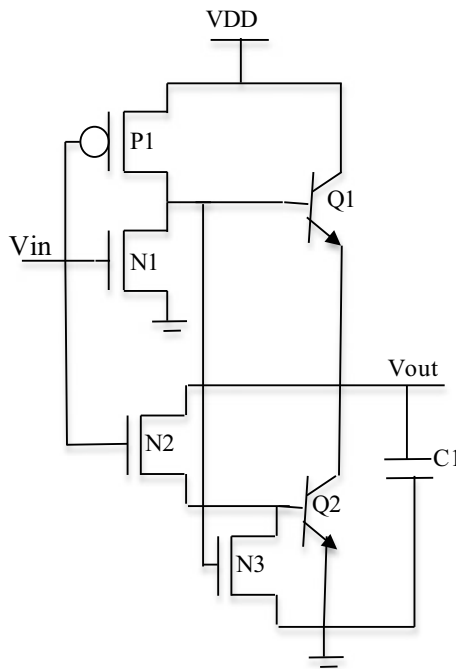
Fig. 1 BiCMOS inverter

Fig. 2 BiCMOS buffer
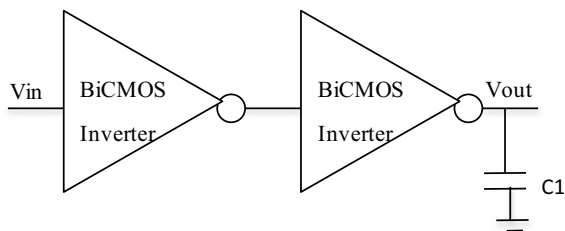
2.2   BiCMOS Schmitt Trigger

In digital circuits, Schmitt trigger [11] circuit is a very useful device. The characteristic of Schmitt trigger depends on positive-going and negative-going threshold. The difference between these characteristics is called hysteresis. Schmitt circuit is used as an effective device to reshape input signals and to minimize the power dissipation, power, and delay.

As shown in Fig. 3, Schmitt trigger is composed of two CMOS inverter and BiCMOS inverter. The second part of Schmitt trigger is work as a latch circuit. The BiCMOS Schmitt trigger circuit operation when the input voltage V_{in} is low, the transistor Q1 is ON and the output V_{out} goes to high, so capacitor C1 is charging. Due to the input voltage V_{in} is high, the transistor Q2 is ON, Q1 is OFF, and the output V_{out} goes to low, so capacitor C1 is discharging. As shown in Fig. 4, the buffer can be designed such as a Fig. 2.

2.3   Tristate Buffer

BiCMOS tristate buffer [12, 13] is composed of three parts: the first part is controlling signal circuit which provides the input signal. As shown in Fig. 5, transistors P1 and N1 are inverting the signal of the input voltage V_{in}. Transistors P4 and N3 are inverting the signal of the control signal (enable/disable). Pass transistors N2 and P2 are used between input and output when the control signal is disabled. These two inverters are controlling the pass transistor. When transistor P3 is turned on, P5 is turn off and N5 is turned on, and similarly, when N4 is turned off, P6 is turned on and N6 is turned off. These two inverters are controlling the pass transistor. When transistor P3 is turned on, the P5 is turned off and N5 is turned on, and similarly, when N4 is turn off, P6 is turned on and N6 is turned off.

When the control signal is disabled, transistors N5 and N6 will be turned on. Due to this effect, the base of BJT transistor NPN Q1 has a low switching effect and NPN Q2 has high switching effect. When a control signal is enabled, transistors P3 and N4 will turn off. Driving is the second part of the tristate buffer circuit diagram. MOS transistors P5, N5, P6, N6, P6, and BJT transistors Q1, Q2 are driving transistors. Transistor Q1 is ON when the N6 transistor is ON, and Q2 is off when
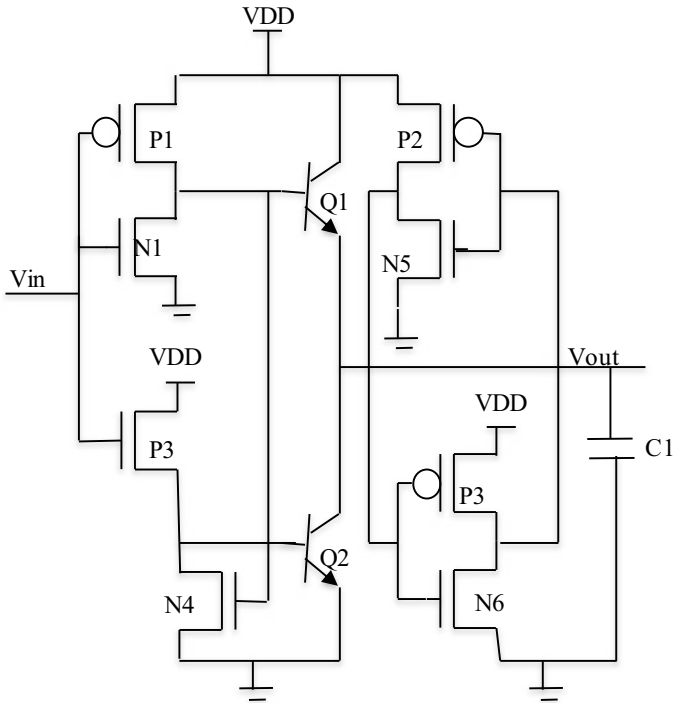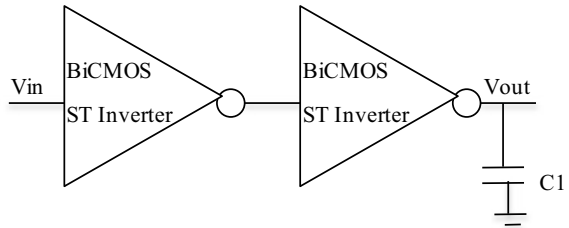
Fig. 3 BiCMOS Schmitt trigger

Fig. 4 BiCMOS Schmitt trigger buffer

the P6 transistor is turned on. N5 and P6 have used for discharge the storage charge when bipolar transistor is turn off. Transistors Q1 and Q2 have large capabilities to drive large capacitive load and a high-speed output circuit. The third part of the tristate buffer circuit diagram is to obtain the output voltage to a full swing on high (V_{dd}) to low (gnd) power supply. Transistors N7, P7, N8, P8, N9, P9 are used to driving the output voltage. When the control signal is high, then output voltage is low, and when the control signal is low, then output voltage V_{out} will depend on input voltage V_{in}.
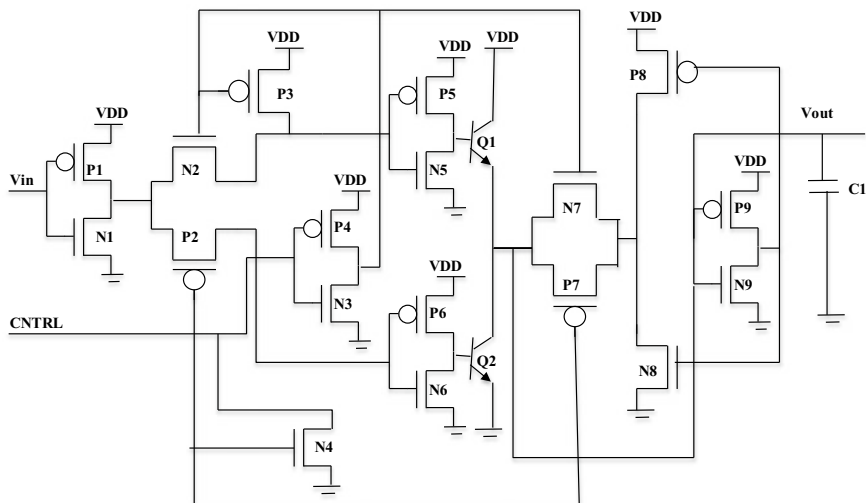
Fig. 5 BiCMOS tristate buffer

2.4   BiCMOS Bidirectional Buffer

In Fig. 6, bidirectional buffer [3, 14, 15] consists of BiCMOS tristate buffer and BiCMOS inverter. Bidirectional buffer is connected to BiCMOS tristate buffers back to back. The application of bidirectional buffer is to amplify a signal for the programmable logic device in both direction, and it is also used in bus transceiver. Due to the control signal is high (logic 1), direction of the bidirectional buffer is A to B via buffer 1, and due to the control signal, control is low (logic 0) and the bidirectional buffer is B to A via buffer 2. The control signal direction of bi-directional buffer.

3   Buffering in MVL Environment

MVL (ternary) logic defines the inverter in a three-way positive ternary inverter (PTI), negative ternary inverter (NTI), and standard ternary inverter (STI). In this paper, standard ternary inverter (STI) is used for designing of buffers.

3.1   MVL Buffer

As shown in Fig. 7, the design of the simple ternary inverter (STI) is composed of transmission gate and inverter. The output of inverter is connected to the
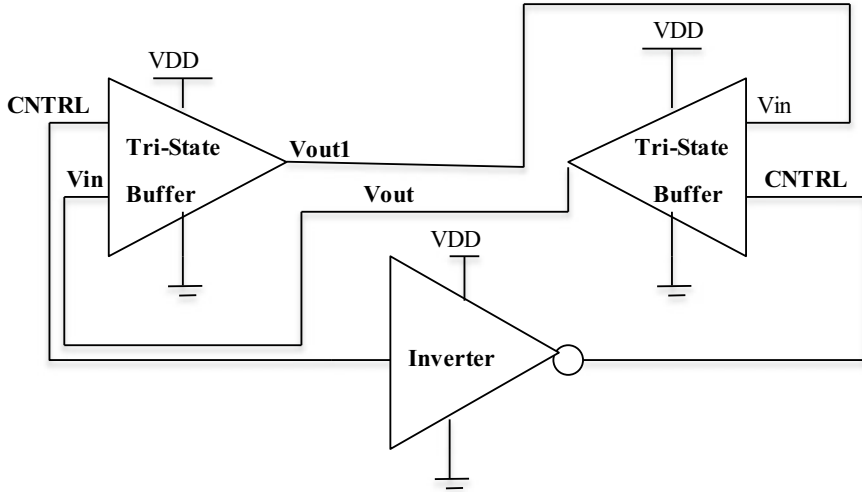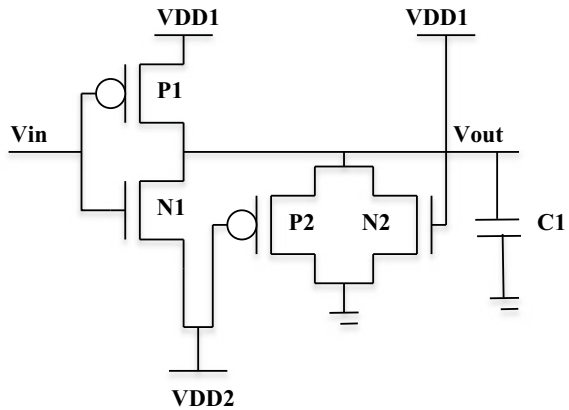
Fig. 6 Design BiCMOS bidirectional buffer

Fig. 7 Design of inverter with MVL logic

transmission gate. The transmission gate transistor PMOS P2 is connected to the negative voltage, and transistor NMOS N2 is connected to positive voltage. According to Mouftah and Garba [16], the resistance of channels is varying when the PMOS and NMOS channel length-to-width ratio will be varying. The transistor's resistance is proportional to L/W ratio. The voltages V_{dd1} and V_{dd2} are power supply positive (+ve) and negative (−ve) voltage. When the input voltage V_{in} is "−1" V, transistor (Fig. 8) P1 will be ON and N2 will be OFF. So, there is no current flow in the transmission gate, and consequently, the output voltage V_{out} goes down to logic "1"; when the input voltage V_{in} is 0 V ($V_{dd}/2$ level), transistor P1 and N1 will be in cut-off region. As a result, V_{out} will be logic 1, and the transmission
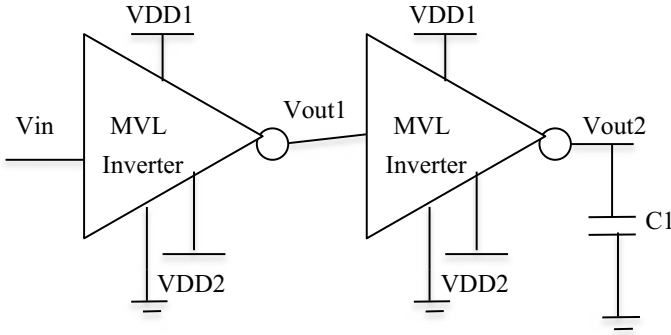
Fig. 8 Design of buffer with MVL logic

gate aids in dragging up a control signal. When input voltage V_{in} is 1 V, transistor P1 will be OFF and N1 will be ON. As a result, V_{out} will be logic "−1". Hence, no current flows in the transmission gate and consequently the output voltage V_{out} go down to logic "0".

3.2 MVL Schmitt Trigger Buffer

Figure 9 shows the voltages V_{dd1} and V_{dd2} are power supply positive and negative voltage. When the voltage V_{in} is "−1", then NMOS N1 and N2 are OFF and the PMOS P1 and P2 are ON in the linear mode of operation, output voltage V_{out} is equal to logic "1", and capacitor C1 gets start charging. Transistor N3 is ON (its drain and gate have the same voltage of V_{dd}), but it also does not carry any current. So, there are no current flows in the transmission gate, and therefore, the output voltage V_{out} goes down to logic "1". When the input voltage V_{in} is logic "1" high, then PMOS P1 and P2 are OFF and the NMOS N1 and N2 are ON and start conducting. Transistor M3 is turned off due to low voltage on the gate. However, the output voltage V_{out} is low voltage, and then, capacitor C1 gets start to discharge. Hence, Schmitt trigger inverters and MVL Schmitt trigger buffer are designed as shown in Fig. 10.

3.3 MVL Tristate Buffer

Figure 11 shows the voltages V_{dd1} and V_{dd2} are power supply positive (+ve) and negative (−ve) voltage. During the control signal, control is low logic "−1"; then output V_{out} is the inverted input signal. During the control signal, control is low logic "0" ($V_{dd}/2$ level), so transistors P3 and N2 will be in cut-off region. As a
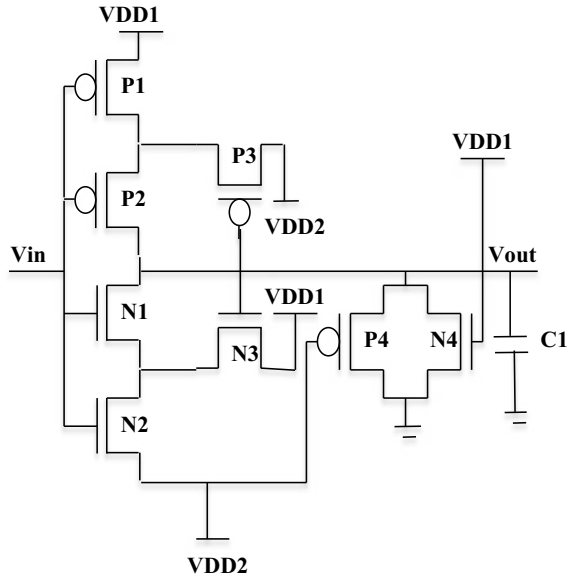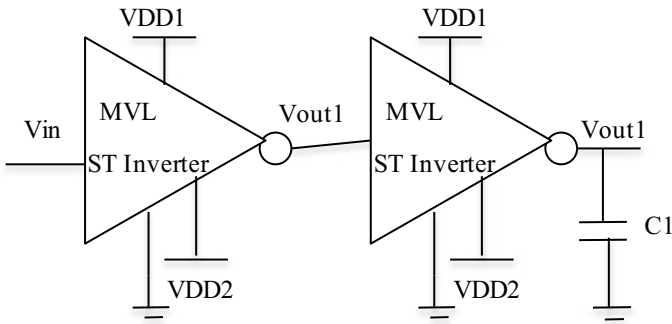
Fig. 9 Schmitt trigger with MVL logic

Fig. 10 Schmitt trigger buffer with MVL logic

result, V_{out} will be logic 1. The transmission gate aids in dragging up a control signal. During the control signal, control is high logic "1"; then output V_{out} disconnected to the input signal, so there is no current flow in the transmission gate, and consequently, the output voltage V_{out} goes down to logic "1". By cascading the two MVL tristate inverters, the MVL tristate buffer is designed as shown in Fig. 12.
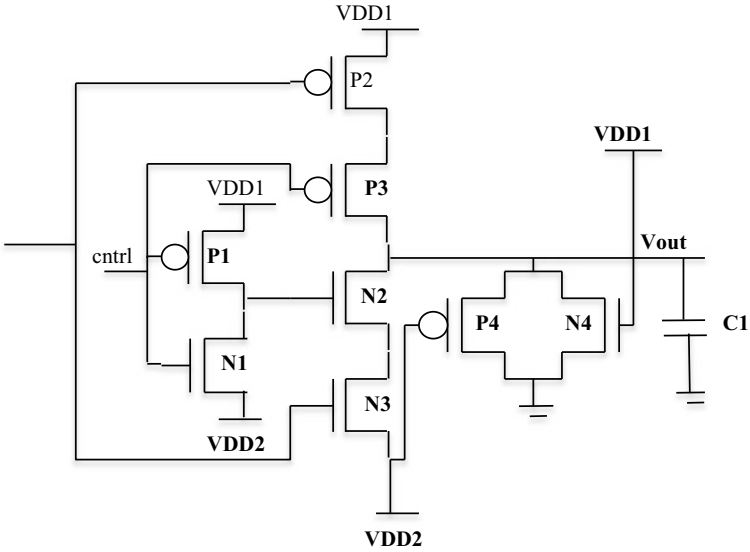
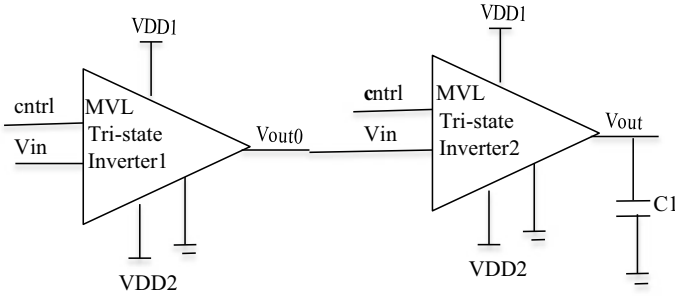**Fig. 11** Design of tristate inverter with MVL logic

Fig. 12 Design of tristate buffer with MVL logic

3.4 *MVL Bidirectional Buffer*

As shown in Fig. 13, the bidirectional buffer is made by connecting two MVL tristate buffer with MVL inverter. The output V_{out1} of tristate buffer 1 is connected to input V_{in} of tristate buffer 2. The control signal of both tristate buffers is connected to MVL inverter. The control signal of MVL buffer 1 is connected to input of MVL inverter, and the control signal of MVL buffer 2 is connected to output of MVL inverter. When the control signal is turn high (logic 1), then the direction of a bidirectional buffer is A to B through tristate buffer 2 and vice versa.
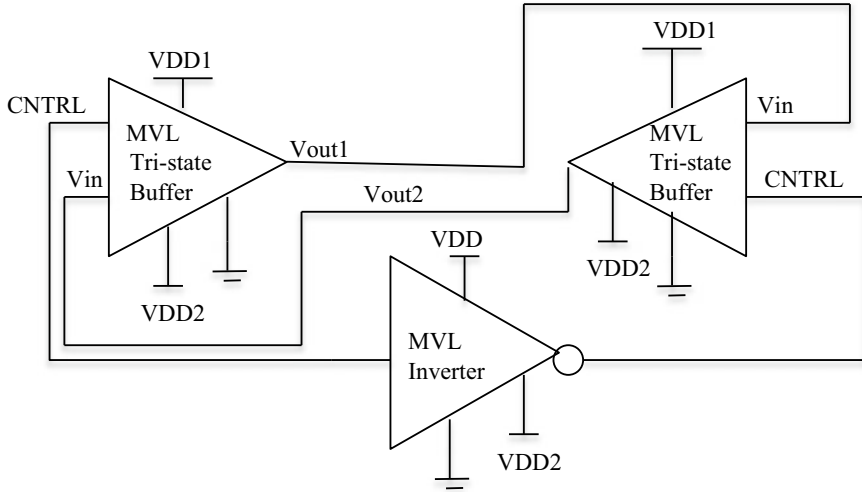
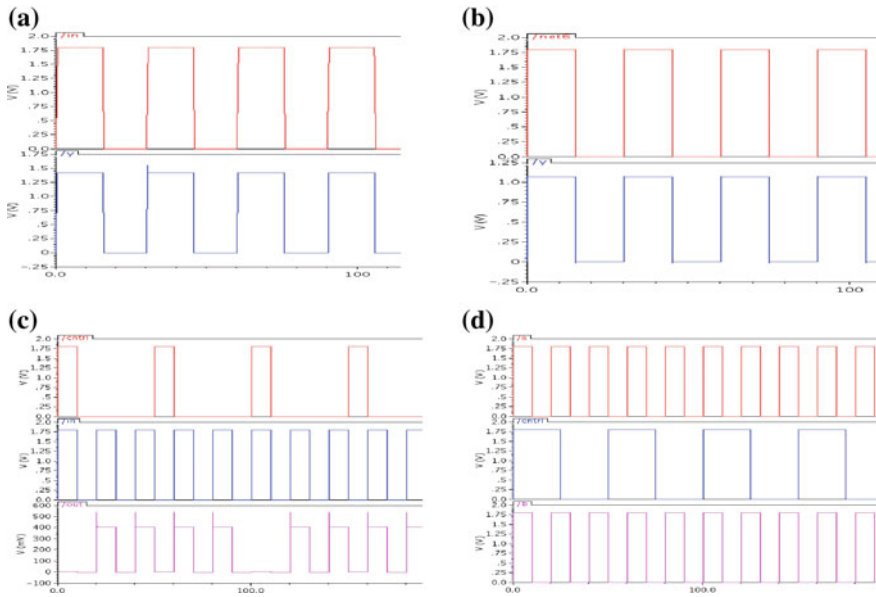**Fig. 13** Design of bidirectional buffer with MVL logic

Fig. 14 Simulation results of **a** BiCMOS buffers, **b** BiCMOS Schmitt trigger buffer, **c** BiCMOS tristate buffer, **d** BiCMOS bidirectional buffer

4 Simulation Results

The result section examines the operation and performance of different buffers on different technologies. The schematic design and verification of all buffers have been done on the Cadence Virtuoso Schematic Editor and ADE simulation tools with gpdk 180 nm technology at 1.8 V supply voltage, respectively. The performance of BiCMOS buffers based on binary logic input and CMOS buffer based on MVL logic input is compared using delay, power dissipation, and noise margin. Figure 14 shows simulation results of BiCMOS buffers, BiCMOS Schmitt trigger buffer, BiCMOS tristate buffer, BiCMOS bidirectional buffer, and Fig. 15 shows the simulation results of CMOS buffer with MVL Logic, CMOS Schmitt trigger buffer with MVL logic, CMOS tristate buffer with MVL logic, and CMOS bidirectional buffer with MVL logic. The load capacitance is connected to the output circuit for a better simulation result. Simulation results of Tables 1 and 2 show that the CMOS MVL logic delay, power dissipation, low and high noise margin are
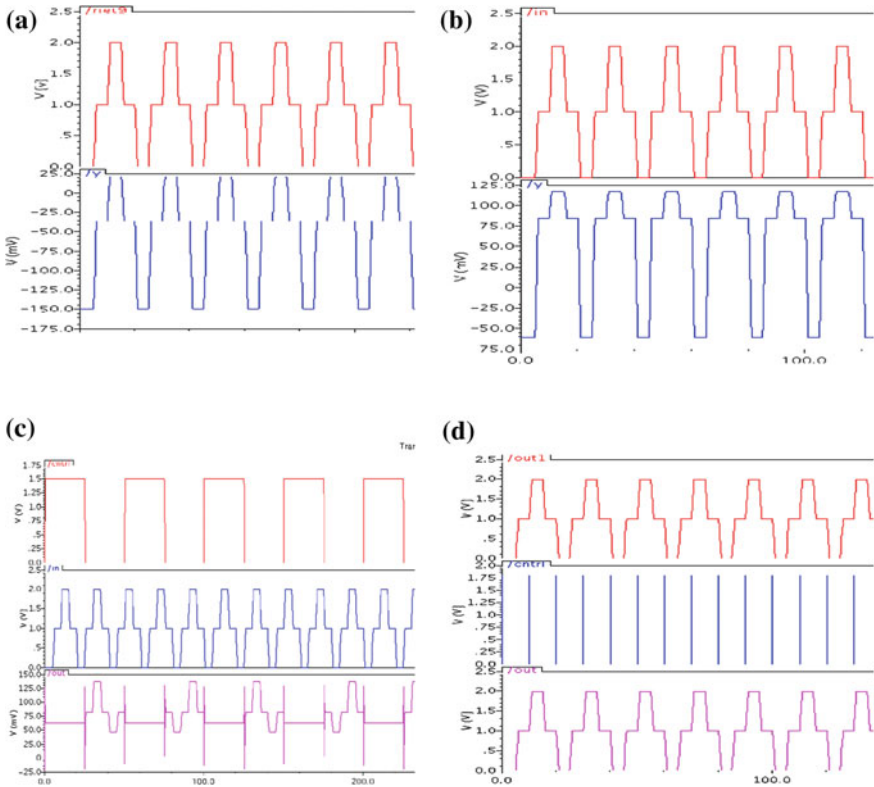

Fig. 15 Simulation results of **a** CMOS buffer with MVL logic, **b** CMOS Schmitt trigger buffer with MVL logic, **c** CMOS tristate buffer with MVL logic, **d** CMOS bidirectional buffer with MVL logic

Table 1 Comparison of BiCMOS technology buffers using parameters like power dissipation (PD), propagation delay, power consumption, and noise margin

Circuit	Wp/L (u)	Wn/L (u)	PD (W)	Power (W)	C_L (pf)	Noise margin	
						NM_L	NM_H
BiCMOS buffer	4/0.18	2/0.18	143.3×10^{-6}	185.9×10^{-9}	1	0.73	0.55
BiCMOS Schmitt trigger buffer	4/0.18	2/0.18	1.814×10^{-3}	2.11×10^{-3}	1	0.72	0.2
BiCMOS tristate buffer	18/0.18	2/0.18	2.015×10^{-3}	217.3×10^{-3}	1	0.9	−0.75
BiCMOS bidirectional buffer	4/0.18	2/0.18	351.9×10^{-3}	26.56	1	0.025	0.05

Table 2 Comparison CMOS MVL logic buffers using parameters like power dissipation (PD), noise margin, power consumption, and propagation delay

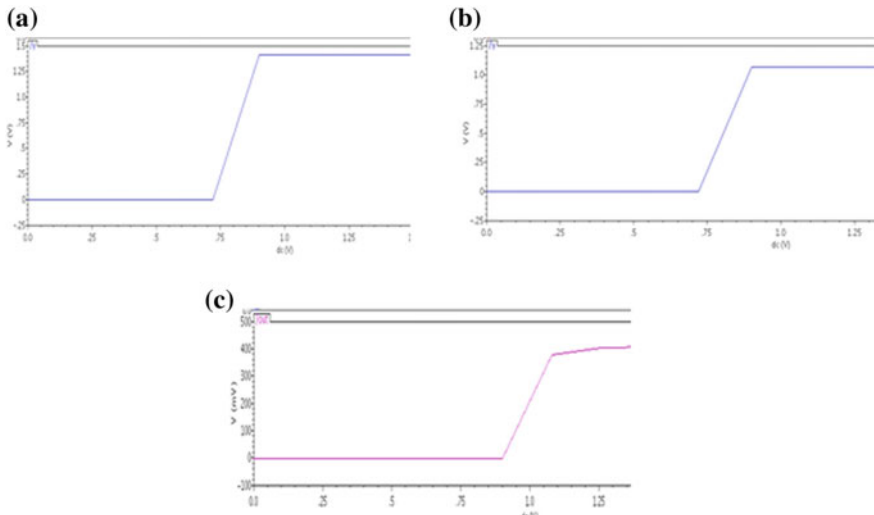| Circuit	Wp/L (u)	Wn/L (u)	PD (mW)	Power (mW)	C_L (pf)	Noise margin	
						NM_L	NM_H
MVL buffer	4/0.18	2/0.18	14.01	15.7	1	0.15	−1.77
MVL Schmitt trigger buffer	2/0.18	2/0.18	7.366	7.192	1	0.06	−1.63
MVL tristate buffer	18/0.18	2/0.18	89.27	55.84	1	0.38	−0.66
MVL bidirectional buffer	18/0.18	2/0.18	39.91	47.33	1	0.5	−0.2

Fig. 16 Voltage transfer characteristics of **a** BiCMOS buffer, **b** BiCMOS Schmitt trigger buffer, **c** BiCMOS tristate buffer

better than BiCMOS by 20.86, 43, 19, and 39.08%, respectively. Therefore, CMOS MVL logic is consumed low power, small area, and less power dissipation and has good noise margin. Figure 16 shows the voltage transfer characteristics of BiCMOS buffer, BiCMOS Schmitt trigger buffer, and BiCMOS tristate buffer.

5   Conclusion

In this work, different buffers such as conventional buffer, Schmitt trigger, tristate and bidirectional buffers are designed with BiCMOS and CMOS MVL logic technology, and comparative performance analysis is presented. Based on the results, CMOS MVL-based buffers exhibit power dissipation, low and high noise margins superior to BiCMOS-based designs by 20, 43, 19, and 39%, respectively. Therefore, CMOS MVL logic consumes low power, small area and has good noise margin. Hence, CMOS MVL-based buffers are the better choices for faster low-power dissipation applications at comparable speeds of BiCMOS-based buffers.

References

1. Saini S, Mahesh Kumar A, Veeramachaneni S, Srinivas MB (2010) An alternative approach to buffer insertion for delay and power reduction in VLSI interconnects. In: 23rd international conference on VLSI design, IEEE
2. Mariyamol PP, Aswathy N (2016) CMOS buffer design approach for low power and lower delay SRAM design. In: Recent advancement and effectual researchers in engineering, science and technology, vol 25. Elsevier, New York, pp 481–488
3. Kaur D, Sulochana V (2013) Crosstalk minimization for coupled RLC interconnects using bidirectional buffer and shield insertion. Int J VLSI Des Commun Syst (VLSICS) 4
4. Elrabaa MS, Elmasry MI (1992) Design and optimization of buffer chains and logic circuits in a BICMOS environment. In: IEEE journal of solid-state circuits, vol 27. IEEE, New York, pp 792–801
5. Butler JT (1991) Multiple-valued logic in VLSI. In: IEEE computer society press technology series. IEEE, New York
6. Wu XW (1990) CMOS ternary logic circuits. In: IEE proceedings, vol 137. IEEE
7. WU CY, Huang HY (1993) Design and application of pipelined dynamic CMOS ternary logic and simple ternary differential logic. In: IEEE journal of solid-state circuits, vol 28. IEEE, New York, pp 895–906
8. Wu X, Prosser F (1991) CMOS design of ternary arithmetic devices. In: Journal of computer science and technology, vol 6. Springer, Berlin, pp 376–382
9. Zhang S, Kalkur TS, Lee S, Chen D (1994) Analysis of the switching speed of BICMOS buffer under high current. In: IEEE journal of solid-state circuits, vol 29. IEEE, New York, pp 787–796
10. Ghorbannia Delavar A, Navi K, Hashemipour O (2007) High-speed full swing current mode BICMOS logical operators. IJE Trans 20:211–220
11. Wang C-S, Yuan S-Y, Kuo S-Y (1997) Full-swing BiCMOS Schmitt trigger. In: IEE proceedings on circuits devices and systems, vol 144. IEEE, New York, pp 303–308

12. Kuo JB, Liao HJ (1993) A high-speed BiCMOS tristate buffer. In: IEEE transactions on circuits and systems-11, vol 40. IEEE, pp 440–443
13. Suriyaamnznranorz C, Dejhtm K, Cheevusuvit F (1999) A high-speed BICMOS tristate buffer circuit. In: The 6th IEEE international conference on electronics, circuits and systems, proceedings of ICECS, IEEE, New York
14. Huang H-Y, Pu R-I (2011) Differential bidirectional transceiver for on-chip long wires. Microelectron J 42:1208–1215
15. Sim J-Y, Sohn Y-S, Heo S-C, Park H-J, Cho S-I (1999) A 1-Gb/s bidirectional I/O buffer using the current-mode scheme. In: IEEE journal of solid-state circuits, vol 34. IEEE, New York, pp 529–535
16. Mouftah HT, Garba AI (1984) VLSI implementation of a 5-trit full adder. In: IEE proceedings, vol 131. IEEE, New York, pp 214–220

On the Electro-Optic Couple Systems of Quantum Station for Quantum Communication Based on Phase Shift Scheme

Vineet Kumar

Abstract Like any other ordinary functions to which the calculus approach of different, for instance differentiation and integration, can apply, the function for a particle term as wave function in similar manner can also be subjected by the different dynamical variables as well that may be either continuous or discrete to gives the information. Using this particle, here as optical one, the concern for confidential communication from past can be resolved as they satisfy the property of non-clonable. Here with in this paper based on the phase shifting scheme for optical pulses, different types of electro-optic system (*EOS*) are discussed, which is essential for the quantum communication. These electro-optic couple systems for both Alice and Bob led to the establishment of quantum station at each, connected by optical fibre links, responsible for generation, controlling, measurement and detection. By the required process of all, the quantum communication which takes place in between the different stations even in the presence of active eavesdropper is secured, as any of its interfere get likely detected by channels of legitimate users.

Keywords Complex exponential function · Light function · Optical fibre link · Quantum channel · Quantum communication · Quantum message · Quantum station

1 Introduction

In accordance with paper [1] by Bennett and Brassard in 1984, it is taken for grant that digital communication in case of conventional information theory and cryptography can always be monitored and copied; therefore, to get rid of this insecure

V. Kumar (✉)
Department of Electrical Engineering,
Kurukshetra University, Kurukshetra 136119, India
e-mail: vineet05k@gmail.com

communication, the transmission must be based on the non-cloning approach that which cannot be monitored and copied. The approach of such non-cloning, on quantum ground, introduce by Wootters and Zurek in 1982 in his paper 'A single quantum cannot be cloned' [2], according to which, no apparatus exists which will amplify an arbitrary polarization.

With the exchange of quantum messages along with obeying of non-clone theorem, the two participants can communicate securely even in the presence of eavesdropper as the attempting of it get likely detected by users, such mode of non-conventional communication here regard as quantum communication. The resource for classical information is bit, i.e. 0 and 1, where the quantum information involves qubit, i.e. in between 0 and 1, with infinite options [3].

The structure of this paper is as follows. It begins with the introduction in Sect. 1 and then followed on by the description of quantum communication in Sect. 2. In Sect. 3, the proposal for the consideration of two quantum stations, which are identical, one for each both Alice and Bob, is made in connection with two-quantum channel to it so that the case of bilateral condition can meet. Next in Sect. 4, the *EOS* of different require for optical pulses for the case of generation, controlling, modulation and detection discussed along with the principle of operation in Sect. 5. Finally, the paper ends with discussion in Sect. 6. Other than equations, in this paper, the numbers of architectures[1] are also used. For the case of representation as types of a given system, the number of trees is also introduced.

2 Quantum Communication

Begin with Auguste Kerckhoff's principle for cryptosystem of 1883, keeping secret of the algorithm does not guarantee for the security, whereas keeping secret of the key does guarantee for the security of same for long [4]. It means, with the resource of proper computation, the encryption and decryption algorithm(s) can be known but the only thing stands long of all is the generated key. Thus, the reliability of the communication system security highly depends upon the security of the key other than the security of the algorithm.

$$Reliability_{\substack{system \\ security}} (algorithm\, secret) < Reliability_{\substack{system \\ security}} (key\, secret)$$

---

[1]The architecture concept used in paper Open Voltage of 2-Port Network Power Line Not Always Longer than Close Voltage, IEEE Xplore, pp. 494–502, 30 October 2017; https://doi.org/10.1109/icstm.2017.8089210; using abbreviations for different as required and/or with mathematical notations of any. This architecture is a way to represent the statement of purpose in simplified manner for better understanding the concept.

Keeping in mind the importance of security of key for a cryptosystem, the following points are mentioned below under *OTP* (or one time pad) scheme introduce by Vernam and Mauborgne [5] in 1926.

- Key must be random
- Key must be non-repeating
- Key must be as long as the message
- Key must be discarded once use.

These conditions can be hold up, by now, by the quantum system only other than the classical system due to the difficulty in process of monitoring and copying.

3   Quantum Stations for Confidential Communication

Message transmission in between the two stations either unilateral or bilateral, here bilaterally, is secured only when the confidentiality remains intact. Based on *OTP* scheme, by using of quantum messenger due to the non-cloning of it, the objective of such confidential transmission can meet. Using the weak coherent optical pulse as messenger through optical fibre link denote by *OFL* regard as quantum channel, one can communicate safely. The quantum channel so consider for communication is the material medium that allows light to propagate through it with conservation of variables. Here, as per requirement as quantum channel two optical fibre links OFL_A and OFL_B are considered for the connectivity in between two locations shown in Fig. 1. The two locations where the operations of different on light quanta like generation, controller, detection and modulation (*GCDM*) can perform are regard as quantum station denote by *QS*. For the quantum communication in between Alice and Bob, bilaterally, the *GCDM* operations must need to take place at both quantum stations QS_1 and QS_2, respectively. Each of the *GCDM* operation on light quanta is done by unique *EOS*, later to be discussed in Sect. 4, coupled to each other in peculiar manner to determine electro-optic couple system.

The principal methods by which the information can encode into the optical pulse are polarization-coded quantum states $(or\ PO - CQS)$ in which each bit of information is code at photon level by given polarization state- and phase-coded quantum states $(or\ PH - CQS)$ in which each bit of information is code through an optical path difference. Out of which two $PO - CQS$ face hurdle due to the lack of polarization conservation over long distance [6–8].

Here $PH - CQS$ method employs for each quantum channel for the quantum communication bilaterally. The two pairs of light quanta travel through each OFL_A and OFL_B are given by P_1^1/P_1^2 and P_2^1/P_2^2, respectively, where the pair P_1^1/P_1^2 originates from QS_1, while the pair P_2^1/P_2^2 originates from QS_2. In a complete process for communication in between two stations, the pair P_1^1/P_1^2 for instance so
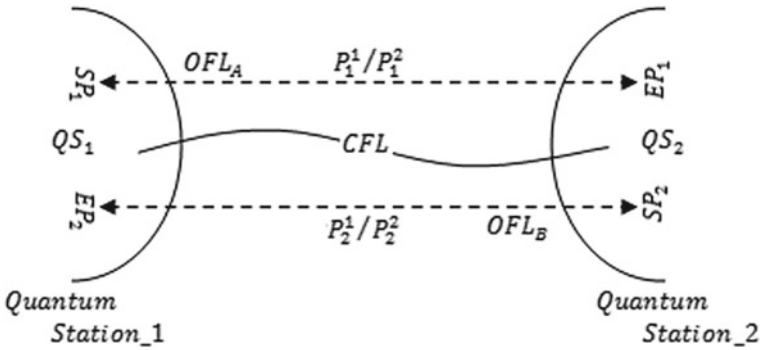
Fig. 1 Schematic of three-channel-based two quantum stations with OFL_A and OFL_B as quantum channel and CFL as classical channel. Each OFL_A and OFL_B carries weak coherent optical pulse train with an average number of less than one light quanta per pulse

originate at QS_1 first comes out from the SP_1 to OFL_A and then goes to EP_1 of QS_2 where the modulation process takes place other than one at QS_1. The pair P_1^1/P_1^2 after QS_2 then backs to QS_1 again, where the other operations take place, similarly for the pair P_2^1/P_2^2 the different operations at both QS_1 and QS_2 takes place. For this back and forth exchange other than quantum channel, the classical channel is also required.

4   Electro-Optic Systems of Quantum Station

The concern for communication to be safer can be possible only when the station that is responsible for sending and receiving the information opt the messenger of a type that is based on non-clonable approach, which is of quantum case. With in this section in continuation of Sect. 3, different *EOS* discussed. Other than unilateral consideration, which determine the case of flow in only one direction as similar to active electrical elements that allows current in only direction like ideal diode, the consideration of bilateral is essential as it allows the flow in either direction like that of current by passive electrical elements which are resistor, inductor, etc. Again, for the case of bilateral confidential communication, the quantum stations are essential, which employs the quantum property posses by particle as messenger, here the optical pulse is considered. At the quantum station of each, the incorporation of different *EOS* is required. This incorporation of different systems is regarded as coupling. The *EOS* requires at each QS consists of four different types one for each operation of optical pulse, given as,

$$EOS : \begin{cases} Electro-optic\ generation \\ \qquad system\ (EOGS) \\ Electro-optic\ controller \\ \qquad system\ (EOCS) \\ Electro-optic\ detector \\ \qquad system\ (EODS) \\ Electro-optic\ modulation \\ \qquad system\ (EOMS) \end{cases} \qquad (A)$$

i.e. Representation of different types of EOS

for different operations on optical pulse.

The te_(A) here represents the different types of *EOS* require at each *QS*, which with the coupling $-\Xi-$ as denotation here determine electro-optic couple system $EOCPS_i \forall i = [1, 2]$ as $EOCPS_i : (EOGS_i - \Xi - EOCS_i - \Xi - EODS_i - \Xi - EOMS_i)$. Next, each of the *EOS*, so introduce, consists of some important components which define below on individual basis.

4.1 Electro-Optic Generation System (EOGS)

This *EOGS* is responsible for the generation of optical pulse at each of the two quantum stations QS_1 and QS_2 indicated by $EOGS_1$ and $EOGS_2$, respectively, which require the components of important given below by its indices as,

$$[EOGS : (EOGS_1|EOGS_2)] : \begin{cases} Fibre\ Coupler : \\ \qquad \left[FC : \left(FC_1^1 \middle| FC_2^1\right)\right] \\ Laser\ Source : \\ \qquad \left[LS : (LS_1|LS_2)\right] \\ Phase\ Modulator : \\ \qquad \left[PM : \left(PM_1^1 \middle| PM_2^1\right)\right] \\ Variable\ Attenautor : \\ \qquad \left[VA : \left(VA_1^1 \middle| VA_2^1\right)\right] \end{cases} \qquad (B)$$

i.e. Representation of four important components for EOGS

with indices for either station.

These te_(B) components at each QS are connect (or couple) to each other in such a manner that the pairs of light quanta P_1^1/P_1^2 and P_2^1/P_2^2 are generate with phase constants φ_1^1/φ_1^2 and φ_2^1/φ_2^2, respectively. Within the *EOGS,* the coupling in between the components of different unlike that of $-\Xi-$ are here denote by ⚹, then,

$$
\begin{array}{c}
EOGS_1: \left[\left(LS_1 \text{ ⚹ } FC_1^1 \text{ ⚹ } VA_1^1 \text{ ⚹ } PM_1^1 \right) \xrightarrow{P_1^1(\varphi_1^1)/P_1^2(\varphi_1^2)} \right] \\[6pt]
\hline \\[-6pt]
EOGS_2: \left[\xleftarrow{P_2^1(\varphi_2^1)/P_2^2(\varphi_2^2)} \left(PM_2^1 \text{ ⚹ } VA_2^1 \text{ ⚹ } FC_2^1 \text{ ⚹ } LS_2 \right) \right]
\end{array} \tag{I}
$$

This arch_e (*I*) represents the components of important for both $EOGS_1$ and $EOGS_2$ which finally cause the generation of pairs of light quantum $P_1^1\left(\varphi_1^1\right)/P_1^2\left(\varphi_1^2\right)$ and $P_2^1\left(\varphi_2^1\right)/P_2^2\left(\varphi_2^2\right)$, respectively, from each QS_1 and QS_2. In paper [9], for key distribution case, a weak coherent pulse train so generate at the Alice side and then send to the Bob for phase difference measurement are in such a way that an average photon number per pulse is less than one. The technique 'chaotic states of semiconductor laser' so they use were able to achieve a sifted key generation rate of 9.0 kbps.

4.2 Electro-Optic Controller System (EOCS)

From Sect. 4.1, it is $EOGS_1$ which cause the generation of optical pulse for confidential key distribution but along by the controlling operation of $EOCS_1$ as one of the *EOS* at QS_1, similarly $EOCS_2$ for $EOGS_2$ at QS_2. The components of important which require at each *EOCS* are given below by its indices as,

$$
[EOCS : (EOCS_1|EOCS_2)] : \begin{cases} Random\,Number \\ \quad Generator : \\ \quad\quad \left[RNG : \left(RNG_1^1\middle|RNG_2^1\right)\right] \\ Voltage\,Controller : \\ \quad\quad \left[VC : \left(VC_1^1\middle|VC_2^1\right)\right] \\ Auxiliary\,Controller : \\ \quad\quad \left[AC : \left(AC_1^1\middle|AC_2^1\right)\right] \end{cases} \tag{C}
$$

i.e. Representation of three important components for EOCS with

indices for either station.

The te_(C) here represents the three important components of *EOCS* require at each *QS*, which are responsible for the operation of *EOGS* at their respective quantum station.

$$
\begin{array}{c}
EOCS_1 : \left[\left(AC_1^1 \, \text{⚥} \, VC_1^1 \, \text{⚥} \, RNG_1^1 \right) \right] \longrightarrow EOGS_1 \\
\hline
EOCS_2 : \left[\left(AC_2^1 \, \text{⚥} \, VC_2^1 \, \text{⚥} \, RNG_2^1 \right) \right] \longrightarrow EOGS_2
\end{array}
\tag{II}
$$

The arch_e (*II*) represents that the signal generates by the respective components of $EOCS_1$ and $EOCS_2$ send to their own $EOGS_1$ and $EOGS_2$ for the generation of pair of light quantum at their QS_1 and QS_2, respectively.

4.3 Electro-Optic Modulation System (EOMS)

This *EOMS* is responsible for the modulation/measurement of optical pulses at each of the two quantum stations QS_1 and QS_2 indicated by $EOMS_1$ and $EOMS_2$, respectively, that which is generated by the station of same and by other as well. Like *EOGS* and *EOCS,* the components of important which require at each *EOMS* are given below by its indices as,

$$
[EOMS : (EOMS_1 | EOMS_2)] : \left\{
\begin{array}{ll}
\textit{Fibre Coupler :} & \textit{Random Number} \\
\quad \left[FC : \left(FC_1^2 \middle| FC_2^2 \right) \right] & \quad \textit{Generator :} \\
\textit{Mirror :} & \quad \left[RNG : \left(RNG_1^2 \middle| RNG_2^2 \right) \right] \\
\quad \left[M : (M_1 | M_2) \right] & \textit{Voltage Controller :} \\
\textit{Phase Modulator :} & \Big/ \left[VC : \left(VC_1^2 \middle| VC_2^2 \right) \right] \\
\quad \left[PM : \left(PM_1^2 \middle| PM_2^2 \right) \right] & \textit{Auxiliary Controller :} \\
\textit{Variable Attenautor :} & \quad \left[AC : \left(AC_1^2 \middle| AC_2^2 \right) \right] \\
\quad \left[VA : \left(VA_1^2 \middle| VA_2^2 \right) \right] &
\end{array}
\right.
$$

<div align="center">

i.e. Representation of different important components for

EOMS with indices for either station.

</div>

$$\tag{D}$$

The te_(D) here represents the different important components of *EOMS* require at each *QS*, which operates only after the operation of *EOGS* and *EOCS* but in two consecutive steps followed by the involvement of both sides. For instance, one pair of light quantum $P_1^1\left(\varphi_1^1\right) / P_1^2\left(\varphi_1^2\right)$ at first the *EOMS* of other quantum station

operates rather than own which is $EOMS_2$ then afterwards $EOMS_1$ of same generating station, similarly for the pair light quantum $P_2^1(\varphi_2^1)/P_2^2(\varphi_2^2)$ as well. Now, by using these components of important the different steps of operation are given below as;

Step: 1

$$EOMS_1: \left[\begin{pmatrix} M_1 \, \text{ʮ} \, FC_1^2 \, \text{ʮ} \, PM_1^2 \, \text{ʮ} \, VA_1^2 \\ \text{ʮ} \\ AC_1^2 \quad \text{ʮ} \quad VC_1^2 \quad \text{ʮ} \quad RNG_1^2 \end{pmatrix} \begin{array}{c} \xleftarrow{P_2^1(\varphi_2^1)/P_2^2(\varphi_2^2)} \\ \xrightarrow{P_2^1(\varphi_2^1\pm\psi_1^1)/P_2^2(\varphi_2^2\pm\psi_1^2)} \end{array} \right]$$

$$EOMS_2: \left[\begin{array}{c} \xrightarrow{P_1^1(\varphi_1^1)/P_1^2(\varphi_1^2)} \\ \xleftarrow{P_1^1(\varphi_1^1\pm\psi_2^1)/P_1^2(\varphi_1^2\pm\psi_2^2)} \end{array} \begin{pmatrix} M_2 \, \text{ʮ} \, FC_2^2 \, \text{ʮ} \, PM_2^2 \, \text{ʮ} \, VA_2^2 \\ \text{ʮ} \\ AC_2^2 \quad \text{ʮ} \quad VC_2^2 \quad \text{ʮ} \quad RNG_2^2 \end{pmatrix} \right]$$

Step: 2

$$EOMS_1: \left[\begin{pmatrix} M_1 \, \text{ʮ} \, FC_1^2 \, \text{ʮ} \, PM_1^2 \, \text{ʮ} \, VA_1^2 \\ \text{ʮ} \\ AC_1^2 \quad \text{ʮ} \quad VC_1^2 \quad \text{ʮ} \quad RNG_1^2 \\ \uparrow \\ P_1^1(\varphi_1^1 \pm \psi_2^1)/P_1^2(\varphi_1^2 \pm \psi_2^2) \end{pmatrix} \xrightarrow{P_1^1(\varphi_1^1\pm\psi_2^1\pm\vartheta_1^1)/P_1^2(\varphi_1^2\pm\psi_2^2\pm\vartheta_1^2)} \right]$$

$$EOMS_2: \left[\xleftarrow{P_2^1(\varphi_2^1\pm\psi_1^1\pm\vartheta_1^1)/P_2^2(\varphi_2^2\pm\psi_1^2\pm\vartheta_1^2)} \begin{pmatrix} M_2 \, \text{ʮ} \, FC_2^2 \, \text{ʮ} \, PM_2^2 \, \text{ʮ} \, VA_2^2 \\ \text{ʮ} \\ AC_2^2 \quad \text{ʮ} \quad VC_2^2 \quad \text{ʮ} \quad RNG_2^2 \\ \uparrow \\ P_2^1(\varphi_2^1 \pm \psi_1^1)/P_2^2(\varphi_2^2 \pm \psi_1^2) \end{pmatrix} \right] \qquad (III)$$

The arch_e (*III*) here represents the required two steps operation on the same light quantum by *EOMS* of either side.

4.4 Electro-Optic Detection System (EODS)

This *EOS*, here, serve the purpose of detection of the phase constant of the emitted light quantum by station of same after being modulated from other station and by the measuring system of itself. The *EODS* for the detection purpose of optical pulse at each of the two quantum stations QS_1 and QS_2 are indicated by $EODS_1$ and $EODS_2$, respectively, which require the components of important given below by its indices as,

$$[EODS : (EODS_1|EODS_2)] : \begin{cases} Mach - Zehnder \\ \quad Interferometer : \\ \quad [MZI : (MZI_1|MZI_2)] \\ Detector : \\ \quad \left[DR : \left(DR_1^1 ; DR_1^2 \middle| DR_2^1 ; DR_2^2 \right) \right] \end{cases} \quad (E)$$

i.e. Representation of two important components

for EODS with indices for either station.

These two *MZI* and *DR* components at each *QS* of *EODS* shown in te_(E) are coupled to each other in a manner that the pair of light quanta $P_1^1\left(\varphi_1^1 \pm \psi_2^1 \pm \vartheta_1^1\right)/P_1^2\left(\varphi_1^2 \pm \psi_2^2 \pm \vartheta_1^2\right)$ so receive can be detected.

$$EODS_1 : \left[\begin{pmatrix} DR_1^1 \\ \quad \backslash \\ \quad / \quad \leftthreetimes MZI_1 \\ DR_1^2 \end{pmatrix} \xleftarrow{P_1^1(\varphi_1^1 \pm \psi_2^1 \pm \vartheta_1^1)/P_1^2(\varphi_1^2 \pm \psi_2^2 \pm \vartheta_1^2)} \right]$$
$$EODS_2 : \left[\xrightarrow{P_2^1(\varphi_2^1 \pm \psi_1^1 \pm \vartheta_2^1)/P_2^2(\varphi_2^2 \pm \psi_1^2 \pm \vartheta_2^2)} \begin{pmatrix} MZI_2 \leftthreetimes & / & DR_2^1 \\ & \backslash & DR_2^2 \end{pmatrix} \right] \quad (IV)$$

This arch_e (*IV*) represents the final operation on optical pulse generate by their own *EOGS* to cause the complete process of quantum communication between Alice and Bob.

5 Principle of Operation of Electro-Optic Couple Systems at Quantum Station

In consideration with earlier Sects. 3 and 4, the *EOS* of different so consider for the case of confidential communication at each station must need to be couple in manner so that it pays the required. It is the controller of $EOCS_1$ which cause the optical pulses P_1^1/P_1^2 to be developed by LS_1 such that the complex exponential term for its electric field is define as $L(t; v) = e^{j2\pi vt}$ where v is the central frequency of the pulse. The term $L(t; v)$ here, regard as light function for which the scalar product l_o determines the amplitude of it. The function $L(t; v)$ in case of optical pulses P_1^1/P_1^2 after getting through PM_1^1 from VA_1^1 of $EOGS_1$ to OFL_A become as $L\left(t; v, \varphi_1^1\right)$ and $L\left(t; v, \varphi_1^2\right)$, respectively, which correspondingly determine by $P_1^1\left(\varphi_1^1\right)/P_1^2\left(\varphi_1^2\right)$ where the element PM_1^1 operate by VC_1^1. The modification in optical pulse P_1^1/P_1^2 is due to the introduction of an additional exponential term to

each given by $X(\varphi) = e^{j\varphi}$ with $\varphi = \varphi_1^1$ and φ_1^2. Therefore, $L(t; v, \varphi_1^1) = L(t; v) \cdot X(\varphi_1^1)$ and $L(t; v, \varphi_1^2) = L(t; v) \cdot X(\varphi_1^2)$. Then,

$$\left.\begin{array}{l} L(t; v, \varphi_1^1) = e^{j2\pi vt} \cdot e^{j\varphi_1^1} \\ \qquad\qquad ; i.e.\, for\, P_1^1(\varphi_1^1) \\ L(t; v, \varphi_1^2) = e^{j2\pi vt} \cdot e^{j\varphi_1^2} \\ \qquad\qquad ; i.e.\, for\, P_1^2(\varphi_1^2) \end{array}\right\} \tag{1}$$

Equation (1) represents the required light functions for optical pulses $P_1^1(\varphi_1^1)/P_1^2(\varphi_1^2)$ from QS_1 to QS_2. The incoming optical pulses $P_1^1(\varphi_1^1)/P_1^2(\varphi_1^2)$ through PM_2^2 of $EOMS_2$ at QS_2 get reflected back to $EOMS_1$ by M_2 but after the phase modulation. This phase modulation at $EOMS_2$ is either over the two elements of sign conventional space denoted by the introduction of an additional exponential term to each given by $Y(\pm\psi) = e^{\pm j\psi}$ with $\psi = \psi_2^1$ and ψ_2^2 so that the output light function for same P_1^1/P_1^2 become as $L(t; v, \varphi_1^1, \pm\psi_2^1) = L(t; v) \cdot X(\varphi_1^1) \cdot Y(\pm\psi_2^1)$ and $L(t; v, \varphi_1^2, \pm\psi_2^2) = L(t; v) \cdot X(\varphi_1^1) \cdot Y(\pm\psi_2^2)$, which correspondingly determine by $P_1^1(\varphi_1^1 \pm \psi_2^1)/P_1^2(\varphi_1^2 \pm \psi_2^2)$ shown in Fig. 2. Then,
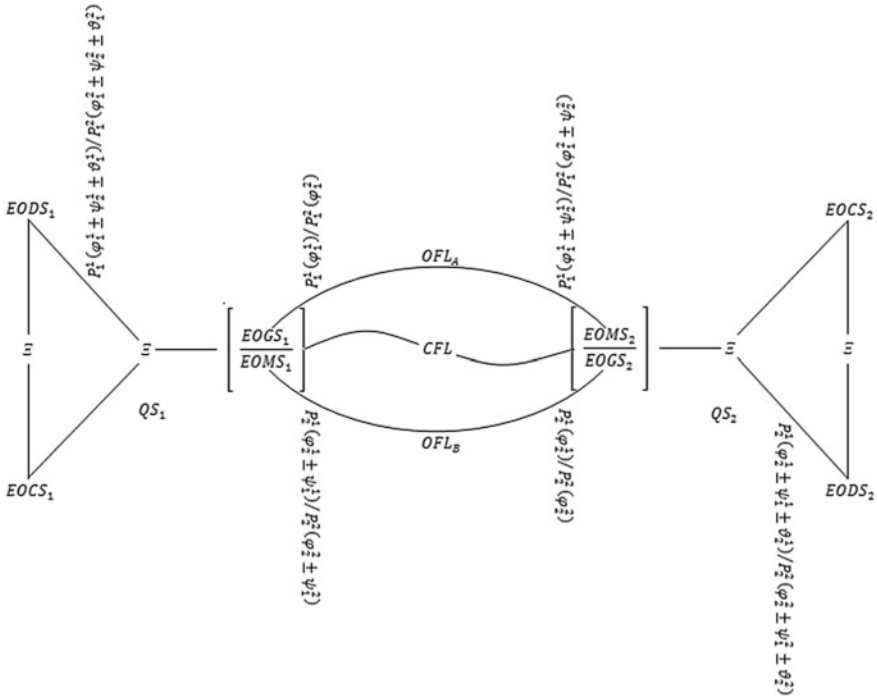
Fig. 2 Representation of the modulated optical pulses at each of the different quantum stations QS_1 and QS_2 for bilateral confidential communication even in the presence of the eavesdropper

$$\left.\begin{aligned}
L\big(t; v, \varphi_1^1, \pm\psi_2^1\big) &= e^{j2\pi vt} \cdot e^{j\varphi_1^1} \cdot e^{j\pm\psi_2^1} \\
&\qquad ; i.e.\, for\, P_1^1\big(\varphi_1^1 \pm \psi_2^1\big) \\
L\big(t; v, \varphi_1^2 \pm \psi_2^2\big) &= e^{j2\pi vt} \cdot e^{j\varphi_1^2} \cdot e^{j\pm\psi_2^2} \\
&\qquad ; i.e.\, for\, P_1^2\big(\varphi_1^2 \pm \psi_2^2\big)
\end{aligned}\right\} \tag{2}$$

Equation (2) represents the required light functions for the modulated optical pulses $P_1^1\big(\varphi_1^1 \pm \psi_2^1\big)/P_1^2\big(\varphi_1^2 \pm \psi_2^2\big)$ from QS_2 to QS_1 through same OFL_A. Like PM_1^1, it is the PM_2^2 which cause the modulation of such at QS_2 after operating by VC_2^2, while the VC_2^1 of $EOCS_2$ is for operation of PM_2^1 to have outgoing coherent optical pulses $P_2^1\big(\varphi_2^1\big)/P_2^2\big(\varphi_2^2\big)$ from $EOGS_2$ at QS_2 to $EOMS_1$ of QS_1 through OFL_B. It is the $EOMS_1$ and then later on $EODS_1$ that has need to perform on P_1^1/P_1^2 but at a state of $P_1^1\big(\varphi_1^1 \pm \psi_2^1\big)/P_1^2\big(\varphi_1^2 \pm \psi_2^2\big)$. Then,

$$\left.\begin{aligned}
L\big(t; v, \varphi_1^1, \pm\psi_2^1, \pm\vartheta_1^1\big) &= e^{j2\pi vt} \cdot e^{j\varphi_1^1} \cdot e^{j\pm\psi_2^1} \cdot e^{j\pm\vartheta_1^1} \\
&\qquad ; i.e.\, for\, P_1^1\big(\varphi_1^1 \pm \psi_2^1 \pm \vartheta_1^1\big) \\
L\big(t; v, \varphi_1^2, \pm\psi_2^2, \pm\vartheta_1^2\big) &= e^{j2\pi vt} \cdot e^{j\varphi_1^2} \cdot e^{j\pm\psi_2^2} \cdot e^{j\pm\vartheta_1^2} \\
&\qquad ; i.e.\, for\, P_1^2\big(\varphi_1^2 \pm \psi_2^2 \pm \vartheta_1^2\big)
\end{aligned}\right\} \tag{3}$$

Equation (3) represents the final modulated light functions for the optical pulses $P_1^1\big(\varphi_1^1 \pm \psi_2^1 \pm \vartheta_1^1\big)/P_1^2\big(\varphi_1^2 \pm \psi_2^2 \pm \vartheta_1^2\big)$ incoming at $EODS_1$ of QS_1 for detection purpose after through $EOMS_1$. In multiplication with Eq. (2) by an additional exponential term $e^{\pm j\vartheta}$ with $\vartheta = \vartheta_1^1$ and ϑ_1^2 equal by $Z(\pm\vartheta)$ to have $L(t; v, \varphi, \pm\psi, \pm\vartheta) = L(t; v, \varphi, \pm\psi) \cdot Z(\pm\vartheta) = L(t; v) \cdot X(\varphi) \cdot Y(\pm\psi) \cdot Z(\pm\vartheta)$ express by Eq. (3) possible only by $EOMS_1$. For the case of phase angles complexity reduction at each quantum station by mean of their own generating optical pulses, the consideration of particulars in concern with same and by limitation as well is essential which are followed by at first the orthogonal condition, then the selection of $\psi_2^1 = (\pi/4\, or\, 3\pi/4)$ with $\psi_2^2 = 0$ or $\psi_2^1 = 0$ and $\psi_2^2 = (\pi/4\, or\, 3\pi/4)$ at second. Due to the presence of both of the two elements of sign conventional space over complex exponential, the rest two options of $-\pi/4$ and $-3\pi/4$ are also possible. In third step likewise second, the selection of $\vartheta_1^1 = \pi/4$ with $\vartheta_1^2 = 0$ or $\vartheta_1^1 = 0$ with $\vartheta_1^2 = \pi/4$ consider.

With the angles selection of such for the detection of optical pulses at $EODS_1$ by two of its components DR_1^1 and DR_1^2 are in such a way that one of it correspond 0 and other 1, let say if DR_1^1 corresponds 0 indicate by $DR_1^1 \to 0$ then DR_1^2 must corresponds 1 indicate by $DR_1^2 \to 1$ or vice versa. With an agreement of binary correspondences of $DR_1^1 \to 0/DR_1^2 \to 1$ means the Alice and Bob at two quantum stations QS_1 and QS_2, respectively, shares an identical bit string. Optically, the indication of bit 0 and 1 here regard by the interference means of constructive (or bright fringe) and destructive (or dark fringe), respectively, where the bright fringe holds the angle difference of $2n\pi$ for $n\epsilon Z$ while the dark fringe holds $(2n + 1)\pi$.

6   Discussion

This paper focuses on the study of different types of *EOS* needs to be installed at each quantum station for the purpose of secure communication bilaterally, at the same time, even in the presence of eavesdropping. This gives the consideration of two quantum stations one for each, both Alice and Bob, connected with least of three channels where two of which are quantum based and the rest one of which is classical based. The components for each *EOS* are coupled in systematic manner such that the collective of which led to cause the development of quantum stations, which are responsible for the operations of different like generation, controlling, modulation and detection. The architecture for each *EOS* is given from (*I*) to (*IV*), where with the help of arch_es (*I*), (*II*), and (*III*) individual complex exponential functions can introduce on optical pulse given by Eqs. (1), (2) and (3), respectively, such that their simple product yield the resultant complex exponential function require to be available at the *EODS* given by arch_e (*IV*).

References

1. Bennett CH, Brassard G (1984) Quantum cryptography: public key distribution and coin tossing. In: Proceedings of the international conference on computers, systems and signal processing, Dec 1984, pp 175–179. http://www.isical.ac.in/~rcbose/internship/lectures2016/rt08bb84.pdf. Republished 2014 in Theoretical Computer Science, Elsevier. https://core.ac.uk/download/pdf/82447194.pdf
2. Wootters WK, Zurek WH (1982) A single quantum cannot be cloned. Nature 299:802–803. https://www.nature.com/articles/299802a0
3. Nielsen MA (2002) Simple rules for a complex quantum world. Sci Am 25–33. http://michaelnielsen.org/papers/SciAmSimpleRules.pdf
4. http://www.petitcolas.net/fabien/kerckhoffs/
5. http://www.ebooklibrary.org/article/WHEBN0000578127/Gilbert%20Vernam
6. Guerreau OL, Merolla JM, Soujaeff A, Patois F, Goedgebuer JP, Malassenet FJ (2003) Long distance QKD transmission using single-sideband detection scheme with WDM synchronization. IEEE J Sel Top Quantum Electron 9(6):1533–1540. https://doi.org/10.1109/jstqe.2003.820929
7. Stucki D, Gisin N, Guinnard O, Ribordy G, Zbinden H (2002) Quantum key distribution over 67 km with a plug & play system. New J Phys 4:41.1–41.8. https://www.idquantique.com/wordpress/wp-content/uploads/njp-2002.pdf
8. Merolla JM, Mazurenko Y, Goedgebuer JP, Porte H, Rhodes WT (1999) Phase-modulation transmission system for quantum cryptography. Opt Lett 24(2):15. https://doi.org/10.1364/OL.24.000104
9. Honjo T, Uchida A, Amano K, Hirano K, Someya H, Okumura H, Yoshimura K, Davis P, Tokura Y (2009) Differential-phase-shift quantum key distribution experiment using fast physical random bit generator with chaotic semiconductor lasers. Opt Express 17(11):9053–9061. https://doi.org/10.1364/OE.17.009053

A Stacked Hollow Low-Profile Dielectric Resonator Antenna with Wide Bandwidth and Enhanced Gain

Sachin Kumar Yadav, Amanpreet Kaur and Rajesh Khanna

Abstract A stacked hollow dielectric resonator antenna (SHDRA) is presented in this article. It consists of two dielectric layers with different permittivity materials etched as a dielectric resonator, stacked, or segmented to each other. This antenna is placing dielectric layers with high permittivity material ($\varepsilon = 9.8$) and low permittivity material ($\varepsilon = 4.4$), fed through a slot (tilted 45°). This paper presents a wideband SHDRA designed with a low profile and high gain. The antenna can achieve gain range 7–8.4 dB, frequency band range 3.7–5.8 GHz, and impedance bandwidth 52.76% at the center frequency of 4.1 GHz.

Keywords High gain antenna · Low-profile antenna · Stacked hollow dielectric resonator antenna · Wideband antenna

1 Introduction

The fast growth of the wireless communication demands for the wideband applications to support a higher data rate. Dielectric resonator antennas (DRAs) have been explored in this field because of several advantages such as light in weight, easy to excitation, low metallic losses, and high radiation efficiency [1]. DRA is made with a dielectric resonator (DR), having relative permittivity 9–100. The different shapes of DR like cylindrical, rectangular, elliptical, triangular, conical, and spherical have been presented that radiate effectively [2, 3]. The different types of feeding techniques are used in DRA like coaxial, microstrip line, conformal strip, aperture-coupled, and coplanar waveguide [4–13].

S. K. Yadav (✉) · A. Kaur · R. Khanna
Thapar Institute of Engineering and Technology, Patiala, Punjab, India
e-mail: yadavsachin1983@gmail.com

A. Kaur
e-mail: amanpreet.kaur@thapar.edu

R. Khanna
e-mail: rkhanna@thapar.edu

In this article, we focus on a hollow DRA that provides wider bandwidth, comparision with its solid counterpart [14–16]. This hollow region is used for additional packaging function, as a light source, amplifier, and coupler [17–19]. Here a stacked hollow DRA with different permittivities, such as high permittivity ($\varepsilon = 9.8$) below that low permittivity ($\varepsilon = 4.4$) material is designed. The stacking concept is used in antenna to help enhance its impedance bandwidth [20].

2 Antenna Design and Configuration

The proposed SHDRA is shown in Fig. 1. It consists of two different rectangular dielectric layers with low permittivity (ε_{rd1}) and upper layer with high permittivity (ε_{rd2}) materials. These two layers have same square length (L_{DR}) but different thicknesses of t_1 and t_2, respectively. The dimensions are selected with follow $L \gg t_1 + t_2$; thus, the SHDRA has almost low profile and resonant frequency around at 4 GHz. The dimension of the antenna is described in Table 1. The antenna feed is given by a slot (rotated 45° angle) coupled from a microstrip line, which is fixed on a substrate having relative permittivity 4.4 and thickness 'h', the slot cut at top ground plane and microstrip feedline is etched on the bottom of the substrate, and the thickness of DRA should be given by

$$t_1 = n\lambda_0/2\sqrt{\varepsilon_{rd1}} \tag{1}$$

$$t_2 = m\lambda_0/4\sqrt{\varepsilon_{rd2}} \tag{2}$$
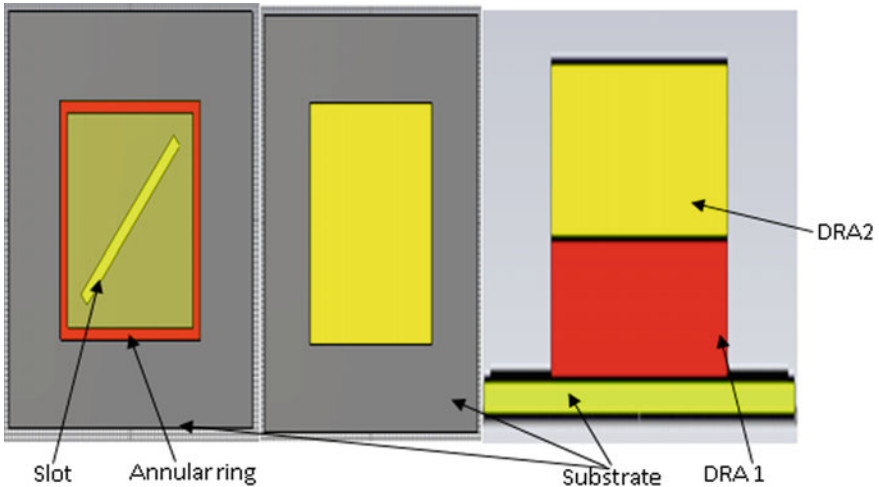
Fig. 1 Different views of SHDRA

Table 1 Dimensions of proposed SHDRA (unit millimeters)

Parameters	Dimensions	Description
$L_s \times W_s$	70 × 70	Substrate length and width
$L_g \times W_g$	70 × 70	Ground length and width
h	0.8	Thickness of substrate
L_{DR}	40	Length square of DR
$L_{max} = L_{DR}$	40	Hollow DR outer dimension
L_{min}	38	Hollow DR inner dimension
t_1	3.2	Thickness of low permittivity material
t_2	4	Thickness of high permittivity material (DR)
L_{slot}	37.5	Slot length
W_{slot}	2.4	Slot width
L_f	1.8	Feedline length
W_f	44.5	Feedline width

where ε_{rd} is an relative permittivity of dielectric resonator, λ_0 is free space wavelength at the resonant frequency, and m and n are an integers.

Figure 1 shows the three dielectric layers, top two DRA layers and bottom substrate layer, that is, completely called SHDRA. All dimension and description of SHDRA are described in Table 1.

3 Simulated Results and Discussion

The SHDRA was designed and simulated in CST MWS V'16 and ANSOFT HFSS V'12. The simulated S_{11} (below −10 dB) with respect to frequencies show in Fig. 2 is presented. The simulated results of antenna parameters are such as impedance
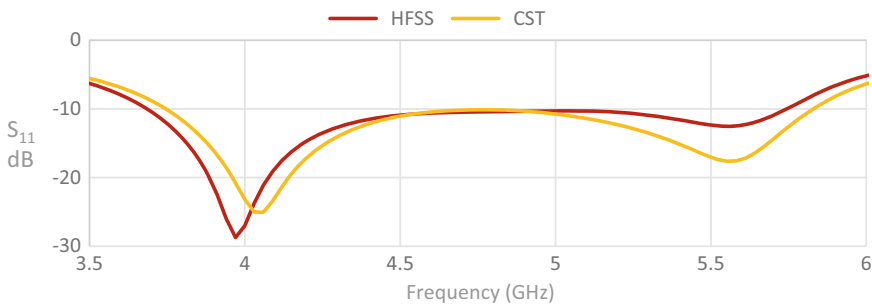
Fig. 2 Simulated reflection coefficient

bandwidth, radiation efficiency, 3-D radiation pattern, and smith chart. Good agreement has been reported to compare results between CST and HFSS.

3.1 Return Loss

Figure 2 shows the return loss of the antenna. As can be seen, the antenna shows an impedance BW (3.7 to 5.8 GHz) of 52.76%. The S11 of the antenna compare with two softwares: HFSS and CST MWS'16. The simulated result of the antenna in both software match, showing a correct simulation.

3.2 Smith Chart

Smith chart of antenna is shown in Fig. 3a, the measures at each frequency and the respective impedance at each frequency.

3.3 Radiation Pattern

In Fig. 3b shows the simulated radiation characteristic with maximum gain 7.38 dB at 4.1 GHz, which shows a good gain of the antenna.

3.4 Antenna Gain and Radiation Efficiency

Figure 4 shows the plot of gain, efficiency, and VSWR with respect to frequency. The antenna shows a peak gain of 8.3 dB, radiation efficiency of 96.2%, and VSWR below than 2 at frequency range 3.7–5.8 GHz.

4 Parametric Study

The performance of SHDRA depends on many parameters like height of DRA, relative permittivity of DRA, and substrate. Figure 5 shows the parametric optimization carried out for height of upper DRA $t2$ = 2.5, 3, 3.5, 4, 4.5, 5.

(a)

Smith Chart 1

Name	Freq	Ang	Mag	RX
m1	4.3417	121.9939	0.2641	0.6892 + 0.3320i
m2	5.5083	-129.8508	0.2793	0.6420 - 0.2987i
m3	6.1500	159.2868	0.6489	0.2197 + 0.1742i
m4	4.1083	158.7360	0.1414	0.7636 + 0.0799i
m5	4.5167	83.5862	0.2948	0.8943 + 0.5738i
m6	5.9403	-162.2775	0.5520	0.2951 - 0.1426i
m7	6.0299	-178.5861	0.6134	0.2396 - 0.0116i
m8	4.9254	-25.3601	0.3018	1.6659 - 0.4737i
m9	3.8507	86.6912	0.1374	0.9782 + 0.2736i

(b)

Type	Farfield
Approximation	enabled (kR >> 1)
Monitor	farfield (f=4.1) [1]
Component	Abs
Output	Gain
Frequency	4.1
Rad. effic.	-0.5008 dB
Tot. effic.	-0.5102 dB
Gain	7.377 dB

dB
7.38
5.07
3.69
2.31
0.922
-2.04
-8.16
-14.3
-20.4
-26.5
-32.6

Fig. 3 a Smith chart and **b** radiation pattern at 4.1 GHz frequency

It can be seen in Fig. 6 that the best result obtained with an upper dielectric resonator height of 4 mm cover the required band and lower dielectric resonator make an annular ring with outer dimension fixed $40 \times 38 \times 3.2$ mm^3.

5 Conclusion

A stacked hollow dielectric resonator antenna consisting of two different permittivity material layers, known as multi-segmentation, has been investigated. It has been proved by the ratio of length and height of the material segmentation and selected two different permittivities, for two different dielectric layers. The antenna
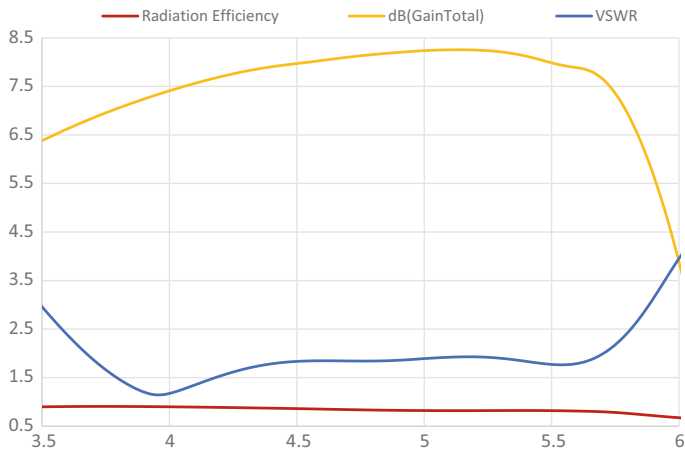
Fig. 4 Antenna gain, radiation efficiency, and VSWR
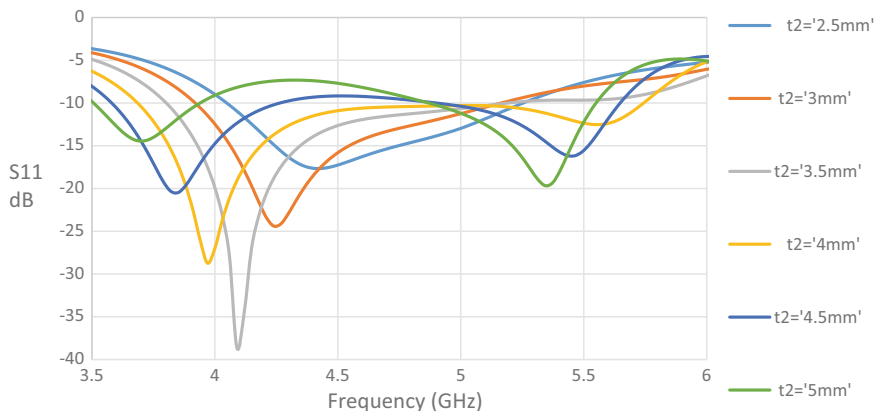
Fig. 5 Reflection coefficient with respect to frequencies varies the height $t2$ of upper DRA

bears a low profile and shows a good gain with wideband characteristics. SHDRA has a simulated maximum gain of 8.3 dB and an impedance bandwidth of 52.76%. The gain can be enhanced approximately to 10 dB if high dielectric permittivity material (low—2.3 and high—28 to 35) is used.
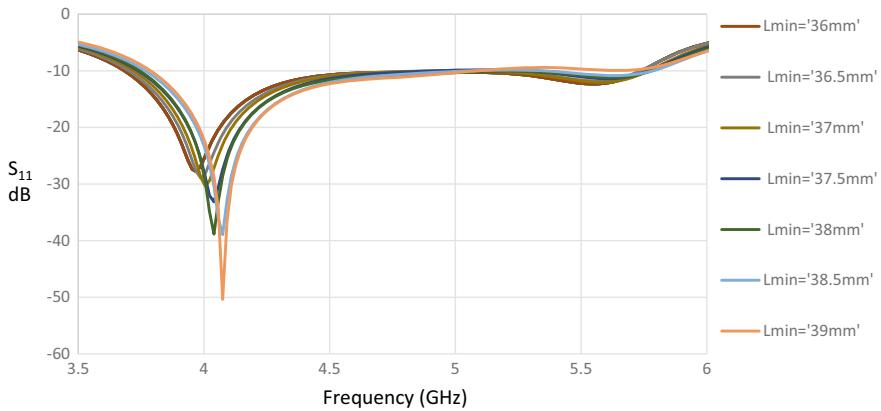
Fig. 6 Reflection coefficient with respect to frequencies, lower DRA inner ring dimensions L_{min} varies

References

1. Petosa A (2007) Dielectric resonator antenna handbook. Artech House, Norwood, MA, USA
2. Luk KM, Leung KW (2003) Dielectric resonator antennas. Research Studies, Baldock, UK
3. Long SA, McAllister M, Conway GL (1983) Rectangular dielectric resonator antenna. Electron Lett 19:218–219
4. Junker GP, Kishk AA, Glission AW (1994) Input impedance of dielectric resonator antennas excited by a coaxial probe. IEEE Trans Antennas Propag 42:960–966
5. Kranenburg RA, Long SA (1988) Microstrip transmission line excitation of dielectric resonator antenna. Electron Lett 28:1156–1158
6. Martin JTHS, Antar YMM, Kishk AA (1990) Dielectric resonator antenna using aperture coupling. Electron Lett 24:2015–2016
7. Leung KW, Luk KM, Lai KYA (1995) Theory and experiment of an aperture coupled hemispherical dielectric resonator antenna. IEEE Trans Antennas Propag 43:1192–1198
8. Leung KW (2000) Conformal strip excitation of dielectric resonator antenna. IEEE Trans Antennas Propag 48:961–967
9. Kranenburg RA, Long SA, Williams JT (1991) Coplannar waveguide excitation of dielctric resonator antennas. IEEE Trans Antennas Propag 39:119–122
10. Al Salmaeh MS, Antar YMM (2002) Coplanar waveguide fed slot coupled rectangular dielectric resonator antenna. IEEE Trans Antennas Propag 50:1415–1419
11. Eshrah IA, Kishk AA, Yakovlev AB (2005) Excitation of dielectric resonator antennas by a waveguide probe: modelling techniques and wideband design. IEEE Trans Antennas Propag 53:1028–1037
12. Eshrah IA, Kishk AA, Yakovlev AB (2005) Theory and implementation of dielectric resonator antenna excited by a waveguide slot. IEEE Trans Antennas Propag 53:483–494
13. Leung KW, Wong WC, Luk KM (1998) Annular slot coupled dielectric resonator antenna. Electron Lett 34:1275–1277
14. Mongia RK, Ittippiboon A, Bhatia P (1993) Electric monopole antenna using a dielectric ring resonator. Electron Lett 29:1530–1531
15. Fang XS, Leung KW (2011) Designs of single- dual-wide-band rectangular dielectric resonator antennas. IEEE Trans Antennas Propag 59:2409–2414

16. Wong KL, Chen NC, Chen HT (1993) Analysis of a hemispherical dielectric resonator antenna with an air gap. IEEE Microw Guided Wave Lett 3:355–377
17. Lim EH, Leung KW (2006) Novel application of hollow dielectric resonator antenna as a packing cover. IEEE Trans Antennas Propag 54:484–487
18. Fang XS, Chen RS (2010) Compact differential rectangular dielectric resonator antenna. IEEE Antennas Wirel Propag Lett 9:662–665
19. Leung KW, Pan YM, Fang XS (2013) Dual function radiating glass for antenna and light covers. IEEE Trans Antennas Propag 61:578–586
20. Pan YM, Zheng SY (2016) A low profile stacked dielectric resonator antenna with high gain and wide bandwidth. IEEE Antennas Wirel Propag Lett 15:68–71

Representation of 3D View of Tumor from 2D Images Using Watershed Algorithm

Kamna Bhandari, B. L. Pal and Arun Vaishnav

Abstract 3D image visualization gives the detailed information of MR images. In this paper, 2D images of different patients have been taken and these are preprocessed, segmented and post-processed. The preprocessing steps include thresholding and skull stripping. Watershed algorithm is applied for segmentation, stacking is performed to arrange different slices of tumor in shape, and interpolation is done to get smoothness between different slices of tumor and lastly rendering (Phong shading applied) which gives realness to the shape of tumor. The developed strategy has been tested on MATLAB 2013a software platform. The dataset of different patients had been taken having no tumor, less tumor, and high tumor.

Keywords Watershed segmentation · Interpolation · Stacking · Phong shading

1 Introduction

Brain tumor is very dangerous as it spreads at very fast speed and it proves a very serious threat to life. For this reason, calculating the volume of tumor is very essential to calculate the stage of tumor. Magnetic resonance imaging (MRI) is the common analysis of the brain tumor, and the combined use of radio waves and magnetic fields gives cross-sectional images of the brain that gives anatomic details of the 3D tumor which are presented as a set of 2D parallel cross-sectional images. 2D MR images of brain tumor do not prove very successful for visualizing the tumor. Interpretations of these images are very difficult to radiologist, which results in a need for 3D reconstruction of the tumor from a set of 2D parallel

K. Bhandari (✉) · B. L. Pal · A. Vaishnav
CSE Department, Mewar University, Gangrar, Chittorgarh, India
e-mail: bhandari.kamna19@gmail.com

B. L. Pal
e-mail: bpal@mewaruniversity.co.in

A. Vaishnav
e-mail: arunv@mewaruniversity.co.in

1055

cross-sectional images of the tumor. The better understanding of tumor can be taken from its 3D view. The 3D view of tumor contributes to a great extent in finding the staging of tumor, surgical planning, and biological research.

2 Literature Survey

We discussed some literature survey works for understanding the background of brain tumor. The techniques which are used by different authors and researchers are C-means clustering, thresholding, genetic algorithm, particle swarm optimization, and so on. The deeper knowledge of brain tumor can be examined by taking into account the deepness of tumor. Many researchers have also worked on 3D image of tumor for this reason, and this field has become an area for research. 3D image gives detailed view of tumor.

Murugavallii and Rajamani [1] in the year 2006 introduced a rapid parallel fuzzy C-means algorithm and cluster center algorithm for cerebrum tumor picture segmentation. This proposed algorithm takes the full use of both consecutive FCM and parallel FCM for the bunching procedure in the division systems. The researchers have decreased the computation time because they have selected actual cluster center and they want to use minimum secondary storage. The new dataset has been generated by the centroid of unit blocks. Gopal and Karnan [2] in the year 2010 displayed an intelligent framework, and their intention is to analyze mind tumor through MRI using image processing clustering calculations like fuzzy C-means with genetic algorithm (GA) and particle swarm optimization (PSO). The performance of tumor detection is done in two stages: preprocessing and enhancement in the main stage and division and grouping in the second stage. The PSO has given the best accuracy results as compare to other techniques.

Resmi and Thomas [3] in the year 2012 displayed a strategy for volume rendering of glioma tumors from fragmented 2D MR images by using morphological operations, and these fragmented tumor cuts are stacked using medical software. Kavitha and Sangeetha [4] in the year 2013 discussed that the variations in type, size, location, and shape of tumor is a very typical job to detect it automatically. For classifying the tumor cells, the neural network is used. With the help of segmentation, the suspicious region can be separated from the background of MR images. An algorithm that can detect tumor automatically is developed using multi-modal MRI. Madhikar and Lokhande [5] in the year 2013 used a simple technique named region growing for detecting the tumor in brain MR. The result of this technique is compared with feedforward neural network and radial basis function network. Two thresholds have been taken: intensity and orientation. Quality rate of algorithm has been used to check the performance of this algorithm. Singh and Kaur [6] in the year 2014 reviewed two image processing techniques, namely watershed segmentation and k-means clustering segmentation that has detected the brain tumor in MR images. These image processing techniques detect brain tumor in early stages, but the area of tumor was not calculated by them. Yu et al. [7] in the year 2014

presented a fully automatic, unsupervised algorithm from which multiple tumors from 3 to 28,079 mm^3 in volume can be easily detected. The detection rate of this technique ranges from 87.84 to 95.30%. Zin and Khaing [8] in the year 2014 presented brain tumor detection and segmentation using watershed segmentation and morphological operation. The preprocessing functions are applied on MR image containing brain tumor. The detection of tumor is done using morphological erosion algorithm. Sharma and Singh [9] in the year 2015 proposed feature detection and roundness metric, and further integration is done decision base alpha-trimmed global mean. This technique is helpful to remove noise. Sindhu and Meera [10] in 2015 presented a review on different image processing techniques. Wakchaure and Khandekar [11] in the year 2015 proposed a technique to visualize 3D view of detected brain tumor and also volume calculation for detection and localization of brain tumor in magnetic resonance imaging. The proposed brain tumor detection and localization framework comprise five steps: image acquisition, preprocessing, edge detection, modified histogram clustering, and morphological operations, but this system does not identify the type of tumor regarding with shapes and structures. Lopes and Jaiswal [12] in the year 2015 presented automatic tumor detection, and also it includes reconstruction of its 3D image that include implementation of various steps of detection and extraction of tumor from the 2D slices of MRI brain images. The two techniques that are used for this purpose are seeded region growing technique and image segmentation. This work can be extended to design software for detection of tumors. Vanitha et al. [13] in the year 2015 used a technique namely morphological image processing to distinguish the tumors from the brain either malignant or non-malignant tumors. For finding location of brain tumor, morphological image processing is used; however, this technique does not calculate volume of tumor. Abdel-Maksoud et al. [14] in the year 2015 presented a proficient image segmentation approach with k-means clustering and fuzzy C-means algorithm with thresholding and segmentation for accurate detection of brain tumor. Kaur and Kaur [15] in the year 2016 proposed a brain tumor detection technique based on object. This technique is compared with neural network, and the accuracy rate is greater in object-based segmentation. Samriti et al. [16] in the year 2016 presented watershed image segmentation technique. Isselmou et al. [17] in the year 2016 presented the image acquisition, image enhancement, threshold, and morphological operation for detection of brain tumor.

From the above literature survey, it is concluded that 3D visualization is very efficient for diagnosing brain tumor. Many efforts have been going on by researchers to visualize tumor in 3D environment with different methods. So due to the fact, this area becomes more interesting for research purpose.

3 Proposed System

The proposed technique is to generate 3D view of brain tumor by applying watershed algorithm by using 2D MR image. This technique composed of mainly three stages which are preprocessing, segmenting, and post-processing. Preprocessing stage involves removing noise, other fine particles, and skull using thresholding. In the second stage, watershed algorithm has been used for segmentation, and in post-processing stage, contouring, stacking, interpolation, and rendering have been done to get 3D volume of tumor (Fig. 1).

Algorithm
Step 1: Obtain 2 MR images of human brain in DICOM format.
Step 2: Perform image preprocessing operations to refine the image, and remove noise on each image slices.
Grayscale conversion

A. First, we will convert color image to grayscale image. If by chance any color image is passed to our system, then our system should recognize the image. The properties of green channel in RGB are same as that of gray image. So, the green channel which is the second one is chosen [18].

$$GrayImage = grayImage(; ; 2); \qquad (1)$$

Fig. 1 Block diagram of proposed algorithm
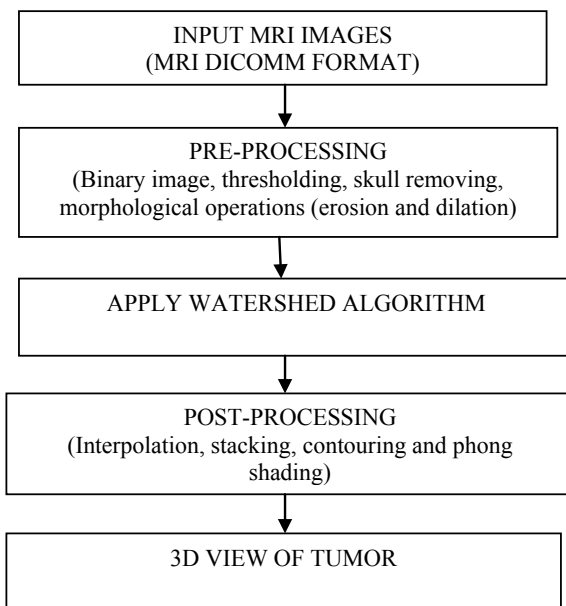
B. Binary conversion

We will find the threshold value. If the value at the pixel position is above the threshold value, then the value will be 1 (white); otherwise, it will be zero (black).

$$\text{BinaryImage} = \text{grayImage} > \text{threshold value};   \tag{2}$$

Step 3: Remove skull part, and extract brain part from the image slices. The human skull image slices of MRI have thickness of 3–4 mm.

$$\text{GrayImage} = \text{grayImage}(3{:}\text{end-3}, 4{:}\text{end-4});   \tag{3}$$

Step 4: Perform morphological operations so that if any part of tumor get extract during skull remove, then by applying morphological operations same pixel points will get back to get tumor mask.

$$\text{BinaryImage} = \text{imfill}(\text{binary Image}, {'}\text{holes}{'});   \tag{4}$$

Imfill function is an inbuilt function in MATLAB, which is used to apply morphological operation. This function is used to fill the empty holes that can be generated if the pixels other than skull got removed during skull removing.

Step 5: Apply watershed algorithm to segment tumor portion.

Watershed algorithm is a type of image segmentation algorithm that divides adjacent pixels in a shape of drainage basin.

$$\text{Bwshed} = \text{watershed}(\text{bw});   \tag{5}$$

This formula returns a matrix of name bwshed that represents watershed regions of matrix bwshed.

Step 6: Detect contour of each tumor slice and stack them one by one to create 3D mesh, and after this, interpolation is performed to get smoothness between images slices.

For interpolation,

$$\text{Interpolated slice} = (1 - \text{interpolated distance}) * \text{first slice} + \text{second slice}   \tag{6}$$

For contouring,

$$\text{Cr} = \text{contourslice}(A, [], [], [1, 2, 3, 4, 5, 6, 7, 8, 9, 10, 11, 12, 13, 14, 15, 16, 17, 18,$$
$$19, 20, 21, 22, 23, 24, 25, 26, 27, 28, 29, 30, 31, 32, 33, 34, 35, 36, 37]);$$
$$\tag{7}$$

Here, we have made a function name contourslice that takes an array(A) which contains interpolated as well as original image slices of brain tumor. Interpolation is performed to get smoothness between slices.

Step 7: Perform Phong shading rendering on 3D mesh to generate 3D realistic tumor shape.

Phong shading is a type of shading technique in which realistic surface is given to the object; interpolation is performed at the normal to the surface. It is also known as Phong interpolation or normal-vector interpolation because interpolation is performed at the surface normals across polygons.

4 Simulation Results

The proposed method is evaluated on the T1-weighted patient dataset with low- and high-grade gliomas obtained from X-NAT [19] public dataset of MRI (Table 1).

Three cases have been discussed here, namely:

(a) Patient is at severe stage of tumor.
(b) Patient is at medium stage of tumor.
(c) Patient is at low stage of tumor.

CASE A: Patient is at severe stage of tumor.
Step 1: The 2D MR images of human brain in DICOM format are shown in Fig. 2. The MR images are grayscale images. All the operations are performed on the binary image, so we convert grayscale image to binary image.

Step 2: In this step, image preprocessing operations are performed to refine the image and remove noise from image slice. Morphological operations and thresholding are used to clean the image that does not contain any unwanted particle.

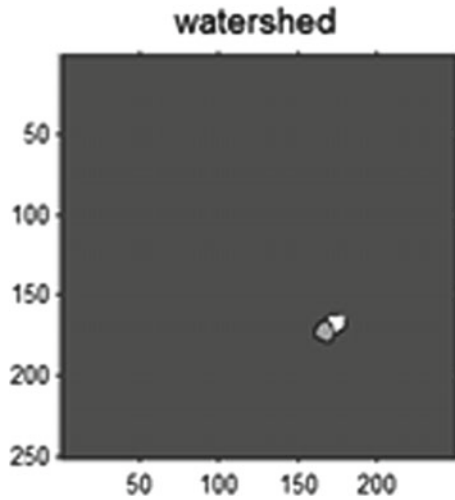**Step 3**: In Fig. 3, skull part has been removed and brain tumor part has been extracted from the image slices.

Step 4: Below two images show the threshold tumor portion of patient which gives clear view of tumor. The next image is the eroded binary image of patient that gives a shape to tumor (Figs. 4 and 5).

Step 5: The result of the watershed algorithm is shown in Fig. 6. Watershed algorithm is used to divide the tumor region into different segments, and tumor gets divided into different segments.

Table 1 Properties of input MRI

No. of MRI slice	20
Type of slice section	Axial
Image size	255×255

Fig. 2 (Case A): Original gray scale image of patient at severe stage of tumor
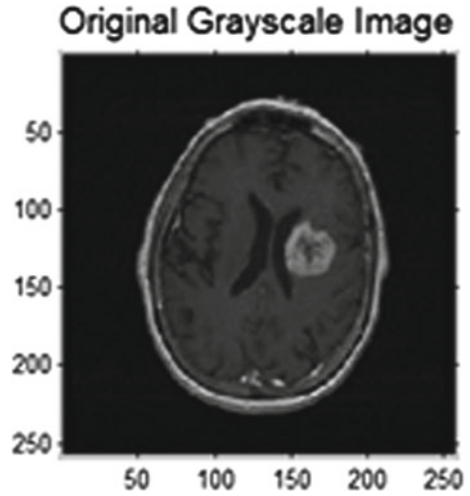
Fig. 3 (Case A): Skull stripped image of patient at severe stage of tumor
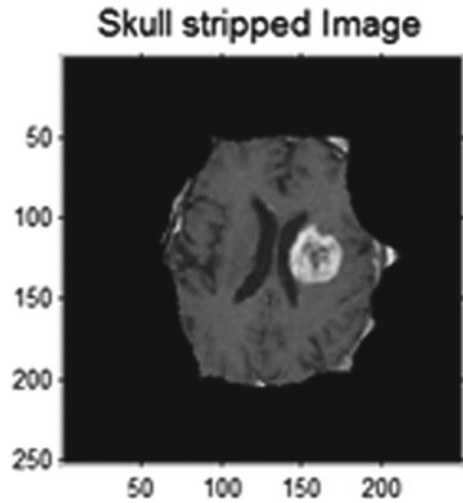
Step 6: Figure 7 is of detecting contour of each tumor slice and stacking them one by one to create 3D mesh. The outline of each image slice of tumor is done in 3D, and stacking of image slice is done to generate a mesh.
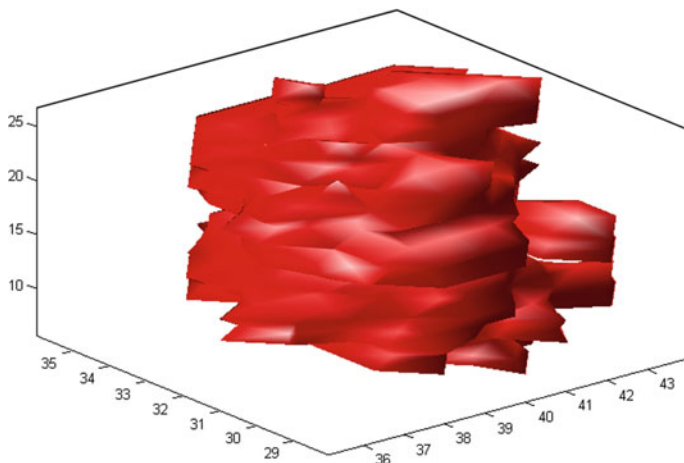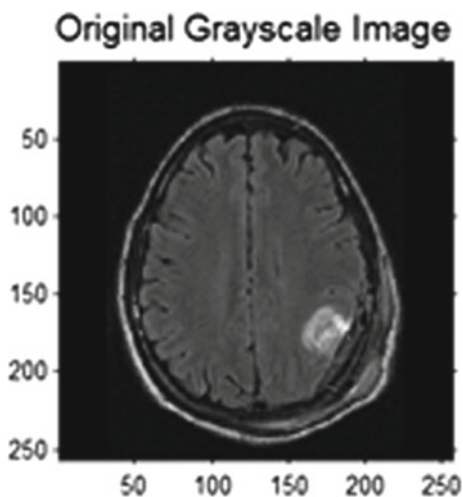
Step 7: The rendered image of tumor is shown in Fig. 8. Rendering is performed on 3D mesh to generate 3D realistic tumor shape. Rendering performs to give a realistic image to 3D mesh generated, by which tumor can be shown in 3D view.

Fig. 4 Thresholded image of patient
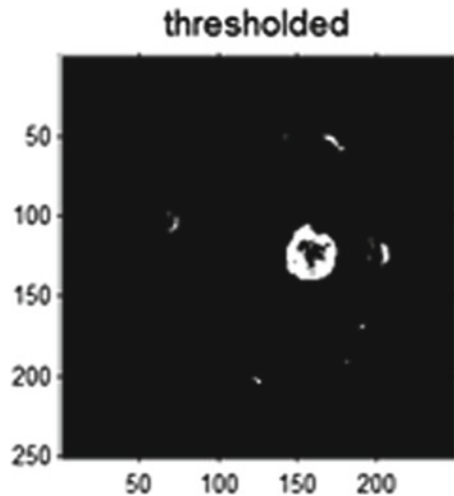
Fig. 5 (Case A): Eroded binary image of patient at severe stage of tumor
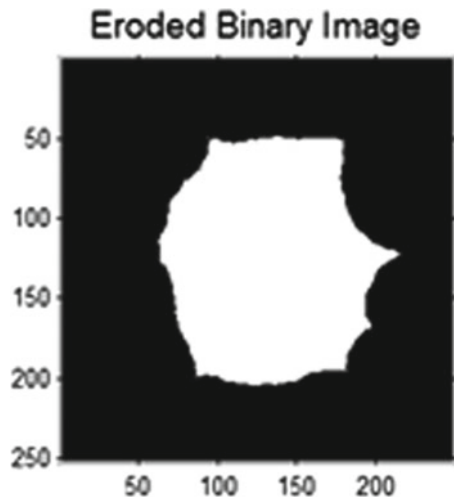
CASE B: Patient is at medium stage of tumor.

Step 1: The 2D MR images of human brain in DICOM format are shown in Fig. 9. The MR images are grayscale images. All the operations are performed on the binary image, so we convert grayscale image to binary image.
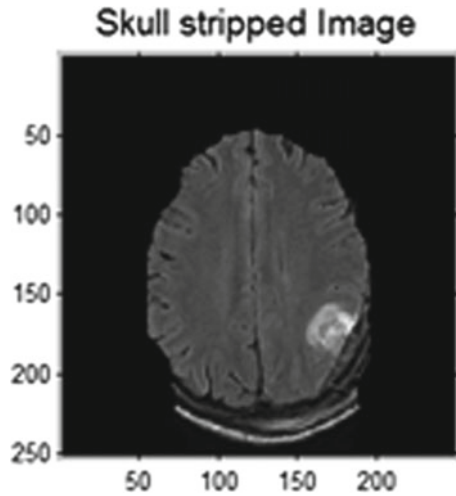
Step 2: In this step, image preprocessing operations are performed to refine the image and remove noise from image slice. Morphological operations and thresholding are used to clean the image that does not contain any unwanted particle.

Image preprocessing operations include morphological operations and thresholding, and these operations are used to clean the image that does not contain any unwanted particle.

Fig. 6 Watershed algorithm is applied on tumor region
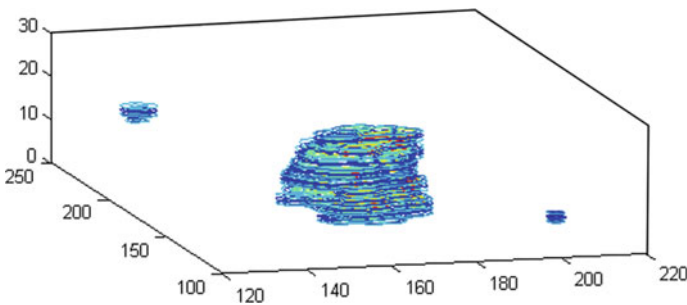
Fig. 7 (Case B): Mesh generation using drawing contours of each slice of MR images at medium stage of tumor

Step 3: In Fig. 10, skull part has been removed and brain tumor part has been extracted from the image slices.

Step 4: Below two images show the threshold tumor portion of patient which gives clear view of tumor. The next image is the eroded binary image of patient that gives a shape to tumor (Figs. 11 and 12).

Step 5: The result of the watershed algorithm is shown in Fig. 13. Watershed algorithm is used to divide the tumor region into different segments, and tumor gets divided into different segments.

Step 6: Figure 14 is of detecting contour of each tumor slice and stacking them one by one to create 3D mesh. The outline of each image slice of tumor is done in 3D, and stacking of image slice is done to generate a mesh.

Fig. 8 (Case A): 3D rendered image of detected tumor along with showing its location in the human brain at severe stage of tumor

Fig. 9 (Case B): Original gray scale image of patient at medium stage of tumor

Step 7: The rendered image of tumor is shown in Fig. 15. Rendering is performed on 3D mesh to generate 3D realistic tumor shape. Rendering performs to give a realistic image to 3D mesh generated, by which tumor can be shown in 3D view.

CASE C: Patient is not suffering from tumor.
Step 1: The 2D MR images of human brain in DICOM format are shown in Fig. 16. The MR images are grayscale images. All the operations are performed on the binary image, so we convert grayscale image to binary image.

Fig. 10 (Case B): Skull stripped image of patient at medium stage of tumor

Fig. 11 Threshold binary image of patient
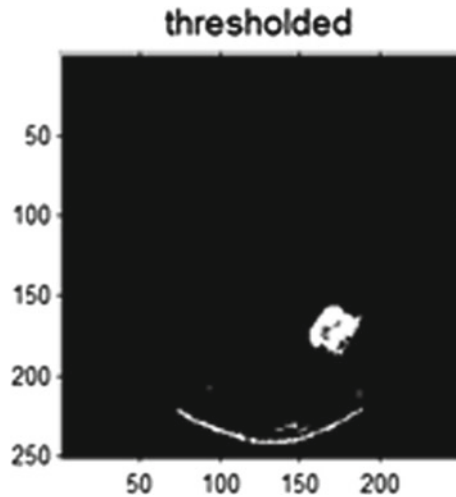
Step 2: In this step, image preprocessing operations are performed to refine the image and remove noise from image slice. Morphological operations and thresholding are used to clean the image that does not contain any unwanted particle.

Step 3: In Fig. 17, skull part has been removed.

Step 4: Figures 18, 19, 20, and 21 are blank because patient is not suffering from tumor.

Fig. 12 (Case C): Eroded binary image of patient having no tumor
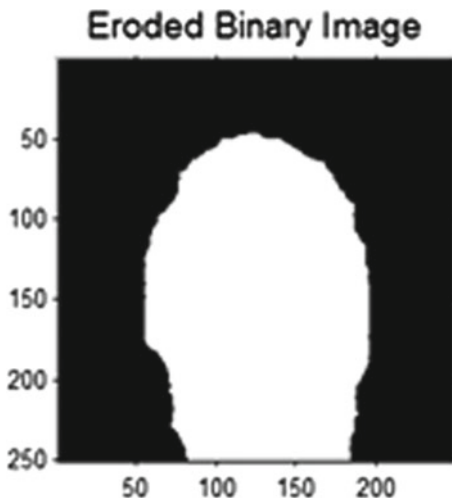
Fig. 13 (Case C): Watershed algorithm of human brain at medium stage of tumor
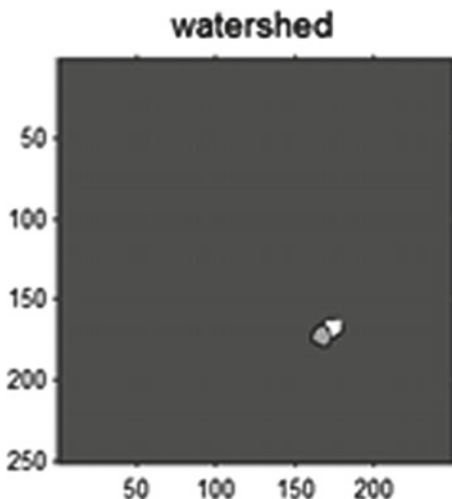
The result of all three cases is shown in Table 2. For clear understanding of algorithm, the first case does not show any 3D view of tumor because patient is not suffering from tumor. The moderate stage of tumor is shown in second case where the tumor is not much deep. The third stage shows the result of algorithm, which is applied on the patient data suffering at severe stage of tumor.
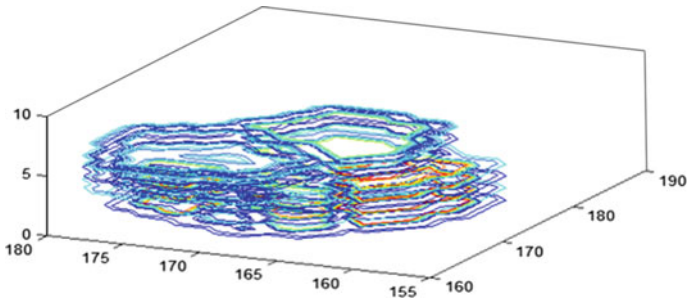
Fig. 14 (Case C): Mesh generation using drawing contours of each slice of MR images having no tumor
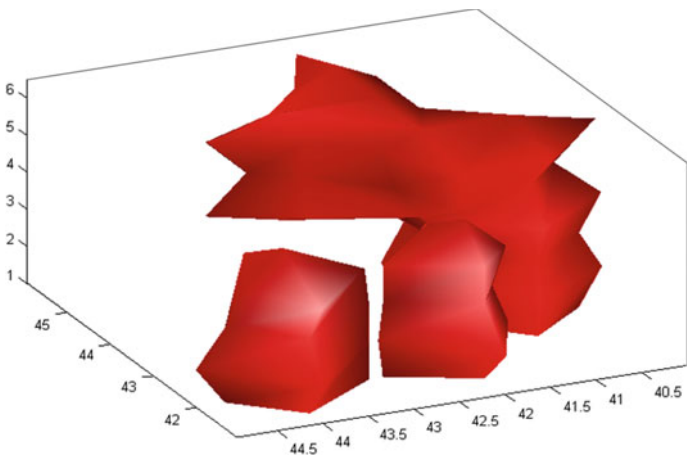
Fig. 15 (Case C): 3D rendered image of detected tumor along with showing its location in the human brain having no tumor

5 Conclusion and Future Scope

In this paper, we have generated 3D view of brain tumor using watershed algorithm. The generated 3D view of tumor shows the deepness of tumor very clearly, and it will be very helpful for the radiologist to diagnose it. Watershed algorithm is applied here to get clear information of deepness of tumor. Preprocessing is

Original Grayscale Image
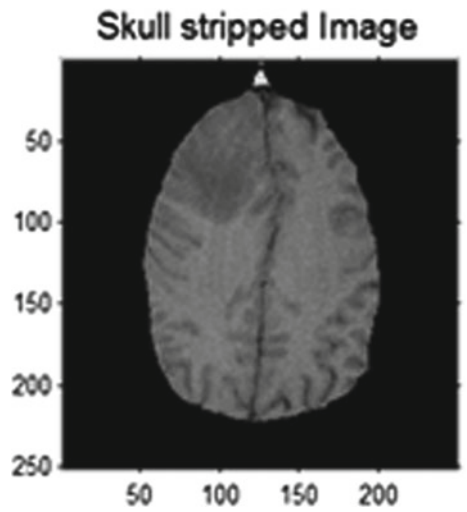
Skull stripped Image

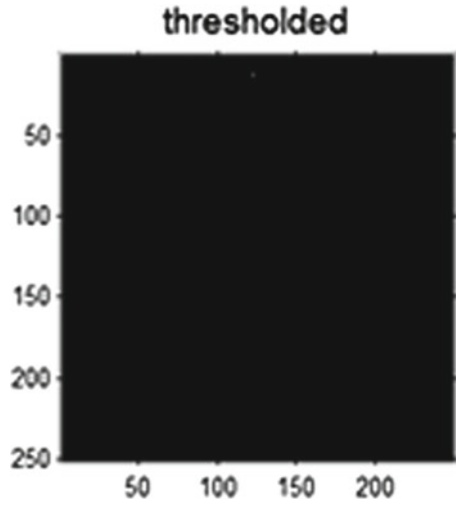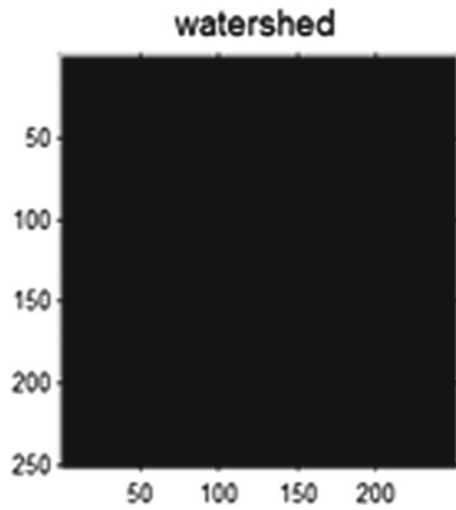**Fig. 18** Threshold image of patient

thresholded

Fig. 19 (Case C): Watershed algorithm of human brain having no tumor
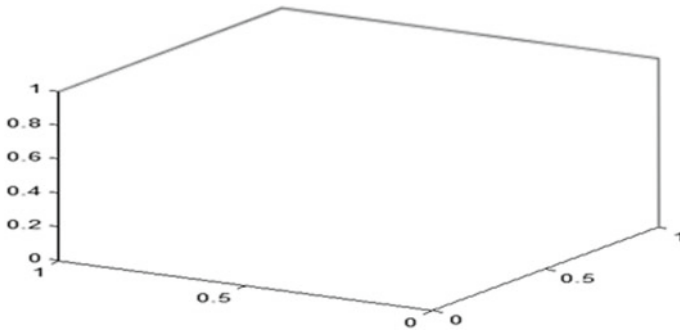

watershed

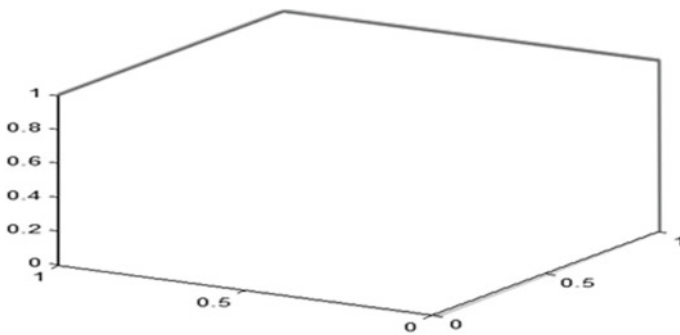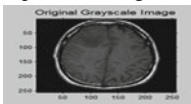**Fig. 20** (Case C): No generation of mesh because person is not suffering from tumor
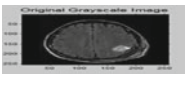
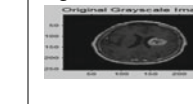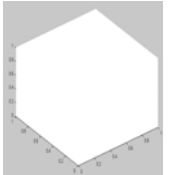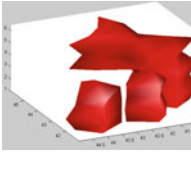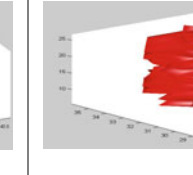**Fig. 21** (Case C): No generation of 3D rendered image of human brain because person is not suffering from tumor or having no tumor

Table 2 Experimental table showing 3D view of tumor at different stages

S. no.	Without tumor	With tumor	
1	Input MR image	Moderate tumor	High tumor
2	Result	Result	Result
3	Remarks No mesh generation because there is absence of tumor	Remarks 3D view of tumor at moderate stage	Remarks Severe stage of tumor, dense growth of cancer cells

necessary to reach to tumor inside skull, and post-processing gives the realistic view of tumor. Three cases had been discussed here namely—higher stage, medium stage, or moderate stage and the absence of tumor. The future scope of this paper is that the dataset of patients had been taken from X-NAT library, which is not a real set of patient data images, and this work can be applied on also real set of patient data in coming future.

References

1. Murugavallii S, Rajamani V (2006) A high speed parallel fuzzy c-mean algorithm for brain tumor segmentation. BIME J 6(1):29–34
2. Gopal NN, Karnan M (2010) Diagnose brain tumor MRI using images processing clustering algorithms such as fuzzy C means along with intelligent optimisation techniques
3. Resmi A, Thomas T (2012) A semi-automatic method of segmentation and 3D modelling of glioma tumors from brain MRI. Biomed Sci Eng 5:378–383
4. Kavitha C, Sangeetha S (2013) Automatic multimodality brain tumor detection. Int J Emerg Technol Adv Eng 3(3):264–268
5. Madhikar G, Lokhande SS (2013) Brain tumor detection and classification by using modified region growing method: a review. IJERT 2(12):2316–2320
6. Singh K, Kaur G (2014) A comprehensive review of various medical image processing techniques for MRI images. Int J Adv Res Comput Sci Softw Eng 4(5):1069–1072
7. Yu C-P et al (2014) 3D blob based brain tumor detection and segmentation in MRI. Institute of Computing, University of Campinas, Brazil
8. Zin S, Khaing AS (2014) Brain tumor detection and segmentation using watershed segmentation and morphological operation. Int J Res Eng Technol 3(3):367–374

9. Sharma P, Singh H (2015) Improvement of brain tumor feature based segmentation using decision based alpha trimmed global mean filter. Int J Comput Appl 121(21):1–8
10. Sindhu A, Meera S (2015) A survey on detecting brain tumor in MR images using image processing techniques. Int J Innov Res Comput Commun Eng 3(1):1–8
11. Wakchaure SL, Khandekar A (2015) Visualization of 3d view of detected brain tumor and calculation of its volume. Int J Tech Res Appl 3(6):120–126
12. Lopes S, Jaiswal D (2015) A methodical approach for detection and 3D reconstruction of brain tumor in MRI. Int J Comput Appl 118(17):0975–0978
13. Vanitha U et al (2015) Tumor detection in brain using morphological image processing. J Appl Sci Eng Methodol 1(1):131–136
14. Abdel-Maksoud E et al (2015) Brain tumor segmentation based on a hybrid clustering technique. Egypt Inform J 16(1):71–81
15. Kaur H, Kaur S (2016) Improved brain tumor detection using object based segmentation. Int J Eng Trends Technol (IJETT) 13(1):1–6
16. Samriti et al (2016) Brain tumor detection using image segmentation. Int J Eng Trends Technol (IJETT) 4(2):1–3
17. Isselmou AEK et al (2016) A novel approach for brain tumor detection using MRI images. Biomed Sci Eng 9:41–52
18. https://www.mathworks.com/help/matlab/function-basics.html
19. www.XNAT.org

Accurate Equivalent Circuit Model for Battery States Estimation

Mohammad Haris Shamsi, Hannan Ahmad Khan and Mohammed Aslam Husain

Abstract To build a battery management system capable of predicting battery behavior, it is necessary to analyze the ongoing dynamic processes inside the battery. Hence, a battery electric equivalent circuit model is proposed in this paper as well as an in-depth analysis is done in MATLAB, this will help the researchers working in the field of renewable energy systems and electric vehicles. The model accounts for all dynamic characteristics of a battery including nonlinear open-circuit voltage, discharge current, and capacity. Effect of temperature is also modeled using a cooling system. The model is validated with test current profiles. Less than 0.1% error between measured and simulated voltage profiles indicates the effectiveness of the proposed model to predict the runtime behavior of the battery. Furthermore, the model is implemented with the energy as well as the power battery pack to explore the differences in battery management systems. The state of charge calculations is performed using the proposed model and the Coulomb counting method and the results indicate only a 4% variance.

Keywords Electrical equivalent Li-ion model · High power lithium cell · High-energy lithium energy cell · State of charge · Electric vehicle

M. H. Shamsi
Energy Technology, Uppsala University, Uppsala, Sweden
e-mail: dcoolshamsi@gmail.com

H. A. Khan
Electrical Engineering Department, AMU, Aligarh, India
e-mail: hannanahmadkhan@gmail.com

M. A. Husain (✉)
REC-Ambedkar Nagar, AKTU, Ambedkar Nagar, India
e-mail: mahusain87@gmail.com

1 Introduction

Electrochemical energy storage [1] is expected to play a crucial role in sustainable solutions for the future mainly due to the efficient energy utilization and zero emission when in use. Electrochemical batteries are now being employed in many electrical systems because of the instant dispatch of energy when required. Although the applications like portable electronics have propelled the battery technologies, such as nickel metal hydride, nickel cadmium, lithium ion, these technologies are not mature enough to meet the progressive energy demands and the size limitations of today's energy systems [2].

A primary concern in the design of the energy systems integrated with electrochemical storage is the management of charge and the battery capacity that is linked with the amount of current taken out from the battery [3]. The state of charge (SoC) relates to the runtime of the battery, and hence, accurate prediction techniques are required for its estimation [4–6]. Researchers have developed different techniques in the past, which involve simple as well as complex algorithms for the estimation of the SoC and the state of health (SoH). However, a perfect estimation tool has not been found yet. Coulomb counting method is one of the basic methods for SoC estimation [7, 8]. As the name suggests, this method calculates the SoC by integrating the SoC flowing in and out of the battery. As far as the SoC precision is concerned, this method suffers from drawbacks such as offset in the measurement sensor resulting in SoC drift. Moreover, the Coulomb efficiency varies with operating states of batteries such as SoC, temperature, current, etc. [9]. Open-circuit voltage method aims to develop a one-to-one correspondence between SoC and open-circuit voltage (OCV) of a cell [10]. This method leads to an accurate estimation of SoC. The disadvantage is long resting time required by batteries to reach the balance potential, i.e., the open-circuit voltage. Also, this method is less likely to be implemented in practical applications because of the high level of accuracy (1 mV) required to estimate SoC in the mid-region of the voltage curve. Careful consideration is needed, as there exists a hysteresis phenomenon in Li-Ion cells [11] because of which the charge OCV and discharge OCV possess different values.

Another major concern relates to the fact that the battery states are not directly measurable by sensors, and hence, these values are usually inferred using model-based estimation algorithms [12]. Accurate battery modeling techniques are, therefore, of utmost importance [13]. Such techniques can enhance the convenience, reliability, and utility of Li-Ion battery packs in real-life applications. However, the complexity of these models remains a critical issue, particularly, due to the large computational effort required. Hence, a trade-off between accuracy and complexity is to be achieved, to utilize these models in microprocessors for accurate results in real time [14].

This paper proposes a high-fidelity computer simulation technique designed in MATLAB environment. The model described in this paper offers a trade-off between the accuracy and the computational effort. The technique described employs a new and intuitive model to predict the running behavior of a Li-Ion

battery pack. The model, known as equivalent circuit model, utilizes active (e.g., capacitors) and passive (e.g., resistors) electrical components to measure the battery performance. In this modeling approach, battery performance can be estimated directly from measuring and monitoring the conditions of cell operation. The associated equivalent circuit is used as a tool to predict battery behavior. Parameters of the model are estimated by performing pulse discharge tests on two different kinds of batteries designed for high energy and high power. The parameter estimation procedure revealed dependencies on SoC, current, and temperature. However, only the effects, due to SoC and current, are implemented using lookup tables that defined the values of parameters. The model is validated using experimental test profiles and then implemented for general simulation purposes. The different dependencies considered in this model render accurate estimation of the SoC.

The paper is organized as follows: Sect. 2 describes the model formulation, Sects. 3 and 4 deal with the experimental tests and the parameter extraction procedure. Sections 5 and 6 state the model formulation in MATLAB and the cell test setup. Section 7 deals with the parameter variation due to SoC and discharge current. Section 8 includes the comparison of simulated and measured test profiles. Section 9 states the conclusions and the future work that would further complement this research work.

2 Model Formulation

An equivalent circuit model (ECM) of a battery consists of different electrical components, namely a voltage source (representing the open-circuit voltage), parallel RC networks (representing the delay in voltage response), and a resistor (representing the internal resistance of the cell). Figure 1 shows the ECM, implemented in this research work.

The model employs active and passive electrical components. The values of these components are variable in nature and change depending on the metrics of the battery.

Previous modeling approaches, compared in [15], have developed ECMs with varying degrees of accuracy. Some have implemented ECMs with only one RC

**Fig. 1** Equivalent circuit model of a battery
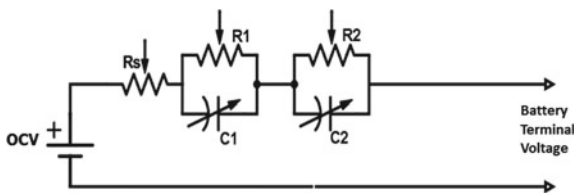
branch [16] while there are ECMs with two or more RC branches [17] offering improved accuracy. However, evaluation studies, such as [18], have proved that adding complexity beyond two RC branches does not justify the increased accuracy with additional computational effort. Some models even include dedicated components to model the effect of hysteresis in Li-Ion batteries [19].

The parallel RC networks in the ECM are used to incorporate the dynamic nature of the cell. These parameters are used to model the transient response. $R1$ and $R2$ are the faradaic contributions to the resistances, which include the charge transfer resistance. $C1$ and $C2$, termed as surface capacitors, represent the surface effects of battery and the internal chemical kinetics of the cell. As marked in Fig. 2, the time constant of the delayed voltage response is modeled using the two RC branches. All the parameters vary with variation of SoC, temperature, and discharge current. In this work, SoC and discharge current are considered in the analysis of the parameters. Effects due to change in temperature are not included and the cells are assumed to function at ambient temperature. However, the cell operation is analyzed in the presence of an external cooling system. The internal resistance of a cell is modeled using a resistor, whose value depends on temperature, SoC, and discharge current. The instantaneous voltage drop, at the beginning of a discharge, arises because of the presence of this resistance.

The OCV of the battery is modeled using a voltage-controlled voltage source. The value of the OCV depends on SoC and varies nonlinearly with SoC. It is measured as a steady-state voltage at different SoC levels. The value of OCV depends on the cell temperature too, but several experimental studies, as in [2], demonstrate that the variation is not evident and can be neglected to reduce the computational effort.

The voltage supplied by the battery to an external load is termed as battery terminal voltage. The value of this voltage differs quite significantly from the open-circuit voltage and is obtained after deducting the voltage drop across the internal resistance and the two RC branches, as shown in Fig. 3.

Fig. 2 Battery characteristic curve representing the different areas of operation of the battery
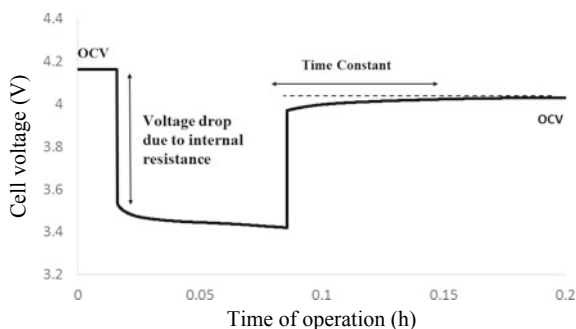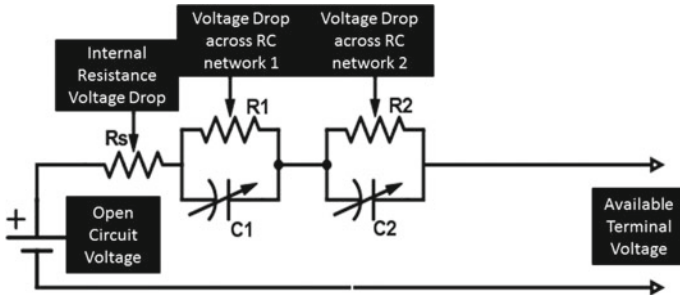
Fig. 3 Different voltage drops inside a battery. The drop is calculated across the different electrical components

3 Experimental Tests

For the parameter estimation, it is necessary to account for the steady state as well as the transient response of each cell in the battery pack. Experimental tests are designed to conveniently obtain the experimental curves [20]. Two main types of tests are performed on each battery.

Pulse discharge test (PDT) includes the discharging of the battery pack by providing the current in the form of constant pulses. There is a rest time included between the applications of two subsequent pulses. The rest time is decided based on the settling of open-circuit voltage to steady state. Discharge pulses are supplied to the pack to reduce the SoC by 15% with each pulse. The duration of each pulse is calculated using the SoC dependency equation on the discharge current. The main aim of these tests is to extract the model parameters, Rs, $R1$, $R2$, $C1$, and $C2$. PDTs are performed at varying pulse current levels to identify the effect of discharge current on the model parameters. These tests are also used to determine the OCV-SoC curves.

Continuous discharge test (CDT) involves the discharging of a battery pack at constant continuous current levels. The current levels remain the same as for the PDTs. These tests are used to identify the effect of different discharge currents on the capacity of the battery pack and of each cell.

4 Model Parameter Extraction

All the parameters proposed in the model are functions of SoC, current, and temperature. However, only the dependency of SoC and current is analyzed as the experiment is conducted in a controlled environment. Previous researches have used electrochemical impedance spectroscopy (EIS) for extracting the parameter values [19]. However, this technique cannot be utilized in practical applications, where the operation is much more dynamic and unpredictable. Another much

simpler theory [2] behind parameter extraction involves Ohm's law, which relates the proportionality between the instantaneous voltage and current. However, the technique works well only if the time step used is smaller than the time constant of the associated reaction so that the change in state can be considered minimal. A much more advanced technique includes the application of curve fitting tools in MATLAB to identify the values of Rs, $R1$, $R2$, $C1$, and $C2$. The value of Rs is determined using the instantaneous change in the value of the voltage at the end of a discharge pulse. The technique proposed in this paper is similar to the one as presented in [20] and uses the parameter estimation tool in Simulink Design Optimization. The model proposed in this paper considers the effect of varying levels of discharge currents, which has not been considered so far in the literature [21].

5   MATLAB Model

The ECM, as proposed in this paper, is modeled in Simulink. An exact equivalent of this model is also designed in Simscape to ease the process of parameter identification. The basic theory behind the modeling in MATLAB involves the following aspects.

With reference to Fig. 2, at the end of any discharge, there is an instantaneous voltage drop due to the presence of Rs in the cell. The values of Rs can be calculated from discharge curves at different current and SoC levels, based on (1). I represents the discharge current and ($V2 - V1$) represents the voltage difference as marked in Fig. 2.

$$Rs = \frac{V2 - V1}{I}. \tag{1}$$

The equations used in the design of the proposed model are:

$$C1\frac{dV2}{dt} + \frac{V2}{R1} = I \tag{2}$$

$$C2\frac{dV3}{dt} + \frac{V3}{R2} = I \tag{3}$$

where I represents the cell current, $V2$ and $V3$ represent the voltages of the two RC networks. These equations represent the model developed using MATLAB. The solution to this equation can be derived analytically as these are first-order RC circuits or using the parameter optimization tool, which enables quick and accurate results. Simulink Design Optimization employs iterative techniques to estimate the parameters. The discharge profile created from the model is compared to the experimental discharge profile and the parameters are updated at each step. The

iteration ends when the simulated voltage at each step matches the experimental voltage. The process is repeated using different discharge profiles. The process will produce 2-D lookup tables, in which the parameters vary with SoC and current. SoC estimation is done using Coulomb counting as well as voltage translation method to check the accuracy of results.

6   Cell Test Setup

Panasonic NCR18650B Energy and A123 Systems AHP14 Power Li-Ion cells are used in the discharge experiments. The energy cells NCR18650B offer a nominal capacity of 3250 mAh and a nominal voltage of 3.63 V. The power cells AHP14 offer a nominal capacity of 14 Ah and a nominal voltage of 3.3 V. These cells have a very low-internal resistance, which averages around 3 mΩ. The cells are discharged at varied levels of current. The charging system consists of a DC power supply. The device enables the battery pack to be charged under constant current-constant voltage regime. For Panasonic NCR18650B Li-Ion cells, a constant current of 1.610 A is used to charge the cells. The voltage is carefully monitored to ensure the safe operating limit of 4.25 V. The power supply is cut off as soon as one of the cells in the pack reaches the maximum voltage or the supply current reduces to 65 mA. The A123 Systems AHP14 power cells are charged using a similar routine but with a constant current of 7.2 A and a constant voltage of 3.6 V. The power supply is cut off as soon as one of the cells in the pack reaches the maximum voltage or the supply current reduces to 100 mA. The discharging system included resistors with a resistance of 6 Ω each. Different values of overall resistance are achieved using a series or parallel combination of the individual ones. The data acquisition board from linear technology is used to measure and store the cell voltages in a computer. The voltages measured by this board have a 16-bit resolution, equivalent to 1 mV and are logged every half a second [22, 23]. Current is measured using digital multimeters with high accuracy. Temperature is monitored using mini thermometers, having a range of −50 to +60 °C and a resolution of 1 °C.

7   Parameter Variations

7.1   With SoC

There occurs a significant variation in the voltage profile as the SoC is decreased from 100 to 0%. The voltage change is steeper for the energy cell than for the power cell. The power cells are designed to work in the mid-SoC region, while the energy cells are designed to work throughout the entire SoC range, as depicted in Fig. 4.

Fig. 4 Variation of
open-circuit voltage with SoC
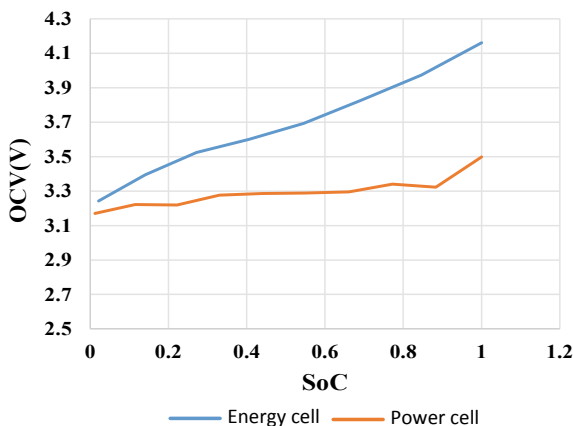
This observation can be used in the design of state estimation algorithms for battery
management systems for Li-Ion batteries. As the battery management systems are
application specific. According to the obtained result shown in Fig. 5a and b, the
value of internal resistance goes high at SoC levels close to zero. Also, the value of
Rs nearly remains constant for other SoC levels. This behavior is more evident for
an energy cell than that for a power cell. The values of the internal resistance of the
power cell are 100 times less than that of the energy cell.

This increase in internal resistance might be implemented in a BMS to detect the
end of charge. Battery capacity is also limited by the value of this resistance. Since
cells having high-internal resistance will have high voltage drops at the end of
discharge, a portion of the capacity remains unused as the BMS shuts off the pack
current when the voltage falls below the cutoff limit. However, if the BMS knows in
prior the value of this resistance, it can compensate for the remaining capacity by
adding the value of internal resistance drops to the measured voltage, thereby,
increasing the energy taken out from the battery.

The resistance values $R1$ and $R2$ of the energy cell and the power cell follow the
same trend as the internal resistance values (Fig. 6a and b). The values attain a high
value at the end of discharge, i.e., 0% SoC (more evident for energy cell). The
capacitance values $C1$ and $C2$ of the energy cell as well as the power cell do not
follow any specific trend with SoC levels and vary abruptly because of the dynamic
nature of the charge movement process inside the battery (Fig. 7a and b).

7.2   With Discharge Currents

The internal resistance values of the energy cells remain almost within a constant
range at different discharge currents for SoC levels in the range of 0.2–1.0 as
evident from Fig. 8. The values undergo a significant increase for low values of
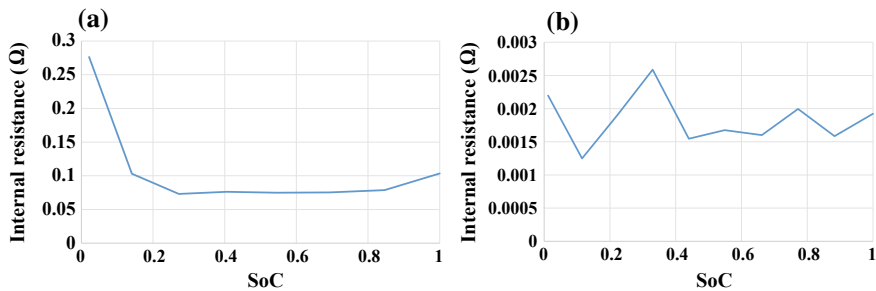
Fig. 5 Variation of the internal resistance of **a** energy cell and **b** power cell with SoC
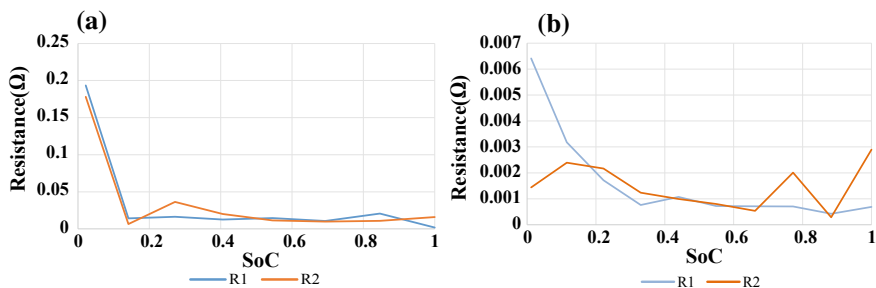
Fig. 6 Variation of parameters $R1$ and $R2$ of **a** energy cell and **b** power cell with SoC
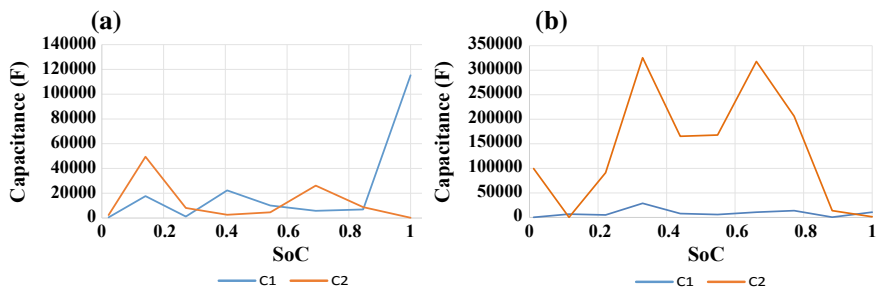
Fig. 7 Variation of parameters $C1$ and $C2$ of **a** energy cell and **b** power cell with SoC

SoC (below 0.2) and the resistance increases with decreasing levels of discharge current values. The variation of parameters OCV, $C1$, $C2$, $R1$, and $R2$ are not found to follow any trend with discharge current. The parameter values of the power cells follow the same trend as the energy cells.

8 Model Validation

A test current profile based on the data provided by a company is created to check
the relevance and functioning of the proposed model. The weakest cell was taken
into consideration for both the energy as well as power cells. The variation of SoC
from cell to cell is also observed using the test profiles. Moreover, SoC estimation is
done using the model as well as the Coulomb counting method and the proximity of
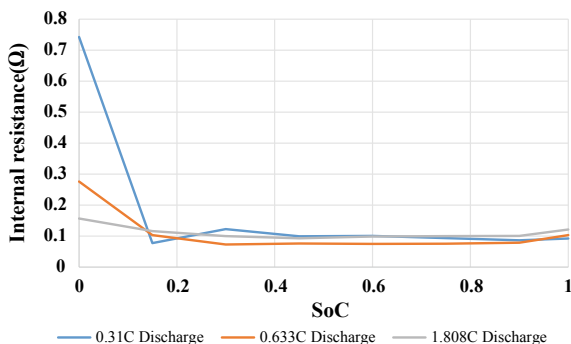the calculated values is taken into consideration. The comparison of the simulated
and measured voltage profile of the energy cell is depicted in Fig. 9a. The test
current profile (negative current values for discharge and positive current values for
charge) is shown in Fig. 9b. For energy cells, the SoC discrepancies from cell to
cell are within a range of 6% as depicted in Fig. 11a. The SoC level across each is
found to vary more with higher discharge currents. As far as the SoC estimation is
concerned, the variation in SoC values estimated using the proposed model and the
Coulomb counting method is found out to be less than 4%.

A similar test profile is analyzed using the model parameters of the power cell.
The simulated and measured voltage profile is depicted in Fig. 10. The test current
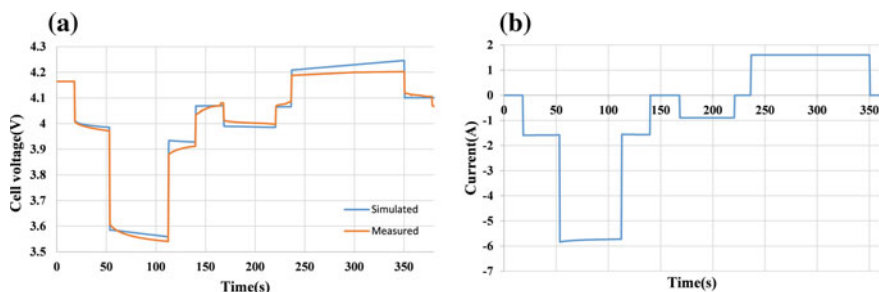
Fig. 9 **a** Measured versus simulated voltage profile of the energy cell. **b** Test current profile of the
energy cell. Negative values of current correspond to the discharging state, while the positive
values correspond to the charging state
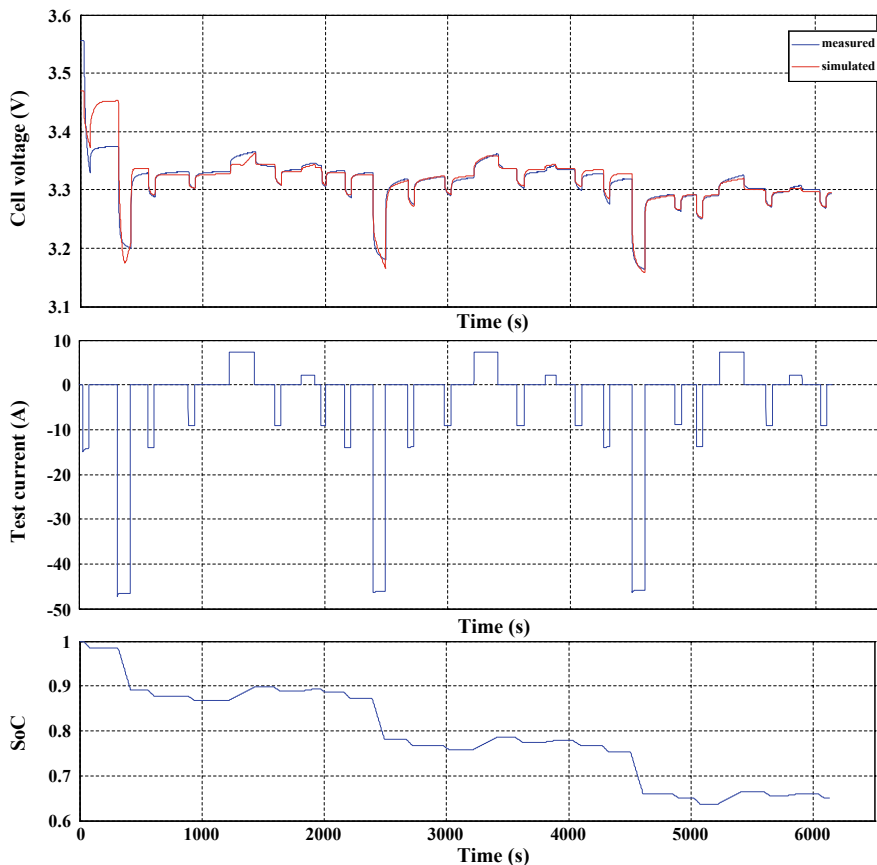
Fig. 10 Simulated versus measured voltage profile, test current profile, and SoC calculations of power cell

profile and SoC calculations are presented alongside in Fig. 10. The simulated voltage profile exactly traces the measured voltage profile, except at the start of the test run. The error between the profiles is encountered to be less than 0.1% for the overall profile with an exception of 2.98% at the beginning of the cycle. The main reason of this discrepancy at the beginning is not known at the moment, but the possible reasons could include dynamic variations in internal resistance, dynamic operating conditions, thermal stresses, etc. For power cells, the SoC discrepancies from cell to cell are within a range of 8% as depicted in Fig. 11b. The discrepancies tend to increase after each high current discharge. As far as the SoC estimation is concerned, the variation in SoC values estimated using the proposed model and the Coulomb counting method is found out to be less than 2%.

Fig. 11 SoC variations across individual cells in **a** energy battery pack and **b** power battery pack

9   Conclusion and Future Work

An accurate, self-corrective and intensive electrical model for a Li-Ion battery has been proposed in this paper. The model captures the dynamic characteristics of a battery. In actual runtime, this model can be implemented to measure the battery performance. Through this modeling approach, the parameters are dynamically updated based on SoC and discharge current variations. The model parame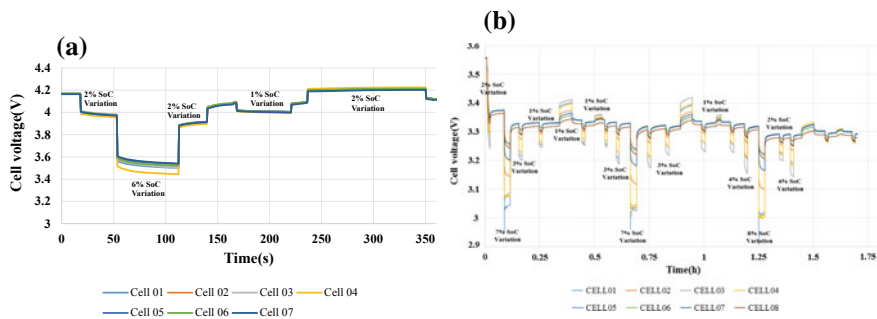ters are extracted using simulation-based approach. The parameters of the proposed model are found to vary with SoC and discharge current. Accurate battery state estimation algorithms are inferred using the discharge profiles as well as the battery model. Integration of these two aspects leads to accurate state estimation when the battery is in operation. Model validation has been performed using the extracted parameters for test current profiles for energy as well as power cells. The simulated profiles are found to match the measured profiles with some discrepancies at the beginning of the test run.

Future work to this research could include the effect of temperature variations on the model parameters. The model has not been investigated from a thermal point of view. Li-Ion batteries are very sensitive to temperature variations. Operating above the specified limits might lead to thermal runaway and a permanent damage to the cells in the battery pack.

References

1. Scrosati B, Garche J (2010) Lithium batteries: status, prospects and future. J Power Sources 195(9):2419–2430
2. Chen M, Rincon-Mora GA (2006) Accurate electrical battery model capable of predicting runtime and I-V performance. IEEE Trans Energy Convers 21(2):504–511
3. Linden D, Reddy TB (2010) Linden's handbook of batteries, 4th edn. McGraw-Hill

4. Huria T, Ceraolo M, Gazzarri J, Jackey R (2012) High fidelity electrical model with thermal dependence for characterization and simulation of high power lithium battery cells. In: 2012 IEEE international on electric vehicle conference (IEVC), Greenville, SC, pp 1–8
5. Hussain MA et al (2012) Modeling and study of a standalone PV system using MATLAB/SIMULINK. i-Manager's J Electr Eng 5(4):30
6. Husain MA, Tariq A (2014) Modeling and study of a standalone PMSG wind generation system using MATLAB/SIMULINK. Univ J Electr Electron Eng 2(7):270–277
7. Welcome to battery university! Retrieved 03 May 2016, from http://batteryuniversity.com/
8. Dell R, Rand DAJ (2001) Understanding batteries. Royal Society of Chemistry, Cambridge. Print
9. Andrea D (2010) Battery management systems for large lithium-ion battery packs. Artech House, Boston. Print
10. Shukla AK, Venugopalan S, Hariprakash B (2001) Nickel-based rechargeable batteries. J Power Sources 100(1–2):125–148
11. Nickel cadmium nicad batteries (2016) Mpoweruk.com. N.p., 2016. Web 16 June 2016
12. Lui R et al (2016) Analysis of the key factors affecting the energy efficiency of batteries in electric vehicle. World Electr Veh J 4:9–13. Print
13. Dunn B, Kamath H, Tarascon J-M (2011) Electrical energy storage for the grid: a battery of choices. Science 334(6058):928–935. Web 4 May 2016
14. Tarascon J-M, Armand M (2001) Issues and challenges facing rechargeable lithium batteries. Nature 414(6861):359–367. Web 4 May 2016
15. Song L, Evans JW (2000) Electrochemical-thermal model of lithium polymer batteries. J Electrochem Soc 147:2086–2095
16. Gomadam PM, Weidner JW, Dougal RA, White RE (2002) Mathematical modeling of lithium-ion and nickel battery systems. J Power Sources 110(2):267–284
17. Dubarry M, Liaw BY (2007) Development of a universal modeling tool for rechargeable lithium batteries. J Power Sources 174(2):856–860
18. Dubarry M, Vuillaume N, Liaw BY (2009) From single cell model to battery pack simulation for Li-ion batteries. J Power Sources 186(2):500–507
19. Knauff M et al (2016) Simulink model of a lithium-ion battery for the hybrid power system testbed. ResearchGate. N.p., 2016. Web 12 May 2016
20. Chiasserini CF, Rao RR (2001) Energy efficient battery management. IEEE J Sel Areas Commun 19(7):1235–1245
21. Jongerden MR, Haverkort BR (2009) Which battery model to use? IET Softw 3(6):445–457
22. Husain MA, Tariq A (2013) Modeling of a standalone wind-PV hybrid generation system using MATLAB/SIMULINK and its performance analysis. Int J Sci Eng Res 4(11)
23. He H, Xiong R, Fan J (2011) Evaluation of lithium-ion battery equivalent circuit models for state of charge estimation by an experimental approach. Energies 4(12):582–598. Web 12 May 2016

Velocity Differential Equation for Electrons at Point Throughout the Volume of Material Space Due to Potential Distribution Function

Vineet Kumar

Abstract Velocity of charge particles is not restricted to be constant at all the points on the volume of material space but rather space-time functions as output each with a nature of different depend upon the nature of input as potential functions presence to the same. This indicates that throughout the space coordinates of different over the volume of material space the velocities so distributed out at any instant along the timeline of positive side, which in correspondent determine the velocity distribution function, are not due to the thermal effect but due to the consideration of potential functions so distributed out for the same. Therefore, based upon the potentials as potential distribution function as input this velocity distribution function as output so find out here with in this paper must not be confused with that of Maxwell's velocity distribution formula. Here, from the respective differential equation the velocity distribution function, so obtained, for charge particles of material space is over the negative element of sign conventional space only, means for electrons, but not over the positive element of it as this does not satisfy the unique integral factor of one for both of mass and charge unlike electrons.

Keywords Current distribution function · Material space · Potential distribution function · Sign conventional space · Velocity differential equation · Velocity distribution function

1 Introduction

Other than mass for the solid of all as measurable of inertness, charge is one of another intrinsic property but for some as they may be neutral as well. Nature wise, this property defines over the two elements of sign conventional space, i.e. $(+)$ and $(-)$, along with magnitude of peculiar denote by $|-e|$ with integral

V. Kumar (✉)
Department of Electrical Engineering, Kurukshetra University, Kurukshetra 136119, India
e-mail: vineet05k@gmail.com

multiple of it. Over the positive element of sign conventional it terms as positive charge, while over the negative element of sign conventional it terms as negative charge. Irrespective to the matching over particles of either, on sign conventional space term neutrality arises and the particle that satisfies the same regard as neutral particle.

This charge particle in case of zero-valued velocity function imposing on it, responsible for the setup of electrostatic field denote by $\vec{E}(x, y, z)$ which in correspondent determine electric force of either attraction or repulsion type in the presence of other with the intrinsic property of the same, but the nature of either like or dislike. In the case of like charge particles the force is repulsive, but in case of dislike charge particles the force is attractive, which as analogy satisfy the truth table of *EX-OR* type logic circuit given by equation of the form $Y = A \otimes B = \overline{A}B + A\overline{B}$ for a system of 2. That is,

A	B	Y
0	0	0; i.e. Repulsive case
0	1	1; i.e. Attractive case
1	0	1; i.e. Attractive case
1	1	0; i.e. Repulsive case

where $\otimes$ denotes the exclusive-*OR* operation. The pair $(0, 0)$ and $(1, 1)$ form the structure for two charge particles represents the case of likeness which in correspondent determine the repulsiveness, while the pair $(0, 1)$ and $(1, 0)$ represents the case of dislike which in correspondent determine the case of attractiveness.

Now, the objective of this paper is to determine the velocity differential equation for charge particle on negative element of sign conventional space throughout the space coordinates of different over the volume of material space not due to the cause of thermal effect but due to the cause of potential functions so distributed on same. The velocity distribution function for charge particle by the solution of its differential equation is an output consequence due to the potential distribution function as input of it over the spatial coordinates of material space on time.

The structure of this paper begins with the introduction in Sect. 1 and then followed on by the description of current function in presence of potential source over negative element of sign conventional space in Sect. 2. In Sect. 3, the mass distribution function for charge particles of type same is concluded, next, in Sect. 4 the differential equation for velocity distribution function is concluded, and finally, it being last by the conclusion in Sect. 5.

2 Current Consideration Over Negative Element of Sign Conventional Space Throughout the Volume of Material Space

Irrespective of the consideration of weight $w > 1$ such that $w \in Z^+$ as a multiple of $-e$ with $|-e| = 1.6 \times 10^{-19}$ C because of the charge is quantized, consider of w here unity only so that electrons as available charge for the material space consider only. Over negative element of sign conventional space, the total charge for the consider charge density $n^-(x, y, z, t)$ on elemental volume $dV(x, y, z)$ as a cube with $dV(x, y, z) = dxdydz$ is $dQ^-(x, y, z, t)$. Where one of the vertexes of elemental volume cube of the material space in three-dimensional space is at point $P(x, y, z)$, while the other opposite diagonal at point $R(x + dx, y + dy, z + dz)$ with $dA_x^{1,2}, dA_y^{1,2}$ and $dA_z^{1,2}$ as the area of six faces along x, y and z axis, respectively, such that $dA_x^1 = dA_x^2 = dydz, dA_y^1 = dA_y^2 = dzdx$ and $dA_z^1 = dA_z^2 = dxdy$. Then, the envelope negative charge is,

$$\partial Q^-(x, y, z, t) = |-e|N^-(x, y, z, t) = |-e|n^-(x, y, z, t)dV(x, y, z) \qquad (1)$$

Other than negative charge concentration of material, there is a positive charge concentration as well given by $n^+(x, y, z, t)$, such that the total number of positive charge particles $N^+(x, y, z, t)$ on elemental volume of same unlike the negative one $N^-(x, y, z, t)$ does not satisfy the relation $N^+(x, y, z, t) = n^+(x, y, z, t)dV(x, y, z)$ as $n^+(x, y, z, t)$ comprises of $n_1^+, n_2^+, \ldots, n_A^+$. Each $n_1^+, n_2^+, \ldots, n_A^+$ so introduce here has corresponding charges of $+e, +2e, \ldots, +Ae$ with A as the atomic number. The only way to represents, the number of positive charge particles on elemental volume is $N^+(x, y, z, t) = \sum_{i=1}^A n_i^+ dV_i(x, y, z)$ with $dV(x, y, z) = \sum_{i=1}^A dV_i(x, y, z)$ such that n_i^+ satisfy peculiar statistical law.

In the absence of any source, the number of charge carriers over either elements of sign conventional space, through the imaginary surface S over the interval of any, being averagely same in number so that the net current is zero. Along x-axis, electric current through the surface having area $dA_x^{1,2} = dS = dydz$ in satisfaction with Eq. (1) can be possible only when an ordered motion with the average velocity function of certain, i.e., $v_x = v_x(x, y, z, t)$, imposed on the chaotic motion of it, which is possible in the presence of nonzero source. The rate of change of negative charge envelope over the elemental volume of same is given by,

$$\frac{\partial}{\partial t} Q^-(x, y, z, t)_x = |-e|n^-(x, y, z, t) \left(\frac{\partial_t n^-(x, y, z, t)}{n^-(x, y, z, t)} dt + 1 \right) v_x dydz \qquad (2)$$

Equation (2), so obtain as component, can yield the vector quantity as well, which is over surface density by considering the components of three as $\frac{\partial}{\partial t} Q^-(x, y, z, t)_x / dydz$, $\frac{\partial}{\partial t} Q^-(x, y, z, t)_y / dzdx$ and $\frac{\partial}{\partial t} Q^-(x, y, z, t)_z / dxdy$ each along the axis of x, y and z, respectively, term as current density vector. This distribution

of current over function of peculiar at each point throughout the volume of material space determines the current distribution function. Again, here, the velocity function of charge is due to the force experience by of electric type only, which satisfies the law of inverse square, i.e., $\propto 1/r^2$, so discussed by Johannes Kepler in 1604 regarding the explanation of spherical expansion of light in space from a point. By experimentation, the conjecture of inverse for electrical found to be in satisfaction suggested the followings as,

1. John Robinson that the repulsive force in between the sphere of similar charges varied as [1]$r^{-2.06}$.
2. J. C. Maxwell that the electric attraction and repulsion must be inversely as some power of the distance between that of the $2 + \frac{1}{50}$ th and that of the $2 - \frac{1}{50}$ th, and there is no reason to think that it differs at all from the inverse duplicate ratio [2, 3].

3 Mass Consideration of Charge Particle Over Negative Element of Sign Conventional Space Throughout the Volume of Material Space

Within the volume of material space, the total number of charge particles so available in the presence of the source can be categorized into the two groups, which is over the either element of sign conventional space. If m_o be the mass of a neutral atom with N and Z as nucleon and mass number, respectively, then, $m_o = Nm_n + Z(m_p + m_e)$, where m_n, m_p and m_e are the mass of neutron, proton and electron, respectively with $A = N + Z$. Irrespective of the mass consideration of negative charge particle, which is always m_e for electron, the mass consideration of a left out positive charge particle is not same in case of all, as it is given by $m_j = Nm_n + Zm_p + (Z - j)m_e; \forall j \leq Z$ with j as a deficit number. This shows that like in case of current consideration for positive charge the mass consideration over volume of same cannot be directly calculated by the simple product of $M^+(x, y, z, t) \neq m_j N^+(x, y, z, t) \neq m_j n^+(x, y, z, t,)dV(x, y, z)$ but by the relation of $M^+(x, y, z, t) = \sum_{j=1}^{A} M_j$ with $M_j = m_j N_j = m_j n_j^+(x, y, z, t,)dV_j(x, y, z)$. The reason for the inequality in direct is due to the availability of range for j from 1 to Z. Here, the only concern is the consideration of mass of electrons over the elemental volume of same as ordinary particles, which at a point and at any instant can be simply obtain by the product of,

$$M^-(x, y, z, t) = m_e N(x, y, z, t) = m_e n^-(x, y, z, t)dxdydz \tag{3}$$

As, this Eq. (3) is of time-dependent type on the volume dV, then, the change in mass over time interval dt is given by,

$$\frac{\partial}{\partial t} M^-(x, y, z, t)_x = m_e n^-(x, y, z, t) \left(\frac{\partial_t n^-(x, y, z, t)}{n^-(x, y, z, t)} \right) dxdydz \qquad (4)$$

This Eq. (4) so obtained as the rate of change of mass distribution function is unlike that of Eq. (2) as in case of time-invariant condition it simply reduces to become zero due to $\partial_t n^-(x, y, z, t) = 0$ while the term $\left(\frac{\partial_t n^-(x,y,z,t)}{n^-(x,y,z,t)} dt + 1 \right)$ for Eq. (2) approaches to one.

4 Differential Equation of Velocity for Charge Particle Over Negative Element of Sign Conventional Space Throughout the Volume of Material Space

In earlier Sects. 2 and 3, the respective differential equations different distribution functions for charge particles throughout the volume of material space over negative element of sign conventional space that are current and mass is conclude from it, which are not in direct dependent of the potential distribution function $\varphi(x, y, z, t)$ but of function $n(x, y, z, t)$ responsible by the presence of same. The potential distribution function $\varphi(x, y, z, t)$ as input so consider here by mean of any is different throughout the space coordinates of material space, such that $\sum_{k=1}^n \left\{ \frac{1}{k!} (\delta x \partial_x + \delta t \partial_t)^k \varphi(x, y, z, t) \right\}$ with $\partial_x = \partial/\partial x$ in conjunction with the function $|-e| n^-(x, y, z, t) dydz$ give the x-component of force as $F_{ax} = |-e| n^-(x, y, z, t) dydz \sum_{k=1}^n \left\{ \frac{1}{k!} (\delta x \partial_x + \delta t \partial_t)^k \varphi(x, y, z, t) \right\}$. This F_{ax} regard as force of non-dissipative type as it is responsible for the motion carrying by the particle, which along with dissipative (or friction) one F_{dx} responsible for the loosening of it gives the resultant of $F_x = F_{ax} - F_{dx}$. Neglecting the friction force acting on a particle and with the consideration of Eqs. (3) and (4), the velocity differential equation for motion yield as,

$$\left(\frac{\partial_t n^-(x, y, z, t)}{n^-(x, y, z, t)} dt + \partial_t \right) v_x(x, y, z, t) =$$
$$\frac{|-e|}{m_e} \left[\sum_{k=1}^n \left\{ \frac{1}{k!} (\delta x \partial_x + \delta t \partial_t)^k \varphi(x, y, z, t) \right\} / dx \right] \qquad (5)$$

Equation (5) so obtained is the required differential equation for velocity of x-component $v_x(x, y, z, t)$ of charge particle over the negative element of sign conventional on material space, which is distribute in accordance with the distribution of potential throughout the volume of material space.

5   Conclusion

As stated earlier, the main objective of this paper is to find the differential equation of the velocity distribution function for charge particle on negative element of sign conventional space throughout the space coordinates of different over the volume of material space due to the potential distribution functions, which is given by Eq. (5). Besides this, the scalar distribution functions of current and mass are also concluded, which is given by Eqs. (2) and (3), respectively.

References

1. Robinson J (1822) A system mechanical philosophy, vol 1, pp 73
2. Maxwell JC (1967) [1879] The electrical researches of the honorable Henery Cavendish. Cambridge University Press, pp 112
3. Sadiku MNO, Principles of electromagnetics. Oxford, 4th edn

Realization of Novel Multi-scroll 2D Chaotic Oscillator Using DVCC

Manoj Joshi and Ashish Ranjan

Abstract In this research work, an autonomous chaotic oscillator is implemented by using differential voltage current conveyor (DVCC) and few passive components. The schematic of the proposed oscillator looks simple, but the behavior is vigorous and attractive. The circuit is examined by its dynamic behavior in addition to control parameters that generate multi-scroll nature without any external periodic signal source. The operational activity of DVCC is verified using 0.18 µm TSMC CMOS parameter. Finally, the viability of chaotic oscillator is justified through PSPICE simulation.

Keywords Nonlinear dynamics · Duffing chaotic oscillator · Differential voltage current conveyor (DVCC)

1 Introduction

In recent time, chaos have proven their prominence in various advanced applications such as artificial intelligence and information security, secured chaotic communication systems, stabilization of circuits, control of chaos in robotics, chaotic synchronization of maps, multi-user mobile communication systems, encryption and storage of information, cryptography, heartbeat analysis, wireless sensor network and many more [1–3].

One of the classical second-order nonlinear dynamical systems that generate chaos called as duffing chaotic oscillator [4]. The mathematical second-order differential equation represents the chaotic behavior as:

M. Joshi · A. Ranjan (✉)
National Institute of Technology Manipur, Imphal 795001, India
e-mail: ashish.ism@rediffmail.com

M. Joshi
e-mail: manojjoshi1506@gmail.com

$$\frac{\mathrm{d}^2 x}{\mathrm{d}t^2} + a\frac{\mathrm{d}x}{\mathrm{d}t} + bg(x) = f(x) \tag{1}$$

where x, $g(x)$, $f(x)$ and (a, b) correspond to displacement, nonlinear function, external driving term, and control parameter for the chaotic oscillator circuit. However, research interest is proceeding to construct the sophisticated nonlinear chaotic oscillator with an active block especially operational amplifier (Op-Amp) [5] and some analog representation of chaotic oscillator with traditional passive components [6–8]. To understand the dynamics of several complex physical system of diverse nature under real-time conditions like nonlinear physical pendulum and duffing oscillator equation [9], forced Duffing-Vander-Pol oscillator [10], non-oscillatory Rayleigh Duffing oscillator [11], Duffing-Holmes [12–15], Silva-Young type oscillator [16] are well reported in the literature. Among these nonlinear oscillators, the occurrence of periodic and non-periodic oscillators may depend on periodic external force known as non-autonomous [9–11] while other oscillatory systems without external periodic signal source termed as autonomous chaotic oscillator [12–14]. The above-mentioned reports are basically based on the mathematical approach and operational amplifier (Op-Amp) based active design approach.

In this paper, an attempt is made for the design of autonomous second-order duffing chaotic oscillator using current mode active building block named as differential voltage current conveyor (DVCC). It provides wider bandwidth, greater linearity, low power consumption, high-dynamic range and few more in comparison with conventional voltage mode Op-Amp [17, 18]. The proposed chaotic oscillator uses three numbers of DVCC, single diode, two resistors, and two capacitors. The workability of chaotic behavior is examined with PSPICE simulation.

2   Circuit Description

A differential voltage current conveyor (DVCC) [19] is a versatile current mode active block whose circuit symbol along with its internal CMOS realization is shown in Fig. 1.

The following matrix form is responsible for the DVCC characteristics as:

$$\begin{bmatrix} V_X \\ I_{Y_{1,2}} \\ I_X \end{bmatrix} = \begin{bmatrix} 1 & -1 & 0 \\ 0 & 0 & 0 \\ 0 & 0 & -1 \end{bmatrix} \begin{bmatrix} V_{Y_1} \\ V_{Y_2} \\ I_Z \end{bmatrix} \tag{2}$$

Here, the two terminals (Y_1 and Y_2) exhibit high-impedance port, while X shows low-impedance port. On the other hand, voltage across the X terminal produces the

(a)

(b)
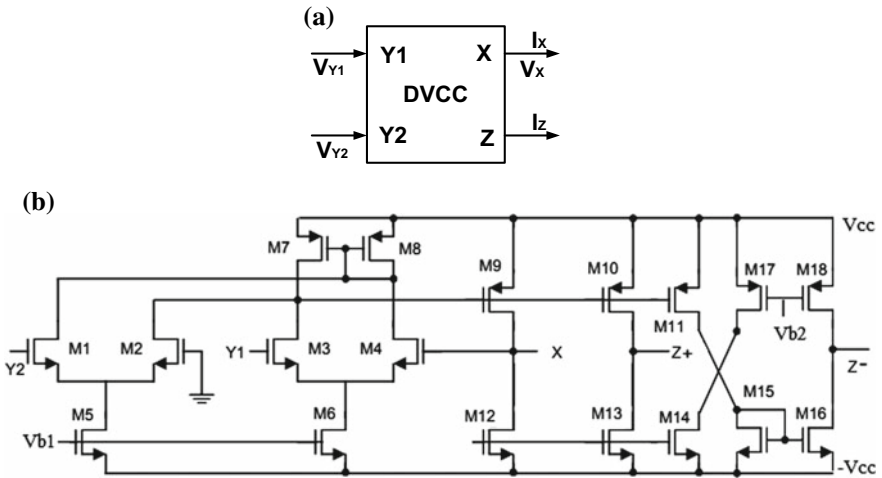
Fig. 1 DVCCC structure **a** circuit symbol, **b** CMOS realization of DVCC

voltage difference of ports Y_1 and Y_2 and the current through X port is the same as that of Z port.

We introduce an alternative scheme for the generation of DVCC-based 2D chaotic oscillator circuit with a diode and some passive components as shown in Fig. 2. The proposed circuit consists of two differentiator circuits and a summer circuit. Our chaotic oscillator is designed on the basis of Eq. (1) as introduced in the introduction section. Here, a practical exponential model is used to exhibit non-linear characteristics, with the help of diode that exhibits the nonlinear diode characteristic as Eq. (3).

Fig. 2 Proposed chaotic duffing oscillator using DVCC
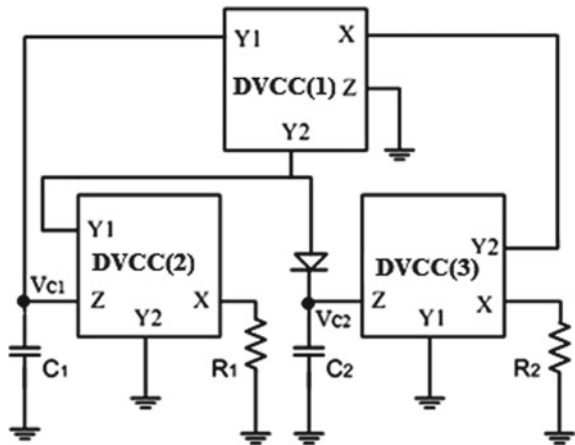
$$I_d = I_s(\exp(V_d/V_T\eta) - 1) \left.\right\}$$
$$V_d = \eta V_T(\ln I_d/I_S) + 1 \qquad (3)$$

where V_T, I_s and η are the thermal voltage at room temperature, reverse saturation current, and ideality factor, respectively. The schematic of chaotic oscillator is examined, by applying Kirchhoff's law where these two differential equations support the mathematical model for chaotic oscillator as:

$$\frac{d}{dt}V_{C1} = \frac{1}{C_1R_1}g(x) \qquad (4)$$

$$\frac{d}{dt}V_{C2} = \frac{1}{C_2R_2}(V_{C1} - g(x)) + \frac{1}{C_2}I_d \qquad (5)$$

Here the term, V_{C1} and V_{C2} are the voltages across capacitors C_1 and C_2, respectively, and $g(I_d)$ is exponential nonlinear function is modeled in term of diode voltage as:

$$g(I_d) = \begin{cases} (V_{C2} - V_d), & V_{C2} > V_d \\ 0, & V_{C2} = V_d \\ -(V_{C2} + V_d), & V_{C2} < V_d \end{cases} \qquad (6)$$

The nonlinear function $g(I_d)$ involves the diode and approximated by the current–voltage characteristic (V-I) of diode as shown in Fig. 3. Here we are considering diode is only forever region. Then the modified expression for Eqs. (4) and (5) can be rewritten as:

$$\dot{x} = a(V_d - y) \left.\right\}$$
$$\dot{y} = b(x - y - V_d) + c\{\exp(y + V_d) - 1\} \qquad (7)$$

Fig. 3 Nonlinear *V-I* characteristic of the ideal diode
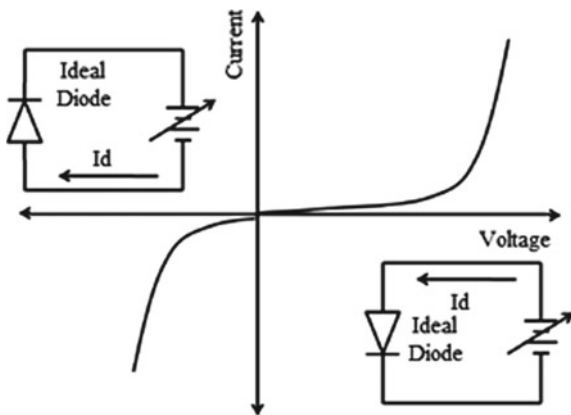
By equating Eq. (7) with the autonomous 2D equation, we found that external driving term is absent and these equations are normalized by dimensionless variable as: $x = V_{C1}/V_T\eta$, $y = V_{C2}/V_T\eta$ and control parameter $a = 1/R_1C_1$, $b = 1/R_2C_2$, $c = 1/V_TC_1$.

where x and y are state variables and (a, b, and c) are positive parameters. According to Eqs. (7) and (8), the parameters a and b depend on diode characteristic. The equilibrium point of Eqs. (7–8) follows:

$$\left. \begin{array}{l} a(V_d + y) = 0 \\ b(x + y - V_d) + c\{\exp(y + V_d) - 1\} = 0 \end{array} \right\} \qquad (8)$$

The general condition of non-dissipative describes mathematically as:

$$\frac{\partial \dot{x}}{\partial x} + \frac{\partial \dot{y}}{\partial x} = -b + c < 0 \qquad (9)$$

where b and c are always positive, hence the system is a dissipative system for ($b > c$) and contracted exponentially ($\mathrm{d}V/\mathrm{d}t = \mathrm{e}^{-(c-b)}$). It signifies volume element (V_0) decreases with respect to flow rate $\mathrm{e}^{-(c-b)t}$ in time domain. As $t \to \infty$, the system trajectory shrinks to zero; therefore, all system orbits are ultimately limited to a specific subset with zero volume and the motion settles onto an attractor.

3 Simulation Results

To verify theoretical observation of the proposed 2D chaotic oscillator based on CMOS DVCC, PSPICE simulation is performed by using 0.18 μm CMOS process parameters [20]. The aspect ratios are given in Table 1. The supply voltages in circuit are +1.25 V, Vb_1=- 0.45 V, Vb_2= 0.30 V. The technical performance of the chaotic oscillator is examined with passive component values R_1 = 6.5 kΩ, C_1 = 40 nF, C_2 = 80 nF and a diode 1N1500. Here the dominant parameter is R_2 whose value varies from few ohms (Ω) to kilo-ohm (kΩ).

The time series chaotic response is shown in Figs. 4 and 5 for double scroll and five scroll. On the other hand, generation of some typical periodic phase portraits

MOS transistors	W (μm)/ L (μm)
M_1–M_6	4.5/0.9
M_7–M_{11}	9/0.9
M_{12}–M_{16}	4.5/0.9
M_{17}–M_{18}	9/0.9
M_1–M_6	4.5/0.9

Table 1 MOS transistors aspect ratio for DVCC

Fig. 4 Time series: V_{C1} and V_{C2} for double scroll
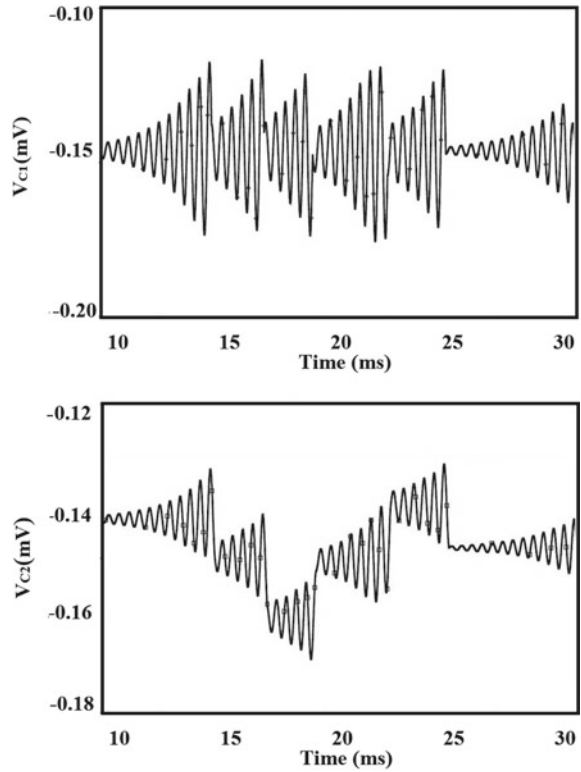
(V_{C1} Vs. V_{C2}) plane is shown in Fig. 6 that exhibits double scroll, five scroll, and multi-scroll for the resistor value (R) 6.5, 8.8, and 1 kΩ, respectively. Finally, a brief comparative study of common autonomous duffing oscillator gives some useful observations as:

- A minimum number of active building blocks and grounded passive components are used [8, 11–14].
- No inductor has been used [11], [13–15].

Fig. 5 Time series: V_{C1} and V_{C2} for multi-scroll
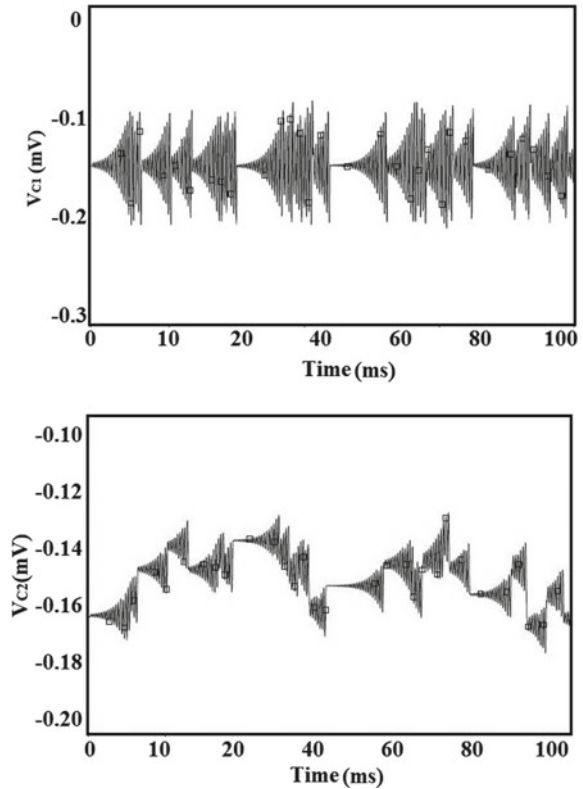
4 Conclusion

In this report, a robust 2D chaotic oscillator is implemented using advance active block as DVCC. The passive components are grounded and give a better sign for integrated circuit design. The entire reported work has explained with the current state of art. Also a new approach has been implemented for the design of chaotic oscillator using advance analog building block which is useful for undergraduate and research student to explore various advanced applications such as artificial intelligence and information security, secured chaotic communication systems [1–3] using chaos theory.

Fig. 6 Generation of phase portraits **a** double scroll with $R = 6.5$ kΩ. **b** Five scroll with $R = 4.5$ kΩ. **c** Multi-scroll with $R = 1$ kΩ
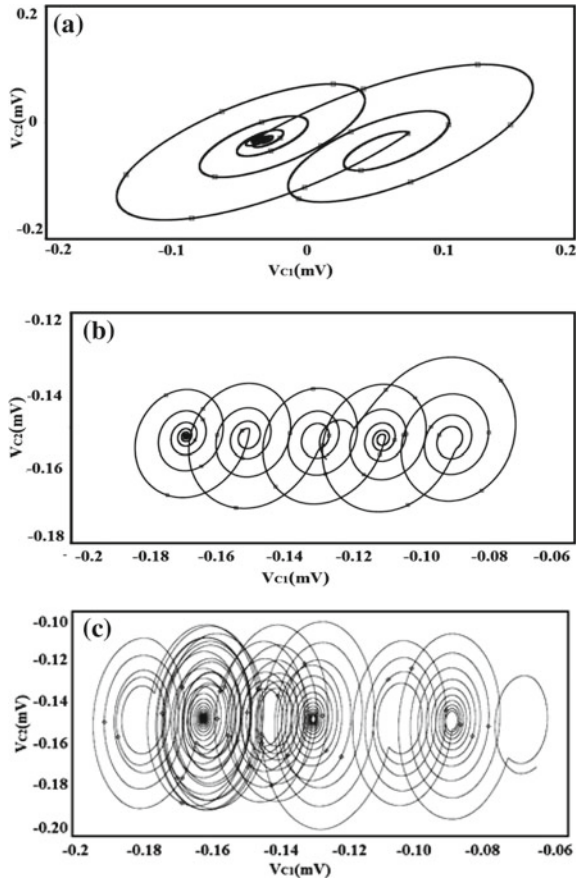
References

1. Dekker A, Farrow P (1994) Creativity, chaos and artificial intelligence. In: Dartnall T (ed) Artificial intelligence and creativity. Studies in cognitive systems, vol 17. Springer, Dordrecht
2. Leon G, Chua and hart rate variability. J Cardiovasc Electrophysiol 10:1358–1360
3. Jin L, Zhang Y, Li L (2013) One-to-many chaotic synchronization with application in wireless sensor network. IEEE Commun Lett 17:1782–1785
4. Ueda Y, Ralph A (1992) Chapter 5: Explosion of strange attractors exhibited by Duffing's equation, nonlinear dynamics. In: The road to chaos
5. Schmitthenner M (2014) Chapter 1: Modeling the Duffing equation with an analog computer. In: Springer proceedings in mathematics & statistics. Springer, Berlin
6. Lakshmanan M (1997) Bifurcations, chaos, controlling and synchronization of certain nonlinear oscillators. In: Kosmann-Schwarzbach Y, Grammaticos B, Tamizhmani KM (eds) Integrability of nonlinear systems. Lecture notes in physics, vol 495. Springer, Berlin
7. Piper JR, Sprott JC (2010) Simple autonomous chaotic circuits. IEEE Trans Circuits Syst II Express Briefs 57:730–734

8. Elwakil AS, Kennedy MP (2000) Improved implementation of Chua's chaotic oscillator using current feedback op amp. IEEE Trans Circuits Syst I Fundam Theory Appl 47:76–79

9. Salas AH, Castillo JE (2014) Exact solution to Duffing equation and the pendulum equation. Appl Math Sci 8:8781–8789

10. Adelakun AO, Njah AN, Olusola OI, Wara ST (2016) Computer and hardware modeling of periodically forced-Van der Pol Oscillator. Act Passiv Electron Compon, 1–7

11. Guin A, Dandapathak M, Sarkar S, Sarkar BC (2017) Birth of oscillation in coupled non-oscillatory Rayleigh Duffing oscillators. Commun Nonlinear Sci Numer Simul 42:420–436

12. Tamaseviciute E, Tamasevicius A, Mykolaitis G (2008) Analogue electrical circuit for simulation of the Duffing-Holmes equation. Nonlinear Anal Model Control 13:241–252

13. Lindberg E, Tamaseviciute E (2009) Autonomous Duffing-Holmes type chaotic oscillator. In: European conference on circuit theory and design, 663–666

14. Tamaseviius A, Lindberg E, Kirvaitis R (2016) Autonomous Duffing-Holmes type chaotic oscillator. Elektron Elektrotech 5:43–46

15. Tamaseviciute E, Mykolaitis G, Tamasevicius A (2011) Autonomous Silva-Young type chaotic oscillator with flat power spectrum. Elektron Elektrotech 9:109–112

16. Kengne J, Kenmogne F (2014) On the modeling and nonlinear dynamics of autonomous Silva-Young type chaotic oscillators with flat power spectrum. Chaos 24

17. Ferri G, Guerrini NC (2003) Low-voltage low-power CMOS current conveyors. Cluwer Academic Publishers

18. Pal K (1989) Modified current conveyors and their applications. Microelectronics J 3:37–40

19. Elwan HO, Soliman AM (1997) Novel CMOS differential voltage current conveyor and its applications. IEE Proc Part G 144:195–200

20. http://lgjohn.ecen.ceat.okstate.edu/5263/processparam/t4bk_lo_epi-params.html

Investigation on Short-Term Wind Power Forecasting Using ANN and ANN-PSO

Neeraj Kumar, Aditi Singh, Nikita Rai and Nihal Chauhan

Abstract The fossil fuels are exhaustible, implying that they draw finite resources that would eventually dwindle. This would as a result become very expensive or too damaging and impactful for the environment. In contrast, the various types of alternative source of energy, commonly the renewable energy sources—solar, wind, and geothermal, are constantly replenished and are nonexhaustible. With the prominent penetration of generation capacity of wind power, the uncertainty and variability of wind energy poses new challenges to power system operations. The major reason for wide acceptance of wind as renewable resource is abundance in nature, economic, and environmental advantages. In the electricity grid at any moment, balance must be maintained between electricity consumption and generation—otherwise, disturbances in power quality or supply may occur. Wind generation is a direct function of wind speed and, in contrast to conventional generation systems, is not easily dispatchable. Managing the variability of wind generation is the key aspect associated with the optimal integration of that renewable energy into electricity grids. The paper explores the combination of artificial neural networks with the particle swarm optimization technique for the forecasting of the month-ahead wind power. This has been incorporated for the model of forecasting along the generalization technique which would be improved. The tool of optimization so selected is PSO which is further used on the weight matrix of ANN for improving the final results. The mean absolute percentage errors, root-mean-square error as well as the *r*-squared for the above-mentioned models were calculated, and accuracy was compared for the month-ahead forecast.

Keywords Wind power · Forecasting · Neural network · Particle swarm optimization

N. Kumar
Electrical and Electronics Engineering Department,
Bharati Vidyapeeth's College of Engineering, New Delhi, India

A. Singh · N. Rai · N. Chauhan (✉)
Bharati Vidyapeeth's College of Engineering, New Delhi, India
e-mail: nihalchauhan16@gmail.com

1   Introduction

Rapidly increasing demand for energy and decrease in the conventional energy resources have led to the use of renewable energy for power generation across the world. The most popular are solar power and wind power. In India, the potential for electricity generation using wind power is approximately of 102 GW. But wind energy cannot be utilized efficiently due to its alternating nature which affects the output power. It is therefore important to forecast the wind power for proper grid operation. It plays a crucial part in planning of the power systems, operation control, distribution, ease of use, consistency of the system, and so on [1].

The utilization of wind for energy generation has gained a lot of attention globally despite the fluctuation in wind speed and other weather factors that affect the wind power [2]. The reliability of the system can be increased by short-term wind power forecasting; this also reduces the operational cost and helps in load management. Forecasting can be done using either physical or statistical procedure.

In this paper, month-ahead wind power is predicted using the statistical model where a relation between generation data and set of variables is found out for the given set of data. This approach uses historical data of a particular location for the construction of model [3]. The parameters for the model is selected, namely the wind speed, day of the week, temperature, and the length of blades for wind generators. The accuracy of the results depends on these parameters. Two modeling techniques have been used, one being the artificial neural networks (ANNs) and the other hybridization of ANN with particle swarm optimization (PSO).

Artificial neural network can be used for the approximation of any nonlinear function, it has a feature of self-learning through which it can familiarize to any change in the surroundings [4]. ANN can be used for mapping a relationship between the given input and the desired output. Since ANN is not an optimization method, we use particle swarm optimization (PSO) for better results [5]. PSO is an optimization method based on the population, and it has a better mechanism for sharing of information and can efficiently solve any optimization problems which includes a lot of constraints. PSO is used to minimize the errors in ANN by modification of the weight matrix and is included in ANN during its training phase [7]. This method is cheap as compared to other techniques, and its implementation is easy.

2   Methodology

The day of the week (D_i), 24-h previous wind power (D_{i-1}), and the 24-h previous wind speed (W_{i-1}) have been given where Y_i the 24-h wind power of the forecasted day and the general form of the predicator is given by [8]:

$$Y_i = f(Y_{i-1}, W_{i-1}, D_i) \tag{1}$$

Thus, we might use the data from the previous power as well as wind speed history along with the type of the day of the week of the forecasted. At the midnight previous day $(i - 1)$, it is, hence, needed to formulate the next day's 24-h prediction (i). This forecasting would further be implemented for arranging and optimizing the power generators of wind used to be started in the day of working (i).

The brief description of wind power generation

In the energy conversion system of wind, kinetic energy of the moving air molecules and wind turbines is used to store the energy in the wind and converts it to the needful electrical power. The following equation can be used to calculate the power (P) contained in the air that flows through the wind turbine [10]

$$P = 0.5 * (S * D * V) * V^2 \tag{2}$$

where

S   Swept area of rotor,
D   Density of air, and
V   Velocity of air at turbine's rotor level.

The hybrid approach model has been presented in the paper for the short-term wind power forecasting, typically, the next 24 h, for India. An observable efficient increase in the efficiency of working has been found after the application of PSO on ANN. Wind speed and wind power inputs have been considered in the proposed model. Historical dependency of data of one year has been incorporated. The wind data of India has been gathered from the National Renewable Energy Laboratory, Western Wind Resources Dataset [11].

Major components of the model

A. *The Neural Network for wind power forecasting*

ANN is inspired by biological nervous systems and consists of simple elements operating in parallel. Training of neural network is done by altering the values of the connections to perform a particular function. Neural networks are trained so that a particular input leads to a specific target output.

The implemented model of artificial neural network basically consists of a two-layered network, namely the input layer, hidden layer as well as the output layer. ANN can be used for modeling of linear and nonlinear systems without the need to make assumptions implicitly. The amount of accuracy depends upon the number of hidden layers in the network and the connection between these layers and output as depicted in Fig. 1. The number of hidden layers used in our model is 30.

The power of the network is determined by the connecting neurons. It consists of weighted inputs, a transfer function, and one output to the inputs. The transfer

Fig. 1 Concept of neural network

Input Layer | Hidden Layer(s) | Output Layer

Fig. 2 Block diagram of the proposed model

Collection of Input Data

Preparation of Input and Target Data

Training of Input data

Testing Of data

Validation of data

Calculation of Accuracy

Result Comparison
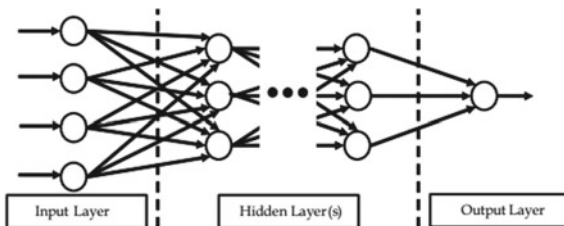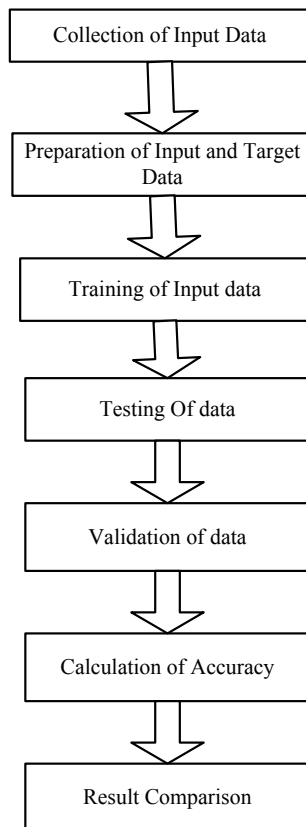
function of a neural network describes its behavior. Since the weights are a parameter that can be adjusted, the whole network is parameterized (Fig. 2).

Pre-processing of data

After the collection of data, the missing data is assumed by taking average of the neighboring data, and then, the data is normalized before feeding it to the neural network.

Network building

In this stage, the user provides the number of hidden layers in the network, the connections between the layer and the output and the transfer function for the given neural network. For multilayer perceptron, the transfer function is given below:

$$Yi = f\left(\sum_{i=1}^{n} WijXi\right) \tag{3}$$

where f is a simple threshold function, Xi is the input signal, and Wij is the strength of the respective connections

Training of data

During training of data, the input weights are so adjusted that the error calculated between the actual and predicted value is the least. The error is calculated using the following formula in Eq. (4)

$$Error\_percent = abs(err)/test * 100 \tag{4}$$

Testing of data

The testing of the input data is performed, and the root mean square is calculated to determine the extent of error produced. The lower the RMSE, the more accurate is the estimation.

Equation (5) gives the formula for calculating the root-mean-square error

$$RMSE = mean(sqrt(r^2)). \tag{5}$$

The r-squared is the regression sum of the squares divided by the total sum of squares. It is also known as the 'coefficient of determination' and denoted by r^2. It is a proportion and is always a number between 0 and 1. It can be calculated using the following equations:

$$SSR : Regression\,sum\,of\,squares = \sum_{i=1}^{n}(\hat{y}_i - \bar{y})^2 \tag{6}$$

$$SSE : Error\,sum\,of\,squares = \sum_{i=1}^{n}(y_i - \hat{y}_i)^2 \tag{7}$$

$$SSTO : Total\,sum\,of\,squares = \sum_{i=1}^{n}(y_i - \bar{y})^2 \tag{8}$$

Hence, the 'coefficient of determination' r^2 is given by:

$$\frac{\text{SSR}}{\text{SSTO}} = 1 - \frac{\text{SSE}}{\text{SSTO}} \tag{9}$$

In certain situations, the ANN model cannot be able to provide great accuracy. Hence, a hybrid mechanism of ANN-PSO is involved, wherein PSO is an evolutionary algorithm which is generally implemented for the set of weight optimization of the ANN.

The mean absolute percentage error (MAPE) is used to examine the forecasting accuracy of the proposed models

$$\text{MAPE}\,[\%] = \frac{1}{N} \sum_{i=1}^{i=n} \frac{|P_{\text{A}}^i - P_{\text{F}}^i|}{P_{\text{A}}^i} \times 100 \tag{10}$$

In Eq. (10), P_{A}^i and P_{F}^i are representing the actual and forecasted energy. N and I are thus representing the number of hours and respective indices.

B. *Particle Swarm Optimization for Weight Optimization of ANN*

Particle swarm optimization (PSO) is a type of evolutionary computation which was initially inspired by the flocking of birds and thus was built with swarm optimization. The algorithm obtains an optimal solution which is designed on the observations from clustering of animals. It is thus, a heuristic methodological approach which was first proposed by Kennedy and Eberhart in 1995 [12] for dealing with the optimization of continuous and discontinuous function decision making. Hence, as the name suggests, it is based on the sociological and biological animal behavior including flock of birds in the search of food.

A basic variant of this algorithm simply functions by using a collection known as swarm of candidate solutions which are generally known as particles. These particles are then made to roam about for the search space with regard to some formulas. This movement of particles is further guided by their own best known position in the search space and the best known position of the entire swarm. When these improved positions are being searched, these will come to guide the swarm's movement. The entire process is repeated with the hope of solution that is satisfactorily optimal. A PSO primarily can be said to have two operators:

- velocity update operator—determining the particle velocity
- position update operator—determining the particle position.

In PSO, each particle is made to flow through the dimensional space of search with random variable as well as velocity which is adaptable with the aim to find the function values that are low (global minimum). In the standard PSO algorithm process of convergence, the particles are manipulated using Eqs. (11) and (12), wherein each particle is accelerated and tries to adjust the velocity in accordance with the best possible positions previously taken which is further saved in the

memory known as personal best. The adjustment is also made in accordance with the previous best position captured via the adjacent particle named global best, thus figuring out to look for a better position. Hence, communication between the particles takes place with a view to spread the information during their search with one another.

$$v_i = \mathrm{w}v_i(t) + r_1 c_1 (p_{\text{best}} - x_i(t)) + r_2 c_2 (g_{\text{best}} - x_i(t)) \tag{11}$$

$$x_i(\mathrm{t}+1) = x_i(\mathrm{t}) + v_i(\mathrm{t}+1) \tag{12}$$

where the variables have the following significance:

|	
w	Inertia weight providing a balance between two explorations, local and global,
v_i	Current velocity for each iteration,
$v_i\ (t+1)$	Modified velocity for each iteration,
c_1	Cognitive component, and
c_2	Social component.

These are the positive numerical to control the movement of particles during every iteration.

r_1 and r_2	uniform distribution numbers ranging from [0, 1],
$x_i(t)$ and $x_i(t+1)$	present and the changed position for every iteration, and N is the number of particles between the input and the hidden as well as the further hidden layers to the final output layers; the connection weights are depicted in two of the matrices, namely w_1 and w_2 with the dimensional size of $(m_1 \times n_1)$ and $(n_1 \times m_2)$, respectively; $x_i(t)$ the present position for each particle that is depicted by $w_i(\mathrm{t}) = \{w_1, w_2\}$. Hence, a set of weights for the present iteration is represented by each particle's position. Using Eqs. (5) and (6), the error of the network is reduced to a minimum value by determining the position for each particle as well as the new velocity. The number of weights that are linked with the network determines the search space dimension. Also, the weight matrix's new position value depicts the fitness value for each particle.

The algorithm flowchart of the proposed method is shown in Fig. 3.

Proposed Algorithm of the technique:

The following algorithm has been used to power the ANN model using the PSO optimization technique.

Fig. 3 Algorithmic flowchart
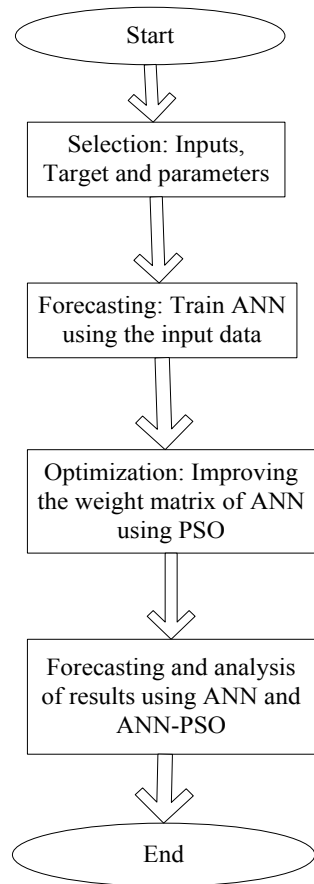
Step **1**: Select the ANN structure. Set the number of neurons and create a feed-forward network to train.

Step **2**: Train the ANN by BP algorithm for selected dataset. The dataset is divided into three different sets like training, validation, and testing datasets. After completion of the training, store the weight matrices for further updates.

Step **3**: Do short-term load forecasting by using the present ANN found in Step 2.

Step **4**: Generate a number of matrix sets called candidate particles from the stored weight matrices in Step 2. This step explores the opportunity of randomness and generates more search spaces.

Step **5**: Initialize local best (pbest), global best (gbest), and other PSO parameters w, c1, and c2 using the standard PSO rules.

Step **6**: Do short-term load forecasting using the ANN having the new weight matrices.

Step **7**: If the performance of Step 6 is better than the previous one, then go to Step 8; otherwise, go to Step 9.

Step **8**: Update pbest and gbest parameters based on the performances of current solution.

Step **9**: In this step, update the present solutions (particles) based on (1–2); thus, a new set of solutions is obtained and the said process repeats.

Step **10**: If stopping criterion is met, take the global best weight matrix set as the solution of the proposed method and go to the next step; otherwise, go back to Step 6 for further exploration.

Step **11**: Put the updated weighted matrix in the ANN structure. The new ANN is constructed by applying PSO. The newly trained ANN powered by PSO optimization generally always performs better than conventional ANN networks as created in Step 3.

Step **12**: Enter training and validation data as input, and results are found for ANN-PSO model.

Step **13**: Compare the performance of Step 3 and Step 12.

Step **14**: Print results.

3   Results and Comparison

In this section, we have demonstrated the outcomes of proposed techniques and their accuracy for the wind power forecasting using MATLAB 2016(a). Figure 4 represents the graph obtained from the ANN method of wind forecasting.

In Fig. 5, the results obtained through ANN powered by PSO are shown. The graph consists of actual (blue) wind power and forecasted (red) wind power curve. It is clearly observed from the graph that forecasted (red) wind power is closely followed the curve of actual (blue) wind power.

Table 1 shows the calculated values of the proposed algorithms, ANN and ANN-PSO of RMSE, MAPE, and R-squared.

The MAPE, RMSE as well as R-squared for the two techniques of forecasting are compared graphically and depicted in Fig. 6. The vertical axis shows the error.

Figures 7 and 8, respectively, show the regression plots of the two techniques used, namely ANN and ANN-PSO, showing a wide area of scattering in the plot of ANN.
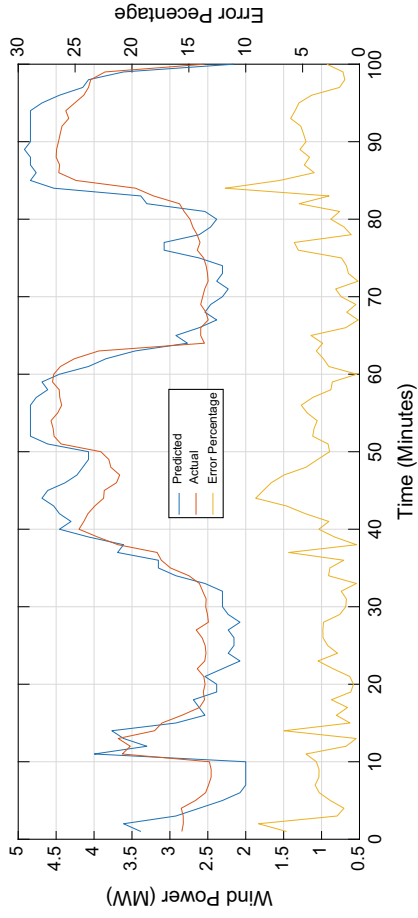
Fig. 4 Actual and forecasted plot of wind power using ANN with error percentage plot
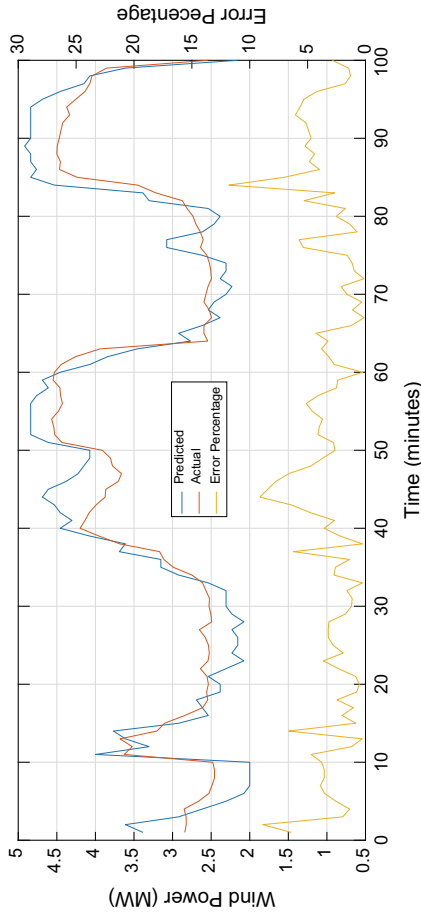
Fig. 5 Actual and forecasted plot of wind power using ANN-PSO and error plot

Table 1 Calculated error values

Algorithm model	RMSE (%)	MAPE (%)	R-squared (%)
ANN	4.1316	2.0534	79.03
ANN-PSO	3.6132	1.8235	82.27

Fig. 6 Graphical representation for errors of ANN and ANN-PSO methods

Fig. 7 Regression plot for ANN

Fig. 8 Regression plot for
ANN-PSO
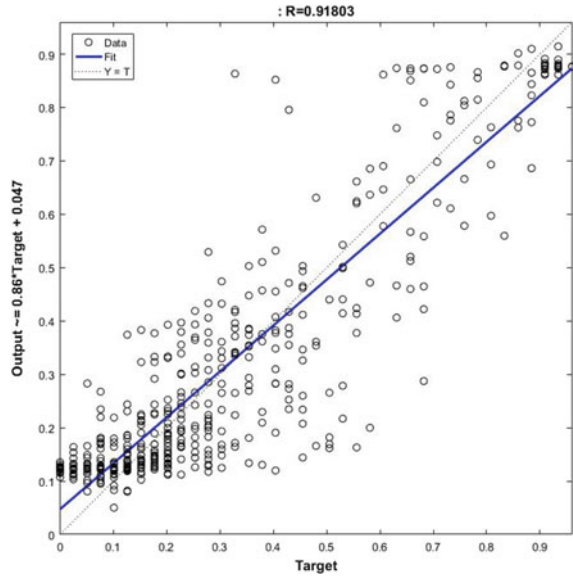
4 Conclusion

This paper proposes ANN and ANN-PSO approaches for short-term wind power forecasting, and forecasting accuracies of the methods are compared. The effectiveness of the proposed methods is thus examined by calculating the MAPE, RMSE, and R-squared values. It has been noticed that the forecasting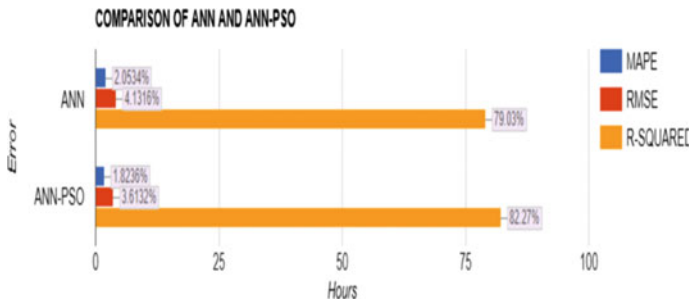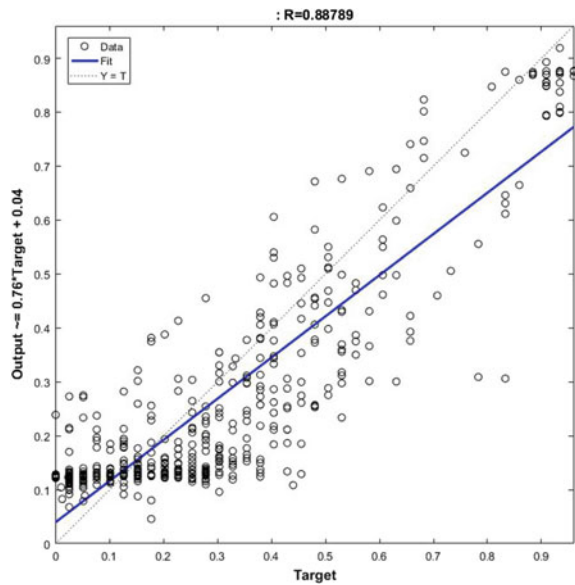 error is reduced due to the optimization of bias weight using PSO to train the ANN network. The MAPE values are 2.0534 and 1.8236% for ANN and ANN-PSO, respectively. The RMSE values are 4.1316 and 3.6132% for ANN and ANN-PSO, respectively. R-squared values are 79.03 and 82.27% for ANN and ANN-PSO, respectively. Hence, the results show the superiority of the PSO-optimized model forecasting over the conventional ANN technique. In future, we can consider the other parameters like wind mill area, the diameter of the wind mill, and direction of wind, weather condition, and height of the turbine to improve the forecasting accuracy.

References

1. Guo Y, Zhang JP, Dai R (2014) Marine navigation. Dalian Maritime University Press, Dalian
2. Rahman S, Hazim O (1993 May) A generalized knowledge-based short-term load forecasting technique. IEEE Trans Power Syst 8(2):508–514
3. Hu X, Zhao G (2008) Forecasting model of coal demand based on Matlab BP neural network. Chin J Manag Sci 10(16):521–525

4. Tsai CF, Wu JW (2008) Using neural network ensembles for bankruptcy prediction and credit scoring. Expert Syst Appl 34(4):2639–2649
5. Srinivasan D, Tan SS, Chang CS, Chan EK (1999 Aug) Parallel neural network-fuzzy expert system for short-term load forecasting: system implementation and performance evaluation. IEEE Trans Power Syst 14(3):1100–1106
6. Xie Z (2010) Matlab statistical analysis and application of 40 case analysis. Beihang University Press, Beijing
7. Kennedy J, Eberhart R (1995) Particle Swarm Optimization. In: Proceedings of IEEE international conference on neural networks, 1942–1948
8. Alex D, Timothy C (1990 Nov) A regression-based approach to short term system load forecasting. IEEE Trans Power Syst 5(4):1535–1550
9. Li G, Hao YL, Zhao YX (2009) Research of neural network to tidal prediction. In: Proceedings of international joint conference on computational science and optimization, 282–284
10. Orwig K, Ahlstrom M, Banunarayanan V, Sharp J, Wilczak J, Freedman J, Haupt S, Cline J, Bartholomy O, Hamann H, Hodge BM, Finley C, Nakafuji D, Peterson J, Maggio D, Marquis M, Recent trends in variable generation
11. National Renewable Energy Laboratory, Western Wind Resources Dataset. Available online: http://wind.nrel.gov/Webnrel/
12. Kennedy J, Eberhart RC (1995) Particle swarm optimization. Proc IEEE Int Conf Neural Netw 4:1942–1948

Impact of the Positioning of a Single Bypass Diode in a PV String on its Reliability

E. Fernandez and Sandhya Prajapati

Abstract The reliability of a solar photovoltaic (SPV) string can be modified by the use of bypass diodes across affected cells suffering an open circuit due to operational problems. Open-circuit conditions are created by mechanical failure of circuit continuity over a period of time or else due to transient conditions like shadow effects which affect one or more cells in the string. Cells in the string that are enclosed between the ends of the bypass diode, if affected, will be bypassed and the chances of power continuity will be improved. In this paper, we attempt reliability evaluation of a single string of 10 solar PV cells in series using a *single* bypass diode that can enclose a variable number of cells of the string between its ends. We assume that only one cell is open circuited in the string. *Monte Carlo* simulations are used to evaluate the LOLP of the string with different bypass diode configurations. The results show that the reliability of power continuity improves as we enclose greater number of PV cells between the bypass diode ends.

Keywords Solar PV modules · Bypass diode · Reliability analysis · Monte Carlo simulation

1 Introduction

Photovoltaic (PV) modules are a very reliable source of electrical energy. Solar photovoltaic (SPV) produces electrical power from sunlight which is a clean, quiet, pollution-free sustainable renewable energy source. SPV systems are recognized as practical alternatives to energy systems for remote, isolated un-electrified locations. Yet, field results [1, 2] indicate that the modules can fail or degrade in a number of ways. In theory, the solar cell modules generally have the life span of about 20 years, but in actual experience due to module packaging technology and other

E. Fernandez (✉) · S. Prajapati
Department of Electrical Engineering, Indian Institute of Technology Roorkee,
Roorkee 247667, Uttarakhand, India
e-mail: eugenefdz@gmail.com

reasons, some solar cell modules, after being used for 8–10 years, will suffer damage. There are two ways in which a solar PV string can fail. In the first instance, there is a regular degradation of the solar array over a period of time due to wear and tear and other natural causes due to atmospheric conditions. In [3], it is listed that various wear and tear causes can include mechanisms external to the cell itself such as solder joints, encapsulant browning, delamination, and interconnection problems. There are a number of studies related to PV module degradation in the field [4–10]. The main conclusion of these studies is that solar modules do not fail in a catastrophic way but experience a steady power degradation over a period of time. Prominent causes are (a) degradation of packaging materials (b) loss of adhesion of encapsulants (c) degradation of cell/module interconnection (d) degradation caused by moisture intrusion (e) degradation of the semiconductor device. Additional causes include ambient weather conditions like temperature, humidity, and radiation. The second way in which a SPV array can fail is when any cell in the series string can get open circuited. This causes the affected string to become non-conducting leading to a reduced power output of the entire array. The open-circuit conditions can be caused due to various causes that basically involve the blocking of light falling on one or more cells. This implies that conditions like cloud shadow, shadows of trees, buildings, poles, and other objects, falling of dirt, paint, bird excreta, dirt layer (after a dust storm), the cracking of the protective glass covering can be potential causes. This condition can be partially or totally eliminated if bypass diodes are used across the affected SPV string (or array/module). In the literature, a number of reports are available that highlight the application of bypass diodes for improving the reliability of SPV systems [11–15]. The second issue is the topic of concern for this paper. We take up the case of a single SPV string of 10 cells in series. The number of bypass diodes has been limited to one only. It is of interest to examine how the reliability of the string will be affected with a single diode connected across a part of the string, when any one cell is randomly open circuited.

2 Role of Bypass Diode

Bypass Diodes are also known as *free-wheeling* diodes. They are connected in parallel with individual solar cells or panels, to provide a bypassing current path around them in the event of a cell or panel becoming faulty or open circuited. Thus, use of bypass diodes allows a series string of connected cells or panels to continue supplying power at a reduced output rather than no power at all. Bypass diodes are connected in reverse bias between a solar cells (or panel) positive and negative output terminals and have no effect on its output. Ideally, there would be one bypass diode for each solar cell, but this may be expensive, and hence, one diode is generally used per small group of series cells. Two types of diodes are available as
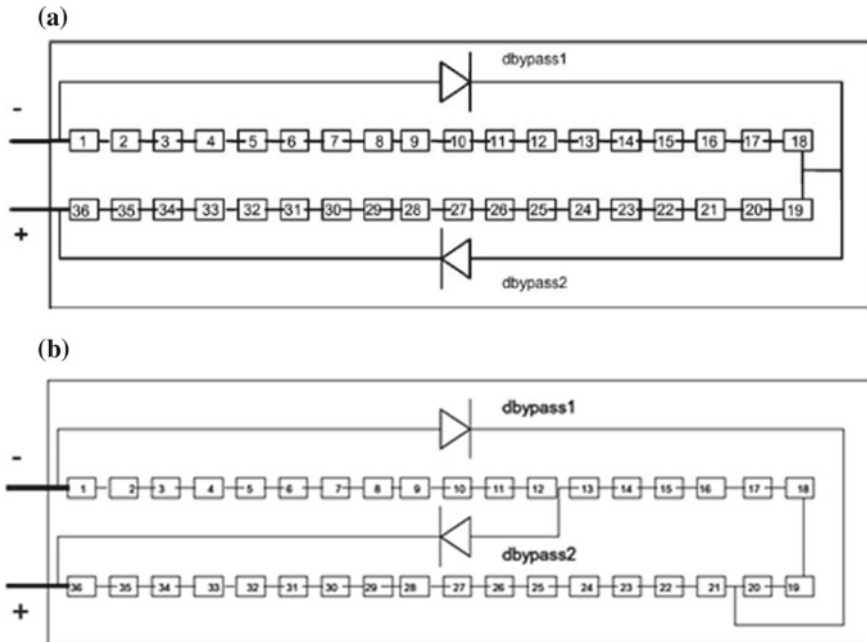
Fig. 1 **a** Bypass diodes in a SPV string without overlap in cells. **b** Bypass diodes in a SPV string with overlap in cells *Source* [12]

bypass diodes for solar panels and arrays, namely the PN-junction silicon diode and the *Schottky* barrier diode. Both types of diodes are available with a wide range of current ratings. The *Schottky* barrier diode has a much lower forward voltage drop of about 0.4 V as compared to the PN type silicon diodes which have a typical voltage drop of 0.7 V. Figure 1a and b shows two possible configurations of bypass diode connections across a string that can be used in practical SPV systems.

Another reason for the use of bypass diodes is to avoid the possibility of "hot spots" formation in partial shadowing conditions of SPV operation [12]. Hot spots appear when a solar cell (normally forming part of a solar cell string of serially connected solar cells) becomes reverse biased and dissipates power as heat. This can happen as a result of mismatch of cell parameters or in the presence of shadows on the PV module. If the power dissipated by the solar cell in hot spot conditions, exceeds the maximum power which can be handled by the cell, it may suffer damage and become open circuited. Thus, the PV array design and the configuration (location) of bypass diodes on the PV modules forming part of the array have an important influence in avoiding possibility of hot spot appearance under partial shadowing conditions.

3   Reliability Evaluation of SPV Systems

SPV-based power systems face many challenges like fluctuating outputs due to non-uniform irradiation, mechanical failures, and loss of efficiency due to degradation. In the event of failure of the system due to one or more of these causes, the supply will be affected. This can have adverse effects on the supply continuity in critical applications particularly in remote area applications depending solely on SPV power generation for electrical needs. Reliability studies are thus important in solar PV systems. In the literature, a number of reports are available dealing with simulations, analysis, and experiences related to reliability estimation and improvement in solar PV systems [16–22].

4   The SPV System for the Study

In this paper, we use a single string module consisting of 10 cells in series ("q" cells). The bypass diode may be used to short "p" cells in series. The remainder (= $q - p$), i.e., "r" cells are not enclosed by the diode ends. Accordingly, the Loss of load Probability (LOLP) can be estimated in terms of inputs and their ratios as variables, i.e., p/q, p/r, and r/q.

Figure 2 shows the SPV string module being considered for the study.

5   Reliability Estimation Using *Monte Carlo*

There are two main categories of power system reliability evaluation techniques, namely analytical and simulation based. Analytical techniques represent the system by analytical models and evaluate the reliability indices from these models using mathematical solutions relying heavily on probability concepts. *Monte Carlo Simulation Methods (MCSM)* estimate the reliability indices by simulating the actual process and random behavior of the system. The method, therefore, treats the problem as a series of experiments [23]. The *Monte Carlo* method is thus the general designation for stochastic simulation using random numbers. The name
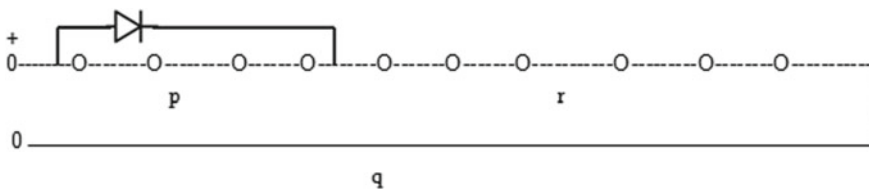

Fig. 2 SPV module for the study
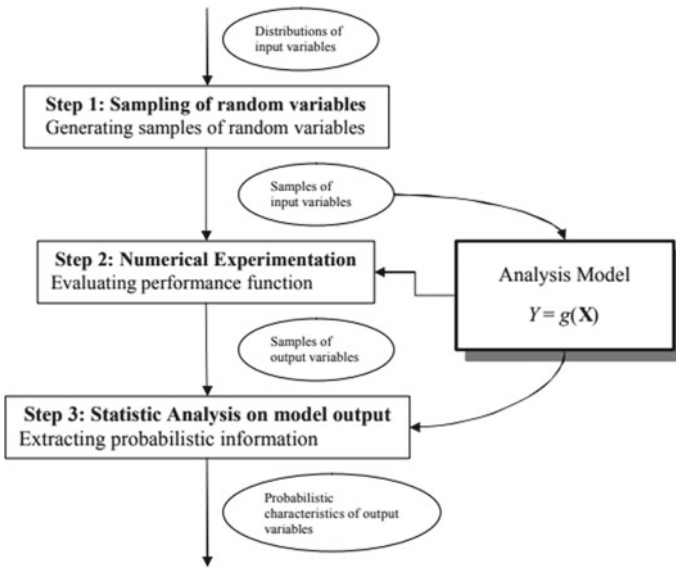
Fig. 3 *Monte Carlo* process. *Source* [31]

"*Monte Carlo*" is derived from a suburb in Monaco made famous by its gambling casino. Since the simulation process involves generating chance variables and exhibits random behaviors, it has been called *Monte Carlo* simulation. The name was also used as the secret code for atomic bomb work performed during World War II involving random simulation of the neutron diffusion process. Evidently then, *Monte Carlo* methods involve random selection techniques to estimate the final outcome. *Monte Carlo* methods have been used in many areas since that time. *Monte Carlo* techniques applications can be found in many fields such as complex mathematical calculations, stochastic process simulation, medical statistics, engineering system analysis, and reliability evaluation. In particular, they are found helpful for reliability analysis [24–30].

6 The Methodology of the Analysis

Reliability of a system can be assessed in a number of ways depending upon how we define "reliability." A system can be considered "reliable" if it performs its function. But whether it is able to perform its function fully or partially, continuously or non-continuously in a given time frame will give rise to different interpretations of what can be considered to mean "reliable." Different criterions are thus involved. In this study, we prefer to adopt the definition of reliability as given in [21]. According to this paper, in a series-parallel type of PV array, the system *fails*

when all n strings (parallel strings) fail. If we consider *only one long string*, then by logical reasoning, we can conclude that this system fails when output of this string is zero. Thus in *Monte Carlo simulation*, we can assume that: (a) the string *will fail* if net output = 0 and (b) the string *will not fail* if the output is any value greater than 0 and up to 100% of the total string output. This assumption may be used in evaluating the reliability of the different one-diode bypass configurations possible in a string by *Monte Carlo* simulations. A basic flowchart of the process summarized in three basic steps is given below (Fig. 2).

The basic steps involved in the *Monte Carlo* Simulation used here are given as follows:

Step 1: Decide on the number of simulations to be carried out (=N) and $N > 10^5$.
Step 2: For $j = 1$, generate any number randomly between 0 and 1. Let the count $C = 0$. The random number generated identifies the solar cell in the string that is deemed to be open circuited in accordance with a predecided system of identification. The random generated number <0.1 refers to a case when no cell is affected in the string.
Step 3: Examine if the continuity of supply of the SPV string is present. This can be X_{failure} or X_{success}. X_{failure} is identified when the continuity is broken by the affected open circuited cell; else, it is X_{success} if $X_j = X_{\text{failure}}$ then $C = C + 1$; $j = j+1$.
Step 4: Repeat steps 3–4 till number of simulation is =N.
Step 5: Calculate LOLP $= \frac{C}{N}$.
Step 6: Repeat steps 2–6 until acceptable value of LOLP or stopping criteria is reached.

7 Results of the Study and Discussions

Tables 1 and 2 show the variation of the LOLP as a function of the variables p, r, and q and also their ratios p/q, r/q, and p/r.

Table 1 Variation of LOLP with p, r, and q

S. No	P	r	q	LOLP
1.	1	9	10	0.8183
2.	2	8	10	0.7273
3.	3	7	10	0.6361
4.	4	6	10	0.5451
5.	5	5	10	0.4541
6.	6	4	10	0.3634
7.	7	3	10	0.2729
8.	8	2	10	0.1789
9.	9	1	10	0.0909

Table 2 Variation of LOLP with p/q, r/q, and p/r

S. No	p/q	r/q	p/r	LOLP
1.	0.1	0.9	0.1111	0.8183
2.	0.2	0.8	0.2500	0.7273
3.	0.3	0.7	0.4285	0.6361
4.	0.4	0.6	0.6666	0.5451
5.	0.5	0.5	1.0000	0.4541
6.	0.6	0.4	1.5000	0.3634
7.	0.7	0.3	2.3333	0.2729
8.	0. 8	0.2	4.0000	0.1789
9.	0. 9	0.1	9.0000	0.0909

7.1 Results

These results are graphically elaborated in Figs. 4, 5, 6, 7, 8.

In order to understand how LOLP will be related to the various input parameters and their ratios, a correlation analysis was conducted.

Table 3 shows the results obtained.

The results as given in Table 3 are in agreement with the observations of Tables 1, 2, and Figs. 4, 5, 6, 7 linear trends (inverse) are shown for variations of p and p/q with LOLP while linear trends (positive) are shown for variations of LOLP with r and r/q. The variation of p/r with LOLP shows an inverse trend which is somewhat nonlinear (not perfectly correlated).
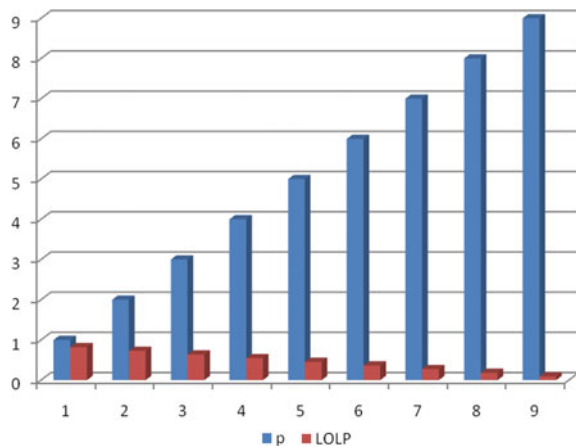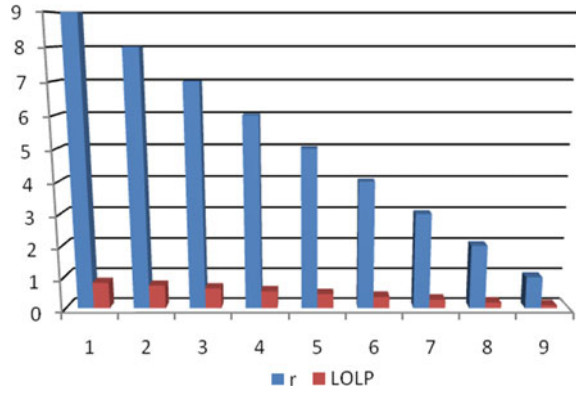
Fig. 4 LOLP versus p

Fig. 5 LOLP versus *r*

Fig. 6 LOLP versus *p/q*
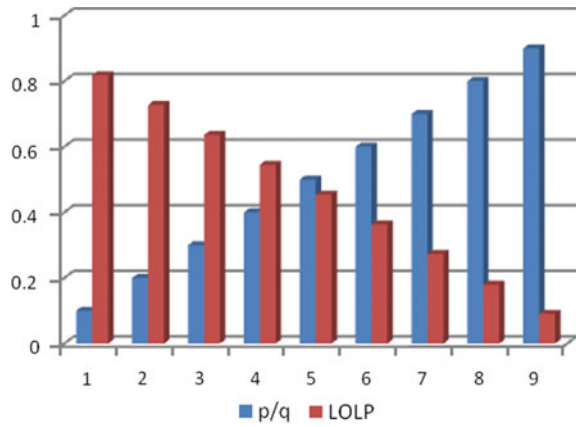
Fig. 7 LOLP versus *p/r*
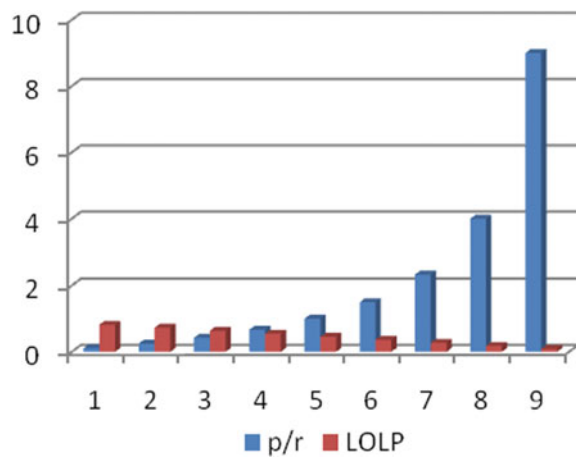
Fig. 8 LOLP versus *r/q*
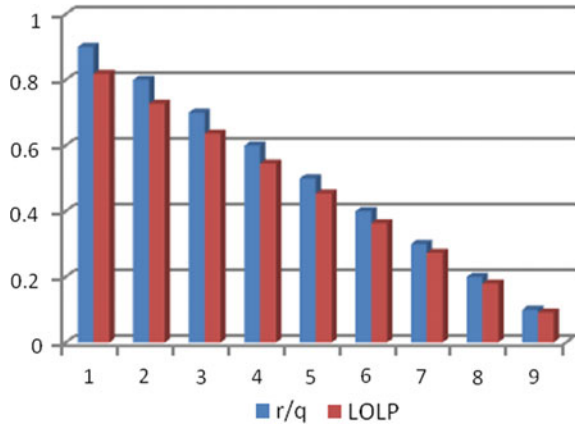
Table 3 Correlation results of LOLP with input parameters and ratios

S. No	Input parameter	Correlation with LOLP
1.	*P*	−1.0000
2.	*R*	0.9997
3.	*p/q*	−1.0000
4.	*r/q*	0.9997
5.	*p/r*	−0.8231

7.2 Discussions

The results lead to the following observations:

(a) As the number of enclosed PV cells between the diode end (=*p*) increases, the LOLP will decrease. This means that the probability of continuity of power delivery will improve even if reduced.

(b) The reverse is the case when the number of unenclosed cells (=*r*) increases, i.e., LOLP will increase.

(c) As *p/q* ratio increases, the LOLP will reduce.

(d) As *r/q* ratio increases LOLP will rise.

(e) As *p/r* ratio increases, LOLP will fall but here unlike the case of (c), the trend is highly nonlinear.

(f) The various graphs (Figs. 3, 4, 5, 6, 7) depict these variations graphically.

(g) The correlation analysis agrees with the observations.

The present study thus leads to the following conclusions:

1. An increase in *p* will lead to a lowering of the LOLP. This implies that the string reliability will improve when *p* increases. The trend is generally linear.

2. An increase in r shows the reverse trend, i.e., LOLP increases with r. Thus, the reliability worsens when the no. of unenclosed cells increases. The trend is mostly linear.
3. Since q remains fixed for the string, the variation of LOLP with p/q and r/q is simply similar in trends to the variations of LOLP with p and q, respectively (albeit of a different scale).
4. The ratio p/r is negatively correlated with LOLP. However, unlike the variation of LOLP with p, this variation is more nonlinear because of the large possible variation in the ratio p/r as compared with the variation of LOLP (which can vary only from 0 to 1).

8 Conclusions of the Study and Scope for Further Research

A study was carried out to evaluate the reliability of a SPV string using a single bypass diode connected across various points in the string. The results show that as the number of enclosed PV cells increases, the LOLP reduces, i.e., reliability improves. It is proposed to carry out further studies to evaluate the LOLP in terms of not only continuity of supply on open circuit of a single cell in the string, but also in terms of the magnitude of acceptable power delivery that the string can deliver in such cases. This will be of greater practical usefulness for actual field operated systems.

References

1. Forman SE (1982) Performance of experimental terrestrial photovoltaic modules. IEEE Trans Reliab R-31:235–245
2. Wohlgemuth JH, Cunningham DW, Nguyen AM, Miller J (2005) Long term reliability of PV module. In: 20th European photovoltaic solar energy conference, Barcelona, Spain, pp 1942–1946
3. Quintana MA, King DL, McMahon TJ, Osterwald RC (2002) Commonly observed degradation in field-aged photovoltaic modules. In: 29th photovoltaic specialists conference, pp 1436–1439
4. Sakamoto S, Oshiro T (2005) Dominant degradation of crystalline silicon photovoltaic modules manufactures in 1990s. In: 20th European photovoltaic solar energy conference, Barcelona, pp 2155–2158
5. Osterwald CR, Benner JP, Pruett J, Anderberg A, Rummel S, Ottoson L (2003) Degradation in weathered crystalline-silicon PV modules apparently caused by UV radiation. In: 3rd world conference on photovoltaic energy conversion, Osaka, Japan, pp 2911–2915
6. Reis AM, Coleman NT, Marshall MW, Lehman PA, Chamberlain CE (2002) Comparison of PV module performance before and after 11-years of field exposure. In: Proceedings of the 29th IEEE photovoltaic specialists conference, New Orleans, Louisiana, USA

7. Muirhead IJ, Hawkins BK (1995) An assessment of photovoltaic power in the Telstra network. In: Solar'95—Proceedings of the annual conference of the australian and new zealand solar energy society, pp 1–8
8. Marion B, Adelstein J (2003) Long-term performance of the SERF PV systems. In: national center for photovoltaics and solar program review meeting, March 2003, pp 1–3
9. Dunlop ED, Halton D (2006) The performance of crystalline silicon photovoltaic solar modules after 22 years of continuous outdoor exposure. Prog Photovoltaics Res Appl 14: 53–64
10. Sakamoto S, Oshiro T (2003) Field test results on the stability of crystalline silicon photovoltaic modules manufactured in the 1990s. In: 3rd world conference on photovoltaic energy conversion, Osaka, pp 1888–1891
11. Shephard NF, Sugimura RS (1984) The integration of bypass diode with terrestrial photovoltaic modules and arrays. In: Proceedings of the 17th IEEE photovoltaic specialists conference, p 676
12. Silvestre S, Boronat A, Chouder A (2009) Study of bypass diodes configuration on PV modules. Appl Energy 86:1632–1640
13. AI-Rawi NA, AI-Kaisi MM, Asfer DJ (1994) Reliability of photovoltaic modules II. Interconnection and bypass diodes effects. Sol Energy Mater Sol Cells 31:469–480
14. Greacen C, Green D (2001) The role of bypass diodes in the failure of solar battery charging stations in Thailand. Sol Energy Mater Sol Cells 70:141–149
15. Giuliano M et al (1981) Bypass diodes design application and reliability studies for solar cell arrays. In: Proceedings of the IEEE PV specialist conference, pp 997–1000
16. Wang Y, Bai X, Ma G (2012) Reliability assessment of grid-integrated solar photovoltaic system. Power Syst Technol 36(10):1–5
17. Ahadi A, Ghadimi N, Mirabbasi D (2014) Reliability assessment for components of large scale photovoltaic systems. J Power Sources 264:211–219
18. Meyer EL, Dyck EE (2004) Assessing the reliability and degradation of photovoltaic module performance parameters. IEEE Trans Reliab 53(1):83–92
19. Dumas N, Shumka A (1982) Photovoltaic module reliability improvement through application testing and failure analysis. IEEE Trans Reliab R-31:228–234
20. Vázquez M, Rey-Stolle I (2008) Photovoltaic module reliability model based on field degradation studies. Prog Photovolt Res Appl. https://doi.org/10.1002/pip.825
21. Gautam NK, Kaushika ND (2002) Reliability evaluation of solar photovoltaic arrays. Sol Energy 72(2):129–141
22. Abouzahr I, Ramkumar R (1991) Loss of probability of stand-alone photovoltaic systems. IEEE Trans Energy Convers 6(1):1–11
23. Youli S, Nagasaka K (2010) Monte Carlo simulation method used in reliability evaluation of a laboratory-based micro grid. In: Proceedings of the international multi conference of engineers & scientists, Hongkong, 17–19 March 2010
24. Billinton R, Li W (1994) Reliability assessment of electric power systems using Monte Carlo methods. Springer Science+Business Media, New York. https://doi.org/10.1007/978-1-4899-1346-3
25. Billinton R, Ghajar R (March 1987) Utilization of Monte Carlo simulation in generation system adequacy evaluation. Canadian Electrical Association, Power System Reliability Subsection, Power System Planning and Operation Section, Engineering and Operating Division
26. Hegazy YG, Salam MMA, Chikhani AY (February 2003) Adequacy assessment of distributed generation system using Monte Carlo simulation. IEEE Trans Power Syst 18(1)
27. Jeon C, Shin J (2014) Long-term renewable energy technology evaluation using system dynamics and Monte Carlo simulation: photovoltaic technology case. Energy 66:447–457

28. Liang H, Cheng L, Liu S (2011) Monte Carlo simulation based reliability evaluation of distribution system containing microgrids. Power Syst Technol 35(10):76–81
29. Wanga H, Zhub N, Baic X (2015) Reliability model assessment of grid-connected solar photovoltaic system based on Monte Carlo. Appl Sol Energy 51(4):262–266
30. Billinton R, Karki R (August 1999) Application of Monte Carlo simulation to generating system well-being analysis. IEEE Trans Power Syst 14(3):1172–1177
31. http://web.mst.edu/~dux/repository/me360/ch8.pdf

Locating Wire Fault in Controller Area Network Based on Kelvin (Four-Wire) Resistance Approach

Ramesh Krishnamurthy, C. Bharatiraja, Yusuff Adedayo, Mohd Tariq and Abdul Azeem

Abstract CAN is a multi-master standard bus interface commonly utilized for transferring the information among electronic control units (ECU's). Fault occurrence in CAN system makes complexity in the data transmission between devices and affects the efficiency of vehicle. Wire faults occur at irregular intervals are not easy to detect and locate in the CAN bus. This paper proposes a method for detecting the open and short wire fault using Kelvin four-wire resistance method in order to reduce approximately 20% of measurement error compared to the existing two-wire resistance measurements and (time-domain reflectometry) TDR approaches. This proposed approach is implemented using Arduino-based CAN controller in order to test the system etiquette. The predetermined threshold resistance values are utilized in detection of open and short wire faults, while the amplitude and time intervals of the reflected signals are used in locating the faults through TDR approach. This proposed system is inexpensive for CAN system troubleshooting and effective in identifying wire faults prior to the user's disruption.

Keywords Controller Area Network · Wire fault · TDR · Kelvin resistance measurement

R. Krishnamurthy · C. Bharatiraja
School of Electrical Engineering, SRM Institute of Science and Technology
(formerly known as SRM University), Kattankulathur Campus, Chennai 603203, India
e-mail: rameshk.tn@gmail.com

C. Bharatiraja
e-mail: bharatiraja@gmail.com

Y. Adedayo
Department of Electrical Engineering, University of South Africa,
Pretoria, South Africa
e-mail: yusufaa@unisa.ac.za

M. Tariq (✉) · A. Azeem
Department of Electrical Engineering, Aligarh Muslim University, 202002 Aligarh, India
e-mail: tariq.iitkgp@gmail.com

A. Azeem
e-mail: azeem.abdul25@gmail.com

1 Introduction

With the rising consumer demand for new features and too many electrical control units (ECU), actuators and sensors are outfitted in contemporary vehicles. These parts are associated via various communication network interfaces and require a high degree of signal integrity. In the intra-vehicular network, the electronic devices were connected through wiring system from one device to another. In the demand of users, many more electronic devices needed to build in vehicles, subsequently the system becomes more complex and too expensive. Therefore, to reduce the cost and complexity, there is a need of replacement of wiring system in-vehicle networks [1, 2].

In 1985, CAN protocol was developed by BOSCH for in-Vehicle network. It is low in cost and prioritized error resistant network. CAN is a multi-master serial bus used for connecting the ECUs. In the vehicular electronics, ECU will act as a gateway for communication between devices over a two-wire bus interface. These wires are 120 Ω twisted pair [3]. In present-day vehicles, there are more than 70 ECUs used for transmission within ABS, power steering, power windows, doors mirror adjustment, and battery recharging, etc. The ECUs will collect the message from actuators and sensors and send to the other ECU for monitoring and controlling the automotive applications [4]. Apart from automobile industry, the CAN network is used in other industries such as aviation and space flight for the data analysis and control systems, i.e., fuel level, pumps, and linear actuators. The Sterile supply technician's use CAN network in Medical equipment. In fact, many hospitals evoked to use CAN network to operate lights, CCTV cameras, X-ray machines, tables, and patient details with CAN systems. The CAN bus is also adopted in embedded applications such as lifts and escalators.

In non-Industrial applications, CAN-based systems are used in telescope, coffee machines, sports cameras, telescopes, automatic doors, and lights. In the need of more security, USA has deployed OBD-II CAN standards, which is mandatory for all cars and light trucks since 1996. CAN bus use one of five protocols of onboard diagnostics standard [5]. To increase the quality, more researches on diagnostics of CAN faults have been conducted in recent years. There are chances of faults occur at irregular intervals may cause system failure, reliability among the users and efficiency of the system reduces. Open wire fault in CAN interrupts the message communication between the ECUs and causes the corruption in transmission of data at irregular interval, these kinds of faults are not easy to find and locate. Therefore, identification and fixing these faults are time-consuming process and complicated for technicians and becomes more challenging to locate and detect intermittent faults.

USA and Europe analyzed to hit upon the reason for road accidents, and they found that many accidents are occurring due to three factors such as road conditions, device failure (brake failure, tire failure and steering and suspension), and abnormal driving speed. Thus, they have introduced safety devices such as ABS, radial tires, and power steering are communicated via CAN bus. ABS CAN system

prevents the wheels from locking up during emergency braking to avoid accidents. The uneven or worn-out tires are the most serious problem leads to catastrophic accidents. Hence, the proposed system is introduced with CAN system for auto checking of tire pressure at regular intervals. Power steering CAN system enables to go around road obstacles to avoid accidents [6]. According to the survey of Georgia uniform vehicle accident report 2010, says that more than 6000 plus roads accidents are happened due to vehicle failure, in that certain accidents are happened due to failure of inter-CAN system. To increase the safety in-vehicle network, CAN plays an important role for maintenance and regular efficiency check for the CAN system.

Gaujal [7] proposed an error frame counter as an online fault diagnosis. If any error occurs, the error frame counter gets incremented upon reaching the threshold value in addition to that, the particular ECU will send a CAN bus failure message to other ECUs. Another robust method is that, if any faulty nodes are detected it sends the information about the faulty node to all the healthy nodes to declare CAN bus is failed. However, these message-oriented approaches were failed to detect open and wire short faults in CAN bus. Physical signal approach consists of inductance, capacitance, and resistance measurement to locate open and short faults [8]. The conventional bus resistance via two-wire resistance approaches introduces the 20% of measurement error, i.e., it adds the device under test resistance plus the lead resistances. As a result, a four-wire Kelvin resistance method is proposed to measure the device under test resistance directly. It measures the bus resistance accurately compared to the existing two-wire method. Several papers are employed with TDR approach to detect the discontinuity in CAN bus. If TDR approach is utilized for detecting the faults at regular intervals in each node then it is much expensive and time consuming process [9]. Our objective is to develop low cost, feasible, and accurate and safety approach to detect the fault by measuring the bus resistance and locate it using simple TDR approach.

2 Overview of Wire Faults in Controller Area Network

2.1 Wire Fault Scenario in CAN Bus

The behavior of the CAN bus in case of wire faults are examined and the CAN apparatus model is designed based on the CAN bus standard. The OSI layer characteristics of the CAN bus are explained in ISO-11898-2 [10]. The physical layer of the CAN plays an important role in CAN communication. It consists of bit encoding and decoding, resynchronization, and bit timing. The sub-layer of the physical layer is realized by transmit data and receive data, which operates with 5 and 3.3 V CAN version. The architecture of the CAN consists of ECUs which transmit and receive messages using transceiver and communicates via twisted pair cable with the terminal resistor 120 Ω at each end. The CAN cable has a maximum length of 40 m at the data rate of 1 MBPS. Moreover, the CAN consists of CAN-H

and CAN-L wires. Both the wires transmit equally divide voltage at the recessive state, but in case of dominant state CAN-H carries higher voltage than the CAN-L wire. In case of short wire fault scenarios, if the voltage on the CAN-H wire increases, resistance on the wire also gets increases. If the wire has open wire fault, voltage and resistance on the CAN wire get decrease [11]. According to the CAN bus Standard ISO 11898-2, the differential resistance of the CAN wires is between 10 and 100 kΩ compared to the terminal resistance 120 Ω.

2.2   Detection of Wire Fault Using Kelvin Measurement

When an ECU does not transmit any messages on the CAN, there is no voltage drop or resistance on the bus. Whenever an ECUs send a message on the bus, the transceiver will detect a bit error and goes to the dominant state. Consequently, there is a voltage drop or decrease in resistance of the wire happens. In order to detect the faults in wire, there is a need of examining the resistance or voltage drop of the CAN wire at regular intervals. For that reason, the resistance of the wire can be measured by using four-wire Kelvin resistance measurements. It will decrease the twenty percent of the measurement error compared to the existing two-wire resistance measurement [12]. To estimate the resistance of the wire, the voltage and the current need to be calculated foremost. While the voltage can be measured by sensing it with the different positions, however, there is no current sensor module available in some of the ECUs. Therefore, low-cost shunt resistor is used to measure the current on the CAN bus. Based on the Kelvin four-wire measurement, unknown resistance can be measured by using known resistance, i.e., 120 Ω terminal resistor. The bus resistance of the CAN wire using Four-Wire Kelvin measurement using resistance computation approach is shown in Fig. 1. Resistance can be measured at regular intervals on the CAN bus. If the measured resistance is within the threshold resistance, there are no faults detected on the CAN bus, however, if the measured resistance is not within the threshold, wire fault has been detected. Threshold resistance of the CAN bus is defined as the differential resistance between the terminal resistance and CAN bus resistance [13].

2.3   Location of Wire Fault Using TDR Approach

In order to locate the fault in CAN Cable, time-domain reflectometry method is used as shown in Fig. 2. The known signal is transmitted to the cable under test and in order to analyze the reflections, the incident signal will be sent out to the CAN Cable (twisted pair cable) and listening to the reflected signal. Based on the reflections, if the cable has normal impedance and is correctly build, then there won't be any reflections and the residual transmitted signal is engrossed at the other
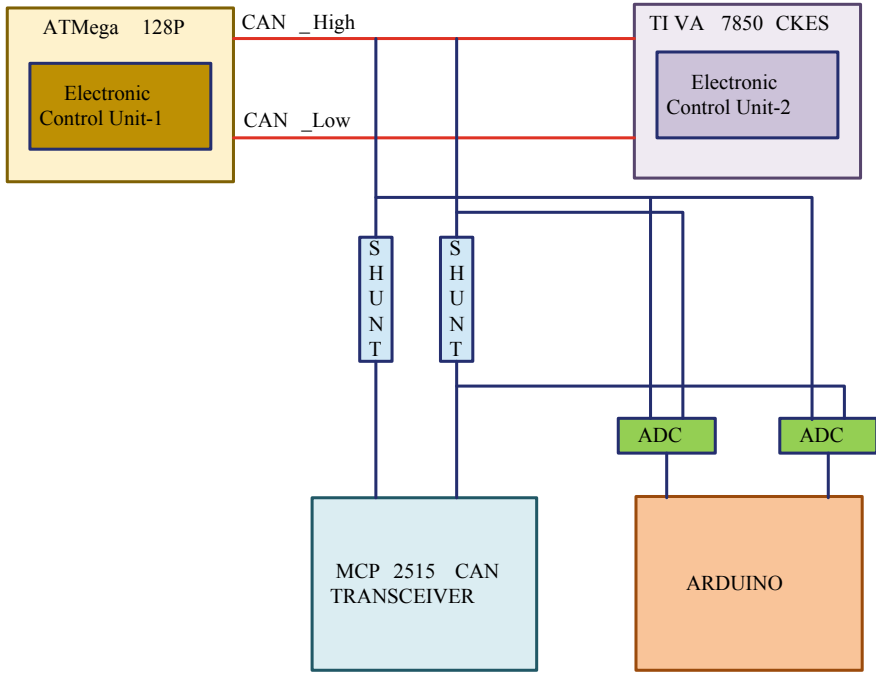
Fig. 1 Wire fault detection circuit

Fig. 2 Time-domain reflectometry system
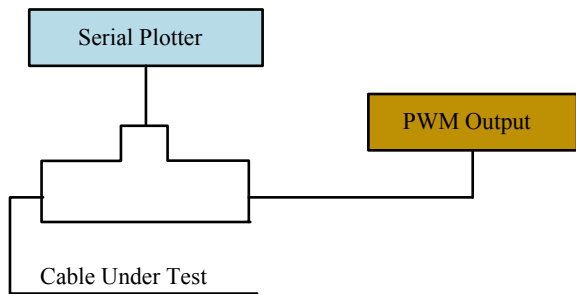
end. However, if any variable impedance is found, then the transmitted signal will be reflected back to the source.

If the incident signal has step increase in the impedance, the same will be replicated in the reflected signal. Contrarily, if there is step decreases in the incident signal, the reflected signal will have the decrease impedance [14]. The amplitude of the reflection not only depends on the resistance change and also loss on the cable. The reflections are marked out as a function of time, and the time difference can be measured as the length of the cable. Thus, amplitude change in signal can be considered as the size of the fault and the reflected signal time difference is

calculated as the length of the cable. The TDR approach can be implemented by means of T-Connector, one end of the connector will have the known signal and opposite end will have the cable which needs to be tested. While the upper end needs to be connected to the device whereas magnitude and time of the signal is estimated [15]. Due to the advancement in electric vehicle technology, there are several ECUs involved in scheduling of EVs for smart charging [16, 17]. Therefore, in order to integrate the charging infrastructure with electric vehicle CAN protocol is mostly used. Many researches are focused on DC motor control for controlling the speed of the contemporary vehicles [18, 19]. For sharing of energy, a solar power system with maximum power point tracking for electric vehicles has been proposed.

3   Results and Discussions

In this work, two ECUs are considered for the demonstration of this approach. One ECU will act as a sender (ATMega128 Microcontroller) includes eight channels PWM signals and 10-bit ADC. The other (Texas instruments—TMS320F28335) ECU will act as a receiver which includes turbo CAN, RS-232, JTAG connector, and onboard USB JTAG emulation. Both ECUs can be communicated by the use of CAN Transceiver (MCP2515 CAN Transceiver). The room temperature can be measured by temperature sensor which is inbuilt within transmitter module and the updated room temperature is successfully transmitted to the receiver.

The interfacing of CAN Transceiver module ATMega128 microcontroller development board (Transmitter Module) with Texas instruments TMS320F28335 CAN Module—MCP2515 (Receiver Module) is shown in Fig. 3.

The CAN communication can be analyzed by using Code Composer Studio Version 7. As shown in Fig. 4, the Data 1 and Data 2 can be successfully sent and received between the ECUs.

In order to check the health of the CAN bus, physical signal-based approach is used to identify the open and short wire fault in CAN bus. In the proposed approach, the bus resistance is measured by using four-wire resistances Kelvin method. If the measured resistance is within the threshold resistance, there are no faults in CAN bus in Fig. 5.

Two-wire measurements introduce nearly 20% additional error compared to the four-wire Kelvin method in Fig. 6.

If the measured resistance is not within the threshold resistance, the fault has been detected and then we are giving alert signal through LED indication as shown in Fig. 7.

In order to locate the fault in CAN Cable, time-domain reflectometry method as discussed the known signal is transmitted to the cable under test. In addition to that, PWM signal can be generated from Arduino ninth Pin on Fig. 8.

Fig. 3 Interfacing of CAN transmitter and receiver module

The room temperature data from the ECU (ATMega128) is transmitted and received using CAN Bus Module (MCP2515 CAN Transceiver
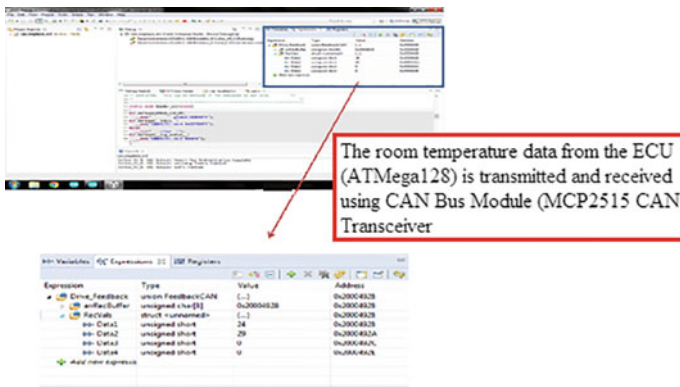
Fig. 4 CAN communication (sending and receiving of data in CC studio V7)

The known signal is transmitted to the cable under test to analyze the reflections. It will send out the incident signal to the CAN Cable (twisted pair cable) and listening to the reflected signal. Based on the reflections, if the cable has normal impedance and is correctly constructed, then there will be no reflections and the remaining transmitted signal is absorbed at the one end. Instead if it is found any

Fig. 5 Four-wire resistance measurement Kelvin method circuit with Arduino

Fig. 6 Comparison between four-wire versus two-wire measurement values

Fig. 7 Wire fault detection (indicated by LED in blinking mode)
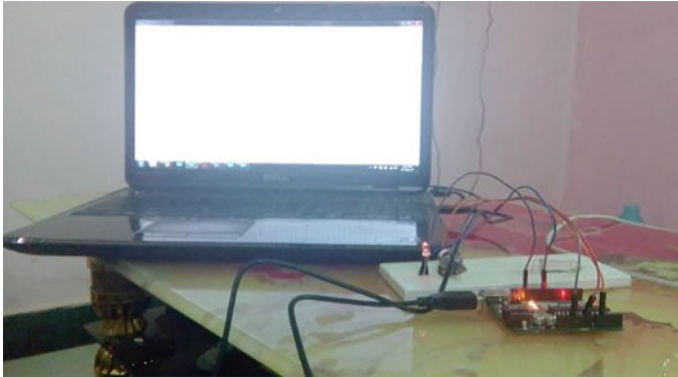
Fig. 8 PWM signal generation circuit from Arduino

variable impedance, then some of the transmitted signals are reflected back to the source. Note that the short wire fault can be detected and measured. The position of wire fault occurred is measured in distance and its corresponding four-wire bus resistance is displayed in serial monitor as shown in Fig. 9.

The parameters calculated and compared between two-wire and four-wire resistance measurements are shown in Table 1.

Let assume V_o is Output Voltage of the PWM signal, t_d denotes the Duration of the pulse, t_r denotes the Repetition time of the pulses, V_{in} as the Input Voltage, I_s as the Current from Shunt Resistor, $R1$ as the Known Resistance 120 Ω, and the V_{avg} denotes average of the module resistors.

Fig. 9 Output in serial monitor

Table 1 Comparison of parameter between two-wire and four-wire method

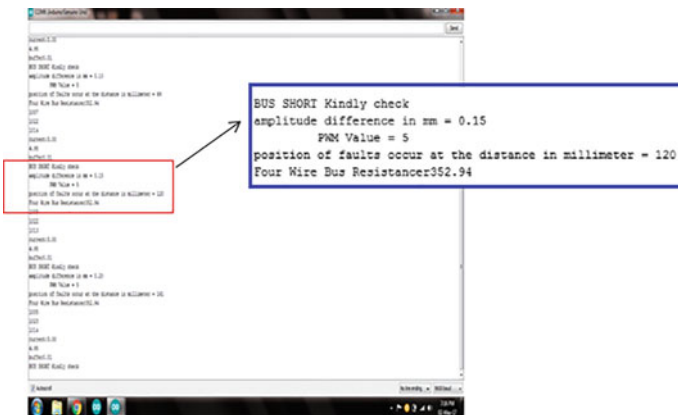| Parameters	Actual value	Measured value in two-wire method	Measured value in four-wire method	Differences	Measurement error with respect to actual value	Error (%)
Voltage (V_{in})	3.3	3	3.2	0.2	0.096	20
Shunt current (I_s)	5	4.66	4.96	0.36	0.992	36
Bus resistance ($R1 * V_{in}/I_s$)	120	113.17	117.65	4.48	0.98	44
Module resistance ($R1/V_{in} * V_{avg}$)	0.85	0.78	0.82	0.04	0.96	4
Size of the fault ($V_o * t_d/t_r$)	0.2	0.16	0.18	0.02	1	2
Location of fault ($t_d/2$)	9.4	6.89	8.46	1.57	1.06	15

4 Conclusion

In this work, we primarily focus on detecting and locating the open and short wire faults in CAN bus wire. It can be detected by measuring the resistance or voltage drop across the CAN bus wire with the help of four-wire Kelvin measurement. Four-wire measurements reduce the lead resistance value by measuring the voltage directly under test in order to eliminate the lead resistance. So we can reduce nearly 20% measurement error compared to the existing two-wire systems. When the measuring resistance is not within the threshold resistance, it can be marked as the fault occurrence. In order to locate the fault in CAN bus, we have generated PWM signal from Arduino and given as the incident signal to the CAN bus. By measuring and analyzing the reflected signal, we can identify the exact size and location of the fault in CAN bus. The experiments have been implemented on an Arduino UNO for both detection and location of faults. So, the results show the new approach, compared to other existing approaches, is robust, accurate, and low cost.

References

1. Robertson T (2014) Network diagnostic flow chart-how to troubleshoot vehicle level CAN communication and CAN diagnostic issues on nissan and infinity vehicles. SAE Technical Paper
2. Huangshui H, Guihe Q (2011) Online fault diagnosis for controller area networks. In: IEEE international conference on intelligent computation and automation (ICICTA), Shenzhen, Guangdong, China
3. Kelkar S, Kamal R (2014) Adaptive fault diagnosis algorithm for controller area network. IEEE Trans Ind Electron 61(10):5527–5537
4. Lei Y, Yuan Y, Zhao J (2014) Model-based detection and monitoring of the intermittent connections for CAN networks. IEEE Trans Ind Electron 61(6):2912–2921
5. Du X, Jiang S, Nagose A, Zhang Y (2016) Locating wire short fault for in-vehicle controller area network with resistance estimation approach. SAE Technical Article
6. Janesch J (2013) Two-wire vs. four-wire resistance measurements: which configuration makes sense for your application. Keithley Instruments, Inc.
7. Gaujal B, Navet N (2005) Fault confinement mechanisms on CAN: analysis and improvements. IEEE Trans Veh Technol 54(3):1103–1113
8. Shi Q, Kanoun O (2014) A new algorithm for wire fault location using time-domain reflectometry. IEEE Sensors J 14(4):1171–1178
9. Yu CQ, Qi ZD, Wang ZY, Wang Y (2011) The fault detection method of CAN bus based on network resistance model. Appl Mech Mater 58–60
10. Furse C, Smith P, Safavi M, Lo C (2006) Feasibility of spread spectrum sensors for location of arcs on live wires. IEEE Sensors J 5(6)
11. Furse C, Chung YC, Lo C, Pendayala P (2006) A critical comparison of reflectometry methods for location of wiring faults. Smart Struct Syst 2(1):25–46
12. Lo C, Furse C (2005) Noise-domain reflectometry for locating wiring faults. IEEE Trans Electromagn Compat 47(1):97–104
13. Smith P, Furse C, Gunther J (2005) Analysis of spread spectrum time domain reflectometry for wire fault location. IEEE Sensors J 5(6):1469–1478
14. Hassen WB, Auzanneau F, Pérès F, Tchangani AP (2013) Diagnosis sensor fusion for wire fault location in CAN bus systems. In: SENSORS, 2013 IEEE, Baltimore, MD, pp 1–4
15. Chokkalingam B, Padmanaban S, Siano P, Krishnamoorthy R, Selvaraj R (2017) Real time forecasting of EV charging station scheduling for smart energy system. Energies 377(10):1–14
16. Ramesh K, Bharatiraja C, Raghu S, Vijayalakshmi G, Sambanthan P (2016) Design and implementation of real time charging optimization for hybrid electric vehicles. Int J Power Electron Drive Syst 7(4)
17. Bharatiraja C, Munda JL, Vaghasia I, Valiveti R, Manasa P (2016) Low cost real time centralized speed control of DC motor using lab view-NI USB 6008. Int J Power Electron Drive Syst 7(3):656–664
18. Bharatiraja C et al (2018) Energy management strategy for rural communities' DC micro grid power system structure with maximum penetration of renewable energy sources. Appl Sci 8 (4)
19. Sadagopan S, Banerji S, Vedula P, Shabin M, Bharatiraja C (2014) A solar power system for electric vehicles with maximum power point tracking for novel energy sharing. In: 2014 Texas instruments India educators' conference (TIIEC), Bangalore, India

The Effect of Liquid Water Content Over the Seas of India and Europe for Ka-Band Satellite Communication

Hitesh Singh, Boncho Bonev, Peter Petkov and Sarang Patil

Abstract In the field of satellite communication, the attenuation caused by rain and clouds is dominant. A lot of studies have been done for rain attenuation, but more need to be done for clouds especially for millimeter waves. In this paper, various studies are conducted in the region of India and Europe. The data were gathered from AMSR-2 satellite. Annual data of liquid water content are collected from two sites, namely Bay of Bengal, India, and Mediterranean Sea, Europe. These data are simulated in cloud model given by ITU-R. Results obtained are compared for two regions. It was observed that due to the climatic conditions, more variations in attenuation are observed in European region as compared to India subcontinent.

Keywords Cloud attenuation · Satellite communication · Millimeter waves · Liquid water content

1 Introduction

It has been observed that the interest over higher frequencies has been increased in the area of satellite communications. This opens the avenues to do propagation studies especially for Ka band for various environmental conditions like rain, cloud, fog, gases, and dust as these frequencies are very sensitive for these conditions. From the past studies, it has been observed that attenuation caused by rain is higher

H. Singh (✉) · B. Bonev · P. Petkov · S. Patil
Technical University of Sofia, Sofia, Bulgaria
e-mail: Hitesh.singh.85@gmail.com

B. Bonev
e-mail: bbonev@tu-sofia.bg

P. Petkov
e-mail: pjpetkov@tu-sofia.bg

S. Patil
e-mail: sarang.p86@gmail.com

than attenuation caused by clouds. The occurence of clouds throughout the year is variable, and their size also varies with time. Thus, the studies done for cloud attenuation have significant impact for designing the radio link.

A cloud consists of tiny drops of water mass, super cool water, crystals of ice, and some suspended particles present in troposphere, which are caused due to the cooling of air at dew point. It is also formed when it gets sufficient moisture from its surroundings in order to raise due point to ambient temperature.

Different types of clouds are present in the atmosphere. They are categorized into three layers, namely low level, middle level, and higher level [1]. The low-level clouds are cumulus clouds, cumulonimbus, and stratus. Cumulus is generally found at the height of 2000–3000 feet. They rarely cause rain except some light showers. Cumulonimbus is found at the height of 2000–45,000 feet. They are found at tropical and temperate regions. Heavy rain and hails are caused by them. At the height of 0–6500 feet, stratus clouds are found. They are very common at costal areas and mountains. They only caused light drizzles.

Medium-level clouds contain altocumulus, altostratus, and nimbostratus. Altocumulus is found at the height of 6500–18,000 feet and causes light rain. Altostratus is found at the height of 6500–16,500 feet. They cause snow and light rain. Nimbostratus is found at 200–1800 feet. They cause heavy rain to moderate rain and snow fall.

High-level clouds are cirrus, cirrocumulus and cirrostratus. At the height of 16,500–45,000 feet cirrus clouds are formed. They are mainly composed of ice crystals. Cirrocumulus is found at the height of 16,500–45,000 feet. They are transition phase between cirrus and cirrostratus clouds. Cirrostratus is found at very height of 20,000–42,000 feet and very difficult to observe.

Different researchers have performed different cloud attenuation models for higher-frequency bands. Some of them are discussed in this section. Goldstein and Kerr [2] have proposed cloud attenuation model in 1951. The parameter used by them is M which is liquid water content in g/m^3, temperature in Kelvin, and wavelength in cm.

The parameters used by Gunn and East [3] were again liquid water content in g/m^3, constant k whose value is given by $(m^2 - 1)/(m^2 + 2)$, where m is $n + jk$ where n is refractive index of material and k is absorption coefficient of material.

Another model proposed by Slobin [4] is specific attenuation and was calculated in dB/km. The parameters used in this model are liquid water content in g/m^3, temperature in kelvin, and wavelength in cm.

Different experimentation studies for cloud attenuation were done by Allen [5]. The parameters used by his model are liquid water content and frequency in GHz.

Altshuler and Marr [6] have proposed his model for millimeter wave frequencies. They used parameters like wavelength in millimeters and density of water droplets in g/m^3.

Most researchers from different part of the world are using ITU-R model [7]. The complete details can be found in [7]. Parameters used in this model are specific attenuation coefficient in (dB/km)/(g/m^3) and liquid water content in g/m^3,

frequency in GHz, and real and imaginary part of dielectric permittivity of water and temperature in kelvin.

From the above discussion, we have seen that the most common parameter almost used by all models is liquid water content in g/m^3. So, it is the most important deciding factor for cloud attenuation. That is why our paper is discussed about this parameter.

2 Experimental Setup

In this work, the values of liquid water content are observed from the Bay of Bengal region of India and Mediterranean Sea of Europe. The readings are taken from the satellite AMSR-2 which is Advanced Microwave Scanning Radiometer [8]. This satellite was launched on 18 May 2001 by JAXA's GCOM-WI spacecraft. It was operated at the height of 700 km from the earth with antenna size of 2-m height swath width of 1450 km. This instrument is dual polarized with conical scanning and passive microwave radiometers. The radio bands on which AMSR-2 works are 6.93, 7.3, 10.65, 18.74, 23.8, 36.5, and 89.0 GHz. The reading is taken annually from May 2016 to May 2017. Figures 1 and 2 show the location of experimentation. The image taken from satellite can be shown in Fig. 3.

3 Experimental Results

From the figures, we calculated the values of liquid water content of clouds present in the area of Bay of Bengal in g/m3. The results are presented in Figs. 4 and 5 for India and Europe. From the results, we can conclude that the value of liquid water content is higher from the month of August 2016 to March 2017 for India. In case of Europe, the values of liquid water content are higher from the month of May to August and from April to May. That means the presence of clouds is higher in this time span over the eastern part of India and Europe. While substituting the values of liquid water content in ITU-R model, we get the results which are presented in Figs. 6, 7, 8, and 9 for both uplink and downlink frequencies. The results clearly show that with the increase in the values of LWC, the value of attenuation also increases while with the decrease in LWC the attenuation also decreases. There changes are higher for higher frequencies especially for uplink frequencies like 24–30 GHz. It has also been concluded that for a particular region, the occurrence of clouds is very with time.

Fig. 1 Political map of India
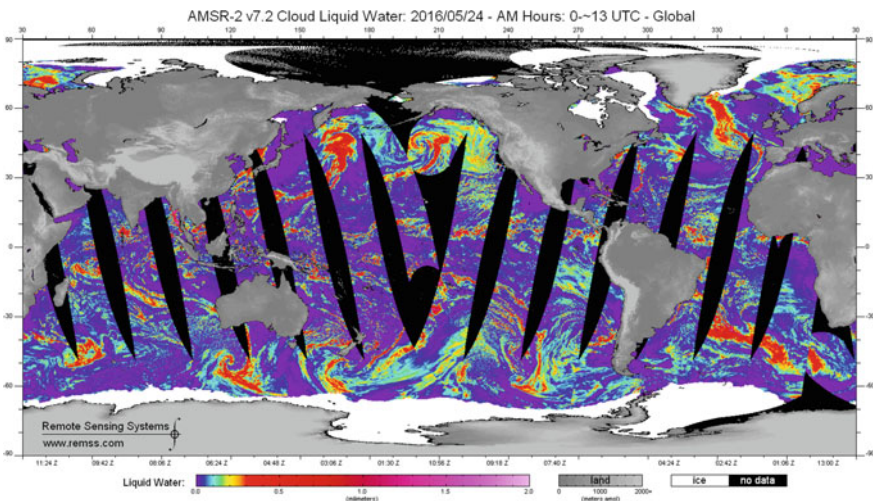
Fig. 2 Political map of Europe

Fig. 3 Cloud liquid water content for the month of May 2016

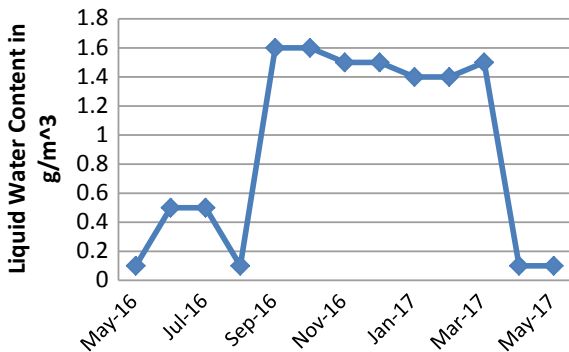**Fig. 4** Annual liquid water content for the Bay of Bengal, India

Fig. 5 Annual liquid water content for the Mediterranean Sea, Europe
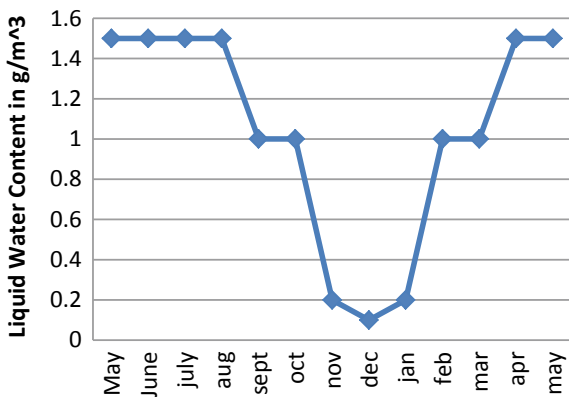
Fig. 6 Specific attenuation for entire year over the Bay of Bengal for uplink
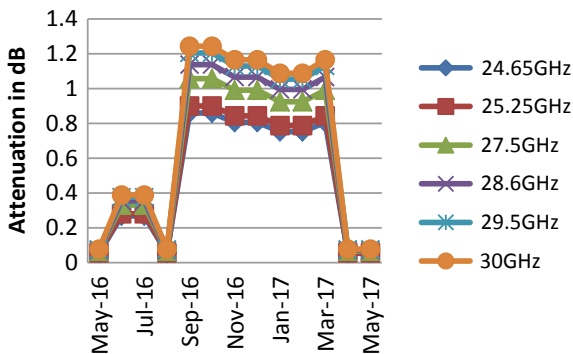
Fig. 7 Specific attenuation for entire year over the Mediterranean Sea, Europe, for uplink
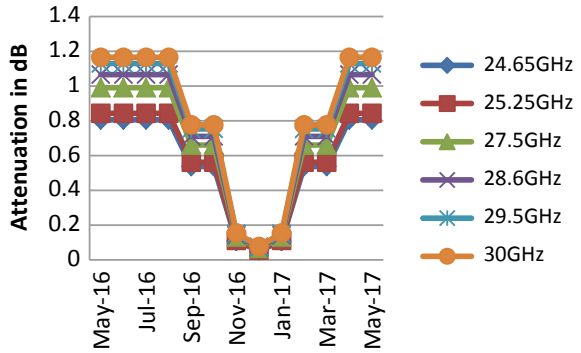
Fig. 8 Specific attenuation for entire year over the Bay of Bengal for downlink

Fig. 9 Specific attenuation for entire year over the Mediterranean Sea, Europe, for downlink

4 Conclusion
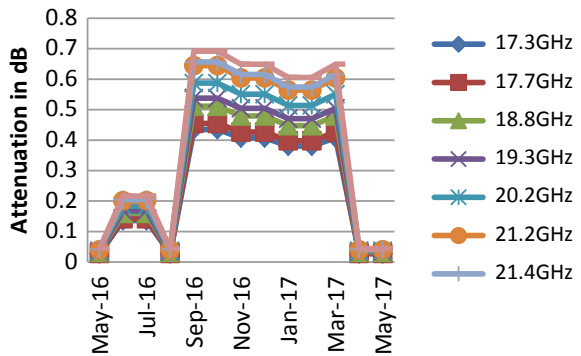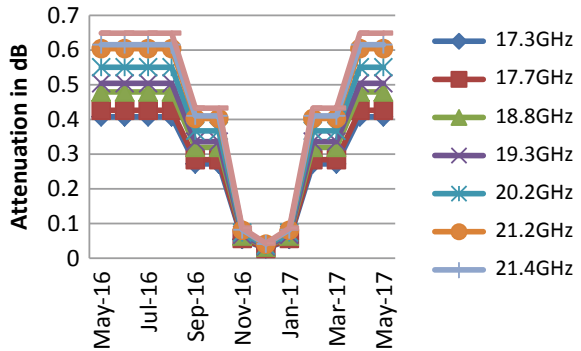
From these experiments, we conclude that the variations of liquid water content in a cloud have a significant impact on the attenuation caused by the clouds in satellite communications. As clouds have complex structure, sometimes heavy clouds are

formed which are called low clouds because of larger water content which may cause larger attenuation, and sometimes, it resides in higher altitude results in lesser attenuations. So, they vary with time. The purpose of this experimentation was to show that more studies need to be performed for designing the satellite links.

Reference

1. World Meteorological Organization (1975) International cloud atlas, vol 1
2. Goldstein H, Kerr DE (1951) Propagation of short radio waves. Mass Inst Tech Radiation Lab Ser 13:588–640
3. Gunn KLS, East TWR (1954) The microwave properties of precipitation particles. Q J Royal Meteorol Soc 80(346):522–545
4. Slobin SD (1982) Microwave noise temperature and attenuation of clouds: statistics of these effects at various sites in the United States, Alaska, and Hawaii. Radio Sci 17(6):1443–1454
5. Allen KC (1983) Attenuati; on of millimeter waves on earth-space paths by rain clouds. NTIA Report 83–132
6. Altshuler EE, Marr RA (1989) Cloud attenuation at millimeter wavelengths. IEEE Trans Antennas Propag 37(11):1473–1479
7. Attenuation due to cloud and fog. Recommendation ITU-R P.840-5. P Series, Radio wave propagation
8. Wentz FJ, Meissner T, Gentemann C, Hilburn KA, Scott J (2014) Remote sensing systems GCOM-W1 AMSR2 [monthly] environmental suite on 0.25 deg grid, Version 7.2. Remote sensing systems, Santa Rosa, CA. www.remss.com/missions/amsr

Real-Time Static Hand Gesture Recognition Using MATLAB

Poras Khetarpal, Neeraj Kumar and Nikita Rai

Abstract This paper proposes static hand gesture recognition that generally consists of recognizing the pre-defined hand signs. Since it is hard for people with disabilities to communicate and providing special training for learning hand gestures communication is a tedious process, hand gesture recognition will decrease the labour. The algorithm is based on segmentation of the image using background subtraction. The aim of this paper is to yield a system of recognition that is efficient and reliable along being cost-effective.

1 Introduction

Hand gesture recognition system is used for creating an interface between computer and humans. For detection of hand gestures firstly, data about the hand have to be collected. Secondly, a decision is made with respect to the nature and source of the data. Two methods which can provide this result are [1]:

- Sensors with gloves attached that measures the position of finger joints.
- An optical method.

This method is chosen, as it is a more practical method, cost-efficient and with without any moving parts, so it is unlikely to be damaged during use in various environments.

P. Khetarpal (✉) · N. Kumar · N. Rai
Bharati Vidyapeeth's College of Engineering, New Delhi 110063, India
e-mail: porask@gmail.com

There are two basic approaches used in the static gesture recognition,

1. A top-down approach, where an image capture image pre-processing feature extraction classification model that was previously created of information which has been collected about hand configurations, is then rendered to some feature in the image coordinates. The rendered image is then compared with the real gesture image so as to figure out if they are the same.
2. A bottom-up approach, which involves extraction of features from the input image and comparing them to the features of images present in the database to obtain the similarities between the two [2].

The first approach requires a large computational effort for reliable recognition which makes it an inferior approach with respect to the second approach. Adequate pre-processing is required in the bottom-up approach for obtaining reliable segmentation [3]. This paper mainly focuses on the latter approach as it is commonly used. The static gesture recognition is divided into various phases where each phase performs a certain task whose result is passed on to the successing phase.

The gestures in this paper are numeric gestures denoting different numerals ranging from 1 to 5. The gestures are not intended to be resembling any sign language though this whole paper points to the promising scope of this technology in this particular field and the benefit it can bring to society.

1.1 Image Processing

Processing of image basically implies the actions in order to receive a substantial result of images or any group of images through the use of mathematical operations with any kind of signal processing for which the input section can be among the following:

- an image,
- a series of images,
- or even a video.

The principal components of a hand recognition system comprise of the data acquisition, hand localization, which can be further classified as segmentation and filtration, hand feature identification, and lastly gesture recognition based on identified features.

The reason for processing images can be listed:

1. Visualization—Observing the objects which are visible.
2. Sharpening of image and its regeneration for creating modified and better images.
3. Retrieval of image—Seeking of interest for the image.
4. Pattern measurement—Various image measuring objects

5. Recognition of the image—Finding and separating the objects which are present in an image.

A. Pre-processing

Pre-processing is the most basic phase that is performed for gesture recognition. We have also used a total of five signs wherein a particular sign with ten images. Pre-processing is done on images for extraction of features from the captured images. Pre-processing consist of two steps

- Segmentation
- Filtration

B. Segmentation

Thresholding methods replace the pixels present in the image with a black pixel if the intensity of the image $I_{i,j}$ is less than a user defined constant T (that is $I_{i,j} < T$), or if the image intensity is greater than the threshold, then the image pixels are replaced by white pixels, i.e. it divides the image into two categories, the foreground and background [4]. This whole process can written mathematically as mentioned

$$\boxed{\begin{aligned} I(x, \mathrm{y}) = 1 \text{ If } F(x, y) > T \\ I(x, \mathrm{y}) = 0 \text{ If } F(x, y) \leq T \end{aligned}}$$

C. Background Subtraction

Detection of moving objects in videos from standalone cameras is most commonly done using background subtraction approach. In this approach, a difference image is obtained by subtracting the current frame from a reference frame. 'Background image' is the term used for reference frame.

D. Filtration

To remove noises from an image, filtration is done.
Basically, two categories of filters can be used to remove salt and pepper noise:

- Mean Filter
- Median Filter

E. Mean Filter

This category of filtration includes a simple sliding-window spatial filter, and it replaces the centre value in the window with the mean value of all the pixels in the window.

F. Median Filter

The median filter is also a sliding-window spatial filter, and it replaces the centre value in the window with median value of all the pixels in the window.

1.2   Image Acquisition

A. **Real-Time Capturing**

The real-time capturing of the image process took full-size skin coloured images of the static hand gestures via the webcam. The images captured are shown in Figs. 1 and 2.

Fig. 1 Captured image 1

Fig. 2 Captured image 2

B. **Image Enhancement and Noise Reduction**

The enhancement of the image was achieved by segmentation and background subtraction, through which the foreground was distinguished from the background [5]. The image was then passed through a median filter so as to reduce the effect of various noises which may incorporate during this whole process.

The image after enhancement and noise reduction are shown in Figs. 3 and 4.

Fig. 3 Captured image 1 after segmentation

Fig. 4 Captured image 2 after segmentation
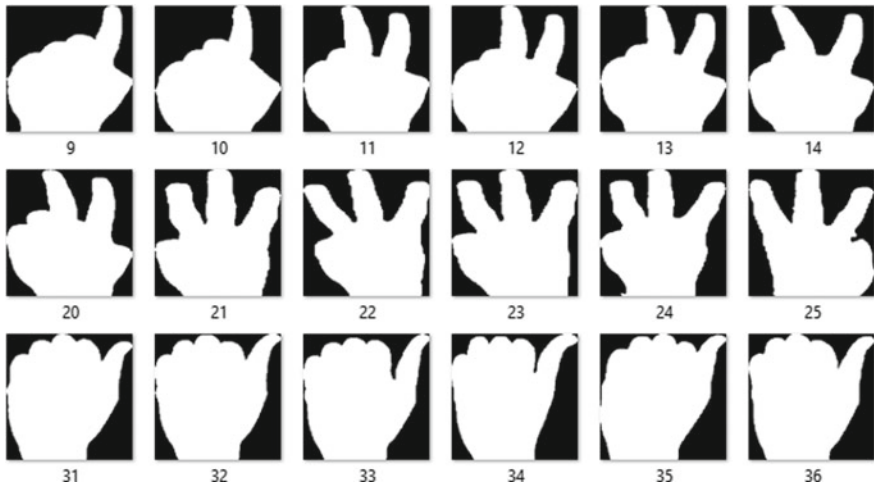
Fig. 5 Database of segmented images

C. **Database Creation**

A database was created of all the pre-defined gestures and was kept as reference for comparing the real-time input [6]. The database constituted of multiple images for a single gesture, 10 per gesture. The images which were in the database where at different angles and orientation so as to minimize the error in result computation (Fig. 5).

These images had already been processed, and the feature extraction was done beforehand.

2   Methodology

The gesture recognition process involved the process of formation of a database of the desired images of the hand gestures. The database is formed by capturing images of the hand gestures via webcam.

A. **Algorithm**

[1] Capture an RGB image using the webcam installed on laptop. For capturing an image using webcam, use the command 'getdata'. Store this image as background image.

[2] Again capture an RGB image and store this as current image. This image is gesture of our hand acting as an input to the system.

[3] Convert background and current images into grayscale image using 'rgb2gray'.

[4] Perform background subtraction by subtracting background image from the present image for obtaining a difference image.

[5] Convert this difference image into binary image by doing threshold segmentation.

[6] Apply median filter to this segmented image to remove salt and pepper noise. Using the command 'medfilt2', we can do this.

[7] Find features of this filtered image using 'regionprops' and resize its pixel to 256 * 256 by using command 'resize'.

[8] Now compare this image with images stored in database using correlation function. Image having the nearest value to 1 after correlation is the recognized image. We have used 'corr2' command for correlation of images.

[9] Display the image with nearest value to 1 after correlation from database and display a dialogue box showing the recognized number and play the sound of the corresponding number [7–9] (Fig. 6).

Fig. 6 Flow chart of proposed method

3 Results

The online during the tests performed the real-time image was captured and after the image was segmented and the background was subtracted, captured image was compared with the images in the database that was generated earlier. After co-relation was performed on the two set of images, the final result was yielded by the system and a warning window, showing the numerical value of the static gesture was displayed alongside it.

The recognition of different gestures is shown in Figs. 7 and 8.

In the above figures, there are two images, namely a test image and the other being the recognition result. The test image is the real-time captured image and after passing it through the algorithm the recognition is generated. Simultaneously, a dialogue box is produced denoting the digit to which the gesture resembles.
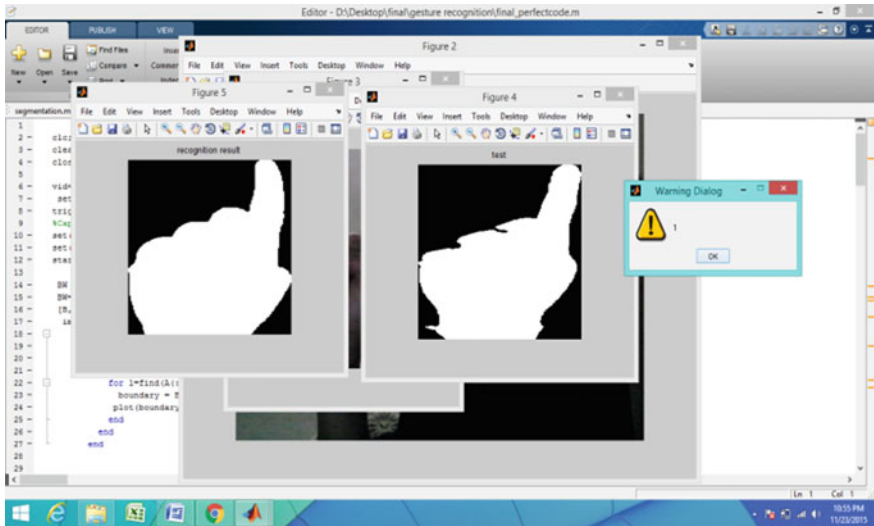

Fig. 7 Recognition of digit 1

Fig. 8 Recognition of digit 2

4 Conclusion

In this paper, the real-time applications of camera are outlined. Using gestures is about increasing the ease of doing a task apart from using it for communication gestures are playing an important part in controlling the technology around and with the upcoming of various techs which more aimed at making the life easier. Gestures in our paper involve just recognition, and they can be used to trigger different functions in a computer. This technique offers great potential and with further improvements in segmentation techniques and by using audio output for the gestures or by incorporating artificial neural networks. Introduction of neural would substantially reduce the programming part and will make it more general model. The developed programme for hand gesture recognition was able to attain a success rate of 95%. This method is useful for people with disabilities as this would decrease labour and be cost-effective.

References

1. Birk H, Moeslund TB (1996) Recognizing gestures from the hand alphabet using principal component analysis. Master's Thesis, Laboratory of Image Analysis, Aalborg University, Denmark
2. Wilson A, Bobick A (1995) Learning visual behaviour for gesture analysis. In: Proceedings of the IEEE symposium on computer vision, Coral Gables, Florida, pp 19–21, Nov 1995

3. Starner T, Pentland A (1995) Real-time American sign language recognition from video using hidden markov models. Technical Report No. 375, M.I.T Media Laboratory Perceptual Computing Section
4. Otsu N (1979) Threshold selection method from gray-level histograms. EEE Trans Syst Man Cybern 9(1):62–66
5. Gonzalez RC, Woods RE (1992) Digital image processing
6. Starner T, Pentland A (1998) Real-time American sign language recognition using desk and wearable computer based video. Pattern Anal Mach Intell IEEE Trans 20(12):1371–1375
7. Park H (2008) A method for controlling the mouse movement using a real time camera. Brown University, Providence, RI, USA, Department of Computer Science
8. Lien C-F. Portable vision-based HCI—a real-time hand mouse system on handheld devices. National Taiwan University, Computer Science and Information Engineering Department
9. Niyazi K, Kumar V, Mahe S, Vyawahare S (2012) Mouse simulation using two coloured tapes. Int J Inf Sci Tech (IJIST) 2(2)
10. Shah KN, Rathod KR, Agravat SJ (2014) A survey on human computer interaction mechanism using finger tracking. Int J Comput Trends Technol 7(3):174–177
11. Gonzalez RC, Woods RE (2002) Digital image processing, 2nd edn. Prentice Hall, Upper Saddle River, New Jersey, 07458
12. Malik S (2003) Real-time hand tracking and finger tracking for interaction. CSC2503F Project Report, 18 Dec 2003
13. Banerjee A, Ghosh A, Bharadwaj K, Saikia H (2014) Mouse control using a web camera based on colour detection. Int J Comput Trends Technol (IJCTT) 9(1)
14. The MATLAB website. Available: http://www.mathworks.com/matlabcentral/fileexchange/2
15. Banos O, Damas M, Pomares H, Rojas F, Delgado-Marquez B, Valenzuela O (2012) Human activity recognition based on a sensor weighting hierarchical classifier. Soft Comput 17 (2):333–343

Probabilistic Load Flow in a Transmission System Integrated with Photovoltaic Generations

B. Rajanarayan Prusty and Debashisha Jena

Abstract This paper compares the performance (solution accuracy and computational efficiency) of two hybrid methods (HMs) for probabilistic load flow (PLF) considering a mixture of discrete as well as correlated Gaussian and non-Gaussian input random variables. The PLF is accomplished on IEEE 118-bus test system with photovoltaic arrays installed at specific buses. The results of the HMs are compared with that of the existing methods such as combined cumulant and Gram-Charlier method, combined cumulant and Cornish-Fisher method, dependent discrete convolution method, and Monte Carlo simulation.

Keywords Hybrid method · Photovoltaic generation · Probabilistic load flow · Transmission system

1 Introduction

Deterministic load flow, traditionally used for the performance evaluation of power systems, ignores the uncertainty associated with the bus power generations and demands [1]. The integration of renewable energy sources like photovoltaic (PV) generation and wind power generation further increases the uncertainty level [2, 3]. Ignorance of the aforementioned uncertainties in load flow study leads to an unrealistic assessment of system performance. Probabilistic load flow (PLF) takes into account these uncertainties in a definite time frame by considering bus powers as random variables (RVs). An increased dimension of uncertainties and the associated correlations are the key factors that make the PLF more challenging.

Numerous methods have been proposed to solve PLF in the literature [4–12]. There is always an increasing interest to introduce a new PLF method that can

B. Rajanarayan Prusty (✉) · D. Jena
Department of EEE, National Institute of Technology Karnataka, Surathkal, India
e-mail: b.r.prusty@ieee.org

D. Jena
e-mail: bapu4002@gmail.com

accurately approximate multimodal probability distributions of result variables. Monte Carlo simulation (MCS) with random sampling is an accurate PLF method in the literature but is computationally burdensome. It acts as a reference method for the accuracy comparison of approximate and analytical methods (AMs). AMs take less time to obtain PLF results; they operate either on the distribution of input RVs or their statistical moments. The latter case is computationally more efficient than the former. Cumulant method (CM), discrete-convolution-based method, and Gaussian mixture approximation (GMA) method are three well-established AMs in the literature. They have certain limitations either in approximating multimodal probability distributions or incorporating input correlations. However, their hybridization yields improvement in the performance of the PLF results.

The authors in [10–12] hybridize CM with GMA technique and sequence operation theory (SOT), respectively, resulting in the hybrid methods (HMs) such as combined cumulant and GMA (CCGMA) and combined cumulant and SOT (CCSOT). On the one hand, univariate CCGMA [10] approximates probability distribution of each non-Gaussian input RV by a gth order Gaussian functions. On the other side, multivariate CCGMA [11] augments together the correlated non-Gaussian input RVs to form a multivariate structure. The probability distribution of the augmented structure is then approximated by a convex summation of gth order multivariate Gaussian functions. The mathematical formulations of both the HMs are elaborated in [10–12]. The solution accuracy and computational efficiency of the CCGMA are related to the order of Gaussian sum, whereas those of CCSOT are related to discrete sequence interval. In [10–12], the values of these performance parameters are assumed fixed, and PLF was accomplished.

In this paper, the effect of change of values of the performance parameters on PLF results is advocated. Besides, a detailed performance comparison of the proposed HMs with that of the MCS and a few other well-established AMs is carried out.

2 Hybrid Methods

The HMs, CCGMA, and CCSOT are elaborated in [10–12]. A short description of both the HMs is provided underneath. Since both the methods hybridize AMs, a sensitivity-matrix-based power system model is adopted for PLF [7].

2.1 CCGMA

In CCGMA, each non-Gaussian input RV or an augmented structure is approximated by a gth order Gaussian sum. In case of a discrete input RV, the approximated Gaussian sum number equals to the number of discrete impulses. The total number of Gaussian components (N_r) essential to approximate the desired RV is

calculated as the product of the Gaussian components pertaining to all non-Gaussian and discrete input RVs. The role of CM in CCGMA is to replace convolution operations of conventional CCGMA [13] with cumulant calculations. Further, input correlations are included in the analysis.

2.2 CCSOT

In CCSOT, the sensitivity coefficients are converted into probability sequences of sequence interval ΔS_1, whereas non-Gaussian and discrete input RVs are converted to probability sequences of sequence interval ΔS_2. The product of the probability sequences pertaining to a sensitivity coefficient and a discrete/non-Gaussian input RV results in a new probability sequence of interval, $\Delta S = \Delta S_1 \Delta S_2$. The role of copula-function-based SOT is to accomplish arithmetic operations and effective inclusion of input correlations. The role of CM formulation in CCSOT is to calculate the PMCC between equivalent Gaussian and non-Gaussian RVs.

3 Measures for Accuracy Comparison

The accuracy of the proposed HMs is ascertained by calculating two types of errors such as average root mean square error (ARMSE) [2, 12] and absolute percentage error (APE) [10]. The ARMSE is calculated as,

$$\text{ARMSE} = \frac{\sqrt{\sum_{i=1}^{N_\text{p}} \left(\text{CDF}_{\text{MCS}_i} - \text{CDF}_{\text{COM}_i}\right)^2}}{N_\text{p}}$$

where, $\text{CDF}_{\text{MCS}_i}$ and $\text{CDF}_{\text{COM}_i}$, respectively, are the ith value on cumulative probability plots using MCS and the comparing method, N_p is the selected number of points in the cumulative probability plots. Value of N_p is set to 100 in this paper.

APE in standard deviation (σ) is calculated as,

$$e_\sigma = \left| \frac{\sigma_{X,\text{MCS}} - \sigma_{X,\text{COM}}}{\sigma_{X,\text{MCS}}} \right| \times 100$$

where, $\sigma_{X,\text{MCS}}$, and $\sigma_{X,\text{COM}}$, respectively, are the standard deviation values of X using MCS and the comparing method.

Aggregate errors (ARMSE and APE) are calculated by summing up the values of error for all the desired RVs. The average error is obtained as the ratio of aggregate error and the total number of desired RVs.

4 Case Study and Comparison of Results

The performance of the proposed HMs is verified on modified IEEE 118-bus test system. The verification includes (i) investigating the accuracy of the HMs with respect to multiple input correlations and (ii) performance assessment (accuracy and computational efficiency) of the HMs as compared to CCGCM, CCCFM, DDC, and MCS. In this paper, the real and reactive power flows in a branch $i - j$ are denoted as P_{Li-j} and Q_{Li-j}, respectively. MATLAB 7.10 is used for developing the programming codes which are executed on a computer with i_7 processor and RAM size of 8 GB. Solar parks are installed at buses 19, 77, 92, 103, and 105 by replacing the original conventional generators. They are denoted respectively as SP-1, SP-2, SP-3, SP-4, and SP-5. Bus and line data for the system are taken from [14]. Table 1 provides the statistical details of the solar parks. The probabilistic description of discrete load powers is given in Table 2. The expected value of a discrete load power is set equal to the specified deterministic data. The real power generations of PV units are assumed to follow Beta distribution with shape parameters a and b [2]. The reactive power capability of all the PV units is neglected. The penetration level of PV units is set to 75% of the local bus load power. The coefficient of variation of PV generation is assumed to be 46.72% [15]. MCS with 24,000 samples is chosen as a comparative reference. This value is obtained by setting variance coefficient parameter $\beta_{\max}$ less than 1% [1, 2] for all the desired RVs.

4.1 Investigation of the Accuracy of the HMs Under Input Correlations

PV units of solar parks 4 and 5 are assumed to be correlated by a PMCC of 0.5 due to their geographical nearness. PMCC between each PV units and the respective

Table 1 Statistical details of solar parks

Particulars		SP-1	SP-2	SP-3	SP-4	SP-5
Bus number		19	77	92	103	105
Number of PV units		1	1	1	1	1
Shape parameters	a	2.697	2.029	1.860	3.618	3.285
	b	5.294	2.406	1.955	17.355	10.845

Table 2 Details of discrete distribution for load power at bus-47

Load power	Real	Probability values
Capacity (pu)	0.34	
Discrete values (pu)	0.23	0.10
	0.24	0.15
	0.36	0.30
	0.38	0.25
	0.39	0.20

local bus load real power is assumed to be 0.3. Real load powers at buses 103, 104, 105, 106, and 107 are assumed to be correlated by a constant PMCC of 0.5. Due to constant load power factor assumption, real and reactive load powers at buses 103, 104, 105, 106, and 107 are completely correlated. Base-case PMCC matrix constituted among the RVs PV_1, PV_2, PV_3, PV_4, PV_5, P_{D19}, P_{D77}, P_{D92}, P_{D103}, P_{D104}, P_{D105}, P_{D106}, P_{D107}, Q_{D103}, Q_{D104}, Q_{D105}, Q_{D106}, and Q_{D107} is provided in Table 3. In base case, load powers at buses 19, 77, 92, 103, 104, 105, 106, and 107 are assumed to follow Gaussian distribution with mean values as specified deterministic data and standard deviation values as 5% of their mean values.

In order to show the capability of the HMs to handle correlated input RVs precisely, aggregate and average ARMSE are calculated and compared in Table 4. The accuracy of multivariate CCGMA is found to be superior to that of univariate CCGMA. In both the cases, ARMSE is minimum for $g = 4$. On the other hand, the accuracy of CCSOT improves when the value of ΔS decreases. The cumulative probability plots of $P_{L100-103}$ is compared in Fig. 1 where WC and BC stand for without correlation and base-case correlation, respectively. Both CCGMA and CCSOT plots are closer to MCS indicating that the proposed HMs are capable of handling input correlations. Due to the consideration of base-case correlation, the standard deviation of $P_{L100-103}$ is increased.

Table 3 Base-case correlation matrix among the input RVs is decided as follows

1.0	0	0	0	0	0.3	0	0	0	0	0	0	0	0	0	0	0	0
0	1.0	0	0	0	0	0.3	0	0	0	0	0	0	0	0	0	0	0
0	0	1.0	0	0	0	0	0.3	0	0	0	0	0	0	0	0	0	0
0	0	0	1.0	0.5	0	0	0	0.3	0	0	0	0	0.3	0	0	0	0
0	0	0	0.5	1.0	0	0	0	0	0	0.3	0	0	0	0	0.3	0	0
0.3	0	0	0	0	1.0	0	0	0	0	0	0	0	0	0	0	0	0
0	0.3	0	0	0	0	1.0	0	0	0	0	0	0	0	0	0	0	0
0	0	0.3	0	0	0	0	1.0	0	0	0	0	0	0	0	0	0	0
0	0	0	0.3	0	0	0	0	1.0	0.5	0.5	0.5	0.5	1.0	0.5	0.5	0.5	0.5
0	0	0	0	0	0	0	0	0.5	1.0	0.5	0.5	0.5	0.5	1.0	0.5	0.5	0.5
0	0	0	0	0.3	0	0	0	0.5	0.5	1.0	0.5	0.5	0.5	0.5	1.0	0.5	0.5
0	0	0	0	0	0	0	0	0.5	0.5	0.5	1.0	0.5	0.5	0.5	0.5	1.0	0.5
0	0	0	0	0	0	0	0	0.5	0.5	0.5	0.5	1.0	0.5	0.5	0.5	0.5	1.0
0	0	0	0.3	0	0	0	0	1.0	0.5	0.5	0.5	0.5	1.0	0.5	0.5	0.5	0.5
0	0	0	0	0	0	0	0	0.5	1.0	0.5	0.5	0.5	0.5	1.0	0.5	0.5	0.5
0	0	0	0	0.3	0	0	0	0.5	0.5	1.0	0.5	0.5	0.5	0.5	1.0	0.5	0.5
0	0	0	0	0	0	0	0	0.5	0.5	0.5	1.0	0.5	0.5	0.5	0.5	1.0	0.5
0	0	0	0	0	0	0	0	0.5	0.5	0.5	0.5	1.0	0.5	0.5	0.5	0.5	1.0

Table 4 Comparison of ARMSEs for the HMs considering input correlations

PLF method		Aggregate ARMSE	Average ARMSE
Univariate CCGMA	$g = 2, N_r = 160$	78.2696	0.1403
	$g = 3, N_r = 1215$	77.9332	0.1397
	$g = 4, N_r = 5120$	77.4433	0.1388
	$g = 5, N_r = 15625$	79.1356	0.1418
Multivariate CCGMA	$g = 2, N_r = 10$	81.7975	0.1466
	$g = 3, N_r = 15$	75.9182	0.1361
	$g = 4, N_r = 20$	71.4296	0.1280
	$g = 5, N_r = 25$	80.6712	0.1446
CCSOT	$\Delta S = 0.001$	425.9772	0.7634
	$\Delta S = 0.0001$	70.5312	0.1264
	$\Delta S = 0.00001$	59.4270	0.1065
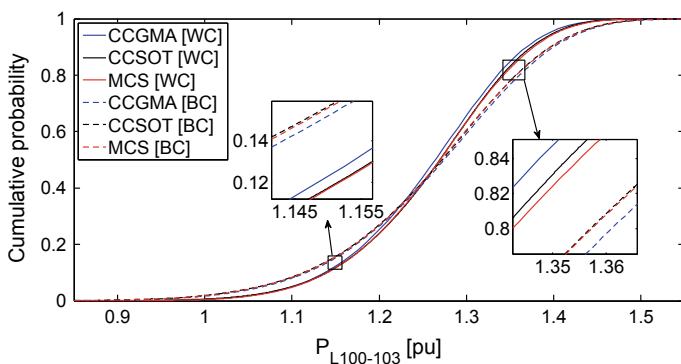
Fig. 1 Comparison of cumulative probability plots of $P_{L100-103}$ with and without considering input correlations

4.2 Performance Assessment of the HMs

The accuracy and efficiency of CCGMA are related to "g", and those of CCSOT are related to ΔS. In order to examine their performance, four different values of "g" such as 2, 3, 4, 5 and three different values of ΔS such as 0.001 ($\Delta S_1 = 0.1$, $\Delta S_2 = 0.01$), 0.0001 ($\Delta S_1 = 0.01$, $\Delta S_2 = 0.01$), and 0.00001 ($\Delta S_1 = 0.001$, $\Delta S_2 = 0.01$) are considered. The average APEs in standard deviation using CCGMA and CCSOT for all the 558 desired RVs are compared with CCGCM, CCCFM, DDC, and MCS in Table 5. The first six cumulants of the desired RVs are calculated in case of CCGCM and CCCFM. The value of ΔS is set to 0.0001 in case of DDC. The average e_σ is highest in case of CCSOT for $\Delta S = 0.001$, i.e., 9.6748%. The minimum in the average e_σ is found in case of CCSOT for $\Delta S = 0.00001$. The cumulative probability plots for P_{L49-54} with various values of

Table 5 Comparison of APEs for various PLF methods under base-case correlations

PLF method		Average e_σ
Multivariate CCGMA	$g = 2, N_r = 10$	4.1267
	$g = 3, N_r = 15$	3.9246
	$g = 4, N_r = 20$	3.7314
	$g = 5, N_r = 25$	3.9828
CCSOT	$\Delta S = 0.001$	9.6748
	$\Delta S = 0.0001$	3.6328
	$\Delta S = 0.00001$	3.1427
CCGCM	First 6 cumulants	4.3028
CCCFM	First 6 cumulants	3.7823
DDC	$\Delta S = 0.0001$	3.5294
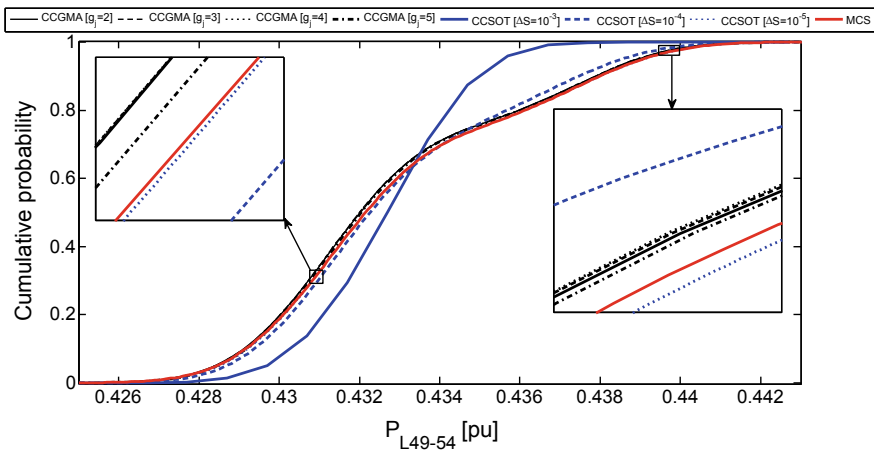
Fig. 2 Comparison of cumulative probability plots of P_{L49-54}

"g" and ΔS are compared in Fig. 2. The CCSOT result with $\Delta S = 0.00001$ is more close to MCS (ARMSE = 0.0316) followed by CCGMA plots for various "g". CCSOT result with $\Delta S = 0.001$ approximates the cumulative probability plot with maximum error, i.e., ARMSE = 0.8931.

Cumulative probability plots for P_{L46-48}, P_{L64-61}, Q_{L45-46}, and Q_{L64-65} under base-case correlation using all the methods are compared in Fig. 3. CCGMA, CCSOT, and DDC plots are closer to MCS plots in all the cases as compared to CCGCM and CCCFM plots.

Further, it is noticed that CCGCM and CCCFM are incapable of approximating multimodal probability distributions of the desired RVs. It is further noticed that CCGCM plots in case of P_{L46-48}, and Q_{L45-46} leads cumulative probability value to exceed unity, whereas probability value goes negative in case of P_{L64-61}.
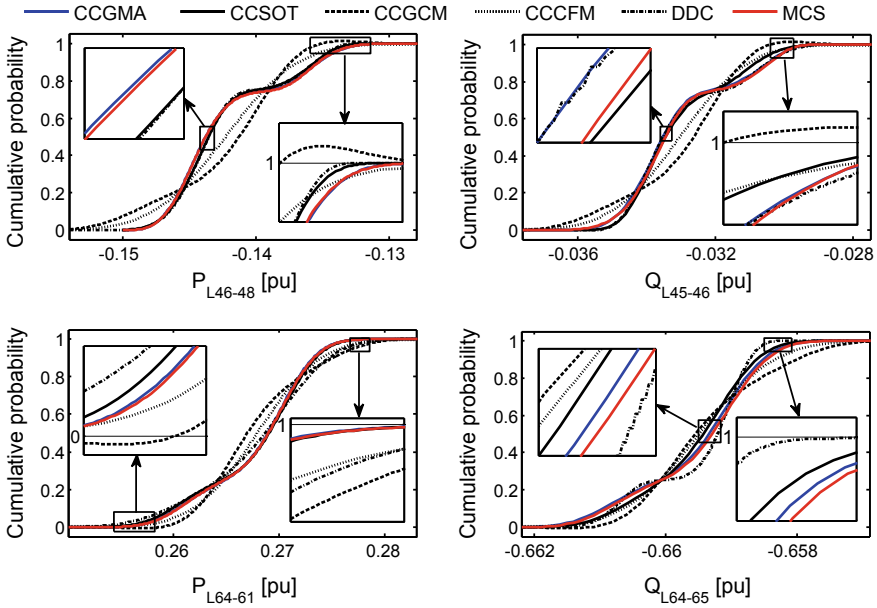
Fig. 3 Comparison of cumulative probability plots of P_{L46-48}, P_{L64-61}, Q_{L45-46}, and Q_{L64-65}

While using CCGMA and CCSOT, the value of "g" and ΔS corresponding to their respective lowest APE is used. In order to obtain the best value of "g" and ΔS that accurately approximates distribution of branch power flows, average APEs are calculated. Average APE for different values of "g" and ΔS are compared in Table 5. It is noticed that for g = 4 and $\Delta S = 0.00001$, CCGMA and CCSOT approximates the distributions of branch power flows with minimum APE, respectively, for the given value of PV penetration and correlation. APE using CCSOT is mainly found to be higher in case of branch power flows with the lower value of variance, whereas for desired RVs with the higher value of variance CCSOT is as accurate as CCGMA, and in few cases, the accuracy of CCSOT is more than CCGMA.

The simulation time required by CCGMA, CCSOT, CCGCM, CCCFM, DDC, and MCS are compared in Table 6. Although simulation time increases significantly with the increase in "g" in case of univariate CCGMA, it does not ensure appreciable decrease in the aggregate APE. On the other hand, computational time in case of multivariate CCGMA is significantly reduced. The values of N_r for various values of g using multivariate CCGMA is extremely less compared to univariate CCGMA. In this study, g = 4 results in minimum ARMSE for both univariate and multivariate CCGMA. CCSOT computational time increases with the decrease in value of ΔS.

Table 6 Comparison of simulation time

PLF method		Simulation time (s)
Univariate CCGMA	$g = 2$, $N_r = 160$	26.96
	$g = 3$, $N_r = 1215$	102.45
	$g = 4$, $N_r = 5120$	398.88
	$g = 5$, $N_r = 15625$	2191.24
Multivariate CCGMA	$g = 2$, $N_r = 10$	14.71
	$g = 3$, $N_r = 15$	15.51
	$g = 4$, $N_r = 20$	16.38
	$g = 5$, $N_r = 25$	17.21
CCSOT	$\Delta S = 0.001$	12.72
	$\Delta S = 0.0001$	117.81
	$\Delta S = 0.00001$	1163.37
CCGCM	First 6 cumulants	60.75
CCCFM	First 6 cumulants	79.30
DDC	$\Delta S = 0.0001$	974.55
MCS	$N_S = 24,000$	1842.15

5 Conclusion

Two HMs for PLF such as CCGMA and CCSOT are successfully applied to modified IEEE 118-bus test system. Uncertainties associated with PV generations and aggregate bus load powers are probabilistically modeled. Accuracy and efficiency of both the HMs are compared. Multivariate CCGMA is found to be more accurate, whereas CCSOT is computationally more efficient than univariate CCGMA. But both the methods obtain the distribution of desired RVs in less time compared to MCS considering input correlations.

References

1. Prusty BR, Jena D (2017) A critical review on probabilistic load flow studies in uncertainty constrained power systems with photovoltaic generation and a new approach. Renew Sustain Energy Rev 69:1286–1302
2. Fan M, Vittal V, Heydt GT, Ayyanar R (2012) Probabilistic power flow studies for transmission systems with photovoltaic generation using cumulants. IEEE Trans Power Syst 27(4):2251–2261
3. Prusty BR, Jena D (2018) Preprocessing of multi-time instant PV generation data. IEEE Trans Power Syst 33(3):3189–3191
4. da Silva AM Leite, Ribeiro SMP, Arienti VL, Allan RN, Do Coutto Filho MB (1990) Probabilistic load flow techniques applied to power system expansion planning. IEEE Trans Power Syst 5(4):1047–1053
5. Gupta N (2016) Probabilistic load flow with detailed wind generator models considering correlated wind generation and correlated loads. Renew Energy 94:96–105

6. Zhang P, Lee ST (2004) Probabilistic load flow computation using the method of combined cumulants and Gram-Charlier expansion. IEEE Trans Power Syst 19(1):676–682

7. Prusty BR, Jena D (2017) A detailed formulation of sensitivity matrices for probabilistic load flow assessment considering electro-thermal coupling effect. In: Proceedings of IEEE PES Asia-Pacific power and energy engineering conference (APPEEC), pp 1–6

8. Su CL (2005) Probabilistic load-flow computation using point estimate method. IEEE Trans Power Syst 20(4):1843–1851

9. Prusty BR, Jena D (2018) An over-limit risk assessment of PV integrated power system using probabilistic load flow based on multi-time instant uncertainty modeling. Renew Energy 116:367–383

10. Prusty BR, Jena D (2016) Combined cumulant and Gaussian mixture approximation for correlated probabilistic load flow studies: a new approach. CSEE J Power Energy Syst 2(2): 71–78

11. Prusty BR, Jena D (2016) Estimation of optimal number of components in Gaussian mixture model-based probabilistic load flow study. In: Proceedings of IEEE India Conference (INDICON), pp 1–6

12. Prusty BR, Jena D (2017) A sensitivity matrix-based temperature augmented probabilistic load flow study. IEEE Trans Ind Appl 53(3):2506–2516

13. Sirisena HR, Brown EP (1983) Representation of non-Gaussian probability distributions in stochastic load-flow studies by the method of Gaussian sum approximations. Proc Inst Electr Eng 130(4):165–171

14. Power Systems Test Case Archive. Available: http://www.ee.washington.edu/research/pstca. Accessed date July 2015

15. Qin Z, Li W, Xiong X (2013) Incorporating multiple correlations among wind speeds, photovoltaic powers and bus loads in composite system reliability evaluation. Appl Energy 110:285–294

Uncertainty Modeling Steps for Probabilistic Steady-State Analysis

B. Rajanarayan Prusty and Debashisha Jena

Abstract This paper endeavors to deliver a detailed probabilistic uncertainty modeling approaches for power system planning and operation. The conventional uncertainty modeling approaches are reviewed, and the modeling challenges under large-scale integration of renewable generations are described. The modeling steps in various timescales (of the time horizons) for different applications are clarified inclusively. It is believed that the paper will help the novice readers in the probabilistic uncertainty modeling area.

Keywords Operation · Planning · Probabilistic steady-state analysis · Time horizon · Timescale · Uncertainty modeling

1 Introduction

In recent days, increasing uncertainties due to load growth, network structural changes, and the introduction of new operating policies pose several technical challenges in power system planning and operation [1]. The conventional deterministic steady-state analysis fails to account for the uncertainties of modern power systems [2]. Ignorance of the aforesaid uncertainty factors in the analysis may lead to either overinvestment or insufficient reliability during planning and operation [3]. The reliability assessments for planning and operation are fundamentally different, mainly the calculation of reliability indices. Planning studies ensure the availability of adequate resources, whereas operational studies maintain the system security. Conceptually, reliability considers adequacy as well as security [4].

Probabilistic steady-state analysis (PSSA) using probabilistic load flow (PLF) reveals the steady-state characteristics of the system by obtaining uncer-

B. Rajanarayan Prusty (✉) · D. Jena
Department of EEE, National Institute of Technology Karnataka, Surathkal, India
e-mail: b.r.prusty@ieee.org

D. Jena
e-mail: bapu4002@gmail.com

tainties in the decision variables derived from the uncertainties of the input random variables (RVs) [5]. PSSA assists in making critical decisions during power system expansion planning, operation (operational planning and real-time operation), and control by identifying the decision variables for which limiting values are expected to exceed. The decision variables in a power system include bus voltage magnitudes, branch power flows, branch power losses, branch temperatures, generator bus reactive powers, slack bus power, etc. [6]. The operational planning establishes an elementary phase before a real-time operation which decides on whether existing facilities satisfy the security criteria or required to be reinforced.

One of the primary tasks in PSSA is uncertainty modeling. It mainly depends on the application, time horizon, and timescale related to the application. In general, power system studies are categorized into grid expansion, operational planning, and real-time system operation [7]. The timescales of subactivities under each of the studies are reviewed in [1]. But, the description of possible uncertainties and various methods for their characterization are not elucidated. Among different uncertainty handling methods, application of a probabilistic method is most appreciated in the literature [8, 9]. Probabilistic uncertainty modeling defines the possible distribution of an input RV with a strict bound based on their historical record. PLF obtains the probability distribution of the decision variables by using an uncertainty handling method [10–14]. Planning studies being associated with longer timescales relies on a highly accurate but computationally more intricate method like Monte Carlo simulation (MCS). However, as operational studies require timely decision, the application of MCS is not feasible, and thus, an analytical method (AM) is preferable.

Conventionally, the uncertainties in power systems are due to load powers and component outages (accounted in steady-state contingency analysis [15]). However, the deepening penetration of renewable generations has introduced several challenges in uncertainty modeling as they are variable, unpredictable, intermittent, and uncontrollable. The uncertainties have two primary components: (i) temporal (related to time) and spatial (related to location). Among various renewable generations, PV resources generate power at varying capacities and hence are greatly favored. Further, PV technology is cost-effective and easily installable. In systems with higher penetrations of PV generations, the system's steady state is significantly affected due to their distinct characteristics which are different from conventional generations. The aforesaid uncertainty factors and associated spatiotemporal complex dependencies lead to modeling challenges [16]. Further, traditional PSSA neglects the weather effect and treats branch parameters as constant. Nevertheless, branch parameters may also have uncertainty content [13, 17]. Consideration of all of the above features leads to effective planning decisions and operational steps.

For different studies, the uncertainty modeling can vary significantly and has never been explicitly described in the literature. Hence, a detailed presentation of the modeling steps and various preeminent aspects in modeling for the planning and

operation of grid-integrated large-scale PV generations is the objective of this paper. It is to mention here that the modeling steps are equally applicable to wind power generation. The ensuing sections reveal in detail about each of the pertinent aspects.

2 Probabilistic Uncertainty Modeling

In power system studies, uncertainties are broadly classified as planning uncertainty and operational uncertainty [2]. While the former corresponds to the analysis of all possible combination of system inputs, the latter corresponds to the forecast errors. On the one hand, planning uncertainties are quantified to make decisions regarding investments (and their economic merits) in locating adequate generation and transmission assets at suitable places and time, thereby ensuring reliable and efficient delivery of real power load when no remedial actions are executed [18]. The quantification of operational uncertainties, on the other hand, is decisive in recognizing whether the system operating limits are within acceptable reliability criteria. Then after the change of system, operating mode is decided by executing remedial actions to minimize the risks associated with the operation (by ensuring reliability through power balance at all the times) [19]. The actions include load transfer, switching actions, protection/control schemes, temporary reconfigurations, etc.

Uncertainty quantification using parametric probability distribution functions either assumed or decided from the operator's experience is not always realistic. Hence, an accurate uncertainty model can only be developed based on the historical data. In PSSA, an input RV X at time t is expressed as $X = \mu_X + \varepsilon_X$ where μ_X and ε_X, respectively, are the expected value and uncertainty component of X. In case of planning study, the daily time series corresponding to a specific time of year is used for uncertainty modeling; the process for obtaining μ_X and ε_X is elucidated in Sect. 3. An operational study considers a time series that constitutes the required number of past values of inputs; μ_X is the point forecasted value of X obtained from the series, and ε_X quantifies the uncertainty associated with the point forecast [20].

2.1 Challenges with Uncertainty Modeling

The requirements of adequate historical data with acceptable accuracy and a sophisticated model to capture spatiotemporal complex dependencies are the significant challenges recognized for an accurate uncertainty model. The historical data inadequacy is due to the irregular source database update. The data inaccuracy is mainly due to the missing values and outliers. In practice, the dependence between different RVs is rarely linear. Therefore, ignorance of nonlinear dependency will

cause significant error in the analysis, and hence, modeling of the concealed dependence structure in case of a higher number of input RVs with arbitrary probability distributions is the challenge.

2.2 Time Horizons and Timescales

Time horizons (long-term, mid-term, and short-term), and timescales (e.g., minutes, hours, days, weeks, months, years, several years, decades, etc.) that a study of interest focuses on, play a significant role in uncertainty modeling. The degree of uncertainty increases significantly from a short timescale in system operation to a larger timescale in expansion planning. For example, based on the current conditions, a system operator has more confidence in forecasting for the next hour than the next month. Nonetheless, the modeling of an operational uncertainty is more intricate than a planning uncertainty.

2.3 Granularity Time Step

The resolution of data in a time series affects the forecasted output. The historical data collected at an hourly interval is referred to as a low-resolution data, whereas an ideal time series of the 1-min time step is referred to as the highest-resolution data.

3 Review of Uncertainty Modeling for PSSA

This section reviews the uncertainty modeling of those PSSA input RVs which are susceptible of being strongly dependent on each other. The uncertainty modeling in conventional, as well as PV-integrated power systems is detailed. Figure 1 provides an overall impression of the time information for modeling uncertainty in various power system studies.

3.1 Conventional Power Systems

Typically, PSSA considers historical time series of inputs to describe the uncertainty components. Either stationarity of the time series is ensured [5, 7, 15, 21] or the expected value and the corresponding confidence interval of the future values are forecasted [5, 7, 21]. The former is generally considered for operational planning, whereas the latter is for expansion planning. The daily peak loads of

⊙ Time-horizon	⊙ Time-scale	⊙ Time-step	⊙ Actions/Decisions

Expansion planning	Long-term	Years-to-decade(s)	Yearly	Grid expansion plans, capacity credit assessment, etc.
	Medium-term	Years	Daily	Infrastructural investment plans
	Short-term	Months	Daily	Installation of protection systems, phase shifters, etc.
Operational planning	Long-term	Year(s)	Daily	Release of transmission equipment(s) for maintenance and scheduled repair
	Medium-term	Month(s)	Daily	Delaying or anticipating the commitment of transmission facilities
	Short-term	Day(s)-to-week	Hourly/daily	Modifying the operational strategy, postponing scheduled outages, etc.
Real-time operation	Long-term	Day-to-day(s)	Hourly	Unit commitment
	Medium-term	Minute(s)-to-day	15 min-to-1 hour	Economic dispatch
	Short-term	Second(s)-to-minute(s)	30 sec-to-5 min	Automatic generation control, storage control, assessment of ramping events, etc.

Fig. 1 Time information for uncertainty modeling in power system planning and operation

substations (each day at the same time) for a period of few months (typically, one up to three months) corresponding to the period of the annual peak are considered for uncertainty modeling. In [15], restriction on the length of time series to one month is to preserve data stationarity. Whereas in [5, 7, 21], the daily peak loads collected for two months have evident trend effects. The stationarity is attained either by data differencing or by fitting a curve (interpreted as the time evolution of expected values) using a set of mathematical functions [21]. Since the data corresponds to a relatively shorter period, the nonlinearities in the load patterns in relation to seasonal change of weather variables are not accounted for; efforts were put only to remove the trend effect from data. The expected value of load power raises by 8% in case of a year-ahead operational planning [15]. The aforesaid short-term (operational) uncertainties are related to short-term factors such as environmental conditions and social effects [21]. In [5, 21], the uncertainties are due to long-term factors such as demographic growth and economic activities. The annual substation peak loads for past several decades are considered for modeling. The load probability distribution for the time horizon is forecasted using the method of linear regression [5]. In all the above cases, the data pertaining to holidays and weekends is removed as they cause a significant reduction in the peak load values. The obtained stationary samples can reasonably be approximated to a continuous density function within a specific range if samples are very close together (i.e., to have small variance) [15]. This procedure dramatically abates computational efforts while applying an AM for PLF. In case of samples not very close together (i.e., to

have large variance), a possible approximated discrete distribution with a definite number of impulses is constructed where the individual probability values sum to unity [15, 21].

The dependencies among load powers usually being linear, Pearson product moment correlation coefficient (PMCC) is used to measure the strength of linear dependencies [5]. The PMCC values can be directly obtained among the stationary samples in operational planning studies and the annual peak load series in long-term expansion planning.

3.2 PV-Integrated Power Systems

For power systems integrated with PV generation, it is very much essential to evaluate the permissible PV penetration level using a probability method which is mainly affected by PV generation distribution, seasonal patterns, fluctuation characteristics, and the associated dependencies among nearby PV generations. In system planning, uncertainty associated with PV generations should be quantified for the determination of the variability of the system power flow, which is essential for system dimensioning. In case of an operational study, uncertainty quantification of PV generation is central in the system management, e.g., optimal operation under high penetration [2].

In recent days, a majority of PV generations are encouraged from the residential rooftop installations located closer to the loads on the transmission systems [22]. But, such installations are suggested not to afford voltage control as per IEEE standard 1547 [23]. Hence, they are utilized as active power resources. This leads to immediate concern of bus voltage magnitude violations under higher penetration levels [24]. Further, uncertainties arising from multiple PV generations and other input RVs, as well as their multiple dependencies, can cause the decision variables to exceed their limiting values. On this line, PLF is carried out at noon to analyze the influence of PV generation uncertainty on the decision variables as PV generation has maximum coefficient of variation (CV) at noon [3]. PV generation and load power historical data collected each day at noon for two years are considered for uncertainty modeling. Such a study can be used for planning-based applications like power balance, peak regulation, etc. Further, how likely the decision variables exceed their allowable limit at the peak hour of PV generation can be known. The authors in [13] used the historical daily time series of ambient temperature along with PV generation and load power for temperature-augmented PLF (TPLF); TPLF is performed at noon. The load power uncertainty model as adopted in [3, 13] can better access the possible state of a power system unlike the conventional model where only peak load powers are considered as the worst-case condition. While peak load values cause low voltage and generation deficiency, light loads give rise to overvoltage conditions [24]. As the data considered for modeling refers to a specific time instant for several years, it conflates predictable and unpredictable components. The unpredictable/uncertainty components in the data are
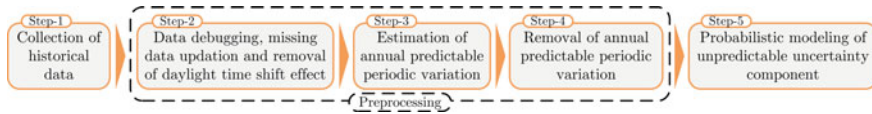
Fig. 2 Uncertainty characterization of a historical daily time series collected for several years

characterized by removing the corresponding predictable components [25, 26]. A step-by-step procedure to accomplish such an uncertainty model is provided in Fig. 2. It is evident from Fig. 2 that step 2 is imperative in preprocessing as historical time series is extremely vulnerable to missing values, outliers, etc. In step 3, the annual periodic variation is characterized using a linear regression model [10, 25, 26]. The residual component in step 4 after filtering out the estimated predictable component refers to the uncertainty component. Finally, in step 5 a probability distribution of the uncertainty component is carried out.

The study carried out in [3] is an example case to evaluate the influence of PV generation and other input uncertainties at a certain time instant. The risk of steady-state bus voltage violation and branch power flow exceedance under various penetration levels and correlations are quantified using over-limit probability indices. Although PV generation has maximum CV at noon, other input RVs have maximum CV values at different other time instants [10]. Hence, a more realistic risk assessment can only be accomplished by executing PLF simulations at many other time instants not just at noon. On this note, an over-limit risk assessment based on multi-time instant uncertainty modeling is carried out in [10]. In multi-time instant uncertainty modeling, the challenge is to develop regression models to trace the complex annual periodic patterns in input data. Such challenges are attempted in [10, 26]. Multi-time instant risk assessment provides useful information for risk-based planning of PV-integrated power systems by estimating over-limit risk indices under various penetration levels [10]. With this information, it is possible to delimit the permissible PV penetration. Further, the assessment of necessary reinforcement can be accomplished. This approach is realistic as the calculated risk indices consider the lower and/or higher limit exceedance of all the system buses and branches. Since the studies in [3, 10] evaluate the uncertainty influence at a specific instant(s) of time, conventional generation dispatch strategies are not accounted for. However, it is an important aspect of PV-integrated power systems to adjust total conventional generation to match the PV generation changes with automatic generation control or day-ahead generation scheduling [27].

In an operational framework, probabilistic forecasting of expected PV generation is of focus for taking strategic decisions [2]. When such uncertainties of PV generations at multiple sites are considered in the analysis, spatial and temporal dependencies are required to be modeled for efficient extraction of critical information for the planning and operation of PV-integrated power systems [28].

4   Conclusion

This paper provides detailed probabilistic modeling approaches for various power system steady-state analysis. Efforts are mainly put to review the current uncertainty modeling steps for the aforesaid applications. The time information for modeling is explicitly detailed. The challenges in modeling for a power system integrated with PV generation are reviewed, and recent modeling approaches are elucidated. It is expected that the review will serve as a reference for novice readers in the area of uncertainty modeling.

References

1. Khuntia SR, Tuinema BW, Rueda JL, van der Meijden MAMM (2016) Time-horizons in the planning and operation of transmission networks: an overview. IET Gener Transmiss Distrib 10(4):841–848
2. Papaefthymiou G, Kurowicka D (2009) Using copulas for modeling stochastic dependence in power system uncertainty analysis. IEEE Trans Power Syst 24(1):40–49
3. Fan M, Vittal V, Heydt GT, Ayyanar R (2012) Probabilistic power flow studies for transmission systems with photovoltaic generation using cumulants. IEEE Trans Power Syst 27(4):2251–2261
4. Li W, Zhou J (2008) Probabilistic reliability assessment of power system operations. Elect Power Comp Syst 36(10):1102–1114
5. Leite da Silva AM, Ribeiro SMP, Arienti VL, Allan RN, Do Coutto Filho MB (1990) Probabilistic load flow techniques applied to power system expansion planning. IEEE Trans Power Syst 5(4):1047–1053
6. Prusty BR, Jena D (2017) A detailed formulation of sensitivity matrices for probabilistic load flow assessment considering electro-thermal coupling effect. In: Proceedings of IEEE PES Asia-Pacific Power Energy Engineering Conference (APPEEC), pp 1–6
7. Leite da Silva AM, Marangon Lima JW, Ribeiro SMP, Arienti VL, Schilling MT, Vieira Filho X, Soares SM (1991) Operational and expansion planning of Brazilian systems based on probabilistic load flow. In: Proceedings of 3rd International Conference on Probabilistic Methods Applied to Electric Power Systems, pp 197–202
8. Prusty BR, Jena D (2017) A critical review on probabilistic load flow studies in uncertainty constrained power systems with photovoltaic generation and a new approach. Renew Sustain Energy Rev 69:1286–1302
9. Aien M, Hajebrahimi A, Fotuhi-Firuzabad M (2016) A comprehensive review on uncertainty modeling techniques in power system studies. Renew Sustain Energy Rev 57:1077–1089
10. Prusty BR, Jena D (2018) An over-limit risk assessment of PV integrated power system using probabilistic load flow based on multi-time instant uncertainty modeling. Renew Energy 116:367–383
11. Prusty BR, Jena D (2016) Combined cumulant and Gaussian mixture approximation for correlated probabilistic load flow studies: a new approach. CSEE J Power Energy Syst 2 (2):71–78
12. Gupta N (2016) Probabilistic load flow with detailed wind generator models considering correlated wind generation and correlated loads. Renew Energy 94:96–105
13. Prusty BR, Jena D (2017) A sensitivity matrix-based temperature augmented probabilistic load flow study. IEEE Trans Ind Appl 53(3):2506–2516

14. Prusty BR, Jena D (2016) Estimation of optimal number of components in Gaussian mixture model-based probabilistic load flow study. In: Proceedings of IEEE India Conference (INDICON), pp 1–6
15. Leite da Silva AM, Arienti VL, Barbosa MH (1987) Probabilistic techniques in load flow analysis-a practical application. In: Proceedings of International Symposium on Probabilistic Methods Applied to Electric Power Systems (ISPMAEPS), pp 643–651
16. Wang Y, Zhang N, Kang C, Miao M, Shi R, Xia Q (2018) An efficient approach to power system uncertainty analysis with high-dimensional dependencies. IEEE Trans Power Syst 33 (3):2984–2994
17. Su CL (2005) Probabilistic load-flow computation using point estimate method. IEEE Trans Power Syst 20(4):1843–1851
18. Zhang P, Lee ST (2004) Probabilistic load flow computation using the method of combined cumulants and Gram-Charlier expansion. IEEE Trans Power Syst 19(1):676–682
19. Peng C, Lei S, Hou Y, Wu F (2015) Uncertainty management in power system operation. CSEE J Power Energy Syst 1(1):28–35
20. Bracale A, Caramia P, Carpinelli G, Di Fazio AR, Varilone P (2013) A Bayesian-based approach for a short-term steady-state forecast of a smart grid. IEEE Trans Smart Grid 4 (4):1760–1771
21. Coutto Filho MBD, Leite da Silva AM, Arienti VL, Ribeiro SMP (1991) Probabilistic load modeling for power system expansion planning. In: Proceedings of 3rd international conference on probabilistic methods applied to electric power systems, pp 203–207
22. Eftekharnejad S, Vittal V, Heydt GT, Keel B, Loehr J (2013) Impact of increased penetration of photovoltaic generation on power systems. IEEE Trans Power Syst 28(2):893–901
23. IEEE 1547 Standard for interconnecting distributed resources with electric power systems, Oct 2003. Available http://grouper.ieee.org/groups/scc21/1547/1547/index.html
24. Fan M (2012) Probabilistic power flow studies to examine the influence of photovoltaic generation on transmission system reliability. Ph.D. dissertation, Arizona State University, Department of Electrical, Computer, and Energy Engineering, Tempe AZ, Apr 2012
25. Fan M, Vittal V, Heydt GT, Ayyanar R (2014) Preprocessing uncertain photovoltaic data. IEEE Trans Sustain Energy 5(1):351–352
26. Prusty BR, Jena D (2018) Preprocessing of multi-time instant PV generation data. IEEE Trans Power Syst 33(3):3189–3191
27. Fan M, Vittal V, Heydt GT, Ayyanar R (2013) Probabilistic power flow analysis with generation dispatch including photovoltaic resources. IEEE Trans Power Syst 28(2): 1797–1805
28. Le DD, Gross G, Berizzi A (2015) Probabilistic modeling of multisite wind farm production for scenario-based applications. IEEE Trans Sustain Energy 6(3):748–758

Analysis of Nonlinear Activation Functions for Classification Tasks Using Convolutional Neural Networks

Aman Dureja and Payal Pahwa

Abstract We give an overview of several nonlinear activation functions in deep neural networks that are used to solve various complex machine learning applications. We make the comparison on effectiveness of using these functions and conduct empirical analysis on the Cat/Dog dataset with the aim of clarifying which function produce the best results overall. We also make the prediction by taking the number of input images on CNN model by applying different activation functions at the number of hidden layers.

Keywords CNN · Activation function · Hidden layers · Deep neural networks

1 Introduction

When making the neural architecture or a deep neural network to perform well in practice, there is need of activation functions. But the choice of activation function also affects the network in terms of optimization and to retrieve the better results. One such decision is the type of layer that composes the neural net, particularly involving the type of activation functions that will be implemented as hidden layers.

The foundation of using such activation function gives the ability to model non-linearity's in the data, which help us to make more complex representation of data so that optimized results can be obtained.

The numbers of nonlinear activation functions like sigmoid and tanh are applied successfully to the number of neural networks for finding the solutions to the number of problem in multilayer's perceptron. But, it fails to train some neural networks due to their nonzero-centered property and slope of the function.

A. Dureja (✉)
USICT, GGSIPU, New Delhi, India
e-mail: amandureja@gmail.com

P. Pahwa
BPIT, Rohini, New Delhi, India
e-mail: pahwapayal@gmail.com

Several activation functions have been introduced in machine learning for many practical applications. These activation functions are used to solve nonlinear complex problems with the real data to train the network and to produce the useful results in classification, regression, etc.

In Sect. 2, we provide the theoretical overview of the activation functions used in our experiments. In Sect. 3, the analysis and the comparison of the performance of five activation functions, mainly Tanh, ELU, Selu, ReLu, and PReLu is done on the convolutional neural network [1] with three hidden layers. We use a dataset of 10,000 images of Cat/Dog for two classes and see how overall accuracies vary accordingly on different activation functions in the network. Based on our results from that analysis, we make the prediction in Sect. 4 by giving input images onto the trained CNN with different activation functions on the layers and conclude which activation function is best suited for CNN.

2 Activation Functions

This section covers the brief description of various activation functions which are used in neural networks. Neural networks are considered as universal function approximators. This means that neural networks can compute and learn any function at all. Almost any process we can think of can be represented as a functional computation in neural networks.

The functions having more than one degree are nonlinear functions, and they have a curvature when we plot them. Now, we need a neural network model that can learn and represent almost anything and any arbitrary complex function which maps inputs to outputs.

Hence it all comes down to this, we need to apply an activation function $f(x)$ to make the network more influential and add capability to it to learn more complex and complicated form of data and represent nonlinear complex arbitrary functional mappings between inputs and outputs. Hence by using a nonlinear activation, we can generate nonlinear mappings from inputs to outputs.

Also another important feature of an activation function is that it should be differentiable. We need it to be this way to perform backpropagation optimization strategy, i.e., while propagating backward in the network to compute gradients of error (loss) with respect to weights and then accordingly optimize weights using gradient descent or any other optimization technique to reduce error.

We are considering the main activation functions in deep neural networks like sigmoid, tanh, exponential linear units (ELU) [2], scaled exponential linear units (Selu) [3], rectified linear units (ReLu) [4], and PReLu [5].

Following are the definitions of the considered activation functions with their respective gradients, by their visualization on the xy-axis.

Most popular types of activation functions:

1. Sigmoid activation function
2. Tanh—hyperbolic tangent
3. ReLu—rectified linear units
4. ELU—exponential linear units
5. Selu—scaled exponential linear units
6. PReLu—parametric ReLu

Sigmoid Function: The sigmoid activation function (Fig. 1) is widely used in machine learning specially for the logistic regression and for the simple neural network implementation. This is an activation function of form

$$f(x) = 1/1 + \exp(-x) \tag{1}$$

and having range between 0 and 1. It is like a S-shaped curve. It is easy to understand and apply but have some disadvantages due to incapable for solving complex problems:

1. Vanishing gradient problem
2. Secondly, its output is not zero-centered. It makes the gradient updates go too far in different directions. $0 < \text{output} < 1$, and it makes optimization harder.
3. Sigmoid functions have slow convergence.

Tanh (Tangent Function): This activation function is represented as (Fig. 2)

$$f(x) = 1 - \exp(-2x)/1 + \exp(-2x) \tag{2}$$

The problem which is raised in the sigmoid function was that its output is not zero-centered, and it is removed in tanh function due to its range in between -1 and 1, i.e., $-1 < \text{output} < 1$. Hence, optimization is easier in this method. But it has still problem of vanishing gradient problem.

Fig. 1 Sigmoid activation function
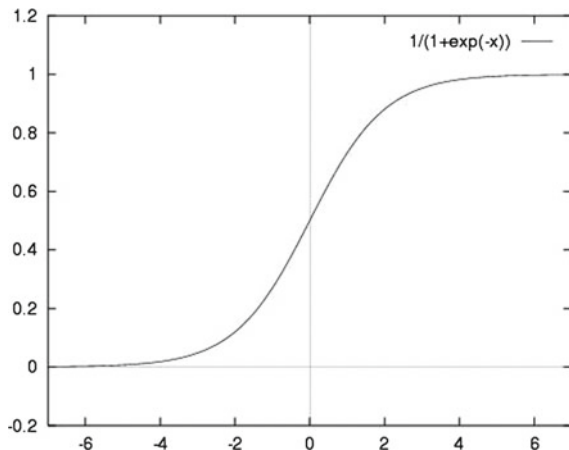
Fig. 2 Tanh activation
function
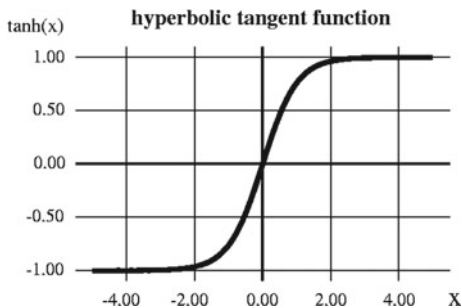
ReLu (Rectified Linear units): It has become very popular in the past couple of years [4]. It was recently proved that it had six times improvement in convergence from tanh function.

$$F(x) = \max(0, x) \quad \text{i.e if } x < 0, \ F(x) = 0$$
$$\text{and if } x \geq 0, \ F(x) = x \tag{3}$$

Hence as seeing the mathematical form of this function, we can see that it is very simple and efficient. Most of the times in machine learning and computer science we notice that most simple and consistent techniques and methods are only preferred and are considered best. Hence, it avoids and rectifies vanishing gradient problem. Almost all deep learning models [6] use ReLu nowadays (Fig. 3).

But its limitation is that it should only be used within hidden layers of a neural network model. Hence for output layers, we should use a Softmax function for a classification problem to compute the probabilities for the classes, and for a regression problem it should simply use a linear function. Another problem with ReLu is that some gradients can be fragile during training and can die. It can cause a weight update which will makes it never activate on any data point again. Simply saying that ReLu could result in dead neurons.

To fix this problem, another modification was introduced called *Leaky ReLu* to fix the problem of dying neurons. It introduces a small slope to keep the updates alive.

We then have another variant made from both ReLu and leaky ReLu called Maxout function (Fig. 3).
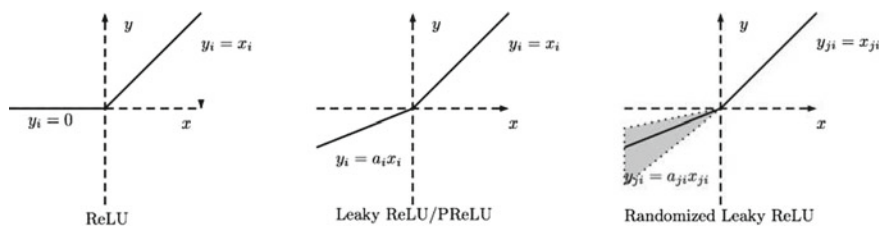
Fig. 3 ReLu activation function
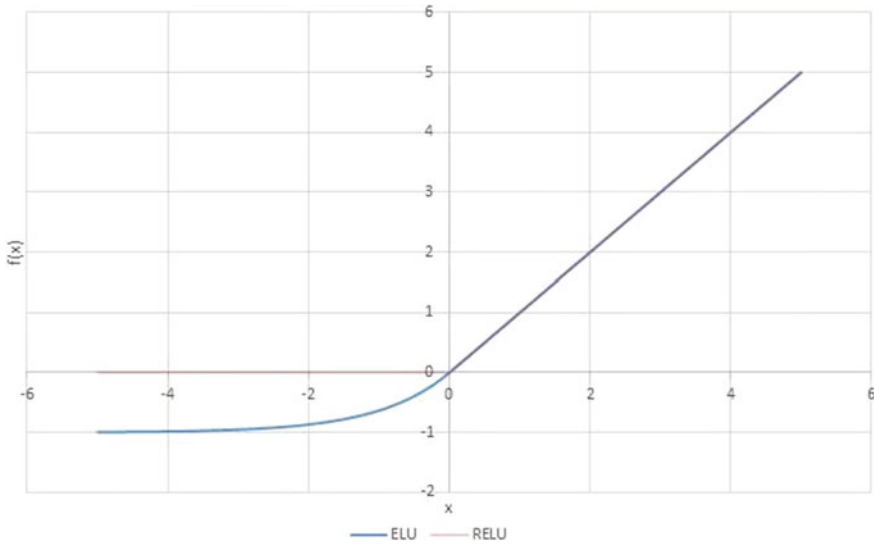
Fig. 4 ELU activation function

ELU (Exponential Linear Unit): ELU function (Fig. 4) produces most accurate results and tends to converge fastly. It has extra alpha constant [2] which is always positive. It is most similar to ReLu, but it does not go for negative inputs.

The problem in tanh and sigmoid function having vanishing gradient problem is solved in ELU. The problem of vanishing gradient is also resolved in ReLu, but ReLu has problem of its mean which is not zero. If we get the mean value is zero, we have fast learning. And ELU has mean value zero.

Selu (Scaled Exponential linear units): Selu is some kind of ELU [3] but different in alpha and delta. α and λ are two fixed parameters, meaning we do not backpropagate through them, and they are not hyperparameters to make decisions about. α and λ are derived from the inputs.

$$\text{selu}(x) = \lambda \begin{cases} x & \text{if } x > 0 \\ \alpha e^x - \alpha & \text{if } x \leq 0 \end{cases} \tag{4}$$

PReLu (Parametric Rectified Linear Unit): PReLu (Fig. 5) improves converging performance systematically. The PReLu learns the parameter α (alpha) and adjusts it through basic gradient descent. PReLu improves model fitting with nearly zero extra computational cost and little overfitting risk.

$$f(x) = \max(0, x) - \alpha \max(0, -x) \tag{5}$$

Fig. 5 PReLu activation
function
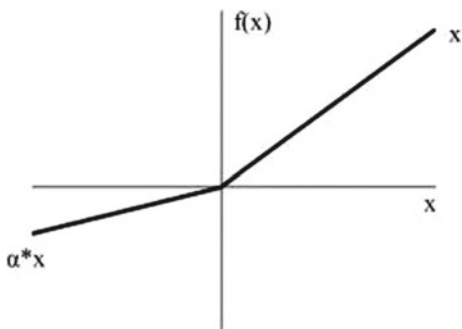
3 Experimental Comparison of Various Activation Functions

In this section, we present the results and discussion about using different activation functions through experiment that compares CNNs by using two classes (Cat/Dog) dataset.

We mainly report the loss at first epoch, accuracy at first epoch, and value loss at first layer, value accuracy at first layer and same as on the last epoch of last layer of CNN for different activation functions.

The configuration for this comparative model is used by using the datasets of two classes (Cat/Dog). The number of convolutional layer used in this network is three, and the pooling layer is also introduced after each layer of CNN layer. The total of the dataset is divided into two parts. Mainly, the first 8000 images are used for training the network, and the second 2000 images are used for testing the network.

We start the experimental comparison by analyzing our network by taking different activation functions on each layer of CNN.

3.1 Tanh

Tanh is the activation function which is used in neural networks and deep neural networks as our baseline model. From Table 1, we can see that there are different values that are getting on first epoch and onto the last epoch.

We notice that as the training error decreases, the validation error always decreases. We also notice that loss at twenty-fifth epoch is very less as compared to loss at first epoch. The value loss and the value accuracy are also noted.

Table 1 Comparison of various nonlinear activation functions in CNN model

Convolutional layer	3	3	3	3	3
Pooling layer	3	3	3	3	3
Activation functions	ReLu	tanh	Selu	PReLu	ELU
Dataset used (training) for two classes	8000	8000	8000	8000	8000
Dataset used (testing) two classes	2000	2000	2000	2000	2000
No of epoch	25	25	25	25	25
Loss at frst epoch	0.6794	0.6575	0.6629	0.6836	0.6575
Accuracy at first epoch	0.5683	0.6085	0.6109	0.5471	0.6001
Value loss at first layer	0.6552	0.6541	0.6041	0.6523	0.6062
Value accuracy at first layer	0.6275	0.6000	0.6540	0.6165	0.6755
Loss at twenty-fifth epoch	0.2937	0.2438	0.3985	0.2692	0.2322
Accuracy at twenty-fifth epoch	0.8748	0.8992	0.8184	0.8859	0.9001
Value loss at twenty-fifth epoch	**0.3912**	0.4307	0.4461	0.4389	0.4539
Value accuracy at twenty-fifth epoch	**0.8320**	0.8295	0.8065	0.8185	0.8125

1. With smaller learning rates, gradient descent is more likely to get stuck in local minima.
2. Smaller learning rates usually require more epoch before an optimal solution if found.

3.2   ELU

ELU is also called exponential linear unit. It is another activation function used in deep neural networks. From Table 1, we see that it gives better results than tanh model. The tanh activation model is likely to incur the vanishing gradient problem.

The property of ELU is that it avoids a vanishing gradient by identifying positive values.

The result shown that the value accuracy at first epoch and the last epoch is higher than the tanh function. The loss at first epoch and the twenty-fifth epoch is less as compared to tanh.

3.3   Selu

Scaled exponential linear unit (Selu) is the same kind of ELU which is used in neural networks and deep architectures as self-normalizing neural network.

The Experiment is performed on the comprising network in CNN by taking Selu. The numbers of factors are observed at the very first epoch and the last (twenty-fifth) of epoch in our experiment. The result shown that (Table 1) the Selu

is well performed than the tanh in value loss at first epoch and the accuracy is better than the tanh and ELU.

The results at various levels are shown in Table 1.

3.4 ReLu

Rectified linear unit (ReLu) is the simplest nonlinear activation function. The advantage of ReLu [7] is that when the input is positive, the derivative is just 1, so there is no squeezing effect you meet on backpropagated errors from the sigmoid function. It is indeed non-saturation of its gradient, which greatly accelerates the convergence of stochastic gradient descent compared to the sigmoid/tanh function. And these advantages give to use within hidden layers [8] of a neural network model. ReLus result in much faster training for large networks.

As shown in Table 1, the ReLu activation function has higher accuracy than tanh, Selu, PReLu, and ELU activation function. The value accuracy at twenty-fifth epoch is 0.8320, and as compared to other it gives better results at hidden layer of CNN.

3.5 PReLu

Parametric ReLu (PReLu) is the activation function that is slightly different from the ReLu and is inspired by LReLu. It has negligible impact on accuracy compared to ReLu. In this paper, we introduce the comparison that when the PReLu is applied in the hidden layer of convolutional layer, it gives almost similar results to ReLu.

PReLu has the same goal as of ReLu: increase the learning speed by not activating some neurons. From Table 2, we can conclude that the ReLu is the best activation function for convolutional neural networks as it achieves highest accuracy on hidden layers.

From the use of various activation functions, we can make our model predictable by taking Cat/Dog dataset that have 8000 training data with 2000 test data.

Prediction

We predict the classification of CNN models by applying different activation functions on hidden layers by inputting the number of images. Table 2 shows the results of prediction, and we can conclude that ReLu is the best activation function as compared to other activation functions at hidden layers of CNN model.

Table 2 Prediction for the number of input images on number of trained (using activation functions at hidden layers) networks

Input images for image classification	Girldog4	Cat	Dog	Girlcat	Girlcat1	Girldog1
Images (Appendix A)	Figure 6	Figure 7	Figure 8	Figure 9	Figure 10	Figure 11
Prediction for two classes (Cat/ Dog) for activation function "ReLu"	Cat	Cat	Dog	Dog	Cat	Dog
Prediction for two classes (Cat/Dog) for activation function "tanh"	Cat	Cat	Cat	Cat	Cat	Cat
Prediction for two classes (Cat/Dog) for activation function "selu"	Cat	Cat	Dog	Dog	Dog	Dog
Prediction for two classes (Cat/Dog) for activation function "PReLu"	Cat	Cat	Dog	Dog	Dog	Dog
Prediction for two classes (Cat/Dog) for activation function "ELU"	Cat	Cat	Dog	Dog	Dog	Dog

4 Conclusion

As with the results finding in the experimental analysis, ReLu, PReLu, ELU, and Selu activation functions give better results in terms of validation error and accuracy on Cat/Dog dataset. With ReLu layer, overall performance and speed of the network is more desirable.

We found that a CNN model with ReLU hidden layers (three hidden layers here) gives best performing results and improves overall performance better in terms of accuracy and speed. This advantage of ReLU in CNN at number of hidden layers is helpful to effective and fast retrieval of images from the databases [9].

To conclude, we can say that the following model is the one which yields the best results:

Activation function: ReLu
Number of epochs: 25
Number of hidden layers: 3
Number of pooling layers: 3
Weight initialization: Uniform

In further work, we can generalize these results to more complex classification tasks onto different datasets.

Appendix A

Input Images

See Figs. 6, 7, 8, 9, 10, and 11.

Fig. 6 Girldog4

Fig. 7 Cat

Fig. 8 Dog
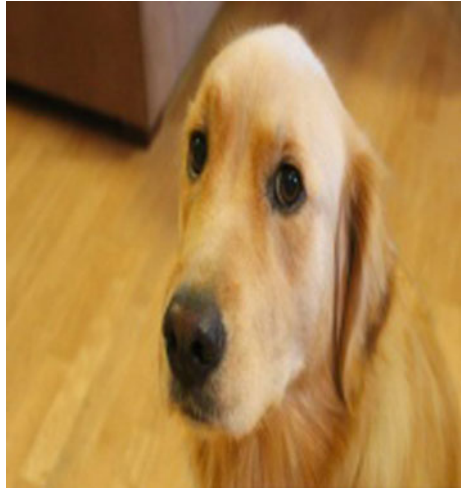
Fig. 9 Girlcat

Fig. 10 Girlcat1

Fig. 11 Girldog1

References

1. Krizhevsky A (2012) ImageNet classification with deep convolutional neural networks. In: NIPS'12 proceedings of the 25th international conference on neural information processing systems, pp 1097–1105, 03–06 Dec 2012
2. Clevert D-A, Unterthiner T, Hochreiter S (2015) Fast and accurate deep network learning by exponential linear units (elus). CoRR, abs/1511.07289
3. Klambauer G, Unterthiner T, Mayr A, Hochreiter S (2017) Self-normalizing neural networks. CoRR, abs/1706.02515
4. Arora R, Basu A, Mianjy P, Mukherjee A (2016) Understanding deep neural networks with rectified linear units. CoRR, abs/1611.01491
5. He K, Zhang X, Ren S, Sun J (2015) Delving deep into rectifiers: Surpassing human-level performance on imagenet classification. In: Proceedings of the IEEE international conference on computer vision, pp 1026–1034
6. Glorot X, Bengio Y (2010) Understanding the difficulty of training deep feed forward neural networks. In: Proceedings of the international conference on artificial intelligence and statistics (AISTATS'10). Society for Artificial Intelligence and Statistics, pp 249–256 (2010)
7. Xu B, Wang N, Chen T, Li M (2015) Empirical evaluation of rectified activations in convolutional network. CoRR, abs/1505.00853
8. Krizhevsky A, Hinton G (2009) Learning multiple layers of features from tiny images
9. Dureja Aman, Pahwa Payal (2018) Image retrieval techniques: a survey. Int J Eng Technol 7 (1.2):215–219

Comprehensive Study of Keyphrase Extraction Metrics for Uncertain User-Generated Data

Muskan Garg and Mukesh Kumar

Abstract Social media analysis has received much attention from academic researchers and practitioners. Twitter is one of the most widely used social media platforms and contains ill-formed, uncertain and user-generated information. The word co-occurrence networks represent the statistical and computational evaluation of contextual data which are also called textual networks. Identifying influential nodes as keywords in textual networks of given data is of theoretical and practical significance. Different network metrics can be used to understand the salient features of textual networks. To overcome this research gap, the comprehensive study of different keyword extraction and keyphrase extraction techniques has been explored which gives useful insight into patterns in word co-occurrence networks. The significant insights obtained from textual networks can be used for different applications for social media analytics. The 'First Story Detection' data set has been used for experimental evaluation to identify significant traditional measures.

Keywords Keyword extraction algorithm · Social media analysis · Word co-occurrence model · Textual network metrics

1 Introduction

Social media analysis is one of the most widely studied areas of research. The field of topic detection and tracking has been introduced [1]. The key idea for social media analysis is keyword extraction and keyphrase extraction. The words which are important in terms of any text are said to be keywords. Similarly, the set of words which occur as a phrase and represent the text are known as keyphrase. The keyphrase represents the topic of discussion which summarizes the textual information.

M. Garg (✉) · M. Kumar
UIET, Panjab University, Chandigarh, India
e-mail: muskanphd@gmail.com

Keyphrase Extraction

The keyphrase extraction is the process of identifying important phrases from the given textual data. It is used to summarize the short text to identify topic of discussion from a set of Twitter posts which are related to the same topic or domain. The topic or domain is very subjective decision to decide if the extracted keyphrase should be about main topic or sub-topics under that topic. For instance, 'floods in Kerala 2018' is a main topic but 'having nothing to eat in XYZ village', 'save us! Water all around' and 'our house drowned in flood' are sub-events. These sub-events help us to determine the emergency conditions. Such topic and emergency conditions can be deduced by identifying keyphrases from many Twitter posts. Tackling this kind of information shall provide useful insights into social media data. In this study, short text is being used for keyphrase extraction; the keyphrase extraction and text summarization are used interchangeably.

Recent progress on word co-occurrence network has added statistical and computational significance over information processing. Graph-based keyphrase extraction measures are usually based on the global network metrics which have been used for keyword extraction. The network metrics have been studied for well-formed data and social media data. It has been observed that the keywords obtained using the random walk-based measures are ranked, and using this information keyphrase is extracted. The application domains for keyword extraction and keyphrase extraction techniques are sentiment analysis, topic and trend detection, event detection, disaster management, outbreak detection and many other applications. The major challenges for identifying keywords in social media data are that the data is unstructured. Due to graphical and statistical approach, the random walk-based keyword extraction from word co-occurrence network has proved to be useful for well-formed data. However, for ill-formed data, traditional network metrics for word co-occurrence network have not been explored.

Word co-occurrence networks are graphical networks which are generated from contextual information. These are also referred to as word adjacency model [2]. There are different types of textual networks which can be framed from given data. For each graph G, node is considered as word and edge is considered as a link connecting two words co-occurring in the given document. In this research work, the document is considered as Twitter feed. Based on the co-occurrence and associativity, construction of graph is decided on three parameters as follows. This paper is organized as follows. In Sect. 2, existing metrics have been implemented on standard Twitter feeds and results have been obtained. In Sect. 3, evaluations and results have been analysed and discussed. Conclusion and future work have been presented in Sect. 4.

2   Evolution of Different Approaches

Graph-based keyword extraction techniques can be both supervised and unsupervised, context dependent and context independent. In this research work, many context-independent unsupervised graph-based keyword extraction techniques have been explored. *KeyWorld* is an automatic indexing system which has been proposed by Matsuo et al. [3] which extracts candidate keywords by measuring their influence on small-world properties. It captures characteristic path length and extended characteristic path length. This algorithm has been inspired by small-world phenomenon and KeyGraph algorithm proposed by Ohsawa et al. [4]. Thereafter, Erkan et al. [5] proposed LexRank which is insensitive to noise in text and calculates importance of sentence (or word) using eigenvector centrality. Mihalcea et al. [6] proposed graph-based TextRank model which has been originated from the concept of PageRank. The author further improved TextRank for text summarization. In 2007, Palshikar [7] proposed hybrid and statistics-based approach for keyword extraction using co-occurrence frequency measure. The author described eccentricity-based keyword identification, other centrality measure-based keyword extractions and proximity-based keyword identification. Litvak et al. [8] proposed HITS-based algorithm for keyword extraction. In 2009, for event detection and tracking in social streams, Sayyadi [9] used KeyGraph algorithm which was proposed earlier by Ohsawa et al. [4]. Later, in 2011, the author introduced DegExt, a graph-based language-independent keyphrase extractor. The author used degree centrality for keyword extraction. In 2013, Boudin et al. [10] compared various centrality measures for graph-based keyphrase extraction from short documents. Abilhoa et al. [11] proposed Twitter Keyword Graph (TKG) algorithm to extract keywords from Twitter data. The author introduced all neighbour edging and nearest neighbour edging for constructing graph, frequency-based and inverse-frequency-based weights in graph and different centrality measures. Besides this, another algorithm named selectivity-based keyword extraction (SBKE) has been proposed by Beliga et al. [12]. The author used degree and strength for each node. There are many such algorithms which have been improved on semantic and linguistic features on textual networks including SingleRank, ExpandRank, word co-occurrence statistical information [13], noun phrase-based keyword extraction, semantic relationships using Wikipedia texts [14], weighted lexical complex network-based keyword extraction Bollen et al. [15], keyword and keyphrase extraction algorithm [16] for word co-occurrence network structure, word topic network model [17] and many more. However, such algorithms have not been considered for keyword extraction from Twitter.

3 Experiments and Evaluation

The traditional techniques for keyword extraction and keyphrase extraction using random walk-based measures and other network metrics have been implemented for Twitter data. The data set which has been used for this study is First Story Detection Petrovic et al. [18] data set in which 27 topics have been mentioned as ground truth. The ground truth topic contains topic id among all the 27 topics in front of every tweet id which are given in data set. Among all the tweets, 3034 tweets have been marked against the topic id correspondingly. The data set has been used by extracting all the tweets for one topic. All the tweets are summarized using keyword and keyphrase extraction technique. Python and NetworkX module have been used for implementation of existing keyphrase extraction technique over Twitter data. For every experimental evaluation, Twitter data has been given as input and top values and bottom values for keywords have been obtained as output.

Word co-occurrence networks have been generated using word co-occurrence architecture. Different basic and derived keyword extraction metrics have been studied for textual networks and evaluated after implementation on Twitter feeds of standard data set of FSD. As per the scores of different metrics, top ten keywords (words with highest value) and bottom ten keywords (words with lowest values) have been collected. Significance of measuring values for words varies from one metric to another. Out of given 18 metrics, one metrics is non-beneficiary (lower the value, better is the significance), fourteen metrics are beneficiary (higher the value, better is the significance), and three metrics have been observed as non-significant. The metrics may have overlapping significance. For each topic, corresponding results have been obtained as shown in Table 1 for first topic 'Death of Amy Winehouse'. Italic font indicates that results obtained are meaningful. The topic is given as ground truth in data set FSD. Each word of topic is considered as keyword.

The given values of recall have been obtained by automatic word-to-word matching. However, due to the presence of ill-formed words, the precision measure

Table 1 Data set considered for keyword extraction

Topic no.	Topic name	Keywords selected
1	Amy Winehouse dead	Amy Winehouse dead
2	Space shuttle Atlantis lands safely, ending NASA's space shuttle programme	Space shuttle Atlantis lands safely ending NASA's programme
4	Richard Bowes, victim of London riots, dies in hospital	Richard Bowes victim London riots dies hospital
5	Flight Noar Linhas Aereas 4896 crashes, all 16 passengers dead	Flight Noar Linhas Aereas 4896 crashes all 16 passengers dead
13	Plane carrying Russian hockey team Lokomotiv crashes, 44 dead	Plane carrying Russian hockey team Lokomotiv crashes 44 dead
18	Gunman opens fire in children's camp on Utoya island, Norway	Gunman opens fire children's camp Utoya island Norway

Table 2 Performance measures obtained for topics using different keyword extraction metrics

S. no.	Keyword extraction algorithm	Precision		Recall		F-measure	
		Top	Bottom	Top	Bottom	Top	Bottom
1	Degree	0.44	0.06	0.532619	0.073571	0.481900	0.066096
2	Strength	0.46	0.06	0.552619	0.073571	0.502074	0.066096
3	Betweenness centrality	0.44	0.04	0.532619	0.045000	0.481900	0.042353
4	Closeness centrality	0.44	0.08	0.532619	0.102143	0.481900	0.089725
5	Eigenvector centrality	0.42	0.06	0.512619	0.073571	0.461710	0.066096
6	Clustering coefficient	0.04	0.42	0.048571	0.512619	0.043871	0.461710
7	Influence	0.44	0.08	0.529841	0.098571	0.480759	0.088320
8	PageRank	0.44	0.02	0.527619	0.025000	0.479843	0.022222
9	TF-IDF	0.08	0.32	0.098571	0.378254	0.08832	0.346697
10	KeyWorld	0.38	0.02	0.457619	0.028571	0.415213	0.023529
11	LexRank	0.44	0.06	0.532619	0.073571	0.481900	0.066096
12	TextRank	0.42	0.06	0.495476	0.073571	0.454627	0.066096
13	Eccentricity	0.06	0.12	0.073571	0.139365	0.066096	0.128960
14	HITS (avg. (H, A))	0.46	0.04	0.552619	0.053571	0.502074	0.045802
15	HITS (max (H, A))	0.48	0.02	0.581190	0.028571	0.525771	0.023529
16	DegExt	0.44	0.06	0.532619	0.073571	0.481900	0.066096
17	TKG	0.46	0.08	0.552619	0.102143	0.502074	0.089725
18	SBKE	0.12	0.06	0.140794	0.065000	0.129568	0.062400

obtained is low. However, manual intervention of results gives meaningful results and better value for precision. For instance, the topic 'Death of Amy Winehouse' may contain two words out of three for degree precision measure, but *dead* and *died* give clear indication for death and hence, precision may be recorded as one. However, in order to keep results unbiased, automatic evaluation has been preferred. But topic 1 has only three words as keywords which may result in poor analysis of precision and recall. Five topics were selected for experiments on the basis of number of keywords obtained from given topic for evaluation. For better examination for precision and recall values, topics having about ten keywords were selected. Further, precision, recall and F-measure have been obtained for each experiment and averaged as shown in Table 2.

4 Discussion

Different performance measures for extracting keywords have been analysed on the basis of experimental evaluation. It has been observed that strength measure and HITS algorithm outperform all the existing techniques on short text as shown in Fig. 1. Also, DegExt, TKG, LexRank, Degree, closeness centrality, eigenvector centrality, betweenness centrality, clustering coefficient and influence measure

Table 3 Inference for different keyword extraction metrics for textual networks

Keyword extraction algorithm	Inference
Degree	Gives the number of words with which word w occurs. Measure of degree centrality for each word
DegExt	
SBKE	Measures the repeated occurrence of word w with its neighbouring words with respect to number of word it is co-occurring with
Strength	Calculated word w frequency
Betweenness centrality	Centrality calculates the measure of number of paths a word w has for word-to-word connectivity
Closeness centrality	
Eigenvector centrality	
TKG	Calculates the significance of word w in Twitter feeds when word co-occurring graph is generated. Performs best by using all neighbouring edge schemes with edge weighing and inverse co-occurrence frequency and closeness centrality
Clustering coefficient	Measures the extent of similarity among neighbours of word w
Influence	Calculates the difference and maximum value among number of predecessors or successors co-occurring with word w
HITS (max (H, A))	
HITS (avg. (H, A))	Calculates the average number of predecessors or successors co-occurring with word w
TF-IDF	Statistical measure of importance of word w
KeyWorld	Based on the average of shortest path measure between two words. Used small-world phenomenon
PageRank	Measures the impact of neighbouring words co-occurring with words on word w using their votes
LexRank	
TextRank	
Eccentricity	Measures reciprocal of number of co-occurrences of pair of words in given feeds. Zero for isolated node

perform omparably significant results. However, eccentricity and SBKE are least significant measures for keyword extraction from uncertain user-generated text. Among all the basic and derived metrics, strength and HITS metrics have proved to be useful in terms of F-measure as observed in Table 2. When F-measure is considered for low-valued elements, it is observed that higher is the value of metrics, better it is for keyword extraction and vice versa. However, it has been observed that small values of clustering coefficient for each node give better keyword extraction. This shows that clustering coefficient is non-beneficiary attribute. Moreover, *Tf-Idf*, eccentricity and selectivity-based keyword extraction have proved to be not much significant measure for keyword extraction from Twitter. Inference for different keyword extraction metrics have been shown in Table 3.

Semantics of textual networks has been observed. Different features can be used as important statistical measure for identifying relevant and influential terms. As per observation, degree measure and DegExt experimentation signify similar semantics
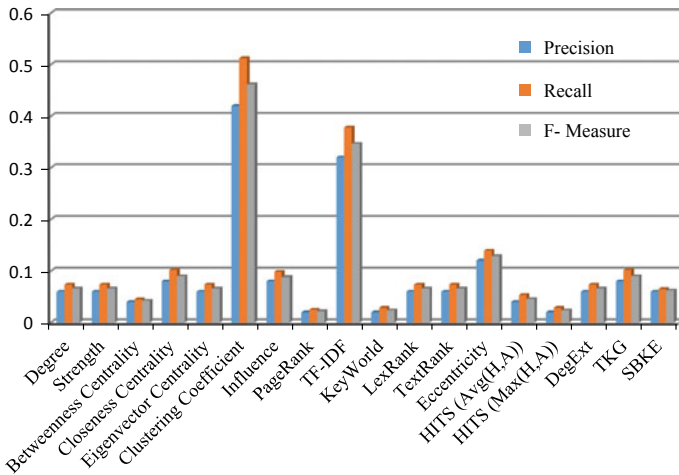
Fig. 1 Graphical representation of performance measures for bottom ten keywords using different keyword extraction metrics

and thus overlap. Metrics with high precision and recall values for top-ranked keywords and low precision and recall values for low-ranked keywords have found to be better than other metrics. On the contrary, clustering coefficient has opposite nature. Although *KeyWorld* metrics marks significantly irrelevant terms, it is computationally expensive and thus is not suitable for large-scale data analysis.

As observed in Table 4, metrics with non-weighted textual graph gives meaningful results. However, strength is a significant measure for textual networks, and thus, edge-based metrics (co-occurrence frequency-based metrics) for weighted textual networks may mark influential words. On the basis of need, adjacent pair and all pair neighbouring models have been used. However, majority of value and centrality-based metrics outperforms using all pair neighbouring model, whereas neighbourhood and its vote-based metrics used adjacent neighbour model for better performance. The inference for this parameter signifies that relation of every word to every other in a document signifies its value as how important the word is for the network and adjacent word pair signifies what impact does influential (important) word have on its neighbour. Similarly, undirected graph is used for neighbourhood-based metrics and directed graph is used for measuring incoming and outgoing links to other words. Also, directed textual network may have better lexical output as sequence of words. Based on this inference, a metric can be developed and it identifies dominant phrase from textual networks which may provide more meaningful results than just keywords.

For each topic, set of different keywords has been obtained. Unique words from this set are represented as ground truth for analysing relevant Twitter feeds. For differently selected metrics, the values have been obtained for each keyword of topic 4. Normalized graph for values of keywords for differently selected metrics has been obtained in Fig. 2. It has been clearly observed that the word 'victim' has

Table 4 Inference for different keyword extraction metrics for textual networks

Keyword extraction algorithm	*F*-measure		Weighted/ non-weighted metrics	All pair neighbour/ adjacent neighbour	Directed/ undirected
	Top	Bottom			
Strength	0.502074	0.066096	Non-weighted	All pair neighbour	Undirected
Betweenness centrality	0.481900	0.042353	Weighted	All pair neighbour	Undirected
Clustering coefficient	0.043871	0.461710	Non-weighted	All pair neighbour	Undirected
PageRank	0.479843	0.022222	Non-weighted	Adjacent neighbour	Directed
HITS (avg. (H, A))	0.502074	0.045802	Non-weighted	Adjacent neighbour	Directed
HITS (max (H, A))	0.525771	0.023529	Non-weighted	Adjacent neighbour	Directed
TKG	0.502074	0.089725	Non-weighted	All pair neighbour	Undirected

not appeared in text. Also, words '*Richard*' and '*Bowes*' are co-occurring and have same values in most of the metrics, and thus, '*Richard Bowes*' may represent candidate keyword or named entity. Also, the last word '*Hospital*' has high clustering coefficient and strength. However, other values for these keywords are low.

Zero value of betweenness centrality indicates that the word has either no in-degree or no out-degree. Also, it can be observed that linking from one word to another, for instance '*London*' to '*Riots*' and '*Riots*' to '*dies*', is dropping and rising in high range of values, and thus, weight edges as strength play pivotal role in identifying co-occurring important words which represent influential nodes in textual networks. As observed from Fig. 2, all measures except strength and clustering coefficient give highest values for '*Richard Bowes*'. The inference for lower value of strength indicates that for each node, number of occurrences has been considered by strength, and thus, most frequently occurring words are given higher values, for instance '*very*' which is not significant.

5   Conclusion and Future Work

The user-generated data on social media is analysed using textual networks. To evaluate the performance of basic and derived metrics for textual networks, we have used Twitter data. In this analysis, unsupervised context-independent graph-based keyword extraction techniques have been implemented and discussed. It is observed that out of 17 identified network-based metrics, 14 metrics proved to be beneficiary and one as non-beneficiary attribute. The two metrics fluctuate with
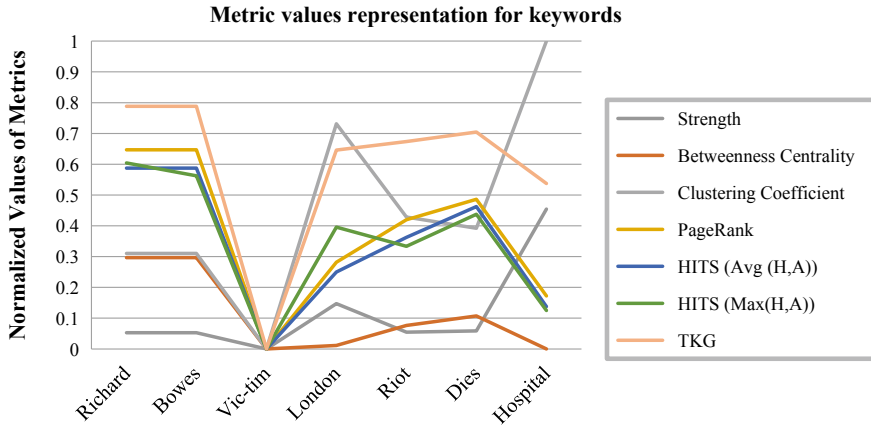
Fig. 2 Normalized metric values for differently selected keyword extraction metrics

change in data set. Differently selected metrics have been analysed, and semantics of textual networks have been discussed. It is observed that in order to maintain lexical sequence of occurrence of words, directed adjacent and weighted graph should be constructed. Majority of network metrics outperforms traditional *Tf-Idf* statistical method. Using this analysis, many useful insights can be obtained for different real-world applications including text mining, topic tracking and detection, event detection and opinion mining. In future, edge-based network metrics can be studied for word co-occurrence directed graph for identifying co-occurring keyphrases.

References

1. Allan J (ed) (2002) Topic detection and tracking: event-based information organization. Kluwer Academic Publisher
2. Amancio DR (2015) Probing the topological properties of complex networks modeling short written texts. PLoS ONE 10(2):e0118394
3. Matsuo Y, Ohsawa Y, Ishizuka M (2001) Keyworld: extracting keywords from document s small world. In: International conference on discovery science, Nov 2001. Springer, Berlin, Heidelberg, pp 271–281
4. Ohsawa Y, Benson NE, Yachida M (1998) KeyGraph: automatic indexing by co-occurrence graph based on building construction metaphor. In: Proceedings. IEEE international forum on research and technology advances in digital libraries, 1998, ADL 98, Apr 1998. IEEE, pp 12–18
5. Erkan G, Radev DR (2004) LexRank: graph-based lexical centrality as salience in text summarization. J Artif Intell Res 22:457–479
6. Mihalcea R, Tarau P (2004) TextRank: bringing order into texts. Association for Computational Linguistics, Barcelona, Spain, pp 104–401

7. Palshikar GK (2007) Keyword extraction from a single document using centrality measures. In: International conference on pattern recognition and machine intelligence, Dec 2007. Springer, Berlin, Heidelberg, pp 503–510

8. Litvak M, Last M (2008) Graph-based keyword extraction for single-document summarization. In: Proceedings of the workshop on multi-source multilingual information extraction and summarization, Aug 2008. Association for Computational Linguistics, pp 17–24

9. Sayyadi H, Hurst M, Maykov A (2009) Event detection and tracking in social streams. In: ICWSM, May 2009

10. Boudin F (2013) A comparison of centrality measures for graph-based keyphrase extraction. In: International joint conference on natural language processing (IJCNLP), Oct 2013, pp 834–838

11. Abilhoa WD, de Castro LN (2014) A keyword extraction method from twitter messages represented as graphs. Appl Math Comput 240:308–325

12. Beliga, S., Meštrović, A., & Martinčić-Ipšić, S. (2016). Selectivity-based keyword extraction method. International Journal on Semantic Web and Information Systems (IJSWIS), 12(3), 1-26.

13. Matsuo Y, Ishizuka M (2004) Keyword extraction from a single document using word co-occurrence statistical information. Int J Artif Intell Tools 13(01):157–169

14. Grineva M, Grinev M, Lizorkin D (2009) Extracting key terms from noisy and multitheme documents. In: Proceedings of the 18th international conference on world wide web, Apr 2009. ACM, pp 661–670

15. Bollen J, Mao H, Zeng X (2011) Twitter mood predicts the stock market. J Comput Sci 2 (1):1–8

16. Lahiri S, Choudhury SR, Caragea C (2014) Keyword and keyphrase extraction using centrality measures on collocation networks. arXiv preprint arXiv:1401.6571

17. Zhou, X., & Chen, L. (2014). Event detection over twitter social media streams. The VLDB journal, 23(3), 381-400.

18. Petrović S, Osborne M, Lavrenko V (2010) Streaming first story detection with application to twitter. In: Human language technologies: the 2010 annual conference of the North American chapter of the association for computational linguistics, June 2010. Association for Computational Linguistics, pp 181–189

Energy Management System for PV—Wind and Battery-Fed DC Microgrid Using Fuzzy-Based Proportional Integral Controller

T. Hari Priya and Alivelu M. Parimi

Abstract This paper focuses on operational analysis and working of PV and wind-fed DC micro-grid under islanded mode. An energy management system (EMS) system based on fuzzy logic + proportional integral (PI) controller has been chosen here to improve the performance of a micro-grid under islanded mode and also to support the peak and pulsating demand using a battery bank. The operational analysis of the proposed system was carried out using MATLAB/Simulink software. The load power tracking along with fuzzy logic + PI controller-based EMS system can maintain equilibrium between the generated power and load demand making the DC micro-gird to provide stable power to the load.

Keywords Energy management system · Fuzzy · Proportional integral controller · Photovoltaic generator

1 Introduction

Micro-grid is a concept of generating power from micro-sources of small capacity which offers improved reliability in service, reduced dependency on the local grid, better economics, and reduced usage of fossil fuels. It is mandatory to use energy storage elements in micro-grids in order to meet the load demand. In general, a micro-grid operates in two modes; the first one is grid-connected mode whose main objective is to avoid propagation of renewable source intermittency and to limit grid-side fluctuations due to load, and the second one is islanded mode whose main objective is to maintain energy balance using storage system.

A lot of research is from the literature available on DC micro-grids; the performance of DC micro-grid (MG) and its control in both isolated and

T. Hari Priya (✉)
EEE Department, VNR VJIET, Hyderabad 500090, India
e-mail: haripriya_t@vnrvjiet.in

A. M. Parimi
Electrical Department, BITS Pilani, Hyderabad Campus, Hyderabad 500078, India

grid-connected modes are explained in [1]. To find the optimal operating strategy and to find the optimal point at which the cost of DC micro-grid is minimum, a mathematical formulation is discussed in [2]. The problem on optimization of energy exchange between distribution network and micro-grid is described in [3]. The objective function and its constraints are presented in [3], along with the evolutionary algorithm technique. The role of energy management system (EMS) and its operation are discussed in [4, 5] where EMS is a collection of computer-aided tools that are used by the grid operators to optimize the generation system performance in addition to monitoring and control. EMS plays a crucial role in micro-grids due to the presence of renewable energy sources of energy. In the literature [6, 7], the EMS with a fuzzy controller is proposed to manage the flow of energy in an isolated mode. The proposed system uses fuzzy-based proportional integral (PI) controller. Use of conventional PI controller in the design of the controller is a common practice because of simplicity in its structure and good performance at a variety of operating conditions. Though they are simple in construction, their performance degrades due to the presence of strong nonlinearities in the system [8]. The nonlinearities present in the system cannot trace the optimal values of proportional and integral constants for change of parameters in the grid system that leads to a significant impact on the performance of the control system in a converter (Fig. 1).

The fuzzy logic controller on the other hand can deal with nonlinearities occurring in the systems and can achieve the optimal solution without doing mathematical modeling of the system [9]. Compared with the PI controller, fuzzy logic controller can control and provide the optimal solution for those dynamic systems which has wide variations in system parameters [10]. The FLC offers advantages like robust and simple in construction; it can be implemented in
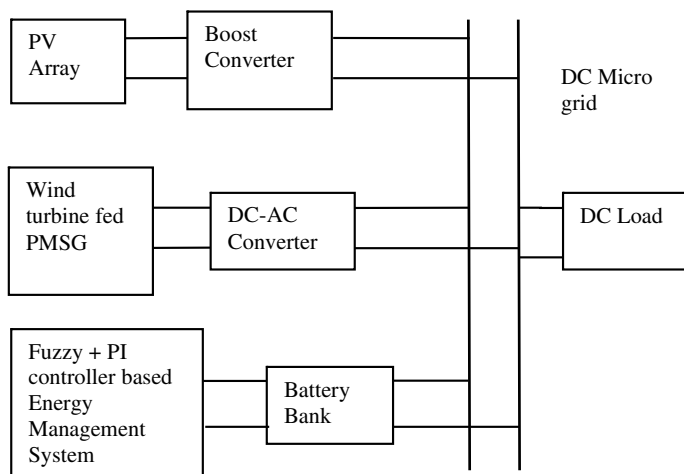
Fig. 1 Proposed topology of DC micro-grid with EMS

multi-input and output applications and provide faster response with low investment cost. Combining the fuzzy logic controller with proportional integral controller is an effective way to overcome the problem of dynamic parameter change. The fuzzy logic of fuzzy-PI controller helps in adjusting the gain parameters of PI controller for any operating conditions. Therefore, application of fuzzy-PI controller for energy management control is proposed in this paper as shown in Fig. 1.

The paper is organized in the proposed manner; Sect. 2 presents modeling of a PV panel. Section 3 provides PMSG-based wind turbine modeling. Then, Sect. 5 discusses about fuzzy-based proportional integral controller for managing energy of the battery. Simulation results and discussion are provided in Sect. 6.

2 Modeling of PV Array

PV array is formed by using basic building block called PV cell, by arranging many solar PV cells in series and parallel fashion the required voltage and currents are achieved. A single solar PV cell consists of a p–n junction semiconductor that generates current when light falls onto it. The simple mathematical model of PV cell is used to perform MATLAB simulation; its equivalent circuit is shown in Fig. 2. It consists of four components, namely series resistance, which is connected in series with parallel combination of three components, namely photocurrent generator (I_{phn}), diode (D), and shunt resistance (R_{sh}) [8, 11].

The characteristic equation relating voltage and current of a PV cell is given by [7–9],

$$I_{phn} = [I_{se} + K_i(T_o - 298)] \times I_r/1000$$

The reverse saturation current of PV module

$$I_{rs} = I_{se}/[\exp(qV_{oc}/N_s knT_o) - 1]$$

Fig. 2 Single-diode model of solar PV cell
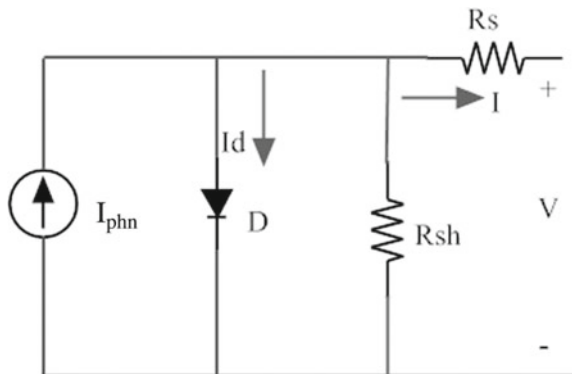
The saturation current of the module is given by,

$$I_{\mathrm{o}} = I_{\mathrm{rs}} \left[\frac{T_{\mathrm{o}}}{T_{\mathrm{r}}}\right]^3 \left[\exp\frac{qE_{\mathrm{g0}}}{nk}\left(\frac{1}{T_{\mathrm{o}}} - \frac{1}{T_{\mathrm{r}}}\right)\right]$$

The PV module output current is given by,

$$I = p\left(N_{\mathrm{p}} \times I_{\mathrm{phe}} - N_{\mathrm{p}} \times I_{\mathrm{o}}\right) \exp\left[\left(\frac{V/N_{\mathrm{s}} + I \times R_{\mathrm{s}}/N_{\mathrm{p}}}{n \times V_{\mathrm{t}}}\right) - 1\right] - I_{\mathrm{p}}$$

$$V_{\mathrm{t}} = \frac{kT_{\mathrm{o}}}{q}$$

$$I_{\mathrm{p}} = \frac{V \times \left(N_{\mathrm{p}}/N_{\mathrm{s}} + I \times R_{\mathrm{s}}\right)}{R_{\mathrm{sh}}}$$

where

I_{phn} is photocurrent delivered in Ampere
I_{r} is irradiation of solar cell
I_{se} is current under short circuit in Ampere
K_{i} is short-circuit current of cell at 1000 W/m^2 irradiation and 25 °C
T_{o} is operating temperature of cell in Kelvin
q is charge carried by an electron
V_{oc} is open-circuit voltage in volt
N_{s} is number of series-connected cells
N_{p} is number of parallel-connected cells
N is ideality factor for diode
T_{r} is nominal temperature in °C
E_{g0} is energy band gap
V_{t} is diode thermal voltage.

The output of PV is connected to DC grid using Boost converter whose modeling is given in [12].

3 Wind Turbine-Fed PMSG Modeling

The wind turbine coupled to the shaft of PMSG extracts the power from wind speed which is given by [10, 13],

$$P = 0.5\rho A V^3 C_p(\lambda, \theta)$$

where

ρ is the density of air in kg/m^3,
A is turbine blade area of cross section in m^2,

V is wind velocity in m/s,
C_p is coefficient of energy conversion which is a function of λ and θ.

$$\rho = (353.05/T) \exp^{-0.034(Z/T)}$$

$$C_p(\lambda, \theta) = \left[\frac{116}{\lambda_i} - 0.4 * \theta - 5\right] 0.5 \exp^{-16.5/\lambda_i}$$

$$\lambda_i = 1 / \left[\frac{1}{\lambda + 0.089\theta} - 0.035/(\theta^3 + 1)\right]$$

$$\lambda = r\left(\frac{\omega}{V}\right)$$

The power output of wind turbine is fed to PMSG which is modeled in MATLAB/ Simulink software. The modeling equations of PMSG are given in [10, 11].

4 Modeling of Battery

A simplified equivalent circuit of battery is shown in Fig. 3, which consists of resistances R_{CC_c} and R_{CC_a}, namely resistance offered between the battery terminal and active electrode, and R_{E1} is the resistance of electrolyte [11]. The double-layer capacitances are given by C_{DL_a} and C_{DL_c} at anode and cathode terminals. The values of capacitance and resistance offered vary as a function of DC current, "state of charge" and "temperature."

The operation of battery during charging mode is influenced by the effect of feeding charging currents of larger magnitude, large internal resistance, SOC of the battery, and fully charging of batteries with constant charging current. At the negative plate, excessive heat is generated due to I^2R losses that occur during discharge and recombination of exothermic oxygen. As heat generated is a function of the flow of current which in turn affects the current flow, hence excessive heat is created in the battery cell [14]. The magnitude and charging rate of the battery are decided by current available for charging and the depth of discharge of the previous stage.

Battery discharge characteristics for lithium-ion battery are given by the expression below in [15] (Fig. 3):

$$V = \text{Vo} - \lambda\,\mu/(\mu - it) + \alpha\,e^{-\beta it}$$

where

V represents voltage across the battery at no load in volts,
Vo   represents fixed voltage in volts,
     represents polarization voltage in volts,
μ represents the capacity of battery in A h,
α represents the exponentially changing voltage in volts, and
β represents the exponentially extracted capacity in $(\text{A h})^{-1}$
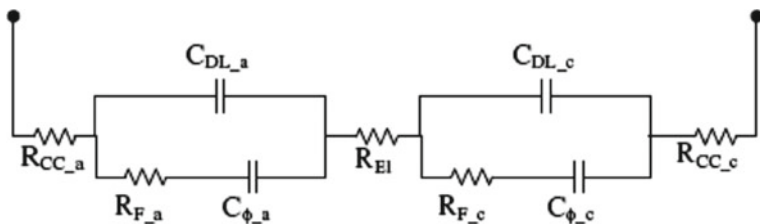
Fig. 3 Equivalent circuit of battery

5 Design of Fuzzy-PI Controller

The block diagram of the proposed fuzzy-PI controller is shown in Fig. 4. Here the proportional and integral constants of proportional integral controller are adjusted dynamically by FLC for different operating conditions, for instance the inputs to FLC, namely error as well as change in error, will characterize its first time derivative in order to find the proportional constant K_p, where error is difference between the generated power and load power. Inference engine along with the rule base which consists of set of if-then rules is framed in terms of two inputs that are used to find the constant K_p.

The fuzzy subsets of input variables, error and change in error, are given by negative large (NL), negative (NE), zero (ZO), positive (PO), and positive large (PL). The fuzzy subsets of output variable K_p are small (SL), moderate (MD), and large (LG). Table 1 shows fuzzy control rule base for gain K_p. In this work, Mamdani's maximum–minimum method is used for inference check [16]. The center of gravity method is used for defuzzification, [17]. The proportional controller K_p is used to find the integral constant K_i dynamically at every instant as shown in Fig. 4.

Fig. 4 Block diagram of fuzzy-PI controller

Fuzzy-PI Controller
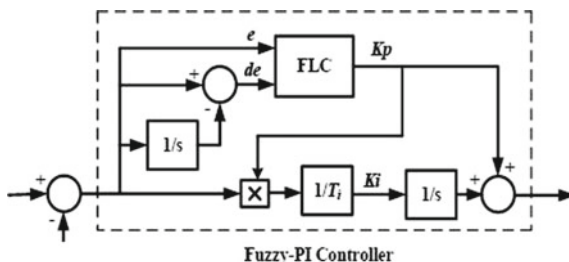
Table 1 Rule base of fuzzy logic controller

e/de	NL	NE	ZO	PO	PL
NL	LG	LG	MD	LG	LG
NE	LG	MD	SL	MD	LG
ZO	MD	SL	SL	SL	MD
PO	LG	MD	SL	MD	LG
PL	LG	LG	MD	LG	LG

6　Results and Discussion

The proposed system as shown in Fig. 1 consists of PV and wind-fed DC micro-grid with battery management system. The ratings of PV and wind-generating systems are shown in Table 2. The output voltage of PV array is scaled up to 240 V using a boost converter and fed to DC micro-grid, whereas the wind turbine-fed PMSG is connected to DC micro-grid using rectifier circuit. The *I–V* and *P–V* characteristics of PV cell are shown in Figs. 5 and 6. The configurations of boost converter circuit are given in Table 3. To meet the load demand, the generated power output of PV and wind sources will supply the power. Due to increase in the demand if the load demand exceeds the generated power, the battery power source will supply the deficit power. In case, if the generated power exceeds

Table 2　PV- and PMSG-fed wind turbine specifications

S. No.	Parameter	Value
1	Voltage under open circuit	44.49 V
2	Voltage at maximum power rating	37 V
3	Current under short circuit	8.199 A
4	Current delivered at maximum power	7.709 A
5	Number of PV cells per module	72
6	Maximum power rating of PV module	269.8 W
7	Voltage constant (V-peak L-L/krpm)	132.55
8	Flux linkage established by magnets	0.1827 Vs
9	Torque constant (Nm/A_peak)	1.0962
10	Nominal mechanical power output of turbine	5000
11	Base power of electrical generator (VA)	211.11
12	Base rotational speed (in p.u.)	1.2
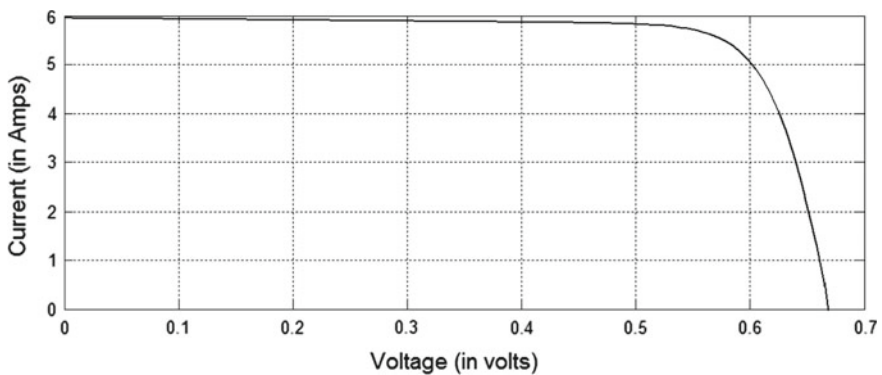
Fig. 5　*I–V* characteristics of PV cell
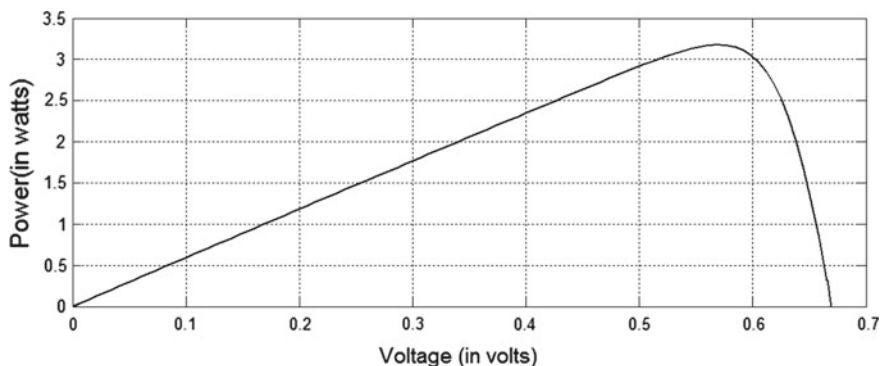
Fig. 6 *P–V* characteristics of PV cell

Table 3 Boost converter-1 specifications	S. No.	Parameters	Rating
	1	Inductor	4.5 mH
	2	Capacitor	550 μF
	3	Switching frequency	2000 Hz
	4	Input voltage	78.5 V
	5	Output voltage	230 V

the load demand, then the battery will store the excess power. The output voltage of series-connected battery cells is 78.5 V which is stepped up to a voltage of 240 V, i.e., the grid voltage using bidirectional buck boost converter circuit, which will act like a boost converter when discharging and buck converter while charging.

To manage the charge and discharge cycle of the battery and to maintain the SOC, the battery energy management system (EMS) is designed. Battery EMS consists of fuzzy + PI controller whose input is error and change in error where error is the difference between the generated power and load power and the output is current signal to the battery. The total power output and the load demand are shown in Fig. 7. The output power delivered by PV and wind-generating systems are 600 and 3200 W, respectively, delivering a total power of 3800 W, but the load demand is 4300 W as shown in Fig. 8a. To meet the excess demand, the battery will discharge 500 W power as shown in Fig. 8b. There is a balance between the power delivered and power consumed by the load due to the existence of battery bank in the circuit as shown in Fig. 8c. The SOC of the battery, the current delivered, and the voltage across the battery during discharge are shown in Fig. 9. As the battery is discharging, the current delivered by the battery is negative.

When the generated power exceeds the load demand as shown in Fig. 10a, the generated power is 3800 W but the load demand is 3200 W. During this period, the battery will start charging as shown in Fig. 10b, where the excess power of 400 W
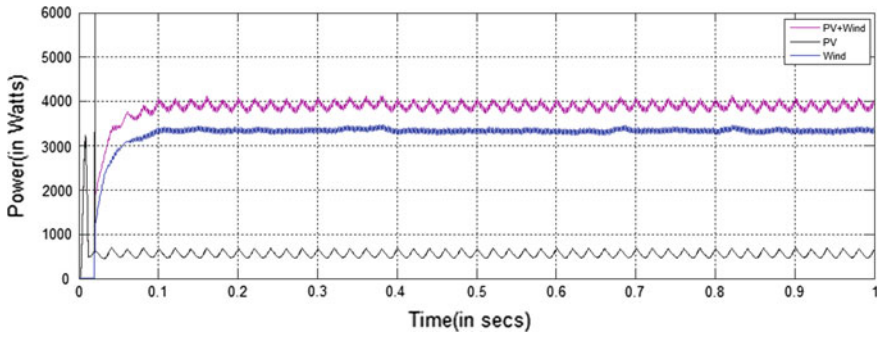
Fig. 7 PV, wind, and combined power generated by both the systems
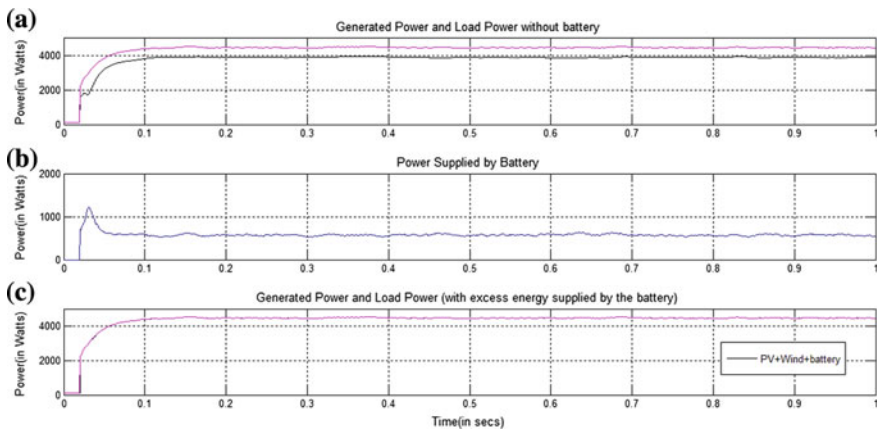
Fig. 8 **a** Generated power and load demand, **b** power delivered by the battery during discharging mode, and **c** balanced power output
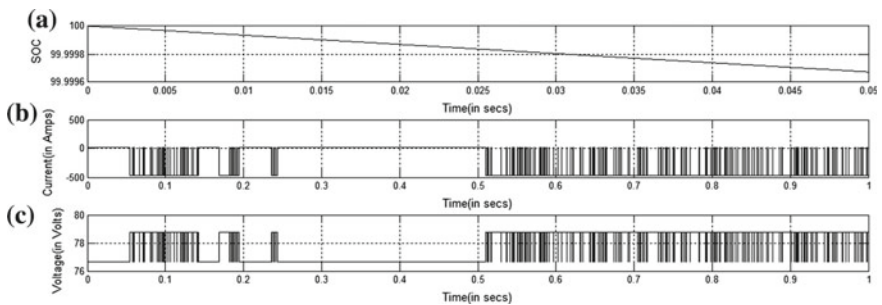
Fig. 9 **a** SOC of the battery, **b** current drawn by the battery, and **c** voltage across the battery
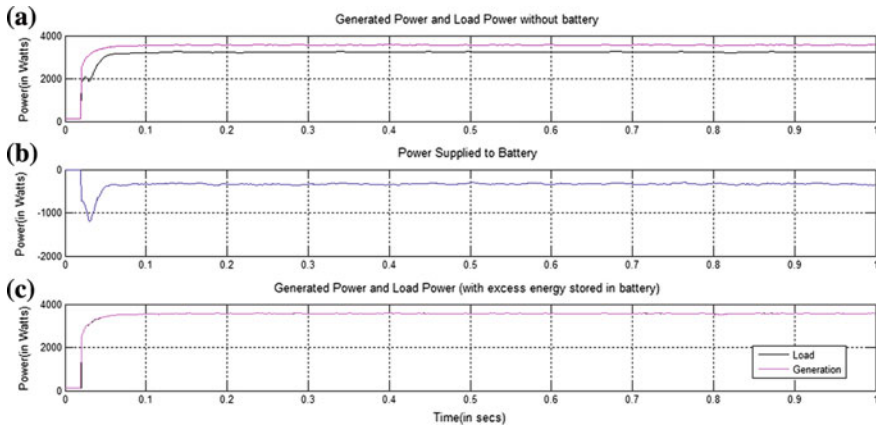
Fig. 10 **a** Generated power and load demand, **b** power drawn by the battery during charging mode, and **c** balanced power output

is stored across the battery. The power delivered and power consumed by the load are balanced as shown in Fig. 10c. The proposed controller is able to manage the battery storage system sensing the load demand and available generation optimally.

7 Conclusion

This paper presents the design and analysis of fuzzy-based proportional integral controller to achieve optimal power flow using energy management system. From the achieved simulation results, it is observed that the system maintains power equilibrium between the generated power and load demand using battery bank whose charging and discharging periods are controlled optimally using fuzzy + PI controller-based EMS. The SOC of the battery is maintained within the range for extension of battery life. Simulation results also ensure that there is stable power supply and efficient operation of the proposed DC micro-grid in islanded operating mode.

References

1. Mutoh N, Ohno M, Inoue T (2006) A method for MPPT control while searching for parameters corresponding to weather conditions for PV generation systems. IEEE Trans Ind Electron 53(4):1055–1065
2. Rongxian H, Zhiwen L, Yaoming C, Fu W, Guoguang R (2010) DC micro-grid simulation test platform. In: Proceedings of the 9th Taiwan power electronics conference, pp 1361–1366

3. Shang C, Srinivasan D, Reindl T (2016) An improved particle swarm optimisation algorithm applied to battery sizing for stand-alone hybrid power systems. Int J Electr Power Energy Syst 74:104–117

4. Xu DL (2010) Control and operation of a DC microgrid with variable generation and energy storage. IEEE Trans Power Electron 25(12):3066–3075

5. Arcos-Aviles D, Pascual J, Marroyo L, Sanchis P, Guinjoan F (2017) Fuzzy logic-based energy management system design for residential grid-connected microgrids. IEEE Trans Smart Grid 99:1–14

6. Roine L, Therani K, Manjili YS, Jamshidi M (2014) Microgrid energy management system using fuzzy logic control. In: 2014 world automation congress (WAC), Waikoloa, HI, USA, Aug 2014, pp 462–467

7. Bhattacharjee C, Roy BK (2016) Advanced fuzzy power extraction control of wind energy conversion system for power quality improvement in a grid tied hybrid generation system. IET Gener Transm Distrib 12(7): 1455–1465

8. Hari Priya T, Parimi AM, Rao UM (2016) Development of hybrid controller for photovoltaic based DC-DC boost converter in DC grid connected applications. In: Proceedings of international conference on circuit power and computing technologies (ICCPCT), pp 1–6

9. Hari Priya T, Parimi AM (2016) Design of adaptive perturb and observe–fuzzy MPPT controller for high voltage gain multi level boost converter. In: Proceedings of IEEE 7th power India international conference, 25–27 Nov 2016

10. Hari Priya T, Parimi AM (2018) Performance analyses of PMSG based WECS using hybrid controller in DC grid connected. Int J Pure Appl Math 118(17):903–913

11. Li X, Hui D, Lai X (2013) Battery energy storage station (BESS)—based smoothing control of photo-voltaic (PV) and wind power generation fluctuations. IEEE Trans Sustain Energy 4 (2):464–473

12. Hari Priya T, Parimi AM, Rao UM (2016) Performance evaluation of high voltage gain boost converters for DC grid integration. In: Proceedings of international conference on circuit power and computing technologies (ICCPCT), 18–19 Mar 2016

13. Yuan X, Wang F, Boroyeivich D et al (2009) DC-link voltage control of a full power converter for wind generator operating in weak-grid systems. IEEE Trans Power Electron 24 (9):2178–2192

14. Reihani E, Sepasi S, Roose L, Matsuura M (2016) Energy management at the distribution grid using a battery energy storage system (BESS). Int J Electr Power Energy Syst 77:337–344

15. Sebastián R (2016) Application of a battery energy storage for frequency regulation and peak shaving in a wind diesel power system. IET Gener Transm Distrib 10(3):764–770

16. Hari Priya T, Parimi AM, Rao UM (2016) Performance evaluation of DC grid connected solar PV system for hybrid control of DC-DC boost converter. In: Proceedings of 10th international conference on intelligent systems and control (ISCO), 7–8 Jan 2016

17. Hari Priya T, Parimi AM, Rao UM (2013) Modeling of DC-DC boost converter using fuzzy logic controller for solar energy system applications. In: Proceedings of IEEE Asia Pacific conference on postgraduate research in microelectronics and electronics (PrimeAsia), 19–20 Dec 2013

Performance Indicators for Assessing Solar Photovoltaic Microgrids in Grid-Connected Mode

K. Pritam Satsangi, G. S. Sailesh Babu, D. Bhagwan Das and A. K. Saxena

Abstract In India, Solar photovoltaic microgrids have become a sustainable energy solution, particularly in remote areas where grid is still unreliable. However, they have stamped their own mark in towns and cities too. Performance assessment of such microgrids is an important aspect in increasing the penetration of PV into grid. In this paper, three different perspectives of assessing the performance of a solar photovoltaic microgrid have been defined. Performance of a 40 kWp SPV microgrid has been investigated for various indicators such as performance ratio, capacity factor, self-consumption, self-sufficiency, and grid interaction. Results obtained indicated that self-consumption in this study is higher than other studies reviewed. This paper focuses on presenting a pool of indicators for better performance assessment of SPV microgrids, particularly in grid-connected mode.

1 Introduction

Dependence on fossil fuels like coal, in power generation, is continuously increasing in India, despite the government's thrust on the use of renewable sources. A recent report by Central Electricity Authority (CEA) reported that coal consumption has increased by 100% in the last decade [1]. By the end of 2016, per capita energy consumption was 1075 kWh and average cost of power supplied was 520 paise/kWh [1]. According to its current climate policy, under Paris agreement (COP21), India is committed to generate 40% of its electrical energy need from

K. Pritam Satsangi (✉) · G. S. Sailesh Babu · D. Bhagwan Das · A. K. Saxena
Department of Electrical Engineering, Dayalbagh Educational Institute,
Dayalbagh, Agra, India
e-mail: pritamsk@gmail.com

G. S. Sailesh Babu
e-mail: babu.sailesh@gmail.com

non-fossil fuels by 2030 [2]. This climate goal motivated the government to revise the target of JNNSM to 100 GW and also the total renewable capacity to 175 GW by 2022. Under similar lines, an ambitious target of replacing conventional vehicles with electric vehicles (EV) by 2030 was also set. All these targets are achievable only through non-fossil, renewable sources of energy. India has huge solar potential, nearly 300 sunny days round the year, geographically. India stands fourth in the world in wind power generation with about 31 GW until March 2017 out of a national target of 60 GW by 2022 [3]. But these sources, being variable generation type, are unreliable during peak load duration most of the times. Intermittency and uncertainty are the two major challenges to overcome and achieve increased penetration of these sources [4]. In this scenario, microgrids (MG) have become a sustainable energy solution throughout the world for more than a decade. They are basically a platform for integrating distributed energy sources (supply), controllable loads (demand), and energy storage units, with the local distribution grid [5]. They work in both grid-connected mode and islanded mode with increased reliability. Typically, supply-side sources are intermittent renewable energy sources, and hence storage units thereby offset the fluctuations in the generation. Monitoring and control are integrated parts of any MG to ensure a smooth transition between grid-connected and islanded mode and thus no loss of load. Introduction of bidirectional metering, incentive-based tariffs, feed-in-tariffs (FiTs), etc. have been instrumental in wider adoption of MG in recent times [6].

2 Performance of Solar Photovoltaic Microgrids (SPVMG)

The performance of MG can be improved by enhancing islanding mode operation. If MG can satisfy the demand variations in islanded mode, then it is expected that it can work in grid-connected mode with high reliability [7]. Considering SPVMG, where solar PV is the primary energy source along with energy storage, loads and local grid, performance studies of such systems can be multifaceted given complex structure of MG. A three-dimensional approach on the performance of such systems is defined under study as follows:

(1) For an SPVMG, performance can be evaluated, treating it as a simple PV system connected to grid, using IEC standards 61724. Though this standard is defined for a grid-connected system (IEC standards), it can also be applied under islanded mode because it does not use any grid metric to assess the performance.

(2) Similarly, the performance of SPVMG can be assessed through self-consumption (SelfC) and grid interaction indices (gridint). However, grid interaction studies are only possible under grid-connected mode.

(3) A power quality perspective can reveal the performance in terms of frequency, voltage magnitude and fluctuations (dips and distortions), impact of MG on local grid.

In this paper, performance indicators of a SPVMG installed in university campus of Dayalbagh Educational Institute are evaluated. This paper presents a performance study of SPVMG in first and second dimensions only. The third dimension is not presented here due to lack of high-resolution (1 s) data from the monitoring system and will be dealt with in future work. The university has a total capacity of 655 kWp, comprising of 11 distributed MGs of different sizes. PV array in each MG is installed on rooftops of the university buildings. A 40 kWp SPVMG is evaluated for performance. It is important to mention here that the performance assessed in this work is specifically applicable only to SPVMG. Unlike many cases, this MG under study comprises of only one distributed energy source (solar PV) along with energy storage (batteries), connected loads, and local grid. Hence, the complexity is little low compared to MGs with multiple energy sources. All the MGs installed in the campus are similar in structure, connected to the same local grid, but without any interconnections between them. This type of real-time system is rarely studied for performance, combining all dimensions together and, therefore, motivated the authors in this direction.

3 Review of Microgrids and Their Performance

A recent article [8] reviewed the status of MGs in India and tabulated number of them deployed typically in rural areas ranging from 1 kWp systems to a large-scale 12,000 kWp systems. These are catering wide range of loads like households, commercial and agricultural. Most of the MG systems were deploying solar PV as one of the distributed energy source, being quite abundant throughout the year. Authors identified three important areas of research, required to increase the penetration of MGs, viz, performance of PV modules, performance of converters and storage, remote monitoring and control of MGs. More studies [6, 9, 10] addressed the challenges and scope of MGs in Indian energy scenario. Some other studies [11–16] have focused on performance evaluation of grid-connected solar photovoltaic plants without batteries. But such plants do not fall under the category of MGs due to lack of storage unit. All such plants have followed standards IEC 61724 for assessing performance. However, there are no studies on the application of IEC 61724 on grid-connected PV systems with energy storage and load. Hence, the authors, in this paper, felt necessary to extend the application of these standards to study the performance of grid-connected PV system with battery and load or simply SPVMG. Many other studies [17–22] focused on self-consumption aspects of distributed solar photovoltaic systems with battery and household loads. Most of these studies reported that adding storage to distributed grid connected PV systems increases the self-consumption of the system. Another way of increasing selfC, by demand-side management, was also presented in the same studies. An increase of relative selfC between 13–24% points using battery and 2–15% points using demand-side management was reported in [22]. Hence, selfC can be considered as a good performance indicator for SPVMG systems. Further studies [23–25] discussed

on grid interaction and load-matching indices of net zero energy buildings with integrated MG system. None of these studies have reported all these indicators specific to SPVMG. However, authors, in this paper, believe that it is necessary to integrate all these performance indicators to assess SPVMG. This approach will help in understanding the performance of SPVMG in a much better way for the benefit of different stakeholders (customer, industry, policymakers) in the microgrid market.

4 Description of Microgrid

As defined in Sect. 1, MG comprises of renewable energy source, energy storage system, flexible loads, and local grid. The campus of Dayalbagh Educational Institute is fully powered by solar PV energy on a bright sunny day. It has an installed capacity of 655 kWp with a total of 11 SPVMGs without any intertie between each of them. In this paper, SPVMG installed in Faculty of Arts is considered for assessing performance, whose configuration is depicted in Fig. 1. Each of these MGs has dedicated controllable loads along with a common local grid. Component-wise specifications are given in Table 1. A 40 kWp PV array is the main source of the system comprising of 24 strings in parallel with 10 modules in each string in series. Three array junction boxes are installed where 8 strings terminate at each AJB before they terminate at a main junction box. A total of 120 batteries with cumulative storage capacity of 96 kWh , 2 V each, are connected in series to make a 240 V DC system voltage. PV array, battery, and inverter input side are connected to DC bus. A 40 kVA grid support conditioner (GSC) comprising of inverter and

Table 1 Specifications of 40 kWp SPVMG

PV array		Inverter		Battery	
Component	Rating	Component	Rating	Component	Rating
Make/model	BHEL/L24170	Type	3-phase	Make/model	EXIDE low maintenance lead acid
V_{OC}	42 V	Output	415 V AC, 50 Hz	Capacity	400 A h
I_{SC}	5.2 A	Input	240–360 V DC	V_{PC}	2 V
V_{MP}	35 V	Rated power	40 kVA	Charging rate	C 10
I_{MP}	4.86 A	Efficiency	94% (rated load)	System voltage	240 V
P_{MAX}	170 Wp	THD	<4%	No. of batteries	120
NOCT	45 °C ± 2 °C			DoD	50%
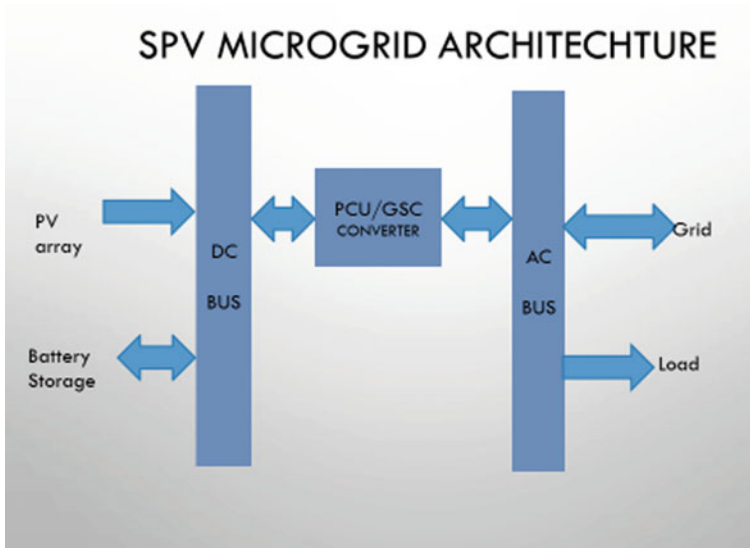
Fig. 1 SPV microgrid

charge controller together is mediating between AC bus and DC bus. The output terminal is connected to 3-ph AC bus, where local grid and controllable loads are also connected. Typical SPVMG architecture is shown in Fig. 1. A data acquisition system is provided along with the inverter with a data resolution of 10 min using which performance analysis is done for a period of 10 months.

5 Performance Indicators

5.1 IEC Standards

IEC 61724 Standards are a traditional way of assessing a grid-connected PV plant and since our SPVMG is also a grid-connected PV system, the following performance indicators are derived and presented for the system under study, given in Eqs. (1)–(5). Y_R is reference radiation input to the PV array, converted into Y_A, after array losses. The array output is fed to inverter and battery through charge controller which has three-terminal input/output. The inverter here has an integrated MPPT/charge controller for two different functions. MPPT is responsible for drawing maximum power from PV array under operating conditions, whereas charge controller is responsible for proper charging/discharging of battery. Y_A output of array is converted into Y_F output of inverter after losses in battery charging/discharging, charge controller losses and inverter losses. All these are

treated as system losses. Performance ratio is the ratio of actual energy output to expected energy output. It includes all the losses occurring in the system. Capacity factor is defined as the actual energy output for a given period of time to the output energy if it were operated at its peak power rating for the same period of time. It gives the degree of utilization of its rated capacity.

$$\text{Reference Energy Yield } (Y_R) = \frac{\text{Measured Insolation in kWh/m}^2}{\text{Reference Irradiation in kW/m}^2} \quad (1)$$

$$\text{Array Energy Yield } (Y_A) = \frac{\text{Array output energy in kWh}}{\text{Nameplate rated output in kW}} \quad (2)$$

$$\text{Final Energy Yield } (Y_F) = \frac{\text{AC energy output in kWh}}{\text{Nameplate rated output in kW}} \quad (3)$$

$$\text{Performance Ratio (PR)} = \frac{\text{Final energy Yield } (Y_F)}{\text{Reference energy yield } (Y_R)} \quad (4)$$

$$\text{Capacity Factor} = \frac{\text{Actual energy ouput of the system}}{8760 * \text{rated power capacity of the system}} \quad (5)$$

5.2 Self-Consumption Indicators

Self-consumption is defined as the fraction of energy utilized by the producer/customer/owner without exporting to grid. Increasing selfC will reduce stress on the local grid and hence it should be encouraged. Self-sufficiency (selfS) reports the degree of on-site generation sufficiency to satisfy the site load needs. Grid interaction index is the ratio of magnitude of net power from grid to the total load demand. All three indices are defined below.

$$\text{SelfC} = \frac{\text{Self consumed PV electricity (kWh)}}{\text{Total PV electricity generated (kWh)}} \quad (6)$$

$$\text{SelfS} = \frac{\text{Self consumed PV electricity (kWh)}}{\text{On-site electricity demand (load)}} \quad (7)$$

$$\text{gridint} = \frac{|\text{Net energy from grid}|}{\text{On-site electricity demand (load)}} \quad (8)$$

6 Results and Discussion

Performance parameters, according to IEC 61724 [26], are assessed for a period of 10 months. Performance ratio and capacity factor of SPVMG are presented in Fig. 2. Annual average PR of 64.2% is recorded. Minimum values are seen in October. Reference yield of 4.10 was recorded during the month, but the array yield was only 2.20 with high array loss of 1.90. This was because of nearby agricultural field where seasonal harvesting takes place in the same month and huge amount of dust is released, accumulated on PV array. Higher PR values are recorded in January and August. An average capacity factor of 9% is recorded for the considered period. An average CO_2 savings of 82 kg/day and a total of 25.72 ton of emission reduction were achieved for the period.

Self-consumption indices are presented in Fig. 3. Annual average self-consumption was found to be 88.5%. Higher values were recorded in May and June. The selfC results obtained in this paper are better than the results in [17–22]. Annual average self-sufficiency of 44% was recorded. Annual average grid interaction of 75% was recorded. This value indicates the grid dependency and can be reduced by controlling the grid charging option for battery bank. The following Figs. 4, 5 and 6 represent the duration curve for each sample day mentioned during different seasons. All these indicate battery bank charging from grid during early and night non-sunshine hours. Spring and summer days also indicate export on negative Y-axis. Power flow on corresponding day in the system is shown in each Figs. 4, 5 and 6, and all the legends plotted are in kW.
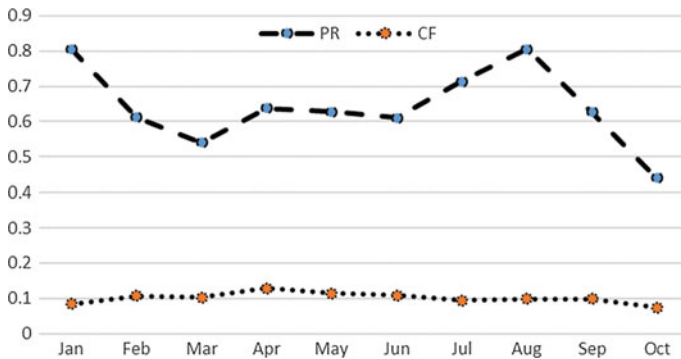
Fig. 2 Variation of PR and CF during 10 months
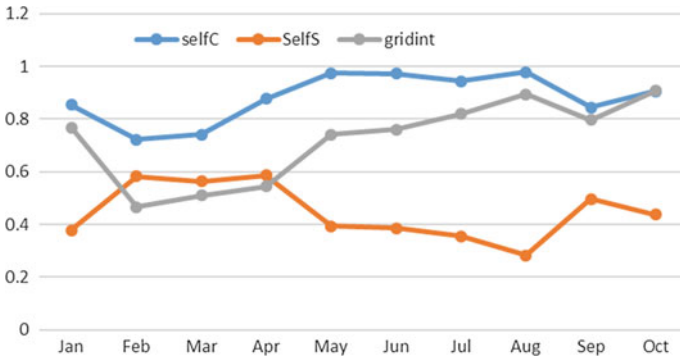
Fig. 3 Variation of self-consumption, self-sufficiency, and grid interaction for 10 months
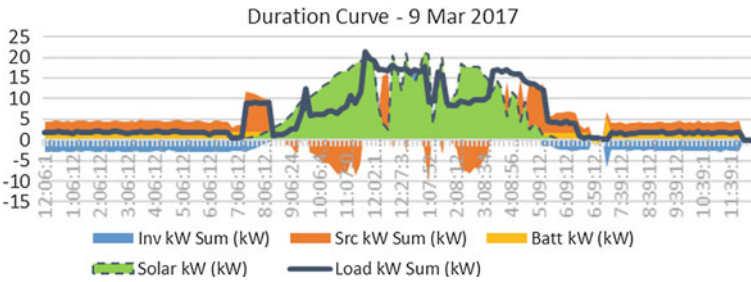
Fig. 4 Duration curve—spring sample day
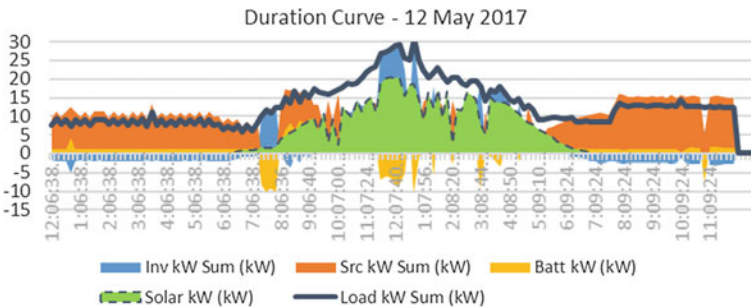
Fig. 5 Duration curve—summer sample day
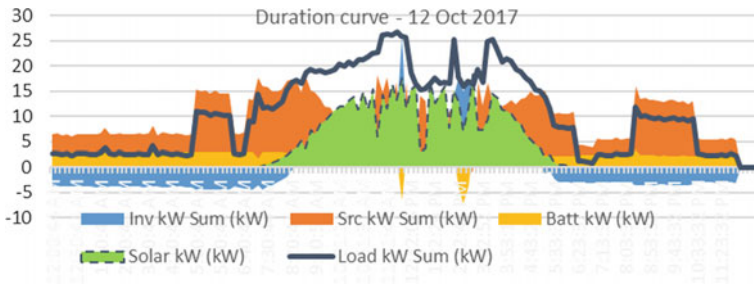
Fig. 6 Duration curve—autumn sample day. Legends: Inv kW—inverter power (positive axis—export; negative axis—import), Src kW—grid power (positive—import; negative—export), Batt kW—battery power (positive—import; negative—export), Solar kW—solar power generated, Load kW—load demand

7 Conclusion

The main conclusions of this paper are summarized as follows:

(i) Solar photovoltaic microgrids are the special case of grid-connected PV systems with storage. Performance of such systems can be assessed based on three different aspects of the systems.

(ii) Using IEC 61724 standards, the traditional way of assessing is accomplished resulting in the performance ratio of 64.2% and a capacity factor of 9%.

(iii) Grid and system interaction perspective revealed that the microgrid under study has a self-consumption of 88%, self-sufficiency of 44%, and grid interaction of 75%.

(iv) Power quality perspective revealing frequency issues, voltage dips or distortions, effect of PV on local grid, etc. can also be studied provided high-resolution (1 s) data is available.

(v) This paper is an attempt to identify and consolidate a pool of indicators to assess the performance of an SPVMG.

References

1. www.cea.nic.in/reports/monthly/executivesummary/2017/exe_summary-08.pdf. Accessed on 16-4-2018
2. https://economictimes.indiatimes.com/news/environment/developmental-issues/indias-dependence-on-coal-to-continue-despite-thrust-on-renewables/articleshow/60173347.cms. Accessed on 19-4-2018
3. Global Wind Energy Council (GWEC) (2016) Indian wind energy, a brief outlook
4. Wang S et al (2018) New metrics for assessing the performance of multi-microgrid systems in stand-alone mode. Int J Electr Power Energy Syst 98:382–388
5. Hatziargyriou N (ed) (2014) Microgrids: architectures and control. Wiley

6. Balijepalli VSKM, Khaparde SA, Dobariya CV (2010) Deployment of microgrids in India. In: 2010 IEEE Power and energy society general meeting, IEEE

7. Bollen M et al (2009) Performance indicators for microgrids during grid-connected and island operation. In: 2009 IEEE Bucharest PowerTech, IEEE

8. Suryad VA, Doolla S, Chandorkar M (2017) Microgrids in India: possibilities and challenges. IEEE Electrification Mag 5(2):47–55

9. Murthy SS (2012) Micro-grid integration with renewable energy in Indian perspective. In: Life senior member, IEEE, pp 1–8

10. Raman P, Murali J, Sakthivadivel D, Vigneswaran VS (2012) Opportunities and challenges in setting up solar photo voltaic based micro grids for electrification in rural areas of India. Renew Sustain Energy Rev 16(5):3320–3325

11. Kumar BS, Sudhakar K (2015) Performance evaluation of 10 MW grid connected solar photovoltaic power plant in India. Energy Rep 1:184–192

12. Sharma V, Chandel SS (2013) Performance analysis of a 190 kWp grid interactive solar photovoltaic power plant in India. Energy 55:476–485

13. Padmavathi K, Daniel SA (2013) Performance analysis of a 3 MWp grid connected solar photovoltaic power plant in India. Energy Sustain Dev 17(6):615–625

14. Sundaram S, Babu JSC (2015) Performance evaluation and validation of 5 MWp grid connected solar photovoltaic plant in South India. Energy Convers Manag 100:429–439

15. Kumar KA, Sundareswaran K, Venkateswaran PR (2014) Performance study on a grid connected 20 kWp solar photovoltaic installation in an industry in Tiruchirappalli (India). Energy Sustain Dev 23:294–304

16. Sharma R, Goel S (2017) Performance analysis of a 11.2 kWp roof top grid-connected PV system in eastern India. Energy Rep 3:76–84

17. Luthander R, Widén J, Munkhammar J, Lingfors D (2016) Self-consumption enhancement and peak shaving of residential photovoltaics using storage and curtailment. Energy 112:221–231

18. Bertsch V, Geldermann J, Lühn T (2017) What drives the profitability of household PV investments, self-consumption and self-sufficiency? Appl Energy 204:1–15

19. Pena-Bello A, Burer M, Patel MK, Parra D (2017) Optimizing PV and grid charging in combined applications to improve the profitability of residential batteries. J Energy Storage 13:58–72

20. Merei G, Moshövel J, Magnor D, Sauer DU (2016) Optimization of self-consumption and techno-economic analysis of PV-battery systems in commercial applications. Appl Energy 168:171–178

21. Castillo-Cagigal M, Caamano-Martín E, Matallanas E, Masa-Bote D, Gutiérrez A, Monasterio-Huelin F, Jiménez-Leube J (2011) PV self-consumption optimization with storage and active DSM for the residential sector. Solar Energy 85(9):2338–2348

22. Luthander R, Widén J, Nilsson D, Palm J (2015) Photovoltaic self-consumption in buildings: a review. Appl Energy 142:80–94

23. Salom J, Widén J, Candanedo J, Sartori I, Voss K, Marszal A (2011) Understanding net zero energy buildings: evaluation of load matching and grid interaction indicators. Proc Build Simul 6:2514–2521

24. Salom J, Marszal AJ, Widén J, Candanedo J, Lindberg KB (2014) Analysis of load match and grid interaction indicators in net zero energy buildings with simulated and monitored data. Appl Energy 136:119–131

25. Berggren B, Widen J, Karlsson B, Wall M (2012) Evaluation and optimization of a Swedish net zebusing load matching and grid interaction indicators. In: Building simulation and optimization

26. International Electrotechnical Commission (1998) Photovoltaic system performance monitoring-guidelines for measurement, data exchange and analysis. International Standard IEC 61724

Analysis of Harmonic Distortion in PV–Wind-Battery Based Hybrid Renewable Energy System for Microgrid Development

Mohammad Amir and Sudhir Kumar Srivastava

Abstract Our proposed methodology is considered as the intelligence-based control framework, which includes a fuzzy-logic-based controller for the control of PWM inverter. Microgrid consists of hybrid-renewable-based energy sources such as a photovoltaic generation unit and a PMSG-based wind generation unit with hill-climbing-based MPPT control algorithms. A battery backup system is also used, which supplies the stored energy during emergency to the variable load as well as the utility grid in such a manner that it maintains the desired load level. Several issues associated with the integration of hybrid-wind-solar-based renewable energy into the utility grid due to its intermittent and uncertainty nature. Various power electronic converters are associated with the grid system, which injects the harmonics and further increases the power quality problems such as harmonic distortion. Total harmonic distortion is a significant measuring parameter, which directly related to the overall power quality measurement of the grid. In this work, an FFT-based THD analysis is carried out to obtain the scale of harmonics at load side and the simulation of proposed methodology is achieved using MATLAB/Simulink environment.

Keywords Fuzzy logic controller (FLC) · Hybrid renewable energy system (HRES) · Maximum power point tracking (MPPT) · Total harmonic distortion (THD)

1 Introduction

To preserve the earth for next generation, environmental friendly energy solution is required to overcome the demanding load and global warming. For that, we need more renewable-based technology that could provide sustainable and pollution-free

M. Amir (✉) · S. K. Srivastava
Madan Mohan Malaviya University of Technology, Gorakhpur, India
e-mail: er.amir123electrical@yahoo.com

S. K. Srivastava
e-mail: sudhirksri05@gmail.com

technology. There are several benefits of the non-conventional technologies offer the potential of clean, less effect on the environment and abundant energy collected from self-renewing resources like sun and wind. In power electronics technology, renewable energy resources are now being use with energy storage systems and this type of integration of more than two technologies [1] are now in trend. Based on the consideration of low technological cost, several environmental benefits and their relative policies, so that penetration of hybrid renewable energy has grown rapidly in last two decades. Later on due to several technological advancements on distributed power generation has given the concept of microgrid, where more than one renewable resource integrate with other sources like the battery storage system could serve the demand power to the load [2]. So, these issues must be suppressed. BESS[1] works as an uninterruptible power backup energy source that is capable to provide a definite amount of power into the desired load, when the combined wind turbine system and solar photovoltaic system cannot meet the overall load demand under all conditions [3]. Our HRES-based proposed technique has designed to deliver continuous power into the load or utility grid. Sudden load-level fall causes several power quality issues such as harmonic distortion. Therefore, FFT-based analysis will be utilized for providing the power quality solution to entire grid system.

1.1 Issues and Recent Developments in the Hybrid-Based Grid System

Each conventional technology is in a several stage of research and development based on the many factors such as availability of different resources, cost, and their potential impact on the environment. There are several disadvantages of BESS such as battery cost as well as there is no guarantee to meet the certain load demands by BESS at all the times, especially when sufficient PV–wind generation to meet the desired load level at good environmental conditions. Conventional energy resources in the form of various renewable-based distributed generations and microgrid with artificial control techniques are emergent technology in the current electrical deregulated power system, because of the growing in power demand and decay in power generation by the fossil fuels for clean environmental aspects. To improve and maintain the power quality, new strategies for better reliability are required with the increasing number of renewable energy resources. The modern artificial-intelligence-based technological advancement has played a vital role such as wavelet-artificial-neural-network-based approach for the short-term day-ahead power production prediction from the base of irradiance and wind speed variation. These intelligence based approach offering the open doors for the grid independent system operator to preplan and management of power dispatch. Today's

---

[1]BESS—battery energy storage system.

population growth rate increasing day by day, which directly leading to the power demand. Several modern techniques of power generation have concerns with growth in power demand, while conservation of the environment stances is an emergent challenge.

2 Description of Proposed Hybrid-Based Grid Integration System

Saib and Gherbi [4] described the concept and principle of the hybrid system and its control. The wind turbine system with PMSG unit which converts wind power into electrical power [5] (generally converts AC into DC power with a rectifier bridge). The Solar PV-System with converter unit, Converts the PV-power into DC power and then both generation units coupled with MPPT system for maximize the power. Both the wind–PV powers fed into common DC link, which is coupled through VSC, where a battery backup system also attached. This BESS is installed to provide the required load power under deficit PV–wind power generation conditions (Fig. 1).
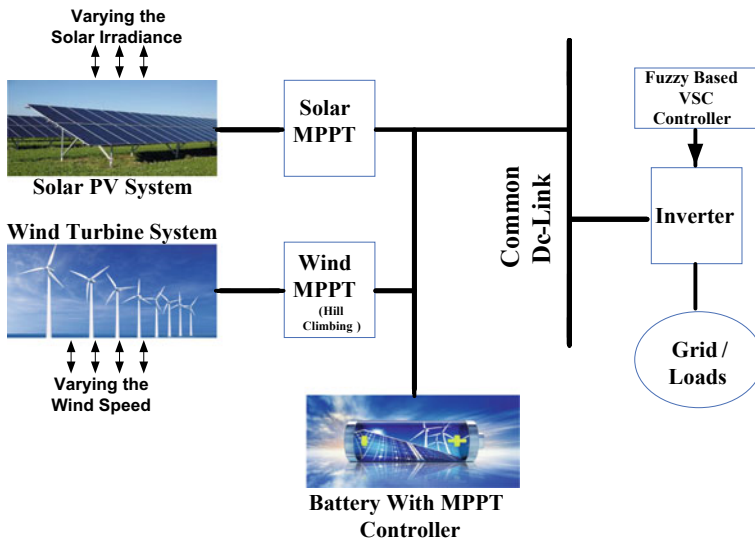
Fig. 1 External layout of a grid system with several sources and their control configurations

2.1 Modeling and System Specification of Proposed Methodology

The aim of this proposed methodology is to control the generation based on load demand [4] and energy storage for the load/utility system comes from the accumulated battery storage system or the hybrid renewable energy based system [6]. Microgrid loads can operate next to the other network or can switch to another utility grid to provide continuously electrical power; otherwise, the energy system of the microgrid can change to a reserve of accumulators, such as a battery source. Hill-climbing-based MPPT techniques provide the maximum amount of power [7, 8], under the variation of atmospheric conditions, which are variable in nature such as variations in solar irradiance (in W/m^2) and wind speed (in m/s^2). (Figure 2, Table 1)
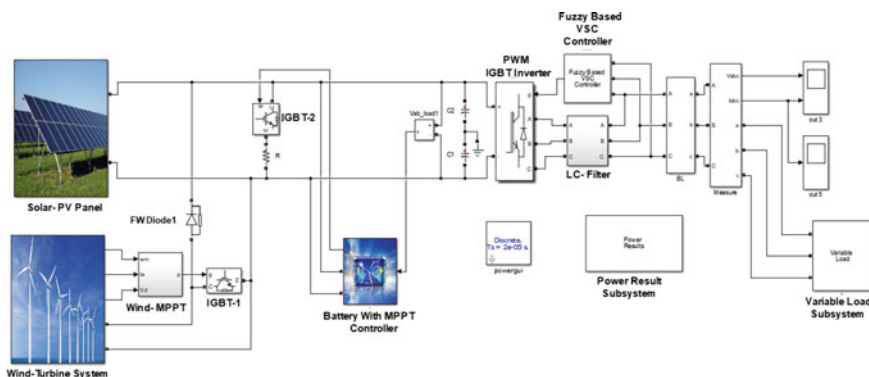
Fig. 2 Demonstration of a hybrid PV–wind-based renewable energy system with a battery backup source using MATLAB/Simulink toolbox [9]

Table 1 Specification of several parameters associated with the hybrid grid system

Grid subsystem	Rating/capacity
First—PV system	P_{OUTPUT} = 9551 W, Maximum irradiance level 1000 W/m^2 V_{MPPT} = 666 V, V_{OC} = 406, I_{SC} = 7.431 amp, R_{SERIES} = 0.005Ω, Standard operating temperature 25 °C, No. of cells in an Array 22, No. of cells in each row = 11, No. of cells in each column = 2
Second—Wind turbine system	P_{OUTPUT} = 8.5 kW, For PMSG a 3Φ, 50 Hz, Salient pole rotor, Inertia = 0.01197 kg/m^2, Friction factor = 1.111189 N.m.s, Viscous damping = 0.001189
Third—Battery energy system	Ni-Metal-Hydride type, Nominal voltage 300 V, Rated capacity = 6.5Ah, with SOC is 60%
Fourth—Filter	Inductance = 90e^{-4} H and Capacitance = 85e^{-6} F
Fifth—Load	A resistive load of 4 kW connected with hybrid system and an additional 10 kW resistive load connected with a circuit breaker in a specified time duration 2–3 s

3 Design of Fuzzy Logic Controller for PWM Inverter Control

The FLC control technique for PWM-based inverter voltage control is capable of providing power balance to the microgrid. These three PV–wind-battery energy sources coupled to a fuzzy-logic-based inverter, which clamps the output voltages of the inverter at a desired level by comprising the inputs such as Errors (E) and Change of Error (COE). Description of fuzzy-based rule matrix with "if and then rule" referred in Table 2. In the proposed modes of operation, a fuzzy-logic-based control strategy regulates the gate pulse so, as to give the desired gate signal to operate the PWM-based inverter [8]. Symmetric rules of 49-rule base applied to the inverter pulse control using "MAMDANI" fuzzy interface method.

A pulse generator is employed to provide the desired gating pulses for IGBT-based inverter as shown in Fig. 3. The FLC control procedure for VSC-based voltage controller is capable of providing balance power conversion to the microgrid. This type of inverter introduces the unusual harmonics, which further feed into the load/utility grid [10].

Table 2 49-rule base of input error and input change of error

Δα		Input error (E)						
		First	Second	Third	Fourth	Fifth	Sixth	Seventh
		NS	NM	NL	Z	PS	PM	PL
Input (COE)	First—NS	'PS'	'PL'	'PL'	'PS'	'NM'	'NM'	'NM'
	Second—NM	'PM'	'PL'	'PL'	'PM'	'Z'	'Z'	'Z'
	Third—NL	'PL'	'PL'	'PL'	'PL'	'Z'	'Z'	'Z'
	Input(COE) fourth —Z	'PS'	'PM'	'PL'	'Z'	'NS'	'NM'	'NL'
	Fifth—PS	'PS'	'PS'	'NM'	'Z'	'NS'	'NM'	'NL'
	Sixth—PM	'Z'	'Z'	'Z'	'NM'	'NM'	'NL'	'NL'
	Seventh—PL	'Z'	'Z'	'Z'	'NL'	'NL'	'NL'	'NL'

Z zero, *PS* positive small, *PM* positive medium, *PL* positive large
NS negative small, *NM* negative medium, *NL* negative large
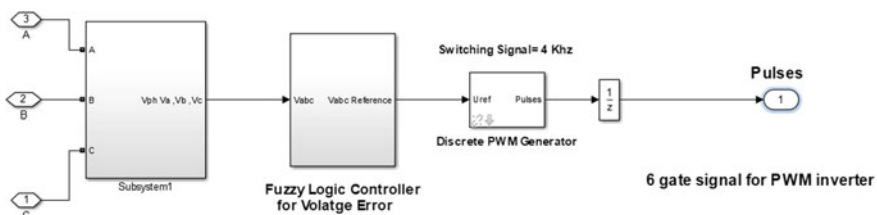
Fig. 3 Subsystem simulink model of IGBT-based inverter control using FLC
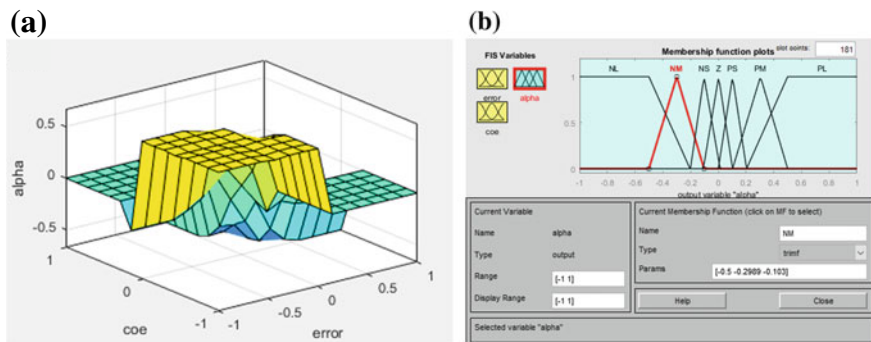
Fig. 4 **a** Three-dimensional surface viewer **b** membership function of desired Output 'α'

In the proposed modes of operation, FLC-based control strategy regulates the gate pulses of 4 kHz. Therefore it provides the desired 6 gate signals to operate the PWM based inverter. Figure 4a, b, respectively, represents that how the output variables are dependent corresponding to the membership function, using fuzzy logic controller for our proposed methodology. Seven-term fuzzy sets are provided earlier with trapezoidal and triangular shapes of the desired output variables, i.e., for alpha output levels are as; NLmf, NMmf, NSmf, Zmf, PSmf, PMmf, and PLmf.

4 Simulation Result of Proposed Hybrid System

There are several operational modes, which includes grid operation with or without the use of battery in such a manner provide continuous power to the 4 kw load. Short-term solar irradiance amplitudes [1000 850 0 500] in W/m^2 are varying corresponding to the time [0, 2, 3 and 5] in s. While the wind speed are varying [5 12 9 0] in m/s^2 with respect to the time variation [0, 5, 3 and 4] in s (Fig. 5).

If the PV–wind generation have sufficient power to maintain the load demand, then the battery energy system is in charging state (0–3 s), else battery is in discharging mode (3.1–6 s) (Table 3).

For maintaining the desired load demand and minimum penalties, it is essential to balance real and reactive power level in the grid system. Due to inductive nature of the load, it causes the reactive power injection, reduction of real power (or useful power), and reduction of overall fundamental power values in the power lines. Therefore, the usage of these quantities must be suppressed which is essential for grid operation under better power quality consideration.

Generally, harmonics are presented and passed through the power line but these limits must be within the definite range, these values are directly affects the overall power quality in such a manner that reactive power and real power must be preceded.
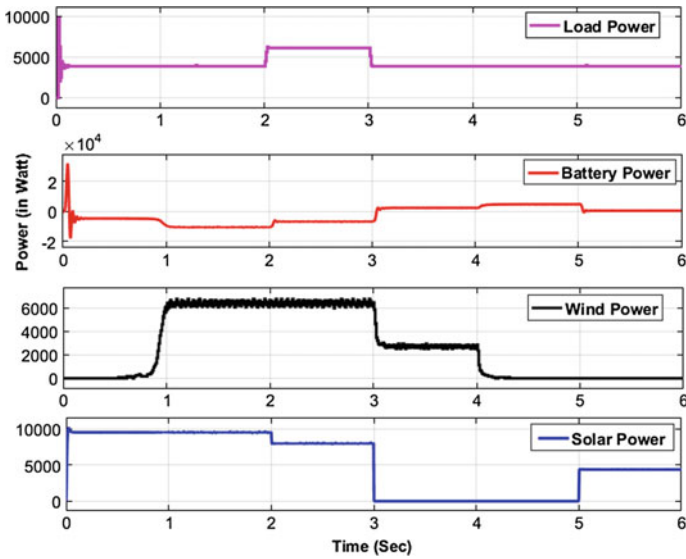
Fig. 5 Characteristics of load power corresponding to generation power ($P_{\text{Wind–PV-Battery}}$)

Table 3 Operational analysis of several parameters associated with the hybrid grid system

Parameters	Time instant					
(In watt) s	At 1 s	At 2 s	At 3 s	At 4 s	At 5 s	At 6 s
P_{Load}	$3.956e^3$	$3.963e^3$	$6.135e^3$	$3.968e^3$	$3.964e^3$	$3.947e^3$
$P_{\text{Battery}}^{\text{a}}$	$-0.94e^4$(**C**)	$-1.06e^3$(**C**)	$-0.68e^3$(**C**)	$0.22e^3$(**D**)	$0.47e^2$ (**D**)	$3.69e^2$(**D**)
P_{Wind}	$5.774e^3$	$6.406e^3$	$6.112e^3$	$2.930e^2$	$3.682e^{-3}$	$3.738e^{-3}$
P_{Solar}	$9.546e^3$	$9.572e^3$	$7.982e^3$	$8.565e^{-6}$	$1.025e^3$	$4.387e^3$
Q_{Load}	$2.531e^{-2}$	$2.752e^{-2}$	$-7.689e^{-1}$	$4.043e^{-2}$	$3.858e^{-2}$	$4.285e^{-2}$

[a]Referred from Table 3, −Sign: Charging State (**C**) and +Sign: Discharging State (**D**)

Table 4 Overall power quality analysis of proposed grid system using FFT

T.H.D of load	Duration	Duration	Duration	Duration	Duration
	1.1–1.9 s	2.1–2.9 s	3.1–3.9 s	4.1–4.9 s	5.1–5.9 s
Va (%)	2.52	2.13	2.69	2.47	2.49
Vb (%)	2.45	2.20	2.96	2.44	2.40
Vc (%)	2.50	2.55	2.69	2.46	2.50
Ia (%)	2.52	2.13	3.05	2.27	2.49
Ib (%)	2.45	2.07	4.53	2.44	2.40
Ic (%)	2.50	2.56	4.86	2.46	2.50

These quantities further relates with the THD [11, 12] using fast Fourier transformation analysis [13]. The THD analysis based on the standard code (according to IEEE-519, necessitates limit is up to 5% for total harmonic distortion [14]) within the definite limit is shown in Table 4.

5 Conclusion

The simulation study shown that PV system and wind energy system with an emergency battery backup system is sufficiently capable to provide the continuous power for maintain the utility/load level. The overall dynamic performance of the wind–PV-battery-based hybrid grid system is achieved using fuzzy-based controller. Our simulation study achieved using fuzzy-logic-based PWM inverter with LC filter, and we can also employ the C-type filter for harmonics reduction effectively. THD analyzed using FFT toolbox to examine the harmonic behavior. The simulation results of HRES-based proposed methodology shown the overall performance and reliability of the generation units to feed the continuous power into the load. The renewable-based wind energy system and solar PV system used as significant energy sources operating with or without use of BESS to get the continuous power to the load. Our proposed methodology maintained the growth of distributed power generation in remote places such as rural areas at reasonable costs.

References

1. Praiselin WJ, Edward JB (2017) Improvement of power quality with integration of solar PV and battery storage system based micro grid operation. In: 2017 Innovations in power and advanced computing technologies (i-PACT), Vellore, pp 1–5
2. Zhao Q, Yin Z (2010) Battery energy storage research of photovoltaic power generation system in micro-grid. In: 2010 fifth international conference on critical infrastructure (CRIS), Beijing, pp 1–48
3. Sekar H, Rajashekar R, Faisal F, Ganpati R, Vijayaraghavan V (2016) Intelligent dynamic grid forecasting algorithm for a grid-connected solar PV based microgrid. In: 2016 IEEE global humanitarian technology conference (GHTC), Seattle, WA, pp 421–427
4. Saib S, Gherbi A (2015) Simulation and control of hybrid renewable energy system connected to the grid. In: 2015 5th international youth conference on energy (IYCE), Pisa, 2015, pp 1–6
5. Althomali R, Alsumiri M (2017) Improved MPPT controllers for wind generation system based on hill climbing technique. In: 2017 international conference on advanced control circuits systems (ACCS) systems & 2017 international conference on new paradigms in electronics & information technology (PEIT), Alexandria, pp 140–143
6. Zade AB, Gaikwad A, Jeevane KPM, Lohote G (2016) Hybrid solar and wind power generation with grid interconnection system for improving power quality. In: 2016 IEEE 1st international conference on power electronics, intelligent control and energy systems (ICPEICES), Delhi, pp 1–6
7. Bahari MI, Tarassodi P, Naeini YM, Khalilabad AK, Shirazi P (2016) Modeling and simulation of hill climbing MPPT algorithm for photovoltaic application. In: 2016

International symposium on power electronics, electrical drives, automation and motion (SPEEDAM), Anacapri, pp 1041–1044

8. Chang EC, Guerrero JM (2011) Fuzzy variable structure control for PWM inverters. In: 2011 IEEE international conference on fuzzy systems (FUZZ-IEEE 2011), Taipei, pp 609–613

9. MATLAB, version 9.0.0341360(R2016a). Natick, Massachusetts: The MathWorks Inc, 2016

10. Berkouk BEM, Ghennam T (2013) Control and energy management of a grid connected hybrid energy system PV-wind with battery energy storage for residential applications. In: 2013 Eighth international conference and exhibition on ecological vehicles and renewable energies (EVER), Monte Carlo, pp 1–11

11. Sinha SS, Shah J, Nerkar H (2016) Harmonics measurement using FFT algorithm in digital signal controller for smart micro-grid system. In: 2016 IEEE region 10 humanitarian technology conference (R10-HTC), Agra, pp 1–5

12. Manjesh, BR (2016) Suppression of harmonics and THD using three-level inverter with C-type filter at the output of the inverter using simulink/Matlab. In: Advances in systems, control and automation, ETAEERE-2016, pp 85–92

13. Pathak G, Singh B, Panigrahi BK, Chandra A, Al-Haddad K (2016) Wind-PV based microgrid and its synchronization with utility grid. In: 2016 IEEE international conference on power electronics, drives and energy systems (PEDES), Trivandrum, pp 1–6

14. IEEE Recommended Practice and Requirements for Harmonic Control in Electric Power Systems—Redline," in IEEE Std 519–2014 (Revision of IEEE Std 519-1992)—Redline, pp 1–213

Output Power Enhancement by Flexible Solar Panel with Optimal Solar Field

Mangila Prasad Tanwar, Anshul Agarwal and Abhishek Mishra

Abstract Most photovoltaic modules which comes for power extraction is flat and subsequently, investigate on board or plate design for photovoltaic frameworks regularly utilizes flat boards or plate. Notwithstanding, the expanded accessibility of thin-film photovoltaic modules opens up potential outcomes for the use of flexible solar cell on curve board or surfaces, including the joining of photovoltaic boards on building rooftops with twofold arch. This paper acquaints a method to analyze the power output for flexible photovoltaic modules on bended surfaces or plate and additionally an idea to organize various such modules on a surface or plate. This mix of geometry arc angle of cell and sun-based investigation gives information that is vital for area design of photovoltaic flexible curve solar panel and analyzation of power output. The calculation of the techniques which is presented is outlined with analysis, for which several parameters have been investigated in an optimized way. Maximum power generation for flexible curve panel are depends on optimal design of field area configuration where flexible curve panels will be installed and collector parameters. The power generation from the field for flexible curve solar panel has been calculated at a different curve angles. The parameter of field area design has been calculated analytically and validated in genetic algorithm (MATLAB).

Keywords Flexible curve panel · Power generation · Field area

M. P. Tanwar · A. Agarwal · A. Mishra (✉)
National Institute of Technology Delhi, New Delhi, India
e-mail: abhishekmishra@nitdelhi.ac.in

M. P. Tanwar
e-mail: akky093@gmail.com

A. Agarwal
e-mail: anshul@nitdelhi.ac.in

1   Introduction

Flexible solar panel is defined as the curvy surfaces of panel which can adopt the considered angle on board. Flexible cell is the bendable cell which can be installed on the curved surface board or plate.

The idea of smart photovoltaic modules has been investigated. The significant advantages and highlights of the proposed idea are examined. The idea of smart photovoltaic modules has been investigated as far as the conceivable power designs and the power generation [1]. Aronescu and Appelbaum [2] formulated the mathematical model to design the photovoltaic field area of panels by considering the dimension of field and radiation collector parameters [2]. Photovoltaic power yield are considered for the establishment of panels in the area where the sun radiation incident is irregular. A photovoltaic device was taken into account under probabilistic power capacity of the hourly radiation of the sun in the region of two different areas for the analyzation of I–V characteristics and to obtain solar-inclined photovoltaic electric device. Contact configuration and cell structure are studied to increase the power capacity [3]. Shading effect is analyzed on fixed tilted sun radiation absorber, and the mathematical equation is formulated. They also described the simulations for the exact tilt angle of panels and generated code to define the function in MATLAB [4]. Tang and Wu [5] analyzed the tilt angle for a stationary collector to optimize the total output energy by formulating mathematical methods.

They considered the monthly incident radiation on flat collectors for analyzing the tilt angle of solar collector in the region of China [5]. Energy generation from the panel installed in the area is considered with possible number of panels to optimize the parameters of configuration in the region of urban areas. They described the mathematical calculation for selection of depending installment parameters [6]. Geometric dimension analyzation introduced for the arrangement of the strip of cell on irregular surface. Triangular strips are introduced to investigate the surface of irregular plate or board [7]. By using the genetic algorithm technique in MATLAB, the irregular curve surface of the plates is optimized [8]. Bended solar cell is considered to operate the propeller of system and electromotor. Mathematical equation is created to study the bended solar cell [9]. Hybrid photovoltaic solar devices are designed to evaluate the average daily power generation efficiency and testing of the field [10]. Solar power-based energy generation is combined with the settled solar collector area and power capacity of the power plant. The different areas of solar panels are examined. Economic advantages of power plants are studied based on areas of different installed solar panel fields [11]. A model is described to evaluate the amount of power generation of photovoltaic solar area [12]. Zier described energy generation index to evaluate the performance in case of partial shading effect by creating binary code technique for varying photovoltaic panel arrays [13]. Sivakumar et al. [14] analyzed the evaluation and maximized the efficiency of panels based on incremental maximum power point tracker (MPPT) technique with unstraight stacked conditions. This consideration focused on rebuild and study for the assessment of the photovoltaic solar panels with unstraight stacked conditions [14].

2 Solar-Field Model

The formulation of objective function for the solar-field model [2].

$$\text{Minimum} A = \frac{\sin \theta}{\theta} \times L \times W \tag{1}$$

Subject to condition,

$$W \geq H \times K \times \cos \beta \, + \, (K - 1) \times D \tag{2}$$

But the bounds are

$$
\begin{aligned}
40 &< L < 100 \\
6 &< K < 11 \\
1 &< D < 3 \\
0^\circ &< \beta < 90^\circ
\end{aligned}
\tag{3}
$$

where

A Solar panel installment area
L Length of the field
W Width of the field
H Width of collector
β Tilt angle
K Number of rows
D Distance of rows
θ Curve angle of the panel.

The maximum power formulation for solar-field area [15].

$$\text{Max.} P = \eta \times A \times I \tag{4}$$

Bound:

$$0.15 < \eta < 0.21 \tag{5}$$

where

P Power generation
H Efficiency of panel
I Irradiation of the sun per day.

3 Genetic Algorithm Implementation

The objective function in the MATLAB is analyzed with the help of genetic algorithm. The power generation and optimum row spacing are investigated which are analyzed as below:

Table 1 shows the power generation by flexible curve panel from the optimum field area A_c = 1102.374 m^2 and panel efficiency considered between the ranges 0.15–0.21. Table 1 shows the optimum power generation of flexible curve panel at 0.21 efficiency and at curve angle θ = 15° which is P_c = 231498.54 W/day.

Table 2 shows that spacing consideration of two adjacent rows of panel, it has provided ranges $1 < D < 3$, and according to this range, the optimal solar-field area is A_c = 1092.56 m^2.

Table 3 shows the power generation by flexible curve panel from the optimum field area A_c = 1092.56 m^2 and panel efficiency considered between the ranges 0.15–0.21. Table 3 shows the optimum power generation of flexible curve panel at 0.21 efficiency and at curve angle θ = 20° which is P_c = 229437.6 W/day.

Table 4 shows that spacing consideration of two adjacent rows of panel, it has provided ranges $1 < D < 3$, and according to this range, the optimal solar-field area is A_c = 1079.96 m^2.

Table 5 shows the power generation by flexible curve panel from the optimum field area A_c = 1079.96 m^2 and panel efficiency considered between the ranges 0.15–0.21. Table 5 shows the optimum power generation of flexible curve panel at 0.21 efficiency and at curve angle θ = 25° which is P_c = 226791.6 W/day.

Table 1 Power generation from the field of flexible panel at curve angle θ = 15°

η_c	A_c (m^2)	I (W/m^2)	P_c (W)
0.15	1102.374	1000	165356.1
0.16	1102.374	1000	176379.6
0.17	1102.374	1000	187403.6
0.18	1102.374	1000	198427.3
0.19	1102.374	1000	209451.1
0.2	1102.374	1000	220474.8
0.21	**1102.374**	**1000**	**231498.5**

The bold values in the table represents the best optimized parameters for maximum power generation in solar panel

Table 2 Optimum row spacing at curve angle θ = 20°

L_c (m)	H_c (m)	K	β	D (m)	A_c (m^2)
40	**1.984**	**11**	**35**	**1**	**1092.56**
40	1.984	11	35	1.5	1288.52
40	1.984	11	35	2	1484.48
40	1.984	11	35	2.5	1680.44
40	1.984	11	35	3	1876.4

The bold values in the table represents the best optimized parameters for maximum power generation in solar panel

**Table 3** Power generation from the field of flexible panel at curve angle $\theta = 20°$

η_c	A_c (m^2)	I (W/m^2)	P_c (W)
0.15	1092.56	1000	163884
0.16	1092.56	1000	174809.6
0.17	1092.56	1000	185735.2
0.18	1092.56	1000	196660.8
0.19	1092.56	1000	207586.4
0.2	1092.56	1000	218512
0.21	**1092.56**	**1000**	**229437.6**

The bold values in the table represents the best optimized parameters for maximum power generation in solar panel

Table 4 Optimum row spacing at curve angle $\theta = 25°$

L_c (m)	H_c (m)	K	β	D (m)	A_c (m^2)
40	**1.984**	**11**	**35**	**1**	**1079.96**
40	1.984	11	35	1.5	1273.66
40	1.984	11	35	2	1467.36
40	1.984	11	35	2.5	1661.06
40	1.984	11	35	3	1854.76

The bold values in the table represents the best optimized parameters for maximum power generation in solar panel

Table 5 Power generation from the field of flexible panel at curve angle $\theta = 25°$

η_c	A_c (m^2)	I (W/m^2)	P_c (W)
0.15	1079.96	1000	161,994
0.16	1079.96	1000	172793.6
0.17	1079.96	1000	183593.2
0.18	1079.96	1000	194392.8
0.19	1079.96	1000	205192.4
0.2	1079.96	1000	215,992
0.21	**1079.96**	**1000**	**226791.6**

The bold values in the table represents the best optimized parameters for maximum power generation in solar panel

Table 6 shows that spacing consideration of two adjacent rows of panel, it has provided ranges $1 < D < 3$, and according to this range, the optimal solar-field area is $A_c = 1046.95$ m^2.

Table 7 shows the power generation by flexible curve panel from the optimum field area $A_c = 1046.95$ m^2 and panel efficiency considered between the ranges 0.15–0.21. Table 7 shows the optimum power generation of flexible curve panel at 0.21 efficiency and at curve angle $\theta = 30°$ which is $P_c = 219859.5$ W/day.

Table 8 shows the power generation by flexible curve panel from the optimum field area $A_c = 1065.018$ m^2 and panel efficiency considered between the ranges

Table 6 Optimum row spacing at $\theta = 30°$

L_c (m)	H_c (m)	K	β	D (m)	A_c (m^2)
40	**1.984**	**11**	**35**	**1**	**1046.95**
40	1.984	11	35	1.5	1234.73
40	1.984	11	35	2	1422.51
40	1.984	11	35	2.5	1610.29
40	1.984	11	35	3	1798.07

The bold values in the table represents the best optimized parameters for maximum power generation in solar panel

Table 7 Power generation from the field of flexible panel at curve angle $\theta = 30°$

η_c	A_c (m^2)	I (W/m^2)	P_c (W)
0.15	1046.95	1000	157042.5
0.16	1046.95	1000	167512
0.17	1046.95	1000	177981.5
0.18	1046.95	1000	188451
0.19	1046.95	1000	198920.5
0.2	1046.95	1000	209390
0.21	**1046.95**	**1000**	**219859.5**

The bold values in the table represents the best optimized parameters for maximum power generation in solar panel

Table 8 Power generation from the field of flexible panel at $\theta = 35°$

η_c	A_c (m^2)	I (W/m^2)	P_c (W)
0.15	1065.018	1000	159752.7
0.16	1065.018	1000	170402.9
0.17	1065.018	1000	181052.1
0.18	1065.018	1000	191703.2
0.19	1065.018	1000	202353.4
0.2	1065.018	1000	213003.6
0.21	**1065.018**	**1000**	**223653.8**

The bold values in the table represents the best optimized parameters for maximum power generation in solar panel

0.15–0.21. Table 8 shows the optimum power generation of flexible curve panel at 0.21 efficiency and at curve angle $\theta = 35°$ which is $P_c = 223653.8$ W/day.

Table 9 shows that spacing consideration of two adjacent rows of panel, it has provided ranges $1 < D < 3$, and according to this range, the optimal solar-field area is $A_c = 1026.65$ m^2.

Table 10 shows the power generation by flexible curve panel from the optimum field area $A_c = 1026.65$ m^2 and panel efficiency considered between the ranges 0.15–0.21. Table 10 shows the optimum power generation of flexible curve panel at 0.21 efficiency and at curve angle $\theta = 40°$ which is $P_c = 215596.5$ W/day.

Table 9 Optimum row spacing at curve angle $\theta = 40°$

L_c (m)	H_c (m)	K	β	D (m)	A_c (m^2)
40	**1.984**	**11**	**35**	**1**	**1026.65**
40	1.984	11	35	1.5	1210.8
40	1.984	11	35	2	1394.94
40	1.984	11	35	2.5	1579.08
40	1.984	11	35	3	1763.22

The bold values in the table represents the best optimized parameters for maximum power generation in solar panel

Table 10 Power generation from the field of flexible panel at curve angle $\theta = 40°$

η_c	A_c (m^2)	I (W/m^2)	P_c (W)
0.15	1026.65	1000	153997.5
0.16	1026.65	1000	164,264
0.17	1026.65	1000	174530.5
0.18	1026.65	1000	184,797
0.19	1026.65	1000	195063.5
0.2	1026.65	1000	205,330
0.21	**1026.65**	**1000**	**215596.5**

The bold values in the table represents the best optimized parameters for maximum power generation in solar panel

Table 11 shows the power generation by flexible curve panel from the optimum field area $A_c = 1003.577$ m^2 and panel efficiency considered between the ranges 0.15–0.21. Table 11 shows the optimum power generation of flexible curve panel at 0.21 efficiency and at curve angle $\theta = 45°$ which is $P_c = 210751.3$ W/day.

Figure 1 shows the optimal field area for flexible curve solar panel. Plot generated in genetic algorithm is based on considered bounds for objective function.

Figure 2 shows the optimum power generation at optimal field area for flexible curve solar panel. Plot generated in genetic algorithm is based on considered bounds for objective function.

Table 11 Power generation from the field of flexible panel at curve angle $\theta = 45°$

η_c	A_c (m^2)	I (W/m^2)	P_c (W)
0.15	1003.577	1000	150536.6
0.16	1003.577	1000	160572.4
0.17	1003.577	1000	170608.2
0.18	1003.577	1000	180643.9
0.19	1003.577	1000	190679.7
0.2	1003.577	1000	200715.5
0.21	**1003.577**	**1000**	**210751.3**

The bold values in the table represents the best optimized parameters for maximum power generation in solar panel
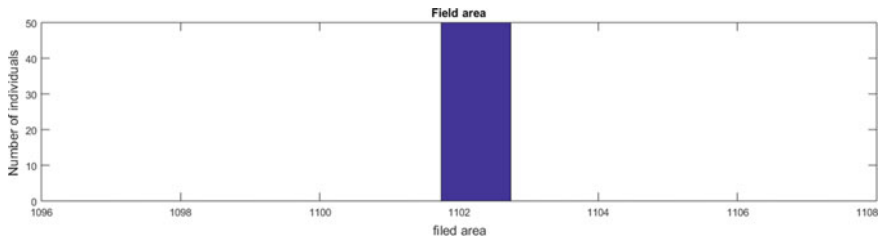
Fig. 1 Optimal field area
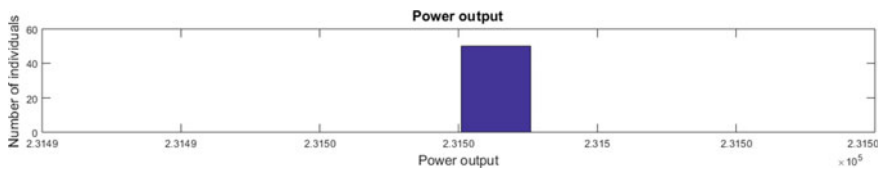
Fig. 2 Optimal power generation

4   Comparison of Power Generation for Flexible Curve Panel

Figure 3 depicts the power generation by optimizing the field area for flexible curve panel at a different curve angles of curve panel by providing the ranges of efficiency based on analytical calculations. The different cases of flexible curve panel are analyzed to compare the power generation from field area. According to the curve angles of curve panel, the optimized area of $A_c = 1102.374$ m^2 and the optimum power generation from the field of flexible panel $P_c = 231498.5$ W/day. The figure depicts the optimum power generation of the flexible curve panel field compared to all considered cases of flexible curve panel field. The optimum value of field area for flexible panel and power generation is validated by using the genetic algorithm (MATLAB).

Fig. 3 Comparison of power output
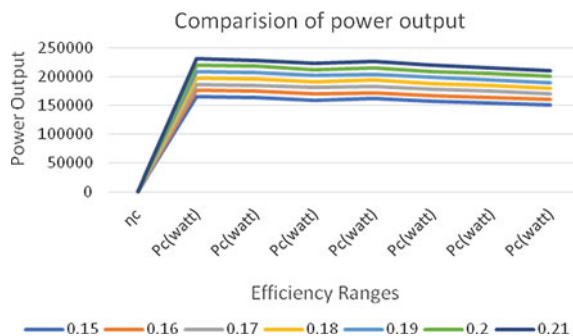
5 Conclusion

This study presents the optimal area design for flexible curve panels by considering field and panel parameters and optimal power generation by considering efficiency ranges of panel, optimum area for the field of curve panels, and radiation from the sun. Some factors are analyzed which can maximize the power generation based on optimization of depending variables. The field area for flexible curve panels is optimized by using genetic algorithm in MATLAB. The analyzation is focused on the power generation of flexible curve solar panel with optimum field area considerations.

References

1. Mazumdar P, Enjeti PN, Balog RS (2012) Smart PV modules—design considerations. In: IEEE international conference on power electronics, drives and energy systems (PEDES), pp 1–6
2. Aronescu A, Appelbaum J (2017) Design optimization of photovoltaic solar fields-insight and methodology. Renew Sustain Energy Rev 882–893
3. Zulkifli NA, Razali NMM, Marsadek M, Ramasamy AK (2014) Probabilistic analysis of solar photovoltaic output based on historical data. In: IEEE 8th international power engineering and optimization conference (PEOCO), pp 133–137
4. Sadineni SB, Boehm RF, Hurt R (2008) Spacing analysis of an inclined solar collector field. In: ASME 2008 2nd international conference on energy sustainability collocated with the heat transfer. Fluids engineering, and 3rd energy nanotechnology conferences, pp 417–422
5. Tang R, Wu T (2004) Optimal tilt-angles for solar collectors used in China. Appl Energy 239–248
6. Rachchh R, Kumar M, Tripathi B (2016) Solar photovoltaic system design optimization by shading analysis to maximize energy generation from limited urban area. Energy Convers Manage 244–252
7. Groenewolt A, Bakker J, Hofer J, Nagy Z, Schlüter A (2016) Methods for modelling and analysis of bendable photovoltaic modules on irregularly curved surfaces. Int J Energy Environ Eng 261–271
8. Cheng Sheng (2009) Curved photovoltaic surface optimization for BIPV: an evolutionary approach based on solar radiation simulation. UCL (University College London), PhD diss
9. Su J, Song B (2008) Curved surface renewable solar cell applied to near space airship energy system. In: Electrical machines and systems, pp 2621–2626
10. Hsu P-C, Huang B, Wu P, Wu W, Lee M, Yeh J, Wang Y, Tsai J, Li K, Lee K (2017) Long-term energy generation efficiency of solar PV system for selfconsumption. Energy Proc 91–95
11. Huang C, Hou H, Hu E, Liang M, Yang Y (2017) Impact of power station capacities and sizes of solar field on the performance of solar aided power generation. Energy 667–679
12. Cook T, Shaver L, Arbaje P (2018) Modeling constraints to distributed generation solar photovoltaic capacity installation in the US Midwest. Appl Energy 1037–1050

13. Ziar H, Mansourpour S, Salimi A, Afjei E (2011) Analysis of shadow effect in photovoltaic arrays using binary coding method. In: Electric power and energy conversion systems (EPECS)
14. Sivakumar P, Kader AA, Kaliavaradhan Y, Arutchelvi M (2015) Analysis and enhancement of PV efficiency with incremental conductance MPPT technique under nonlinear loading conditions, pp 543–550
15. Lan H, Dai J et al (2015) Optimal tilt angle of photovoltaic arrays and economic allocation of energy storage system on large oil tanker ship 11515–11530

Enhancement of the Voltage Profile for an IEEE-14 Bus System by Using FACTS Devices

Faiz Ahmad

Abstract The voltage instability is one of the major problems in the power system network. Voltage collapse due to instability causes the system voltage to dip to such a value which is not acceptable for stable operation and not capable to recover, which leads to interruption to the supply in the system. Developments in the field of FACTS devices have paved the way to mitigate the problem of voltage instability in the power system network. They also enable the flexible operation of the power system. In the present work, I have simulated Standard IEEE-14 Bus model with standard test data using PSAT software and obtained the results. Then I have increased the reactive load in the system by 5, 10, and 20% in succession, and on comparing the results I have found that Bus 9 and Bus 14 are the weakest buses in the system and hence more prone to the voltage collapse. The FACTs devices have been connected to the buses which are the weakest in the system to improve the voltage stability problem.

Keywords FACTS · PSAT · Voltage stability

1 Introduction

Voltage stability of the power system has been acknowledged as a significant problem for stable system operation for many decades [1]. There are many instances of major blackouts in the power system caused instability problems have proven the importance of the voltage instability phenomenon [2]. A number of blackouts have been listed in the past due to voltage instability. Instability in the voltage causes the voltage to fall to such a level from which it is not capable to make progress leading to

F. Ahmad (✉)
Electrical Engineering Department,
Muzaffarpur Institute of Technology, Muzaffarpur, India
e-mail: faizahmad831@gmail.com

disruption in power supply [3]. Recent developments in the field of FACTS devices have paved the way to mitigate the problem of voltage instability in the power system. They also enable flexible operation of the power system [4].

2 PSAT

PSAT stands for power system analysis toolbox. It is based on MATLAB, which is a extremely useful tool for sparse matrix functions and vectorized computations to optimize the performances. To carry out precise and complete analysis of power system, it supports various models of static as well as dynamic systems [5].

3 IEEE-14 Bus Model

Figure 1 shows IEEE 14 Bus power system topology as a single-line diagram. It comprises of two alternators using IEEE type 1 exciters—three synchronous compensators which are exclusively used for the compensation of reactive power. A total of 11 loads are connected at different buses in the system [6].

The PSAT programs have been used to achieve *P-V* curve and voltage profile of different buses of the standard IEEE 14 Bus power system [7, 8].

4 Simulation Model and Results at Base Load

See Fig. 2.

The results found by simulating the model shown in Fig. 2 with PSAT are provided in Figs. 3 and 4.

5 Results on Increasing Reactive Load

Figures 5, 6, and 7 give voltage profiles of different buses at 5, 10, and 20% overloading, respectively.

From Table 1, it is clear that voltage variations are most in the case of Bus 14 and Bus 9. Thus, Bus 14 and Bus 9 are the weakest buses in the system and are more prone to voltage collapse. Hence, a special protection scheme using FACTS devices is incorporated to avoid voltage instability in the system.
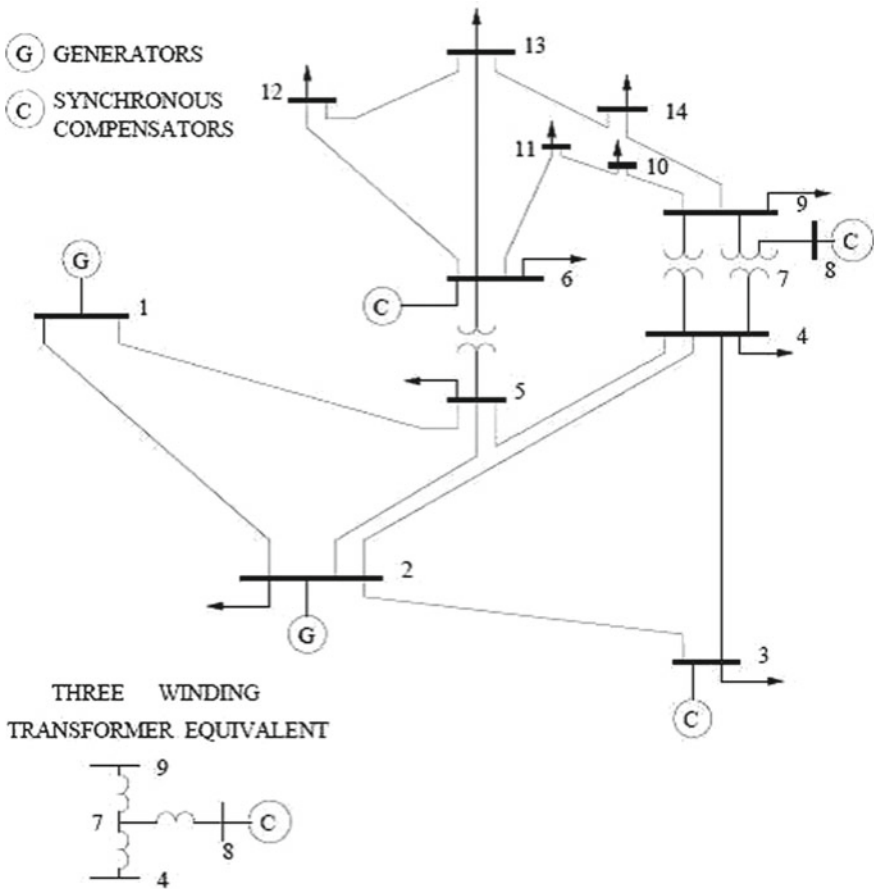
Fig. 1 IEEE 14-bus test system

6 Voltage Profile Enhancement Using SVC

The simulation model of Standard IEEE-14 Bus power system incorporating SVC at bus number 14 is shown in Fig. 8.

The results of Fig. 8 simulation model are shown in Figs. 9 and 10.

7 Voltage Profile Enhancement Using STATCOM

The simulation model of Standard IEEE-14 Bus power system incorporating SVC at bus number 14 is shown in Fig. 11.
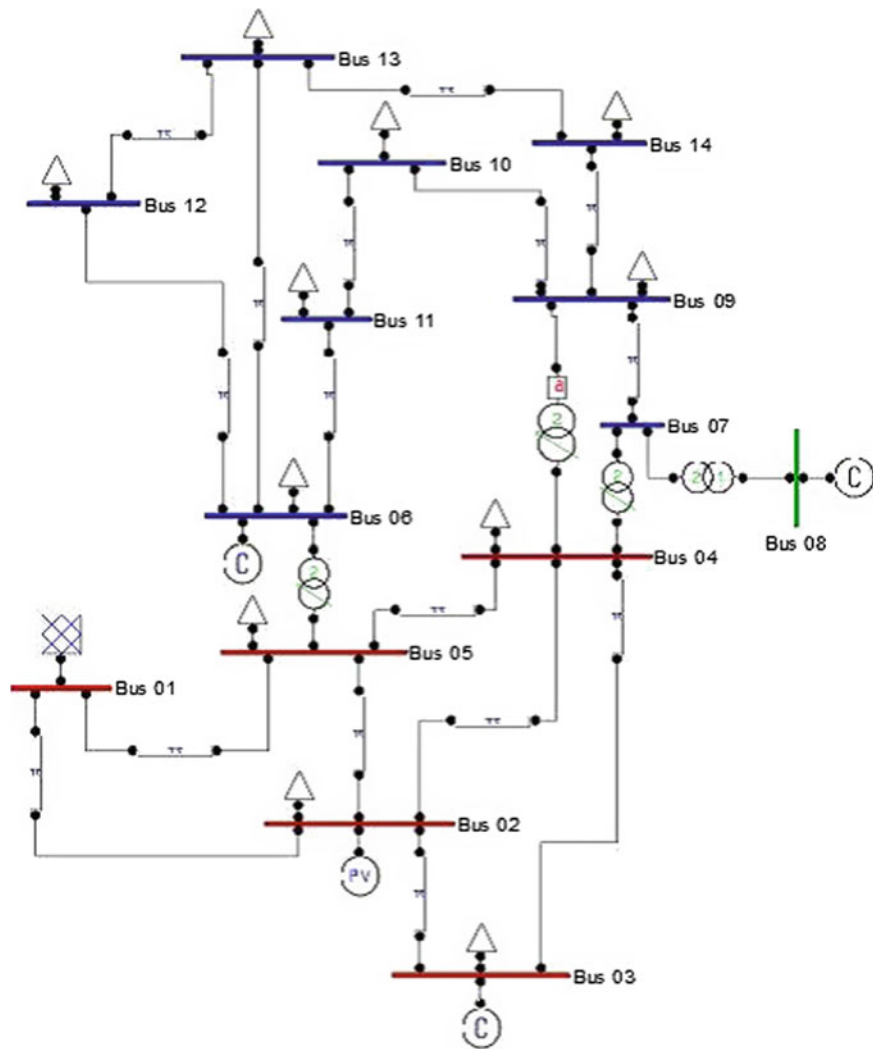
Fig. 2 Simulink model for IEEE 14 bus system
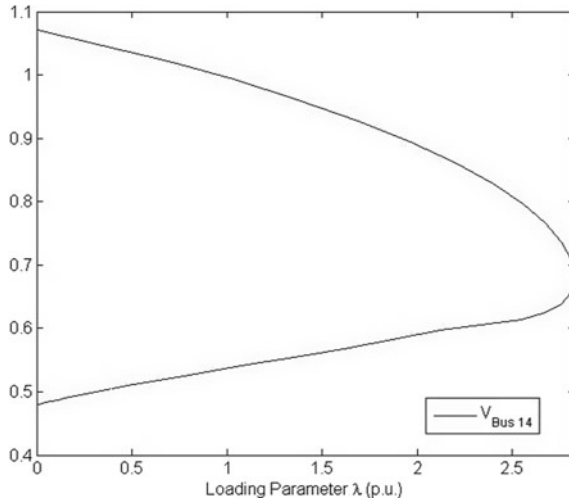
Fig. 3 Voltage bus 14 versus loading parameter. Maximum loading parameter (λ) = 2.904
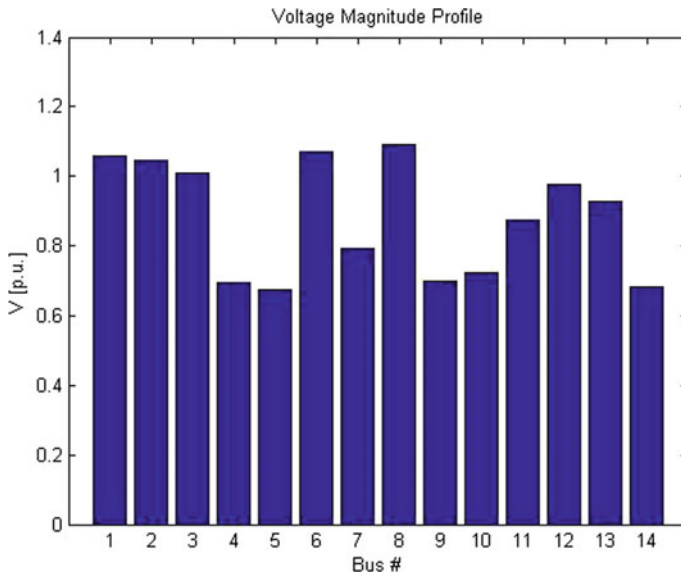
Fig. 4 Voltage profile of system at base load
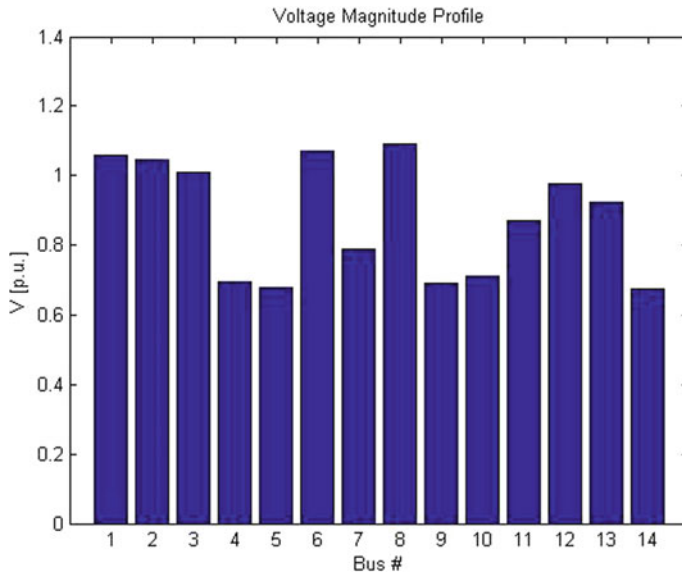
Fig. 5 Voltage profile at 5% overload
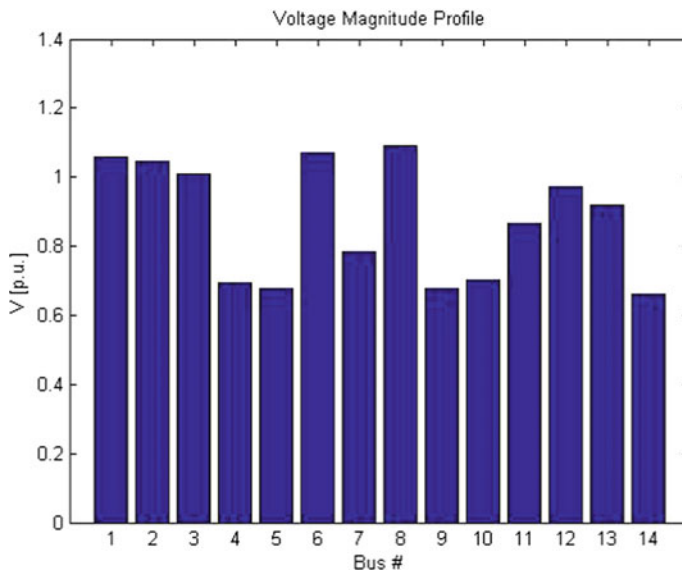
Fig. 6 Voltage profile at 10% overload
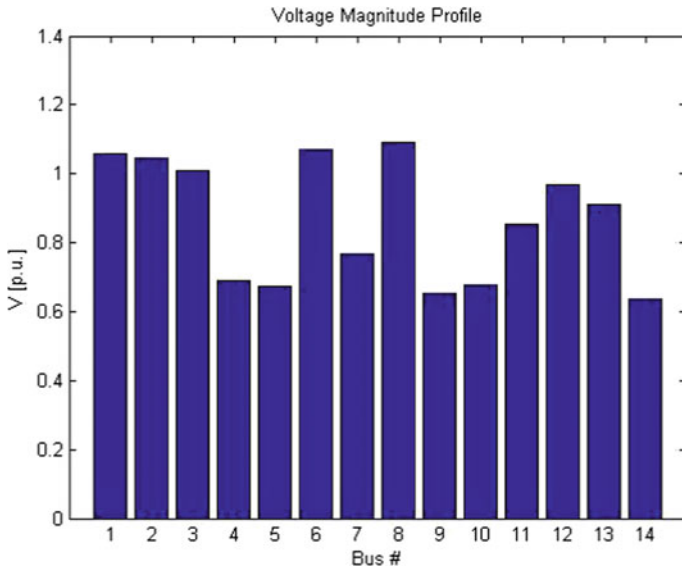
Fig. 7 Voltage profile at 20% overload

Table 1 Results obtained by varying reactive load standard IEEE-14 Bus simulation model

Bus voltage	Base case	Set 1 (5%)	Set 2 (10%)	Set 3 (20%)
V_1	1.060	1.060	1.060	1.060
V_2	1.045	1.045	1.045	1.045
V_3	1.010	1.010	1.010	1.010
V_4	0.688	0.694	0.692	0.681
V_5	0.665	0.677	0.676	0.667
V_6	1.070	1.070	1.070	1.070
V_7	0.837	0.787	0.782	0.740
V_8	1.090	1.090	1.090	1.090
V_9	0.797	0.688	0.677	0.598
V_{10}	0.806	0.712	0.701	0.624
V_{11}	0.918	0.870	0.864	0.822
V_{12}	1.010	0.974	0.972	0.957
V_{13}	0.993	0.922	0.919	0.894
V_{14}	0.984	0.672	0.660	0.576

Fig. 8 Simulation model of IEEE-14 Bus system with SVC
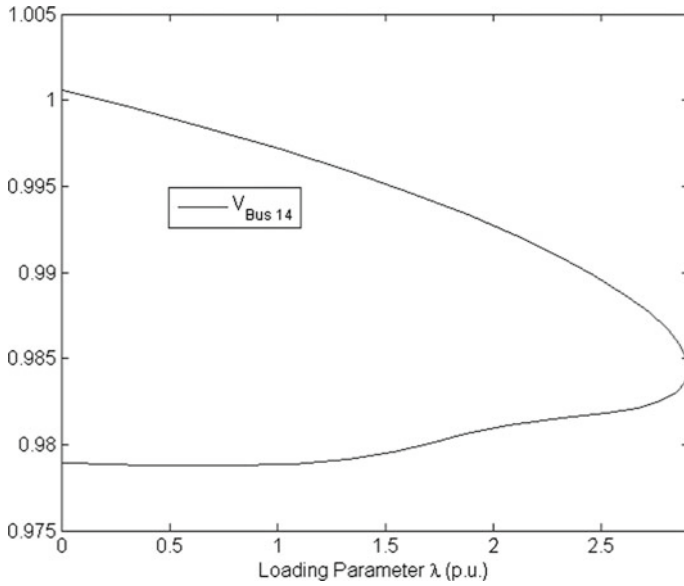
Fig. 9 Voltage bus 14 versus loading parameter. Maximum loading parameter (λ) = 2.908
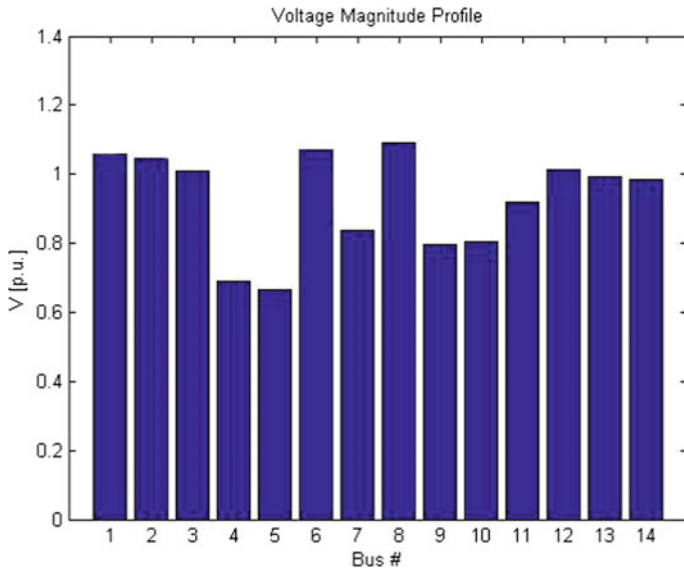
Fig. 10 Voltage profile at different buses
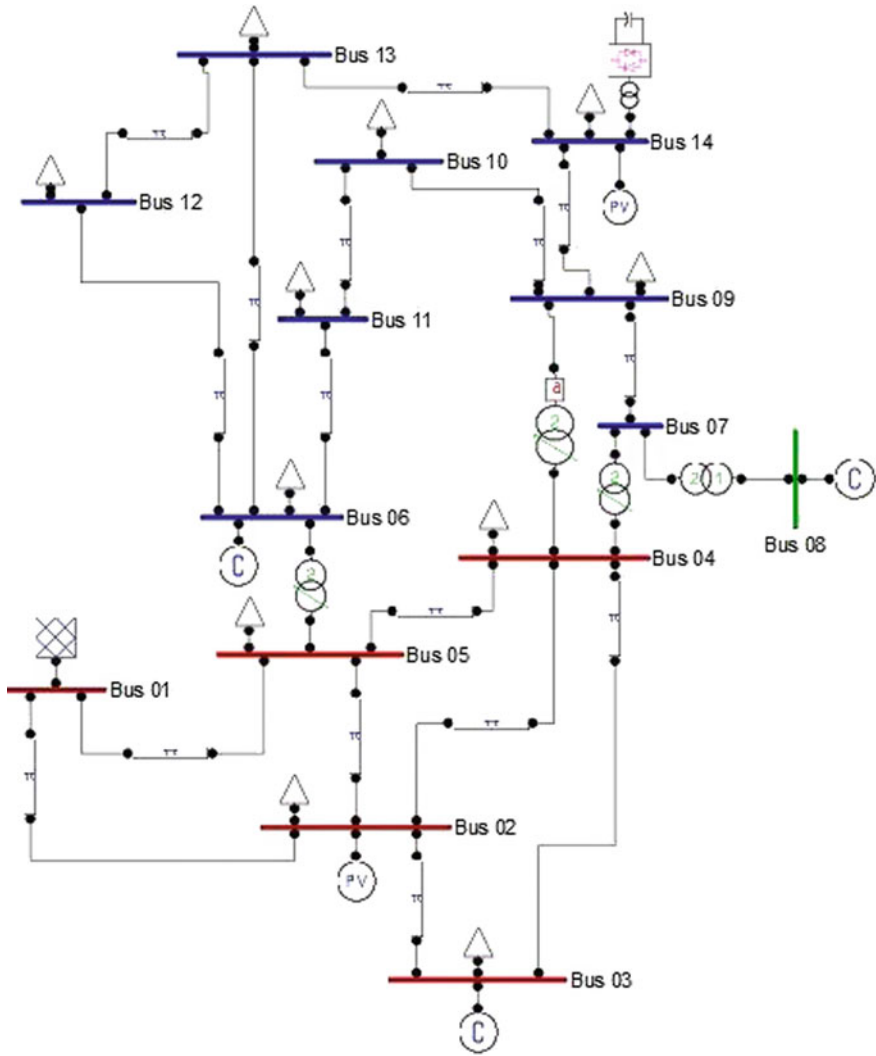
Fig. 11 Simulation model of IEEE-14 Bus system with STATCOM
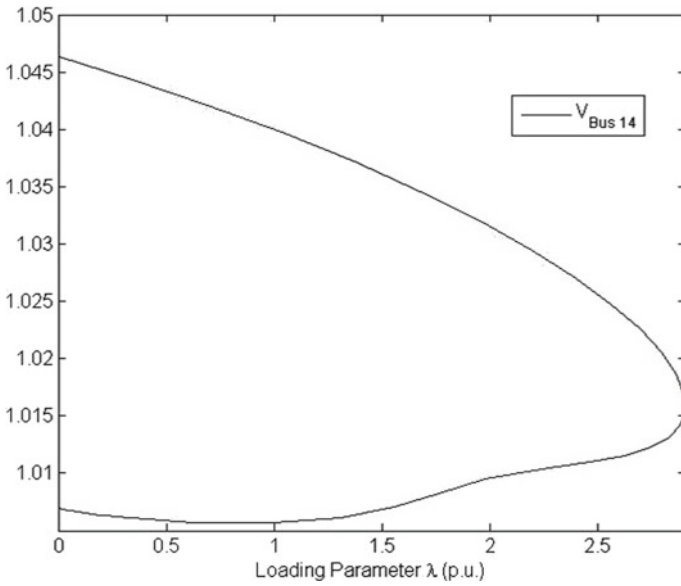
Fig. 12 Voltage bus 14 versus loading parameter. Maximum loading parameter (λ) = 2.904
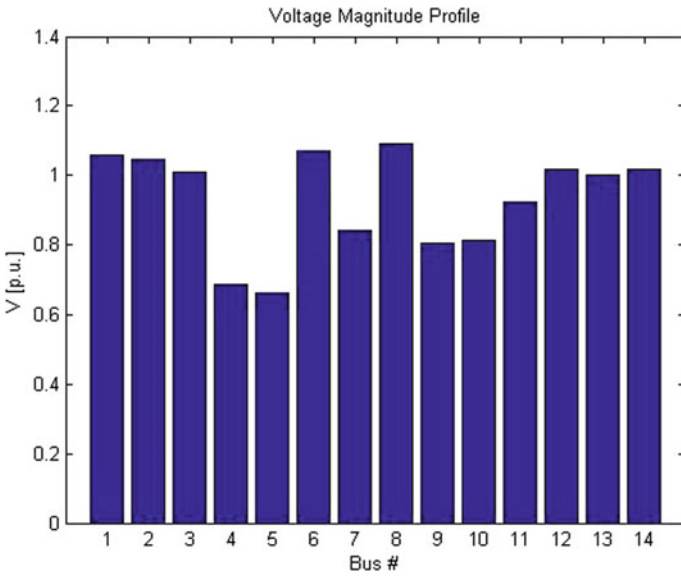
Fig. 13 Voltage profile at different buses

The results of the simulation of Fig. 11 Simulink model are shown in Figs. 12 and 13.

8   Voltage Profile Enhancement Using UPFC

The simulation model of Standard IEEE-14 Bus power system incorporating SVC at bus number 14 is shown in Fig. 14.

The results of the simulation of Fig. 14 Simulink model are shown in Figs. 15 and 16.
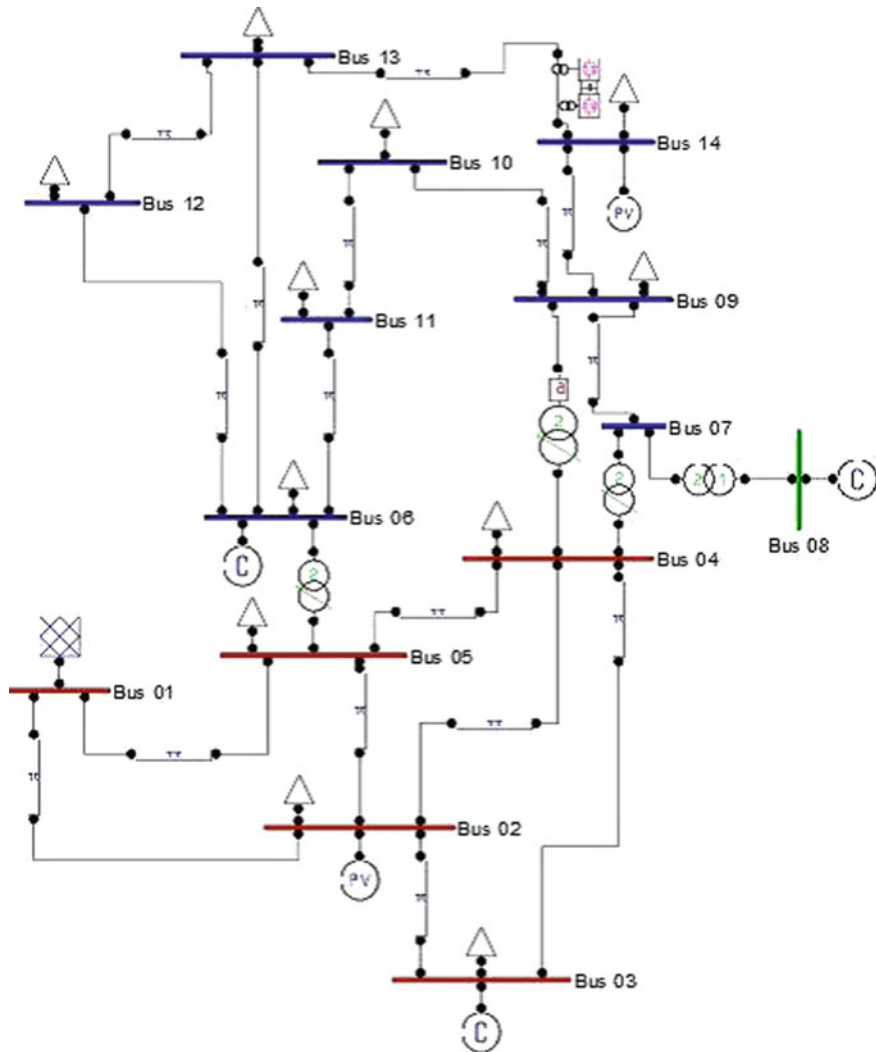
Fig. 14 Simulation model of IEEE-14 Bus model incorporating UPFC
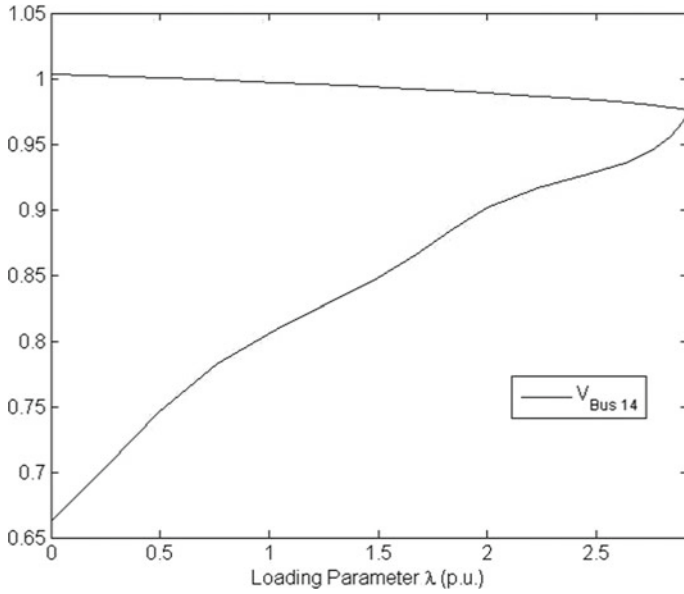
Fig. 15 Voltage bus 14 versus loading parameter. Maximum loading parameter (λ) = 2.917
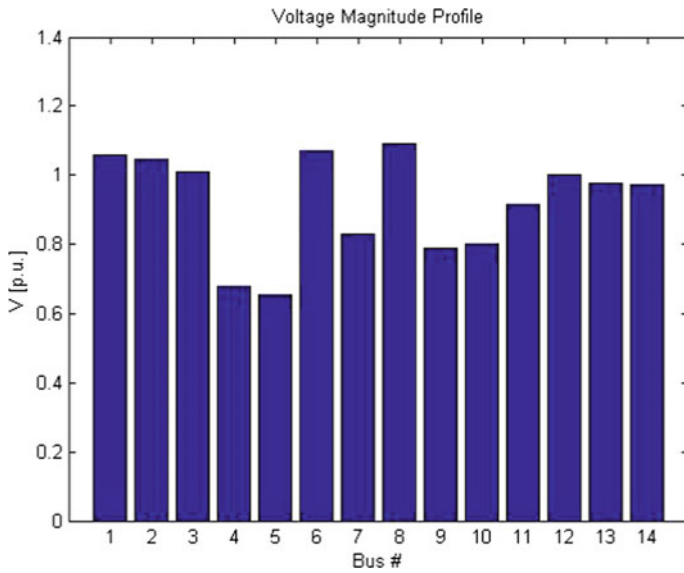
Fig. 16 Voltage profile at different buses

Table 2 Voltages at different buses under different FACTS devices

Bus No.	V (p.u.) without FACTS	V (p.u.) SVC	V (p.u.) STATCOM	V (p.u.) UPFC
1	1.06	1.06	1.06	1.06
2	1.045	1.045	1.045	1.045
3	1.01	1.01	1.01	1.01
4	0.692	0.688	0.685	0.677
5	0.675	0.665	0.660	0.651
6	1.07	1.07	1.07	1.07
7	0.791	0.837	0.839	0.831
8	1.09	1.09	1.09	1.09
9	1.697	0.797	0.806	0.789
10	0.720	0.806	0.813	0.799
11	0.875	0.918	0.922	0.915
12	0.976	1.01	1.01	1.001
13	0.925	0.993	0.999	0.974
14	0.681	0.984	1.015	0.973

Table 3 Maximum loading parameter (λ_{max}) under different FACTS devices

	Base model without FACTS	SVC	STATCOM	UPFC
$\lambda_{maximum}$	2.8286	2.908	2.917	2.917

9   Comparison of Results with and without Facts Devices

See Tables 2 and 3.

10   Conclusion

It is clear from Table 1 that on increasing the reactive load on Standard IEEE-14 Bus model, the voltage profile at bus 14 and bus 9 is the most affected. Hence, bus 14 and bus 9 are the weakest buses in the system and are more prone to voltage collapse. To avoid voltage collapse and hence the failure of the system, special protection scheme by employing FACTS devices is incorporated into these buses. Tables 2 and 3 show the results obtained under different FACTS devices. Table 2 clearly shows that the voltage profile at weakest buses has improved significantly. From Table 3, I see that the maximum loading parameter (λ_{max}) has improved after employing FACTS devices at the weakest bus.

References

1. Ghahremani E, Kamwa I (2013 May) Optimal placement of multiple type FACTS devices to maximize power system loadability using a generic graphical user interphase. IEEE Trans Power Syst 28(2):764–777
2. Basavaraja B, Sathish Kumar K, Sank er ram BV (2014) Optimal placement of FACTS devices with available transfer capability enhancement. In: IEEE Conference 2014. 978-1-4799-4103-2/14
3. Anand B, Ebenezer Jeyakumar A (2011) Load frequency control of interconnected hydro system with fuzzy logic controller. In: International conference on process automation control and computing
4. Musunuri S, Dehnavi G (2010) Comparison of STATCOM, SVC, TCSC, and SSSC performance in steady state voltage stability improvement. In: North American power symposium 2010
5. Milano F (2005 Aug) An open source power system analysis toolbox. IEEE Trans Power Syst 20(3)
6. Kumar S, Kumar A, Sharma NK (2015) Analysis of power flow continuous power flow and transient stability of IEEE-14 bus integrated wind farm using PSAT. In: International Conference on Energy Economics and Environment (ICEEE) (ICEEE) IEEE, pp 1–6, 27–28 Mar 2015
7. Nanda J, Mishra S, Saikia LC (2009) Maidan application of bacterial foraging-based optimization technique in multi area automatic generation control. IEEE Trans Power Syst 24 (2):602–609
8. Nanda J, Mangla A, Suri S (2006) Some new findings on automatic generation control of an interconnected hydro thermal system with conventional controller. IEEE Trans Energy Convers 21(1):187–194

Tremor Observer Models and Tremor Rejection Methods for Robotic Surgery

Harish Parthasarathy, Vijyant Agarwal and Ritika Agarwal

Abstract In this work, tremor is treated as disturbance, and a very general kind of disturbance observer based on Lyapunov energy theory has been proposed for robotic disturbance estimator and more generally for nonlinear state variable systems. The disturbance observer dynamics is based on the instantaneous state and not on its derivative. This guarantees easy implementation.

Keywords Tremor · Disturbance · Lyapunov energy

1 Introduction

Here, we describe the general kind of disturbance observer used in nonlinear systems and more specifically in robotics based on the idea investigated in [1, 2]. A flexible and simple solution to inverse kinematics and trajectory planning with performance criteria for a redundant manipulator through modification in fuzzy c-means is proposed in [3]. A generalized linear feedback matrix is investigated in [4] for robotics to track the wanted trajectory in the presence of stochastic noise. The proposed algorithm builds from Itos stochastic calculus to minimize the conditional expectation of the instantaneous error energy differential with respect to the feedback matrix subject to energy constraints. A method to track and reject disturbances changing with time is proposed in [5], using only joint position variables, unlike other works where derivative of position variables is also needed. The overall master–slave dynamical system is abstracted in [6], into a stochastic delay

H. Parthasarathy · V. Agarwal (✉)
Netaji Subhas University of Technology, Dwarka 110078, New Delhi, India
e-mail: vijaynt.agarwal@gmail.com

H. Parthasarathy
e-mail: harisignal@yahoo.com

R. Agarwal
ABV IIITM, Gwalior, India
e-mail: ritikaagarwal646@gmail.com

differential system with random fluctuations in the parameters. This system is then changed into a common stochastic differential system with an infinite dimensional state vector. The stochastic environment force is specified in [7] by obtaining the maximum likelihood estimate (MLE) of controller-gain parameters $\widehat{\mathbf{K}}$ of the slave robot. Lyapunov method has been used in [8] to examine the stability and convergence of state, disturbance, and parametric estimates of a robot. The idea for the design of the disturbance observer is that its governing differential equations should be based on only the instantaneous angular position and velocity of the robot or equivalently only on the current state of the nonlinear system governed by the state variable dynamics. It should not involve the acceleration of the robot or equivalently, the derivative of the state of the nonlinear system. Without taking into account random noise in the state dynamics, we evaluate the rate of change of the Lyapunov energy of the disturbance estimation error and derive conditions under which this error converges to zero as time goes to ∞ under the condition that in this asymptotic limit, the disturbance converges to a constant DC level. After taking random noise into account, we evaluate the performance in the sense of mean value of the rate of change of the Lyapunov energy and study conditions under which this value is asymptotically bounded.

2 Proposed Method

Consider the robot system

$$M(q)q'' + N(q, q') = \tau(t) + d(t) + w(t) \tag{1}$$

where q is the angular position vector of the links, τ is the external torque, d is the disturbance, and w is WGN. Consider the equations

$$\hat{d}(t) = z(t) + p(q'(t)), \tag{2}$$

$$z'(t) = L(q(t), q'(t))\big(\tau(t) - N(q(t)\, q'(t)) - \hat{d}(t)\big) \tag{3}$$

Then, we have

$$\begin{aligned}
\hat{d}'(t) &= L\big(N - \tau - \hat{d}\big) + p'(q')q'' \\
&= L\big(N - \tau - \hat{d}\big) + p'(q')M(q)^{-1}(\tau - N + d + w)
\end{aligned} \tag{4}$$

Choosing

$$L = p'(q')M(q)^{-1} \tag{5}$$

we get

$$\hat{d}'(t) = L\big(d - \hat{d} + w\big) \tag{6}$$

Assume that

$$w_1 = d - \hat{d} \tag{7}$$

is WGN. Then writing $\varepsilon = w_1 + w$, it follows that ε is also WGN. So our system of equations for the state and disturbance observer after disturbance rejection becomes

$$M(q)q'' + N(q, q') = \tau + d - \hat{d} + w = \tau + \varepsilon, \hat{d}' = L(q, q')\varepsilon \tag{8}$$

and the EKF can be applied to this system. Consider a system in the general form:

$$x'(t) = f(t, x(t)) + d(t) + w(t) \tag{9}$$

where $x(t), d(t), w(t) \in R^n$. The explicit dependence of f on time arises because of a known input. d is the disturbance, and w is WGN. We design the disturbance observer as follows:

$$\hat{d}(t) = z(t) + p(x(t)) \tag{10}$$

where

$$z'(t) = -L(t, x(t))\big(f(t, x(t)) + \hat{d}(t)\big) \tag{11}$$

Then, we get

$$\hat{d}'(t) = p'(x(t)((f(t, x(t)) + d(t) + w(t)) - L(t, x(t))\big(f(t, x(t)) + \hat{d}(t)\big) \tag{12}$$

Assume that

$$L(t, x(t)) = p'(x(t)) \tag{13}$$

Then,

$$\hat{d}'(t) = p'(x(t))\big(d(t) - \hat{d}(t) + w(t)\big) \tag{14}$$

which is appropriate for a disturbance observer provided that $p'(x(t))$ is positive definite.

Lyapunov energy-based disturbance observer: Let $w(t) = 0$ and define

$$V(t) = (1/2)(d(t) - \hat{d}(t))^{\mathrm{T}} J(x(t)) (d(t) - \hat{d}(t)) \tag{15}$$

Then,

$$V'(t) = -(1/2)(d(t) - \hat{d}(t))^{\mathrm{T}} \left[K(x(t))^{\mathrm{T}} J(x(t)) + J(x(t)) K(x(t)) \right.$$
$$\left. - \sum_i J_{,i}(x(t)) x_{i'}(t) \right] (d(t) - \hat{d}(t)) \tag{16}$$

where

$$K(x) = p'(x) \tag{17}$$

and we neglect $d'(t)$, i.e., at large times, the disturbance is nearly a DC disturbance. Let $\max_{i,t} x_{i'}(t) = v$ and $\min_{i,t} x_{i'}(t) = u$. Then, if we can ensure that $J(x)$ is positive definite and simultaneously

$$K(x)^{\mathrm{T}} J(x) + J(x) K(x) - \sum_i v_i J_{,i}(x) \tag{18}$$

is positive definite, where each v_i is either v or u, then our disturbance observer will converge to the true disturbance. More precisely, for the rate of change of the Lyapunov energy to be negative, it is sufficient that

$$K(x)^{\mathrm{T}} J(x) + J(x) K(x) - v_0 \left(\sum_i \| J_{,i}(x) \| \right) I \geq 0 \tag{19}$$

where $\|\cdot\|$ is the spectral norm of matrices and $v_0 = \max_{i,t} |x_i(t)|$.

3 Conclusion

Using the Lyapunov energy method, a general kind of disturbance observer was designed based on the instantaneous state of a nonlinear dynamical system and applied to the robotic dynamics. The disturbance observer guarantees that in the absence of noise, and the condition that the disturbance converges to a constant DC value, the disturbance error will converge to zero. In the presence of random noise, we need to make an analysis of the ensemble averaged Lyapunov energy rate of change. This is the future scope of work.

References

1. Li S, Yang J, Chen W-H, Chen X (2014) Disturbance observer-based control. CRC Press, pp 283–284
2. Agrawal V, Parthasarathy H (2016) Disturbance estimator as a state observer with extended Kalman filter for robotic manipulator. Nonlinear Dyn 84(4):2809–2825
3. Agarwal V (2012) Trajectory planning of redundant manipulator using fuzzy clustering method. Int J Adv Manuf Technol (Springer; Impact factor 1.5) 61:727–744
4. Nagpal N, Agarwal V, Bhushan B (2018) Real time state observer based controller for stochastic robotic manipulator. IEEE Trans Ind Appl 54(2):1806–1822
5. Agrawal V, Parthasarathy H (2016) Disturbance estimator as a state observer with extended Kalman filter for robotic manipulator. Nonlinear Dyn (Springer; Impact factor: 3) 84(4):1–17
6. Singla R, Agarwal V, Parthasarathy H, Rana R (2016) Feedback optimization problem for master-slave teleoperation tracking in the presence of random noise in dynamics and feedback. Nonlinear Dyn (Springer) 1–28. https://doi.org/10.1007/s11071-016-2908-9
7. Nagpal N, Bhushan B, Agarwal V (2016) Estimation of stochastic environment force for master-slave robotic system. Sadhana (Springer) 1–11. https://doi.org/10.1007/s12046-017-0643-7
8. Singla R, Parthasarathy H, Agarwal V (2017) Classical robots perturbed by Levy processes: analysis and Levy disturbance rejection method. Nonlinear Dyn (Springer). https://doi.org/10.1007/s11071-017-3471-8

Socio-Economic Aspects of PV Roof-Top Installations for Residential Colonies

Prasidh Kumar, Namita Arora and Rajneesh Kaushal

Abstract As an alternative source of electric power, roof-top solar photovoltaic (PV) systems stand out above all other options because of their wide distribution and potential to generate electricity at the point of demand, making electric energy a fungible commodity having a high price elasticity of demand. Such installations are particularly closely connected with prospects of improvements in the standard of living of dwellers in colonies. Continuous affordable access to electricity and the Internet helps the population become part of a more global culture. Solar PV has risen as a technology to solve climate change problems by reducing dependency on conventional electricity generation techniques in order to aim at Sustainable Development Goals (SDGs). The objective of this research is to assess the economics of various roof-top solar PV technologies (Renewable Energy Technologies (RETs)) and financial frameworks in the context of a residential society and to find the best working models and practices that can lead to increased efficiency while optimizing cost in the roof-top segment covering various aspects of the entire value chain.

P. Kumar
School of Renewable Energy and Efficiency, National Institute of Technology,
136119 Kurukshetra, Haryana, India
e-mail: prasidhkumar26@gmail.com

N. Arora (✉)
Department of Electrical Engineering, National Institute of Technology,
136119 Kurukshetra, Haryana, India
e-mail: aroranamita33@gmail.com

R. Kaushal
Department of Mechanical Engineering, National Institute of Technology,
136119 Kurukshetra, Haryana, India
e-mail: rajneesh@nitkkr.ac.in

1 Introduction

The objective of this study is to realize the PV potentials and provide recommendations to use this potential, while taking into account economical and social constraints, as an aftermath. Technical, economic and social parameters of the PV energy provides potential under the policy of a net-metering law and same kind of conditions can be seen in order to realize under which condition and for what type of consumer it is profitable to adopt PV in the reference of Socio Economic aspects.

The less final energy prices can have a strong impression on the income received by selling energy at differential rates, additionally in the savings due to self-consumption as from installing a certain PV system. For various residential case studies [1], income and savings are recouped for a system size of 4 kWp (kilowatt peak). For various case studies shown the income produced by selling energy to the grid is five times higher than the savings made due to self-consumption per kWh. This is due to comparatively low demand of the residential case studies and it would be favorable to increase the total income generated by a PV system of a certain system size. Undeliberately, income earned by selling electricity to the grid is higher compared to self-consumption of electricity in spite of the differential tariff described by net-metering law comparable to the feed-in tariff for energy of PV systems [2]. In case of residential, savings on self usage is lower, but earnings on selling electricity are more in most of these cases. Levelised Cost of Electricity (LCOE) and Net Present Value (NPV) could be calculated for economical aspects and following formulas can be implied for this.

For LCOE

$$\text{LCOE} = \frac{\sum_{t=1}^{n} \frac{\text{Expenditures}_t}{(1+i)^t}}{\sum_{t=1}^{n} \frac{\text{Electricity generated}_t}{(1+t)^t}} \quad \left(\frac{\text{USD}}{\text{MWh}}\right) \tag{1}$$

For NPV

$$\text{NPV} = \sum_{t=1}^{n} \frac{\text{CF}_t}{(1+i)^t} \, (\text{USD}) \tag{2}$$

where n is the average life, t refers to the year, i is the rate of discount and CF_t is the cash flow for the ongoing year [3].

For a Net Energy Metering (NEM) policy to be achievable and get an investment, price of electricity generated from PV should be lower or comparable to retail electricity cost. NEM schemes may be varied according to how the net energy during a billing period is used to bill the customer. In case this net energy is greater than zero (i.e. the usage is greater than generation) the consumer may be billed only for this value of net energy at the retail electricity price, known as "full netting".

Presently, Delhi residential consumers pay about Rs. 8.75/kWh, which shows it is the market segment with the highest roof-top potential for solar installations at

1.24 GW. The proposed study can play a crucial role as various public policies are introduced for green and clean environment and social issues to be addressed immediately have been taken into consideration by Ministry of New and Renewable Energy (MNRE), especially planning laws, strategize to implement and promote new projects to inculcate residential solar roof-top segment. It is clear that, in the Indian scenario large amount of funds are released in form of subsidies by Government of India to promote roof-top solar PV in residences and institutions.

In regard to social aspects, a detailed survey has been done with support of DISCOM, Tata Power Delhi Distribution Limited in which feedback from customers, who have withdrawn their solar power plant installation interest, was noted. In the results it was found that different people from almost the same area of Delhi were having different reasons to not install solar power plants on their roof-tops. Some people want to use their roof-tops for other applications, which they realized after showing interest in solar roof-top installation, some were finding the installation with average price INR 50,000/kW [4] to be expensive and are waiting for the prices to decrease by technology development while others are totally not prepared for this type of power production.

The social aspects of solar roof-top on which further work can be done are:

1.1 Job Creation

While solar roof-top installations may create jobs, there is high need of skilled local labor to install solar plant at roof-top. If local residents are unqualified for the jobs, outside labor will be brought in. Since residential solar plant installation creates relatively few jobs, and the bulk of these jobs are temporary, solar energy development has little effect on population growth.

1.2 Fiscal Impacts

It is difficult to generalize the fiscal impacts of extractive facilities because taxation systems vary by State. An influx of new workers will create a demand for more stores and restaurants, which will in turn hire workers who will spend their incomes locally.

1.3 Quality of Life

The sentiments of the people who have installed, or are going to install solar PV roof-top system, gets disturbed as some people consider solar roof-top system a burden on them and have a negative impression of solar roof-top installation;

further studies can be done on these people as to how they ponder upon the installation of solar roof-top. The impact on the quality of life of different class of the population i.e. poor class, middle class and rich class after going for solar roof-top can thus be studied in detail.

1.4   Social Cohesion

Tensions may arise in the minds of people if the profits are not shared equally or if the solar electricity producer does not get adequate returns after installation of plant [5]. For e.g. in a NEM system, if the government utility stops buying electricity from the solar producer or buys at a very cheap price, then problems may arise in a way that residential owners will not opt for large capacity solar power plants, as they will not be paid for producing surplus energy through a solar power plant.

1.5   Utility in Loss

Solar photovoltaic installations are been negotiated globally at a fast pace in upcoming years due to overage tariff affecting size of future residential PV investments. These tariffs credit electric energy generated by the solar system, but not consumed by the household and thus transferred back to the utility, at a rate below the going retail electricity rate. This results into net metering policy forces the utility to buy surplus electricity at the going retail rate for electricity, though it could procure the same power at the lower wholesale rate. Thus making them run into losses [6].

2   Load Assessment of Delhi

Figure 1 shows the load assessment of Delhi for a period of 3 days i.e. from 30th January to 1st February 2018. The electricity consumption for State of Delhi is characterized by high time homogeneity, having high loads at morning and evening rush hours.

Other than this, there are disruptive impacts of solar roof-top installations. By installing solar panels, a consumer pays the utility less and, for the first time, becomes an energy producer rather than a consumer only. Net metering rules—which allow homeowners to sell surplus electricity from their solar panels back to the grid—are being challenged as well. Utilities are seeking additional restrictions on net metering or to reduce the price they pay homeowners for this surplus power. Also, no body knows what to do with PV modules after a lifespan of 25–30 years. Can there be a way to utilize used panels in a profitable way?
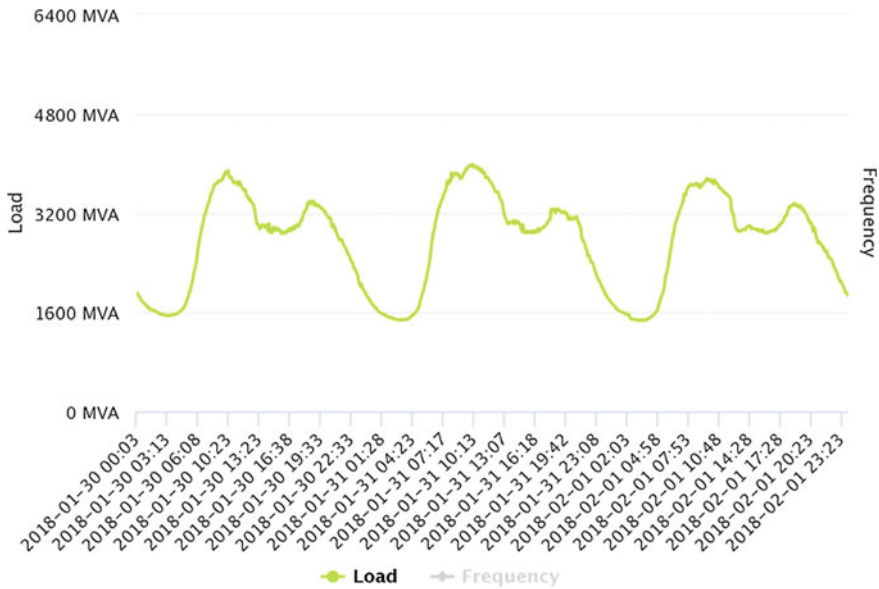
Fig. 1 Delhi electrical load assessment [7]

3 Model Formulation Framework

Technological capabilities for development of new PV installations at the places of the studies can be found out. A top-bottom approach can be used for optimizing the technical PV potential [8]. Firstly, the net solar radiation in an hourly time-step format for a year for the locations defined in the case studies are found (the theoretically calculated PV capability). Secondly, the solar radiation as well as temperature data are inducted to a PV model to calculate hourly energy output for every location (technical potential) accepting as true, the installation capacity of one kWp.

The study will lead to promotion of Renewable Energy with an already identified scope i.e. the presence of a provincial planning and specific laws, the presence of technologies and renewable resources and also the potential for interaction between multiple factors already inculcated [9]. Also, the limiting problems i.e. lack of knowledge and diffusion, less profitability, stoppages on the concerned sectors, less confidence in government policies and also lack of local generation potential can be dealt with.

For solar to be acceptable to residential consumers, a payback period of 5–7 years is preferred. A seven-year payback for 5 kW PV system corresponds to equity internal rate of return (**IRR**) of 15%, which would make returns from solar significantly higher than alternate, low-risk investments. Under these conditions, residential solar will reach parity [10].

4 Support to People

Supporting the wide spread network of Renewable Energy Technologies means supporting people, not technologies. This support is extended on the basis of motivation, financial possibilities, energy needs and risk averse. A survey was conducted approaching potential investors and knowing their possible motives for investing into PV metering (Table 1) [2].

According to this, Households and Industrialists are into distributive RETs, whilst Unknown Investing people and Big Utilities move towards centralized arrangements. Municipalities and Energy Producers may use the two systems. Moreover not all investors are applying heat and electricity producing systems to the same levels. Preferring some investor types over others means inculcating specific RET, which are-various stages of RET market introduction. The more the potential investor gets economically motivated, the more relevantly RET has to be spread over the market. Hence the pioneer investors, which are mainly non-commercially motivated, contribute the introduction of RET to the market. Its capability also vary from one country to other. Certainly House Owners and Industry can do much more higher in the long run compared to Energy Communities or Anonymous Investors and will become more and more important in the future [11]. Depending on the stage of market introduction, different investor types should be approached.

4.1 Anonymous Investors

Anonymous Investors contribute seeing ideal structure influencing them to pick up a high pay and spare to return on speculations. High devaluation stipends are appealing for Anonymous Investors with high wage. No potential client ought to be rejected from the help. Co-agents, utilities and outside financial specialists ought to have the capacity to apply for this help [4]. Remote financial specialists increase exceptional significance as it is imperative to guide cash-flow to the destinations with good normal conditions. At the present Anonymous Investors want to put resources into power creating RET. They are of developing significance for the prominence of expansive RET.

Table 1 Investors and their motives for profit

Investor type	Large motive	Energy community
Motivation of investors	Economical, strategic	Ecological, political
Importance	Medium	High
Operator	Self	Self
Purchaser of produced energy	Own grid	Grid, third parties
Readiness for financial risks	Low	High

4.2 Industry

State-possessed temporary workers like Energy Agencies go for broke beginning from long pay-back circumstances with modern interests in RET. Beyond any doubt reserves is another approach to decrease the individual dangers because of probability about future vitality buy [12]. Additionally changes in the administrative and lawful structure could upgrade crafted by temporary workers. Reasonable conditions for the entrance to the power lattice cultivate power creating RET. In spite of different conceivable modern uses of RET, actuating the mechanical RET potential will remain an intense errand.

4.3 Large Utilities

Huge Utilities, for example, wind ranches or half breed sunlight based warm power plants, are imperative for huge scale RET. Since their hierarchical structure is pointed on extensive unified power plants and vitality circulation. Upgrades in the administrative casing fill in and additionally access to people in general endowment spending plans persuade them to put resources into RET. In any case, this must be considered, that Large Utilities acquire cash because of the present status of the vitality framework. As profit for ventures picked up by ordinary vitality sources will be higher than return on placing cash in RET, Large Utilities will just put ineffectively in RETs [3].

4.4 House-Owners

There is a high potential in heat creating RET in private structures. Private House Owners are a key component for popularizing appropriated RET. Coordinate gifts diminish capital needs of the financial specialist and demonstrate to them people in general affirmation. In this manner, open acknowledgment is raised and open mindfulness is picked up. Low loan fee credits replicate the vitality cost structure to which the private vitality consumer is utilized to. Self-fabricated RET are alluring for individuals with low salary [13].

4.5 Municipalities

Municipalities are viewed as the perfect edge for a general advancement of the entire neighborhood vitality framework under practical and social viewpoints. In addition regions can offer help to conquer a wide range of issues. Districts having

introduced RET out in the open structures have a critical multiplicatory part in turning into a core through that RET of different financial specialists are started. Coordinate city RET ventures can be improved by changing the spending control and in addition by presenting Energy Service Companies.

4.6 Energy Communities

There isn't a strict fringe in Anonymous Investor write and Energy Communities, Motivation profiles and degree of profitability prerequisites of financial specialists of the two kinds can be extremely undifferentiated. Energy Communities have not been made in many nations yet, in spite of the fact that the fundamental thought is very like the customary, co-agent and city driven vitality supply framework. As pioneers, Energy Communities exhibit the attainability of RET [13]. They assume a critical part as an opponent for the built up players on the vitality advertise. Neighborhood acknowledgment of RET can be raised. Regardless of whether their immediate effect as far as the quantity of introduced RET may be not high their aberrant effect is important. Therefore Energy Communities ought to have a similar access to all endowment sources as alternate financial specialists [14].

5 Smart City-Ajmer Data Case Study

The details of the various projects implemented and Energy availability and reduction of outages in the city of Ajmer has been studied. Ajmer smart city limited is incorporated under company act 2013 Ajmer has been selected in round 2, after Round 1 and fast track of smart cities project with a total budget of Rs. 1770.5 Crore [6]. According to a study following steps are taken to procure Renewable Energy Technologies over there.

  (i) Replacement of conventional street lights with LED bulbs; 31,000 replaced —100% LED coverage by end of July 2016.
 (ii) Ajmer Municipal Corporation has installed 30 kW solar PV system at head office to harness solar energy. ADA (84 kW) and AVVNL are also in the process of tapping solar energy.
(iii) All city based substations of AVVNL are on SCADA and currently being controlled from a centralized location.
 (iv) Geographic Information System mapping for the electric utility is in progress and to be completed to support Document Management System implementation by 2015.
  (v) Transmission and Distribution losses have come down from 20 to 12% during 2014-2016 (Source: Ajmer Vidyut Vitran Nigam Limited).

(vi) The budget allocated (in Crore) for different sectors related to utility company is as follows

- **Energy Security**

    Solar power generation—48.58
    Power distribution strengthening—56.42

- **Green and Blue grid**

    Anasagar promenade—110.69
    Innovative use of public open spaces—35
    Green buildings—16

5.1 How to Achieve Convergence

Solar Roof toping shall seek support from Ministry of New and Renewable Energy to get 30% subsidy. Solar energy generation in the ABD area has been proposed in public buildings and open parks with a total cost of Rs. 48.58 Crores and amount of Rs. 14.57 Crores has been converged though Ministry of New and Renewable Energy subsidy under Solar Policy and the remaining amount of Rs. 34 Crore would be covered under Smart City Mission [15].

5.2 Consumer Details

Total no. of consumers—139,860
Total sanctioned load—388.793 MW
Sanctioned load of net meter—2512.48 kW
On-grid solar photovoltaic installed—2009.984 kW (assuming 80% sanctioned load as solar PV installed)
By smart city policy, 10% of energy should be generated by solar energy i.e. 38.87 MW
Left over capacity for smart city—36.861 MW.

6 Conclusion

As the demand for renewable energy is increasing so are its socio-economic aspects. This paper has dealt with these aspects and how they affect the lives of people and utility. As the units are being fed back to the utility grid there is advantage during peak load hour the energy is stored for the consumption and the units used from grid are reduced during the time photovoltaic energy is being

consumed during peak load hours energy from utility would be available easily for use. Moreover as power is injected to the grid locally, losses due to transmission are being reduced to a greater extent. It is useful where electricity rates are high. For solar photovoltaic module to be successful, least cost of electricity through this method should be less than retail electricity price. Hence here we successfully conclude this paper.

References

1. Langniss O (2006) Paper on Instruments to foster renewable energy investments in Europe a survey under the financial point of view. German Aerospace Research Establishment (DLR), Pfaffenwaldring 38-40, 70569 Stuttgart, Germany
2. Comello S, Reichelstein S (2016) Cost competitiveness of residential solar PV: the impact of net metering restrictions
3. Paper by Lamport L (1994) Latex: a document preparation system, 2nd edn. Addison-Wesley, Reading, Ma
4. Journal on Solar Energy Corporation India Limited (2018) (A Government of India Enterprise)
5. Goel M (2016) Solar rooftop in India: policies, challenges and outlook. Green Energy Environ
6. Report on survey of incentivization of net-metering schemes and policies by Tata Power (2017)
7. https://www.delhisldc.org/rtmap1.aspx?mode=NDPL
8. Langniss O (2018) Instruments to foster renewable energy investments in Europe, a survey under the financial point of view. Renewable Energy
9. Briano JI, Báez MJ, Morales RM (2015) PV grid parity monitor
10. Energy Research Centre of the Netherlands (2012) Grid parity definition
11. Ramirez Camargo L, Franco J, Sarmiento Babieri N, Belmonte S, Escalante K, Pagany R, Dorner W (2016) Technical, economical and social assessment of photovoltaics in the frame of the net-metering law for the Province of Salta, Argentina. Energies
12. Poullikkas A, Kourtis G, Hadjipaschalis I (2013) A review of net metering mechanism for electricity renewable energy sources. Int J Energy Environ 4:975–1002
13. High-performance home technologies: guide to determining climate regions by county. In: Building America best practice series, Chap. 7.3, PNNL-17211 Rev. 3, PNNL. 2015
14. NREL, Building America house simulation protocols (2014). Technical Report. National Renewable Energy Laboratory
15. Smart city project to help development of chosen areas (Chandigarh). The Times of India, 1 Feb 2016 Issue

Microcontroller-Based Control of Ceiling Fans for Household Power Reduction and Human Comfort

Arpit Jadon, Akshay Varshney, Saif Wakeel and Abdul Hudaif

Abstract Concerns regarding the unnecessary power consumption are ubiquitous in today's world but still, there are certain small gaps to be filled. One such problem of unnecessary power consumption caused due to a large number of ceiling fans functioning all over the world is addressed. The solution of which further leads to human comfort. Also, the capability of present system to allow human intervention-free control of ceiling fan leads to an ease for elderly and disabled people. The present approach deals with the microcontroller-based automatic control of the ceiling fan with the regularly changing power supplied to the fan. Power to be supplied being dependent on varying parameters. Two of the most important and salient parameters considered for this work are ambient temperature and the presence of a human in the room. To verify the feasibility, a laboratory prototype is designed and tested.

Keywords Firing angle · Zero crossing detector · PIR · Temperature sensor

1 Introduction

With the passage of time, energy has transformed into one of the most essential and basic infrastructures for economic development of a country. Therefore, energy security is indispensable for the sustained growth of an economy [1]. Non-renewable energy resources which are finite and exhaustible resources are the ones that are dominating the net power production in the current world scenario. But these resources are rapidly decreasing, and therefore, extensive research is going on to harness electrical energy from renewable energy resources [2] that are capable of being renewed and are not affected by the rate of their consumption.

A. Jadon (✉) · A. Varshney · S. Wakeel · A. Hudaif
Aligarh Muslim University, Aligarh 202002, Uttar Pradesh, India
e-mail: arpit.jadon47@gmail.com

A. Varshney
e-mail: akshayvarshney.001@gmail.com

Despite the large-scale steps that are taken towards energy production from renewable resources, renewable energy technologies are still in their development stage. One of the examples is the continuous efforts to approach the technology capable of harvesting solar energy in a cost-effective manner [3]. With such major emphasis on large-scale electrical energy conservation, there are certain impactful gaps that are still left uncovered at the small scale. Non-essential power consumption due to various commonly used electrical appliances is one such problem. In a rapidly growing populous country like India [4], electricity consumption has been increasing in homes and has even tripled since 2000. Moreover, the percentage of households with access to electricity has increased from 55% in 2001 to more than 80% in 2017 and as per 2014 estimates, an electrified Indian household consumed about 90 units (kWh) of electricity per month on an average [5]. There are various efforts that have been made to combat the electricity consumption in households like energy conservation initiatives were taken by the Government of India [6], energy efficiency programmes [7], etc., but these efforts have not been able to leave any significant impact on people and expected results are not visible. The attitude of masses towards electricity consumption is still oblivious to a great extent. The energy consumption in households is majorly due to the usual electrical appliances like electric (ceiling) fans, televisions, refrigerators and air conditioners. Moreover, electric fan is the most sought-after electrical appliance followed by television, refrigerators and then air conditioners [8, 9]. With the increasing incomes, the number of electrical appliances owned by a household will also increase. Thus, there is a need to develop technologies that are capable of saving power without human intervention, i.e. automated smart power reduction technologies. As electric fan accounts for the largest portion of electrical appliances commonly used throughout the country, this work is directed towards the development of a prototype of the automatic system capable of reducing unnecessary power consumption caused due to ceiling fans or fans running on AC supply in general. A ceiling fan consists of a permanent-split capacitor (PSC) and single-phase induction motor [10]. Air conditioners used in homes consume much more power than ceiling fans. People often forget or feel uncomfortable to switch off or change the speed of their fans even when ceiling fans at their lesser speed suffice for the necessary cooling required in the room. Many such other instances lead to unnecessary power consumption due to ceiling fans. The main reason behind this consumption is the manual control of ceiling fan speed using common voltage controllers independent of ambient temperature or any other factor. Therefore, an automatic ceiling fan speed control system is developed where speed of the ceiling fan is varied automatically according to the ambient temperature and presence of humans in the surrounding. Thus, this system not only helps in cutting down the unnecessary power consumption but also leads to a reduction in human effort by eliminating the human intervention in varying the fan's speed.

2   Implementation Insight and Concepts

A TRIAC-based circuit using AC phase control is utilized to control the power supplied to the fan accompanied by a microcontroller-based triggering circuit. A TRIAC is a power electronic device capable of conducting in both directions and is extensively used for power control in AC circuits. A TRIAC will conduct only when a triggering signal is applied at its gate terminal. Therefore, in order to control the power in a TRIAC-based AC circuit, gate triggering system forms a crucial part as it decides when the TRIAC would conduct and hence the time for which load will receive power. In principle, there are many triggering circuits used to trigger the TRIAC at suitable phase angle like monostable triggering circuit, R triggering circuit, RC triggering circuit, UJT-based triggering circuit, etc. [11].

But since in this approach, TRIACs' gate is required to be triggered in conjunction to various sensors data fed-back to the system, microcontroller based digital firing scheme is utilized, because of its suitability in similar situations. So, it is basically a digitally automated single-phase full-wave voltage controller controlled using AC phase control to connect the load to the source for a part of each half-cycle of the input voltage [12], thus leading to a reduction in supplied power. Temperature measurement and motion detection are accomplished by using an LM35 temperature sensor and passive infrared sensor (PIR), respectively. The outputs of the LM35 and PIR sensor act as the feedback inputs for the microcontroller-triggering system. Sensing the outputs via temperature and PIR sensor is a very crucial as well as important part of the present system.

3   Working Method

Main challenge involved in designing a circuit for a temperature-based speed control of single-phase induction motor is varying the firing angle of the TRIAC as per the change in temperature. Delaying the firing pulse by an angle leads to the control of load voltage and the power supplied to the motor, thus controlling the speed. Moreover, the firing angle is measured from the zero crossing point of the supply voltage [13], i.e., zero crossing of the input supply voltage acts as a reference for measuring the firing angle. Therefore, the first step involved in this approach is to determine the zero crossings of the input supply voltage. For this purpose, a zero crossing detector (ZCD) circuit involving an optocoupler (IC 4N25) is used. The input voltage signal (sine wave) coming from a 230/12 V single-phase transformer is rectified and then fed to an optocoupler. The ZCD outputs a digital signal which goes high when rectified input voltage signal reaches the zero value, i.e. at positive and negative zero crossing of the input sine wave. The digital output signal of ZCD is then supplied to the digital input of microcontroller which sets the detected zero crossing as a reference for firing pulses. The output of the zero crossing detector as recorded on the digital storage oscilloscope (DSO) is as shown in Figs. 1 and 2.

Fig. 1 Blue: rectified input supply voltage and yellow: ZCD output
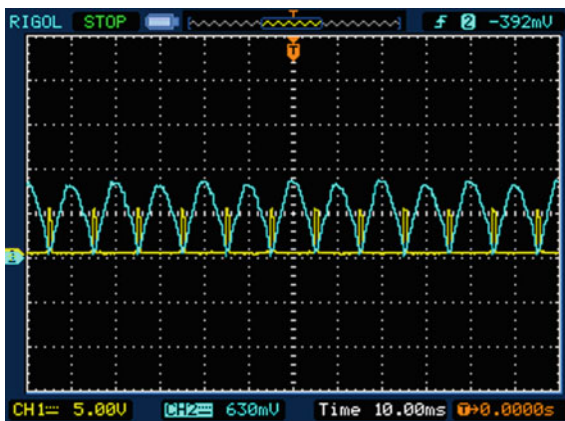
Fig. 2 Blue: rectified input supply voltage and yellow: ZCD output
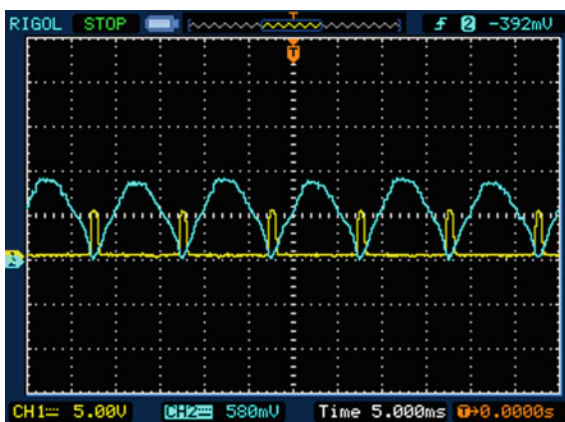
As can be seen from the figures, a high pulse is generated whenever the rectified signal approaches zero voltage, and for the rest of the time, ZCD output remains low. The ambient temperature is sensed utilizing the LM35 temperature sensor, and consequently, a delay in firing pulses is provided according to the ambient temperature of the room. Six temperature intervals of 5 °C each are considered, and apart from the ambient temperature, the activation of the whole system is governed by the output signal of PIR sensor which detects the motion in the room. A high output from PIR sensor activates the system for a period of 30 min by default, and the control is transferred to the temperature sensor output. Thus, a firing pulse is given to the TRIAC driver circuit only when the PIR sensor gives the high output, and hence, the fan or the motor remains in an off condition until the PIR sensor detects motion in the room. After 30 min, the system again goes to off state and waits for the motion to be detected. Note that this running period of 30 min and temperature intervals are changeable as per the ease and comfort of the user. LM35 temperature sensor continues to measure and supply the ambient temperature output

to the microcontroller. Thus, according to the prevailing ambient temperature interval, TRIAC gate is triggered at varying suitable phase angles by the triggering pulses sent to the gate terminal of the TRIAC by the digital output pin of the microcontroller. Thus, firing or phase angle has a direct relation with ambient temperature and power supplied to the motor. A high firing angle (a large delay in firing pulse with respect to the zero crossing) will lead to a low conduction period and thus a low power output, on the other hand, a small firing angle (a small delay in firing pulse with respect to the zero crossing) will lead to a larger conduction period and hence greater power output. Thus, varying power output will result in varying speed of the ceiling fan motor.

4 Overall System and the Experimental Set-up

Therefore, as quite visible from the previous sections, the overall circuit consists of a zero crossing detector (ZCD) circuit, a digital triggering circuit based on a microcontroller interfaced with an LM35 temperature sensor and PIR sensor. This low-voltage digital circuit containing the microcontroller is isolated from the high-voltage power circuit including the single-phase induction motor using an opto-isolator (moc3021 IC).

The diagram of the laboratory experimental set-up and overall process is shown in Figs. 3 and 4, respectively.
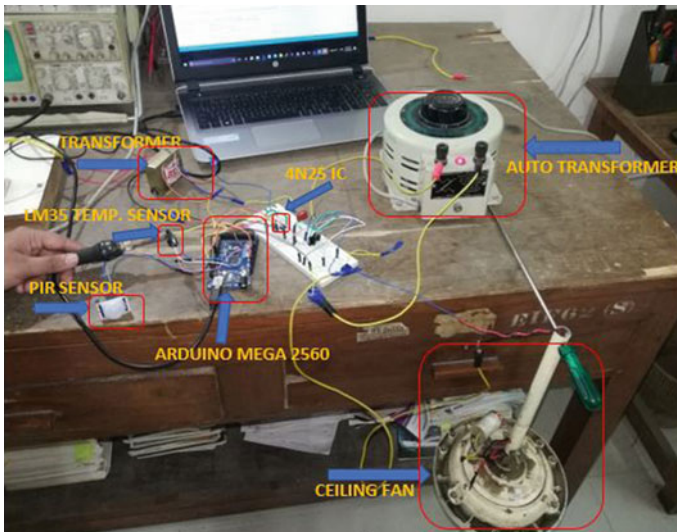
Fig. 3 Laboratory experimental set-up
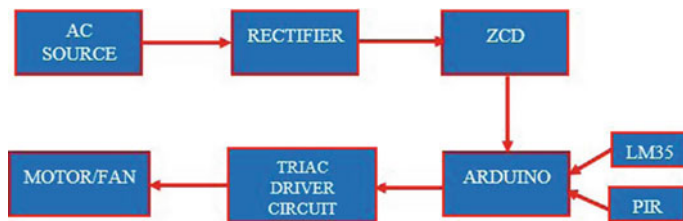
Fig. 4 Block diagram of the complete system

5 Algorithm

The program for the microcontroller is written in the Arduino IDE. As soon as the microcontroller receives a high signal from PIR sensor, the complete system is activated for a period of 30 min after which system is deactivated and Arduino waits for the PIR to detect any motion in the surrounding. As soon as the system is activated, Arduino reads the digital output fed to its interrupt pin by the ZCD. At the rising edge of high-pulse output of ZCD, an interrupt occurs and an interrupt service routine (ISR) is called which checks for the interval in which the ambient temperature lies by reading the temperature sensor data and accordingly a delayed triggering signal (from the digital output of Arduino) is given to the TRIAC driver circuit which corresponds to a specific speed of the motor. In this work, six temperature intervals at a gap of 5 °C each are taken. In each temperature interval, the speed of the fan is different. There is a minimum temperature below which fan remains in the off state, and there is a maximum temperature above which fan runs at the maximum speed. The flow diagram of the algorithm is shown in Fig. 5.

6 Results and Discussion

As can be seen from Figs. 6, 7, 8, 9 and 10, as the firing angle increases the conduction area of the voltage waveform shown in yellow decreases, thus leading to the reduction in output voltage and output current (shown in blue). Hence, the power supplied to the load decreases causing a decrement in the speed of the motor. As the motor is running under no load, back-emf is present and can be seen in the results as well.

During switching on speed conditions, i.e., if the supply is connected while the rotor is already rotating, there is a negative peak because of the transient generator action due to the rotation in transient flux [14]. But there is no significant impact on the smooth speed control of the AC ceiling fan due to this process. The circuit board developed for the same application is shown in Fig. 11.
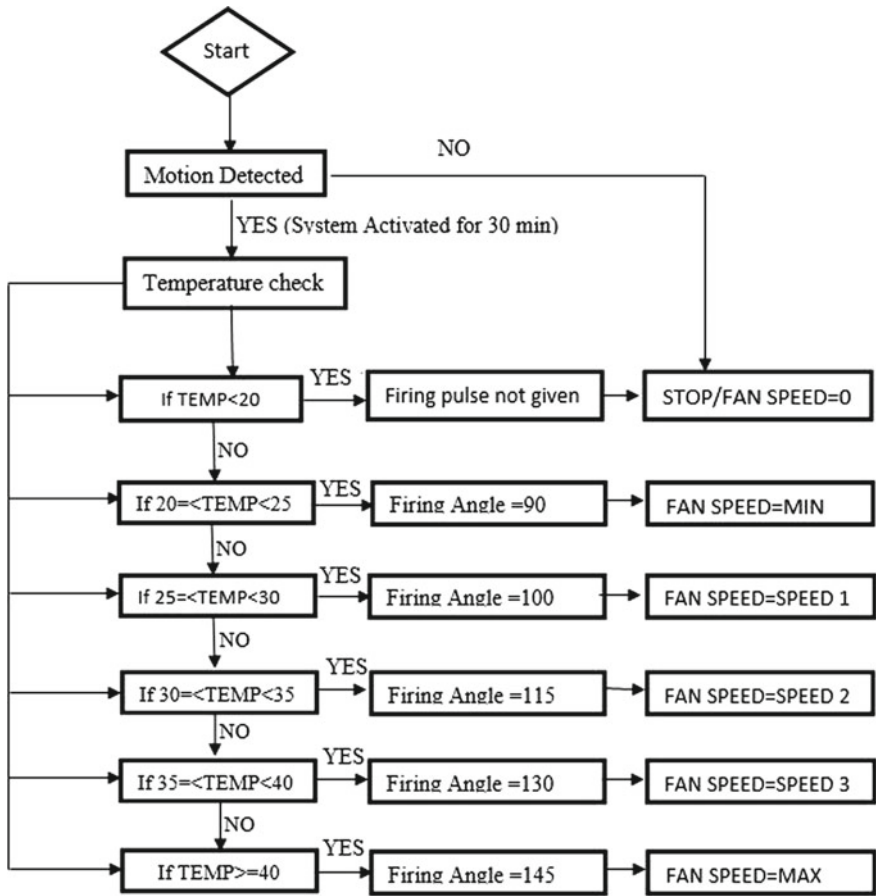
Fig. 5 Complete algorithm flow diagram

Fig. 6 Output voltage and current waveforms for firing angle = 90°

Fig. 7 Output voltage and current waveforms for firing angle = 100°
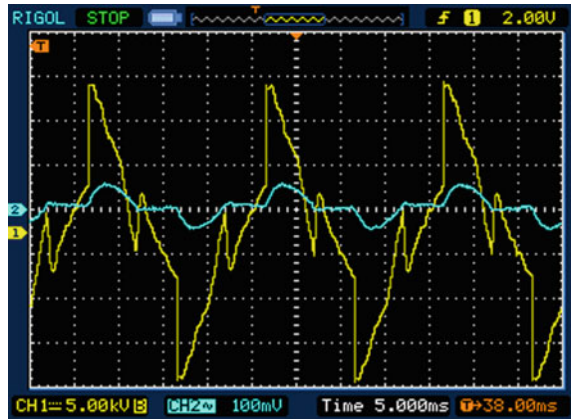
Fig. 8 Output voltage and current waveforms for firing angle = 115°

Fig. 9 Output voltage and current waveforms for firing angle = 130°

Fig. 10 Output voltage and current waveforms for firing angle = 145°

Fig. 11 Developed circuit board
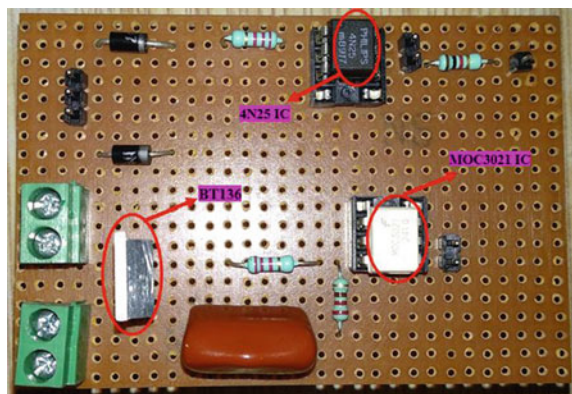
7 Conclusion

The developed microcontroller-based automated system will not only save the unnecessary power consumption caused due to ceiling fans but also fulfil the necessary demand of most of the modern automatic systems, i.e. comfort to the user because of the system's capability to vary the speed of ceiling fan according to the ambient temperature and presence of humans in the room. It will certainly reduce the problems of elderly people and people with disabilities by reducing the need of any human intervention in the control of ceiling fan. The low cost of the resultant circuit, Arduino microcontroller, LM35 temperature sensor and PIR sensor make this product a highly feasible one for a typical household usage. The same system can be implemented on other electric fans working on AC power supply like a table fan.

Future Scope

We considered single-phase AC induction motor ceiling fan for our experiment, which is in the majority usage in various average economy countries like India. However, with the rise of modern technology, BLDC motor ceiling fans are also gaining attention. Therefore, our future research work will be based on these BLDC motor ceiling fans for incorporating better and smart performance.

References

1. Khan B (2006) Non-conventional energy resources. Tata McGraw-Hill Education
2. Panwar N, Kaushik S, Kothari S (2011) Role of renewable energy sources in environmental protection: a review. Renew Sustain Energy Rev 15(3):1513–1524
3. Lewis NS (2007) Toward cost-effective solar energy use. Science 315(5813):798–801
4. India at Glance—Population Census 2011 (2011) http://census2011.co.in/p/glance.php. Last accessed 2018-02-02
5. Trends in India's Residential Electricity Consumption (2017) http://www.cprindia.org/news/6519. Last accessed 2018-02-08
6. Nandi P, Basu S (2008) A review of energy conservation initiatives by the government of india. Renew Sustain Energy Rev 12(2):518–530
7. Bureau of Energy Efficiency (2018) https://beeindia.gov.in/content/programmes. Last accessed 2018-02-08
8. Parikh KS, Parikh JK (2016) Realizing potential savings of energy and emissions from efficient household appliances in India. Energy Policy 97:102–111
9. Rathi S, Chunekar A, Kadav K (2012) Appliance ownership in india: evidence from nsso household expenditure surveys 2004–05 and 2009–10. Pray. Energy Gr
10. Ishak D, Tiang T, Choy S (2015) Performance evaluation of permanent split-capacitor single-phase induction motor for ceiling fan application. In: 2015 18th international conference on electrical machines and systems (ICEMS). IEEE, pp 1865–1870
11. Asghar MJ (2004) Power electronics. PHI Learning Pvt, Ltd
12. Bimbhra P, Kaur S (2012) Power electronics, vol 2. Khanna publishers
13. Rashid MH (2017) Power electronics handbook. Butterworth-Heinemann
14. Slater R, Wood W (1967) Constant-speed solutions applied to the evaluation of induction-motor transient torque peaks. In: Proceedings of the institution of electrical engineers, vol 114. IET, pp 1429–1435

Extraction of Solar PV Module Parameters Using Back Search Optimization Algorithm

P. Anandhraj and K. Mohana Sundaram

Abstract The electrical energy produced from solar panels has gained more attentions due to its non-polluting nature and lessening cost over the years. The accurate modeling of PV modules is necessary to extract maximum power and also identify the finest PV modules from the manufacturers. However, exact modeling of PV module is difficult task due to certain parameters are not mentioned in the manufacturer's datasheet. In this work, a technique based on back search optimization algorithm is utilized to find that parameters in various environmental conditions. The MATLAB simulation results have successfully validated the effectiveness of back search optimization algorithm for PV module parameters extraction.

Keywords Back search optimization algorithm (BSA) · Photovoltaic (PV) · Convergence curve · Solar Irradiance

1 Introduction

Renewable energy sources are abundant in contrast to conventional energy sources like fossil fuels, thereby non-renewable energy sources can be preserved by using alternate forms of energy. Among non-conventional energy sources, energy obtained from solar is identified as the most feasible source due to inexhaustibility, non-polluting nature, and maintenance free [1, 2]. Considering the need, researchers around the world have published various research papers in the area of solar photovoltaic system. Important research area in this system is unknown parameters extraction, i.e., optimizing the parameters not given in manufacturer's datasheet [3, 4]. The mathematical and analytical approaches are used for parameters

P. Anandhraj (✉) · K. Mohana Sundaram
Vel Tech Multi Tech Dr. Rangarajan Dr. Sakunthala Engineering College, Chennai, India
e-mail: anandpannerselvam@gmail.com

K. Mohana Sundaram
e-mail: kumohanasundaram@gmail.com

extraction and these approaches utilize supplier's datasheet values such as (i) short-circuit current (ii) open-circuit voltage (iii) voltage at maximum power point (V_{mp}), current at maximum power point (I_{mp}), current temperature coefficient (k_i), and voltage temperature coefficient (k_v) [5–7]. Neverthlessly, the conventional approach is not suitable for different environmental conditions and then it drives into the inappropriate parameters identification; thereby, invalid results will occur [8–10]. On the other hand, individual point of authentic electrical characteristics is obtained by mathematical extraction techniques, and it is suitable for all environmental conditions. The numerical approaches produce all data points in the electrical characteristics which lead to difficult calculation. For that reason, many optimization techniques are utilized for PV parameters extraction [11–14]. The most commonly used techniques are genetic algorithm [15], Bacterial Foraging Algorithm [16], Bird Mating Algorithm [17], Pattern Search Algorithm [18]. Some algorithms require broad search to choose chromosomes from primary set of population which makes the calculation very difficult and inaccurate. The initial parameter selection and tuning are a difficult task in other methods. In this paper, back search optimization algorithm is tried to find the unknown PV parameters with fast convergence and accuracy.

2 PV Module Mathematical Modeling

For less complexity, the single diode model is analyzed in this article and it is shown in Fig. 1. An ideal solar cell contains current source and antiparallel diode. The structural resistance and leakage current are presented in practical PV system, thereby series and shunt resistance is added to the ideal PV electrical characteristics.

The output current of the solar cell is represented in Eq. (1). Where I_{PV}—Photo Voltaic current, I_D—Diode Current, R_p—Parallel Resistance, V_D—Voltage Drop.

$$I = I_{PV} - I_D - \left(V_D/R_p\right) \tag{1}$$

The expanded solar current equation for single diode model [6–9] is given as:
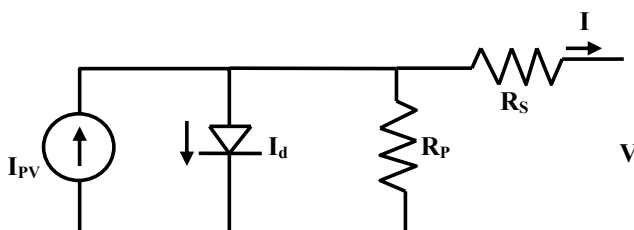
Fig. 1 Single diode solar cell model

$$I = I_{PV} - I_0[\exp((V + R_sI)/V_ta) - 1] - (V_D/R_sI)/R_p \tag{2}$$

In Eq. (2), five parameters such as photo-generated current (I_{PV}), shunt resistance (R_p), series resistance (R_s), diode ideality factor (a), diode saturation current (I_0) are not given in the manufacturer's technical specifications. The intention of this study is to find this unknown parameter. To reduce the burden, in this p work, 'I_{PV}', 'I_0' is calculated analytically. The diode ideality factor 'a' is chosen randomly between 1 and 2 which is based on the other parameters of the PV model [19, 20]. The remaining two parameters of 'R_s', 'R_p' are optimized using back search optimization algorithm. It is clear from the previous work that these parameters are varied based on the environmental conditions.

The photo-generated current of single diode solar cell [7] is given by

$$I_{PV} = (I_{sc} + k_i dT) + G/G_n \tag{3}$$

The diode saturation current for the single diode model relies on the photo-generated current and open-circuit voltage [8].

$$I_0 = I_{PV}/\exp[((V_{oc} + k_v dT) * V_t)/a] - 1 \tag{4}$$

At maximum power point, the voltage across the solar cell is V_{mp}, and current through the solar cell is I_{mp}, and differentiation of power is zero with respect to voltage. With this condition, the unknown parameters are extracted in this article.

$$(dP/dV) = 0 \tag{5}$$

$$d(V * I)/dV = V(dI/dV) + I \tag{6}$$

$$|(dI/dV)|_{(V_{mp}, I_{mp})} = (I_0\Psi\exp\{\Psi(V_{mp} + I_{mp}R_s)\} - G_P)/ \\ (1 + I_0\Psi R_s\exp\{\Psi(V_{mp} + I_{mp}R_s)\} - G_PR_s \tag{7}$$

$$J = (dI/dV) + (I_{mp} + V_{mp}) \tag{8}$$

where $G_P = 1/R_p$ represents the reciprocal of shunt resistance, $\Psi = 1/aV_t$ reciprocal of diode ideality factor and thermal voltage. The unknown parameters are extracted for the lowest value of fitness function (J).

Fig. 2 Flowchart of back
search optimization algorithm
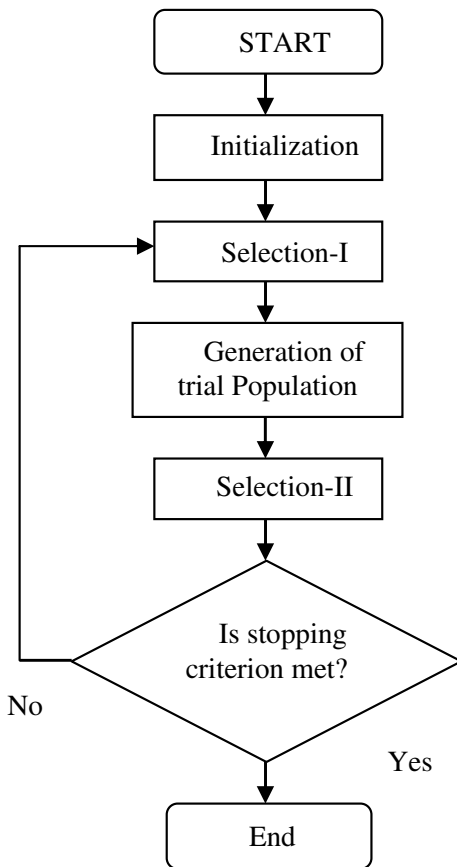
3   Back Search Optimization Algorithm-Based Solar Cell Parameter Extraction

BSA is a new evolutionary algorithm for resolving various mathematical optimization problems. It is operated with single control parameter, easy structure and is capable to solve multimodal problems. The trial population in the BSA consists of two mutation and two crossover operators. Unlike other techniques, the current and historical populations are employed in BSA. The operation of BSA comprised five sections such as initialization, selection-I, mutation, crossover, and selection-II (Fig. 2).

Table 1 Solar model parameters estimated with back search optimization algorithm for different irradiance

Parameters	SVL 0250P
$G = 1000$ W/m^2	
R_s	0.146
R_p	324
$G = 750$ W/m^2	
R_s	0.492
R_p	168.244
$G = 500$ W/m^2	
R_s	1.374
R_p	282.789

4 Simulation Results and Its Discussion

A MATLAB/Simulink model is developed to verify the back search optimization algorithm. SVL 250Wp solar module datasheet provides the technical specifications such as open-circuit voltage (V_{oc}), short-circuit current (I_{sc}), maximum power point current (I_{mp}), maximum power point voltage (V_{mp}), voltage temperature coefficient, and current temperature coefficient. Nevertheless, these parameters are inadequate for exact P-V characteristics modeling, and it requires extra parameters such as series resistance (R_s), parallel resistance (R_p), and diode ideality factor (a). These parameters are obtained using back search optimization algorithm. The initial value of series resistance (R_s) is choosing randomly within the range of [0 2] and initial boundary limit for parallel resistance (R_p) between 50 and 500. The selected value of diode ideality factor (a) ranges from 1 to 2.

Fig. 3 Convergence curve of back search optimization algorithm
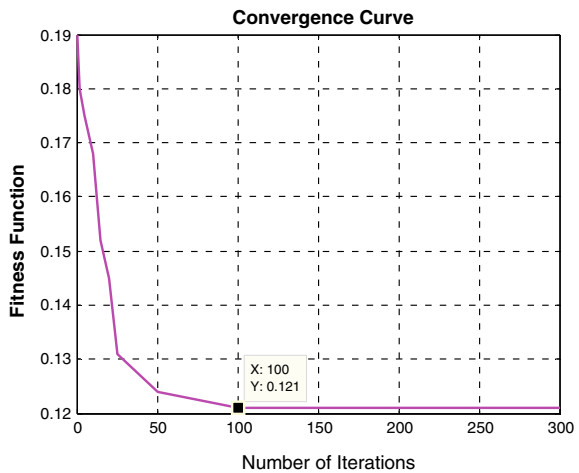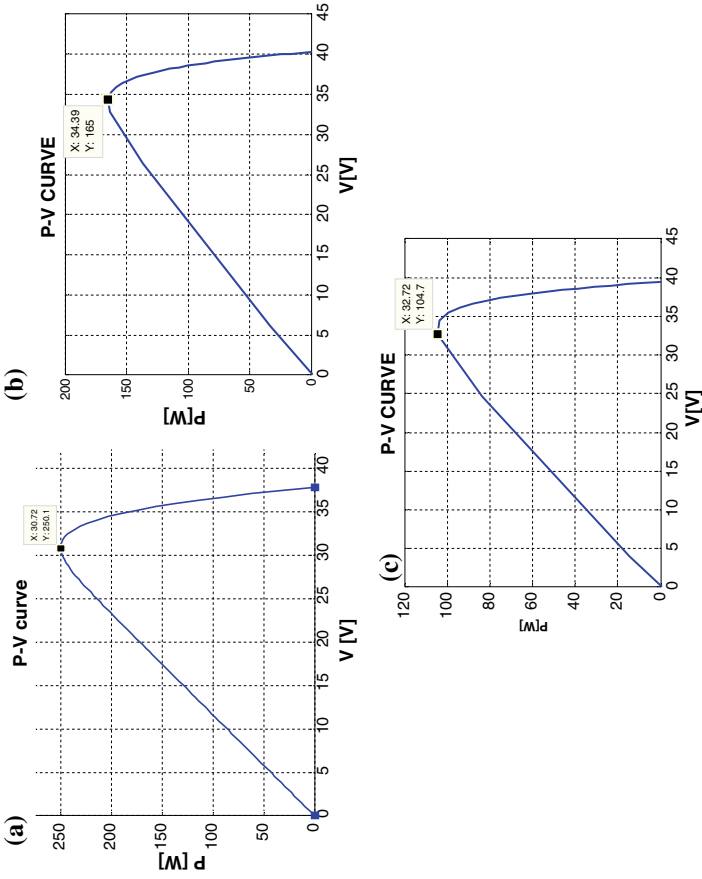
Fig. 4 **a** P-V characteristics at standard test condition, **b** P-V characteristics for Irradiance (*G*) = 750 W/m², **c** P-V characteristics for Irradiance (*G*) = 500 W/m²

In Table 1, it can be concluded that lower value of series resistance and higher value of parallel resistance lead the P-V plot toward the maximum power point (MPP).

With all the above data, MATLAB/Simulink model is computed for BSA. After several instances, the best convergence curve is achieved and minimum fitness value in that curve determines the accuracy of the algorithm. The convergence curve of back search optimization algorithm is presented in Fig. 3.

Figure 4a–c represents P-V characteristics of 250Wp solar module (SVL0250P) for different environmental conditions. At standard test condition, voltage and power at maximum power point are 30.72 V and 250.1 W which is indicated in the figure by data cursor. At $G = 750$ W/m^2, maximum power point voltage and power are 34.39 V and 163 W. At $G = 500$ W/m^{2,} voltage and power at maximum power point are 32.2 V and 102.7 W. The graphs clearly indicate the variation of significant PV parameters, i.e., open-circuit voltage (V_{oc}), short-circuit current (I_{sc}), voltage, and current at maximum power point based on environmental conditions.

5 Conclusion

In this article, back search optimization algorithm has been implemented successfully to extract solar cell's unknown parameters with fast convergence and accuracy. The objective function has been converged with less number of iteration, selection of initial population has been performed without complexities, and this technique has been operated with single control parameter. Thus, back search optimization algorithm is the fastest and appropriate computational algorithm for PV module parameter extraction.

References

1. Chan DSH, Phang JCH (1987) Analytical methods for the extraction of solar-cell single- and double-diode model parameters from I-V characteristics. IEEE Trans Electron Dev 34:286–293
2. Solanki CS (2015) Solar photovoltaics—fundamentals, technologies and applications hardcover, 3rd ed. PHI Learning, New Delhi
3. Villalva MG, Gazoli JR (2009) Comprehensive approach to modeling and simulation of photovoltaic arrays. IEEE Trans Power Electron 45:1198–1208
4. Jordehi AR (2016) Parameter estimation of solar photovoltaic (PV) cells: a review. Renew Sust Energy Rev 354–371
5. Chan DSH, Phang JCH (1987) Analytical methods for the extraction of solar-cell single- and double-diode model parameters from I-V characteristics. IEEE Trans Electron Dev 286–293

6. De Soto W, Klein SA, Beckman WA (2006) Improvement and validation of a model for photovoltaic array performance. Sol Energy 78–88
7. Sachin VR, Vivek JP (2015) Simulation and comparison of perturb and observe and incremental conductance MPPT algorithms for solar energy system connected to grid. Sadhana 139–153
8. Chien-Chih L, Chih-Yen C, Chi-Yuan W (2008) Physical parameters extraction from current–voltage characteristic for diodes using multiple nonlinear regression analysis. Solid State Electron 839–843
9. Mohana Sundaram K, Anandhraj P, Vimalraj Ambeth V (2018) PV-fed eleven-level capacitor switching multi-level inverter for grid integration. Lecture Notes in Electrical Engineering
10. Barukcic MC, Ćorluka V, Miklosevic K (2015) The irradiance and temperature dependent mathematical model for estimation of photovoltaic panel performances. Energy Convers Manage 229–238
11. El-Naggar KM, AlRashidi MR, AlHajri MF, Al-Othman AK (2012) Simulated annealing algorithm for photovoltaic parameters identification. Sol Energy 266–74
12. Jing Jun S, Kay-Soon L (2012) Photovoltaic model identification using particle swarm optimization with inverse barrier constraint. IEEE Trans Power Electron 3975–3983
13. Askarzadeh A, dos Santos Coelho L (2015) Determination of photovoltaic modules parameters at different operating conditions using a novel bird mating optimizer approach. Energy Convers Manage 608–614
14. Askarzadeh A, Rezazadeh A (2013) Artificial bee swarm optimization algorithm for parameters identification of solar cell models. Appl Energy 943–949
15. Zagrouba M, Sellami A, Bouaıcha M, Ksouri M (2010) Identification of PV solar cells and modules parameters using the genetic algorithms: application to maximum power extraction. Sol Energy 860–866
16. Rajasekar N, Kumar Neeraja K, Venugopalan R (2013) Bacterial foraging algorithm based solar PV parameter estimation. Sol Energy 255–265
17. Askarzadeh A, Rezazadeh A (2013) Extraction of maximum power point in solar cells using bird mating optimizer-based parameters identification approach. Sol Energy 123–133
18. AlHajri MF, El-Naggar KM, AlRashidi MR, Al-Othman AK (2012) Optimal extraction of solar cell parameters using pattern search. Renew Energy 238–245
19. Carrero C, Amador J, Arnaltes S (2007) A single procedure for helping PV designers to select silicon PV module and evaluate the loss resistances. Renew Energy 2579–2589
20. Walker G (2001) Evaluating MPPT converter topologies using a matlab PV model. J Elect Electron Eng 45–55

Author Index